NASA/CP—1999–209092

NASA Microgravity Materials Science Conference

Compiled by
D.C. Gillies
Marshall Space Flight Center, Marshall Space Flight Center, Alabama

D.E. McCauley
University of Alabama in Huntsville, Huntsville, Alabama

Proceedings of a conference held in
Huntsville, Alabama, July 14–16, 1998

February 1999

The NASA STI Program Office...in Profile

Since its founding, NASA has been dedicated to the advancement of aeronautics and space science. The NASA Scientific and Technical Information (STI) Program Office plays a key part in helping NASA maintain this important role.

The NASA STI Program Office is operated by Langley Research Center, the lead center for NASA's scientific and technical information. The NASA STI Program Office provides access to the NASA STI Database, the largest collection of aeronautical and space science STI in the world. The Program Office is also NASA's institutional mechanism for disseminating the results of its research and development activities. These results are published by NASA in the NASA STI Report Series, which includes the following report types:

- TECHNICAL PUBLICATION. Reports of completed research or a major significant phase of research that present the results of NASA programs and include extensive data or theoretical analysis. Includes compilations of significant scientific and technical data and information deemed to be of continuing reference value. NASA's counterpart of peer-reviewed formal professional papers but has less stringent limitations on manuscript length and extent of graphic presentations.

- TECHNICAL MEMORANDUM. Scientific and technical findings that are preliminary or of specialized interest, e.g., quick release reports, working papers, and bibliographies that contain minimal annotation. Does not contain extensive analysis.

- CONTRACTOR REPORT. Scientific and technical findings by NASA-sponsored contractors and grantees.

- CONFERENCE PUBLICATION. Collected papers from scientific and technical conferences, symposia, seminars, or other meetings sponsored or cosponsored by NASA.

- SPECIAL PUBLICATION. Scientific, technical, or historical information from NASA programs, projects, and mission, often concerned with subjects having substantial public interest.

- TECHNICAL TRANSLATION. English-language translations of foreign scientific and technical material pertinent to NASA's mission.

Specialized services that complement the STI Program Office's diverse offerings include creating custom thesauri, building customized databases, organizing and publishing research results...even providing videos.

For more information about the NASA STI Program Office, see the following:

- Access the NASA STI Program Home Page at ***http://www.sti.nasa.gov***

- E-mail your question via the Internet to help@sti.nasa.gov

- Fax your question to the NASA Access Help Desk at (301) 621–0134

- Telephone the NASA Access Help Desk at (301) 621–0390

- Write to:
  NASA Access Help Desk
  NASA Center for AeroSpace Information
  800 Elkridge Landing Road
  Linthicum Heights, MD 21090–2934

NASA/CP—1999–209092

NASA Microgravity Materials Science Conference

Compiled by
D.C. Gillies
Marshall Space Flight Center, Marshall Space Flight Center, Alabama

D.E. McCauley
University of Alabama in Huntsville, Huntsville, Alabama

Proceedings of a conference held in
Huntsville, Alabama, July 14–16, 1998

National Aeronautics and
Space Administration

Marshall Space Flight Center • MSFC, Alabama 35812

February 1999

Available from:

NASA Center for AeroSpace Information
800 Elkridge Landing Road
Linthicum Heights, MD 21090–2934
(301) 621–0390

National Technical Information Service
5285 Port Royal Road
Springfield, VA 22161
(703) 487–4650

Foreword

The 1998 Microgravity Materials Science Conference was held July 14-16 at the Von Braun Center, Huntsville, Alabama. It was organized by the Microgravity Materials Science Discipline Working Group, sponsored by the Microgravity Research Division at NASA Headquarters, and hosted by the NASA Marshall Space Flight Center and the Alliance for Microgravity Materials Science and Applications (AMMSA). It was the third NASA conference of this type in the microgravity materials science discipline. The microgravity science program sponsored approximately one hundred and twenty investigations and one hundred and six principal investigators in FY98, all of whom made oral or poster presentations at this conference. In addition, some twenty posters covering Advanced Technology Development projects sponsored by the Microgravity Research Division at NASA Headquarters, NASA microgravity facilities, and commercial interests were exhibited. The conference's purpose was to inform the materials science community of research opportunities in reduced gravity in preparation for a NASA Research Announcement (NRA) scheduled for release in late 1998 by the Microgravity Research Division at NASA Headquarters. The conference was aimed at materials science researchers from academia, industry, and government. A tour of the MSFC microgravity research facilities was held on July 16, 1998. This volume is comprised of the research reports submitted by the Principal Investigators after the conference.

Page intentionally left blank

Table of Contents

Principal Investigator/Research Reports **Page**

Agenda

Tuesday, July 14, 1998

8:30 a.m.	Introductions	Dr. Bradley M. Carpenter, NASA HQ
8:35 a.m.	Welcome from the Directorate, Marshall Space Flight Center	Mrs. Carolyn Griner, NASA MSFC
8:40 a.m.	Microgravity Research Program	Mr. Robert C. Rhome, NASA HQ
9:00 a.m.	The Current Microgravity Materials Science Program	Dr. Donald Gillies, NASA MSFC
9:20 a.m.	The Route to Flight	Mr. Joel Kearns, NASA MSFC
9:50 a.m.	International Space Station: An Overview from the Microgravity Perspective	Mr. Ned Penley, NASA JSC
10:15 a.m.	Break	
10:35 a.m.	Remarks to PI's and Comments to Prospective Proposers	Dr. Michael J. Wargo, NASA HQ
10.55 a.m.	Question and Answer Session	
11:15 a.m.	INVITED PAPER: Nucleation and Properties of Undercooled Metallic Melts: Results of the TEMPUS MSL-1 Mission	Dr. Ivan Egry, DLR
12:00 p.m.	Lunch (boxed lunches provided)	
1:15 p.m.	Parallel Session I	
2:45 p.m.	Break	
3:00 p.m.	Parallel Session II	
6:00 p.m.	Dinner at the Huntsville Depot Roundhouse Buses depart from in front of Hilton Hotel beginning at 5:50 p.m. and return to the Hilton beginning at 9:45 p.m.	

Wednesday, July 15, 1998

8:00 a.m.	Parallel Session III
10:00 a.m.	Break
10:15 a.m.	Parallel Session IV
11:45 a.m.	Lunch and Poster Session (boxed lunches provided)
2:00 p.m.	Parallel Session V Materials Science/Radiation Shielding Review (Salon II)
3:30 p.m.	Break
3:45 p.m.	Parallel Session VI

Thursday, July 16, 1998

8:00 a.m.	Parallel Session VII Materials Science/Radiation Shielding Review (Salon II)
10:00 a.m.	Break
10:15 a.m.	Parallel Session VIII
11:45 a.m.	Lunch (boxed lunches provided)
1:00 p.m.	Escorted Tour of Marshall Space Flight Center Buses will depart from the North Hall of the Von Braun Center Estimated time of return 5:30 p.m. **Foreign Nationals must have pre-registered for this tour and must have their passports in their possession in order to be allowed to enter Marshall Space Flight Center.**

Tuesday, July 14, 1998
Parallel Session I: 1:15 to 2:45 p.m.

North Hall	Salon 1	Orchestra Rehearsal Room
Solidification I		Undercooling I
Chair: Dr. P Voorhees, Northwestern University		Chair: Prof. J. Perepezko Univ. of Wisconsin-Madison
Lehoczky, Dr. Sandor L. NASA/Marshall Space Flight Center *Crystal Growth of II-VI Semiconductor Alloys by Directional Solidification (30 min)*		Trinh, Dr. Eugene H. Jet Propulsion Laboratory *Dynamically Induced Nucleation of Deeply Supercooled Melts and Measurement of Surface Tension and Viscosity*
Fripp, Dr. Archibald L. NASA/Langley Research Center *Growth of Compound Semiconductors in a Low Gravity Environment (30 min)*		Spaepen, Prof. Frans Harvard University *Kinetics of Nucleation & Growth from Undercooled Melts*
Curreri, Dr. Peter A. NASA/Marshall Space Flight Center *Fundamental Studies of Solidification in μg Using X-Ray Microscopy*		Robinson, Dr. Michael B. NASA/Marshall Space Flight Center *A Study of Undercooling Behavior of Immiscible Metal Alloys in the Absence of Crucible-Induced Nucleation*
		Bayuzick, Prof. Robert J. Vanderbilt University *Investigation of the Relationship Between Undercooing and Solidification Velocity*

Tuesday, July 14, 1998
Parallel Session II: 3:00 to 5:00 p.m.

North Hall	**Salon 1**	**Orchestra Rehearsal Room**
Metals and Alloys I	Thermophysical Properties	Undercooling II
Chair: Dr. R. Hopkins, Northrup-Grumman	Chair: Dr. T. Anderson, Univ. of Florida	Chair: Dr. M. Robinson, NASA/MSFC
Voorhees, Dr. Peter W. Northwestern University *Coarsening in Liquid-Solid Mixtures*	Banish, Dr. Michael University of Alabama in Huntsville *Self-Diffusion in Liquid Elements (SDLE) (30 min)* Presenting: Dr. Iwan Alexander	Perepezko, Prof. John H. University of Wisconsin *Analysis of Containerless Processing & Undercooled Solidification Microstructures*
Poirier, Prof. David R. University of Arizona *Comparison of Structure & Segregation in Alloys Directionally Solidified in Terrestrial and Microgravity Environments*	Matthiesen, Dr. David H. Case Western Reserve University *Diffusion Processes in Molten Semiconductors (30 min)*	Katz, Dr. Joseph L. The Johns Hopkins University *Measurement of Liquid-to-Solid Nucleation Rates in Undercooled Metallic Melts*
Andrews, Prof. J. Barry University of Alabama at Birmingham *The Effect of Convection on Morphological Stability During Coupled Growth in Immiscible Systems*	Banish, Dr. Michael University of Alabama in Huntsville *Themophysical Property Measurements of Te-Based II-VI Semiconductor Compounds* Presenting: Dr. Iwan Alexander	Rhim, Dr. Won-Kyu X. Jet Propulsion Laboratory *Thermophysical Property Measurement of Molten Semiconductors in 1-G and Reduced Gravity Conditions*
Kassemi, Dr. Mohammad Ohio Aero Space Institute at LeRC *Identification of Gravity-Related Effects on Crystal Growth from Melts with an Immiscibility Gap*	Rosenblatt, Prof. Charles S. Case Western Reserve University *Paramagnetic Liquid Bridge in a Gravity-Compensating Magnetic Field.*	Manning, Dr. John R. National Institute of Standards & Technology *Thermophysical Properties of High Temperature Liquid Metals & Alloys* Presenting: Dr. Shankar Krishnan

Wednesday, July 15, 1998
Parallel Session III: 8:00 to 10:00 a.m.

North Hall	**Salon I**	**Orchestra Rehearsal Room**
Oxides	Electronic Materials I	Solidification II
Chair: Dr. L. Schioler, NSF	Chair: Dr. R. Hopkins, Northrup-Grumman	Chair: Prof. P. Voorhees, Northwestern University
Witt, Prof. August F. Massachusetts Inst. of Technology *Identification &Control of Gravity Related Defect Formation During Melt Growth of Electro-optical Single Crystals: Sillenites*	Bachmann, Dr. Klaus J. North Carolina State University *Fundamental Aspects of Vapor Deposition and Etching under Diffusion Controlled Transport Conditions*	Anderson, Prof. Timothy J. University of Florida *An Electrochemical Method to Visualize Flow and Measure Diffusivity in Liquid Metals*
Hofmeister, Prof. William H. Vanderbilt University *Microgravity Processing of Oxide Semiconductors*	Krishnan, Dr. Anantha CFD Research Corporation *Influence of Natural Convection and Thermal Radiation on Multi-Component Transport and Chemistry in MOCVD Reactors*	Lehoczky, Dr. Sandor L. NASA/Marshall Space Flight Center *Growth of Solid Solution Single Crystals (30 min)*
Brezinsky, Dr. Kenneth University of Illinois at Chicago *Combustion Synthesis of Materials in Microgravity*	Su, Dr. Ching-Hua NASA/Marshall Space Flight Center *Crystal Growth of ZnSe and Related Ternary Compound Semiconductors by Vapor Transport*	Wilcox, Prof. William R. Clarkson University *Use of Microgravity to Control the Microstructure of Eutectics*
Brady, Prof. John F. California Institute of Technology *Dispersion Microstructure and Rheology in Ceramics Processing*	Wiedemeier, Prof. Heribert Rensselaer Polytechnic Institute *Defect Generation in CVT Grown* $Hg_{1-x}CdTe_x$ *Epitaxial Layers under Normal and Reduced Gravity Conditions*	Gillies, Dr. Donald C. NASA/Marshall Space Flight Center *Solidification of II-VI Compounds in a Rotating Magnetic Field*
Weber, Dr. Richard Containerless Research Inc. *Process-Property-Structure Relationships in Complex Oxide Melts*	Dudley, Prof. Michael State University of New York at Stony Brook *Combined Synchrotron White Beam X-Ray Topography and High Resolution Triple Axis X-Ray Diffraction Characterization and Analysis of Crystals Grown in* μg *and Ground-Based Experiments*	Alexander, Dr. Iwan Case Western Reserve University *Analysis of Residual Accerleration Effects on Transport and Segregation During Directional Solidification of Tin-Bismuth in the MEPHISTO Furnace Facility*
Weber, Dr. Richard Containerless Research Inc. *Microgravity Studies of Liquid-Liquid Phase Transitions in Undercooled Alumina-Yttria Melts*	Holmes, Dr. Douglas E. Electronic Materials Engineering *Dimensional Stability of Supermatrix Semiconductors*	

Wednesday, July 15, 1998
Parallel Session IV: 10:15 to 11:45 a.m.

North Hall	**Salon I**	**Orchestra Rehearsal Room**
Solidification III	Electronic Materials II	Nanomaterials
	Chair: Dr. M. Vlasse, NASA/MSFC	Chair: Dr. F. Rose, NASA/MSFC
Trolinger, Dr. James D. MetroLaser, Inc. *Investigation of the Influence of μg on Transport Mechanisms in a Virtual Space Flight Chamber*	Matthiesen, Dr. David H. Case Western Reserve University *Study of Dopant Segregation Behavior During the Growth of GaAs in Microgravity (30 min)*	Voecks, Dr. Gerald E. Jet Propulsion Laboratory *Investigation of Controlled Zeolite Nucleation & Crystal Growth Development*
Trolinger, Dr. James D. MetroLaser, Inc. *A Proposal to Further Investigate the Influence of μg on Transport Mechanisms in a Virtual Space Chamber*	Szofran, Dr. Frank R. NASA/Marshall Space Flight Center *Reduction of Defects in Germanium Silicon*	Dutta, Dr. Prabir K. The Ohio State University *Reverse Micelle-Based Synthesis of Microporous Materials in Microgravity*
Fedoseyev, Dr. Alexandre University of Alabama in Huntsville *Theoretical and Experimental Investigation of Vibrational Control of the Bridgman Crystal Technique*	Wiedemeier, Prof. Heribert Rensselaer Polytechnic Institute *Vapor Growth of Alloy Type Semiconductor Crystals (30 min)*	El-Shall, Dr. Samy Virginia Commonwealth University *Studies on Nucleation, Polymerization and Nano-particle Composites in Supersaturated Vapors under μg Conditions*
Maxworthy, Dr. Tony Univ. of Southern California *Numerical and Laboratory Experiments on the Interactive Dynamics of Convection, Flow, and Directional Solidification* Meng Zhang presenting		

Wednesday, 15 July, 1998
Parallel Session V: 2:00 - 3:30 p.m.

North Hall	**Salon I**	**Orchestra Rehearsal Room**
Metals and Alloys II	Microstructure Formation I	Electronic Materials III
Chair: Prof. J. Perepezko, Univ. of Wisconsin-Madison	Chair: Dr. J. Dantzig, Univ. of Illinois, Urbana-Champaign	Chair: Dr. T. Anderson, Univ. of Florida
Trivedi, Prof. Rohit Iowa State University *Interface Pattern Selection Criteria for Cellular Structures in Directional Solidification (IPSIDS) (30 min)*	Jackson, Prof. Kenneth A. University of Arizona *Non-Equilibrium Phase Transformations*	Singh, Dr. N. B. Northrop-Grumman Corporation *Flight Experiment to Study Double Diffusive Instabilities in Silver-Doped Lead Bromide Crystals*
Abbaschian, Prof. Reza University of Florida *In-Situ Monitoring of Crystal Growth Using MEPHISTO) (30 min)*	Brown, Dr. Robert A. Massachusetts Institute of Technology *Application of Parallel Computing for Two-and Three-Dimensional Modeling of Bulk Crystal Growth and Microstructure Formation*	Larson, Prof. David J. State University of New York at Stony Brook *Orbital Processing of High Quality Cadmium Telluride (30 min)*
Glicksman, Prof. Martin E. Rensselaer Polytechnic Institute *Isothermal Dendritic Growth Experiment (IDGE) (30 min)* Dr. Matthew Koss presenting	Gokhale, Dr. Arun M. Georgia Institute of Technology *Effect of Gravity on the Evolution of Spatial Arrangement of Features in Microstructure: A Quantitative Approach*	Kaforey, Dr. Monica L. Case Western Reserve University *Dislocation Formation During Growth of Semiconductor Crystals*
	Kelton, Prof. Kenneth F. Washington University *Phase Formation and Stability: Composition and Sample Size Effects*	Ostrogorsky, Prof. Aleksandar G. Rensselaer Polytechnic Institute *Space- and Ground-based Crystal Growth Using a Magnetically Coupled Baffle*

Wednesday, 15 July, 1998
Parallel Session VI: 3:45 - 5:15 p.m.

North Hall	**Salon I**	**Orchestra Rehearsal Room**
Solidification IV	Magnetic Field Solidification	Glasses
Chair: Dr. R. Trivedi, Iowa State Univ.	Chair: Dr. D. Watring, NASA/MSFC	Chair: Dr. L. Schioler, NSF
Larson, Prof. David J. State University of New York at Stony Brook *Orbital Processing of Eutectic Rod-Like Arrays (OPERA)*	Fripp, Dr. Archibald L. NASA/Langley Research Center: *Melt Stabilization of PbSnTe in a Magnetic Field*	Johnson, Dr. William L. California Institute of Technology *Physical Properties & Processing of Undercooled Metallic Glass Forming Melts*
Andrews, Prof. J. Barry University of Alabama at Birmingham *Coupled Growth in Hypermonotectics (30 min)*	Li, Prof. Ben Q. Washington State University *Study of Magnetic Damping Effect on Convection and Solidification Under G-Jitter Conditions*	Day, Dr. Delbert E. University of Missouri at Rolla *Kinetics of Nucleation & Crystal Growth in Glass Forming Melts in Microgravity*
Karma, Prof. Alain S. Northeastern University *The Role of Dynamic Nucleation at Moving Boundaries in Phase and Microstructure Selection*	Szofran, Dr. Frank R. NASA/Marshall Space Flight Center *Magnetic Damping of Solid Solution Semiconducting Alloys*	Rhim, Dr. Won-Kyu X. Jet Propulsion Laboratory *Undercooling Limits & Thermophysical Properties in Glass Forming Alloys*
	Walker, Prof. John S. University of Illinois at Urbana *Models of Magnetic Damping for Bridgman Semiconductor Crystal Growth in Microgravity*	

Thursday, 16 July, 1998
Parallel Session VII: 8:00 - 10:00 a.m.

North Hall	**Salon I**	**Orchestra Rehearsal Room**
Microstructure Formation 2	Polymers	TEMPUS
Chair:	Chair: Dr. J. Rabolt, Univ. of Delaware	Chair: Dr. J. Rogers, NASA/MSFC
Koss, Dr. Matthew B. Rensselaer Polytechnic Institute *Transient Dendritic Solidification Experiment (TDSE)*	Pojman, Prof. John A. University of Southern Mississippi *Frontal Polymerization inμg*	Flemings, Dr. Merton C. Massachusetts Institute of Technology *Alloy Undercooling Experiments in Microgravity Environment (30 min)*
Glicksman, Prof. Martin E. Rensselaer Polytechnic Institute *Evolution of Local Microstructures: Spatial Instabilities of Coarsening Clusters* Dr. Don Frazier presenting	*Preforms*El-Shall, Dr. Samy Virginia Commonwealth University *Studies on Nucleation, Polymerization and Nano-particle Composites in Supersaturated Vapors under μg Conditions*	Bayuzick, Prof. Robert J. Vanderbilt University *Experiments on Nucleation in Different Flow Regimes (30 min)* Prof. William Hofmeister presenting
Ardell, Dr. Alan J. University of California, Los Angeles *Ostwald Ripening of Liquid and Solid Droplets in Liquid Metal Matrices*	Wettlaufer, Prof. John University of Washington *Thin Film Mediated Phase Change Phenomena: Crystallization, Evaporation and Wetting*	Johnson, Dr. William L. California Institute of Technology *Thermophysical Properties of Metallic Glasses and Under-Cooled Liquids (30 min)*
Dantzig, Dr. Jonathan University of Illinois *Adaptive Grid Methods for Phase Field Models of Microstructure Development*	Altan, Dr. M. Cengiz: University of Oklahoma *Microgravity Impregnation of Fiber Preforms*	Flemings, Dr. Merton C. Massachusetts Institute of Technology *Measurement of the Viscosity and Surface Tension of Undercooled Melts under μg Conditions, and Supporting Magnetohydrodynamic Calculations (30 min)*
Beckermann, Prof. Christoph University of Iowa *Equiaxed Dendritic Solidification Experiment (EDSE) (30 min)*	Talham, Dr. Daniel R. University of Florida *The Features of Self-Assembling Organic Bilayers Important to the Formation of Anisoptropic Inorganic Materials in μg Conditions*	
	Paley, Dr. M. Steven Universities Space Research Association *Gravitational Effects on the Morphology and Kinetics of Photo-deposition of Polydiacetylene Films from Monomer Solutions*	

Thursday, 16 July, 1998
Parallel Session VIII: 10:15 - 11:45 a.m.

North Hall	**Salon I**	
Modeling	Metals and Alloys III	
Chair: Dr. J. Dantzig, Univ. of Illinois, Urbana-Champaign	Chair: Prof. R. Trivedi, Iowa State University	
Derby, Prof. Jeffrey J. University of Minnesota *Atomistic Simulations of Cadmium Telluride: Toward Understanding the Benefits of µg Crystal Growth*	German, Prof. Randall M. The Pennsylvania State University *Gravitation Effects on Distortion in Sintering*	
Cha, Dr. Soyoung Stephen University of Illinois at Chicago *Three-Dimensional Velocity Field Characterization in a Bridgman Apparatus: Technique Development and Effect Analysis*	German, Prof. Randall M. The Pennsylvania State University *Gravitational Role in Liquid Phase Sintering (30 min)*	
Meiburg, Prof. Eckart University of Southern California *Potential Flow Interaction with Directional Solidification* Sudhir Buddhavarapu presenting	Stefanescu, Prof. Doru M. University of Alabama *Particle Engulfment and Pushing by Solidifying Interfaces (30 min)*	

Poster Presentations

1. Apfel, Dr. Robert E. - Yale University
   Nucleation and Growth Mechanisms Underlying the Microstructure of Polymer Foams Produced by Dynamic Decompression and Cooling

2. Bernholc, Prof. Jerry - North Carolina State University
   Growth and Properties of Carbon Nanotubes

3. Cebe, Prof. Peggy - Tufts University
   Study of Development of Polymer Structure in Microgravity Using Ellipsometry

4. Chernov, Prof. Alexander A. - Universities Space Research Association
   Morphological Stability of Stepped Interfaces Growing From Solution

5. Courtney, Prof. Thomas H. - Michigan Technological University
   Gravity Induced Settling in Interconnected Liquid-Solid Systems

6. Cucinotta, Dr. Francis A. - NASA Johnson Space Center
   Improved Radiation Transport Code and Nuclear Data Base for Evaluation of Spacecraft Shielding

7. Derby, Prof. Jeffrey J. - University of Minnesota
   Theoretical Analysis of 3D, Transient Convection and Segregation in Microgravity Bridgman Crystal Growth

8. Ducheyne, Dr. Paul - University of Pennsylvania
   Surface Transformation of Reactive Glass in a Microgravity Environment

9. El-Shall, Dr. Samy - Virginia Commonwealth University
   Gas Phase Polymerization and Nucleation Experiments in Microgravity

10. Evans, Prof. James W. - University of California at Berkeley
    Exploiting the Temperature Dependence of Magnetic Susceptibility to Control Convection in Fundamental Studies of Solidification Phenomena

11. Feigelson, Dr. Robert S. - Stanford University
    Investigation of the Crystal Growth of Dielectric Materials by the Bridgman Technique Using Vibrational Control

12. Friedli, Dr. Adrienne C. - Middle Tennessee University
    Development of Anionic Polyelectrolyte for Solid Battery Applications

13. Greenberg, Dr. Alan R. - University of Colorado at Boulder
    Influence of Solutocapillary Convection on Macrovoid Defect Formation in Polymeric Membranes

14. Grugel, Dr. Richard N. - Universities Space Research Association
    Novel Directional Solidification Processing of Hypermonotectic Alloys

15. Grugel, Dr. Richard N. - Universities Space Research Association
    Utilizing Controlled Vibrations in a Microgravity Environment to Understand and Promote Microstructural Homogeneity during Floating-Zone Crystal Growth

16. Gupta, Dr. Prabhat K. - Ohio State University
    Interdiffusion in the Presence of Free Convection

17. Halas, Dr. Naomi Jean - Rice University
    Metal Nanoshell Functionalization and Materials Assembly: Effects of Microgravity Conditions

18. Heilbronn, Dr. Lawrence H. - Lawrence Berkeley National Laboratory
    Radiation Transmission Properties of In-Situ Materials

19. Hunt, Dr. Arlon - Lawrence Berkeley National Laboratory
    Porosity and Variations in Microgravity Aerogel Nano-Structures

20. Kassemi, Dr. Mohammad - Ohio AeroSpace Institute/NASA LeRC
    Effect of Marangoni Convection Generated by Voids on Segregation During Low-g and 1-g Solidification

21. Kou, Prof. Sindo - University of Wisconsin at Madison
    Physical Simulation of Marangoni Convection in Weld Pools

22. Krishnan, Dr. Shankar - Containerless Research, Inc
    Atomic Structure of High Temperature and Supercooled Liquids

23. Lewis, Dr. Jennifer A. - University of Illinois at Urbana Champaign
    Colloidal Stability in Complex Fluids

24. Li, Dr. Ben Q. - Louisiana State University
    A Comparative Modeling Study of Magnetic and Electrostatic Levitation in Microgravity

25. Mayti, Richard - University of Wisconsin
    High Resolution Triple Axis X-Ray Diffraction Analysis of II-VI Semiconductor Crystals

26. McFadden, Dr. Geoffrey B. - National Institute of Standards and Technology
    A Phase-Field/Fluid Motion Model of Solidification: Investigation of Flow Effects During Directional Solidification and Dendritic Growth

27. Megaridis, Dr. Constantine - University of Illinois at Chicago
    Microgravity Investigation on the Formation of Oxides and Adsorbed Oxygen Films in Solder Jetting Applications Pertinent to the Electronics Manufacturing Industry

28. Myerson, Dr. Allan S. - Polytechnic University
Thermodynamic and Spectroscopic Studies of Secondary Nucleation in Microgravity

29. Naumann, Prof. Robert J. - University of Alabama in Huntsville
Reduction of Convection in Closed Tube Vapor Growth Experiments

30. Palosz, Dr. Witold - Universities Space Research Association
Investigation of Crystal Growth of Ternary II-VI and IV-VI Compounds by Physical Vapor Transport

31. Regel, Dr. Liya L. - Clarkson University
Improved Crystal Quality by Detached Solidification in Microgravity

32. Sacco, Jr., Dr. Albert - Northeastern University
Modeling of Macroscopic/Microscopic Transport and Growth Phenomena in Zeolite Crystals Under Microgravity Conditions

33. Sridhar, Prof. K. R. - University of Arizona
Development of Superior Materials for Layered Solid Oxide Electrolyzers Based on Mechanical and Thermal Failure Testing and Analysis

34. Wilson, Dr. John - NASA Langley Research Center
Improved Spacecraft Materials for Radiation Shielding

35. Zugrav, Dr. Maria I. - University of Alabama in Huntsville
Ground Based Experiments in Support of Microgravity Research Results - Vapor Growth of Organic Nonlinear Optical Thin Film

Numbers above correspond to the panel where the poster will be placed at the Von Braun Center.

In-Situ Monitoring of a Bismuth-Tin alloy solidification using MEPHISTO

Reza Abbaschian[1], Kirk M. Beatty[2], Fuwang Chen[2], Henry de Groh III[3],
Gerard Cambon[4]

1. University of Florida, Materials Science & Engineering, 224 MAE Building, Gainesville, Florida 32611, tel. (352) 392-6609, FAX (352) 392-7219, rabba@mail.mse.ufl.edu,
2. UF, MSE, tel. (352) 392-1462, FAX (352) 392-7219, kbeat@mail.mse.ufl.edu
3 NASA/Lewis Research Center, Cleaveland OH,
Phone (216) 433-5025, FAX (216) 433-5033, email: henry@sarah.lerc.nasa.gov
4 Centre National d'Etudes Spatiales (CNES), Toulouse, France
Phone 33-5-61-273481, FAX 33-5-61-282959

Abstract

Experiments were carried out to study the morphological stability of Bi- 1 atomic % Sn alloys using the MEPHISTO directional solidification apparatus aboard Space Shuttle Columbia (STS-87, launched Nov. 19, 1997) and in ground-based studies. The Seebeck signal and temperature measurements indicate that convection was significant for ground-based studies. In the space-based experiments, interface breakdown was observed at growth velocities of 6.7, 27, and 40 μm/sec, but not at 1.8 and 3.3 μm/sec.

Introduction

An investigation of the solidification of Bi- 1 atomic % Sn was performed using both ground- and space-based experiments. The solidification experiments for this faceted alloy used an apparatus developed by Centre National d'Etudes Spatiales (CNES, Toulouse, France) and Commissariat à l'Energie Atomique (CEA, Grenoble, France) called MEPHISTO, which stands for Materiel pour l`Etude des Phenomenes Interessant la Solidification su Terre et en Orbit apparatus. The apparatus was developed for investigating directional solidification of metallic alloys and doped semiconductors. The space-based experiments were performed aboard the Fourth United States Microgravity Payload (USMP-4), and built upon results from the three previous Microgravity Payload missions.

The interface between a crystalline solid and its liquid can be either faceted or non-faceted (which are smooth or rough, respectively, on an atomic scale). The growth of a faceted interface is dominated by the nucleation and lateral growth of new layers, or if the interface contains dislocations, by layers generated by a combination of nucleation and dislocation based growth. For a rough interface, on the other hand, growth can take place at sites throughout the solid-liquid interface. The kinetics of solidification for faceted and rough interfaces are markedly different, such that the undercooling required to maintain a given growth rate on a smooth interface of reasonable size can be orders of magnitude greater than required on a rough interface.[1,2,3,4,5] The morphological stability threshold (plane front to cellular transition) has also been found to depend on crystalline orientation in a faceted material. During the Second United States Microgravity Payload (USMP-2) Mission, the solidification of a bismuth- 0.1 atomic % tin alloy was studied using experiments at different growth velocities and growth distances. As expected, under suitable growth conditions the alloy began solidification with a planar interface, but eventually broke down into a cellular growth mode. However, dramatic differences in the distance to break down were found in adjacent grains with different orientations. [6] Though differences in breakdown distance for different growth directions are predicted by models of morphological stability, the results for the Bi-Sn alloy are not fully understood.

These observations suggest that kinetics and growth anisotropy have a strong influence on the stability of planar solidification for a faceted material. To extend our understanding of these effects requires experiments in which the growth velocity, interface undercooling, liquid and solid composition, solid orientation and microstructure, thermal profile, segregation coefficient, and liquid diffusion coefficient are known or can be measured. To this end, the space experiments offer a unique opportunity as convective effects are eliminated, thus enabling accurate measurements and/or calculations of the diffusional profiles ahead of the interface

Equipment and Samples

The MEPHISTO apparatus (which has been described previously [7,8]) is capable of simultaneous processing of three rod shaped samples, each of which is approximately 900 mm in length and 6 mm in diameter. The central part of MEPHISTO consists of two furnaces each with a neighboring heat sink. One of the furnace-heat sink structures is stationary, while the other is on a moving platform. Between the heaters special reflectors and insulation are used to maintain a nearly uniform temperature. In the experiments to be described the furnaces were heated to 750° C, while the cold zones were kept near 50° C, resulting in a molten zone in the middle of each sample. When the movable furnace-heat sink structure is translated away from the fixed furnace the extent of the hot zone is lengthened, increasing the extent of the molten zone in the sample. Near the solid-liquid interfaces, which are located between each furnace and its accompanying heat sink, temperature gradients on the order of 200° C/cm are established.

The alloy used for the experiments was Bi with 1 atomic % Sn. Bi and Sn form a simple eutectic, with a maximum solubility of 1.63 atomic % Sn at the eutectic temperature of 140° C. The melting temperature of bismuth is 271.4°C, and the distribution coefficient for Sn in Bi is approximately 0.03. Each of the three samples consisted of a rod of Bi-1 atomic % Sn alloy approximately 900 mm in length and 6 mm in diameter within a quartz tube. A 2 mm ID, 3 mm OD quartz capillary is located on the moving furnace side, which extends about 250 mm into the sample. Thin quartz capillaries (approximately 0.6 mm OD) for the thermocouples were also inserted for the thermocouples in the two of the three samples.

Each of the three samples, which will be referred to as the “Quenching”, “Peltier”, and “Seebeck” samples, have a special purpose in the study of alloy solidification. The Quenching sample is used to measure the rate of solidification using the resistance change across the sample during processing and to produce a short section of quenched sample. The quench is achieved using a mechanism that pulls the sample about 2 cm towards the cold zone in approxiamtely 0.5 seconds. The Peltier sample has connections to allow marking the sample with short electrical pulses which cause heating or cooling at the solid-liquid interface according to the equation:

$$Q_P = -(\pi_S - \pi_L)J\Delta t.$$

Q_P is the heat generated at the solid-liquid interface, π_S and π_L are the Peltier coefficients of the solid and liquid alloy respectively, J is the current (positive for flow from solid to liquid), and Δt is the pulse duration. If the current direction results in cooling at the interface, the rate of solidification will momentarily increase and there will be a build up of solute at the interface. The accompanying change in the composition of the solid can be revealed with etching and optical microscopy. Details of Peltier interface demarcation for a Bi-1 wt % Sb alloy is discussed in reference. [9] The Seebeck sample is used to measure the difference between the temperature of the stationary and moving solid-liquid interfaces. If the structural and compositional dependence of the Seebeck coefficient of the solid are neglected, the relation of the temperature of the two interfaces and the Seebeck signal, E_S, is

$$T_{MI} = T_{SI} + \frac{E_S}{\eta_S - \eta_L},$$

where T_{MI} and T_{SI} is the temperature of the moving and stationary interfaces repsectively. [8,10] η_S and η_L are the Seebeck coefficient of the solid and liquid near the melting temperature.

Experiments and Growth Conditions

The flight experiments were performed with the help of Société Européene de Propulsion (SEP) by telecommanding. The experiments were initiated by heating the movable and stationary furnaces to 750°C. This established a liquid zone approximately 340 mm long. Melting and solidification experiments were performed by commanding the apparatus to move the mobile furnace/heat sink structure. The fully open position was referenced as 0 mm and the fully closed 150mm. Increasing the furnace position corresponded to freezing, and decreasing the furnace position to melting. Figure 1 is a plot of the MEPHISTO movable furnace position during the USMP-4 mission. Many of the experiments consisted of a freezing period where the furnace position was increased, a hold period where the furnace was kept stationary, and a melt period where the furnace was moved back to the original position for the cycle with the opposite velocity of the freezing period. Figure 2 is an example with a start position of 115 mm, freezing for 15 mm at 13.5 μm/s, and a hold period of ½ hour, and then melting back to the 115 mm position at 13.5 μm/s. The detailed analysis of the Seebeck, resistance and thermocouple measurements will benefit from the large number of experiments performed aboard USMP-4. As shown in figure 1 the experiments included thirty-five freeze-hold-melt cycles during the mission and eleven periods of final solidification. The experiments were over a range of solidification rates from 0.74 to 40 μm/s.

Preliminary Results

The thermal profile in the MEPHISTO apparatus was monitored using several thermocouples located in each of the furnace diffusers and heat sinks. The thermocouples in the heater and heat sink diffusers were used to control the overall thermal conditions of the furnace. Since the thermal profile is not fully determined by the temperatures imposed at the diffusers, but also on the properties of sample being processed, four additional thermocouples were placed inside small quartz capillaries located in the Quench and Peltier samples. Based on the thermocouples located within the Quartz and Peltier samples, the temperature gradient in the liquid, G_L, for the ground-based mission was approximately 90 °C/cm, while the temperature gradient in the liquid for the space-based experiments was approximately 200 °C/ cm. The significant small significantly smaller than G_L for the ground-based experiments is evidence of hydrodynamic mixing on the ground-based experiments, (as well as the differences in the heat transfer coefficient between the metals, the quartz tube, and the surrounding graphite diffuser).

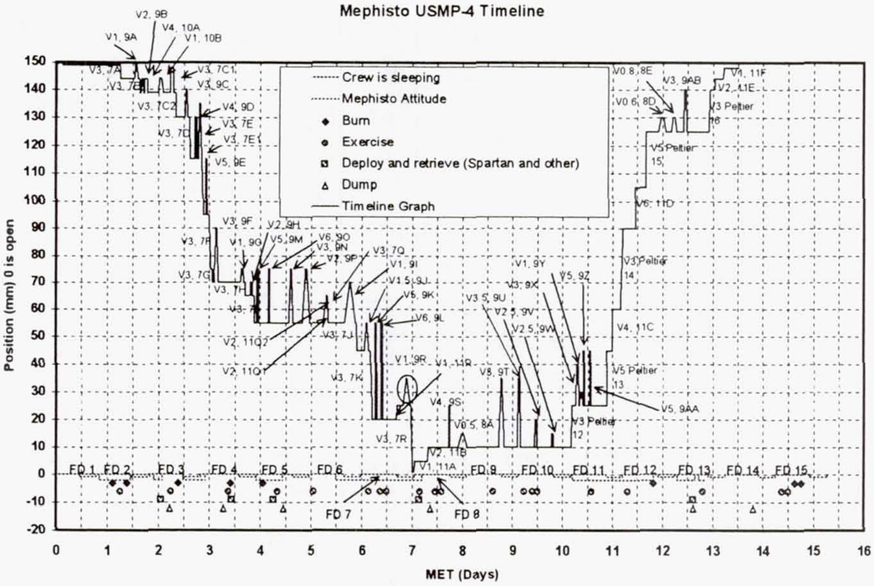

Figure 1: The MEPHISTO moving furnace position as a function of days into USMP-4 mission. The velocities for V0.5, V0.6, V0.8, V1, V1.5, V2, V2.5, V3, V3.5, V4, V5, V6 are 0.74, 1.11, 1.48, 1.85, 2.59, 3.7, 5.2, 6.7, 10, 13.3, 26.7 and 40 μm/s respectively.

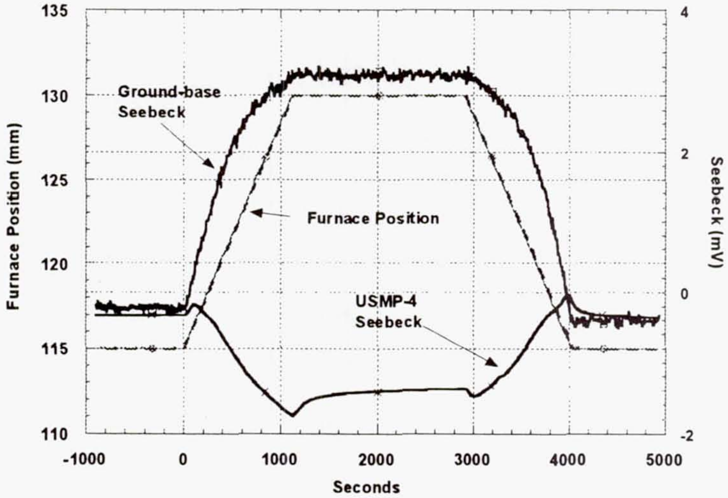

Figure 2: Seebeck signal and position for ground- and space-based experiments for solidification at 13.5 μm/s. The moving furnace position as a function of time into the experiment is very similar for the two experiments. The ground-based experiments have noticeable fluctuations in the Seebeck signal, presumably from hydrodynamic mixing in the melt.

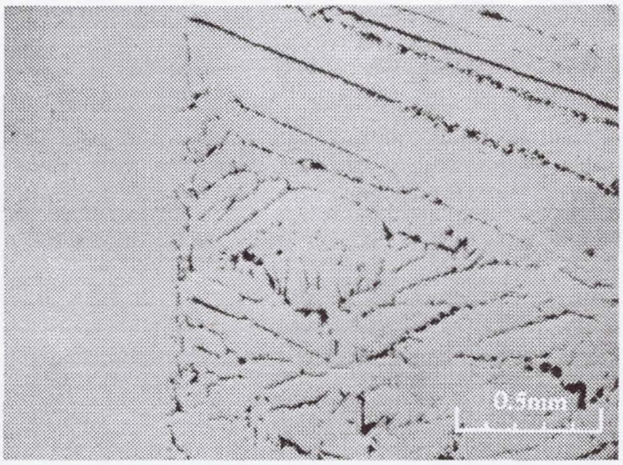

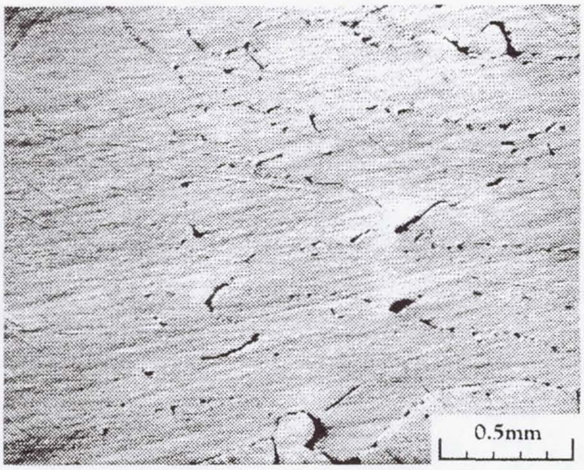

Figure 3, on the left, shows the transition from growth at 1.85 μm/sec to a quench. Figure 4, on the right, is another picture of the quench sample. The region pictured in figure 4 resulted from translation the moving furnace at 6.7 μm/sec, a period of no translation, and then translation at 40 μm/sec. The scale bar in each is 0.5mm long, and the growth direction was to the right.

Figure 2 gives the Seebeck signals acquired for a ground- and a space-based experiment. Each consisted of solidification, hold, and melt. The Seebeck signal for the ground-based experiment rose during freezing, fluctuated around an average value for the hold, then decreased during melting. The fluctuations in the signal are due to hydrodynamic mixing in the liquid. It was observed that the magnitude of the fluctuations strongly depended on the temperature of the melt. The signal for the space-based experiment had an initial increase, then decreased during freezing. After the furnace stopped, the signal increased at a decaying rate. During melting the signal decreased, then increased back to near its initial value before the freeze-hold-melt cycle was begun. The simplified equation relating the Seebeck signal and the stationary and moving interface temperature does not explain these results. Instead a more general relationship which includes, for example, the structure of the solid must be used to determine the moving interface temperature.

The quench sample from the USMP-4 mission was sectioned and polished to reveal the microstructure. The section of the sample from the end of the growth capillary (approximately 90 mm furnace position) to the end of the quench zone included growth velocities of 1.85, 3.7, 6.7, 26.7 and 40 μm/sec. Evidence of interfacial breakdown was not found at the regions grown at 1.85 and 3.7 μm/sec. However, evidence of breakdown was found in the regions grown at 6.7, 26.7, and 40 μm/sec and the quenched region. Figure 3 shows the transition from growth at 1.85 μm/sec to the quench. Figure 4 is a picture of the microstructure resulting from a transition from holding the furnace at a stationary position to translation of the furnace at 40 μm/sec. Preliminary findings are the distance to interfacial breakdown was about 2.0 cm for the 6.7 μm/sec growth region and less than 0.3 mm for the growth at 26.7 and 40.0 μm/sec. Accurate analysis will be based on additional results from the Peltier and Seebeck samples including interface position during solidification.

Summary

Over 45 cm of directionally solidified Bi- 1 at % Sn alloy was recovered from the USMP-4 mission. The Seebeck signal and resistance were measured during the entire solidification process, and Peltier pulses were successfully administered. Seebeck signals and temperature gradient in the liquid for the space and ground-based experiments are markedly different. These results indicate a strong influence of convection on ground-based solidification experiments. Breakdown of the solid-liquid interface is observable for growth rates of 6.7, 26.7, and 40 µm /sec., but not at 1.85 and 3.7 µm /sec (over the distances observed). Analysis of results from Seebeck and Peltier samples including interface shape and position, and Seebeck signals will enable accurate tests of theories of morphological instabilities

Acknowledgments

The authors would like to thank CEA and the Société Européene de Propulsion (SEP, France) for their support during ground-based experiments and flight preparations. We would also like to acknowledge the entire USMP-4 team, especially Philippe Beaugrand, Vincent Gounot, Philippe Le, Regis Rieu, Sam Coriell, Graham de Vahl Davis, Eddie Leonardi, Bill Foster, Gil Santoro, Minwu Yao, Nick Barbosa, Jeff Mileham, Jeff Clancy, and Gordon Seuell. The superb support of the NASA Marshall USMP-4 team, and the financial support of the program by NASA is gratefully acknowledged.

References:

1. S.D. Peteves and R. Abbaschian, Met. Trans. A 22A (1991), 1259
2. S.D. Peteves and R. Abbaschian, Met. Trans. A 22A (1991), 1271
3. W. Obretenov, D. Kashchiev, V. Bostanov, J. Crystal Growth 96 (1989) pp. 843
4. T.F. Ciszek, J. Crystal Growth 10 (1971) p 263
5. T. Abe, J. Crystal Growth, 24/25 (1974) p 463
6. R.Abbaschian, A.B. Gokhale, J.J Favier, G. Cambon, S.R. Coriell, H.C. de Groh III and R.L. DeWitt, 33rd AIAA Aerospace Sciences Meeting, Reno, Jan. 1995, AIAA 95-0608.
7. A. Rouzard, J.J. Favier and D Thevenard, Adv. Space. Res. 8, (1988) p 49
8. Reza Abbaschian, Kirk M. Beatty, Fuwang Chen, Tyler Lenzi, Henry de Groh III, Gerard Cambon, Graham de Vahl Davis, and Eddie Leonardi, 10th EMMMS conference, Feb. 1998
9. Q. Li, H. Nguyen Thi, B. Billia J. Crystal Growth 167 (1996) pp. 277
10. B.Sixou, A. Rouzaud J.J. Favier, J. Crstal Growth 137 (1994) p. 605

Study of Interesting Solidification Phenomena on the Ground and in Space (MEPHISTO)

J. Iwan D. Alexander, J.-J. Favier†, J.-P. Garandet†,
National Center for Microgravity Research on Fluids and Combustion
and Department of Mechanical and Aerospace Engineering,
Case Western Reserve University, Cleveland, Ohio, USA.
ida2@po.cwru.edu: (216) 368 6045
†Comissariat à l'Energie Atomique, DTA/CEREM/DEM/SPCM,
17 Rue des Martyrs, Grenoble Cedex 9, France

Abstract

Real-time Seebeck voltage variations in a Sn-Bi melt during directional solidification in the MEPHISTO spaceflight experiment flown on the USMP-3 mission, have been correlated with well-characterized thruster firings and an Orbiter Main System (OMS) burn. The Seebeck voltage measurement is related to the response of the instantaneous average melt composition at the melt-crystal interface. This allowed us to make a direct comparison of numerical simulations with the experimentally obtained Seebeck signals. Based on the results of preflight and real-time computations, several well-defined thruster firing events were programmed to occur at specific times during the experiment. In particular, we simulated the effects of the thruster firings on melt and crystal composition in a directionally solidifying Sn-Bi alloy. The relative accelerations produced by the firings were simulated by impulsive accelerations of the same magnitude, duration and orientation as the requested firings. A comparison of the simulation results with the Seebeck signal indicates that there is a good agreement between the two. This unique opportunity allows us to make the first quantitative characterization of actual g-jitter effects on an actual crystal growth experiment and to calibrate our models of g-jitter effects on crystal growth.

Introduction

The MEPHISTO program is the result of a cooperative effort that involves the French nuclear and space agencies Comissariat à l'Energie Atomique, CEA - Centre National d'Etudes Spatiales, CNES) and the National Aeronautics and Space Administration (NASA). Six space flights on the USMP carrier were initially planned, with odd-numbered missions being the responsibility of the French scientific teams and the even-numbered missions being the responsibility of the US. During the first flight of MEPHISTO in October 1992, bismuth-doped tin samples (Sn:0.5 at.% Bi) were used and experiments were carried out both below and above the morphological stability threshold. Exciting results were obtained [1] that opened new perspectives for research.

The first objective of the USMP-3 flight was to investigate the g-jitter induced solutal segregation in planar front solidification. We requested well-controlled gravity perturbations, mainly in the form of Primary Reaction Control System (PRCS) burns. The other main scientific objective was to track the morphological stability threshold (i.e. the instability where the growth front goes from planar to cellular) with the highest possible accuracy. In comparison with the first flight, the USMP-3 alloys were slightly more concentrated (1.5% at. Bi), in order to check a possible soluto-convective effect.

MEPHISTO is a directional solidification furnace, in which three samples are simultaneously processed. A unique property of the apparatus is that there are two heating/cooling subsystems [2,3]. One of these is held at a fixed position and provides a reference interface. The other is programmed to translate along the furnace axis to facilitate solidification and melting of the alloy samples. One of the samples is dedicated to a measurement of the Seebeck voltage between the two ends. In other words, the sample acts as its own thermocouple, with a "cold" and a "hot" reference junction (respectively the moving and fixed interfaces). The Seebeck voltage is then a measure of the undercooling at the growth front, and most importantly, the signal is obtained in real time. It is thus possible to run many experimental cycles on the same sample. This, in turn, allows for a test of the reproducibility of the process and to ensure a better accuracy of the results. The second sample is used to record the position and the velocity of the moving interface. These are obtained from a resistance measurement. At the end of each experimental cycle, a quench freezes the structure of the solid-liquid front. Peltier pulse marking performed on the third sample allows the determination of the shape of the interface at given time intervals. Moreover, in the second and third samples, thermocouples present in the liquid phase are used to determine the temperature gradient and possible thermal fluctuations. The MEPHISTO facility ran for 312 hours, including 216 hours dedicated to scientific operation. During that time period, 24 solidification/fusion cycles were carried out. Five growth rates were preprogrammed (1.7, 3.7, 5.7, 12 and 24 mm/h) before the flight, but, thanks to telescience operations, we were able to different growth rates to track the morphological stability threshold. Controlled gravity perturbations were realized through planned thruster firings and maneuvers. In all 9 PRCS burns, ranging in duration from 10 to 25 seconds were carried out. In addition, an OMS burn and a 360° X-axis roll were also performed (see Table I). (See table 1)

Table 1 MEPHISTO PRCS and OMS burns and rolls

Velocity	*MET*	*Duration [sec]*	*Type*	*Orientation*
V3	5/21:45	25	PRCS	+Z
V3	6/00:00	15	PRCS	+Z
V2	6/22:00	10	PRCS	+Z
V2	7/00:25	10	PRCS	+X
V1	10/12:30	15	PRCS	+Z
V3	12/12:25	15	PRCS	-Z*
V3	12/14:25	15	PRCS	+Y
V3	12/14/28	15	PRCS	-Y
V3	12/16:28		360° X-axis roll	
V3	13/12:50	15	PRCS	+Z*
V3	13/14:03	30	OMS burn	dominantly X

During the first flight of the MEPHISTO directional solidification experiment on NASA's USMP-1 mission in 1992, the impact of sudden effective gravity perturbations were clearly evidenced [1]. Real-time Seebeck voltage variations across a Sn-Bi melt showed a distinct variation that can be correlated with thruster firings [1]. The Seebeck voltage measurement is related to the response of the instantaneous average melt composition at the melt-solid interface [4]. This permitted a direct comparison of numerical simulations (and acceleration data) with the Seebeck signals obtained on USMP-1. Motivated by the results of the comparison, we used numerical simulations to predict the response of the Seebeck signal to thruster firings of various magnitudes and durations. The behavior of the signal is directly related to changes in interfacial composition caused by thruster-induced convective disturbances. Motivated by the observations made on USMP-1, one of the objectives of the USMP-3 MEPHISTO experiments was to quantitatively characterize g-jitter effects on an actual crystal growth experiment. To plan the USMP-3 MEPHISTO experiments, simulations were carried out for different solidification rates and g-jitter scenarios.

There were several differences between the USMP-3 and USMP-1 experiments. First, a more concentrated alloy was solidified on USMP-3, and, second, Primary Reaction Control System (PRCS) thruster burns were requested at particular times during four separate growth runs. The Seebeck signal was recorded continuously and down-linked in real-time to the MEPHISTO experiment team at NASA's Marshall Space Flight Center. This allowed for quantification of the effects of "g-jitter" on convective-diffusive transport in the melt through the changes in average interfacial composition obtained from the Seebeck measurement. In addition, guided by SAMS acceleration data, we carried out simulations for comparison with the recorded Seebeck signals. The effects of thruster firings on the average composition was monitored in six separate experiments and for eleven separate acceleration disturbance events. Selected results from our ongoing post-flight analysis are described below.

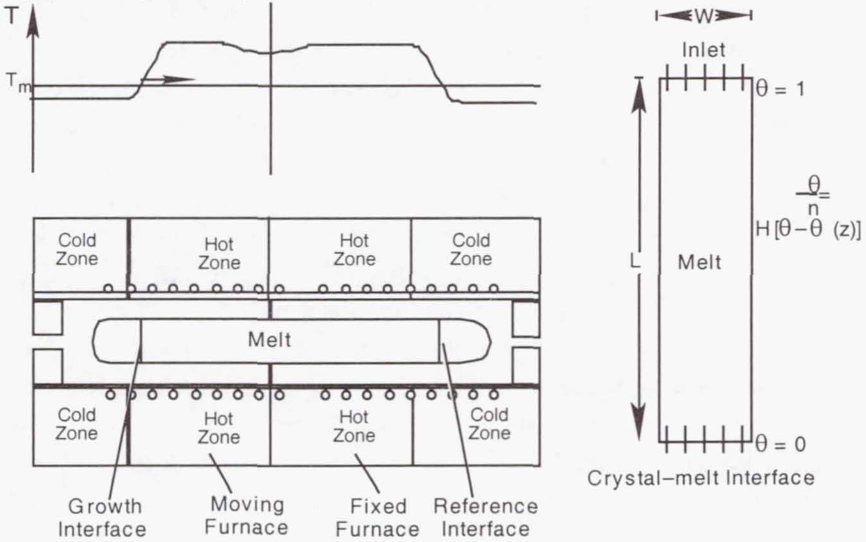

Fig. 1 The MEPHISTO set-up (bottom-left), temperature profile (top left) and computational model (right). T_m denotes the melting temperature.

Approach

A sketch of the experiment set-up is shown in Fig. 1 . There are two furnaces. One is fixed. The other is translated. The applied temperature profile shown in Fig. 1 leads to a central cylindrical melt volume bounded by a moving and a stationary (or reference) solid-liquid interface. The melt composition at the moving and the stationary reference interfaces is not the same. For Sn-Bi there is a dependence of melting temperature on concentration. Thus, it follows that the melting temperature at the two interfaces will also be different. The Seebeck effect gives rise to a small but measurable voltage difference between these two interfaces. Measurement of this voltage difference allows us to determine the average temperature and, thus, the average composition of at the growing interface. The MEPHISTO set-up and the Seebeck measurements are discussed in more detail in [4].

The numerical model used to simulate the response of the tin-bismuth melt to particular types of g-jitter has been described elsewhere [5-7]. The essential features are outlined below. Solidification takes place as the furnace is translated along the ampoule (see Fig. 1). Directional solidification due to the furnace translation is simulated by supplying a two-component melt of bulk composition $c_{\bullet}$ at a constant velocity Vg at the top of the computational space (inlet), and withdrawing a solid of composition $c_s = c_s(x,t)$ from the bottom (See Fig. 1). The crystal-melt interface is located at a distance L from the inlet; the width of the ampoule is W. The temperature at the interface is taken to be T_m, the melting temperature of the crystal, while the upper boundary is held at a higher temperature T_h. In the actual experiment, the temperature gradient along the ampoule wall ahead of the growing interface was essentially linear (195 K cm-1). Thus, we set a linear temperature gradient along the wall in the simulations. Furthermore, since we wish to confine our attention to compositional nonuniformities caused by buoyancy-driven convection, rather than variations resulting from non-planar crystal-melt interfaces, the interface is held flat. We expect that, given the large temperature gradient, changes in melting temperature due to compositional non-uniformity will not lead to significant changes in interface shape due to interfacial compositional inhomogeneity. Furthermore, because of the melt's low Prandtl number and the low magnitude accelerations, convection does not lead to significant deviations of the temperature from the conductive state, Thus, changes in the interface shape due to changes in the thermal field will be negligible. In an actual experiment, owing to the finite length of the ampoule, there is a gradual decrease in length of the melt zone during growth. In this model, transient effects related to the change in melt length are ignored. Since the MEPHISTO experiments involve melt lengths that far exceed the ampoule diameter, this does not preclude us from calculating the compositional transient. That is, we can start the calculations by solidifying from an initially uniform composition melt.

The dimensionless governing equations governing coupled convective-diffusive heat mass and species transfer in the melt were assumed to be those for a Boussinesq fluid with a linear dependence of density on temperature and composition. The boundary conditions imposed were those corresponding to plane front directional solidification at a translation rate Vg with a linear temperature gradient applied to the ampoule walls. Solute was preferentially rejected at the crystal-melt interface ($k = 0.27$ for this Sn-Bi alloy). The equations were solved using a Chebyshev spectral method.

Results

The PRCS firings produced an impulse acceleration with the largest component parallel to the solid liquid interface. Figure 2 shows the actual (uncorrected for drift) and predicted Seebeck signal for an experiment subject to two thruster burns (25 seconds and 10 seconds in duration) that produced an acceleration oriented parallel to the crystal-melt interface (i.e. perpendicular to the ampoule axis. Before the first burn, the Seebeck signal decreases monotonically. Immediately following the burn, the signal increases rapidly and reaches a maximum about 100 seconds after the termination of the burn. The signal then decreases slowly and eventually takes on almost the same slope that it had before the burn. The same behavior occurs following the second burn. After translation of the furnace was stopped. Solidification then ceases and the Seebeck signal increases as the average interfacial concentration decreases.

Note that the actual Seebeck measurement shown has not been corrected for drift and, thus, the voltage does not return to its original value. For the response of the Seebeck signal predicted by computer simulation, there is an immediate rapid response to each of the firings. In addition, we see that the time taken for the Seebeck signal to reach a maximum value is approximately the same for the computed and measured signals.

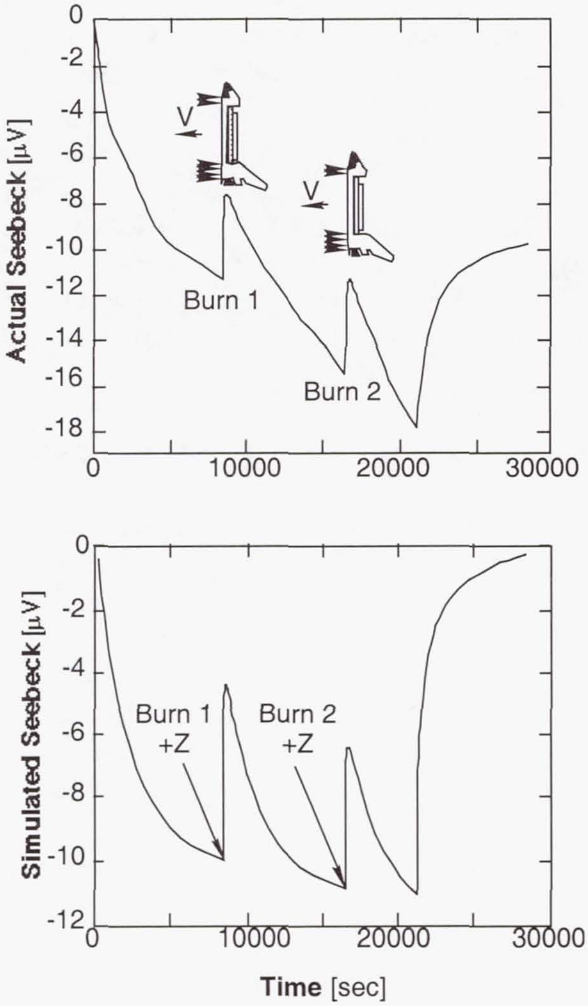

Fig. 2 (a) Actual and (b) predicted Seebeck signal for a 25 second and 15 second burn oriented parallel to the crystal-melt interface.

Summary

The USMP-3 MEPHISTO experiments permitted a quantitative correlation between well-characterized g-jitter recorded by spacecraft accelerometers and the response of a directionally solidifying alloy. Furthermore, the comparison of the results of the experiment with the predictions of numerical simulations carried out on the Alabama Research and Education Network's C-90 Supercomputer, will allow us to verify the degree to which such simulations can accurately predict experiment sensitivity to g-jitter accelerations. Without quantitative experimental verification, such predictions are of limited use and could lead to unnecessary design restrictions, an undesirable low gravity environment, or unsuitable experiment operating conditions

Ongoing work involves corrections of the raw Seebeck data, analysis of residual acceleration data measured by NASA's Space Acceleration Measurement System, estimation of the degree of melt homogeneity following remelting cycles and refinement of the computational simulations. This unique experiment showed use of simulations to assist in changes in experiment strategy greatly enhances the scientific return from limited opportunity spaceflight experiments. It is expected that ongoing work will yield benchmark comparisons between measured and predicted residual acceleration effects.

Acknowledgments

This work was carried out within the framework of the GRAMME agreement between CNES and the CEA, and was supported by the National Aeronautics and Space Administration through Grant NAG3-1740 and by the State of Alabama through the Center for Microgravity and Materials Research the Alabama Research and Education Network.

References

[1] J.J. Favier, J.P. Garandet, A. Rouzaud and D. Camel, J. Crystal Growth 140 (1994) 237.

[2] A. Rouzaud, J. Comera, P. Contamin, B. Angelier, F. Herbillon and J.J. Favier, J. Crystal Growth, 129 (1993) 173

[3] A. Rouzaud, J.J. Favier and D. Thevenard, Adv. Space Res., 8 (1988) 49

[4] J.-J. Favier, J.P. Garandet, A. Rouzaud and D. Camel, J. Crystal Growth, 113 (1991) 21.

[5] J.-J. Favier and A. Rouzaud, Revue Phys. Appl. 22 (1987) 713.

[6] J.I.D. Alexander, J. Ouazzani and F. Rosenberger, J. Crystal Growth 97 (1989) 285.

[7] J.I.D. Alexander, S. Amiroudine, J. Ouazzani and F. Rosenberger, J. Crystal Growth 113 (1991) 21.

[8] J.I.D. Alexander, in Materials and Fluids under Low Gravity, L. Ratke, H. Walter and B. Feuerbacher, eds.(Springer, Berlin, 1995) p. 95-102.

[9] J.I.D. Alexander, J.P. Garandet, J.J. Favier and A. Lizèe, "G-jitter effects on segregation during directional solidification of tin-bismuth in the MEPHISTO furnace facility", J. Crystal Growth 178 (1997) 657.

MICROGRAVITY IMPREGNATION OF FIBER PREFORMS

M. Cengiz Altan
School of Aerospace and Mechanical Engineering
University of Oklahoma, Norman, OK 73019, U.S.A.
405-325-1737; altan@ou.edu

Introduction

It is well known that the spreading of liquids and wetting of solid surfaces in space exhibit a number of significant fluid management challenges as well as numerous interesting phenomena. Many of these phenomena are also technologically important in fabricating high-performance parts in space such as the structural components needed to build the space station or medium to large panels needed for repair in space. The ability to manufacture geometrically complex, lightweight and high performance composite parts in space primarily depends on understanding and subsequent controlling of flow processes such as filling a mold cavity, spreading or coating a solid surface, and impregnation of a porous fiber preform. For example, most high-performance molding operations involve impregnation of a fibrous preform where the balance between viscous and surface forces as well as nonisothermal effects significantly affect the fluid behavior. It is believed that microgravity provides the necessary means to mold much stronger/stiffer composite materials due to achieving higher volume content of the reinforcing preform. In addition, the complete process can be accomplished with much simpler, lighter, and inexpensive tooling and molding equipment.

The objective of the current research is to contribute to the understanding of microgravity impregnation and wetting of porous media, and to develop low-pressure molding methodologies to fabricate high-performance composite materials. Investigating the effects of capillary forces and gravity on mold filling will be among the primary objectives. The flow through porous media induced during the filling of a centergated mold cavity will be studied under 1-g and microgravity conditions. The proposed experiments aim at understanding the effects of fluid viscosity, external pressure (i.e., impregnation pressure), surface tension, and microstructure of the wetted porous media on the flow kinematics.

Effects of Gravity on Mold Filling

In the absence of gravity or in filling operation in which gravity can be neglected, free surface shape in a planar mold cavity would be symmetric with respect to its midplane. The assumption that gravity can be neglected is used by most researchers studying resin transfer molding (RTM) [1-3]. The presence of gravity deforms the fluid front causing it to sag towards the bottom mold surface. Due to this spreading, the bottom of the free surface advances ahead of the top. The difference between the radial location of the bottom and top of the free surface contact lines is defined as spreading. Initial experiments showed that spreading can be quite significant under certain processing conditions. In the absence of a fibrous preform, Figs. 1 and 2 show approximately 0.75 in. and 1.5 in. of spreading of the fluid front, respectively. With low viscosity fluids or for low filling rates, significant spreading up to 2 to 6 times the gap thickness is observed. During the filling of a mold, transient pressure distribution on the top and bottom mold walls can differ markedly in flows with considerable spreading.

In the absence of a fibrous preform in the mold, spreading at a radial location in a centergated disk shaped cavity can be characterized by the Reynolds, Bond, Capillary numbers and the contact angle, α. For the filling of a mold, the first three non-dimensional parameters can be expressed as,

$$\mathrm{Re} = \frac{\rho u L}{\mu}; \qquad Ca = \frac{\mu u}{\sigma}; \qquad Bo = \frac{\rho g L^2}{\sigma}, \tag{1}$$

where ρ, σ, and μ are the fluid properties density, surface tension, and viscosity; L is the gapwidth; and u is the average local velocity. These numbers are defined at the location of the first fluid front probe (r=2.0 in.), thus the velocity, u, represents the average velocity at r=2.0 in. For macroscopic analysis, a Reynolds number to characterize the flow regime can be expressed in terms of the volume flow rate as

$$\mathrm{Re}_Q = \frac{\rho Q}{\mu L} \tag{2}$$

The dependence of spreading on Reynolds, Bond, Capillary numbers and contact angle needs to be fully understood through carefully designed experiments. Towards this end, the following physical parameters can be changed in filling experiments: gapwidth, L; volume flow rate, Q; viscosity of the fluid, μ. For a given fluid and the mold surface the contact angle can be determined. Then two of the remaining three non-dimensional parameters need to be kept constant while changing the third one. This requires the adjustment of all the physical parameters (i.e., L, Q, and μ) in a unique manner. Experiments are designed and being conducted to identify the effects of Reynolds, Bond, and Capillary numbers on spreading.

Experimental Setup

An experimental molding setup for observing and characterizing flow during the filling of a disk shaped cavity has been constructed. The experimental setup consists of the following components: an assembled mold cavity, a peristaltic pump and tubing system for fluid transfer, and a data acquisition system. The 9.0 in. radius centergated disk shaped mold cavity, depicted in Fig 3., is formed by placing spacer plates between 1.0 in. thick Plexiglas mold walls. Spacer plates are cut from 20x20-inch aluminum or acrylic sheets with an 18-inch diameter disk shaped cut from its center. Several spacer plates with thicknesses ranging from 1/16 to 1/2 inch are fabricated and can be combined to provide gap widths from 1/16 to 1 in. Fluid is injected by the peristaltic pump at constant flow rate through an inlet gate with a diameter that can be varied from 0.125-0.375 in. Figure 3 shows the radial locations of pressure transducers and fluid front sensors which are connected to the data acquisition system. Figure 4 provides a closer view of the fluid front sensors and how they detect spreading. Figure 4a shows a typical fluid front as it might appear without spreading in the absence of gravity, while Fig. 4b shows a front which has sagged due to gravity. The sensors are mounted at three radial locations in the disk, r=2, 4, and 6 in., and each consists of two small pairs of terminals mounted on the top and bottom walls. Each has a power terminal and three numbered sensing terminals as illustrated in Fig. 4.

A sensing circuit in conjunction with the data acquisition system detects when the front contacts each sensing terminal by measuring a resistance drop. The three sharp voltage increases shown in Fig. 5 represent the fluid front contacting the three terminals. The spreading S can be calculated from the two known radii R_a and R_b and these three fluid front contact times t_1, t_2, and t_3 [4]. Initially, it is assumed that the free surface travels at the average velocity of the flow at any given radius. The average velocity, V, is known to be inversely proportional to the radius, r, since the fluid is injected at a constant flow rate, Q.

$$V(r) = \frac{dr}{dt} = \frac{c}{r}, \tag{3}$$

where c is a constant. Integrating this expression from R_a to R_b (t_3 to t_2) yields,

$$\frac{1}{2}(R_b^2 - R_a^2) = c(t_2 - t_3)\,. \tag{4}$$

The constant is determined from Eq. (3) as $c = V_b R_b$. Equation (4) is rearranged to yield an expression for the velocity at b,

$$V_b = \frac{(R_b^2 - R_a^2)}{2R_b(t_2 - t_3)}\,. \tag{5}$$

Equation (3) can also be integrated for the bottom of the fluid front which travels from R_b to R_c over the time interval t_1 to t_2 to determine the final radius, R_c,

$$R_c = \sqrt{R_b^2 + 2V_b R_b (t_2 - t_1)}\,. \tag{6}$$

From R_c, the distance between the top and bottom of the fluid front can be calculated as spreading, $S=R_c-R_b$.

The velocity at b calculated from Eq. (5) is referred to as *V measured* in the results section, as this is the velocity calculated from the measurements taken by the fluid front sensing probes. It is useful to calculate the velocity in a second way from the known volume flow rate and the area the fluid flows through at a given radius r,

$$V(r) = \frac{Q}{2\pi r L}\,. \tag{7}$$

This velocity is referred to as *V calculated* in the figures and results section and is used to quantify the effect of gravity on the velocity field during filling.

In addition to spreading, transient pressure distribution during mold filling is measured and compared with theoretical models. From Darcy's law, the transient pressure, *p*, in a disk being filled at constant flow rate is calculated to be,

$$p(r) = \frac{Q\mu}{(1-\phi)2\pi L K_{rr}} \ln \frac{R^*}{r}, \tag{8}$$

where K_{rr} is the permeability of the preform in the radial direction, R^* is the location of the fluid front at a given time, r is the location at which the pressure is being calculated, and ϕ is the volume fraction of the preform.

Results

Filling experiments have been conducted with 0 to 35% preform (i.e., stacked layers of chopped glass fiber mats) placed in the cavity. Channeling and gravity are measured to have notable effects on the flow kinematics and spreading during filling, dependent on the fiber volume fraction, fluid viscosity, mold gapwidth, and the inlet velocity.

Spreading results from three experiments are presented in Table 1, and the corresponding velocities are given in Table 2. Run 1 is a filling experiment having a volume fraction of 18% chopped glass strand preform in a gapwidth of 0.5 in. Corn syrup having a viscosity of 140 cp is injected from the bottom of the cavity at a flow rate of 1.1×10^{-5} m^3/s. Run 2 has identical fill conditions, except the fluid is injected from the top mold wall to clearly identify gravity effects. Run 3 has the following conditions: L=0.25 in., μ=110 cp, ϕ=27%, and Q=6.0×10^{-6} m^3/s. In runs 1 and 2, gravity effects on spreading can be clearly seen. Run 1 shows nearly 2 in. of spreading at r=2 in., with a decrease in spreading as r increases. Run 2 shows the top of the fluid front is ahead of the bottom (indicated by negative spreading) at r=2 in. due to the fluid being injected from the top. The front sags due to gravity downstream. The measured velocity at the top wall in run 1 is higher than the velocity calculated from the flow rate. This is expected since spreading decreases drastically by r=6 in. Run 2 has less spreading and measured velocities are in better agreement with the calculated velocities. Run 3 is a flow with negligible spreading primarily due to smaller gapwidth and higher fiber volume fraction, thus depicting good agreement between the measured and predicted velocities.

Figure 6 contains transient pressure curves at three radial locations for a 516 cp glycerol water mixture injected at a flow rate Q=5.26×10^{-6} m^3/s into a cavity containing 18% chopped glass fiber mats. In Fig. 6, the permeability is calculated to be 4×10^{-8}m^2 by curve fitting Eq. (8) to pressure data at r =1.5 in. This permeability value is consistent with permeability values reported in literature [5-7]. The two other curves in Fig. 6 are generated using this permeability, and are shown to match the experimental data at the other radial locations well.

References

1. Bruschke, M.V. and Advani, S.G., "A finite element/control volume approach to mold filling in anisotropic porous media", *Polymer Composites*, **11(6)**, 398-405, (1990).
2. Young, W.B. and Lai, C.L., "Analysis of the edge effect in resin transfer molding", *Composites Part A*, **28A**, 817-822 (1997).
3. Parnas, R.S. and Salem, A., "A comparison of the unidirectional and radial in-plane flow of fluids through woven composite reinforcements", *Polymer Composites*, **14(5)**, 383-394, (1993).
4. Olivero, K.A. and Altan, M.C., "Gravity effects on preform impregnation during resin transfer molding", 14th meeting of the Polymer Processing Society, **PPS-14**, 786-787, (1998).
5. Parnas, R.S., Flynn, K.M., and Dal-Favero, M.E., "A permeability database for composites manufacturing", *Polymer Composites*, **18(5)**, 623-633, (1997).
6. Sheard, J., Senft, V., Mantell, S.C., and Vogel, J.H., "Determination of corner and edge permeability in resin transfer molding", *Polymer Composites*, **19(1)**, 96-105, (1998).
7. Lai, Y-H., Khomami, B., and Kardos, J.L., "Accurate permeability characterization of preforms used in polymer matrix composite fabrication processes", *Polymer Composites*, **18(3)**, 368-377, (1997).

Table 1: Spreading at three radial locations for three different fill conditions.

S (in)	S (r =2in.)	S (r =4in.)	S(r =6in.)
Run 1	1.98	0.24	0.02
Run 2	-0.29	0.11	0.08
Run 3	0.10	0.00	-0.04

Table 2: Measured and calculated velocity at three radial locations.

V (in./s)	V(r =2in.)	V(r =4in.)	V(r =6in.)
Probe Run 1	0.195	0.134	0.055
Probe Run 2	0.130	0.065	0.055
Calculated 1&2	0.129	0.064	0.043
Probe Run 3	0.167	0.076	0.054
Calculated 3	0.160	0.080	0.053

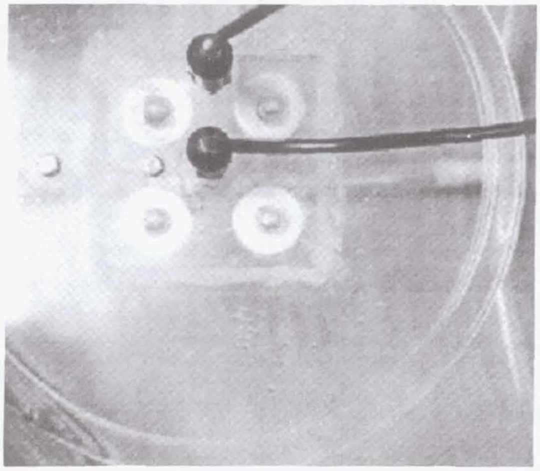

Figure 1: Spreading observed during filling in the absence of a preform: μ=412cp, Q=2.13*10^{-5} m^3/s, L=0.25 in., Re$_Q$=10.2.

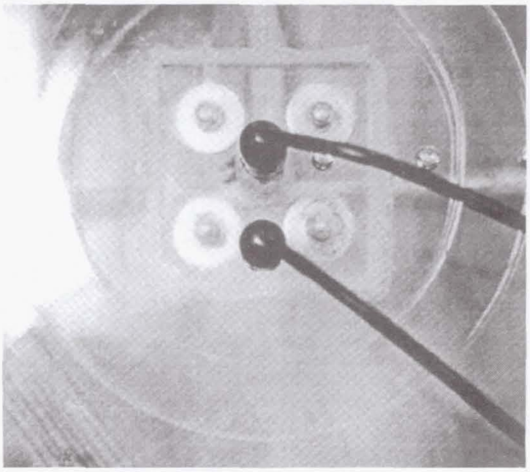

Figure 2: Spreading observed during filling in the absence of a preform: μ=113cp, Q=8.69*10^{-5} m^3/s, L=0.25 in., Re$_Q$=151.3.

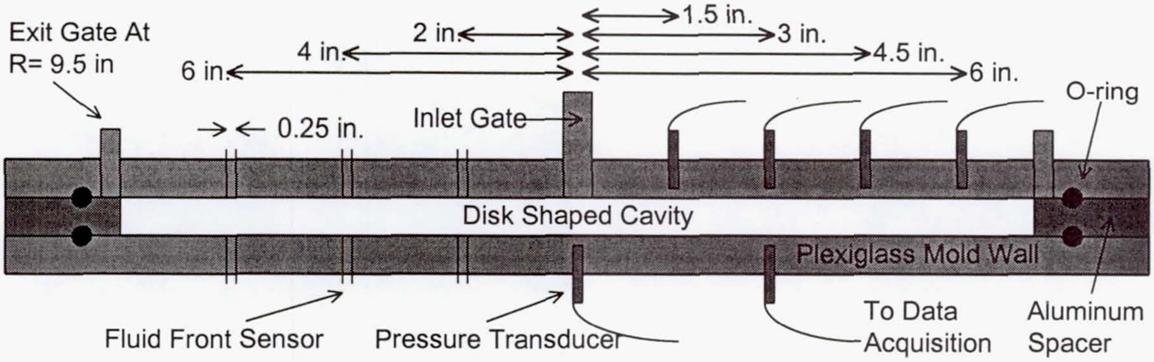

Figure 3: Cross section of experimental mold cavity.

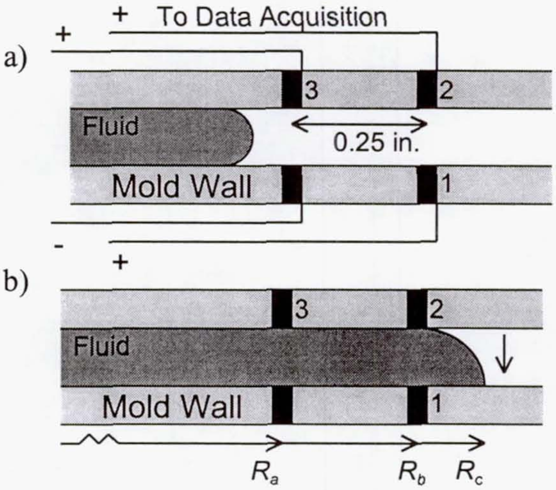

Figure 4: Schematic cross section of fluid front probe and a fluid front, a) without spreading; b) with spreading due to gravity.

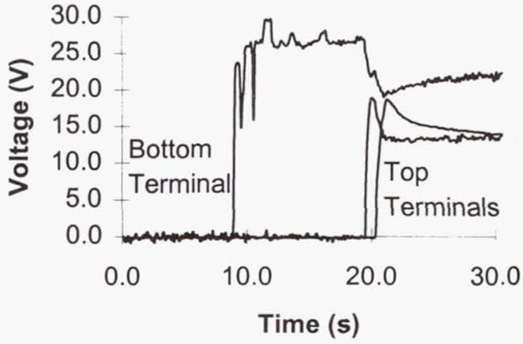

Figure 5: Voltage data from fluid front sensors: r=2 in, 15% preform μ=110cp, Q=1.75*10^{-5} m^3/s, L=0.5 in.

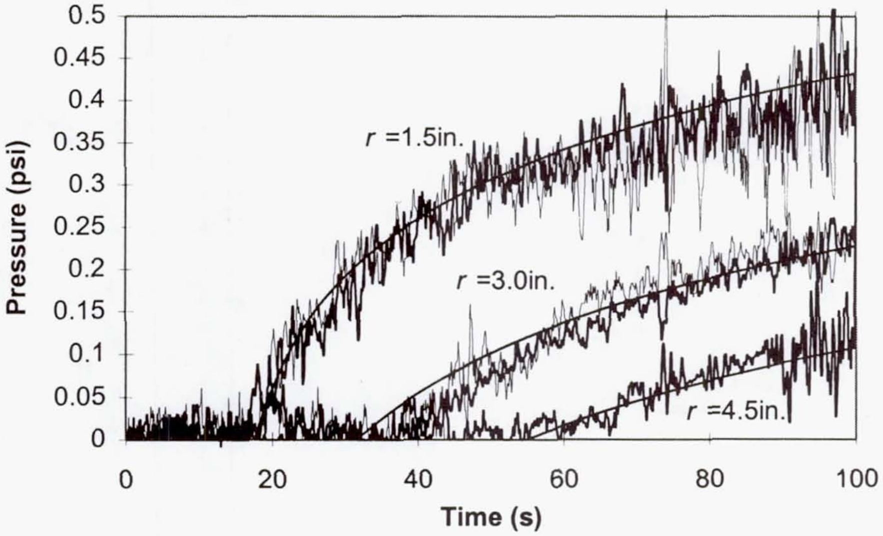

Figure 6: Transient pressure for Q=5.26*10^{-6} m^3/s, μ=516 cp, 18% preform. Re=0.04, Bo=8.2, Ca=0.02. K_{rr} calculated to be 4*10^{-8}m^2.

AN ELECTROCHEMICAL METHOD TO VISUALIZE FLOW AND MEASURE DIFFUSIVITY IN LIQUID METALS

T.J. Anderson
University of Florida
Gainesville, FL 32611
352-392-0882; tim@nersp.nerdc.ufl.edu

R. Narayanan
University of Florida
Gainesville, FL 32611
352-392-9103; ranga@gibbs.che.ufl.edu

Introduction

The main objective of this program is to develop and demonstrate a novel electrochemical sensor for determining the fluid dynamic state in low Prandtl number, opaque liquid metals at high temperature. The basic idea is to use solid state electrochemical cells constructed along the container boundaries to control and detect the concentration of a tracer species. In this project, yttria stabilized zirconia (YSZ) is used as a solid oxygen-ion-conducting electrolyte and separates a 'working' liquid metal electrode from a 'reference' electrode. Atomic oxygen, dissolved in the liquid metal at the ppm concentration level, is detected by electrochemical cells operating in the galvanic mode. The same cell configuration is also used to establish localized concentration boundary conditions through coulometric titration of oxygen. Information about the dynamic state of the liquid metal is then obtained by perturbing the oxygen distribution in the liquid and observing the dynamic response of the measured EMF of the detection cells[1-2].

Although a variety of methods have been used to study the fluid dynamics of high temperature, opaque liquid metal systems,[3-5] many of these techniques are of low sensitivity, intrusive, or not easily adaptable to flight-based experimentation. In contrast, this tool is non-intrusive (the oxygen levels are typical of those present in liquid metal processing) and capable of detecting velocities as low as 10^{-4} cm/sec. This technique is also highly adaptable to flight experimentation given power, weight, safety and signal level requirements. The electrochemical method to visualize flow provides a fresh approach to a difficult problem that has the potential not only to enhance our understanding of the fluid dynamics of low Prandtl number fluids, but also provide a critical experimental link between computational fluid dynamics and processed material properties.

The magnitude of convective velocities encountered in the microgravity processing of liquid metals (e.g., bulk crystal growth of semiconductors) can be comparable to diffusive velocities. Thus accurate values of the oxygen diffusivity are necessary to separate the diffusive component of the oxygen flux from the convective component. Unfortunately, gravity driven convection in the melt prevents accurate measurement of the mass diffusivity of oxygen in liquid metal systems on earth. A complimentary objective of this project is to perform the necessary ground-base investigations that will lead to the flight definition of a series of microgravity experiments to measure the temperature dependent diffusivity of oxygen in liquid metals. In addition to providing accurate values of the oxygen diffusivity for the flow visualization studies, these results should provide the research community with a benchmark for the development of improved ground-base cell configurations. Another science objective of this study is to establish the constitutive behavior of "Fickian" diffusion of oxygen in liquid metals.

Experimental Methods

Flow Visualization Cells A schematic of the electrochemical system used to visualize the flow is shown in Figure 1a. The ampoule was constructed from a flat, closed-one-end cylinder of recrystallized alumina with 3-mm holes drilled along the periphery (1cm-height intervals, 90° spacing, and one at the bottom). Stubs of the YSZ solid electrolyte were fitted into the holes and sealed with a high temperature ceramic cement. Porous platinum electrodes were sintered onto the outside stub ends and contacted with Pt wires. Each electrochemical sensor used the melt as the common working electrode, with a separately contacted air/Pt reference electrode. The tube with inner radius R was filled with either Sn or Pb to a height H to yield a fluid aspect ratio $\beta = H/R$. Dissolved oxygen was used as the tracer species, which could be injected or extracted locally at one or more of the sensor locations by electrochemical titration. The dissolved oxygen concentration was monitored as a function of time at the other cell locations on the melt/electrolyte boundary by operating the cells in the galvanic mode. The whole apparatus was inserted into a gradient furnace to establish a temperature gradient and thus vary the dynamic state in the melt.

A typical flow visualization experiment was conducted by filling the ampoule with an etched metal charge to a specified height. After bringing the cell to operating temperature, a uniform oxygen concentration was established in the melt by applying a constant potential for several hours. Oxygen was then introduced at the lower electrode by applying a lower potential or removed from this electrode by applying a higher potential. The change in oxygen concentration at each of the other electrochemical sensors at various heights was then monitored as a function of time by measuring the open-circuit potentials. The value of the Rayleigh number was progressively increased by changing the ΔT across the melt, and the titration experiment was repeated.

Diffusivity Measurements. A schematic diagram of the electrochemical cell assembly used in the diffusivity measurements is shown in Figure 1b. It consisted of a working liquid metal electrode sandwiched between two solid YSZ electrolyte discs (9.5 mm OD, 1.6 mm thick) through which oxygen could be titrated. The working electrode materials were high purity zone-refined bars of Sn or Pb. After casting and machining, these metals were contained in fused silica tubes (3 to 7 mm heights) of circular (7.3-mm ID) or square (5.0-mm sides) cross-section. Equimolar mixtures of Cu and Cu_2O powders of purity 99.95% formed the reference electrode material. After loading the metal the YSZ discs were cemented to the fused silica containers. A 1-mm hole was drilled through the upper electrolyte disc at its center to allow for the overflow of excess tin or lead. A cylindrical copper sheath (25.4-mm OD) to improve the isothermal conditions surrounded the cell. The method of purification of the argon blanket gas, the procedure for sealing the electrolytes with the reference electrode material and other experimental details are described elsewhere.[6]

The diffusivity of oxygen in liquid Sn or Pb was determined either by a transient experiment or by a steady state experiment. In the transient mode, the initial oxygen concentration in the liquid metal was established by transporting oxygen in or out of the metal through an applied voltage across both oxygen concentration cells. When the oxygen potential in the melt was uniform and stable, a large voltage was imposed between the two electrodes of one of the oxygen concentration cells (either upper or lower) such that an essentially zero oxygen concentration boundary condition was established at one of the liquid metal surfaces. The open circuit electromotive force (emf) was then measured at the other oxygen concentration cell as a function of time. The response was related to the oxygen diffusivity through the one-dimensional linear diffusion equation.

In the steady state experiments, constant but different voltages well above the saturation potential of the liquid metal with respect to the reference electrodes were applied to each oxygen concentration cell. When steady state was reached, a uniform flux of oxygen, as measured by either cell current, was established. Using literature values for the saturation solubility,[7-9] the concentration of oxygen was calculated for the individual cells, which allowed calculation of the concentration gradient, and with the flux, determination of the oxygen diffusivity.

Summary of Results

To explore the limits of this novel technique and to validate its robustness a series of experiments have been designed using model fluids and geometries. Liquid Sn was selected as the model fluid because of its low vapor pressure and well-defined thermophysical properties. Both cylindrical and rectangular geometries are being investigated experimentally as a function of the imposed temperature gradient, aspect ratio, and tilt. A technique was developed to locate YSZ sensors in the walls of alumina tubes to avoid the problem of ionic conduction within the wall when using YSZ tubes. Successful experiments were performed in a cylindrical geometry to determine the flow orientation as a function of Ra and aspect ratio. Transitions from an unicellular flow pattern to an axisymmetric flow configuration and to a stacked flow arrangement were observed upon increasing the aspect ratio. At high values of Ra, the observed flow patterns and estimated velocities were comparable to the predictions of Hardin et al.[10]. Additional experiments were performed with variable temperature gradients and measurement modes (e.g., pulsing input, galvanic or potentiostatic titration) to understand the limits of the technique.

As an example, the onset of oscillatory flow was recorded at various aspect ratios by varying the applied temperature gradient. Figure 2 shows the temperature recorded by 4 thermocouples placed along the outside that were 2 cm above the bottom and at 90° spacing for a container aspect ratio of 5.3. The value of the Rayleigh number was determined to be $1.80 \pm 0.1 \times 10^5$ from the measurement of the ΔT (35 K) and the thermophysical properties of Sn. Figure 3 shows the corresponding oxygen concentration at the 4 electrochemical sensors adjacent to the 4 thermocouples. The oscillations are clearly complex and a phase difference exists between the sensors. Fourier transform of the thermocouple and oxygen sensor signals revealed three underlying frequencies with the fundamental frequency at 0.015 Hz. The agreement between the frequencies estimated from the thermocouple signals and the oxygen signals is good.

Work was also initiated on measuring the convective flow in square geometries. Since very little modeling effort has been devoted to this geometry, 3-dimensional simulation studies were performed. Both steady (torroidal, unicellular, multiple cells) and oscillatory flow configurations were calculated depending on the aspect ratio and Ra. The tracer atomic oxygen species balance was solved to allow a complete simulation of the electrochemical visualization technique. These simulations were used to design experiments, which are now underway. As an example, oscillatory flow was predicted by a series of calculations performed as a function of Ra at Pr=0.008 and an aspect ratio=0.25. The value of Ra at which steady, non-oscillatory flow patterns appeared was 200,000, while the onset of oscillatory flow occurred at a value Ra=300,000. The results of calculations conducted for time steps of 0.1 sec are shown in figure 4. The calculations employed a three-dimensional, finite-element algorithm developed by Gupta[11]. Figure 4 shows two-dimensional slices through the x-z plane in the vector space. The results show the initiation of a complex steady oscillatory flow pattern.

Coulometric titration procedures have long been used to determine values of the diffusivity of elements in liquid metals. The results of this study strongly indicate that convection driven by thermal or solutal gradients is present in most ground-base experiments. The measured values of the oxygen diffusivity depended on the cell size and experimental configuration. Measurements taken in configurations that gave rise to gravity driven convective flows also gave larger values of diffusion coefficients than measurements taken in configurations where the convective flows were apparently weaker. A detailed numerical model with a sophisticated 3-D code was developed to predict the effects of imperfections such as tilts and radial heat losses. It is concluded that even slight imperfections affect the diffusivity measurements for all of the cell configurations studied.

For example, taller cells, which were associated with large time constants, increased the measurement error because of mass transfer through an overflow port to accommodate the expansion of tin upon heating. The initial oxygen concentration and cell dimensions both influenced the hydrostatic stability of the tin sample during a transient diffusion experiment. This is not surprising as the transport process is essentially the transient version of the Rayleigh-Bénard problem and the aspect ratio and Rayleigh number are two parameters which are found to define the stability criterion in that problem.

As an example, the oxygen diffusivity in liquid Sn was measured as a function of temperature for several different aspect ratios. The results for a circular geometry are shown in Figure 5a and the results for a square geometry in Figure 5b. Both transient and steady state measurements were made. In both figures, the diffusivities measured using the transient method by initially removing oxygen at the top cell gave higher values of the diffusivity than those measurements made by initially removing oxygen at the bottom cell. Removing oxygen from liquid Sn increases the density. Thus oxygen removal at the top side produces an unstable density variation over the short diffusion length to produce convection that adds to the diffusive flux. Similar but less pronounced results are evident in the steady state mode when the oxygen gradient is reversed. The differences in the measured oxygen diffusivity observed between the square and circular geometries, as well as the scatter with aspect ratio further support convective contributions to oxygen mass transfer.

It is concluded that this novel technique holds considerable promise for use in a microgravity environment to detect low level flows and to accurately measure diffusivities. Furthermore, gravity driven convection in the melt prevents accurate measurement of the mass diffusivity of oxygen in metal systems by coulometric titration. This situation represents a clear example where a reduced gravity environment is necessary to obtain meaningful values of this important physical property.

References

1. Sears, B., Narayanan, R.N., Anderson, T.J., and Fripp, A.L., J. Crystal Growth, 125, 404 (1992).
2. Sears, B., Narayanan, R.N., Anderson, T.J., Fripp, A.L., Debman, W.J., and Woodall, G.A., J. Crystal Growth, 125, 415 (1992).
3. Hurle, D.T.J. and Jakeman, E., J. Fluid Mech., 64, 65 (1974).
4. Stewart, M.J. and Weinberg, F., J. Crystal Growth, 12, 228 (1971).
5. Kakimoto, K., Eguchi, M., Watanabe, H. and Hibiya, T., J. Crystal Growth, 94, 412 (1989).
6. Sears, B., Anderson, T.J., Narayanan, R. and Fripp, A.L., Metall. Trans. B, 24B, 91 (1993).
7. Szwarc, R., Oberg, K.E. and Rapp, R.A., High Temp. Sci., 4, 347 (1972).
8. Ramanarayanan, T.A. and Rapp, R.A., Metall. Trans., 3, 3239 (1972).
9. Belford, T.N. and Alcock, C.B., Trans. Faraday Soc., 61, 443 (1965).
10. Hardin, G.R., Sani, R.L., Henry, D., and Roux, B., Int. J. Num. Meth. Fluids, 10, 79 (1990).
11. Gupta, N. Natural Convective Flow of Low Prandtl Number Fluids Confined in a Rectangular Box Heated from Below, M.S. Thesis, University of Florida, 1998.

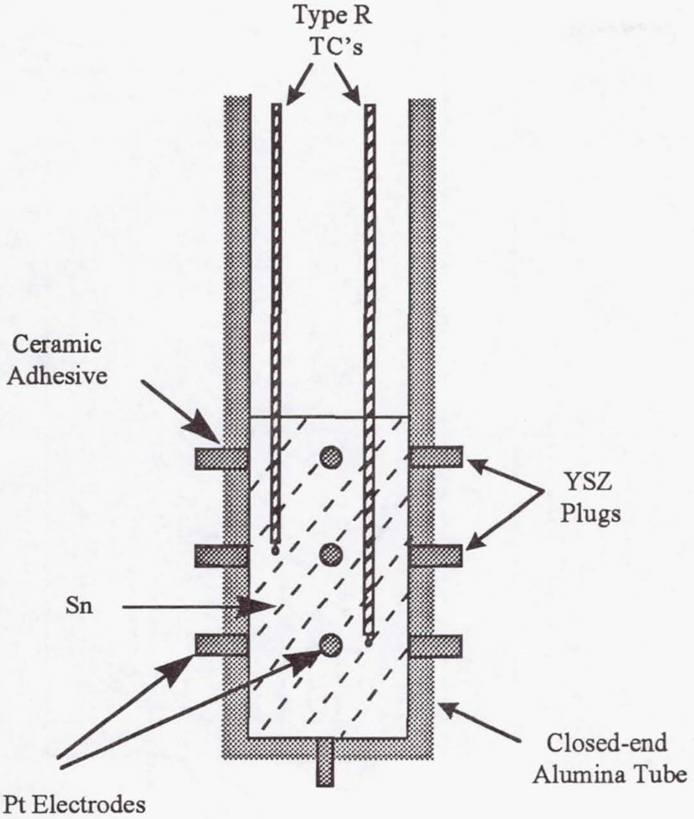

Figure 1a. Schematic of Flow Visualization Cell

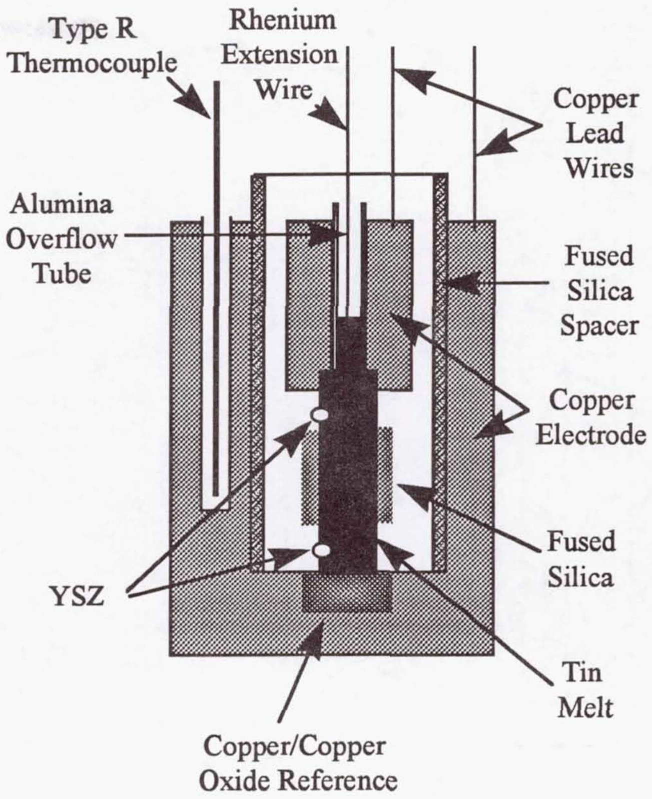

Figure 1b. Schematic of Diffusivity Measurement Apparatus

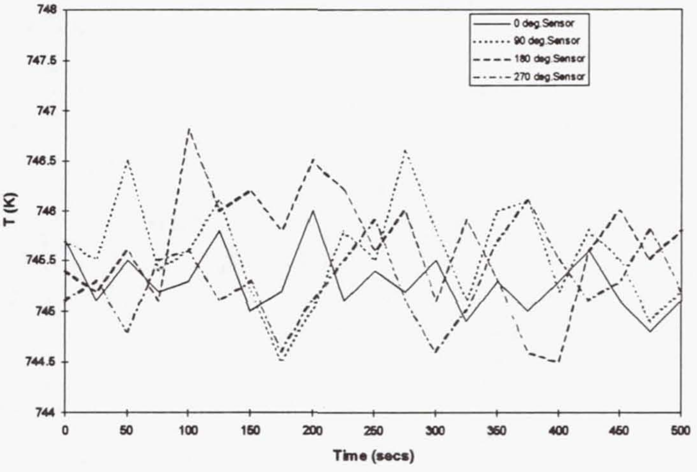

Figure 2

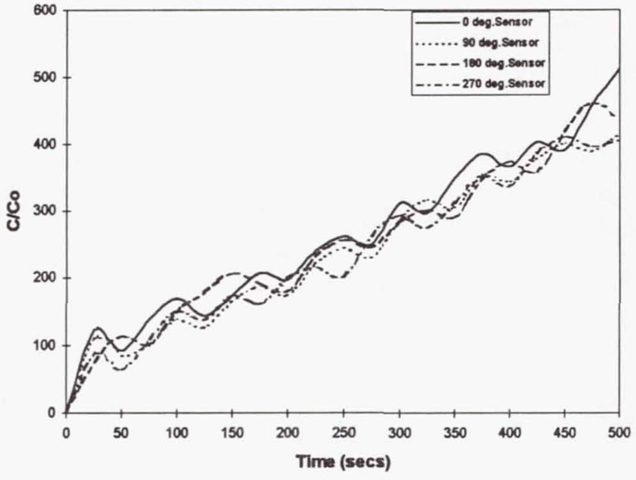

Figure 3

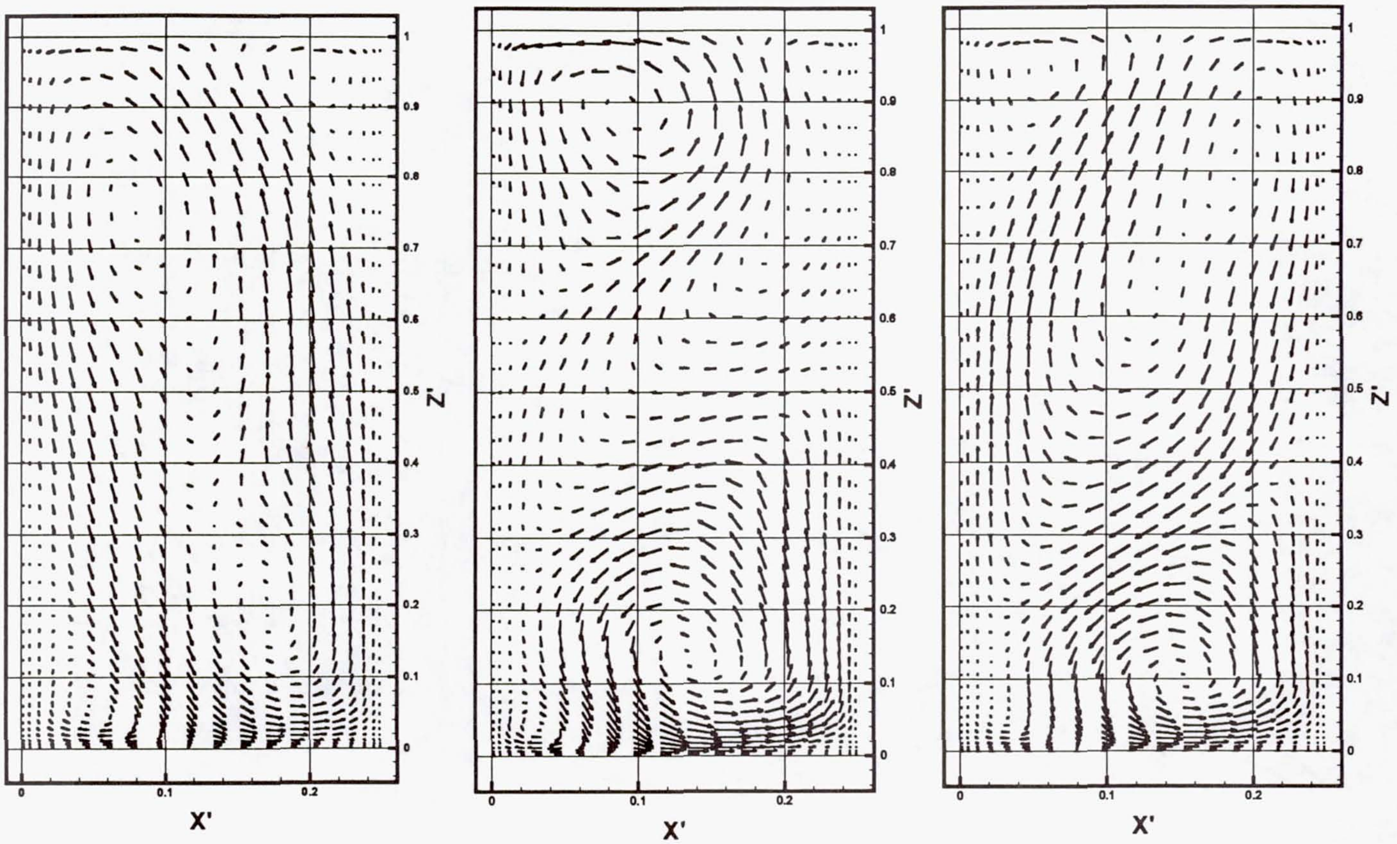

Figure 4

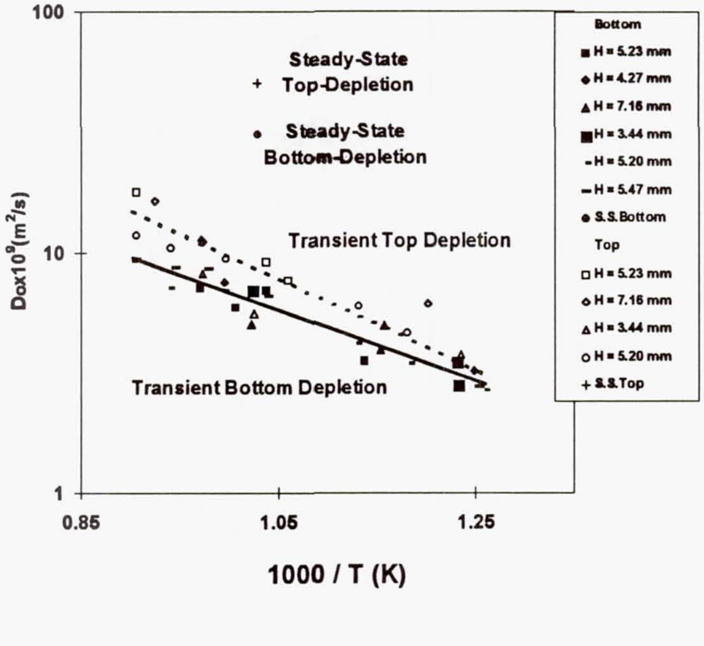

Figure 5a. Experimental Results for the Diffusivity of Oxygen in Liquid Sn (Circular Base Geometry)

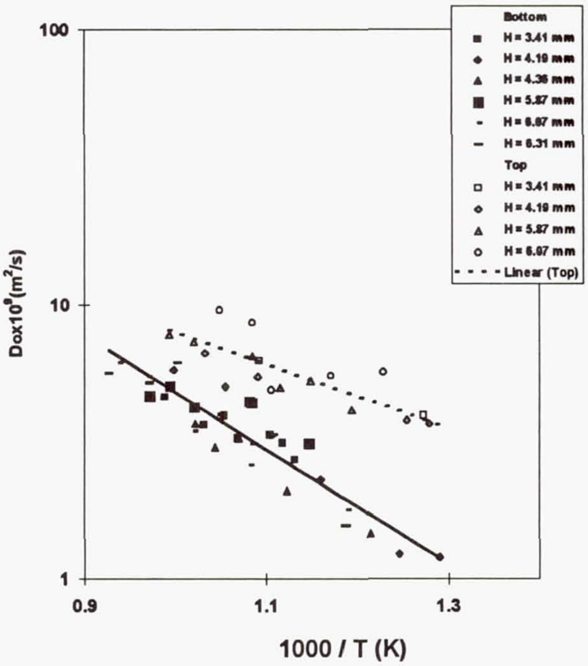

Figure 5b. Diffusivity Results with Liquid Sn in a Square Cross Sectional Geometry

COUPLED GROWTH IN HYPERMONOTECTICS (Primary Experiment)
AND
WETTING CHARACTERISTICS OF IMMISCIBLES (Glovebox Investigation)

Barry Andrews
Materials and Mechanical Engineering
University of Alabama at Birmingham

Sam Coriell
Metallurgy Division
National Institute of Standards and Technology

Introduction

The objective of this continuing investigation is to gain an improved understanding of solidification processes in immiscible alloy systems. A portion of the Coupled Growth in Hypermonotectics (CGH) study involves the development of experimental techniques which will permit solidification of immiscible alloys to produce aligned microstructures.[1] A parallel effort is underway to develop a model for the solidification process in these alloy systems.[2] Results from experimentation will be compared to those predicted from the model and utilized to improve the model. In order to permit solidification under the conditions necessary to form fibrous structures in these immiscible alloys, experimentation must be carried out under low-gravity conditions.

The first phase of the CGH experiment flew aboard the Life and Microgravity Spacelab (LMS) mission during the summer of 1996. Processing conditions were controlled in an attempt to force the production of an aligned fibrous phase in the microstructure of processed samples. This capacity could prove important in some of the proposed applications of immiscible alloys which include use as superconductors and as high performance magnetic materials. The Advanced Gradient Heating Facility (AGHF) was used to directionally solidify the immiscible alloys. Alloys in the aluminum indium system were studied and specialized aluminum nitride ampoules were used in order to control several undesirable effects that are sometimes observed during low gravity processing.

A separate but related investigation entitled Wetting Characteristics of Immiscibles (WCI) was carried out using the microgravity glovebox aboard the USMP-4 flight in the fall of 1997. This investigation was designed to study segregation mechanisms in immiscible alloys. The most common segregation mechanism in an immiscible alloy is gravity-driven sedimentation of the higher density immiscible liquid phase. This difficulty usually occurs during normal one-g processing in an attempt to form a dispersed microstructure. Microgravity processing should provide a solution to this problem. However, segregation has also be observed in low gravity processed immiscible alloys.[3-8] There are obviously some critically important factors that could influence segregation during microgravity processing. These factors include the interfacial energies between the phases,[9] alloy/ampoule reactions,[10] droplet migration due to gradients in surface tension brought about by temperature and compositional inhomogeneities,[8] the relative volume fractions of the immiscible phases,[5] and alloy/ampoule wetting characteristics.[5, 10-12]

Experimental Approach

Coupled Growth in Hypermonotectics. The CGH project involves the directional solidification of a range of alloy compositions over a range of growth rates. For the Life and Microgravity Spacelab mission, three alloy compositions in the aluminum-indium immiscible system were directionally solidified at the same rate of 1.0 μm/s. The samples were sealed under vacuum in aluminum nitride ampoules which contained several sample segments, pistons and a spring in order to maintain the desired growth conditions during processing. Thermocouples embedded in grooves in the exterior wall of the ampoule were used to monitor temperatures and determine thermal gradients and growth rates.

In order to avoid free surfaces generated due to contraction of the sample prior to and during solidification, a piston and high temperature carbon spring were utilized. In an attempt to reduce any residual gasses, which could have led to bubble formation, the alloys were vacuum induction melted. In addition, the ampoule components were all vacuum degassed at 1250° C for more than 6 hours. Samples were loaded and sealed under a vacuum of at least 1×10^{-4} Torr.

Wetting Characteristics of Immiscibles. For the WCI investigation, it was important that nucleation events, droplet coalescence and droplet migration be directly observable. This requirement dictated the use of a transparent analog sample (succinonitrile-glycerin) and a transparent cell assembly. Cells were constructed from standard 25mm x 75mm x 1mm microscope slides, separated by a 0.13mm thick Teflon® gasket. Nucleation on or droplet migration to the Teflon® gasket surface was monitored during the investigation. Fine gauge thermocouples were embedded in the gasket material on each edge of the cells in order to monitor nucleation temperatures and verify the thermal history of the cells during processing.

For processing, the sample cells containing the succinonitrile-glycerin mixtures were first heated to 90° C using a thermal chamber. The cells were held at this temperature from 15 to 25 minutes in order to allow homogenization. Once homogenized, the crew removed the cells from the thermal chamber and placed them on a backlit holder for observation using a stereo microscope during cooling. The microscope was outfitted with a video camera. The camera image was displayed on a laptop computer screen within the shuttle middeck area and was downlinked to the ground to permit simultaneous observation by the investigators. Twelve sample cells, with compositions covering the miscibility gap were processed.

Results and Discussion

Coupled Growth in Hypermonotectics. Several difficulties were encountered during processing of the CGH samples during the LMS mission. The first difficulty concerned a thermal gradient in the flight furnace that was substantially lower than that observed using the engineering model of the furnace. This reduced thermal gradient is expected to have a detrimental influence on the ability to maintain a stable solidification front, especially for the highest composition alloy. Another difficulty involved the loss of data telemetry from the AGHF during processing of the 18.5% In alloy. Unfortunately, there is no data recording capability within the AGHF facility, so all data on furnace position and sample temperatures were lost for this sample.

Radiographic analysis of the flight and ground based samples (see Figures 1 & 2) revealed the presence of several significant sized voids in two of the flight samples. In addition, the carbon springs had been destroyed in several samples when the aluminum-indium alloy leaked past the piston into the spring area. The voids that were present were undesirable for several reasons. First, voids provide free surfaces, which, with the high thermal gradients in this experiment can allow surface tension induced flow and undesirable mixing in the sample. There is also a potential problem with inconsistency in the growth conditions along the sample. The voids will obviously change the local cross-sectional area of the sample and result in local variations in both thermal gradient and growth rate. These variations in local conditions will make analysis of the results much more difficult.

One of the first questions being addressed in this study concerns the source of the voids. This information is especially important since additional flight experiments are planned. As a result, the primary focus of this project to date has been on determining the source of the voids. Dr. Witold Palosz at the Marshall Space Flight Center has been using a specially designed apparatus to determine residual gas content in fused silica ampoules used in semiconductor processing. Dr. Palosz's approach has been to break open an ampoule in a small vacuum chamber and determine the gas composition by slowly lowering the temperature and monitoring pressure changes. By noting the temperatures at which pressure drops occur (due to condensation) it is possible to identify the gases present.

A typical pressure vs. temperature plot obtained from the residual gas in an AlN flight ampoule is shown in Figure 3. This figure also contains calibration curves for nitrogen (open circles) and carbon monoxide (open triangles) which are the most difficult gases to distinguish by this technique. Compositional analysis of the gas obtained from the flight ampoules revealed that a significant amount of nitrogen was present in all cases. Preliminary indications are that carbon monoxide was also present in two of the ampoules. However, additional calibration runs are necessary to verify the presence of carbon monoxide. Work is continuing in this area.

Wetting Characteristics of Immiscibles. In the WCI glovebox investigation, a real-time video downlink was made available during the cooling phase for each sample to permit observation of the results and facilitate crew/investigator interaction during processing. The field of view was set so that events at the gasket edge could be observed. The magnification of the microscope was initially set so that the width of the video frame was approximately 1mm.

The first cells processed were those which were high in glycerin content. In the 70-55wt% GLY samples, succinonitrile-rich droplets appeared to nucleate more or less uniformly throughout the cell without preferential nucleation on the gasket. While droplets were found at the gasket surface, the contact angles were relatively high ($\approx 45^{\circ}$). However, dramatic changes took place when the glycerin content was lowered slightly.

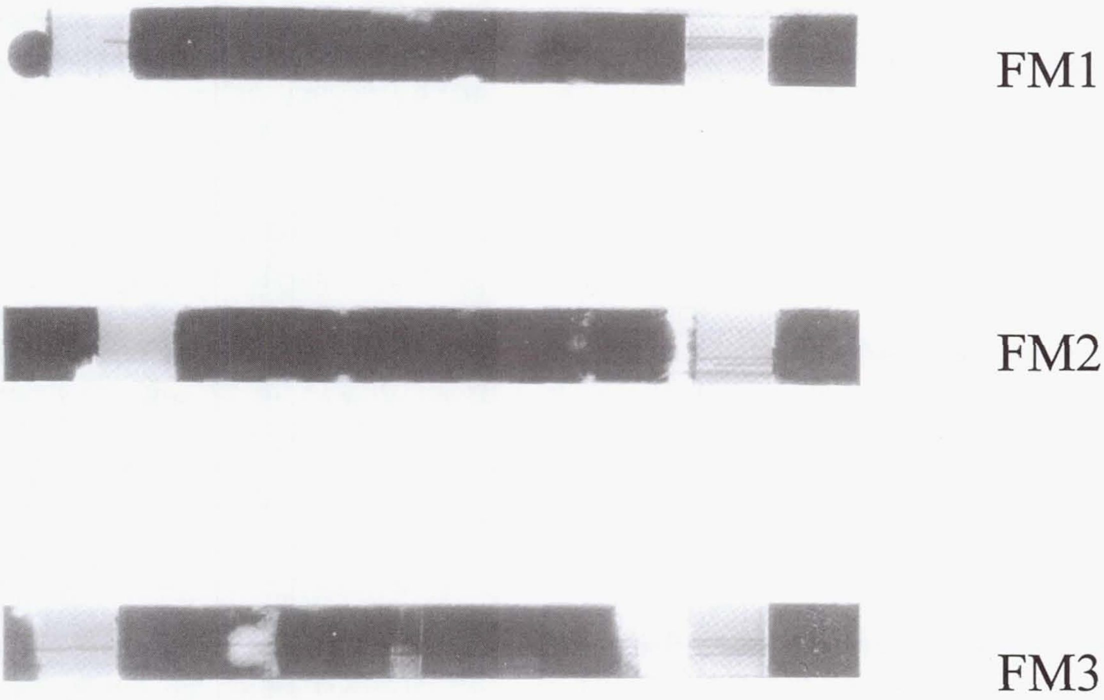

Figure1. Radiograph of the flight samples directionally solidified aboard the LMS mission.

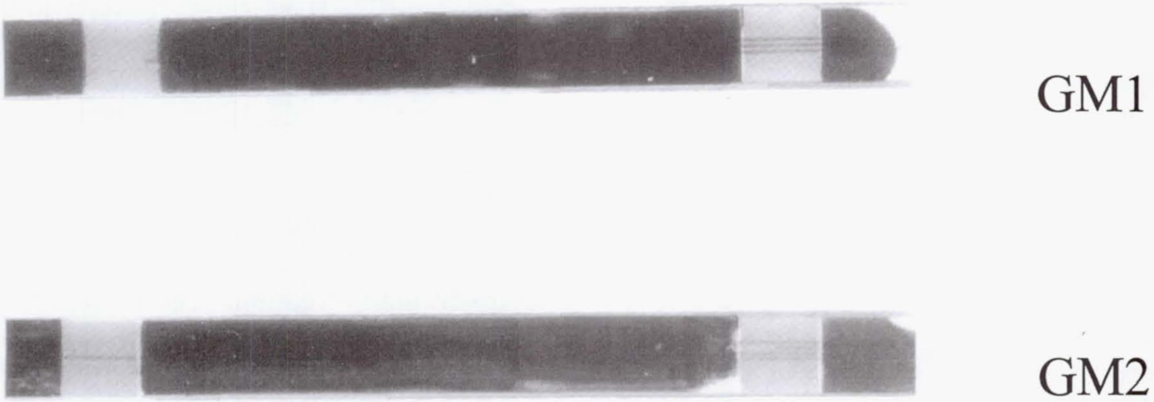

Figure 2. Radiograph of the ground processed samples GM1 and GM2.

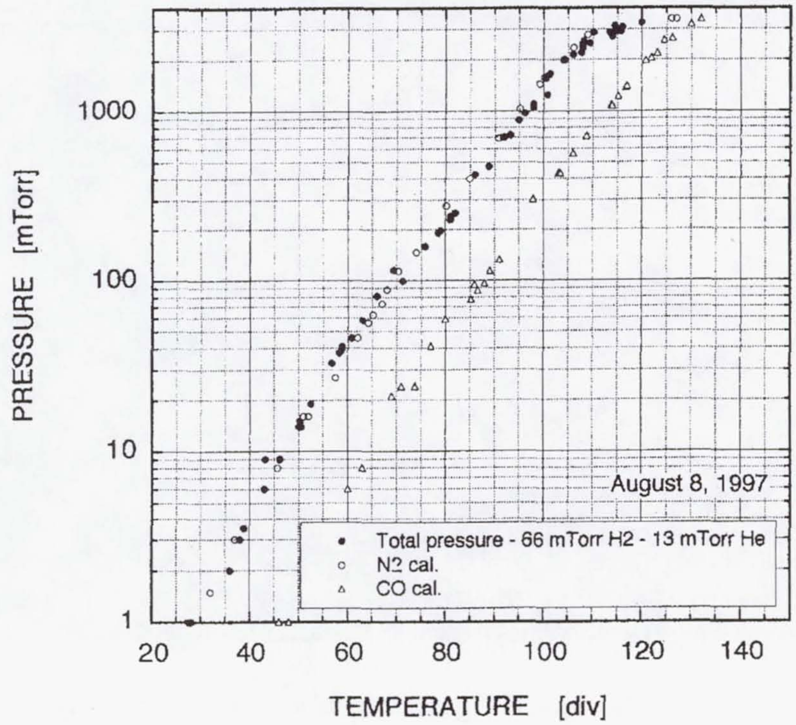

Figure 3. Pressure vs. temperature variations during a typical residual gas analysis. The open circles represent a nitrogen calibration curve while the open triangles represent a carbon monoxide calibration curve. The temperature scale covers a range of roughly 20K to 120K.

Cahn's analysis of wetting in immiscible systems indicates perfect wetting is anticipated between one of the immiscible liquid phases and a solid surface for compositions near the center of the miscibility gap. The range over which this perfect wetting occurs is anticipated to vary with the alloy systems and with the solid surface. For the system under study it appears this transition occurred somewhere between 55 and 50wt% GLY.

During cooling of the 50wt% GLY sample, events that were within the field of view appeared to be very similar to those observed previously. However, when the field of view was moved in order to scan around the perimeter of the cell it was apparent that the succinonitrile-rich liquid had accumulated around the edge of the cell in many locations. Contact angles approaching zero were observed in many areas and a film of succinonitrile-rich liquid was present in some locations, as shown in Figure 4.

It is unfortunate that the events of interest for this sample took place outside the field of view of the microscope. It would have been most informative to observe these events in order to determine if preferential nucleation took place at the gasket surface or if the film formed due to droplet migration alone. The next sample processed (45wt% GLY) exhibited similar behavior to the 50wt% GLY sample. Unfortunately, this sample had started to degrade due to the unusually high cabin temperature during this mission. As a result, there are too many unknowns to permit a sound analysis of this sample.

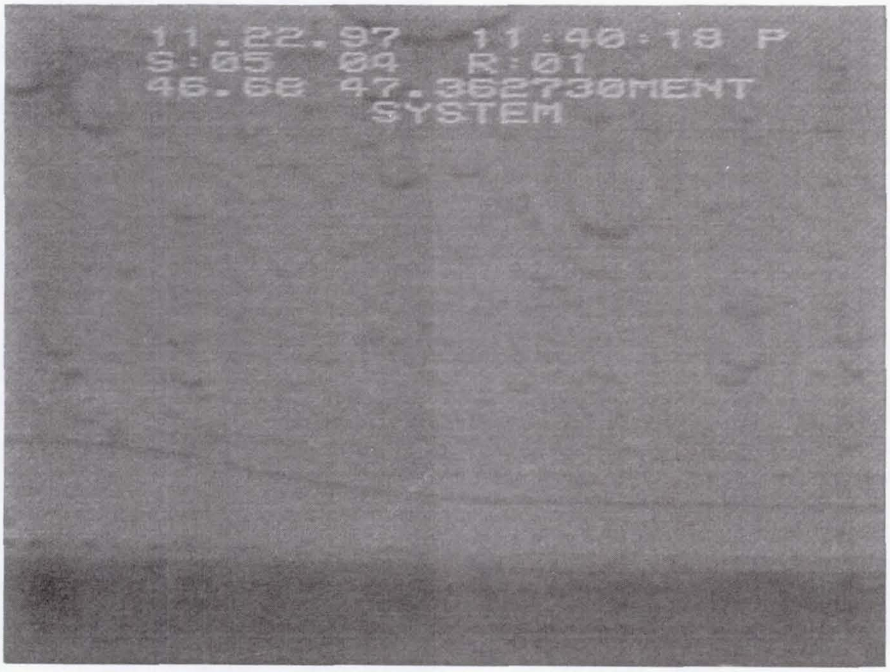

Figure 4. Perfect wetting of the Teflon® gasket in a succinonitrile-55wt% glycerin sample processed in the microgravity glovebox during USMP-4.

The remaining samples (most of which had a longer shelf life) were on the succinonitrile-rich side of the miscibility gap. Therefore, during cooling these samples all formed glycerin-rich droplets in a succinonitrile-rich liquid. In all cases the glycerin-rich droplets did not perfectly wet the Teflon® gasket. This non-wetting behavior permitted the formation of a uniform dispersion in most of these samples.

The last sample processed contained the least amount of glycerin (15wt% GLY) and exhibited unanticipated behavior. Samples of this composition had always produced a fairly uniform structure when processed on the ground. However, during microgravity processing, droplets of the glycerin rich liquid appeared to move away from the gasket surface yielding a small droplet-free region. It is assumed this behavior resulted because the glycerin rich droplets were completely non-wetting on the gasket surface.

Summary

To summarize our findings to date, three immiscible aluminum indium samples were directionally solidified during the LMS mission. Two of these samples contained voids that were sufficient in size to modify the solidification parameters locally during processing. In addition, the aluminum-indium alloy leaked past the uppermost piston in two of the flight ampoules and one of the ground based ampoules and destroyed the carbon spring. Most work to date has concentrated on identifying the gas present in the voids in order to help determine their source. Residual gas analysis revealed that the voids contained primarily nitrogen with some ampoules also containing smaller amounts of another gas, which, at this stage is thought to be carbon monoxide. Additional testing is being carried out to verify this finding.

Twelve samples in the transparent model system, succinonitrile-glycerin, were processed during the USMP-4 mission in the fall of 1997. A transparent cell assembly was utilized to permit direct observation of the events taking place. Sample compositions covered the majority of the composition range of the miscibility gap. A small composition range was identified in which the cell gasket surface was perfectly wet by the minor liquid phase. This perfect wetting led to the formation of a film of the minor phase along the perimeter of the cell. This behavior may explain difficulties encountered by some investigators in producing a uniform dispersion in microgravity processed immiscible alloy systems. An unexplained observation was made at one of the composition extremes where droplets were found to move away from the gasket surface leaving a depleted region during processing. Further analysis of the data is underway.

References

1. J.B. Andrews, J.S. O'Dell, A. Cheney, Y. Arikawa and L.J. Hayes, "Ampoule Design and Testing for Microgravity Experimentation on Coupled Growth in Hypermonotectics," Proceedings, 8th International Conference on Experimental Methods for Microgravity Materials Science, A Publication of the Minerals, Metals and Materials Society, R.S. Schiffman editor, 1996.

2. S.R. Coriell, W.F. Mitchell, B.T. Murray, J.B. Andrews and Y. Arikawa, "Analysis of Monotectic Growth: Infinite Diffusion in the L_2-Phase," Journal of Crystal Growth, 179, pp 647-657, 1997.

3. S.H. Gelles and A.J. Markworth, AIAA Journal, Vol. 16, No. 5, pp 431-438, 1978.

4. T. Carlburg and H. Fredriksson, "Microgravity Studies in the Liquid-Phase Immiscible System: Aluminum-Indium," Met. Trans. A, Vol. 11, pp 1665-1676, 1980.

5. J.B. Andrews, A.C. Sandlin and P.A. Curreri, "Influence of Gravity Level and Interfacial Energies on Dispersion-Forming Tendencies in Hypermonotectic CuPbAl Alloys," Met. Trans. A, Vol. 19, pp 2645-2650, 1988.

6. H.C. deGroh III and H.B. Probst, "Effects of Crucible Wetting During Solidification of Immiscible Pb-Zn," NASA Technical Memorandum 101872, 1988.

7. A. Deruyterre, L. Froyen, "Melting and Solidification of Metallic Composites," Proceedings for the Workshop on Effect of Gravity of Solidification of Immiscible Alloys, Stockholm, ESAS, SP-219, pp 65-67, 1984.

8. L. Ratke, W.K. Thieringer, H. Fishchmiester, "Coarsening of Immiscible Liquid Alloys by Ostwald Ripening," Proceedings of the Norderney Symposium on Scientific Results of the German Spacelab Mission D1, pp 332-341, 1986.

9. P.A. Curreri, J.M. Van Alstine, D.E. Brooks, S. Bamberger, R.N. Snyder, Marshall Space Flight Center Preprint Series No. 85-0156, Marshall Space Flight Center, Huntsville, Alabama, 1985.

10. A.B. Cheney, J.B. Andrews, "The Evaluation of Ampoule Materials for Low-g Processing of Immiscible Alloys," Proceedings of the 6th International Symposium on Experimental Methods for Microgravity Materials Science, R.S. Schiffman editor, pp 191-198, 1994.

11. S.H. Gelles, NAS8-32952, Final Post Flight Report, MEA A1 Experiments, 1984.

12. C. Potard, Materials Processing in the Reduced Gravity Environment of Space, Elsevier Science Publishing Co., New York, New York, pp 543-551, 1982.

THE EFFECT OF CONVECTION ON MORPHOLOGICAL STABILITY DURING COUPLED GROWTH IN IMMISCIBLE SYSTEMS

Barry Andrews
Materials and Mechanical Engineering
University of Alabama at Birmingham

Sam Coriell
Metallurgy Division
National Institute of Standards and Technology

Introduction

The objective of this study to determine the influence of convection on the morphological stability of the solid-liquid interface during directional solidification in immiscible systems. Recent findings[1,2] indicate that gravity level has a dramatic influence on the structure obtained during directional solidification in these systems. Evidence from ground based experimentation by the investigators indicates this variation in microstructure may be due to fluid flow which occurs on both a microscopic scale at the solid-liquid interface and on a macroscopic scale during the solidification process.[1-3] The overall fluid flow generated appears to reduce the stability of the solidification front during coupled growth influencing the development of desired fibrous microstructures.[1-4]

This study combines observations made utilizing transparent metal-analog systems with a detailed analysis of fluid flow on a microscopic and macroscopic scale. One segment involves a theoretical analysis to determine the anticipated fluid flow at the solidification front. Another segment involves experimentation to either verify or disclose weaknesses in the theoretical portion of the analysis. The findings will make a significant contribution to a better understanding of the role of fluid flow on steady state solidification and coupled growth in immiscible alloys.

Background

It should be theoretically possible to process a hypermonotectic alloy under conditions that would result in coupled growth between the L_2 and S_1 phases.[1-5] Solidification under these conditions result in an aligned fibrous microstructure consisting of fibers of the L_2 phase in a higher volume fraction than that found for the monotectic composition. The composition variations and temperature gradients during solidification of a hypermonotectic sample could be maintained such that the liquid temperature never fell into the region of liquid immiscibility. As a result, the primary phase, which is L_2 in this case, would not form in advance of the solidification front and the sedimentation problems usually associated with processing hypermonotectic alloys could be avoided.[1-4]

Unfortunately, alloys processed under conditions which should easily result in morphological stability and a macroscopically-planar solidification front usually do not produce the desired microstructure.[1-4] A simple analysis reveals that steady-state directional solidification in a hypermonotectic alloy results in a composition profile that causes the liquid density to increase with distance from the solidification front. This variation can lead to convective instability.

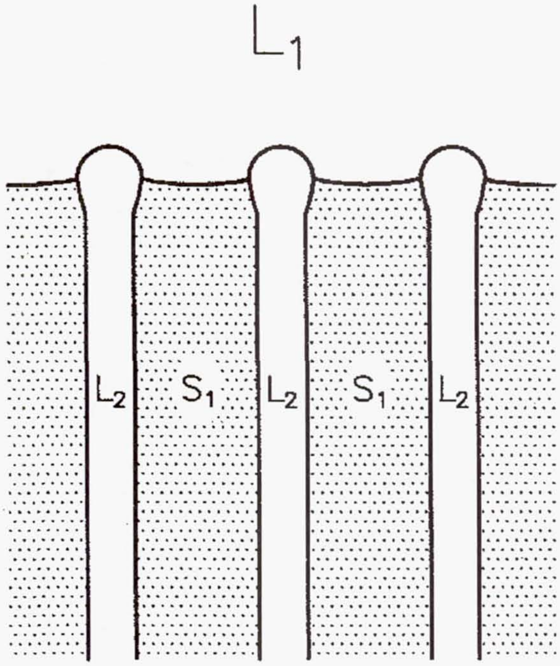

Figure 1. Schematic of the solidification front observed during coupled S_1-L_2 growth in hypermonotectic samples.

Recent results indicate a strong dependency of the microstructure on gravity level and thus convection during processing[1,2]. Low-gravity conditions obtained using NASA's KC-135 zero-g aircraft resulted in the formation of an aligned fibrous microstructure during directional solidification of metallic samples, while a less desirable, dispersed microstructure was produced during the high-g (1.8g) portions of flight. These results support the hypothesis that the breakdown of coupled growth is due, at least partially, to buoyancy driven flows.

Development of the Model

The first step in development of the model involves determining the temperature and solute distribution in the liquid at the solidification front, which must be done both on a microscopic and macroscopic scale. Figure 1 shows the typical structure at the solidification front which is being utilized as a starting condition for the model. Obviously, the thermal and solutal fields will lead to density variations in the liquid which will tend to drive convection. The model under development takes into account the microscopic density variations in the liquid between the fibers at the solidification front and the macroscopic density variation brought about due to the general depletion of solute in advance of the solidification front for a hypermonotectic alloy.

For growth of a bulk sample of hypermonotectic composition, two distinct length scales appear, namely, the interrod spacing, which is of the order of micrometers, and the sample size, which is of the order of centimeters. We are initially considering these as separate problems, and will only attempt to study their interaction after a thorough understanding of each is developed. For growth at the monotectic composition, the central problem is understanding the microscale phenomena, while for growth at hypermonotectic compositions, there is the possibility of bulk convection which may disrupt the coupled growth of composite structures.

At the microscale level, the coupled growth of a monotectic has many similarities with the coupled growth of eutectics. Recently, the theory of coupled eutectic growth, which is based on the Jackson and Hunt theory,[6] has been extended by numerical computations[7] and the underlying assumptions have been elucidated.[8-10] Initially, we extend the Jackson-Hunt eutectic theory to monotectic growth. While the basic geometry of eutectic and monotectic growth are similar, in eutectic growth it is an excellent approximation to neglect diffusion in the two solid phases. For monotectic growth, one of the phases formed is now a liquid and diffusion is clearly important in this phase.[11] In addition, in monotectic growth there is a fluid-fluid interface which can give rise to fluid flow driven by gradients of surface tension.

On the macroscopic level, except for growth at the monotectic composition, the solute concentration changes from approximately the monotectic composition at the interface to the bulk composition far from the interface. To treat the macroscopic flow problem, we propose to average over the microscopic features. Basically, this will provide boundary conditions at the interface, which will differ from the single phase problem, but will allow us to treat the bulk flow using methods previously developed.[12] Such calculations would determine the processing conditions, namely, temperature gradients, growth velocity, and bulk composition, necessary to avoid the onset of thermosolutal convection. For hypermonotectic compositions sufficiently far from the monotectic, the system will be convectively unstable. We have begun use of a finite element code to model the fluid flow in the unstable regime. Such calculations provide flow velocities and determine macrosegregation during monotectic growth. The further development of this model will lead to a better understanding of the relative significance of the factors effecting solidification in immiscible systems.

Experimental Verification

Experimentation is being carried out for verification of the model. Directional solidification is carried out using a temperature-gradient-stage microscope and is archived using time-lapse video tape recording. This approach facilitates determination of the flow velocities for comparison with velocities predicted from the model. The succinonitrile-glycerol $(CH_2CN)_2$-$(C_3H_5(OH)_3)$ system is being utilized for this study. Polystyrene microspheres will be used in some of the cells as tracer particles to monitor flow.

Initial experimentation was carried out with very small cell spacings (approximately 10µm). It was felt that the small spacing between cell walls would result in a very large damping effect on fluid flow. In addition, the first sets of experiments are being carried out using a horizontal (i.e. flat) cell orientation in order to minimize gravity driven flow during processing. This approach permits an estimation of the influence of surface tension driven flow on the solidification process without the added complication of extensive bouyancy driven flow. Interface stability has been obtained in hypermonotectic samples for this thin, horizontally oriented cell configuration (see Figure 2). In addition, several interesting observations have been made concerning surface tension driven flow and Marangoni droplet migration when the interface is marginally unstable (see Figure 3). Small scale mixing due to surface tension driven flow is obvious under these conditions.

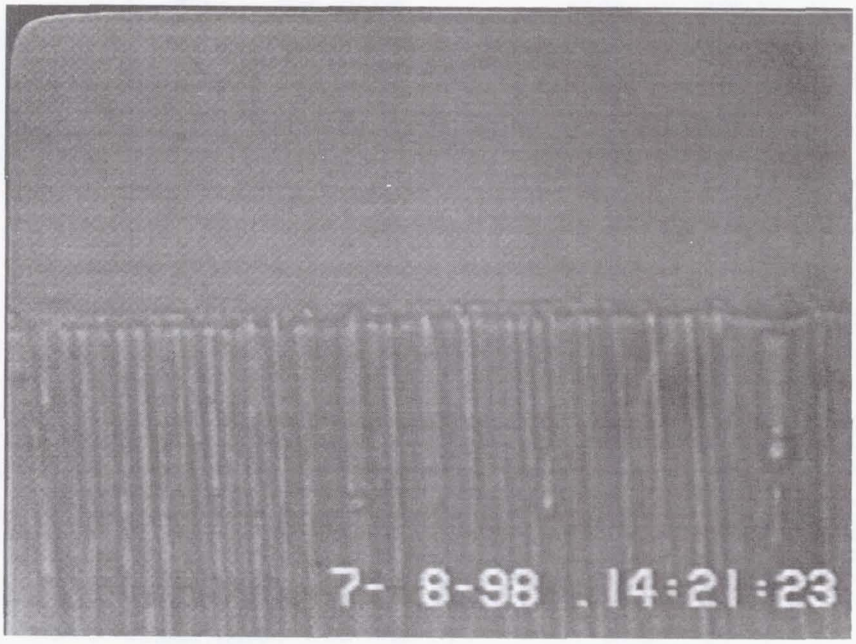

Figure 2. Interface stability during directional solidification of a hypermonotectic succinonitrile-glycerol sample.

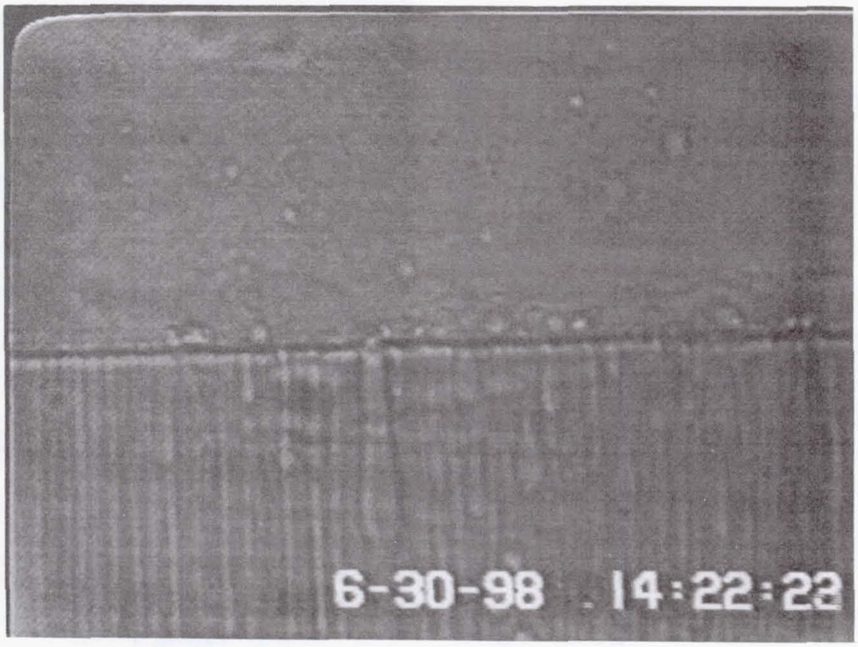

Figure 3. A marginally unstable solidification front obtained during directional solidification of a hypermonotectic succinonitrile-glycerol sample.

After the influence of these surface tension driven flows are understood and documented, the cell orientation will be changed to allow normal vertical directional solidification. After results are obtained for a small cell spacing, the cell thickness will be increased slightly in order to decrease damping and the experimentation repeated. Close attention will be paid to any changes in fluid flow resulting from the reduced damping. The thickness of the cells will be systematically increased and the effect of reduced damping quantified. The resulting increase in fluid flow is expected to eventually lead to disruption of the coupled growth process at the solidification front.

Summary

This study will investigate the influence of fluid flows on processes at the solidification front and the structures obtained during directional solidification of immiscible alloys. The first portion of the investigation involves the development of a model describing fluid flow during the solidification of immiscible materials. Another portion of the project involves experimentation designed to test the ability of the theoretical model to predict fluid flow in samples processed under one-g conditions and the effect of this fluid flow on sample morphology. Fluid flow will be regulated through the use of thin sample cells that will help damp fluid motion. The findings from this study will result in a dramatic improvement in the level of understanding of immiscible alloys and the influence of fluid flow on the coupled growth process.

References

1. J.B. Andrews, A.L. Schmale and A.C. Sandlin, "The Influence of Gravity Level During Directional Solidification of Immiscible Alloys," Journal of Crystal Growth, 119, pp 152-159 (1992).

2. L.J. Hayes and J.B. Andrews, "The Influence of Convection on Coupled Growth in Al-In Hypermonotectic Alloys," Proceedings, 6th International Conference on Experimental Methods for Microgravity Materials Science, A Publication of the Minerals, Metals and Materials Society, R.S. Schiffman editor, pp 167-174 (1994).

3. J.B. Andrews, L.J. Hayes, and S.R. Coriell, "Instabilities During Coupled Growth of Hypermonotectics" Advances in Space Research, Vol. 16, pp(7)177-(7)180 (1995).

4. L.J. Hayes and J.B. Andrews, "The Effect of Convective Instability on Coupled Growth in Hypermonotectic Alloys," Solidification and Gravity, Transtec Publications, Vol 215-216, pp 233-240, (1996).

5. B. Andrews, L. Hayes, Y. Arikawa, S. O'Dell and A. Cheney, "Coupled Growth in Immiscible Alloys," Space Processing of Materials, Proceedings SPIE - The International Society for Optical Engineering, ed. N. Ramachandran, Vol. 2809, pp 12-22, (1996).

6. K.A. Jackson and J.D. Hunt, "Lamellar and Rod Eutectic Growth," Transactions of the Metallurgical Society of AIME, 236 (1966) 1129-1142.

7. D.A. Kessler and H. Levine, J. Crystal Growth 94 (1989) 871.

8. K. Brattkus, B. Caroli, C. Caroli, and B. Roulet, J. Phys. France 51 (1990) 1847.

9. P. Magnin, R. Trivedi, "Eutectic Growth: A Modification of the Jackson and Hunt Theory", Acta Metall. Mater. Vol. 39, No. 4, pp. 453-467, 1991.

10. B. Drevet, D. Camel, J.J. Favier, "Solute Boundary Layer and Convection in Solidification of Eutectic Alloy", Proceedings VIIth European Symposium on Materials and Fluid Sciences in Microgravity, Oxford, UK, 10-15 September, 1989, ESA SP-295 (January, 1990) pp. 101-108.

11. S.R. Coriell, W.F. Mitchell, B.T. Murray, J.B. Andrews and Y. Arikawa, "Analysis of Monotectic Growth: Infinite Diffusion in the L_2-Phase," Journal of Crystal Growth, 179, pp 647-657, 1997.

12. S.R. Coriell and G.B. McFadden, "Instability During Directional Solidification: Gravitational Effects," Progress in Low-Gravity Fluid Dynamics and Transport Phenomena, J.N. Kostes and R.L. Sani, Editors, (AIAA), (1990).

NUCLEATION AND GROWTH MECHANISMS UNDERLYING THE MICROSTRUCTURE OF POLYMER FOAMS PRODUCED BY DYNAMIC DECOMPRESSION AND COOLING

Robert Apfel and David Wu
Department of Mechanical Engineering
Yale University
New Haven, CT 06520-8286
203-432-4346, robert.apfel@yale.edu
203-432-4256, d.wu@yale.edu

Abstract

The control of the microstructures of lightweight polymers, polymer blends, polymer-metal composites, and amorphous metals depends in large part on the procedures by which these materials are created and on an understanding of the nucleation and growth mechanisms underlying these procedures. We are further developing a novel approach for producing lightweight, foam structures — Dynamic Decompression and Cooling (DDC) — and using this approach for systematically providing data to new models for the underlying nucleation and growth mechanisms.

DDC involves heating and mixing polymer (and/or other source) materials under pressure in the presence of a volatile phase. Non condensable gas super-pressurizes the mixture. The rapid decompression of this mixture results in the boiling of the volatile phase (aided by the supersaturation of the non-condensable gas), and the cooling of the melt due to latent heat of vaporization of the volatile phase. The result is a solid, open-foam structure of low density possessing microstructures that differ greatly from those commonly found in polyethylene and polypropylene foams commercially available. The reasons for the difference stem from the greatly different nucleation and growth mechanisms as compared to extruded foams.

These mechanisms are shrouded in the complexity of the process. In particular, there are several nucleation and growth mechanisms occurring in a short period of time. Upon decompression, there is supersaturation of the non-condensable gas and superheating of the volatile phase. Bubble nucleation and growth follow, controlled by evaporation of the volatile phase and diffusion of the non-condensable phase. Supercooling of the melt occurs as the volatile phase takes its latent heat of vaporization from the melt. Growth is dependent on transport properties including the temperature-dependent viscosity and heat conductivity. Solidification may or may not involve a latent heat of fusion depending on whether crystallization occurs or an amorphous phase is formed.

In order to understand these nucleation and growth mechanisms, we must be able to vary the operating parameters over a wide range, and we must be able to follow the transient process in detail. Therefore, we shall use high speed video to record the process, which occurs in a fraction of a second, and to instrument the cell to record the time-dependent temperature and pressure in the mixture as it is decompressed. This data will provide input to the theoretical formalism, and will complement post-analysis data ranging from mechanical testing to electron micrographs and x-ray diffraction. We shall document the conditions at which the structure of foams changes

from closed cell to open cell, and we shall correlate microstructure with nucleation and growth mechanisms.

The microgravity environment may aid in providing idealized conditions for such tests. In particular, phase separation, and layering and stratification effects are minimized so that uniform initial states can be achieved prior to decompression. Also, non-uniform heating produces convective effects that are absent in zero-g, allowing for the study of transient processes and the resulting foams, which should be isotropic. These considerations are especially important when considering polymer blends and polymer-metal composites intended for high temperature applications (e.g. significantly above 200°C) because of phase separation and density stratification effects. Ground-based studies will provide a baseline for future microgravity work.

Motivation to understand mechanisms underlying foam production

Although polymer foams have been manufactured for decades and the state of the art in the production of polymer and polymer blended foams is advanced in many respects [1], models of the nucleation and growth processes that allow for the accurate prediction and control of both the microstructure and the macrostructure (e.g. foam cell size and other characteristics) have been conspicuously absent, and empiricism has dominated. We are left with a number of unanswered questions. The primary one has to do with the development of an understanding of the underlying nucleation and growth mechanisms in the generation of crystalline polymer foams. Whereas much has been done in industry to apply closed cell foams, their appears to be far less known about open cell foams produced by highly transient processes. The micro-structures and morphologies of such foams possess many intriguing properties, which may lead to practical applications of new materials, if the process can be controlled.

Recent applications of DDC to polymer foams

Our most recent work has focused on polymers. Experimental work has proceeded with polybutylene terephthalate (PBT) and polyolefins, polyethylene and polypropylene (PE and PP). Whereas earlier work focused on immiscible droplet dispersions as the blowing phase, the current work has employed various organic solvents, which have neglibile solubility of the solid phase at room temperature, but which dissolve into the polymer at the melt temperatures of the respective materials and at elevated pressures which prevent the volatile phase from boiling until rapid decompression.

We have begun with PBT because it has become an important engineering thermoplastic polyester for many applications requiring good solvent resistance, mechanical properties, dimensional stability, and good processability.[2] It has a relatively high crystallinity (60%), which is hard to suppress by conventional cooling methods even though it has a glass transition temperature above room temperature (Tg= 67°C).[3],[4] High crystallinity means relatively low impact resistance and toughness, which excludes PBT from some important applications, such as automobile body panels.

We have also begun with PE and PP, because they are the world's most widely used polymers for numerous applications, and have a large potential market as lightweight cellular plastics due to excellent chemical and physical properties and low price.[5] Like many crystalline thermoplastics, PE and PP are difficult to produce as highly expanded cellular materials by conventional foaming processes.[6] A sharp decrease of their viscosity over a narrow temperature range above the melting point makes expansion hard to control. In addition, the rapid crystallization rate and relatively slow cooling rate for the bulk polymer lead to the collapse of cell structure in the stabilization phase of the expanded polymer. Although this processing difficulty is eliminated by crosslinking PE before the foaming process, the need for expensive processing techniques has caused the cost per unit volume to exceed that of low density polystyrene (PS) and polyurethane foams.[7],[8] Dow Chemical developed "Ethafoam" polyethylene foaming technology (without crosslinking) in the 1960s[9], and has been improving the technology by altering the blowing agents from chlorofluorocarbon (CFC) to isobutane since then.[10],[11]

We have processed PBT, PET, HDPE, LDPE, LLDPE, PP resins as well as PBT/PP and HDPE/PP blends in our DDC apparatus. All resulting materials are open, porous and interconnected foams with a density as low as 10% of the original resins. They readily modify the toughness and strength of the original polymers. Preliminary examination of the processed materials by SEM show a variety of foam structures with fibers, granules and sheets quite prevalent. We summarize some of the microstructures observed for PBT, HDPE and PP in Table 1. Specific data of micrographs follow.

Table 1: Microstructures Observed in Initial Polymer Studies

Polymer resin	**original density** (g/cm^3)	**foam density** (g/cm^3)	**microstructure** (SEM imaging)
PBT	1.310	0.13~0.26	fibers, granules, sheets
HDPE	0.955	~0.08	sheets, granules, ribbons network, multilamellas, mushroom-like crystals
PP	0.900	~0.08	sheets, multilamellas, granular film

SEM imaging description

Figure 1 shows the basic microstructures of PBT foams produced by the DDC process using chloroform as blowing agent. In figure 1a, we see a band of thin fibers with diameter as small as 100 nm, indicating that the polymer chain orientation is involved in the process. In figure 1b, we see granular aggregates with a diameter of several micron. There are pores as small as micron in the aggregates. This structure looks somewhat like that of phases separated from polymer solution. In figure 1c, we see the fiber web combined with some granules. This is very unusual structure, which is ideal to enhance the foam strength, but hard to imagine how the structure was generated. In figure 1d, we see a curved fiber which corresponds to one part at failure after tensile deformation. The specimen is drawn at room temperature (below Tg of PBT). The fiber is extended and necked with drawing. After failure, the internal stress drives it to shrink.

Figure 2 shows some unique microstructures found for HDPE, PP and PP/PBT blended foams produced from the DDC process. In figure 2a, we see the folded sheets (HDPE foams) composed of multilayers with different end edges on the surface of the sheets. Each thin layer is polyethylene lamellae. The multilamellar structure looks like polyethylene hedrites grown from

Fig. 1

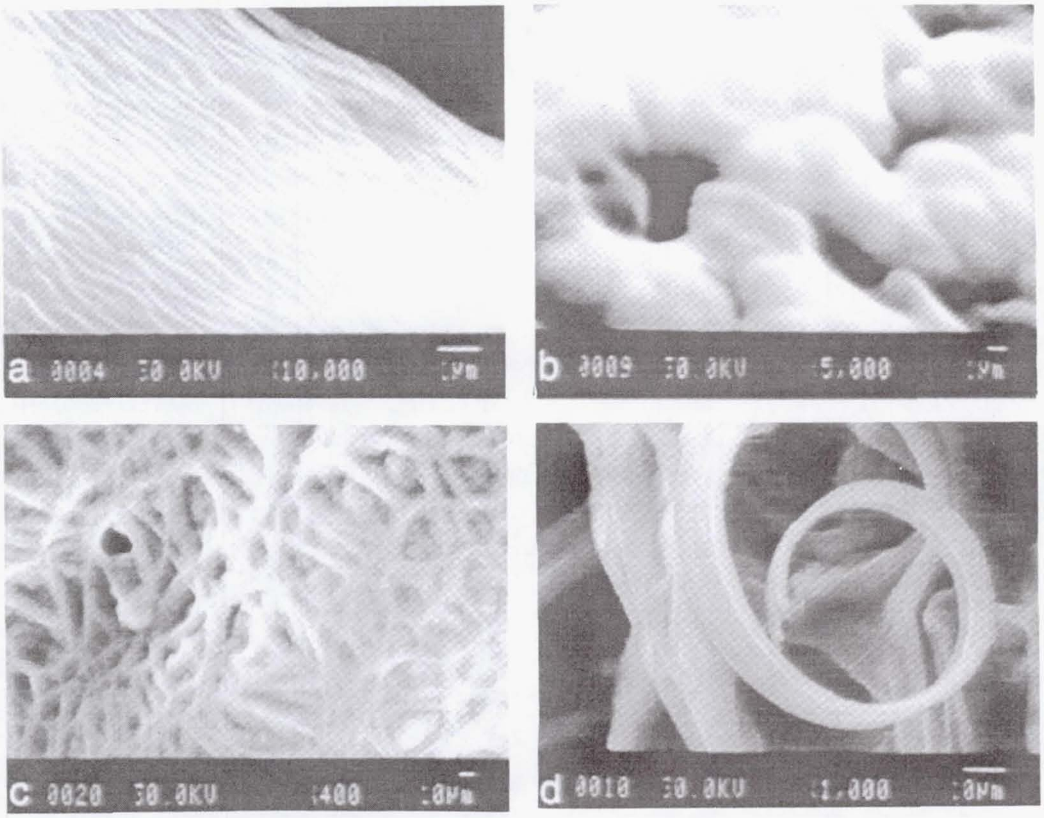
a 0004 30.0KV X10,000 1μm
b 0009 30.0KV X5,000 1μm
c 0020 30.0KV X400 10μm
d 0010 30.0KV X1,000 10μm

Fig. 2

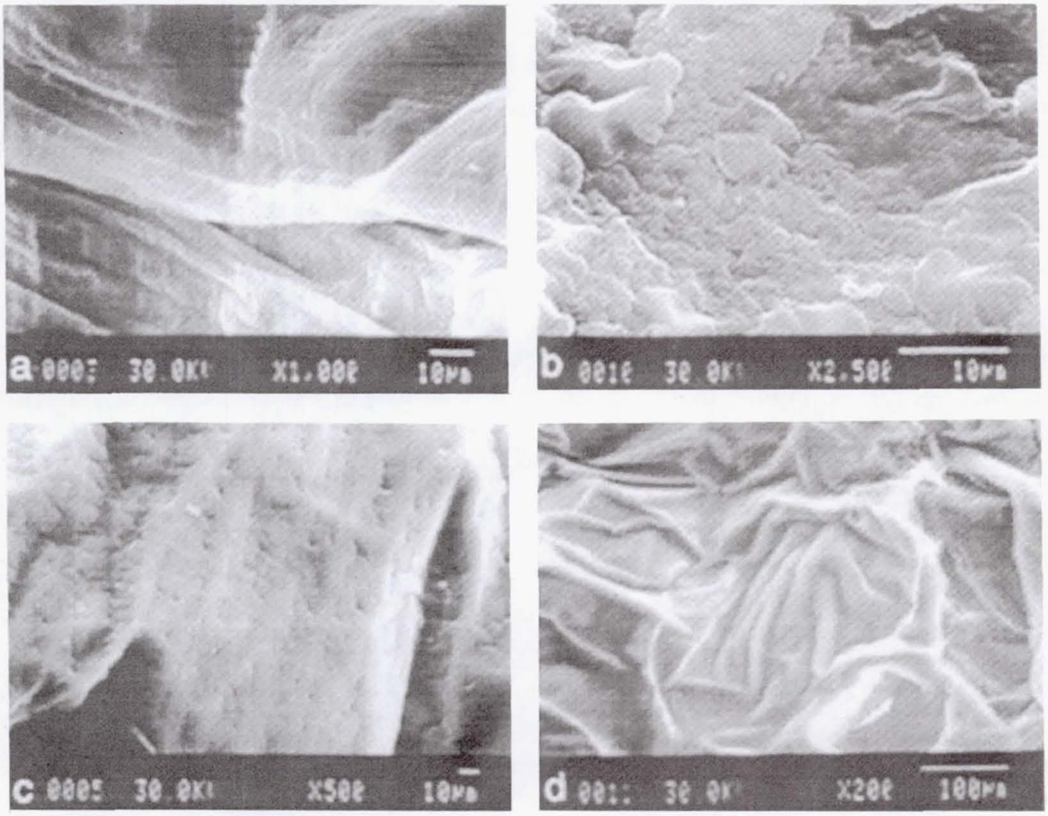
a 0003 30.0KV X1,000 10μm
b 0016 30.0KV X2,500 10μm
c 0005 30.0KV X500 10μm
d 0011 30.0KV X200 100μm

a supercritical solution[12] but with much condensed geometry. In figure 2b, we see mushroom-like structures for HDPE foams. These order structures are polyethylene crystals but are not the same as usual polyethylene spherulites grown from a melt. In the figure 2b, we also see ribbon networks in the background. They are not totally amorphous because HDPE has as high as 90% crystallinity, and the mushroom-like crystals are clearly grown from them. Note that all these regular structures are generated in the DDC transient process. In figure 2c, we see the granular sheets for PP foams. The granules are regularly arranged in the sheets. In figure 2d, we see the folded sheets structure for PP/PBT (80/20) blended foams. Although many microstructures are observed for either PP or PBT foams, we do not see them for the blend. This indicates that homogeneous mixtures may be generated by DDC process, even though PP and PBT are not miscible by conventional thermal/mechanical mixing.

Questions posed by initial DDC tests with polymers

DDC can produce lightweight polymeric materials with a variety of microstructures. Although we can produce a variety of microstructures by the DDC process, we do not understand the nucleation and growth mechanisms involved in the foaming process. How are microstructures generated in the transient DDC process? This essential question is being addressed through experimental and theoretical studies of nucleation and growth mechanisms in polymer foam synthesis using DDC. A better understanding of the underlying processes should permit some degree of control of the microstructure for a variety of applications.

Nucleation and growth modeling

The nucleation and growth process that is being developed assumes crystalline polymers. Instead of exploiting the glass transition temperature of a polymer to freeze in the foam structure, the process operates above the crystalline polymer's melting point. The initial state is a solution of polymer and a volatile solvent. As decompression is effected above the boiling temperature of the solvent, the solvent nucleates gas bubbles, which then grow and cool the solution. When the solution enriched in polymer is cooled below the crystallization temperature, nucleation of polymer crystallite begins. This process thus involves the nucleation and growth of bubbles, which induce the nucleation of polymer crystallites, followed by simultaneous growth of bubbles and crystals. The rationale for using this double nucleation and growth process is that, depending on the type of solvent used and the decompression schedule, the microstructure of the crystalline polymer (such as percent crystallinity or the distribution of grain orientations and grain sizes) within the microcellular foam structure may also play a role in determining the final property of the foam. To successfully model this process from a fundamental point of view, a large number of parameters are required to calculate the nucleation and growth rates of both the gas bubbles and the polymer crystals, which must be coupled thermally by heat flow calculations and chemically by diffusion calculations. The details of the nucleation and growth modeling are described in detail in the proposal submitted to NASA.

Broad parameter study of polymer foam synthesis

The materials that result from the DDC process have very complex structures both in cell or pore macrostructures and in microstructures, which may, in some instances, follow a fractal growth mechanism. Our challenge is to produce a particular structure by systematic variation of processing parameters. At our disposal for variation are: polymer material (including blends), blowing material (various solvents and/or immiscible dispersions), mass fraction of blowing material, non-condensable gas pressure (beginning and end), initial starting temperature (above melt temp. or somewhat below). We are focusing on the following systems: PE, PP, PBT, PBT/PP blends, PE/PE blends, and PP/metal alloy blends.

Apparatus Characteristics and Capabilities

It is clear that if the theoretical modeling of nucleation and growth in this very complex system is to provide useful predictions, there must be specific data provided to the model from our experimental program. The heart of the experimental apparatus is a pressure cell in which the ingredients can be added, heated under pressure, stirred, and decompressed. A pressure cell (1500 psi max pressure) will host the polymer composition. The heating (and cooling) will be done actively by circulating a temperature-controlled hot oil (e.g. silicone oil) through a sealed copper tube wrapped around the bottom of the container holding the melt and blowing matterial. (Alternatively, we will use resistance heating and fluid cooling.) The bottom of the container will be aluminum or aluminum-clad to aid in thermal conduction. The upper portion of the container will be glass or quartz, for viewing purposes. Just prior to decompression, the fluid circulating though this system will be switched to a cold, low viscosity fluid in order to remove heat from the container so that reheating effects are minimize, preserving the sample. Instrumentation to measure the temperature and pressure as a function of time, as well as to film at least the initial stages of decompression, will permit real-time pressure measurement in the cell as a function time, real-time temperature in the melt as a function of time, filming and light scattering, measurement of liquid-vapor interfacial tension, and inferred properties such as the liquid-solid interfacial tension. Post-test diagnostic measurements will include optical microscopy and SEM, x-ray diffraction, thermal analysis (DSC), thermal mechanical analysis (TMA), mechanical properties analysis, and surface properties-BET. These characterizations will not only allow us to understand the process of microstructure formation for this dynamic process, but also help us to infer areas of possible application for these unique materials.

References

---

[1] See, for example, D. Klempner and K.C. Frisch, eds. Handbook of Polymeric Foams and Foam Technology, Hanser, Munich, 1991.

[2] A. T. Chen, Automotive Plastics, RETEC'87, Pbul. by Soc of Plastics Engineers, Brookfield Cent, CT, USA. p 272 (1988).

[3] P. Cebe and M. V. Brillhart, "processing of semicrystalline polymers", NASA Conference Publication 3250, p 215 (1994).

[4] I. Avramov and N. Avramova, "Calorimetric study of poly(ethylene terephthalate)/Poly(butylene terephthalate blends", J. Macromol. Sci.-Phys., B30 (4), 335 (1991).

[5] R. B. Seymour and T. Cheng, Eds, Advances in Polyolefins: The world's Most Widely Used Polymers, Plenum Press, New York, 1985.

[6] C. L. Tice, "Design properties of foamed crystalline engineering resins", J. Cellular Plastic, 26, 411 (1990).

[7] G. Burillo and E. Adem, in Polymeric Materials Encyclopedia, J. C. Salamone, Ed., CRC Press, Inc., 1996; vol 8, "polyethylene foams", 6015.

[8] R. D. Deanin, in Polymeric Materials Encyclopedia, J. C. Salamone, Ed., CRC Press, Inc., 1996; vol 4, "foamed plastics", 2554.

[9] D. S. Chisholm, et al, U.S. Patent 3,065,190 (1962).

[10] K. W. Suh, in Encyclopedia of Chemical Technology", Fourth Eds, 1994; vol 11, "foamed plastics", 730.

[11] C. P. Park, "expandable polyolefin compositions and preparation process utilizing isobutane blowing agent", U.S. Patent, 4,640,933 (1987).

[12] P.J. Bush, D. Pradhan, and P. Ehrlich, Macromolecules, 24, 1439 (1991).

OSTWALD RIPENING OF LIQUID AND SOLID "DROPLETS" IN LIQUID METAL MATRICES

H. Gan, S. Prikhodko and A. J. Ardell
University of California, Los Angeles
Department of Materials Science and Engineering
School of Engineering and Applied Science
6531-G Boelter Hall
Los Angeles, CA 90095-1595
(310) 825-7911; aardell@ucla.edu

Introduction

Ostwald ripening (coarsening) involves the growth of large particles at the expense of small ones in a polydisperse array. The driving force for coarsening is the reduction of interfacial area, hence energy, that accompanies growth as solute atoms are transported by diffusion from small to large particles. The theory of diffusion-controlled coarsening by Lifshitz and Slyozov[1] and Wagner[2] (the LSW theory) predicts that the average radius, $\langle r \rangle$, of the particles in the minor (dispersed) phase increases with aging time, t, according to the familiar kinetic law

$$\langle r \rangle^3 - \langle r_o \rangle^3 = kt, \tag{1}$$

where $\langle r_o \rangle$ is the value of $\langle r \rangle$ at the onset of coarsening ($t = 0$) and k is a rate constant. There is always a small decrease in the residual supersaturation, $X_\alpha - X_{\alpha e}$, with t during coarsening, where X_α is the average solute concentration in the continuous (α) phase at t. and $X_{\alpha e}$ is the solute concentration at thermodynamic equilibrium. $X_\alpha - X_{\alpha e}$ obeys the asymptotic relationship[1]

$$X_\alpha - X_{\alpha e} \approx (\kappa t)^{-1/3}, \tag{2}$$

where κ is another rate constant.

The LSW theory was formulated for an infinitely dilute dispersion, i.e. one for which the volume fraction, f, is zero, strictly speaking. The theory must therefore be modified in some way to account for the fact that in any system in which f is finite there must be diffusional interactions, or overlapping diffusion fields, that affect the rate at which individual precipitates grow. Also, when f is large physical encounters among the growing particles can become important. Considerable theoretical effort has been directed towards finding a quantitative solution to this problem. The differences among the theories and the extent to which they have succeeded in predicting the effect of f on coarsening behavior have been reviewed[3-5]. All theories predict that finite f accelerates the growth rates of individual particles because the diffusion distances decrease as f increases. The temporal dependence of $\langle r \rangle$ is unaffected by f, but k in equation (1) must be replaced by $k_f = kF(f)$, where $F(f)$ is a function of f that depends on the particular theory [in the LSW limit $f = 0$ and $F(0) = 1$. There is also an effect of f on κ, such that κ becomes $\kappa_f = k_f/(\ell\langle u \rangle)^3$, where ℓ is the capillary length, $\langle u \rangle = \langle r \rangle / r^*$ and r^* is the radius of a particle that is neither growing nor shrinking at time t (in the LSW theory $\langle u \rangle = 1$, i.e. $r^* = \langle r \rangle$). When $f > 0$, $\langle u \rangle < 1$; the extreme value[6] of $\langle u \rangle$ in the limit $f = 1$ is $\langle u \rangle = 8/9$.

Ostwald ripening has been intensively investigated in solid alloys in which the dispersed phase is coherent with the continuous phase. Coherency introduces the issues of the influence of elastic energy on the morphology of individual particles and spatial correlations among groups of precipitates. The motivation for investigating coarsening in liquid systems is that the underlying assumptions of the LSW theory are ideally fulfilled when the continuous phase is a liquid. In a liquid matrix the particles of the dispersed phase, be they liquid or solid, are usually spherical in shape, and both the continuous and dispersed phases are free of the internal stresses that complicate Ostwald ripening of coherent precipitates in solid systems. Furthermore, since all the theories predict that $k(f)$ increases most rapidly with f when f is small (< 0.05), quantitative evaluation of the different theories is, in principle, best accomplished by experiments on specimens containing relatively dilute dispersions. Microgravity is essential for successfully conducting experiments on liquid-based dispersions because differences between the mass densities of the continuous and droplet phases induce particle motion due to gravity-driven sedimentation forces.

Experimental Approach

Dependence of Electrical Resistivity on Solute Concentration

Experiments on coarsening in liquids under microgravity conditions can yield a much greater quantity of reliable data if the investigation does not rely exclusively on post-mortem metallographic examination. This is because of the difficulties involved in quenching-in the coarsened "microstructure" from the liquid state without disturbing it during solidification. Preserving the as-coarsened, predominantly liquid, two-phase structure must become increasingly difficult as f decreases, which is unfortunate because the regime of small f is the desired one for experimentation. The objective of this research is to investigate coarsening by continuously monitoring the electrical resistivity, ρ, of the liquid as a function of t. The scientific basis for this approach is the dependence of ρ on X_α. In principle, ρ is affected by both the precipitate and matrix phases in any two-phase alloy, but for a dilute dispersion of spherical particles in the limit of small f, the resistivity of the two-phase alloy is given by[7]

$$\rho \cong \rho_m\left(1+\frac{3f}{2}\right). \tag{4}$$

where ρ_m is the resistivity of the continuous (matrix) phase. When ρ depends linearly on X_α, which is often the case for dilute solutions, we can write

$$\rho_m - \rho_A = KX_\alpha, \tag{5}$$

where ρ_A is the resistivity of the pure solvent (A) and K is a calibration constant. Therefore, when f is very small $\rho = \rho_m$, which then depends uniquely on X_α.

There are two factors that can influence the accuracy of the data. One is a potential limitation imposed by the physics of the coarsening process itself and the other is a limitation associated with temperature control. Using values of the parameters relevant to the coarsening of liquid Pb in Zn at 450 °C published by Kneissl et al.[8], and taking $\langle u\rangle = 1$, it can be shown that $\kappa = 1.34 \times 10^{13}\ s^{-1}$. This value of κ is 9 to 12 orders of magnitude larger than those typical of solid systems[9]. Such a large value of κ implies that between 10 and 1000 s, the concentration of Pb in solution can be expected to decrease by $\approx 1.53 \times 10^{-5}$, i.e. by only about 15.3 appm at 450 °C. The changes in solute concentration accompanying coarsening in liquids will generally be the order of tens of parts per million! Using data on the variation of ρ with solute concentration in liquid Zn-Pb alloys[10], the resistivity can be expected to change by 0.027 nΩ·m between 10 and 1000 s at 450 °C. Changes this small are measurable, in principle, using modern instrumentation, and variations much smaller than this should be detectable. However, the temperature coefficient of ρ of liquid metals is very large, and without a unique experimental arrangement, the expected temperature fluctuations during normal temperature control would completely eliminate any chance of measuring the changes in ρ estimated above.

There are therefore 2 formidable challenges to the successful execution of this research project. One of them is the design and implementation of a containerless method of measuring ρ, which involves measuring the change in inductance of mutual inductance coils; several such methods are in use today[11-15]. The other is the design of a furnace that meets the criteria of extremely small temporal fluctuations and small temperature gradients. We believe we have succeeded in designing and constructing a novel furnace that fulfills the necessary objectives. It is described in the following section.

Furnace Design

The major positive progress to date is the successful design and construction of a novel furnace consisting of heating elements placed in the interior of a water-cooled jacket. It is depicted schematically in Fig. 1 (not to scale). The jacket is constructed from concentric quartz tubes, 450 mm long, and configured so that water flows in the 6 mm wide channel between them. The outer diameter of the larger outer tube is 18 mm, while the inner diameter of the smaller inner tube is 10 mm. The heating element is nichrome wire 0.32 mm in diameter, insulated using Al_2O_3 tubes 0.8 mm in outer diameter and attached to another quartz tube with an inner diameter of 3 mm; it is this tube that is intended to contain the specimen during an experiment. The continuous wire strand is parallel to the axes of the water-cooled tubes, and the entire assembly fits comfortably inside the inner water-cooled tube. The method of "winding" is non-inductive. However, the temperature gradients are extremely sensitive to the geometry of the insulation used between the heating elements and the inner water-cooled tube. A satisfactory configuration was attained by trial and error using thin rings of Al_2O_3 spaced at different intervals; it is shown in Fig. 2. The temperature profile inside the furnace, measured with an Al rod inserted in the interior, is also shown in Fig. 2 at two different levels of temperature resolution. It is evident that the gradients have been reduced so that the maximum variation along a length of slightly less than 200 mm does not exceed ±0.5 °C when the average temperature inside the furnace is 552.6 °C. Even these gradients could undoubtedly be reduced by minor adjustments of the positions of the thin Al_2O_3 rings or the introduction of several new ones. Attaining the operating temperature requires a power input of only ~225 Watts (150 V DC at ~1.5 A). Temperature measurements over a period of 6 h indicate a temperature fluctuation of only ±0.5 °C using a Sorensen DCR-B 300-9B power supply with voltage stability of 0.1% for 8 h after warming up for 30 min. This furnace design meets all the requirements for conducting the proposed coarsening experiments, and its only shortcoming is its relatively large outer diameter, which limits the size of the induction coils and hence the filling factor for the induction measurements.

While the design of the furnace is disarmingly simple, the effort required to produce the temperature profile shown in Fig. 2 proved extremely formidable. The initial design used a double-helical coil of nichrome wire wound directly on the tube housing the specimen. The double-walled chamber surrounding the tube was only 10 mm in diameter. This design minimizes the diameter of the entire assembly, thereby maximizing the filling factor for the induction coils in the bridge circuit, which improves the sensitivity of the electrical measurements, in principle. However, it proved impossible to control temperature fluctuations along the length of the furnace because they were extremely sensitive to the spacings of the individual wires in the double-helical arrangement. It proved impossible to adjust the local spacings of the windings in such a way that the variation of temperature along the length would vary by less than ± 25 °C. Initial experiments using vacuum between the double-walled quartz chamber, rather than water-cooling, were also a failure. After considerable effort the initial design was abandoned in favor of the one depicted in Fig. 2. The temperature profile for the design in Fig. 2 is highly sensitive to the geometry of the insulating material placed between the heating element and the concentric water-cooled quartz tubes. Many combinations of wall thicknesses and lengths of the insulating material were explored before arriving at the one shown in Fig. 2.

There are other parameters associated with the design that have not been varied, so their influence is unknown. In particular, the flow rate of the cooling water is 0.1 l/s and its temperature is 13.8 °C. The cooling water supply originates from the recirculating water system on the UCLA campus, and would certainly have to be replaced by a much smaller one for use in a non-terrestrial environment. We have also not yet explored the temperature range over which the furnace can operate, but the power input required to reach an operating temperature of 500 °C is easily attained with the stabilized power supply currently in use.

Design of the Bridge Circuit

Electrical resistivity will be measured using an induction bridge circuit, one leg of which contains the active specimen and the other leg a dummy specimen maintained at exactly the same temperature. The composition of the dummy specimen will be chosen to match, as closely as possible, that of the liquid matrix of the actual specimen so that the output of the bridge circuit will be as sensitive as possible to changes in solute concentration of the matrix of the active specimen. The output of the bridge circuit should therefore depend only on the difference in concentration between the actual and dummy specimens, and should be unaffected by small temperature fluctuations since both the actual and dummy specimens are always at exactly the same temperature. The frequency of the bridge circuit will be chosen so that the resistance of the bulk liquid is measured, rather than the surface resistance, but it is not difficult to show that the skin depth exceeds a typical specimen diameter (e.g. 2 mm) at readily accessible frequencies (~10 kHz).

A sensitive lock-in amplifier manufactured by Stanford Research, Inc. has been purchased for detecting the small changes in mutual induction that obtain when the concentration of solute in the matrix changes with aging time during coarsening. Mutual induction coils have been wound, and experiments are in progress to measure the sensitivity of the bridge circuit. In experiments to date the circuit we have constructed is easily balanced to within about 300 nV at f = 10 kHz. The signal generated when a rod of a solution-treated 6xxx Al alloy is inserted into the furnace is about 650 nV. For the chosen configuration length and diameter of the primary and secondary coils, number of turns, input voltage and frequency, the observed sensitivity is inadequate for conducting the experiments on coarsening. We have not attempted to optimize the myriad parameters affecting the sensitivity of the bridge circuit, so much work in this area remains to be done. However, the bridge circuit has been tested with the furnace heated to ~553 °C, and the response is identical to that when the furnace is cold, indicating that there is no interaction between the heating elements and induction coils.

Summary

A small, novel furnace has been designed, constructed and tested. It is, in principle, suitable for conducting experiments on coarsening of "droplets" in liquid metals using a contactless method of measuring the change in electrical resistivity of the specimens during coarsening of the dispersed droplets. However, the circuitry necessary for successfully carrying out the experiments has not been satisfactorily built. It is not known at this stage whether it is possible to design and construct a bridge circuit with the necessary sensitivity.

References

1. I. M. Lifshitz and V. V. Slyozov, J. Phys. Chem. Solids, 19, 35 (1961).
2. C. Wagner, *Z. Elektrochem.* **65** (1961) 581.
3. P. W. Voorhees, *Annu. Rev. Mater. Sci.* **22** (1992) 197.
4. P. W. Voorhees, *J. Stat. Phys.* **38** (1985) 231.
5. A. J. Ardell, in *Phase Transformations '87*, ed. by G. W. Lorimer, Institute of Metals, London (1988), p. 485.
6. A. J. Ardell, *Acta Met.* **20** (1972) 61.
7. P. L. Rossiter, *The Electrical Risistivity of Metals and Alloys*, Cambridge University Press, Cambridge, England (1987), p. 169.
8. A. Kneissl, P. Pfefferkorn and H. Fischmeister, in *Proc. 4th European Symposium on Material Sciences Under Microgravity*, European Space Agency Rept. SP-191 (1984), p. 55.
9. J. Ardell, Interface Science, 3, 119 (1995).
10. V. Y. Asonovich, I. T. Sryvalin and V. A. Kozlov, *Russian Metallurgy* **4** (1969) 137.
11. D. W. Nyberg and R. E. Burgess, *Can. J. Phys.* **40** (1962) 1174.
12. R. C. Callarotti, *J. Appl. Phys.* **43** (1972) 3949.
13. A. J. Hamdani, *J. Appl. Phys.* **44** (1973) 3486.
14. W. Wejgaard and V. S. Tomar, *J. Phys. E: Sci. Instr.* **7** (1974) 395.
15. W. Bauhofer, *J. Phys. E: Sci. Instr.* **10** (1977) 1212.

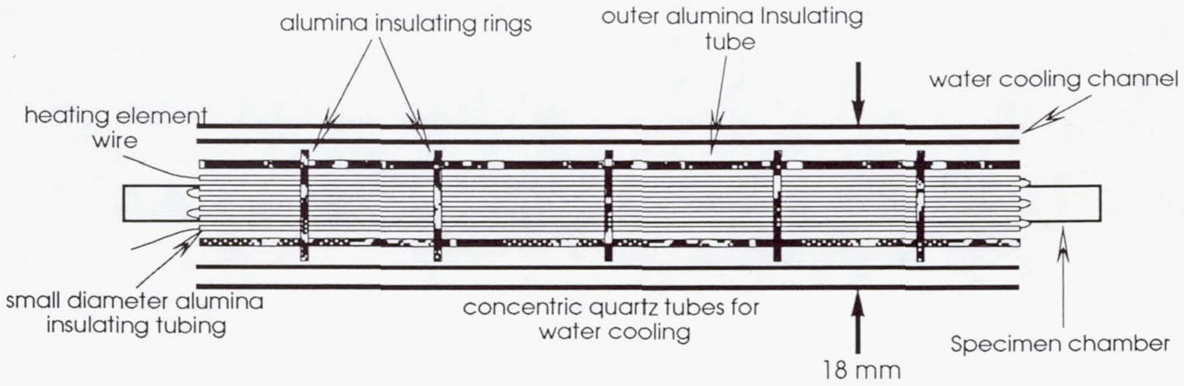

Figure 1. Schematic cross-section of the furnace, illustrating its essential details.

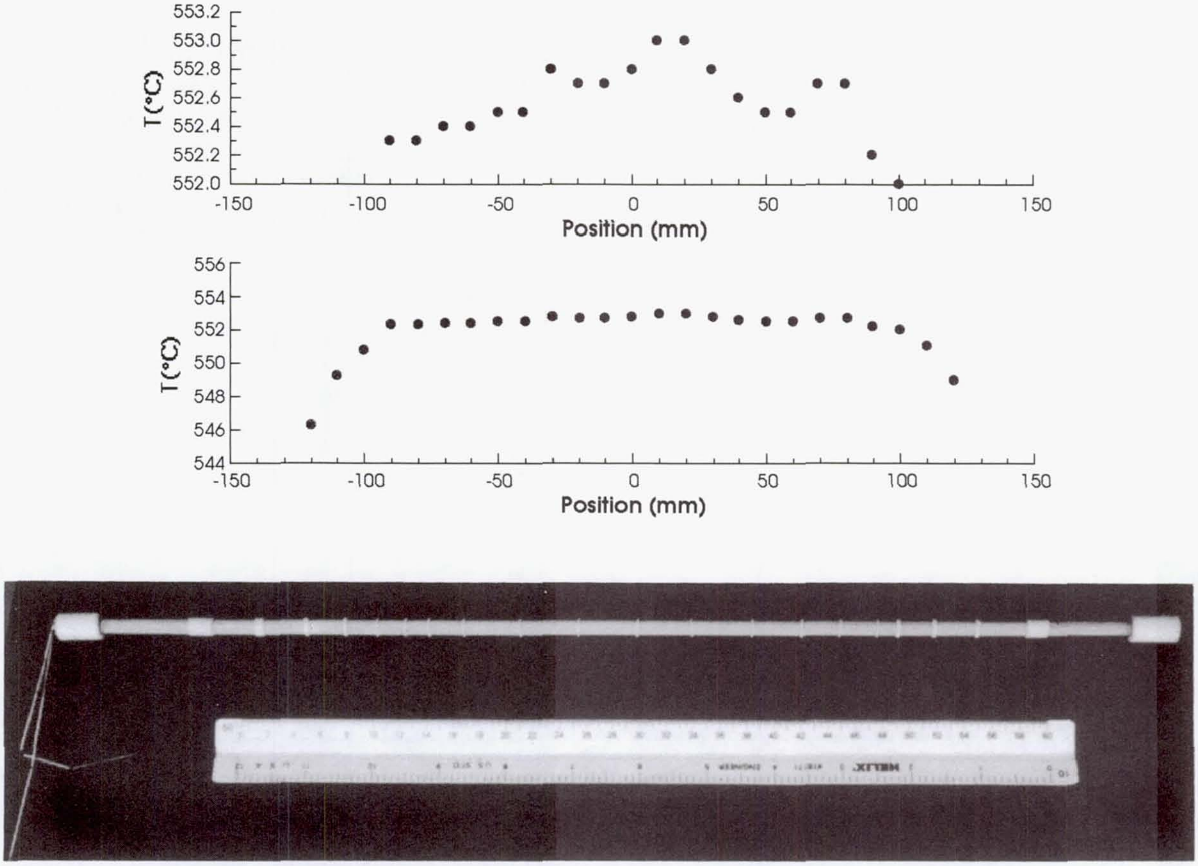

Figure 2. Photograph of the furnace heating element. When inserted into the water-cooled housing, which is 18 mm in diameter (see Fig. 1) and heated using a power-input of ~225 W, the resulting temperature profile is as shown in the graphs above the photo. The white features distributed along the length of the element are the Al_2O_3 rings shown schematically in Fig. 1. The ends of the nichrome heating wire are visible at the left of the photo.

Chemical Vapor Deposition at High Pressure in a Microgravity Environment

Sonya McCALL[A], Klaus BACHMANN[A], Stacie LeSURE[A], Nkadi SUKIDI [A,B]
and Fuchao WANG[A]

In this paper we present an evaluation of critical requirements of organometallic chemical vapor deposition (OMCVD) at elevated pressure for a channel flow reactor in a microgravity environment. The objective of using high pressure is to maintain single-phase surface composition for materials that have high thermal decomposition pressure at their optimum growth temperature. Access to microgravity is needed to maintain conditions of laminar flow, which is essential for process analysis. Based on ground based observations we present an optimized reactor design for OMCVD at high pressure and reduced gravity. Also, we discuss non-intrusive real-time optical monitoring of flow dynamics coupled to homogeneous gas phase reactions, transport and surface processes. While suborbital flights may suffice for studies of initial stages of heteroepitaxy experiments in space are essential for a complete evaluation of steady-state growth.

1. Objectives and Approach

The overall objective of the work described in this paper is to extend chemical vapor deposition to super-atmospheric pressure. The specific objective of the experiment in space is to provide conditions of laminar flow for the evaluation of the validity of selected process models and input parameter sets that are needed for analysis and control of chemical vapor deposition at elevated pressure. The motivation for extending chemical vapor deposition to high pressure is to maintain stoichiometric single phase surface composition of materials that are characterized by large decomposition pressures at their optimum elevated processing temperatures. An example is indiumnitride, which under conditions of conventional OMCVD at subatmospheric pressure, is limited to processing temperatures < 823 K$^{1)}$. This restriction limits the control of formation and propagation of extended defects in this material, and is one of the reasons why at present, confined $Ga_xIn_{1-x}N$ heterostructure devices (e.g., diode lasers$^{2)}$) do not include indium-rich compositions. This in turn restricts quantum well depth and thereby the accessible color range. Here we focus onto deposition temperatures ≥ 900 K, requiring nitrogen pressure ≥ 100 atm to suppress surface decomposition$^{3)}$. Since at $p \geq 100$ atm the mean free path becomes comparable to molecular dimensions interactions between reactive gas phase constituents are inevitable. For growth of InN we select trimethylindium (TMI) and ammonia as source compounds, which decompose in the hot vapor atmosphere in the vicinity of the heated substrate. Therefore, without special preventive measures, interactions of reactive decomposition products of source materials in the vapor phase are likely to occur. Thus homogeneous gas phase nucleation of InN particles above the hot substrate becomes possible, competing and interfering with nucleation and well defined growth of InN epitaxial films on the substrate surface. In order to avoid this problem separately controlled flows of TMI and ammonia or hydrazine are injected into the reactor in a timing sequence that assures maintainance of their separation by plugs of pure nitrogen carrier gas, as illustrated in Fig. 1. Thus indium and nitrogen precusors to growth never exist simultaneously in the vapor volume above the substrate. A special problem of group III-nitride epitaxy is the absence of lattice matching substrates, resulting in strained layer overgrowth. Thus far SiC and sapphire are the most widely used substrate materials for group III nitride growth to which we add for InN heteroepitaxy GaP coated silicon as a possible alternative.

A Department of Materials Science and Engineering, North Carolina State University, Raleigh, NC 27695, U.S.A.
B Present Address: Motorola Company, Mesa, AZ 85202, U.S.A.

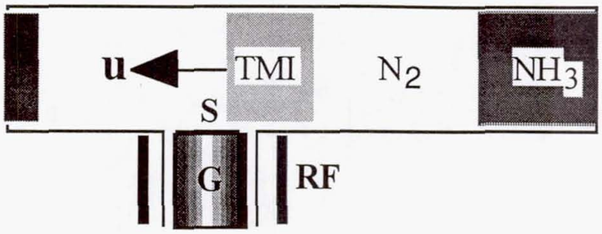

Figure 1. Schematic representation of channel flow at center line velocity $\mathbf{u}_o$ across heated substrate S, employing plugs of source vapor (TMI and NH_3 or N_2H_4) separated by plugs of pure N_2 gas; RF rf coil, G SiC coated graphite susceptor.

For GaP heteroepitaxy on silicon substrates we have developed pulsed chemical beam epitaxy (CBE) using p-polarized reflectance (PRS) for real-time optical process monitoring and triethylgallium (TEG) and tertiary-butylphosphine (TBP) as source vapors4)-7). Here we focus onto recent results concerning initial stages of heteroepitaxy that, in conjunction with theoretical predictions of gas phase kinetics, help in estimating the time requirements for the envisioned experiments. Figure 2 shows PRS intensity as a function of time for three experiments employing continuous flow of TBP and pulsed flow of TEG at 0.3 s pulse width at 0.2 Hz repetition rate. Three distinct stages - verified by atomic force microscopy and high resolution cross sectional transmission electron microscopy studies8) - are observed:

(i) In the initial incubation period of length $t \leq \tau_i$ surface reactions result in gradual build-up of products of source vapor decomposition on the surface of the silicon substrate. During this stage no structure coinciding with the arrival of the TEG pulses exists in the PR signal.

(ii) Once the critical supersaturation for nucleation of GaP islands is reached steps in the PR signal are observed, coinciding in time with the arrival of TEG pulses, and indicating GaP nucleation and island growth on the silicon surface 5), 8).

(iii) At $t = \tau_h$ the contributions to the PRS signal-associated with the early stages of nucleation and overgrowth that are described by effective medium theory-join smoothly into the slow oscillations in reflectivity-associated with interference of partial waves reflected at the ambient/film and film/substrate interfaces4) for steady-state growth of a contiguous GaP film.

In view of efficient heat transfer from the hot susceptor and substrate surfaces to the vapor phase at high pressure, homogeneous gas phase reactions replace pyrolysis of source vapor molecules on the substrate surface under conditions of CBE.

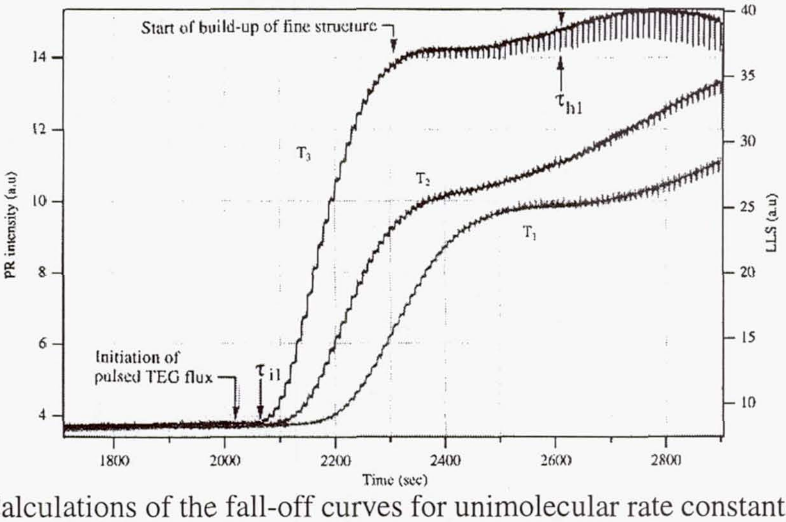

Figure 2. P-polarized reflectance as function of time for growth of GaP on Si(100): T_1=350 °C, T_2=420 °C, T_3=490 °C; τ_{i1} = 160 s, τ_{i2} = 95 s, τ_{i3} = 50 s. $\tau_{h1} \approx$ 10 min, $\tau_{h2} \approx$ 13.5 min s, $\tau_{h3} \approx$ 16 min.

Calculations of the fall-off curves for unimolecular rate constants on the basis of Rice-Ramsperger-Kassel-Marcus theory9) predict at ~ 100 atm pressure and T ≈ 900 K faster group III alkyl decomposition rates than observed under the conditions of CBE5). Also, the flux reactive molecular fragments instead of intact source vapor molecules to the surface at higher temperature than accessible under conditions of low pressure growth can be expected to result in faster kinetics of surface reactions, surface transport and incorporation of constituent atoms into the lattice of the nuclei and, in later stages, of the growing epitaxial film. Of course, diffusivities decrease with increasing pressure. However this is compensated, in part, by access to higher temperature, which increases transport rate, and, in part, by the possibility to sustain at high pressure steeper concentration gradients. Therefore, we expect that short periods of time will suffice for studies of incubation and nucleation, which thus can be addressed on suborbital flights. Such studies are important since both type and distribution of defects in the epitaxial film are determined during initial stages of island growth prior to coalescence8). However, a complete investigation, including steady-state growth, takes substantially longer uninterrupted experiment time than accessible with suborbital flights, that is, requires access to an experiment in space.

2. Need for Processing at Reduced Gravity

A necessary condition for realizing pulsed high pressure OMCVD is the absence of contamination of the flow by buoyancy-driven recirculation, which would result in mixing of the separately injected plugs of source vapors. Based on results of simulations of flow for a variety of reactor geometries we conclude that channel flow at high center-line velocity indeed eliminates residual buoyancy driven recirculation for Richardson number $Ri \equiv Gr/Re^2 >> 1$10). Gr and Re stand for the Grasshof and Reynolds numbers, respectively. This sets a lower limit for flow velocity, $|\mathbf{u}| >> (z_o g \beta \Delta T)^{1/2}$ and consequently a lower limit for $Re = \rho \left| \mathbf{u} \right| z_o / \eta$, where z_o, g, ρ, β, η and ΔT refer to the characteristic channel dimension, length of the gravity vector, gas density, volume expansion coefficient, dynamic viscosity and temperature difference across the channel, respectively. At $p \geq 100$ atm for a conventional reactor design (see section 3) $Re > 10^4$ on the ground, which makes onset of turbulence likely. Turbulent flow involves interactions between many degrees of freedom over wide ranges of spatial and temporal scales and thus cannot be adequately simulated with present computer technology. Attempts have been made at reducing complexity by eliminating inessential degrees of freedom, e.g., on the basis of observations of organized structures (eddies) in turbulent flows at low Re11). Proper orthogonal decomposition (POD)12), in particular, represents the fluctuating velocity field $\mathbf{u}(\mathbf{r},t)$ by the sum over a denumerably infinite set of POD modes $\{\Phi_j^{(m)}(\mathbf{r})\}$ that are functions of position $\mathbf{r} = c_i\mathbf{r}_i + c_j\mathbf{r}_j + c_k\mathbf{r}_k$ and are weighted by random coefficients $\alpha_m(t)$ that depend on time t. The POD modes are mutually orthogonal eigenfunctions of two-point correlation tensor $R_{ij}(\mathbf{r},\mathbf{r}') = <u_i(\mathbf{r})u_j^*(\mathbf{r}')>$, where subscripts refer to components parallel to basis vectors $\mathbf{r}_i$, $\mathbf{r}_j$ and $< >$ represents an averaging operation. The set $\{\lambda^{(m)}\}$ of eigenvalues associated with $\{\Phi_j^{(m)}\}$ is ordered so that $\lambda^{(p)} > \lambda^{(q)}$ for any pair of integers $p < q$. For specific cases of low Re channel flow it has been shown 13) that major parts of kinetic energy and turbulence generation can be captured by a limited set of low order modes $\Phi^{(m)}$. However, the same set may not represent other properties of the flow, that is, a substantial number of POD modes may be required for adequate representation. Although significant progress has been made during the past decade with regard to direct numerical simulations of turbulent flow14), their viability for simulations of heteroepitaxy presently is not assured, since local variations in reaction rates, associated variations in composition, and localized generation/consumption of heat result in a strong interdependence of the evolutions of turbulent flow and heteroepitaxial growth. For these reasons, it appears prudent to address this problem as far as possible experimentally, so that future progress in computational methods can be tested against experimental results. Reliable results can be obtained by experimentation at reduced gravity, where the flow velocity needed for suppression of buoyancy driven recirculation and thereby Re are reduced. Thus laminar flow conditions can be realized for high pressure OMCVD processes. In this case, the coupling to chemical reactions and transport can be simulated reliably on the basis of known physico-chemical models with proven mathematical methods and validated by experiment.

3. Description of a Ground-Based Reactor

Figure 3 shows a photograph of the reactor section of a high pressure OMCVD system for ground-based studies at relatively low pressure ($p \leq 7$ atm) constructed at North Carolina State University. The innermost reactor shell R is made from fused silica, and is mounted on base plate B. Under operating conditions R is sealed in pressure bearing stainless steel second confinement shell C (raised in Fig. 3 for installation of R). Active controls are provided for a selected small pressure differential between inside and outside of R and for the absolute pressure inside C. The design provides for flexibility in the evaluation of variations in reactor geometry by exchange of fused silica reactors without need for changes in pressure bearing parts of the system. For real-time monitoring of growth rate, and of changes in surface composition due to sequential pulsed exposure of the hot surface to TMI and NH_3 or N_2H_4 we have made provisions for p-polarized reflectance spectroscopy (PRS), that is, admission of a chopped p-polarized laser beam through a window on the perimeter of C and tube 1 and recovery of the reflected beam through tube 2 for phase sensitive detection by a photodiode outside C. In order to establish pulsed exposure of the substrate surface to precursors to growth at high pressure, flows of source vapor/carrier gas mixtures are either directed into the run line connected to entrance tube 3 on R or into a vent line bypassing R. When a source vapor is added to the run line flow a matching flow of nitrogen carrier gas is subtracted from the run line flow and redirected into the vent line. Thus the total flow through the reactor remains unchanged. The gas flow is passed over the substrate wafer mounted on a susceptor in vertical fused silica tube 4 attached to R, so that the wafer surface is flush with the bottom channel wall and the susceptor is located inside single-turn rf-coil RF. Waste products are exhausted through tube 5. Errors in positioning S, resulting in a step in the bottom of the channel at the location of the substrate wafer, or irregularities in the channel side walls, can trip

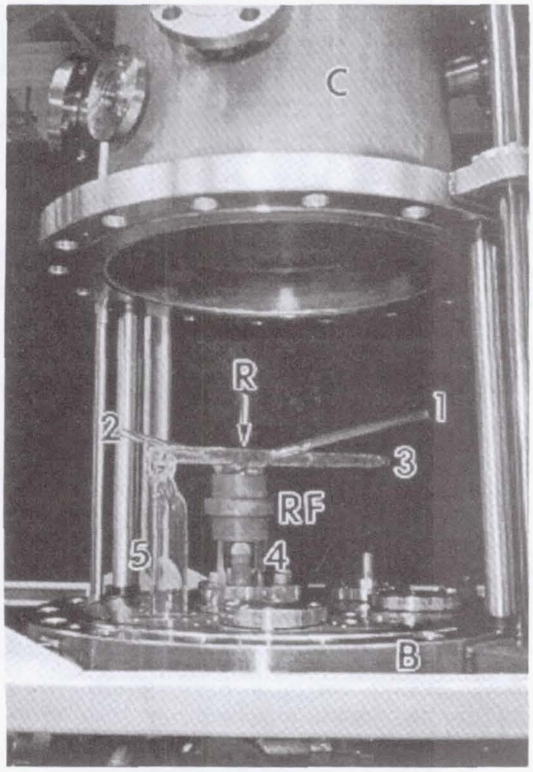

Figure 3. Photograph of the reactor section of a high pressure OMCVD system.

eddies in the flow even at low Re. This is demonstrated in Fig. 4 by flow visualization using injection of smoke.

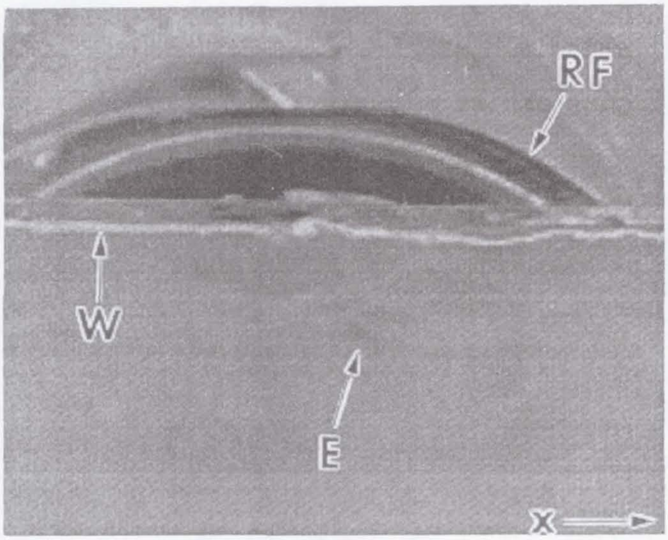

Figure 4. Visualization by smoke injection of an eddy marked E in a flow of nitrogen through R in x-direction for Re = 300 near a large irregularity in channel sidewall W.

Therefore, even under the conditions of low Re flow localized flow instabilities can exist that are likely to affect process uniformity. In order to prevent this problem and to verify laminar flow conditions, improvements of reactor design and characterization of the flow dynamics as part of the experiment are necessary requirements.

Figure 5 shows the design of a prototype high pressure reactor for work at reduced gravity and has

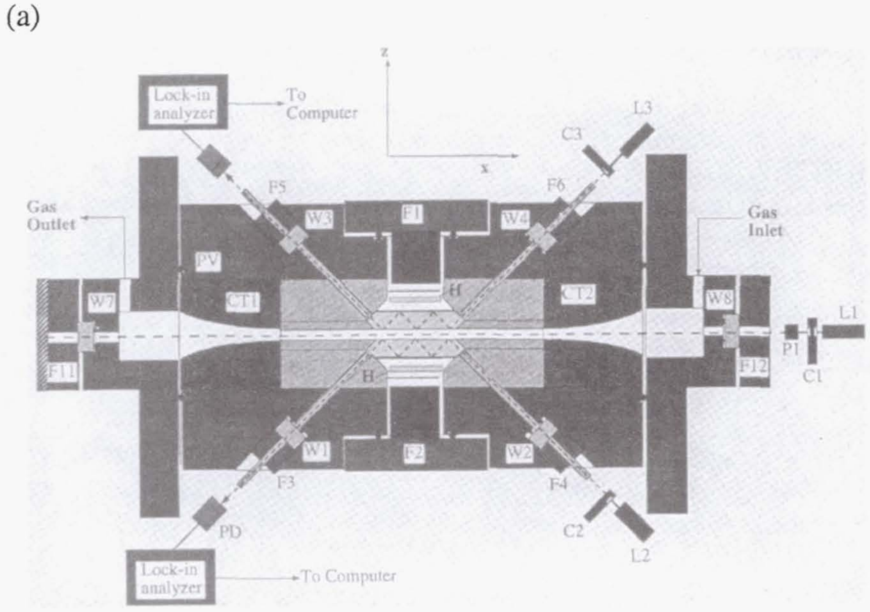

Figure 5. Schematic representation of a reactor for high pressure OMCVD at µg: W1-W8 fused silica windows, H heater ribbons, S substrate prisms, PV pressure vessel, F1-F12 flanges. CO collecting optics, E Fabry-Perrot etallon, M monochromator, D detector, BA boxcar averager, CCD camera, FG frame grabber, P polarizer, C1-C3 choppers, L1-L3 lasers.

(b)

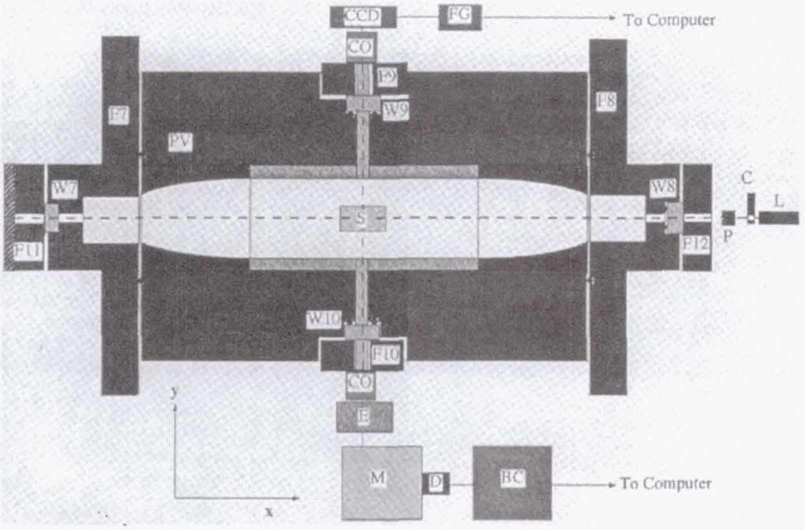

the following improved features: absence of purge flows perturbing the channel flow and composition of the nutrient phase in the vicinity of the substrates, pairing of heated substrate prisms that are incorporated into the top and bottom channel walls achieving high symmetry, and continuous cross section of the channel from entrance to exit ports of the reactor.

References

1) S. Bedair, F.G. McIntosh, J.C. Roberts, E.L. Piner, K.S. Boutros and N.A. El Masry, J. Crystal Growth 178 (1997) 113
2) S. Nakamura, M. Senoh, S. Nagahama, N. Iwasa, T. Yamada, T. Matsushita, H. Kiyoku and Y. Sugimoto, Jpn. J. Appl. Phys. 35 (1996) L74
3) J. MacChesnay, P.M. Bridenbaugh, and P.B. O'Connor, Mater. Res. Bull. 5 (1970) 783
4) N. Dietz and K.J. Bachmann, Mater. Res. Bull.20 (1995) 133
5) N. Dietz and K.J. Bachmann, Vacuum 47(1996) 133
6) K.J. Bachmann, C. Hoepfner, N. Sukidi, A.E. Miller, C. Harris, D.E. Aspnes, N. Dietz, H.T. Tran, S. Beeler, K. Ito, H.T. Banks and U. Rossow Appl. Surf. Sci. 112 (1997) 38
7) K.J. Bachmann, N. Sukidi, C. Hoepfner, C. Harris, N. Dietz, H.T. Tran, S. Beeler, K. Ito and H.T. Banks, J. Crystal Growth 183 (1998) 323
8) N. Sukidi and K.J. Bachmann, J. Electrochem. Soc. (1998) to be published
9) N.I. Buchan and J. Jasinski, J. Crystal Growth 106 (1990) 605
10) K.J. Bachmann and G. Kepler, Proc. IEEE 3123 (1997) 64
11) S.J. Kline, W.C. Reynolds, F.A. Schraub and P.W. Runstadler, J. Fluid Mech. 30 (1967) 741
12) G. Berkooz, P. Holmes and J.L. Lumley, Ann. Rev. Fluid Mech. 25 (1993) 539
13) P. Moin and R.D. Moser, J. Fluid Mech. 200 (1989) 471
14) P. Moin and K. Mahesh, Ann. Rev. Fluid Mech. 30 (1998) 539

Acknowledgements

The authors are indebted to Prof. N. Dietz for helpful comments and suggestions, to Dr. C. Hoepfner - presently with Spire Corporation, Bedwell, MA - for valuable assistance in the construction of the ground-based reactor. Also, we thank Prof. B.H. Bairamov of A.F. Ioffe Physico-Technical Institute, St. Petersburg, Russia, for sharing of information regarding the use of etalons in high resolution Raman spectroscopy. Furthermore, we acknowledge support for this work by NASA Collaborative Agreement NCC8-95 and DOD MURI Grant F-49-620-95-1-0447.

Thermophysical Property Measurements of Te-based II-VI Semiconductors

R. Michael Banish and J. Iwan. D. Alexander*
Center for Microgravity and Materials Research
University of Alabama in Huntsville
Huntsville, AL 35899
banishm@email.uah.edu ; 256-890-6050

*Department of Mechanical and Aerospace Engineering
Case Western Reserve University
Cleveland, OH 44106
ida2@po.cwru.edu

Introduction

The experimental determination of transport properties such as diffusivities and conductivities is often contaminated by buoyancy-driven convective effects. The accurate determination of transport properties requires convective flow velocities to be eliminated or significantly suppressed. This is generally not possible under terrestrial conditions. While it can be argued that mass diffusivity measurement techniques such as nuclear magnetic resonance and inelastic neutron scattering, that probe rapid molecular motion, are insensitive to convective contributions, they are not as precise as macroscopic, averaging techniques. However, all macroscopic measurement techniques yield diffusivity data prone to be contaminated by gravity-driven convection. The use of narrow capillaries to suppress convective transport has suggested poorly understood wall effects. Magnetic fields, widely used for suppressing convection in conducting liquids, modify the diffusive motion itself. Earlier liquid (metal) diffusion studies conducted on spacecraft have demonstrated the gain in precision resulting from the drastic reduction of convection in a low-gravity environments.

Simple scaling illustrates the difficulty of obtaining purely diffusive transport in liquids. In a system of diffusivity 10^{-5} cm^2/s and a typical diffusion distance of 1 cm, the characteristic diffusion velocity is of order 10^{-5} cm/s. Hence, if true diffusion is to be observed, convective flow velocities parallel to the concentration gradient must be of order 10^{-7} cm/s, i.e. 10 Å/s, or less! Thus, in liquids, the attainment of diffusion-dominated transport over macroscopic distances at normal gravity is obviously not a simple task. This is illustrated by modelling results [1] for diffusive-convective transport in capillaries with realistic thermal boundary conditions, which indicate that temperature nonuniformities as low as 0.1K, across samples of mm dimensions, are sufficient to cause convective domination of transport. Numerical modelling results from our research indicate that at the high magnetic fields necessary to decrease the convective flow velocity of 1% of the diffusive velocity, a similar, significant influence on the diffusive motion will occur.

Thermal diffusivity measurements in melts are also prone to be contaminated by convective contributions. The use of small measuring volumes increases the likelihood that asymmetries and imperfections in the measurement apparatus itself leads to errors. The use of larger cell volumes on the other hand is prone to result in convective contamination. These problems can be especially troublesome with II-VI semiconductors, since their thermal conductivity is smaller than that of typical container materials. Levitated drop techniques offer little relief of this problem due to the high vapor pressure of II-VI compounds. Modelling of these convective contributions is at best problematic since the assumptions for estimating or modelling these contributions depends on ground-based data already influenced by convection. The above analysis can be applied to thermal diffusivity and/or conductivity measurements as well, although the requirements are not quite as stringent as for mass diffusivity [2,3]. Assuming a thermal conductivity of 0.0108 W-cm/K (CdTe) the melt thermal diffusivity is 0.010 cm^2/s. Then for a 1 cm cell, convective velocities need to be less than 0.0001 cm/sec to obtain precise thermal diffusivity values. Earlier liquid thermal conductivity/diffusivity studies conducted on spacecraft have demonstrated the gain in precision, and lower absolute values, resulting from the drastic reduction of convection in a low-gravity environments [2].

Diffusivity and thermophysical properties for the tellurium based II-VI binary semiconductors (CdTe, HgTe and ZnTe) have been studied quite extensively in the solid state. However, for the molten state only few values exist, and the temperature dependence is practically unknown. We will extend our presently employed "novel" diffusivity technique to the

- measurement of binary- and (selected) impurity- diffusivity in melts of Te-based II-VI compounds over a temperature range approximately 100 °C above the melting point.

In addition, we will measure the following interrelated thermophysical parameters:

- density change on melting and the volume expansion coefficient of the melt for pure and doped materials,
- melt thermal conductivity and thermal diffusivity.

Mass diffusivity measurements

For our MSAD funded proposal to study self-diffusion in molten melts we choose a direct or tracer technique utilizing a mathematical algorithm developed by Codastefano [4]. Our experimental hardware was designed to accommodate this mathematical algorithm. This technique had previously not been applied to liquids, particularly for diffusivity measurements at several temperatures in a single experiment run. This approach is particularly suited to the limited availability of experiment time on space flights. Diffusivities are deduced in-situ and in real-time from consecutive concentration profiles obtained from radioisotope emission using a multiple detector arrangement. Two detectors are positioned symmetrically about the half-length L/2 of the capillary; where the location of the detectors is determined by the sample length at the (individual) measurement temperature. However, by a judicious choice of detector positions, 4 detectors (2 high, 2 low) may be used for measuring the diffusivity at several temperatures. At periodic time intervals, the activity is simultaneously monitored at the two locations. A single temperature hardware unit utilizing this approach to measure diffusion coefficients in molten indium metal has flown under NASA sponsorship on a MIR flight. The self-diffusivity values we have measured both on the ground and in space are among the lowest values reported for this material.

The cell to be used for diffusion measurements is schematically shown in the Self-diffusion in Liquid Elements paper in this volume. A small section of activated materials (typically 1 mm long) is placed in an ampoule with a precast, nonradioactive, section (29 mm long, 3 mm ϕ) of the diffusion matrix material. Please see table for the isotopes to be used. A plunger, spring [19] and screw cap are then added to complete the final ampoule assembly. The ampoule is then placed in a metal cartridge (stainless steel) and welded closed.

The completed cartridge is then positioned in the concentric isothermally heater liner/shield with holes that act as collimators. After melting, as the radiotracer diffuses through the sample its' photon predominately escape though the precisely positioned collimation bores in the sides of the liner/shield. The diffusion of the radiotracer is monitored in real-time by a series of CdZnTe detectors with their associated electronics. TTL pulses from the radiation detectors are displayed and recorded for later data analysis.

Since, in this method, the diffusivity determination does not depend on any particular initial condition the sample temperature may be changed at any time. Estimates of the time necessary at each temperature are precalculated. However, in actual practice, the sample temperature is changed from preliminary analysis of the displayed data.

The three compounds to be used in these studies are CdTe, HgTe, and ZnTe. The radioactive tracers of the II-VI elements, to be used in the binary and ternary-dopant (at 5 or 10 mole% deviations from stoichiometry) diffusivity measurements are listed in the Table below. In addition, we will determine the diffusivity of widely used, extrinsic dopants at concentrations of about 0.1%. Their radiotracers are also listed in the Table.

Radiotracer	Half-life [days]	Photon Energies [keV]
Te-(123-131)	120 (ave)	27, 160
Zn-65	244	1115
Hg-203	46	279
Cd-109	464	24, 88
In-114m	50	24, 190
Ag-110	250	22, 657
Au-195	183	65, 98,120
Cu-67	62	184

Thermal conductivity and/or diffusivity measurement

Both these parameters will be determined a small graphite cell which is schematically shown in Figure 1. A CdTe melt (1-5 cm^3) is contained in the crucible with a spring-loaded [19] graphite plunger to assure good thermal contact with the melt. The cell/material is isothermally heated to the measurement temperature using a close-fitting heatpipe arrangement. The input energy is transmitted to the graphite cell via a silica optical fiber coupled to a argon laser (not shown). The shape of the cell will be optimized for maximum sensitivity, thus the "H" shaped depicted in Fig. 1 may not be the final configuration. Depending on whether the thermal conductivity or diffusivity is to be measured, this input is pulsed or cw, respectively.

The temperature measurement system for this cell consists of a series of fine blackbody optical fibers with associated (commercial) electronics, with a temperature resolution of 0.01 °C. The use of blackbody optical fibers represents a major improvement in the resolution of temperature measurement [5-8]. Blackbody optical fibers are capable of temperature resolutions of 0.01 °C at 1200°C with a repeatability of 0.05% or 0.6 °C at 1100 °C [9].The final position of the optical fibers' location will be chosen after numerical modelling of the conductive/convective heat transfer in the cell; therefore the positions shown here are for illustration only.

We will determine the thermal conductivity and diffusivity for the three Te-based semiconductors and with various impurities starting at 10 mole%. If no effect is noticed at this concentration we do not plan to determine either with lower impurity concentrations.

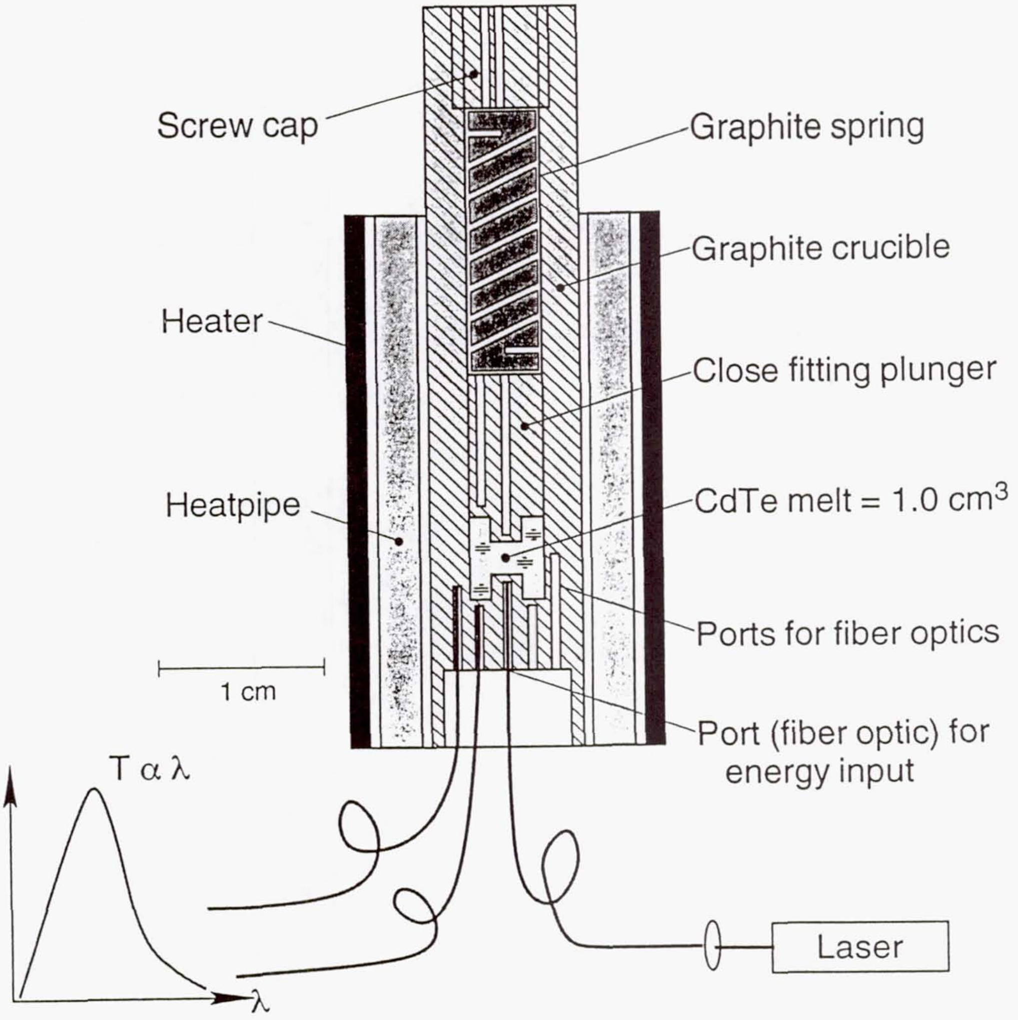

Figure1. Cell for determining thermal conductivty

Thermal and solutal expansion measurements

The additional thermophysical parameters that we propose to determine, the melt volume expansivity, the volume expansion on melting, do need not be measured in a low-gravity environment. These parameters are important in establishing a data base for modelling of heat and species transport. In addition they are necessary for establishing the correct sample length for our mass diffusion measurements. It should be noted that although various authors typically cite individual different references for each of the thermophysical parameters discussed in this proposal, most of these can be traced back to a single source [10]. The values given there determined by dilatometry or hydrostatic weighing, with a total error of 1.5% for the density (5.67 gm/cm^3 at the mp). At the same time, however, this group reported a melt volume expansion coefficient of 2×10^{-5}/K and a density change on fusion of 0.4%; i.e., in both cases the measurement error exceeds the measured change by several hundred percent! Thus, obviously, more definitive values need to be determined. With respect to thermal diffusivity only one reference is known for either pure CdTe [11] or HgTe [12], in both only two measurements were conducted and with the author in [11] noting a large discrepancy in the between the data sets.

The thermal and solutal expansion of solids and nonreactive liquids, at temperatures below about 600°C, is readily measured by X-ray diffraction [13] or pycnometric techniques [14,15], respectively. For higher temperature melts thermal expansion measurement by X-ray absorption is accurate to better than 1% [16-18]. However, for reactive liquids, such as the Te-based semiconductor alloys, with their low reported thermal expansion coefficients of 2×10^{-5}/K [10], the X-ray absorption or pycnometric techniques do not provide sufficient resolution. However, surfaces of these materials reflect visible light. Therefore, we plan to measure the thermal and solutal expansion of these melts with an interferometric technique, see below.

The thermal expansivity of CdTe, ZnTe and HgTe melts will be determined via an optical reflection (interference) technique. A collimated He-Ne laser beam will be reflected from the melt surface and recombined with a reference beam to set up an interference fringe pattern. Changes in the position of the melt surface will be determined by a counting the shift of the fringes. Changes in position of the melt surface not due to thermal expansion of the melt will be detected by reflection of part of the beam from a reference mirror. From the corrected fringe count, the known mass of the sample and the geometry of the ampoule, the thermal expansivity of the melt can be readily evaluated.

In the high temperature setup, we have to expect severe beam distortions. Hence, we assume that the resolution for surface displacements will be limited to one fringe shift. For typical dimensions of sample and ampoule, this results in a resolution for volume changes of 0.001%, compared to the 1.5% of the earlier determinations [5] discussed above. We are also investigating the use of a "low-coherence" length laser source. This would allow us to decrease our sensitivity to 0.1%, which may be more reasonable for these systems.

Bubble formation within the melt may lead to fringe shifts. For instance, the formation of a 100 mm bubble is sufficient to cause one fringe shift. We assume that will either rise to the surface, causing a sudden (detectable) shift in the fringes, or remain entrapped in the melt. Trapped bubbles will result in some detectable hysteresis.

We will determine the expansion coefficient for the three Te-based alloys, undoped and with a selection of dopants (Section 3.1) starting at 10 mole%.

Density change on melting

The density change on melting will be determined in the "T"-shaped silica glass cell schematically shown in Fig 2. This cell consists of a reservoir for the alloy ($\approx$ 15 cm^3) and an upper arm ($\approx$ 5 cm^3) with optical windows. After inserting the sample, the cell will be backfilled with xenon prior to sealing. A heatpipe will be used to achieve the best possible temperature uniformity.

As schematically shown in the figure, an optical beam will be passed times through the upper arm of the cell to set up an interferometric fringe pattern. On sample melting, the compression of the xenon gas will change the effective optical path length in the gas. This leads to a shift of the interference fringes. For a total optical path length of 5 cm and a practical ratio of sample volume to cell volume, again assuming that detectable path length changes are limited to a whole fringe shift, this arrangement results in a resolution for density changes of 0.03 %. The earlier determinations discussed above had a resolution of 1.5%.

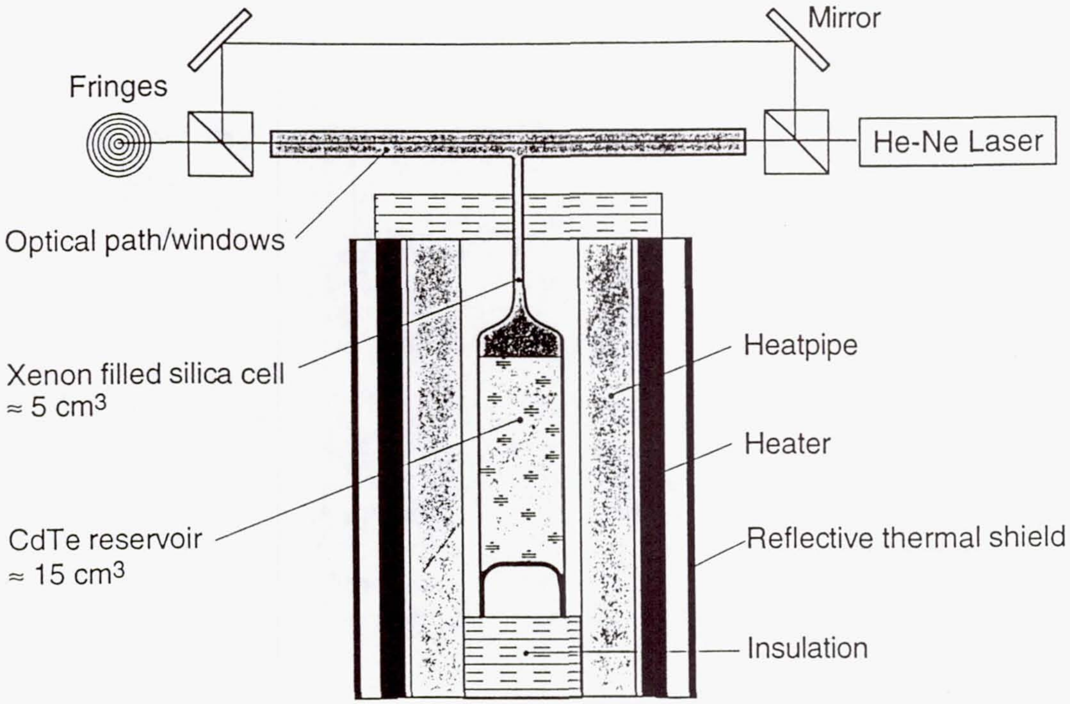

Figure 2. Cross section of cell for determining volume change on melting

References

[1] J.I.D. Alexander, J-F. Ramus and F. Rosenberger, Microgravity Sci. Tech (submitted).
[2] S. Nakamura, T. Hibiya, F. Yamamoto and T. Yokota, , International J. of Thermophysics, 12, 783 [1991].
[3] C. Harrison and F. Weinberg, Metallurgical Transactions B, 16B, 355 [1985].
[4] P. Codastefano, A. Di Russo and V. Zanza, Rev. Sci. Instrum. **48,** 1650 (1977).
[5] J.P.Davis, A. Samouris, L.C.Bobb and D.C. Larson, Fiber Optic and Laser Sensors VI, SPIE vol. 985, 53 (1988).
[6] A. Hu, M. Corke, F. Gillham and D. Stowe, Fiber Optic and Laser Sensors VI, SPIE vol. 985, 34 (1988).
[7] C.J. Nie, J.M. Yu, F. Wu and Y.P. Gao, Fiber Optic and Laser Sensors IX, SPIE vol. 1584, 87 (1991).
[8] A. Dandridge and A.D. Kersey, Fiber Optic and Laser Sensors VI, SPIE vol. 985, 34 (1988).
[9] Accufiber, Model 100, Luxtron Inc, New Jersey.
[10] G.G. Glazov, S.N. Chizhevskaya and N.N. Glagoleva, Liquid Semiconductors, Plenum Press, New York (1969), and V.M. Glazov, S.N. Chizhevskaya and S.B. Evgen'ev, Russ. J. Physical Chemistry, 43, 201 (1969).
[11] S. Sen, et al., J. Crystal Growth, 86, 110 [1986].
[12] L.R. Holland, J. Vacuum Science and Tech, A1, 1615 (1983).
[13] P.C. Dorsey, et. al., J. Applied Physics, 79, 3517 [1996].
[14] P.S. Fiske and J.F. Stebbins, Review of Sci. Instruments, 65, 3258 [1994].
[15] D. Chandra and L.R. Holland, J. Vacuum Science and Tech, A1, 1620 (1983).
[16] W.D. Drothing, J. of the Less-Common Metals, 96, 223 [1984].
[17] W.D. Drothing, High Temperatures-High Pressures, 13, 441 [1981].
[18] P.M. Nasch and S.G. Steinmann, Phys. Chem. Liquids, 29, 43 (1995).
[19] H. Buhl and R. Weiss, J. Crystal Growth, 131, 470 (1993).

Self-diffusion in Liquid Elements

R. Michael Banish, Lyle Jalbert and J. Iwan. D. Alexander*
Center for Microgravity and Materials Research
University of Alabama in Huntsville
Huntsville, AL 35899
banishm@email.uah.edu ; 256-890-6050

*Department of Mechanical and Aerospace Engineering
Case Western Reserve University
Cleveland, OH 44106
ida2@po.cwru.edu

Introduction

With increasing conceptual insight into transport and segregation in solidification and crystal growth, reliable data for diffusivities in liquid metals and semiconductors have become essential for guidance in process development. However, at this point even *self*-diffusion in elemental liquids is not well understood, let alone binary diffusion. In particular, there is little insight into the temperature dependence of diffusivities, D(T), and its correlation to the temperature-dependent structure of the liquid. Although various theories for D(T) have been developed over the years, the uncertainties associated with most diffusivity data are too large to allow for an unambiguous evaluation of these theoretical models. Currently, the differences between several theoretical predictions are often less than those between different sets of data for the same system. In addition, most D(T) data are limited to relatively narrow ranges in temperature beyond an element's melting point. Hence, for both theoretical and technological developments, there is a clear need for diffusivity measurements of improved accuracy and precision over wide temperature ranges for a variety of elements.

In the planned space experiments, the self-diffusivities of select liquid elements will be measured. A technique will be used that yields diffusivities at several temperatures with one sample. Thus, wide temperature ranges can be covered with a small number of samples. In this approach, which circumvents solidification of the diffusion sample prior to the concentration profiling, the evolution of the concentration distribution of a radiotracer is followed in real time using two pairs of radiation detectors. Furthermore, by employing an isotope which emits photons at (two) sufficiently different energies, transport in the bulk of the sample and near the container wall will be distinguished.

The scientific objectives of the proposed space experiments include the

- accurate measurement of self-diffusivities over a wide range in temperature in elements selected for their class-like liquid structure properties;
- interpretation of the measured diffusivities in terms of diffusion mechanisms and associated, temperature-dependent liquid structures; and
- quantification of the "wall effect" believed by some to contaminate diffusivity measurements in capillaries.

In the following we cover selected topics that either were not addressed during the 1996 Microgravity Materials Science Conference, or have been completed following this Conference. In December of 1997 the Science Concept Review was held for SDLE. We successfully passed that review. Additional tasks assigned by the Review panel will be addressed in the next Conference proceeding.

Background

For this research to study self-diffusion in molten melts we choose a direct or tracer technique utilizing a mathematical algorithm developed by Codastefano [1]. Our experimental hardware was designed to accommodate this mathematical algorithm [2]. This technique had previously not been applied to liquids, particularly for diffusivity measurements at several temperatures in a single experiment run. This approach is particularly suited to the limited availability of experiment time on space flights. Diffusivities are deduced in-situ and in real-time from consecutive concentration profiles obtained from radioisotope emission using a multiple detector arrangement. Two detectors are positioned symmetrically about the half-length L/2 of the capillary; where the location of the detectors is determined by the sample length at the (individual) measurement temperature. However, by a judicious choice of detector positions, 4 detectors (2 high, 2 low) may be used for measuring the diffusivity at several temperatures. At periodic time intervals, the activity is simultaneously monitored at the two locations. A single temperature hardware unit utilizing this approach to measure diffusion coefficients in molten indium metal has flown under NASA sponsorship on a MIR flight. The self-diffusivity values we have measured both on the ground and in space are among the lowest values reported for this material.

Application of technique to indium-terrestrial and low-gravity results

Experimental runs were performed at a single temperature as a verification of the method and hardware, both on Earth and aboard the space station Mir. In the ground-based tests we also investigated the effect of the initial source activity levels on the signal-to-noise ratio. To ensure mission success the hardware for these measurements included a backup set of detectors placed 180° from the primary set (left/right detectors). All experiments were run until diffusant/emitter uniformity was obtained throughout the sample. Typically this requires 100 hours at the low temperatures used in these experiments.

The first ground-based runs were performed at temperatures near 200 °C. In addition to verifing viability of this technique for liquid diffusion measurements, these runs established tha approximately 1 mCi of source activity would be sufficient for our experiments Radiation counts were taken continuously and summed every 10 seconds. Diffusant source parameters and apparent diffusivity results are summarized in Table 1.

Table 1. Summary of ground-based results at 200 °C.

Source activity [μCi]	Self-diffusivities in indium [10^{-5} cm^2/s]			
	Left detectors		Right detectors	
	190 keV	24 keV	190 keV	24 keV
53	2.44±0.16	(3.74)*	(only one pair used)	
75	2.60±0.17	2.47±0.16	2.64±0.17	2.43±0.16
150	2.46±0.16	(3.69)*	2.46±0.16	(2.36)*
600	2.14±0.14	2.16±0.14	2.21±0.14	2.24±0.14
5000	2.33±0.15	2.04±0.13	2.24±0.14	2.06±0.13

* ground loop/stray capacitance problems: calibration shifts during experiment.

All three runs performed on Mir utilized samples with an initial activity of 1 mCi. In runs 1 and 3 the Microgravity Isolation Mount (MIM) was operated in the latched mode, i.e., without g-jitter isolation. Run 2 was performed with active isolation. Unfortunately, due to hardware problems and time constraints, the planned defined input g-pulse runs were not carried out. The resulting apparent diffusivities are summarized in Table 2.

Table 2. LMD Mir results.

Run	Temperature [° C]	Self-diffusivities in indium [10^{-5} cm^2/s] Left detectors 190 keV	Left detectors 24 keV	Right detectors 190 keV	Right detectors 24 keV
1(latched)	186.5 ± 0.8	1.99±0.13	2.07±0.13	1.98±0.13	2.06±0.13
2(isolated)	185.0 ± 0.4	2.09±0.13	1.98±0.13	2.07±0.13	unusable
3(latched)	186.5 ± 0.4	2.08±0.13	2.09±0.13	2.05±0.13	unusable

Several aspects of these results are noteworthy. First, within the experimental uncertainty, the results are reproducible. Furthermore, the agreement between the left and right detector pairs indicates that at these low temperatures either convective transport contributions are insignificant or, less likely, affect the concentration distribution in the measurement plane rather symmetrically. The latter could result from a convection roll that is oriented normal to the plane of measurement.

Another important result is that the data obtained in space and on Earth are essentially the same. However, what is important it the low scatter of the Mir-acquired data. It is significant to note that the 6 data sets (three runs, high and low energy for each run) are within *one-half* a standard deviation of each other. It is not surprising that the space measurements reveal no g-jitter effects; due to both the rather low value of g and the g-jitter on the Mir and the relatively high viscosity of the melt at the measurement temperature .

Overall, these results are on the low end of the range of published values for D_{In}(200°C) which are from (2.2 - 3.8) × 10^{-5} cm^2/s.

Several diffusion runs with indium were carried out. Each run covered three consecutively lower temperatures. The results are summarized in Table 3, together with the self-diffusivities of In measured by other authors [3-7] are plotted in Fig. 1. The wide scatter of the data well illustrates that diffusivities obtained in liquids at normal gravity are prone to be contaminated by uncontrollable convection. As emphasized for liquid diffusivity measurements by Verhoeven [8], any horizontal component of a density gradient results in convection without a threshold. We have recently estimated convective contributions to transport in our experiments [9]. The numerical modeling results for self-diffusion in In at 730 °C in 30 mm long capillaries with 3 mm diameter, show that at normal gravity convective contributions become significant when an applied horizontal temperature non-uniformity ΔT_h exceeds 0.01 K. Often, flow due to horizontal density gradients can be reduced by keeping, as is the case in our experiments the top of the sample slightly warmer than its bottom. However, the above simulations [9] show that this can be rather ineffective and under certain conditions may even increase the apparent diffusivity.

Table 3. Apparent self-diffusivities obtained with indium at the two photon energies in four experiments.

Temperature [°C]	190 keV [10^5 D cm^2/sec]	24 keV [10^5 D cm^2/sec]
800	9.84 ± 0.59	10.07 ± 0.61
600	7.69 ± 0.48	8.02 ± 0.50
400	5.25 ± 0.34	5.01 ± 0.34
700	7.72 ± 0.47	-
500	6.20 ± 0.39	-
300	4.60 ± 0.33	-
900	8.95 ± 0.54	8.61 ± 0.52
800	9.80 ± 0.59	10.16 ± 0.61
700	8.93 ± 0.55	9.62 ± 0.60
900	11.75 ± 0.70	11.63 ± 0.59
600	8.04 ± 0.49	8.09 ± 0.50
300	4.54 ± 0.29	4.78 ± 0.31

From the above, it is not surprising that our data show evidence of convection in the samples. For instance, the apparent *D* at 700 °C deduced from the 900 - 700 °C run is significantly higher than that of the 700 - 300 °C run. This may be due to the longer time the first sample was at high temperature before the measurement at 700 °C was made. Thus there was more time for convective contamination of the diffusive transport. Note however, that the uncertainties for the two measurements at 900 °C do not overlap. We assign this to convective contributions

Finally, it should be noted that for all data, transport in the bulk of the sample and near the container wall were indistinguishable, i.e., no 'wall effect' was detected.

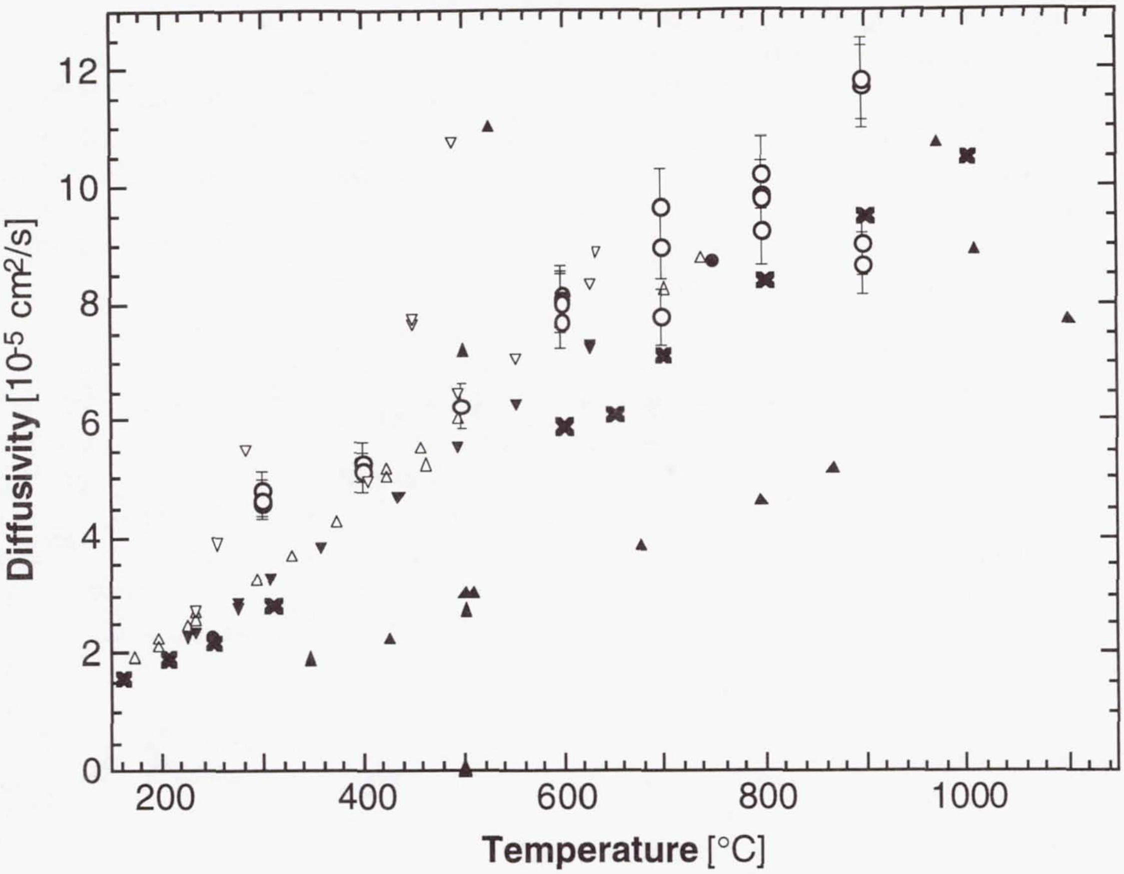

Fig. 1. Experimental data for self-diffusivities in indium: (○) this work ; (▲) Foster and Reynik [6]; (Δ) Lodding [4]; (●) Mathiak et al. [5]; (∇) and (▼) Carreri, Paoletti and Vincentini [3] with 1.6 and 0.83 mm diameter capillary, respectively, (✖) Oglobya, Lozovoi and Chumakov [7] with 0.5 mm diameter capillary.

Application of technique to tellurium

We have applied the multiple temperature hardware to ^{123m}Te/Te over the temperature range 500-740 °C. The two samples investigated had activities of approximately 200 μCi and 17 μCi, respectively. The diffusivity results for these experiments are shown in Table 4. Due to the low initial activity we were only able to measure at two temperatures in the first run and a single temperature in the second run.

Table 4. Apparent self-diffusivities obtained with tellurium.

Temperature [°C]	159 keV [10^5 D cm^2/sec]	27 keV [10^5 D cm^2/sec]
740	9.76 ± 0.59	9.60 ± 0.58
580	5.82 ± 0.36	6.02 ± 0.37
500	4.53 ± 0.28	4.26 ± 0.26

In comparison to the published values [10], our measurement at 500 °C produced a lower diffusivity. This can be attributed to less convective contamination of the transport using our technique. The two diffusion coefficients at 580°C and 740°C are the only existing measured values at higher temperatures. There is again no apparent difference between transport (diffusion) in the bulk and near the wall. Within this small data set there does not appear to be any abrupt change in diffusion at higher temperatures. This supports the gradual structural rearrangements noted in the neutron scattering data after the initial change at just above T_m.

Determination of Collimator Geometry

Geometric factors as well as radiation properties of the shielding material must be considered in optimizing the collimator geometry. Obviously, the radiation shield must be thick enough to absorb a large fraction of the radiation. Otherwise the detector signal is not representative of the radiation escaping through the collimation bores. Furthermore, due to the conical shape of the radiation beam transmitted by the collimation bore, r_c's larger than the sample diameter will not result in a commensurate increase of the radiation dose received by the detector. These arguments are further complicated by the scattering of and fluorescence induced by the primary radiation [11]. Our samples (^{114m}In) emit about 95% gamma and 5% beta radiation, with the average beta energy in excess of 750 keV. Both cause fluorescence in the shield. In addition, gamma radiation is Compton-scattered in the shield and, in particular, upon grazing incidence on the collimator surface. Each scattering process reduces the energy of the radiation. Thus, multiple scattering and fluorescence can lead to photons that are counted in energy windows different from those corresponding to the primary photons and beta particles.

We have experimentally investigated various collimator geometries for their effect on total radiation received by the detector. Hence, we used lead for the collimator optimization experiments, that were conducted at room temperature. Collimation holes of 1, 1.5, 2 and 3 mm diameter were drilled into lead shields of 12.7, 25.5 and 38.3 mm thickness. A 3 mm diameter cylindrical radioactive indium sample was placed consecutively behind the collimation bores. The detector signals were energy-discriminated; see Sect. IV.C. Table 5 summarizes the results. The signal-to-noise ratio is defined as the signal amplitude obtained in the energy window (± 0.3 keV about the chosen energy) divided by the sum of amplitudes measured in all other channels outside the energy window.

From these data, we can draw the following conclusions. Since the signal to noise ratio (SNR) for the 1 mm collimator hole is essentially 1, the smallest usable diameter is 1.5 mm. As expected, with the 3 mm sample diameter very little additional radiation is received on expanding the collimator diameter to more than 2 mm and, hence the SNR remains essentially unchanged or even decreases. Furthermore, the signal-to-noise ratio increases with the increase in the thickness of the radiation shield, from 12.7 mm to 25.5 mm, while a 38.3 mm thickness results in little further improvement.

Table 5. Signal to noise ratios obtained with various collimator geometries

Diameter [mm]	Lead Thickness [mm]	Signal/Noise at 24 keV	Signal/Noise at 190 keV
1	12.7	1.1	1.1
1.5	12.7	1.4	1.25
2	12.7	1.67	1.5
3	12.7	2.1	2.0
1	25.5	1	1
1.5	25.5	1.6	1.6
2	25.5	2.0	1.8
3	25.5	2.0	2.1
1	38.3	1	1
1.5	38.3	1.9	1.5
2	38.3	2.2	1.9
3	38.3	1.7	2.2

Copper, initially planned as the high-temperature radiation shield material, showed intolerably high fluorescence levels. For the actual high-temperature experiments, the radiation shield consisted of gold with a wall thickness of 15.5 mm. As calculated from absorption data [11], this wall thickness provides the same absorption for 190 keV photons as the 25.5 mm of lead used above. This results in an overall diameter of the radiation shield/isothermal liner of 41 mm. With this collimator geometry and 10 mm square detectors, the maximum distance between the outside edge of the collimator and detector must not exceed 30 mm if all radiation from the collimators is to be collected.

References

[1] P. Codastefano, A. Di Russo and V. Zanza, Rev. Sci. Instrum. **48,** 1650 (1977).

[2] Lyle B. Jalbert, R. Michael Banish and and F. Rosenberger, Physical Review E. **57**, 1727 (1998).

[3] G. Careri, A. Paoletti and M. Vincentini, Nuovo Cimento **10**, 1088 (1958).

[4] V.A. Lodding, Z. Naturforschg. **11a**, 200 (1956).

[5] G. Mathiak et al., J. Non-Crystalline Solids **205-207**, 412 (1996).

[6] J.P. Foster and R.J. Reynik, Metallurgical Transactions **4**, 207 (1973).

[7] V.I. Oglobya, V.I. Lozovoi and A.G. Chumakov, Phys Metals **9**, 455 (1990).

[8] J.D. Verhoeven, Trans. Met. Soc. AIME **242**, 1937 (1968).

[9] I. Alexander , J.-F. Ramus and and F. Rosenberger, Microgravity Science and Technology **9**, 158 (1996).

[10] D.H. Kurlat, C. Potard and P. Hicter, Phys. Chem. Liqu. **4**, 183 (1974).

[11] W.H. Tait, *Radiation Detection*, (Butterworths, London 1980).

Page intentionally left blank

Experiments on Nucleation in Different Flow Regimes

R. J. Bayuzick, W.H. Hofmeister, and C.M. Morton
Department of Chemical Engineering, Vanderbilt University
M.B. Robinson
Space Sciences Laboratory, MSFC

Introduction

The vast majority of metallic engineering materials are solidified from the liquid phase. Understanding the solidification process is essential to control microstructure, which in turn, determines the properties of materials. The genesis of solidification is nucleation, where the first stable solid forms from the liquid phase. Nucleation kinetics determine the degree of undercooling and phase selection. As such, it is important to understand nucleation phenomena in order to control solidification or glass formation in metals and alloys.

Early experiments in nucleation kinetics were accomplished by droplet dispersion methods [1-6]. Dilitometry was used by Turnbull and others, and more recently differential thermal analysis and differential scanning calorimetry have been used for kinetic studies. These techniques have enjoyed success; however, there are difficulties with these experiments. Since materials are dispersed in a medium, the character of the emulsion/metal interface affects the nucleation behavior. Statistics are derived from the large number of particles observed in a single experiment, but dispersions have a finite size distribution which adds to the uncertainty of the kinetic determinations. Even though temperature can be controlled quite well before the onset of nucleation, the release of the latent heat of fusion during nucleation of particles complicates the assumption of isothermality during these experiments.

Containerless processing has enabled another approach to the study of nucleation kinetics [7]. With levitation techniques it is possible to undercool one sample to nucleation repeatedly in a controlled manner, such that the statistics of the nucleation process can be derived from multiple experiments on a single sample. The authors have fully developed the analysis of nucleation experiments on single samples following the suggestions of Skripov [8]. The advantage of these experiments is that the samples are directly observable. The nucleation temperature can be measured by noncontact optical pyrometry, the mass of the sample is known, and post processing analysis can be conducted on the sample. The disadvantages are that temperature measurement must have exceptionally high precision, and it is not possible to isolate specific heterogeneous sites as in droplet dispersions.

Experimental Method

Levitation processing of refractory materials in ultra high vacuum provides an avenue to conduct kinetic studies on single samples. Two experimental methods have been identified where ultra high vacuum experiments are possible; electrostatic levitation in ground based experiments and electromagnetic processing in low earth orbit on TEMPUS [9]. Such experiments, reported here, were conducted on zirconium. Liquid zirconium is an excellent solvent and has a high solubility for contaminants contained in the bulk material as well as those contaminants found in the vacuum environment. Oxides, nitrides, and carbides do not exist in the melt, and do not form on the surface of molten zirconium, for the materials and vacuum levels used in this study.

Ground based experiments with electrostatic levitation have shown that the statistical nucleation kinetic experiments are viable and yield results which are consistent with classical nucleation theory [9]. The advantage of low earth orbit experiments is the ability to vary the flow conditions in the liquid prior to nucleation. The purpose of nucleation experiments in TEMPUS was to examine the effects of fluid flow on nucleation.

The primary evidence for a change in nucleation behavior is a shift in the mean undercooling. It is not necessary to know the functional form of the nucleation rate equation, or the operative mechanism to make the comparison of nucleation behavior under two different flow conditions. Simply stated, if the nucleation rate is different for two experimental conditions, then the parent distribution of nucleation events is different and the mean undercooling is different.

Null hypothesis testing is used to determine if the difference in means of two samples reflects a significant difference in the means of parent distributions for two experimental conditions. Two sets of data (A and B) can be compared by analysis of means using the null hypothesis.

The null hypothesis (H_o) is:

The mean nucleation temperature in experiment A and experiment B are identical.

and, the alternate hypothesis (H_1) is:

The mean nucleation temperature in experiment A and experiment B are different.

If H_0 is rejected and H_1 supported, then the means of the parent distributions are different and therefore the nucleation rate as a function of temperature is different.

The central limit theorem states that the means of samples from a population will be distributed normally, even if the population is not normally distributed. Nucleation temperature distributions, particularly those at low activation energies, are not normally distributed. However, in invoking the central limit theorem, no assumptions about the underlying distributions are necessary, and the means of two samples can be compared by using Student's "t" distribution [10].

Results and Conclusions

Statistical distributions of undercoolings were generated in “free cooling” experiments on TEMPUS. During free cooling the heater power is set to the lowest value, and the power input to the sample comes from the positioning field. One sample was repeatedly melted and cooled to freezing, holding all experimental variables constant except for the positioner power settings on cooling. Two different power supply settings were used; the lowest positioner power capable of stable positioning of the sample, and a high positioner power. The pure radiation cooling rate for this sample is $53Ks^{-1}$. At the low positioner power the cooling rate was $50Ks^{-1}$, and at the high positioner power the cooling rate was $48Ks^{-1}$. Fluid flow calculations for the lower positioner power indicate the undercooled liquid is in the laminar flow regime with flows of approximately 4 cm s^{-1} and Reynolds numbers of about 200[11]. Modeling is continuing to characterize the flow regime corresponding to the higher positioner power which is know to be greater than the low power. The experiments were interspersed to minimize any effect of sample history on the comparison.

The distributions of undercoolings for these experiments and the nucleation kinetic fits are shown in figure 1. A t-test for mean undercooling at the 95% confidence level supports the null hypothesis and rejects the alternate hypothesis. These experiments revealed there is no significant change in the nucleation behavior in the range of flow conditions tested.

The kinetic determinations made from the distributions, assuming the classical nucleation expression [12] are given in table I. These kinetic determinations are consistent with ground based experiments on zirconium using the electrostatic levitator. The kinetic values are similar to those for arc melted samples, and are lower than the maximum values (ΔTmean=348K, $K_v=10^{43}$, $\Delta G^*=88kT$) obtained on a machined sample in the electrostatic levitator. The kinetic determinations are believed to be lower because of the temperature measurement uncertainty caused by sample translations on MSL-1. The maximum mean undercoolings from MSL-1 scale to the maximum achieved in the ESL if volume and cooling rate are considered.

Other experiments were conducted to determine the surface tension and viscosity of the undercooled melt [13], and to examine the heat capacity by noncontact modulation calorimetry [14]. To accomplish these experiments in the undercooled melt, the heater power was used to hold liquid samples at the desired temperature and pulsing or modulation of the heater was used to excite surface oscillations or to modulate the temperature of the sample. Experiments at low temperatures (and heater powers) were followed by free cooling to the nucleation temperature, which, in all cases was within the bounds of the distributions in the previous experiments. In experiments near the melting temperature, at heater voltages above 220 V, the undercooling of the samples was significantly limited as shown in figure 2. At 220 V heater the flows are estimated to be 50 cm s^{-1}. Initial analysis by Hyers and Trapaga indicates that at these flows the dynamic pressure is equal to the static pressure in the samples, a condition which is known to cause cavitation in fluid flows [15]. The collapse of cavitation bubbles creates sufficient pressures to raise the melting point of the material through the Clapyeron equation such that nucleation of the solid occurs [16-18].

Additional evidence of nucleation by cavitation can be found in the modulation experiments. A compilation of specific heat/total hemispherical emissivity (Cp/ϵ) determinations from the drop tube, electrostatic levitator and TEMPUS is shown in figure 3. The drop tube data was derived by measuring the release temperature of Zr pendant drops, the free fall time to recalescence in vacuum, and the nucleation temperature. In 135 experiments with masses around 0.23 g, the average ratio of specific heat to total hemispherical emissivity was 1.57 with a one sigma standard deviation of 0.03. In the electrostatic levitator, 332 cooling curves (four samples, mass range from 0.013 to 0.057 g) were evaluated by a sliding boxcar fit of the cooling curves to the radiation cooling equation solving for Cp/ϵ. The average value over the temperature range was 1.54 ± 0.12 (1σ). The TEMPUS modulation Cp/ϵ data falls within the bounds of these other determinations except for the experiment at the melting temperature. This determination is apparently 13-15% higher than the rest of the data. Other determinations indicate that there is no temperature dependence of Cp/ϵ in the measured range and do not support the findings of the TEMPUS modulation experiment at the melting temperature. In essence, the melting temperature data showed a smaller modulation in temperature for the applied power modulation. The temperature modulations in this experiment were 10K above below the melting temperature at a frequency of 0.1Hz. A cyclic phase transformation including nucleation by cavitation and subsequent remelting provides a heat source during cooling and a heat sink during melting which explains the decrease in the temperature modulation around the melting point. This explanation is consistent with the above fluid flow calculations.

These experiments indicate that fluid flow has no effect on nucleation until the cavitation phenomenon occurs, and that cavitation induced nucleation is responsible for limiting bulk undercooling in the higher flow regimes.

References

1. D. Turnbull, J. Chem. Phys., **20** (3), 411 (1952).
2. D. Turnbull, J. Chem. Phys. **18**, 198 (1950).
3. J.J. Richmond, J.H. Perepezko, S.E. LeBeau, and K.P. Cooper, in "Rapid Solidification Processing: Principles and Technologies III" (R. Mehrabian, ed.), pp. 90-95, NBS, Gaithersburg, MD, 1982.
4. J.H. Perepezko, S.E. LeBeau, B.A. Mueller, and G.J. Hildeman, in "ASTM Conference on Rapidly Solidified Powder Aluminum Alloys" (M.E. Fine and E.A. Starke, Jr., eds.), pp. 118-136, ASTM-STP 890. Philadelphia, PA, 1985.
5. W.T. Kim, D.L. Zhang and B. Cantor, Met. Trans. A **22A**, 2487 (1991).
6. G.A. Merry and H. Reiss, Acta. Metall. V. 32, no. 9 (1984) p. 1447.
7. C.W. Morton, W.H. Hofmeister, R.J. Bayuzick, and M.B. Robinson, Mat. Sci. Eng. **A178** (1-2), 209 (1994).
8. V.P. Skripov, in "Current Topics in Materials Science, Crystal Growth in Materials, Vol. 2" (E. Kaldis and H.J. Scheel, eds.), p. 328, North Holland Publishing Co., New York, 1977.
9. C.W. Morton, W.H. Hofmeister, R.J. Bayuzick, A. Rulison, J. Watkins; submitted to Acta Materialia.
10. G.K. Bhattacharyya and R.A. Johnson; "Statistical Methods and Concepts", John Wiley and Sons, New York, 1977.
11. R. W. Hyers and G. Trapaga, MIT, personal communication.
12. D. Turnbull, and J.C. Fisher, J. Chem. Phys., **17** (1), 71 (1949).
13. I. Egry; J. Mat. Sci. 26 (1991) 2997-3003.
14. H.J. Fecht and W.L. Johnson; Rev. Sci. Instrum. V. 65, no. 5 (1991) p. 1299.
15. I.S. Pearsall; I. Mech. E., CME, July 1974, p. 79.
16. J.D. Hunt and K.A. Jackson; J. Appl. Phys. V. 37, no. 1 (1966) p.254.
17. R. Hickling; Nature, v. 206, no.4987 (1965) p. 915.
18. J.J. Frawley and W.J. Childs; Trans. AIME, v. 242, Feb. 1968, p.256.

Table I: Results of kinetic determinations of nucleation distributions from MSL-1R. The Classical Turnbull-Fisher expression was used to fit the distributions.

Positioner Power	Mean Undercooling $\Delta T_{avg} \pm 1\sigma$ (K)	log K_v ($\sigma \approx 3.0$)	ΔG^* (kT) ($\sigma \approx 7.0$)
Low	333.8 ± 4.8	29	62
High	334.7 ± 3.2	34	72

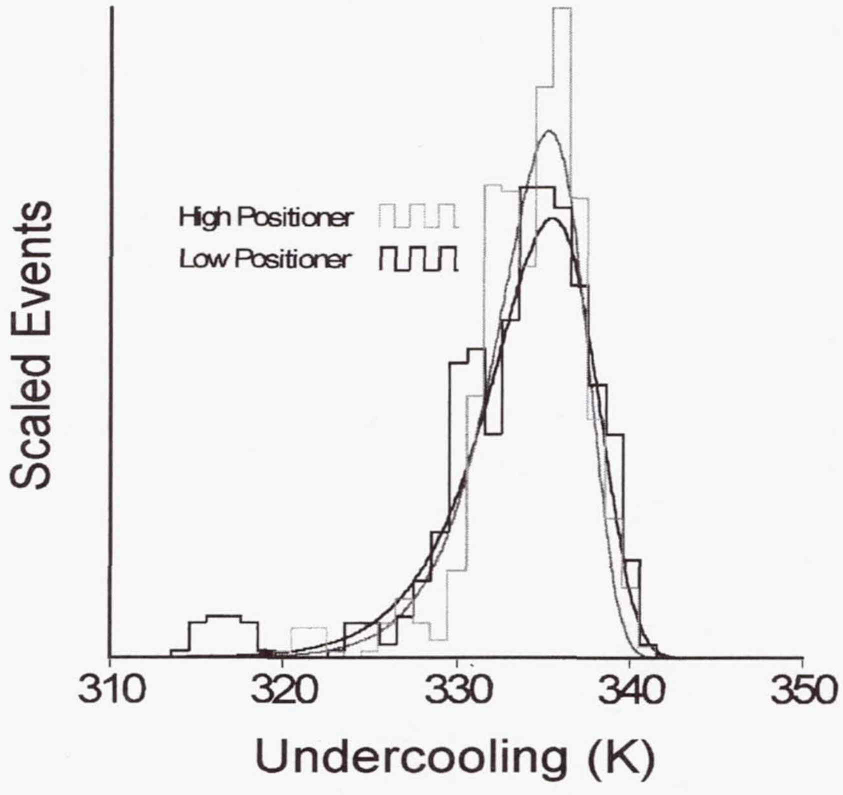

Figure 1: Two distributions from "free cooling" experiments on MSL-1R. The Low Positioner distribution is in the laminar flow regime and the High Positioner is believed to be in a transitional flow regime.

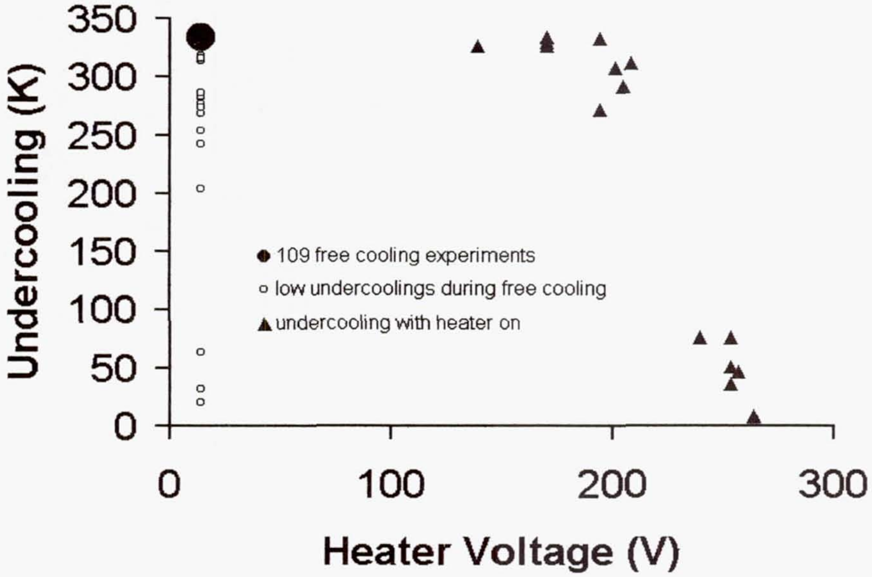

Figure 2: All zirconium undercoolings from two samples are compiled in this graph as a function of heater voltage applied during the cycle. Both distributions in figure 1 are contained in the large circle at the upper left. Samples processed above 220 V heater would not undercool to the same level as those cooled with less heater voltage applied.

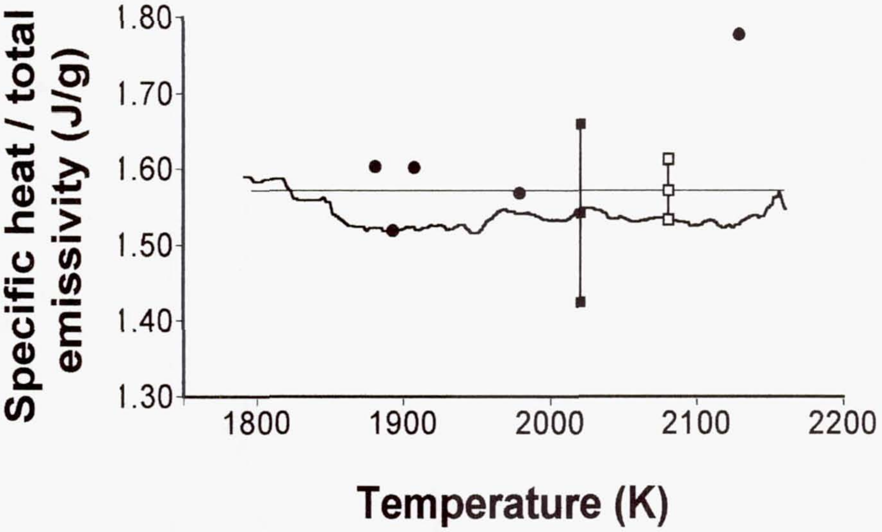

Figure 3: The ESL data as a function of temperature is plotted as the thick black line. The average ESL data over the temperature range is represented with filled squares. The drop tube data temperature range is represented with a thin straight line and the mean and one sigma points as open squares. The modulation calorimetry results from TEMPUS are given as filled circles.

INVESTIGATION OF THE RELATIONSHIP BETWEEN UNDERCOOLING AND SOLIDIFICATION VELOCITY

B.T. Bassler, A. Altgilbers, W.H. Hofmeister and R. J. Bayuzick
Department of Chemical Engineering, Vanderbilt University,
Nashville, TN 37235

INTRODUCTION

The overarching driver for this work is the heart of Materials Science, namely the understanding of microstructure and its genesis. For solidification processing, two dominant factors for microstructural development are undercooling and solidification speed but these are not, at this time, nominally fully utilized as parameters. One reason is that the effects of undercooling and solidification velocity on microstructure are not quantitatively understood. Furthermore, the relationships between undercooling and solidification velocity are not completely understood. Two pivotal aspects of the lack of understanding are disagreement between theory and experimental results on "bulk" samples and the disagreement between experimental results.

Thus, the principal objective of this work is to accurately and systematically quantify the solidification velocity as a function of deep undercooling for pure metals and alloys. The primary hypothesis to be tested is that present theories on the effect of undercooling on solidification velocity do not predict the actual behavior. Within this framework and the framework of flight definition, another objective is to pinpoint the adequacy of ground based experimentation and, conversely, the need for microgravity experimentation.

The general approach is to use direct imaging at high frame rates (up to 1,000,000 frames per second) to measure the speed of solidification at high undercoolings. Electromagnetic and electrostatic levitation techniques are to be used to limit heterogeneous nucleation and to obtain an unobstructed direct view. Pure nickel, pure titanium, pure silicon, nickel based alloys and titanium based alloys are the materials of interest.

EXPERIMENTAL METHOD

Utilizing electromagnetic levitation, six millimeter specimens are levitated, heated, melted and cooled. At chosen undercoolings, nucleation is triggered by touching the side of the sample with a needle. The specimen is observed over its lower hemisphere through a mirror by a high speed array of photodiodes to track the solidification event[1]. Because of the release of the heat of fusion, a thermal field defining hot solid and undercooled liquid is produced with the interface clearly delineated by the brightness difference. The instrumentation that has been developed to follow the trace of the interface over the lower hemisphere consists of a 10x10 array of 2.5 mm square photodiodes. Voltage outputs from each photodiode is monitored simultaneously for up to a total of 8192 frames of data acquisition at speeds ranging from 2 msec to 1 μsec per frame at 8 bits per channel per image. The position of the interface is located by the voltage responses and spatial transformations are used to place the position of the solidification interface within the specimen over time. From this, the solidification velocity (V) can be obtained with an error of about 10 % V.

EXPERIMENTAL RESULTS

Table 1 shows a summary of alloys processed along with the range of undercoolings within which solidification velocities have been determined. Figures 1, 2 and 3 give the graphical representations of the solidification velocity determined as a function of undercooling for the nominally pure nickel specimens. Figure 4 is an overlay of the previous three figures. Differences shown are attributed to effects of interstitial solute on the solidification velocity. Nickel processed in He/H_2 results in a reduction of residual oxygen content as compared to pure nickel. On the other hand, processing nickel with a leak results in an increase of oxygen content as compared to pure nickel.

The effects on solidification velocity/undercooling relationships for carbon additions to nickel are graphically illustrated in Figure 5. The graphs are overlaid in Figure 6. Significant effects of the carbon additions on solidification velocity are evident. Figure 7 shows the behavior of solidification velocity with undercooling for nickel-1.2a/o titanium and Figure 8 illustrates the graphical comparison between the alloy and pure nickel. The solidification velocity dependence on undercooling for pure titanium is shown in Figure 9.

COMPARISONS TO THEORY

The theory according to Boettinger, Coriell and Trivedi (BCT theory)[2] is a theory relating solidification velocity to undercooling that is somewhat further along the evolutionary ladder in that, in essence, it attempts to describe behavior at higher undercoolings with non-equilibrium interface conditions. Hence, the theory is being used as a benchmark with which to compare experimental results. Figure 10 shows some comparisons.

In all cases given in Figure 10, there is a major departure from the theory at high undercoolings. The theory predicts a continual increase with undercooling whereas actual behavior shows an arrest in the solidification velocity. Also, at low undercoolings, conformation with theory is obtained only if a smaller stability constant than that used by BCT is applied. In contrast to the other materials studied, pure titanium does not exhibit an arrest in solidification velocity with undercooling in similar undercooling regimes. In addition, no conformation with theory can be obtained by simply changing the stability constant. Furthermore, in the nickel-carbon alloys as well as in nickel containing residual elements, it is noted that solute effects are indicated in a regime which is expected to be thermally dominated.

Figure 11 represents an attempt at comparing experimental results for nickel-carbon alloys with BCT theory at lower undercoolings, incorporating solute drag[3] into the theory. The correlation is less than satisfactory. Solute drag incorporation for Nickel-2.8a/o C predicts the form of the dependence but would predict lower solidification velocities as a function of undercooling. In Ni-1.7a/o C alloys there is an indication of a fit but only in a limited portion of the undercooling regime.

OBSERVED TRENDS

Some trends are evident from the data obtained thus far. With the exception of the behavior in pure titanium, at high undercoolings, a transition in the dependency of solidification velocity on undercooling is indicated at a critical undercooling. The undercooling and solidification velocity at the transition is a function of material, solute type, solute concentration and processing environment. A second transition is indicated at intermediate undercooling in higher solute alloys.

Three different stages of solidification velocity dependency are also indicated by microstructural analysis. Stage 1 would correspond to coarse widely spaced dendrites; stage 2 would correspond to refinement and closer spacing of dendrites; and stage 3 would correspond to closely spaced dendrites without secondary arms. Since theory is based on a model of an isolated dendrite, stage 3 would depart significantly from the assumptions, resulting modeling, and resulting predictions of the theory. Stage 2 would likewise be compromised.

In nickel and the nickel alloys, the BCT theory correlates with experiment in the lower undercooling regimes if the stability parameter is changed from the $1/4\pi^2$ value of Langer and Müller-Krumbhaar[4]. Fits are obtained using $1/8\pi^2$ for Ni processed in He/H_2. For Ni, Ni-0.6a/o C, and Ni-1.2a/o Ti, fits are obtained if the stability parameter is set at $1/12\pi^2$. The results for titanium can not be made to correlate with the theory utilizing the Langer/Müller-Krumbhaar value or any modification thereof.

Incorporation of solute drag into the theory brings experiment and theory closer together for the higher nickel-carbon alloys. However, significant discrepancy remains.

NEAR TERM DIRECTIONS

The data base utilizing electromagnetic levitation and heating will be expanded. Work in nickel-carbon alloys and nickel-titanium alloys will be continued. To this will be added experiments in nickel-silicon and nickel-tin alloys. In addition, various titanium alloys will be investigated. Experiments utilizing electrostatic levitation is of great interest. Development of the equipment and techniques for conducting these experiments will continue. At the earliest opportunity, electrostatic levitation experiments will be carried out.

REFERENCES

1. B.T. Bassler, R.S. Brunner, W.H. Hofmeister, and R. J. Bayuzick, "Ultra High Speed Imaging System for the Measurement of Solidification Velocity Via Direct Observation of Rapid Solidification," to be published in Review of Scientific Instruments, April, 1997.

2. W.J. Boettinger, S.R. Coriell, and R. Trivedi, "Application of Dendrite Growth Theory to the Interpretation of Rapid Solidification Microstructures": in *Rapid Solidification Processing: Principles and Technologies, IV*, R. Mehrabian and P.A. Parrish, eds., Claitor's Publishing Division, Baton Rouge, LA, 1988, pp. 13-25.

3. M.J. Aziz and W.J. Boettinger, "On the Transition from Short-range Diffusion-limited to Collision-limited Growth in Alloy Solidification," Acta Metallurgica et Materialia,42, 2, 1994.

4. J.S. Langer and H. Müller-Krumbhaar, "Theory of Dendritic Growth," Acta Met, 26, 1978.

Material	Processing Environment	Liquidus Temperature T_M	Minimum Undercooling	Maximum Undercooling
Nickel	UHP He	1726 K	4.4 $\%T_M$	15.5 $\%T_M$
Nickel	He w/air leak	1726 K	5.0 $\%T_M$	13.7 $\%T_M$
Nickel	He-20H_2	1726 K	4.6 $\%T_M$	15.8 $\%T_M$
Titanium	UHP He	1933 K	8.0 $\%T_M$	14.4 $\%T_M$
Ni-0.6 a/o C	UHP He	1723 K	3.2 $\%T_M$	14.1 $\%T_M$
Ni-1.7 a/o C	UHP He	1712 K	5.6 $\%T_M$	14.9 $\%T_M$
Ni-2.8 a/o C	UHP He	1699 K	5.4 $\%T_M$	13.6 $\%T_M$
Ni-1.2 a/o Ti	UHP He	1712 K	4.1 $\%T_M$	14.1 $\%T_M$

Table 1. Undercooling ranges of processed alloys.

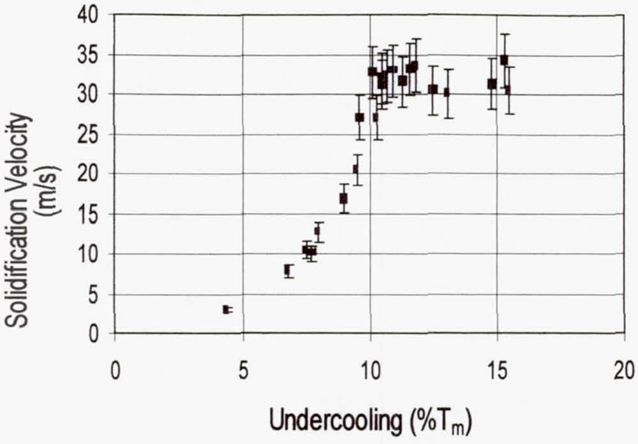

Figure 1 - Solidification velocity as a function of undercooling for pure nickel processed in UHP He. The error b`ars represent ±10% of the velocity value.

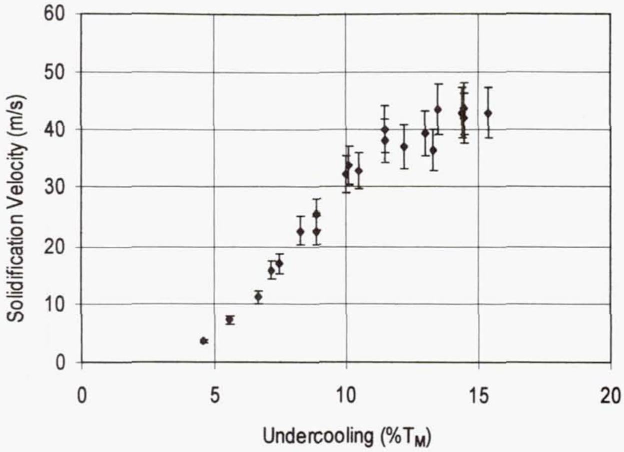

Figure 2 - Solidification velocity as a function of undercooling for pure nickel processed in He-20w/o H_2. The error bars represent ±10% of the velocity value.

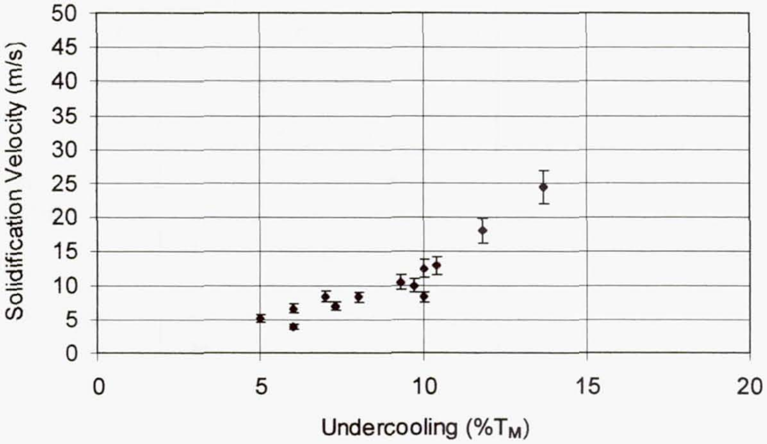

Figure 3 - Solidification velocity as a function of undercooling for pure nickel processed in UHP He with an air leak in the gas inlet to the electromagnetic levitator. The error bars represent ±10% of the velocity value.

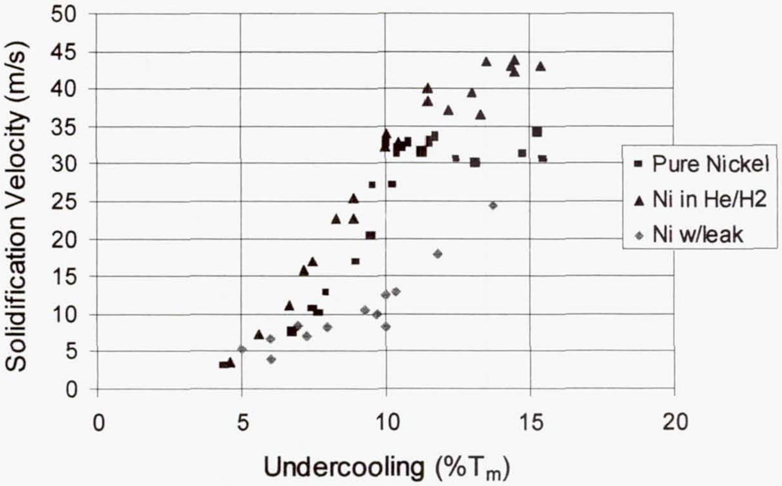

Figure 4 - Solidification velocity as a function of undercooling for pure nickel processed in different gas environments. The error bars of ±10% of the velocity value are not shown in order to present the data as clearly as possible.

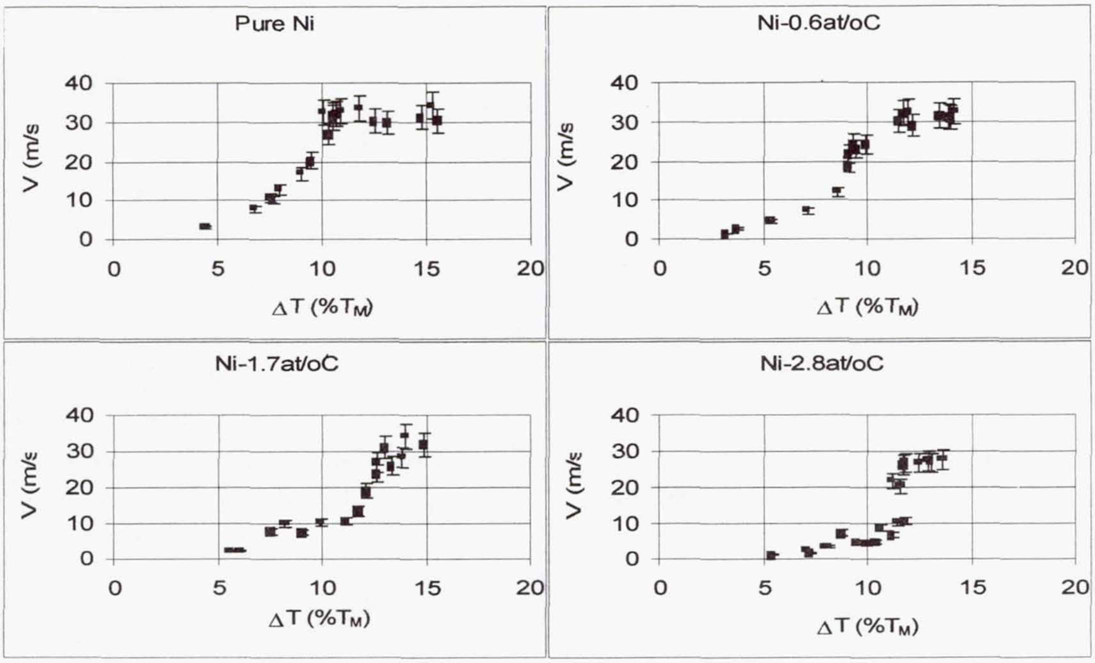

Figure 5 - The results for the solidification velocity as a function of undercooling for Ni in UHP He, Ni-0.6a/o C in UHP He, Ni-1.7a/o C in UHP He, and Ni-2.8a/o C in UHP He. The error bars represent ±10% of the velocity value.

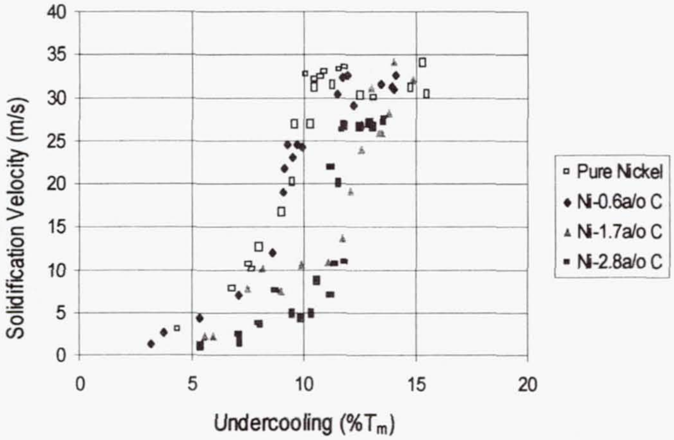

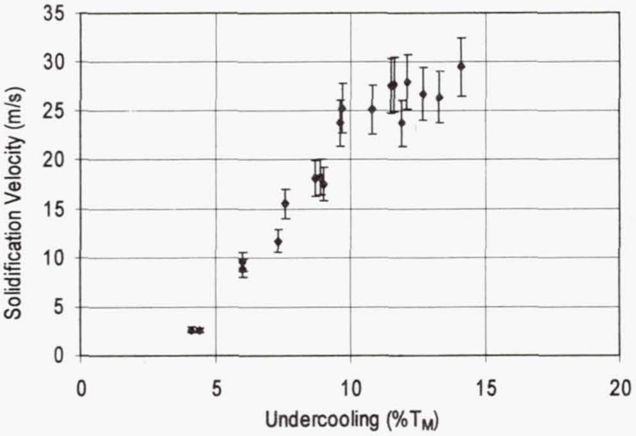

Figure 6 - Graph of all of the nickel-carbon together with the results for pure nickel. The data illustrates the increasing effect of carbon concentration on the solidification velocity of nickel with increasing concentration. The error bars of ±10% of the velocity value are not shown in order to present the data as clearly as possible.

Figure 7 - Graph of the solidification velocity as a function of undercooling for Ni-1.2a/o Ti processed in UHP He. The error bars represent ±10% of the velocity value.

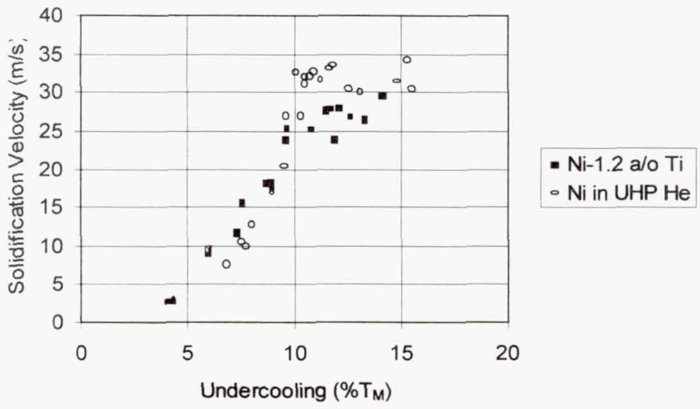

Figure 8 - Ni-1.2a/o Ti results plotted along with the solidification velocity results for pure nickel in UHP He. The error bars of ±10% of the velocity value are not shown in order to present the data as clearly as possible.

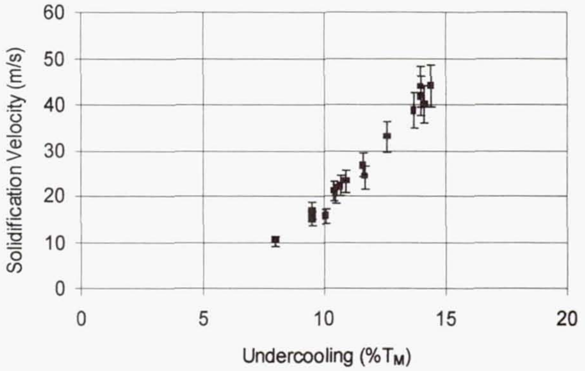

Figure 9 - Solidification velocity as a function of undercooling for pure titanium processed in UHP He. The error bars represent ±10% of the velocity value.

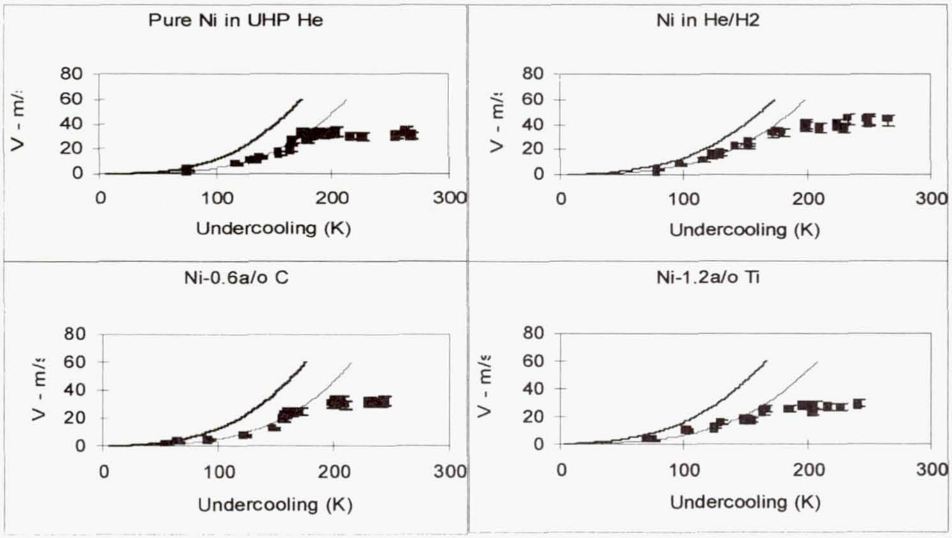

Figure 10 - The experimental data for pure nickel, Ni processed in He/H_2, Ni-0.6a/oC, and Ni-1.2a/oTi are shown along with the theoretical predictions of the BCT theory. The heavy black line in each graph was calculated using $\sigma^*=1/4\pi^2$. The thin lines were calculated for Ni in UHP He using $\sigma^*=1/12\pi^2$, for Ni in He/H_2 using a concentration of 0.005a/o H_2 and $\sigma^*=1/8\pi^2$, for Ni-0.6a/oC using $\sigma^*=1/12\pi^2$, and for Ni-1.2a/oTi using $\sigma^*=1/12\pi^2$.

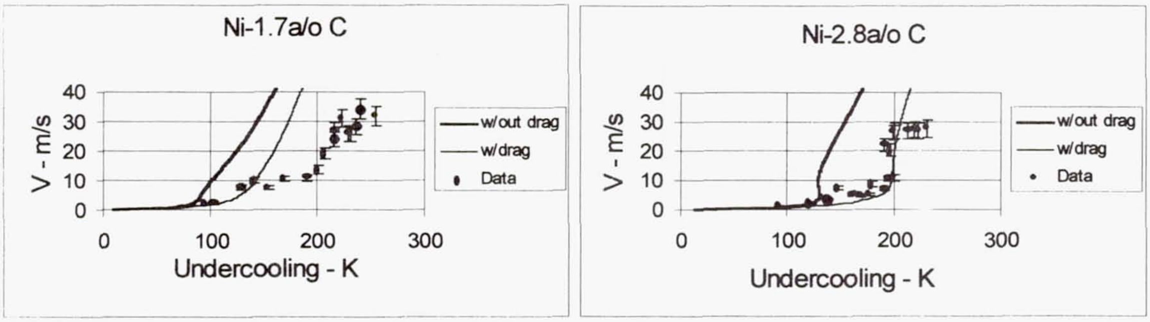

Figure 11 - BCT predictions without and with solute drag for Ni-1.7a/oC and Ni-2.8a/oC. Both curves were calculated using the smallest k_E of each alloy and $\sigma^*=1/4\pi^2$.

EQUIAXED DENDRITIC SOLIDIFICATION EXPERIMENT (EDSE)

C. Beckermann, Professor
Department of Mechanical Engineering
The University of Iowa
Iowa City, IA 52242-1527

Co-Investigators:
I. Steinbach, ACCESS e.V.
A. Karma, Northeastern University
H.C. deGroh III, Nasa Lewis

OBJECTIVES

The objective of the research is to quantitatively determine and understand the fundamental mechanisms that control the microstructural evolution during solidification of an assemblage of equiaxed dendritic crystals. A microgravity experiment will be conducted to obtain benchmark data on the transient growth and interaction of up to four equiaxed crystals of a pure and transparent metal analog (succinonitrile, SCN) under strictly diffusion dominated conditions. Of interest in the experiment are the transient evolution of the primary and secondary dendrite tip speeds, the dendrite morphology (i.e., tip radii, branch spacings, etc.) and solid fraction, the tip selection criterion, and the temperature field in the melt for a range of initial supercoolings and, thus, interaction "strengths" between the crystals. The experiment thus extends the microgravity measurements of Glicksman and coworkers for steady growth of a single dendrite [Isothermal Dendritic Growth Experiment (IDGE), first flown on USMP-2] to a case where growth transients are introduced due to thermal interactions between neighboring dendrites – a situation more close to actual casting conditions. Corresponding earth-based experiments will be conducted to ascertain the influence of melt convection. The experiments are supported by a variety of analytical models and numerical simulations. The data will primarily be used to develop and test theories of transient dendritic growth and the solidification of multiple interacting equiaxed crystals in a supercooled melt.

NEED FOR MICROGRAVITY

Experimental validation of present equiaxed dendritic solidification models is very limited, with only a few bulk solidification experiments conducted (on earth) using metal alloys [1]. There are basically four issues that have hampered the testing of such models: (i) the inability to control and quantify nucleation, (ii) the presence of uncontrolled, gravity-driven melt convection and crystal movement, (iii) the difficulty to observe growth in metallic systems, and (iv) the complications associated with coupled thermal and solutal undercoolings when using alloys. The Equiaxed Dendritic Solidification Experiment (EDSE) is designed to be simple, yet overcomes all of these limitations. In particular, even with an initially isothermal sample, gravity-driven convection caused by latent heat release can only be minimized in a microgravity environment. Due to our inability to analyze solidification microstructure evolution in the presence of this convection, it is important to first generate benchmark data for the diffusion limit.

RESULTS

The research to date has concentrated on:

- (i) development of the science requirements for the proposed microgravity experiment;
- (ii) design, construction, and testing of a ground-based version of the experiment;
- (iii) modeling of the growth of an assemblage of equiaxed dendritic crystals.

These efforts have culminated in the passing of the Science Concept Review (SCR) held at Nasa Lewis in February of 1998. The research team is now preparing for the Requirements Definition Review (RDR). Some of the experimental and theoretical research is described in greater detail below.

Ground-Based Experiments

We have conducted preliminary experiments involving an assemblage of equiaxed crystals using a setup that is functionally similar to the planned EDSE. A schematic of the setup together with a photograph taken during an experiment is shown in Figure 1.

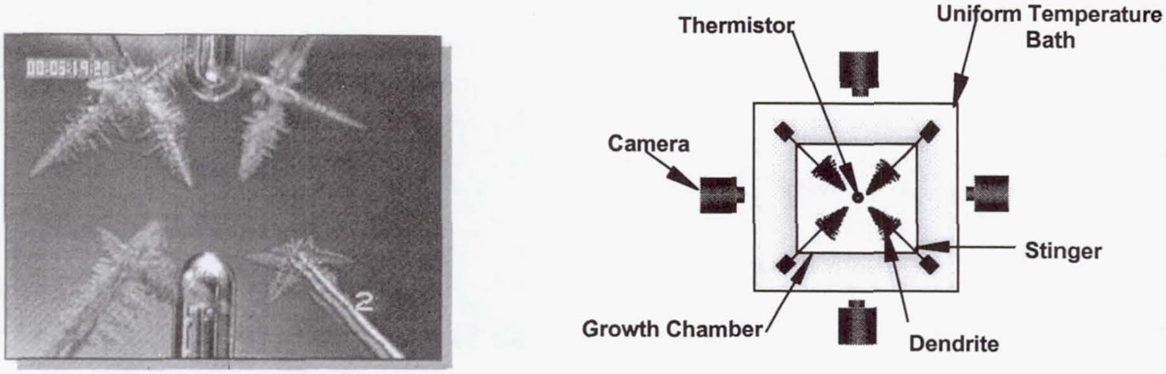

Tetrahedron Arrangement of Dendrites **Dendritic Solidification Apparatus**

Fig.1 Schematic of the equiaxed dendritic solidification apparatus and a photograph showing the tetrahedron arrangement of the dendrites

A glass growth chamber is contained within a temperature regulated bath. Four CCD cameras, with light sources, provide orthogonal images from four sides. The growth chamber contains pure SCN, several thermistors, and four stingers on which the dendrite growth is initiated. The tips of the stinger tubes are located at the corners of a tetrahedron with edge lengths, and hence spacing between the tips, of 10 mm. Thermoelectric coolers are mounted on the stinger ends opposite to the tips. An experiment starts by melting the SCN, then cooling the liquid to establish the desired supercooling in the growth chamber. The thermoelectric coolers are initiated and, after some time, dendrites start to emerge at the stinger tips. Although the present setup does not yet allow for a quantitative evaluation of the growth phenomena, we have performed image analysis in order to demonstrate some of the measurement techniques. We have also used this setup to examine numerous issues regarding the design of the planned microgravity experiment, including dendrite initiation, imaging requirements, stinger design, and others. We have clearly established the feasibility of the proposed experiment and measurement techniques.

Modeling

The proposed microgravity experiment is supported by several modeling efforts, that are not only intended to provide the theories that will be tested using the microgravity data, but will also be used to simulate the experiment. Work has concentrated on the development of four models:

(i) Modified Ivantsov Theory

A modification to the Ivantsov theory describing the heat flow around a dendrite tip has been proposed that takes into account the presence of other dendrites at a finite distance. This theory relies on the presence of a quasi-steady growth regime and the validity of the usual tip selection criterion. Figure 2 shows the predicted effect of interactions on the growth Peclet number for SCN and four crystals. By measuring the variation of both the tip velocity and radius in the planned microgravity experiment it will be possible to verify this theory.

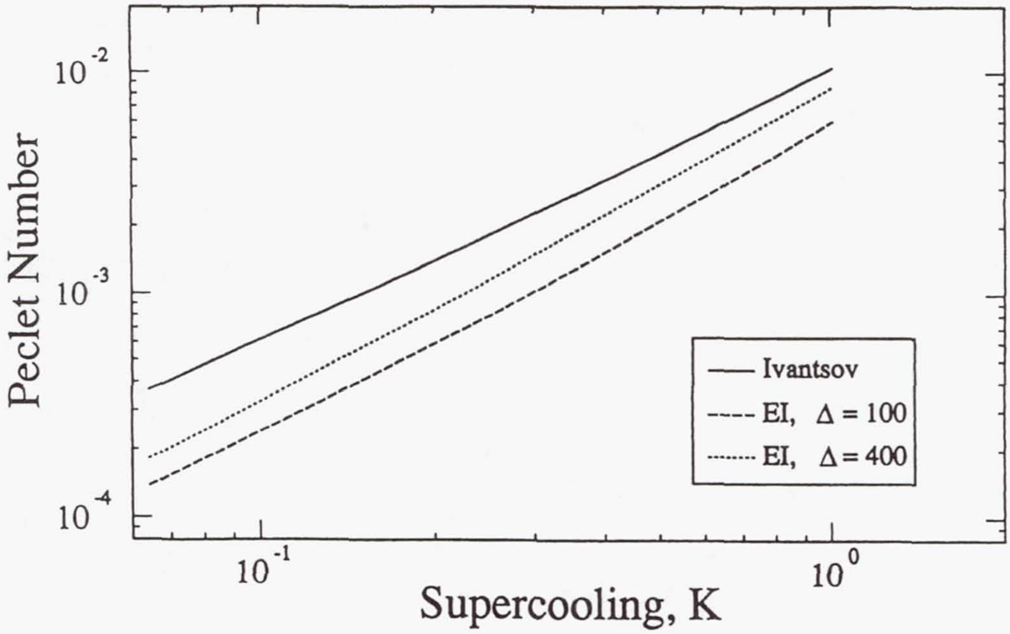

Fig. 2 Modified Ivantsov theory (EI): predicted effect of the dendrite proximity parameter, Δ, on the Peclet number-supercooling relation for an assemblage of four equiaxed crystals (SCN); the solid line is for an infinitely large proximity parameter (no interactions).

(ii) Modified Unit-Cell Model

We have developed a modified unit-cell model for predicting the internal solid fraction evolution in equiaxed dendritic solidification. Such unit-cell models can be used as micro-models in simulations of casting processes. While the original model for a single crystal was recently verified using data from the IDGE (Figure 3a) [2], the modified model is designed for an assemblage of multiple crystals and will be validated using EDSE data. As shown in Figure 3b, it predicts a transient variation in the tip speeds, as well as a transition from a fully dendritic structure to a more globulitic structure with increasing thermal interaction.

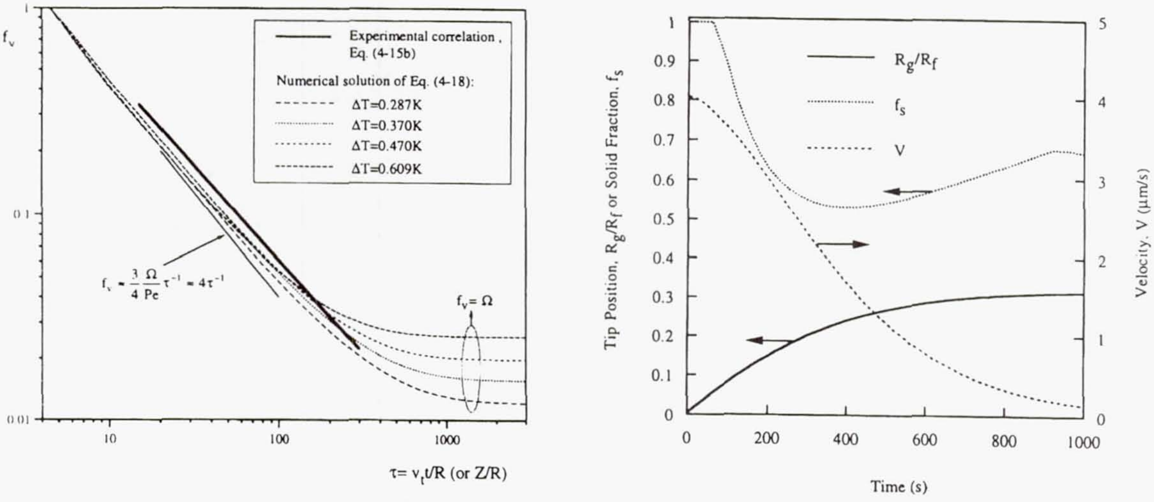

(a) (b)

Fig. 3 Unit-cell model: (a) predicted evolution of solid fraction for a single dendrite and comparison with IDGE data [2]; (b) predicted evolution of solid fraction, tip position, and tip velocity for an assemblage of equiaxed crystals (initial supercooling is 0.2K, SCN).

(iii) Mesoscopic Model

In this model [3, 4], the thermal interactions between the equiaxed crystals are fully accounted for by numerically calculating the three-dimensional, transient temperature field in the supercooled melt. The shape evolution and crystallographic orientation of the crystal envelopes are calculated by linking the numerical solution with a local analytical solution for the dendrite tip speeds. The mesoscopic model was validated for the steady growth of a single crystal using IDGE data. The full model is used to establish the requirements and parameters for the planned EDSE. Ultimately, we also plan to use the model to simulate the microgravity tests, in order to quantify the thermal field in the growth chamber and to test the validity of the local analytical solution under transient growth conditions. An example of simulation results for multiple equiaxed crystals is shown in Figure 4. Presently, the simulations are limited to diffusion dominated (microgravity) conditions.

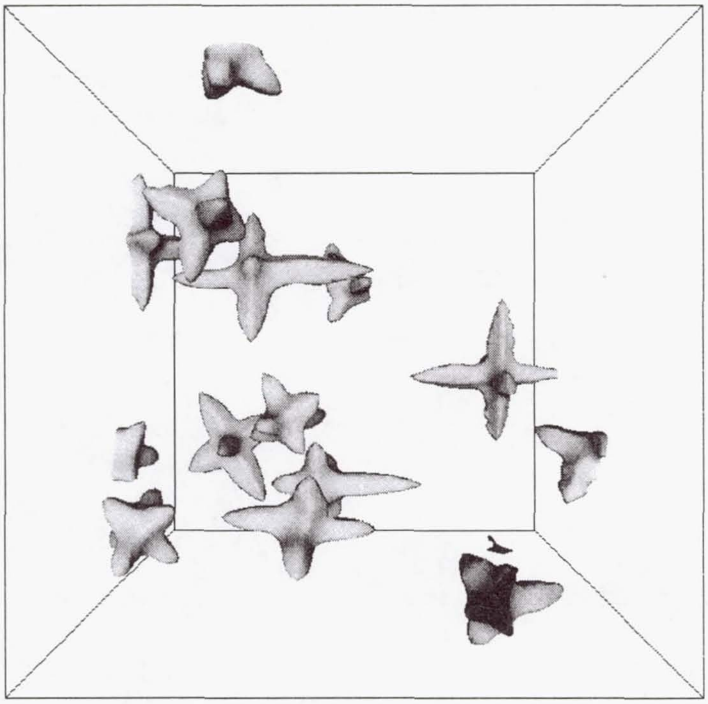

Fig. 4 Simulation results for the growth of multiple equiaxed crystals using the mesoscopic model; shown are the dendrite envelopes at an intermediate growth time (SCN, supercooling is 0.4K).

(iv) Phase-Field Model

We have also performed direct numerical simulations on a microscopic scale using the phase-field model [5, 6] to study the growth interactions of equiaxed dendrites and the resulting transients in the dendrite tip speeds and radii. An example of such simulations is shown in Figure 5. While simulations cannot yet be achieved for the conditions of the planned experiment, they do provide fundamental insight into issues such as dendrite tip operating point selection in the presence of growth interactions and transients.

REFERENCES

[1] Beckermann, C., "Modeling Segregation and Grain Structure Development in Equiaxed Solidification with Convection", Journal of Metals, Vol. 49, No. 3, March, 1996, pp. 13-17.

[2] Li, Q., and Beckermann, C., "Scaling Behavior of Three-Dimensional Dendrites", Physical Review E, Vol. 57, 1998, pp. 3176-3188.

[3] Steinbach, I., Kauerauf, B., Beckermann, C., and Guo, J., "Modeling of the Growth and Interactions of Equiaxed Dendrites on a Mesoscopic Scale", in Solidification 1998, eds. S.P. Marsh et al., TMS, Warrendale, PA, 1998, pp. 5-14.

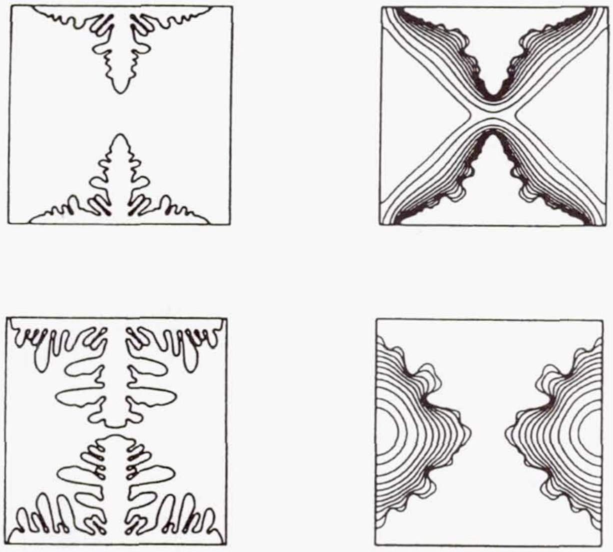

Fig. 5 Example of a phase-field simulation of two interacting equiaxed dendrites growing towards each other (left panels: phase-field contours, right panels: isotherms).

[4] Steinbach, I., Kauerauf, B., Beckermann, C., Guo, J., and Li, Q., "Three-Dimensional Modeling of Equiaxed Dendritic Growth on a Mesoscopic Scale", MCWASP VIII, eds. B.G. Thomas and C. Beckermann, TMS, Warrendale, PA, 1998, pp. 573-580.

[5] Diepers, H.J., Beckermann, C., and Steinbach, I., "A Phase-Field Method for Alloy Solidification with Convection", in Solidification Processing 1997, eds. J. Beech and H. Jones, Dept. Engineering Materials, The University of Sheffield, Sheffield, UK, 1997, pp. 426-430.

[6] Tong, X., Beckermann, C., and Karma, A., "Phase Field Simulation of Dendritic Growth with Convection", MCWASP VIII, eds. B.G. Thomas and C. Beckermann, TMS, Warrendale, PA, 1998, pp. 613-620.

Investigations of Carbon Nanotube Growth and Mechanical Properties

Jerry Bernholc and Christopher Roland
Department of Physics, NC State University, Raleigh, NC 27695

Introduction

The discovery of carbon nanotubes [1-3] has revitalized and refocused much of the fullerene research. The interest and excitement in carbon nanotubes derives largely from their unusual structural and electronic properties. Experiments and theory indicate that they are superstrong fibers, with a remarkable resilience to extreme conditions of strain. Simply put, because of the uniqueness of the graphene sp^2 bond, carbon nanotubes may be the ultimate strength fibers produced by nature. Furthermore, nanotubes hold considerable promise as composites, catalysts, field emitters, photonic material, molecular straws, molecular devices, and as MicroElectricalMechanical Structures (MEMS) materials [4-10], which should allow for unique space-oriented applications.

In this brief report, we give a description of some of our recent theoretical investigations of carbon nanotubes, with a focus on aspects of their growth and mechanical properties. This research has been carried out with a series of complementary theoretical methods covering different length and time scales, including *ab initio*, classical molecular dynamics and kinetic Monte Carlo simulations.

Noncatalytic Growth of Nanotubes

The problem of nanotube growth remains an important issue that needs to be understood if nanotubes are ever to reach their full potential as a technological material. Because carbon nanotubes typically form under highly nonequilibrium conditions, the kinetics of their growth represents a problem of considerable complexity. While nanotubes were first produced in carbon arcs [1-3], they have since been synthesized through laser vaporization, catalytic combustion, chemical vapor deposition and ion bombardment [10-16]. Given these different methods of synthesis, it is likely that a variety of mechanisms are operating in the formation of the tubes and in their assembly into nanoropes [13-19]. However, two common features have emerged. First, the type of nanotube that is produced is sensitive to the presence and/or absence of catalysts: multiwalled nanotubes are the primary product formed in the absence of catalysts, while single-wall nanotubes are the dominant product in the presence of transition metal catalysts. Second, experiments have shown that carbon nanotubes actually remain open during noncatalytic growth [3]. This is surprising, because the large number of dangling bonds present at the open tips definitely favor a closed-tube geometry.

A number of reasons have been given to explain the open-ended growth. Initially, it was believed that it is the high electric fields present at the nanotube tips that keep them open during growth [20]. However, detailed *ab initio* simulations [17,21], and the subsequent development of other non-arc methods of synthesis, show that the electric field cannot be responsible for keeping the tubes open. Similarly, other reasons such as the temporary saturation of the dangling bonds with hydrogen, or thermal gradient effects, may similarly be eliminated. There are, however, strong indications from theory that tube closure is associated with the formation of curvature-inducing defects such as adjacent pentagon pairs and other related structures [17]. This suggests that nanotube growth may indeed proceed in an open-ended fashion provided that the formation of such defects is somehow suppressed. Energetically, we have shown that the formation of these defects is favored only for narrow nanotubes, so that tubes with diameters greater than about 3 nm should remain open. Under conditions of catalytic growth, it is believed that the presence of small metal particles encased by the nanotube [17,22], a root growth mechanism [18], or the action of Co or Ni atoms on the tips of the nanotubes (the so-called "scooter" mechanism) prevents the nucleation of such defects and leads to the formation of single-wall nanotubes with narrow diameters [19].

Multiwall carbon nanotubes, however, have another kinetic alternative open to them in the form of the so-called "lip-lip" interaction [13]. Such an interaction arises when atoms or small clusters deposit themselves at the tips of the nanotubes. These then form bridges or "spot-welds" between the adjacent tube tips, which are thereby kept open for continued growth. Lip-lip interactions are also conjectured to be particularly important in stopping the unraveling of carbon nanotube under conditions of field emission [9].

To investigate the importance of the lip-lip interactions in keeping carbon nanotubes open, we have carried out extensive molecular dynamics (MD) simulations [23]. Surprisingly, we find that the lip-lip interaction itself does not stabilize open-ended growth, but rather facilitates the closing of the tubes by mediating the transfer of atoms between the inner and outer shells. Details of our simulations are as follows. Carbon atoms were modeled with a classical many-body Tersoff-Brenner potential, which is known to adequately reproduce many of the important features of carbon bonding [24]. We then constructed a number of double wall tubes, with a height of 12 to 24 atomic layers. These were uniformly heated up to 3000 K over a 40 ps period of time, keeping the bottom layer of the tube fixed. Although there was no initial interaction between the open tube tips, bridging bonds were first observed to form at about 900 K, when the radial distortions were large enough to bring the carbon atoms of the tips within the interaction range. These bonds have a fluctuating character, breaking and reforming into similar configurations on a time scale of several picoseconds. Continuing with the annealing process, we find that the various double-wall tubes close spontaneously on a time scale of hundreds of picoseconds, as illustrated in Fig. 1. Because of the fluctuating nature of the lip-lip interactions, at some point a curvature-inducing defect nucleates on the inner tube, which then curves inwards. However, because of the lip-lip interaction connecting the two tubes, the outer shell is also forced to curve inwards and there is a transfer of atoms between the two shells further enhancing the inward bending of the nanotube tips. Ultimately, there is a general collapse of the upper parts of the tubes, which then forms a two-layer cap closing off the double-wall tubes. Simulations of nanotubes with different numbers of shells and different chiralities display similar behavior, showing that the lip-lip interaction itself cannot maintain the tubes open, and that the time scale for tube closure is set by the diameter of the inner tube.

How then can growth proceed in the absence of catalysts? A possible scenario is that initially a single nanotube with a reasonably large diameter forms. Shells can then readily nucleate and grow via a "step-flow" and/or coalescence mechanism, using the initial nanotube surface as a template. This process is under current investigation. For step flow, atoms or small clusters landing on the surface of the nanotube make their way via diffusion over to edges of shells, where they are more readily incorporated into the growing tube. Diffusion itself takes place via a kick-out mechanism, with an energy

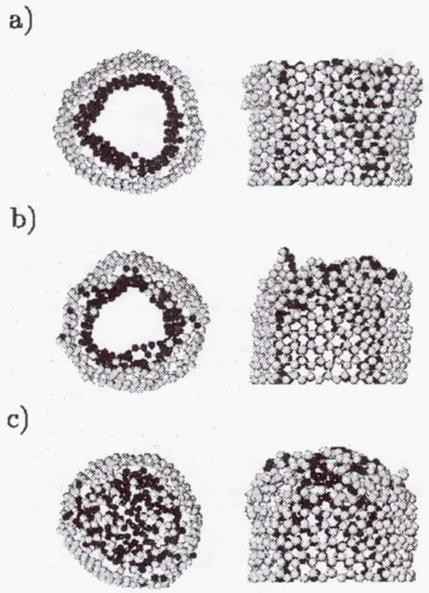

Figure 1: Top and side views of (18,0)@(21,0) double-wall tubes from top and side. (a) 0 ps; (b) 45 ps; (c) 180 ps.

barrier that is about 1 eV [25]. Larger nanotube fragments on the surface of the nanotube are actually expected to be more mobile, because of the relatively weak interaction between the different nanotube shells. Provided that there is sufficient feedstock and the carbon flux is sufficiently high, the outer shell is likely to catch up with the inner tube. The growth of the resulting multiwalled tube will then continue for some transient period of time, and then the tube will close. These notions are supported by the apparent independence of the lengths of different shells, the varying number of shells per nanotube, and the observations of multiwalled nanotubes with nested inner caps of varying lengths.

If the lip-lip interaction does not prevent nanotube closure, the maximum time to closure of the inner tube severely limits the lengths of nanotubes that can be formed during growth. To address this issue, we have carried out an extensive annealing study of the time to closure of open, single-wall tubes, both as a function of temperature and tube diameter [25]. We concentrated on single-wall tubes, as the time to closure of the largest and the smallest diameter shells provide both an upper and lower bound estimate for the closing of a given multiwalled tube within the context of the lip-lip interaction. In turn, these estimates were combined with the fastest growth rate for defect-free growth, as obtained from MD simulations. This procedure gives an upper bound estimate for the length of carbon nanotubes that can be grown. Qualitatively, the results are as follows. As expected, the higher the temperature, the shorter the length of nanotube that can be formed. This is due to a more rapid nucleation of defects at higher temperatures and suggests that lower temperatures are needed to optimize the lengths of non-catalytically grown nanotubes. Indeed, these results are consistent with experimental data from both carbon arc and laser ablation methods. For instance, laser ablation leads to defect-free nanotubes with diameters in the 2-20 nm range and with lengths of about 200-300 nm at about 1500 K, consistent with our theoretical results. At lower temperatures of about 1200 K, nanotube with a large number of defects are observed to form. This is likely due to a chamber growth rate that is larger than the maximum rate for defect-free growth. In a carbon arc growth temperatures are consistently higher, in the 2400-3000 K regime. Here, large diameter 10 nm tubes are observed to grow out to several _m's, which is also in agreement with our theoretical results.

Mechanical Properties

Many of the unique applications of carbon nanotubes are intimately related to their mechanical properties. For instance, there is considerable experimental and theoretical evidence that nanotubes display a remarkable resistance to bending, twisting, and other deformations [4,26,27]. Our theoretical investigations show that it is the extraordinary flexibility of the hexagonal network that allows the system to sustain very large bending angles, kinks and other highly distorted regions. In addition, nanotubes are observed to be extremely resilient, suggesting that even largely distorted configurations can be due to elastic deformations with no atomic defects involved.

Our recent investigations of the mechanical properties of nanotubes have focused on the strain release mechanisms under both uniaxial tension and compression [27]. Using dynamical first-principles and classical molecular dynamics simulations, we have been able to identify the initial stages of the mechanical yield of tubes. Beyond a critical value of the tension, the system releases its excess strain via the spontaneous formation of topological defects. The first defect to form corresponds to a 90 degree rotation of a carbon-carbon bond about its center, the so-called Stone-Wales transformation [28], which produces two pentagons and two heptagons coupled in pairs (5-7-7-5). Static calculations under a fixed dilation show a crossover in the stability of this defect with respect to the ideal hexagonal network. This crossover is observed at about 5% tensile strain in (5,5) and (10,10) armchair tubes. For example, in a (5,5) tube, the formation of such defects costs about 2.34 eV in the absence of strain. Under a 10 % strain, such a defect costs -1.77 eV, showing that this defect is effective in releasing the excess strain energy in a nanotube under tension. Moreover, through its dynamical evolution, this defect acts as a nucleation center for the formation of dislocations in the ideal graphitic network and is the cause of possible plastic behavior in carbon nanotubes. An example of this shown in Fig. 2, which illustrates a long-time 2.5 ns simulation of a (10,10) tube at 2000 K under 10 % axial strain. Within the first 1.1 ns a few (5-7-7-5) defects are formed in the tube, and each one remains localized in its region of formation. After 1.5 ns another defect forms with a distinctive time evolution. Approximately 100 ps after its formation, the two pentagon-heptagon pairs split and eventually one of them starts diffusing within the helical structure of the tube, while the other defect remains trapped in its original position. After another 350 ps, the 5-7 defect that has migrated transforms into a (5-7-5-8-5), i.e., an octagon and a pair of pentagons were added to the original pentagon-heptagon pair.

The introduction of topological defects can change the index of the nanotubes. A 5-7 defect is the smallest defect that can change the tube index or chirality without drastically altering the local curvature of the nanotube. What we observe during the simulation is actually an index change in the (10,10) tube, and the strain-induced formation of a (10,10)/(10,9)/(10,10) heterojunction. This is produced by the splitting of the two pentagon-heptagon pairs comprising the original defect. It is important to note that a (5-7-7-5) defect does not introduce any changes in the tube index. Similarly, the addition of an octagon and a pair of pentagons to the pre-existing pentagon-heptagon pair, as in the last simulation, also leaves the index unchanged. The unique electronic and transport properties of heterojunctions formed by joining carbon nanotubes of different indices have already been extensively investigated [29]. Here, we show that the formation and splitting of the (5-7-7-5) defect, followed by dislocation glide, can also lead to the formation of heterojunctions.

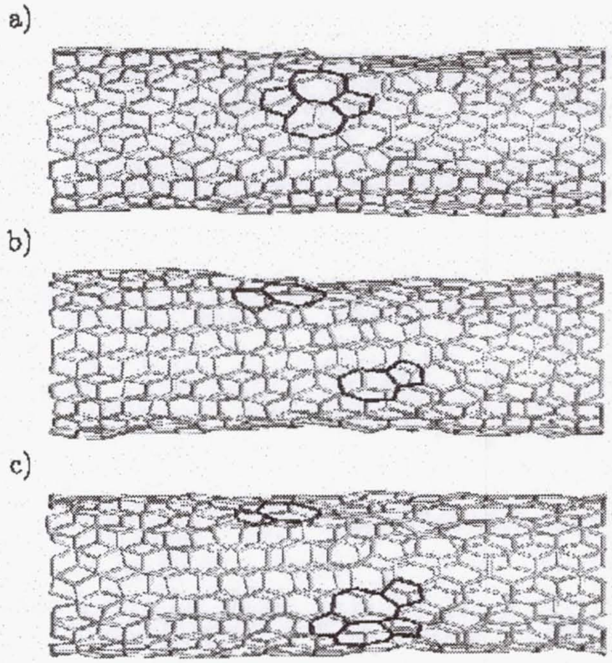

Figure 2: Time evolution of a particular (5-7-7-5) defect from a classical simulation for a (10,10) tube at 2000 K under 10 % uniaxial strain. The defect structure is highlighted in black. (a) Formation of defect; (b) defect splits and starts to diffuse; (c) another bond rotation leads to the formation of a (5-7-5-8-5) defect.

Summary

In summary, we have investigated aspects of both carbon nanotube growth and their mechanical properties with both quantum and classical molecular dynamics simulations. Our recent investigations of nanotube growth have focused on the role of the so-called lip-lip interaction, which is important during the noncatalytic growth of multiwalled carbon nanotubes. We have shown that the lip-lip interaction does not keep the tubes open for growth, but actually aids in the closure of the outer tube by facilitating the transfer of atoms between the inner and outer nanotube shells. Based on this mechanism for closure, we have estimated the lengths of defect-free nanotubes that can be formed as a function of temperature and nanotube radius. Turning to the mechanical properties, we investigated the behavior of nanotubes under uniaxial tension. At high temperatures, the spontaneous formation of a double pentagon-heptagon pair was observed for tubes under strains greater than about 5 %. These topological defects act as nucleation centers for the formation of dislocations in the originally ideal graphite network, and mark the onset of plastic or brittle behavior. The mechanism of the formation, the energetics and kinetic transformations of these and similar defects as a function of the nanotube indices are under current investigation.

References

1. S. Iijima, Nature (London) **354**, 56 (1991).
2. T.W. Ebbesen and P.M. Ajayan, Nature (London) **358**, 220 (1992).
3. S. Iijima, P.M. Ajayan and I. Ichihashi, Phys. Rev. Lett. **69**, 3100 (1992).
4. S. Iijima, C. Brabec, A. Maiti and J. Bernholc, J. Chem. Phys. **104**, 2089 (1996); B.I. Yakobson, C.J. Brabec and J. Bernholc, Phys. Rev. Lett. **76,** 2511 (1996).
5. P. Calvert, Nature (London) **357**, 365 (1992).
6. P. Ross, Sci. Am. **265** No. 6, 16 (1991).
7. J. Broughton and M. Pederson, Phys. Rev. Lett. **69**, 2689 (1992).
8. F.J. Garcia-Vidal, J.M. Pitarke and J.B. Pendry, Phys. Rev. Lett. **78**, 4289 (1997).
9. A.G. Rinzler, J.H. Hafner, p. Nikolaev, L. Lou, S.G. Kim, D. Tomanek, P. Nordlander, D.T. Colbert and R.E. Smalley, Science **269**, 1550 (1995).
10. See for example: M.S. Dresselhaus, G. Dresselhaus and P.C. Eklund, *Science of Fullerenes and Carbon Nanotubes* (Academic Press, San Diego 1996); J. Bernholc, C. Roland, and B. I. Yakobson, Cur. Opinion in Solid State and Mat. Sci., **2**, 706 (1997).

11. D.T. Colbert, J. Zhang, S.M. McClure, P. Nikolaev, Z. Chen, J.H. Hafner, D.W. Owens, A.G. Rinzler, and R.E. Smalley, Science **266**, 1218 (1994).

12. A. Thess, R. Lee, P. Nikolaev, H. Dai, P. Petit, J. Robert, C. Xu, Y. Hee Lee, S.G. Kim, A.G. Rinzler, D. Tomanek, and R.E. Smalley, Science **173**, 483 (1996).

13. T. Guo, D. Nikolaev, A.G. Rinzler, D. Tomanek, D.T. Colbert and R.E. Smalley, J. Phys. Chem. **99**, 10694 (1995).

14. S. Witanacheki and P. Mukherjee, J. Vac. Sci. Tech. A **13**, 1171 (1995).

15. S. Iijima and T. Ichihashi, Nature (London) **363**, 603 (1993).

16. D.S. Bethune, C.H. Kiang, M.S. de Vries, G. Gorman, R. Savoy, J. Vasues, and R. Beyers, Nature (London) **363,** 605 (1993).

17. A. Maiti, C. Brabec, C. Roland and J. Bernholc, Phys. Rev. Lett. 73, 2668 (1994); Phys. Rev. B 52, 14850 (1995); C. Brabec, A. Maiti, C. Roland and J. Bernholc, Chem. Phys. Lett. **236,** 150 (1995).

18. A. Maiti, C. Brabec and J. Bernholc, Phys. Rev. B **55,** R6097 (1997).

19. A. Thess, R. Lee, P. Nikolaev, H. Dai, P. Petit, J. Robert, C. Xu, Y.H. Lee, S.G. Kim, A.G. Rinzler, D.T. Colbert, G.E. Scuserua, D. Tomanek, J.E. Fischer, and R.E. Smalley, Science **273,** 483 (1996); Y. Hee Lee, S.G. Kim and D. Tomanek, Phys. Rev. Lett. **78,** 2393 (1997).

20. R.E. Smalley, Mater. Sci. Eng. B **19**, 1 (1993).

21. L. Lou, P. Nordlander and R.E. Smalley, Phys. Rev. B **52**, 1429 (1995).

22. H. Dai, A.G. Rinzler, P. Nikolaev, A. Thess, D.T. Colbert and R.E. Smalley, Chem. Phys. Lett. **260,** 471 (1996).

23. M. Buongiorno Nardelli, C. Brabec, A. Maiti, C. Roland and J. Bernholc, Phys. Rev. Lett. **80,** 313 (1998).

24. J. Tersoff, Phys. Rev. Lett. **56,** 632 (1986); **61,** 2879 (1988); Phys. Rev. B **37,** 6991 (1988); D.W. Brenner, Phys. Rev. B **42**, 9458 (1990).

25. M. Buongiorno Nardelli, C. Roland and J. Bernholc, unpublished.

26. M.R. Falvo, G.J. Clary, R.M. Taylor II, V. Chi, F.P. Brooks, S. Washburn and R. Superfine, Nature (London) **389,** 582 (1997).

27. M. Buongiorno Nardelli, B.I. Yakobson and J. Bernholc, Phys. Rev. B **57**, R4280 (1998).

28. A.J. Stone and D.J. Wales, Chem. Phys. Lett. **128,** 501 (1986).

29. B.I. Dunlap, Phys. Rev. B **46,** 1933 (1992); L. Chico, V.H. Crespi, L.X. Benedict, S.G. Louie and M.L. Cohen, Phys. Rev. B **54,** 2600 (1996); V.H. Crespi, M.L. Cohen and A. Rubio, Phys. Rev. Lett. **79,** 2093 (1997).

DISPERSION MICROSTRUCTURE AND RHEOLOGY IN CERAMICS PROCESSING

J. F. Brady
Division of Chemistry and Chemical Engineering
210-41
California Institute of Technology
Pasadena, CA 91125
USA
Phone: 626-395-4183
Fax: 626-568-8743
email: jfbrady@caltech.edu

Introduction

Ceramics provide a potentially very useful class of materials owing to their physical properties; they are light, hard, resistant to abrasion, chemically inert, stable at high temperatures, and excellent thermal and electrical insulators [1]. Further, by casting from a liquid suspension and subsequently sintering, many complex parts and shapes can be fabricated [2]. Although the resultant properties of ceramics can be outstanding, they often suffer from extreme brittleness. This brittleness is caused by the propagation of cracks, which is in turn due to microstructural defects. These defects may be caused by a number of different factors, such as particle agglomeration, migration or segregation prior to sintering, or due to inhomogeneous volume change upon sintering. If a ceramic's microstructure can be controlled and rendered homogeneous prior to (and after) sintering optimal material properties may be realized in an economic way.

Typically, high-performance ceramics are produced using monodisperse submicron-sized particulate suspensions from which the ceramics are cast. By controlling the size and processing a dense uniform microstructure may be formed prior to sintering. This route has met with limited success even though the maximum volume fraction of ceramic particulates that can be achieved prior to sintering is 0.74. The limited success may stem from the fact that a perfect crystal of mono-sized particles has slip planes that yield easily, and from the fact that there is still a large amount of void space that must be eliminated upon sintering.

An alternate approach is to use a mixture of particle sizes [3,4]. It is well know that solids fractions of 90% can be obtained with a bidisperse suspension of spherical particles. And even greater loadings are possible with tridisperse systems. Crystalline slip planes can be eliminated with a mixture of particle sizes. In addition to achieving high solids fractions, and therefore reducing potential sintering inhomogeneities, a mixture of two different types of particles can also impart desirable properties in a 'composite' ceramic. For example, zirconia in alumina has been used to arrest crack propagation owing to the transformation toughening of zirconia under stress [5]. Of critical importance for processing is the fact that particles that differ in size or composition are subject to gravitational phase separation. Hence, processing in a gravity-reduced environment offers substantial benefits.

Research Objectives

For bi- or poly-disperse suspensions to be successful, the microstructure must be controlled during processing. It has been observed experimentally that for the same total volume fraction, a mixture of two particle sizes leads to a reduction in the suspension viscosity, with obvious advantages for ease of processing [6-14] . Although there are several heuristic models to explain this viscosity reduction phenomena, there is no fundamental explanation and very little theoretical work has been done. Furthermore, the viscosity reduction is only one factor. Of much greater importance is the microstructure formed during processing, for this determines the ultimate success or failure of the ceramic. As an example of the importance flow has on microstructure, figure 1 shows the flow-induced ordering that can occur in monodisperse Brownian suspensions [15,16]. To date there have been no studies of microstructure formation during flow of bidisperse suspensions.

Results

Figure 2 shows the results for the steady shear viscosity of a bidisperse suspension of Brownian hard-spheres at a total volume fraction of 0.45 determined by Brownian Dynamics. The size ratio is 2 to 1. The figure shows the variation in the total viscosity as a function of the fraction of small particles, X_s, and nondimensional shear rate or Peclet number based on the radius of the small particles, $Pe_s = \gamma a^2/D$, with a the radius of the small particles and λa that of the large. The bidisperse viscosities are intermediate between the monodisperse results as one would expect. This is in agreement with the intuitive notion that the maximum packing of solids is largest at this ratio and therefore at a total solids content of 0.45, one is further from the maximum packing than at either extreme of large or small particles. The shear thinning viscosities can all be collapsed onto a single curve if the Peclet number is based on the volume mean particle size, $Pe = \gamma\langle a^2\rangle/\langle D\rangle$, and $\langle D\rangle = kT/6\pi\eta\langle a\rangle$. These results are in agreement with the recent experiments of Rodriguez et al [8] and Shikata, et al [18].

Also of interest is the microstructure formed during shear. As seen in figure 1 the monodisperse suspension at the same solids concentration and shear rate orders completely into flowing strings. For the bidisperse suspension at $X_s = 0.25$ the small particles are disordered, but the large particles order, although not as completely as the monodisperse case. How this ordering extends over a range of total solids concentration, size ratio and fraction of small particles is not known.

Future Work

Future work will be to extend the simulations to a greater range of volume fractions and size ratios. Over what range does the ordering persist? Can one see evidence of phase separation by depletion forces? And how is this influenced by flow? Also, the simulation results are for Brownian particles that do not interact hydrodynamically. For the shear thinning behavior shown here, it is known that hydrodynaimc interactions have only a quantitative, and not qualitative, effect on the results. Does this carry over to mixtures as recent experiments suggest? At high shear rates, however, hydrodynamically interacting hard-spheres show shear thickening due to the formation of lubricationally bound clusters of particles. Will these clusters be disrupted by the addition of small particles that can get into the lubrication gaps between the large particles and break the connectivity and thereby prevent shear thickening? To answer this question, we will need to improve the speed of the simulation of hydrodynamically interacting particles, and work is in progress in developing a fast O(N ln N) Accelerated Stokesian Dynamics simulation capability.

References

1. National Research Council 1989 *Materials Science and Engineering for the 1990s*, National Academy Press.
2. Somiya, S. 1989 *Advanced Technical Ceramics*, Academic Press.
3. Reed, J.S. 1988 in *Ceramic Transactions, Ceramic Powder Science II*, The American Ceramic Society, p.601.
4. Brook, R.J., Tuan, W.H. and Xue, L.A. 1988 in *Ceramic Transactions, Ceramic Powder Science II*, The American Ceramic Society, p.811.
5. Hannink, R.H.J. and Swain, M.V. 1994 *Ann. Rev. Mater. Sci.* **24**, 359.
6. Ferris, K.J. 1968 *Trans. Soc. Rheol.* **12**, 281.
7. Chong, J.S., Christiansen, E.B. and Baer, A.D. 1971 *J. Appl. Polym. Sci.* **15**, 2007.
8. Rodriguez, B.E., Kaler, E.W. and Wolfe, M.S. 1992 *Langmuir* **8**, 3282.
9. Hoffman, R. 1992 *J. Rheol.* **36**, 947.
10. Shapiro, A.P. and Probstein, R.F. 1992 *Phys. Rev. Lett.* **68**, 1422.
11. Chang, C. and Powell, R.L. 1993 *J. Fluid Mech.* **253**, 1.
12. Chang, C. and Powell, R.L. 1994 *J. Rheol.* **38**, 85.
13. Woutersen, A.T.J.M. and de Kruif, C.G. 1993 *J. Rheol.* **37**, 681.
14. Wagner, N. J. and Woutersen, A.T.J.M. 1994 *J. Fluid Mech.* **278**, 267.
15. Phung, T.N. 1993 *Ph.D. Thesis*, California Institute of Technology.
16. Phung, T.N., Brady, J.F. and Bossis, G. 1996 *J. Fluid Mech.* **313**, 181.
17. Shikata, T., Niwa, H and Morishima, Y. 1998, *J. Rheol* (to appear).

Bidisperse Ordering: $X_s = 0.25$
$Pe_s = 1000$, vorticity-gradient plane

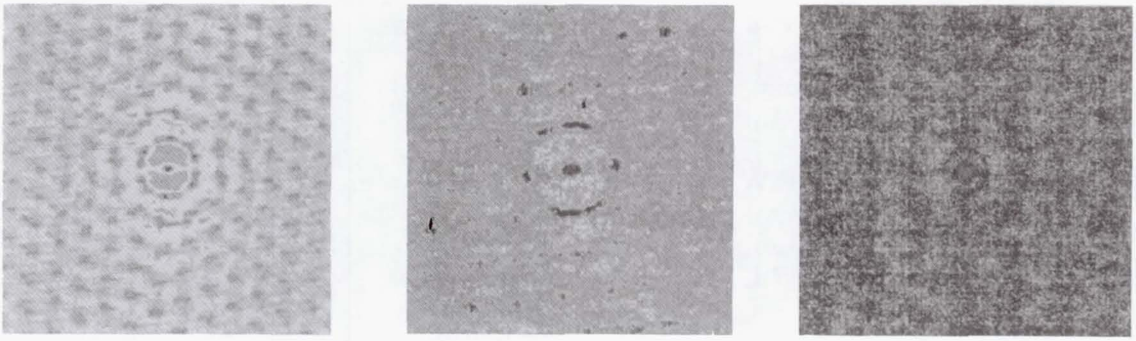

monodisperse **large-large** **small-small**

Figure 1. Projections of the pair-distribution function for monodisperse and bidisperse suspensions of Brownian hard-spheres at a volume fraction of 0.45 determined by Brownian Dynamics simulation. The size ratio is 2 to 1. The projections are in the velocity-gradient -- vorticity plane and show the suspension to be completed ordered into strings in the flow direction (monodisperse), partial ordering of the large particles and no ordering of the small particles in the bidisperse suspension. The nondimensional shear rate or Peclet number is 1000 based on the radius of the small particles.

Shear thinning for all relative concentrations

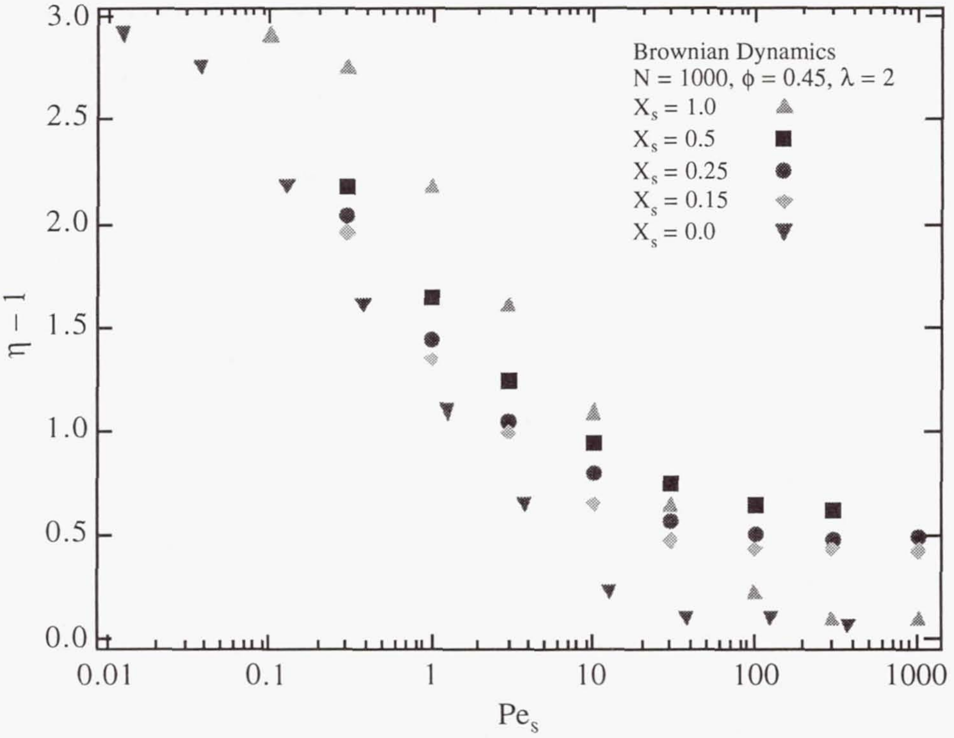

Figure 2. Shear thinning viscosities determined by Brownian Dynamics simulation for a bidisperse mixture of hard-spheres at a total volume fraction of 0.45. The size ratio is 2/1. The viscosities for intermediate fractions of small to large (by volume) particles X_s fall between those for the monodisperse suspensions.

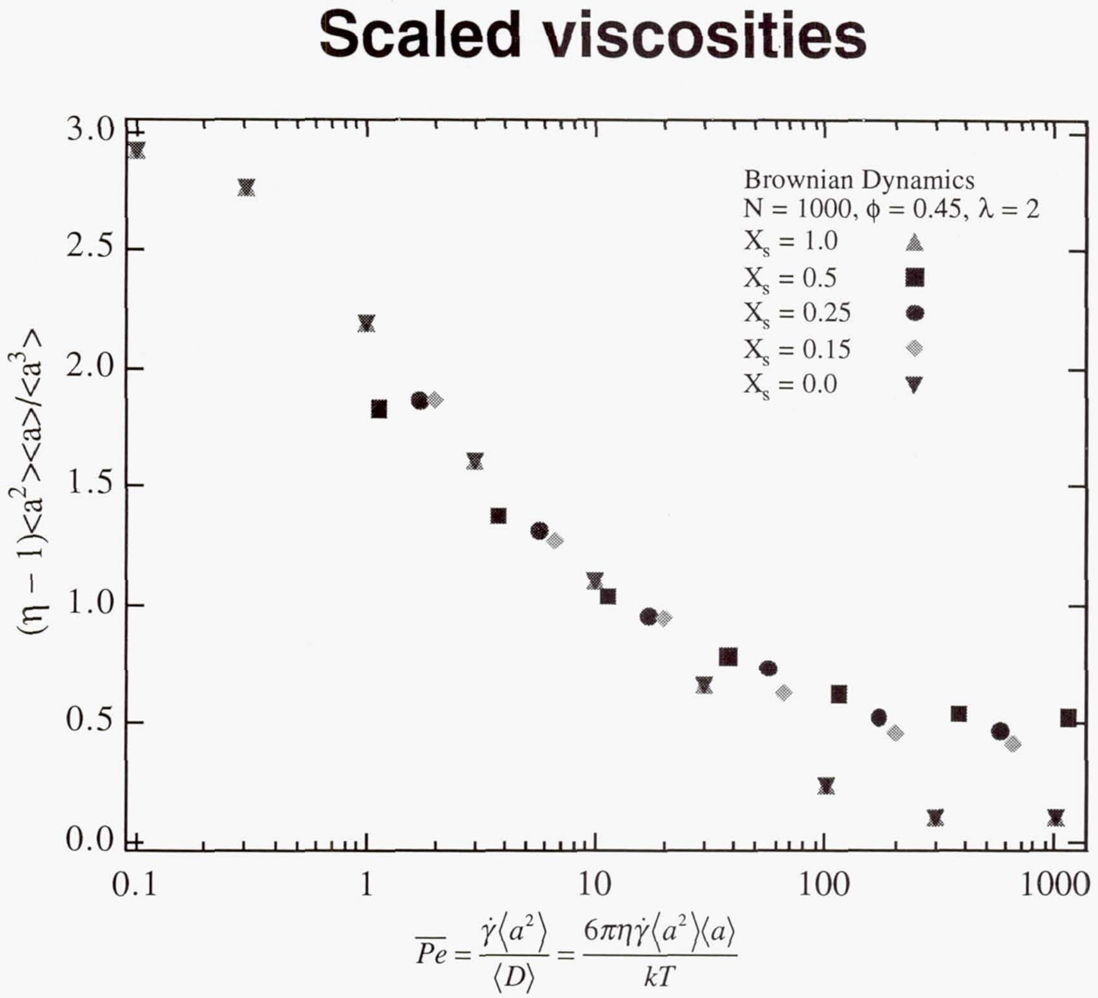

Figure 3. Scaled shear thinning viscosities determined by Brownian Dynamics simulation for a bidisperse mixture of hard-spheres at a total volume fraction of 0.45. The size ratio is 2/1. The viscosities for intermediate fractions of small to large (by volume) particles X_s fall between those for the monodisperse suspensions. The shear rate is scaled with the volume averaged particle size and self diffusivity.

Combustion Synthesis of Titanium Nitride under Fluidization

Kenneth Brezinsky, Principal Investigator
(kenbrez@uic.edu, 312-996-9430)
and
Kyeong-Ook Lee, Jon J. Cohen

Department of Chemical Engineering
University of Illinois at Chicago
810 S. Clinton Street
Chicago, IL 60607-7000

INTRODUCTION

Several investigators have studied the self propagating high temperature synthesis (SHS) of titanium nitride during the past decade and found that one of the most important scientific issues is increasing the conversion yield of the nitride. In general, conversion yield has been limited by the melting of titanium particles during the combustion synthesis because the melting point of titanium is lower than the combustion temperature. The titanium liquid tends to penetrate into interstitial spaces between the unreacted or unmelted particles especially in earth gravity leading to reduced reactant porosity. The reduction in porosity leads to less contact of nitrogen with the remaining titanium particles and low nitride conversion results. Recently, a technique was developed to increase the conversion yield of titanium nitride by using a fixed powder bed and supercritical nitrogen [1]. The high initial nitrogen density at the supercritical condition provides the reactant particles with enough initial nitrogen that the conversion yield achieved was 74%, without significant formation of liquid barriers. The yield achieved was a significant improvement over those obtained by other techniques.

PRELIMINARY EXPERIMENTAL RESULTS

In order to increase the yield further, the fixed powder bed has been transformed into a fluidized bed with homogenous uniform dispersion. The dispersion is produced in a quartz tube thirteen-millimeters in diameter. The dispersion is comparable to the static dispersion to be achieved eventually in microgravity. The fluidized dispersion obtained in the laboratory and which is being studied in preparation for microgravity experiments is created by purging particles through a dual particle injection system into a co-flowing nitrogen stream that has passed through a sintered stainless steel base plate, Fig. 1. The titanium particle dispersion appears to be both homogenous and uniform. As a result of fluidization, the interparticle distances are increased and controllable so that nitrogen accessibility to the titanium surface is increased. Testing of the yield dependence of the combustion synthesis on nitrogen accessibility is achieved by using a tungsten igniter coil affixed medially in the quartz tube.

For the tungsten igniter to be able to initiate the combustion synthesis process, the fluidized bed must provide a homogenous dispersion of titanium dense enough to reach the ignition limits in nitrogen. Particle loading and corresponding densities have been found for successful ignition of the fluidized titanium particles. Successful ignition leads to propagation of a flame counter to the direction of the flow of fluidizing nitrogen. The dispersion density necessary for flame propagation is maintained by the addition of purging particles throughout the experiment including an observed afterburn period. During this afterburn period, after the propagation of the flame, conversion to nitride continues apparently without significant melting of the remaining titanium. The final titanium nitride product recovered from the successful fluidized bed experiments is a sintered matrix with some unreacted titanium particulates as indicated by scattered silver colored titanium particles in a mostly yellow-brown titanium nitride matrix. The titanium nitride from these investigations shows a spherical morphology with diameters ranging from sixty to one hundred microns, Fig. 2. These spherical products are produced from rodlike titanium precursors. The titanium nitride product also is more porous than that reported in published investigations and is probably due to the fluidization process. During fluidization, the percolating titanium-nitrogen mixture aids in dissipating heat as well as forming the dispersion. This additional heat dissipation decreases the molten titanium that has lowered the yield in reported investigations. The product from these experiments do not show regions of molten titanium plated by titanium nitride, rather a sintered matrix of titanium nitride with some titanium sparsely intermixed. The measured yield of this sintered matrix of titanium nitride based on the weight of the initial titanium powder is approximately 61%. This yield is much higher than the value of 24% obtained at much higher pressures (2.28MPa) in room temperature nitrogen [1]. Fluidization clearly improves conversion yield.

FUTURE WORK

Currently, the morphology of the titanium nitride product is examined using scanning electron microscopy (SEM). Photographs of the initial pure titanium as well as the titanium nitride are taken using SEM for comparison and are the basis for the discussion above. In future experiments, X-ray diffraction analysis also will be performed to determine the microstructure of the resultant titanium nitride. Similarly, in future experiments the flame propagation speed will be measured using two type-C thermocouples (W-5%Re by W-26%Re) as a function of temperature fluctuations at the flame fronts.

Preparations are currently underway to continue these investigations using supercritical nitrogen in the KC-135 parabolic flight plane, where microgravity effects will be attained. Better results in microgravity are expected since a true homogenous, non-stratified dispersion can be created without gravitational field effects and without the mixing effects due to the turbulent flow required to maintain fluidization on earth. Without turbulence, microgravity is expected to further increase the conversion yield and produce a dispersed particulate product instead of the sintered product presently found. The KC-135 will be used for these investigations due to the long observation time in the SHS of titanium nitride, which surpasses the five seconds allotted by the drop tower. The use of supercritical nitrogen has already been shown to increase the yield [1].

Before progressing to microgravity conditions, further investigations aimed at optimizing the fluidized bed will be conducted at normal gravity. Further investigations are expected to lead to a more uniform product and increased product yield based on recent preliminary experiments with a fluidized bed of spherical titanium particles, Fig. 3. The combustion synthesis of TiN from these particles showed better fluidization, more well defined flame propagation and more spherical product particles.

REFERENCES

1. Brezinsky, K., Brehm, J.A., Law, C.K. and Glassman, I.; "Supercritical Combustion Synthesis of Titanium Nitride", Twenty-Sixth Symposium (Int'l) on Combustion, The Combustion Institute, 1996, pp.1875-1881.

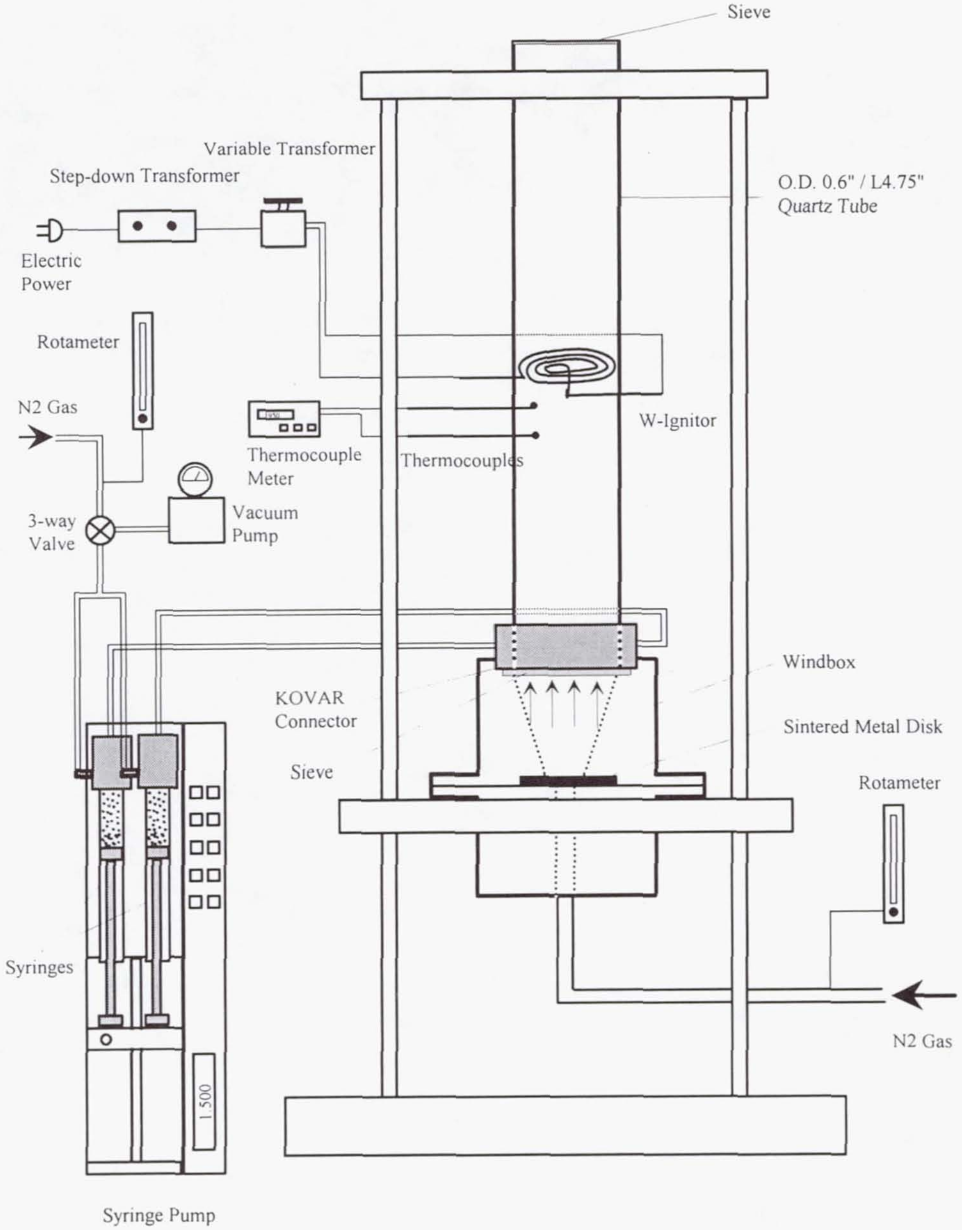

Figure 1. Schematic of Fluidized-bed Dispersion/Combustion System

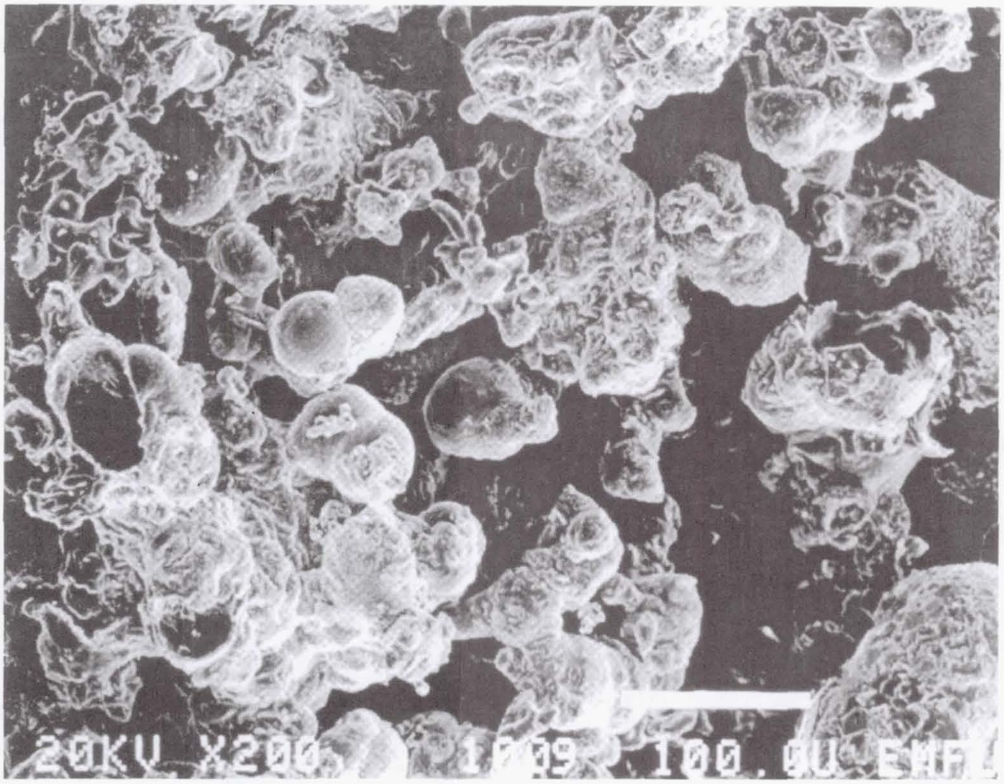

Figure 2. Morphology of titanium nitride product

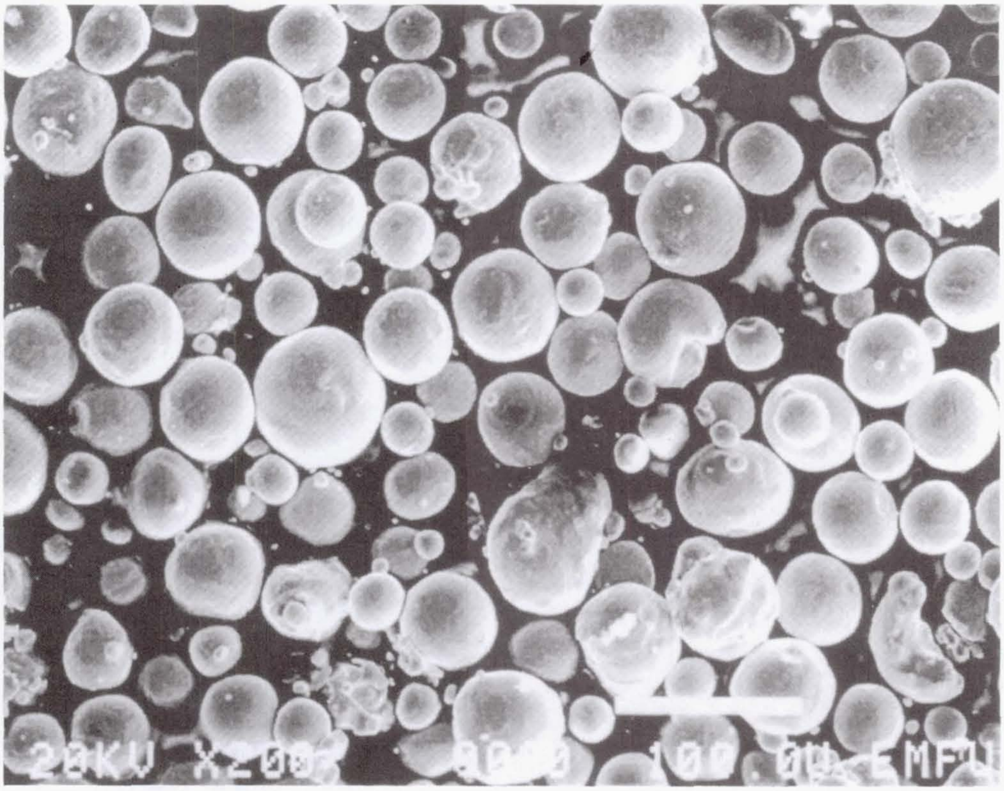

Figure 3. Morphology of spherical titanium powder

Application of Parallel Computing for Two- and Three-Dimensional Modeling of Bulk Crystal Growth and Microstructure Formation

Robert A. Brown
Department of Chemical Engineering
Massachusetts Institute of Technology
Cambridge, MA 02139
Phone: (617) 253-5726
E-mail: rab@mit.edu

Introduction

The quality of metal oxide and semiconductor crystals grown from the melt depends fundamentally on heat, mass, and species transport in the melt and crystal and on the interactions of these fields with the formation of microstructure, microdefects, dislocations, and voids in the grown crystal. Modeling of these individual processes for understanding their complex interactions is essential to the successful growth of crystals in a microgravity environment and to the interpretation of experiments from ground-based and microgravity research. The complexity of mathematical models of these phenomena makes numerical simulation essential. The goal of this project is to develop modern numerical simulation methods for calculation of complex models of transport processes in crystal growth and of microdefect formation using modern scaleable parallel computing.

Research to date has focused on the development of numerical methods for two types of mathematical models: development of parallel numerical algorithms for solutions of complex models of transport processes in material processing, and the development of algorithms for computation of mesoscale microstructure in materials processing. In parallel, we have continued our investigation of the dynamics of small-scale crystal growth systems of interest in microgravity applications, especially of the thermal-capillary and hydrodynamic dynamics of small-scale floating zone systems. This later research will not be discussed in this report.

Parallel Solution of Materials Processing Models

In the first study, implementation of scaleable parallel numerical algorithms are developed for the solution of the large, sparse systems of linear algebraic equations that arise when Newton's method is applied to the solution of the nonlinear algebraic equations formed from finite element discretization of transport problems, such as the description of natural convection in crystal growth melts, or of the free-boundary problem that describes heat transfer, phase change, and convection in solidification systems. Here we have focused on the development of Schwarz-Krylov methods for solution of the discrete modified-Stokes problems that arise at Newton iterations of nonlinear fluid mechanical problems. We have developed a block preconditioned Krylov iterative method based on the bi-conjugate gradient stabilized (Bi-CGSTAB) algorithm. The preconditioner is a Schur compliment factorization of the Jacobian based on the pressure variables and coupled with an additive Schwarz, domain decomposition iterative solution of the associated linear system. A coarse-grid preconditioner for the pressure variables also is used and direct LU decomposition is applied to the coarse-grid problem and to the domain-sized problems within the additive Schwarz method. This block-preconditioned Bi-CGSTAB method was implemented for a prototype problem of nonlinear, two-dimensional natural convection and tested on a single processor Hewlett Packard 735 computer. The iterative method compared well with a state-of-the-art direct solution method for varying Grashof number. Because the i of Schwarz-Krylov method does not require the storage of any zeros, larger problem sizes also are tractable than for the direct method.

The Schwarz-Krylov method was implemented in parallel using the recursive spectral dissection method to partition elements to processors, as implemented in the program CHACO. The code was written in the MPI language. Parallel efficiencies scaled well with increasing problem size and number of processors. These results suggest that the Schwarz-Krylov method will be robust for the solution of much more complex materials processing problems; application to a representative solidification problem is underway.

Parallel Simulation of Microstructure in Silicon Crystals

The second class of applications has been the development of models and numerical algorithms for simulation of microdefect formation in crystalline silicon, as occurs during the cooling during Czochralski and floating zone crystal growth. Although commercial semiconductor silicon is nearly perfect, comparison of the predictions of our models with experiments have shown that native point defects — self-interstitials and vacancies — in silicon diffuse, combine, and aggregate to form mesoscopic clusters that affect semiconductor device performance. We have constructed models of point defect dynamics and aggregation using statistical mechanical concepts for diffusion-limited reaction to model the interactions of point defects as chemical reactions. The distribution of point defect aggregates is modeled by combining discrete kinetic rate equations for small cluster sizes ($n < 20$) and a continuous size distribution governed by a Fokker-Planck equation for the description of very large cluster sizes ($20 < n < 1 \times 10^{10}$). The numerical solution of these equations combines two very different discretizations: a variable finite difference approximation constructed to maintain the monotonicity of the continuous cluster size distribution for discretization of the n-space Fokker-Planck equation and a Galerkin finite element discretization of variables in physical space. Because clusters of point defects cannot diffuse, the Fokker-Planck and discrete rate equations describing their dynamical evolution are hyperbolic equations in physical space and diffusive only in the state-space n of the size distribution, as written in the Fokker-Planck equation.

The solution of these models involves parallel implementation transient methods for simultaneous solution of the models describing point defect formation and aggregation. We have developed a mesoscale-macroscale splitting method for time integration formed from a couple discontinuous finite element/finite-volume solution of the Fokker-Planck equation and discrete rate equations for the non-diffusing clusters with an implicit transient finite element analysis of the reaction-diffusion point defect equations. The result gives a decoupled algorithm in which the discretized representations of the defect distributions are easily computed sequentially at each point in the crystal, and so are very amenable to parallel computing by considering simultaneous solution along parallel solution characteristics. This approach, coupled with implementation of the Schwarz-Krylov method for solution of the discrete-diffusion reaction problem, will yield a highly parallel and robust algorithm for simulating very complex microdefect formulation.

The application of these models is already bearing fruit. Comparison of experiments and quasi-one-dimensional simulations for the formation of microvoids — voids in silicon of 50 to 500 nm in radius — that are formed by vacancy aggregation during crystal growth show the accuracy of the calculations for predicting the formation of these defects in silicon and for connecting microdefect formation with macroscale processing conditions. These simulations are the first detailed description of the formation of microdefects in silicon and are the foundation for detailed analysis of the evolution of defects throughout silicon processing. The parallel transient analysis will yield the first fully two-dimensional simulation of microdefect dynamics in silicon.

Effects of Melt Processing on Evolution of Structure in PEEK

Georgi Georgiev[1], Patrick Shuanghua Dai[1], Elizabeth Oyebode[1],
Peggy Cebe[1] *, and Malcolm Capel[2]

[1] Department of Physics and Astronomy, Tufts University, Medford, MA 02155
[2] Biology Department, Brookhaven National Laboratory, Upton, NY 11973
* To whom correspondence should be addressed

Abstract

We report on the effects of melt processing temperature on structure formation in Poly(ether-ether-ketone), PEEK. Real time Small Angle X-ray Scattering, SAXS, and thermal analysis are used to follow the melting behavior after various stages of processing. Assignment of peaks to structural entities within the material, the relative perfection of the crystals, and the possibility of their reorganization, are all influenced by the melt processing history. With the advent of high intensity synchrotron sources of X-radiation, polymer scientists gain a research tool which, when used along with thermal analysis, provides additional structural information about the crystals during growth and subsequent melting.

PEEK is an engineering thermoplastic polymer with a very high glass transition temperature (145 °C) and crystal melting point (337 °C). PEEK has been the subject of recent studies by X-ray scattering in which melt and cold crystallization were followed in real-time. X-ray scattering and thermal studies have been used to address the formation of dual endothermic response which has been variously ascribed to lamellar insertion, dual crystal populations, or melting followed by re-crystallization. Another important issue is whether all of the amorphous phase is located in interlamellar regions, or alternatively whether some is located in "pockets" away from the crystalline lamellar stacks. The interpretation of scattering from lamellar stacks varies depending upon whether such amorphous pockets are formed. Some groups believe all of the amorphous phase is interlamellar. This leads to selection of a smaller thickness for the crystals. Other groups suggest that most amorphous phase is not interlamellar, and this leads to the suggestion that the crystal thickness is larger than the amorphous layer within the stacks. To investigate these ideas, we used SAXS and Differential Scanning Calorimetry to compare results of single and dual stage melt crystallization of PEEK using a treatment scheme involving annealing/crystallization at T_{a1} followed by annealing at T_{a2}, where either $T_{a1}<T_{a2}$ or $T_{a1}>T_{a2}$.

We proposed a model to explain multiple melting endotherms in PPS, treated according to one or two-stage melt or cold crystallization. Key features of this model are that multiple endotherms: 1. are due to reorganization/recrystallization after cold crystallization; and, 2. are dominated by crystal morphology after melt crystallization at high T. In other words, multiple distinct crystal populations are formed by the latter treatment, leading to observation of multiple melting.

PEEK 450G pellets (ICI Americas) were the starting material for this study. Films were compression molded at 400 °C, then quenched to ice water. Samples were heated to 375 °C in a Mettler FP80 hot stage and held for three min. to erase crystal seeds before cooling them to T_{a1} = 280 °C . Samples were held at T_{a2} for a period of time, then immediately heated to 360 °C. In the second treatment samples were held at T_{a1} = 310 °C for different crystallization times t_c, then cooled to 295 °C and held 15 min.

In situ (SAXS) experiments were performed at the Brookhaven National Synchrotron Light Source with the sample located inside the Mettler hot stage. The system was equipped with a two-dimensional position sensitive detector. The sample to detector distance was 172.7 cm and the X-ray wavelength was 1.54 Å. SAXS data were taken continuously during the isothermal periods and during the heating to 360 °C at 5 °C/min. Each SAXS scan was collected for 30 sec. Since the samples were isotropic, circular integration was used to increase the signal to noise ratio.

After dual stage melt crystallization with $T_{a1}<T_{a2}$, the lower melting endotherm arises from holding at T_{a1}. During cooling a broad distribution of crystals forms, and the low-melting tail is perfected during T_{a1}. Heating to T_{a2} melts these imperfect crystals and allows others with greater average long spacing to form in their place. After dual stage crystallization with $T_{a1}> T_{a2}$, the amount of space remaining for additional growth at T_{a2} depends upon the holding time at T_{a1}. The long period of crystals formed at T_{a2} is smaller than that formed at T_{a1} due to growth in a now-restricted geometry.

Perfection of crystals is seen as an increase of the intensity of the population scattering at higher s, while the intensity of the population scattering at lower s stays constant. During heating from below to above the minor endotherm, we see rapid decrease of the intensity of the X-ray scattering corresponding to the population of crystals scattering in the shoulder. Another important observation is that after the sample is annealed at 295 °C, the shoulder intensity is restored once again. The population scattering at higher s remains longer before it disappears in the sample treated to the second stage of melt crystallization, compare to the sample crystallized with a single stage. This could be interpreted as an effect of continued perfection of the less perfect population, which is also reflected in the increased melting temperature of the smaller endotherm as the holding time at 295 °C increases. In the corresponding DSC scans we see a shift in the area and the peak temperature of the lower melting endotherm with an increase of the annealing time.

Research was supported by NASA Grant NAG8-1167.

THREE-DIMENSIONAL VELOCITY FIELD CHARACTERIZATION IN A BRIDGMAN APPARATUS: TECHNIQUE DEVELOPMENT AND EFFECT ANALYSIS

James S. Slepicka, Yi Ge, and Soyoung Stephen Cha
University of Illinois at Chicago
Chicago, IL 60607
312-996-9612; SSCha@uic.edu

Introduction

The integrity of crystal structures is strongly influenced by the existence of thermally-induced flows as well as local nucleation particles and their growth in the melt, which may act in a detrimental manner. In both ground-based and microgravity experiments, these physical properties that involve three-dimensional (3-D) fluid or particle motions need be characterized to identify their effects on material processing. In spite of the efforts to alleviate detrimental flow problems, their influence cannot be completely eliminated. Such 3-D flows make instantaneous gross-field evaluation practical impossible with existing point probes. Two-dimensional two-component measurement methods such as particle imaging velocimetry (PIV) can provide valuable information but still pose limitations in investigating 3-D fields. Consequently, providing means for detecting 3-D three-component (3-C) velocity or particle fields and characterizing pertinent solidification parameters is very important for crystal growth experiments in optimizing production parameters. It is also vital to validation and improvement of numerical modeling for material processing.

In the effort to overcome the intrinsic limitations of the current techniques, two complementary optical techniques have been developed and tested for measurement of 3-D 3-C particle or flow motions, which reflect the peculiar aspects of restricting experimental conditions in crystal growth and material processing. One, termed Holographic Diffraction Image Velocimetry (HDIV),[1,2] utilizes double-reference-beam off-axis holographic recording and reconstruction of two independent time-sequence images of a particle field. The other, called Stereoscopic Imaging Velocimetry (SIV),[3] is based on dual solid-state camera observation from different vantage points. These two techniques are believed to meet a broad range of experimental requirements, being complementary with respective strengths and limitations. The HDIV technique offers velocity extraction of an extended area with high spatial resolution and dynamic range from a single observation direction but it does not provide a real-time capability. It is also complex in setup. In contrast, the SIV technique is appropriate for observing a restricted area only with limited resolution and dynamic range but it allows continual near-real-time velocity monitoring. Its experimental configuration is also simple, including hardware and software. In both of these techniques, the illumination beam is not restricted to any specific plane of focus as in PIV, and can be reasonably thick to provide true volume illumination since the images are recorded in three-dimensions.

Description of the Methods and Experimental Results

In HDIV, two successive exposures of a displacing particle field are recorded on a single holographic plate, using a separate reference beam for each exposure. It thus provides the capability of measuring an instantaneous 3-D 3-C velocity field from a single observation direction. After recording, each individual scene of particle diffraction is independently reconstructed and scanned section-by-section with a solid state camera without requiring specific particle focusing. Intensity data from the resulting local particle fields is then computationally processed by employing statistical correlation algorithms for matching local sections in the time-sequence 3-D images to extract velocity components. The HDIV system provides a large effective angular aperture defined as the smallest value among scattering lobe angle of the particles, subtended angle θ of the holographic plate, and angular aperture of the imaging system. This serves to give the technique the capability to reconstruct a 3-D particle field with high resolution and short depth of field.

In the research, a breadboard setup for HDIV has been built and testing has been conducted for evaluation of the concept, data acquisition system, and processing algorithms. Initially, some simple experiments were performed using spherical particles 10μm in diameter dispersed on a plane surface or imbedded in a transparent plastic volume. In the plate-field experiment, the entire particle fields were captured twice on a holographic plate, once before and again after rotation of the plane. These rotations thus produced known particle displacements for assessing measurement accuracy, which increase with distance from the center of rotation. Figure 1 shows a typical results for out-of-plane displacement measurement. Our experiments with static particles undergoing in- and out-of-plane rotations demonstrated the ability of the HDIV technique to extract 3-D 3-C particle displacements with good accuracy and dynamic range. While in-plane accuracy was shown to be limited by the finite pixel size of the CCD array, typical uncertainty in out-of-plane detection from these experiments was found to be on the order of $\sim 0.2d^2/\lambda$, where $d=\lambda/\theta$ is the in-plane resolution corresponding to the smallest identifiable image structure and λ is the laser wavelength. This is without interpolation in correlation peak detection and with a relatively low resolution translation stage. It is a significant improvement over other techniques which generally can only produce lower out-of-plane resolutions. Further testing was conducted with a 3-D flow for the flow around a 12mm diameter sphere, which was dropped in a vertical test section containing glycerin seeded with 5μm diameter polystyrene spherical particles. A double-pulsed laser was employed to holographically record a horizontally illuminated particle volume including the bottom-front quarter of the sphere. The resulting velocity field at a typical plane is shown in Fig. 2. Without the exact field known for comparison, only qualitative interpretation is possible for this experiment. As can be seen, the symmetrical character of this type of flow is evident as well as the increase in velocity for planes closer to the sphere. For some of the upper scans, velocity vectors did not show at the points where the surface of the sphere was present.

The HDIV technique was tested in various situations and operational modes for fundamental investigations to characterize the important experimental parameters, which affect its performance, as well as to identify some remedial solutions to minimize the effects. These include emulsion shrinkage, wavelength change, and plate mispositioning in recording and reconstruction. To further enhance the out-of-plane resolution, the approach of comparing the intensity variances of the diffraction images of individual particles is being investigated. The approach appears to be promising to provide the measurement accuracy much better than the current value of $0.2d^2/\lambda$.

The SIV measurement consists of camera calibration, particle identification through superposed image decomposition and centroid detection, particle tracking for each camera image, stereoscopic 3-D matching of individual particle tracks, and velocity vector extraction and validation. Images of individual particles or equivalently data points are not completely recoverable. The data loss mostly occurs during the processes of centroid identification of individual particles and the optimization phase of particle tracking. The lost becomes more prominent as the particle density increases. In order to maximize the data recovery and to enhance the measurement accuracy, artificial neural networks were implemented in these two phases of processing. A very important feature of these networks is their adaptive nature, where learning by example replaces programming in solving problems.[4,5] The back propagation neural network has proven to be very useful in particle identification and overlap decomposition because of its ability and efficiency in pattern recognition and classification. The test results demonstrated higher efficiency and speed in identifying single or superimposed particles as compared with conventional models. The tracking algorithm takes as its input the particle positions found in the particle identification process. It then provides the output of particle image track assignments across time-sequence image frames. The Hopfield neural network was utilized to select an ideal track from the database of potentially-valid tracks found through four time-sequential frames. It identifies those that correspond to a global optimization scheme in order to get a high successful recovery rate. The utilization of the Hopfield neural network has proven to be very successful in attaining valid tracks.

For the SIV approach, computer simulations and experimental measurements have been conducted with the developed prototype hardware and software to assess the performance of the technique. The results have shown that on the average the success rates for particle identification decomposition are better than 98%, 87%, and 91% for single, double, and triple particles, respectively. The particle tracking was also tested but with the synthetically generated data in order to compare its output with the tracks contained in a known flow field. The particles position in the flow were randomly produced. Figure 3 shows the flow field with 600 particle tracks. The success rates for tracking were 100%, 98.5%, and 97.7% with 200, 400 and 600 particles, respectively, in the field. To investigate and test the performance in a more realistic manner, a laminar water jet emerging from a circular tube was measured with the SIV system. At the tip the velocity profile was parabolic, as expected, in good agreement with the analytical profile.

Conclusions

Our initial testing has proven HDIV and SIV to be a viable candidate for reliable measurement of 3-D 3-C flow velocities of a particle field, intentionally seeded or formed by natural nucleation. The strengths of the technique include greater experimental freedom in volumetric field illumination and observation, both of which can be arbitrary in direction and shape unlike conventional PIV and in-line holographic techniques. For SIV, the results have demonstrated significant advantages in using the neural networks. For HDIV, no specific particle focusing is required and seeding of higher concentration particles is possible during recording unlike other two-dimensional techniques. These features of HDIV and SIV are very appropriate in conducting flow experiments. With current activities are focused on further improving the processing efficiency and overall accuracy and automation, it is believed that these methods can become important flow diagnostic tools with the ability to meet the increasing demands for applications to flow velocity and particle size characterization of crystal growth and material processing. Future investigation will be focused on the applications to crystal growth investigations including microgravity experiments. These involve miniaturization of the experimental systems and further refinement of the processing algorithms.

References

1. J.S. Slepicka and S.S. Cha, AIAA J., 35, 1201 (1997).
2. J. S. Slepicka and S. S. Cha, in SPIE Proc. on Optical Technology in Fluid, Thermal, and Combustion Flow III, 3172, 318 (1997).
3. Y. Ge, V. Em-Udom, and S. S. Cha, AIAA Paper 98-2812 (1998).
4. D. E. Rumelhart, G. E. Hinton, and R. J. Williams, Learning internal representations by error propagation; parallel distributed processing, the MIT press, Cambridge, 1986.
5. B.D. Ripley, Pattern Recognition and Neural Networks, Cambridge University Press, Cambridge, 1996.

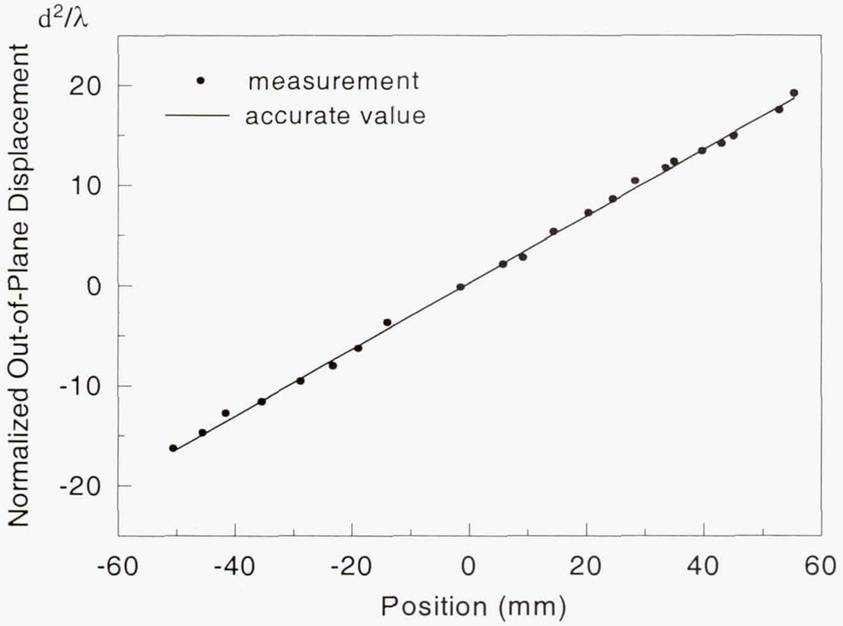

Figure 1. Measured out-of-plane displacements from a rotated plane particle field.

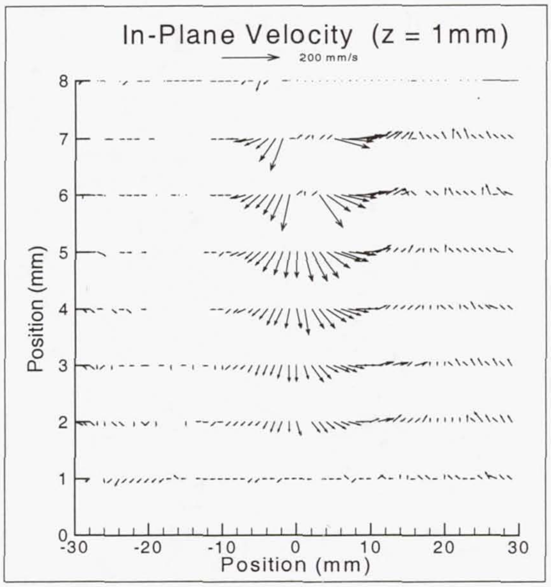

Figure 2. In-plane velocity components for a typical plane in the flow around a falling sphere.

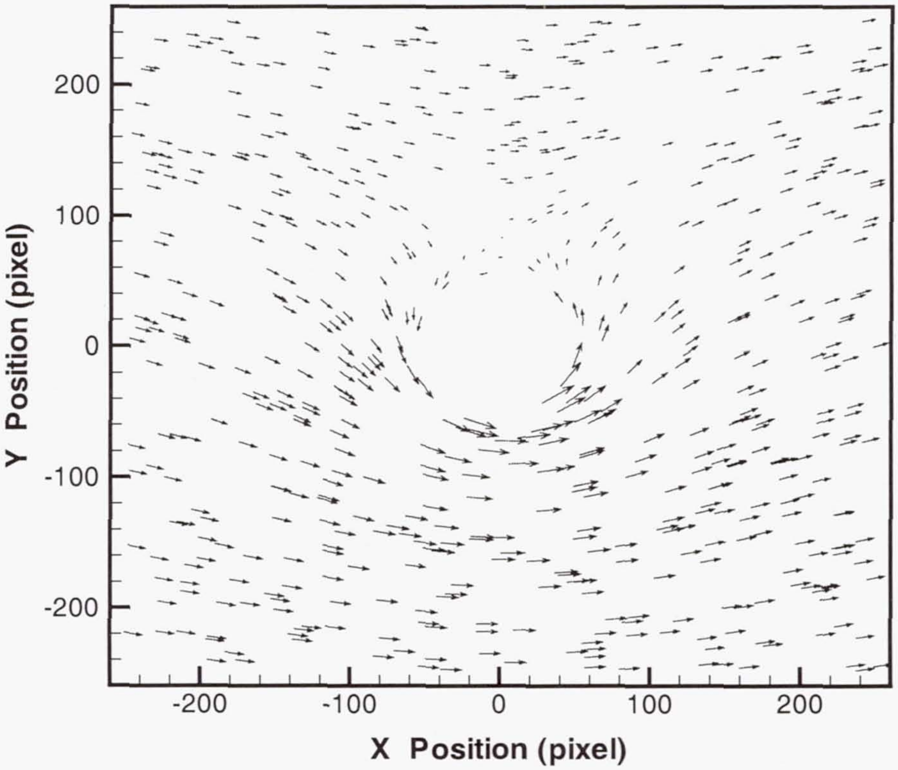

Figure 3. Flow field with 600 particles.

Page intentionally left blank

Step Bunching: Influence of Impurities and Solution Flow

A.A. Chernov*, P.G. Vekilov, S.R. Coriell***, B.T. Murray***, G.B. McFadden*****

*** Universities Space Research Association/MSFC, 4950 Corporate Drive,**
Ste. 100, Huntsville, AL 35805
**** University of Alabama in Huntsville, Huntsville, AL**
*****National Institute of Standards and Technology, Gaithersburg, MD 20899**

1. The Problem

Step bunching results in striations even at relatively early stages of its development and in inclusions of mother liquor at the later stages. Therefore, eliminating step bunching is crucial for high crystal perfection. At least 5 major effects causing and influencing step bunching are known:

1. Basic morphological instability of stepped interfaces. It is caused by concentration gradient in the solution normal to the face and by the redistribution of solute tangentially to the interface which redistribution enhances occasional perturbations in step density due to various types of noise.

2. Aggravation of the above basic instability by solution flowing tangentially to the face in the same directions as the steps or stabilization of equidistant step train if these flows are antiparallel [1-4].

3. Enhanced bunching at supersaturation where step velocity v increases with relative supersaturation s much faster than linear [5]. This $v(s)$ dependence is believed to be associated with impurities. The impurities of which adsorption time is comparable with the time needed to deposit one lattice layer may also be responsible for bunching [6, 7].

4. Very intensive solution flow stabilizes growing interface even at parallel solution and step flows [5].

5. Macrosteps were observed to nucleate at crystal corners and edges [8, 9]. Numerical simulation, assuming step-step interactions via surface diffusion also show that step bunching may be induced by random step nucleation at the facet edge and by discontinuity in the step density (a ridge) somewhere in the middle of a face. The corresponding bunching patterns produce the ones observed in experiment [10-12].

The nature of step bunching generated at the corners and edges and by dislocation step sources, as well as the also relative importance and interrelations between mechanisms 1-5 is not clear, both from experimental and theoretical standpoints. Furthermore, several laws controlling the evolution of existing step bunches have been suggested [13, 14], though unambiguous conclusions are still missing. Addressing these issues is the major goal of the present Project.

2. Theory [15]

Linear perturbation analysis was applied to a stepped interface on which step density is, respectively linear and non-linear functions of supersaturation and also to the case when the step rate is a non-linear function of supersaturation. The approach and codes developed earlier [1-4] were employed.

2.1 Linear increase of vicinal slope with supersaturation.

First vicinal slope, p, is kept constant. This is the case of, e.g., lysozyme faces or prismatic, KDP/ADP faces on which steps are generated by strong dislocation sources at high supersaturation. If $p = \text{const} = 5.10^{-3}$ and the solution is stagnant, the interface is unstable within the area surrounded by solid line in Fig. 1. This solid line presents the perturbation wavevector k_x as a function of the normal growth rate, $V = p\nu$. As the solution flow velocity in the stabilizing (counter, or up-step) direction rises, this area of instability shrinks and disappears at a certain shear flow ($\sim < 1 s^{-1}$ for the ADP growth parameters). The instability area expands if the flow is destabilizing (down-step).

If the vicinal slope p linearly increases with relative supersaturation ($p=0.117s$), the interface is stable in the area inside the dashed line in Fig. 1. In this case the instability region expands at higher growth rate rather that shrink, contrary to the region surrounded by the solid line and corresponding to p = const. Such dramatic change in behavior comes from much stronger sensitivity of the surface self stabilization to the average step density than to step velocity inducing the self stabilization.

2.2 Non-linear increase of step velocity and hillock slope with supersaturation.

Step velocity was chosen to fit the experimental data for prismatic ADP face making use of the following relationship

$$\nu = \beta_2 \{b_1+(b_2-b_1)/[1 + \exp [b_3(1-s/s^*)]]\}s \qquad (1)$$

with $b_1 = 4.0\ 10^{-3}$cm/s, $b_2 = 3.10^{-2}$cm/s. $b_3 = 20$, $s^* = 0.041$. The square brackets present the stepwise function of s with the change from $\beta_2 \cong b_1$ at $s<<s^*$ to $\beta_2 \cong$ at $s>>s^*$.

The resulting stability areas at different shear flows are seen in Fig. 2. The slope varied with supersaturation as $p = 0.117 \cdot s$. Besides the instability area in the upper right part of Fig. 2, similar to the one shown in Fig. 1, the instability also occurs at supersaturations $s \simeq s^*$ where the kinetic coefficient changes most steeply with s. This confirms the experimentally observed and intuitively clear weaker stability of the interface to perturbations at the supersaturations corresponding to the strongest response of the interface to the local supersaturation changes i.e. impurity induced instability [5].

As it can be seen from Fig. 2 by comparing stability borders at various solution flow shear rates, S, the stability strongly depends on solution flow: the instability region in the middle of Fig. 2 may shrink to zero at high stabilizing shear flows, $S > 0$, and expands at $S < 0$. Experimentally, the impurity induced instability actually remains at any flow rates while theory predicts its elimination at sufficiently intense stirring. However, no systematic measurements at various flow rates have been performed so far.

If we assume that the hillock slope approaches constant value at rising supersaturations as it happens for powerful dislocation step sources, then the region in the upper right corner of Fig. 2 naturally disappears.

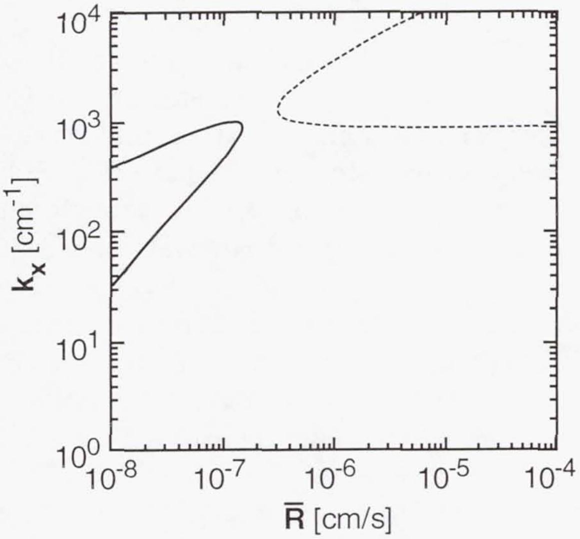

Fig. 1. The spatial wave numbers at which the system is neutrally stable as a function of growth velocity for linear kinetics ($b_0 = 0$, $b_1 = b_2 = 4.0 \times 10^{-3}$ cm/s) for p = 0.005 (solid curve) and p = 0.117 s (dashed curve).

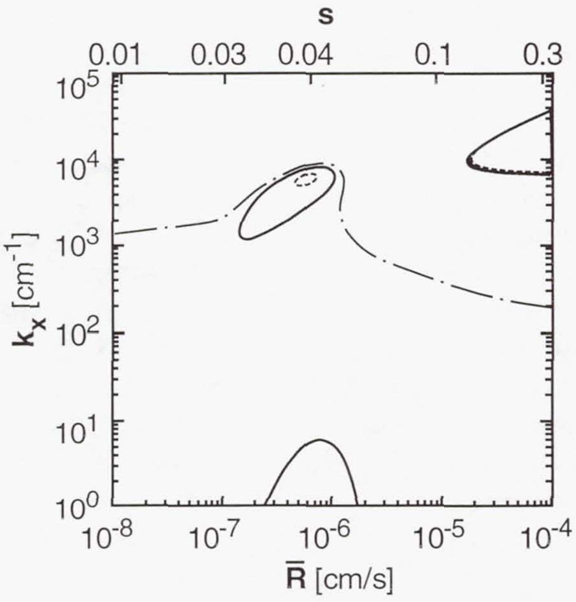

Fig. 2. The spatial wave numbers at which the system is neutrally stable as a function of growth velocity and supersaturation (upper axis) for nonlinear kinetics ($b_0 = 0$, $b_1 = 4.0 \times 10^{-3}$ cm/s, $b_2 = 3.0 \times 10^{-2}$ cm/s, $b_3 = 20.0$, $s^* = 0.041$) for p = 0.117 s and shear rates S of 0.5 (dashed), 0 (solid), and -0.5 (chain dashed) s^{-1}.

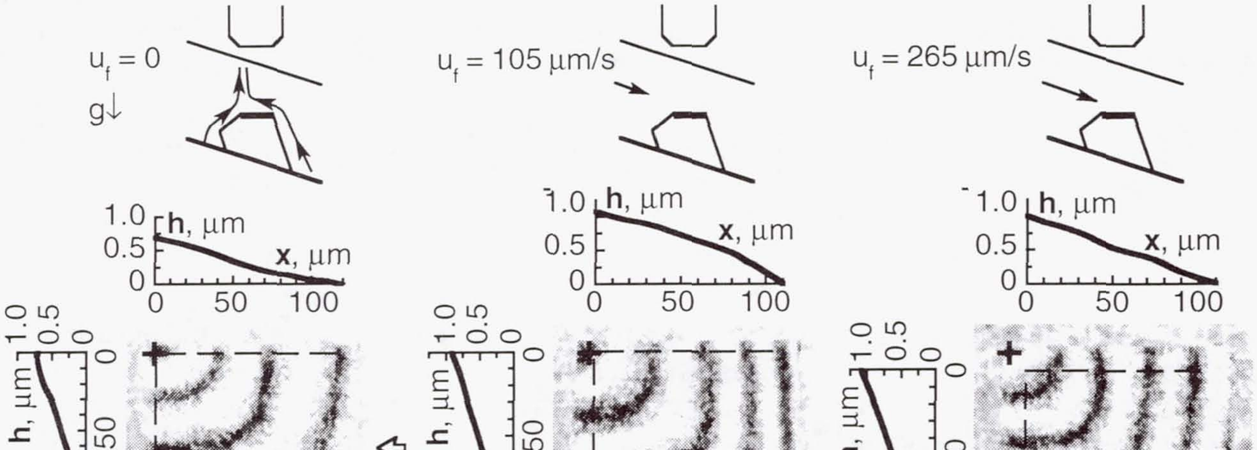

Fig. 3. Schematic of the experiment (upper row) of lysozyme crystal growing under conditions of natural convection (a), and forced flow at the average flow rates u = 105 μm/s (b) and 265 μm/s (c). The face profiles shown at the interferograms were determined by interference pattern intensity along the vertical and horizontal dashed lines.

3. Experiment

3.1 The average surface profile.

So far, stability of lysozyme bipyramidial face was studied. The experimental setup was described earlier [11]. The observation scheme and flows are shown in Fig. 3, upper row. The face profile was determined from interferograms. The local face growth rate and local vicinal slope, i.e. the step density, were measured in points #1, 2, 3 marked by crosses on each of the face interferograms (Fig. 3, lower row). Point #1 is in the upper left corner, point #2 is the upper right, and point #3 is the lover left. In each point, the interface positions by two adjacent laser beams, ca. 3μm apart was simultaneously measured. Each testing point includes such pair of laser beams with the pair oriented normal to the average step direction (interference fringes). Techniques for measurement and evaluation of these fluctuations were described in ref. [11]. As the interferograms demonstrate. The step source was located in the upper left corner of the face. This source is probably of dislocation origin because there was no growth cessation at supersaturation $s \simeq 0.4$. In the experiments under consideration, $s \simeq 1$.

The surface profiles h(x) along the dashed lines in horizontal and vertical cross sections are attached to the corresponding interferograms. The profiles in the direction normal to the flow (between the points #1 and #3) shown at the left from each interferogram in Fig. 3. These profiles are about flat, in Figs. 3b and c, while in Fig. 3b this profile is concave.

The profiles along the flow behave differently. Under conditions of only natural convection, Fig. 3a, the h(x) profile shows that the face is slightly concave in the region $30 < x < 80$μm/s.

At the forced flow rate u=105 μm/s (Fig. 3b) the face is convex. The profile convexity disappears if the crystal is turned by some 20° or more around the axis normal to the face and solution flow. Such a turn means changes in flow patterns and, also, that mutual azimutal orientation of the flow and step directions changes significantly.

At flow rate, u=265 μm/s the hillock slope is about constant. The face flatness may be attributed to a deeper kinetic control of the growth and thus essentially more constant supersaturation along the face.

3.2 Fine Structure of the Surface: Fluctuations.

Figs. 4, 5 and 6 corresponding to the Fig. 3a, b, and c, present the temporal fluctuations of normal growth rate and local slopes in testing points #1, #2 and #3.

These temporal fluctuations are the result of step bunches passing through the testing points, possessing different slopes, p, and thus providing different local normal growth rates, $V = pv$.

No essential difference can be seen between fluctuations in a and c of Figs. 5, and 6. This might be expected since the flow in all cases is essentially parallel to the steps in testing points #1(a) and #3(c) and thus should not strongly influence step bunching. A larger amplitudes of normal growth rate fluctuations can be noted in test point #2 as compared to #1 under conditions of natural convection (Fig. 4). In this case, indeed, the flow is stabilizing in #2 and destabilizing in #1. This effect was reported earlier in [1, 5, 12].

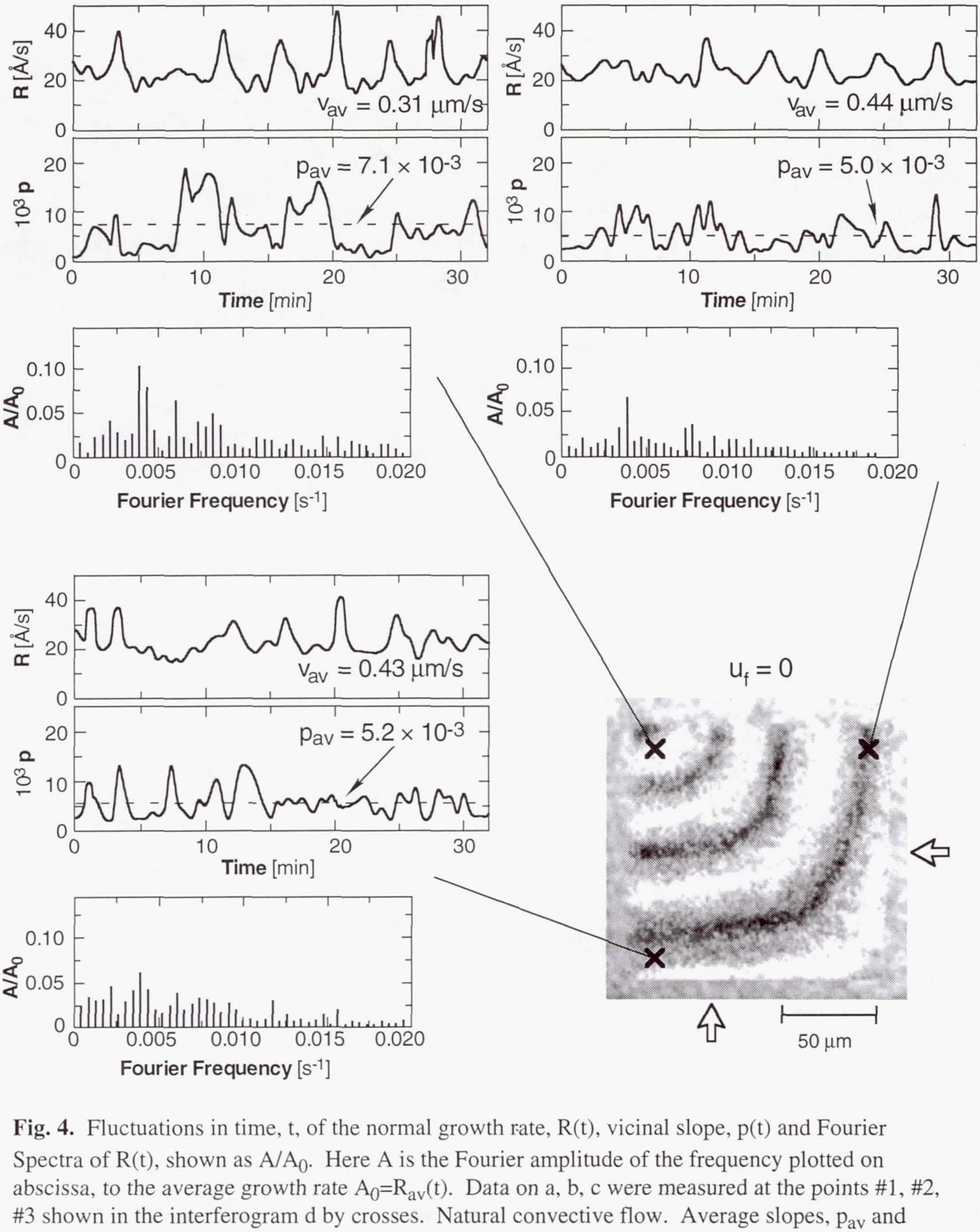

Fig. 4. Fluctuations in time, t, of the normal growth rate, R(t), vicinal slope, p(t) and Fourier Spectra of R(t), shown as A/A_0. Here A is the Fourier amplitude of the frequency plotted on abscissa, to the average growth rate $A_0=R_{av}(t)$. Data on a, b, c were measured at the points #1, #2, #3 shown in the interferogram d by crosses. Natural convective flow. Average slopes, p_{av} and effective step rates, v_{av}, are shown.

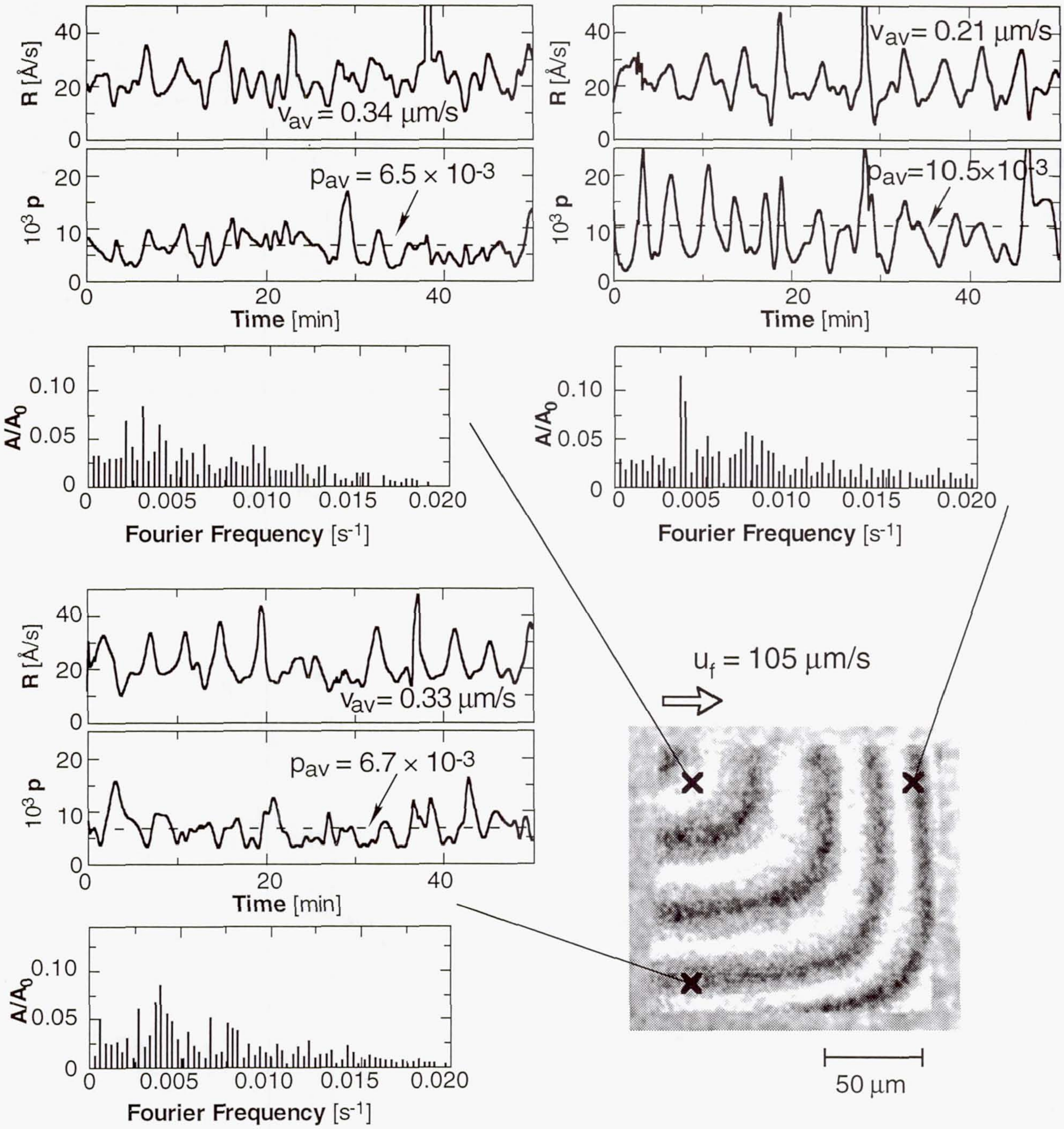

Fig. 5. Same as Fig. 4, forced solution flow rate u = 105 μm/s.

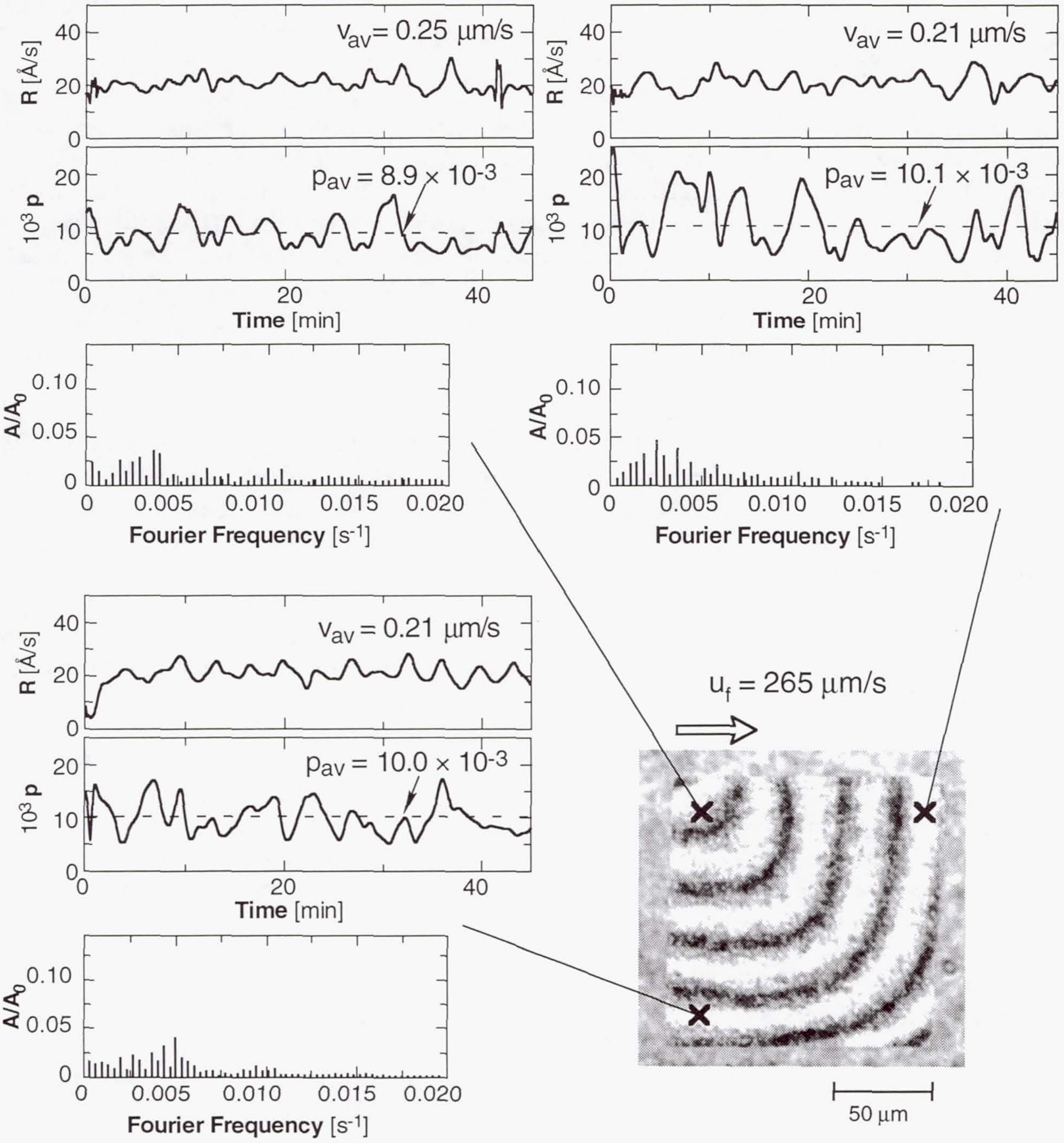

Fig. 6. Same as Fig. 4, forced solution flow rate u = 265 µm/s.

Comparing the fluctuation amplitude , in a and b in Figs. 5 and 6, we note that fluctuations are stronger in Figs. 5b, 6b as compared to Figs. 5a, 6a. This corresponds to an increase in average slope, p_{av}, from a to b. Similarly, the fluctuation are stronger in Fib 4b at larger $p_{av}=7.10^{-3}$ as compared to Fig. 4b at resulting $p_{av}=5.10^{-3}$. Corresponding decrease in average step rate, ν_{st}, with increase of p_{av}, may also be noted since the average normal growth rate, $R_{av} = (p\nu)_{av}$ remains unchanged. The numbers for p_{av} and v_{av} are given in the figures.

Much stronger effect have the increase in the flow rate from 105µm/s to 265 µm/s: fluctuations in normal growth rate in Fig. 5 are noticeably less intense than these in Fig. 6, i.e., the flow rate rise essentially damps the fluctuations. This effect takes place in both the upstream and the downstream testing points #1 and #2 in Figs. 6a and b. Simultaneously, an increase of the p(t) and R(t) fluctuations measured in the downstream points #2(b), as compared to the upstream point #1(a) can be seen in Fig. 5.

4. Discussion and Conclusions

The role of bulk transport in formation of the overall face profile, i.e. the h(x) and p(x) dependencies (Fig. 4), can be estimated making use of convectional boundary layer thickness above thin plate. With $R=2\cdot10^{-7}$cm/s, $D=10^{-6}$cm^2/s, $\nu=10^{-2}$g/cm.s, crystal size ~ 100µm and the ratio of the protein concentration in crystal to the one in solution $\simeq$ 30, this estimate suggest the diffusion boundary layer thickness $\simeq 2.3\cdot10^{-2}$cm and about 10% decrease in supersaturation along the face. This is insufficient to provide the observed slope change of the order of 100%.

This large slope increase may be associated with step bunching resulting in effectively lower average kinetic coefficient of the face. The corresponding modeling based on strong step-step interaction is consistent with this large increase — cf. Figs. 9 and 16 in reg. [10].

Existence of fluctuations corresponding to step bunches passing the test point #1, close to the step source, along with the ones in #2 and #3, suggests that the experimentally observed bunching might occur at the very beginning, during the step generation and is merely enhanced in course of propagation along the face. Therefore, the theory analyzing only onset of instability is probably insufficient to treat the data: evolution of bunches, along with their generation at the dislocation and/or nucleation sources is needed.

The mechanism of step bunching in the close proximity to the step source is not clear. One may think of step pairing noted on the KDP crystals by AFM [17], on bunching provided by irregular step generation at the edge with essential contribution of surface diffusion [12], on the coupled impurity adsorption, step nucleation and propagation [18] at supersaturations close to the transfer from the dislocation to the 2D nucleation driven growth and at the supersaturations close to the impurity assisted non-linear steep increase of the step rate with s, like the one discussed in Sec. 2.

Suppression of fluctuations by the faster solution flow may be associated with weaker coupling of step generation by either dislocations or 2D nucleation (both non-linearly dependent on supersaturation) with diffusion and impurity adsorption in the very vicinity of the step generation area.

Enhanced fluctuations in the downstream portion of the step train is qualitatively consistent with the theory developed in Sec. 2. However, extension of the theory to the evolution of the already formed surface corrugations to form the more pronounced dissipative step structure in needed. Equally important are relevant future experiments.

5. Acknowledgment

The Authors acknowledge the support of the NASA Microgravity Science and Applications Division through grants NAG8-1354 and NAG8-1454.

6. References

1. A.A. Chernov, Y.G. Kuznetsov, I.L. Smol'ski, V.N. Rozhanski, Sov. Phys. Crystallography **31** (1986) 859.
2. A.A. Chernov, J. Cr. Gr. **118** (1992) 705.
3. A.A. Chernov, S.R. Coriell, B.T. Murray, J. Cr. Gr. **132** (1993) 405.
4. S.R. Coriell, B.T. Murray, A.A. Chenrov, G.B. McFadden, J. Cr. Gr. **169** (1996) 773, Met. Matls Trans. **27A** (1996) 687.
5. L.N. Rashkovich and B.Y. Shekunov, J. Cr. Gr. **100** (1990) 133.
6. F.C. Frank, in Growth and Perfection of Crystals, Ed. R.H. Doremus, B.W. Roberts, D. Turnbull (Chapman and Hill, London, 1958) p. **411**.
7. J. P. van der Eerden and H. Müller Krumbhaar Electrochim. Acta **31** (1986) 2431.
8. A. Papapetrou, Zs. f. Kristallografie **92** (1935) 89.
9. A.A. Chernov, J. Cryst. Gr. **24-25** (1974) 122.
10. P.G. Vekilov, H. Lin and F. Rosenberger, Phys. Rev. E **55** (1997) 3202.
11. P.G. Vekilov, L.A. Monaco and F. Rosenberger, J. Cryst. Gr. **146** (1995) 289.
12. P.G. Vekilov, J.I.D. Alexander and F. Rosenberger, Phys. Rev. **55** (1996) 6650.
13. A.A. Chernov, Sov. Phys. Usp **4** (1961) 116.
14. D.G. Vlachos, L.D. Schmidt, R. Aris, Phys. Rev. B **47** (1993) 4896.
15. S.R. Coriell, A.A. Chernov, B.T. Murray, G.B. McFadden, J. Cryst. Gr. **183** (1998) 669.
16. Carlson, ref. 6, p. **421**.
17. J.J. DeYoreo, T.A. Land, B. Daiz, Phys. Rev. Lett. **73** (1994) 838.
18. A.A. Chernov, V.F. Parvov, M.O. Kliya, D.V. Kostomarov, Y.G. Kuzentsov, Sov. Phys. Crystal **52** (1981) 185.

Page intentionally left blank

Dynamic Reduction and the Creation of Fine-Grained Ceramics from Inviscid Oxide/Silicate Melts

Reid F. Cooper
Department of Materials Science and Engineering
University of Wisconsin
1509 University Avenue
Madison, WI 53706
Phone: (608) 262-1133
E-mail: cooper@engr.wisc.edu

The overall materials science objectives of this research program are to discern, characterize, and develop a useful approach to the creation of fine-grained ceramics from inviscid (low-viscosity) ionic melts. The scientific problem centers on the need to control the density and spatial distribution of crystalline nuclei in such melts. We (my graduate students and I) have identified a new, unique "alternative" approach to controlled nucleation, for which microgravity containerless processing is required: dynamic reduction. In transition-metal-cation-bearing, multicomponent ionic melts, the redox dynamics are such that relatively rapid processing is possible.

Melts that contain multiple cations can be forced to undergo a dynamic reduction reaction, given appropriate control of the activity of oxygen of the process environment. In the case where a transition metal oxide component is a minority constituent of the melt, such a reaction can result in the uniform distribution of metal (either as fine crystals or as fine, discrete droplets, depending on the temperature) within the (now) transition-metal-cation-depleted ionic melt. Because of the presence of the transition metal cation species, the kinetics of the process involves the diffusive motion of cations that is charge-compensated by the rapid motion of electronic defects (i.e., polarons: localized electrons or electron holes); as such, reduction should occur at an internal front. (One objective of the research, then, is to characterize the morphology and possible variations of morphology of such reduction dynamics in melts.) In this approach, then, the finely and uniformly dispersed metal phase can act as a substrate for the heterogeneous crystalline nucleation of the remaining ionic melt upon its cooling. This reduction approach could prove effective, too, in controlling the coarsening of the metal nuclei: Ostwald ripening processes would require redox reactions at the metal/ceramic interface, which could be rate limiting. At present, we are pursuing control experiments on Fe^{2+}-doped aluminosilicate melts, which are sufficiently viscous to be effectively suspended by refractory wire in a conventional furnace. Initial reaction morphologies match the cation-diffusion-dominated and rate-limited reduction dynamics articulated above; theoretical analysis/modeling of these dynamics are underway. The extension to inviscid liquids will be first approached on ferromagnesian orthosilicate, prepared by melting natural and synthetic ferromagnesian olivine, $(Fe_x,Mg_{1-x})_2SiO_4$. The control experiments on aluminosilicate and orthosilicate liquids will be extended to AeroAcoustic Levitation (AAL). The AAL experiments involve levitation on a gas jet of controlled oxygen activity, created by reacting mixtures of H_2 and CO_2 gasses. Initial levitation of specimens will be at an oxygen activity in which the material is stable against reduction; subsequent treatment will drive the reduction reaction.

The postulate for these experiments was founded on the results of oxidation studies of melts and glasses, previously supported by the NASA Microgravity Sciences program. In these earlier experiments, we were able to prove unequivocally the applicability of the "semiconductor condition" to the understanding of redox dynamics in iron-bearing aluminosilicate melts and glasses. Specifically, the polaron behavior decouples the diffusive motion of cations and anions; one consequence is that, when exposed to a gradient in the chemical potential of oxygen, the dynamic response allowing internal oxidation can avoid the motion of an oxygen species (ionic or atomic/molecular) altogether. While we were able to demonstrate "isothermal undercooling" via oxidation that resulted in the uniform, internal heterogeneous nucleation of silicate phases on internal-oxidation-induced ferrite precipitates (homogeneously nucleated at the oxidation front), one difficulty was the coarsening of the ferrite nuclei. The dynamics of reduction should be the mirror-image, kinetically, of oxidation in such materials (our present work will confirm/deny this hypothesis).

Microgravity and containerless requirements merge in this research as both chemical and physical constraints of the surface condition are critical process parameters, as well as the need for quiescence in the melt droplet and the need to avoid gravity-effected separation of metal and ceramic liquid phases.

Understanding the dynamics of redox reactions in transition-metal-cation-bearing aluminosilicate melts, specifically because of this research, has already resulted in an important technological spin-off. We have recently successfully learned to push upward the maximum temperature for the "float" processing of silicate glasses (i.e., so as to form very flat sheet), from 1100 °C (the maximum temperature for float processing of soda-lime-silicate glass on pure molten tin) to approximately 1450 °C. The temperature transition allows the float processing of more refractory aluminosilicate compositions for application (e.g., in high-value-added flat-panel displays). The breakthrough required the combination of solution thermodynamics (the float medium is an exothermic, liquid metallic alloy) with the ability to control, by appropriate doping, the chemical diffusion process in the silicate melt that allows for its reduction.

The results of this present melt-reduction research will also impact our understanding of our solar system: the reduction morphology witnessed in chondrules in the most primitive chondritic meteorites (natural microgravity processing of ceramic melts) is similar to that seen in our preliminary experiments. We may, thus, be able to articulate thermodynamic/kinetic constraints on the evolution of the protosolar nebula.

Gravity Induced Settling in Interconnected Liquid-Solid Systems: Simulation

T. H. Courtney, J. A. Spencer and S. Z. Lu
Department of Metallurgical and Materials Engineering
Michigan Technological University
Houghton, MI 49931

Research Objectives

Settling (sedimentation) of the solid phase in a two-phase solid-liquid mixture takes place in a gravity environment. If the solid phase is less dense than the liquid, the solid floats; if it is more dense, it sinks. The two-phase morphology can be divided into three categories. In one, isolated solid particles are distributed in a liquid matrix, and sedimentation is rapid and its rate apparently described by Stokes law. A second morphology is called "interconnected;" that is, both the solid and liquid phase have a skeleton-like structure. In this case, sedimentation rates, although much less than for the previous situation, remain rapid enough so that observable sedimentation is observed on time scales on the order of hours. A third morphology is described by pockets of liquid isolated within a continuous the solid phase. In this situation, sedimentation rates are much less than for the two previous cases.

Our work focuses on sedimentation in interconnected structures for the mechanism(s) by which this takes place remain unresolved. In brief, there are two schools of thought on the matter. One holds that for a system in which the solid phase is denser than the liquid, creep of the solid takes place as a result of its self weight (compensated for to some extent by liquid buoyancy)[1-3]. However, there are problems with this concept. First, the solid head is minimal and, thus, the creep rates should also be [4].[1] Second, the creep rate is predicted to increase with the solid phase volume fraction [1]. This is both counter-intuitive and at variance with experimental observations [5]. Third, the model cannot account for the (inverse) settling observed in systems in which the solid has a lesser density than the liquid. In this situation, there is no "head" that could cause creep.

Work sometime ago in our laboratory [6] argued that sedimentation is due to particle "extrication." That is, occasionally a particle "works itself" free from the solid skeleton, settles a distance about equal to the interparticle spacing, and reattaches (by sintering) itself to the skeleton. Repetition of the process results in the slow "slumping" observed in interconnected liquid-solid structures. Support for this view was provided by selected experiments in which a two-phase compact was suspended in a liquid having the same composition as the liquid in the two-phase mixture. It was found that particles did, in fact, extricate themselves from the skeleton and either float to the top of the liquid (for Fe-Cu mixtures) or sink to its bottom (for W-(Ni,Fe,W) mixtures). However, extrication here takes place at the surface of the two-phase mixtures (that is, at the interface between the

---

[1]- When the solid is not contiguous, creep rates can be substantial. The matter has been treated by several authors[7-9].

two-phase mixture and the liquid). The process should occur more rapidly there than in the interior of the two-phase mixture. (This is so due to the greater connectivity of solid particles in the interior.)

In this program we hope to unequivocally unravel the mechanism of sedimentation in interconnected two-phase liquid-solid mixtures. This is to be accomplished by a combination of modeling and experiment. The program only initiated in the spring of this year and experimental results to date are modest. Thus, this paper focuses on how we model sedimentation and presents initial results of such modeling. We also describe selected experiments that will be used in our attempt to delineate the settling mechanism.

Relevance to Microgravity

Since settling takes place in, and as a result of, a gravity environment, it would occur only minimally in a microgravity environment. Thus, our work is linked to the gravitational force. In addition, a variety of other phenomena - including some related to materials processing - are affected by sedimentation of the type with which we are concerned. Liquid phase sintered structures, the focus of our experimental work, is one such area. But so are phase separation in polymer blends and settling instigated coagulation during processing of colloidal ceramics. In addition, hyper-monotectic alloy solidification in a gravity environment results in a settling-induced phase separation not unlike that we are studying. ("Sedimentation" kinetics, of course, are much more rapid in monotectic solidification.) Thixotropic processing of solid-liquid slurries and certain geological phenomona also have things in common with the topic of this program.

Preliminary Modeling Studies

As noted, experimental studies have just initiated. Their crux is described later. However, we have carried out some initial modeling studies and have their results to report. In this section we also describe the basic approach taken in the modeling and the physics on which it is based.

Consider an interconnected solid-liquid mixture. Although the solid has a skeletal form, it can be viewed as a collection of particles of effective radius r making contacts with similar particles. Solid contiguity is determined by the neck size of the contacts and the number of contacts per particle. Neck size is dictated by the relative values of the solid-solid and solid-liquid surface energies (low solid-liquid surface energies result in lesser neck size/particle radius ratios) while the number of contacts per particle increases with solid phase volume fraction (V_p). We designate the number of particles per unit volume as N_V; V_p is related to N_V and r through $N_V r^3 = \alpha V_p$ where α is a constant having a value of order unity. (Its precise value depends on the relative surface energies and on the number of contacts per particle.)

We take a slab of length L having, to begin with, a uniform distribution of the solid along its length. The slab is placed in a gravity environment, and sedimentation begins.

The situation can be mimicked numerically as follows. We divide the slab into N sections of thickness δx. As a result of the gravity force, particles of solid "drift" into each specific slab and also drift out of it . Boundary conditions are stipulated, of course. Particles do not drift out of the "Nth" slab; they only accumulate there. Further, they do not drift into the first slab, but only out of it. The situation can be described by the finite difference equation:

$$[\delta N_V/\delta t]_i = -[N_V/\tau]_i + [N_V/\tau]_{i-1} \quad (1)$$

Equation (1), as written, is generic. That is, the sedimentation time constant (τ) can be made a function of V_p (for the extrication model, it is expected to increase with V_p) and particle radius. Because of the latter, concurrent particle coarsening (the rate of which also depends on V_p) can be incorporated into the simulation. But it is always best to start with a simple case, and Fig. 1 shows the results of one such simulation where τ is taken constant. Input data for the simulation include N_V, *r* and V_p (only two of these variables are independent). Model output is converted into a graph of V_p vs. distance along the sample length for different sedimentation times. We have permitted, in this initial modeling, a value of V_p=1 to be obtained at one end of the sample. In reality, the effective maximum value of V_p is less than this and corresponds to the situation where isolated liquid pores form in the two-phase mixture. The value of V_p at which this transition takes place is system specific. In this initial effort we have neglected this factor. It can be easily be incorporated into later simulations.

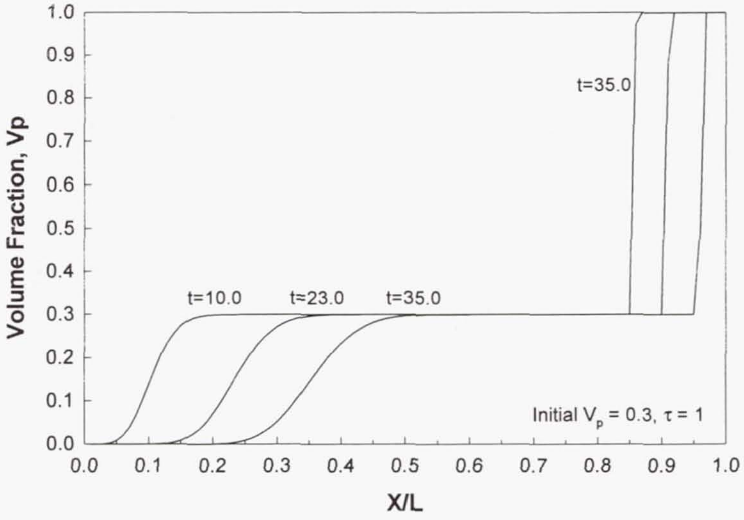

Figure 1: Variation of solid phase volume fraction with position in a sample in a gravity environment for different sedimentation times. Gravity force is from left to right. In this simulation, the settling "time constant" was taken constant (i.e., independent of solid particle radius and volume fraction) and the initial volume fraction of solid - uniform along the length - was equal to 0.3

As indicated by Fig. 1, when τ is constant the particle volume fraction is, excepting for the zones at the sample ends, constant along the sample length. (This result can be intuitively deduced from Eq. (1).) Figure 2 displays results for different initial values of V_p, still keeping τ constant; the behavior is qualitatively similar to that shown in Fig. 1. The extent of the solid denuded zone can be plotted as a function of sedimentation time (Fig. 3). The incubation time for formation of this zone depends mildly on V_p.[2] The slopes of the lines in Fig. 3 represent effective "creep" rates; i.e., d(x/L)/dt has dimensions of inverse time. Were the denuded zone length to be measured experimentally, the rate at which it extends could be tied to an effective sedimentation creep rate or, in the case of the extrication mechanism it could be linked to the particle extrication time.

The unnormalized slopes of Fig. 3 represent "velocities." They are tied to the partial differential representation of Eq. (1) which has the form

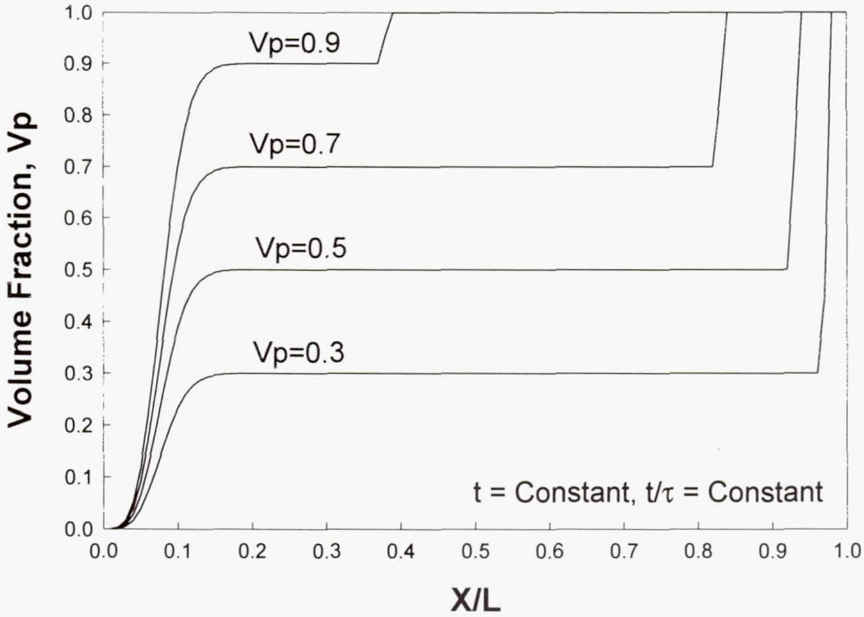

Figure 2: Variation of solid phase volume fraction along sample length for different values of the initial, uniformly distributed, solid phase volume fraction. The results pertain to a specific sedimentation time. As in Fig. 1, the characteristic settling time constant is taken as a constant.

---

[2] - We have defined the incubation time as the time required to reduce V_p in the first slab to 0.001. Likewise we have defined any slab to be solid free when its volume fraction has a value less than 0.001.

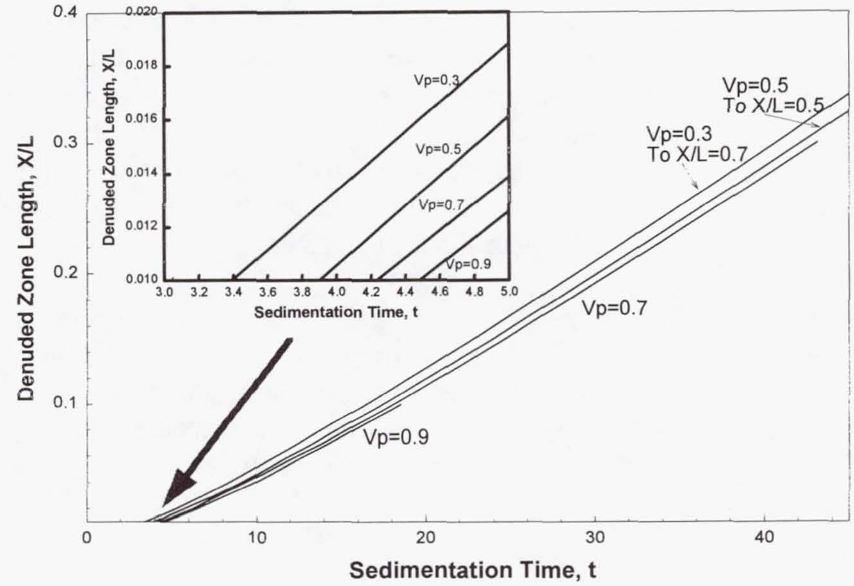

Figure 3: Extent of solid denuded zone as a function of sedimentation time for different initial solid phase volume fractions. The slopes of the lines indicate a modest dependence of sedimentation rate on particle volume fraction, even when - as assumed in constructing this figure - the characteristic settling time constant is taken as constant. The inset shows that the incubation time for formation of a denuded zone also scales - almost linearly - with initial solid phase volume fraction.

$$\partial N_V/\partial t + (2r/\tau)(\partial N_V/\partial x) = 0 \quad (2)$$

and a general solution to this equation is [7]

$$N_V = f(t - (x\tau/2r)) \quad (3)$$

The "velocity" of Eq. (3) in this instance is the slab width divided by the extrication time. On a fundamental basis, the slab width selected should be on the order of the particle diameter in which instance the velocity is simply $2r/\tau$.[3]

Future Work

Modeling such as that described here is but a framework within which to analyze experimental results. For example, measurement of the sedimentation rate and how V_P

---

[3] - As noted, a lower limit on slab width is $2r$. In the examples shown, we have used 1000 slabs. Assuming a 2 cm long sample, this corresponds to a particle diameter of 20 μm. Such a particle size is typical of liquid phase sintered structures.

varies with distance along the gravity direction permits estimation of τ by means of "curve fitting." In and of itself, such a procedure is not of much fundamental use. A physical interpretation of τ is called for. This can be done in (at least) two ways. First, particle extrication times can be measured (albeit with some uncertainty for reasons noted previously). These times should relate directly to the sedimentation time constants. Good correlation with experimental settling rates would buttress the extrication model for settling. If such correlation is not obtained, the experimentally derived settling times can be correlated to creep models [8,9]. In this instance, the resulting creep "time constant" should directly relate to measured sedimentation time constants.

Sedimentation studies in Pb-rich Pb-Sn alloys have just commenced. This is a convenient system to study for alterations in alloy composition and settling temperature permit extensive variations in solid phase volume fraction and liquid composition. (The latter should affect the neck-to-particle diameter ratio as a result of the change in liquid-solid surface energy with liquid composition.) In addition, we will investigate settling in tungsten heavy alloys. There is a considerable extant data base on settling in these materials and this will aid in analysis.

Conclusions

We have presented preliminary results on numerical mimicking of settling in solid-liquid interconnected systems. Such modeling can be couched in terms of an effective time constant for settling. The settling rate relates directly to this constant and, when the constant does not depend on solid phase volume fraction, the solid phase concentration is - excepting for regions near the sample ends - uniform along the sample length. When the settling time constant increases with V_p, this variation is not as uniform.

Modeling results will be used in conjunction with experimental studies in an attempt to determine the mechanism of solid phase sedimenation in solid-liquid interconnected structures. This will be done by reconciliation of experimental results with numerical simulations of the type described here.

References

1. Y. Liu, D. F. Heaney and R. M. German, Acta Metall. et Mater., 43, 1587, (1995).
2. A. Bernabe Rodriguez and J. Gil Sevilano, *Tungsten and Tungsten Alloys - 1992*, Metal Powder Industries Federation, Princeton, N.J., 61, (1992).
3. J. Gil Sevillano and A. Bernabe Rodriguez, Mater. Sc. and Eng., A175, 159, (1995).
4. T. H. Courtney, Scripta Mater., 35, 567, (1996).
5. T. H. Courtney, Metall. Trans. A., 15A, 1065, (1984).
6. A. N. Niemi and T. H. Courtney, Acta Metall., 31, 1393, (1983).
7. William Ted Martin and Eric Reissner, *Elementary Differential Equations*, Addison-Wesley, Cambridge, Mass., (1956)
8. G.M. Pharr and M. F. Ashby, Acta Metall., 31, 129, (1983).
9. R. Raj and C. K. Chyung, Acta Metall., 29, 159, (1981).

EVALUATION OF SPACECRAFT SHIELDING EFFECTIVENESS FOR RADIATION PROTECTION

Francis A. Cucinotta[1] and John W.Wilson[2]
[1]NASA Johnson Space Center, Houston TX 77058
[2]NASA Langley Research Center, Hampton VA 23681

Abstract:

The potential for serious health risks from solar particle events (SPE) and galactic cosmic rays (GCR) is a critical issue in the NASA strategic plan for the Human Exploration and Development of Space (HEDS). The excess cost to protect against the GCR and SPE due to current uncertainties in radiation transmission properties and cancer biology could be exceedingly large based on the excess launch costs to shield against uncertainties. The development of advanced shielding concepts is an important risk mitigation area with the potential to significantly reduce risk below conventional mission designs. A key issue in spacecraft material selection is the understanding of nuclear reactions on the transmission properties of materials. High-energy nuclear particles undergo nuclear reactions in passing through materials and tissue altering their composition and producing new radiation types. Spacecraft and planetary habitat designers can utilize radiation transport codes to identify optimal materials for lowering exposures and to optimize spacecraft design to reduce astronaut exposures. To reach these objectives will require providing design engineers with accurate data bases and computationally efficient software for describing the transmission properties of space radiation in materials. Our program will reduce the uncertainty in the transmission properties of space radiation by improving the theoretical description of nuclear reactions and radiation transport, and provide accurate physical descriptions of the track structure of microscopic energy deposition.

Introduction

Estimating the effectiveness of spacecraft shielding on reducing the health effects galactic cosmic rays (GCR) and solar particle events (SPE) is a major issue for HEDS. Spacecraft shielding composed of low Z materials is expected to be advantageous because of reduction of high energy and charge ions (HZE), and target fragments, especially neutrons, in comparison to higher Z materials such as aluminum. Projectile fragmentation reactions in shielding are advantageous because lower charged ions of equal velocity are less biologically damaging than the projectile ion. Materials composed of lower atomic mass atoms are more efficient per unit mass in producing projectile fragmentation. Target fragmentation events are highly dependent on material type. These events are the major nuclear reaction effect for SPE's and are an important contributor to GCR transmission. Quantitative evaluations for material selection must rely on physical descriptions of radiation transmission properties including nuclear reactions. An important factor in the development of nuclear cross section databases is the ability to describe nuclear structure and clustering aspects of specific materials constituents and GCR components. The quantum based QMSFRG model has been shown in previous limited studies to provide this capability. Source terms for nuclear fragments can be included in the state-of-the-art, radiation transport codes, GRNTRN/BRYNTRN and used for space applications. We are developing theoretical descriptions of nuclear interactions and radiation transport, and fast computational software that will provide accurate predictive capability and an engineering design tool in support of the HEDS enterprises.

An objective of the HEDS Strategic Plan is to understand the effects of space radiation on humans including possible unique effects from heavy ions. The relationship between the transmitted radiation fields at organ sites and biological risk is poorly understood and awaits fundamental understanding in molecular and radiation biology. Determination of the impact of biological counter-measures will be dependent on knowledge of transmitted radiation for specific materials and the microscopic energy deposition events of heavy ions since it is expected that such countermeasures will work on some but not all GCR components. Radiobiology experiments to understand biological risks and potential countermeasures are supported by the Code UL Office of Life and Microgravity Sciences and Applications. Our research program will support these efforts by providing tools to study the combined effects of risk mitigation areas, including relationships between shielding properties and biological counter-measures. We will study the effectiveness of shielding material using conventional risk assessment, and track structure models that quantitatively represent proton and HZE biological response data.

Radiation Transport in Materials

The physics of high-energy heavy ion transport in single or multi-layered materials has been developed at Langley Research Center over the last 25 years by Wilson and co-workers [1]. Several computer codes were developed for application to space or laboratory boundary-value problems. The BRYNTRN code describes the transport of laboratory or space light-ion beams (p,n,d,t,h, and α) and the local distribution of heavy target fragments and recoils (A>4). The HZETRN code solves the Boltzmann equation using the straight-ahead approximation for GCR transport in multi-layer materials. The GRNTRN code solves the laboratory heavy ion transport code and is being developed for space application. The HZETRN code contains BRYNTRN as a subroutine and the GRNTRN code is being extended in this manner. Other developments of the model include a multi-group approach for low-energy neutron transport [2] and future extensions of the codes to include meson, muons, and electrons. In Table I we show comparisons of the HZETRN/BRYNTRN code to measurements on-board the space shuttle on STS-81 [3] where several polyethylene spheres were flown with TEPC's inserted. Good agreement for both dose and dose equivalent comparisons are found, however spectral components show larger differences and have indicated areas for improvement in the codes [2,4].

Table I. Comparison of HZETRN/BRYNTRN to GCR Measurements on STS-81 [3]

Diameter	Measured Dose	Calculated Dose	Measured Dose Eq.	Calculated Dose Eq.
0.0, g/cm^2	.147 mGy/day	.135, mGy/day	.479, mSv/day	.521, mSv/day
1.934	.138	.138	.441	.400
4.322	.129	.118	.316	.368
7.903	.128	.113	.371	.322
12.68	.116	.111	.290	.298

Nuclear Data Bases: The QMSFRG Model

Nuclear interaction cross section data bases are required for the transport of cosmic rays with energies below 10 MeV/amu to energies above tens of GeV/amu, including a large number of projectile and target material combinations. The types of cross sections required for transport involve total yields and secondary energy spectra for one-dimensional transport and double differential cross sections in angle and energy for three-dimensional transport. Neutron and proton cross sections have been studied at some length in the past. Nuclear-reaction modeling is required, especially for both light and heavy ion projectiles, to understand the basic physical processes, and to extrapolate limited experimental data between projectile energies and projectile-target combinations. Our efforts in data base developments have focused largely on quantum multiple scattering theories (QMST), Monte-Carlo approaches to nuclear reactions use an intra-nuclear cascade that imitates the QMST, however neglecting quantum interference effects and nuclear structure effects. In the QMST a the many-body integral-equation for the transition operator for nucleus-nucleus scattering [5] is considered,

(1) $T = K + K\,G\,T$

where K is the interaction kernel and G the Bethe-Salpeter propagator representing two nuclei in intermediate states. The kernel is the sum of all irreducible diagrams for projectile-target constituents. The solution of (1) is made using appropriate high energy approximations for momentum and energy transfers typical of nuclear reactions, development of bound state function models for transitions of interests, and new methods to deal with many particle phase problems for the description of fragmentation channels.

The microscopic QMST theory for the description of nuclear fragmentation, denoted QMSFRG, proceeds by summing the QMST for heavy ion reactions in terms of response functions for an arbitrary number of particle knockouts for the heavy ion abrasion dynamics [5]. The microscopic theory can be shown [5] to reduce to the optical-model formulation of abrasion and the geometric abrasion model. The reaction dynamics for fragmentation processes are unified by the development of a single function, the multiple scattering amplitude, in terms of the momentum vectors of all secondary reaction products. The production cross sections for the fragments are found by considering the phase space for an arbitrary final state where there are n abraded particles, leaving a projectile pre-fragment with energy denoted E_{F*}. Conserving energy in the pre-fragment formation after interactions with the target are complete, the scattering amplitude f_{fi} and cross sections are related by [5-7]

(2) $d\sigma = \Sigma_X\, \Pi^{n}_{j=1}[d\mathbf{k}_j/(2\pi)^3]\delta(E_i - E_f)\, dE_{F*}\, d^2q\, |f_{fi}|^2$

where the $\mathbf{k}_j$ are the abraded nucleon wave vectors, E_i and E_f are the energies in the initial and final states, and q is the total transverse momentum in the reaction. Equation (2) is summed over the final states of the target nuclei, X. In the abrasion-ablation model there is a causal assumption that separates the time evolution of ablation processes from the abrasion. It follows that for the emission of v nuclei from the excited pre-fragment with energies E_r we have $E_{F*} = E_F + \Sigma^{v}{}_{r} E_r$ where r=0 is allowed in order to include the possibility that the pre-fragment excitation energy is below the lowest particle-emission channel. The abraded particle momentum distribution is

$$(3) \qquad d\sigma/d\mathbf{k} = \Sigma_n \Sigma_X \int \Pi^n{}_{j=2}[d\mathbf{k}_j/(2\pi)^3] dE_{F*}\, d^2q\, |f_{fi}|^2$$

where we are integrating over all variables except the momentum of one abraded particle. The excitation spectra of pre-fragment nuclei are obtained from equation (2) as

$$(4) \qquad d\sigma / dE_{F*} = \Sigma_X \int \Pi^n{}_{j=1}[d\mathbf{k}_j/(2\pi)^3]\, d^2q\, |f_{fi}|^2$$

The decay of the pre-fragment nuclei into the final fragment opens the phase space further, and this description is required for predicting the final mass yields as well as momentum distributions of ablated nucleons or light nuclei. Good accuracy for predicting proton and neutron production in heavy ion collision's [6] is found with the model. The development of the scattering amplitude in terms of abrasion response functions has been made using the eikonal approximation. For proton-nucleus and light ion-nucleus collisions, the Watson or Faddeev multiple scattering theories are used directly to perform cluster summations with the eikonal approximation for four-point functions that occur in the expansion. Important interference effects are seen in these calculations (ref. [5] and earlier references cited therein) that are neglected in a Monte-Carlo approach. Many-body response functions are modeled as convolutions of one-body response functions using the shell model. Figure 1 shows results of the model for ^{16}O fragmentation. Ablation is described by solving the Master equation for de-excitation of the pre-fragments [5,7]. For light nuclei (A<16) experimental decay paramters are used.

Track Structure and Space Radiation Risk Assessment

Particle energy spectrum for shielding/mission scenarios as determined by transport equations can be used to determine biological risk after a biological response function is defined. Conventional risk assessment uses LET dependent quality factors and risk coefficient's decided on by committee to estimate cancer risk. Track structure models predict [8] that biological response will depend on several aspects of particle tracks including the radial extension and the δ-ray energy spectra, and the spatial structure of biological target molecules. Deviations from LET dependence are especially important when considering complicated radiation fields and are supported by experimental data. Track structure models are applied to represent biological response data for protons, neutrons, and heavy ions [8]. These models are than used to evaluate shield material characteristics using radiation transport codes [9]. Important deviations are seen on material properties when using conventional or track structure models. This approach to studying shield effectiveness has been recently recommended by the National Academy of Science's Space Science Board. We are continuing these studies using improvements in the physical description of particle tracks [10,11] and new models [12] of radiobiology experiment's supported under NASA's Radiation Health Program. Figure 2 shows comparisons of the track model [10] to the average specific energy deposited as a function of radial distance from 14 MeV/u Ge ions in 0.5 and 1.0 μm sites. A similar approach has been developed for nanometer volumes [11]. The model can also be extended to describe micro-electronics damage by heavy ion tracks.

References

1.Wilson JW et al., Transport Methods and Interactions for Space Radiations. NASA RP-1257 (1991).

2. Shinn JL, Cucinotta FA, Simonsen LC, Wilson JW, Badavi FF, Badhwar GD, Miller J, Zeitlin C, Heilbronn RK, Clowdsley MS, Heinbockel JH, and Xapsos MA, Validation of a Comprehensive Space Radiation Transport Code. *IEEE Nucl. Sci.* (in press) (1998).

3. Badhwar GD and Cucinotta FA, Depth Dependence of Absorbed Dose, Dose Equivalent, and LET in Polyethylene and Comparison with Model Calculations. *Radiat. Res.* **149**, 209-218 (1998).

4. Cucinotta FA, Wilson, JW, Badavi F, and Badhwar GD, Effects of Target Fragmentation on Evaluation of LET Spectra from Space Radiation. *Radiat. Meas.* **26**, 923-934 (1996).

5. Cucinotta FA, et al., Computational Procedures and Data-Base Development. In: NASA Workshop on Shielding Strategies for Human Space Exploration. Eds. Wilson JW, Miller J, Konradi A, and Cucinotta FA, NASA CP 3360 (1997).

6. Cucinotta FA, Wilson JW, and Townsend LW, Abrasion-Ablation Model for Neutron Production in Heavy Ion Collisions, *Nucl. Phys. A* **619**, 202-212 (1997). Cucinotta F A, Forward Production of Protons From ^{12}C in Heavy Ion Collisions. *J. Physics G.* **20**, 1803-1815 (1994).

7. Cucinotta FA et al., Assessment and Requirements of Nuclear Reaction Data Bases for GCR Transport in the Atmosphere and Structures. *Adv. in Space. Res.*, (in press) (1998). Cucinotta FA, Wilson JW, Tripathi RK, and Townsend LW, Microscopic Fragmentation Model for Galactic Cosmic Ray Studies. *Adv. in Space. Res.,* (in press) (1998).

8. Cucinotta F A, Wilson JW, Shavers MR, and Katz R, The Effects of Track Structure and Cell Inactivation on the Calculation of Heavy Ion Mutation Rates in Mammalian Cells, *Int. J. Radiat. Biol.* **69**, 593-600 (1996).

9. Wilson JW et al., Issues in Space Radiation Protection, *Health Phys.* 68, 50-58 (1995).

10. Cucinotta FA, Katz R, and Wilson JW, Radial Distributions of Electron Spectra From High-Energy Ions. *Radiat. & Environ. Biophys.* (in press) 1998.

11. Cucinotta F A, Nikjoo H, and Goodhead DT, Comment on the Effects of Delta-Rays on the Number of Particle-Track Transversals Per Cell in Laboratory and Space Exposures, *Radiat. Res.* **150**, 115-119 (1998). Cucinotta FA, Nikjoo H, and Goodhead DT, Radial Distribution of Frequency Distributions in Nanometer Volumes from HZE Particles (submitted), 1998.

12. Cucinotta FA,Dicello, JF, Williams JR, Dillehay LE, Zhang YG, Wilson JW, and Mabry M, Cell Cycle Progression in Low Dose-Rate Exposures to Ionizing Radiation. *Adv. in Space. Res.* (1997).

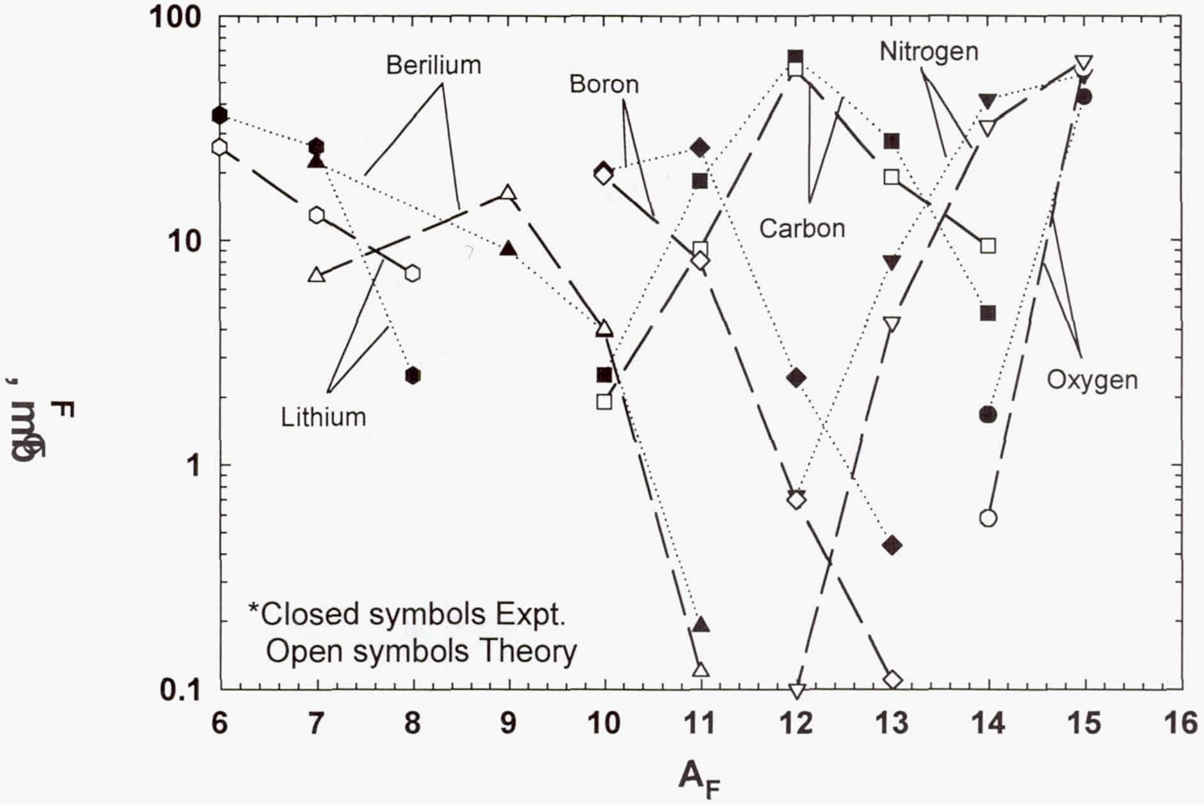

Fig. 1. Comparison of QMSFRG to experiments for 2.1 GeV/u ^{16}O fragmentation on ^{12}C

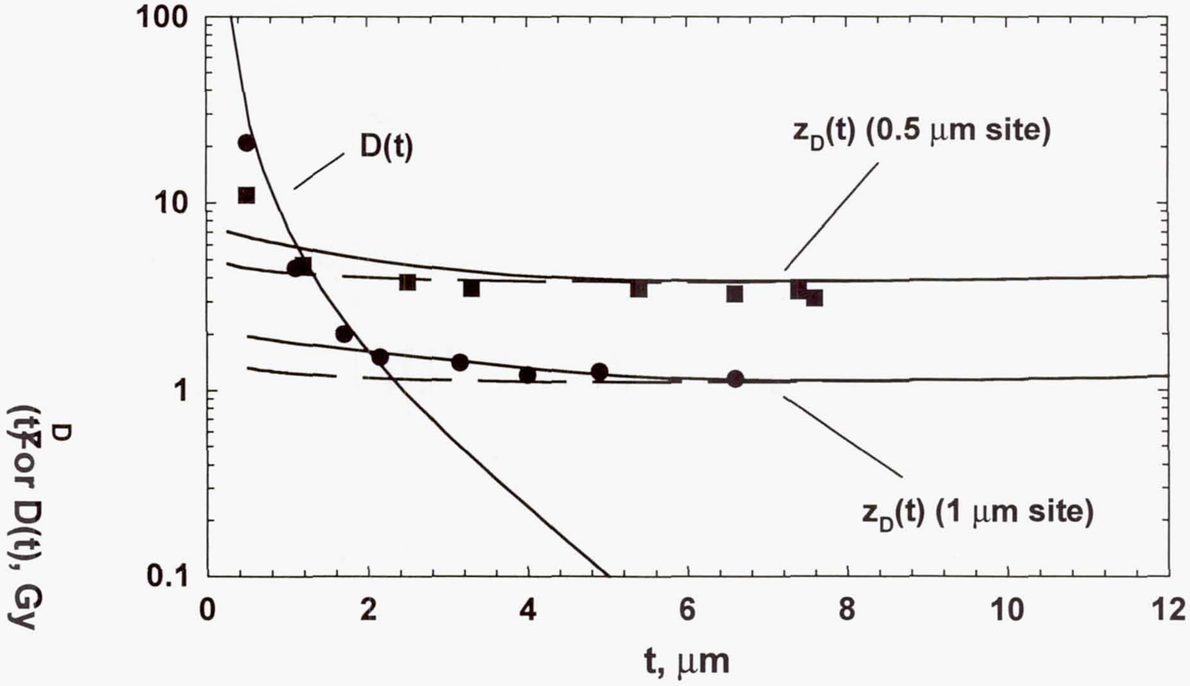

Fig. 2. Comparison of track model to mean specific energy as function of radial distance from ion.

Fundamental Studies of Solidification in Microgravity Using Real-Time X-Ray Microscopy

Principal Investigator: Dr. Peter A. Curreri; NASA Marshall Space Flight Center (MSFC)
Co-Principal Investigator: Dr. William Kaukler; University of Alabama, Huntsville
Co-Investigators: Dr. Subhayu Sen; Universities Space Research Association
Dr. Biliyar N. Bhat; NASA Marshall Space Flight Center

Introduction

This research applies a state of the art X-ray Transmission Microscope, XTM, to image (with resolutions up to 3 micrometers) the solidification of metallic or semiconductor alloys in real-time. We have successfully imaged in real-time: interfacial morphologies, phase growth, coalescence, incorporation of phases into the growing interface, and the solute boundary layer in the liquid at the solid-liquid interface [1-9]. We have also measured true local growth rates and can evaluate segregation structures in the solid; a form of in-situ metallography. During this study, the growth of secondary phase fibers and lamellae from eutectic and monotectic alloys have been imaged during solidification, in real-time, for the first time in bulk metal alloys.

Current high resolution X-ray sources and high contrast X-ray detectors have advanced to allow systematic study of solidification dynamics and the resulting microstructure. We have employed a state-of-the-art sub-micron source with acceleration voltages of 10-100 kV to image solidification of metals. One useful strength of the XTM stems from the manner an image is formed. The radiographic image is a shadow formed by x-ray photons that are not absorbed as they pass through the specimen. Composition gradients within the specimen cause variations in absorption of the flux such that the final image represents a spatial integral of composition (or thickness).

The ability to image these features in real-time enables more fundamental and detailed understanding of solidification dynamics than has previously been possible. Hence, application of this technique towards microgravity experiments will allow rigorous testing of critical solidification models.

XTM Results:

The XTM has been applied to obtain information fundamental to solidification of metallic systems. (Refer to ref. [2,6,8] for a good description of the technique.) A diverse array of alloys have been studied with the XTM:

1. The solid-liquid planar interface of *pure* aluminum was studied with and without second phase insoluble particles (spherical voids, cylindrical holes, and zirconia spheres).
2. Single-phase alloys of Al with Cu, Ag, Au, and Mg were examined to observe solutal distribution effects at the interface, interface instabilities from planar to cellular, or interactions with the interface shape due to the thermal field perturbations caused by insoluble second phase particles both at equilibrium and during solidification. One major aspect of this was the study of particle pushing in support of the PEP flight experiment. The dynamics of solid/liquid interface shape evolution near an insoluble particle showed the limits to the applicability of some analytical models.
3. Two-phased eutectic alloys of Al with $CuAl_2$ or $AuAl_2$ were studied to observe lamellar and fibrous growth morphologies respectively.
4. Two-phased monotectic alloys of Al with In, Bi, or Pb were studied to observe growth morphologies and solute distributions. Fibers were observed to form in Al-Pb and Al-Bi.
5. Al-Mn-Si alloys were examined for nucleation and growth of precipitates in the melt.
6. Planar interfaces in pure Zn were observed to demonstrate that other base materials than Al could be used.

Solid-Liquid Interface in the Vicinity of an Insoluble Particle in the Melt

The distribution of insoluble particles in a metal casting depends primarily on the interaction of the particles with the solid/liquid (s/l) interface during the solidification process. This is true whether the particles are solid, liquid or gaseous. It has been experimentally demonstrated that there exists a critical interface velocity, V_{cr} at which the transition from particle pushing to engulfment occurs and V_{cr} decreases as particle radius increases, following a power law.

It has been postulated that the thermal conductivity ratio, μ between the particle and the liquid matrix affects the transition from particle pushing to engulfment. When $\mu<1$ the particle acts as a heat sink and this results in a lower temperature and faster growth velocity of the interface just below the particle. Subsequently a convex protuberance or a bump is formed on the solidification front behind the particle. For systems with $\mu>1$ the particle acts as a source of heat and this lowers the growth velocity of the interface behind the particle. This results in a trough formation or a concave depression below the particle. Finally, when $\mu=1$ the thermal field is unperturbed and consequently, the interface remains planar. Neglecting forces due to convective flow and gravitational acceleration, the two main forces acting on a particle suspended in liquid metal are due to drag and interfacial energies. The (attractive) drag force between the particle and the s/l interface is expressed as:

$$F_D = 6\pi\eta V \frac{R^2}{d} \mu^2 \qquad 1$$

where F_D= drag force, h = viscosity, V= interface velocity, R = particle radius and d = distance between the interface and the particle. Equation 1 accounts for the contribution of localized deviations from planarity when the interface approaches the particle. The (repulsive) interfacial force is expressed as :

$$F_l = 2\pi R \Delta\sigma_o \left(\frac{a_o}{a_o + d} \right)^2 \mu \qquad 2$$

where, F_l = interfacial force, $\Delta\sigma_0$ = difference in interfacial energies between particle/liquid and particle/solid and a_0 = interatomic distance. Equations 1 and 2 show that the force field acting on the particle is influenced by the localized deviation of the s/l interface in the proximity of the particle. Furthermore, the localized deviation will also effect the critical velocity for engulfment. Hence, the objective of this investigation was to experimentally quantify the nature and extent of this deviation as a function of μ, particle radius, R , and the distance between the particle and the interface, d.

Figure 1 illustrates the effect of a 500 μm diameter ZrO_2 particle on a stationary and a growing interface [1]. When the stationary interface has almost made contact with the particle, that is $d\approx8$ μm (Figure 1a), a convex perturbation or a bump formation on the interface is noticed. The behavior of a growing s/l interface interacting with 500 μm diameter ZrO_2 particle is, however, different compared to a stationary interface. With a translation velocity of 3 μm/s, a distinct depression or trough formation was noticed on the tip of the original convex protuberance (Figure 1b), at a distance of d=40 μm. Whereas, for a stationary interface interacting with the particle no such trough was detected.

The two dimensional analytical solution (in spherical co-ordinates) which describes the shape of an interface near a particle has several simplifying assumptions. For example, it neglects the effect of latent heat of fusion of the matrix and the particle heat capacity. Further, the thermal conductivities of the liquid and solid matrix are assumed to be equal. Consequently, the effect of these parameters is not accounted for by this analytical model. After applying appropriate boundary conditions, the isotherm for the melting point of the interface is described as:

$$Cos\theta = \frac{(R+d)\left[1+\frac{a}{b}\right]}{r\left[1+a\left(\frac{R}{r}\right)^3\right]} \qquad 3$$

where, $a = \dfrac{1-\mu}{2+\mu}$ and $b = \left(1+\dfrac{d}{R}\right)^3$.

By definition, the interfacial radius of curvature, R_I, below the particle can be expressed as:

$$R_I = \frac{2a-b}{3a}(R+d) \qquad 4$$

Here, only the analytical solution for interface shape prediction is compared to the experimental results. Fig. 2(a) shows the experimental results and the analytical solution for a pure Al stationary interface at a distance of 8 μm from a 500 μm diameter spherical ZrO_2 particle. Since the thermal conductivity of ZrO_2 is less than liquid Al, a protuberance is expected at this separation. Indeed, the analytical model is in agreement with the experimental measurements. Fig. 2(b) is a comparison of the shape of the growing interface with that predicted by the analytical model. The analytical model predicts a convex protuberance for these conditions, in contradiction with the experimental observations. In the absence of latent heat effects, the predictions of the analytical model are consistent with the experimental results for equilibrated interfaces. However, the analytical model fails in the case of a moving interface probably due to the continuous evolution of latent heat. Based on the above analysis it can be stated that the initial stages of interaction between a particle and an interface is not a steady state process. There appears to be a constant adjustment of the equilibrium distance between the particle and the interface as dictated by the thermal field and the force field (attractive and repulsive). The thermal field is not only dictated by the thermal conductivity ratio but also the latent heat entrapment between the particle and the interface during solidification.

Eutectic and Monotectic Second Phase Structures

The application of XTM for the study of solidification fundamentals was *initially* limited to a resolution of 25 μm for real-time imaging. The study of the dynamics of formation of secondary eutectic and monotectic droplets and fibers required a resolution on the order of 5 μm. Our recent advances in XTM furnace design have increased the real-time magnification (during solidification) for the XTM from 40X to160X. The increased magnification has enabled for the first time XTM imaging of real-time growth of fibers and particles with diameters of 3-8 μm and of eutectic lamellae with 12 μm spacing. Figure 4 and 3a, illustrate these respectively. To ensure the lamellar features observed were not artifacts, the lamellar spacings were measured during growth and after growth by sectioning and conventional metallography. All the spacings measured were consistent with themselves and with previously published measurements; Figure 3b.

At low growth rates (2 μm/sec) rejection of solute into the liquid by the solid was frequently observed using XTM in the Pb and In based Al monotectic alloys. The solute boundary layer was also observed in Bi monotectic specimens but unlike the In and Pb monotectics, was found to be clear of precipitated droplets. Generally, the solute layer was observed to extend 75 to 100 μm from the solid into the melt at the s/l interface for the growth rates used.

We have studied the kinetics of formation and morphological evolution of secondary fibers and particles in Al-Bi monotectic alloys. We observed a previously unreported velocity dependent thermo-capillary depletion mechanism for Bi-rich liquid which can penetrate many fiber diameters. At a reduced velocity approaching zero, the secondary liquid (L2) rods intersecting the interface began to 'drain' or exude from their cylindrical cavity and form droplets at the solid-liquid interface that grew to about 22 μm diameter. They detached and moved quickly up the thermal gradient. Within about 3 minutes the Bi-rich L2 rods were depleted to a distance of about 50 μm into the solid. This is illustrated in Figure 4a. Some Bi-rich droplets were seen to migrate up the gradient *during* solidification as well. Contrast this to the formation of droplets within the solute layer in the melt of the Al-Pb and Al-In monotectics. These droplets stayed where they formed only to be engulfed by the matrix. One hypothesis is that the alternate behaviors stem from interfacial energy differences between the three systems. We feel from the rate of depletion effects, and the observed migration of the droplets during solidification, that the phenomenon be considered in solidification kinetic models for monotectics.

Figure 4b shows the real-time image resulting from a translation rate increase from zero to 5 μm/sec. This image was taken following the 'depletion' scenario described above. The depleted zone behind the interface is visible in this radiomicrograph. The solidification transient developed a band of solid aluminum with very little bismuth. Only in a few places can some fibers or droplets be seen to form until composite growth is established as seen on the left side of this image. The solute had to build-up to a sufficient degree for the formation of the second phase precipitates. At the 5 μm/sec translation rate, it required about 100-200 μm of growth to permit the formation of the fully developed composite interface structure.

As far as we know, we have made the first real-time observations of bulk solidification morphology for Al-7.4 weight % Au on-eutectic alloy. Examples are shown in Figure 6. We observed this alloy with 5 μm resolution forming Al_2Au fibers (Figure 6a) or plates (Figure 6b, depending on growth rate) in an Al matrix. Additionally, the intermetallic fibers in this system were found to grow in advance of the s-l interface for growth rates above the fiber-plate transition velocity of ~1 μm/sec (Figure 6b). The extended Al_2Au phase fibers survived in the melt after translation was set to zero velocity for approximately 2 minutes. We noted thickening (ripening) of these Al_2Au phase fibers at this time. Some ripened fibers were about 25 μm thick and extended about 100 μm into the melt. It was observed over time (several minutes), that the coarsened, extended portions of the intermetallic phase eventually loosened from the matrix and settled to the bottom of the crucible. The existence of such a process and subsequently its kinetics would be nearly impossible to study with conventional solidification and quench techniques. We are not aware that this phenomena has been previously reported.

Solute Distribution in the Melt

Recently, the work focused on the quantification of the solute distribution in the melt in the vicinity of the s-l interface. A gas-quench apparatus was installed into the XTM furnace to permit post-solidification composition analysis. Very dilute (0.34 and 0.84 weight %) Al-Au alloys were solidified around the planar-cellular transition and gas-quenched. Quench rates were not sufficiently high (to date) to prevent cellular or dendritic breakdown of the interface. The resulting microsegregation made high-resolution solute profiling impossible. Fortunately, the solute boundary layer extends up to 2000 μm or more depending on growth rate so the solute concentration variation could be measured with lower resolution. Solute profiles were measured from low magnification film radiographs of the specimens grown at various rates. The quenched interface profile was measured as an intensity average across a 1 mm wide strip of the sample for 4 mm. One example growth rate will be shown here and compared to a model.

This measured profile was used to create a two-dimensional synthetic radiograph image such that the shade of gray used depended on the intensity value at each point along the profile. Using image processing techniques, this image was reduced in contrast (mathematically the profile amplitude was linearly reduced) until the gray level of the solid side of the interface matched the gray level of the specimen radiograph. This produced an image that matched the original in appearance. Each step required a different computer program because some steps require operator interaction and because a similar approach was taken to create a synthetic radiograph image from a model.

Using the Tiller, Rutter et al. model for interface diffusion and phase diagram data, a solute concentration curve was determined for Al-0.8Au growing at 5 μm/sec with the solute diffusion coefficient of 3×10^5 cm^2/sec.

These images were assembled into a single composite graphic shown in Fig. 5 a. Instead, the comparison needs to be made from graphs of these intensities or compositions. Figure 5b shows how well the images above match graphically. This figure superimposes the normalized gray level plots of the measured profile with the modeled profile for direct comparison. For profile measurements made on other specimens (not shown here), the solute distribution (concentration variation into the melt) in the quenched melt is nearly linear at the interface. The concentration profiles do not have the classic exponential rise to the interface. The model comes quite close with its diffusion limited profile shape and depth.

Acknowledgments

Thanks are extended to Pat Salvia in the foundry at Materials & Processes Lab. for casting the alloys and having the chemical analysis performed. We wish to thank NASA's Microgravity Science Division NRA Program for funding this work.

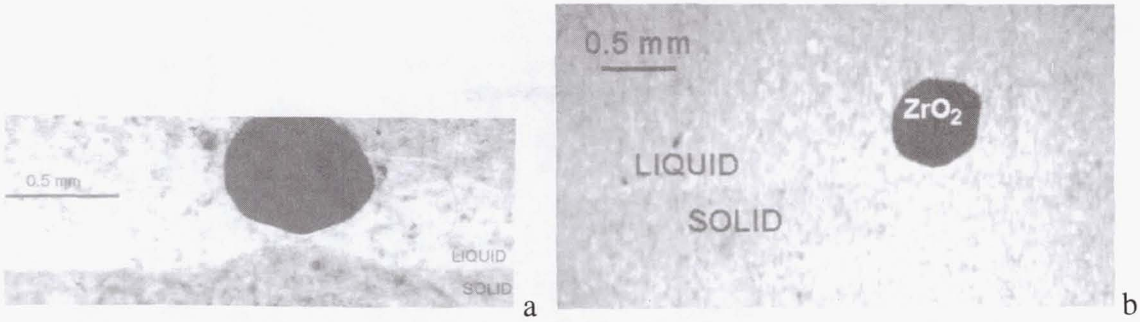

Fig. 1. (a) A x-ray radiograph of a planar s/l Al interface interacting with 500 μm diameter ZrO$_2$ particle at a distance of *d*=8 μm and (b) a video image of a transient s/l Al interface at a distance of *d*=40 μm from the ZrO$_2$ particle.

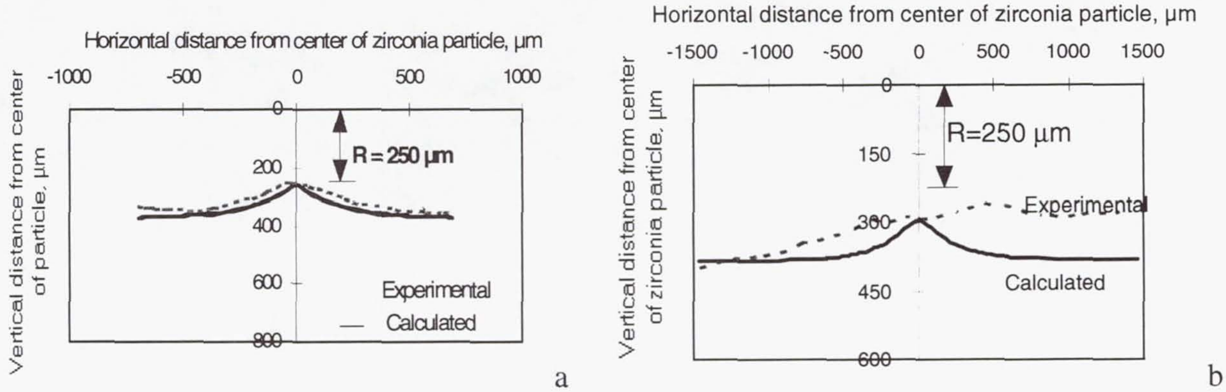

Fig. 2. Experimental results and analytical solutions for (a) a stationary s/l Al interface interacting with a 500 μm diameter ZrO$_2$ particle. The interface is at a distance of *d*=8 μm from the particle and (b) a moving s/l Al interface interacting with a 500 μm diameter ZrO$_2$ particle. The interface is at a distance of *d*=40 μm from the particle.

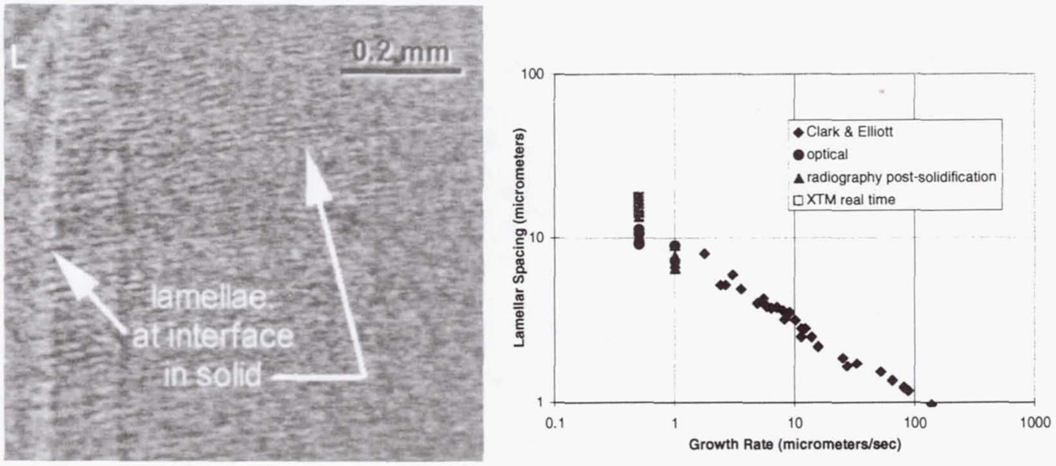

Figure 3 a and b. A) Digitally enhanced image showing lamellar morphology forming at solid-liquid interface. Translation rate 0.5 μm /sec, gradient 4160 K/m, $\lambda \approx 15$ μm. L is liquid. The lamellae are growing at a slight angle to the interface isotherm. B) Measured lamellar spacings compared to literature values. Optical and radiographic measurements coincide and all are consistent with Clark & Elliott.

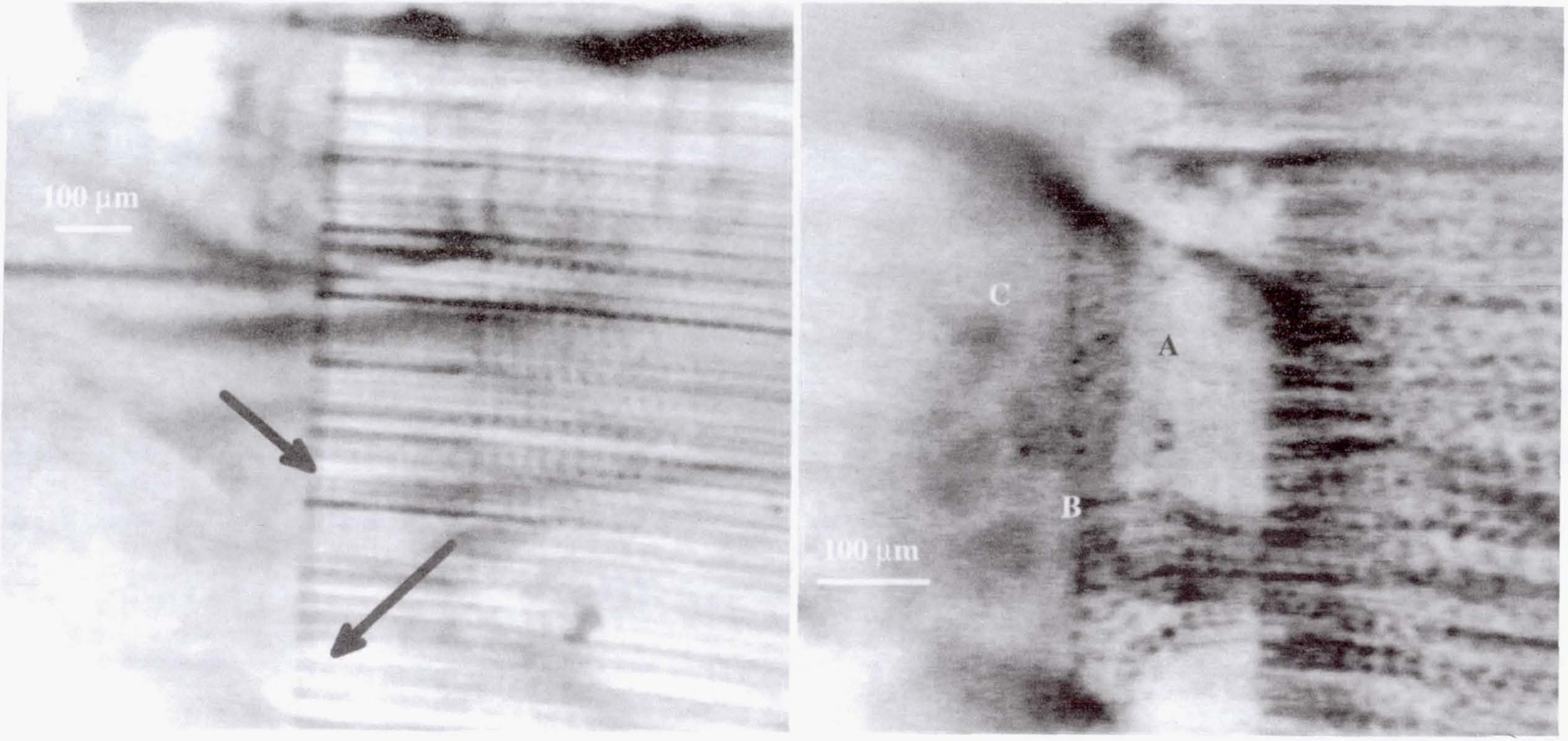

Fig. 4 a,b. Real-time XTM images of Al-3.4 Bi monotectic. a) The translation at 3 µm/sec was halted for a few minutes and some of the liquid-2 fibers at the interface ejected themselves leaving a whiter region behind (arrows). Note also the 3D particle array on the right. b) Captured during the resumption of the growth, now at 5 µm/sec translation rate. Here, a band of solid with lower Bi concentration [A] is seen adjacent to the previously halted interface with some sporadic liquid-2 fibers and droplets forming within this transition [B]. The solid-liquid interface has returned to a composite structure [C].

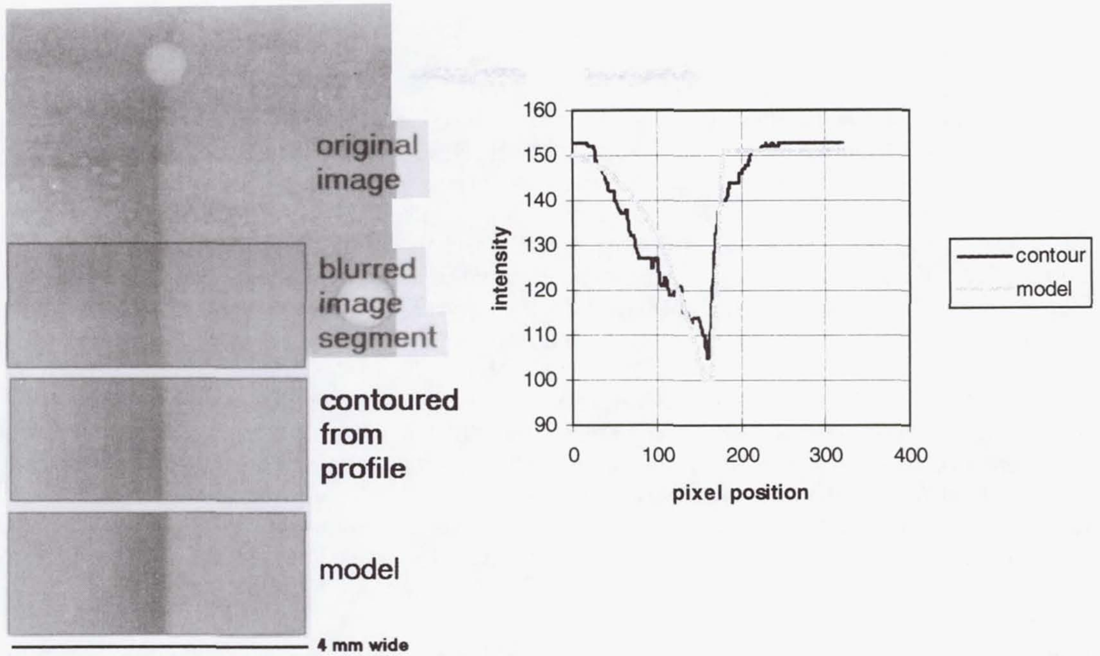

Figure 5 a and b. Results from comparison of synthetic radiographs from diffusion model to measured solute concentration induced intensities. a) Top shows post-quench radiograph of Al-0.8 Au grown at 5 µm/sec. Melt is on the left of interface. Next, is a segment smoothed by unidirectional blurring and then below that the synthetic radiograph made from a 2-D contour plot of the measured intensity profile from a 1 mm wide band in the radiograph. The bottom image was constructed from a diffusion model for the same solidification conditions and selective x-ray absorption by the constituents for the x-ray spectrum applied. b) The gray level intensities from the bottom 2 images in a) are superposed to show the reasonable fit between the model and the radiograph. Note how the measured composition contour has a linear form in the melt.

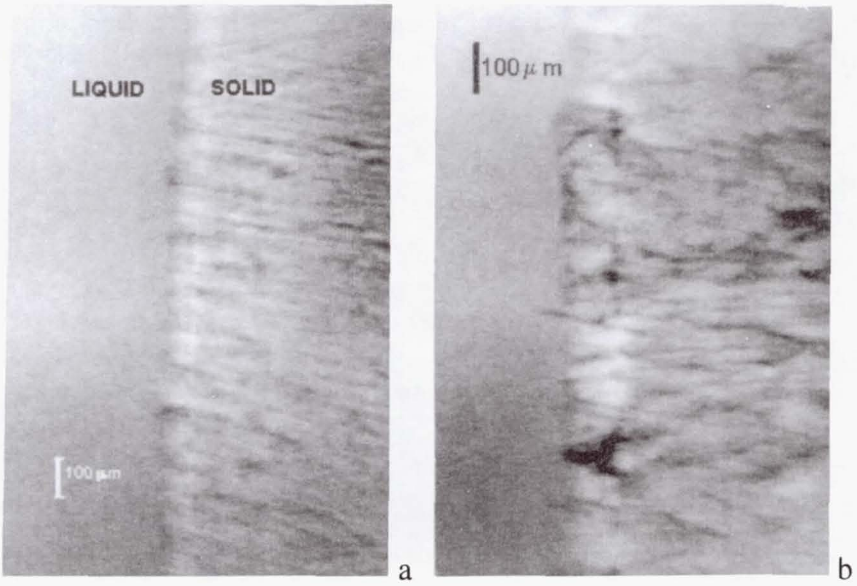

Figure 6 a (left, rate of about 2 µm/sec) and b (right, rate of about 1 µm/sec). Radiomicrographs of Al-Au eutectic during solidification. The microstructure is fibrous $AuAl_2$ in an Al matrix in a. b shows the degeneration of the fibers into plate-like features. The growth direction is to the left in a thermal gradient of 52 K/cm .

References

1. S. Sen, W. F. Kaukler, P. Curreri and D. M. Stefanescu (1997)"Dynamics of Solid/Liquid Interface Shape Evolution near an Insoluble Particle - An X-ray Transmission Microscopy Investigation",: Metallurgical and Materials Transactions A, 28A, pp. 2129-2135.
2. Kaukler, W. F. and P. A. Curreri (1996) "Advancement of X-ray Microscopy Technology and it's Application to Metal Solidification Studies," presented at the 1996 SPIE Technical Conference in Space Processing of Materials, Aug. 4, 1996, Ed. N. Ramachandran, 2809:34-44.
3. Curreri, P. A., Kaukler, W. F., Sen, S. and Peters, P. "Application of real-time X-ray Transmission Microscopy to Fundamental Studies of Metal Alloy Solidification", Spacebound 97 Proceedings, Canadian Space Agency; joint meeting with 9th International Symposium on Experimental Methods for Microgravity Materials Science, May 11-15 1997, Montreal Canada:72-84.
4. Curreri, P.A. and W. Kaukler (1996) "X-Ray Transmission Microscopy Study of the Dynamics of Solid/Liquid Interfacial Breakdown During Metal Alloy Solidification," Presented at 8th International Symposium on Experimental Methods for Microgravity Materials Science, Feb 4-8, 1996, Anaheim, CA, 125 TMS Annual Meeting, available on CD from TMS.
5. Kaukler, W. F. and P.A. Curreri, (1996) "X-Ray Transmission Microscopy of Al-Pb Monotectic Alloys During Directional Solidification," Presented at 8th International Symposium on Experimental Methods for Microgravity Materials Science, Feb 4-8, 1996, Anaheim, CA, 125 TMS Annual Meeting, available on CD from TMS.
6. Kaukler, W., F. Rosenberger, and P. A. Curreri (1997) "In-situ Studies of Precipitate Formation in Al-Pb Monotectic Solidification by X-ray Transmission Microscopy," Metallurgical Transactions, 28A:1705-1710.
7. Curreri, P. A., Kaukler, W. F. and Sen, S. "Real-time X-ray Transmission Microscopy for Fundamental Studies of Solidification: Al-Al_2Au Eutectic", CP420 Space technology and Applications International Forum-1998, The American Institute of Physics, 389-396.
8. Curreri, P.A. and W. F. Kaukler (1996) "Real-Time X-Ray Transmission Microscopy of Solidifying Al-In Alloys," Metallurgical Transactions 27A (3):801-808.
9. Curreri, P.A. and W. F. Kaukler (1995) "Real-Time X-Ray Transmission Microscopy of Solidifying Al-In Alloys," presented at The Metallurgical and Materials Society Annual Meeting, Las Vegas, NV, Feb. 12-16, 1995) published in Proceedings of 7th International Symposium on Experimental Methods for Microgravity Materials Science, Robert Schiffman, Ed., The Minerals, Metals and Materials Society, 93-101.

ADAPTIVE-GRID METHODS FOR PHASE FIELD MODELS OF MICROSTRUCTURE DEVELOPMENT

Nikolas Provatas[†,*], Nigel Goldenfeld[*] and Jonathan A. Dantzig[†]
[†]Department of Mechanical and Industrial Engineering
[*]Department of Physics
University of Illinois at Urbana-Champaign

Dendrites are the primary component of solidification microstructures in metals. Their properties have been a topic of intense study in the past 10-15 years. Experiments [1, 2] by Glicksman and coworkers on succinonitrile (SCN) and other transparent analogues of metals have provided tests of theories of dendritic growth, and have stimulated considerable theoretical progress [3–5]. The experiments have clearly demonstrated that naturally growing dendrites possess a unique steady state tip, characterized by its velocity, radius of curvature and shape, which leads the to a time-dependent sidebranched dendrite as it propagates.

Insight into the steady state dendrite problem was first obtained from local models [6–9] describing the evolution of the interface, and incorporating the features of the bulk phases into the governing equation of motion for the interface. These models showed that a nonzero dendrite velocity is obtained only if a source of anisotropy – for example, anisotropic interfacial energy – is present in the description of dendritic evolution. It was then shown that the spectrum of allowed steady state velocities is discrete, not continuous, and the role of anisotropy was understood theoretically, both in the local models and the full moving boundary problem [5, 10, 11]. Moreover, only the fastest of a spectrum of steady state velocities is stable, thus forming the operating state of the dendrite. It is widely believed that sidebranching is generated by thermal or other statistical fluctuations on a microscopic scale, which are amplified by advective diffusion. This body of theoretical work is generally known as solvability theory.

Brute force solution of the time-dependent Stefan problem requires front tracking and lattice deformation to contain the interface at predefined locations on the grid [12]. The *phase-field* model avoids this problem by introducing an auxiliary continuous order parameter $\phi(\mathbf{r})$ that couples to the evolution of the thermal field. The phase field interpolates between the solid and liquid phases, attaining two different constant values in either phase, with a rapid transition region in the vicinity of the solidification front. The level set of $\phi(\mathbf{r}) = 0$ is identified with the solidification front, and the dynamics of ϕ are designed to follow the evolving solidification front [13–23]. The phase-field parameters can be derived from parameters of the Stefan problem [14, 24], however this mapping is not very sensitive to the precise form of the phase-field model [25].

While the phase-field model finesses the problem of front tracking, it is still prohibitively expensive for large systems, because the grid spacing must be small enough everywhere that the phase-field model converges to the the sharp interface limit [14, 24]. Caginalp and Chen [26] showed rigorously that the phase field model converges to the sharp interface limit when the interface width (and hence the grid spacing) is *much smaller* than the capillary length. This result is necessary for acceptance of the phase field model, but is not sufficient for computational tractability in the experimentally relevant regime.

However, more recently Karma and Rappel [24] presented a different asymptotic analysis in powers of the ratio of the interface width to the diffusion length. Their procedure allows selection of parameters such that the phase field model corresponds to the sharp interface limit when the interface width (and hence the grid spacing) is *of order* the capillary length - a much more tractable regime. Furthermore, their improved analysis allows the kinetic coefficient to be tuned to zero, which corresponds to the experimentally realized situation at low undercooling in succinonitrile [2]. Karma and Rappel's numerical results are in excellent agreement with solvability theory at dimensionless undercoolings as low as 0.30, but fail to access the range of experimentally-realizable undercoolings near 0.1. What is needed is an effective adaptive technique [27] which dynamically coarsens the grid spacing away from the front.

In this work we show how the phase field model can be solved in a computationally efficient manner that opens a new large-scale simulational window on solidification physics. Our method uses a finite element, adaptive-grid formulation, and exploits the fact that the phase and temperature fields vary significantly only near the interface. We illustrate how our method allows efficient simulation of phase-field models in very large systems, and verify the predictions of solvability theory at intermediate undercooling. We then present new results at low undercoolings that suggest that solvability theory may not give the correct tip speed in that regime.

We model solidification using the phase-field model used by Karma and Rappel [24]. We rescale temperature T by $U = c_P(T - T_M)/L$, where c_P is the specific heat at constant pressure, L is the latent heat of fusion and T_M is the melting temperature. The order parameter is defined by ϕ, with $\phi = 1$ in the solid, and $\phi = -1$ in the liquid. The interface is defined by $\phi = 0$. We rescale time by τ_o, a time characterizing atomic movement in the interface, and length by W_o, a length characterizing the liquid–solid interface. The model is given by

$$\begin{aligned} & \frac{\partial U}{dt} = D\nabla^2 U + \frac{1}{2}\frac{\partial \phi}{\partial t} \qquad (1) \\ A^2(\vec{n}) \ & \frac{\partial \phi}{dt} = \nabla \cdot (A^2(\vec{n})\nabla\phi) + (\phi - \lambda U(1-\phi^2))(1-\phi^2) \\ + \ & \frac{\partial}{\partial x}\left(|\nabla\phi|^2 A(\vec{n})\frac{\partial A(\vec{n})}{\partial \phi_{,x}}\right) + \frac{\partial}{\partial y}\left(|\nabla\phi|^2 A(\vec{n})\frac{\partial A(\vec{n})}{\partial \phi_{,y}}\right), \end{aligned}$$

where $D = \alpha\tau_o/W_o^2$ and α is the thermal diffusivity, and where λ controls the coupling of U and ϕ. Anisotropy has been introduced in Eqs. (1) by defining the width of the interface to be $W(\vec{n}) = W_o A(\vec{n})$ and the characteristic time by $\tau(\vec{n}) = \tau_o A^2(\vec{n})$ [24], with $A(\vec{n}) \in [0, 1]$, and $A(\vec{n}) = (1-3\epsilon)\left[1 + \frac{4\epsilon}{1-3\epsilon}\frac{(\phi_{,x})^4 + (\phi_{,y})^4}{|\nabla\phi|^4}\right]$. The vector $\vec{n} = (\phi_{,x}\hat{x} + \phi_{,y}\hat{y})/(\phi_{,x}^2 + \phi_{,y}^2)^{1/2}$ is the normal to the contours of ϕ, and $\phi_{,x}$ and $\phi_{,y}$ represent partial derivatives with respect to x and y. The constant ϵ parameterizes the deviation of $W(\vec{n})$ from W_o. We expect the results to be similar for other definitions of anisotropy [14].

We use the asymptotic relationships given in [24] to select the parameters in Eqs. (1) such that it operates in the sharp interface limit, defined by U at the interface satisfying $U_{\text{int}} = -d(\vec{n})\kappa - \beta(\vec{n})V_n$. The variable $d(\vec{n})$ is the capillary length, κ is the local curvature, $\beta(\vec{n})$ is the interface attachment kinetic coefficient and V_n the normal speed of the interface, all in dimensionless form. In terms of $A(\vec{n})$, $d(\vec{n}) = d_o\left[A(\vec{n}) + \partial_\theta^2 A(\vec{n})\right]$, where $d_o = 0.8839/\lambda$ and θ is the angle between $\vec{n}$ and the x-axis. In this formulation, the constants W_o, τ_o and λ may be chosen so as to simulate arbitrary values of β. In particular, $\lambda = 1.5957D$ makes $\beta = 0$ [24], a limit which is appropriate for SCN.

We compute four-fold symmetric dendrites in a quarter-infinite space, initiated by a small quarter disk of radius R_o centered at the origin. The order parameter is initially set to its equilibrium value $\phi_o(\vec{x}) = -\tanh((|\vec{x}| - R_o)/\sqrt{2})$ along the interface. The initial temperature decays exponentially from $U = 0$ at the interface to $-\Delta$ as $\vec{x} \to \infty$.

We simulate Eqs. (1) on an adaptive grid of linear isoparametric quadrilateral and triangular finite elements, formulated using Galerkin's method. Following Ref. [28], elements are arranged on a two dimensional quadtree data structure, which makes our code scalable when implemented using dynamic memory allocation. The largest system sizes we have considered thus far correspond to 2D uniform lattices having $2^{17} \times 2^{17}$ grid points. The grid is locally refined to have a higher density of elements in the vicinity of the interface, identified by large fluxes in a composite field based on both ϕ and U. Typically, the grid is adapted about every 100 time steps, which permits ϕ and U to remain within the refined range between regriddings. We allow a difference of at most one level of refinement between neighboring quadrilateral elements. In such a case the quadrilateral element of lower level of refinement has an extra side node. The extra nodes are resolved with triangular elements.

On an adaptive grid, the concept of a grid spacing is replaced by that of a minimum grid spacing Δx_{min}, representing the finest level of spatial resolution. We found that for solutions to converge properly, the grid must be *layered* such that the highest density of elements appears around the ϕ interface, while the U-field, whose width is of order D/V_n can be encompassed by a mesh of larger grid spacing. Convergence of our solutions is relatively insensitive to Δx_{min}. For a test case of dendrites grown at $\Delta = 0.55$, $D = 2$, $\epsilon = 0.05$, and integration time step $dt = 0.016$, our solutions for the steady state velocity converge to that given by solvability theory to within a few percent for $0.3 \leq \Delta x_{\text{min}} \leq 1.6$.

Fig. 1 shows a dendrite 10^5 time steps into its evolution computed using our adaptive grid method, using the parameters just mentioned above. The system size is 800×800, with $\Delta x_{\text{min}} = 0.78$, and about half of the computational domain is shown. Sidebranching is evident, and arises due to numerical noise. This calculation took approximately 10 cpu-hours on a Sun UltraSPARC 2200 workstation.

We examined the cpu-scalability of our algorithm with system size by growing dendrites in systems of various linear dimension L_B and measuring the cpu time R_t^a for the dendrite branches to traverse the entire system. We once again use the same parameters as above, except $\Delta x_{min} = 0.4$. The relationship between R_t^a and L_B is shown in Fig. 2, where we see that $R_t^a \sim L_B^2$. The number of calculations performed, per time step, is proportional to the number of elements in our grid, which is set by the arclength of the interface being simulated multiplied by the diffusion length D/V_n. For a parabolic shape the arclength $\sim L_B$. Thus, since the dendrite tip moves at a constant velocity V_n, then $R_t^a = [R_o^a D V_n^2/\Delta x_m^2] L_B^2$, where R_o^a is a constant that depends on the implementation. The cpu time R_t^u needed to compute the same case on a uniform grid scales as $R_t^u = [R_o^u/(V_n \Delta x_m^2)] L_B^3$. For large system sizes, $R_t^a/R_t^U \sim L_B$.

We tested the effective anisotropy of our dynamically adapting lattice in two ways. Following the method outlined by Karma [24], we find an equilibrium shape for the interface when the background field is adjusted dynamically so as to maintain the velocity of the interface at zero. The effective anisotropy is inferred by fitting an equation to the computed interface. We found ϵ_{eff} to be within 5% of the intended value for input $\epsilon = 0.02 - 0.04$. We also tested for grid anisotropy by rotating the grid by 45 degrees, which should represent the lowest accuracy for square elements. In this case, the steady state tip-velocity was within 1% of its value in the original orientation.

We further verified our algorithm by comparing measured tip-velocities and shapes for dendrites grown using the same undercoolings, parameter sets and systems sizes reported in [24]. We found very good agreement for $\Delta = 0.65, 0.55, 0.45, 0.30$. We next investigated the effect of system size. Fig. 3 shows the time evolution of tip-velocity for several undercoolings and system dimensions. The two cases for $\Delta = 0.65$ are typical of results at intermediate Δ, showing a relatively rapid leveling to an asymptotic speed within a few percent of that predicted by solvability theory.

At lower Δ, however, we found that the tip-velocity deviates from that predicted by solvability theory. Fig. 3 also shows the evolution of the tip-velocity for $\Delta = 0.25$ in two different sized boxes. Whereas the computed tip-velocity falls a few percent below the solvability value in the 6400×400 box, it exceeds by 8% the solvability value in the 6400×3200 box. This effect is even larger at $\Delta = 0.1$, also shown in Fig. 3, where the tip speed is about 3 times larger than that predicted by solvability theory.

The explanation for this behavior is that at low Δ, the thermal fields of the two dendrite branches overlap, violating the assumptions of solvability theory, which models an isolated single dendrite. At large undercooling, each dendrite arm quickly outruns the other's thermal boundary layer, and solvability theory should apply. (See Fig. 1, $\Delta = 0.65$.) The conditions of solvability theory can also be approximated at lower undercooling if simulations are performed in a domain which is small in one direction. For the simulation performed with $\Delta = 0.25$ in the small box (6400×400), the branch in the y-direction is extinguished by its interaction with the wall and agreement with solvability theory is obtained. However, when both branches are present, as in the simulation with $\Delta = 0.25$ in the larger box (6400×3200), their interaction leads to an increased tip-velocity because the dendrites are embedded in a circular rather than parabolic diffusion field. This is clearly seen in Fig. 4, where the dendrite shape and its associated field are shown for $\Delta = 0.10$ ($D = 13$, $d_0 = 0.043$, $\epsilon = 0.05$, $\Delta x = 0.78$, $dt = 0.08$). The dendrite arms never became free of each other in this simulation, causing the observed deviation from solvability theory shown in Fig. 3. This latter simulation was performed in a 102400×51200 domain, chosen to contain about $10D/V_n$. We note that the ratio of the largest to smallest element size in this simulation is 2^{17}. A fixed mesh having the same resolution would contain 9×10^9 grid points, clearly beyond current computing capability.

We can estimate the time $t^\star$ when the growth of the dendrite tip crosses over from the transient regime where the branches interact to that where they become independent by equating the length of the full diffusion field, $3(Dt^\star)^{1/2}$, to the length of a dendrite arm, $V_n t^\star$. This gives the crossover time as $t^\star = 9D/V_n^2$. The values for $t^\star$ corresponding to the cases $\Delta = 0.65$, 0.25 and 0.10 in Fig. 3 are 2.5×10^3, 1.6×10^4 and 5.9×10^7, respectively. Inspection of Fig. 3 confirms this scaling.

These results have important implications when comparing theory to experimental observations at low undercooling. We find that in this regime, the appropriate theory to use is one which explicitly takes into account the long range effects of other branches [29]. In particular, study of real dendrites with sidebranches, growing at low undercooling, will require such treatment. An investigation of this effect, as well as results in 3D, applications to directional solidification and other solidification processes, and a more detailed description of our algorithm will appear in future publications.

We thank Wouter-Jan Rappel for providing the Green's function steady-state code used to test some of our simulations, and Alain Karma for generously providing us with his unpublished results. We also thank Robert Almgren and Alain Karma for helpful discussions of our results at low undercooling. This work has been supported by the NASA Microgravity Research Program, under Grant NAG8-1249.

References

[1] S.-C. Huang and M.E. Glicksman, Acta. Metall., **29**, 701 (1981)]

[2] M. E. Glicksman, Materials Science and Engineering, **65** (1984).

[3] J.S. Langer, Rev. Mod. Phys. **52**, 1 (1980);

[4] J.S. Langer, "Lectures in the Theory of Pattern Formation", in *Chance and Matter*, Les Houches Session XLVI, edited by J. Souletie, J. Vannenimus and R. Stora (North Holland, Amsterdam, 1987), p. 629.

[5] D.A. Kessler, J. Koplik and H. Levine, Adv. Phys. **37**, 255 (1988).

[6] R. Brower, D. Kessler, J. Koplik, and H. Levine, Phys. Rev. Lett., **51**, 1111, (1983).

[7] E. Ben-Jacob, N. Goldenfeld, J.S. Langer and G. Schön, Phys. Rev. Lett., **51**, 1930 (1983).

[8] E. Ben-Jacob, N. Goldenfeld, B.G. Kotliar, and J.S. Langer, Phys. Rev. Lett., **53**, 2110 (1984).

[9] D. Kessler, J. Koplik, and H. Levine, Phys. Rev. A, **30**, 3161 (1984).

[10] E. Brener, and V. I. Melnikov, Adv. Phys. **40**, 53 (1991).

[11] Y. Pomeau and M. Ben Amar, *Dendritic growth and related topics*, in *Solids far from equilibrium*, ed. C. Godrèche, (Cambridge, 1991) 365.

[12] R. Almgren, J. Comp. Phys. **106**, 337 (1993).

[13] J. S. Langer, in *Directions in Condensed Matter* (World Scientific, Singapore, 1986), 164.

[14] G. Caginalp, Arch. Rat. Mech. Anal. **92**, 205 (1986); G. Caginalp, Anal. of Phys. **172**, 136 (1986); G. Caginalp, and E. Socolovsky, SIAM J. Sci. Comp. **15**, 106 (1991).

[15] J. B. Collins and H. Levine, Phys. Rev. B, **31**, 6119 (1985).

[16] J. A. Warren and W. J. Boettinger, Acta Metall. Mater. A **43**, 689 (1995)

[17] A. A. Wheeler, W.J. Boettinger, and G. B. McFadden Phys. Rev. A **45**, 7424 (1992) (1996).

[18] A. Karma, Phys. Rev. E **49**, 2245 (1994).

[19] K. R. Elder, F. Drolet, J. M. Kosterlitz, and M. Grant, Phys. Rev. Lett. **72**, 677 (1994).

[20] A. A. Wheeler, G. B. McFadden, and W.J. Boettinger, Proc. Royal Soc. London A **452**,

[21] R. Kobayashi, Physica D **63**, 410 (1993).

[22] N. Provatas, E. Elder, M. Grant, Phys. Rev. B, **53**, 6263 (1996).

[23] S-L. Wang and R. F. Sekerka, Phys. Rev. E **53**, 3760 (1996).

[24] A. Karma, and W.-J. Rappel, Phys. Rev. E **53**, 3017 (1995); A. Karma, and Wouter-Jan Rappel, Preprint (1997).

[25] M. Fabbri and V. R. Voller, J. Comp. Phys. **130**, 256 (1997).

[26] G. Caginalp and X. Chen, *On The Evolution Of Phase Boundaries*, edited by M.E. Gurtin an d G.B. McFadden (Springer-Verlag, New York, 1992), p.1.

[27] R. J. Braun, and B. T. Murray, J. Cryst. Growth **174**, 41 (1997).

[28] N. Palle, and J. A. Dantzig, Met. Trans. A, **27A**, 707 (1996).

[29] R. Almgren, W. S. Dai and V. Hakim, Phys. Rev. Lett., **71**, 3461 (1993).

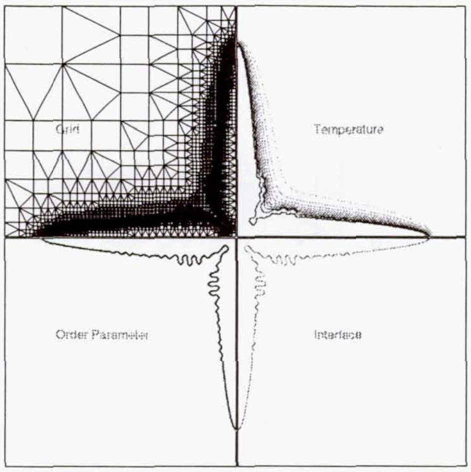

Figure 1: A dendrite grown using the adaptive-grid method for $\Delta = 0.55$, $D = 2$, $\epsilon = 0.05$. Clockwise, beginning at the upper right the figures show contours of the U-field, the contour $\phi = 0$, contours of the ϕ-field and the current mesh.

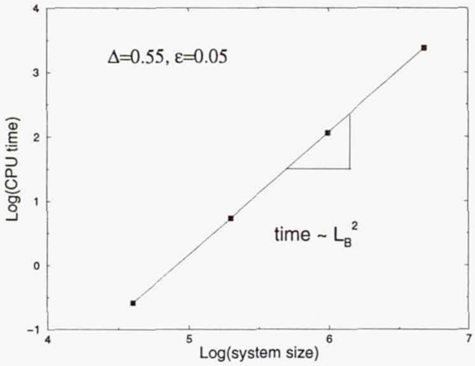

Figure 2: CPU time vs. the system size, illustrating the computing time for a dendrite to move through the system of linear dimension L_B using our adaptive mesh method.

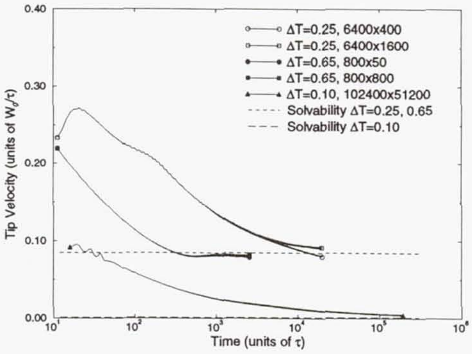

Figure 3: The time evolution of the tip-velocity for undercooling $\Delta = 0.65, 0.25$ and 0.10.

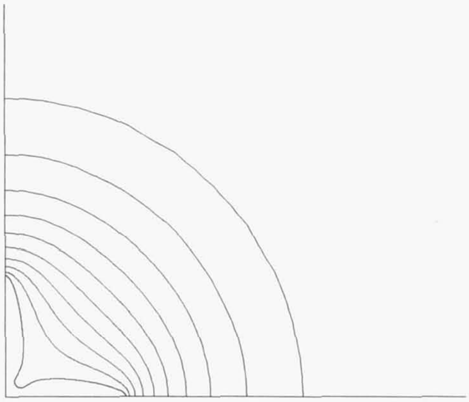

Figure 4: Dendrite silhouette and isotherms from -0.01 to -0.9 for undercooling $\Delta T = 0.1$. Full domain dimensions are $102,400 \times 51,200$. The dendrite tip is approximately $1,300$ units from the origin, while the temperature field spreads to about $5,000$ units.

KINETICS OF NUCLEATION AND CRYSTAL GROWTH IN GLASS FORMING MELTS IN MICROGRAVITY

NASA Contract: NAG8-1465

Delbert E. Day and Chandra S. Ray
Ceramic Engineering Department and Graduate Center for Materials Research
University of Missouri-Rolla, Rolla, MO 65409.
573-341-4354; day@umr.edu

Introduction

This is a flight definition project with the specific objective to investigate the kinetics of nucleation and crystal growth in microgravity for high temperature inorganic oxide melts that have the potential to form glass when cooled. The present project is related to of our previous NASA project[1] that was concerned with glass formation for high temperature containerless melts in microgravity. The previous work culminated in two experiments[2, 3] which were conducted aboard the space shuttle in 1983 and 1985 and which consisted of melting levitated, spherical (6 to 8 mm diameter) samples in a Single Axis Acoustic Levitator (SAAL) furnace at 1500° C.

Of special relevance to the present project was the finding that glass formation for a CaO-Ga_2O_3-SiO_2 composition melted in microgravity was nearly three times more likely than for the same composition melted at 1-g (on earth). This finding was based on the comparison of the critical cooling rate for glass formation (defined as the slowest rate at which a melt can be cooled without crystallizing) for the identical composition measured at 1-g (on earth) with the cooling rate which the containerless melt experienced in micro-g (space), see Fig. 1. The improvement in glass formation for the containerless melt prepared in micro-g was attributed to the suppression of heterogeneous nucleation that usually occurs at the melt-container interface on earth (1-g). Unfortunately, the maximum improvement in glass formation for containerless melts in microgravity could not be determined because of the unplanned termination of the third flight experiment due to the Challenger accident.

A second important finding of equal importance was that the glass obtained from the space melted sample, which had been prepared from a deliberately, chemically inhomogeneous (hot-pressed) sample, was considerably more chemically homogeneous than the control sample prepared on earth (1-g). Melt homogenization or mixing at 1-g is known to be caused primarily by gravity-driven convection. Why a glass prepared in micro gravity, where gravity-driven convection is ideally absent and the melt would be more nearly stagnant, was more chemically homogeneous, remained unclear.

It is interesting to note, however, that similar results have been obtained from other microgravity experiments[4-9], even for glasses processed in containers. The following list summarizes the most important results that have been consistently reported for glass forming melts in microgravity.

(1) *Glass formation is enhanced for melts prepared in space*[2-4].

(2) *Glasses prepared in microgravity are more chemically homogeneous*[2-8] *and contain*[6-8] *fewer and smaller chemically heterogeneous regions than identical glasses prepared on earth.*

(3) *Heterogeneities that are deliberately introduced such as Pt particles are more uniformly distributed*[7,8] *in a glass melted in space than in a glass melted on earth.*

(4) *Glasses prepared in microgravity are more resistant to crystallization*[4,6,9]*, and have*[6] *a higher mechanical strength and threshold energy for radiation damage.*

(5) *Glasses crystallized in space have a different microstructure, finer grains more uniformly distributed, than equivalent samples crystallized on earth*[4,8].

The preceding results are not only scientifically interesting, but they have considerable practical implications. These results suggest that the microgravity environment is advantageous for developing new and improved glasses and glass-ceramics that are difficult to prepare on earth. However, there is no suitable explanation at this time for why a glass melted in microgravity will be more chemically homogeneous and more resistant to crystallization than a glass melted on earth.

A fundamental investigation of melt homogenization, nucleation, and crystal growth processes in glass forming melts in microgravity is important to understanding these consistently observed, but yet unexplained results. This is the objective of the present research. A lithium disilicate ($Li_2O.2SiO_2$) glass will be used for this investigation, since it is a well studied system, and the relevant thermodynamic and kinetic parameters for nucleation and crystal growth at 1-g are available. The results from this research are expected to improve our present understanding of the fundamental mechanism of nucleation and crystal growth in melts and liquids, and to lead improvements in glass processing technology on earth, with the potential for creating new high performance glasses and glass-ceramics.

Hypothesis

The solidification of high temperature melts is controlled by the kinetics of nucleation and crystal growth. A melt forms a glass when nucleation and subsequent crystal growth does not occur or can be avoided during cooling the melt. Understanding the kinetics of nucleation and crystal growth for a melt is also the basis for understanding glass formation for that melt. According to the classical theory of nucleation and crystal growth, the volume fraction, V_c/V (= x), that crystallizes in a melt during cooling can be related to the nucleation rate, I_v, and crystal growth, U as[10],

$$x = 1 - \exp [- (4\pi/3) \int I_v (\int U\, dt'')^3\, dt'] \quad \ldots \quad \ldots \quad \ldots \quad \ldots(1)$$

If x in the quenched melt is below the lower detection limit, which is currently about 10^{-6}, the resulting material is considered a glass.

The simplified forms of I_v and U at a temperature T are given in Eqs. 2 and 3,

$$I_v = (n_v D / \lambda^2) \exp (- W^* / kT] \quad \ldots \quad \ldots \quad \ldots \quad \ldots \quad \ldots(2)$$

$$U = (f D / \lambda) [1 - \exp (V_m \Delta G_v /RT) \ldots \quad \ldots \quad \ldots \quad \ldots \quad \ldots(3)$$

where W^* is the thermodynamic barrier for nucleation, ΔG_v is the free energy difference between unit volumes of the crystal and liquid phases, n_v is the number of molecules or formula units of the nucleating phase per unit volume, k is the Boltzmann constant, and λ is a jump distance on the order of atomic dimensions, V_m is the molar volume of the crystal phase, R is the gas constant, and f is an interface site factor which refers to the fraction of sites on the interface to which an atom can attach. For melts with an entropy of fusion of less than 2R which is approximately true for most glass forming melts, the site factor f is close to unity. D is the effective diffusion (self) coefficient and is related to the viscosity of the melt, η, at the temperature T as,

$$D = kT / 3\pi\lambda\eta \quad \ldots \quad \ldots \quad \ldots \quad \ldots \quad \ldots \quad \ldots \quad \ldots(4)$$

None of the above equations involves gravity (g) *per se* , and it is hard to not clear why the kinetics of nucleation or crystal growth (or, conversely, the kinetics of glass formation) for a melt in microgravity will be different from those at 1-g. However, the experimental results suggest differently.

It is suspected that gravity-driven convection at 1-g introduces a high rate of mass transfer in melts, which could affect the structure of the melt in several ways.

(1) Materials dissolved from the container walls may continually be convected (carried) into the melt at 1-g thereby, creating chemical inhomogeneities and potential sites for heterogeneous nucleation and crystallization. Due to lack of gravity-driven convection in micro-g, any materials dissolved from the container could be confined to a thin layer at the melt-container interface leaving the bulk of the melt essentially free from these impurities (or nucleation sites). If there is less mixing in a melt in micro-g then the overall nucleation rate is expected to be lower and chemical homogeneity would be better than for a glass melt at 1-g.

(2) High temperature melts, particularly, multicomponent melts containing two or more

components of differing density can experience localized compositional fluctuations which favors the formation of clustered regions whose chemical compositions differ from the overall composition of the melt. Rapid quenching of a melt freezes these compositionally different (microheterogeneous) regions in the glass, which are potential nucleation sites for crystallization. A higher rate of mass transfer can induce a larger compositional fluctuation in a melt at 1-g forming microheterogeneous regions of larger size and number. As a consequence, a glass prepared on earth can be less chemically homogeneous and have a higher nucleation rate or crystallization tendency compared to the same glass prepared in space.

The above two hypotheses basically imply that the perturbation induced by gravity-driven convection causes the effective diffusion coefficient, D (Eq. 4) to be larger in a melt at 1-g. Experiments show[11,12] values of D that are 30 to 40% lower for melts in space compared to the best values reported for melts on earth. A lower value of D in space experiments will reduce both the nucleation and crystal growth rates (Eqs. 2 and 3), resulting in an overall increase in the tendency for glass formation (Eq. 1) of the melt compared to that of a melt on earth.

The formation of microheterogeneous regions can be viewed qualitatively as a demixing effect (shown schematically in Fig. 2), which is enhanced by gravity-driven convection. If there is no Marangoni flow, a melt in micro-g would be essentially stagnant and the effect of demixing would be much smaller. The equilibrium level of homogeneity at 1-g can be attained in a shorter time, but it is expected to always be less than what can be achieved in space.

A third hypothesis stems from the reported[13,14] pseudoplastic character of glassy materials. This means that a glass under an applied stress will have a lower effective viscosity, η (or higher D, Eq. 4), compared to a stress-free glass at the same temperature. In other words, a stressed glass will have a higher tendency for crystallization than an unstressed glass. Since a melt at 1-g is under constant convection compared to a near quiescent melt in micro-g, it is suspected that a glass prepared at 1-g will have a higher stress and will be more susceptible to crystallization than a glass prepared in space.

Experiment

The hypotheses mentioned above, namely, (1) the reduction of nucleation and crystal growth rates, (2) improvement in chemical homogeneity, and (3) reduction of stress for the glasses prepared in space compared to those for the glasses prepared on earth will be tested through flight and ground based experiments. As mentioned before, a lithium-disilicate ($Li_2O.2SiO_2$ or LS_2) will be used as the test composition.

The flight experiments will include melting an LS_2 composition in sealed platinum capsules at temperatures between 1100 and 1500° C and cooling the melts at predetermined rates. While a part of the samples will be returned to earth as their as-quenched condition for various property measurements, others will be given a two stage heat treatment in space between 420 and 700° C for 30 min to 12 h for nucleation and crystal growth. Conventional microscopic techniques will be used to determine the rates for nucleation and crystal growth of the glasses as a function of temperature and to evaluate the microstructure of the crystallized samples. These data will be compared with that for the control samples from similar measurements at 1-g.

Differential thermal analysis (DTA) will be used to compare the crystallizing tendency for the space and earth melted glasses. A few selected properties that are likely to be affected by the degree of homogeneity and stress of a glass such as the density, refractive index, and optical transmission in the UV, visible, and IR, will be measured and compared for these glasses. Any difference in the structure of space and earth melted glasses will also be investigated by x-ray photoelectron spectroscopy (XPS), neutron diffraction, and Raman and IR spectral analysis.

Work Performed / Undertaken

The work for this project was started with investigating the effect of melting temperature on the crystallization of an LS_2 glass. Since the microheterogeneous regions discussed earlier form in the liquid state, it is reasonable to expect that melting temperature might have an effect on the size and number of these regions and, hence, on the overall crystallization behavior of the glass. Glasses (50 g) were prepared by melting a homogeneous batch of the LS_2 composition in a platinum crucible at 1450° C for 15 min. The melt was then stirred with an alumina rod and held at temperatures between 1050 and 1450° C at 50° C intervals for 2 h before quenching between steel plates.
A 50 mg sample of each glass with particle size between 425 and 500 μm was analyzed by DTA at a heating rate of 10° C/min. No effect of melting temperature of this LS_2 glass was apparent in the DTA thermograms. The peak temperature of the glass transition endotherm and crystallization exotherm in DTA occurred at 481±1° C and 658±2° C, respectively, for all the glasses melted at different temperatures.

The IR spectra for these glasses as measured by KBr pellet technique from 450 to 2000 nm are also essentially identical and do not show any effect of melting temperature.

The LS_2 glasses prepared by melting at different temperatures are now being used to measure the nucleation and crystal growth rate as a function of temperature using conventional optical microscopy. Neutron diffraction, XPS, and Raman spectra measurements for these glasses are continuing.

References

1. Day D. E. and Ray, C. S., *Containerless Processing of Glassforming Melts in Space*, NASA contract NAS8-34758; *NASA Technical Memorandum #4069*, vol. 2, pp. 537-556 (1988).
2. Ray C. S. and Day D. E., *Proc. Mat. Res. Soc.*, **87**, 239 (1987).
3. Ray C. S. and Day D. E., *JASMA*, **7**, 94 (1990).
4. Barta C., Stourac L., Triska A., Kocka J. and Zavetova M., *J. Non-Cryst. Solids*, **35-36**, 1239 (1980).
5. Barta C., Trnka J., Triska A. and Frumar, *Adv. Space Res.*, **1**, 121 (1981).
6. Petrovskii G. T., Ryumin V. V. and Semeshkin I. V., *Steklo i Keramika*, **1**, 5 (1983).
7. Braetsch V. and Frischat G. H., *Proc. ESA on Mat. Sci. Under Micrgravity*, Bordeaux, France 2-5 dec. 1986, pp. 259-262 (ESA SP-256, 1987); *Naturwissen Schaffen*, **73**, 368 (1986).
8. Frischat G. H., *J. Non-Cryst. Solids*, **183** 92 (1995).
9. Tucker D. S., Scripa R. N., Wang B. and Rigsbee J. M., *Proc. 18th Int. cong. On Glass*, San Francisco, CA, 5-10 July, 1998.
10. Scherer G. W., *Materials Science and Technology*, vol. 9, chapter 3 (Eds. Cahn R. W., Hassen P. and Krammer E. J.), VCH Publications, New York, 1991.
11. Ukanaw A. O., *M 558-Skylab Results, NASA-MSFC*, 1979, p.427.
12. Frohberg G., Kraatz K. H. and Wever H., *ESA-SP-222*, 1984, p. 201.
13. Deubener J. and Brückner R, *J. Non-Cryst. Solids*, **209**, 96 (1997).
14. Dobreva-Veleva A., Rüssel C. and Gutzow I., *Proc. 18th Int. cong. On Glass*, San Francisco, CA, 5-10 July, 1998.

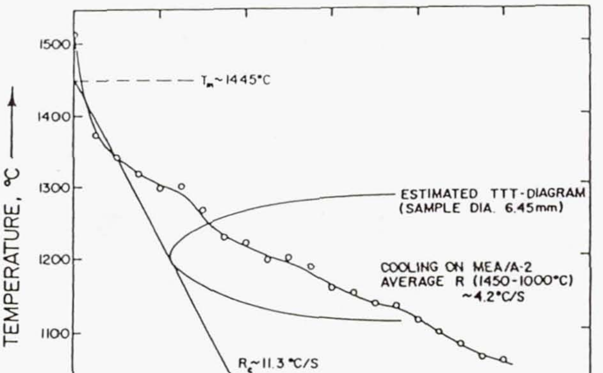

Fig. 1. The TTT diagram for a 25 SiO_2-35.7CaO-39.3Ga_2O_3, mol% glass determined at 1-g and the actual cooling rate used in space experiment (ME A/A-2) for this melt.

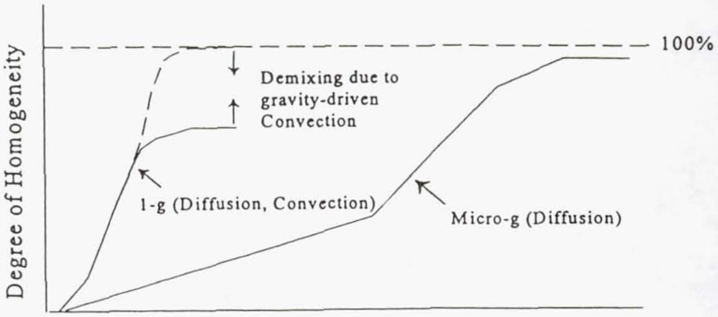

Fig. 2. A most likely situation for melt homogenization in micro-g and at 1-g. At 1-g, the melt may be homogenized in a shorter time, but degree of homogenization will be less due to possible demixing induced by gravity-driven convection.

Atomistic Simulations of Cadmium Telluride: Toward Understanding the Benefits of Microgravity Crystal Growth

J.J. Derby (PI) and J.R. Chelikowsky (Co-PI)
Department of Chemical Engineering and Materials Science
University of Minnesota
151 Amundson Hall
421 Washington Avenue, S.E.
Minneapolis, MN 55455-0132

Telephone: (612) 625-1313
Fax: (612) 626-7246
E-mail: derby@tc.umn.edu, jrc@msi.umn.edu

Introduction and Objectives

Progress in crystal growth on earth or in space will depend on a more fundamental understanding of the important coupling between atomistic-scale processes which control the properties of grown crystalline material and the macroscopic transport conditions imposed by the growth system. Our long-term goal is to understand the mechanisms which influence crystal quality through the hierarchy of length and time scales relevant to these atomistic-scale and macro-scale processes. The immediate goal of the research summarized here is to employ atomistic simulation to understand better the melt growth of cadmium telluride (CdTe) and its alloy cadmium zinc telluride (CdZnTe). These materials are employed in a variety of technologically important electronic and electro-optical devices; however, the growth of high-quality, large-area single crystal substrate has proven to be extremely difficult under terrestrial conditions. We seek to obtain a more fundamental understanding of the properties of cadmium telluride so that the physical mechanisms responsible for growth can be elucidated. A secondary objective of our work is the prediction of high-temperature thermophysical properties of liquid and solid CdTe.

Relationship to Microgravity Research

Recent growth experiments of $Cd_{0.96}Zn_{0.04}Te$ in a microgravity environment aboard USML-1 resulted in material which was far superior in structural perfection compared to earth-grown material under similar conditions. These dramatic results were attributed to the elimination of hydrostatic pressure from the melt column overlaying the crystal due to microgravity conditions, thereby reducing the hoop stresses that occur in a crystal as it grows and cools. In addition, it was speculated that the near absence of hydrostatic pressure allowed for the melt to solidify with minimal wall contact, thereby eliminating deleterious wall interactions. We will utilize atomistic simulation to understand the dynamics of the liquid/solid interface and of the solid material under the stress conditions corresponding to micro-gravity and terrestrial conditions. The work to be performed in this project will support current microgravity research on the melt growth of CdTe compounds and will provide for a quantitative, unambiguous method to understand the subtle effects of microgravity in these systems.

The primary thrust of this work will be to clarify the role of microgravity in interpreting the USML-1 results described above; however, this work promises to support future microgravity research in other substantial ways. Atomistic simulations will provide predictions of the high-temperature thermophysical properties of CdTe and its alloys. Accurate high-temperature properties are needed for reliable materials processing models, but such data are extremely difficult to obtain from experimental measurements (many of which have been undertaken in microgravity environments). The prediction of these properties using atomistic simulation clearly complements ongoing and future microgravity process modeling and experimental property measurement efforts. Another likely benefit from this work is that a more complete understanding of the structure of molten CdTe and alloys will aid the development of seeding procedures for melt growth. For earth-based processes, reliable seeding techniques have not yet been developed for these materials, yet such procedures have been identified as one of the most needed process improvement to increase yields. Undoubtedly, as further microgravity experiments on the melt growth of CdZnTe are performed, seeded growth experiments will be desired and the knowledge obtained from atomistic simulations will be invaluable.

Methodology and Results

We have successfully employed *ab initio* pseudopotentials to compute the electronic structure of solid and liquid CdTe. Subsequent work focused on performing first principles molecular dynamics simulations on the liquid state using interatomic forces between atoms to calculate the atomic trajectories and integrate the equations of motions to simulate the liquid. The liquid was modeled by considering a 64 atom unit cell with periodic boundary conditions; the atoms were randomly place in this cell and initially heated to a very high temperature. After cooling the system to a temperature slightly above the melting temperature, we analyzed the resulting liquid.

We have determined the pair correlation function, the self-diffusion of the Cd and Te atoms, and have performed an analysis of the liquid structure. We compared the theoretical results for the pair correlation function to experimental x-ray and neutron work. Our initial comparisons are quite encouraging; the predicted and experimental distributions are quite similar. Likewise, our computed diffusion coefficients are consistent with experiments.

We have submitted a manuscript entitled "*Ab Initio* Molecular Dynamics Simulation of Liquid CdTe and GaAs: Semiconducting versus Metallic Behavior" to *Physical Review Letters*. All semiconductors of IV row, such as silicon, and III-V materials, such as gallium arsenide, assume metallic behavior when melted. This is in contrast to some II-VI semiconductors such as CdTe which retain their semiconducting behavior in both the liquid and the solid state. In order to understand this difference, we have performed *ab initio* molecular dynamics simulations of liquid GaAs and CdTe. Using the Kubo-Greenwood formalism, we predict the conductivity of both liquids and confirm the differences observed experimentally. We relate the conductivity differences between II-VI and III-V semiconductors to strong structural differences occurring within the melt.

Theoretical Analysis of 3D, Transient Convection and Segregation in Microgravity Bridgman Crystal Growth

J.J. Derby (PI) and A. Yeckel (Co-PI)
Department of Chemical Engineering and Materials Science
University of Minnesota
151 Amundson Hall
421 Washington Avenue, S.E.
Minneapolis, MN 55455-0132

Telephone: (612) 625-1313
Fax: (612) 626-7246
E-mail: derby@tc.umn.edu, yecke003@tc.umn.edu

Introduction and Objectives

Key to the advancement of crystal growth processing is a better understanding of the dominant influence of buoyancy-driven convection on segregation and morphological stability during crystal growth on earth. Since these effects in turn play a critical role in establishing the structure and properties of grown materials, considerable interest has developed for their study by use of the microgravity environment provided by space flight. However, space flight experiments are still subject to accelerations that rapidly vary in magnitude and direction, and such variations complicate experiments by the introduction of significant transient and three-dimensional effects. We propose to develop rigorous process models that account for such three-dimensional, transient phenomena during melt crystal growth under microgravity conditions.

With this model, we will perform fundamental studies of transient acceleration and g-jitter effects – significant advances in the understanding of segregation phenomena are to be expected. In addition, there is an immediate and continuing need of the microgravity flight experiment program for three-dimensional growth models coupled with realistic heat transfer models that describe current NASA flight furnaces, such as the Advanced Automated Directional Solidification Furnace (AADSF) and Crystal Growth Furnace (CGF). The codes developed here will enable the unambiguous interpretation of flight experiments, and will, perhaps even more importantly, provide a tool to design the conditions needed in future flight experiments to best study the effects of microgravity on segregation theory.

Relationship to Microgravity Research

There has long been interest in employing the microgravity environment of space to process advanced materials. Growing crystals in space has the alluring potential to reduce convective flow velocities to the point where diffusion-controlled growth is possible, thus promoting the growth of higher quality crystals and enabling the detailed study of segregation phenomena. Early space experiments confirmed that microgravity processing could significantly reduce the level of melt convection. Uniform doping was not achieved, however, indicating that convection was not completely damped in the melt. Recent experiments conducted on the First United States Microgravity Laboratory (USML-1) also indicated that convection was not totally damped. Clearly, reducing the magnitude of the gravitation force alone was not sufficient to achieve diffusion-controlled growth in these experiments. Other effects can also complicate the microgravity environment, especially those associated with time-dependent changes in the direction and magnitude of the gravity vector (g-jitter). These effects induce flow in the melt that is three-dimensional and time-dependent.

Another three-dimensional effect that arises during microgravity crystal growth experiments concerns the dewetting of the melt from the ampoule walls, resulting in bubbles or free surfaces. Such events can lead to significant Marangoni flows driven by gradients in surface tension along the free surface of the melt. Of interest in these situations are the effects of these three-dimensional flows on segregation and the effects of the free surface on reducing mechanical interactions between the solidifying charge and the ampoule. Growth experiments of $Cd_{0.96}Zn_{0.04}Te$ aboard USML-1 resulted in material that was far superior in structural perfection compared to earth-grown material under similar conditions. It was speculated that the near absence of hydrostatic pressure allowed for the melt to solidify with minimal wall contact, thereby eliminating deleterious wall interactions. To truly quantify the conditions needed to promote dewetting and explain the resultant phenomena associated with the presence of the melt free surface requires a fully three-dimensional modeling capability.

Previous attempts to model the effects of g-jitter and dewetting have relied on an assumption of 2D, axisymmetric behavior that greatly simplifies analysis. The proposed work will directly address the limitations of these models. The rigorous simulation of three-dimensional, transient effects will allow, for the first time, quantitative analyses of segregation phenomena in microgravity systems. This capability will be extremely important for the unambiguous interpretation of flight experiments, and, perhaps more importantly, will provide a tool to design the conditions needed in future flight experiments to best study the effects of microgravity on segregation theory.

Methodology and Results

We employ the finite element method coupled with a fully implicit time-integration technique to solve the transient, three-dimensional momentum, continuity, and transport equations. The Newton–Raphson iterative scheme is used to solve the resulting equation set at each time step, and the GMRES (Generalized Minimal Residual) iterative scheme is used to solve the linear systems arising in the Newton–Raphson iterations. We have implemented this algorithm on the Cray T3E, a massively parallel, distributed memory supercomputer, at the University of Minnesota Army High Performance Computing Research Center.

While we have made substantial progress in our capability to compute three-dimensional, transient flows, there are several areas in which our software needs to be extended to enable the detailed modeling of Bridgman crystal growth under microgravity. Two extensions have already been completed. In order to accurately represent effects caused by the ampoule and container, we have modified the code to solve for heat transfer through multiple domains with unequal physical properties. We have also implemented a rigorous, self-consistent methodology to solve for the location and shape of the moving melt/crystal interface location. These extensions have allowed us to compute the flow, temperature distribution, and interface location in a prototype problem of steady-state solidification in a solid-liquid system.

Several additional extensions are required to complete our code development. One extension is to solve for coupled, time-dependent mass transport, to enable segregation studies throughout a growth run. Another is to provide for realistic thermal boundary conditions by coupling our code with an appropriate representation of global (furnace) heat transfer. Also to be implemented are provisions to represent free-surface traction boundary conditions caused by surface tension gradients, so that three-dimensional Marangoni flows can be calculated. This approach will be needed to consider imperfections caused by bubbles or melt dewetting. We anticipate that implementing the above code modifications will be straightforward and have confidence in the current capabilities of the underlying algorithm and implementation.

Reactions and Surface Transformations of a Bone-Bioactive Material in a Simulated Microgravity Environment

S. Radin[1], P. Ducheyne[1], and P.S. Ayyaswamy[2]
Center for Bioactive Materials and Tissue Engineering
University of Pennsylvania
Philadelphia, PA 19104-6315

[1] Department of Bioengineering
School of Engineering and Applied Sciences

[2] Department of Mechanical Engineering and Applied Mechanics
School of Engineering and Applied Sciences

A comprehensive program to investigate the expeditious *in vitro* formation of three-dimensional bone-like tissue is currently underway at the University of Pennsylvania. The study reported here forms a part of that program. Three-dimensional bone-like tissue structures may be grown under the simulated microgravity conditions of NASA designed Rotating Wall Bioreactor Vessels (RWV's). Such tissue growth will have wide clinical applications. In addition, an understanding of the fundamental changes that occur to bone cells under simulated microgravity would yield important information that will help in preventing or minimizing astronaut bone loss, a major health issue with travel or stay in space over long periods of time.[1] The growth of three-dimensional bone-like tissue structures in RWV's is facilitated by the use of microcarriers which provide structural support. If the microcarrier material additionally promotes bone cell growth, then it is particularly advantageous to employ such microcarriers.

We have found that reactive, bone-bioactive glass (BBG) is an attractive candidate for use as microcarrier material.[2] Specifically, it has been found that BBG containing Ca- and P- oxides upregulates osteoprogenitor cells to osteoblasts.[2] This effect on cells is preceded by BBG reactions in solution which result in the formation of a Ca-P surface layer. This surface further transforms to a bone-like mineral (i.e., carbonated crystalline hydroxyapatite (c-HA)). At normal gravity, time-dependent, immersion-induced BBG reactions and transformations are greatly affected both by variations in the composition of the milieu in which the glass is immersed and on the immersion conditions.[3] However, the nature of BBG reactions and phase transformations under the simulated microgravity conditions of RWV's are unknown, and must be understood in order to successfully use BBG as microcarrier material in RWV's. In this paper, we report some of our recent findings in this regard using experimental and numerical methods.

BBG composition 45S5, the most reactive among known bone-bioactive glasses,[4] was chosen for the study. BBG 45S5 behavior in physiological solutions was tested in simulated microgravity and compared with that at normal gravity. On the basis of our numerical study,[5] we have chosen the BBG granule size to be in the range 40-70 μm, and a RWV rotational speed of 10 rpm. Our numerical study has shown that these parameters enable the microcarrier to remain suspended in the medium without experiencing collisions with the wall of the vessel. Immersion-induced changes in the solution composition and the material surface were analyzed after immersion.

Materials and Methods

Immersion experiments were conducted in tris(hydroxylmethyl)aminomethane buffered solution (pH 7.4 at 37 °C) both in the simulated microgravity environment of a High Aspect Ratio Vessel

(HARV-50 ml, Synthecon, Houston, Texas) and in normal gravity. Melt-derived bone-bioactive glass (BBG) 45S5 (W,%: 45.3 % SiO_2, 23.9 % CaO, 24.8 % Na_2O and 6.2 % P_2O_5) granules (MO-SCI Co., Rolla MO) were immersed at 1 mg/ml weight-to-solution volume (W/V) ratio for 1, 3, 6, 10 and 24 hours.

Prior to studying the immersion-induced reactions of BBG under the simulated microgravity conditions, we conducted an experiment with gold coated BBG particles in order to observe the tracjectories of the particles in the HARV at 10 rpm and the 1 mg/ml W/V ratio. The particles were sputter coated with a thin (about 200 Å) layer of gold to make them visible in solution. This experiment with gold-coated particles confirmed that most of the particles, in an inertial frame, circled around the center of the rotating chamber during immersion up to 24 hours. Particles employed for the actual immersion study were without gold coating.

After immersion, the solutions were analyzed for changes in the Si, Ca and P-concentrations using atomic absorption spectroscopy (5100, Perkin-Elmer, Norwalk CT) and colorimetry (Ultraspec Plus Spectrophotometer, Pharmacia LKB, Piscataway NJ). The BBG surface was analyzed prior to and after immersion using Fourier transform infrared spectroscopy (FTIR, 5DXC, Nicolet, Madison WI).

Results and Discussion

Figures 1 a-c show changes in the P, Ca- and Si-concentrations as a fuction of immersion time of BBG granules in tris buffered solution both under simulated microgravity (HARV) and unit gravity conditions. The data indicate that the following reactions have occurred in both environments: an initial leaching of all ions, subsequent uptake of P-ions and solution saturation with Si-ions. Although the sequence of these reactions was similar under both conditions, the kinetics were different as indicated by a remarkable increase in the rate and amount of both release and uptake under simulated microgravity conditions. Specifically, whereas the amounts of P- and Ca-ions released during the initial stage (prior to uptake) under unit gravity were 10 ppm (0.32 mM) and 80 ppm (2 mM) respectively, a two-fold increase to 180 ppm Ca (4.5 mM) and 70 % increase to 17 ppm P (0.55 mM) were observed under simulated microgravity. These observations suggest that the enhanced release of Ca- and P-ions in the HARV environment led to a dramatic rise in solution supersaturation with regard to Ca-P phases. The data also showed that the time to detectable P-uptake, indicative of precipitation of Ca-P phases, was reduced from 3 hours under unit gravity to 1 hour under simulated microgravity. Moreover, the amount of P-uptake, i.e. the difference between the highest and the lowest concentrations measured prior to uptake and at 24 hours respectively, was increased from 8.7 ppm at unit gravity to 14.4 ppm at simulated microgravity suggesting an significant increase of the amount of Ca-P precipitates. The HARV environment also affected the pattern of Ca-uptake; it was observed after 1 hour immersion in HARV, but was not detected under unit gravity. Concerning Si-release, the saturation concentration of 65 ppm was reached after 3 hours in the HARV environment in comparison to 6 hours in normal gravity.

Chemical and structural changes of the BBG surface resulting from the immersion-induced reactions are indicated by the FTIR spectra shown in Fugure 2. The FTIR spectrum of unreacted (before immersion) particles shows absorption bands characteristic of silica network of unreacted 45S5 glass.[4] Bands assigned to P-O and C-O vibrations were present in the spectra after 6 hours of immersion under both unit gravity and simulated microgravity conditions. The appearance of these bands suggests the formation of a carbonated Ca-P phase on the glass surface. Splitting of the lower energy P-O band indicates that the phase was crystalline and as such is carbonated hydroxyapatite (c-HA). The analysis also points out that, although the formation of the c-HA layer on the BBG surface occurred under both conditions, the layer formed under simulated microgravity was significantly thicker than that formed under unit gravity. This was indicated by a greater P-O/Si-O intensity ratio in the lower energy region of the spectrum of BBG after immersion in the HARV environment compared to that in unit gravity.

The combined solution and surface analyses suggest that the following events occurred upon immersion of BBG granules under both testing conditions: dissolution of BBG (indicated by the release of Si- Ca- and P-ions); saturation of solution with Si-ions and supersaturation of originally Ca-P-free solution with these ions followed by precipitation of Ca-P phases (indicated by P- and Ca-uptake); growth of Ca-P precipitates with immersion (suggested by continuous uptake). The analysis also revealed that, although the sequence of the events was similar under both conditions, the kinetics were significantly affected by the simulated microgravity environment, i.e. both dissolution and precipitation reactions were enhanced. In addition, the surface analysis (FTIR) pointed out that a layer (~ 1 μm thick) of bone-like apatite, i.e. carbonated crystalline hydroxyapatite (c-HA) was formed on glass granules after 6 hours of immersion in both conditions; however, this surface layer was significantly thicker on granules which reacted under simulated microgravity in comparison to those in unit gravity. This finding suggests that crystallization of Ca-P precipitates, essential for the bone-bioactive behavior of BBG, was also enhanced by the simulated microgravity conditions.

Conclusions

The study has demonstrated that the simulated microgravity environment remarkably enhances the kinetics of BBG reactions that are associated with bone-bioactive behavior.

Our ongoing study on the effect of simulated microgravity on the BBG reactions, associated with bone-bioactivity, includes testing BBG in solutions closely mimicking the electrolyte and organic content of plasma, as well as expanding the number of measurements in order to produce statistically significant data in all solutions.

References

1. L.E. Freed and G. Vunjak-Novakovic, *Biotech. Bioeng.*, 46, 306 (1995).
2. P. Ducheyne, ch. 9 in: "Hip surgery: New materials and developments," L. Sedel and M. Cabanela, eds., Martin Dunitz, London (1998).
3. S. Radin *et al.*, *J. Biomed. Mat. Res.*, 37, 363-375 (1997).
4. L.L. Hench, *J. Am. Cer. Soc.*, 74, 1487-1510 (1991)
5. H. Gao *et al.*, *Microgravity Sci. Technol.*, X1/1 (1998).

Acknowledgment

This work was supported by NASA-NRA grant NAG 8-1483.

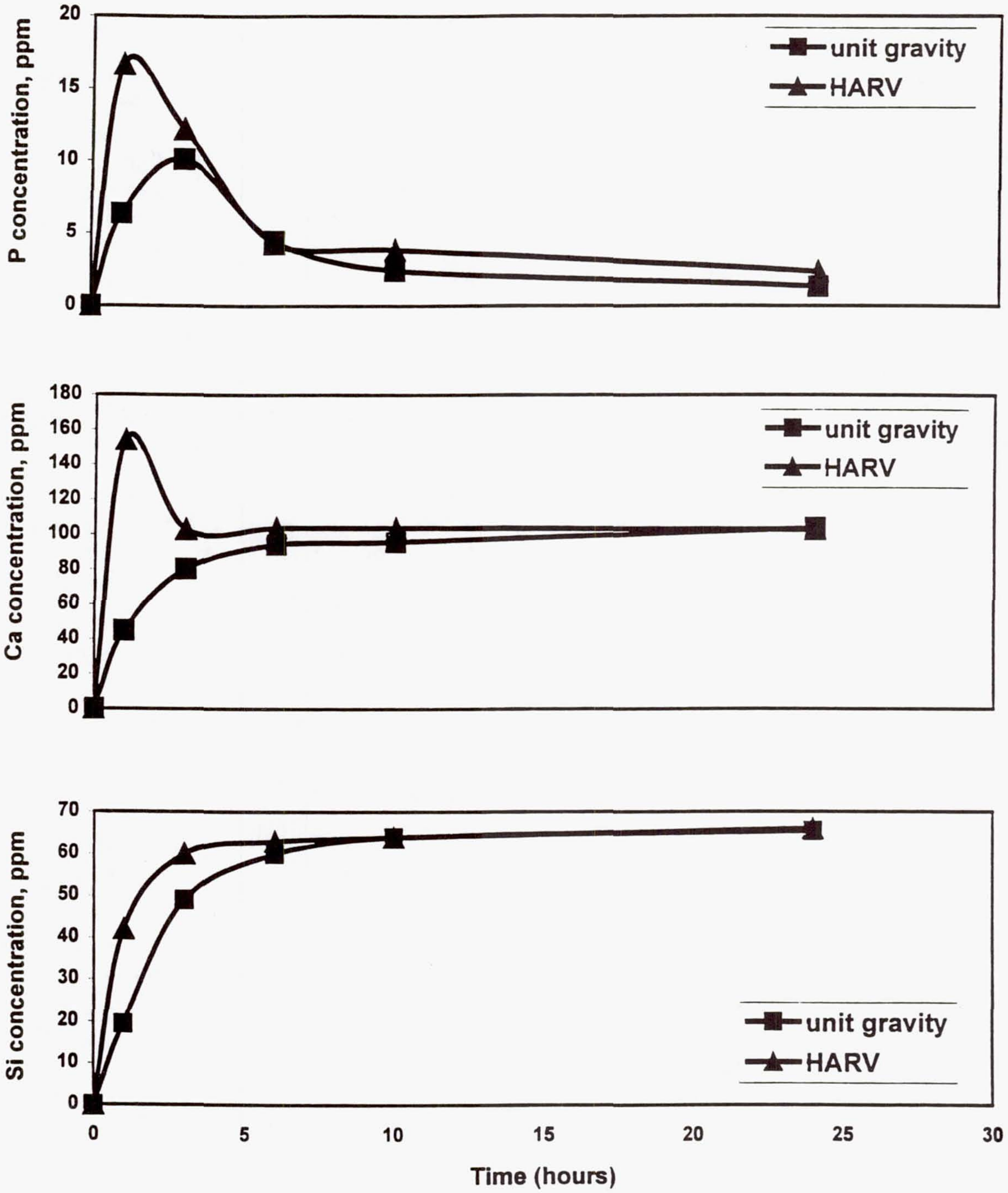

Figures 1 a-c. Changes in the concentrations of P-, Ca- and Si-ions as a fuction of immersion time in tris buffered solution (pH 7.4 at 37^{0}C) under simulated microgravity (HARV) and unit gravity conditions.

A remarkable increase in the rate and the amount of initial release of all ions (dissolution) and the following uptake of P- and Ca-ions (precipitation) was observed in the simulated microgravity environment of the HARV.

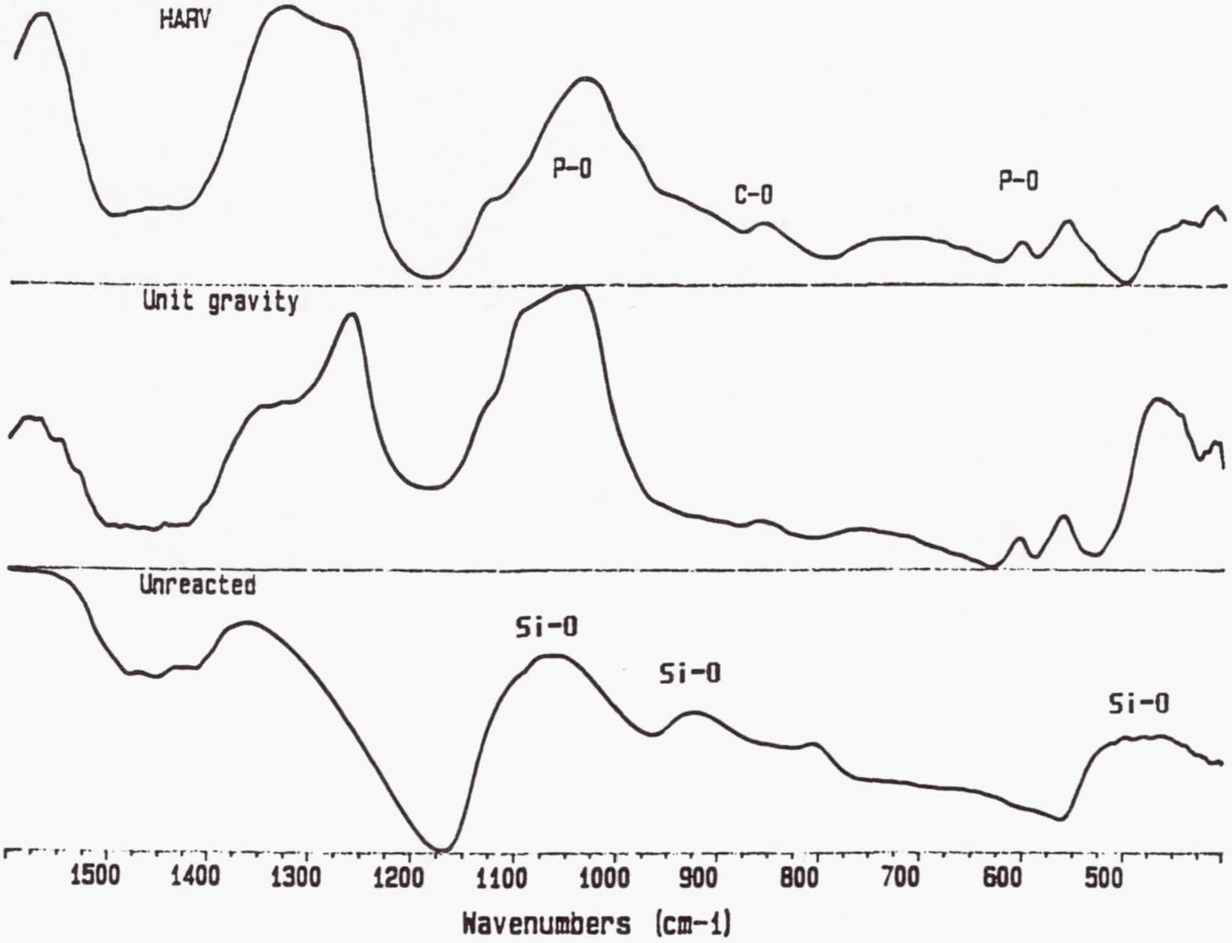

Figure 2. FTIR spectra of BBG granules before immersion (unreacted) and after 6 hours of immersion in tris buffered solution under simulated microgravity (HARV) and unit gravity conditions. The appearance of P-O and C-O bands (which were not present before immersion) on both spectra of reacted granules indicates formation of a layer of crystalline carbonated hydroxyapatite (c-HA), bone-like apatite, on the glass surface. However, the apatite layer formed under simulated microgravity was significantly thicker than that formed under unit gravity (as suggested by a greater ratio of the P-O/Si-O intensity in the lower energy region).

Page intentionally left blank

COMBINED SYNCHROTRON WHITE BEAM X-RAY TOPOGRAPHY AND HIGH RESOLUTION TRIPLE AXIS X-RAY DIFFRACTION CHARACTERIZATION AND ANALYSIS OF CRYSTALS GROWN IN MICROGRAVITY AND GROUND-BASED ENVIRONMENTS

M. Dudley (P.I.),
Dept. of Materials Science & Engineering,
SUNY at Stony Brook, Stony Brook NY 11794-2275
(516)-632-8500; FAX (516)-632-8052; e-mail: mdudley@ccmail.sunysb.edu

R.J. Matyi (Co-I.),
Dept. of Materials Science & Engineering,
University of Wisconsin-Madison, 1500 Engineering Drive, Madison WI 53706
(608)-263-1716; FAX (608)-262-8353; e-mail: matyi@engr.wisc.edu

Research Objectives and relevance to Microgravity

The objective of the research proposed here is to carry out detailed studies of defect and general distortion distributions in crystals grown in both microgravity and ground based environments (e.g. using modified Bridgman, Vapor Transport or Traveling Heater Method techniques) using a combination of synchrotron white beam X-ray topography (SWBXT)[1] and high resolution triple crystal X-ray diffractometry (HRTXD).[2] This unique combination of techniques is expected to reveal detailed differences between crystals grown in these two different environments and to enable meaningful assessment to be made of the influence of a microgravity environment on various aspects of the quality of crystals grown therein. SWBXT and HRTXD are complementary analytical techniques which are most sensitive and useful at contrasting ends of the "scale" of defect densities in crystals. By applying both techniques to the same crystals, it will be possible to provide detailed and quantitative assessments of the defect structure from regions that range from highly perfect (where SWBXT is expected to be the superior characterization tool) to highly imperfect (where HRTXD should be the superior method). This unified and continuous view of the defect structure should lead to valuable insights into the effect of growth conditions on the defect generation process. The proposed research program will draw upon the extensive experience that has been gained at the State University of New York - Stony Brook and University of Wisconsin - Madison in the analysis of defects in semiconductors using advanced methods of X-ray diffraction. Prof. Michael Dudley of SUNY - Stony Brook has worked closely with the crystal growth community at NASA's Marshall Space Flight Center (MSFC) in applying methods of SWBXT to numerous semiconductor crystals grown both on earth and in microgravity. His counterpart, Prof. Richard Matyi of UW - Madison, has been actively engaged in demonstrating the capabilities of HRTXD to a variety of semiconductor materials. By combining these complementary techniques it should be possible to obtain a deeper understanding of the process of defect generation than would be possible with either technique alone, or perhaps by any structural probe.

The significance of the research described here is that it will directly determine the influence of a microgravity environment on the detailed defect and distortion distribution in crystals produced in flight experiments, and will enable direct comparison to be drawn with crystals produced in ground based experiments. Confirmation has already been obtained that effects resulting from the limited flight times available for microgravity crystal growth experiments can exert control over the microstructure of the crystals grown, potentially detracting from the intended assessment of the influence of the magnitude of the gravity vector on these processes. Determination of the influence of cooling rate on the defect microstructure of crystals is crucial for selection of experimental conditions under which the effects of the gravity vector on crystal growth quality can be usefully investigated. Once such selection has been optimized, differences in microstructure observed in microgravity grown crystals may be safely attributed to the influence of the gravity vector and not to artifacts related to compressed growth schedules.

Significant Results to Date and Future Plans

In the past year, cooperative studies have been carried out on the following materials: ground-based ZnSe,[2] grown by Dr. C.-H. Su; ground-based $Hg_{1-x}Cd_xTe$, grown by Dr. D.C. Gillies; and ground-based and flight-based CdZnTe,[3,4,5] grown by Dr. D.J. Larson Jr. (USML1). Selected results from ZnSe (figure 1) and $Hg_{1-x}Cd_xTe$ (figure 2) will be presented here. Preliminary comparison of results obtained by these two techniques further emphasizes their complementary nature and usefulness for complete, quantitative characterization of crystal growth quality, and for the assessment of the influence of growth conditions thereon.

For ZnSe, two as-grown boules (43 and 45) as well as several individual wafers cleaved from different boules, all grown by Dr. C.-H. Su, have been studied in detail using SWBXT. A preliminary correlation between HRTXD and SWBXT data from one of these boules (43) and one of these wafers (32) has already been carried out. Selected results from boule 43 are presented here. HRTXD analysis was performed on a large $(0\bar{1}1)$ facet on the surface of the boule. SWBXT in reflection mode was carried out over all facets and surfaces of the boule. Topographs and HRTXD scans, recorded from the large $(0\bar{1}1)$ facet, are shown in figure 1.

SWBXT clearly reveals that boule 43 is extensively twinned (twinning in ZnSe appears to follow the theory of Hurle,[6] recently modified by Dudley et al[7,8]). Both triple axis diffraction scans and double axis rocking curves recorded from position **A** reveal the presence of peak splitting. This is due to the x-ray footprint (in this case $3\times0.1mm^2$) partially straddling the twin boundary leading to contributions from both matrix and twinned regions. Even though the $0\bar{2}2$ and $02\bar{2}$ reciprocal lattice vectors, respectively from matrix and twin regions, are nominally parallel, there is a slight lattice misfit at the twin boundary leading to the small degree of lattice rotation which becomes apparent on the triple and double axis scans as well as on the $0\bar{2}2$ topograph. The distortion associated with the inclusion at **B** is evident in both sets of results. Good agreement between the topography and both double and triple axis results is apparent.

For the case of $Hg_{1-x}Cd_xTe$, research was carried out on several wafers sliced from boules grown, using the traveling solvent zone method (Te solvent), both in the presence and absence of an applied magnetic field. Since the composition in the crystal varied along the two boules, adjacently sliced wafers, with similar composition were studied using SWBXT and HRTXD.

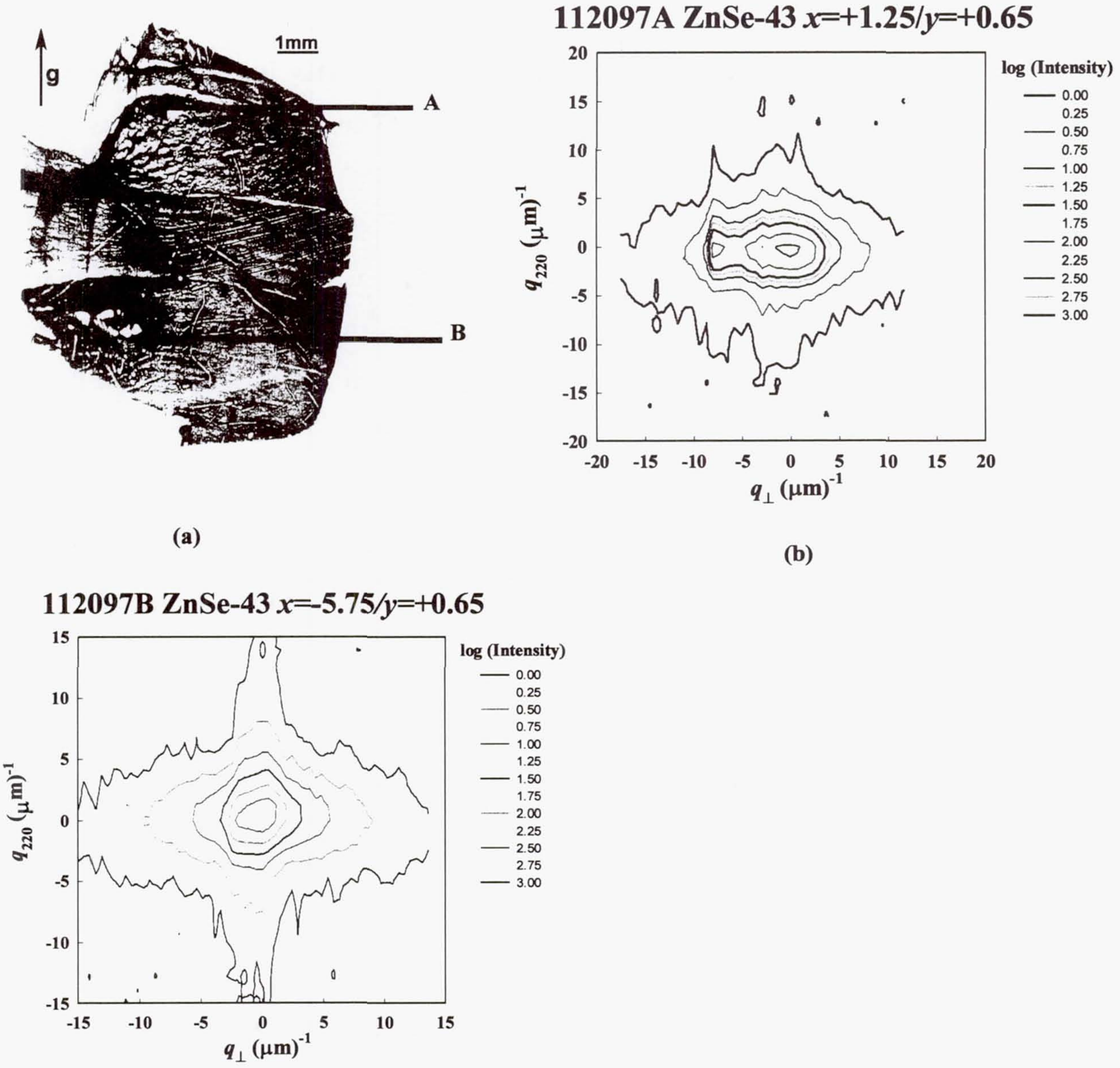

(a)

(b)

(c)

Figure 1. (a) SWBXT image, recorded in reflection mode, from large $(0\bar{1}1)$ facet on ZnSe boule 43 - $0\bar{2}2$ reflection exhibiting the absence of orientation contrast, showing contributions from matrix and twin; (b)-(c) triple axis diffraction scans from regions marked A and B in (a).

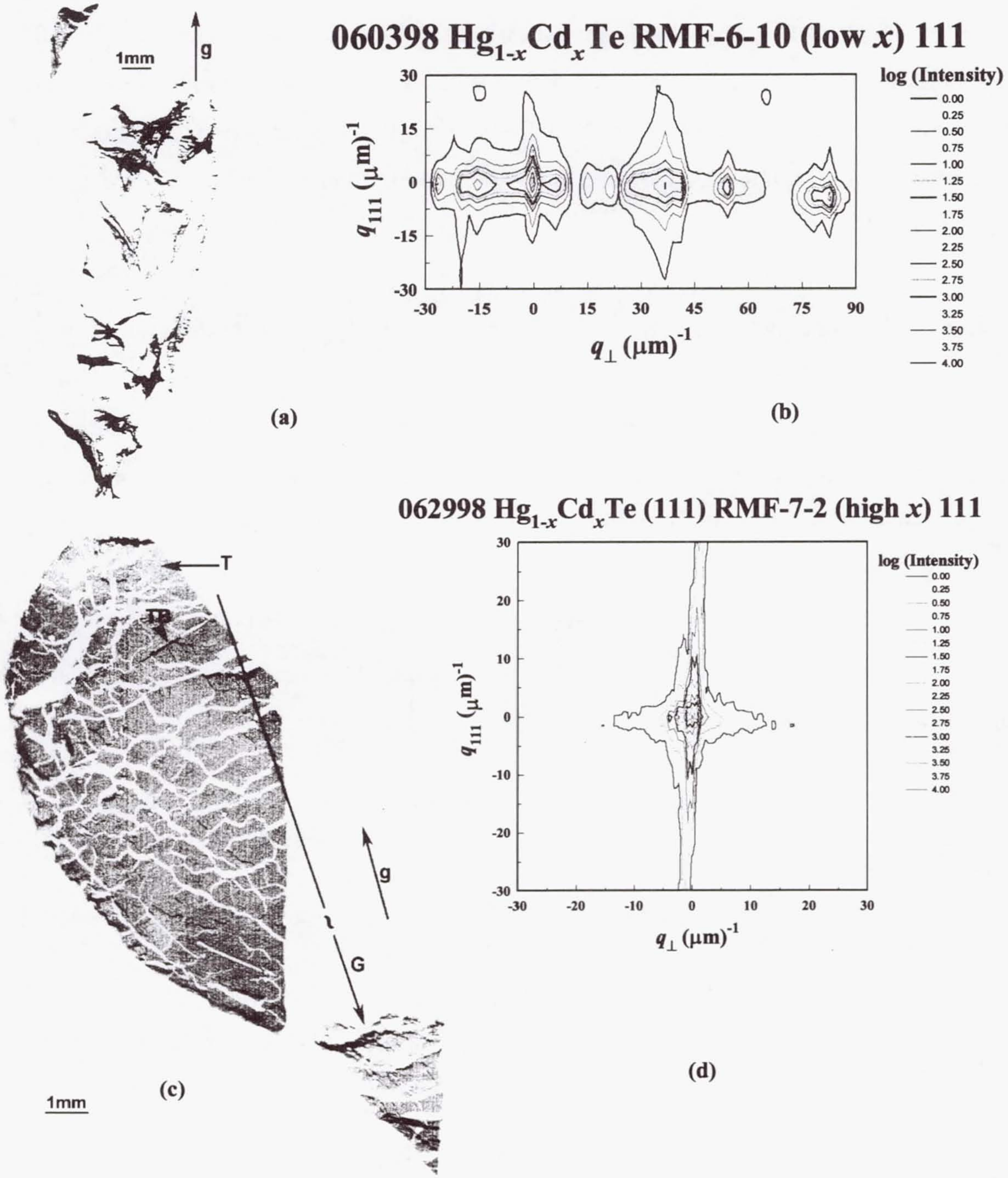

Figure 2. (a) SWBXT image from a low *x* value $Hg_{1-x}Cd_xTe$ wafer grown in the absence of field; (b) HRTXD scan from similar low *x* value wafer to that in (a); (c) SWBXT image recorded from a high *x* value wafer grown in the presence of an applied magnetic field; (d) HRTXD scan from similar high *x* value crystal.

SWBXT images and HRTXD scans recorded from both high and low x value wafers, with and without an applied magnetic field, are shown in figure 2. Both techniques reveal clear differences, with the crystals grown in the presence of the field exhibiting much higher structural quality. Small angle boundaries, with tilt angle between 0.5 and 2.5 minutes of arc are evident on the topograph. The HRTDX footprint is smaller than the average grain size and so does not readily reveal these boundaries.

In future work, a complete description will be sought of the type and distribution of all defects present in the crystals to be examined. Crystals will initially be examined in boule form using both SWBXT and HRTXD in reflection geometry in order to reveal the overall distribution of defects and distortion around the crystal surface. This will help determine the optimal wafering geometry to be adopted for the next stage of the research. SWBXT and HRTXD will then be used, in sequence, to examine the defect and distortion distributions in each of the wafers. Information so gathered will then be compiled to reconstruct to complete three dimensional defect and distortion distributions in the as-grown boule. This reconstructed information can then be used to compare with the predictions of growth models.

1. M. Dudley, in "Applications of Synchrotron Radiation Techniques to Materials Science", D.L. Perry, R. Stockbauer, N. Shinn, K. D'Amico, and L. Terminello (Eds.) **Mat. Res.Soc. Symp. Proc., 307**, 213-224, (1993).
2. J. Su, H. Chung, Y. Guo, M. Dudley, H.M. Volz, C. Salles, and R.J. Matyi, **Advances in X-ray Analysis**, **41**, 1998 (In Press).
3. H. Chung, Ph.D Thesis, Stony Brook, (1997).
4. B. Raghothamachar, H. Chung, M. Dudley, D. Larson, Jr., **Advances in X-ray Analysis**, **41**, 1998 (In Press).
5. M. Dudley, D.J. Larson Jr., H. Chung, and B. Raghothamachar, Proceedings of 31st COSPAR Scientific Assembly, Birmingham, UK, July 14-21, 1996, **Advances in Space Research**, (1998) (In Press).
6. D. T. J. Hurle, **J. Cryst. Growth, 147**, 239 (1995).
7. H. Chung, M. Dudley, D. J. Larson, Jr., D. T. J. Hurle, D. F. Bliss and V. Prasad, **J. Crystal Growth**, **187,** 9-17, (1998).
8. M. Dudley, B. Raghothamachar, Y. Guo, X.R. Huang, H. Chung, D. T. J. Hurle, and D. F. Bliss, **J. Crystal Growth,** (1998), (In Press).

Reverse Micelle-Based Synthesis of Microporous Materials in Microgravity

Prabir K. Dutta
Department of Chemistry
The Ohio State University
Columbus, OH 43210; dutta.1@osu.edu

Introduction

Microporous materials are crystalline frameworks with well defined cages and channels of molecular dimensions varying from 2 to 8 Å.[1] Various elements such as silicon, aluminum, zinc, phosphorus, gallium and transition metals can form the backbone of the framework. These elements, abbreviated as T and T' make up the framework through T-O-T' linkages. The most commonly used microporous frameworks are aluminosilicate zeolites. These find extensive use in detergents and catalysts. The ion-exchange of the extraframework ions are exploited in detergent use. The catalytic behavior arises because superacidity can be introduced into these frameworks and the topography of the channels and cages influence product formation. Discovery of novel frameworks can have significant impact on practical applications, as in the recent introduction by Unilever of a new zeolite in detergents and the use of ZSM-5 in petroleum cracking. Thus, there is considerable effort worldwide in the synthesis of new frameworks. Microporous materials are typically made under hydrothermal conditions. Influence of the nature of starting reactants, structure directing agents, pH, temperature, aging -- all have profound influence on microporous material crystallization.[2] This is primarily because the most interesting open frameworks are not stable structures in the synthesis medium. Thus, the discovery of new structures is often tied to finding the right reaction conditions that allow for kinetic stabilization of the structure. Because of the complexity of the synthesis process, most advances in microporous materials synthesis are made by trial and error. There has been a concerted effort over the past few decades to gain a comprehensive understanding of the crystal growth process, which would result in more directed synthesis of these materials.

The important issues in crystal growth are:

- molecular structure and assembly of the nuclei
- nature of the nucleation process
- growth of nuclei into crystals
- factors influencing morphology
- transformation of frameworks into subsequent structures.

The NASA-funded research described here is involved in exploring all the above issues of microporous materials nucleation and crystal growth. Our synthetic approach is significantly different from conventional synthesis because our focus has been to design methods that will be eventually tested in microgravity. We summarize below our recent results. Experimental aspects of our research can be found in several publications.[3-5]

Results and Discussion

A New Route of Synthesis: Conventional synthesis of microporous materials usually involves mixing together reactants in an aqueous medium and results in immediate formation of an amorphous material, usually referred to as the gel from which crystal growth occurs. The complexity of the reaction mixture makes it difficult to examine the process. An advance has been to examine synthesis from clear solutions.[6] However, even in these clear solutions there are nanometer sized particles that are thought to play a critical role in the nucleation process. In our synthesis procedure, reactants are dispersed in small droplets of water in a oil-like medium with the help of detergents. These nanoclusters of water are called reverse micelles and a schematic of such a micelle is shown in Figure 1. The reactants in two different micelles can exchange with one another upon collision and if the conditions are appropriate, nucleation can occur.

The detergents that are responsible for dissolving the water pool in the hydrocarbon come in a variety of forms and we have discovered that they have a profound influence on the crystallization process of microporous materials. This dependence in itself has provided some insight on the crystallization process. Figure 2 shows the three detergents that have been examined in this program.

Our focus has been on the synthesis of zincophosphates, referred to as ZnPO. The detergent AOT has been extensively examined in the literature for formation of reverse micelles and used in synthesis of semiconductors and metal particles.[7] Our initial focus was with this detergent. Figure 3 shows the first microporous material, zincophosphate sodalite that was made using reverse micelles, along with the powder diffraction pattern and electron micrograph.

Synthesis of Open Frameworks: Considerable efforts were made to make other framework structures by primarily changing the Zn and phosphate concentrations in the AOT reverse micelles. More condensed phases than sodalite, such as hopeite and P6l could be formed, but all attempts at synthesizing more open structures (especially ZnPO-X) failed. Careful IR spectroscopy of the water in AOT reverse micelles showed that the presence of Na^+, the neutralizing ion for the sulfonate group of AOT was disrupting the structure of water that was necessary to nucleate the open-pore framework of ZnPO-X. This led us to examine a neutral surfactant, Tween 85, shown in Figure 2b. All attempts with Tween 85 based reverse micelle also led to the formation of sodalite or more condensed phases such as hopeite. We did not investigate this system in as much detail as we did AOT, but concluded that it was difficult to get the appropriate water loading into the micelle. Experiments with the cationic reverse micelles, Figure 2c, led to the formation of open framework ZnPO-X. Figure 4 shows the framework structure, SEM and the diffraction pattern. It is unclear as yet if the surface of the DODMAC reverse micelle is playing an added role in the nucleation of ZnPO-X. This may indeed be true because tetramethylammonium ion, (TMA^+) is used as a structure directing agent for ZnPO-X, and two of the methyl groups in DODMAC point into the inside of the reverse micelle (resembles half a TMA ion), the site for ZnPO-X nucleation. The fact that the open structure ZnPO-X could only be grown from DODMAC reverse micelles indicates that the structure of water and cation-water complexes plays an important role in the nucleation of open frameworks. A hypothesis of this action is that the particular ordering of the phosphate ions can be influenced by the competition between cation (such as Na^+) ordering of water and the ordering imposed by the template ion, TMA^+.

Control of Crystal Growth We have also discovered that reverse micelles provide an effective way to control supersaturation and therefore the route to crystal growth. Experiments are done by reacting a zinc containing reverse micelle with a phosphate micelle. As these micelles collide with each other, they build a distribution of micelles with varying zinc and phosphate contents in the micelles. Depending on the intramicellar pH which determines the types of phosphate species, the supersaturation conditions will only exist in a certain fraction of the reverse micelles. This control of supersaturation has a profound influence on the crystal growth mechanism, dynamics and eventual morphology of the crystals. This was best demonstrated in the case of sodalite growth using the AOT reverse micelle system. The supersaturation was controlled by intramicellar pH which led to formation of a different distribution of phosphate species. Under conditions where pH was high, the supersaturation condition for zincophosphate precipitation was not exceeded. This led to a slow crystal growth process in a layer-by-layer fashion. On the other extreme, at low intramicellar pH, the supersaturation conditions were exceeded for a large number of zinc and phosphate containing reverse micelles, and there was extensive precipitation of amorphous zincophosphate. In the low supersaturation case, the nuclei that were developed in a small fraction of reverse micelles were fed by nutrients from the other reverse micelles. This is only possible in a reverse micellar system because it is possible to maintain quite different compositions in different reverse micelles, but all in the same reaction system. If supersaturation is exceeded as in the reverse micelles at low pH, then crystal growth occurs by restructuring of the amorphous gel via a surface mediated solution mechanism. This has the counterpart in conventional microporous material synthesis, where crystal growth occurs in the presence of the amorphous gel. Intermediate levels of supersaturation can also be obtained by careful control of intramicellar pH, in which crystal aggregates are formed.

Influence of Sedimentation on Crystal Growth We have had less experience with crystal growth in the Tween-85 and DODMAC systems. But the preliminary results are similar to that of the AOT system. In particular, we were interested in the method of crystal growth at low supersaturation where single crystals were growing in a layer-by-layer fashion. It was apparent that if these crystals could be suspended for longer periods of time, then larger crystals could be grown. In order to suspend crystallites for longer periods of time, we built a rotation cell and tested it with the sodalite/AOT system. Even though this accomplished the purpose of suspension, there was enough motion that crystallites assumed different shapes. This is an indication that motion of nutrients around growing crystals influences morphology. Another attempt to examine the effect of suspension was to grow crystals in a long narrow column and collect crystallites at different periods of time. These experiments were tried out with ZnPO-X/DODMAC system. The octahedral crystals gradually increase in size with suspension time. In summary, the reverse micelle system has led to the following advances in understanding of microporous materials synthesis:

a. Role of water and cation/water structure in synthesis.
b. Control of crystal growth process by adjusting supersaturation conditions.
c. Distinguishing different pathways of crystal growth for the first time.
d. By using different detergents, we have established the generality of the reverse micelle method for growing microporous materials.
e. Discovery of a layer-by-layer growth provides opportunity for growing large crystals if conditions for suspension can be maintained.

Crystal Dissolution and Convection Effects One of the critical issues in microporous materials crystal growth is the nature of the building blocks that assemble to form the growing crystal. There has been considerable speculation in the literature about secondary building units, but there has been no direct evidence for such structures. In order to observe these building units, it is clear that a spectroscopic tool is required. The problem is that every spectroscopic tool measures properties of the whole system, whereas the specific building units are few in number. Thus, the problem is to discriminate the signal of a small number of building units from a large background and to the best of our knowledge, this has not been done.

Another approach is to examine dissolution of crystals. Here, the issue of background signal is absent and spectroscopic analysis becomes straightforward. We have taken this strategy with ZnPO-X. The probe of choice is Raman spectroscopy, which via vibrational spectroscopic data provides information on the structural changes. We have also made another significant advance in the crystallization of ZnPO-X. Typically, ZnPO-X grows as octahedra with the (111) faces exposed. These crystals are of the size of 10-20 μm. It is difficult to properly focus the Raman excitation light on the crystal and any motion disrupts the focal plane because of the sloping geometry of the (111) face relative to the focused laser light (about ~5 μm). However, if a single twin fault plane is introduced into the octahedron, then a flat crystal is obtained. We have discovered conditions in which we can grow large platelet (>100 μm) crystals of ZnPO-X, which makes it possible to study the flat (111) face.

Raman microprobe spectroscopy of the surface of the ZnPO-X crystal was measured at various pH's. Under acidic pH conditions, the ZnPO-X crystal dissolves. ZnPO-X has two types of cages (Figure 4). Tetramethylammonium ion, trapped within the smaller sodalite cages exhibits the symmetric C-N stretching frequency higher than that of free TMA ion. Thus, this band is a direct measure of the presence of sodalite cages in the ZnPO-X structure. Comparison of the intensity of this band versus the P-O stretching modes characteristic of ZnPO-X could for example suggest if the sodalite unit is maintained while the P-O-Zn structure connecting the sodalite cages is disrupted.

The Raman spectra of the surface was monitored as a function of dissolution time with the whole system being stirred. The intensity of the TMA^+ peak decreased at the same rate as that of the phosphate peak of ZnPO-X indicating that there was no particular stabilization of the sodalite unit. The experiment was repeated under static conditions, with the crystal in a still solvent environment. Both the spectroscopy as well as the morphology of the crystals observed during the dissolution process under these static conditions was different from the stirred system. The Raman spectrum shows the formation of hopeite. Optical microscopy shows that the morphology is conserved. Electron microscopy indicates that the morphology of the crystal is maintained because hopeite forms an outer cover on the ZnPO-X. This happens because under the nonstirred conditions, as the ZnPO-X dissolves, it forms a transient acidic environment around the crystal, which leads to immediate precipitation of hopeite. This suggests that under convection-free conditions, it may be possible to spectroscopically examine the intermediates of dissolution since their residence times on the surface is going to be considerably longer.

Proposed Experiments in Microgravity There are two aspects of microgravity that we want to exploit. These include lack of sedimentation and absence of buoyancy driven convection. As we have shown above, under particular conditions of reverse micelle composition, crystal growth in a layer-by-layer fashion becomes possible. Avoiding sedimentation in these systems will lead to growth of larger crystals. Light scattering will be used to follow the growth of crystals. Seeding experiments to grow larger crystals is also possible, something that has not been accomplished in conventional synthesis.

The second aspect of the microgravity experiments will focus on microprobe Raman studies on crystal dissolution with primary focus on ZnPO-X. The idea is to evaluate if particular surface intermediates can be distinguished during dissolution. How the crystal falls apart provides information of stability of certain building units and thereby information about the crystal growth process.

References

1. Dyer, A. An Introduction to Zeolite Molecular Sieves, Wiley, Chichester, 1988.
2. Davis, M.E. and Lobo, R.F. *Chem. Mater*. 4, 756 (1992).
3. Dutta, P.K.; Reddy, K.S.N.; Salvati. L.; Jakupca, M. *Nature* 374, 44 (1995).
4. Reddy, K.S.N.; Salvati, L.; Dutta, P.K.; Abel, P.; Su, K.; Ansari, R.R. *J. Phys. Chem.*, 100, 9870 (1996).
5. Castagnola, M.J. and Dutta, P.K. *Microporous and Mesoporous Mater.* 20, 149 (1998).
6. Schoeman, B.J. *Zeolites*, 18, 97 (1997).
7. Fendler, J.H. *Chem. Rev.* 87, 877 (1987).

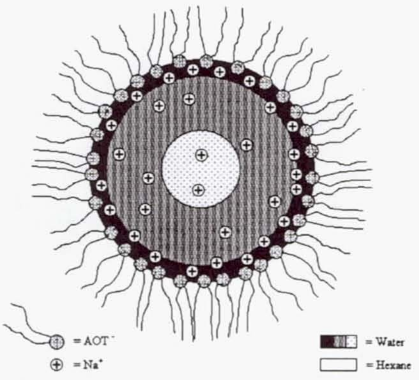

Figure 1. Schematic of a reverse micelle.

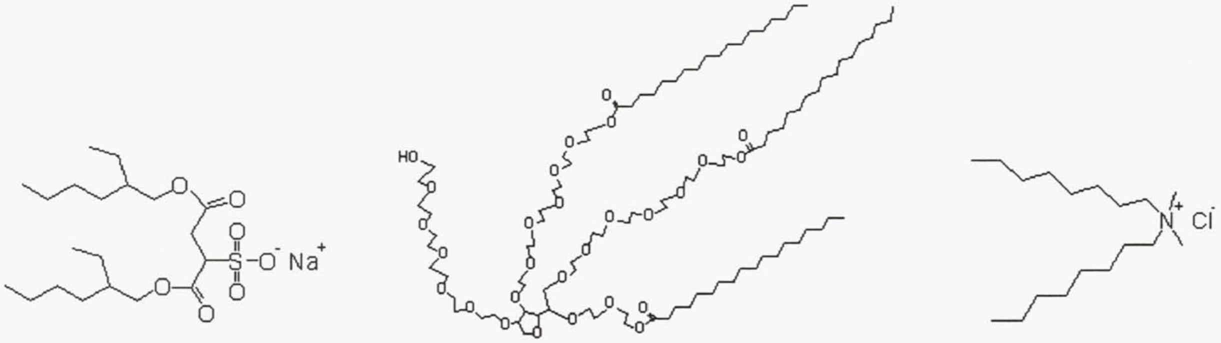

AOT
(a)

Tween-85
(b)

DODMAC
(c)

Figure 2. Different detergents used in this study.

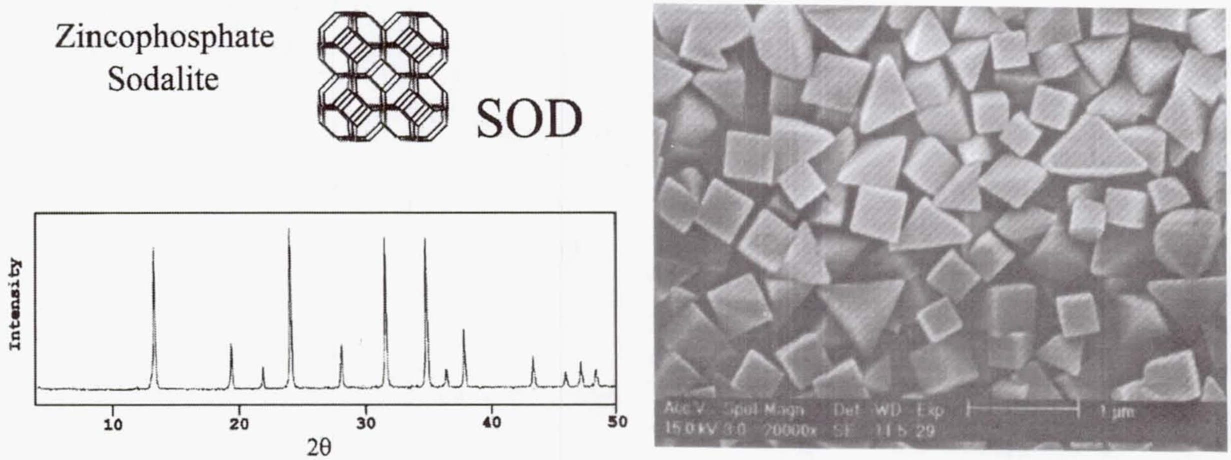

Figure 3. Structure, scanning electron micrograph and diffraction pattern of sodalite formed from AOT reverse micelles.

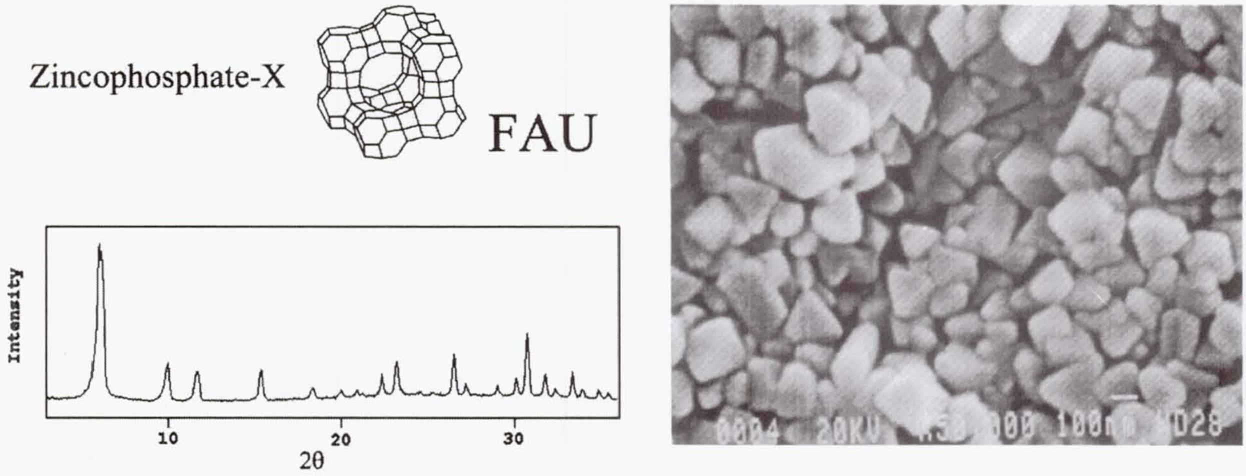

Figure 4. Structure, scanning electron micrograph and diffraction pattern of ZnPO-X formed from DODMAC reverse micelles.

SYNTHESIS OF SEMICONDUCTOR AND METAL OXIDE NANOPARTICLES BY LASER VAPORIZATION-CONTROLLED CONDENSATION TECHNIQUES

M. Samy El-Shall
Department of Chemistry
Virginia Commonwealth University
Richmond, VA 23284-2006
Phone: (804) 828-3518; Fax: (804) 828-8599
E-Mail: SELSHALL@GEMS.VCU.EDU

Introduction

Nanoparticles often exhibit novel properties, which are different from the bulk materials' properties[1,2]. Many of these properties show strong dependence on size, shape and surface preparation[1,2]. The characterization of these properties can ultimately lead to identifying many potential uses, particularly in the field of catalysis. Research in this area is motivated by the possibility of designing nanostructured materials that possess novel electronic, optical, magnetic, photochemical and catalytic properties. Such materials are essential for technological advances in photonics, quantum electronics, nonlinear optics and information storage and processing.

The primary objective of this work is to develop a novel technique to synthesize nanoparticles of controlled size and composition[3-7]. Our technique combines the advantages of pulsed laser vaporization with controlled condensation (LVCC) in a diffusion cloud chamber under well-defined conditions of temperature and pressure. It allows the synthesis of a wide variety of nanoparticles of metal oxides, carbides and nitrides. Furthermore, the same method can be coupled to plasma and ionic polymerization techniques, thus allowing the incorporation of the metallic nanoparticles within the polymer films. The application of this method under a microgravity environment is expected to allow better control of the microstructure and morphology of these particles since size-induced segregation effects will bw dramatically reduced relative to ambient conditions. It should be possible to grow clusters of well-defined sizes and make layered structures of controlled compositions. The use of laser vaporization will make it possible to vaporize several different metals either simultaneously or sequentially and deposit multilayers of engineered compositions and particle size distributions.

The characterization of the surface-oxidized Si nanocrystals and their photoluminescence (PL) properties of will be discussed here. One of the main goals of this work is to compare the results of the PL from the solid surface-oxidized particles that were previously studied, with those from the incorporated particles in polymer films. We also study the properties of the photochromic nanoparticles of molybdenum and tungsten trioxides prepared by the LVCC method.

Experimental Method

The LVCC method is based on the formation of nanoparticles by condensation from the vapor phase. Previous work was based on using thermal evaporation or sputtering to produce supersaturated metal vapors[1,2]. The LVCC process consists of pulsed laser vaporization of a metal target into a selected gas mixture in a modified diffusion cloud chamber. The laser vaporization produces a high density vapor within a very short time, typically 10^{-8} sec, in a directional jet that allows directed deposition. Desorption is possible from several targets simultaneously, yielding mixed particles. An important feature is the use of an upward diffusion cloud chamber, at well defined temperatures and pressures. A temperature differential between the end plates produces a convection current into which the metal is evaporated. A sketch of the chamber with the relevant components for the production of nanoparticles is shown in Figure 1.

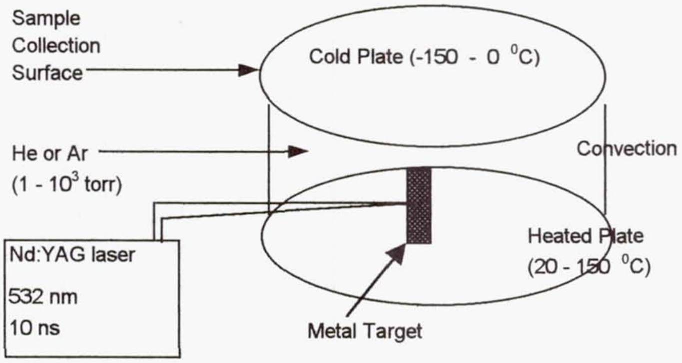

Figure 1. Experimental Set-up for the Synthesis of Nanoparticles by the LVCC Method.

The chamber consists of two horizontal, circular stainless steel plates, separated by a glass ring. A metal target of interest is set on the lower plate, and the chamber is filled with a pure carrier gas such as helium or Ar (99.99% pure) or a mixture containing a known composition of a reactant gas (e.g. O_2 in case of oxides; N_2 or NH_3 for nitrides, CH_4 for carbides, etc.). The metal target and the lower plate are maintained at a temperature higher than that of the upper one (temperatures are controlled by circulating fluids). The top plate can be cooled to less than 150 K by circulating liquid nitrogen. The large temperature gradient between the bottom and top plates results in a steady convection current which can be enhanced by using a heavy carrier gas such as Ar under high pressure conditions (10^3 Torr). The metal vapor is generated by pulsed laser vaporization using the second harmonic (532 nm) of a Nd-YAG laser (15-30 mJ/pulse, 10^{-8} s pulse). The laser beam is moved on the metal surface in order to expose new surface to the beam and assure good reproducibility of the amount of metal vapor produced. Following the laser pulse, the ejection of the metal atoms and their eventual interaction with the ambient atmosphere take place. Since the target surface where evaporation occurs is located near the middle of the chamber (about 0.5 reduced height) and the ambient temperature rapidly decreases near the top plate, it is likely that maximum supersaturation develops within the upper half of the chamber above the surface target (closer to the target than to the top plate). This supersaturation can be made as large as desired by increasing the temperature gradient between the chamber plates. The higher the supersaturation, the smaller the size of the nucleus required for condensation. Both diffusion and convection affect the removal of the small particles away from the nucleation zone (once condensed out of the vapor phase) before they can grow into larger particles. Under microgravity conditions, convection is absent and it is possible to operate the chamber in the flow mode in order to control the transport of the nanoparticles to the cold plate. By controlling the temperature gradient, the total pressure and the laser power (which determines the number density of the metal atoms released in the vapor phase), it is possible to control the size of the condensing particles.

Results and Discussion

Using the LVCC method, several nanoscale metal oxide, carbide and nitride particles (10 - 20 nm) of well - defined composition have been prepared. The particles aggregate into a novel weblike microstructure, which results in a material with unusually high surface area. This is an important factor in catalysis and in using the nanoparticles as reinforcing agents for liquid polymers.

The SEM of the weblike aggregates of the Si nanocrystals produced by the LVCC technique show particles with ~ 5-8 nm diameters but the Raman shift suggests the presence of particles as small as ~ 4 nm. The Raman spectrum of the surface - oxidized Si nanocrystals, produced by the LVCC method exhibit a sharp peak at about 510 cm^{-1}. This is close to the Raman allowed optical phonon characteristic of microcrystalline silicon at 520 cm^{-1}. This peak shifts to higher frequency by increasing the amount of O_2 added during the particles' synthesis. The downshift of this band compared to the bulk sample is attributed to size and strain effects. We note that porous Si samples prepared under various etching conditions show Raman shifts which have been correlated to the particle size. For example; Raman shifts of 517 cm^{-1}, 515 cm^{-1}, 507 cm^{-1}, and 501cm^{-1} were correlated to particle sizes of 7 nm, 4.8 nm, 2.5 nm and ~ 1.6 nm, respectively[1,5]. Based on the Raman shift of our sample, the average particle size can be estimated as ~ 4 nm. This is considerably smaller than the particle size shown by the SEM micrographs and this suggests that particles smaller than the SEM is able to detect may be present in the sample. The weblike aggregates of coalesced Si nanocrystals, passivated by a SiO_x barrier layer exhibit intense red PL upon excitation with visible or UV light. The freshly prepared Si nanoparticles do not show the emission unless a passivated layer stabilizes the nanocrystal surface by saturating all the dangling bonds. FTIR of the freshly prepared sample shows weak peaks due to the stretching, bending and rocking vibrations of the Si-O-Si bonds indicating the presence of the surface oxidized layer SiO_x, but no red or blue emission is observed until more complete development of the oxide layer has been achieved. This appears to be essential for efficient passivation of the nanocrystal surface. It is also important to note that fully oxidized Si nanoparticles with SiO_2 composition and completely amorphous phase do not show the red PL upon UV or visible excitations.

The particles show luminescence properties that are similar to those of porous Si and Si nanoparticles produced by other techniques. Dispersed luminescence spectra obtained with two different excitations are shown in Figure 2. Both blue and red emissions are observed. The blue emission is very weak under the cw excitation since the lifetime associated with it is short (less than 20 ns) compared to the lifetimes of the red emission (80 - 130 μs at 300K). The shape of the blue emission appears similar to that from SiO_2 nanoparticles and it is probably due to the oxidized surface layer of the Si nanoparticles[4,5]. The red PL from the Si particles shifts to longer wavelength with decreasing the excitation energy. The red emission has a lifetime that ranges from 80 to over 130 μs (at 300 K), increasing with emission wavelength. The features of the red emission are similar to those observed for porous Si [5]. The results are consistent with the quantum confinement mechanism as the source of the red photoluminescence The emission of visible from the Si nanocrystals has potential applications in designing new photonic Si-based devices.

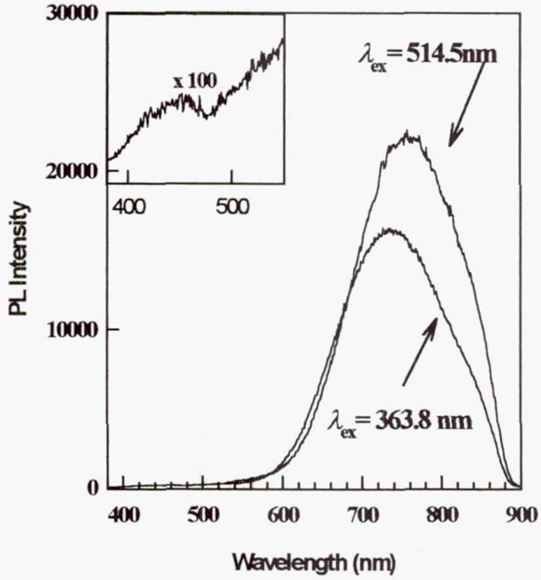

Figure 2. Photoluminescence from Si Nanocrystals

Different methods to incorporate the Si nanocrystals into polymeric films of polystyrene and polyvinyl acetate have been used. The quenching of the photoluminescence of the nanoparticles by organic electron acceptor molecules (nitro- and cyano-substituted aromatics) in solution has also been investigated. The quenching effect results in decreasing both the intensity and the lifetime of the red emission. The results suggest an electron transfer mechanism for the photoluminescence quenching. This work is currently in progress in order to understand the mechanism of the photoluminescence quenching from the Si nanocrystals by the organic electron acceptor molecules.

Molybdenum and tungsten trioxides are photochromic materials which change color upon going from one oxidation state to another by absorption of light[8-10]. The photochromic materials have potential practical applications in areas such as displays, imaging devices, "smart windows", and solar energy conversion[8-12]. In the last two decades, intense interest has been focused on the bulk photochromic materials, while nanoscale particles have not been given much attention. In this paper, we study the photochromic properties of MoO_3 nanoparticles and find that the color change for the nanoparticles is one order of magnitude larger than that observed for bulk MoO_3. We also present a brief characterization of the tungsten oxide nanoparticles.

Molybdenum oxide is the second most studied transition oxide material with electro- and photochromic properties after tungsten oxide. However, few studies have been carried out to characterize this material at the nanoscale level. The MoO_3 nanoparticles appear a white-pale-green color. The bulk MoO_3 obtained from Aldrich is gray. It is interesting that blue Mo oxide nanoparticles are obtained when the O_2 content in the reaction chamber (using He as carrier gas) is in the range of 1% to 90%. The white nanoparticles made in a pure O_2 environment are molybdenum trioxide particles, while the blue particles contain the Mo(V) oxide composition.

The MoO_3 nanoparticles show a strong photochromic effect. The dependence of the UV-vis absorption spectra of the white molybdenum trioxide sample (prepared in 800 torr O_2 in the reaction chamber) on the irradiation time of an excimer laser (308nm, 72mJ/pulse) is shown in Figure 3. The change in absorbance is seen across the visible range; the largest change occurs from 600 nm to 860 nm. For example, the change of absorbance at 750 nm is 0.7409 after the nanoparticle sample is irradiated for 36 min. For comparison, a series of UV-vis spectra of the commercial MoO_3 (Aldrich) were also measured at different irradiation times under the same conditions as the nanoparticle sample and the results are shown in Figure 4. The change of absorbance at 750 nm is only 0.0506 for the bulk MoO_3 after irradiation with the excimer laser for 36 min. The color change in the nanoparticle sample after 36-min irradiation is 15 times stronger than that of the bulk sample.

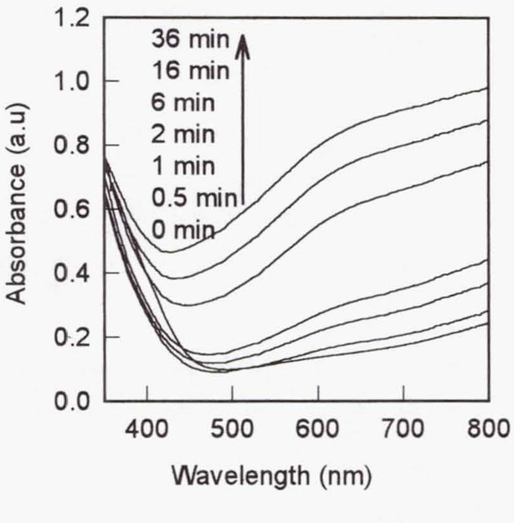

Figure 3. UV-vis spectra of white MoO_3 nanoparticles as a function of the irradiation time.

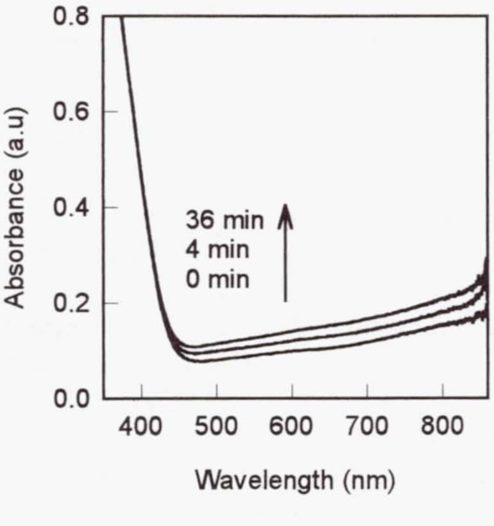

Figure 4. UV-vis spectra of bulk MoO3 as a function of the irradiation time.

The X-ray diffraction pattern of WO_3 nanoparticles indicates a monoclinic crystalline structure similar to the bulk material. The color of bulk WO_3 is yellow while the WO_3 nanoparticles prepared by the LVCC method exhibit a white color. This white color changes to blue upon irradiation of the nanoparticles with the second harmonic of the Nd:YAG laser (532 nm) in air. We measured the IR and the Raman spectra of the particles before and after the irradiation and the spectra measured after irradiation clearly shows all the features associated with the reduction of WO_3 to W_2O_5.

These features include the decrease in the IR absorption at 800 cm^{-1} and the disappearance of the Raman bands at 802 cm^{-1} and 716 cm^{-1}, which are the characteristic IR and Raman features of WO_3. The observed laser induced reaction of the white WO_3 nanoparticles appears to be a multiphoton process. We observed an interesting quenching effect by the WO_3 nanoparticles. The PL spectra taken from colloid solutions of the Si nanocrystals in ethanol after successive additions of WO_3 particles and excitations with 266 nm show systematic loss of the PL intensity with increasing the concentration of the WO_3 nanoparticles. This quenching effect can be explained by an electron transfer mechanism from the Si to the WO_3 nanoparticles.

Conclusions and Future Work

The photoluminescence properties of the Si nanocrystals are similar to those observed for porous Si [5]. The results are consistent with the quantum confinement mechanism as the source of the red photoluminescence. The emission of visible from the Si nanocrystals has potential applications in designing new photonic Si-based devices. Molybdenum and tungsten oxide nanoparticles have been prepared by the LVCC method. The nanoparticles show a very strong photochromic effect: the color change is one order of magnitude larger than for the bulk materials.

Future work will focus on the incorporation of the nanoparticles in polymeric films and understanding the factors that control the weblike microstrucures of the aggregated nanoparticles. The control of the weblike morphology and the degree of porosity of the nanoparticles under microgravity conditions is expected to yield high surface area materials which would have important applications in the areas of calalysis and novel composites.

References

1. See for example: "*Nanomaterials: Synthesis, Properties and Applications*", Editors: A. S. Edelstein and R. C. Cammarata, Institute of Physics Publishing, 1996.
2. G. M. Chow and K. E. Gonsalves (Eds.), Nanotechnology: Molecularly Designed Materials, ACS Symposium Series 622, Washington DC, (1996).
3. M. S. El-Shall, W. Slack, W. Vann, D. Kane and D. Hanley, J. Phys. Chem. **98** (1994) 3067.
4. M. S. El-Shall, S. Li, T. Turkki, D. Graiver, U. C. Pernisz and M. E. Baraton, J. Phys. Chem. **99** (1995) 17805.
5. S. Li, S. Silvers and M. S. El-Shall, J. Phys. Chem., **101**, 1794 (1997).
6. S. Li, S. Silvers and M. S. El-Shall, in "*Advances in Microcrystalline and Nanocrystalline Semiconductors - 1996*", Editors: P. M. Fauchet, R. W. Collins, P. A. Alivisatos, I. Shimizu, T. Shimada and J. C. Vial, Vol. **452**, Materials Research Society Symposium Proceedings Series, 389-394 (1997).
7. M. S. El-Shall and Shoutian Li, SPIE, **3123**, 98-109 (1997).
8. Durr, H; Bouas-Laurent, H. *Photochromism – Molecules and Systems*, PP.5, Elsevier: Amsterdam, Oxford, New York and Tokyo, 1990.
9. Mortimer, R. *J. Chem. Soc. Rev*. 26, 147, 1997.
10. Yao, J. N.; Hashimoto, K.; Fujishima, A. *Nature*, 355, 624, 1992.
11. Bechinger, C.; Ferrere, S.; Zaban, A.; Sprague, J.; and Gregg, B. A. *Nature*, 383, 608, 1996.
12. Yao, J. N.; Loo, B. H.; Hashimoto, K.; Fujishima, A. *J. Electroanal. Chem*. 290, 263, 1990.

GAS PHASE POLYMERIZATION AND NUCLEATION EXPERIMENTS IN MICROGRAVITY

M. Samy El-Shall
Department of Chemistry
Virginia Commonwealth University
Richmond, VA 23284-2006
Phone: (804) 828-3518; Fax: (804) 828-8599
E-Mail: selshall@hsc.vcu.edu

Introduction

The proposed research is focused on two categories namely, gas phase / aerosol droplets polymerization and vapor to liquid homogeneous nucleation.

A. Gas Phase and Aerosol Polymerization Studies

Understanding the fundamental mechanisms that govern polymerization reactions is an important question in a number of scientific disciplines as well as practical applications. Despite the fact that solutions and bulk liquids are the preferred medium for many industrial and laboratory polymerization processes, our fundamental understanding of the polymerization reactions in solution remains limited. Under normal circumstances, polymerization is conducted in condensed systems (monomer liquid or solution) in which multiple reactions (initiation, propagation, chain transfer, termination, etc.) are occurring simultaneously. Information regarding the exact nature of each mechanistic step and understanding of elementary events occurring in the course of polymerization remain largely unavailable. In solution the problem is further complicated by reaction within the solvent. In cationic polymerization, the very high reactivity of cationic monomers cause the reaction rates to be unmeasurably fast, thus obscuring the kinetic and mechanistic details. Furthermore, cationic polymerization often stops before complete monomer consumption since the ion pair eventually recombines and terminates the process.

In order to arrive at a clearer understanding of these processes, the first step must be the elucidation of the detailed mechanism of the early stages of polymerization reactions in the gas phase. The fundamental significance of gas phase polymerization can be illustrated by considering the following items involving, as an example, cationic polymerization:

1. In the gas phase there is the possibility of observing the direct formation, in real time, of product polymeric ions of a chosen size. In contrast, in the liquid phase, one is usually forced to infer what has happened by the qualitative and quantitative analysis of the products.
2. In the gas phase it is possible to suppress the process of termination, as well as the process of chain transfer.
3. In the gas phase, it is sometimes possible to study in isolation, elementary steps (e.g. initiation, propagation, recombination, etc.) of a multistep reaction.

4. It is of interest to study polymerization in a poor solvent since the polymer is likely to adopt a globule rather than a coil configuration and the rate, and possibly the mechanism of reaction, could be dramatically affected. Perhaps the poorest "solvent" is represented by the vapor so that the development of gas phase methods could contribute to studies of this kind. The rate could also be affected by the competition between intrapolymer and polymer-solvent energy transfer processes.

The importance of gas phase polymerization and its potential for use in industry cannot be minimized. This solvent free approach eliminates the need for distillation, drying and solvent recovery and therefore, the operating costs and energy consumption associated with these processes. Furthermore, gas phase polymerization can lead to the synthesis of defect-free, uniform thin polymeric films of controlled morphology and tailored compositions with excellent electrical and optical properties for many technological applications such as protective coatings and electrical insulators. Unfortunately, the achievement of true homogeneous gas phase polymerization for the synthesis of high molecular weight polymers is very difficult, and has not really been accomplished successfully in the past. The main problem is the extreme involatility of the large polymers, rendering it impossible to keep them in the gas phase

Study of the Early Stages of Cationic Polymerization

We have studied the early stages of cationic polymerization using the Laser Vaporization High Pressure Mass Spectrometry (LV-HPMS) technique.[1-6] In this method, the gas phase reactions of the selected monomer are probed by mass spectrometry following the laser vaporization / ionization of a metal target placed inside a high pressure cell (1-2 torr). A schematic diagram of the experimental set up for the metal catalyzed reactions is shown in Figure 1. For uncatalyzed reactions, the monomer ions are generated within the high pressure cell, containing a suitable carrier gas such as N_2, by using a pulsed electron gun or laser multiphoton ionization.

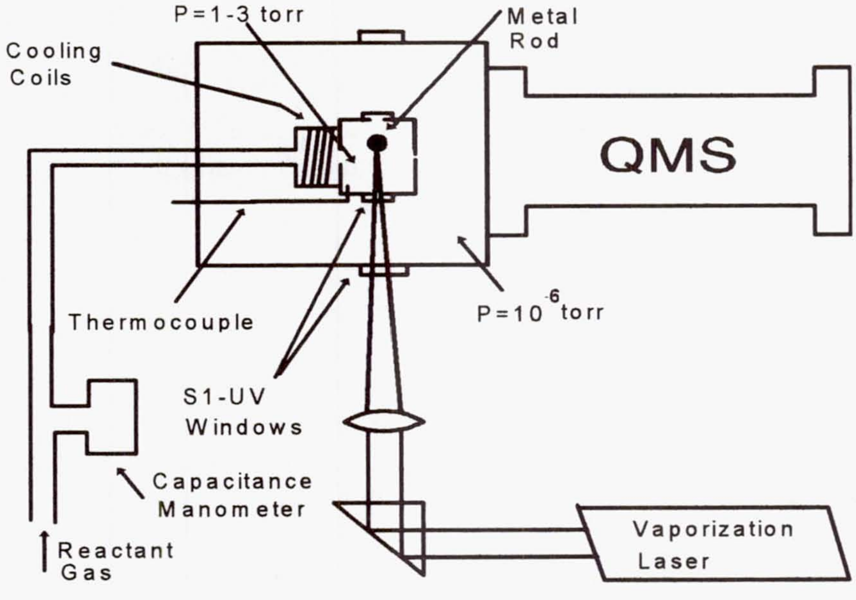

Figure 1. Schematic for the Laser Vaporization-High Pressure Mass Spectrometry (LV-HPMS) source.

Metal-Catalyzed Polymerization

The majority of olefin polymerization processes are catalytic, most often involving a heterogeneous catalyst. The reactions taking place following the process of metal ion generation in the presence of unsaturated hydrocarbons are of considerable interest because these reactions may provide a better understanding of related processes involving supported metal catalysts and the polymerization of olefinic monomers.

Recent research in our laboratory has lead to the discovery of a novel technique for polymerization using metal ions generated in the gas phase by laser vaporization techniques. The ions are pulled toward the monomer liquid by applying appropriate electric fields across the reaction chamber.[7,8] Using this method, high molecular weight polymers (10^6 units, polyisobutylene) have been synthesized. The polymeric materials also contain micron - and submicron - sized metal particles. The surface morphology of the polymer film obtained is dependent on experimental conditions such as laser power, temperature, pressure and electric field strength. This is a significant result since the incorporation of ultrafine metal particles and clusters into the polymer matrices would greatly extend the scope of these polymeric materials in, for example, electrical, magnetic and optical applications.

In another application, we were able to polymerize liquid films of isobutene on Si substrate using laser vaporization of Ti metal in isobutene vapor at a total pressure of 10^{-3} bar. Interestingly, depending on the temperature of the substrate, we could form either polymeric microbeads or long stripes as shown in Figure 2.

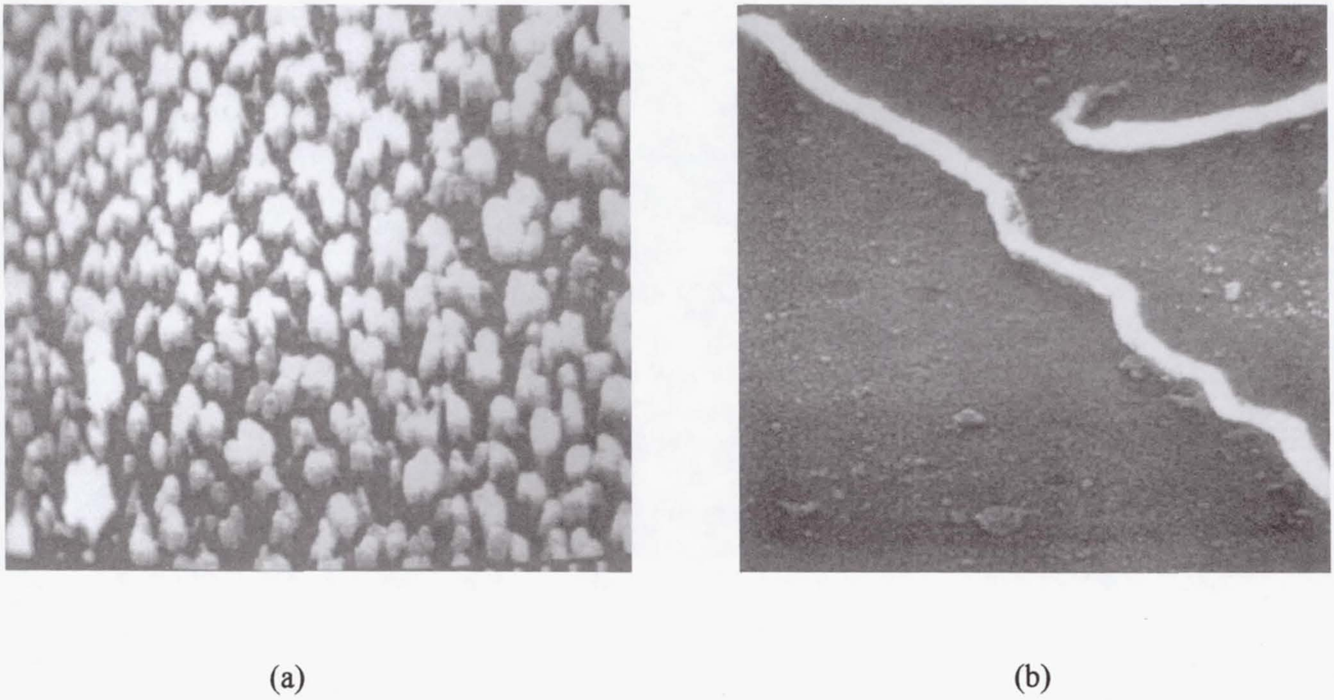

(a) (b)

Figure 2. SEM micrographs of polyisobutene prepared by laser vaporization of Ti in presence of a liquid film of isobutene monomer at (a) –10 °C and (b) –110 °C.

We believe that the control of these microstructures is hampered by the gravity effects which introduce convection and non-homogeneous conditions. By carrying out these experiments in space, it should be possible to control the microstructures and the size distribution of the polymer beads or the polymer modified silica particles. In the flight experiments, the use of plasma polymerization of the thin monomer liquid films as a simple alternative to laser vaporization can also be applied. These new directions which are explored for the first time, could lead to the production of new polymeric films with unique material properties.

We have extended these experiments to other monomers such as styrene and siloxanes. Using this technique, we were able to synthesize silica particles modified with polymerized polystyrene as shown in Figure 3. In these experiments, the silica particles were prepared by laser vaporization of a Si target in the presence of a small amount of oxygen with simultaneous polymerization of styrene. It should be noted that use of silica as a reinforcing filler provides many beneficial properties for the polymeric materials including heat resistance, hardness, stiffness and modulus.

Figure 3. Oxidized Si particles in polystyrene.

Proposed Gas Phase and Aerosol Polymerization Experiments in Microgravity

Gas phase polymerization can be initiated by photon irradiation or electron beam ionization of the monomer vapor. Another initiation method may involve plasma polymerization. The size of the product polymer particles is again limited in normal gravity by gravitational settling. Polymerization can be terminated by recombination, or by the injection of inhibitors. In the microgravity experiments, polymerization will be initiated by irradiation by a high-pressure Hg / Xe UV lamp, or by electron irradiation using an electron gun based on a hot filament, or by plasma ionization using RF-field between two electrodes (distance of 2 cm at a pressure of 0.1-0.5 mbar). The growth of the particles will be monitored by scattering of a test laser beam introduced perpendicular to the photoinitiating UV light or by a CCD camera. The product particles will be collected and the particle size distribution will be analyzed microscopically.

Polymerization within small compartmentalized volumes of monomer liquid droplets is widely used in suspension and emulsion polymerization. An analogous new process of compartmentalized polymerization in liquid droplets suspended in the vapor can be used in microgravity since large nucleating droplets can be suspended indefinitely, without the presence of the solvent. While analogous in principle, the substitution of volatility vs. solubility requirements will allow the extension of compartmentalized polymerization to previously inaccessible systems. Furthermore, physical differences, such as the solution vs. gas phase mobility of reactive species will allow the comparative study of suspension vs. aerosol / nucleating droplets polymerization, enhancing the basic understanding of both processes.

In these experiments, we will generate an aerosol of monomer droplets by mechanical dispersion from a reservoir. We will then use pulsed irradiation by a UV lamp to initiate polymerization in the monomer vapor and/or within the monomer droplets. Initiation in the aerosol droplets will be achieved by two mechanisms. First, the UV irradiation will generate radicals in the gas phase that will proceed to polymerize. The living polymerizing particles can then be absorbed into a monomer droplet and continue polymerizing. Alternatively, the UV irradiation can generate a radical within an already formed droplet.

B. Vapor Phase Nucleation Studies

Nucleation is one of the most ubiquitous and important phenomena in science and technology. The nucleus for homogeneous nucleation remains one of the most elusive entities known in chemical physics, and has never been observed directly. Only the consequences of its presence, e.g. droplet formation, precipitation, etc. are observed. The typical measurements of vapor to liquid nucleation rates involve light scattering from liquid droplets that fall, under the influence of gravity, from the supersaturated vapors. One of the very important current issues in nucleation research is whether the observed effect of a carrier gas is due to convection and instability in the operating conditions of the nucleation chamber under 1-g or if it actually represents a real contribution to the nucleation process. There is no other way to answer this question except by complete elimination of the convection and other instability conditions by carrying out the nucleation experiments in microgravity. Recent nucleation experiments in diffusion cloud chambers have shown that the pressure of the carrier gas has an apparent effect on the measured nucleation rates.[9,10] Our hypothesis is that the pressure effect arises from the dynamics of growth and motion of the droplets and not from a pressure dependence of the kinetics of homogeneous nucleation. Because of the coupling between high pressure and convection, it is not possible to examine the effect of carrier gas pressure on the nucleation rate over a wide temperature range without introducing convection effects which limit the window of stable operation of the cloud chamber. Another factor that can affect the accuracy of the nucleation rate measurements in diffusion cloud chambers is the thermophoretic effect. Thermophoresis is thought to be more effective when the temperature gradient becomes steeper. In normal gravity, the natural convection which is also induced by the temperature gradient has an influence on the behavior of droplets. When the temperature gradient becomes steep, the effect of natural convection becomes a dominant one and makes it difficult to determine the thermophoretic effect. A recent measurement of this effect in microgravity has shown that the measured thermophoretic velocities are much higher than the corresponding values estimated from proposed theoretical equations. The micogravity measurements have also indicated that the data obtained in previous studies under normal gravity conditions are erroneous.[11]

Convection may also occur within the droplets once they reach macroscopic sizes, affecting the structure and, in binary or multicomponent systems, the intra-droplet concentration profiles. Due to these effects, the measured nucleation rates may reflect convective transport effects, and the interpretation the measured effects is uncertain.

The convection effects will be absent in microgravity, and the nucleation and droplet growth rates will be determined purely by diffusion and condensation / evaporation processes. This will allow the purest test of nucleation theories. By comparison, the results will also yield the effects of convection terms in normal gravity. Unlike in normal gravity, the ultimate particle size will not be limited by gravitational settling. This will allow unique studies on growth rates of large droplets.

Summary and Conclusions

The study of gas phase polymerization is an important intellectual and technological frontier which promises unique results not only for a fundamental understanding of polymerization reactions, but also for the development of new materials with unique properties. In the past it has been almost impossible to study gas phase chain polymerization because the involatile product molecules condensed out of the gas phase. The application of microgravity to the study of gas phase polymerization is expected to result in a better control of the process and may also lead to important technological advances

The growth of nuclei in supersaturated vapors under microgravity conditions is expected to provide a more accurate and reliable picture of the growth process that can now be used to test the validity of different nucleation theories. This is the second objective of the proposed research.

References

1. Daly, G. M.; El-Shall, M. S., J. Phys. Chem., **98**, 696 (1994).
2. Daly, G. M.; Y. B. Pithawalla, Y. B.; Yu, Z.; El-Shall, M. S., Chem. Phys. Letters , **237**, 97 (1995).
3. Meot-Ner, M.; Sieck, L. W.; El-Shall, M. S.; Daly, G. M. J. Am. Chem. Soc., **117**, 7737 (1995).
4. El-Shall, M. S.; Daly, G. M.; Yu, Z.; Meot-Ner, M., J. Am. Chem. Soc., **117**, 7744 (1995).
5. El-Shall, M. S.; Yu, Z., J. Am. Chem. Soc., **118**, 13058 (1996).
6. Pithawalla, Y. B.; J. Gao, J.; Yu, Z.; El-Shall, M. S. Macromolecules, **29**, 8558 (1996).
7. El-Shall, M. S.; Slack, W., Macromolecules, **28**, 8456 (1995).
8. El-Shall, M. S. Applied Surface Science, **106**, 347 (1996).
9. Bertelsmann, A.; Stuczynski, R.; Heist, R. H. J. Phys. Chem. **100**, 9762 (1996).
10. Kane, D. B.; El-Shall, M. S. J. Chem. Phys. **105**, 7617 (1996).
11. Toda, A.; Ohi, Y.; Dobashi, R.; Hirano, T. J. Chem. Phys. **105**, 7083 (1996)

EXPLOITING THE TEMPERATURE/CONCENTRATION DEPENDENCE OF MAGNETIC SUSCEPTIBILITY TO CONTROL CONVECTION IN FUNDAMENTAL STUDIES OF SOLIDIFICATION PHENOMENA

J. W. Evans, Dong Xu and W. Kinzy Jones, Jr.
Dept. of Materials Science and Mineral Engineering
University of California, Berkeley CA 94720
(510) 642-3807 (tel)   (510) 642-9164 (fax)
evans@socrates.berkeley.edu

Frank R. Szofran
Marshall Space Flight Center, NASA

INTRODUCTION

The objective of this new research project is to demonstrate by experiment, supplemented by mathematical modeling and physical property measurement, that the effects of buoyancy driven convection can be largely eliminated in ground-based experiments, and further reduced in flight, by applying a new technique. That technique exploits the dependence of magnetic susceptibility on composition or temperature. *It is emphasized at the outset that the phenomenon to be exploited is fundamentally and practically different from the magnetic damping of convection in conducting liquids that has been the subject of much prior research.*

The concept suggesting this research is that all materials, even non-conductors, when placed in a magnetic field gradient, experience a force. Of particular interest here are paramagnetic and diamagnetic materials, classes which embrace the "model alloys", such as succinonitrile-acetone, that have been used by others investigating the fundamentals of solidification. Such alloys will exhibit a dependence of susceptibility on composition. The consequence is that, with a properly oriented field (gradient) a force will arise that can be made to be equal to, but opposite, the buoyancy force arising from concentration (or temperature) gradients. In this way convection can be stilled.

The role of convection in determining the microstructure, and thereby properties, of materials is well known. Elimination of that convection has both scientific and technological consequences. Our knowledge of diffusive phenomena in solidification, phenomena normally hidden by the dominance of convection, is enhanced if we can study solidification of quiescent liquids. Furthermore, the microstructure, microchemistry and properties of materials (thereby practical value) are affected by the convection occurring during their solidification. Hitherto the method of choice for elimination of convection has been experimentation in microgravity. However, even in low Earth orbit, residual convection has effects. That residual convection arises from acceleration (drag on the spacecraft), displacement from the center of mass or transients in the gravitational field (g-jitter). There is therefore a need for both further reducing buoyancy driven flow in flight and allowing the simulation of microgravity during ground based experiments.

PREVIOUS INVESTIGATIONS

Two publications of great relevance to this investigation are those of Braithwaite et al. (1) and Beaugnon et al. (2). These investigators at the Centre de Recherches sur les Très Basses Température in Grenoble, have described how a material in a magnetic field gradient is subjected to a force (per unit volume)

$$F = -\left(\frac{\chi}{2\mu_0}\right)\nabla(B^2) \qquad (1)$$

where χ is the magnetic susceptibility, μ_0 is the permeability of vacuum and B is the magnetic flux density.

If the susceptibility varies with the temperature in a fluid with a temperature gradient, then the effect is to enhance or oppose the normal buoyancy driven convection. The effect can be described by a magnetic Rayleigh number given by these works as

$$Ra_m = Ra\left(1 + \frac{F}{g}\left(1 + \frac{\gamma}{\beta}\right)\right) \qquad (2)$$

where Ra is the usual Rayleigh number, g is the acceleration due to gravity (or microgravity), β is the volumetric expansion coefficient and γ is the fractional rate of change of susceptibility with temperature:

$$\gamma = \left|\frac{1}{\chi}\frac{d\chi}{dT}\right| \qquad (3)$$

In the case where the magnetic force is aligned opposite to the gravitational force (F and g have opposite signs), the magnetic Rayleigh number is reduced to zero at some value of $\nabla(B^2)$ for any liquid, halting buoyancy driven flow.

Fig. 1 is taken from the results of these French investigators; these are measurements of heat flux (expressed as a Nusselt number) from a hot to a cold plate separated by a paramagnetic solution (gadolinium nitrate in water). The apparatus was located in a superconducting magnetic and the parameter on the curves is the value of ∇B^2 in T^2/m. With the magnetic force applied opposite to gravity, convection was suppressed, apparently being eliminated at 15 T^2/m.

By obvious extension of the work of these investigators, solutal convection should be suppressed in the case of a solution with a concentration dependent susceptibility when

$$Ra'_m = Ra\left(1 + \frac{F}{g}\left(1 + \frac{\gamma'}{\beta'}\right)\right) \qquad (4)$$

equals zero, where Ra'_m is the magnetic Rayleigh number for solutal convection

$\beta' = \left|\frac{1}{\rho}\frac{d\rho}{dC}\right|$ is the fractional change of density with concentration

$\gamma' = \left|\frac{1}{\chi}\frac{d\chi}{dC}\right|$ is the fractional change of susceptibility with concentration.

Again it is emphasized that this halting of buoyancy driven flows is different from the usual magnetic damping. Conventional magnetic damping relies on induced currents arising from the cross product of the velocity vector and the magnetic flux density; if the velocity is zero (or if the material is non-conducting) the damping force is zero, i.e., the force is only operative when motion exists and should therefore completely halt the flow only in the limit of an infinite magnetic field. Furthermore, because model alloys are usually non-conducting (being transparent for ease of observing the solidification) they cannot be arrested by this conventional magnetic damping. The opportunity for controlling flow by exploiting the variation in dependence of susceptibility of the fluid has been noted by Edwards and co-workers (3).

RESEARCH PROJECT DESCRIPTION

The investigation, extending over four years, entails construction of an apparatus in which buoyancy driven flows can be measured during solidification of transparent liquids, selection of suitable liquids (model alloys) by physical property measurement, running the apparatus in the High Magnetic Field Solidification Facility at MSFC to demonstrate that convection can be controlled or eliminated, and mathematical modeling of the convection within a magnetic field. The apparatus will then be used for studying convection free solidification as well as other phenomena (e.g., Soret effect) that require minimization of convection.

THEORY

The total (gravitational plus magnetic) body force components acting on a material placed within a magnet with axial symmetry are

$$F_{z\,\mathrm{Tot}} = \rho g - \frac{\chi}{\mu_0}\left(B_z\frac{\partial B_z}{\partial z} + B_r\frac{\partial B_r}{\partial z}\right) \tag{5}$$

$$F_{r\,\mathrm{Tot}} = -\frac{\chi}{\mu_0}\left(B_z\frac{\partial B_z}{\partial r} + B_r\frac{\partial B_r}{\partial r}\right)$$

For the moment it will be assumed that a region can be found inside the magnet where the axial magnetic body force

$$F_{z\,\mathrm{Mag}} = -\frac{\chi}{\mu_0}\left(B_z\frac{\partial B_z}{\partial z} + B_r\frac{\partial B_r}{\partial z}\right) \tag{6}$$

is uniform (showing no variation in the axial or radial direction), i.e., $B_z\frac{\partial B_z}{\partial z} + B_r\frac{\partial B_r}{\partial z}$

is constant. Furthermore it is assumed that the radial component of the force is negligible. If buoyancy driven by concentration gradients is to be eliminated,

$$\frac{dF_{Tot}}{dC} = 0 \tag{7}$$

Introducing the fractional variation of density (β') with concentration (C), there will be no buoyancy driven convection when

$$B_Z \frac{\partial B_Z}{\partial z} = g\rho\beta' \mu_0 / \frac{d\chi}{dC} \tag{8}$$

The magnetic field and magnetic forces for a material with the susceptibility of water located within the superconducting magnet of the High Magnetic Field Solidification Facility at MSFC have been calculated and are depicted in Figs. 2 and 3 respectively. The current through this magnet is controllable and the units in Fig. 2 are T/Amp while in Fig. 3 they are N/m^3A^2. The origin of the co-ordinate system is at the center of the magnet and the region depicted is from that center to the inner radius of the magnet (radially) and to just above the mouth of the magnet (vertically). The magnetic field appearing in Fig. 2 is the anticipated one; the field is strongly axial inside the magnet, diverging as the mouth is approached. It appears from Fig. 3 that the assumption of a uniform axial force and zero radial force is approximately satisfied over a volume of 10cms height and 10cms radius roughly halfway between the center and mouth of the magnet. It is in this volume that the experiment is to be conducted.

EXPERIMENTAL

A sketch of the experiment to be incorporated in the superconducting magnet appears in Fig. 4. The model alloy under investigation is contained in a chamber, with temperature controlled walls, located in the bore of the magnet. The motion of the liquid is to be followed as a function of the current of the magnet. The intended technique for measuring the liquid motion is particle image velocimetry. This is a technique whereby motion of particles suspended in the fluid is tracked by a digital camera and velocity maps extracted from the frame-to-frame movement by commercial software. It can only be successful if the terminal velocity of the particles is negligible; in the present case this must hold for terminal velocities resulting from magnetic, as well as gravitational, forces. The particles in one plane are illuminated by a sheet of laser light from the optical scheme shown in Fig. 4. Prior to such experimental work it is necessary to decide on appropriate model alloys. In addition to the usual requirements of mimicking the solidification of practical materials (such as metallic alloys) and transparency, the alloy chosen must exhibit significant variation of susceptibility with composition. Unfortunately, although the susceptibilities of pure liquids are available in the literature, there is little published on susceptibility of solutions. It has therefore been necessary to embark on susceptibility measurements. Fig. 5 shows preliminary results of measurements on ammonium chloride-water which has been used by others (4) as a model alloy. The measurements were made using a Quantum Design magnetic property measurement system (SQUID) with a field strength of 2 Tesla.

REFERENCES

(1) Braithwaite, D., Beaugnon, E. and Tournier, R., *Nature* 354, 1991, 134.
(2) Beaugnon, E. et al., *J. Phys. I France* 3, 1993, 399.
(3) Edwards, B.F., Gray, D. D. and Huang, J., Third Microgravity Fluid Physics Conference, 1996, 711.
(4) Beckermann, C. and Viskanta, R., 1988, *PhysicoChem. Hydrodyn.* 10, 195.

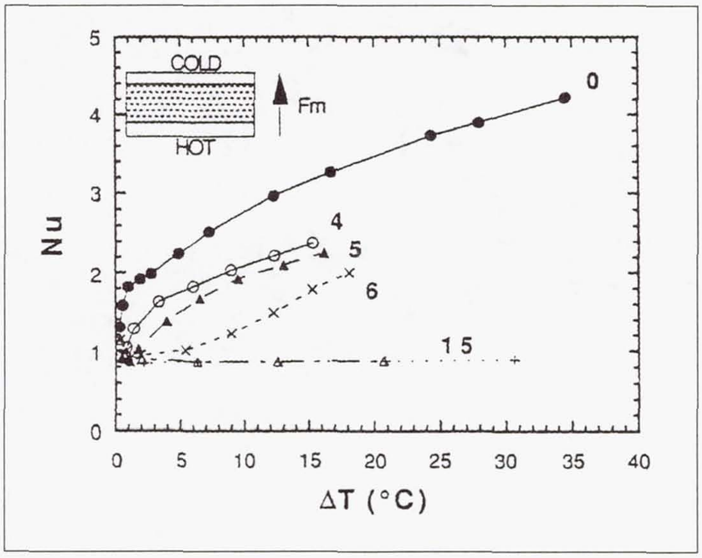

Fig. 1 Plot of Nusselt number versus thermal gradient (taken from ref. 3).

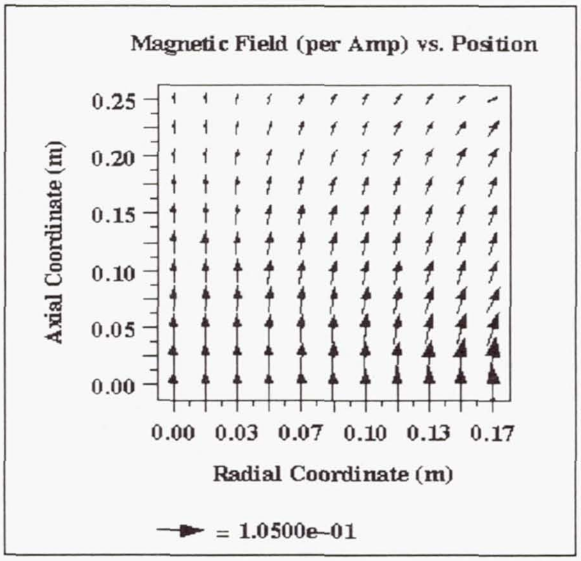

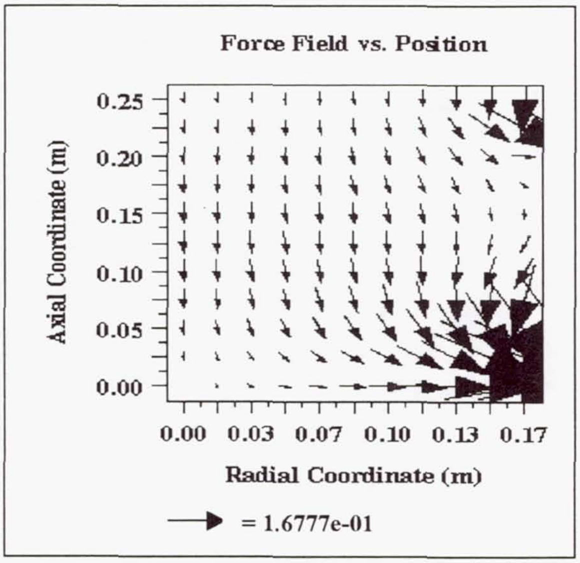

Fig. 2 Plot of magnetic field versus position for the superconducting magnet of the HMF Facility at MSFC.

Fig. 3 Plot of magnetic forces for the superconducting magnet of the HMF Facility at MSFC.

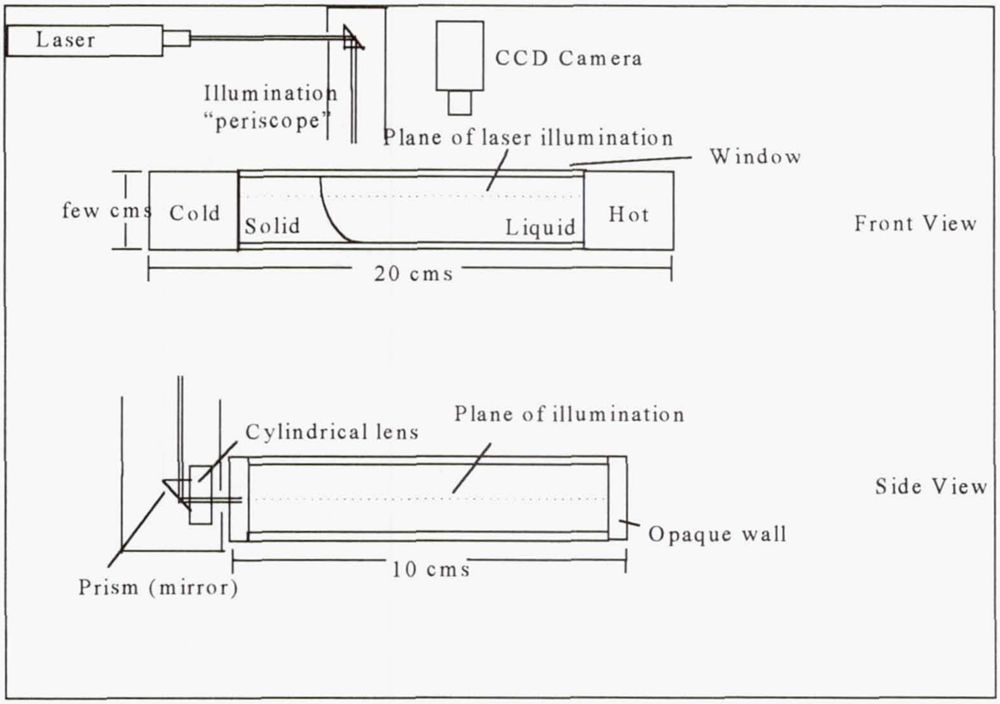

Fig. 4 Sketch of experiment for use in HMF Facility at MSFC.

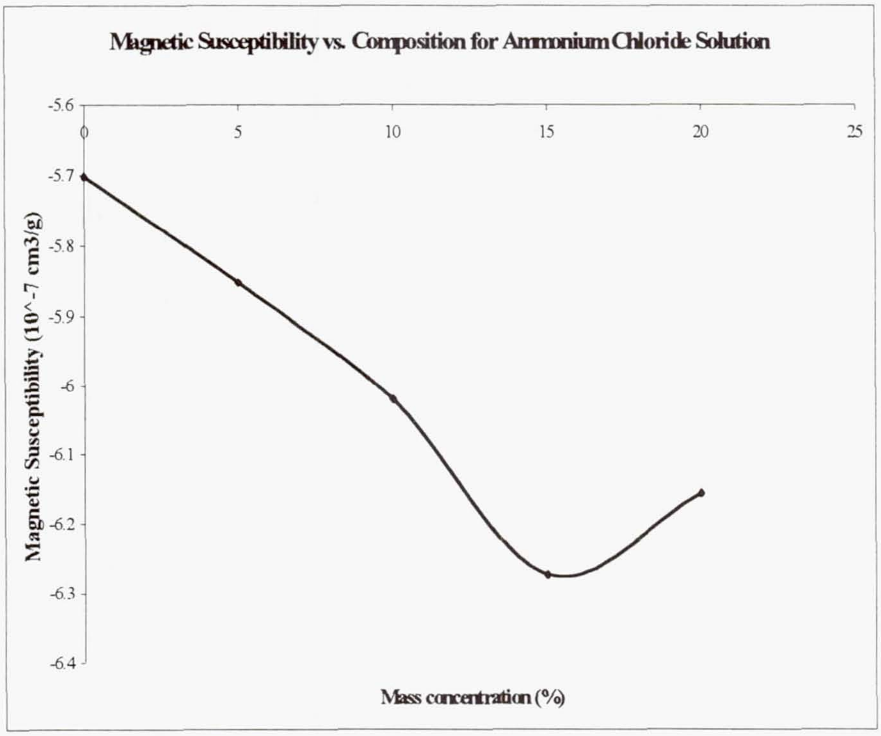

Fig. 5 Plot of magnetic susceptibility versus concentration for ammonium chloride solution.

INVESTIGATION OF VIBRATIONAL CONTROL OF THE BRIDGMAN CRYSTAL GROWTH TECHNIQUE

Alexandre Fedoseyev

Center for Microgravity and Materials Research, University of Alabama in Huntsville,
Huntsville, Alabama 35899, E-mail: alex@cmmr.uah.edu

1. Introduction and objectives

The objective of this ongoing research is to characterize and quantify using vibrational control of convective flows and, thus, to provide defined convective contributions to both heat and mass transport of Bridgman crystal growth. It has been recognized that oscillatory, or pulsatile, flow significantly alters the transfer of mass, heat and momentum in fluid systems. Our research involves a fundamental theoretical investigation, facilitated by numerical analysis, complemented by ongoing and planned experimental flow visualizations and crystal growth studies at the Stanford University and the General Physics Institute.

Research project objectives are to

- conduct a parametric theoretical and numerical investigation of vibro-convective buoyancy-driven flow in differentially heated cylindrical containers
- investigate buoyant vibro-convective transport regimes in Bridgman-type systems with a focus on the use of vibration to suppress, or control, convection in order to achieve *transport* control during crystal growth.
- assess the feasibility of vibro-convective control as a means of offsetting "g-jitter" effects under microgravity conditions
- exchange information with the experimental group of Prof. E. Zharikov at the General Physics Institute (GPI) of the Russian Academy of Science and Prof. R. Feigelson at Stanford University who are undertaking a complementary experimental program [1].

2. Significance and justification for microgravity research

The character of natural buoyant convection in rigidly contained inhomogeneous fluids can be drastically altered by vibration of the container boundaries or through the introduction of vibration sources into the interior of the fluid.

Control of convective transport continues to be an important aspect of crystal growth research. Control of convection through static and rotating magnetic fields is being actively pursued by several groups. However, there are many instances, whether due to materials properties or other practical considerations, use of magnetic fields to induce stirring or suppress flow may not be an option. In such cases, vibrational control could become an attractive alternative.

While active vibration isolation can be a partial solution, it will not solve the problems that might arise due to the quasi-steady and very low-frequency acceleration components related to the gravity gradient and other orbital factors. Thus as an alternative to vibration isolation, one might envisage using vibration to either suppress flow or to provide flow regimes tailored to particular crystal growth experiments. These flows would not be accessible under terrestrial conditions due to strong natural convection effects.

3. Theory and numerical modeling

Bouyancy driven vibro-convective motion occurs when oscillatory displacement of a container wall induces the acceleration of a container wall relative to the inner fluid. The vibration may be viewed as a time-dependent modulation of steady gravity. In a closed container the fluid will move as a rigid body with a container. If, however, the fluid density is nonuniform, fluid motion may ensue. The magnitude of this motion, of course, depends on the orientation of the vibrational direction with respect to the local density gradients. Note that similar to Rayleigh-Bernard configurations there may be a "critical" threshold for the coupled vibrational frequency and amplitude, to cause convection. Interestingly, in case of a constant density fluid with annular vibration, fluid motion may also take place (example: angular vibration). A review and relevant theoretical and experimental research can be found in [2] and publications [3-9].

3. 1 The physical model

Calculations are being made for two basic physical set-ups. The first involves purely thermo-vibrational convection in a differentially cylindrical cavity with no consideration of solidification. These calculations are being performed for identification and characterization of the thermal vibrational flow and in conjunction with the ongoing flow visualization model experiments being conducted by Zharikov et al.. The second set-up will be closer to a practical solidification situation and will involve explicit consideration of plane or curved front solidification in a long cylindrical ampoule using a similar to [10] approach.

3.2. Translational vibration

Translational vibration corresponds to a linear displacement such as, for example, **u** = **d**cosωt, where **d** is a real vector corresponding to the displacement amplitude. Thus, a point is displaced back and forth upon the same line. For a reference frame fixed to the vibrating ampoule these types of vibrations result in momentum equation of the following form

$$\frac{\partial \mathbf{v}}{\partial t} + (\mathrm{v}\cdot\nabla)\,\mathbf{v} = -\nabla p + \mathrm{Pr}\,\nabla^2\mathbf{v} + \mathrm{Ra}_T\mathrm{Pr}(\Theta + \alpha\,C)\,\mathbf{k} + \mathrm{Pr}\,\mathrm{Ra}^*_T(\Theta + \alpha\,C)\,f(w,t) \qquad (1)$$

where length, time and velocity are scaled by R_0, R_0^2/κ and κ/R_0, R_0 is the ampoule radius and κ is the thermal diffusivity. Continuity and heat-mass transfer equations complete problem formulation. The Prandtl, Schmidt, Rayleigh and solutal -thermal buoyancy ratio are given by

$$\mathrm{Pr} = \frac{\nu}{\kappa},\ \mathrm{Sc} = \frac{\nu}{D}\ \mathrm{Ra}_T = \frac{\beta\Delta T g R^3}{\nu\kappa},\ \alpha = \frac{\beta_c c_\infty}{\beta\Delta T},\quad \mathrm{Ra}^*_T = \frac{d\omega^2\beta\Delta T R^3}{\nu\kappa},$$

where β and β_s are the thermal and solutal expansion coefficients and ΔT, g, ν and D are the characteristic longitudinal temperature difference in the melt, gravitational acceleration, kinematic viscosity and solute diffusivity, respectively. The dimensionless number Ra^*_T is a vibrational Rayleigh number and $\mathrm{Ra}^*_s = \alpha\,\mathrm{Ra}^*_T$.

Average equations for small amplitude vibration. The dimensionless group Ra^*_T in equation (1) should not be confused with the vibrational Rayleigh number Ra_v of Gershuni, $Ra_v = (\beta_T \omega^2 R \Delta T)^2/\kappa\nu$ [3], which arises for monochromatic vibration as follows. If the amplitude $|\mathbf{d}|$ of a sinusoidal vibration is small, i.e., $|\mathbf{d}| << \min(R/\beta\Delta T, R/\beta c_\infty)$, the velocity, temperature and concentration fields may be represented as the superposition of mean (averaged) fields and small oscillating components.

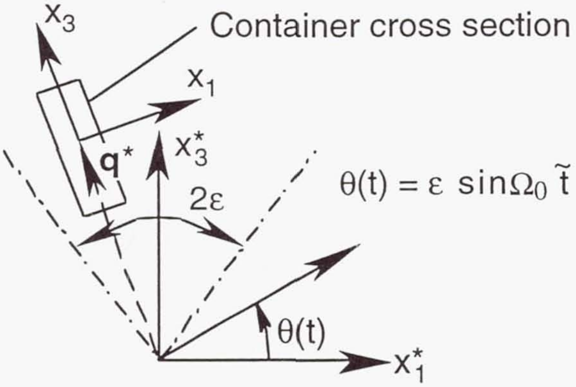

Fig. 1. Diagram of the rotational vibration. The container is rotated at an angle θ(t) about a center of rotation at $\mathbf{x}^* = \mathbf{0}$. The vector $\mathbf{q}^*$ connects the center of rotation to the mass center of the container.

3.3. Rotational vibration

The equations of motion for angular vibrations take on a more complicated form (see Fig.1). A container of length L is subjected to an angular vibration θ(t) in the x_1^*-x_3^* plane. The position vector to the mass center of the cylinder is parallel to the side of the cylinder and is given by $\mathbf{q}^* = R_0[-\sin\theta \mathbf{i}_1^* + \cos\theta \mathbf{i}_3^*]$ where R_0 is the distance from the origin $\mathbf{0}^*$ to the mass center of the cylinder and $\theta(t) = \varepsilon \sin\Omega_0 t$, where t is time. In the new reference frame the equations of motion have the form

$$\rho \frac{D\underset{\sim}{\mathbf{v}}}{Dt} = \operatorname{div} \mathbf{T} - \rho g(\sin\theta \mathbf{i}_1 + \cos\theta \mathbf{i}_3) + \rho[2\widetilde{\Omega}\mathbf{v} - \widetilde{\Omega}^2 \mathbf{x} + \dot{\widetilde{\Omega}}\mathbf{x} + \varepsilon^2 \Omega_0^2 R_0 \cos^2 \Omega_0 t\, \mathbf{i}_1], \quad (2)$$

where D/Dt denotes the material derivative, $\mathbf{v}$ is the velocity of the fluid relative to the unstarred frame, ρ is the density of the fluid and $\mathbf{T}$ is the stress tensor. The fluid is taken to be Newtonian, with a constant viscosity and the Boussinesq approximation is assumed to hold. The dimensionless equations governing the transport of momentum, mass and heat in the cylinder are obtained, after using L, L^2/κ, κ/L, and $\Delta T = T_H - T_C$ to scale, respectively, length, time, velocity and temperature. The parameters are $\Omega = \Omega_0 L^2/\kappa$, the dimensionless frequency and $\vartheta = R_0/L$. The Prandtl, Pr, Rayleigh, Ra, vibrational Rayleigh Ra_Ω, and Ekman, E, numbers are

$$Pr = \frac{\nu}{\kappa},\ Ra = \frac{\beta\,\Delta T\, g L^3}{\kappa\nu},\ Ra_\Omega = \frac{\beta\,\Delta T\,\Omega_0^2 L^4}{\kappa\nu},\ E = \frac{\nu}{\Omega_0 L^2},$$

where β, ν, g and κ are the coefficient of thermal expansion, kinematic viscosity, gravitational acceleration and thermal diffusivity, respectively. This system of equations differ from the usual equations in the absence of rotation in that two additional terms are present; the Coriolis term which is proportional to $\varepsilon Pr/E$, and the centrifugal term which is proportional to $\varepsilon^2 \vartheta Ra_\Omega Pr$ at $\mathbf{x} = \mathbf{0}$ and varies with position in the ampoule. The importance of the latter term depends on the dimensions of the amplitude of the angular vibration, ε , and the ratio ϑ. The centrifugal terms give rise to periodic forcing that fluctuates about a mean value at twice the period of the angular vibration.

Since the above system of equations has not been well studied, we propose a conservative approach for the study of angular vibrations and confines our investigation to a parametric study of flow regimes and transitions for thermo-vibrational situations only without solidification.

3.4. Solution method

The equations are solved in primitive variable form (velocity-pressure, temperature, etc.) using a Finite Element Method package *Femina/3D* developed by the Principle Investigator. ***Femina/3D*** simultaneously considers the continuity equation directly with the momentum equations at each solution step. This eliminates many problems related to boundary conditions and places only slight limitations on the time step size for transient problems (due to the physical nature of the problem). Proposed regularization for the incompressibility condition makes solution procedure more efficient, allows same order finite element approximation for $\boldsymbol{v}$ and p and a use of fast iterative solution methods [11].

4. Significant results of the investigation

We implemented a 3D model of convective buoyancy-driven melt flow in differentially heated cylindrical containers using the FEMINA/3D code. This code was carefully tested on benchmarked experimental and numerical data for a variety of 2D/3D viscous and thermo-convective flow problems [12,13].

In our model we accounted for the influence of the Coriolis force. This is characterized by the Ekman number, which can be of the order 10^{-4} to 10^{-5} for frequencies ~1Hz. This results in large coefficients, *Pr/E,* for Coriolis terms in the governing equation and causes difficulties in the numerical solution. To resolve this we implemented a high accuracy solution method using preconditioning by high order incomplete decomposition. This allowed us to obtain high precision solution, with an accuracy up to 10^{-9}, and reducing the computation time by two order of magnitude over currently available commercial codes.

We have also investigated the validity of the Boussinesq model. A question of the validity of this model for binary alloys and for thermal convection under microgravity conditions has been discussed recently by P. S. Perera, R. F. Sekerka [14], V. Pukhnachev [15] and G. Gershuni, D. Lyubimov [3]. The estimates show that the Boussinesq model is quite adequate for our case of a closed ampoule and the range of parameters under investigation.

A parametric study of the general buoyant-vibrational flow in a Bridgman growth system is being performed. The first phase includes the cases of translational and rotational vibrations under typical microgravity and Earth conditions for typical semiconductor melts. Typical flow pattern is presented in Fig. 2. Even in the total absence of gravity we have found flows, i.e. characterized by a fluid flowing up one side and down the other. The temperature distribution remain almost unperturbed (due to the low *Pr*).

We have considered the influence of both translational (polarized) vibrations and rotational (angular) vibrations on a melt flow. Comparison with the results obtained experimentally and using the average equations for small amplitude vibrational displacements has been performed.

The angular orientation between the direction of vibration and ampoule axis (with imposed T-gradient) has been studied for translational vibrations. As intuitively expected, when that angle is zero, there is no influence of the vibration on a flow even if vibrational Raleigh number is very high. The maximum observed effect corresponds to an angle of 90 degrees. Here transport is significantly enhanced.

We have started to define the parameter space where translational and angular vibrations can cause average melt flow for a typical semiconductor growth. For a given vibration amplitude and frequency, rotational (angular) vibrations result in more intensive melt flow than translational ones. In the light of these results we discuss the use of vibration as a practical means of flow control and also discuss the relative importance of Coriolis force for flows generated by rotational vibrations. Typical flow patterns for different flow regimes have been identified.

As an outgrowth of this finding we have started to investigate the influence of forced vibration on g-jitter induced flows (Fig. 3).

References

[1] R. Feigelson and E. Zharikov, Investigation of the crystal growth of dielectric materials by the Bridgman techniques using vibrational control, *NASA Micr. Mat. Sci. Conf.*, 1998.

[2] A. Fedoseyev and J.I.D. Alexander, *NASA Microgravity Mat. Sci. Conf.*, 1996, 205-210

[3] G. Gershuni, D. Lyubimov, *Thermal Vibrational Convection*, Wiley, N.Y., 1997

[4] Y.C. Lu, J.-J. Shiau and R.S. Feigelson, *J. Crystal Growth*, **102** (1990) 807-813.

[5] R.C. DeMattei and R.S. Feigelson, *J. Crystal Growth*, **128** (1993) 1062-1068.

[6] A. Lizee, J.I.D. Alexander, *Phys. Rev. E* **56** (1997) 4152

[7] K.K. Gabdrahmanov, V.G. Kozlov, *Microgravity Q.*, 5 (1995) 146-151

[8] V.G. Kozlov, V.V. Rivola, Mean heat convection in a cavity rotating around a horizontal axis, *Proc. Xth European symposium on Phys. Sci. in Microgravity*, Moscow, 1997, 266

[9] V.S. Yuferev at al. Effect of space craft rotaion on convection and transport. Ibid, 37

[10] A.I. Fedoseyev and J.I.D. Alexander, *J. Comp. Phys.*, 130 (1997) 243-255.

[11] A.I. Fedoseyev and J.I.D. Alexander. An efficient method for modeling of incompressible viscous flow, thermal and vibrational convection, *16th Int. Conf. Numer. Meth. Fluid Dynamics,* Arcachon, France, 6-11 July, 1998.

[12] A.I. Fedoseyev, B.V. Alexeev, *Math. and Computers in Simulation* (1998) (accepted)

[13] A.I. Fedoseyev, B.V. Alexeev. High order continuum model for incompressible viscous flow and application to numerical modeling of thermo-vibrational convection. *Proc. of CMDS9 Symposium*, World Scientific, 1998 (in print).

[14] P.S. Perera and R.F. Sekerka, *Physics of Fluids* **9** (1997) 376-391

[15] V. Pukhnachev. Microconvection in a vertical layer, *Fluid Dynamics*, 5 (1994) 76-84.

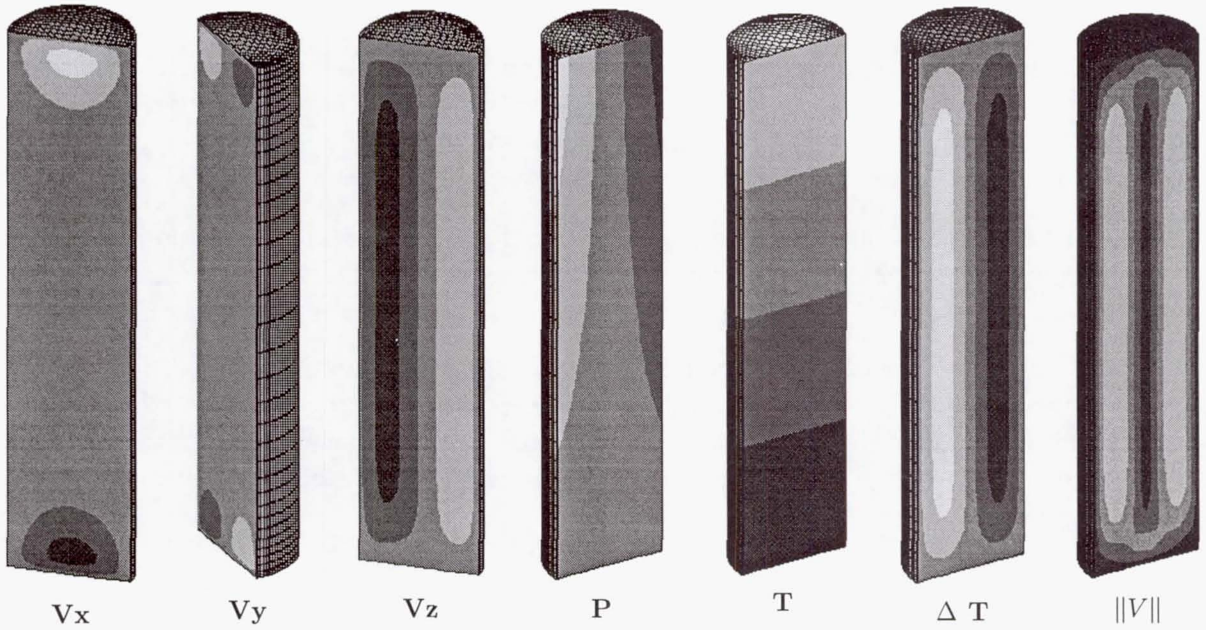

Figure 2: Melt flow patterns for translational vibrational convection, $Ra = 0$, $Ra_v = 7.25 \cdot 10^4$, lateral vibration: V_x, V_y,V_z are velocity components, p, T - pressure, temperature and ΔT, $||V||$ - temperature perturbation and velocity module

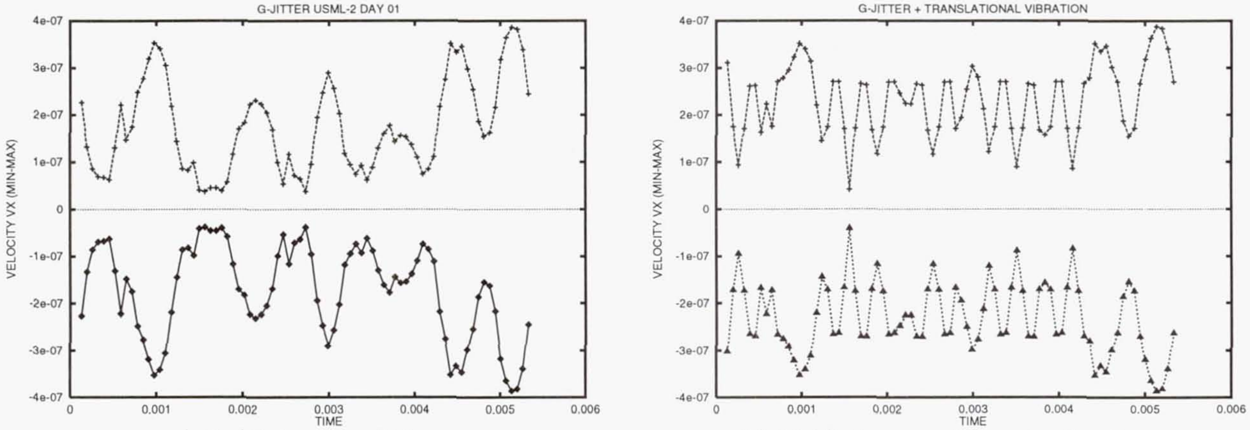

a) $V_x(t)$ due to g-jitter

b) $V_x(t)$ due to g-jitter + vibration

Figure 3: Comparison of the melt flow response to (a) g-jitter, UMSL-2 mission SAMS data, and (b) g-jitter + vertical vibration, $Ra_v = 7.25 \cdot 10^4$. Min-max values of V_x component versus time are shown

INVESTIGATION OF THE CRYSTAL GROWTH OF DIELECTRIC MATERIALS BY THE BRIDGMAN TECHNIQUE USING VIBRATIONAL CONTROL

Robert S. Feigelson, Principal Investigator
Stanford University
Stanford CA
Evgenii Zharikov, Co-Principal Investigator
General Physics Institute
Moscow,Russia

OBJECTIVES OF INVESTIGATION:

The principal goal of this ground-based program, which started in February 1998, is to investigate the influence of low frequency vibrations on the fluid flow and quality of dielectric oxide crystals grown by the vertical Bridgman method. This experimental program, a collaborative effort between Stanford University and the General Physics Institute of the Russian Academy of Sciences in Moscow , includes a strong emphasis on both physical modeling and the growth of some technologically important materials. It is in close collaboration with the theoretical and numerical investigations of A. Fedoseyev and I. Alexander in another NASA sponsored program. This latter program involves a study of vibro-convective buoyancy-driven flows in cylindrical configurations with the expectation of being able to use vibrational flows to control buoyancy driven fluid transport to off-set the effect of "g-jitter" during microgravity Bridgman crystal growth. These two programs taken together, will lead to a new parametric control variable which can be used to either supress or control convection, and thereby heat and mass transport during Bridgman crystal growth. It is expected to be effective in either a terrestial or space environment.

The experimental program is designed to verify and refine the results of the predictions made in the theoretical program, lead to the design of vibration controlled growth systems which can adapted to NASA flight ready crystal growth furnaces, and provide recommendations for the use of this vibrational technology in space growth experiments.

The specific objectives of the program are as follows: 1) Investigate how applied low frequency vibrations affect fluid flow during Bridgman crystal growth and develop relationships between vibro-convective-mediated flows and crystal quality. This part of the program will involve extensive experimental physical modelling using noncrystallizing water-glycerine mixtures and low temperature, transparent model growth systems, 2) Establish the most appropriate mode(s) for introducting low frequency vibrations into crystal growth systems, and optimize parameters for producing desireable fluid flow regimes (heat and mass transport conditions) in crystal growth systems with different physical and material properties. Solve the specific technical problems associated with the introduction of vibrations into real growth systems. Design,and construct apparatus for fluid flow and crystal growth experiments,, 3) Correlate vibration induced flows with a) interface shape and position, b) striations c) microsegregation, d) dopant distribution and e) crystal perfection , etc., 4) Demonstrate the effectiveness of vibroconvection control during the growth of nominally pure and doped technologically important dielectric oxide single crystals, 5) Verify and refine the theoretical predictions derived from mathematical modelling research, 6) Develop quantitative laws for predicting the most appropriate growth conditions for a specific material and system geometry and, 7) Provide recommendations for the use of vibrational technolgoy in space and terrestrial growth experiments

BENEFITS TO MICROGRAVITY RESEARCH

It is well known that natural buoyant convection in terrestrial crystal growth systems has a profound (often negative) influence on crystal quality (defects and homogeneity) and growth rates. Recent numerical modeling work has confirmed that vibrations can be used to supress buoyancy-driven flows. It has been indicated that such suppression might be very effective at reduced gravity levels of 10^{-4} g or less. This has raised the possiblity that, under microgravity conditions, controlled vibrations might be used to mask the undesirable "g-jitter" induced convective effects. Such g-jitter convection can be caused by quasi-steady residual acceleration (due to gravity gradients and atmospheric drag effects) and to transient and oscillatory acceleration disturbances) One approach to vibration isolation might be the use of low frequency vibrations to either suppress flow or to provide stable flow regimes tailored to a particular set of crystal growth experiments which essentially overwhelm the unstable flows. experiments.

SIGNIFICANT RESULTS

Since the program began a few months ago the construction of a video accessible, computer controlled transparent Bridgman furnace has been designed and built by the Russian group and special ampoules designed for the vibrational studies.

The electromechanical vibrators being used in this study have a wide amplitude range (up to 1.5 mm) and allow for frequencies in the 0-300 Hz range. The experimental studies were carried out using model liquids (distilled water) and $NaNO_3$ melts, for which the basic thermophysical parameters are given in table 1.

Sensors for measurement of temperature and flow rates in the distilled water were a needle type thermoanemometers for the indirect heating of a microthermisistor (MT-54). Temperature in the melt was measured by chromel-alumel thermocouples. For temperature sensor positioning, a two-coordinate device was rigidly fixed on the top rod. Accuracy was better than 0.5 mm. Before the beginning the measurements, the temperature sensors were calibrated. The error did not exceed 0.5 ° C.

The flow visualization was obtained by the addition of 20 microns diameter aluminum particles into the liquid. Observation and photographing the spatial form of the flows under steady-state conditions was accomplished using a flat vertical beam of light. Visual observation of flows structures and measurements of their characteristic sizes was made with the help of a binocular microscope which could measure distances to within 10 microns.

Table 1. Thermophysical Properties of the model Liquids [1]

Property	**Water** **(t = 30^{o}C)**	**$NaNO_3$** **(t = 310^{o}C)**
Melting point, ^{o}C	0.0	307.0
Liquid density, g*cm^{-3}	0.996	1.889
Dynamic viscosity, g*cm^{-1}*s^{-1}	8.01×10^{-3}	2.78×10^{-2}
Kinematic viscosity, cm^{2}*s^{-1}	8.0410^{-3}	1.4710^{-2}
Thermal diffusivity cm^{2}*s^{-1}	1.48×10^{-3}	1.58×10^{-3}
Coefficient of volumetric expansion, K^{-1}	2.8×10^{-4}	6.6×10^{-4}
Prandtl number	5.4	9.3

A schematic of the experimental set up for physical modeling with distilled water is given in a fig. 1. The ampoule used for these model experiments was a cylindrical glass vessel (4) with an internal diameter 36.0 and 41.0 mm and a height of 73.5, 110 and 146 mm. The ampoule was placed between two copper heat exchangers (1) at temperatures TB and TT. The ampoule was placed in a rectangular dish made from acrylic plastic (6), with the temperature of the internal wall TL. The vibrating body (3) was fixed on a rod (2), which was attached to the vibration generator (5). The vibrating block was rigidly fixed on a stand (8). Misalignment of the ampoule and body did not exceed 0.1 mm. Uncontrollable vibrations of the ampoule were minimal due to the rigidly of the design and the massive plate for vibration isolation (9).

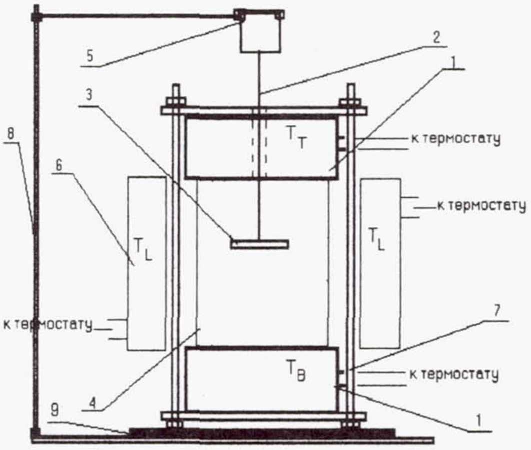

Fig.1.Setup for study of convective flows in distilled water.

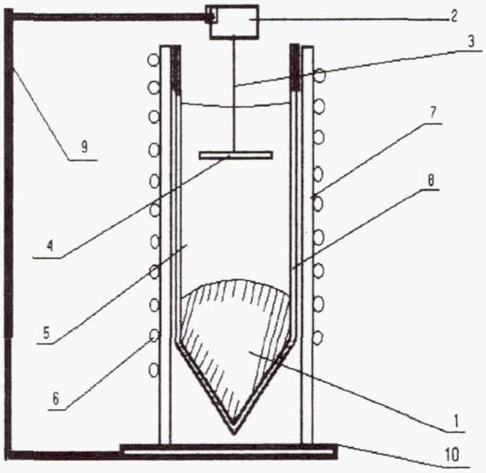

Fig.2. Set up for study of convective flows in $NaNO_3$ melts.

The schematic of the experimental set up for the $NaNO_3$ Bridgman simulation is given in a fig. 2. The ampoule (8) was made of quartz and was filled with sodium nitrate (1). The external ampoule was made of quartz to allow observation of the flow patterns in the melt. The ampoules were located on a support fixtures (9). The vibrator (2), rod (3), vibrating body (4), and isolation plate (10) are also shown.

Most of these studies were carried out in ampoules of internal diameter D = 16.8 mm. The height of the melt H, being equal to 36 mm. The thermal boundary conditions on the wall of the ampoules were T1max = 360°C. Heating and cooling rates were 5 °C/min. After reaching the operating temperature, the system was maintained there for at least 1 hour to stabilize the thermal conditions.

For comparison of various vibrating modes, the vibrating Reynolds number R_{ev} was used:

$$R_{ev} = 2\pi fAR/\nu \qquad (1),$$

where f is the vibration frequency, A the vibration amplitude, ν the dynamic viscosity, and R the vibrating body radius.

The geometrical parameter giving the relationship between the area of the gap between the internal walls of the ampoule and the vibrating body, and the area of the vibrating body has been chosen as

$$S(k) = (D^2/d^2)-1 \qquad (2),$$

where D is the internal diameter of ampoule and d the diameter of the vibrating body. This is the characteristic section area through which a liquid undergoing vibrational mixing goes in a given system.

Previous experiments [2] have shown that vibrations in an ampoule with the liquid surface capped will not generate fluid flow under isothermal conditions. The liquid in this case behaves as a solid. The vibrations of an ampoule with a liquid possessing a free surface can produce rather intensive flows. In the preliminary study reported on here our basic attention was limited to the flow patterns occurring under a vibrating body inserted into the melt. In the current work, the vibrating body acts as the generator of additional convective flows. This can act as the active adjustable control factor during crystal growth.

Several different vibrator configurations were studied including spheres, cubes, and cylinders (the latter with variously shaped bottom faces). In the case of a vibrating cylinder or disc, the flow patterns in a vertical section of an ampoule (fig.3) is similar to that which occurs under vibration of a cube. However in this case the vortices have cylindrical symmetry and the liquid goes from the edge of a body to its axis and further along the axis of the ampoule.

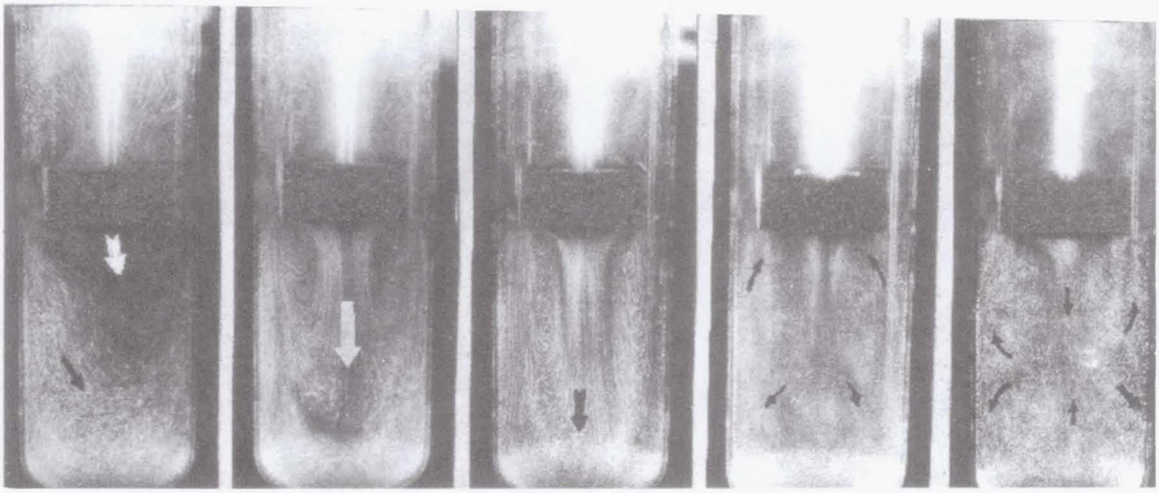

Fig. 3. Flow patterns under axial vibrations of the cylinder in an ampoule with a diameter D = 41,0 mm: a) f = 80,0 Hz, A = 50 _m, Rev = 1,3; b) f = 80.0 Hz, A = 100 _m, Rev = 5.0; c) f = 80,0 Hz, A = 200 _m, Rev = 20,1; d) f = 80,0 Hz, A = 300 _m, Rev = 45,2; e) f = 80,0 Hz, A = 500 _m, Rev = 322.

The simplest way found so far to get axially symmetric vortices and, correspondingly, control of the flows in a liquid volume is to use a vibrating disk. In experiments with distilled water with a temperature gradient the presence of a motionless body suppressed the temperature oscillations. The vibrator body acted as a heat shield, preventing heat exchange between hot and cold regions and also changed the natural convection flow patterns. The application of vibrations resulted in the formation of vortices of a vibrating nature near the disk, which increased with increasing amplitude and in considerable ordering when R_{eV} = 1290. Larger amplitudes caused unstable vibrating vortices, which lost axial symmetry and covered whole ampoule volume.

In experiments on $NaNO_3$ without vibrations, the growth interface was convex. The application of vibrations resulted in the occurrence of strong vortices in a melt. Vibrating flows decreased along the ampoule axis from the vibrator body downward to the crystal interface, and caused a displacement and shape change of the solid-liquid interface. The appropriate selection of amplitude-frequency parameters can give a nearly flat crystallization front (fig. 4)

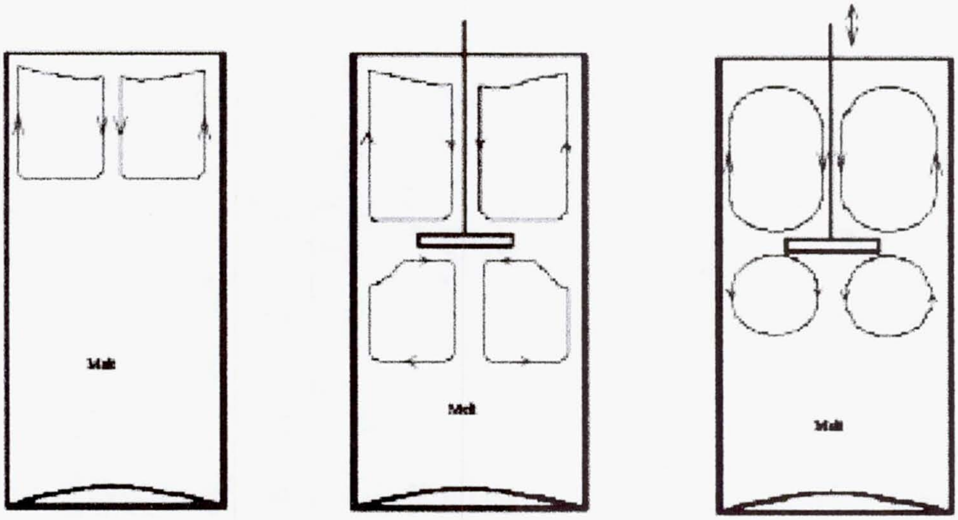

Fig. 4. Flow patterns in NaNO$_3$ melt, (ν= $1.47x10^{-2}$ cm^2/sec a) free melt;
b) melt with a motionless vibrating body; c) vibration f = 50 Hz, A = 200 _m, R_{eV} = 684.

With use of a system with the parameter S_k equal to 2.33, the introduction of a vibrating body into the melt did not change the thermal flow patterns. Under the influence of vibrations, the structure of the flows was maintained, only being increased in scale with increasing of amplitude. In the area close to the interface an almost isothermal, motionless layer of melt existed and its thickness was maximal in the free melt and decreased with increasing of vibrations amplitude.

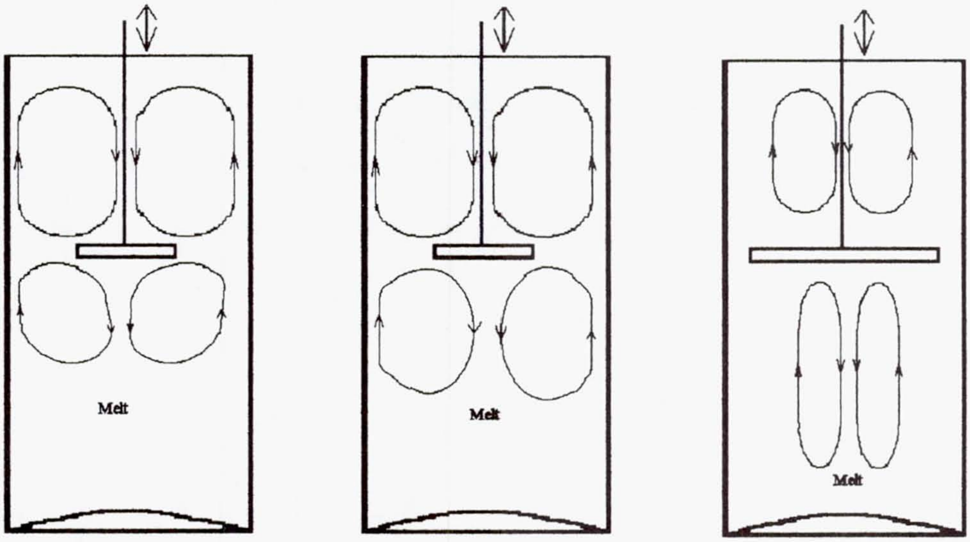

Fig. 5. Patterns in NaNO3 melt with amplitude A = 300 m, (ν = $1.47x\ 10^{-2}$ cm^2/sec):
a) f = 66 Hz, Sk = 2,33, Re_v = 1354; b) f = 50 Hz, Sk = 2,33, Re_v = 1026;
c) f = 50 Hz, Sk = 0,96, Re_v = 1026.

In a system with parameter S_k equal to 0.96, (all other conditions constant), an increase in disk size has much more influence on the change in the convective flow patterns. Their intensity sharply increases with a decrease in S_k. In contrast to the previous case, all flows became non axially symmetric when $R_{eV} = 1300$. When the vibrating flows reached the crystal surface, it resulted in a deflection of crystallization front towards the crystal (fig. 5)

The U.S. program has focussed its initial efforts on the effect of induced vibrations on fluid flow in a simulated Bridgman growth system. The particular case being studied involves two orthogonal vibrations normal to the crucible axis (equal amplitude, phase difference 90°) which has been shown to produce high rates of fluid flow in a terrestrial enviornment (4,5). Data previously collected on the relationship of fluid flow to the Reynolds number, Froude number, dimensionless amplitude of vibration and crucible aspect ratio has been recently analyzed. This analysis shows that two of the independent parameters are gravity dependent. We are continuing to study this latter method to understand the effect of reduced gravity on the fluid flow rates.

CONCLUSIONS

The hydrodynamic flow patterns for variously shaped vibrating bodies, various heating conditions, and with an appropriate temperature distribution in the liquid phase (both the model and crystallizing systems) were studied.

The vibrating body, its location to the crystallization front, the geometrical parameters associated with the area of the ampoule walls and the vibrating body, and the height of the liquid column were found to have a considerable influence on the vibroconvective flow patterns and temperature distributions in the liquid phase. Vibroconvective flows greatly influenced the position and shape of the solid-liquid interface in real crystallizing systems.

REFERENCES

1. Schwabe D., Scharmann A., Preisser R., Order R. Experiments on surface tension driver flow in floating zone melting. J. Crystal Growth, vol. 43, 3, 1978, pp. 305-312.
2. J.I.D. Alexander. "Low gravity experiment sensitivity to residual acceleration." A review "Microgravity Sciense and Technology", III, 1990, p. 52.
3. Gershuni G.Z., Zhukhovitsky E.M. "Vibrational thermal convection in space." In "Hydromechanics and transfer processes in space", Acad. Sci, Sverdlovsk, 1983. pp.86-105. (in Russian)
4. Liu, W.S., Wolf, M.F., Elwell,D., and Feigelson, R.S., “Low frequency vibrational stirring: A new method for rapidly mixing solutions and melts during growth”J. Crystal Growth, 1987, vol 82, pp. 589-597.
5.. Lu Y.-C., Shiau J.-J., Feigelson R.S. and Route R.K.. "Effect of vibrational stirring on the quality of Bridgman growth of CdTe." J. Cryst. Growth, 1990, vol. 102, pp. 807-813.

Page intentionally left blank

ALLOY UNDERCOOLING EXPERIMENTS IN A MICROGRAVITY ENVIRONMENT

"Recent results from the STS-83 and STS-94 missions"

Merton C. Flemings and Douglas M. Matson
Department of Materials Science and Engineering
Massachusetts Institute of Technology
77 Massachusetts Avenue Room 8-407
Cambridge, MA 02139

Phone : (617) 253-3233
E-mail : flemings@mit.edu, matson@mit.edu

Objectives

The focus of this program is the study of the effect of microgravity on metastable solidification of ternary steel alloys. By observing changes in the mechanism for nucleation of the stable phase following primary recalescence from undercooled melts, the role of convection in phase selection may be evaluated.

Microgravity

Undercooling in containerless processing has shown promise in producing metastable phases and materials that exhibit improved chemical homogeneity and ultra-fine grain sizes. One aim of this research is to develop an understanding of the role of convection in the metastable to stable transition that has been observed in multi-component systems, notably in Fe-Ni and Fe-Cr-Ni alloys. The mechanism for nucleation of the second phase and the delay time observed in this transformation appear to be dependent on solid movement and coalescence, probably the result of convective flow.[1] Ground-based electromagnetic (EM) levitation experiments require maintaining a balance between the levitation force and gravity, while space experiments need far less energy to position the sample. With a reduction in melt convection[2] in μg, we have investigated the apparent changes in phase selection for these two different environments. Microgravity is thus an integral requirement for the successful attainment of the goals of this program.

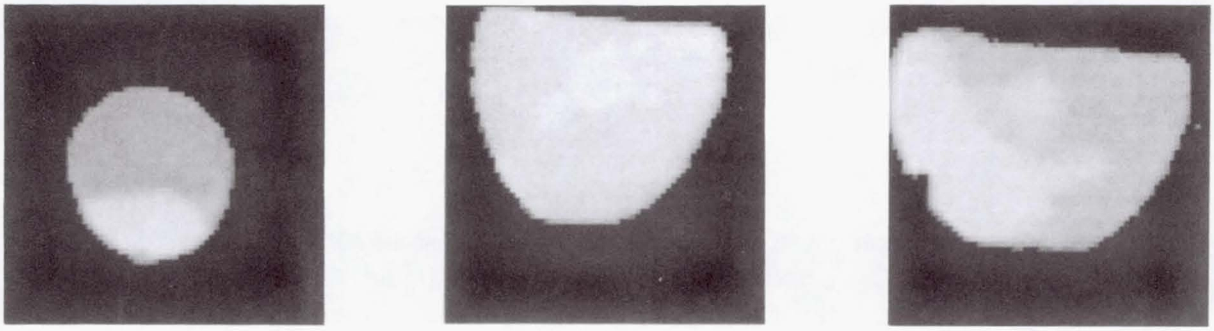

(a) Triggered nucleation undercooled ΔT=145°
(b) γ growth in semi-solid undercooled ΔT=218°
(c) edge nucleation event undercooled ΔT=130°

Figure 1 - Digital images of growth competition in ground-based steel alloy solidification

Ground-based Electromagnetic Levitation Results

In collaboration with our Co-Investigator Wolfgang Löser of Institut für Metallische Werkstoffe (IFW-Dresden), the rapid solidification of two ternary steel alloys, a Fe-12wt%Cr-16wt%Ni and a Fe-16wt%Cr-12wt%Ni alloy, were investigated under containerless processing conditions. A high-speed digital video technique was used to image growth into the undercooled melt for both the metastable ferritic phase and the stable austenitic phase[3-4]. Above a critical undercooling, the metastable δ-phase nucleates first and, after a delay, a second thermal rise is observed during transformation to the stable γ-phase. Double recalescence events were observed at temperatures consistent with the T_o temperature of the bcc phase defining a value of the critical undercooling for metastable nucleation which is significantly lower than previously predicted.[1, 5-8]

Figure 1 contains digital images taken at an acquisition rate of 40,500 frames/second during steel alloy double recalescence events[9]. In the first image, primary metastable phase nucleation was initiated at a known site using a stimulation trigger with subsequent growth into the undercooled liquid; growth of the second phase follows soon thereafter from the same nucleation site. In the second image, spontaneous nucleation of the second phase is seen, both from the primary nucleation site (in the center) and in other sites distributed within the semi-solid. The third image shows nucleation of the stable phase at the growing metastable phase front with subsequent competitive growth of both phases into the undercooled liquid. As seen in these images, ground-based double recalescence events show three types of mechanisms for nucleation of the second phase, two within the semi-solid and one at the interface between primary phase and liquid.

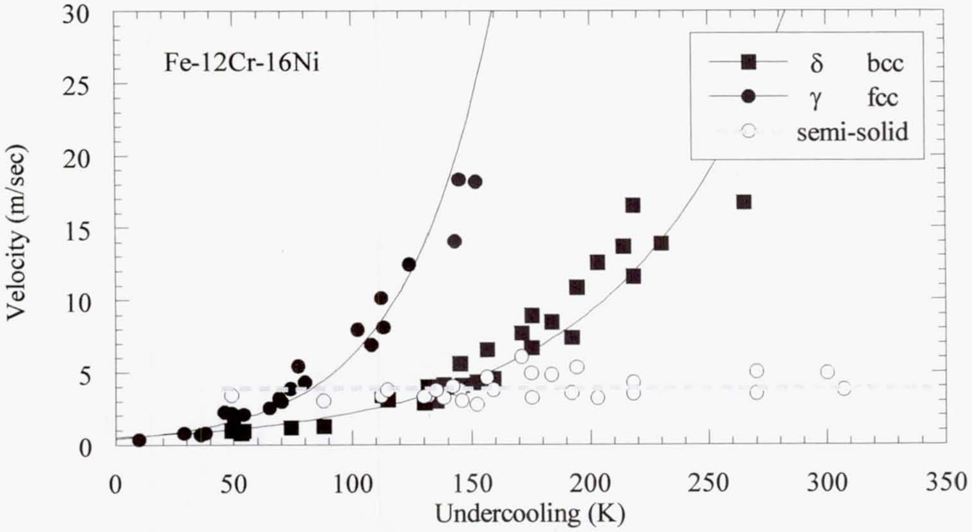

Figure 2 - Growth rate of each phase as measured in ground-based EM levitation testing
Solid symbols indicate growth into undercooled liquid
Open symbols indicate growth into the semi-solid following primary recalescence

As shown in Figure 2, at a given temperature the rate of growth into the undercooled liquid for the fcc gamma phase is greater than for the bcc delta phase. The velocity of the stable phase growing into the semi-solid which forms during primary metastable recalescence was also measured and, as seen in Figure 2, is independent of the initial undercooling. This effect has previously been observed in other ternary steel alloys[9]. The behavior arises because the driving force for growth under these conditions is approximately constant given that the temperature following primary recalescence is always nearly the same at a given composition.

Depending upon the delay time between nucleation events, the bcc phase may be growing into the liquid at the same time as the fcc phase is growing into the semi-solid. During simultaneous growth at temperatures below the undercooling where the velocities of the two phases are equal, the metastable phase grows into the liquid faster than the stable phase grows within the semi-solid and thus a distinct double recalescence event is observed. Above this temperature, the equilibrium phase can overwhelm the slower metastable phase and break into the undercooled liquid. Such a double recalescence event can therefore appear as a single event. A model based on competitive growth of the two phases successfully predicts the limit where double recalescence events may be detected as a function of the geometric relationship between the sensor and the nucleation site.

Flight Results

Molten samples of the ternary steel alloys were successfully processed in a containerless fashion using the TEMPUS electromagnetic levitation facility aboard the shuttle Columbia. The solidification rate was measured as a function of undercooling using a combination of live video downlink and the onboard recording of a perpendicular set of two high-speed pyrometers. Nucleation was induced within the field of view using a ZrO_2-coated stimulation needle.

Figure 3 shows a comparison between the growth rate of the metastable phase into the undercooled liquid for ground-based and MSL-1 microgravity experiments. By employing a two-sided t-test we found that there is no significant difference between these two conditions to a confidence level of 88%. In a similar manner, the velocity for growth of the stable phase into the semi-solid following primary recalescence was also evaluated and found to be the same in space and on the ground with a confidence level of 97%.

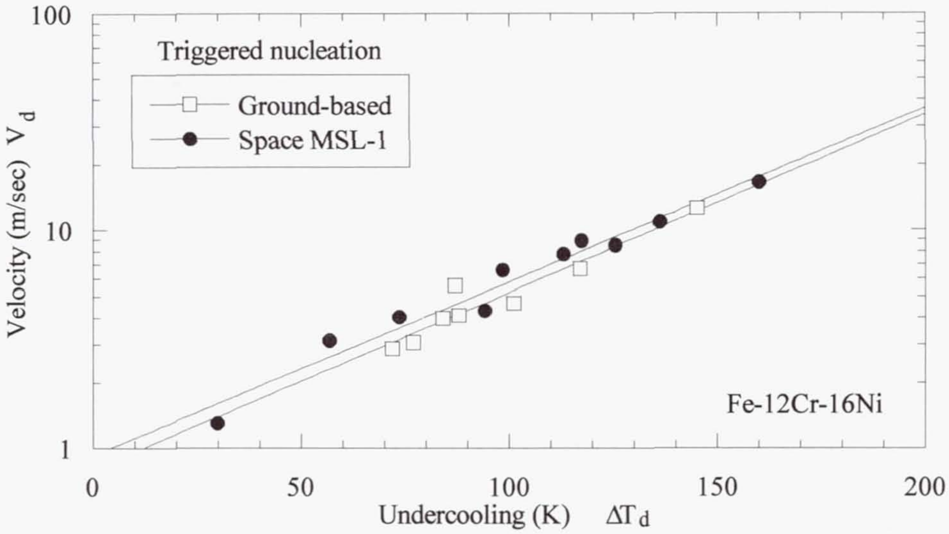

Figure 3 - Growth rate of the metastable phase into the liquid during primary recalescence

Figure 4 shows a comparison between the observed delay times measured adjacent to the nucleation stimulation point in space and on the ground; significant positive deviation (to a confidence level of 99%) is observed in space. These results are consistent with our hypothesis that convection may influence the formation of secondary nucleation sites.

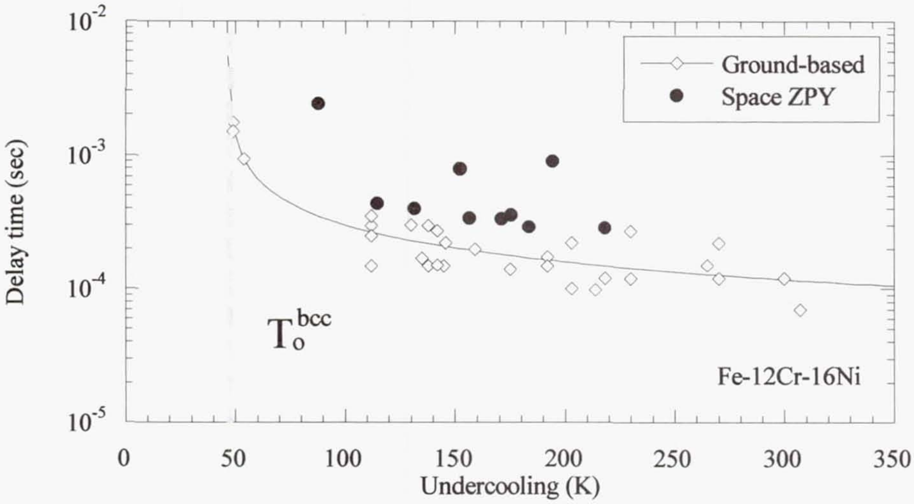

Figure 4 - Delay times under ground-based and space conditions

A growth competition model was developed to predict which phase would be seen, given a known relationship between the nucleation site and the location of the sensor used to monitor the passage of each of the fronts during recalescence. This model was based on ground-based measurements of the propagation velocities and delay times and includes the assumption that secondary nucleation will occur within the semi-solid – either at the primary site or distributed within the semi-solid. The model was intentionally designed to fail to include edge nucleation events as these are assumed statistical in nature. In the case where a single recalescence event is detected when a double recalescence event was predicted, ground-based results show that this occurrence is associated with the edge nucleation mechanism. In terrestrial tests on the flight Fe-12Cr-16Ni master alloy this was observed to occur in 71% of the tests below an undercooling of 150° and in none above this undercooling. In μg tests during MSL-1, this was never observed at any undercooling level and we therefore associate the occurrence of the edge nucleation mechanism with ground-based conditions.

In addition to being able to predict which phase will be observed, the growth competition model allows prediction of what the delay time should be, as a function of sensor position relative to the nucleation site. Using the growth competition model, we have defined a deviation parameter,

$$\theta_d = \left(\frac{\tau_o}{\tau_p}\right) - 1$$

based on the ratio of the observed, τ_o, to predicted, τ_p, delay times. This parameter may then be used to compare the ground-based and space results to a common theoretical baseline.

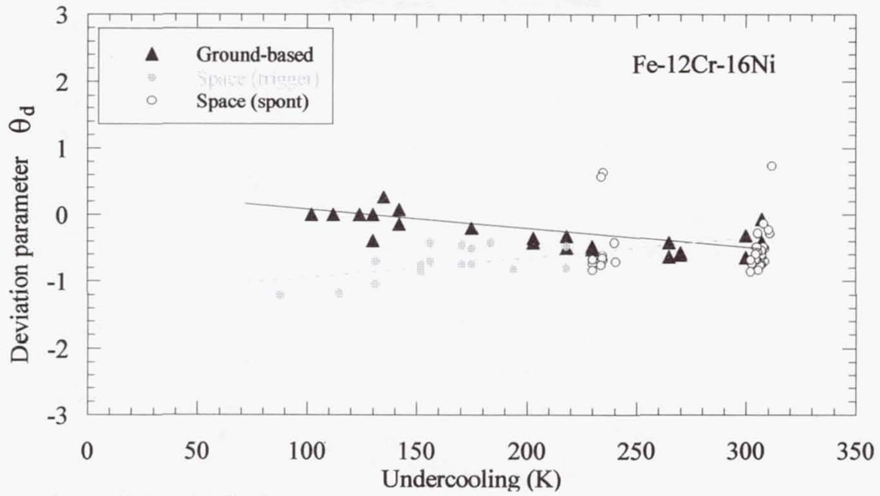

Figure 5 - Variation of the deviation parameter

This comparison is shown in Figure 5 where significant negative deviation is seen for flight experiments at low undercoolings. This effect is due to the increased delay times observed during MSL-1 compared to those measured in ground-based tests, as seen earlier in Figure 4.

Conclusions

Double recalescence events were observed in hypoeutectic ternary steel alloys at much lower undercoolings than previously reported. Using a high speed imaging technique, we are able to identify and characterize the mechanism for nucleation of the stable phase after the initiation of metastable phase growth. We have shown evidence that nucleation of the stable phase at the interface between the growing metastable phase and the liquid may be suppressed in microgravity.

When comparing the growth rate under ground-based and microgravity conditions, there is no significant difference for the observed growth of the metastable phase into the undercooled liquid over the range of undercoolings investigated. There is also no significant difference in the growth rate of the stable phase into the semi-solid that formed during primary recalescence. There is, however, a significant difference in the delay between primary and secondary recalescence.

We have successfully developed a model that combines :

(1) simultaneous growth of competing phases,
(2) the delay between recalescence events,
(3) assumptions on the mechanism for secondary nucleation of the stable phase, and
(4) given a known relationship between the sensor and the nucleation events

to explain the role of growth competition in phase selection during rapid solidification of undercooled hypoeutectic Fe-Cr-Ni alloys. Using this model, we have demonstrated that a difference exists between the high convective environment of ground based electromagnetic levitation and that attainable in microgravity.

References

1. T. Koseki and M.C. Flemings, Met. Trans., 26A, 2991 (1995).
2. G. Trapaga, D.M. Matson, R. W. Hyers, and M.C. Flemings, in **Proc. Julian Szekely Memorial Symposium on Materials Processing**, H. Y. Sohn, J. W. Evans, and D. Apelian, eds.,TMS Warrendale PA, 453 (1996).
3. D.M. Matson, in **Solidification 1998**, S.P. Marsh *et al.*, eds.,TMS Warrendale PA, 233 (1998).
4. J.W. Lum, D.M. Matson, and M.C. Flemings, , Met. Trans., 28B, 865 (1996).
5. T. Koseki and M.C. Flemings, Met. Trans., 27A, 3226 (1996).
6. T. Volkmann, W. Löser, and D.M. Herlach, Met. Trans., 28A, 453 (1997).
7. T. Volkmann, W. Löser, and D.M. Herlach, Met. Trans., 28A, 461 (1997).
8. S. Moir and D.M. Herlach, Acta Mater., 45(7), 2827 (1997).
9. D.M. Matson, A. Shokuhfar, J.W. Lum, and M.C. Flemings, in **Solidification science and processing**, I. Ohnaka and D.M. Stefanescu, eds.,TMS Warrendale PA, 19 (1996).

THE MEASUREMENT OF THE VISCOSITY AND SURFACE TENSION OF UNDERCOOLED MELTS UNDER MICROGRAVITY CONDITIONS AND SUPPORTING MHD CALCULATIONS

Robert Hyers, Gerardo Trapaga, and Merton C. Flemings
Department of Materials Science and Engineering
Massachusetts Institute of Technology
(617) 253-3236
rwhyers@mit.edu, trapaga@navier.mit.edu, flemings@mit.edu

Objectives of the Investigation

The scientific and technical objective of our experiment in the MSL-1 space shuttle mission was to utilize the electromagnetic levitation (EML) system, TEMPUS, for the experimental determination of the surface tension and the viscosity of metallic melts, in both the superheated and the undercooled state, using the unique attributes of microgravity. This objective was achieved on both the STS-83 and STS-94 shuttle missions for several different metals.

In addition, the development of a mathematical model aimed at representing the magnetohydrodynamic phenomena in levitated samples represented an important component of the project. This model has provided the means for the understanding of the role of the different processing parameters on the behavior of the samples during the experiments, as well as an important tool for the design of the actual experiments.

Necessity of Microgravity

Ground based experiments with the oscillating droplet technique introduce an inherent systematic error in the measurement of surface tension. In addition, the perfect symmetry of the samples, possible only in microgravity conditions, eliminates the splitting of oscillation modes that is observed in ground-based experiments. Based on purely theoretical grounds, Cummings and Blackburn [1] have developed a correction for gravitational and electromagnetic effects on the apparent surface tension; one of the accomplishments of the IML-2 flight was to provide the first experimental results suggesting the validity of the correction factor. Surface tension data from the MSL-1 flights suggest that this correction factor, while only about 1-3% for microgravity experiments, is still relevant even for these experiments.

The reason for performing measurements of viscosity under microgravity conditions is quite different. Under earthbound conditions, the levitation forces needed are quite high and the associated rotational component of that force (the curl of JxB) gives rise to transitional or turbulent flows, making the measurement of viscosity impossible for normal metals. However, in microgravity, this internal flow velocity may be greatly reduced because much smaller positioning forces (i.e., about 300 times smaller than under earthbound conditions) are needed to contain the sample. These reduced forces allow a laminar flow condition which will not interfere with the droplet oscillations.

Significant Results to Date

Successful containerless measurement of the viscosity of a liquid metal was demonstrated for the first time during these microgravity experiments, both for the superheated and undercooled regimes. Also, high-precision containerless measurements of surface tension were performed as a part of these experiments.

In a typical experiment, a thermal cycle is prescribed where a sample is heated, melted and superheated, and then allowed to cool. As the droplet cools, the heating field is pulsed to excite surface oscillations. This sample processing is illustrated in Fig. 1 where seven pulses are shown during the cooling step. Each of these pulses represents a measuring point providing surface tension and viscosity data for a particular temperature range.

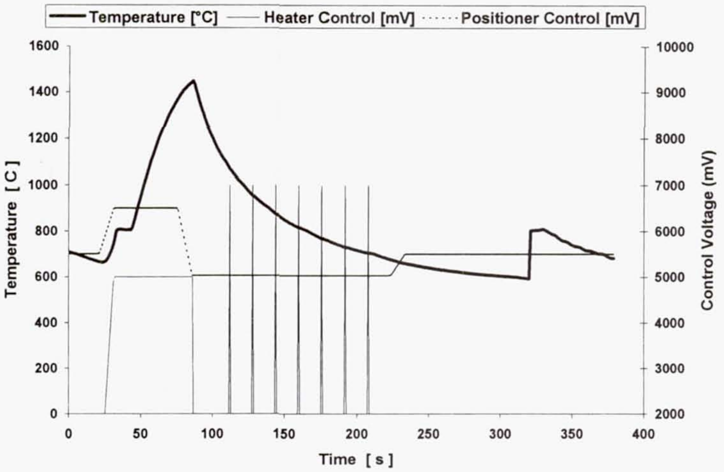

Fig 1: Typical thermal profile for droplet oscillation experiments in TEMPUS. Sample is melted As the droplet cools, the heating field is pulsed to excite surface oscillations. The sample recalesces and is fully solidified, then mechanically damped in preparation for the next cycle.

The surface oscillation are recorded on a video. The apparent area of the droplet is measured for each frame yielding the measured area-time signal (Fig. 2.a). A Fourier power spectrum is taken of this signal to find the frequency of the surface oscillation (Fig. 2.b) which is related to the surface tension by Rayleigh's equation:

$$\omega_l^2 = \frac{l(l-1)(l+2)\gamma}{\rho R_o^3} \qquad \text{(eq. 1)}$$

where ω_l is the angular frequency of oscillation mode l , for a droplet of surface tension γ , density ρ, and radius R_o . The mode $l = 2$ is the fundamental mode of surface oscillations.

A band-pass filter (flat-topped Hamming widow) is used to isolate the component of the area-time signal which is due to surface oscillations (Fig. 2.c). The damping time τ of this oscillations is related to the viscosity, μ, by Lamb's equation:.

$$\tau_l = \frac{\rho R_o^2}{(l-1)(2l+1)\mu} \qquad \text{(eq. 2)}$$

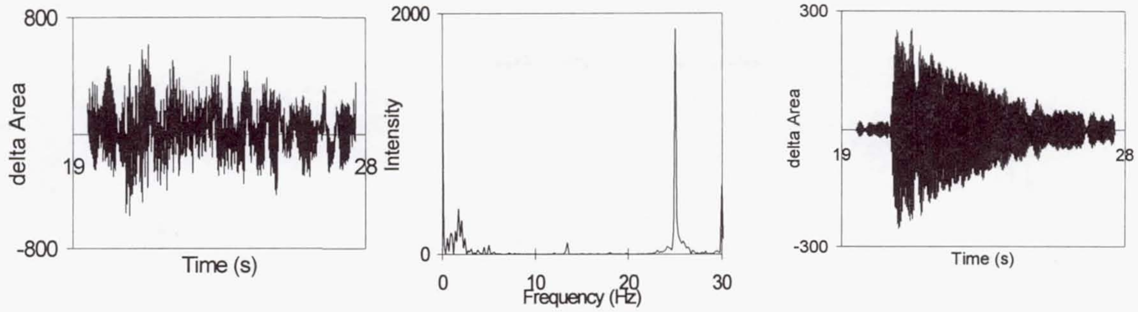

(a) Unfiltered Oscillations (b) Power Spectrum (c) Filtered Oscillations

Fig 2: MSL-1(STS-83) experimental data Pd-18Si sample, excited oscillations at 1215C. Power Spectrum of the unfiltered oscillation shows a surface tension peak visible at 25.0 Hz, which corresponds to a surface tension of 1.7 N/m and (c) filtered oscillations with exponential damping constant of 3.42s, giving viscosity 9.0 mPa-s.

Surface tension and viscosity data are presented in Figs. 3 and 4 for a Pd-18Si alloy for a wide range of temperatures (725 - 1425C), covering up to 100 C of undercooling and 650 C of superheat.

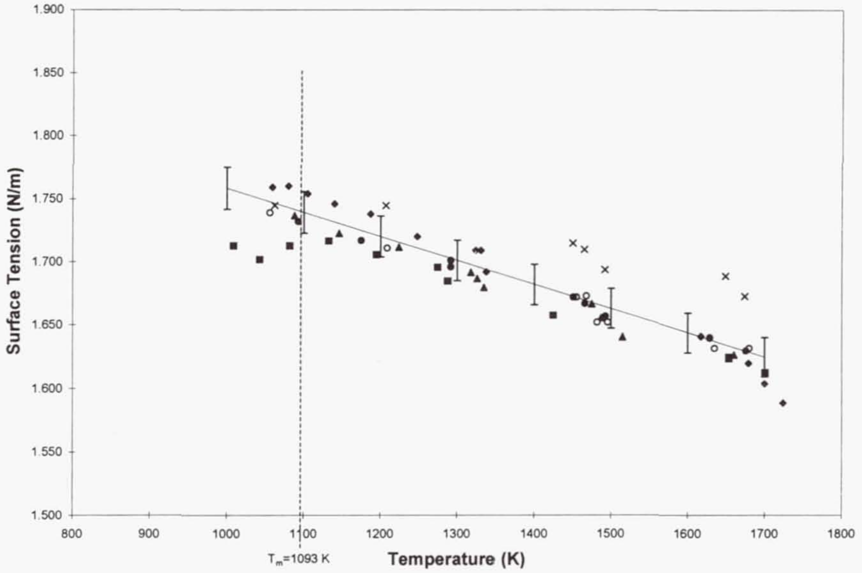

Fig 3: Corrected surface tension data for Pd-18Si.

Surface tension data are corrected and fitted as a function of temperature as $\gamma = 1.949 - 1.91 \times 10^{-4} T$, for surface tension γ in N/m and T in Kelvin, to a standard error of better than 1%. The application of Cummings and Blackburn's correction for electromagnetic forces to these points provides a significant improvement in the scatter of these data.

Measurements of viscosity for this alloy may be correlated as a function of temperature, as $\mu = 0.1917 \exp(5754 / T)$, for viscosity μ in mPa-s and temperature T in Kelvin. The viscosity data presented in Fig 4, are compared with experimental correlations reported by other authors [2]-[4] for this and similar glass-forming alloys. These data are in very good agreement and prove that the oscillation drop technique is capable of providing containerless measurements of viscosity.

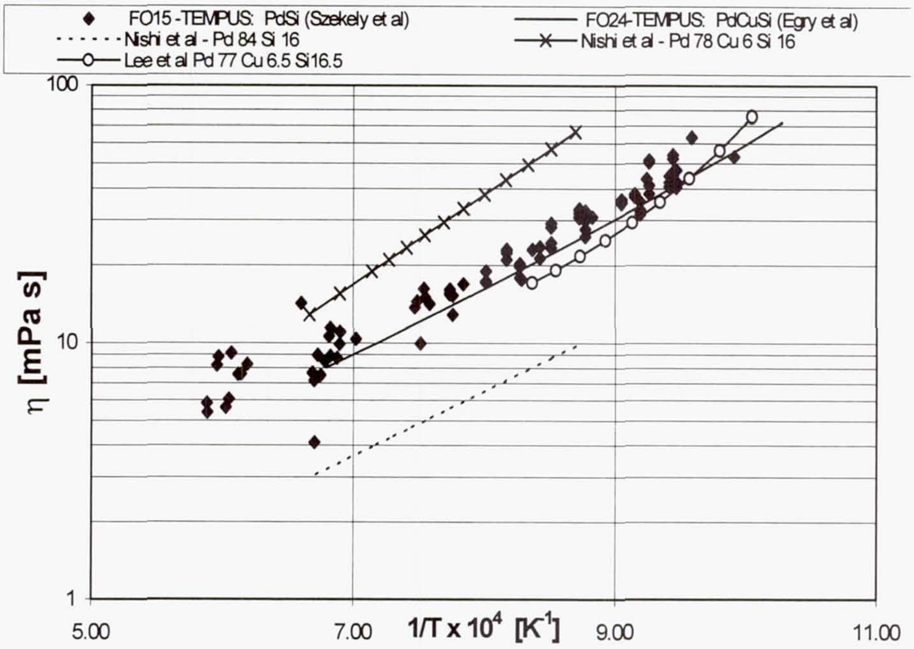

Fig 4: Viscosity data for Pd-18Si. Other relations from [2-4].

The results described above represent a small portion of the data acquired on the MSL-1 missions. Additional results are forthcoming for other alloy systems: PdSi, Zr, FeCrNi, ZrNiCuAlNb and TiZrCuNi

Calculations of the magnetohydrodynamic flow in the droplets allow comparison of flow conditions between different experiments and samples. These calculations were an important part of the planning of these experiments, and contributed significantly to the importance and utility of the results. Due to lack of space only two illustrations are presented in this report.

Characteristic internal flow patterns in the droplet are determined depending on the parameters employed during specific experiments. Fig.5 shows calculated flow fields for a 7mm Zr sample in TEMPUS for a constant coil positioner current (100A) and various coil heating currents. These computed results illustrate possible control regimes of the flow and the transition from positioning- dominated to heating-dominated flow, within this range of parameters.

The figure indicates that as the current in the heating coil is increased, the forces from the heating field oppose the flow of the positioner's equatorial recirculating loops and augment the flow of the positioner's polar loops. Because the force due to the heating field is directed inward at the equator, this force should augment loops with flow inward near the equator and out at the poles and suppress circulations with the opposite direction. Thus, the original four-loop (positioner-dominated) flow pattern, becomes a two-loop (heater dominated) pattern, as the heater current is increased and the outward-flowing equatorial loops of the positioner-dominated pattern slow to extinction. During this flow transition, the droplet mean and maximum velocities undergo a decrease, as the faster loop of the positioner-dominated pattern is slowed, but when the heater forces become dominant, the velocity resumes the expected increase with increasing heater current.

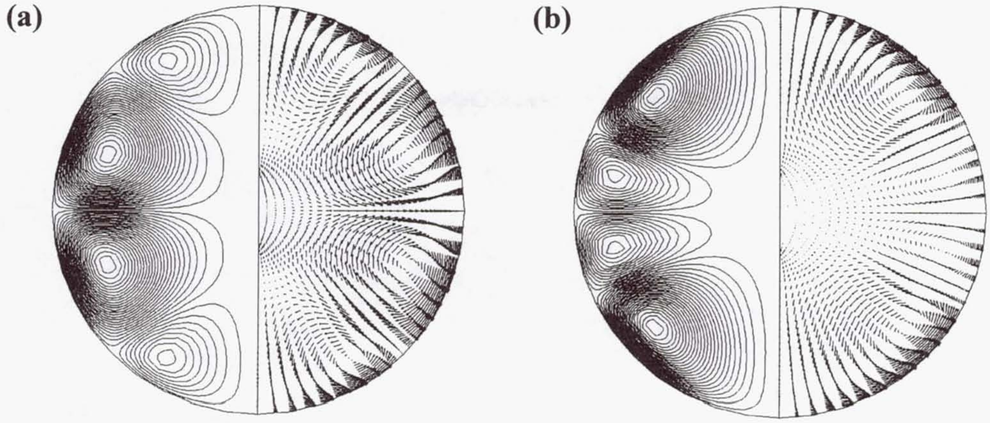

Pos=100A heat=16.2A
max. Velocity = 3.41 cm/s
Reynolds Number = 176

Pos=100A heat=22.4A
max. velocity = 3.25 cm/s
Reynolds Number = 168

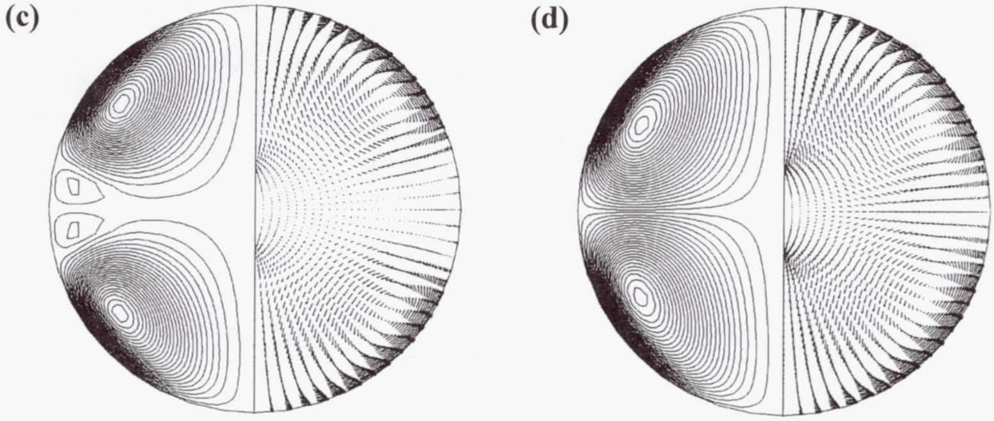

Pos=100A heat=26.3A
max. Velocity = 3.23 cm/s
Reynolds Number = 167

Pos=100A heat=30.9A
max. velocity = 3.58 cm/s
Reynolds Number = 185

Fig 5: Development of flow pattern for increasing heating current at constant positioning current of 100A for 7mm Zr sample. The heating forces oppose the rotation of the faster positioner loop, so the increasing heating forces cause the faster loop of the positioner flow to slow and disappear, while the slower positioner loop becomes faster.

Another important result of the modeling work involves the analysis of the role of fluid flow during nucleation experiments in microgravity for Zr samples (in collaboration with the Vanderbilt team[5]). These experiments found that the maximum undercooling was independent of the applied heating field only up to about 200V in the heater oscillating circuit, and that undercooling was inhibited at higher voltages.

The MHD model suggests that this effect was caused by cavitation. The calculations show a locally reduced pressure in the recirculation loops; this reduction would give a negative local pressure for a heating field corresponding to 225V (Fig. 6). This local state of hydrostatic tension provides a driving force for cavitation. The collapse of bubbles then promotes the nucleation of the solid phase.

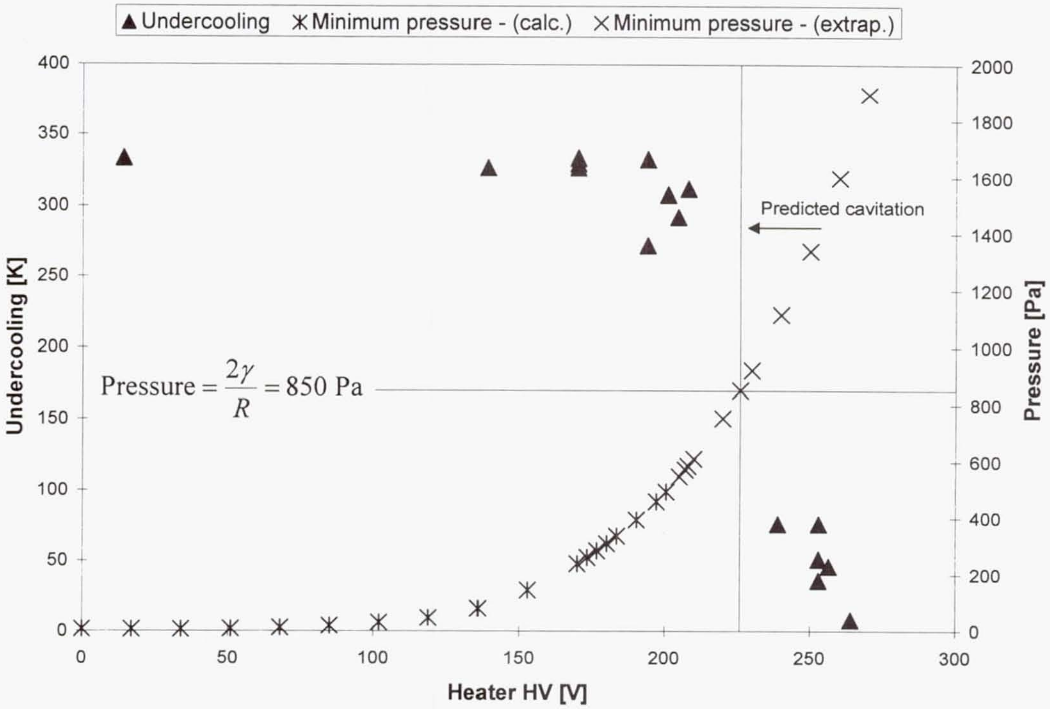

Fig 6: Undercooling as a function of applied heater voltage for a 7mm Zr sample.

Summary

Experiments carried out during the STS83 and STS94 mission provided successful containerless viscosity measurements using EML for a wide range of temperatures and viscosities. Also resulted precise, containerless measurement of surface tension and its temperature dependence over a wide temperature range. Analysis of surface tension data indicated that Cummings and Blackburn's correction, while only 1-3 % for these microgravity experiments, is still important.

The theoretical analysis, based on the use of mathematical modeling techniques, proved to be very useful to provide important information for the design and analysis of EML experiments. As illustrated in this report, the modeling work allowed to obtain some important insight into the role of internal flows on the behavior of the droplet for different samples and type of experiments, for example by providing a sound explanation of the ocurrence of dynamic nucleation in nucleation experiments for Zr.

References

[1] D.L. Cummings and D.A. Blackburn, "Oscillations of Magnetically levitated Aspherical Droplets", *J. Fluid Mech.*, Vol. 224, 395-416 (1991).
[2] Y. Nishi, N. Kayama, S. Kiuchi, K. Suzuki and T. Masumoto, "Viscosities and Glass Formation of $Pd_{84}Si_{16}$ Alloy and $Pd_{78}Cu_6Si_{16}$ Alloy" *J. Japan Inst. Metals*, Vol. 44, No. 12, pp. 1336-1341 (1980).
[3] S.K. Lee, K.H. Tsang and H.W. Kui, "Viscosity of molten $Pd_{77}Cu_{6.5}Si_{16.5}$ and the Principle of Corresponding States", *J. Appl. Phys.*, Vol. 70, No. 9, pp. 4842 (1991).
[4] I. Egry, G. Lohöfer, *et al.*, MSL-1 Results for PdCuSi, priv. comm.
[5] R. Bayuzick, W. Hofmeister, *et al.*, MSL-1 Results for Zr, priv. comm.

POLYELECTROLYTES FOR BATTERY APPLICATIONS: SYNTHETIC APPROACHES AND PRECURSOR PROPERTIES

Mu Zheng, Jason T. Manka, and Andrienne C. Friedli*
Department of Chemistry, Middle Tennessee State University
Murfreesboro, TN 37132
615-898-2071; acfriedli@acad1.mtsu.edu

Introduction. Widespread interest exists for the development of polymer electrolytes for use in solid state batteries.[1] These devices have applications in energy storage and power supply for the human exploration and development of space (HEDS), as well as for communications devices on Earth. On a molecular level, the polyelectrolytes must be flexible enough to promote ion migration, yet have diffuse charges to prevent trapping of the ions at a given site.[1] Here we report our progress toward new well-defined polyelectrolyte materials.

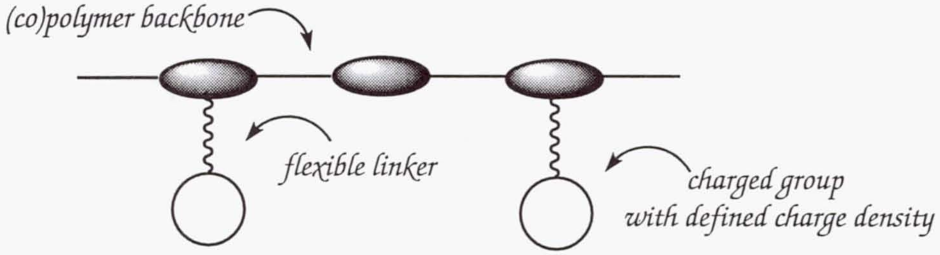

Figure 1. Design for polyelectrolyte materials.

The polyelectrolyte design (Figure 1) includes a semi-rigid polymer backbone, connected using a flexible chain to pendent anions. The key feature is the identity of the charged groups, which affect mobility of counterions. We have selected boron clusters, initially $CB_{11}H_{12}^{-1}$, in hopes of synthesizing the first example of a polyelectrolyte with non-nucleophilic anionic groups (pK_a of conjugate acid<-10). Carboranes have the added advantage of low toxicity, spherical charge distribution, insensitivity to pH, and ease of functionalization at carbon. The linking groups are oligoethylene glycol chains, which are flexible, and promote conductivity of cations.[2] To simplify polymer synthesis and characterization, the polymerization method should promote a narrow distribution of molecular weights and be tolerant of charged groups. Given these restrictions, ring opening metathesis polymerization (ROMP) seemed a reasonable route. ROMP of 7-oxabicyclo[2.2.1]hept-2-ene derivatives such as **1a** may be carried out in aqueous solutions, and results in low polydispersity, stable polymers with semi-rigid backbone structures.[3] Ease of synthetic access to **1a** and closely related starting materials, established ROMP methodology to form **poly(1a)** and close derivatives,[4] as well as some understanding of the resulting polymer microstructure,[3] make this backbone structure ideal for our purposes. **Poly(1c)** has the potential to be a water-soluble, non-toxic, stable polymer with a variety of charged groups, and is expected to be a good candidate for batteries.

SCHEME 1.

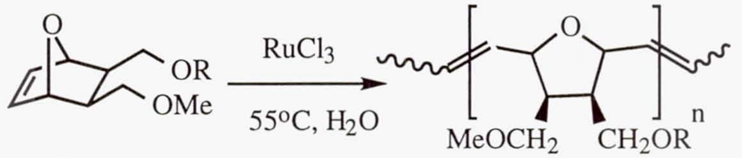

1

poly(1)

1a R = Me
b R =-$(CH_2CH_2O)_2CH_2CH_2Cl$
c R =-$(CH_2CH_2O)_2CH_2CH_2CB_{11}H_{11}^-$
d R =-$(CH_2CH_2O)_2CH_2CH_2NMe_3^+$

Monomer Synthesis. The synthetic strategy for obtaining key intermediate **1b** is shown in Scheme 2. Literature procedures[3-5] were used to obtain **2** from furan and maleic anhydride, followed by reduction to **3**, and Williamson ether synthesis to give **4**. The same etherification conditions were used to obtain **1b** from **4** and **5**.[4] Tetraethylene glycol ditosylate[6] or -dibromide gave mixtures of products which were difficult to separate. Heating of the reaction mixture while forming **1b** resulted in elimination rather than increased conversion.

SCHEME 2.

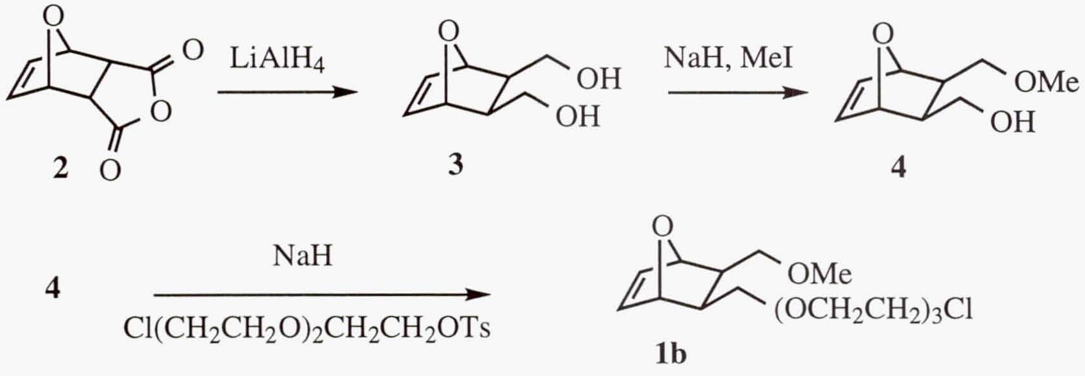

2 **3** **4**

4 **1b**

5

Scheme 3 illustrates our efforts to convert **1b** to charged monomers. Treatment of **1b** with $CB_{11}H_{11}^{2-}$ resulted in a small amount of the carbadodecaborate derivative (**1c**). Presumably, conversion of **1b** to the more reactive iodide will improve the yield of **1c**, in analogy to alkylation of $CB_{11}H_{11}^{2-}$with alkyl bromides and iodides.[7] Reaction of **1b** with trimethylamine readily produced a cationic monomer with a pendent trimethylammonium group (**1d**).[5]

SCHEME 3.

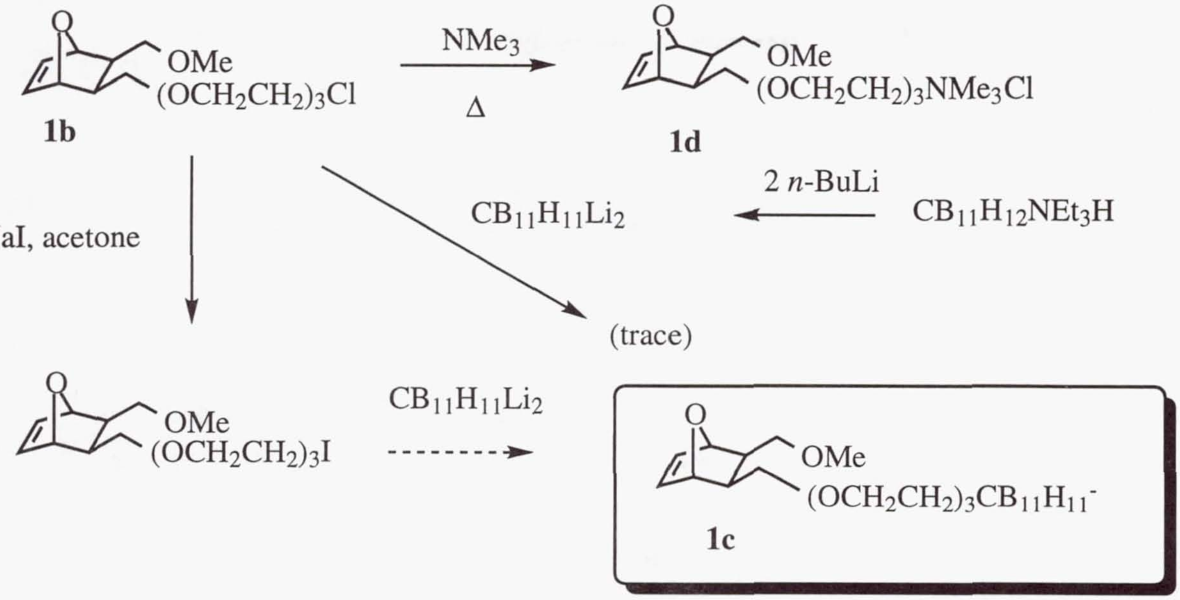

Polymer Synthesis. Once pure monomers were synthesized, they were polymerized to the structures shown in Scheme 1 (except **poly(1c)**), using literature[3] conditions: water containing recycled $RuCl3$ catalyst. Thus far, six neutral polymers and copolymers have been prepared. Polymerization of **1d** also proceeded smoothly under the same conditions as the neutral monomers, and related ROMP catalysts have been reported to polymerize trimethylammonium derivatives of oxabicyclo[2.2.1]heptenes in water.[8] Based on the successful polymerization of **1a** in the presence of $Na_2B_{12}H_{12}$, which is isoelectronic with $NaCB_{11}H_{12}$, it is expected that polymerization of **1c** will also occur. Polymerization of **1a**, **1b**, and **1d**, and copolymerization of **1a** and **1b** proceeded in yields of 70% and greater, however the polymers contained some impurities presumed to come from the catalyst that were difficult to remove. Isolation and purification of the anionic polymers are likely to be more difficult due to the high solubility of boron clusters in organic and aqueous media.

Polymer Properties. The physical properties of **poly(1c)** are expected to approximate the properties of **poly(1a)**, **poly(1b)**, copolymers of **1a** with **1b** and other derivatives, and especially **poly(1d)**. For most of the polymers measured, neither a T_g, nor a T_m was observed by Differential Scanning Calorimetry (DSC), but a T_d onset was observed near 300 ^oC by DSC and Thermogravimetric Analysis. **Poly(1d)** had a T_g at 192 ^oC and T_d at 309 ^oC. Copolymers of **1a** and **1b** decomposed between 274 and 294 ^oC. No T_g was observed for monomer ratios of 1: 0.5, 2, and 3 of **1a** and **1b**, but at a 1:1 ratio, a T_m was observed at 195 ^oC. All polymers were sparingly soluble in organic solvents and water. **Poly(1d)** swelled to a gel in water. Tetrahydrofuran solutions of the neutral polymers and copolymers were analyzed by Gel

Permeation Chromatography to give molecular weights (M_n) ranging from 0.51-3.7 x 10^6 with narrow polydispersities, but instrument conditions and an appropriate standard have not yet been worked out for charged polymers.[5]

Conclusions. The synthetic phase of the research is well underway, and two charged monomers have been synthesized, but reaction conditions were not optimized. Future work will involve the improvement and scaling up of the synthesis, as well as investigation of the properties of anionic polymers and copolymers.

Acknowledgments. Financial support for the development of cationic and neutral polyelectrolytes was provided by the Petroleum Research Fund (PRF #30202-GB7) and Middle Tennessee State University. We thank Dr. Andrew Douglass for refining the procedures for starting materials and working on the first approach to appending a linking group.

References

1. Gray, F. *Solid Polymer Electrolytes*; VCH: New York, 1991.
2. Reed, C. A. *Acc. Chem. Res.* **1998**, *31*, 133-139.
3. Novak, B. M. Ph.D. Dissertation, California Institute of Technology, 1989; Novak, B. M.; Grubbs, R. H. *J. Am. Chem. Soc.* **1988**, *110*, 7542-7543; *ibid.* pp. 960-961.
4. Lu, S.-Y.; Quayle, P.; Heatley, F.; Booth, C.; Yeates, S. G.; Padget, J. C. *Macromolecules* **1992**, *25,* 2692-2697.
5. Zheng, M. D. A. Dissertation, Middle Tenneessee State University, 1997.
6. Douglass, A. G.; Zheng, M.; Friedli, A. C.; Kaszynski, P. *Polym. Prepr.* **1996**, *37*, 634.
7. Jelínek, T.; Baldwin, P.; Scheidt, W. R.; Reed, C. A. *Inorg. Chem.* **1993**, *32*, 1982-1990.
8. Grubbs, R. H. *J. Am. Chem. Soc.* **1998**, *120*, 1627-1628.

GROWTH OF COMPOUND SEMICONDUCTORS IN A LOW GRAVITY ENVIRONMENT:
MICROGRAVITY GROWTH OF PbSnTe

A.L. Fripp[a], W.J. Debnam[b], W.R. Rosch[c], N.R. Baker[d], and R. Narayanan[e]

The growth of the alloy compound semiconductor lead tin telluride (PbSnTe) was chosen for a microgravity flight experiment in the Advanced Automated Directional Solidification Furnace (AADSF), on the United States Microgravity Payload-3 (USMP-3) and on USMP-4 Space Shuttle flights in February, 1996, and November, 1997.

The objective of these experiments was to determine the effect of the reduction in convection, during the growth process, brought about by the microgravity environment. The properties of devices made from PbSnTe are dependent on the ratio of the elemental components in the starting crystal. Compositional uniformity in the crystal is only obtained if there is no significant mixing in the liquid during growth. Lead tin telluride is an alloy of PbTe and SnTe. The technological importance of PbSnTe lies in its band gap versus composition diagram which has a zero energy crossing at approximately 40% SnTe. This facilitates the construction of long wavelength (>6 μm) infrared detectors and lasers. The properties and utilization of PbSnTe are the subject of other papers.[1,2]

PbSnTe is also interesting from a purely scientific point of view. It is, potentially, both solutally and thermally unstable due to the temperature and density gradients present during growth. Density gradients, through thermal expansion, are imposed in directional solidification because temperature gradients are required to extract heat. Solutal gradients occur in directional solidification of alloys due to segregation at the interface. Usually the gradients vary with both experiment design and inherent materials properties.

In a simplified one dimensional analysis with the growth axis parallel to the gravity vector, only one of the two instabilities work at a time. During growth, the temperature in the liquid increases ahead of the interface. Therefore the density, due to thermal expansion, is decreasing in that direction. However, the phase diagram shows that the lighter SnTe is preferentially rejected at the interface. This causes the liquid density to increase with distance away from the interface.

---

[a]. NASA, Langley Research Center, Hampton, VA 23681 (retired)

[b]. NASA, Langley Research Center, Hampton, VA 23681

[c]. NRC, Langley Research Center, Present address: Northrop Grumman STC, Pittsburgh, Pa 15235

[d]. Lockheed Martin Engineering and Sciences Co., Hampton, VA 23681

[e]. Department of Chemical Engineering, University of Florida, Gainesville, FL 32611

The PbSnTe growth experiment on USMP-3 consisted of three separate crystals grown in a single segmented ampoule. The crystals were grown in series, one in each of the three primary orientations with respect to the residual gravity vector. The growths on USMP-3 were roughly analogous to hot-on-top, cold-on-top, and horizontal growth.

The work on USMP-4 was to grow two sets of three crystals, again in segmented ampoules. The hot on top orientation was chosen for all growths. The variables, this time, were to be ampoule translation rate, thermal gradient, internal pressure, and nucleation procedure. The growth rate, which is related to the translation rate, is a key growth parameter under control of the experimenter. Higher growth rates produce steeper solutal gradients but less penetration of this vital diffusion zone into the convecting fluid flow. Thus, the growth rate presents a dichotomy of effects; a high growth rate produces a steeper concentration gradient while a low growth rate allows the diffusion tail to extend into the thermal convection cells. A change in thermal gradient has the obvious effect of changing the temperature dilatation contribution to the convective driving force. The internal pressure, at elevated temperatures, was adjusted by the amount of excess tellurium in the compound, and it was thought that it may affect pore formation in the crystals. The nucleation procedure was studied by using both seeded and unseeded growths and tests the influence of the evolution of latent heat on initial growth.

For the combined two flights we designed a set of nine experiments in three different ampoules to measure the effect of the gravitational body force on the convective properties of alloy compound crystal growth as modified by reduced gravity and other crystal growth parameters. As is often the case, especially in new and difficult experimental arenas such as found using the microgravity laboratory, nature may have her way with even the best laid plans of human endeavor and can wreck total havoc with strategies such as ours.

Ampoule #1 processed without any problems that were telemetered to the ground. Recalescence was observed in cells 1 and 2, and due to failure of the uppermost thermocouples (not a surprising event due the operating limits of the 20 mil diameter sheaths) was not expected to be observed in cell 3.

The observations, as seen on the ground, for our second ampoule (the third ampoule on the USMP-4 flight) were not so gratifying. On this part of the experiment, anomalies were observed in the sample thermocouples during the initial melting of the samples. When control thermocouples failed on the furnace booster heater, a cell (ampoule) failure and leakage from one of the lead tin telluride samples was suspected. To protect the two experiments already processed, the furnace drive was sent to the store position (full insertion), and growth was started in a gradient freeze manner by selectively powering down the different furnace zones. The experiment was terminated when the main heater control thermocouples failed.

The actual anomalies were only identified during sample retrieval at the Kennedy Space Center in February 1998. Clearly, the anomaly first occurred in ampoule # 1 not our second ampoule as was suspected. Cell 1, of ampoule #1, was intact and cell 2 was broken with approximately one third the length of the crystal still in the broken ampoule. The Inconel cartridge was swollen along its length starting near the cold end of cell 1, which was heated to 1000 C; the swelling

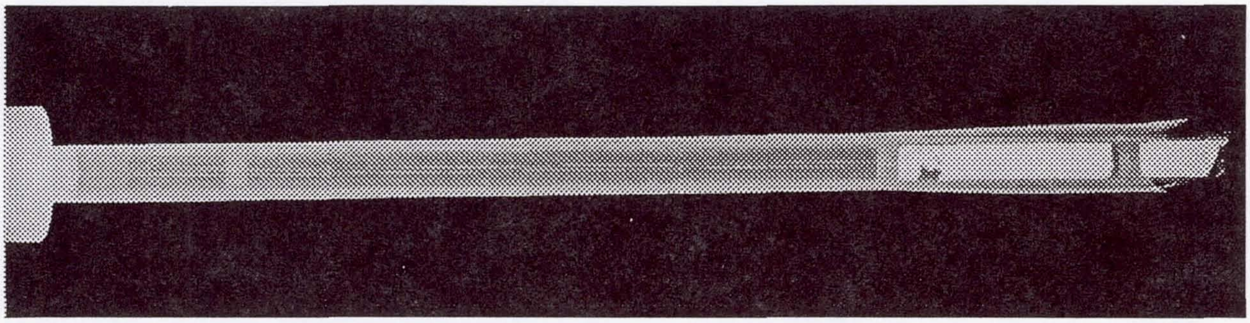

Figure 1. X-ray of sample AF-1 showing intact cell1, broken crystal in cell 2, and the swollen and torn Inconel cartridge.

increased at the beginning of cell 2, where the temperature had increased to 1150 C; and then the cartridge appeared ripped apart in the vicinity of the ampoule breakage. The remainder of the cartridge and ampoule were deposited in the furnace and caused the observed problems during the space processing of ampoule #2.

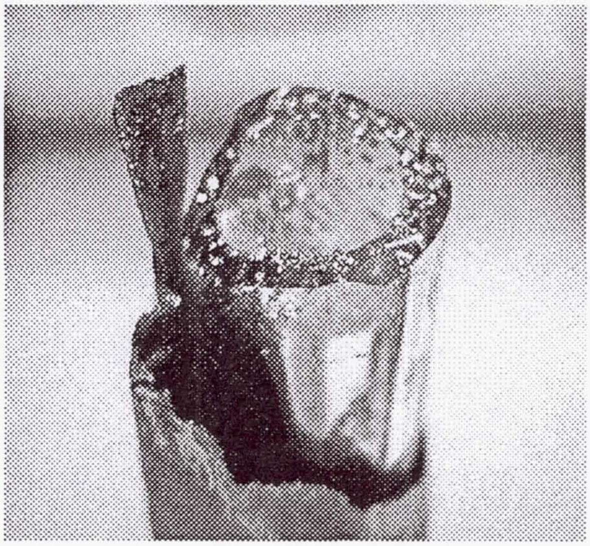

Figure 2. Photograph on the broken crystal and torn cartridge of AF-1.

The experimental ampoules, that is, what is left of them, are still impounded by the Marshall Space Flight Center awaiting further analysis of the anomaly; hence sample analysis must await their release. The remainder of this paper will discuss the observations made to date and attempts to duplicate the cartridge swelling that apparently caused the anomaly.

Figure 1 is an x-ray of the ruptured sample showing the completed cell 1 and the broken sample in cell 2 along with swelling of the cartridge. Figure 2 is a photograph of the broken end on cell 2. The metal cartridge appears forcibly torn and not corroded by PbSnTe vapors, and the remaining crystal in cell 2 appears to be broken and not just decanted from spilled liquid.

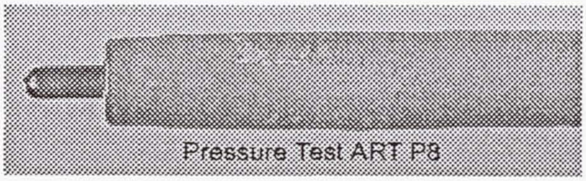

Figure 3. Result of pressure test where cartridge was pressurized to 75 psig.

A set of experiments was conducted at the Langley Research Center to determine if excess pressure within the cartridge (that is, the space between the sealed quartz ampoule and the Inconel cartridge) could have caused the cartridge to swell to a diameter greater than the 0.75 inch diameter of the radiation shield insert in the insulation zone of the furnace. The maximum excess pressure within the cartridge during growth in the AADSF is approximately 10 psi if the cartridges are sealed at 12 psia. In these post- flight tests the argon pressure was actively controlled at pressures up to 100 psig to simulate the remote possibility that the flight sample was over pressurized during sample preparation. Table 1 summarizes these tests and figure 3 shows one of the tubes after failure where the maximum bulge reached 0.70 inches only in the area of the failure. Three separate Inconel tubes were taken to failure (that is, an observation of pressure drop in the cartridge), but none produced sufficient swelling to have caught on the radiation shield and caused the tearing of the cartridge as observed on the flight sample.

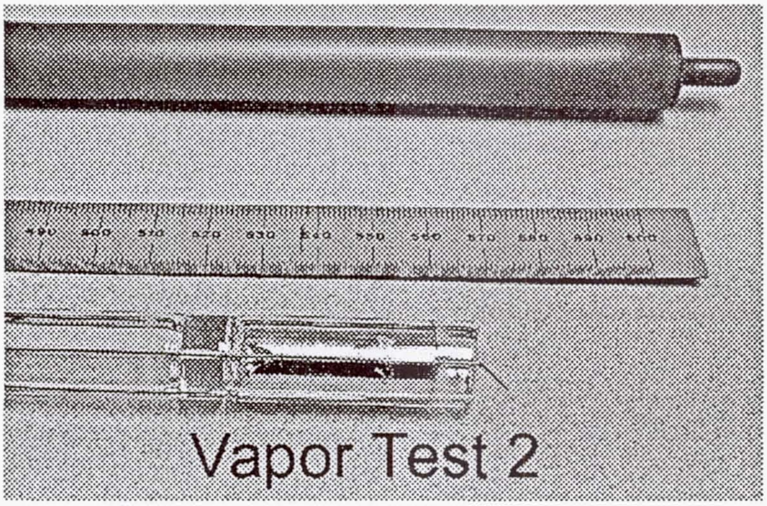

Figure 4. Setup for a PbSnTe vapor test on the integrity of the Inconel cartridge. The PbSnTe resides in the open ended quartz ampoule.

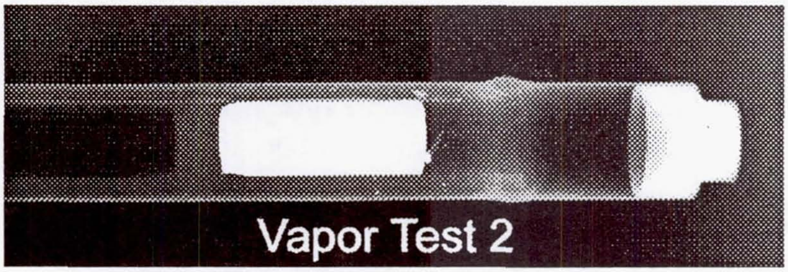

Figure 5. X-ray of loaded test cartridge after failure. Note that the only appreciable swelling (~0.66 inch) is immediately ahead of the open end of the ampoule.

Another set of tests looked at the hypothesis that one of the cells developed a crack and leaking PbSnTe vapor weakened the Inconel to allow the concomitant swelling. (Note: had the quartz containing the PbSnTe broken and liquid come in contact with the Inconel then the metal would have lost its integrity within seconds relieving any pressure differential.) As a cracked ampoule is difficult to simulate, we used an open ended ampoule that was maintained vertical to prevent any PbSnTe - Inconel contact. Figure 4 shows the open ended ampoule with the PbSnTe and the Inconel muffle tube which will contain it, and figure 5 is an x-ray of the sample after the failure as demonstrated by a pressure drop. Note that the only appreciable swelling occurred at the end of the open ampoule but even that was insufficient to bind on the AADSF insert.

The ampoules and furnace reside at the Marshall Space Flight Center awaiting deposition by the Anomaly Resolution Team. The two ampoules, still in their cartridges, have only been examined by computer aided tomography, x-rays, and photography. Further results must wait for the release of the samples and the subsequent analysis.

REFERENCES:

1. T.C. Harman; "Control and Imperfections in Crystals of PbSnTe, PbSnSe and PbSSe"; J.Nonmetals 1 (1973) 183.

2. S.G. Parker and R.W. Johnson; "Preparation and Properties of PbSnTe"; in Preparation and Properties of Solid State Materials vol 6, Ed. W.R. Wilcox, Marcel Dekker, Inc., New York 1981, p 1.

Table 1: Effect of Pressure, Temperature, and Time on Muffle Tube Expansion

This series of experiments examine the combined effect of temperature, pressure and duration on the expansion of the Inconel muffle tubes. All tubes used were from the same batch as the flight (AF1-105) tube, and the tests were conducted in the Bridgman furnace at Langley. ART-P1 through P6 involved heating the muffle tubes during the day, cooling overnight, and measuring the tube diameter, before proceeding to the next heat/cool/measure cycle. ART-P9 is a variation of the P7 and P8 tests, but without cooling and measuring the tube diameter after the 24 hours at 1000 C and 75 psig.

Number	**Dates**	**psig**	**Temp °C**	**Time hr**	**Post-Test Tube Dia, inches**	**(increase)**	**Notes**
ART-P1	3/18/98	15	1000	7:00	0.624	(0.000)	Muffle Tube # N25
ART-P2	3/19/98	15	1150	6:30	0.627	(0.003)	Followed ART-P1, same tube (N25)
ART-P3	3/20/98	25	1150	6:20	0.629	(0.002)	Followed ART-P2, same tube (N25)
ART-P4	3/23/98	45	1150	6:46	0.638	(0.009)	Followed ART-P3, same tube (N25)
ART-P5	3/24/98	75	1150	6:53	0.665	(0.027)	Followed ART-P4, same tube (N25)
ART-P6	3/25/98	100	1150	0:44	0.687	(0.022)	Leak developed in N25, test terminated.
ART-P7	4/2/98	75	1000	24:00	0.645	(0.021)	Muffle Tube # N27
ART-P8	4/6/98	75	1150	0:36	0.685 0.700 at split	(0.040)	Leak developed in N27, test terminated. Tube split 2" from tip.
ART-P9	4/8/98	75	1000	24:00	Not measured		Muffle Tube # N28 Straight to 1150C
ART-P9#2	4/9/98	75	1150	0:47	0.674	(0.050)	Leak developed in N28, test terminated.

MELT STABILIZATION of PbSnTe in a MAGNETIC FIELD

Archibald L. Fripp[a], William J. Debnam[b], William Rosch[c], Arnon Chait[d], Minwu Yao[e], and Frank R. Szofran[f]

1. INTRODUCTION

Both the experimental observation [1] and numerical simulation [2] indicate that the Bridgman growth of PbSnTe under the microgravity environment in space is still greatly influenced by buoyancy-induced convection. The application of a magnetic field during the semiconductor growth can dampen the convective flow in the metal-like melt [3-5]. However, for Bridgman growth of PbSnTe on earth (with either vertical or horizontal configuration), both experimental observation [6] and numerical modeling [7] suggest that even with a strong magnetic furnace (5-Tesla constant axial magnetic field), the convective flow in the melt still cannot be sufficiently suppressed to reach the diffusion-controlled level. In order to completely dampen the buoyancy-induced convection on earth, estimates based on scaling analysis indicate that for common experimental conditions, an extremely high magnetic field is required, far beyond the capacity of the experimental apparatus currently available. Therefore, it is proposed that only the combination of microgravity environment and magnetic damping will produce the desired diffusion-controlled growth state for this particular material.

The primary objectives of this study are to provide a quantitative understanding of the complex transport phenomena during solidification of non-dilute binarys, to furnish a numerical tool for furnace design and growth condition optimization, to provide estimates of the required magnetic field strength for low gravity growth, and to assess the role of magnetic damping for space and earth control of the double-diffusive convection. As an integral part of a NASA research program, our numerical simulation supports both the flight and ground-based experiments in an effort to bring together a complete picture of the complex physical phenomena involved in the crystal growth process.

---

[a]. NASA, Langley Research Center, Hampton, VA 23681 (retired)

[b]. NASA, Langley Research Center, Hampton, VA 23681

[c]. NRC, Langley Research Center, Present address: Northrop Grumman STC, Pittsburgh, Pa 15235

[d]. NASA, Lewis Research Center, Cleveland, OH 44135

[e]. Ohio AeroSpace Institute, Brook Park, OH 44142

[f]. NASA Marshall Space Flight Center, Huntsville, AL 35812

2. MATHEMATICAL MODEL

2.1 Magnetohydrodynamic Models

In the literature [8], there are mainly three approximations for the MHD equations. The most complex approximation incorporates the interaction between fluid flow and the magnetic field and its derivation can be found in [9]. This model is valid for describing MHD effects in electrically conducting melts of non-magnetic metals or semiconductors in which Ohm's law is valid and the fluid velocity is small compared to the speed of light.

The second is a more restrictive approximation which assumes that the fluid flow does not disturb the externally applied field with the Lorentz force still being present. This approximation is valid if the magnetic Reynolds number and the magnetic Prandtl number are both small which is the case in typical crystal growth of semiconductors. The derivation of the governing MHD equations can be found in [10].

The third and simplest MHD model is the so-called induction free approximation. In this approximation, any induced electrical field is set to be identically zero and thereby the MHD effects of the imposed field can be solely expressed through the Lorentz force term in the momentum equation. Because the magnetic Reynolds number is negligibly small under the growth conditions considered herein, this model applies well to our case and is used in the present study.

2.2 Governing Equations

In this paper, the liquid pseudo-binary mixture of LTT is assumed to behave as a Newtonian fluid and its motion is described by the Navier-Stokes equation. Other governing equations include the incompressibility condition, energy equation and concentration equation, plus the phase change conditions at the solid/liquid interface and the appropriate boundary conditions.

2.3 The FEM Model

We consider vertical and horizontal Bridgman growth configurations. For bottom seeded (vertical) Bridgman growth with axisymmetric boundary conditions, it is reasonable to assume that the heat, species and flow fields are all axisymmetric.

The so-called pseudo-steady-state model (PSSM) [11] is adopted in the present work. In PSSM, the directional steady movement of the solid/liquid interface during the steady growth is modeled by letting melt enter at its hot end with a uniform growth velocity and composition and by removing the crystal from the cold end at a speed that conserves the mass of the alloy in the system. This simplification is valid for long ampoules and melts with low Prandtl numbers, in which the transient effects on heat transfer are small [12].

The axisymmetric and 2-D FEM models are built with the 4-node bilinear element, in which velocity, temperature and species are approximated by bilinear shape functions. The pressure is approximated as piecewise constant. The moving solid-liquid interface is modeled by the front-tracking technique [13]. To update the interface position and remesh the interior domains, a method of spines [14,15] is used. The nonlinear algebraic system resulting from the FEM discretization procedure is solved by a segregated solution approach. Details of the FEM formulation in FIDAP are documented in [14]. The nonlinear iteration termination is controlled by a specified tolerance of for the relative error norms of velocity, residual and free surface update.

3. NUMERICAL RESULTS

The action of an axial magnetic field on convection in the melt is to interfere with the radial velocity component. At large magnetic field strength, the magnitude of the radial velocity is inversely proportional to the square of the strength of magnetic field [11]. The axial velocity component is not affected by the magnetic field except in the coupling through the incompressibility condition. When the field is large enough, an almost uniaxial flow can always be obtained. One of the goals of this study is to quantitatively determine the required magnetic field levels at which the diffusion-controlled growth can be achieved in orbit. In this section we provide a typical analysis of magnetic damping for vertical Bridgman growth at a low gravity of . Our numerical results suggest that the influence of magnetic damping on the convective flow in the melt is indeed very effective. There are two large counter-rotating flow cells throughout the liquid region indicating the existence of significant convection caused by both thermal and solutal buoyancy forces. At 3kG, the convective flow is greatly affected and the flow cells become much smaller corresponding to much weaker convective strength. It is interesting to note that there is a critical value between 3.0 and 3.14kG for this specific problem. When B exceeds this critical value, the flow cells are completely suppressed. At B=9.6kG, the streamlines become perfectly straight which suggests that a diffusion-dominated growth state has been achieved.

We next examine the effects of magnetic damping on the solute segregation. Solute segregation phenomena on the macroscopic scale can be divided into two classes; namely longitudinal (axial) macro segregation caused by mixing on the melt length scale and transverse (radial) segregation caused by low levels of mixing near the interface and by interface curvature. As analyzed by D.H. Kim et al [11], these two forms of segregation are a function of convection level in the melt. In our computation, we consider variable-level magnetic damping under a constant gravity level and a fixed set of furnace parameters. Consequently the convective strength, and hence the solute segregation, is directly related to the strength of the imposed magnetic field. The solute field is visualized via iso-concentration contour plots, which illustrates qualitatively how solute segregation changes with increase of magnetic field. The axial solute segregation is greatly reduced at 3 kG and an almost diffusion-dominated growth (characterized by the thin diffusion boundary layer near the interface) is reached at 9.6 kG.

In order to quantitatively describe the effects of magnetic damping and the transition from growth with intensive laminar convective mixing to diffusion-controlled growth (without bulk convection), we compute three representative quantities. The first is the maximum total velocity, which can be used as a measure of the convective strength in the melt. Note that the total velocity includes a constant translation velocity (the growth rate) and the buoyancy-induced convective flow velocity. The results are given in Figure 1. The U_{max} v.s. B curve given in

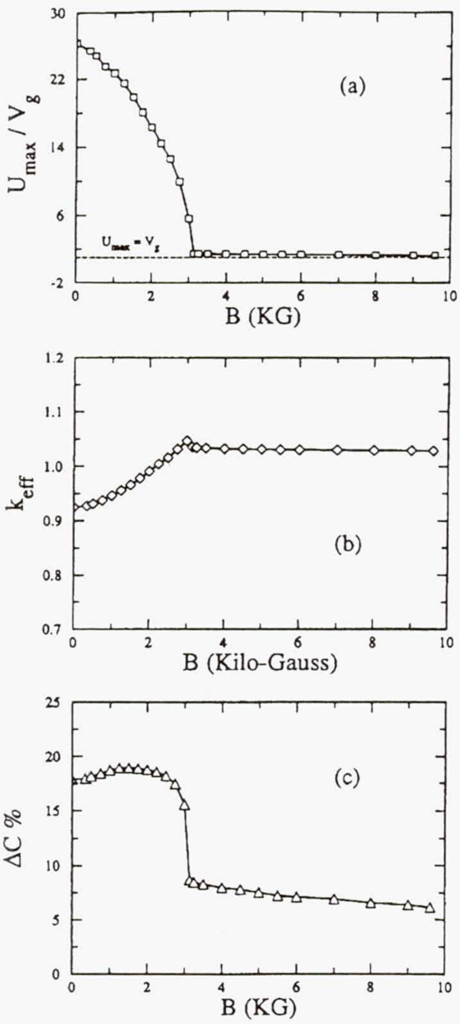

Figure 1. Quantitative descriptions of the effect of magnetic damping on convective flow strength and solute segregation in the PbSnTe melt. (a) The total maximum velocity; (b) The effective segregation coefficient, (c) The percentage radial segregation.

Figure 1(a) shows that there are two stages during the magnetic damping process. The first is a rapid change stage in which the strength of the convective flow in the melt is greatly reduced with an increase of B. The second is a slow (asymptotic) change stage during which the velocity decreases very slowly with the increase of B. These two stages are divided by the critical field value, B_c (in this particular example) and can be clearly seen in Figure 1(a). In this case, over 90% of the original strength of convection is damped when is increased from zero to about 3 kG. However it requires an additional 6 kG or more to eliminate nearly all of the original velocity strength.

The second quantified parameter is the effective segregation coefficient k_{eff}. The third is the percentage radial segregation. Radial segregation results show that both weak and strong convection levels produce low radial segregation, while intermediate convection levels produce high radial segregation [16]. The computed segregation coefficients for vertical growth are plotted as a function of levels in Figures 1(b) and (c). The two stages mentioned above can be easily distinguished. It is seen from Figure 1(b) that increases effectively in the first stage ($0<B<B_c$) and then asymptotically approaches unity at the second stage ($B>B_c$). $k_{eff}\sim1$ indicates quantitatively that the desired diffusion-controlled growth state is indeed achieved at B=9.6kG. Figure 1(c) shows how radial segregation changes with increasing B, while the expected qualitative behavior of the radial segregation is evident from Figure 1(c), it is clear that during the first stage, the reduction in flow strength only minimally affects the local segregation conditions near the interface. The almost complete stoppage of convection around has a dramatic effect on the radial segregation with a slow asymptotic regime at higher magnetic field strength.

The analysis presented in this section is limited to the vertical growth under microgravity. At high gravity levels (e.g. at full earth gravity level), our results suggest that the axially imposed magnetic field is not effective for suppressing convective flow in the PbSnTe melt. A typical example of magnetic damping for the vertical growth of PbSnTe on earth was shown in [17], which suggests that the maximum fluid velocity is still about 1000 times higher than crystal growth rate at 60 kG and the decrease of the fluid velocity is much slower than that at the microgravity gravity levels.

4. EXPERIENTIAL

The Earth based experiments are relatively straight forward. Crystals are grown in a magnetic field. After growth they are evaluated for compositional uniformity and defect structure. The experimental parameters are ampoule dimensions, temperature gradient, and magnetic field strength and orientation. The solutal driving force can be varied by both changing the growth rate, the temperature gradient, ampoule size, and by changing the starting ratio of SnTe to PbTe. Numerical analysis helps select the experimental matrix.

Experimental results to date of 1 cm diameter crystals grown in a 80 C/cm thermal gradient with growth rate as a parameter are indistinguishable from the totally mixed results obtained without magnetic fields, even with the 5T field. This result, for these conditions, was predicted by our numerical analysis.

5. CONCLUSIONS

For Bridgman growth of PbSnTe under microgravity (with both vertical and horizontal configurations), the simulations suggest that a moderate axial magnetic field of only a few kilo-Gauss in strength could effectively eliminate buoyancy-induced convection in the melt and control solute segregation. Therefore, this work confirms the idea that the combination of microgravity environment and the magnetic damping will indeed be sufficient to produce the desired diffusion-controlled growth state for PbSnTe.

REFERENCES

[1] A.L. Fripp, R.K. Crouch, W.J. Debnam, G.A. Woodell, I.O. Clark, F.M.Carlson, and R.T. Simchick: in Microgravity Science and Applications Flight Programs - Selected Papers, NASA Tech. Memorandum 4069, October 1988.

[2] M. Yao, A. Chait, A.L. Fripp and W.J. Debnam; Microgravity Sci. Tech., Vol. 8 (1996) pp. 214-225.

[3] H.P. Utech and M.C. Flemings; J. Appl.Phys., Vol. 37 (1966) pp. 2021-2024.

[4] H.P. Utech and M.C. Flemings; Crystal Growth, ed. H.S. Peiser, Pergamon Press, Oxford, 1967.

[5] H.A. Chedzey and D.T.J. Hurle, Nature, Vol. 210 (1966) p. 933.

[6] A.L. Fripp, (private communication), 1995.

[7] M. Yao, (unpublished numerical results), 1995.

[8] J. Baumgartl and G. Muller; Proc. 8th European Symposium on Materials and Fluid Science in Microgravity, Brussels, Belgium, 12-16 April, 1992, pp.161-164.

[9] P.H. Roberts; An Introduction to Magnetohydrodynamics, Longmans, London, 1967.

[10] L.D. Landau, E.M. Lifshitz and L.P. Pitaevskii; Electrodynamics of Continuous Media, Translated by J.B. Sykes, J.S. Bell, and M.J. Kearsley, 2nd ed., Pergamon Press, New York, 1984.

[11] D.H. Kim, P.M. Adornato and R. Brown; J. Crystal Growth, Vol. 89 (1988) pp. 339-356.

[12] T.J. Jasinski, W.M. Rohsenow and A.F. Witt; J. Crystal Growth, Vol. 61 (1983) p. 339.

[13] J. Crank; Free and Moving Boundary Problems, Clarendon Press, Oxford, 1984.

[14] M. Engleman; FIDAP Theoretical Manual (version 7), Fluid Dynamics International, Inc., 500 Davis St. Suite 600, Evanston, IL 60201, 1993.

[15] H. Saito and L.E. Scriven; J. Comp. Phys., Vol. 42 (1981) p. 53.

[16] M.A. Brown, AIChE J, Vol.34 (1988), pp. 881-911.

[17] M. Yao, A. Chait, A.L. Fripp and W.J. Debnam, Proceedings of the 6th FIDAP Users Conference, Chicago, IL, 4/30-5/2, 1995; also NASA Technical Memorandum 106996.

Gravitational Role in Liquid Phase Sintering

Randall M. German and Ronald G. Iacocca
P/M Lab, 118 Research West
The Pennsylvania State University
University Park, PA 16802-6809; tel 814-863-8025, email rmg4@psu.edu

Introduction

Liquid phase sintering (LPS) is a common process for the fabrication of dense, net-shape structures. Despite extensive industrial use, several processing difficulties trace to gravity. One easily recognized problem is solid-liquid separation. Like sand settling in water, differences in densities between the solid and liquid phases induce microstructure and compositional segregation. Consequently, only alloys with small quantities of liquid are fabricated on Earth. The tungsten heavy alloys (W-Ni-Fe or W-Ni-Cu) are particularly sensitive to gravitational effects since the liquid-solid density difference is nearly 9 g/cm^3. In this research, we have documented that after sintering on Earth there is a significant gradient in grain coordination number, grain size, grain shape, and solid phase contiguity with the position in the compact. Further, there is a slight difference in grain size due to the compressive stresses during Earth-based sintering. Grain coalescence occurs at gravity induced contacts, giving gradients from the stress in the microstructure due to gravity. It was on the basis of these observations that microgravity and parallel ground-based experiments were performed.

Gravity effects are evident at the macroscale as compact distortion. An excess of liquid causes shape loss, with the formation of the "elephant foot" geometry or even puddles of solid-liquid. The factors causing distortion in LPS are not understood. Previous work suggested that it was simply due to the solid-liquid ratio; however, experiments have produced compacts with more than 60 vol.% liquid that retain shape. Compositions that slump on Earth also distorted in microgravity, but in the latter case they spheroidized. Our analysis and modeling efforts now explain distortion during sintering (from both gravitational and surface tension stresses, thug applicable to both ground-based and microgravity samples) as arising from three features - solid-liquid ratio, dihedral angle, and solubility change when the liquid forms.

Microgravity LPS experiments have been performed in recent years, and the Penn State research team was involved in analysis of samples form flights starting in 1992 (SLJ, IML-2, MSL-1, and MSL-1R). Each investigator has adopted different questions, compositions, and sample preparation techniques. Although each study provides insight, a unified view is missing. Therefore, one goal of the research was to perform cross-study experiments where these various alloys will be processed under similar conditions. This showed the lack of care in prior sample preparation greatly affected the findings and compromised final conclusions. Further, reports from ground-based experiments often proved inadequate to fully document sintering and microstructure findings. One success was the stability of the Large Isothermal Furnace and the support hardware. No malfunction of the flight hardware directly involved in the liquid phase sintering experiments was encountered in microgravity. In this regard, the original plan to use microgravity experiments to isolate gravitational effects on microstructure evolution during liquid phase sintering was very successful. The contrast and comparison of ground-based and microgravity samples, processed from the same powders, in the same furnace, using the same cycles provided the needed separation of variables. Modeling efforts conducted in parallel with the experiments provide a basis for assessing current understanding. The initial phase of the microgravity research was focused on variations in sintering time and solid content using W-Ni-Fe compositions with a constant Ni:Fe ratio of 7:3, but varying W content from 78 to 98%. With improved understanding of the LPS system, we were successful in extending the flight samples to new composition regions with high liquid contents.

Significant Findings

A model for grain growth during liquid-phase sintering is presented. A Rayleigh grain size distribution is assumed based on both experimental and theoretical results. This asymmetric distribution provides a continuous driving force for coarsening. The model uses the solid grain contiguity to calculate the relative solid-state and liquid-phase contributions to coarsening. The level of grain agglomeration affects both the mean diffusion distance and interface area over which diffusion occurs. A cumulative grain growth rate is calculated assuming independent solid and liquid contributions to coarsening. Consequently, only the liquid volume fraction and solid-liquid dihedral angle are required to predict the change in grain coarsening rate with solid-liquid ratio. A prior empirical correlation between the grain growth rate constant and the liquid volume fraction is compared to the resulting analytic form, showing excellent agreement. The new model is projected to be generically applicable to microstructure coarsening in multiple phase materials, including porous structures.

Liquid phase sintering (LPS) is a process for the densification of particulate materials such as tungsten carbide, silicon nitride, bronze, low alloy steels, stainless steels, tool steels, and various cermets. The liquid provides a capillary force and high transport rate that give rapid densification. However, the high diffusivity leads to progressive microstructural coarsening. Several authors have considered the problem of solid-liquid coarsening. Most of the models applied to liquid phase sintered structures are extrapolations of classic Ostwald ripening concepts developed for dilute solid contents. A dispersed grain structure allows use of a mean field concept for calculation of the coarsening rate. This has some substantiation in that the grain size typically increases with the cube root of isothermal hold time. The growth or contraction of a specific grain depends on the local environment, as established by various observations..

Semisolid systems, ranging from liquid phase sintering materials to metal-ceramic composites, evidence coarsening behavior very different from the assumptions in Ostwald ripening models. These materials have intertwined liquid and solid phases that coarsen at elevated temperatures. Consequently, there are many deficiencies with extending Ostwald ripening theories to semisolid alloys.

Liquid phase sintering is limited by Earth's gravity, because there are few systems where the solid and liquid densities are equal. Mechanical stability dictates multiple grain contacts to avoid collapse of the solid grain structure under the action of gravity. At these contacts, the grains form bonds. Once a steady-state is achieved, the bond size depends only on the grain size and the dihedral angle, while the number of bonds per grain depends largely on the liquid content. Net-shaping via LPS is most successful with less than 40 vol.% liquid and an intermediate dihedral angle (15° to 60°), giving sufficient rigidity to resist distortion. At high temperatures, the skeletal structure is not so strong that it inhibits densification. Consequently, the final microstructure consists of intertwined and connected solid and liquid networks. Grain agglomeration is a natural consequence of neck growth between contacting grains. Thus, dilute solid systems exhibit solid grain agglomeration when processed in microgravity or neutral buoyancy conditions.

Liquid phase sintering systems have varying dihedral angles (depending on the grain misorientations), and even nonspherical grain shapes. Except for a few cases the existing models do not allow for grain contact. They are only applicable to dilute solid suspensions without agglomeration, theoretically possible at low solid contents, probably below 20 vol.% solid. Most importantly, Ostwald ripening theories underestimate the grain growth rate constant for LPS systems. Another problem with extending Ostwald ripening to LPS is with systems that contain two solid phases. In these cases the reduced solid-liquid interface area gives slower growth. This has been traced to a change in contiguity or increase in dihedral angle. Several studies further show grain growth in LPS includes coalescence. Thus, the possibility of testing Ostwald ripening theories with LPS systems in fundamentally impeded by solid-solid grain contacts.

In spite of the difficulties in translating Ostwald ripening theory to grain growth in liquid phase sintering, one major success is evident. That is the general consensus that grain growth by diffusion through the liquid, termed solution-reprecipitation, follows a cubic law with an Arrhenius temperature dependence with an activation energy that correlates with diffusion through the liquid.

This model differs from the several dilute solid content coarsening theories. The current model works in the LPS range, typically with less than 40 vol.% of second phase. Note the Ostwald ripening models should not be extrapolated into the LPS range, and the LPS coarsening model should not be extrapolated into the Ostwald ripening range. The reasonable fit to available experimental LPS grain growth data is worthwhile. This behavior appears to be valid over the composition range typical to Earth-based liquid phase sintering with less than 40 vol.% liquid.

The paper shows how grain growth during liquid-phase sintering has been understood with unique observations from microgravity and ground-based samples. The findings show a high level of grain agglomeration at all solid contents. This is an energetically favorable situation as compared to dispersed grains as typically treated in Ostwald ripening theory. The grain agglomeration affects the mean diffusion distance and interface area over which diffusion occurs. Coarsening in liquid phase sintering depends on several factors that change with solid volume fraction. Critical findings from the microgravity experiments gives rules needed to fully model the coarsening process. An important observation is a cumulative grain size distribution that follows the Rayleigh distribution. This distribution gives a growth rate calculation that brings both solid and liquid contributions into the overall grain growth rate. The assumption is that independent solid and liquid contributions lead to the overall observed rate of coarsening.

Consequently, only the liquid volume fraction and solid-liquid dihedral angle are required to predict the change in grain coarsening rate with solid-liquid ratio. An empirical correlation between the grain growth rate constant and the liquid volume fraction to the inverse two-thirds power is compared to the new analytic form derived from the microgravity studies, showing excellent agreement.

Summary of Key Findings

A universal grain size distribution for LPS materials has been isolated and described mathematically, and this distribution agrees with recent independent findings.

The volume fraction of liquid has been mathematically linked to the grain growth rate constant and solid-liquid density difference for LPS materials, giving the first universal coarsening law applicable to the solid contents characteristic of LPS.

A model has been created for slumping and distortion during LPS. This model describes the role of gravity, component size, substrate friction, and surface tension on reshaping processes. Analysis has shown an important role of grain connectivity and dihedral angle on shape preservation during LPS. Evidence exists that grain boundary wetting by newly formed liquid is a key factor in distortion.

Grain agglomeration has been predicted and observed in dilute solid content systems. The weak agglomeration force was first modeled for LPS, but may be applicable to many situations including solid-liquid, liquid-liquid, solid-vapor, and liquid-vapor systems. The agglomeration event was observed in microgravity samples sintered by Kohara and Ekbom.

Based on pore stabilities in the microgravity samples, we have revisited the derivation of Young's equation and found Gibbs' original treatment is incorrect since a gravity term was dropped from the derivation.

Coalescence has been documented in a zero dihedral angle LPS system conclusively to prove Ostwald ripening theories are incorrect in ignoring this effect. Further, grain rotation as part of coalescence has been measured during long time LPS. Electron channeling experiments will show the emergence of preferred grain orientations for coalescence during long term LPS.

Early evidence shows a nonrandom radial distribution function in the grain size of LPS heavy alloys.

The settled region of Earth-based LPS samples has been analyzed for the density difference effect and the terminal skeletal structure for no solid-liquid density difference. A model for the solid content versus position in the settled solid structure accurately explains all previous observations.

A new generalized idea of grain coordination number versus effective pressure has emerged that may have applicability to loosely packed particles. The model expresses the mean coordination number as a function of the effective pressure. Ground-based experiments are being performed to test this model.

Pore structure observations in microgravity LPS samples show a high stability. This suggests buoyancy may be important to densification during LPS on Earth. A complication is the lack of a reducing atmosphere during microgravity sintering, but under identical ground-based LIF experiments a gravity role is evident.

Some Publications For In-Depth Study

C. M. Kipphut, A. Bose, S. Farooq and R. M. German, "Gravity and Configurational Energy Induced Microstructural Changes in Liquid Phase Sintering," *Metall. Trans.,* 1988, vol. 19A, pp. 1905-1913.

R. M. German and S. Farooq, "An Update on the Theory of Liquid Phase Sintering," *Sintering '87,* vol. 1, S. Somiya, M. Shimade, M. Yoshimura and R. Watanabe (eds.), Elsevier Applied Science, London, UK, 1989, pp. 459-464.

S. C. Yang, S. S. Mani and R. M. German, "The Effect of Contiguity on Growth Kinetics in Liquid Phase Sintering," *J. Met.,* 1990, vol. 42, no. 5, pp. 16-19.

S. C. Yang and R. M. German, "Gravitational Limit of Particle Volume Fraction in Liquid Phase Sintering," *Metall. Trans.,* 1991, vol. 22A, pp. 786-791.

S. S. Mani and R. M. German, "Gravitational Effects on Microstructural Parameters During Liquid Phase Sintering," *Adv. Powder Met.,* 1991, vol. 4, pp. 195-212.

S. C. Yang and R. M. German, "Generic Grain Size Distribution for Liquid Phase Sintering," *Scripta Met. Mater.,* 1992, vol. 26, pp. 95-98.

R. M. German, A. Bose and S. S. Mani, "Sintering Time and Atmosphere Influences on the Microstructure and Mechanical Properties of Tungsten Heavy Alloys," *Metall. Trans.,* 1992, vol. 23A, pp. 211-219.

R. G. Iacocca and R. M. German, "Experimental Design for Liquid Phase Sintering in Microgravity," *Adv. Powder Met. Part. Mater,* 1993, vol. 2, pp. 181-194.

R. M. German, "Microstructure of the Gravitationally Settled Region in a Liquid Phase Sintered Dilute Tungsten Heavy Alloy," *Metall. Mater. Trans.*, 1995, vol. 26A, pp. 279-288.

R. Raman and R. M. German, "A Mathematical Model for Gravity-Induced Distortion During Liquid Phase Sintering," *Metall. Mater. Trans.,* 1995, vol. 26A, pp. 653-659.

Y. Liu, D. F. Heaney and R. M. German, "Gravitational Effects on Solid Grain Packing in Liquid Phase Sintering," *Tungsten and Refractory Metals,* A. Bose and R. Dowding (eds.), Metal Powder Industries Federation, Princeton, NJ, 1995, pp. 121-128.

Y. Liu, D. F. Heaney and R. M. German, "Gravity Induced Solid Grain Packing During Liquid Phase Sintering," *Acta Met. Mater.,* 1995, vol. 43, pp. 1587-1592.

R. M. German, R. G. Iacocca, J. L. Johnson, Y. Liu and A. Upadhyaya, "Liquid-Phase Sintering Under Microgravity Conditions," *J. Met.,* 1995, vol. 47, no. 8, pp. 46-48.

Y. Liu, R. Iacocca, J. L. Johnson, R. M. German and S. Kohara, "Microstructural Anomalies in a W-Ni Alloy Liquid Phase Sintered under Microgravity Conditions," *Metall. Mater. Trans.,* 1995, vol. 26A, pp. 2485-2486.

R. G. Iacocca, Y. Liu and R. M. German, "Microstructural Examination of Tungsten Heavy Alloys Sintered in a Microgravity Environment," *Adv. Powder Met. Part. Mater.* , 1995, vol. 1, pp. 4.239-4.249.

D. F. Heaney, R. M. German and I. S. Ahn, "The Gravitational Effects on Low Solid-Volume Fraction Liquid-Phase Sintering," *J. Mater. Sci.,* 1995, vol. 30, pp. 5808-12.

Y. Liu and R. M. German, “Relationship Between Contact Angle and Surface Tensions,” *Sintering 1995*, R. M. German, G. L. Messing and R. Cornwall (eds.), Marcel Dekker, New York, NY, 1996, pp. 229-236.

R. M. German, "Grain Agglomeration in Solid-Liquid Mixtures Under Microgravity Conditions," *Metall. Mater. Trans.,* 1995, vol. 26B, pp. 649-651.

Y. Liu and R. M. German, "Contact Angle and Solid-Liquid-Vapor Equilibrium," *Acta Mater.,* 1996, vol. 44, pp. 1657-1663.

R. M. German and Y. Liu, "Grain Agglomeration in Liquid Phase Sintering," *J. Mater. Synth. Process.,* 1996, vol. 4, pp. 23-34.

J. L. Johnson and R. M. German, “Solid-State Contributions to Densification During Liquid Phase Sintering,” *Metall. Mater. Trans.,* 1996, vol. 27B, pp. 901-909.

Solidification of II-VI Compounds in a Rotating Magnetic Field

D. C. Gillies, M. P. Volz, K. Mazuruk, Marshall Space Flight Center, Huntsville, AL
S. Motakef, Cape Simulations Inc., Newton, MA
M. Dudley, State University of New York at Stony Brook, Stony Brook, NY
R. Matyi, University of Wisconsin - Madison, Madison, WI

Background

This project is aimed at using a rotating magnetic field (RMF) to control fluid flow and transport during directional solidification of elemental and compound melts. Microgravity experiments have demonstrated that small amounts of residual acceleration of less than a micro-g can initiate and prolong fluid flow, particularly when there is a static component of the field perpendicular to the liquid solid interface.[1] Thus a true diffusion boundary layer is not formed, and it becomes difficult to verify theories of solidification or to achieve diffusion controlled solidification. The RMF superimposes a stirring effect on an electrically conducting liquid, and with appropriate field strengths and frequencies, controlled transport of material through a liquid column can be obtained. As diffusion conditions are precluded and complete mixing conditions prevail, the technique is appropriate for traveling solvent zone or float zone growth methods in which the overall composition of the liquid can be maintained throughout the growth experiment. Crystals grown by RMF techniques in microgravity in previous, unrelated missions have shown exceptional properties.[2] The objective of the project is two-fold, namely (1) using numerical modeling simulate the behavior of a solvent zone with applied thermal boundary conditions and demonstrate the effects of decreasing gravity levels, or an increasing applied RMF, or both, and (2) to grow elements and II-VI compounds from traveling solvent zones both with and without applied RMFs, and to determine objectively how well the modeling predicts solidification parameters.

Microgravity Relevance

The traveling heater method (THM) of crystal growth potentially involves both temperature and solutal gradients and thus is considerably subject to buoyancy driven convection on earth. When the driving force for convection is reduced, as in a flight experiment, then transport through the solvent zone is predominantly by diffusion and the technique becomes prohibitively slow, and far too susceptible to variations in the microgravity environment such as g-jitter and the direction of the residual acceleration component. The application of a rotating magnetic field in unit gravity and in microgravity leads to a dramatic increase in the flow within the zone and to increased transport of solute material through the zone.

Cadmium telluride dissolved in liquid tellurium has been used to model a typical traveling solvent zone. During crystal growth a single crystal seed of CdTe is in contact with the zone at the solidifying end, while a source of polycrystalline CdTe is dissolved into the tellurium rich zone as the zone is translated. The aspect ratio of zone length to sample diameter is normally between ½ and 1. The temperature is set such that the zone maximum temperature is between the melting point of the solvent and the solute. In the case of CdTe-Te, a zone of approximately 750°C is used. This leads to a solute concentration of approximately 12% CdTe.

Modeling incorporates the momentum balance as governed by the incompressible Navier-Stokes and the continuity equations, but with three velocity components to account for the azimuthal flow. The force term includes thermal and solutal buoyancy forces and also the electromagnetic stirring force. Thermal boundary conditions are imposed on the THM system, and it is assumed that the dissolution and growth rates are equal. The complete model has been described in a journal article.[3]

In Figure 1a, the THM technique is shown as configured for terrestrial gravity. This technique has proved to a useful method of producing CdTe, but suffers from the time required to transport the material through the zone. Too fast a translation leads to increased tellurium inclusions. The figure shows the flow pattern, superimposed on the CdTe concentration field. It can be seen that the solidifying interface is a complex shape with the curvature mainly concave as seen from the melt. Under these conditions any defects that are propagated from the edges of the sample will continue to grow through the crystal. In Figure 1b, the same geometry and thermal field have been applied for the conditions of $10^{-3}g_0$. In this case the transport is purely diffusion controlled and the flow rates are considerably slower. The composition varies almost linearly through the zone. The interface shape, now convex as seen from the melt, has been modified and is now more favorable for the growth of high quality crystals. Defects propagating from the interface will be eliminated upon reaching the walls. Figure 1c shows the effect of applying a 8 mT rotating magnetic field of 60 Hz on the ground. The single roll cell has been replaced by a complex, mainly double cell arrangement as the buoyancy induced cell is pushed upwards by a recirculating Ekman cell at the interface. While, in principle, an increase in field strength should result in two cells, the flow velocities become very large and the solutal transport is too intense to be modeled. The interface shape is, however, improved as compared to the non-magnetic case. This two-dimensional representation does not show the azimuthal flow which attains a maximum of approximately 1 mm/sec for each 1mT of applied field. Transport rates through the zone are considerably increased. In figure 1d the RMF is applied to a zone in low gravity. The RMF produces two Eckman recirculating cells which overwhelm the residual convection and result in efficient transport of material. At higher field strengths than shown here, the two cells are more uniform. This illustration is meant to show the onset of the double Ekman cell configuration. The situation is ideal for controlled transport, even when the acceleration level is only as low as $10^{-3}g_0$. Thus the combination of low, but not exceptionally low, acceleration levels with a weak applied rotating magnetic field is able to produce controlled flow ideally suited for zone growth.

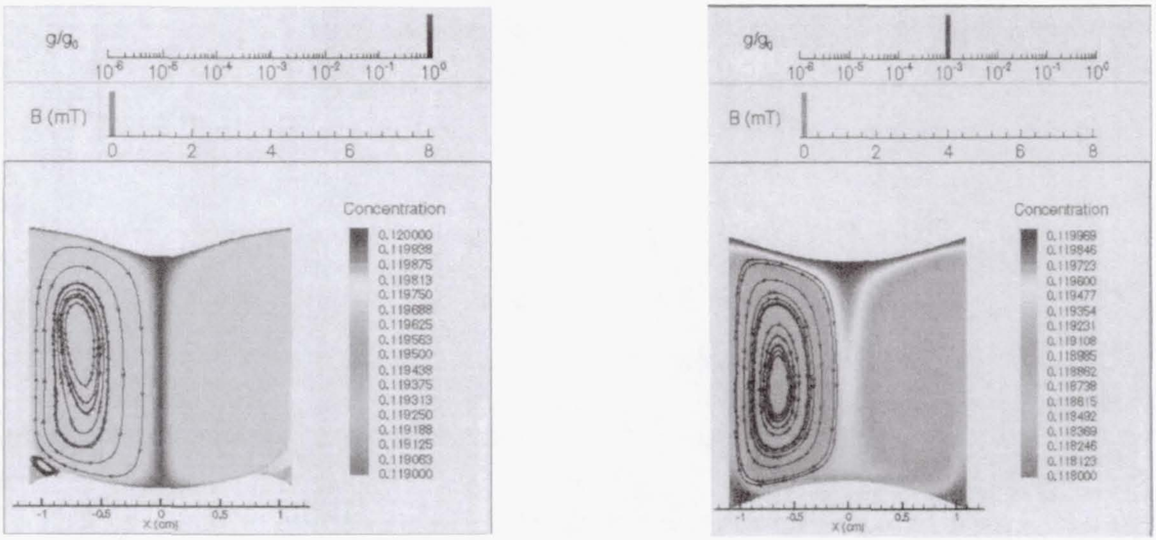

a. Terrestrial Gravity, No Field

b. Microgravity, No Field

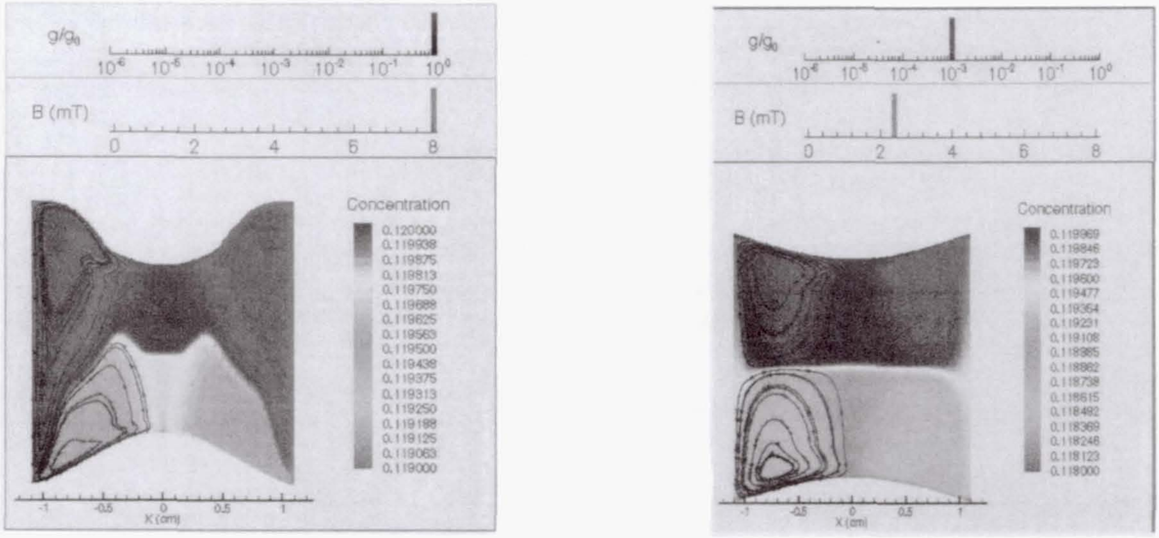

c. Terrestrial Gravity, 8 mT

d. 10^{-3} g_0, 2.2 mT

Figure 1. Calculated Flow Patterns and concentration fields in cadmium telluride within a tellurium solvent zone

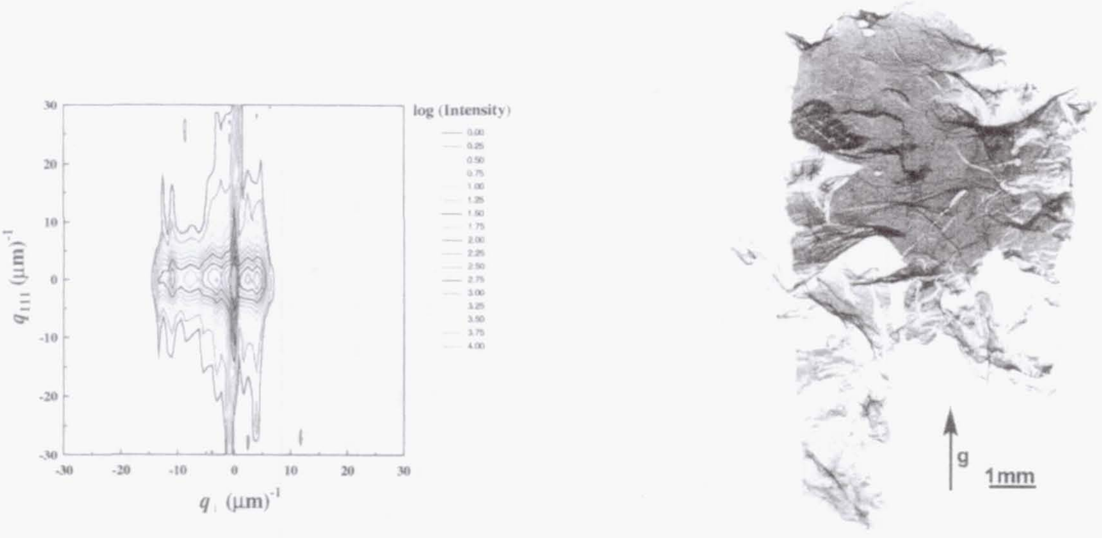

Figure 2. Typical results of growth of a high Cd HgCdTe alloy grown by traveling heater method with an applied rotating magnetic field
a. Triple axis x-ray diffraction b. Synchrotron white beam topograph

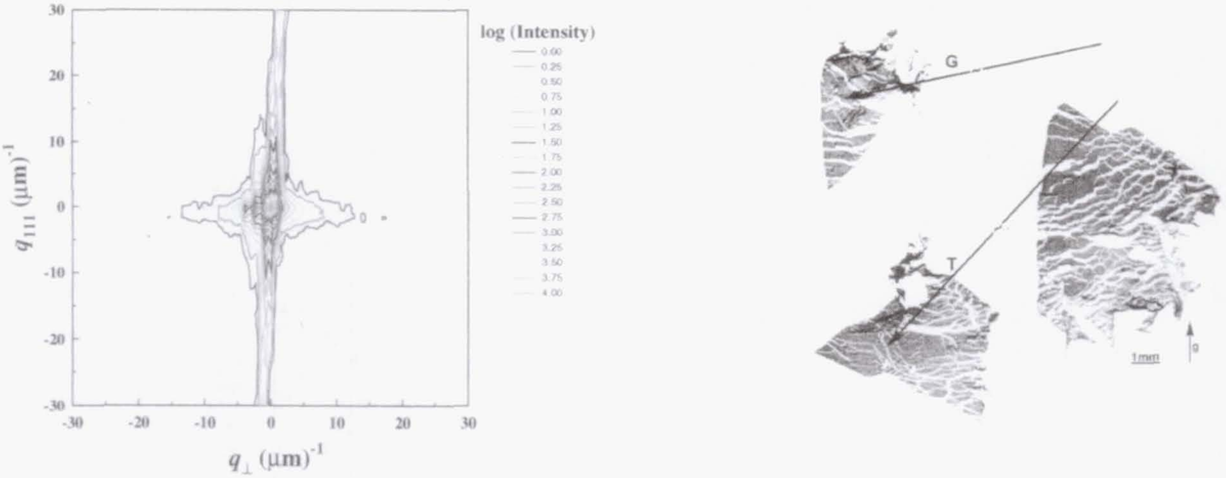

Figure 3. Typical results of growth of a high Cd HgCdTe alloy grown by traveling heater method – conventional (no magnetic field)
a. Triple Axis Diffractometry b. White Beam X-ray Synchrotron Topograph

Experimental Results

Several systems have been examined as candidates for the THM technique. While the original proposal called specifically for II-VI compounds, the possibility of examining transport in simpler systems with materials, particularly elements, which are easier to characterize, has also been contemplated. Of the possible selections, the growth of the group IV elements, particularly germanium has been considered. Growth of germanium from a lead solution has been tried, but the solubility is low and there is a need to process at above 820°C to achieve the desired zone configuration. The resulting crystal of germanium contained lead inclusions. We are now proceeding with the growth of germanium from a germanium-silver eutectic. The eutectic temperature is 651°C and so growth will be at temperatures similar to those used for growth of II-VI compounds. While the modeling has been done for pure CdTe, compounds have been grown, namely CdZnTe and HgCdTe. In all cases the thermophysical properties of the zone were assumed to be those of pure tellurium. The measurement of the viscosity, electrical conductivity and density of the tellurium alloys will be made with an oscillating cup viscometer.[4] The modeling effort is now being extended to include the HgCdTe alloys.

The growth configuration consists of four separate heaters on one translating stand. Of these small, single zone furnaces, two are equipped with rotating magnetic fields and two are not. Thus, we run parallel experiments, with and without the field. Some typical early results for HgCdTe alloys grown with a translation speed of 1 mm/day are shown in Figure 2 and 3. When the zone is translated with the field applied, the result is a structure in which there are many low angle boundaries and a mosaic structure results. Figure 2a shows results from a triple axis x-ray diffractometer which maps reciprocal lattice space. The multiple peaks confirm the presence of sub-grains, and the breadth of the peaks illustrate a high defect density. Figure 2b, taken from an adjacent wafer, is a reflection white beam x-ray synchrotron photograph in which the diffraction spot is enlarged to show the structure. The material has a very high defect density with a myriad of overlapping segments to the reflections. The photograph confirms that the quality of material is not high. Other wafers from the same boule showed similar results. Results from the parallel experiment with HgCdTe grown conventionally without the field are shown in Figure 3. In Figure 3a, the triple axis diffraction demonstrates a strong “surface streak” running vertically. This is an indication of good crystal quality. The material, however is not free of low angle boundaries. This structure is typical of the THM method. The improvement can be seen more dramatically in Figure 3b, where the white lines delineate low angle boundaries, as do the dark lines within the sub-grains. The sub-grain size is large fractions of mm, however, and is another indication of high quality. In this case the tilt across small angle boundaries is 1-4 minutes, while the dislocation density within the sub-grains is 10^4 - 10^5 /cm^2. Modeling analysis, which was done for the simpler case of CdTe, shows that the flow in the ground based sample is extremely complex in the presence of the field (see figure 1c), while low gravity conditions with the field applied would lead to a superior product as the flow across the interface would control the thermal field (figure 1d). The more complex cases of the II-VI alloys are now being modeled.

Conclusions

Numerical modeling has demonstrated that, in the growth of CdTe from a tellurium solution, a rotating magnetic field can advantageously modify the shape of the liquid solid interface such that the interface is convex as seen from the liquid. Under such circumstances, the defect structure is reduced as any defects which are formed tend to grow out and not propagate. The flow of liquid, however, is complex due to the competing flow induced by the rotating magnetic field and the buoyancy driven convection. When the acceleration forces are reduced to one thousandth of gravity, the flow pattern is much simplified and well controlled material transport through the solvent zone can be readily achieved.

Triple axis diffractometry and x-ray synchrotron topography have demonstrated that there is no significant improvement in crystal quality for HgCdTe grown on earth from a tellurium solution when a rotating magnetic field is applied. However, modeling shows that the flow in microgravity with a rotating magnetic field would produce a superior product

References

1. Donald C. Gillies, Sandor L. Lehoczky, F. R. Szofran, Dale A. Watring, Helga A. Alexander and Gregory A. Jerman, J. Crystal Growth, 174 (1997),
2. M. Fiederle, C. Eiche, W. Joerger, M. Salk, A. S. Senchenkov, A. V. Egorov, D. G. Elbing and K. W. Benz, J. Crystal Growth, 166 (1996), 256-260.
3. Chahid K. Ghaddar, Cheo K. Lee, Shariar Motakef and Donald C. Gillies, To be published in Journal of Crystal Growth.
4. Konstantin Mazuruk, Ching-Hua Su, Sandor L. Lehoczky and Franz Rosenberger, J. Appl. Phys. 77 (10), 15 May 1995, 5098-5102.

The Isothermal Dendritic Growth Experiment (IDGE)

M.E. Glicksman (518/276-6721), <glickm@rpi.edu>
M.B. Koss (518/276-2844), <kossm@rpi.edu>
A.O. Lupulescu (518/276-2023), <lupula@rpi.edu>
J.C. LaCombe (518/276-8068), <lacomj@rpi.edu>
J.E. Frei (518/276-6130), <freij@rpi.edu>
Materials Science and Engineering Department
Rensselaer Polytechnic Institute
Troy, NY, 12180-3590

And

D.C. Malarik (216/433-3203), < Diane.Malarik@lerc.nasa.gov>
Microgravity Science Division
MS 500-217
NASA Lewis Research Center
Cleveland, OH 44135

Introduction

Dendrites describe the tree-like crystal morphology commonly assumed in many material systems--particularly in metals and alloys that freeze from supercooled or supersaturated melts. There remains a high level of engineering interest in dendritic solidification because of the role of dendrites in the determination of cast alloy microstructures. Microstructure plays a key role in determining the physical properties of cast or welded products. In addition, dendritic solidification provides an example of non-equilibrium physics and one of the simplest non-trivial examples of dynamic pattern formation, where an amorphous melt, under simple starting conditions, evolves into a complex ramified microstructure [1].

Although it is well-known that dendritic growth is controlled by the transport of latent heat from the moving solid-melt interface as the dendrite advances into a supercooled melt, an accurate, and predictive model has not been developed. Current theories consider: 1) the transfer of heat or solute from the solid-liquid interface into the melt, and 2) the interfacial crystal growth and growth selection physics for the interface. However, the effects of gravity-induced convection on the transfer of heat from the interface prevent either element from being adequately tested solely under terrestrial conditions [2].

The Isothermal Dendritic Growth Experiment (IDGE) constituted a series of three NASA-supported microgravity experiments, all of which flew aboard the space shuttle, *Columbia*. This experimental space flight series was designed and operated to grow and record dendrite solidification in the absence of gravity-induced convective heat transfer, and thereby produce a wealth of benchmark-quality data for testing solidification scaling laws [3,4].

The first flight of the IDGE flight, on STS-62, took place in March, 1994, on the second United States Microgravity Payload (USMP-2) [5], with a second flight on STS-75, in February/March, 1996, on USMP-3. Both flights used ultra-pure succinonitrile (SCN) as the test material. SCN is an organic crystal that forms dendrites similar to the BCC metals when it solidifies. Thus, SCN provides a nearly ideal physical model for ferrous metals. The third and final IDGE flight (USMP-4) launched on STS-87, in December and March of 1997, employed a different test material. This flight used pivalic acid (PVA)---an FCC organic crystal that solidifies like many non-ferrous metals. PVA, like SCN, has convenient properties for conducting benchmark experiments. However, unlike SCN, PVA exhibits a large anisotropy of its solid-melt interfacial energy, which is a key parameter in the selection of dendritic operating states.

USMP-2 (SCN)

The main conclusions drawn from comparing the on-orbit data to terrestrial dendritic growth data, obtained using the same apparatus and techniques, are that: 1) convective effects under terrestrial conditions cause growth speed increases up to a factor of 2 at the lower supercoolings ($\Delta T < 0.5$ K), and convection effects remain discernible under terrestrial conditions up to supercoolings as high as 1.7 K, far beyond what was thought. 2) In the supercooling range above 0.47 K, microgravity data remain virtually free of convective or chamber-wall effects, and may be used reliably for examining diffusion-limited dendritic growth theories. 3) The diffusion solution to the dendrite problem, combined with a unique scaling constant, σ^*, will not provide accurate prediction of the growth velocity and dendritic tip radii. 4) Growth Péclet numbers calculated from Ivantsov's solution deviate systematically from the IDGE data observed under diffusion-limited conditions. 5) The scaling parameter σ^* does not appear to be a constant, independent of supercooling. Finally, 6), the σ^* measurements from the terrestrial and microgravity data are in good agreement with each other, despite a difference of over six orders of magnitude in the quasi-static acceleration environment of low-earth orbit and terrestrial conditions [6,7].

USMP-3 (SCN)

The second IDGE flight on USMP-3/STS-75 mostly supported the above conclusions. However, at present at a still non-final stage of the analysis, there are some important modifications. With sufficient repeated observations [8], it now appears that the terrestrail and microgravity σ^* are distinguishable, with the microgravity σ^* larger the those measured under terrestrial conditions. However, even with the built up statistic of repeated experiment cycles, the functional dependence of σ^* with supercooling remains ambigious. Some of the additional data supports the conclusion of USMP-2 that there is a functional dependence on supercooling, while some of the additional data argues against such a dependence.

The second flight also clarified some issue at the lower supercoolings as to the role of convection, wall proximity or other explanations by showing definitively that it is not convection [9,10] and argued to what extend the low temperature effects are due to wall proximity effects [11]. Finally, the second flight yielded sufficient data to make a three-dimensional reconstruction of the non-parabolic, non-body-of-revolution dendritic tip shape [12,13].

Moving Heat Source Analysis

The method of moving heat sources is applied to the problem of dendritic growth in order to examine how the actual, non-paraboloidal shape of the dendrite tip and its trailing side branch structure affects the transport process. The model describes the diffusive thermal transport processes around a body of revolution (representing the dendrite) advancing into a quiescent melt at a constant rate. The latent heat produced at each of the points along an advancing solidification front is superposed to determine the net change in temperature at an arbitrary point in the surrounding melt. The calculation is performed by specifying the interface shape used in the model to be a shape-preserving body of revolution, which advances into the melt at a constant velocity. Once the shape and the growth velocity are specified, we solve the heat equation (formulated by the moving heat source method) to determine the supercooling experienced by the tip of the interface that is necessary to support the specified growth conditions.

Results of this work indicate that when corrections to Ivantsov's classical, infinite, parabolic tip shape are incorporated, enhanced agreement with experimental data is obtained, relative to the Ivantsov solution. This result is obtained by making modifications to the interface shape in a manner reflecting actual observed SCN dendrite tip shapes. When done, the predicted Pe vs. Δ (Δ is the dimensionless supercooling) relationship is shifted from the Ivantsov result. In general, the model indicates that for interface shapes that are wider than a parabola, Pe will be lower than Ivantsov's result for a given Δ. Conversely, an interface shape narrower than a parabola will raise Pe relative to Ivantsov's result.

The superposition of the latent heat sources (mentioned above) is accomplished by integration starting at the tip, and extending back to the interface areas behind the tip. When done in this manner, it is seen to be unnecessary to integrate back an infinite distance behind the tip. Instead, far from the tip, the contributions to the tip's required supercooling become small. This indicates that there is some "range of influence" which affects the heat transport at the tip of the dendrite, beyond which contributions become negligible. The size of this range is observed to be a strong function of the growth Peclét number, $Pe=VR/2\alpha$, where V is the growth rate, R is the radius of curvature of the tip, and α is the thermal diffusivity of the melt. The important question this raised was whether or not this range would extend into the region of the dendrite where side branches were present, and the assumed interface shape was not valid.

The model was next applied to the case of the IDGE experiment's range of Peclét numbers and supercoolings. Using the upper end of the experimental Peclét range, *Pe* ~0.01, the integration range was limited to the region of the dendrite that is not dominated by the side arms (i.e. the tip region, within 12*R* of the tip). When this is done (Figure 1),

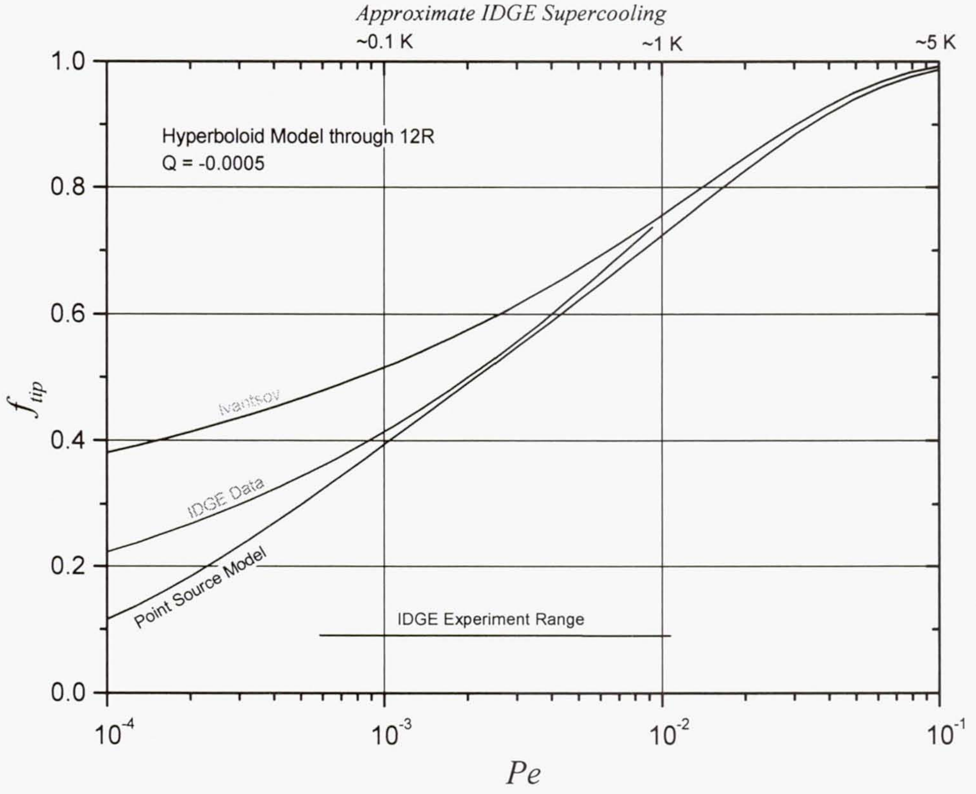

Figure 1. Fractional contribution to *Pe* from dendrite tip.

at most, only ~75% of the tip supercooling is accounted for. This indicates that at least 25% of the tip's supercooling derives from the side branch region of the dendrite—a region that is clearly not described by any simple function (and clearly, neither is Ivantsov's paraboloid). For the lower Peclét numbers seen in the IDGE experiments, the side branch region contributes up to ~60% of the tip supercooling. This observation joins earlier work by Schaefer [14] in suggesting that under the conditions of the IDGE experiment, the side branch region of a dendrite contributes significantly to the thermal conditions at the tip itself. Furthermore, since there is a considerable stochastic aspect to the side branch structure, it would follow that the scatter in the IDGE data may be Figure

2explained by the variations in the side branch structure, and the corresponding influence that this region has upon the transport processes underway at the tip.

USMP-4

The data and subsequent analysis from the final flight experiment are currently at a preliminary stage, based on images received using telemetry from space. We compared the dendritic growth speed of PVA as a function of the supercooling to both terrestrially measured PVA data, and an estimate scaled from prior SCN microgravity data. The preliminary results of these tests indicate that the PVA data are in good agreement with the SCN data (Figure 2). This implies that dendritic growth in PVA is, like SCN, diffusion-limited, with little, if any, kinetic response. This observation conflicts with the conclusion reached by other investigators that there are large interfacial kinetic effects in PVA. Currently we are extracting more accurate velocity and tip radius, shape, and side-branching measurements from post-flight 35mm film and videos.

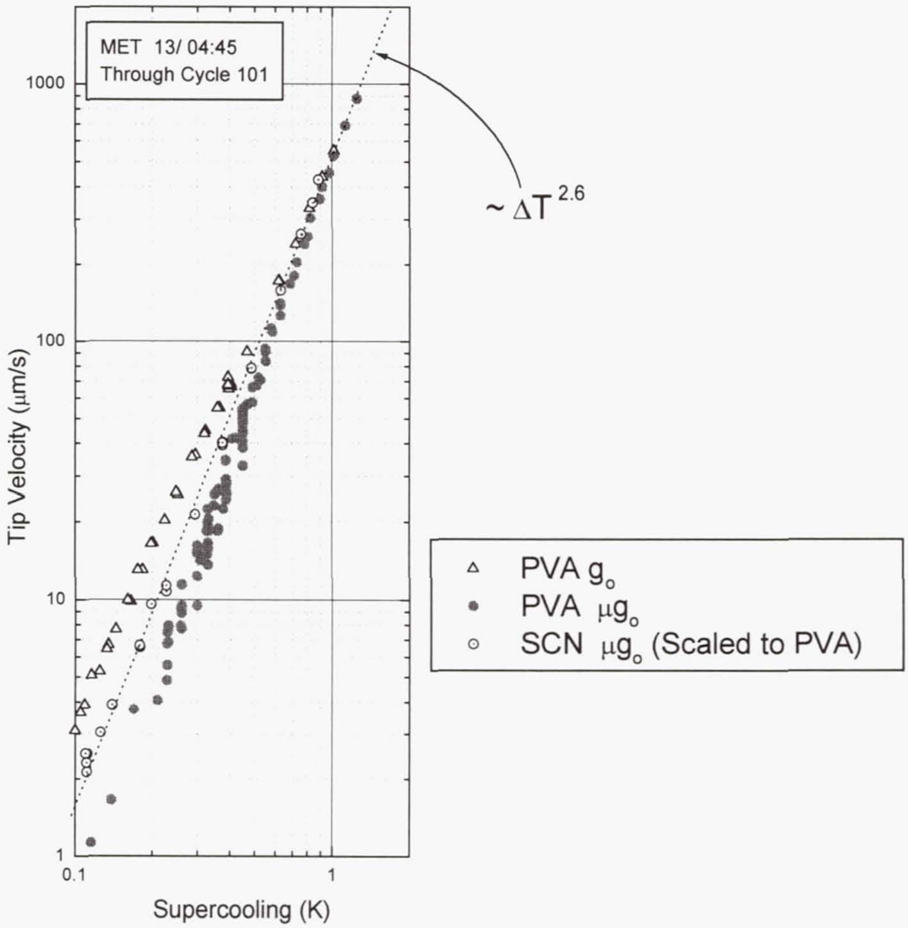

Figure 2. Velocity versus supercooling for PVA.

Figure 3 shows some preliminary data assessing the nature of these boundary layer interactions in PVA. We see that when the nearest neighbor distance exceeds about two thermal diffusion distances, λ, where the diffusion distance $\lambda=\alpha/v$ (α is the diffusivity and v is the tip speed) the velocity levels off at its maximum steady–state rate. When nearest neighbor spacings fall below about 2λ, the velocity is reduced through thermal interactions of the boundary layers. This phenomenon of neighbor interactions has never been observed before, because microgravity conditions are needed to insure growth limited by thermal diffusion from the solid–melt interface.

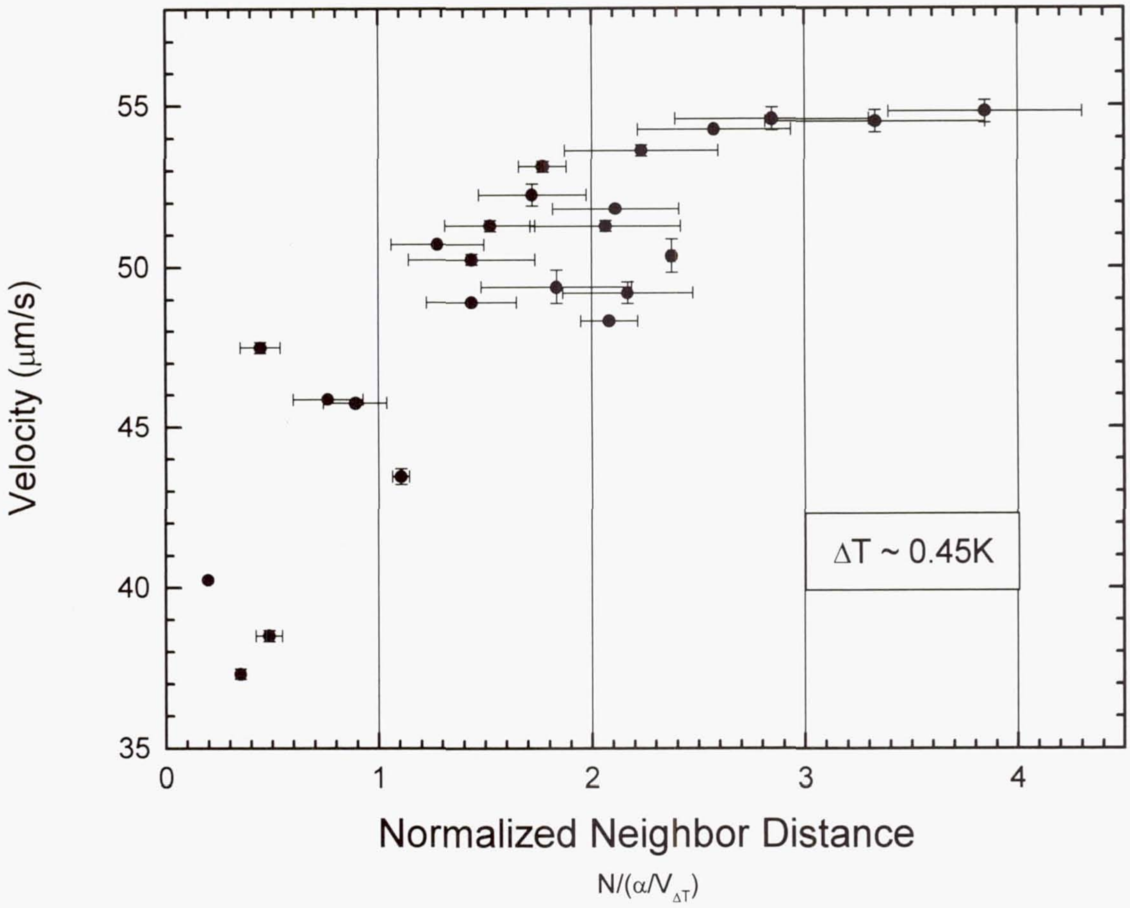

Figure 3. Dendrite velocity versus distance to nearest neighbor.

Telescience

In addition to our investigation of dendritic solidification kinetics and morphology, the IDGE has been part of the development of remote, university-based teleoperations. These teleoperation tests point the way to the future of microgravity science operations on the International Space Station (ISS). NASA headquarters and the Telescience Support Center (TSC) at LeRC, set a goal for developing the experience and expertise to set up remote, non-NASA locations from which to control space station experiments. Recent IDGE space shuttle flights provide proof-of-concept and tests of remote space flight teleoperations [15].

Summary and Conclusions

The data and analysis performed on the dendritic growth speed and tip size in SCN demonstrates that although the theory yields predictions that are reasonably in agreement with experiment, there are significant discrepancies. However, some of these discrepancies can be explained by accurately describing the diffusion of heat. The key finding involves recognition that the actual three-dimensional shape of dendrites includes time-dependent side-branching and a tip region that is not a paraboloid of revolution. Thus, the role of heat transfer in dendritic growth is validated, with the caveat that a more realistic model of the dendrite then a paraboloid is needed to account for heat flow in an experimentally observed dendrite. We are currently conducting additional analysis to further confirm and demonstrate these conclusions.

The data and analyses for the growth selection physics remain much less definitive. From the first flight, the data indicated that the selection parameter, σ^*, is not exactly a constant, but exhibits a slight dependence on the supercooling. Additional data from the second flight are being examined to investigate the selection of a unique dendrite speed, tip size and shape.

The IDGE flight series is now complete. We are currently completing analyses and moving towards final data archiving. It is gratifying to see that the IDGE published results and archived data sets are being used actively by other scientists and engineers. In addition, we are also pleased to report that the techniques and IDGE hardware system that the authors developed with NASA, are being currently employed on both designated flight experiments, like EDSE, and on flight definition experiments, like TDSE.

References

1. M.E. Glicksman and S.P. Marsh, *The Dendrite*, Handbook of Crystal Growth, ed. D.J.T. Hurle, Vol 1b, p.1077, (Elsevier Science Publishers B.V., Amsterdam, 1993).
2. M.E. Glicksman and S.C. Huang, *Convective Heat Transfer During Dendritic Growth*, Convective Transport and Instability Phenomena, ed. Zierep and Ortel, Karlsruhe, 557, (1982).
3. M.E. Glicksman, E.A. Winsa, R.C. Hahn, T.A. LoGrasso, S.H. Tirmizi, and M.E. Selleck, Met. Trans. A, **19A**, 1945, (1988).
4. M.E. Glicksman, M.B. Koss, and E.A. Winsa, JOM, **47(8)**, 49, (1995).
5. M.E. Glicksman, M.B. Koss, and E.A. Winsa, Phys. Rev. Lett., **73**, 573, (1994).
6. M.E. Glicksman, M.B. Koss, L.T. Bushnell, J.C. LaCombe, and E.A. Winsa, ISIJ, **35(6)**, 604, (1995).

7. M.B. Koss, L.A. Tennenhouse, J.C. LaCombe, M.E. Glicksman, and E.A. Winsa, (Manuscript submitted to Metallurgical and Materials Transactions, 1998).
8. A.O. Lupulescu, M.B. Koss, J.C. LaCombe, M.E. Glicksman, and L.A. Tennenhouse, Rensselaer Polytechnic Institute, Troy, NY, unpublished research, (1998).
9. M.B. Koss, L.T. Bushnell, M.E. Glicksman, and J.C. LaCombe, Chem. Eng. Comm., **152-153**, 351, (1996).
10. L.A. Tennenhouse, M.B. Koss, J.C. LaCombe, and M.E. Glicksman, J. Crystal Growth, **174**, 82, (1997).
11. L.A. Tennenhouse, M.B. Koss, J.C. LaCombe, A.O. Lupulescu, and M.E. Glicksman, Rensselaer Polytechnic Institute, Troy, NY, unpublished research, (1998).
12. J.C. LaCombe, M.B. Koss, V.E. Fradkov, and M.E. Glicksman, Phys. Rev. E, **52**, 2278, (1995).
13. J.C. LaCombe, D.C Corrigan, M.B. Koss, L.A. Tennenhouse, A.O. Lupulescu, and M.E. Glicksman, Rensselaer Polytechnic Institute, Troy, NY, unpublished research, (1998).
14. R.J. Schaefer, J. Crystal Growth, **43,** 17, (1978).
15. M.B. Koss, M.E. Glicksman, L.T. Bushnell, J.C. LaCombe, and E.A. Winsa, 8th International Symposium on Experimental Methods for Microgravity Materials Science, ed. R.A. Schiffman, The TMS, Warrendale, PA, (1996).

Title: Evolution of Local Microstructures (ELMS): Spatial Instabilities of Coarsening Clusters

Principal Investigator: Martin E. Glicksman, *Rensselaer Polytechnic Institute*

Co-Investigators: Donald O. Frazier*, Jan R. Rogers*, William K. Witherow*,
J. Patton Downey*, Barbara R. Facemire*
**NASA Marshall Space Flight Center, Space Sciences Laboratory*

Introduction

This work examines the diffusional growth of discrete phase particles dispersed within a matrix. Engineering materials are microstructurally heterogeneous, and the details of the microstructure determine how well that material performs in a given application. Critical to the development of designing multiphase microstructures with long–term stability is the process of Ostwald ripening. Ripening, or phase coarsening, is a diffusion–limited process which arises in *polydisperse* multiphase materials. Growth and dissolution occur because fluxes of solute, driven by chemical potential gradients at the interfaces of the dispersed phase material, depend on particle size. The kinetics of these processes are "competitive," dictating that larger particles grow at the expense of smaller ones, overall leading to an increase of the average particle size. The classical treatment of phase coarsening was done by Todes, Lifshitz, and Slyozov, (TLS)[1,2] in the limit of zero volume fraction, V_V, of the dispersed phase. Since the publication of TLS theory there have been numerous investigations, many of which sought to describe the kinetic scaling behavior over a range of volume fractions. Some studies in the literature report that the relative increase in coarsening rate at low (but not zero) volume fractions compared to that predicted by TLS is proportional to $V_V^{1/2}$, whereas others suggest $V_V^{1/3}$. This issue has been resolved recently by simulation studies at low volume fractions in three dimensions by members of the Rensselaer/MSFC team.[3-5]

Background and Objectives

Our studies of ripening behavior using large–scale numerical simulations suggest that although there are different circumstances which can lead to either scaling law, the most important length scale at low volume fractions is the diffusional analog of the Debye screening length. This screening length places limits on the extent and applicability of a mean–field description and can result in local divergences from mean-field behavior. The numerical simulations we employed exploit the use of a recently developed "snapshot" technique and identify the nature of the coarsening dynamics at various volume fractions. Preliminary results of numerical and experimental investigations, focused on the growth of finite particle clusters, provide important insight into the nature of the transition between the two scaling regimes. The companion microgravity experiment centers on particle growth within finite clusters and follows the temporal dynamics driving microstructural evolution using holography.

This research effort will extend our preliminary ground-based results and develop a critical microgravity experiment to observe these phenomena in a suitably quiescent environment. Work accomplished to date shows that the critical cross–over between the two scaling regimes ($V_V^{1/2}$ versus $V_V^{1/3}$) is a function of both the volume fraction, which, intuitively, affects the screening length and the cluster size, n, where n is the number of particles comprising the cluster. Specifically, the cross–over occurs at a critical volume fraction for which $V_V \approx 1/(3n^2)$. One also expects that the volume fraction itself fluctuates from region–to–region, because the local size and distribution of particles vary. Thus, spatial variances should arise in the local kinetics. One of the scientific objectives of this work is to identify the nature of these microstructural fluctuations. This added level of understanding will be of importance in the development of more predictive models for microstructural evolution in heterogeneous materials.

Theory

We begin with a discussion of infinitely dilute coarsening systems based on the TLS mean–field solution to coarsening kinetics which is restricted to zero volume fraction of droplet phase. The continuity equation requires that neither nucleation nor coalescence occur, only smooth growth and dissolution:

$$\frac{\partial F}{\partial t} + \frac{\partial}{\partial R}\left[\nu(R) \cdot F\right] = 0 \qquad 1.$$

Our approach in this work is to seek to measure and predict ν(R), the time rate of change of the radius, R, of a particle, in a given cluster. To obtain ν(R), certain simplifying assumptions are required:

1. Kinetics are limited by volume diffusion in the matrix, and

2. Diffusion remains quasi-static.

Therefore, the diffusion equation describing the concentration field, c(r), in the matrix phase reduces to the Laplace equation:

$$\nabla^2 \varphi = 0\,, \qquad 2.$$

where $\varphi = (c - c_0)/c_0$, and c_0 is the equilibrium solubility.

The boundary conditions at the surface of the *i*-th particle are specified through the Gibbs-Kelvin local equilibrium relation

$$\varphi_i = \frac{\lambda}{R}, \tag{3.}$$

where λ is the capillary length given by, $\lambda = 2\gamma\Omega/(k_B T)$, through which all quantities of length are scaled in this mean-field treatment; γ is the droplet-matrix interfacial energy; Ω is the atomic volume of the dispersed phase; and k_B is Boltzmann's constant.

Solution to the Laplace equation, subject to the Gibbs–Kelvin boundary condition, may be written in terms of the Coulomb potential

$$\varphi_i = \left(\frac{z_i e}{4\pi\varepsilon}\right)\left(\frac{1}{r}\right), \tag{4.}$$

where φ_i is the coulomb potential at a distance r from an ion of charge $z_i e$.

The diffusion potential is, therefore,

$$\varphi(r) = \sum_i \frac{\lambda B_i^{TLS}}{|r - r_i|} + \varphi_\infty. \tag{5.}$$

The diffusion analog of electrostatic charge is source/sink strength (volume flux), B_i^{TLS}, given by

$$B_i^{TLS} = \left(1 - \frac{R_i}{R^*}\right), \tag{6.}$$

where R* is the critical radius given by, $R^* = \lambda/\varphi_\infty$, and φ_∞ is the background matrix potential, assumed uniform throughout the matrix phase. The zero volume fraction restriction in TLS theory results in the total neglect of direct interactions among particles. A more realistic approach which introduces the influence of volume fraction on coarsening kinetics was employed by Marqusee and Ross.[6] Their approach applies a spatially coarse–grained background diffusion potential, which is the diffusion analog of the electric potential arising from a given charge density, ρ. An expression for electric potential influenced by ρ is,

$$\nabla^2\varphi = -\frac{\rho}{\varepsilon_o}. \tag{7.}$$

The diffusion analog is, therefore,

$$\nabla^2\varphi = -4\pi\sigma, \tag{8.}$$

where σ, a source/sink density in the matrix space, is analogous to ρ from electrostatics. σ introduces a coarse–grained local background potential, $\varphi(\mathbf{r})$, due to droplets surrounding a coarsening droplet centered at point r in the matrix,

$$\varphi(r) = \sum_i \frac{\lambda B_i}{|r - r_i|} \exp(-\kappa \cdot |r - r_i|) + \varphi_\infty . \qquad 9.$$

The volume flux, B_i, is now,

$$B_i = \left(1 - \frac{R_i \varphi_\infty}{\lambda}\right)(1 + \kappa R_i) = B_i^{TLS}(1 + \kappa R_i), \qquad 10.$$

where κ represents the natural cut-off distance for direct particle interactions via the diffusion field, beyond which the particles are isolated from each other by the intervening two-phase medium.

For droplet clusters comprising finite coarsening systems, one may define physically distinct coarse-grained length scale parameters; among them are:

- the Debye screening radius, $\Lambda_D \equiv \kappa^{-1}$.
- the average droplet radius in the cluster, $\Lambda_R \approx \langle R \rangle$,

  therefore, $\Lambda_D = [4\pi N_V \langle R \rangle]^{-1/2}$. As in electrostatics, for large Λ_D (sparse particle density), the screened potential approaches the unscreened potential.

- the extent of the total coarsening system, Λ_{tot}, is defined for a "spherical cluster" by

$$\Lambda_{tot} = \left(\frac{4\pi}{3}\right)^{-1/3}\left(\frac{n}{N_V}\right)^{1/3}, \qquad 11.$$

  where *n* is the total number of particles remaining at a given time, and for $\Lambda_D \geq \Lambda_{tot}$, screening is not a factor.

One can now relate the time-rate of change of radius,

$$v(R_i) = -\frac{2\lambda D c_o \Omega}{R_i^2} B_i , \qquad 12.$$

whereby B_i is now representative of the volume flux of a droplet in a finite coarsening cluster. The experimental parameters for determining the time-rate of change of each droplet within a given cluster are accessible through physicochemical measurement and holography.

Experiment

Experimental objectives of ELMS are:

- to measure $\nu(R_i)$ of each droplet cluster by using holography
- to determine, in a mixed–dimensional system (3-*D* droplets undergoing 2-*D* diffusion), the existence, if any, of spatial instabilities in microstructural homogeneity due to a heretofore undefined "screening length"
- to verify in a fully 3-*D* system in microgravity the TLS coarsening rate deviation dependence on local volume fractions for global volume fractions ≤ 1%, where the volume fraction for a finite coarsening cluster is,

$$V_v = \frac{\sum_{i=1}^{n} (4/3)\pi R_i^3}{(4/3)\Lambda_{tot}^3}. \qquad 13.$$

The experimental approach is comprised of ground–based work to extend prior mixed-dimensional studies and a flight experiment to study finite coarsening kinetics in three dimensions.

A. Ground-based experiment

The ground-based experimental study of diffusional coarsening will proceed in a liquid–liquid two–phase system. Ideally, one performs the experiment at an isopycnic point to maximize reduction of gravity–driven convective disturbances. This would allow observations over the long times required to investigate diffusional coarsening. A holographic technique has been instrumental in prior work on this subject and will continue to be the primary method to study both the influence of local environmental conditions on individual droplet size histories and measurements of global averages. Most of the ground-based coarsening data will be collected during two-dimensional diffusion of three–dimensional droplets attached to a glass surface (mixed–dimensional case).[4,5]

Ground-based studies will proceed as follows:

- Prepare droplet distributions for sparse and densely populated clusters for finite coarsening systems undergoing 2–*D* diffusion;

- Configure a pre–programmed x–y translator with predetermined droplet positions in tandem with a sharp tool for scoring pinpoint defects onto high–quality, pristine cell walls. This should induce heterogeneous nucleation at desired positions;

- Fabricate an optimal cell for achieving predictable cluster size and number distributions, and perform experiments;

- Study temporal correlation of droplet size and number distribution for mixed–dimensional coarsening.

B. Flight Experiment

The space–based coarsening study requires long–duration, quality microgravity to prevent phase separation via Stokes settling. In this instance, there is no wall attachment to prevent sedimentation, so establishing microgravity conditions is an imperative. As the estimated time of the experiment is almost four months, a Space Station facility will ultimately be required.

In order to understand the need for quality microgravity, it is helpful to examine the velocity of a 100μm diameter droplet (the largest size anticipated) at a temperature near the isopycnic point. The Hadamard-Rybczynski relation provides the velocity of droplets,

$$V_s = \frac{2}{3}\frac{\left[r^2(\rho_2 - \rho_1)\left(\frac{\eta_2}{\eta_1} + 1\right)a\right]}{\left[3\eta_2 + 2\eta_1\right]}, \qquad 14.$$

where ρ_2-ρ_1 is the mass density difference between the droplet and matrix phases, η_1 is the viscosity of the matrix fluid, and η_2 is the viscosity of the droplet phase fluid. The Hadamard-Rybczynski relation is valid provided that the droplet surface is clean, and the Reynolds number, $Re \equiv \rho|V_s|r/\eta_1$, is small compared to unity. Droplets are assumed to remain spherical. Assuming the use of a succinonitrile-water system, and using a succinonitrile–rich droplet phase with a 0.1K deviation from the isopycnic temperature, $\Delta\rho \equiv 3.85 \times 10^{-5}$ g/cm^3. Such a deviation could occur from either experimental uncertainties in the isopycnic set point and the temperature measurement system, as well as from cycling or drift caused by the temperature control system. The magnitude of the velocity of such a droplet at 10^{-4}g is 1 x 10^{-4}mm/hr. In 1-g, the same droplet would fall 1mm in 1hr, and would reach the bottom of the test cell before noticeable ripening had occurred. The dispersion would become rapidly depleted of larger ripening droplets. The relative position of the droplets would also vary significantly in time. It would not be possible to explore local microstructural effects from diffusion, because the droplet population would be altered more rapidly by sedimentation effects. This and other factors, such as distortion around the diffusion field, would obscure the kinetics. These factors impose the imperative for microgravity investigation of three–dimensional coarsening kinetics and observation of evolution of microstructure.

Preparation for microgravity studies will begin by assessing two approaches for droplet dispersion:

1. Jet break-up in microgravity to control the distribution of droplets in each cluster.

From Tomitika, the Rayleigh stability criterion, q, is expressed as,

$$q = \frac{\gamma}{2\eta_2}\left(1 - x_d^2\right)\phi\left(x_d, \frac{\eta_2}{\eta_1}\right), \qquad 15.$$

where η_1 and η_2 are viscosities of the fluids; γ is the interfacial tension; R is radius of liquid cylinder; and $x_d = 2\pi R/\lambda_d$. λ_d is the wavelength of disturbance caused by, e.g., vibrations or nozzle roughness. For appropriate jet velocity and nozzle wetting characteristics, the average droplet size in a cluster is approximately twice the nozzle diameter. For $q < 0$, disturbances damp out; for $q = 0$, disturbances remain stable, resulting in oscillating waves; for $q > 0$, disturbances become capillary waves which lead to liquid cylinder breakup [pressure limits drop size].

Table 1. Results from prototype: distribution of butyl–benzoate droplets in water[7]

d_N(μm)	<d>(μm)	σ(μm)	<d>/d_N
77	149	±66	1.9
153	284	±130	1.9
203	348	±190	1.7

d_N is the nozzle diameter; <d> is the average cluster droplet diameter; σ is the standard deviation within the cluster from average cluster droplet diameter.

2. Site saturation method [Nucleation of Crystals from Solution (NCS)][8] for forming droplet clusters by quench.

Finally, holographic imaging is the optical tool selected for observing these phenomena. Figure 1 contains a sequence of holograms during the mixed-dimensional coarsening of succinonitrile-water. Figure 2 represents maps of local diffusion fields derived from spatial and size distributions of all droplets observed in the corresponding holograms of Figure 1 using monopole approximations. Clearly, holography provides more data than does conventional optical imaging techniques. A reconstructed hologram is amenable to various optical characterization techniques, *e.g.*, *in situ* microscopy, and interferometry. An especially important aspect of the experimental study includes determining the extent of modifications required to allow incorporation of holography within the operating envelope of the millikelvin thermostat (MITH) hardware.

References

1. O.M. Todes, J. Phys. Chem (Sov) **20**, 629 (1946).
2. I.M. Lifshitz and V.V. Slyozov, J. Phys. Chem. Solids **19**, 35 (1961).
3. V.E. Fradkov, M.E. Glicksman, S.P. Marsh, Phys. Rev. E. **53**(3), 3925 (1996).
4. J.R. Rogers, J.P. Downey, W.K. Witherow, B.R. Facemire, D.O. Frazier, V.E. Fradkov, S.S. Mani, and M.E. Glicksman, J. Electronic Mat. **23**(10), 999 (1994).
5. V.E. Fradkov, S.S. Mani, M.E. Glicksman, J.R. Rogers, J.P. Downey, W.K. Witherow, B.R. Facemire, and D.O. Frazier, J. Electronic Mat. **23**(10), 1007 (1994).
6. J.A. Marqusee and J. Ross, J. Chem. Phys. **80**, 536 (1984).
7. J.R. Rogers, Ph.D. Dissertation, University of Colorado, 1992
8. R.L. Kroes, D.A. Reiss, and S.L. Lehoczky, Microgravity Sci. Technol. VIII/1 52-55, (1995).

Holograms of mixed-dimensional coarsening of succiononitrile-water system in pyrex cells: discrete phase is succinonitrile rich.

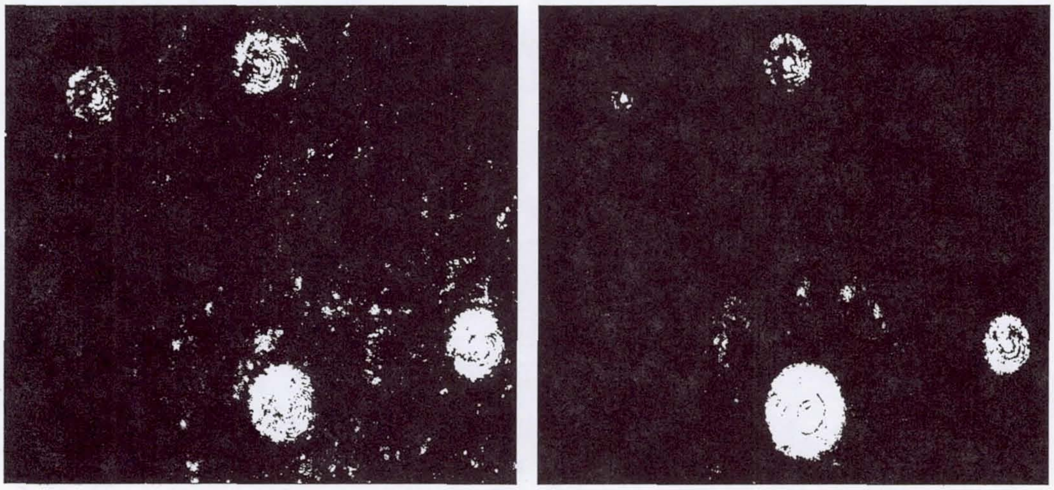

Hologram 100

Hologram 129

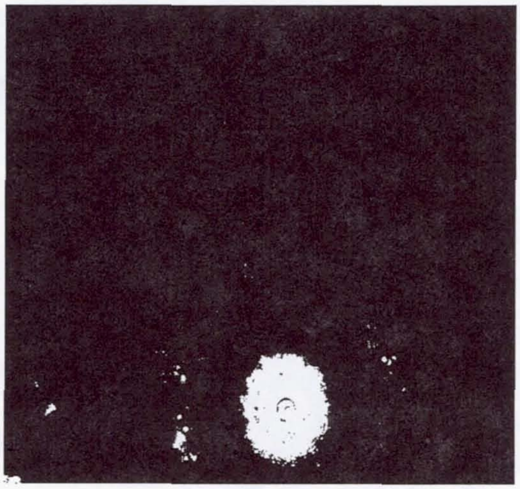

Hologram 151

Figure 1.

Holographic data for mixed-dimensional coarsening, with mapping of local diffusion fields using monopole approximations. Black circles show particle sizes, shades of blue indicate areas of solute depletion, whereas shades of red show enrichment.

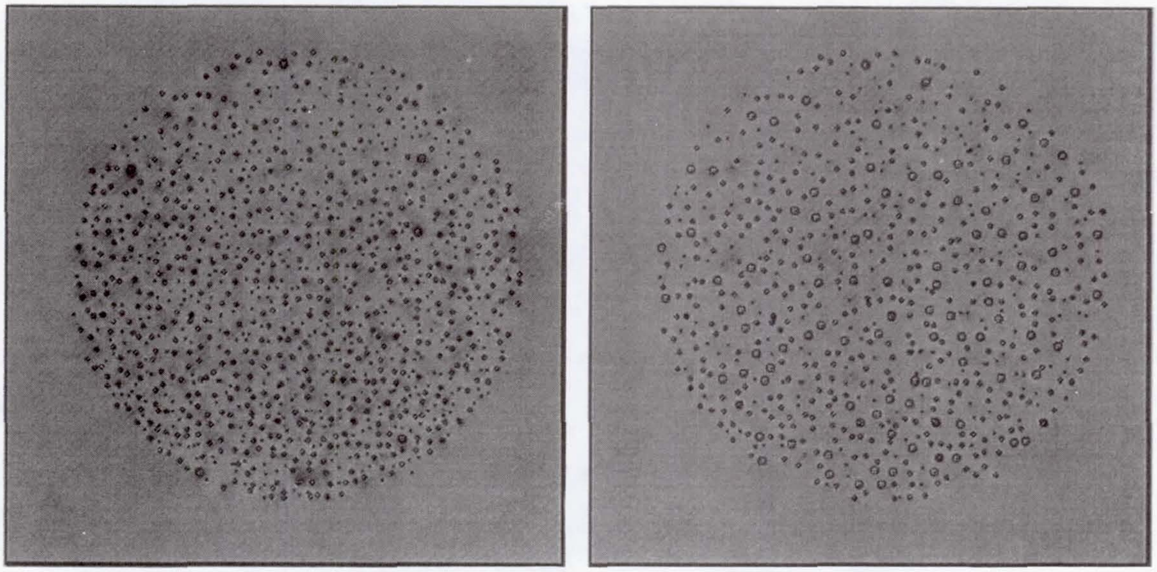

Hologram 100 Hologram 129

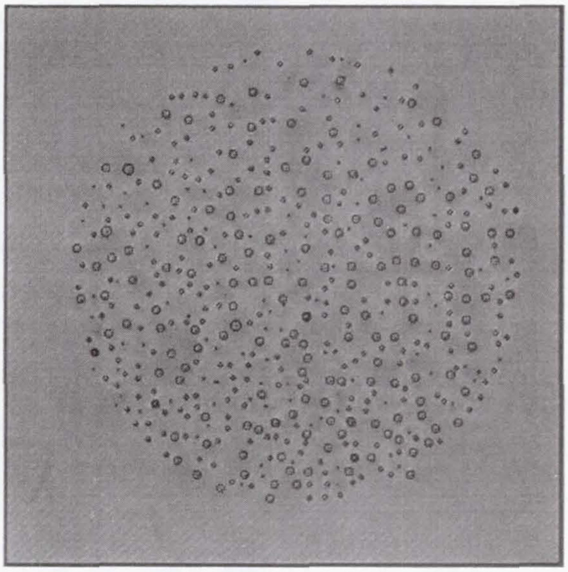

Hologram 151

Figure 2.

EFFECT OF GRAVITY ON MICROSTRUCTURAL EVOLUTION DURING LIQUID PHASE SINTERING: A QUANTITATIVE APPROACH

Arun M. Gokhale, Asim Tewari, and Tom Mirabelli
School of Materials Science and Engineering, Georgia Institute of Technology
Atlanta, Georgia-30332-0245

INTRODUCTION

Evolution of global microstructural attributes and spatial arrangement of microstructural features are important aspects of microstructure development. These microstructural characteristics may be significantly affected by gravity, particularly, if liquid phases are present during the evolution processes. Understanding of the role that gravity plays in microstructure development is expected to enhance our understanding of how the intrinsic materials processes govern the microstructural evolution. Therefore, it is of interest to quantitatively characterize effects of gravity on the kinematics of microstructural evolution in three-dimensional space by using unbiased stereological and image processing techniques. Objective of this research program is to develop flexible and practical quantitative metallographic procedures to quantify three-dimensional microstructure in an assumption-free, unbiased, and efficient manner, and apply these techniques to gauge the role of gravity in microstructural evolution during liquid phase sintering of tungsten heavy alloys. The practical and efficient procedures are being developed to estimate the topological characteristics such as number and connectivity of grains in three-dimensional microstructure, moments of grain volume distribution, and descriptors of spatial arrangement of grains such as radial distribution function, pair correlation function, higher order (n-point) correlations [1-3], nearest neighbor distribution and higher order neighbor distributions, etc. The research involves development of digital image analysis procedures, development of computer codes to extract the spatial distribution information from the image analysis data, development and applications of stereological procedures, development of efficient serial sectioning procedures, and computer simulations of three-dimensional microstructure. These techniques are utilized to quantify the evolution of microstructural attributes, and spatial arrangement of tungsten grains and pores during liquid phase sintering of a series tungsten heavy alloys. This part of the research is in collaboration with Professor R.M. German and his group at Pennsylvania State University. The ground based as well as microgravity environment liquid phase sintering experiments have been performed by Professor German and his colleagues at Penn. State. The research program at Georgia Tech involves quantitative characterization of evolution of microstructure in these liquid phase sintered specimens. The quantitative data on the evolution of the spatial arrangement of tungsten grains are used to address the questions such as: How does the gravity affect the kinetics of liquid phase sintering? How does gravity affect topology of three-dimensional microstructure?, Does the spatial distribution of distances between tungsten grain centers reach a pseudo-static form when appropriately normalized by a microstructural scale factor?, Are there any spatial correlations among the sizes of tungsten grains?, How does the gravity affect the distance distributions and the spatial correlations? , etc. We have made very significant progress towards these goals. Some of our important recent results are presented in this paper; these results were not presented in our annual progress reports [4]. In this paper, we present our work on reconstruction of three-dimensional microstructure from montage serial sections, and unbiased three-dimensional microstructural data on the mean grain volume, variance of grain volume distributions, number density, and connectivity of grains in liquid phase sintered microstructures, and gravitational effects on these attributes of microstructures. The next section of the paper gives a brief description of the image analysis and stereological procedures developed in this research program. In the subsequent section, these techniques are applied to quantify the effect of gravity on microstructural evolution of tungsten grains during liquid phase sintering of 83wt% W-Ni-Fe alloy.

DIGITAL IMAGE ANALYSIS AND STEREOLOGICAL TECHNIQUES

It is well known that the microstructural attributes such as number density and connectivity of grains, average grain volume (average size), variance of grain volume distribution etc. in three-dimensional microstructure can not be estimated in an unbiased manner from any measurements whatsoever performed on random two-dimensional metallographic planes[5]: serial sectioning of three-dimensional microstructure is essential for estimation of these microstructural attributes. In the past, serial sectioning has been performed by recording microstructural image of one field of view in a metallographic plane followed repeated polish-photograph-polish procedure to generate a stack of serial sections of one field of view . The small volume of three-dimensional microstructure created by such a stack of serial sections having cross-sectional area of one field of view is not useful for extracting quantitative three-dimensional microstructural information in a statistically robust manner, and it is of no use at all for quantitative characterization of spatial arrangement of microstructural features in three-dimensions. Further, manual matching of serial sections (as used in the earlier studies) can lead to significant error in the estimation of the sampled microstructural volume. Note that it is essential to know the sampled microstructural volume to estimate the attributes "per unit volume". We have developed digital image analysis procedures to recreate a large volume of three-dimensional microstructure by using the "montage" serial sectioning technique developed in this research program. The technique involves creation of a montage of large number of perfectly matching (within one pixel) high resolution contiguous microstructural fields [2,3]. A stack of such montages is generated by serial sectioning, which leads to creation of microstructural volume that may be 25 to 50 times larger than the one created by conventional serial sectioning procedures, for the same effort. Such large microstructural volume is very useful for statistically reliable estimates of microstructural attributes, and it is essential for quantitative characterization of spatial arrangement of microstructural features in three-dimensional space. We have utilized digital image analysis to precisely match the image montages of successive serial sections, and to recreate three-dimensional microstructure. Figure-1 represents a very small portion (about 4%) of volume rendered image of recreated three-dimensional microstructural volume of 83wt% W-Ni-Fe alloy specimens liquid phase sintered in microgravity at 1500° C for one minute and one hundred and twenty minutes. It is possible to remove the matrix from these volume rended images and generate surface rendered microstructure of the tungsten grains as shown in Figure-2. There is a significant evolution of microstructure with time. Observe that, although these specimens were liquid phase sintered in the microgravity environment, most of the tungsten grains are inter-connected in three-dimensions. The three-dimensional microstructure appears to be consisting of a connected network of linear chains of tungsten grains that have branches and

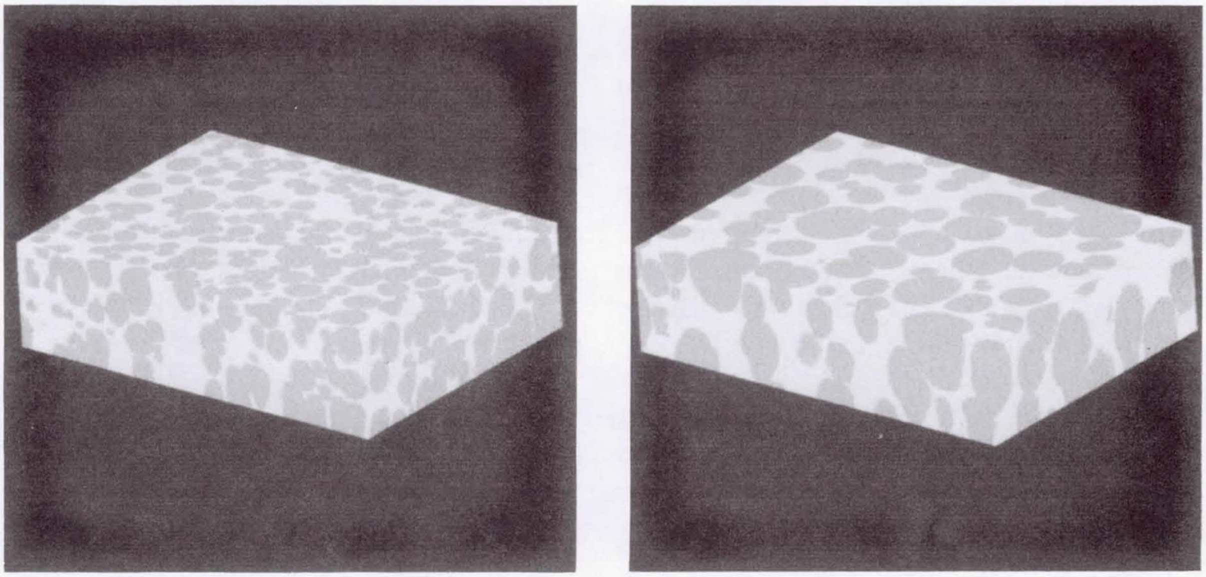

Figure 1: Volume rendered 3D microstructure of W-grains in 83 wt.% W-Ni-Fe alloy liquid phase sintered in microgravity for (i) 1 min (ii) 120 min

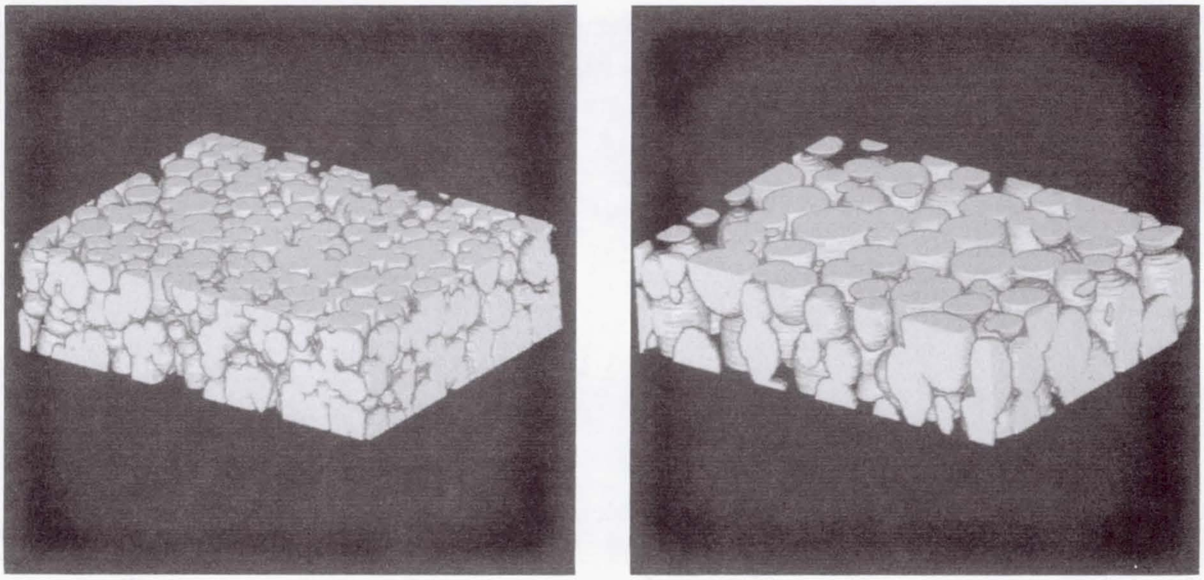

Figure 2:Surface rendered 3D microstructure of W-grains in 83 wt.% W-Ni-Fe alloy liquid phase sintered in microgravity for (i) 1 min (ii) 120 min

nodes. The generation of large three-dimensional microstructural volumes via our montage serial sectioning technique enables us to quantitatively characterize the effect of gravity on the evolution of microstructure, microstructural connectivity, and spatial arrangement of grains in these liquid phase sintered microstructures. Note that the montage serial sectioning and image analysis procedures developed in this research program are quite general and they are useful for quantitative characterization of any three-dimensional microstructure.

Sterio [6,7] has developed an unbiased procedure for estimation of number density of grains (or any microstructural feature) from simple counting measurements on set of pairs of serial sections called disector. The technique involves observations on a pair of planes (serial sections) separated by a small distance, and it involves counting features present in one plane that are not present in the second plane and vice-versa. We have combined this unbiased stereological counting procedure with montage serial sectioning and digital image analysis to evolve a very efficient and practical techniques for unbiased estimation of number density of microstructural features in three-dimensional space. This technique is applied for estimation of number density of tungsten grains and necks between tungsten grains in the liquid phase sintered microstructures. A ratio of the number density of necks and the number density of grains gives one quantitative measure of the extent of connectivity of grains in three-dimensional microstructure.

Gundersen and Jensen [8] have developed a stereological method for estimation of volume weighted average volume of grains (or particles) of any arbitrary sizes and shapes from measurements of point-sampled intercepts. We have developed image analysis procedure to perform these measurements automatically so that statistically reliable estimate of volume weighted average grain volume can be obtained from large number of measurements performed by using digital image processing. The volume weighted average volume is useful for unbiased and assumption-free estimation of the variance of the distribution of the grain volumes in three-dimensional microstructure.

RESULTS AND DISCUSSION

Table-I gives data on unbiased and assumption-free estimates of average grain volume of tungsten grains in three-dimensional microstructure of specimens of 83wt% W-Ni-Fe alloy liquid phase sintered in normal gravity and microgravity environments at 1500° C. *Note that in all the specimens, all the measurements were performed in the region 1.5 mm to 3 mm from the specimen bottom.*

Table-I

Sintering time	Normal Gravity	Microgravity
1 minute	7.6×10^3 $(\mu m)^3$	4.6×10^3 $(\mu m)^3$
120 minutes	42×10^3 $(\mu m)^3$	25×10^3 $(\mu m)^3$

As expected, the average grain volume increases significantly with time. Further, at a given sintering time, microgravity specimen has smaller average grain volume than the specimen liquid phase sintered in normal gravity. Note that all the processing parameters for microgravity and normal gravity specimens were exactly the same [9]. The data clearly show that gravity affects the kinetics of the liquid phase sintering (LPS) process. Such observations have been made in earlier studies based on two-dimensional microstructural data [9]. However, these are the first unbiased and assumption-free three-dimensional measurements that demonstrate effect of gravity on the kinetics of LPS process. Table-II gives data on the variance [$\sigma^2(V)$] and covariance [$\sigma(V)$/(mean grain volume)] of the three-dimensional grain volume distribution of tungsten grains in LPS microstructures 83wt%W-Ni-Fe alloy sintered in normal gravity and microgravity environments at 1500° C. It is interesting to observe that, for the specimens sintered for one minute, the variance (and covariance) of grain volume distribution is much smaller for the specimen processed in microgravity: the microgravity grain volume distribution is significantly narrower than that corresponding specimen processed in normal gravity.

Table-II

Sintering time	Normal Gravity		Microgravity	
	Variance	Covariance	Variance	Covariance
1 minute	$13.4 \text{X} 10^6\ (\mu m)^6$	0.23	$1.2 \text{X} 10^6\ (\mu m)^6$	0.06
120 minutes	$608 \text{X} 10^6\ (\mu m)^6$	0.35	$265 \text{X} 10^6\ (\mu m)^6$	0.40

It is interesting to observe that the covariance of the grain volume distribution of the specimens processed in the normal gravity does not change significantly with time, whereas there is a significant increase in the covariance of the grain volume distribution of the specimens processed in microgravity. Therefore, in the normal gravity, the normalized grain volume distribution appears to have reached a time invariant form, whereas microgravity specimens do not appear to have reached a time invariant normalized grain volume distribution. This shows that the <u>path</u> of evolution of grain volume distribution is different in normal gravity and microgravity. To the best of our knowledge, this is the first set of data that reveal the effect of gravity on <u>distribution</u> of grain volumes during microstructural evolution. Table-III gives the data on the number density of grains N_V, number density of necks between grains, N_C, and number of necks per grain C for the same set of specimens.

Table-III

Sintering time	Normal Gravity			Microgravity		
	N_V	N_C	C	N_V	N_C	C
1minute	$9 \text{X} 10^{-5}\ (\mu m)^{-3}$	$15 \text{X} 10^{-5}\ (\mu m)^{-3}$	1.7	$12 \text{X} 10^{-5}\ (\mu m)^{-3}$	$17 \text{X} 10^{-5}\ (\mu m)^{-3}$	1.4
120 minute	$1.8 \text{X} 10^{-5}\ (\mu m)^{-3}$	$3.6 \text{X} 10^{-5}\ (\mu m)^{-3}$	2.0	$2.4 \text{X} 10^{-5}\ (\mu m)^{-3}$	$3.5 \text{X} 10^{-5}\ (\mu m)^{-3}$	1.5

Observe that the number density of grains is somewhat higher in the normal gravity specimens as compared to the corresponding microgravity specimens, and there is a marginal increase in this ratio with time. The number of necks per grain is between 1.5 to 2.0 with microgravity values somewhat smaller than the values for corresponding normal gravity specimens. The low values of the number of necks per grain suggests a connected grain structure consisting of linear chains of grains that have branches and nodes, which is in agreement with the visual observations on the reconstructed three-dimensional microstructures shown in Figures-2 and 3.

SUMMARY AND CONCLUSIONS

(1) Serial sectioning and image processing techniques are established to recreate **large volume high-resolution** three-dimensional microstructure of tungsten heavy alloys.

(2) Combination of serial sections, reconstructed three-dimensional microstructure and stereological methods permit **unbiased and assumption-free** estimation of following parameters:

i. Average volume of W grains

ii. Variance of grain volume distribution

iii. Number density of necks and grains

(3) The variance of grain volume distribution is smaller in micro-gravity processed specimens, which implies a narrower grain volume distribution.

(4) There is a significant difference in the evolution of grain volume distribution in the specimens processed in normal gravity and micro-gravity

(5) The data reveal that kinetics of LPS process are slower in micro-gravity.

(6) The 3D microstructural reconstruction and connectivity data suggest that these LPS microstructures consist of linear chains of connected grains having branches and nodes.

REFERENCES

[1] B.D. Ripley, **J. Royal Stat. Soc.**, Vol. 39, PP. 212- 222, 1977

[2] P. Louis and A.M. Gokhale: "Computer Simulation of Spatial Arrangement and Connectivity of Particles in Three- Dimensional Microstructure: Application to Model Electrical Conductivity of Polymer Matrix Composite", **Acta Materiallia**, Vol.44, PP. 1519-1528, 1996.

[3] S. Yang, A. Tewari, and A.M. Gokhale: "Modelling of Non-Uniform Spatial Arrangement of Fibers in a Ceramic Matrix Composite", **Acta Materiallia**, Vol.45, PP. 3059-3069, 1997.

[4] A.M. Gokhale: Annual Progress Report for NASA project NAG-1245, April 1997 and April 1998.

[5] R.T. DeHoff and F.N. Rhines: **Quantitative Microscopy**, McGraw Hill, New York, 1968.

[6] D.C. Sterio: "Unbiased Estimation of Number and Size of Arbitrary Particles Using Disector", **Journal of Microscopy**, Vol.134, PP. 127-136, 1984.

[7] L.M. Cruz-Orive and E.R. Wiebel: "Recent Stereological Methods for Cell Biology", **American Journal of Physiology**, Vol.258L, PP. L148-L56, 1990.

[8] H.J.G. Gundersen and E.B. Jensen: "Stereological Estimation of Volume Weighted Mean Volume of Arbitrary Particles", **Journal of Microscopy**, Vol.138, PP. 127-142, 1985.

[9] R.M. German, Y. Liu, and A. Griffo: "Gravitational effects on Grain Coarsening During Liquid Phase Sintering", **Metall. and Mater. Trans.-A**, Vol. 28A, PP. 215-221, 1997.

Influence of Solutocapillary Convection on Macrovoid Defect Formation in Polymeric Membranes

Sanjay Konagurthu, Matthew R. Pekny, Paul Todd, Alan R. Greenberg*, and William B. Krantz
Departments of Chemical and Mechanical* Engineering
University of Colorado, Boulder, CO 80309-0424

1 Introduction

The majority of polymeric membranes can be formed via a phase separation/inversion process by which a polymer solution (in which the solvent is the continuous phase) inverts into a swollen three-dimensional macromolecular network or gel (where the polymer is the continuous phase). Polymeric membranes, formed by a phase-inversion process in a thin-film solution cast on a smooth surface, are rich in structure which strongly influences their selective permeation properties. Certain combinations of properties cannot be achieved owing to the formation of oversized pores called "macrovoids" (MVs). The presence of MV pores in large numbers can result in compaction and/or collapse of polymeric membranes and hence in a reduction of flux in high pressure applications such as reverse osmosis. Therefore, it is desirable to control the final membrane morphology by optimizing the casting conditions. In order to avoid MV formation, a compromise is made whereby thicker skin layers are tolerated than would be desired to obtain the maximum permeation rates through the membrane (Sourirajan and Matsuura, 1984). If more could be learned about the nature and causes of MV growth, it might be possible to obtain very thin permselective skin layers while avoiding MV formation.

The dry-cast process is the focus of the research. The dry-cast process for polymeric membrane formation involves dissolving the polymer in an appropriate volatile solvent containing a small amount of nonsolvent to form a single-phase solution. Subsequent evaporation of the solvent causes a phase separation to occur at a sufficiently low solvent concentration. The resulting nonsolvent-rich dispersed phase forms the pores, whereas the polymer-rich phase forms the matrix structure of the membrane. Thus, in the cellulose acetate (CA)/acetone/water system, acetone evaporates, CA becomes the continuous phase, and water forms the pores. There are two contrasting hypotheses that have been advanced to explain the growth of MV pore structures observed in polymeric membranes formed by the wet- or the dry-cast processes. One of these hypotheses is based on a diffusive growth mechanism which is totally independent of body forces such as gravity (Reuvers, 1987). According to this hypothesis, macrovoids grow by the pure molecular diffusion of nonsolvent and solvent from the surrounding casting solution. Since only diffusion and no force balance is implicit, MV growth by this mechanism should not be influenced by any body forces such as gravity.

The alternative hypothesis is based on a solutocapillary convection force which is opposed by viscous drag and buoyancy forces(Shojaie, 1992, 1994). The rationale behind this hypothesis is as follows: The evaporation of acetone from the liquid/gas interface during the dry-casting process induces a water concentration gradient, which in turn creates a surface-tension gradient, which pulls the growing macrovoid downward into the bulk casting solution. Therefore, MV growth is facilitated by convective diffusion due to bulk flow induced by interfacial (solutal marangoni) convection, and opposed by both viscous drag and buoyancy forces since the surrounding casting solution is more dense than the growing macrovoid. Since neither surface tension nor gravity are important in the first hypothesis, varying these two parameters should allow one to distinguish which (if either) of these hypotheses is correct. Thus, four objectives are being pursued in this research:

1.1 To measure the number and volume of macrovoids formed in dry-cast cellulose acetate/acetone/water membranes under varied levels of inertial acceleration using low-gravity experiments on the NASA KC-135A aircraft. If the hypothesis advanced by Shojaie *et al.* is correct, it is expected that a wider range of casting solution compositions should give rise to MV-containing membranes when cast in microgravity, and MVs formed in low-g should be larger and more numerous. Opposite effects are expected for membranes cast under increased inertial acceleration. In preliminary experiments, membranes cast by Konagurthu (1995) under low- and high-gravity conditions confirmed these expectations.

1.2 To test the role of surface-tension-gradient-driven forces by adding surfactant solutes to the casting solution, with careful attention to effects on the phase diagram.

1.3 Real-time video microscopy of simulated dry casting to monitor the simultaneous motion of the phase inversion front and the migrating, growing macrovoids using casting solutions of various compositions including surfactants.

1.4 A complete model of MV growth due to solutocapillary flow that combines experimental measurements with Marangoni convection theory. This model is being coupled with an existing theory for the solvent-casting membrane formation process developed by Shojaie (1992) to yield a completely predictive model for polymeric membrane formation via the dry-cast process. Details concerning the modeling effort are under development and are not presented in this report.

2. Experimental

2.1 Low-Gravity Membrane casting on the KC-135

2.1.1 Materials and Methods

Cellulose acetate (Eastman 398-10 with a MW of 40,000 and DS of 2.45) was dried at 110 °C under vacuum for several days. Reagent-grade acetone (Baker, Inc.) was used as received. De-ionized distilled water was used in preparing the polymer solutions which were mixed (minimum of 8 hours) with a magnetic stirrer. In order to avoid premature phase separation during preflight storage the solutions were ultracentrifuged at 10,000 rpm for one hour in a Sorvall RC-5C plus centrifuge to remove any undissolved polymer and the heavy end of the polymer molecular weight distribution. The supernatant was immersed in a bath of methyl alcohol to precipitate the remaining dissolved polymer. The polymer was collected by vacuum filtration, and the retentate was dried in a vacuum oven at 60°C for two hours. The desired casting solution compositions in the range 8-11 wt.% CA, 60-63 wt.% acetone, and 28-31 wt.% water then were made from this regenerated dried polymer; the resulting casting solutions were found to be stable against phase separation for at least one week. Initial casting-solution compositions were selected based on the model predictions of Shojaie *et al.* (1992, 1994a) and were selected insure that the phase-separation process and MV growth occur well within the limited low-g time available on a KC-135 flight (~ 25 seconds). The membrane casting was done on the specially designed and integrated MCA (Membrane Casting Apparatus) designed by Konagurthu (1995) and the same apparatus is proposed to be used for future low-gravity casting.

The morphological characterization of the membranes cast in both the ground-based and the low-g experiments was done using a Cambridge Stereoscan 250 Mk3 scanning electron microscope after gold coating with a Denton DV-502A evaporator/sputter-coating apparatus.

2.1.2 ***Results: Preliminary Low-g casting*** *experiments*

Figure 1 shows scanning electron micrographs of MVs formed during the dry-casting of polymeric membranes on the KC-135 flights.

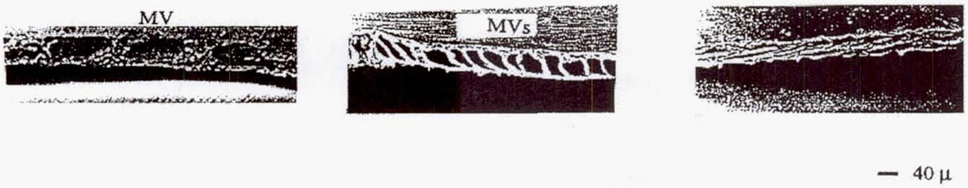

Figure 1: SEMs of macrovoids formed in polymeric membranes dry-cast from a casting solution having a thickness of 200 µm and composition of 11 wt.% CA, 60 wt.% acetone and 29 wt.% water at 23 °C. Left, cast on the ground at

1-g showing a few large MVs; center, on KC-135 aircraft at 0.01 g showing unique morphology consisting mostly of MVs; right, on KC-135 aircraft at 2-g showing no detectable MVs.

These preliminary results are encouraging, since they are consistent with, but do not yet prove, the solutocapillary hypothesis of macrovoid formation; namely, more macrovoid formation occurred in low gravity, and macrovoids could not be seen after casting in 2-g experiments.

2.2 Effect of surfactant additives

2.2.1 Theory

An independent confirmation of the solutocapillary hypothesis could be achieved through the casting of membranes on the ground (and in low-g and increased-g) in the presence and absence of trace amounts of surfactant solutes that drastically reduce the total interfacial tension and hence the interfacial tension gradient -- the driving force for solutocapillary flow. Berg and Acrivos (1965) showed that the addition of a surface active agent (surfactant) can stabilize fluid/fluid interfaces against Marangoni convection. This stabilizing effect is attributable primarily to the effects of surface elasticity. The latter arises owing to the following mechanism. Solutocapillary or marangoni forces will cause the free body to move in the direction opposite to the surface tension gradient (downward from the planar liquid/gas interface). If a surfactant is added to the casting solution, it will adsorb at the interface between the growing macrovoid pore and the surrounding polymer rich continuous phase. The viscous drag owing to the downward motion of the self-propelled macrovoid pore will cause the adsorbed surfactant to accumulate preferentially at the upper or trailing end of the macrovoid. Since the reduction in surface tension is proportional to the surfactant concentration, its accumulation at the rear of the macrovoid will cause a reduction in the surface tension gradient and thereby will reduce the Marangoni driving force. This then constitutes the stabilizing mechanism known as surface elasticity.

2.2.2 Materials and Methods

Cellulose acetate (CA) used in this study was the same grade employed for the microgravity experiments. A total of seven surfactants were used to perform the ground-based membrane casting experiments. Among them were Triton X-100 (Polyoxyethylene iso-octyl phenyl ether) obtained from J.T. Baker Co., Span-80 (sorbitan monooleate) obtained from Fisher scientific, and a range of 3M Fluorad fluorosurfactants: FC129 (anionic), FC-170C (nonionic with hydroxyl), FC-171 (nonionic without hydroxyl), FC-135 (cationic) and FC-430 (polymeric nonionic). The surfactants were added at levels of 10 ppm (below the CMC), 100 ppm, and 300 ppm to nonsolvent (water) which in turn was used to make up the casting solutions at concentrations which resulted in macrovoids.

2.2.3 Results: Effect of surfactants on membrane morphology

Surfactants that reduce the interfacial tension gradient between the growing MV and the surrounding casting solution were identified, and were shown to decrease the number and size of MVs, suggesting again that the solutocapillary hypothesis is correct. If the diffusion hypothesis were correct, the addition of surfactants should not have had a significant impact on macrovoid formation. Membranes were cast using casting solutions at the concentrations of surfactants specified above. The most promising results were obtained with the nonionic surfactants viz. Triton X-100, Span-80, and the FC-170C. This is to be expected since the nonionic surfactants in general have little or no interaction with the polymer, whereas the other surfactants employed in this study do. Figure 2 summarizes the results in a bar graph which plots macrovoid linear density (MVs/mm) as a function of the surfactant employed.
The macrovoids observed were fewer in number, and in general, smaller in size along the longitudinal axis. Figure 3a) shows a typical cross-section of a membrane cast on the ground with Span-80 used as a surfactant. As can be seen, the macrovoids are greatly diminished in size and they are more oblate in shape than tear-drop shaped, implying that interfacial properties were affected as opposed to the control – figure 3b) (without surfactant).

The anionic and the cationic surfactants did not influence the macrovoid phenomena to a large extent. This is probably because of the nature of the surfactant chemistry and interactions with the polymer/solvent mixtures. We propose to employ the non-ionic surfactants as they had the most effect on membrane morphology in general, and mitigated macrovoid occurrence in particular. These are the surfactants which we are planning to use for the low-gravity experimentation on board the KC-135.

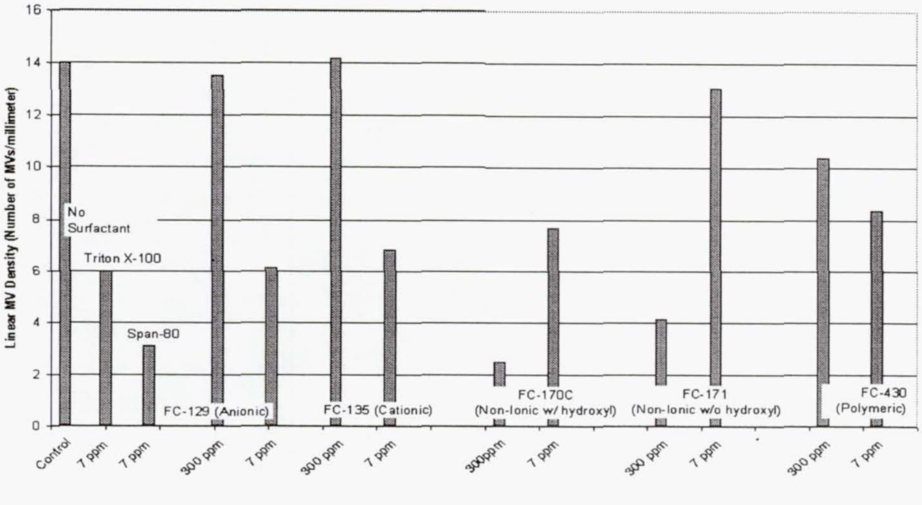

Figure 2: Linear macrovoid density(MVs/mm) as a function of surfactant type and composition

Figure 3. a) SEM of a membrane cast with Span-80 as surfactant, and b) without surfactant (control)

2.3 Video microscopy of macrovoid growth in real-time

To the best of our knowledge, real-time monitoring of macrovoid growth in dry-cast polymeric membranes has never been attempted before. Nerad et al (1986) reported video microscopy studies of macrovoid growth under wet-cast conditions. A drop of the casting solution was confined between two glass microscope cover slips; contact with the nonsolvent was facilitated by capillary wicking of water into the closely spaced microscope cover slips; the initiation and growth of macrovoids then could be followed using video microscopy. This simple experimental design provides considerable information on the macrovoid growth process. The same approach was utilized for the video-microscopy experiments in the dry-cast process as outlined below.

2.3.1 Materials and Experimental set-up

Figure 4 shows the schematic of the videomicroscopy approach employed for the real-time monitoring of macrovoid growth for the dry-cast process. A small amount of casting solution is injected between two microscope cover slips as shown in the figure. A Nikon EFD-3 optical microscope is mounted such that it is directly above the casting solution/gas interface and is connected to a CCD camera (JVC-TK 1270) which captures the images to be stored either on a video tape or a computer with NIH imaging capability so that the images can be analysed for eliciting the relevant information. The casting solutions used were the same composition that were used for generating macrovoids as before. We also employed this technique to monitor macrovoid growth when surfactants were added to the system. We used a nonionic surfactant (FC-129C) which had given us the most promising results in mitigating macrovoids as outlined in the earlier section.

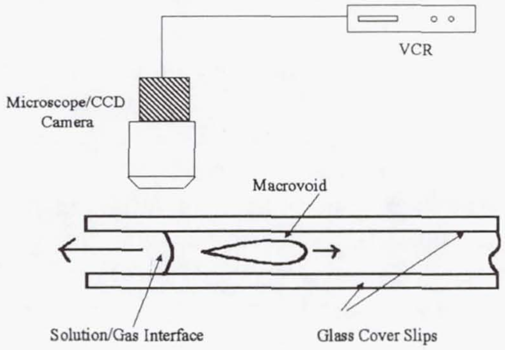

Figure 4. Schematic of the video microscopy set-up for monitoring macrovoid growth

2.3.2 Results: Video Microscopy

A full factorial matrix was designed for the video microscopy experiments in which we systematically varied the mass-transfer coefficient by varying the diffusion-path length, for different compositions with and without surfactants. The compositions we chose were those that resulted in macrovoids via regular casting. Figure 5 shows time-lapse video micrographs at various times after injection of the casting solution between the cover slips. These macrovoids were observed for higher mass transfer rates which is consistent with the solutocapillary hypothesis that higher water concentration gradients (which are a result of high solvent mass-transfer) are required for macrovoid growth. The concentration employed was 30 wt.% water, 60 wt.% acetone, and 10 wt. % CA. The results are summarized below:

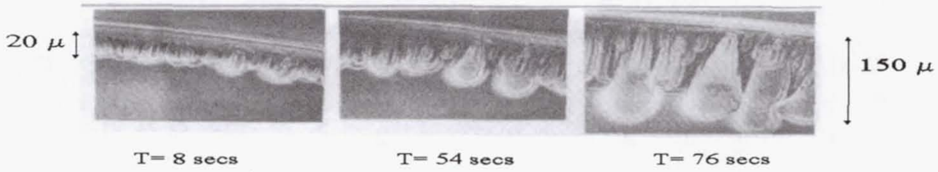

Figure 5. Time lapse images of MVs obtained via video microscopy

1. Only the higher mass-transfer coefficient resulted in macrovoids.

2. The macrovoids grow until the demixing/gelation front overtakes them and arrests their growth in time and space.
3. The macrovoids are unskinned as opposed to wet-casting where they are skinned. This was confirmed by Paulsen et al. (1994) in their work on wet-cast CA membranes.
4. The addition of trace amounts of surfactant resulted in dampening out the macrovoids.
5. These are the first documented studies in which macrovoid growth was observed in real-time for dry-cast CA membranes. These are also the first known studies in which the three-dimensional demixing front was observed in real-time for dry-cast CA membranes.

3 Conclusions and Discussion

Based on the work done so far, body forces do seem to play a role on macrovoid growth in dry-cast CA membranes. Also, surface tension gradients appear to be responsible for macrovoid growth in these membranes as seen in the surfactant experiments. We propose to combine the effect of varying-g along with the surfactant addition in the upcoming KC-135 flight in October, 1998 to observe the relative effects of body forces vis-à-vis surface tension gradients. This will provide insight into the dominating factor for macrovoid growth. The real-time video microscopy of simulated dry-casting reveals the simultaneous motion of the phase inversion front and the migrating, growing macrovoids using casting solutions of various compositions including surfactants. The MV growth patterns definitely suggest a convective rather than a diffusive process. These experiments are critical for the proposed comprehensive model for macrovoid growth due to solutocapillary flow that combines the experimental measurements with the marangoni convection theory.

4. References

1. Konagurthu, S., Krantz, W. B., and Todd, P., "Use of Low Gravity to Test Alternative Hypotheses for Macrovoid Growth in Polymeric Membranes" , Proceedings of Euromembrane, Vol. 1, 256-261, 1995.
2. Nerad, B. A., K. J. Gleason and W. B. Krantz, in Thin Liquid Film Phenomena, AIChE Symposium Series, 82 (252), 167-178 (1986).
3. Paulsen, F.G., S.S. Shojaie, and W.B. Krantz, J. Mem. Sci., 91, 265-282 (1994)
4. Reuvers, A. J., Diffusion Induced Demixing Processes in Ternary Polymeric Systems, Ph. D Dissertation, Twente University of Technology,Enschede, The Netherlands (1987).
5. Shojaie, S. S., Polymeric Dense Films and Membranes via the Dry-Cast Phase-Inversion Process: Modeling, Casting and Morphological Studies, PhD Dissertation, University of Colorado, Boulder (1992).
6. Shojaie, S. S., W. B. Krantz, and A. R. Greenberg, J. Mat. Proc. & Mfg. Sci., 1, 181-194 (1992).
7. Shojaie, S. S., W. B. Krantz, and A. R. Greenberg, J. Mem. Sci. 94, 255-280 (1994a).
8. Shojaie, S. S., W. B. Krantz, and A. R. Greenberg, J. Mem.Sci. 94, 281-298 (1994b).
9. Sourirajan, S. and T. Matsuura, Reverse Osmosis and Ultrafiltration, Division of Chemistry, National Research Council of Canada, Ottawa (1984).

UTILIZING CONTROLLED VIBRATIONS IN A MICROGRAVITY ENVIRONMENT TO UNDERSTAND AND PROMOTE MICROSTRUCTURAL HOMOGENEITY DURING FLOATING-ZONE CRYSTAL GROWTH

Richard N. Grugel
Universities Space Research Association
c/o Marshall space Flight Center
MS - ES75
Huntsville, AL 35812

telephone: (256) 544-9165
fax: (256) 544-8762
e-mail: richard.grugel@msfc.nasa.gov

ABSTRACT

It has been demonstrated in floating-zone configurations utilizing silicone oil and nitrate salts that mechanically induced vibration effectively minimizes detrimental, gravity independent, thermocapillary flow. The processing parameters leading to crystal improvement and aspects of the on-going modeling effort are discussed. Plans for applying the crystal growth technique to commercially relevant materials, e.g., silicon, as well as the value of processing in a microgravity environment are presented.

JUSTIFICATION FOR MICROGRAVITY RESEARCH

Gravity driven flow which occurs during float-zone processing is minimized in a microgravity environment and thus permits thermocapillary flow to be singularly investigated. Here, utilizing incremented and calibrated vibration, the consequence of flow velocities on microstructure can be controlled and systematically investigated, not just acknowledged. The microgravity environment will minimize unit-gravity induced biases such as static shape distortion and buoyancy flow. Here then is an opportunity to evaluate crystal growth and homogeneity in association with a stable and dimensionally optimized floating-zone.

BACKGROUND

The floating-zone technique for crystal growth of semiconductor materials has proven invaluable to the semiconductor industry. Unfortunately, significant convective flow in the liquid, both natural and induced is inherent to float-zone processing (Muhbauer *et al.*, 1983), both of which degrade crystal quality. Convection phenomena common to all floating-zone arrangements and relevant here are: A) surface tension induced flow (Marangoni or thermocapillary) and B) gravity induced flow (buoyancy). It should also be appreciated that flow induced by density differences can be minimized in a microgravity environment, whereas thermocapillary convection is *independent* of gravity level.

Many experimental and theoretical investigations have been conducted with the intent of understanding the influence of thermocapillary (TC) convection on crystal uniformity (e.g., Eyer *et al*, 1984; Eyer *et al.*, 1985; Cröll *et al.*, 1987). Schwabe *et al.* (1978, 1990) reported temperature oscillations in a $NaNO_3$ floating zone which was induced by surface flow and, based on a sounding-rocket experiment, also noted that oscillatory TC convection occurs in microgravity (Schwabe *et al.*, 1982). Jurisch and Loser (1990) and Jurisch (1990) showed striations of W in Mo single crystals which were attributed to oscillatory thermocapillary convection. A model (Young and Chait, 1990) where a floating-zone is simulated in a thin sheet in the absence of gravity revealed that convection and the presence of curved solid/liquid interfaces promoted lateral solute segregation; it was further suggested that a flat interface does not necessarily ensure uniform dopant distribution.

EXPERIMENTAL ASPECTS

Some studies toward understanding the effect of vibration on float-zone processing have been conducted (Anilkumar *et al.*, 1993; Grugel *et al.*, 1994; Shen *et al.*, 1996). A floating half-zone was simulated (Anilkumar *et al.*, 1993), Figure 1, by placing silicone oil between two vertical, 6.4mm diameter, aluminum rods which were separated by 2.5mm. Thermocapillary flow was initiated by imposing a temperature gradient (~20Kcm^{-1}) on the system via a resistance heater on the upper rod. As seen in Figure 1 top, this flow can be visualized by the addition of ~50μm diameter tracer particles which are illuminated by a He-Ne (10mW) laser sheet 0.5mm thick. In conjunction with the bottom rod is a vibrator that operates at a frequency of 70 Hertz and oscillation amplitude of ~100μm. The induced surface streaming flow, due to end-wall vibration of the float-zone, counteracts the thermocapillary flow which results in a balance, Figure 1 center. By increasing the vibration amplitude, the flow can be reversed (Figure 1 bottom).

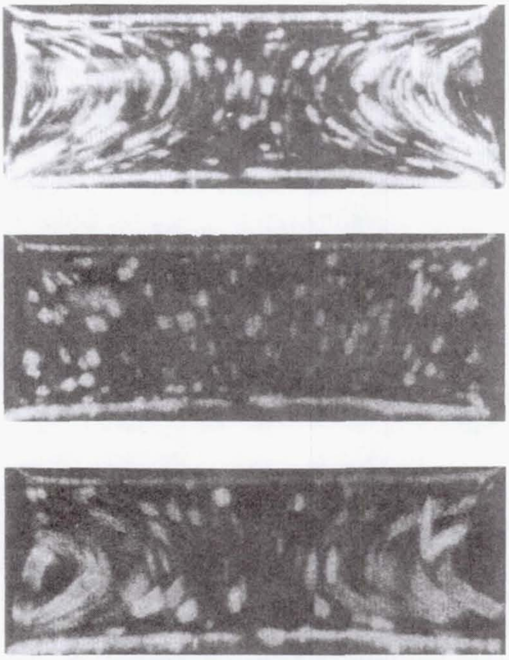

Fig. 1. Photographs (1/2 s exposures) of particle trajectories in the central section of a model half-zone of silicone oil (20cS) showing: (top) thermocapillary convection resulting from heating at the top, (center) balancing of the flow field through vibration of the bottom end-wall, and (bottom) reversal of the flow through imposition of higher vibration amplitude.

Using a fine (0.1mm dia.) k-type thermocouple it was also found that the radial temperature gradients smoothed considerably, thus suggesting a means to control thermocapillary flow and thereby improve crystal quality.

This innovative approach was expanded to investigate its effect in a traveling floating-zone of a model compound, sodium nitrate ($NaNO_3$) (Shen *et al.*, 1992). The choice of $NaNO_3$ has many advantages; when liquid allows direct observation and recording of flow patterns can be made, it has been successfully used in previous studies, and some of the thermophysical parameters are similar to a germanium or silicon melt. A traveling ring-heater assembly was constructed and used to float-zone process 6mm diameter $NaNO_3$ rods. When vibration, at a frequency of ~1.5kHz and amplitude of ~10μm, to the liquid zone was induced through the upper $NaNO_3$ rod the corresponding interface improved, i.e., became essentially planar, and flow decreased considerably. Again, radial temperature profiles improved and it was found that increasing the frequency effectively reversed the flow.

With these results, it was sought to *demonstrate improved microstructural* homogeneity. "Alloys" of the eutectic composition $NaNO_3$ - 18wt pct $Ba(NO_3)_2$ (Grugel *et al.*, 1994) were cast into 6mm diameter rods for float-zone processing with the intent of comparing distribution of the respective phases.

When the eutectic was solidified by the float-zone method, without vibration, at a rate $\approx$ 2.6mmhr^{-1} the $Ba(NO_3)_2$ phase is flake-like and distinctly finer in the center whereas on the sample periphery it is branched and coarser. When vibration is introduced to the system the solid/liquid interface, as in pure $NaNO_3$, flattens and subsequent examination reveals a uniformly coarse microstructure as a result of a uniform temperature gradient.

DISCUSSION

The effect of controlled vibrations on damping float-zone convection and improving microstructural homogeneity has been demonstrated. Still, considerable ground-based experimental and theoretical work is necessary. Here we will concentrate on defining the role various processing parameters play in promoting microstructural uniformity during floating-zone crystal growth. In particular float-zone dimensions, aspect ratios, oscillation frequency, and amplitude will be evaluated with the intent of understanding how thermocapillary flow is negated

In addition to experiments a comprehensive theoretical framework is being developed. An initial study has been completed (Lee, C.P., et al., 1996). This pointed out that the vibration-driven flow field is a subset of a large family of changeable flow fields set-up due to the non-linear oscillations of liquid bridges; flow fields changing direction and number of loops as the forcing frequency and/or the Reynolds number is changed. This streaming is due to the net body force imposed on the bulk of the column by the vibration.

Using the experimental parameters and properties of the silicone oil to calculate the Bond and thermal Marangoni numbers it was revealed that the latter, i.e., surface tension driven flow would clearly dominate over buoyancy. The impact of vibration on viscous flow can be estimated using the pulsating Reynolds number (Gershuni and Lyubimov, 1998). Finally the interaction between surface tension and imposed vibration can be characterized by the Weber number. These estimations of non-dimensional numbers are preliminary in nature; they are, however, very useful to ensure that the numerical model indeed represents the experimentally observed phenomena.

Transient numerical model was implemented using a finite element code (FIDAP, 1993). The typical one vortex structure of the flow with dominant thermocapillary convection (left side of the zone) is represented on Figure 2 and can be compared to Figure 1 (top). Dominant vibrational flow is shown on Figure 3. This flow has two vortices that represent wave motion initiated by moving rod. Small vortices close to the corner of computational domain on Figure 3 can be either secondary wave motion or flow generated by Schlichting mechanism (Gershuni and Lyubimov, 1998). Finally, Figure 4 pattern of reverse flow is presented, e.g., Figure 1 (bottom). It appears that this flow structure occurs within narrow parameter range.

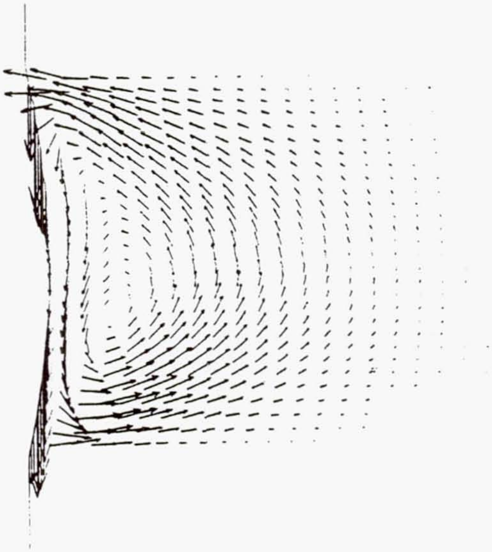

Fig. 3. Flow due solely to thermocapillary convection.

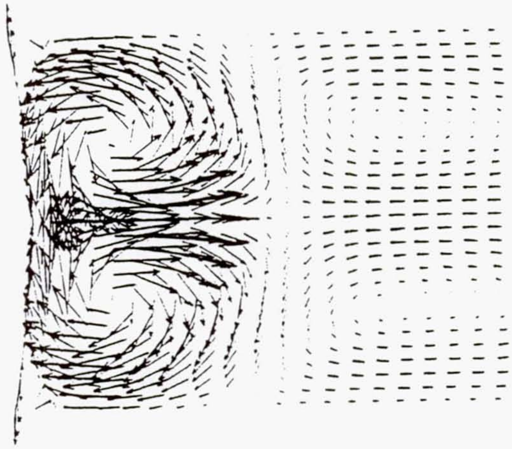

Fig. 4. Flow due solely to vibration at a moment when the rod movement is about to change direction.

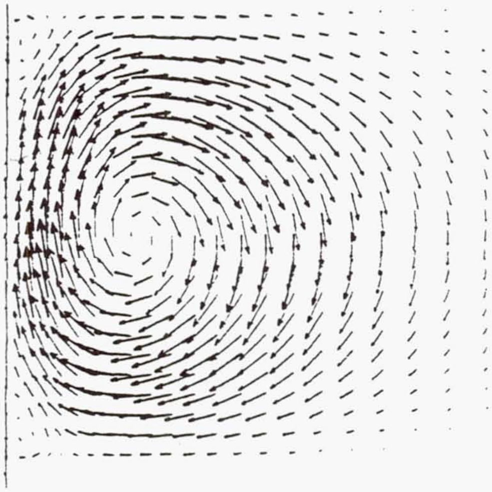

Fig. 5. Flow reversal due to interactions of thermocapillary convection and induced vibration.

Further investigation is necessary to accurately determine this range of parameters. The numerical data are in qualitative agreement with experimental findings; additional effort is required to obtain quantitative agreement.

Microgravity Extension

Gravity driven flow which occurs during float-zone processing is minimized in a microgravity environment and thus permits thermocapillary flow to be singularly investigated. Here, utilizing incremented and calibrated vibration, the consequence of flow velocities on microstructure can be controlled and systematically investigated, not just acknowledged. The microgravity environment will minimize unit-gravity induced biases such as static shape distortion and buoyancy flow; furthermore, sedimentation of tracer particles will be minimized. Here then is an opportunity to evaluate crystal growth and homogeneity in association with a stable and dimensionally optimized floating-zone.

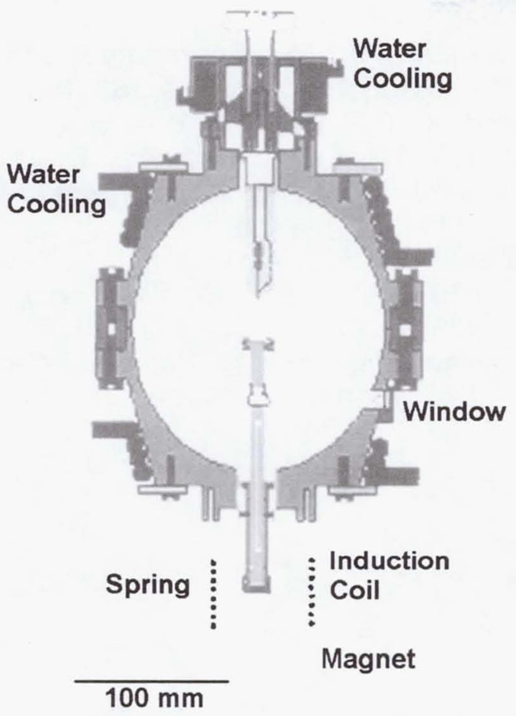

Fig. 5. Schematic of the monoellipsoid furnace (ELLI) with ampoule for float-zone experiments in conjunction with vibration.

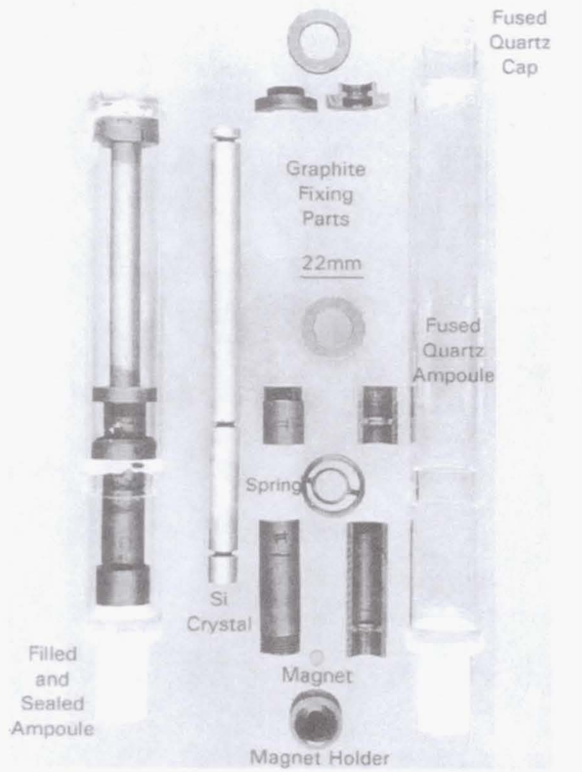

Fig. 6. Filled and sealed ampoule capable of inducing vibration to the liquid zone (left), and the individual components.

Investigating Si and Ge-based materials is an advantage in that thermocapillary convection dominates and promotes microsegregation even in a microgravity environment. Growth of the silicon and/or germanium-based semiconductors can be conducted in the Paraboloid-Ellipsoid Mirror Furnace (Elli) which was developed for growing crystals in space and used during the D2 mission, Figure 5. Figure 6 is a photograph of the components that will induce vibration to the growing crystal.

ACKNOWLEDGMENTS

The author wishes to express appreciation to his co-investigators and researchers C.P. Lee, A.V. Anilkumar, T.G. Wang, X.F. Shen (Vanderbilt University, Nashville, TN), A. Cröll (Kristallographisches Institut, Freiburg i. Br., Germany), and A. Bune (USRA) Support from NASA grant NAG8-1230 is gratefully acknowledged.

REFERENCES

Anilkumar, A.V., R.N. Grugel, X.F. Shen, C.P. Lee, and T.G. Wang, *J. Appl. Physics*, **73,** 4165 (1993).

Cröll, A., W. Muller, and R. Nitsche, *Proc. 6th Symp. on Materials Sciences under Microgravity Conditions*, p. 87, ESA/ESTEC Noordwijk (1987).

Eyer, A., H. Leiste, and R. Nitsche, Proc. *5th Europ-Symp. on Materials Sciences under Microgravity*, pp. 173-181, ESA-SP222 (1984).

Eyer, A., H. Leiste, and R. Nitsche, *J. Crystal Growth*, **71**, 173 (1985).

FIDAP Theory Manual Version 7.0, Fluid Dynamics International, Inc., (1993).

Gershuni, G.Z. and D.V. Lyubimov, *Thermal Vibrational Convection*, p. 365, John Wiley & Sons (1998).

Grugel, R.N., X.F. Shen, A.V. Anilkumar, and T.G. Wang, *Journal of Crystal Growth*, **142,** 209 (1994).

Grugel, R.N., Fay Hua, and T.G. Wang, *J. Materials Science Letters*, **13**, 1419 (1994).

Jurish, M. and W. Loser, *J. Crystal Growth*, **102,** 214 (1990).

Jurish, M.: *J. Crystal Growth*, **102,** 223 (1990).

Lee, C.P., A.V. Anilkumar, and T.G. Wang, *Phys. Fluids*, **8**, 12 (1996).

Muhbauer, A., W. Erdmann, and W. Keller, *J. Cryst. Growth*, **64,** 529 (1983).

Schwabe, D., A. Scharmann, F. Preisser, and R. Oeder, *J. Crystal Growth*, **43** 305 (1978).

Schwabe, D., R. Velten, and A. Scharmann, *J. Crystal Growth*, **99,** 1258 (1990).

Schwabe, D., A. Scharmann, and F. Preisser, *Acta Astron.*, **9,** 183 (1982).

Shen, X., R.N. Grugel, A.V. Anilkumar, and T.G. Wang, *Microstructural Design by Solidification Processing,* pp.173-182, TMS (1992).

Shen, X.F., A.V. Anilkumar, R.N. Grugel, and T.G. Wang, *J. Crystal Growth*, **165**, 438 (1996).

Young, G.W. and A. Chait, *J. Crystal. Growth*, **106,** 445 (1990).

NOVEL DIRECTIONAL SOLIDIFICATION PROCESSING OF HYPERMONOTECTIC ALLOYS

Richard N. Grugel
Universities Space Research Association
c/o Marshall space Flight Center
MS - ES75
Huntsville, AL 35812

telephone: (256) 544-9165
fax: (256) 544-8762
e-mail: richard.grugel@msfc.nasa.gov

ABSTRACT

Gravity driven separation precludes uniform microstructural development during controlled directional solidification (DS) processing of hypermonotectic alloys. It is well established that liquid/liquid suspensions, in which the respective components are immiscible and have significant density differences, can be established and maintained by utilizing ultrasound. A historical introduction to this work is presented with the intent of establishing the basis for applying the phenomena to promote microstructural uniformity during controlled directional solidification processing of immiscible mixtures. Experimental work based on transparent organics, as well as salt systems, will be presented in view of the processing parameters.

BACKGROUND

With the intent of producing uniform composites, solidification processing of hypermonotectic alloys in a microgravity environment began with the 1973 Skylab mission and has continued since. In review, the results of later experiments are essentially no different, i.e. extremely disappointing. In microgravity, despite the favorable reduction in acceleration, gravity *independent* factors cause coalescence and massive segregation of the liquid phases. This results in a highly inhomogeneous structure. The proposed work would negate these detrimental factors by utilizing ultrasonic energy to initiate and maintain a uniform dispersion of the excess L_{II} phase. A thorough experimental and modeling effort will be coordinated with the intent of understanding and optimizing the processing parameters necessary to produce a uniformly aligned hypermonotectic composite during controlled directional solidification. If successful, this technique could be used in conjunction with a low gravity environment to give ideal processing conditions.

The binary miscibility gap system of interest is characterized by 1) a region where two distinctly different liquids are in thermodynamic equilibrium and 2) the monotectic reaction, $L_I = S_I + L_{II}$. Note that, although similar in form to the well studied eutectic, one of the reaction product phases is a liquid. Microstructural development at the solid/liquid interface for these alloys has been theoretically discussed by Chadwick[1)] and Cahn[2)] and experimentally investigated by Livingston and Cline[3)] and Grugel and Hellawell[4,5)].

Alloy compositions to the right of the monotectic reaction are termed hypermonotectic and, upon cooling, pass through the two liquid miscibility gap. Solidification of these alloys for application as, e.g., slide bearings is hampered by the inherent, usually large, density differences between the L_I and L_{II} phases. This leads to rapid separation, coalescence and, consequently, a highly inhomogeneous structure. It was envisioned that processing in a microgravity environment would eliminate the density differences and a uniform composite of aligned or finely dispersed L_{II} (eventually S_{II}) in the S_I matrix could be produced. Unfortunately, microgravity experiments still resulted in highly macrosegregated structures[6)]; ref. 10 lists many papers reporting similar results.

A number of explanations for these poor results have been posed. They include droplet coalescence by Ostwald ripening and/or thermocapillary convection and preferential wetting of the container by one of the liquid phases. These factors, which are both detrimental to microstructure *and* gravity independent, merit consideration.

Earlier experiments where hypermonotectic alloys were directionally solidified[7-9)] served to demonstrate the detrimental effects of phase separation on microstructure. While the above mentioned coarsening and wetting cannot be eliminated, they may be used to some advantage. It has been shown[10-13)] that these gravity independent effects could be accommodated through the inclusion of fibers which served to accrue and uniformly distribute the L_{II}. As the directional solidification front advances the fibers and adhering L_{II} are uniformly incorporated into the S_I + L_{II} matrix. This process, however, does necessitate fibers.

To this end it is suggested to apply an ultrasonic field to the bulk liquid which, upon cooling, will initiate and maintain a uniform dispersion of the precipitated liquid, L_{II}. The microgravity environment would then serve to eliminate density differences, i.e., settling, between the liquids. With droplet coalescence minimized, controlled directional solidification should promote a uniformly aligned, composite microstructure.

The study of acoustic waves on initiating and maintaining suspensions in two-liquid systems is well established. In 1927 Wood and Loomis[14)] reported using high-frequency sound-waves of great intensity to form emulsions. Shortly after, Richards[15)] used lower intensities of sound and was able to emulsify many liquid immiscibility systems. Mechanisms for emulsification by ultrasonic waves were further investigated in a series of papers published in the 1930's by Sollner, *et al.*[16)] and they were able, using energies of 100mA and more, to emulsify a maximum of 6g mercury in 1 liter of water. Schmid *et al.*[17)] (late 1930's) applied ultrasonics to a number of pure metal and alloy melts. Overall, upon solidification, a comparatively much finer microstructure resulted. They also produced a dispersion of lead in the immiscible aluminum-lead system that was considerably finer at the top. A number of papers reporting the results of applying ultrasonic energy to solidifying melts have since been published [e.g. 18-26]; again overall finer and more uniform microstructures resulted.

Clancy et al., realizing the need for a uniform distribution of droplets and/or particles prior to solidification processing in a microgravity environment, developed an ultrasonic mixing system for use with existing Spacelab furnace hardware[27)]. Subsequently, microstructural examination of a hypermonotectic zinc - 5 wt pct lead alloy, (microgravity environment provided by TEXUS sounding rockets) showed a better distribution of the Pb-phase with acoustics applied than without[28,29)]. In a similar microgravity experiment, Takahashi et al.[30)] solidified hypermonotectic aluminum - 30 wt pct indium alloys subjected to ultrasonic energy; again considerably better dispersions were found.

The above experiments examined metallic, miscibility gap systems from which microstructural development must be inferred after solidification is complete. This hindrance may be circumvented by using transparent materials which simulate solidification phenomena in metals and alloys, a well established technique[31)].

EXPERIMENTAL ASPECTS

With reference to the succinonitrile - glycerol phase diagram, Fig. 1, consider the following demonstration[32)].

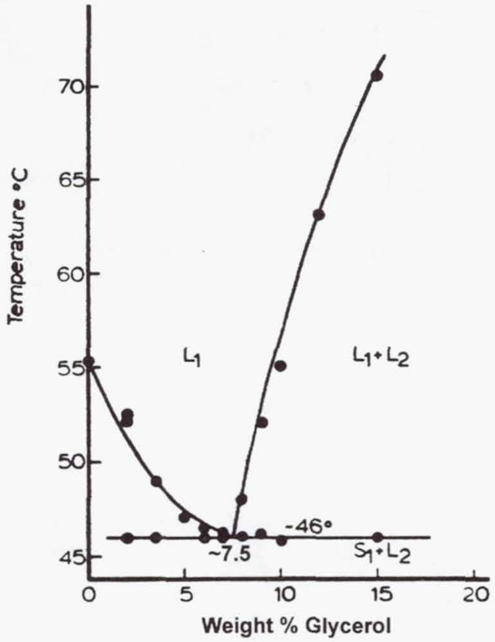

Fig. 1 Partial Succinonitrile - Glycerol phase diagram[33)].

Hypermonotectic succinonitrile - 15 wt pct glycerol "alloys" were made and placed in 12mm I.D test tubes. The samples were instrumented with a thermocouple and submerged in the water bath of a commercial ultrasonic cleaner, the initial bath temperature being ~90°C. When the bath, and sample, cooled to ~73°C precipitation of the excess L_{II} phase (glycerol) initiates. After 45 minutes, ~ 51°C, the coalesced glycerol fully occupies the sample bottom, Figure 2 - left. Subsequent solidification results in a highly segregated structure. The right side of Fig. 2 shows a similar sample which was subjected to ultrasonic energy during cooling. At ~50°C and 105 minutes, after precipitation of the L_{II} phase initiated, a uniform dispersion of the excess liquid is maintained.

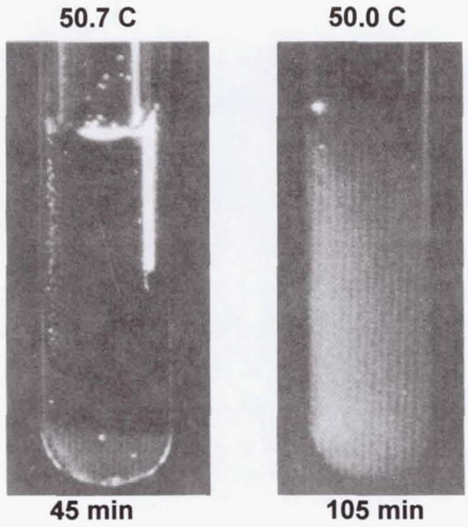

Fig. 2 Left: Settling and coalescence of L_{II} (glycerol) as the sample cools through the miscibility gap. Right: L_{II} droplets remain suspended in an ultrasonic field.

Controlled directional solidification experiments generally consider four processing parameters, i.e., growth rate (V), temperature gradient (G), composition (C_o), and gravity (*g*). Applying ultrasonics introduces many additional variables. These include frequency, amplitude, sample dimensions, heat generation, and melt-probe interactions and must be considered. For example, the effect of amplitude is demonstrated in Figure 3. Here a given amount of tin was melted in a zinc chloride - sodium chloride flux after which ultrasonic energy (20 kHz) was introduced for ~1 minute. In Figure 3a the amplitude was 64µm, in Figure 3b the amplitude was 137µm; an obviously finer droplet dispersion is observed as a consequence of the higher amplitude.

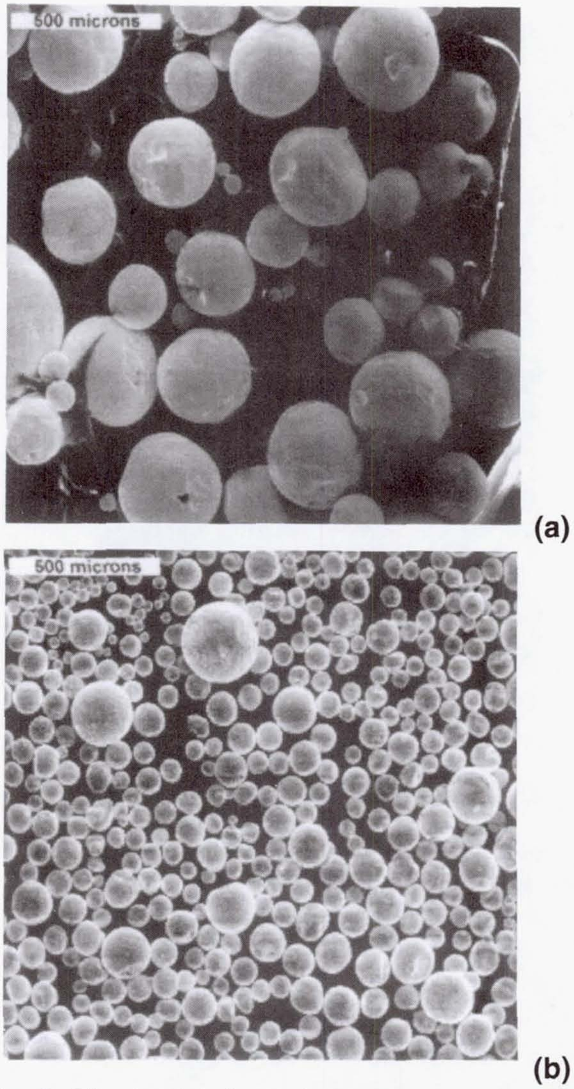

Fig. 3 Tin droplet dispersions as a consequence of applying ultrasonic (f = 20 kHz) energy with a probe amplitude of **(a)** 64μm and **(b)** 137μm for ~1 minute.

A schematic representation of the directional solidification apparatus used in this investigation is depicted in Figure 4. Here the sample and probe are fixed with the heating-cooling units translated at the desired rate. The heater consists of a resistance winding (~1cm intervals) around a quartz tube which permits direct observation and recording of events at the solid/liquid interface.

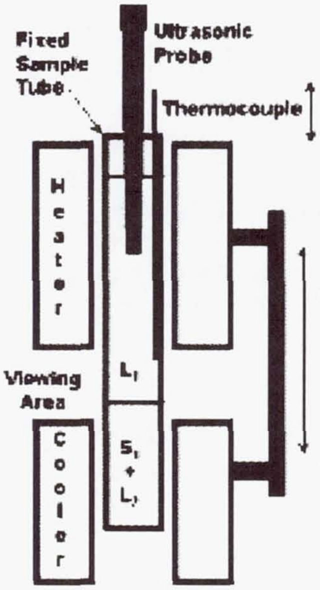

Fig. 4 Schematic representation of the directional solidification apparatus used in this investigation.

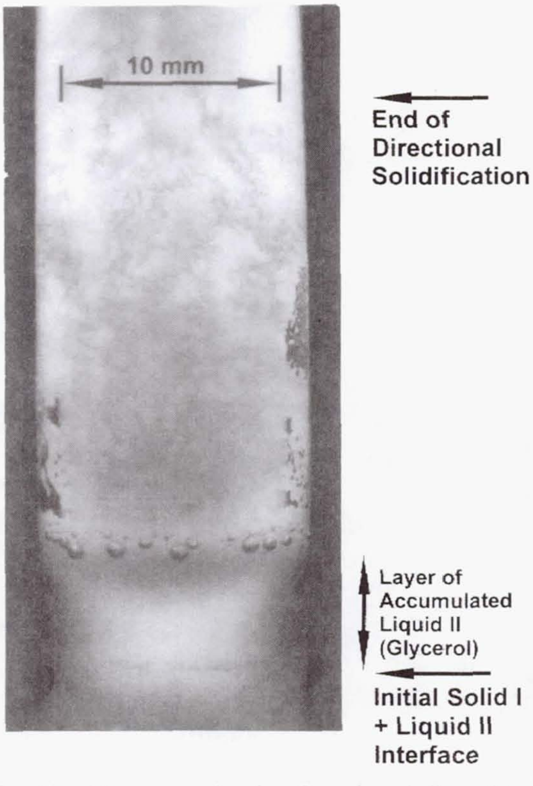

Fig. 5a Macrograph of a Succinonitrile - 15 wt pct Glycerol "alloy" directionally solidified at 5μms^{-1}. The layer of Liquid$_{II}$ (glycerol) forms during melting prior to reaching equilibrium. Note that the sample tube is 12mm OD, 10mm ID.

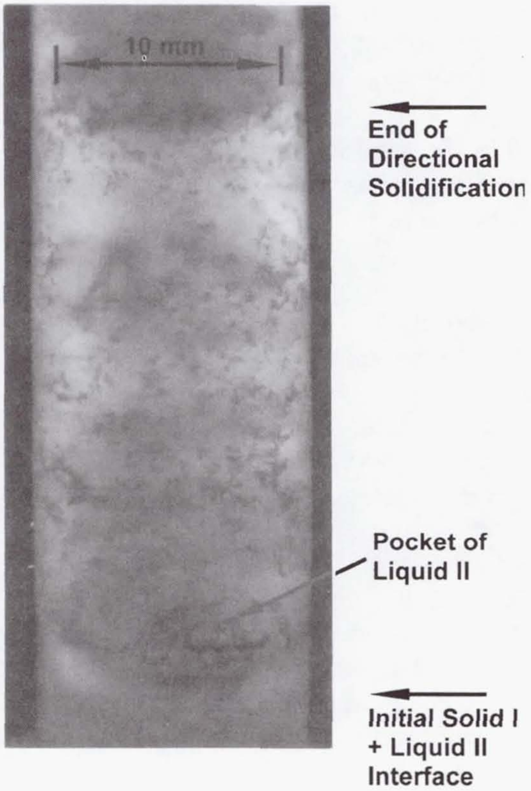

Fig. 5b Improved microstructural uniformity as a consequence of applying ultrasonic (f = 20 kHz) energy with a probe amplitude of 137μm for 0.1 second/second during controlled directional solidification.

The macrostructure of a hypermonotectic "alloy" which has been directionally solidified in the above mentioned furnace is shown in Figure 5a. Clearly visible is a layer of excess, denser, L_{II} that has accumulated at the (now) equilibrium S_I + L_{II} interface as established by the temperature gradient. From observation, the layer of glycerol initially forms once the sample is placed into the furnace. Initially, as it heats up, the mixture passes through the two liquid region prior to reaching an equilibrium L_I temperature. During this time precipitated L_{II} can sink and accumulate; if heating was instantaneous this would be minimized. Secondly, it takes time for the S_I + L_{II} interface to stabilize. As it slowly melts back and passes through the miscibility gap the denser glycerol contributes to the L_{II} layer. Conversely, the less dense succinonitrile-rich L_I develops under the L_{II} layer until a sufficient mass is developed which then releases, passes through the layer, and contributes to the upper bulk liquid. Obviously, the desired microstructural homogeneity is compromised by this process.

In contrast, Figure 5b shows an identical sample that was directionally solidified in the presence of an applied ultrasonic field. Here only a small pocket of L_{II} accumulated at the S_I + L_{II} interface. The horizontal banding is a result of manually moving the probe tip in relation to the advancing interface. It is envisioned that the L_{II} pocket can be further minimized (or eliminated) by optimizing the processing parameters. Banding will be controlled by modifying the experimental apparatus such that the probe moves in conjunction with the heating and cooling units. Further work involves scaling and applying the processing parameters to a metallic sample from which microstructural and compositional analysis will be facilitated.

SUMMARY

A review of the literature and some initial experiments have illustrated that ultrasonic energy can promote and maintain finer and more uniform dispersions during solidification processing of immiscible alloy systems. Directional solidification experiments of transparent materials demonstrated sedimentation, a consideration that is minimized by introducing ultrasonic energy. Processing in a microgravity environment will minimize sedimentation, but not coalescence, during melting and subsequent solidification; this makes a case for including ultrasonic capabilities. Furthermore, we might expect the microgravity environment to extend the volume fraction of a suspended dispersion as well as provide benchmark samples to which mathematical models and Earth-processed samples can be unequivocally compared.

ACKNOWLEDGMENTS

Appreciation is expressed to Mr. Don Lovell and Mr. Curtis Bahr for their technical assistance. Support from NASA grant NCC8-1231 is gratefully acknowledged.

REFERENCES

1. G.A. Chadwick: *Brit. J. Appl. Phys.*, **16** (1965) 1095.
2. J.W. Cahn: *Metall. Trans. A*, **10A** (1979) 119.
3. J.D. Livingston and H.E. Cline: *Trans. TMS-AIME*, **245** (1969) 351.
4. R.N. Grugel and A. Hellawell: *Metall. Trans. A*, **12A** (1982) 669.
5. R.N. Grugel and A. Hellawell: Materials Research Soc., Proc., Vol. 19, Elsevier, (1982) 417.
6. T. Carlberg and H. Fredriksson: *Metall. Trans. A*, **11A** (1980) 1665.
7. R.N. Grugel, T.A. Lograsso, and A. Hellawell: Materials Processing in the Reduced Gravity Environment of Space, Elsevier, (1982) 553.
8. S. Shah et al: *Metall. Trans. A*, **19A** (1988) 2677.
9. R.N. Grugel and Shinwoo Kim: *Adv. in Space Research*, **13** (1993) 225.
10. R.N. Grugel: *Metall. Trans. B*, **22B** (1991) 339.
11. R.N. Grugel and S. Nourbakhsh: AIAA Paper No. 92-0352, (1992).
12. R.N. Grugel and S. Nourbakhsh: 4th International Symposium, Experimental Methods for Microgravity Materials Science Research, TMS, (1992) 81.
13. R.N. Grugel: U.S. Patent No. 5,246,508, (1993).
14. R.W. Wood and A.L. Loomis: *Phil. Mag.*, **7** (1927) 417.
15. W.T. Richards: *J. Amer. Chem. Soc.*, **51** (1929) 1724.
16. K. Sollner et al.: *Kolloid-Zeit*, **60** (1932) 263; *Trans. Faraday Soc.*, **31** (1935) 835; *Ibid*, **31** (1935) 843; *Ibid*, **32** (1936) 556; *Ibid*, **32** (1935) 616.
17. G. Schmid et al.: *Zeit. Fur Elecktrochem*, **43** (1937) 869; *Zeit. fur Elecktrochem*, **45** (1939) 769; *Zeit. fur Elecktrochem*, **46** (1940) 87.
18. A.H. Freedman and J.F. Wallace: *Trans. Amer. Foundryman's Soc.*, **65** (1957) 578.
19. D.H. Lane, et al: *Trans. AIME*, **218** (1960) 985.
20. D.H. Lane, and W.A. Tiller: *Trans. AIME*, **218** (1960) 991.
21. M. Weinstein: *Trans. AIME*, **230** (1964) 321.
22. H.E. Bates and M. Weinstein: *J. Electrochem. Soc.*, **112** (1965) 693.
23. H.E. Bates and M. Weinstein: *J. Electrochem. Soc.*, **114** (1967) 259.
24. J.A. Bailey and J.R. Davila: *J. Inst. Metals*, **97** (1969) 248.
25. Y. Hayakawa, Y. Sone, K. Tatsumi, and M. Kumagawa: *Japan. J. Appl. Phys.*, **21** (1982) 1273.
26. W. Fengquan, C. Shiyu, H. Deping, W. Bingbo, and S. Guangji: *J. Materials Sci.*, **29** (1994) 3997.
27. P.F. Clancy,et al: Acta Astronautica, **7** (1980) 877.
28. P.F. Clancy, W. Heide, and D. Langbein: 4th European Symposium on Materials Science under Microgravity, ESA SP-191 (1983) 99.
29. P.F. Clancy, and W. Heide: Workshop on the Effect of Gravity on Solidification of Immiscible Alloys, ESA SP-219 (1984) 73.
30. T. Takahashi, et al: *J. Japan Inst. Light Metals*, **34** (1984) 479.
31. R.N. Grugel and R. Trivedi: Metallography: Past, Present, and Future (75th Anniversary Volume), ASTM STP 1165, (1993) 393.
32. R.N. Grugel: Unpublished research, Vanderbilt University, 1994.
33. R.N. Grugel: Ph.D. Thesis, Michigan Technological University (1983).
34. R.N. Grugel, et al: *J. Crystal Growth*, **121** (1992) 599.
35. G.M. Swallowe, J.E. Field, C.S. Rees and A. Duckworth: Acta Metall., **37** (1989) 961.

INTER-DIFFUSION IN THE PRESENCE OF FREE CONVECTION

Prabhat K. Gupta
Department of Materials Science & Engineering
The Ohio State University
2041 College Road
Columbus, OH 43210
email: gupta.3@osu.edu

NAG8-1470
(Microgravity Materials Science Conference, July 1998)

Abstract

Because of their technological importance, establishment of the precise values of interdiffusion coefficients is important in multicomponent fluid systems. Such values are not available because diffusion is influenced by free convection due to compositionally induced density variations. In this project, earth based diffusion experiments are being performed in a viscous fluid system PbO-SiO2 at temperatures between 500-1000 C. This system is chosen because it shows a large variation in density with small changes in composition and is expected to show a large free convection effect. Infinite diffusion couples at different temperatures and times are being studied with different orientations with respect to gravity. Composition fields will be measured using an Electron
Microprobe Analyzer and will be compared with the results of a complementary modeling study to extract the values of the true diffusion coefficient from the measured diffusion profiles.

Introduction:

Interdiffusion describes the evolution of compositional inhomogeneities in systems containing more than one component. Since most material systems of technological importance are not single component and since interdiffusion is the rate controlling step in most processing operations involving compositional changes (e.g., crystal growth, melting, dissolution, precipitation, and sintering), establishment of precise values of interdiffusion coefficients and of their variations with respect to composition and temperature is of much interest. While techniques for measuring interdiffusion coefficients are available, values of interdiffusion coefficients in liquids (and supercooled liquids) are available only for a few systems and that too with limited precision. One of the reasons is the influence of free convection due to *compositionally induced density variations* in interdiffusion composition profiles.

To determine the interdiffusion coefficients accurately, there are two possible approaches. One is to design experiments in which the effect of free convection is suppressed or reduced. The other is to develop a theory to correctly account for the presence of free convection in interdiffusion.

Much of the effort in the past has followed the first approach. For ground based experiments, the obvious way to reduce the influence of gravity is to have the density increase in the direction of gravity. However, this does not completely eliminate the effect of the potential energy on the composition profiles. For example, in equilibrium, the composition will not be uniform - the denser component will be segregated at the bottom. Another method makes use of capillary tubes [1] to contain the two liquids of differing compositions relying on capillary forces to counteract free convection. Frischat et al [2] have recently shown this method to be problematic due to the variation in the values of interfacial tension (between liquid and the capillary surface) with liquid composition. Further, this method does not always work in ternary or higher component systems because an initially stable system (with density increasing along the direction of gravity) may become unstable at later times by compositional induced density changes. A third method uses complex experimental set ups to simulate zero gravity conditions in ground based experiments [3].These methods, because of their inherent complexity (especially in the case of high temperature melts) are not suitable for generating experimental data on diffusion coefficients in a large number of systems. It is, therefore, desirable to follow the second approach and develop analytical schemes for taking into account the presence of free convection in simple experimental designs (like an infinite couple) which can be conveniently performed in most laboratories. This forms the motivation for this research program.

Objectives:

The objective of this research program is to provide a detailed understanding of the influence of free convection during interdiffusion. More specifically, the program aims:
a) to develop theoretical procedures for the evaluation of the interdiffusion coefficients from infinite couple experiments taking into account the presence of free convection, and b) to test the validity of these theoretical procedures by applying them to measured composition fields obtained in ground based experiments in a suitably chosen controlled-viscosity, isothermal, and isobaric binary liquid (or supercooled liquid) system and comparing the computed diffusion coefficient values with the corresponding values obtained in identical experiments in micro-gravity conditions where free convection is absent.

Relevance to Microgravity:

Free convection makes the interpretation of interdiffusion experimental results in liquid and supercooled liquid systems difficult. Temperature induced free convection can be eliminated by conducting the experiments isothermally. However, density variations as a result of compositional changes cannot be eliminated in a diffusing system. If the measurements of the diffusion coefficients have to be made in systems in which compositionally induced density variations are large, then a microgravity environment is most desirable for measurement of interdiffusion coefficients.

Review of Relevant Research:

Because of the importance of interdiffusion in the processing of materials, a large amount of effort has been invested over several decades to measure the interdiffusion coefficients in various kinds of materials, and the progress has been summarized in many excellent reviews [4,5]. Diffusion coefficients are generally determined by analyzing the measured isothermal and isobaric evolution of a step composition profile. This configuration is known as an 'infinite couple' provided the end compositions are not perturbed by diffusion. The resulting composition fields are typically measured most conveniently by an Electron Microprobe Analyzer [6]. While the experimental procedure is straight forward, the analysis of the measured composition profiles for the purpose of extracting the diffusion coefficients is not because a) the interdiffusion coefficients are composition dependent, b) there is, in general, a volume change in the system upon diffusion, and c) free convection is present in liquid systems. The first two effects have been well studied as they are also present in solid systems where much interdiffusion work has been reported. For example, procedures, extending the Matano analysis (a technique for extracting the composition dependent values of the interdiffusion coefficient from measured composition profile), are available to account for volume changes [7]. However, there does not exist a procedure to account for free convection effects which are always present in fluid systems. Much of the previous work on interdiffusion in liquids and supercooled liquids has been analyzed under the assumption of absence of free convection.

Presence of free convection in interdiffusion experiments has been recognized by several investigators [1,2,3]. Most efforts have been directed at designing experiments to reduce the presence of free convection. Hunold and Bruckner [1] used the capillary method to avoid natural convection in glass melts during interdiffusion experiments. To further reduce natural convection, glass of higher density was always placed in the lower part of the capillary. Herr and Frischat [3] have also used the capillary method to study interdiffusion in Na_2O-Rb_2O-SiO_2 melts. Up to 1000°C, no influence of convection was observed. Above 1000°C, they observed that that composition contours were no longer planar. In a later publication, Frischat and coworkers [2] point out the adverse influence of variation of the interfacial tension values between the two melts and the surface of the capillary tube (e.g., the contact angle at the interface is not 90° with respect to the tube wall causing the interface to be nonplanar).

Description of the Research Program:

The research under this program is being carried out along two parallel but intertwining paths. Fluid dynamical modeling of interdiffusion in presence of free convection constitutes one path. The goal of this part is to develop a procedure (analytic if possible and numerical if necessary) to calculate the values of the composition dependent interdiffusion coefficients from composition profiles obtained in infinite couples (with vertical and horizontal orientations) taking account of the presence of natural convection. The other path of the research program consists of experimental studies of binary interdiffusion under isothermal isobaric conditions free from fluid dynamic instabilities. Experiments will be carried out both in conditions of strong free convection and in conditions of weak free convection. These experimental results will be analyzed for interdiffusion coefficients using the procedure developed in the modeling studies. Comparison of the results under conditions of weak and strong free convection will provide a rigorous test of the developed procedure. At some time in the future, it is hoped that interdiffusion experiments will be performed in microgravity environment where compositionally induced free convection is absent. These experiments will provide the true values of the interdiffusion coefficients in the chosen system.

Fluid dynamic modeling of interdiffusion in the presence of free convection:

There are essentially four equations that govern the evolution of an isothermal binary diffusing system. The first is the continuity equation (i.e., equation for total mass balance):

$$\partial\rho/\partial t + \nabla . (\rho V) = 0 \qquad (1)$$

where ρ is the total density and V is the mass average velocity. The second is the diffusion equation (written for component A):

$$\partial\rho_A/\partial t + \nabla . (\rho_A V) = \nabla . (D \nabla\rho_A) \qquad (2)$$

where D is the interdiffusion coefficient, and ρ_A is the mass density of component A. The third is the momentum balance equation. It governs the evolution of the three components of the mass average velocity V.

$$\rho\, [\partial V/\partial t + V . (\nabla V)] = -\nabla p + \mu\nabla^2 V + \rho g \qquad (3)$$

Here p is the pressure, μ is the shear viscosity, and g is the acceleration due to gravity. The fourth equation is the equation of state for the system:

$$\rho = \rho(T, p, \rho_A)$$

The following approximation can be used for the equation of state for a condensed system:

$$\rho = \rho_0 + (\partial\rho/ \partial\rho_A)_0 (\rho_A - \rho_{A0}) + (\partial\rho/ \partial p)_0 (p - p_0) \qquad (4)$$

Since we are interested in interdiffusion in an isothermal system, the energy balance equation can be ignored. The main problem in solving these four equations for the four unknowns (ρ, ρ_A, p, and V) lies in the fact that this system of equations involves non-linear coupled partial differential equations.

The 'infinite' diffusion couple will be in the shape of a cylinder (Radius, R) and of finite length (2L) along the axis. The initial composition profile will be a step function in the axial direction (the x-direction). Vanishing of the flux will be imposed as a condition at all boundaries of the cylinder reflecting their closed nature. The velocities (tangential as well as normal components) will be taken as zero at the boundaries.

It is useful to put the governing equations in a dimensionless form. To do so, lengths are normalized by radius R. Time is made dimensionless by scaling it with R^2/D. The mass densities are scaled by the density difference, $\Delta\rho$, for the two end compositions. The velocities are scaled by U which is given by:

$$U = g\,\Delta\rho\,(R\sin\theta)^2/(\rho_0\,\nu) \qquad (5)$$

Here ν is the kinematic viscosity, θ is the orientation of the cylinder axis with respect to the vertical direction, and ρ_0 is the density of the average composition. Under these conditions, the Rayleigh number Ra (which is the product of Grashof and Schmidt numbers) is a measure of the influence of free convection in the interdiffusion process:

$$Ra = U R / D \qquad (6)$$

For horizontal orientation ($\theta = 90$) Ra is much larger than 1 for typical supercooled viscous liquids [8], indicating that the free convection is not negligible even in highly viscous liquids.

Experimental program:

To keep the experiments and the theoretical analysis simple, diffusion will be studied isothermally. This will also eliminate temperature induced free convection. In an isothermal system, free convection can still occur due to compositionally induced density changes (the effect which we investigating) and the undesired Marangoni effect (capillary induced free convection) due to the variation of surface tension with composition. This capillary induced flow can be eliminated by choosing a system where the surface tension does not vary with composition. However, this is possible only with very few systems in limited temperature and composition ranges. A better approach is to eliminate free surfaces by covering them with inert films. This can be used with any system and will be used in our experiments.

Since the main objective is to understand the role of free convection in interdiffusion, a binary system will be chosen as this is the simplest multicomponent system. Higher component systems involve the complexity of having many diffusion coefficients. It is hoped that sometime in future, after the theory is validated for the binary system, experiments will be proposed in ternary systems.

After diffusion treatment, the entire two dimensional composition field of an infinite couple will be measured by a technique such as the Electron Microprobe Analyzer. Simple liquids are not suitable for this purpose since composition profiles do not remain frozen at room temperature. On the other hand, solid systems are also not suitable for this purpose since they do not exhibit effects of free convection. Glasses, which are solid at room temperature and supercooled liquids at temperatures above their glass transition temperatures, are best candidates for our experiments.

Because of these considerations, we have chosen to use the PbO - SiO_2 system. This system offers the following advantages:

a) a large single phase liquid field at temperatures above 765°C.

b) a large variation of density with respect to change in composition [8].

c) relative ease of measurement of composition profiles using an Electron Microprobe Analyzer.

References:

1. K. Hunold and R. Bruckner, Glasstechn. Ber., 53, 207, (1980).
2. M. Braedt and G. H. Frischat, J. Am. Ceram. Soc., 67, C-54, (1984)
3. M. Meier and G. H. Frischat, Phys. and Chem. of Glasses, 34, 71, (1993)
4. J. Philibert, "Atom movements: diffusion and mass transport in solids", Les Editions de Physique, (1991).
5. P. K. Gupta and A. R. Cooper, Physica, 54, 39, (1971).
6. J. Ganguly, R. Bhattacharya, and S. Chakraborty, Am. Mineralogist, 73, 901, (1988).
7. F. J. J. van Loo, Acta Met, 18, 1107, (1970).
8. N. P. Bansal and R. H. Doremus, Handbook of Glass Properties, Academic Press, (1986).

Optical Resonances of Gold Nanoshells

R. D. Averitt, S. J. Oldenburg, S. L. Westcott, T. R. Lee*, N. J. Halas
Department of Electrical and Computer Engineering and the Center for
Nanoscale Science and Technology, Rice University, Houston, TX 77005
*Department of Chemistry, University of Houston, Houston, TX 77204

Metal nanoshells, consisting of a dielectric core with a metallic shell of nanometer thickness, are a new, composite nanoparticle whose optical resonance can be "designed in" in a controlled manner. By varying the relative dimensions of the core and shell, the optical resonance of these nanoparticles can be varied over hundreds of nanometers in wavelength, across the visible and into the infrared region of the spectrum. These nanoparticles can serve as constituents in a new class of materials that are capable of uniquely controlling radiation in the visible and infrared spectral regions. Our current research focuses on two types of nanoshells: naturally occurring gold-coated Au_2S nanoshells and gold-coated silica nanoparticles that are formed utilizing colloid reduction chemistry and self-assembly[1, 2].

Solid metallic nanoparticles are well known for their attractive optical properties: a strong optical resonance and an extremely large and fast nonlinear optical (NLO) polarizability associated with their plasmon frequency[3]. These optical properties are accounted for extremely well by classical electromagnetic theory (Mie scattering theory)[4]. Although the general Mie scattering solution for a spherical particle consisting of concentric layers has been known for decades[5], it was only recently theoretically established that a configuration consisting of a nanometer-scale metallic shell covering a submicron dielectric core should result in a particle with a plasmon-derived optical resonance tunable over large regions of the electromagnetic spectrum[6]. Figure 1 shows calculations using Mie scattering theory for a series of gold nanoshells with a shell thickness of 2 nm and a core radius that increases from 2 to 15 nm in going from a) to c). In this case the plasmon peak is shifted from ~550 nm to greater than 900 nm.

In order to construct nanoshell particles that will have their plasmon resonance shifted beyond the near infrared, a shell thickness/particle radius ratio of 10^{-2} to 10^{-4} is required. To achieve good optical quality in this regime, a high degree of sphericity of the dielectric core particles, a monodisperse distribution of dielectric core particles upon which to grow the metal nanoshell, and isotropic metal nanoshell growth onto the core particles is required. The growth and study of micron-scale spherical particles in space has a long history, dating from the Apollo program. During missions Apollo 14 and 16, the effect of reduced gravity on the electrophoresis of polystyrene latex spheres was studied. Extensive research into the reduced gravity growth of latex spheres, directed by Vanderhoff et al., flew on early Space Shuttle missions STS-003, STS-004, STS-006, STS-007, and STS-011[7]. The conclusions of this project were that highly monodisperse spherical latex particles in the micron size range could be grown with a higher degree of sphericity than was achievable on earth. Since we are exploring a similar size regime for our composite particles, it is apparent that a microgravity environment will result in higher quality particle growth, reducing deleterious effects such as sedimentation during growth. This will yield a more monodisperse distribution of nanoshells, which will in turn improve the optical quality by reducing inhomogeneous broadening of the plasmon resonance.

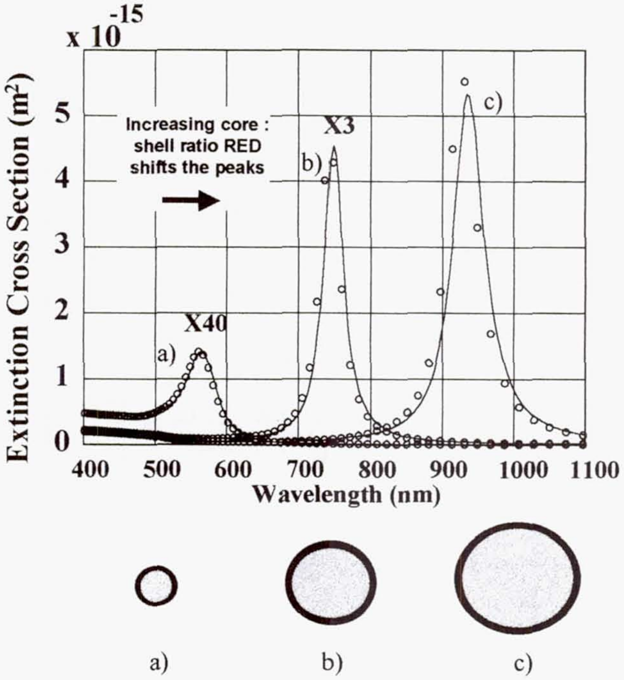

Figure 1: Mie scattering calculations of the plasmon resonance for metal nanoshells: (a) core radius = 2nm, shell thickness = 2nm; (b) core radius = 8 nm, shell thickness = 2nm; (c) core radius = 15 nm, shell thickness = 2 nm.

Gold-Coated Au_2S Nanoshells

We have recently confirmed the original theoretical predictions of Mie scattering for the nanoshell geometry by studying the growth of gold sulfide (Au_2S) nanoparticles in a series of ground-based experiments. These nanoparticles, formed via reduction of $AuCl_4^-$ with HS^- in water, are gold-terminated during growth, providing a naturally occurring metal nanoshell system. These nanoparticles typically manifest a large (200-300 nm) optical resonance red shift, followed by a sizeable blue shift, during particle growth. The solid lines in Figure 2 show a series of UV-vis spectra of the gold nanoshells during their growth. The peak at 520 nm is due to the simultaneous formation of solid gold nanoparticles. The shifting peak is associated with the gold nanoshells and the observed shifting is due to the changing core/shell ratio. The dashed lines are calculations using Mie scattering theory. At all times during the reaction, the calculations agree with experiment. This analysis has allowed us to show that these optical resonance shifts correspond to a two-stage growth model, where first the core and then the shell grow linearly as a function of time[1].

We have also studied the ultrafast electron dynamics of gold-coated Au_2S nanoshells embedded in poly-vinyl alcohol films via femtosecond pump-probe spectroscopy utilizing a cavity-dumped Ti:sapphire laser[8]. The induced change in the transmission of the gold nanoshell films studied has a lifetime of ~1.6 ps. Figure 3 (a) and (b) shows the UV-vis

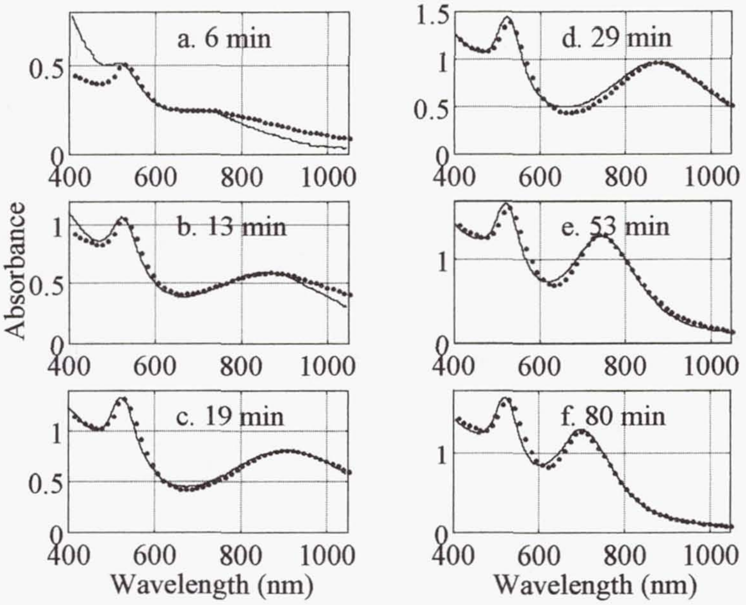

Figure 2: Uv-vis spectra of Au-coated Au_2S nanoparticles at various stages of growth. Solid line: experimental data. Dotted line: theory. Radii: (a) core = 4.1 nm, shell =1.0 nm; (b) core = 8.6 nm, shell = 1.3 nm; (c) core = 13.1 nm, shell = 1.7 nm; (d) core = 15.1 nm, shell = 2.2 nm, (e) core = 15.1 nm, shell = 3.4 nm; (f) core = 15.1 nm, shell = 4.1 nm.

and the corresponding transient induced changes in the transmission of this film. In tuning the laser from 780 nm to 840 nm, we observe a change from induced bleaching to induced absorption. Our analysis indicates that the origin of the measured signal is due to the creation of a hot electron distribution within the gold shell. The hot electrons return to equilibrium via energy-dissipative interactions with the nanoparticle core and the embedding medium.

Gold-Coated Silica Nanoparticles

In the gold-terminated Au_2S metal nanoshell system, the range over which the optical resonance is tunable (~ 600 to 1000 nm) is limited by the constraints of its complex growth chemistry. Thus, we have developed an approach to the construction of metal nanoshell particles that combines techniques of molecular self-assembly with the reduction chemistry of metal colloid synthesis. This approach is general and can potentially be adapted to a variety of core and shell materials allowing for the fabrication of nanoparticles whose plasmon resonance lies in the infrared. We have grown monodisperse silica nanoparticles via the Stober method as our cores[9]. Organosilane molecules (3-aminopropyltriethoxysilane) are then adsorbed onto these nanoparticles. These molecules bond to the surface of the silica nanoparticles, extending their amine groups outward as a new termination of the nanoparticle surface. After isolating the silane coated silica particles from residual reactants, a solution of very small gold colloid (1-2 nm in diameter) is added[10]. The solid gold nanoparticles bond covalently to the organosilane linkage molecules via the amine group. Subsequently, the gold-decorated silica nanoparticles are used as nucleation sites for the reduction of an aged mixture of chloroauric acid and potassium carbonate by a solution of sodium borohydride. This results in an increasing coverage of gold on the nanoparticle surface.

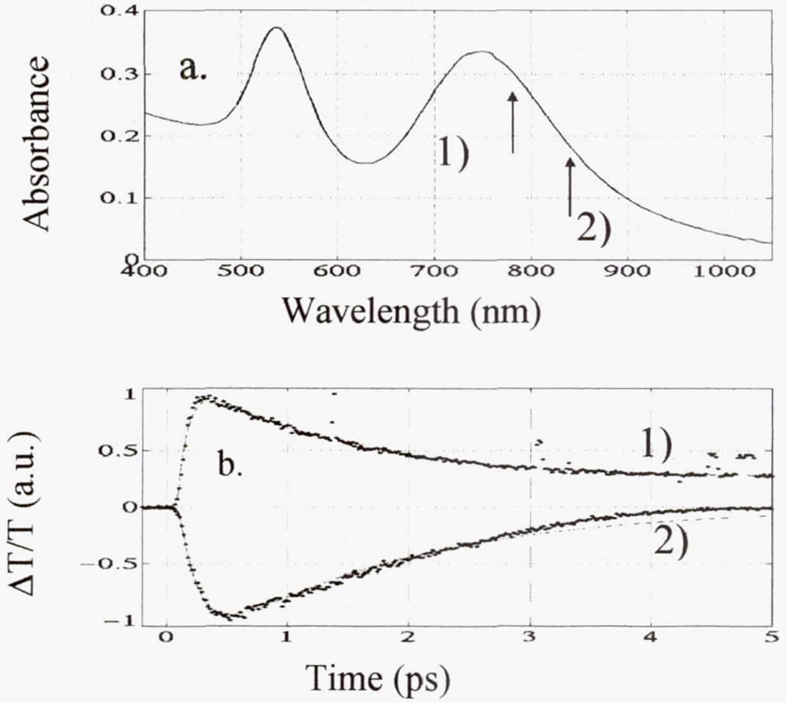

Figure 3: (a) UV-vis of gold nanoshell film. The labeled arrows correspond to the wavelength at which the time-resolved induced change in transmission was measured. (b) In tuning the Ti:sapphire laser from 780 nm to 840 nm the signal changes from induced bleaching to induced transmission.

In Figure 4(b-f), a sequence of transmission electron microscope (TEM) images of 120 nm diameter nanoparticles illustrates the progression in metal nanoshell growth that occurs during the reduction. Initially, the seed colloid absorbates increase in size as reduction ensues (b,c). Then, the seed colloids begin to coalesce on the nanoparticle surface (d,e), until finally the apparent formation of a continuous metallic nanoshell (f) on the dielectric nanoparticle surface can be observed. Nanoshell growth is typically completed in a few seconds with a yield greater than 95 percent.

These dramatic changes in nanoshell structure give rise to a detailed optical signature of nanoshell formation and growth. This is shown in Figure 5, where (a) 120 nm and (b) 340 nm diameter silica spheres were used as the dielectric nanoparticle substrates. As the nanoshell growth progresses, these sequential UV-visible spectra increase in absorbance. In the initial stages of nanoshell growth, when gold is reduced exclusively onto the colloidal adsorbates, the spectrum is identical to that expected for gold colloid in solution. As the colloidal adsorbates grow, their plasmon peak becomes slightly red shifted. As the growing colloidal adsorbates begin to coalesce and form islands on the nanoparticle surface, this peak becomes distorted into a broad shoulder characteristic of particles with a distribution of aspect ratios ratios, a lineshape similar to that previously observed in spectroscopic studies of gold platelets in solution[11].

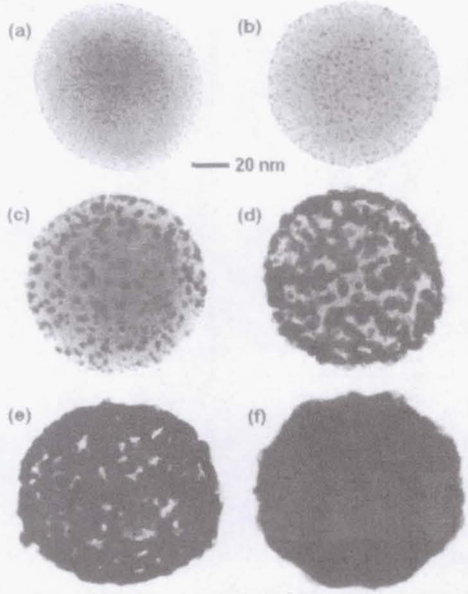

Figure 4: (a-f) TEM images of nanoshell growth on 120 nm diameter silica dielectric nanoparticle. (a) Initial gold colloid-decorated silica nanoparticle. (b)-(e) gradual growth and coalescence of gold colloid on silica nanoparticle surface. (f) completed growth of metallic nanoshell.

A pronounced nanoshell resonance peak abruptly rises when the shell growth is "complete". In Figure 5(a), the peak of the plasmon absorbance has shifted from 520 to over 800 nm while in Figure 5(b), a much greater shift is observed, leaving only the shoulder of the initial nanoshell peak observable for this core/shell ratio within our spectrophotometer range. At this stage, quantitative agreement between Mie scattering theory, the observed UV-visible absorption, and structural measurements obtained by TEM is achieved. A generalized version of Mie scattering theory incorporating the higher order multipoles of the scattering expansion is required here, since these slightly larger nanoparticles are no longer in the quasistatic limit. The higher order contributions give rise to the secondary peak to the left of the plasmon resonance in Figure 5(a) and the modulated peak in Figure 5(b). The relative positions and magnitudes of the secondary peaks with respect to the dipole resonance and the degree of absorbance versus scattering is a strong function of the overall particle size. Thus, in addition to core/shell ratio, the absolute size of the metal nanoshell provides additional control over the wavelength dependent optical response of the composite nanoparticles.

Future Directions

Current efforts in our laboratory focus on optimizing the present nanoshell growth process and extending and adapting this method to a broader range of core and shell materials.
Within these studies, the limitations induced by terrestrial gravity regarding size and shape uniformity of nanoparticle cores and homogeneity of shell growth are being assessed. Several molecular functionalization strategies of these nanoparticles are being pursued, with the ultimate goal of condensing nanoshells into crystalline structures and well-ordered thin films.

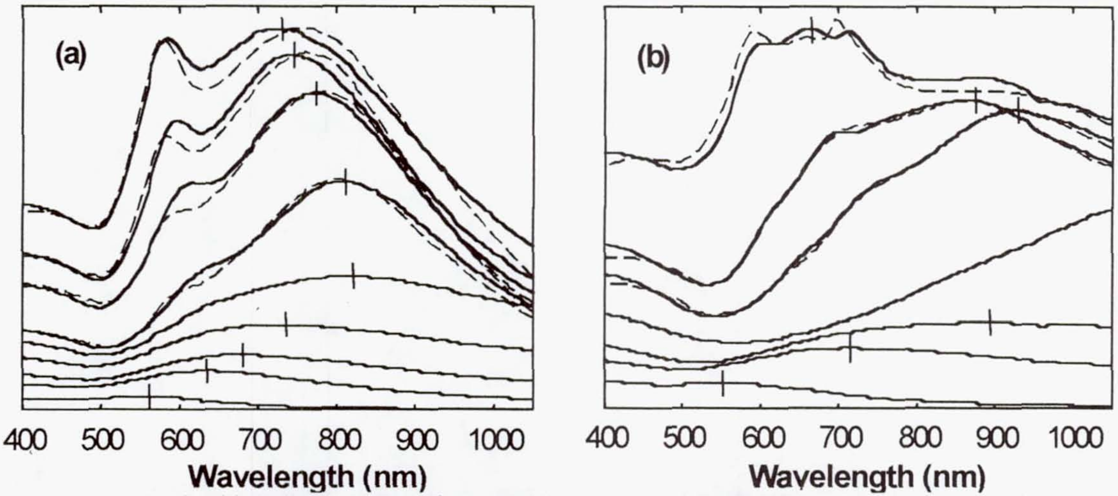

Figure 5 : (a) Growth of gold shell on 120 nm diameter silica nanoparticle. The lower spectral curves follow the evolution of the optical absorption as coalescence of the gold layer progresses. This is responsible for the initial red shift in the peak absorbance from 550 nm to 800 nm. Once the shell is complete, the peak absorbance is shifted to shorter wavelengths. Corresponding theoretical peaks are plotted with dotted lines. From right to left these spectra correspond to theoretical shell thicknesses of 14, 17, 24 and 30 nm. Experimental shell thicknesses determined by TEM are slightly larger at 20, 26, 29, 33 nm ± 4 nm. This discrepancy is attributed to the ± 4 nm surface roughness present on both the interior and exterior surfaces of the shell layer. The hash marks indicate the peak of each spectrum. (b) Growth of gold shell on 340 nm diameter silica nanoparticles. Here the peak shifts are much more pronounced with only the shoulder of the middle curve visible in our spectrophotometer range. The dotted lines from right to left, correspond to shell thicknesses of 17, 35, 48 nm. TEM determined shell thicknesses were 18, 39, 53 ± 12 nm.

These crystallization and deposition studies will provide another experimental arena where terrestrial gravitational effects are expected to be sizeable and where a microgravity environment may provide the opportunity to produce crystalline structures not obtainable using a ground-based approach.

References

1 R. D. Averitt, D. Sarkar, N. J. Halas, Phys. Rev. Lett. **78**, 4217 (1997).

2 S. J. Oldenburg, R. D. Averitt, S. L. Westcott, N. J. Halas, Chem. Phys. Lett. **288**, 243 (1998).

3 F. Hache, D. Ricard, C. Flytzanis, App. Phys. A **47**, 347 (1988).

4 U. Kreibig, M. Vollmer, *Optical Properties of Metal Clusters* (Springer, New York, 1995).

5 A. L. Aden, M. Kerker, J. App. Phys. **22**, 1242 (1951).

6 A. E. Neeves, M. H. Birnboim, J. Opt. Soc. Am. B **6**, 787 (1989).

7 J. W. Vanderhoff, *et al.*, J. Dispersion Sci. Tech. **5**, 231 (1984).

8 R. D. Averitt, PhD thesis, Rice University, Houston, 1998.

9 W. Stober, A. Fink, E. Bohn, J. Colloid Interface Sci. **26**, 62 (1968).

10 D. G. Duff, A. Baiker, Langmuir **9**, 2301 (1993).

11 J. Weisner, A. Wokaun, Chem. Phys. Lett. **157**, 569 (1989).

RADIATION TRANSMISSION PROPERTIES OF *IN-SITU* MATERIALS

Lawrence Heilbronn
MS 29-100
Lawrence Berkeley National Laboratory
Berkeley, CA 94720
510-486-4002
gunner@LBL.gov

Larry Townsend
Department of Nuclear Engineering
Pasqua Engineering Building
University of Tennessee
Knoxville, TN 37996-2300
423-974-5048
ltownsen@utk.edu

Introduction

In order to accurately determine the radiation risk to astronauts from Galactic Cosmic Rays (GCR) and Solar Particle Events (SPE), the nature of the secondary radiation field created by the fragmentation of GCR and SPE in shielding and tissue must be understood. Due to their high penetrabilities, neutrons are an important component of the secondary radiation field, especially for astronauts protected by thick shielding on lunar or Martian bases[1-3]. Because of their relatively short lifetimes, free neutrons are not present in the primary GCR. The predominant source of neutrons, then, is interactions of GCR and SPE in shielding materials. These interactions span the full range of GCR ions (protons, helium, and HZE) and GCR energies (100 MeV/nucleon and up); hence neutrons are produced from an enormous set of varied and different interactions. Some studies have been conducted at ground-based accelerator facilities in regards to the production of neutrons from GCR-like interactions, but because accelerator resources are limited and because neutron experiments require a large amount of the time available at those accelerators, the best approach to the problem of determining the amount of neutron radiation behind shielding is through a calculational approach. New and innovative materials involving the use of local regolith are being developed and studied for their usefulness in lunar and Martian base design. One important design criterion is the ability of those materials to shield human personnel from the radiation environment in which such bases will exist. Because neutrons will be a significant component of the radiation environment inside those bases, it is critical that computer models be developed which can accurately predict the production of neutrons from GCR and SPE interactions with *in-situ* materials. The primary thrust of the research program described here is to develop an accurate neutron production model, with an emphasis on neutron production from composites comprised of *in-situ* materials. Because models used to calculate neutron production behind thick shields will need cross-section and thick-target production data for verification of model input and output, emphasis will also be placed on completing analysis of existing neutron-production data and compiling a set of experimental neutron production data which is relevant to model development.

The research program described here is a four-year program started in 1998. A general description of the theory program and experimental-data-base development program follows, along with expected goals and milestones of the overall program. In addition, some preliminary results from analysis of experimental data is presented.

Theory Program

Shown in Figure 1 is a plot of thick-target neutron spectra from 435 MeV/nucleon Nb stopping in Nb, at the indicated laboratory angles. The solid lines show calculations of the data using the Boltzmann-Uehling-Uhlenbeck (BUU) equation. Although the calculation does a reasonable job of matching the data at large angles, it misses the data at forward angles by a large margin. In addition to the fact that BUU calculations are unable to predict the entire spectrum of neutrons, they use a Monte-Carlo code which requires too much computer time to be effectively used in engineering applications where the physical properties and layout of shielding materials are changed often in order to determine the best overall shielding scenario. A simple, physically realistic yet accurate neutron production model is needed. Such a model, based upon a two-stage, quantum-mechanical abrasion-ablation collision formalism is proposed herein. The initial version of this model was found to reproduce the measured 0° energy spectra of secondary neutrons produced in Ne-NaF and other reactions quite well[4]. Finishing the model development and validating it is the goal of this proposed work.

I. Theoretical Approach

In an abrasion-ablation fragmentation model, the projectile nuclei, moving at relativistic speeds, collide with target nuclei. In the abrasion (knockout) step, those portions of the nuclear volume that overlap are sheared away by the collision. The remaining projectile piece, called a prefragment, continues its trajectory with essentially its precollision velocity. As a result of the dynamics of the abrasion process, the prefragment is highly excited and subsequently decays by the emission of gammas and/or nuclear particles. This step is the ablation stage. The abrasion or knockout process can be analyzed with classical geometric arguments[5] or with quantum scattering theory[6-8]. The ablation stage can be analyzed using geometric arguments[5] or methods based upon Monte Carlo or intranuclear cascade techniques[6]. These models have been very successful for accurately predicting mass yields in heavy ion collisions. However, until recently, they have met with little success in predicting nucleon production, including momentum distributions.

In the abrasion-ablation model to be used in this work[4], the nucleon momentum distribution from abrasion is written as:

$$\left(\frac{d\sigma}{dk}\right)_{abr} = \sum_{n}\binom{A_p}{n}\frac{1}{(2\pi)^2}\int d^2q\,d^2b\,d^2b'\,\exp\left[iq\bullet\left(b-b'\right)\right]P^{A_p-n}\left(b,b'\right)\frac{dN_1}{dk}\int dT_{F^*}\Lambda_{n-1}\left(b,b',T_{F^*},k\right) \tag{1}$$

where A_p is the projectile mass number, n is the number of abraded (knocked out) nucleons, k is the wave number of the emitted neutrons, and T_{F^*} is the prefragment recoil energy. The spectral function for single nucleon removal is

$$\left(\frac{dN_1}{dk}\right) = \frac{1}{(2\pi)^3}\int dr\,dr'\exp(ikr)\rho(r,r')\exp\left[-2\,\mathrm{Im}\,X^{(-)}(y)\right]Q_l^{+}(b'-s')Q_l(b-s) \tag{2}$$

where Q represents the profile functions from Glauber theory optically-averaged over target coordinates, $X^{(-)}$ describes the final-state interaction with the prefragments and $\rho(r,r')$ is the projectile nuclear density matrix. The functions $\Lambda_{(n-1)}$ in Eq. (1) describe multiple nucleon knockout (n > 1) and include energy-conserving effects.

After the projectile-target collision, the prefragment nuclei have a distribution of excitation energies. This excitation spectrum is treated as an average state with a single or small number of average excitation energies used to describe the prefragment. The strength of each state is determined by the total abrasion cross section σ_{abr}. Therefore, the momentum distribution for neutron production by ablation in the projectile nucleus rest frame is

(3)

$$\left(\frac{d\sigma}{dk}\right)_{abl} = \sum_j \sigma_{abr}\left(A_j, Z_j, E_j^*\right) P_n(j,k)$$

where the probability P_n that the j^{th} prefragment with mass number A_j, charge number Z_j, and excitation energy E_j, emits a neutron of momentum k is estimated using Weisskopf-Ewing statistical decay model. Neutrons from the evaporation of the target prefragment are neglected in these calculations. The higher order cascade effects of projectile knockouts interacting with projectile prefragments is also neglected. The calculations also do not account for the production of nucleons through the decay of isobars produced in the collision.

The overall approach in the proposed work is to first compare the existing model with recent measurements of secondary neutron production. Second, the additional contributions to neutron production described in the previous paragraph will be incorporated into the model and ultimately be compared with the available data and with the data to be obtained in the experimental phase of this program.

II. Scheduled Milestones

First Year

1. Initiate validation process for the existing model by comparing model calculations with available experimental data

2. Begin modifications to the existing model in order to incorporate higher order cascade effects.

Second Year

1. Continue validation comparisons with existing experimental data.

2. Complete modifications to model to incorporate higher-order cascade effects.

Third Year

1. Continue development of the abrasion-ablation model by incorporating production and decay of nucleon isobars into the model.

2. Continue validation comparisons with experimental data.

Fourth Year

1. Complete development and validation of the abrasion-ablation neutron production model.

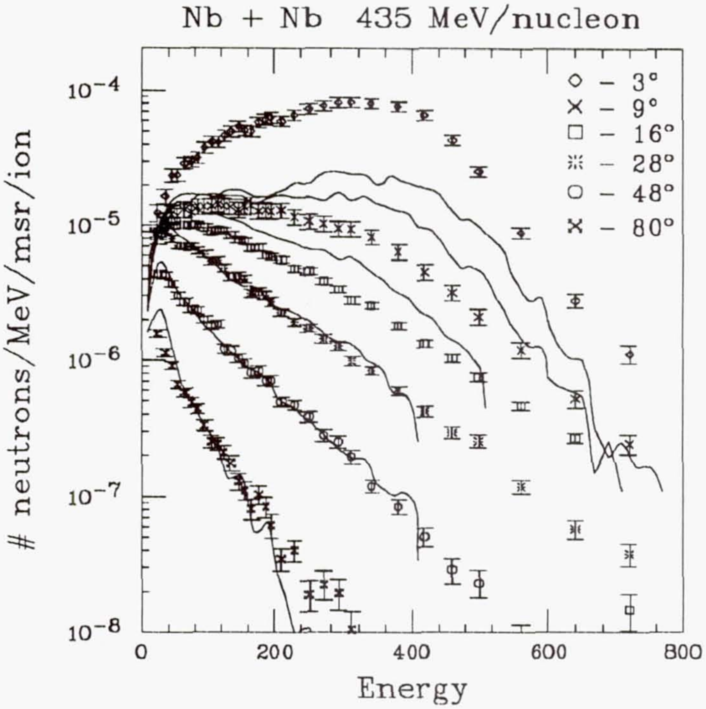

Fig 1. Thick-target neutron spectra from the 435 MeV/nucleon Nb + Nb system at the indicated angles. The solid lines come from a fit to the data using BUU calculations.

Experimental Program

In addition to the 435 MeV/nucleon Nb + Nb data shown in Fig. 1, this program has also recently completed analyses of 272 MeV/nucleon Nb stopping in targets of Nb and Al, 155 MeV/nucleon He stopping in Al, and 155 MeV/nucleon C stopping in Al. These data sets will be eventually included into a comprehensive experimental-data base comprised of proton-induced and heavy-ion-induced neutron production cross sections and thick-target yields.

Scheduled Milestones (experimental program)

First Year

1. Complete analysis of the stopping target data taken with 155 MeV/nucleon He and C beams in an aluminum target. Publish results.

Second Year

1. Complete analysis of the thin-target cross section data taken with 155 MeV/nucleon He and C beams, and with a 75 MeV/nucleon C beam.

Third Year

1. Begin compilation of data base of all existing neutron-production data sets (experimental data) relevant to NASA's materials and shielding programs.

References

1. L.C. Simonsen, J.E. Nealy, L.W. Townsend and J.W. Wilson, SAE Technical Paper 901346, 1990.

2. L.C. Simonsen and J.E. Nealy, NASA Technical Paper 3079, 1991.

3. F.A. Cucinotta, NASA Technical Paper 3354, 1993.

4. F.A. Cucinotta, J.W. Wilson and L.W. Townsend, Nucl. Phys. A 619, 1997.

5. J.D. Bowman, W.J. Swiatecki and C.F. Tsang, LBL-2908, 1973.

6. J.Hufner, K. Schafer and B. Schurmann, *Phys. Rev. C* 12, 1975.

7. L.W. Townsend, *Can. J. Phys.* 61, 1983.

8. L.W. Townsend, F. Khan, and R.K. Tripathi, *Phys. Rev. C* 48, 1993.

Page intentionally left blank

MICROGRAVITY PROCESSING OF OXIDE SUPERCONDUCTORS

James R. Olive, William H. Hofmeister, and Robert J. Bayuzick
Vanderbilt University
Nashville, TN 37235

Marcus Vlasse, Marshall Space Flight Center, Huntsville, AL 35812

Introduction

Considerable effort has been concentrated on the synthesis and characterization of high T_c oxide superconducting materials. The YBaCuO system has received the most intense study, as this material has shown promise for the application of both thin film and bulk materials. There are many problems with the application of bulk materials; weak links, poor connectivity, small coherence length, oxygen content and control, environmental reactivity, phase stability, incongruent melting behavior, grain boundary contamination, brittle mechanical behavior, and flux creep. The extent to which these problems are intrinsic or associated with processing is the subject of controversy. This study seeks to understand solidification processing of these materials, and to use this knowledge for alternative processing strategies, which, at the very least, will improve the understanding of bulk material properties and deficiencies.

In general, the phase diagram studies of the YBaCuO system have concentrated on solid state reactions and on the Y_2BaCu0_x + liquid → $YBa_2Cu_3O_{7-\delta}$ peritectic reaction. Little information is available on the complete melting relations, undercooling, and solidification behavior of these materials. In addition, rare earth substitutions such as Nd and Gd affect the liquidus and phase relations[1]. These materials have promising applications, but lack of information on the high temperature phase relations has hampered research. In general, the understanding of undercooling and solidification of high temperature oxide systems lags behind the science of these phenomena in metallic systems. Therefore, this research investigates the fundamental melting relations, undercooling, and solidification behavior of oxide superconductors with an emphasis on improving ground based synthesis of these materials.

Experimental Results

Significant progress has been made in understanding the above mentioned phenomena. Two techniques of containerless processing were utilized, Aero-Acoustic Levitation and drop tube processing. The liquidus of the $YBa_2Cu_3O_{7-\delta}$ has been determined to be 1820 °C, a considerably higher temperature than reported in the literature[2,3]. In addition, deep undercooling of these materials has been accomplished. In many cases tetragonal $REBa_2Cu_3O_x$ was solidified directly from the melt, demonstrating that formation of the intermediate phases in these systems can be avoided by melt processing and undercooling.

Aero-Acoustic Levitation (AAL) experiments provided a means for direct observation of large (2.5 mm) samples during processing[4]. The Ultra High Speed Thermal Imaging (UHSTI) system developed at Vanderbilt has proven to be useful for obtaining spatial thermal information during melting and solidification. Upon rapid solidification, several thermal events were observed, most notably a low temperature (~1080 K) slow moving event which led to a cellular structure with tetragonal $YBa_2Cu_3O_x$ being the primary solidification phase. When full melting of the sample was obtained, single phase tetragonal $YBa_2Cu_3O_x$ was formed upon recalescence[5].

Drop tube experiments at Vanderbilt University have concentrated on determining the high temperature phase relations in $YBa_2Cu_3O_{7-\delta}$, $NdBa_2Cu_3O_x$, and partial substitutions of Nd for Y. These experiments involved melting small powders (50 - 100 μm) in a pure oxygen environment using a 2 meter drop tube. Melted powders solidified in free fall. The resulting samples were examined microstructurally using scanning electron microscopy, energy dispersive spectroscopy (EDS) and optical microscopy. Powder x-ray diffraction was performed for phase identification. Because these materials possess a low thermal conductivity, the smallest resultant samples were used for comparison based on the fact that they were more likely to reach the furnace temperature during free fall. Table 1 lists the compositions processed and the ranges of processing temperatures in these experiments. Experiments were performed at 25 ° increments within each range.

Sample Material	*Temp. (°C)*
$YBa_2Cu_3O_{7-\delta}$	1650-1800
$Y_{.9}Nd_{.1}Ba_2Cu_3O_x$	1650-1800
$Y_{.8}Nd_{.2}Ba_2Cu_3O_x$	1650-1800
$Y_{.7}Nd_{.3}Ba_2Cu_3O_x$	1575-1800
$Y_{.5}Nd_{.5}Ba_2Cu_3O_x$	1525-1800
$Y_{.3}Nd_{.7}Ba_2Cu_3O_x$	1475-1800
$Y_{.1}Nd_{.9}Ba_2Cu_3O_x$	1450-1800
$NdBa_2Cu_3O_x$	1400-1800

Table 1. Drop Tube Experiments Performed.

Microstructural analysis using energy dispersive spectroscopy along with powder X-ray diffraction on the resultant samples provides for developing a clear picture of the phases that solidify. Figure 1 summarizes these analyses for all of the drop tube experiments which have been performed in this study. The lines indicate the primary solidification phase as a function of composition and drop tube processing temperature. At processing temperatures above the solid line, the samples were completely molten, then undercooled to below the RE-1:2:3 peritectic to solidify single phase tetragonal RE-1:2:3 from the melt. Below this line the existence of facted, high temperature phases indicates that the samples were processed in a solid + liquid region of the phase diagram. Therefore, this line defines the liquidus between pure Y-1:2:3 and Nd-1:2:3. The data show a decreasing trend in the liquidus with increasing Nd to and including the composition $Y_{.1}Nd_{.9}Ba_2Cu_3O_x$. At that composition, the liquidus temperature reaches a minimum of 1500 °C (± 25 °C). For the pure Nd-1:2:3 samples, the liquidus increases markedly to 1600 °C (± 25 °C).

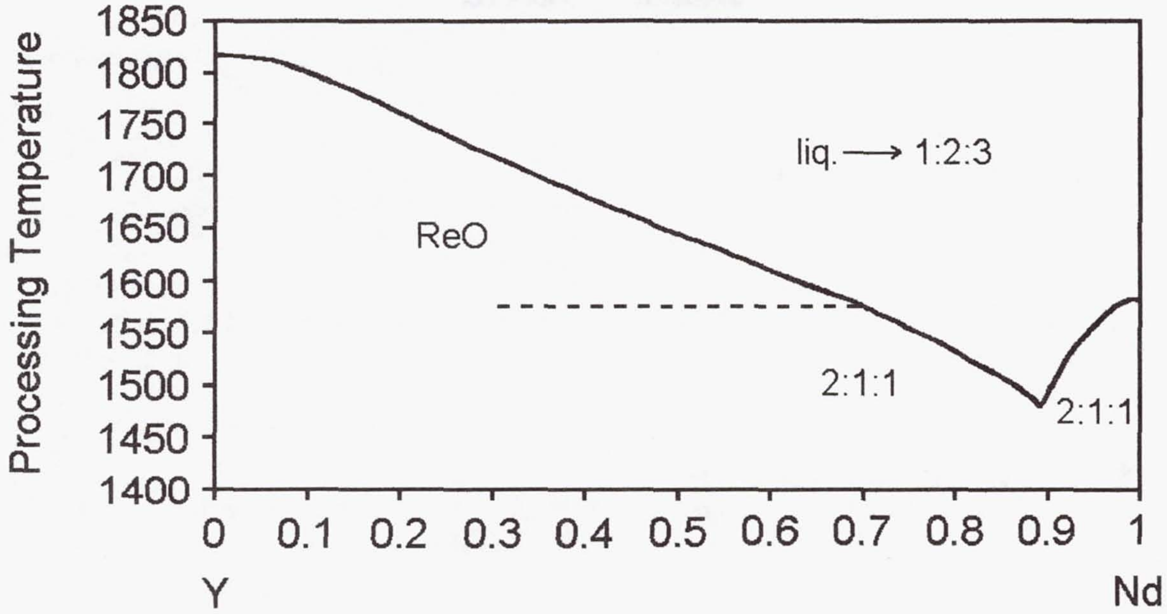

Figure 1. Schematic diagram of Nd atoms/unit cell vs. drop tube processing temperature showing the primary solidification phase. Phases are as follows: 2:1:1 = Y_2BaCuO_5, ReO = Rare earth oxide, 1:2:3 = tetragonal $RE_{1(Y+Nd)}Ba_2Cu_3O_x$.

A typical micrograph from a sample that did not melt completely is shown in figure 2. This result is from a sample of pure $YBa_2Cu_3O_{7-\delta}$ processed at 1775 °C. Here, four distinct phases can be seen. Particles of Y_2O_3 (dark gray) are seen accompanied by dendrites of the darkest phase. The darkest phase corresponds to Y_2BaCuO_5. The surrounding matrix is eutectic in nature and is composed of at least two different Ba Cu oxide phases. This morphology appears frequently when samples are not completely molten prior to solidification. In this case, samples reached temperatures within the Y_2O_3 + liquid region of the phase diagram. Once they passed out of the hot zone and began cooling, the Y_2BaCuO_5 phase nucleated on the surfaces of these particles. Upon further cooling, the remaining liquid solidified as a Ba Cu oxide eutectic.

Figure 3 shows a sample of $Y_{.8}Nd_{.2}Ba_2Cu_3O_x$ processed at 1775 °C in the drop tube. Here, tiny feathery dendrites of Y_2BaCuO_5 are observed within a matrix of Ba Cu oxides. In this case, the sample was nearly, but not completely molten in free fall. Enough solid RE_2O_3 remained to nucleate Y_2BaCuO_5. Figure 4 shows a sample of $Y_{.3}Nd_{.7}Ba_2Cu_3O_x$ processed at 1675 °C where large dendrites and grains of pure $Y_{.3}Nd_{.7}Ba_2Cu_3O_x$ formed. Microstructures of this type are an indication that the samples were completely molten prior to solidification. Upon cooling, samples undercooled to below the $Y_{.3}Nd_{.7}Ba_2Cu_3O_x$ peritectic and solidified tetragonal 1:2:3 phase directly from the melt.

Nd substitution affects phase selection in the following ways. First, as the Nd content increases, the tendency for the formation of RE oxide from the melt decreases. At a Nd content of 0.7 atoms/unit cell, RE oxide does not appear in the resultant samples. Secondly, for intermediate compositions ($0.5 \geq x \geq 0.3$), the 2:2:3 phase exists at high temperatures. This phase is previously unreported and occurs only in the presence of 1:2:3. Figure 5 is a micrograph of a $Y_{.5}Nd_{.5}Ba_2Cu_3O_x$ sample processed at 1725 °C where the 2:2:3 phase appears between large grains of $RE_1Ba_2Cu_3O_x$.

The decreasing tendency for RE oxide to form and the overall lowering of the liquidus with increasing Nd content additionally alters phase selection in that the RE-1:2:3 phase forms more readily. This is coupled with a decrease in the number of second phases and off-stoichiometric compounds that appear in the final microstructure. This effect can clearly be seen in figure 1. Samples low in Nd possess at least 7 different phases in the post-processed material over a range of 150 degrees. Samples high in Nd possess only 4 different phases in a range up to 400 degrees. Hence, Nd is a 1:2:3 stabilizer.

The Need for Microgravity Experiments

The difficulties of processing these materials in one g present a clear case for microgravity processing. For example, the large density differences in these multi-component systems cause sedimentation in the melt. Also, $YBa_2Cu_3O_{7-\delta}$ and rare earth (RE) substituted $YBa_2Cu_3O_{7-\delta}$ have a very low thermal conductivity, such that moderate heating and cooling rates develop large thermal gradients in the melt, thereby driving convection. Furthermore, these materials react with all known containing media, but the poor electrical conductivity at room temperature prevents the use of more conventional electromagnetic containerless processing techniques. For various reasons, other techniques for containerless processing are not appropriate because control of the processing environment is crucial to maintaining oxygen stoichiometry and preventing contamination by other gasses such as CO_2. Furthermore, heat capacity, viscosity and surface tension measurements on the undercooled liquid melt cannot be done on earth but can be obtained in microgravity. Fundamental studies of the melting, undercooling, and solidification behavior under the highly controlled conditions possible in a microgravity environment will lead to a greater understanding of these materials. In addition, it will be possible to produce benchmark materials in space.

Future Work

Containerless melt processing has proven to be a novel technique for gaining valuable information about the phase relationships in oxide superconductor systems. In particular, the techniques put forth in this study allowed for obtaining information unavailable using conventional processing methods due to the avoidance of any container contamination effects.

Experiments are planned to continue the fundamental high temperature phase relationships using the 2-meter drop tube at Vanderbilt. In addition, aero-acoustic levitation experiments will be performed on 2.5 mm drops to determine the viability of this technique for ground based containerless processing on these systems.

An additional goal of this program is to develop collaboration with other groups and provide access to the unique processing strategies developed by the microgravity program. Ultimately this research effort will lead to a proposed flight experiment where investigators from industry, national laboratories, and universities could participate in highly controlled experiments on the melting and solidification behavior of oxide superconducting systems.

References

1. R.W. McCallum, M.J. Kramer, T.J. Folkerts, S.R. Arrasmith, B.D. Merkle, S.I. Yoo, Youwen Xu and K.W. Dennis, *Containerless Melt Processing of* $REBa_2Cu_3O_{7-x}$ *{RE=Y, Gd, Nd} High Temperature Superconductors,* in Physical and Materials Properties of High Temperature Superconductors, S.K. Malik and S.S. Shah eds. (Nova Science Publishers, Inc. 1992) p. 667.

2. R.S. Roth, K.L. Davis and J.R. Dennis, *Adv. Ceram. Mater.* **3B**, v. 2, (1987) 303.

3. K. Osamura and W. Zhang, *Z. Metallkunde* **82**, (1991) 408.

4. J.K.R. Weber, D.S. Hampton, D.R. Merkley, C.A. Rey, M.M. Zatarski, and P.C. Nordine, *Ceram. Bull.* **70**, 71 (1991).

5. J.R. Olive, W.H. Hofmeister, R.J. Bayuzick, G. Carro, J.P. McHugh, R.H. Hopkins, M. Vlasse, J.K.R. Weber, P.C. Nordine, and M. McElfresh, *J. Mater. Res.* **9**, no. 1, 1 (1994).

Figure 2. Micrograph of a Y-1:2:3 sample processed in pure O_2 at 1775 °C in the drop tube indicating incomplete melting.

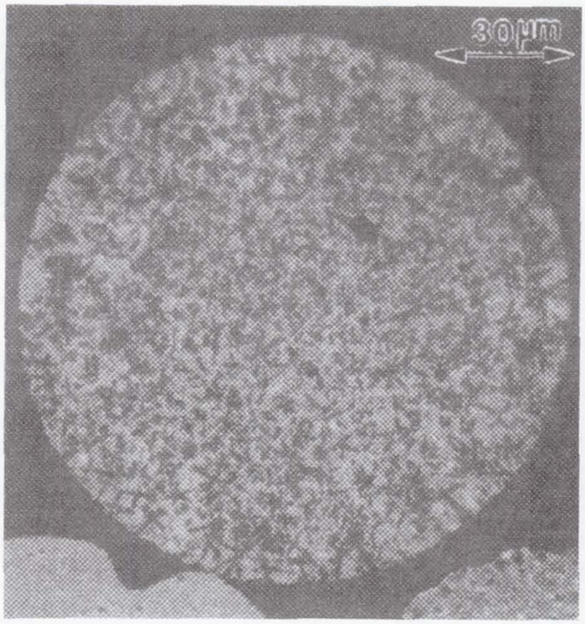

Figure 3. Characteristic micrograph of $Y_{.8}Nd_{.2}Ba_2Cu_3O_x$ processed in pure O_2 at 1775 °C in the drop tube.

Figure 4. Micrograph of $Y_{.3}Nd_{.7}Ba_2Cu_3O_x$ processed in pure O_2 at 1675 °C in the drop tube showing primary RE-1:2:3 solidification.

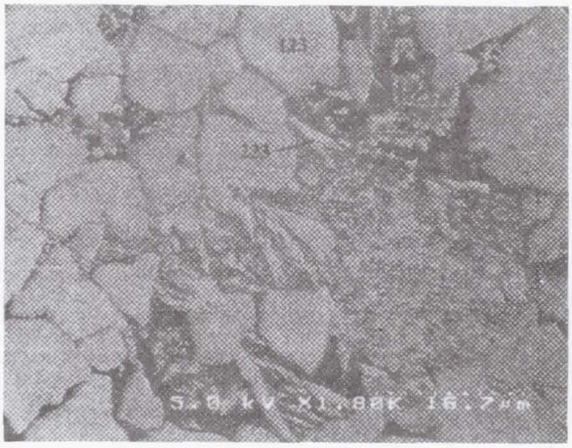

Figure 5. Micrograph of $Y_{.5}Nd_{.5}Ba_2Cu_3O_x$ processed in pure O_2 at 1725 °C in the drop tube. The lighter dendritic phase corresponds to 2:2:3.

Dimensional Stability of Supermatrix Semiconductors

D.E. Holmes and J.H. Cho
Electronic Materials Engineering
829 Flynn Road
Camarillo, CA

Supematrix Semiconductors (SMS) are *in-situ* composite semiconductor materials produced by directional solidification of eutectics in which the phases form in oriented, periodic, and crystallographically oriented arrays in 3 dimensions. SMS technology makes possible the 3-dimensional superlattice, the Quantum Cable, and materials with new or enhanced electronic, optoelectronic, electro-optic, and photorefractive properties. Objectives of the program are two-fold: (1) to demonstrate microgravity as an enabling environment for producing SMS materials with a high degree of microstructural control required for device applications; (2) to establish a broader scientific understanding of growth-property relationships of multi-phase solidification. To date, it has been demonstrated that the microstructure of the Ge/GeAs SMS is both dramatically and beneficially impacted when produced under conditions of simulated microgravity.

Our approach to simulating microgravity conditions has been to apply magnetic damping to crystal growth from a small, low-Rayleigh-number melt. Three tasks have been addressed. First, a low-pressure Czochralski crystal growth system with an integrated 7 kgauss electromagnet has been designed and constructed, as shown in Fig. 1, and a liquid encapsulated growth process has been established for Ge/GeAs, the SMS chosen for study. Emphasis in the design of the system was placed on achieving high thermal symmetry to minimize temperature gradients across the melt. The diameter and height of the starting melt are both 2.6 cm, and the weight is100 grams. Crystals (i.e., two-phase ingots containing Ge rods aligned along the axis of solidification in a GeAs matrix) of between 50 and 100 grams, as shown in Figs. 2 and 3, are typically grown.

Establishment of sample preparation and characterization procedures has also been addressed as a part of this task. Crystals are sliced by using an annular I.D. saw, lapped, and polished with colloidal silica. The microstructure of as-polished samples is revealed by using Normarski microscopy without preferential etching due to differential polishing of the two components.. Automated image analysis has been used to assist in detailed microstructural characterization.SEM, EDAX, TEM, HREM, X-ray diffraction, Hall effect measurements, and photoluminescence are also being applied.

Characterization of thermohydrodynamic properties of the encapsulated melt is the second program task. Temperature fields and temperature spectra (i.e., temperature versus time at constant probe position) have been determined with and without magnetic damping by using a movable, multi-channel temperature probe. Results show (1) that the condition of the undamped melt is laminar, and (2) that the application of a magnetic field has a major impact on the temperature field further enhancing the hydrodynamic stability.

For example, in the absence of a magnetic field, the temperature within the melt is uniform to within ± 3 deg C, as shown in Fig. 4, and the temperature distribution (bottom hotter than top) is consistent with an axis non-centrosymmetric flow pattern. Vertical gradients increase from 0.9 deg C per cm to 5.2 C per cm with the application of a 6 kgauss field, as shown in Fig. 5, apparently as a result of the suppression of convective heat transfer. Horizontal gradients, on the other hand, are independent of field strength above about 2 kGauss, which appears to be a threshold possibly related to the re-orientation and alignment of the undamped flow pattern to the magnetic field. Saturation of the temperature gradient with field strength is also observed at about 5 kgauss. Temperature spectra with and without an applied field show no significant and identifiable fluctuations associated with turbulent conditions. In addition, empirical Rayleigh numbers on the order of 4000 are close to published values for the laminar-to-conductive transition.

The third program task is to establish cause-effect relationships between microstructural features and conditions of solidification, including the solidification rate, crystal rotation, and magnetic field strength. A matrix of growth experiments is being conducted, and available data is summarized below.

Three important results have been obtained to date. First, dimensional stability depends on both seed rotation and magnet field strength. Continuity of the microstructure along the axis of solidification exhibits a dramatic dependence on magnetic field strength as the length of Ge rods increases by about 300% under super-threshold fields. Furthermore, cross-sectional uniformity is enhanced by employing slow seed rotation, and a figure of merit of non-uniformity improves from 25% to 10% as super-threshold fields are applied.

Second, the application of a magnetic field refines the microstructure, and the average inter- rod spacing decreases by about 30% under magnetic damping.

Finally, a natural tendency of the microstructure in undamped growth to coarsen as solidification proceeds has been established.

A picture is emerging supported by the data that dimensional stability is promoted by hydrodynamic stability and magnetic damping. However, cause-effect relationships are not clear, and the results have not been reconciled with available models despite the fact that some parallel behavior has been reported for space growth experiments. Although additional analysis remains, a more refined technique of materials characterization, such as interface demarcation, may be required to elucidate the physical mechanisms.

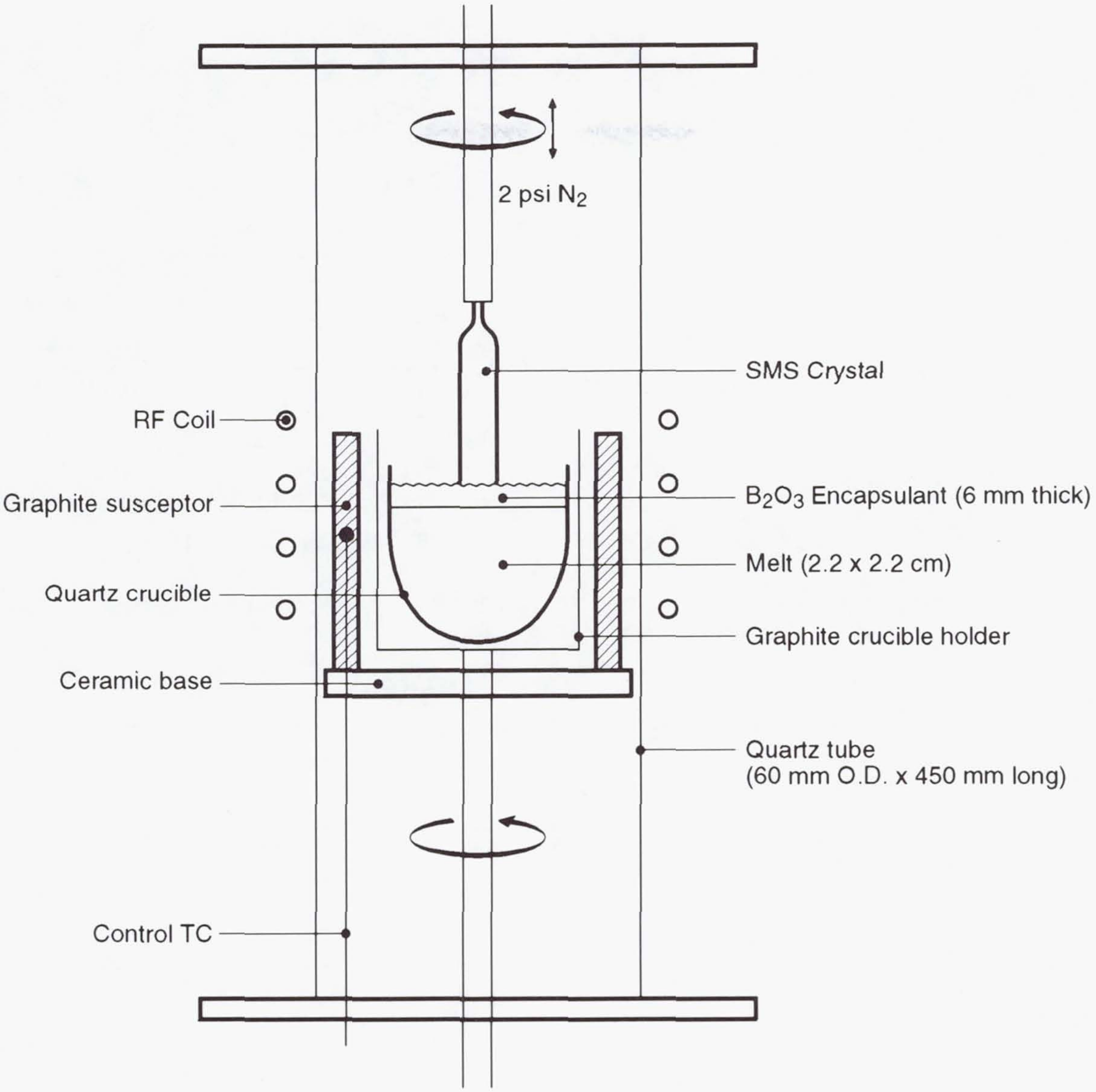

Figure 1. Schematic of LEC Growth System for Ge/GeAs SMS

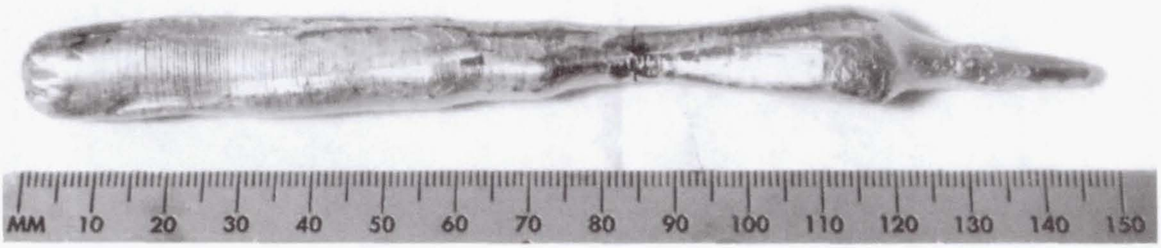

Figure 2. Photograph of typical Ge/GeAs Crystal

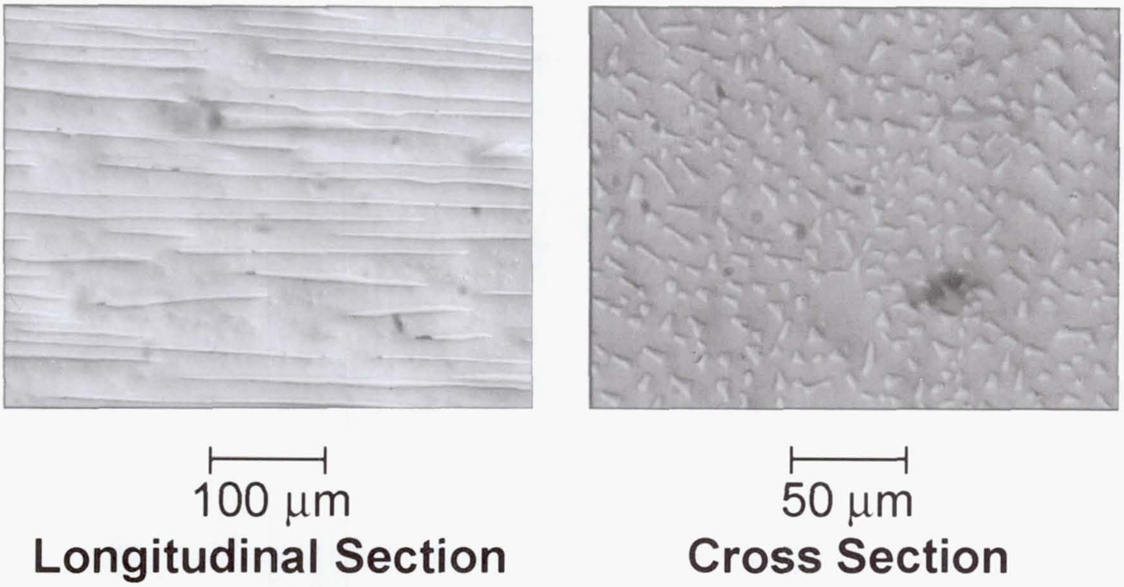

Figure 3. Dependence of Vertical and Horizontal Gradients on Magnetic Field Strength

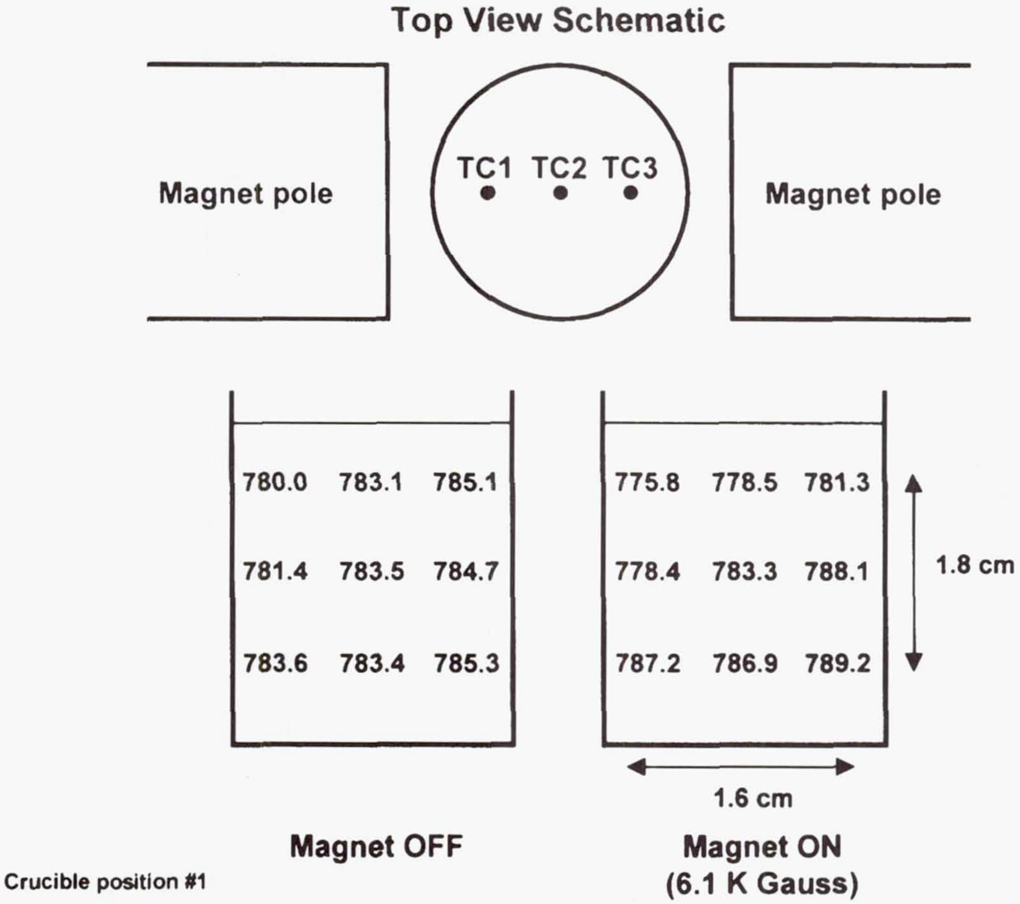

Figure 4. Temperature profiles of Damped and Undamped Melt

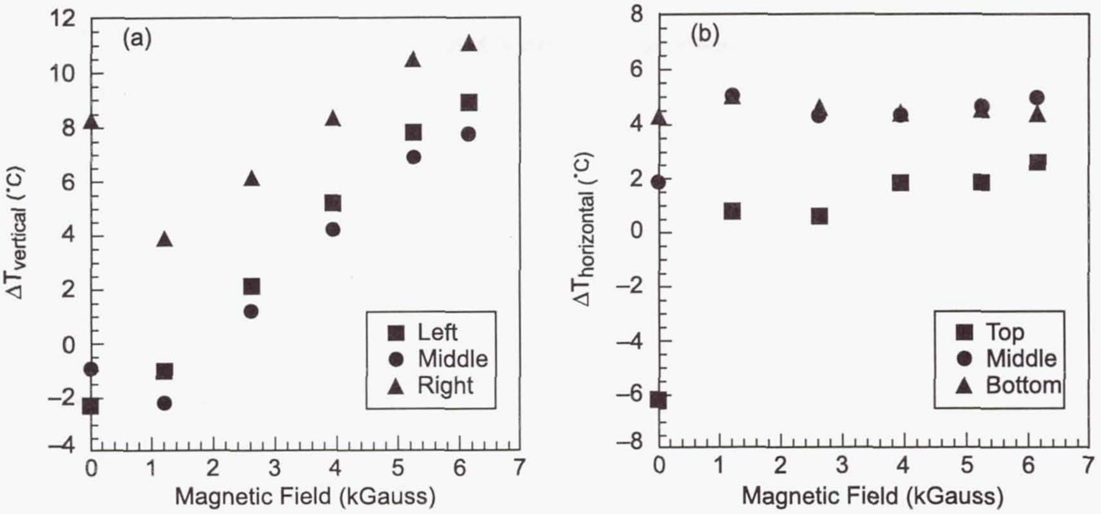

Figure 5. Dependence of Melt Temperature on Magnetic Field Strength (Crucible position #2)

Table 1. Summary of Microstructural Characterization

- Magnetic damping refines microstructure, 30% effect @ 6 kG
- Magnetic damping increases rod length by 250-300%
- Slow rotation improves on-wafer uniformity, FOM down to 10%

Page intentionally left blank

EFFECTS OF MICROGRAVITY ON THE FORMATION OF AEROGELS

A. J. Hunt, M. R. Ayers,
Lawrence Berkeley National Lab.,
University of California,
Berkeley, CA 94720
510-486-5370; ajhunt@lbl.gov

R. J. Cronise, D. A. Noever
NASA/Marshall Space Flight Center
Huntsville, AL 35812
256-544-5493
Raymond.Chronise@.msfc.nasa.gov

L. Sibille
Universities Space Research Association,
NASA/Marshall Space Flight Center,
Huntsville, AL 35812
256-544-5221
Laurent.Sibille@.msfc.nasa.gov

Introduction

This paper describes research to investigate fundamental aspects of the effects of microgravity on the formation of the microstructure of metal oxide alcogels and aerogels. We are studying the role of gravity on pore structure and gel uniformity in collaboration with Marshall Space Flight Center (MSFC) on gelling systems under microgravity conditions. While this project was just initiated in May 1998, related research performed earlier is described along with the plans and rationale for the current microgravity investigation to provide background and describe newly developing techniques that should be useful for the current gellation studies

The role of gravity in materials processing must be investigated through the study of well-mastered systems. Sol-gel processed materials are near-perfect candidates to determine the effect of gravity on the formation and growth of random clusters from hierarchies of aggregated units. The processes of hydrolysis, condensation, aggregation and gellation in the formation of alcogels are affected by gravity and therefore provide a rich system to study under microgravity conditions. Supercritical drying of the otherwise unstable wet alcogel preserves the alcogel structure produced during sol-gel processing as aerogel. Supercritically dried aerogel provides for the study of material microstructures without interference from the effects of surface tension, evaporation, and solvent flow.

Aerogels are microstructured, low density open-pore solids. They have many unusual properties including: transparency, excellent thermal resistance, high surface area, very low refractive index, a dielectric constant approaching that of air, and extremely low sound velocity. Aerogels are synthesized using sol-gel processing followed by supercritical solvent extraction that leaves the original gel structure virtually intact.

These studies will elucidate the effects of microgravity on the homogeneity of the microstructure and porosity of aerogel. The presence of poorly controlled microporosity in aerogel leads to material non-uniformity that gives rise to increased light scattering. Investigation of the effect of gravity driven solute flows within microclusters and their effect on condensation and agglomeration reactions will enable us to improve the preparation and properties of aerogel. Increased clarity of images viewed through aerogel and decreased scattering from the pores of aerogel will significantly improve the prospects for large-scale adoption of aerogel in such applications as transparent insulating windows, high performance thermal insulation, and Cherenkov detectors.

Experimental Method

We are investigating alternative methods to initiate gellation in alkoxide sols. In conventional sol-gel processing, catalysts are introduced in the water-containing phase prior to initiating the reactions by mixing with the alkoxide. Our new approach involves ultraviolet radiation to control the catalysis. This approach was developed for two principle reasons. First, to study the effect of controlling catalysis and associated solvent releases and heat generation in microgravity conditions. Ultraviolet initiated catalysis offers a unique ability to effect the rate of gellation and condensation reactions on demand. Secondly, the approach is better suited to space based experimental conditions. Rapid mixing of the alkoxide-solvent and water-solvent-catalysis solutions is usually achieved by modified syringe pump setups that break a membrane between two opposing volumes and rapidly mix the two components. This process is often associated with bubble formation that can persist in microgravity conditions. These bubbles interfere with several sample analysis techniques used to determine material properties.

Short-wave UV is capable of cleaving many of the bonds found in alkoxide-based silica sols, such as, O-H, O-R, C-C, and C-H. However, the only effects of UV on SiO_2 gels has been reported for thin-films [1, 2]. In these cases, UV exposure significantly increased the rate of gellation and the densification of the final xerogel. However, the effects of UV on the microstructure and porosity of large silica monoliths was not reported until this work.

The effects of pH on gel microstructure, porosity, and clarity have been reported earlier [3-6]. These show a strong dependence on pH in both primary particle growth and aggregation of particles and clusters into a gel. Additionally, even small amounts of acid or base catalysts greatly increase the rate of gellation in alkoxide-derived silica sols. As we desired to study sols with long gel times, we studied the effects of UV on sols with no added catalyst, and report the microstructural characteristics of the resulting gels and aerogels, determined by light scattering, surface area measurements, TEM and x-ray diffraction.

Gel preparation utilized precondensed TEOS (“Silbond H-5”, Silbond Corp.), anhydrous ethanol (UV grade), and high purity water. The sol was prepared by mixing two solutions prepared from the starting compounds. The mixed sol was divided into 4 equal portions and poured into fused-silica tubes and sealed by PTFE plugs with viton o-rings. Samples were exposed to ultraviolet light from two 15 Watt germicidal Hg-vapor lamps, in an enclosed light-box. Samples were exposed for various lengths of time (T_{UV}), including, no exposure, 5 hours, T_{UV} = gel time and continuous exposure. After exposure, the samples were kept in the dark. The temperature of the samples in the light box were kept constant at about 25 ^{o}C).

The evolution of light scattering with time was measured at 532 nm with a doubled Nd-YAG c.w. laser at a 90^{o} scattering angle. Samples were removed from UV exposure at regular intervals and their scattering measured and calibrated against a sealed CS_2 standard. When the scattering intensity stabilized with respect to time for all samples, the gels were removed from their holders and soaked in 30% H_2O/ethanol for 48 hours. Water was removed from the gels by four successive soaks in 200 proof ethanol for 24 hours each. The aged alcogels were dried using standard CO_2-substitution and supercritical drying in a 300 ml Polaron critical-point dryer. Single-point B.E.T. surface area measurements of the dried aerogels were obtained from the desorption isotherm of 30% N_2/He using a Quantasorb analyzer. UV-visible transmission spectra, X-ray diffraction powder patterns, and high resolution TEM images were taken. Samples for TEM analyses were ground in acetone, and evaporated onto holey carbon-Cu grids.

Results and Discussion

Table 1 lists several physical of the characteristics of UV-catalyzed neutral silica sols, gels, and aerogels. First, a significant decrease in the gel time (to about one third) is observed with continuing UV irradiation times. This is consistent with a general increase in the rate of hydrolysis and condensation reactions leading to gellation.

Table 1. Characteristics of UV catalyzed sol, gel, and aerogels.

Sample	**T_{UV}**	**T_{GEL}**	**~Slope**	**$\%T = A\exp(-Bt/l^4)$**		**Surface area**
	hours	hours	(scat. vs. time)	(A)	(B)	m^2/gm
1	0	720	6	0.5762	0.3260	480
2	5 (<<T_{GEL})	720	6	0.5570	0.3370	550
3	250 (= T_{GEL})	250	6, then 2	0.5724	0.3651	520
4	1900 (>>T_{GEL})	250	6	0.5504	0.3790	400

Light scattering is an effective monitor of the evolving structure of gel systems [7]. The technique is most sensitive during the formation of clusters and their aggregation into a network gel [8]. The growth characteristics of these clusters can be observed by plotting the log of the scattering intensity vs. the log of time. Spherical or compact cluster growth has a characteristic a slope of six (acid catalyzed) and linear growth in higher surface charge conditions produces a slope of two (base catalyzed) [7]. This occurs because volume evolves as the cube of time for spherical growth (and polarizability to the sixth power), while linear growth produces a first power volume (and second power polarizability) increase with time. In this study, the neutral silica sols all show a slope of six, consistent with the formation of weakly acidic Si-OH groups formed by the initial hydrolysis of Si-OR groups. A dramatic exception to this is seen when UV light exposure is ceased at T_{GEL} wherein the slope changes to two when UV is discontinued. As the aggregation of clusters during gellation is controlled by the surface potential of the clusters, it is likely that recombination products of photo-degraded species increase the surface charge on growing clusters. This in turn affects the formation behavior by shifting the manor of assembly from cluster like to chain like aggregation.

Light scattering from internal features such as the large pore fraction is the primary cause of the wavelength-dependent Rayleigh scattering and result in the bluish cast of dried silica aerogels[9]. Larger features, in the aerogel such as surface damage due to solvent flows, scratches, and larger occlusions such as bubbles, can also contribute to scattering. These two effects can be separated and quantified using the equation [7]:

$$T = A \exp(-Bt / \lambda^4)$$

where T is the % transmittance of an aerogel of thickness, *t,* at a wavelength, l, and A and B are constants. Fitting the UV-visible spectrum of an aerogel to this equation gives A (the wavelength independent portion of scattering, due to large features) and B (the wavelength dependent portion, due to the internal gel structure). Values of A and B appear in Table 1. All samples show an increase in B with longer UV exposure, indicating a coarsening of the gel structure due to UV light. A general decrease in surface area of the dried aerogels is also seen with prolonged UV exposure of the alcogel. Both of these effects indicate an enhancement of dissolution and re precipitation reactions leading to both pore and particle growth.

TEM images for dried aerogels where $T_{UV} = T_{GEL}$, and $T_{UV} >> T_{GEL}$ show rather large primary particles (compared to base-catalyzed aerogels) in accord with the lower surface area of these aerogels. The image of the $T_{UV} = T_{GEL}$ sample shows a rather open structure as anticipated for a gel with a certain amount of linear cluster aggregation. The sample with $T_{UV} >> T_{GEL}$ shows a more dense compacted structure, consistent with spherical cluster growth. Both samples appeared predominantly amorphous to the electron beam. However, *some areas* of the sample $T_{UV} = T_{GEL}$ showed higher levers of crystallinity.

The X-ray powder patterns showed typical amorphous pattern for samples with $T_{UV} = 0$, $T_{UV} >> T_{GEL}$. However, the $T_{UV} = T_{GEL}$ sample shows a significantly different pattern, that is very broad (as expected for <10 nm particles), but similar to that found for dehydrated $H_2Si_4O_8$ precipitates [10]. Long-term aging of sol-gel sodium aluminosilcate gels has been shown to form increased numbers of crystallization nuclei compared to gels dried soon after gellation [11]. However, in our study, crystallinity is only observed when UV exposure was ceased at the gel point, and then only in a portion of the aerogel. It is likely that UV exposure forms dense SiO_2 particles by enhancement of internal condensation reaction of surface -OH groups. These particles can then act as crystallization centers as particle growth continues very slowly after ceasing UV exposure.

Future Plans

Increased comprehension of gel formation processes will benefit the broad understanding of sol-gel chemistry. In particular, the clarification of the effect of solvent flows on cluster growth and gel aggregation processes measured under microgravity conditions in KC 135 and shuttle flights will help settle controversy over which of the various models of gel formation is correct. Time resolved light scattering measurements will be used in studies of sol growth and gel formation. Additional measurements on supercritically dried aerogels including angle and polarization dependent Mueller scattering matrix determination, High Resolution Transmission Microscopy, x-ray, and BET pore size analysis will provide detailed information as to the uniformity and size of the micropore structure. Thus, research into microgravity effects will advance both practical applications for aerogel as well as fundamental sol-gel science. Aerogel is being developed for a range of applications in the commercial and aerospace arenas. Thus improvements in processing gained through microgravity research can be used to produce better aerogel products.

References

1. Van de Leest R.E., App. Surface Sci. 86 278(1995).
2. Niwano M., Kinashi, K., Saito K.,Miyamoto N., and Honma K., J. Electrochem. Soc. 141 1556(1994).
3. Brinker C.J., and Scherer G. W., **Sol-Gel Science** (Academic Press, San Diego, 1990).
4. Cao W., and Hunt A. J., J. Non-Cryst. Solids 176 18(1994).
5. Tewari P. H., Hunt A. J., K.D. Lofftus, and Lieber J. G., M.R.S. Symp. Proc. 73 195(1986).
6. Russo R.E., Hunt A.J., J. Non-Cryst. Solids, 86 219(1986).
7. Hunt A. J., J Non-Cryst. Solids, in press (1998).
8. Lofftus K. D., K.V.S. Sastry, A.J. Hunt, Advanced Materials Proceedings 229(1990).
9. Hunt A. J., and Berdahl P., **Better Ceramics Through Chemistry**, Vol 32, North Holland Press, New York, 275(1984).
10. Lagaly, G., Beneke, K., Kammermeier, H., Z. Naturforsch., B: Anorg, Chem., Org. Chem 34B(5) (1979) 666.
11. Cook J. K., Thompson R. W., Zeolites 8 322(1988).

Page intentionally left blank

NON-EQUILIBRIUM PHASE TRANSFORMATIONS

Kenneth A. Jackson, P.I.
Department of Materials Science and Engineering
University of Arizona
4715 East Fort Lowell Road
Tucson, AZ 85712
(520) 322-2981
kaj@shadow.aml.arizona.edu

Objectives

The goal of this research is to develop an understanding of the structure and properties of multi-component materials produced by phase transformations which occur under conditions which are far from equilibrium. These conditions often produce segregation effects and microstructures which are quite different from those produced by near-equilibrium transformations. The development of a sound physical understanding of these non-equilibrium phase transformations in alloys is perhaps the most important and challenging outstanding basic problem in materials science today. There have been many experimental studies designed specifically to explore this regime, but the underlying physical processes have not been properly understood. Ad hoc equations have been used to fit experimental data and these have remained essentially unchanged for the past decade. We are using Monte Carlo modeling based on the Ising model to study these crystallization processes in alloys. These are similar to the simulations which played a major role in developing our understanding of the atomic level processes which control the crystallization of pure materials. The computer modeling provides a powerful tool to help us to understand the experimental results, to develop a detailed understanding of the processes involved, and as a predictive tool for guiding experiment.

Microgravity

The field of Materials Science centers on the control and characterization of the properties of materials. Crystallization is a primary method used to control both the structure (e.g. phase distribution, degree of crystallinity, grain size) and composition (e.g. segregation effects). The standard quasi-equilibrium description of crystallization of alloys works well near equilibrium, but there is considerable experimental evidence demonstrating that it does not work at large undercoolings or supersaturations, where glasses crystallize, and where many of the commercial powders used in powder metallurgy and ceramics are formed.

Projects supported by NASA are making major experimental contributions to our understanding of nucleation and crystallization in the regime where these effects are important, including the microstructure of rapidly solidified small droplets, the growth rate discontinuities observed during dendritic solidification of alloys, the extended solid solubility ranges observed due to rapid solidification, and the distribution of the component elements resulting from nucleation and growth in containerless processing. Our simulations and modeling provide a new framework for the interpretation of these experiments.

Significant Results

Monte Carlo modeling using a Spin-1 kinetic Ising model has been used to simulate non-equilibrium binary alloy solidification. The simulations are based on bond energies derived from the equilibrium properties of the alloy system to be modeled. In the simulations, the atoms can make random diffusive motions in the liquid [1-5], and join or leave the crystal at random with probabilities based on their local bonding environment. The algorithms are very simple in principle, but result in realistic behavior, as illustrated in figure 1.

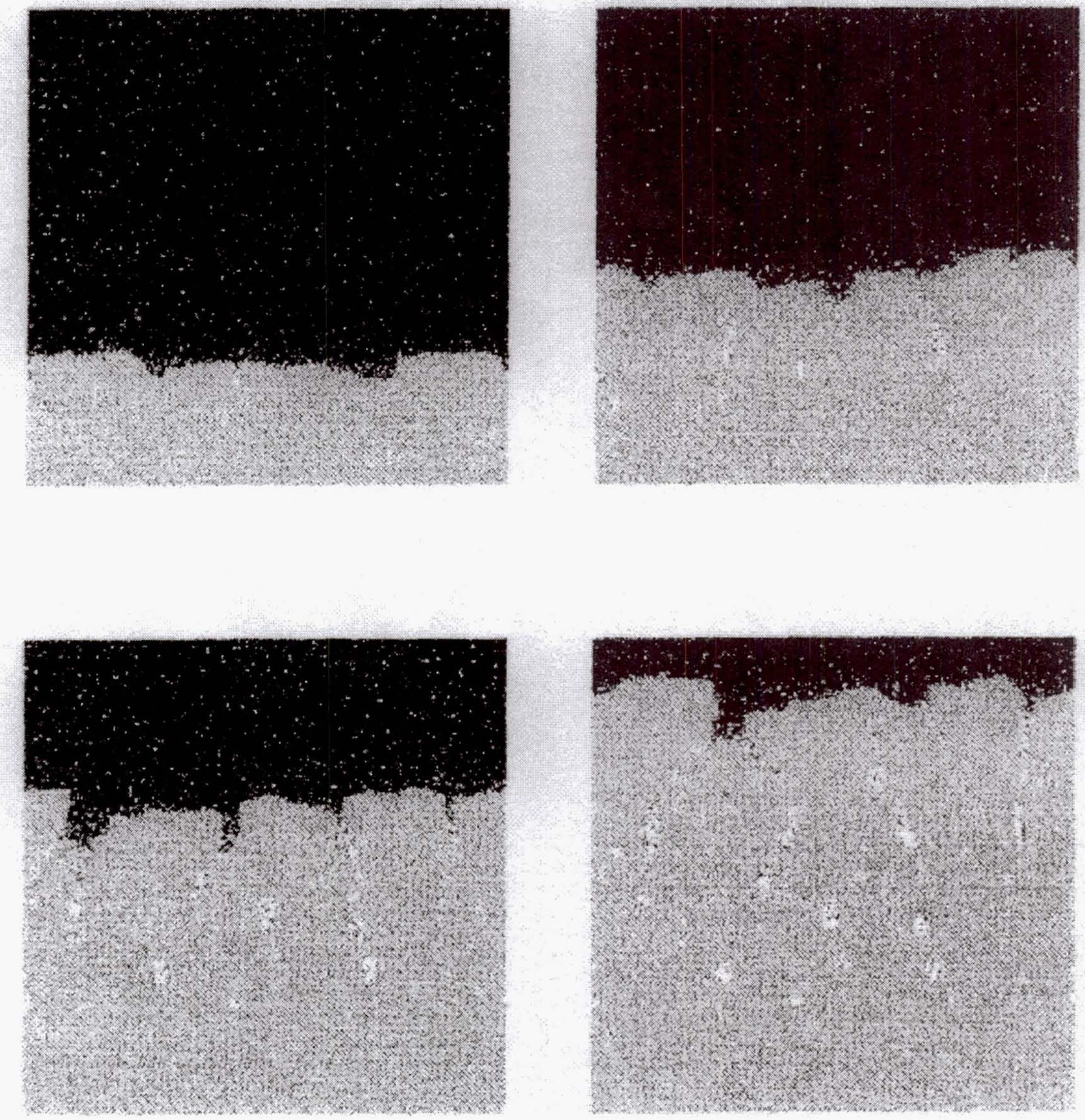

Figure 1. *Typical configurations for four sequential positions of an interface during growth. The liquid atoms of the primary component are black, the solid atoms of the primary component are gray, and the dopant atoms are white. The interface becomes unstable, depressions rich in dopant develop, and pockets of liquid form which contain high concentrations of the dopant.*

Simulations have been carried out for various growth temperatures, growth rates, surface roughness, liquid diffusivities, equilibrium segregation coefficients, entropies of fusion, and compositions of the liquid. The non-equilibrium segregation coefficient, **k** (the ratio of the solid composition to the liquid composition at the interface), increases with increasing growth velocity, and decreasing liquid diffusivity and surface roughness. Overall, the Monte Carlo results are consistent with experiment. The non-equilibrium segregation coefficient was also found to increase with concentration of the liquid, but the effect is small at low concentrations.
For simulations of the growth of pure silicon, the bonding structure was based on the diamond cubic crystal structure, and the roughening transition was scaled to correspond to the experimental roughening transition. Growth on the (111) face at small undercoolings depended on the rate of nucleation of new layers, as expected on a faceted interface. Figure 2 is a plot of the growth on the (111) face as a function of time at several different temperatures. The time scale

was compared directly with experiment by matching growth on the (100) face to the measured solidification rate of (100) silicon. The mean time between nucleation events can be determined from these data. This nucleation rate was fitted to a poly-nuclear growth model, resulting in a specific step free energy which was about 10% of the specific surface free energy. Extrapolation to Czochralski growth rates gives an undercooling of about 5° for the (111) facet, which agrees well with estimates based on experiment.

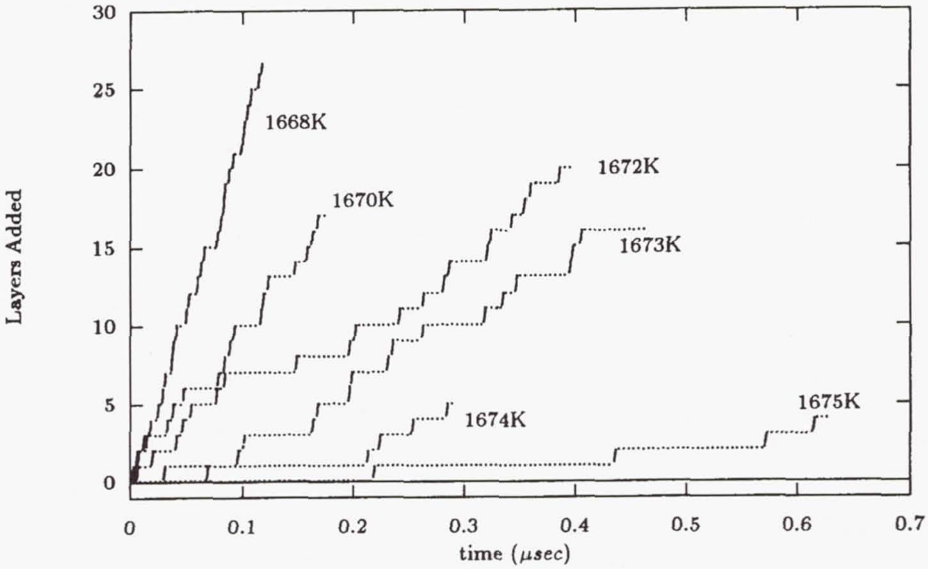

Figure 2. *Number of layers added to the crystal as a function of time for growth normal to the (111) face of silicon. The melting point of silicon is 1688° K and the growth temperatures are indicated.*

The non-equilibrium distribution coefficient was investigated as a function of orientation for various growth rates using simulations [4]. The thermodynamic properties and crystal structure were chosen to correspond to bismuth-doped silicon, with an equilibrium **k**-value of 7×10^{-4}. Values for **k** were obtained as a function of growth rate for several orientations of the solid/liquid interface along the zone axis between [111] and [100], as shown in figure 3. For the same growth rate, **k** was found to be greatest for solid/liquid interfaces parallel to the (111) plane, as is found experimentally. The orientation dependence of the **k**-value in the simulations compares well with the experimental orientation dependence reported by Aziz et al. [6], although there is a discrepancy in the growth rate dependence. The kink site density at the interface was determined and found to depend on orientation in the simulations, and on undercooling for the (111) face. The net growth rate at the kink sites was found to vary linearly with undercooling, as expected, and the overall growth rate was found to be the product of the step density and kink-site velocity. The incorporation of dopant was found to depend on the parameter β, which is discussed below.

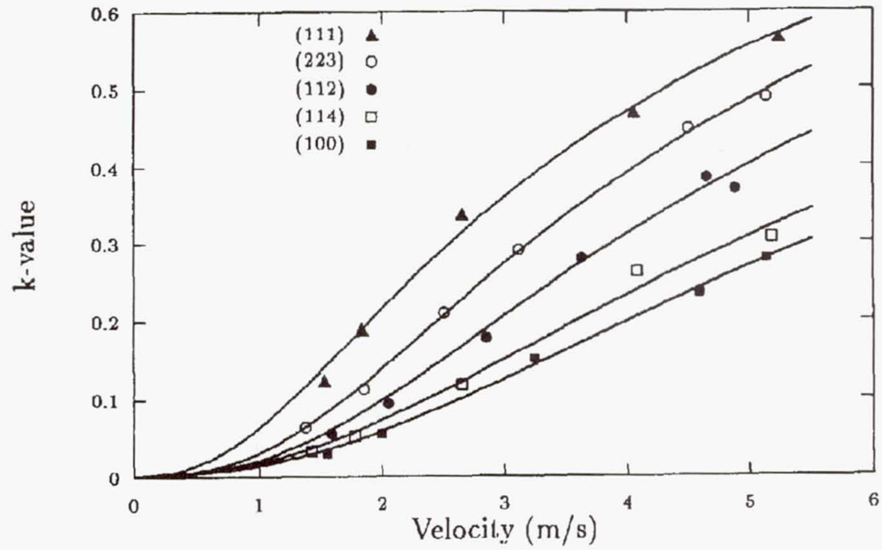

Figure 3. *Simulation results for the growth rate and orientation dependence of the distribution coefficient in bismuth doped silicon.*

Analytical Model

A novel analytical model for the non-equilibrium incorporation of dopants during crystallization has been developed. The model relies heavily on insights gained from the Monte Carlo computer simulations. It is based on a physical picture of the ability of the interface to transfer, between species, the chemical potential required for crystallization. This happens when a dopant atom cannot move fast enough to escape the advancing interface. The model has three parts. The first is a pair (for a binary alloy) of equations, one for the rate of crystallization of each component of the alloy, which incorporate the possibility of the transfer of the "chemical potential for crystallization" between the species at the interface. These equations are based on the standard expression for the growth rate of a pure material, and they reduce to the usual thermodynamic description of the alloy system at equilibrium. The second component is the relationship between the crystallization time for a fluctuating interface and the diffusional jump time, which sets the relative time scale for a dopant atom to escape from the advancing interface. This relationship is embodied in the parameter $\beta = av\Delta\mu/Dk_BT$, where a is the interatomic spacing, v is the growth rate, $\Delta\mu$ is the chemical potential difference driving the crystallization process, D is the diffusion coefficient, and k_BT is Boltzmann's constant times the temperature. For a rough interface, the growth rate **v** is proportional to the driving force, $\Delta\mu$, so that for this case, β is proportional to v^2/D. The same relationship had been found earlier by Temkin [7] in his analyses of alloy crystallization. The third component of the model depends on the motion of dopant atoms at the interface within the time allowed by the advancing interface. This depends on the details of the interface configurations, and, although the general features of this relationship are clear, its detailed functional form can apparently vary somewhat.

The analytical expressions for the growth velocity were developed to closely match the Monte Carlo simulation data. The equation for the net growth rate of the **A** component of a binary alloy is given by:

$$v_A = v_A^0\left[C_A^L - C_A^S \exp\left(\frac{(1-P)\Delta\mu_A^0 + P\Delta F^0}{k_BT}\right)\right] \qquad (1)$$

and for the **B** component is given by:

$$v_B = v_B^0\left[C_B^L - C_B^S \exp\left(\frac{(1-P)\Delta\mu_B^0 + P\Delta F^0}{k_B T}\right)\right] \tag{2}$$

Here the C's are the concentrations of the A and B components in the solid (S) and liquid (L) at the interface, $\Delta\mu_i$ is composition-dependent difference in chemical potential between the solid and the liquid for the corresponding species, $\Delta F^0 = C_A^S\Delta\mu_A^0 + C_B^S\Delta\mu_B^0$ is the free energy difference between the solid and the liquid. The superscript 0 on the chemical potential and free energy differences indicate that the explicit concentration terms are not present.

The quantity P is related to a "trapping probability", given approximately by

$$P \approx \frac{A\beta^g}{1 + A\beta^g} \tag{3}$$

where A is a constant, and $g \approx 1/2$.

At equilibrium, $v_A = 0 = v_B$, and $\beta = 0$, so that $P = 0$, and equations 1 and 2 reduce to the usual equality of chemical potentials in the two phases for each species at equilibrium: $\Delta\mu_A = 0 = \Delta\mu_B$. These equations also reduce to the quasi-equilibrium model for alloy crystallization for $P << 1$.

P approaches 1 for large β, when diffusion is very slow compared to the growth rate. $P = 1$ for diffusionless growth ($D = 0$), in which case the atoms crystallize without diffusive motions. The composition does not change during crystallization, and so $C^L = C^S$ for both species. The concentrations can be taken out of the square brackets in equations 1 and 2, making both equations similar. The growth rate for both species goes to zero when $\Delta F^0 = 0$, which defines the temperature $\mathbf{T_0}$.

Eqns. 1 and 2 can thus be used to calculate a variety of "kinetic" phase diagrams, depending on the magnitude of the magnitude of P. $P = 0$ gives the equilibrium phase diagram, and for $P = 1$, the solidus and liquidus lines collapse onto the $\mathbf{T_0}$ line. Intermediate values of P give a range of "kinetic" phase diagrams going continuously between these two limits. These "kinetic" phase diagrams define the extended range of solid solubilities to be expected during rapid quenching as well as the non-equilibrium distribution coefficient.

A simple approximate expression for the distribution coefficient for component B can be derived from equations 2 and 3:

$$k \approx k_e^{\frac{1}{\left(1 + A\beta^g\right)}} \tag{4}$$

where $\mathbf{k_e}$ is the equilibrium distribution coefficient.

The orientation dependence of the **k**-value shown in figure 3 arises because there is a different relationship between the growth rate and the undercooling (or $\Delta\mu$) for a smooth interface such as the silicon (111) interface and a rough interface such as the silicon (100) interface. For a smooth interface, a larger $\Delta\mu$ is required for the same overall growth rate, (the step velocity, which depends linearly on $\Delta\mu$, must be faster because the step density is smaller) and so the **k**-value is larger than for the rough interface, as illustrated in figure 3. When plotted as a function of $\beta = av\Delta\mu / \Delta k_B T$, all of the data for the various orientations in figure 3 superimpose [4].

Summary

The model outlined above predicts a non-equilibrium **k**-value which compares well with Monte Carlo computer simulations and with experimental results. The quantities involved in β are known or can be estimated for many systems, and so the magnitude and onset of non-equilibrium effects can be predicted from these equations. Although relevant experimental data are limited, the factor A in equations 3 and 4 seems to be independent of alloy system within the limitations imposed by uncertainties in the values of the materials parameters involved. The model seems to have significant predictive capabilities, and can be used to predict velocity-dependent "kinetic" phase diagrams, which define the range of applicability of the quasi-equilibrium model and can be used to predict the extended solid solubilities found during rapid crystallization, as well as non-equilibrium distribution coefficients.

References

[1] K. A. Jackson, G. H. Gilmer, D. E. Temkin, J. D. Weinberg and K. Beatty, J. Crystal Growth, 128 (1993) 127.
[2] K. A. Jackson, G. H. Gilmer and D. E. Temkin, Phys. Rev. Lett. 75 (1995) 2530.
[3] K. A. Jackson, G. H. Gilmer, D. E. Temkin, and K. M. Beatty, J. Crystal Growth, 163 (1996) 461.
[4] K. M. Beatty and Kenneth A. Jackson, J. Crystal Growth, 174 (1997) 28.
[5] K. M. Beatty, Ph. D. Dissertation, University of Arizona, 1997.
[6] M.J. Aziz and C.W. White, Physical Review Letters 57 (21), 2675-2678 (1986).
[7] D. E. Temkin, Sov. Phys. Cristall., 17 (1972) 405.

Physical Properties and Processing of Undercooled Metallic Glass Forming Liquids, W.L. Johnson, D.S. Lee, C. Hays, and J. Schroers, 138-78 Keck Laboratory of Engineering, California Institute of Technology, Pasadena, CA 91125

Abstract

The High Vacuum Electrostatic Levitation (HVESL) technique as developed by Rhim and collaborators at Jet Propulsion Laboratory provides a method of levitating metallic alloy droplets of size ranging up to several mm under high vacuum conditions with relatively quiescent conditions. The levitated sample can be heated and melted using either a focused quartz lamp or a laser. When combined with non contact temperature measurements, such a system provides an ideal platform for the study of liquid metals and alloys under ultra-clean and containerless conditions. The HVESL method has been initially applied to the study of the undercooling behavior and thermophysical properties of metallic glass forming liquids in both the equilibrium liquid and undercooled states. Studies of crystal nucleation and growth kinetics in undercooled glass forming liquids have enabled direct measurements of the CCT and TTT-diagrams throughout the undercooled liquid range for a number of bulk metallic glass forming systems. As a representative example, technique has been used to directly quantify the influence of low level impurities (e.g. oxygen) on the crystal nucleation kinetics in a bulk metallic glass forming system. Preliminary experiments, suggest that it is feasible to implement an AC modulation calorimetry measurement on the HVESL platform. We are also examining the potential use of the HVESL platform to carry out studies of atomic diffusion and thermal transport in bulk metallic glass forming liquids.

Objectives

The objective of this work is to carry out undercooling studies and thermophysical property measurements on liquid metallic alloys which form bulk metallic glasses. Specifically, we will carry out the following types of measurements:

1) Time-Temperature-Transformation (TTT) diagrams and Continuous Cooling Transformation (CCT) diagrams for the crystallization kinetics of the glass forming liquids.

2) AC Modulation Calorimetry measurements to determine the specific heat and thermal conductivity of the equilibrium and undercooled liquid alloys.

3) Molar volume measurements using high resolution imaging of the liquid drop.

4) Measurements of atomic diffusion constants in the undercooled liquid state over the temperature range from the glass transition to the thermodynamic melting point of the crystalline phases.

Background

In recent years, bulk metallic glass forming alloys have been developed for which the liquid alloys solidify to the glassy state at low cooling rates. The nucleation an growth of crystalline phases from the undercooled melt is exceedingly sluggish in these systems.

The High Vacuum Electrostatic Levitation method (HVESL) method provides a platform for containerless processing of relatively large liquid droplets (3mm diameter) using laser heating and non-contact temperature measurements under high vacuum conditions. In turn, this allows one to control the influence of heterogeneous nucleation (at the container wall or on foreign particles) and obtain optimum conditions for undercooling. As applied to bulk metallic glass forming alloys, the HVESL permits measurements of a variety of physical properties, e.g. specific heat [1,2] , thermal conductivity [1,2] , viscosity, surface tension, thermal expansion of the liquid [3], and atomic diffusion coefficients, through the entire undercooled liquid range. The proposal to use ESL in the determination of atomic diffusion coefficients is to our knowledge, a new and novel approach to studying transport in liquids as one approaches the glass transition from higher temperatures. It offers the opportunity to test current theories of atomic diffusion and its relationship to the fluidity of liquids.

Experimental Methods

Our earliest ESL studies [4,5] were carried out in collaboration with Dr. W. Rhim of Jet Propulsion Laboratory using the JPL ESL facility. More recently, we have used the HVESL facility currently located at Marshall Space Flight Center and originally developed at Loral Space Systems (Palo Alto, CA) by A.J. Rulison and J. Watkins. to carry out studies of metallic glass forming liquids. Here, we confine our attention to recent work at the Marshall facility. This facility is described in detail by Rulison et. al. [6]. The Marshall HVESL was used to process two bulk glass forming alloys:

1. $Ti_{34}Zr_{11}Cu_{47}Ni_8$ (Vit 101)
2. $Zr_{57}Nb_5Ni_{12.6}Al_{10}Cu_{15.4}$ (Vit 106)

These alloys are referred to as Vitreous Alloys 101 and 106 (Vit. 101 for short). Prior to all processing the ESL chamber is evacuated with a turbo molecular pump to a pressure of 2-5 x 10^{-7} mbar. The levitated samples are heated by a continuous wave 50 W, Nd:YAG laser operating at 1.064 μm. The laser beam is focused with a silica lens down to a spot size of about 1-2 mm diameter. The heating laser power is varied by a 0-5 V analog control signal. The specimen temperature is monitored remotely with a single color optical pyrometer that uses a thermoelectrically cooled InGaAs detector with built in preamplifier. For control of the experimental temperature, the pyrometer emissivity setting is held constant throughout the experiments and initially set to obtain agreement with the known melting point (solidus temperature) of each alloy. Other details of the experimental set up can be found in ref. [6].

The samples used in these studies were prepared from high purity elemental metals using an arc melting system equipped with a turbo-molecular pump to achieve base pressures in the 10^{-7} mbar range and high purity (1ppm) argon gas when conducting melting. Small pieces (typically 35-60 mg) of the arc melted button (typically 10-25 grams) are then remelted in a hemispherical indentation on the base plate of the arc melter to produce a roughly spherical specimen of diameter ranging from 2-3 mm. These samples were then deployed in the HVESL.

Results

In the present paper, we present selected results which illustrate the capabilities of the HVESL in the study of these glass forming alloys. Our earliest studies have focused on determining the undercooling behavior of melt. A typical melting an undercooling cycle for Vit 101 is shown in Fig. 1. The example shown was melting cycle 33. the sample has already undergone previous melting and solidification cycles. The figure shows the laser control voltage vs. time as well as the measured sample temperature vs. time. The sample is initially heated to a temperature of 1480 K with a laser power in the 10 W range (control voltage of ~4V). The laser power is then dropped to less than 0.1 W (control voltage less than 3 V) and the sample undergoes free radiative cooling to an undercooling of ΔT ~ 220 K (T = 940 K) with respect to the known liquidus temperature (1160 K) of the alloy. This is followed by a recalescence event and subsequent further cooling of the solid. The crystallized sample is then reheated through the melting transition when the laser power is once again increased to its initial value.

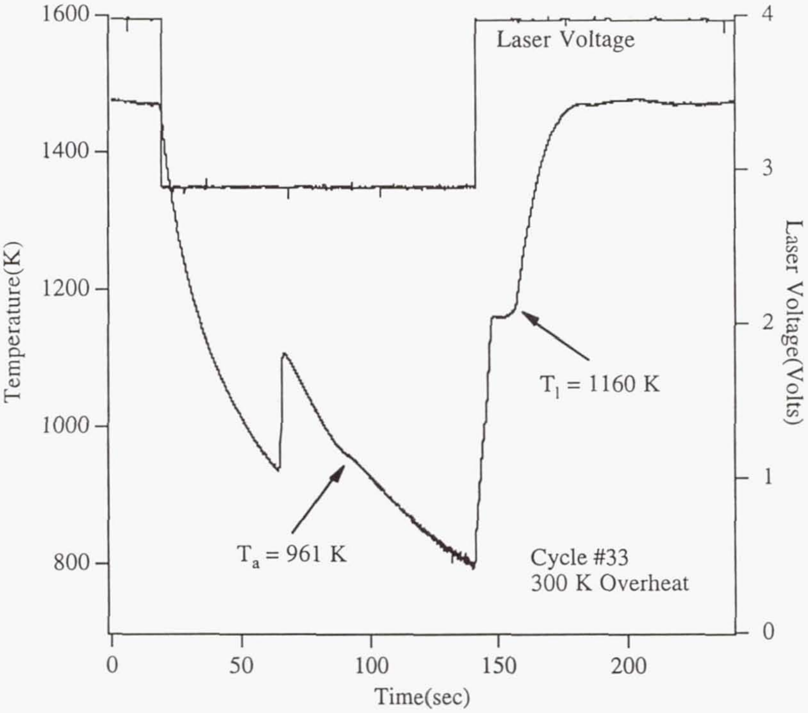

Fig.1 Example of a melting and undercooling cycle carried out on a Vit. 101 sample in the HVESL

The undercooling obtained varied during processing and was generally found to increase with increasing number of melt cycles and increasing amounts of "overheat". Here, "overheat" refers to the maximum temperature (with respect to the liquidus temperature of 1160 K) reached by the molten alloy prior to free radiative cooling. Undercooling results for the Vit 101 sample are displayed in Fig. 2 as a function of the number of melt cycles. The various symbols refer to the degree of overheating used in each cycle. Note that the last cycle was carried out with only 100 K of overheat. The undercooling is nearly the same as the next last melting cycle in which 300 K of overheating was used. This demonstrates that the increased undercooling observed after repeated melting does not directly depend on overheat and suggest that heterogeneous nucleants in the sample are gradually dissolved and eliminated by repeated melting. For such samples, the degree of undercooling depends on previous processing and suggests

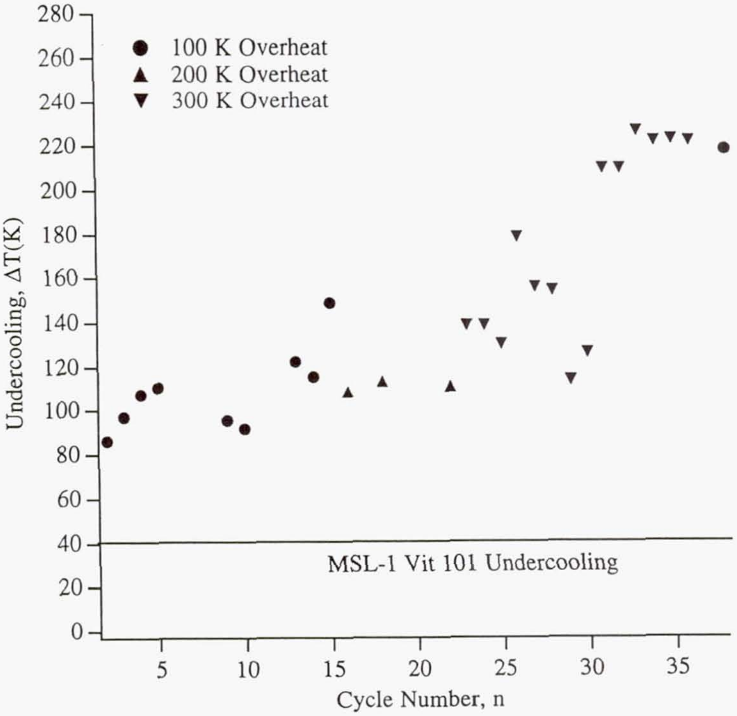

Fig. 2 Undercooling achieved in a Vit. 101 sample in the HVESL as a function of melting cycle number. Various symbols indicate he maximum overheat used in each cycle. Undercooling obtained during processing of an 8mm drop in the TEMPUS facility during MSL-1 mission is shown for comparison.

that the achievable undercooling is controlled by heterogeneous nucleants which can be dissolved or "fluxed" away by repeated melting. Further, notice that during the last 5-6 melting cycles, the undercooling behavior did not appear to change further. In fact, it has been found that the maximum achievable undercooling appears to "saturate" after a sufficient number of cycles. In this case, many melting cycles are required to achieve this maximum.

The behavior seen above is not characteristic of all samples studied in the ESL. Other specimens (e.g. Vit 106) show undercooling behavior which becomes reproducible after a small number (1-3) of initial melting cycles. In this case, one can use repeated melting cycles to map a TTT-diagram for crystallization. In such experiments, the sample is initially overheated to a prescribed temperature, then allowed to radiatively cool until a predetermined temperature is reached. At this point, the laser power is toggled up to a level required to a maintain steady state temperature. This power level is determined by initially measuring sample temperature vs. laser power to construct steady state temperature-laser power curve. Using this method, one can obtain a thermal history curve consisting of a free cooling segment followed by an isothermal plateau. On then measures the time elapsed to sample recalescence (onset of crystallization) as a function of the isothermal plateau temperature. Combining these data allows for the construction of a TTT-diagram. The diagram shows the elapsed time to recalescence at various isothermal plateau temperatures. Strictly speaking, the radiative cooling time to reach the plateau cannot be neglected in comparison to the elapsed time at the plateau temperature. As such, the diagram determined is not strictly a TTT-diagram. On the other hand, the radiative cooling segment is identical for all undercooling cycles so that the effect is systematic for all cycles. The TTT-diagram of a Vit 106 specimen so-obtained is shown in Fig. 3. One can clearly observe that two

---

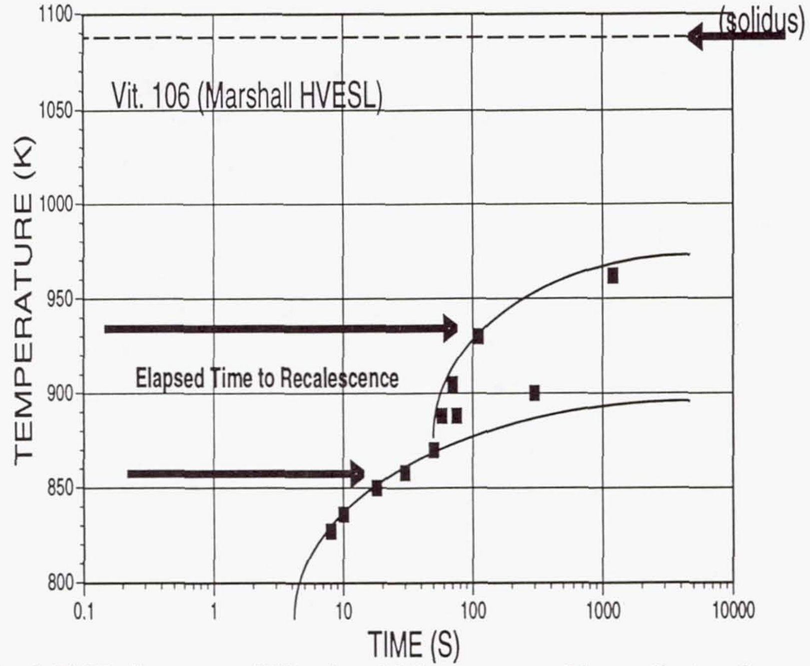

Fig. 3 TTT-diagram of Vitreloy 106 constructed by radiative free cooling followed by isothermal "plateau" curves in the HVESL. Notice evidence of two distinct nucleation events.

independent nucleation events are observed in the TTT-diagram. It is also apparent that to bypass nucleation altogether, one must pass the "nose" of the lower nucleation curve. This nose occurs at a time of several seconds. This suggests a critical cooling rate of the order of 30-100 K/s will be required to form a glass in this alloy (i.e one must cross a temperature interval of the order of 100 K in a time scale of the order of a few seconds).

The above examples illustrate how the ESL can be used to study undercooling and construct TTT-diagrams. These diagrams in turn can be used to determine the experimental time scales available in which to carry out thermophysical properties measurements on the undercooled melt prior to the onset of crystallization. Below we discuss future plans for exploiting this capability.

Thermophysical Properties Studies

We have carried out preliminary experiments to demonstrate the implementation of the AC Modulation Calorimetry (ACMC) technique using the ESL platform [1,2]. To implement the ACMC method on the ESL platform, we use modulation of the laser heating power superimposed on a baseline dc power level. In preliminary work, we have used step modulation of the laser power whereby the laser control voltage is repeatedly toggled between two levels. Using this method, we have been able to measure the external relaxation time constant (τ_1) of sample droplets. The reader is referred to refs. 1 and 2 for details of the method. From these measurements, we have demonstrated that we can accurately measure the ratio c_p/ε of the specific heat to the total hemispherical emissivity of the sample. Further work will evolve calculating the power coupling from the laser beam to the specimen and will allow separation of c_p from ε, this the determination of the sample heat capacity.

Other work involves the development of a method to measure atomic diffusion constants of various atomic species in the undercooled and equilibrium states of the liquid for bulk metallic glass forming alloys. The TTT-diagrams will be used to determine the range of temperatures and time scales which are experimentally accessible for diffusion studies. Specifically, we plan to carry out tracer diffusion studies of Ni, Cu, Al and other species in the liquid glass forming alloys by deploying the tracer elements on the surface of the metallic glass sphere. The sphere will then be levitated and rapidly heated with the laser to a predetermined isothermal plateau temperature. Diffusion of the tracer into the sphere will occur at the plateau temperature. The time scale available for heating and interdiffusion is determined from the previously measured TTT-diagram. Following interdiffusion, the sample will be "quenched" by radiative cooling to capture the diffusion profile of the tracer in the sphere. It is expected that the diffusion profiles will be influence by gravity driven convection in ground-based experiments and by Marangoni convection as well. The importance of Marangoni convection will be determined by the magnitude of temperature gradients within the sample during the heating and isothermal plateau phases of the experiment. Current efforts are focused on assessing the role of gravity driven convection and Marangoni convection on the time evolution of the diffusion profiles and the interpretation of the diffusion data. We will assess the merits and advantages of carrying out such experiments under μg-conditions where gravity driven convection can be avoided.

Summary

We have used the HVESL platform to carry out containerless processing studies of glass forming metallic liquids. We have demonstrated the use of the HVESL to determine TTT- and CCT-diagrams which describe the undercooling behavior and crystal nucleation kinetics of the alloys. Further experiments are under development to utilize the ESL platform to carry out specific heat, thermal conductivity, and atomic diffusion measurements on glass forming alloys.

References

1. H.J. Fecht and W.L. Johnson, Rev. Sci. Instr., **62**, 1299 (1991)
2. R.K. Wunderlich, D.S. Lee, W.L. Johnson, and H.J. Fecht, Phys. Rev., **B55**, 26 (1997)
3. K. Ohsaka, S.K. Chung, W.K Rhim, A. Peker, D. Scrugges, and W.L. Johnson, Appl. Phys. Lett., **70**, 726 (1997)
4. Y.J. Kim, R. Busch, W.L. Johnson, A.J. Rulison, and W.K. Rhim, Appl. Phys. Lett., **68**, 1057 (1996)
5. Y.J. Kim, R. Busch, W.L. Johnson, A.J. Rulison, and W.K. Rhim, Appl. Phys. Lett., **65,** 2136 (1994)
6. A.J. Rulison, J.L. Watkins, and B. Zambrano, Rev. Sci. Instrum., **68**, 2856 (1997)

Thermo-physical Properties of Undercooled Metallic Glass Forming Alloys - An Experiment on MSL-1

S.C. Glade, D.S. Lee, and W.L. Johnson, 138-78 Keck Laboratory, Calif. Inst. of Tech.,
Pasadena, CA 91125

Wunderlich and H.J. Fecht, Technical University Berlin, Inst. of Metals Research, Hardenberstr.
36, PN 2-3, 10623, Berlin, Germany

Abstract

Thermo-physical properties of two bulk metallic glass forming alloys, $Ti_{34}Zr_{11}Cu_{47}Ni_8$ (VIT 101) and $Zr_{57}Nb_5Ni_{12.6}Al_{10}Cu_{15.4}$ (VIT 106), were investigated in the stable and undercooled melt. Our investigation focused on measurements of the specific heat in the stable and undercooled liquid using the method of AC modulation calorimetry [1,2]. The VIT 106 exhibited a maximum undercooling of 140 K in free radiative cooling. Specific heat measurements could be performed in stable melt down to an undercooling of 80 K. Analysis of the specific heat data indicate an anomaly near the equilibrium liquidus temperature. This anomaly is also observed in the temperature dependencies of the external relaxation time, the specific volume, and the surface tension; it is tentatively attributed to a phase separation in the liquid state. The VIT 101 specimen exhibited a small undercooling of about 50 K. Specific heat measurements were performed in the stable and undercooled melt. These various results will be combined with ground based work such as the measurement of T-T-T curves in the electrostatic levitator and low temperature viscosity and specific heat measurements for modeling the nucleation kinetics of these alloys.

Objectives

The primary scientific objective of the experiments conducted in the MSL-1 spacelab mission was the measurement of the specific heat capacity in the stable and undercooled liquid of the two bulk metallic glass forming alloys

$Ti_{34}Zr_{11}Cu_{47}Ni_8$	VIT 101
$Zr_{57}Nb_5Ni_{12.6}Al_{10}Cu_{15.4}$	VIT 106

From the free temperature decay of the specimen between bias temperature T_1 and T_2, the rate of radiative heat loss was measured from which the total hemispherical emmisivity of the specimen as function of temperature can be inferred if the specific heat is known. Furthermore, the method of AC modulation calorimetry employed for the measurement of the specific heat allows the determination of the effective thermal conductivity of the liquid alloy. In cooperation with different scientific groups participating in the TEMPUS experiment on MSL-1, it was also planned to share these specimens for the measurement of the temperature dependencies of specific volume, surface tension, and viscosity.

Background

In recent years, bulk metallic glass forming alloys, which can be produced with dimensions relevant for their use as structural materials, have attracted considerable attention. This is in part due to their improved mechanical properties, such as increased tensile strength, hardness, and corrosion resistance, making these materials interesting candidates for engineering applications. On the other hand, the exceptional stability of these materials in the metastable undercooled melt makes the undercooled liquid amenable to physical investigations not possible before. The formation of metallic glasses by cooling the liquid alloy from temperatures well above the equilibrium melting point depends critically on the cooling rate, or equivalently on the stability of undercooled melt with regard to crystallization. Following classical nucleation theory, the nucleation rate is determined by kinetic factors such as the viscosity, expressing the mobility of atoms or groups of atoms, and by thermodynamic factors, expressing the driving force for the formation of a crystalline nucleus in the melt. The latter is composed of a surface energy term and the difference in the Gibbs free energy between the undercooled liquid and the competing crystalline phase. The Gibbs free energy difference can be obtained from measurements of the specific heat capacity, in the metastable liquid and crystalline phase, and the heat of fusion. Combining the specific heat and viscosity data with measurements of the nucleation kinetics, such as T-T-T curves, can serve to model nucleation kinetics. Thus, differences in the nucleation kinetics and glass forming ability of different alloy compositions may be systematically assessed. Investigations of the nucleation kinetics of these alloys have been performed in a ground based program with the electrostatic levitator (ESL). These experiments also allow the determination of the ratio of the specific heat to the total hemispherical emissivity.

Methods of data acquisition and analysis

Measurements of the specific heat capacity were performed on 8 mm diameter specimens with the containerless electromagnetic processing device TEMPUS. Specimens are positioned by an radio-frequency (rf) electromagnetic quadrapole field and heated by a dipole field. Containerless conditions are required to avoid heterogeneous nucleation of the undercooled melt by contact of the specimen with container walls. Furthermore, heating due to the strong levitation forces required for containerless electromagnetic processing would not allow one to perform these experiments under clean ultrahigh vacuum conditions in a 1-g environment.

The heat capacity of the specimen is determined by AC modulation calorimetry. In short, the heating power input to specimen at bias temperature T_o is sinusoidally modulated at frequency ω. This results in a temperature response at ω with amplitude ΔT_{mod} such that $\Delta T_m / T_o << 1$, with c_p given by:

$$c_P = \frac{P_{mod}}{\omega \Delta T_{mod}} f(\omega, \tau_1, \tau_2)$$

P_{mod} is the amplitude of modulated power component. $f(\omega, \tau_1, \tau_2)$ is a correction function accounting for the finite thermal conductivity, with internal relaxation time τ_2, and heat loss, with external relaxation time τ_1. Due to the typically large difference in the external and internal relaxation times for metallic specimens, there is a frequency where $\Delta T_{mod}(\omega)$ is frequency independent, characterizing the isothermal regime with $1 - f(\omega,\tau_1,\tau_2) < 10^{-2}$. Experimentally, this regime can be identified by a phase shift of 90° between the heater current modulation and the temperature response. Calibration of P_{mod} is performed by application AC modulation calorimetry to the crystalline phase with known specific heat. The temperature dependence of the calorimeter constant thus obtained can be determined from measurement of the specific volume and the resistivity, as obtained from the current and voltage data from the rf-generator. Fig. 1 shows a typical experimental run with the VIT 106 alloy depicting melting and overheating (1), rapid cooling into the undercooled melt (2), and performing AC modulation calorimetry (3). The sample subsequently recalesces (4), possibly into a metastable crystalline phase.

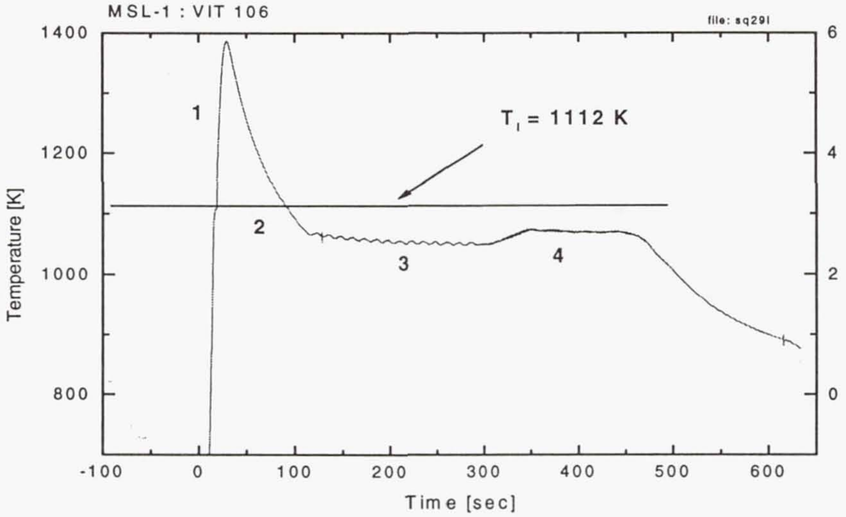

Fig. 1. Typical MSL-1 experiment with VIT 106

Determination of ΔT_{mod} is performed by application of a baseline drift correction, with external relaxation time τ_l, and subsequent Fourier analysis, as shown in Fig.2. The frequency components at 1.2 and 1.5 Hz are due to harmonic motions of the specimen in the potential well of the positioning field and do not represent true temperature variation. Alternatively, a FFT low pass filter is applied to the raw signal and a running average over modulation cycles is performed. The two methods agree within the statistical error of the running average, typically to within 0.1 K. As such, with $\Delta T_{mod} \approx 3$ K, a relative error in c_p determination of $< 4\%$ is obtained. From a step function change in the heating power input, τ_l can also be determined from the transient behavior of the modulation signal. The data shown in Fig. 3 can be very well represented by a single exponential fit as expected for transients with a small temperature difference.

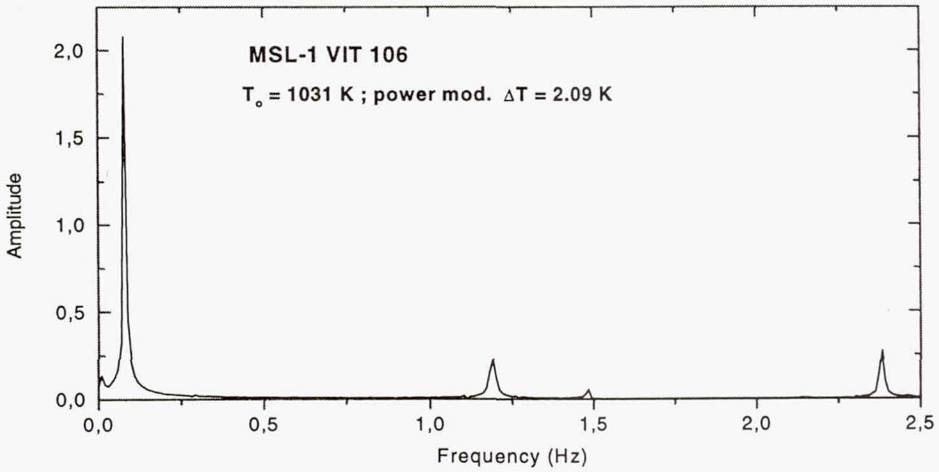

Fig. 2. Fourier transform of temperature signal (3) from Fig.1 after correcting for signal drift

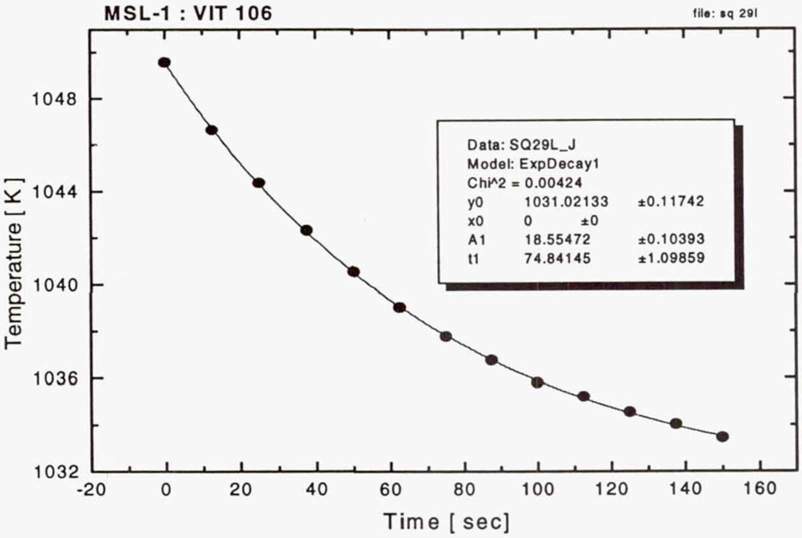

```
Data: SQ29L_J
Model: ExpDecay1
Chi^2 = 0.00424
y0      1031.02133     ±0.11742
x0      0       ±0
A1      18.55472       ±0.10393
t1      74.84145       ±1.09859
```

Fig3. Position of modulation maxima as function of time for τ_1 determination. ● data points, — single exponential fit

Flight results compared with ground results

Fig. 4 shows results for the external relaxation time τ_1 obtained in the flight experiment for VIT 106 together with similar values obtained in the ESL. The good agreement between these values demonstrates the consistency of the experimental approach. The solid line represents a T^{-3} scaling of τ_1 for constant specific heat capacity. As such, the deviation of the experimental data from this scaling reflects the strong increase of the specific heat with decreasing temperature for the undercooled melt. Furthermore, a singular point near T_l is observed suggesting an unusual behavior in c_p. Further evidence is provided in Fig. 5, with values of the specific heat from AC modulation calorimetry normalized to the heater coupling coefficient. The temperature dependence of the coupling coefficient has not yet been taken into account. Nonetheless, the anomaly exhibited in the external relaxation time is also present in the specific heat in the same temperature range. Furthermore, the temperature dependence of the specific volume also appears to change in this temperature range. This behavior is suggestive of a phase separation just above the liquidus temperature. In order to test this hypothesis further, laboratory experiments to analyze the solidification microstructure after rapidly quenching the liquid from different temperatures are under way. AC modulation calorimetry could be performed for this alloy up to an undercooling of 70 K. The agreement of data points at similar temperatures is very good and demonstrates the precision of this method.

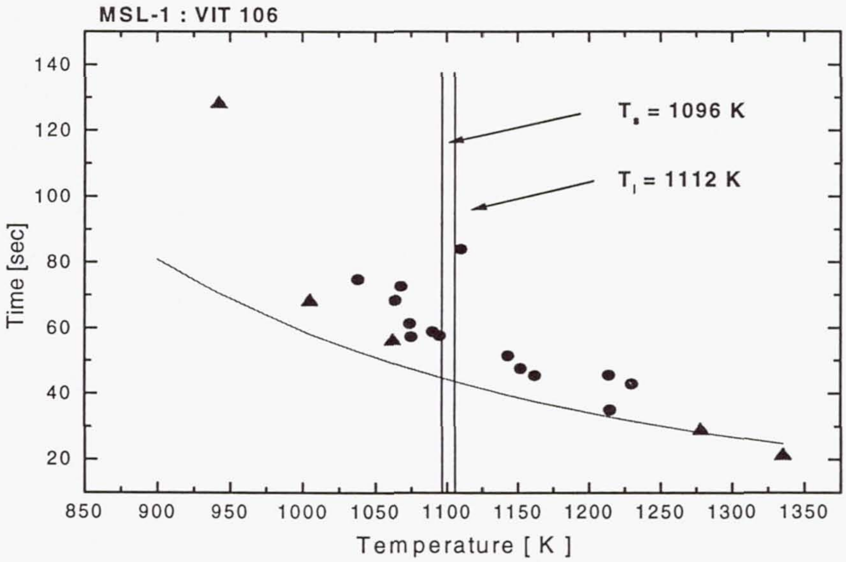

Fig. 4. External relaxation time as a function of temperature for VIT 106

●: MSL-1, Δ : ESL- ground based results.

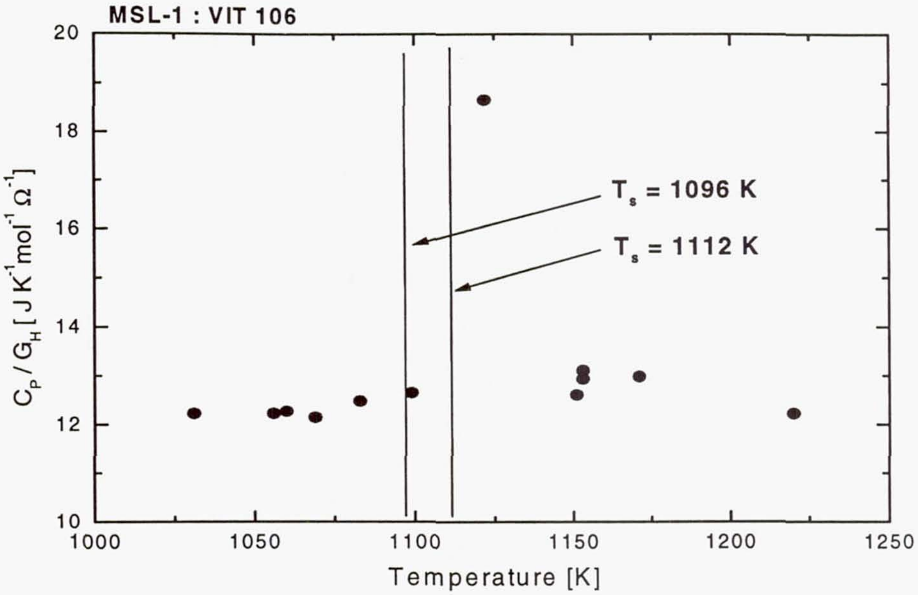

Fig 5. Specific heat capacity of VIT 106 normalized to heater coupling coefficient G_H.

As compared to ESL ground based experiments where undercooling of over 200 K could be obtained, the VIT 101 flight specimen showed only an undercooling of 45 K, which is attributed to the presence of minor impurities. Specific heat capacity data in the stable melt and the slightly undercooled melt were obtained. It should be pointed out that no anomaly in τ_1 or c_p similar to VIT 106 could be observed. The same holds for the measurements performed by the Fecht group on two bulk glass forming alloys of different composition.

Other ground based work includes analysis of solidification microstructure and phase selection in the flight specimen (VIT 101) solidified from the undercooled liquid under mg conditions. Comparison will be made with a 1-g reference specimen, as well with those phases crystallizing at high undercooling by heating the glass into the undercooled melt. Results of an electron microprobe analysis are shown in Table 1, exhibiting two phases of almost complementary composition in (ZrTi) ≈ 50 at% and (NiCu) ≈ 50 at%. We will further identify the structure of these phases and investigate the dependence of their formation on impurity levels.

Tab. 1 EDX spot analysis of $Ti_{34}Zr_{11}Cu_{47}Ni_8$ (VIT 101) flight specimen

Phase	Zr at%	Ti at%	Ni at%	Cu at%
1	7.45	36	12.97	36.42
2	18.99	22.44	8.12	50.44
3	3.27	47.44	3.05	46.24

Conclusions

The specific heat capacity of two glass forming metallic alloys was measured by AC modulation calorimetry in the stable and undercooled (for VIT 106) melt. The temperature dependence of the specific heat as well of the external relaxation time and the specific volume appear to exhibit an anomaly tentatively identified as phase separation in the liquid. This would constitute an important finding as phase separation is suggested to occur frequently in glass forming metallic melts. However, with a few exceptions, experimental evidence of this is rare. Further work will include investigation of the phase selection in these alloys as well as viscosity measurements at high undercooling. These data can be combined with high temperature viscosity data and undercooling experiments with the ESL to model the nucleation kinetics in these alloys. Future perspectives also include the implementation of AC modulation calorimetry in the ESL.

References

1. H.J. Fecht and W.L. Johnson, Rev. Sci. Instr., **62**, 1299 (1991)

2. R.K. Wunderlich, D.S. Lee, W.L. Johnson, and H.J. Fecht, Phys. Rev. **B55**, 26 (1997)

Page intentionally left blank

DISLOCATION FORMATION DURING GROWTH OF SEMICONDUCTOR CRYSTALS

Dr. Monica L. Kaforey, Dr. David H. Matthiesen, and Dr. Arnon Chait
Case Western Reserve University
10900 Euclid Ave. White 330
Cleveland, OH 44106
(216) 368-4219 phone
(216) 368-3209 fax
e-mail: mlk14@po.cwru.edu

In the ongoing efforts to produce higher quality semiconductor materials, there is a continuous search for ways to consistently make materials with fewer defects. Thus, improvements in the understanding of how and why defects form would be extremely beneficial. This research examined one of the factors believed to affect dislocation formation during the growth of semiconductor crystals.

During directional solidification of semiconductor crystals, dislocations propagate from the existing crystal to the growing crystal at the melt/solid interface and from the solid/crucible surface into the growing crystal. Modeling efforts have shown that the interaction between the crucible wall and the sample in the region of the melt/solid interface has a significant effect on dislocation formation. Previous experimentation in microgravity has shown that when the melt is not in contact with the wall of the crucible, the resulting crystal will have a lower dislocation density. It is hypothesized that the increased ability of the crystal to relieve stresses is responsible for the lower dislocation density. The research done under the current ground-based funding will help to prepare for future space flight investigations of the effect of forced contact versus detachment of the melt from the crucible wall on dislocation structure during directional solidification of semiconductor crystals. The current research also involved characterization of a spring that would be necessary for maintaining melt/crucible contact during future flight experimentation.

Background

Dislocations are one of the primary defects found in semiconductors. Dislocations can result in semiconductor crystals for a variety of reasons. Two of the main reasons are (1) propagation from the seed crystal, and (2) shear strains due to mechanical or thermal stresses[1].

One approach to reducing the dislocation density has been to dope the material such that the critical resolved shear stress (CRSS) is increased so that the applied stress will not exceed the slip threshold[2-6]. An alternate approach to reducing the dislocation density would involve decreasing the applied thermal stress. Stresses in crystals grown by the Czochralski method have been studied[7-12]. Rosch and Carlson[5] summarize the results of these studies by stating that for crystals smaller than one diameter in height, a significant amount of stress is located near the solid-liquid interface and near the seed crystal. For crystals longer than 2 diameters, all of the significant stress is found at the interface. Also, the stress is higher near curved rather than flat interfaces. Significant amounts of stress found at the perimeter and center of the interface will cause more dislocations to form in these regions, while fewer dislocations form in the intervening region. Experimental results agree with the modeling efforts; reducing the thermal stress resulted in a crystal with a lower dislocation density.

The third possible approach to reducing the dislocation density is to reduce the applied mechanical stress. There are various potential sources of applied mechanical stress for a crystal grown using the vertical Bridgman method in which the melt is in contact with the crucible. The first source is at the location of the melt-solid interface. Semiconductors expand upon solidification. Thus, if the melt is in contact with the crucible when it solidifies, the crystal will be constrained by the crucible. This results in a compressive stress on the crystal. This mechanical stress may be removed by processing in microgravity where the melt may form a free surface such that the melt is not in contact with the crucible wall at the melt-solid interface. If the melt is not in contact with the crucible wall, the solidifying crystal is free to expand without experiencing the compressive stress due to the crucible.

The second source of mechanical stress from the crucible occurs in cases where the crucible contracts more than the crystal upon cooling. In this case, the crucible applies a compressive stress to the crystal. If, on the other hand, the crystal contracts more than the crucible, the crystal may stick to the crucible, partially stick, or detach from the crucible wall. Rosch and Carlson[5] computed stress fields in GaAs during vertical Bridgman growth. They found that the crystal-crucible interaction was the most important parameter in determining dislocation generation. This source of mechanical stress has been minimized in the proposed experiments through the use of a pyrolytic boron nitride (PBN) crucible. The germanium crystal will contract more than the PBN crucible upon cooling.

In ground based experiments, the melt will remain in contact with the crucible wall due to the pressure of the hydrostatic head during vertical Bridgman crystal growth. One method which eliminates contact with a crucible is float-zone crystal growth. In this method, the melt is held in place, in opposition to gravity, between two ends of a rod by surface tension. This limits the diameter of the crystals that can be grown to a few mm[13]. Vertical Bridgman growth can be used to grow much larger crystals.

Hypothesis

It is hypothesized that during crystal growth in microgravity a free surface may form on the surface of the melt. If the free surface forms in the region of the melt-solid interface, the defect concentration in the resulting crystal is expected to be reduced from that found in a crystal grown with forced contact with the crucible.

Objective

The objective of the proposed research is to comprehensively study the effect of free surface formation on the dislocation density of directionally solidified doped semiconductor crystals and to correlate these results with appropriate numerical modeling efforts.

Justification for Microgravity Research

Traditionally, solidification experiments have been done in microgravity due to the significant reduction in buoyancy driven convection that can be achieved in this environment. In this research, it is the desire to form a free surface in the region of the melt/solid interface that necessitates a microgravity environment. In a 1-g environment, the hydrostatic pressure of the melt is sufficient to keep the melt in contact with the wall of the crucible during vertical Bridgman crystal growth. In microgravity, the pressure on the melt is reduced or eliminated depending on the orientation of the acceleration vector. This can lead to the formation of a free surface on the melt. Ideally, this free surface will form in the region of the melt-solid interface and thus provide a crystal in which to study the effect of the free surface on defect formation.

Microgravity is necessary to investigate the case of a melt detached from the crucible wall. If this program is selected for flight in the future, two types of experiments are proposed to be done in microgravity. One type of experiments would employ a spring to prevent the formation of a free surface on the melt and one would, hopefully, result in the formation of a free surface at the solidification interface.

Experimental Plan

The current ground based research was designed to determine knowledge that would be necessary for future microgravity experiments. The characterization methods to be used on the samples were developed, including an etch pit density technique for determining the dislocation density in germanium and gallium arsenide samples.

Gallium doped germanium (Ga/Ge) crystals are being grown using the vertical Bridgman technique. Crystals grown in contact with a PBN crucible and grown with a boric oxide encapsulant are being examined to determine the effect of the encapsulant on the resulting dislocation density. It was hypothesized that the use of an encapsulant would allow the crystal to relieve stresses similarly to the case of a detached melt.

Numerical simulations are being performed by the Computational Materials Laboratory at NASA Lewis Research Center and Florida Atlantic University. The dislocation density predictions generated from the numerical simulations will be compared to the experimental results.

PBN (pyrolytic boron nitride) leaf springs have been used in previous GaAs crystal growth experiments in microgravity (GTE Get Away Special[14] and United States Microgravity Laboratory 1 and 2[15]) to insure that the melt remained in contact with the container. As part of the current ground-based program, a statistically sound design of experiments was developed for determining the spring constant of a stack of PBN leaf springs. The experiments have been completed and analysis of the results is in progress. A fully quadratic empirical model will be developed in terms of the leaf radius, width, height, and the number of leaves in the stack. This will enable the prediction of the force applied on the melt from a stack of leaf springs of a given size. In addition, a theoretical model will be compared to the empirical model.

The theoretical model for a portion of a cylinder that is simply supported at both ends with a line force applied at the center was needed. Exact solutions are known for the deflection of a flat plate and a half cylinder which are simply supported at opposite sides with a line force applied at the center. Solutions to these and many other cases may be found in Young[16] and Timoshenko and Woinowsky-Krieger[17]. However, the intermediate case of just a portion of a cylinder is not available in the literature. This intermediate case was solved for an exact solution and an overview of the derivation is included here.

From a cylinder of radius, *r*, a section is cut having a width, *w*, a depth, *b*, and a thickness, *h*, as shown in Figure 1. A coordinate system defined in terms of *c* and *y* with the origin at the center of the cylinder is also shown in Figure 1(a). Figure 2 shows, in 2 dimensions, the force, *P*, applied at the center of the cylindrical section which is simply supported at the edges. Also shown is the coordinate *x* which is the perpendicular distance from the edge of the section of interest to the applied force.

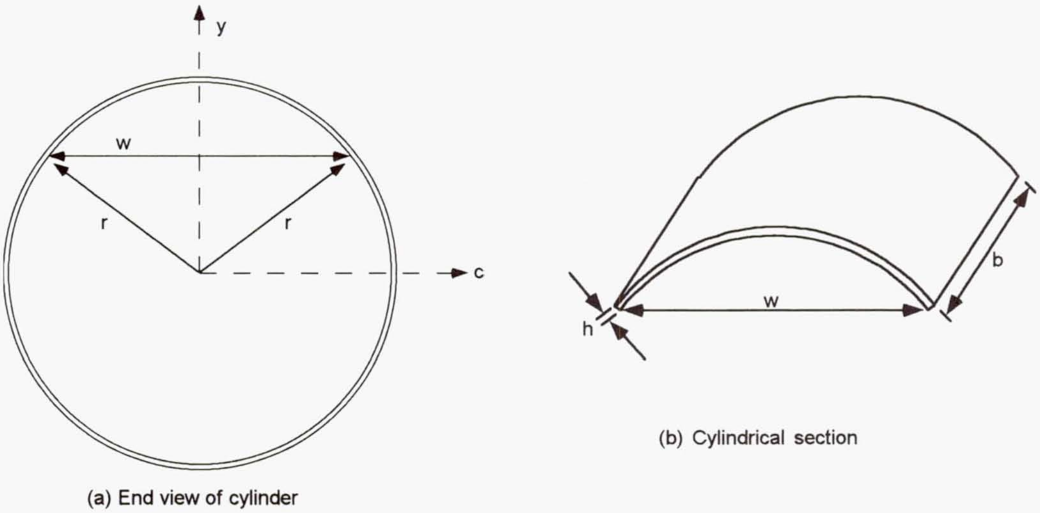

(b) Cylindrical section

(a) End view of cylinder

Figure 1. (a) End view of cylinder showing radius, *r*, and width, *w*. Also shown is *c-y* coordinate system. (b) Cylindrical section showing width, *w*, depth, *b*, and thickness, *h*.

From the equation of a circle,

$$y = \sqrt{r^2 - c^2} \tag{1}$$

Taking the derivative with respect to *c* gives

$$y' = \frac{-c}{\sqrt{r^2 - c^2}} \tag{2}$$

and then

$$1 + (y')^2 = 1 + \frac{c^2}{r^2 - c^2} = \frac{r^2}{r^2 - c^2} \tag{3}$$

In general, the arc length, *l*, of any curve *f(x)* from *x=a* to *x=b* is given by Rade and Westergren[18] to be

$$l = \int_a^b \sqrt{1 + f'(x)^2}\, dx \tag{4}$$

so for the cylindrical section, the arc length, *a(x)*, from $c = -\frac{w}{2}$ to $c = -\frac{w}{2} + x$ is

$$a(x) = \int_{c=-\frac{w}{2}}^{c=-\frac{w}{2}+x} \frac{r}{\sqrt{r^2 - c^2}}\, dc \tag{5}$$

Integrating equation (5) gives the arclength at any point along the section as

$$a(x) = r\left[\arcsin\left(\frac{-\frac{w}{2}+x}{r}\right) - \arcsin\left(\frac{-\frac{w}{2}}{r}\right)\right] \tag{6}$$

Considering only one half of the section, since it is symmetrical about the centerline, evaluating equation (6) gives

$$a_{\min} = 0 \tag{7}$$

when $x = 0$ and

$$a_{\max} = r\arcsin\left(\frac{w}{2r}\right) \tag{8}$$

when $x = \frac{w}{2}$.

Rearranging equation (6) to find *x(a)* gives the perpendicular distance to any point point on the cylindrical section from the plane of the applied force as

$$x(a) = \frac{1}{2}\left\{w + 2r\sin\left[\frac{a}{r} - \arcsin\left(\frac{w}{2r}\right)\right]\right\} \tag{9}$$

The momentum, *M*, at any point along the cylindrical section is

$$M = \frac{P}{2}x = \frac{P}{4}\left\{w + 2r\sin\left[\frac{a}{r} - \arcsin\left(\frac{w}{2r}\right)\right]\right\} \tag{10}$$

Castigliano's Theorem[19] states that, in general, the deflection, *d*, is the partail derivative of energy with respect to the applied force,

$$d = \frac{\partial U}{\partial P} \tag{11}$$

where *U* is the energy and

$$U_{bending} = \frac{1}{2EI}\int_L M^2\,dL \tag{12}$$

where *L* is the length of interest, *E* is the modulus, and *I* is the moment of inertia.

Considering the arclength for one half of the cylindrical section as the length of interest and then adding the 2 halves to get the total energy gives

$$U = \frac{1}{EI}\int_{a_{\min}}^{a_{\max}} M^2\,da \tag{13}$$

Substituting equations (7), (8), and (10) into equation (13) gives

$$U = \frac{1}{EI}\int_0^{r\arcsin\left(\frac{w}{2r}\right)} \frac{P^2}{16}\left\{w + 2r\sin\left[\frac{a}{r} - \arcsin\left(\frac{w}{2r}\right)\right]\right\}^2 da \tag{14}$$

Integrating equation (14) gives

$$U = \frac{P^2 r}{16EI}\left\{-4rw + 2rw\sqrt{4 - \frac{w^2}{r^2}} + 2r^2\arcsin\left(\frac{w}{2r}\right) + w^2\arcsin\left(\frac{w}{2r}\right) - r^2\sin\left[2\arcsin\left(\frac{w}{2r}\right)\right]\right\} \tag{15}$$

Substituting equation (15) into equation (11) and taking the partial derivative with respect to the applied force gives the deflection

$$d = \frac{Pr}{8EI}\left\{-4rw + 2rw\sqrt{4-\frac{w^2}{r^2}} + 2r^2\arcsin\left(\frac{w}{2r}\right) + w^2\arcsin\left(\frac{w}{2r}\right) - r^2\sin\left[2\arcsin\left(\frac{w}{2r}\right)\right]\right\} \quad (16)$$

Equation (16) is the deflection for any cylindrical section of width, *w*, and radius, *r*, which is simply supported at opposite edges with a force, *P*, applied along the centerline.

For dimensions such that the thickness of the section is much smaller that the width, the moment of inertia for a rectangular beam (see for example Beer and Johnston[20]) is

$$I = \frac{1}{12}bh^3 \quad (17)$$

Substituting equation (17) into equation (16) gives

$$d = \frac{3Pr}{2Ebh^3}\left\{-4rw + 2rw\sqrt{4-\frac{w^2}{r^2}} + 2r^2\arcsin\left(\frac{w}{2r}\right) + w^2\arcsin\left(\frac{w}{2r}\right) - r^2\sin\left[2\arcsin\left(\frac{w}{2r}\right)\right]\right\} \quad (18)$$

Applying this result to PBN leaf springs, for any one leaf spring, the spring constant, k, is given by

$$k = \frac{P}{d} \quad (19)$$

where d is given by equation (18). For a stack of leaves, the deflection of the stack is the sum of the deflections of the individual springs. Thus, the spring constant of the stack is

$$k_{stack} = \frac{P}{nd} \quad (20)$$

From this, a prediction of the spring constant was made for each set of experimental conditions in the DOE.

Value of Research

The knowledge gained from the current ground-based experiments will be useful when ampoules are designed for space station era experiments in microgravity. In addition, the ability to predict the force of a stack of PBN leaf springs makes the potential use of this type of spring much greater for many other applications. The knowledge gained from future flight experiments combined with a vigorous modeling effort is expected to contribute significantly to the understanding of how and why dislocations form during the growth of semiconductors. This information will be useful to ground-based research efforts that are trying to reduce the number of defects in semiconductor crystals.

Dislocations are detrimental to the performance of semiconductors in device applications. Optical properties[13], hardness[21-23], and electrical properties such as electron mobility[24] are sensitive to the dislocation density in semiconductors. This study should result in a significant improvement in the understanding of dislocation formation during semiconductor crystal growth due to an applied mechanical stress. This knowledge could be used to improve terrestrial processes so that they can consistently produce single crystal semiconductors with fewer defects.

References

1. C. Elbaum, Prog. Met. Phys. **28**, 1959, p. 203.
2. Robert A. Brown, "Theory of Transport Processes in Semiconductor Crystal Growth from the Melt," in Microelectronics Processing, ed. by Dennis W. Hess and Klavs F. Jensen, 1989, American Chemical Society, Washington, D. C., p. 35-103.
3. G., Jacob, M. Dusuaux, J. P. Farges, M. M. B. Van den Boom, and P. J. Roksnoer: J. Cryst. Growth **61**, 1983, p. 417.
4. A. Jordan, A. Von Neida and R. Caruso, J. Crystal Growth **70**, 1984, p. 555.
5. William Rosch and Frederick Carlson, J. Crystal Growth **109**, 1991, p. 75-81.
6. H. Kohda, K. Yamada, H. Nakanishi, T. Kobayashi, J. Osaka, and K. Hoshikawa: J. Cryst. Growth **71**, 1985, p. 813.
7. J. Lambropoulos, J. Crystal Growth **80**, 1987, p. 245.
8. J. Lambropoulos and C. Delametter, J. Crystal Growth **92**, 1988, p. 390.
9. C. Schvezov, I. Samarasekera and F. Weinberg, J. Crystal Growth **84**, 1987, p. 219.
10. C. Schvezov, I. Samarasekera and F. Weinberg, J. Crystal Growth **85**, 1987, p. 142.
11. C. Schvezov, I. Samarasekera and F. Weinberg, J. Crystal Growth **92**, 1988, p. 489.
12. Shahryar Motakef, J. Crystal Growth **114**, 1991, p. 47-58.
13. W. R. Wilcox: AIAA 91-0507, 1990.
14. A.H. Bellows, D.H. Matthiesen, G.A. Duchene, and G. Chen, "A Versatile GAS Furnace for Materials Processing in Space", No. 92-0787, 30th AIAA Aerospace Sciences Meeting (1992).
15. M.L. Kaforey, J.M. Bly and D.H. Matthiesen, "Void Formation In Gallium Arsenide Crystals Grown In Microgravity", J. Crystal Growth 174 (1997) 112.
16. W.C. Young, Roark's formulas for stress and strain, 6th ed., 1989, McGraw-Hill, New York.
17. Timoshenko, S. and Woinowsky-Krieger, S., 1959, *Theory of Plates and Shells*, 2nd ed., McGraw-Hill, New York.
18. Rade, L. and Westergren, B., 1995, *Mathematics Handbook for Science and Engineering,* Birkhauser, Sweden, p. 145.
19. Castigliano, 1879, *Théorème de l'équilibre des systèmes élastiques et ses applications*, Paris. English translation in Andrews, E. S., *Elastic Stresses in Structures*, Scott, Greenwood, London. For explanation, see for example Boresi, A. P. and Sidebottom, O. M., 1985, *Advanced Mechanics of Materials*, John Wiley & Sons, New York, Chapter 4.
20. Beer, F. P. and Johnston, E. R., Jr., 1984, *Vector Mechanics for Engineers,* 4th ed., McGraw-Hill, New York.
21. R. S. Feigelson and R. K. Route: J. Cryst. Growth **49**, 1980, p. 399.
22. J. C. Fisher: Dislocations and the Mechanical Properties of Crystals, 1957, Wiley, New York.
23. H. G. Van Bueren: Imperfections in Crystals, 2nd ed., 1961, North-Holland, Amsterdam.
24. J. R. Dale and J. C. Brice: Solid State Electronics **3**, 1961, p. 105.

ROLE OF DYNAMIC NUCLEATION AT MOVING BOUNDARIES IN PHASE AND MICROSTRUCTURE SELECTION

Alain Karma, Department of Physics, Northeastern University, Boston, MA 02115, and Rohit Trivedi, Ames Laboratory of the Department of Energy and Department of Materials Science and Engineering, Iowa State University, Ames, Iowa, 50011

INTRODUCTION

Solidification microstructures that form under steady-state growth conditions (cells, dendrites, regular eutectics, etc.) are reasonably well understood in comparison to other, more complex microstructures, which form under intrinsically *non-steady-state* growth conditions due to the competition between the nucleation and growth of several phases. Some important practical examples in this latter class include microstructures forming in peritectic systems [1], in highly undercooled droplets [2], and in strip cast stainless steels [3]. Prediction of phase and microstructure selection in these systems has been traditionally based on (i) heterogeneous nucleation on a static interface, and (ii) comparing the relative growth rate of different phase/microstructures under steady-state growth conditions. The formation of new phases, however, occurs via nucleation on, or ahead of, a moving boundary. In addition, the actual selection process is controlled by a complex interaction between the nucleation process and the growth competition between the nuclei and the pre-existing phase under non-steady-state conditions. As a result, it is often difficult to predict which microstructure will form and which phases will be selected under prescribed processing conditions.

This research addresses this critical role of nucleation at moving boundaries in the selection of phases and solidification microstructures through quantitative experiments and numerical modeling in peritectic systems. In order to create a well characterized system in which to study this problem, we focus on the directional solidification of hypo- and hyper-peritectic alloys in the two-phase region, imposing a large enough ratio of temperature gradient/growth rate (G/V_p) to suppress the morphological instability of both the parent (α) and peritectic (β) phases, i.e. each phase alone would grow as a planar front. Our combined experimental and theoretical results show that, already in this simplified case, the growth competition of these two phases leads to a rich variety of microstructures that depend sensitively upon the relative importance of nucleation, diffusion, and convection [4, 5, 6, 7].

GROUND BASED EXPERIMENTS

A set of systematic experiments was carried out to characterize the formation of microstructures in the Sn-Cd. These experiments exploit a new experimental technique developed [4] to directionally solidify several samples simultaneously in capillary tubes with a range of diameters from 0.2 mm to 6 mm, which allows one to systematically reduce and study the effect of convection. The most significant results are the following.

(1) In the hyperperitectic region, an oscillating structure with seemingly distinct isolated bands was observed. This structure has been widely reported in the literature at large G/V_p ratio (see [6] and references to earlier work therein). Successive polishing of the samples, however, revealed that this structure is actually made up of two *continuous* interconnected phases in three dimensions. In particular, the microstructure consists of a large tree-like domain of primary α phase that is embedded inside the peritectic β phase (Fig. 1a). This result is important in that it shows that the widely observed structure is not made up of discrete bands and, hence, is not controlled by nucleation after the first β band is formed.

(2) This tree-like structure was found to disappear as the sample diameter was reduced, which demonstrates that this structure is the result of the convection present in the bulk liquid. In the hyperperitectic region, only a single α to β transition is observed (Fig. 1b) in a sample of 0.6 mm diameter where convection is suppressed, as predicted by the diffusive model.

(3) In the same 0.6 mm diameter sample where convection is suppressed, bands (Fig. 2) that grow by repeated nucleation of the primary and peritectic phases, were observed in a window of composition inside the hypoperitectic region. This result is the first experimental confirmation of the existence of nucleation-controlled *discrete*, as opposed to continuous, band formation in a purely diffusive regime, which had been theoretically predicted but not observed [8].

(4) The microstructure in the diffusive regime is not unique (Fig. 2) and seems to depend in a complex way on the growth conditions and the nucleation undercoolings of the two phases. In 0.6 mm diameter samples, discrete bands were consistently observed with a large spacing on the order of one mm that is consistent with the prediction of the diffusive model. This spacing, however, was irregular, indicating that the nucleation undercoolings of the two phases can themselves vary in the course of the experiment, most likely due to spatial variations in heterogeneous sites along the sample walls. In 0.4 mm diameter samples, we observed discrete bands that spanned the cross-section either fully or partially leading to the formation of "islands" of the peritectic phase. In addition, coupled growth structures were observed.

MODELING

Numerical modeling studies were carried out to understand the origin of the different microstructures observed in the convective and diffusive regimes as a function of sample size, composition, and nucleation undercoolings.

A model of convection was developed [5] which shows that the oscillatory microstructures observed in experiments in the hyperperitectic region form due to the presence of oscillating convection in the melt. In this study, the Navier-Stokes equations in the Boussinesq approximation and the heat and solute transport equations are solved numerically inside a two-dimensional rectangular cavity with both horizontal and vertical temperature gradients. These equations are written in a coordinate system that is fixed with respect to the uniformly moving solid-liquid interface. The solid-liquid interface is assumed to remain planar. This assumption renders the computations tractable and makes it possible to captures the main effect of convection on the oscillating microstructures. Numerical calculations were carried out for conditions characteristic of solidification for Sn-1.3 wt% Cd at a growth rate of 3 μm/s in tubes of inner diameter ranging from 0.6 mm to 6.0 mm. The microstructure for a 0.6 mm diameter is diffusion controlled with a sharp transition from α to β (Fig. 1d). In contrast, for

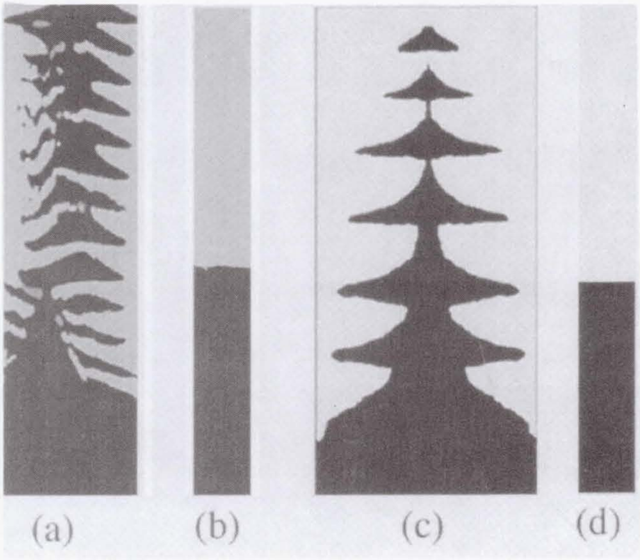

Figure 1: Experimental (a and b) and numerically calculated (c and d) microstructures for a Sn-1.3 wt%Cd alloy for tube diameters $d = 6$ mm (a and c), and $d = 0.6$ mm (b and d), $V_p = 3\mu$m/s and $G = 13.5$ K/mm.

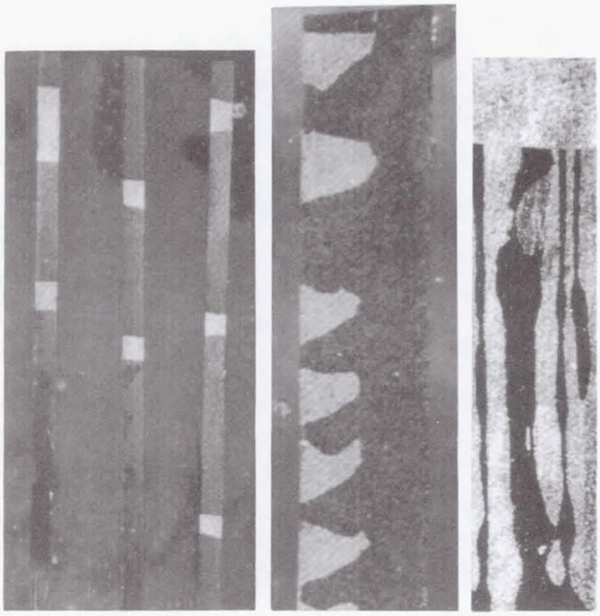

Figure 2: Experimental micrographs showing the variety of possible microstructures in a purely diffusive regime: discrete bands (left, $d = 0.6$ mm, $C_0 = 0.9$ wt% Cd, $V_p = 3\mu$m/s, $G = 23$ K/mm), islands (middle, $d = 1$ mm, $C_0 = 0.75$ wt% Cd, $V_p = 4\mu$m/s, $G = 23$ K/mm), and coupled growth (right, $d = 2$ mm, $C_0 = 0.1.3$ wt% Cd, $V_p = 1\mu$m/s, $G = 13.5$ K/mm).

a 6 mm diameter the convective flow drives an oscillating concentration profile at the interface, which gives rise to an oscillatory coupled growth of the two phases. This oscillatory growth, in turn, generates a tree-like microstructure (Fig. 1c) that is in good qualitative agreement with the experimentally observed one (Fig. 1a).

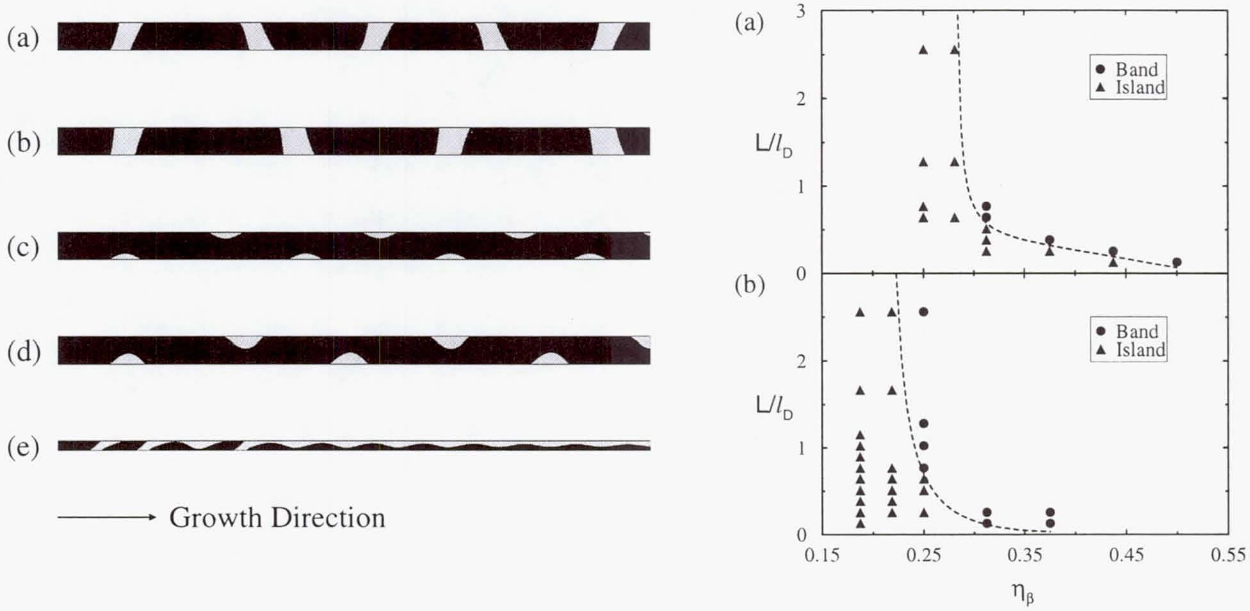

Figure 3: **Left:** Phase-field model simulated microstructures for $GD/(V|m_\alpha|\Delta C) = 1.116$ and (a) $\Delta\tilde{T}_N^\alpha = 0.135, \Delta\tilde{T}_N^\beta = 0.0438, L/l_D = 0.512, \eta_\beta = 0.125$, (b) $\Delta\tilde{T}_N^\alpha = 0.174, \Delta\tilde{T}_N^\beta = 0.0563, L/l_D = 0.512, \eta_\beta = 0.125$, (c) $\Delta\tilde{T}_N^\beta = 0.0250, L/l_D = 0.512, \eta_\beta = 0.05$, (d) $\Delta\tilde{T}_N^\beta = 0.0312, L/l_D = 0.512, \eta_\beta = 0.075$, (e) $\Delta\tilde{T}_N^\alpha = 0.0193, \Delta\tilde{T}_N^\beta = 0.0312, L/l_D = 0.128, \eta_\beta = 0.437$. **Right:** morphology diagram as a function of system size and volume fraction of the β-phase for two different nucleation undercoolings: (a) $\Delta\tilde{T}_N^\beta = 0.0312$ and (b) $\Delta\tilde{T}_N^\beta = 0.0250$. Here $\Delta\tilde{T}_N^{\alpha,\beta} \equiv \Delta T_N^{\alpha,\beta}/(|m_\alpha|(C_p - C_\alpha))$ where C_α and C_p are the equilibrium composition in α and liquid phases at the peritectic temperature, η_β is the volume fraction of the β phase defined by $\eta_\beta C_\beta + (1-\eta_\beta)C_\alpha = C_0$, and $l_D = D/V_p$.

The microstructure in the diffusive regime was investigated by numerical simulation of a fully dynamical phase-field model of peritectic solidification for a generic peritectic phase diagram [7]. The equations of the model were simulated in a rectangular geometry and the microstructure was studied at fixed G/V_p ratio as a function of the width, L, of the sample (analogous to the sample diameter d in the experiments), the composition C_0 inside the hypoperitectic region, measured here in terms of the equilibrium volume fraction of the peritectic phase η_β, and the nucleation undercoolings ΔT_N^α and ΔT_N^β.

The simulation results summarized in Fig. 3 show that, below a minimum sample size, L_{min}, discrete bands of the peritectic phase only fill the sample partially, thereby forming "islands" of this phase, whereas above this minimum they span its entire cross-section. The existence of this minimum size can be understood by noting that partial bands should be formed when the time for the excess solute rejected by the parent phase to diffuse across the sample is shorter than the time for the peritectic phase to spread across the sample. Since these two times are proportional to $\sim L^2/D$ and L/V_s^β, respectively, where V_s^β is the lateral spreading velocity of the peritectic phase on the parent phase, equating them yields the estimate $L_{min} \sim D/V_s^\beta$.

This estimate contains only one part of the physical mechanism that controls the transition from islands to bands. In particular, our numerical results show that L_{min} is a function of composition (dashed line in Fig. 3) and becomes infinite at a critical composition, which decreases with increasing nucleation undercooling of the peritectic phase. Below this critical composition β islands form no matter how wide is the sample. The existence of this critical composition can be understood qualitatively by noting that mass conservation implies that the β phase acts as an 'impurity sink' that depletes the boundary layer of solute ahead of the growing α-phase at a rate proportional to $1 - \eta_\beta$. Hence, for η_β sufficiently small, this sink effect can become large enough to overcome the driving force for the β-phase to spread laterally independently of the sample size.

When the parent phase renucleates on the peritectic phase, it covers it completely only if the sample is smaller than some maximum width L_{max}. For $L > L_{max}$, the parent phase only partially fills the sample and the β phase grows continuously after the first band. In contrast to L_{min}, which decreases with nucleation undercooling of the peritectic phase, L_{max} increases with nucleation undercooling of the parent phase. This finding can also be explained semi-quantitatively by comparing the time $\sim L/V_s^\alpha$ for the α-phase to spread across the sample to the time $\sim D/V_p^2$ for the temperature of the α-liquid interface to fall below the peritectic temperature, which yields the estimate $L_{max} \sim DV_s^\alpha/V_p^2$. The fact that V_s^α increases with ΔT_N^α explains our numerical finding that L_{max} increases with the same quantity.

These results demonstrate that when only a single nucleus is allowed to form on the sample walls, discrete band formation in a diffusive regime is only possible over a finite range of system sizes $L_{min} < L < L_{max}$ and a finite range of hypoperitectic compositions. Moreover, these ranges depend crucially on the nucleation undercoolings of the two phases. These results also show that other structures than discrete bands can form, which include discrete islands of the β and α phases for certain ranges of nucleation undercoolings and $L < L_{min}$ and $L > L_{max}$, respectively, as well as more chaotic microstructures.

NEED FOR MICROGRAVITY AND FUTURE DIRECTIONS

Our results demonstrate unambiguously that convection is playing an especially important role in peritectic systems alloys in comparison to other solidification systems. For example, the basic morphology of cellular, dendritic, or eutectic microstructures is typically influenced quantitatively, but not destroyed, by convection. In contrast, here, convection has a stronger role in that it prevents the formation of nucleation-controlled discrete bands and other more complex microstructures, and leads instead to the continuous growth of oscillating tree-like structures. This is a consequence of the fact that the formation of this class of microstructures is controlled by a delicate competition between growth and nucleation, which is very sensitive to local variations in composition. Thus, future experiments conducted in a microgravity environment will be critically needed to test the microstructural predictions of the diffusive models in large samples.

The phase-field model results so far agree qualitatively with the experiments in that the the microstructure that forms in a diffusive regime depends sensitively on the sample width. A detailed experimental study, however, is now needed to test the model predictions. In addition, the simulations have provided an understanding of the different microstructures that can form in a diffusive regime when only a single nucleus of the new phase is allowed to spread from the walls of the sample. While this restriction is applicable to narrow samples, it is not realistic for wide samples where multiple nuclei can spread simultaneously. Phase-field simulations will be extended to model the formation of microstructures resulting from (i) multiple nucleation events as a function of the composition and the nucleation undercoolings, and (ii) a smaller G/V_p ratio where one or both phases become morphologically unstable.

For a large G/V_p ratio, we expect that there should exist a range of nucleation undercoolings where alternate discrete layers of the two phases can form over the entire sample width. In particular, this banded microstructure should form if the mean spacing between β-nuclei is larger than L_{min}, and the mean spacing between α-nuclei is smaller than L_{max}. More complex microstructures that involve the stochastic formation of islands of one phase should be expected to form for other conditions. For a smaller G/V_p ratio, the simultaneous presence of morphological instability and nucleation of one or both phases should lead to the formation of an even richer class of microstructures that largely remain to be explored.

ACKNOWLEDGMENTS: This research was performed in collaboration with P. Mazumder, T.S. Lo, J.S. Park, and M. Plapp, and supported by NASA grant NAG8-1254.

References

[1] H.W. Kerr and W. Kurz, Int. Mater. Rev. **41**, 129 (1996).

[2] J. H. Perepezko, Mat Sci. Eng. A**178**, 105 (1994).

[3] Y. Wu, T. J. Piccone, Y. Shiohara, and M. C. Flemings, Metall. Trans. **18**A, 915 (1987).

[4] J. S. Park and R. Trivedi, J. Cryst. Growth **187**, 511-515 (1988).

[5] P. Mazumder, R. Trivedi and A. Karma, "Mechanism of Layer Structure formation in Peritectic Alloys", Materials Research Society (MRS) Procedings, Edited by E. Ma et al., (1998) 39-44.

[6] A. Karma, W.-J. Rappel, B.C. Fuh, and R. Trivedi, "Model of Banding in Diffusive and Convective Regimes during Directional Solidification of Peritectic Systems", Metall. Mater. Trans. **29**A, 1457-1470 (1998).

[7] T.S. Lo, A. Karma, and M. Plapp, "Phase-Field Modeling of Nucleation-Controlled Microstructure Formation in Peritectic Alloys", (to be published in Phys. Rev. E).

[8] R. Trivedi, Metall. Mat. Trans. **26**A, 1583 (1995).

Effect of Marangoni Convection Generated by Voids on Segregation during Low-G and 1-G Solidification

M. Kassemi[1], A. Fripp[2], N. Rashidnia[1], and H. de Groh[3], [1]NCMR, NASA LeRC, Cleveland OH, [2]NASA LaRC, Hampton, VA, [3]NASA LeRC, Cleveland OH

1. Introduction and Objective

Solidification experiments, especially microgravity solidification experiments are often hampered by the evolution of unwanted voids or bubbles in the melt. Although these voids and/or bubbles are highly undesirable, there are currently no effective means of preventing their formation or eliminating their adverse effects, particularly, during low-g experiments. Marangoni Convection caused by these voids can drastically change the transport processes in the melt and, therefore, introduce enormous difficulties in interpreting the results of the space investigations. Recent microgravity experiments by Matthiesen (Study of Dopant Segregation Behavior During the Growth of GaAs in Microgravity, 1994), Andrews (Coupled Growth in Aluminum-Indium HyperMonotectics, 1997) and Fripp (Lead-Tin-Telluride, Growth in a Low-G Environment, 1997) are all good examples of how the presence of voids and bubbles affect the outcome of costly space experiments and significantly increase the level of difficulty in interpreting their results.

In this work we examine mixing caused by Marangoni convection generated by voids and bubbles in the melt during both 1-g and low-g solidification experiments. The objective of the research is to perform a detailed and comprehensive combined numerical-experimental study of Marangoni convection caused by voids during the solidification process and to show how it can affect segregation and growth conditions by modifying the flow, temperature, and species concentration fields in the melt.

While Marangoni convection generated by bubbles and voids in the melt can lead to rapid mixing that would negate the benefits of microgravity processing, it could be exploited in some terrestial processing to ensure effective communication between a melt/solid interface and a gas phase stoichiometry control zone. Thus we hope that this study will not only aid us in interpreting the results of microgravity solidification experiments hampered by voids and bubbles but to guide us in devising possible means of minimizing the adverse effects of Marangoni convection in future space experiments or of exploiting its beneficial mixing features in ground-based solidification.

2. Background and Microgravity Relevance

The results of the PbSnTe solidification experiment on USMP3 (Fripp, 1997) together with the preliminary numerical simulations of thermocapillary convection generated by bubbles in both 1g and low-g environments (Kassemi and Rashidnia, 1996 and 1997) are good examples of how creation of voids or bubbles in the melt during the solidification process can affect the outcome of costly space experiments.

2.1 Lead-Tin-Telluride Low-G Growth Experiment

In the Lead-Tin-Telluride low-g growth experiment, crystals were grown using the Bridgman technique in AADSF facility. During the flight, three separate crystals were processed in a single,

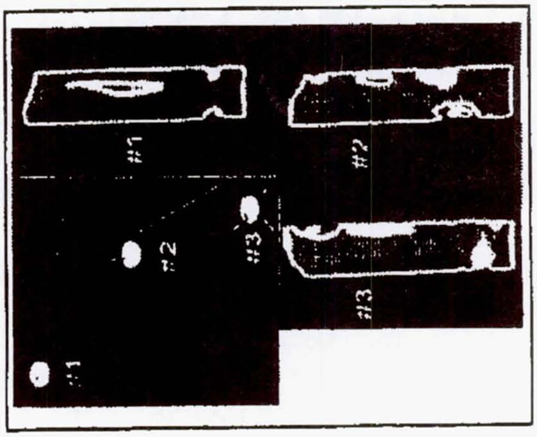

Figure 1. CAT Images of Void Formation in The Three Lead-Tin-Telluride Samples.

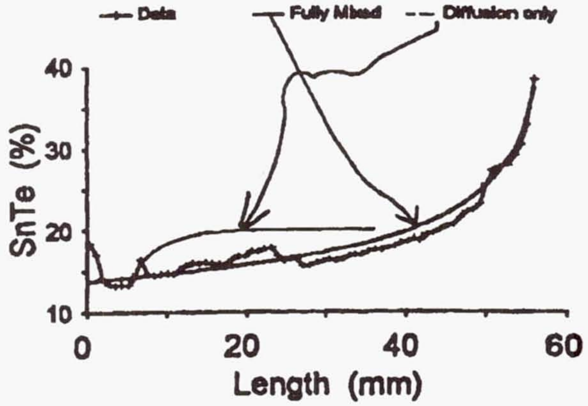

Figure 2. Fripp's Experimental Composition Profile for Solidification of PbSnTe in Cell #1 (Top-Heated). The Fully-Mixed and Diffusion-Only Theoretical Profiles Are Also Shown.

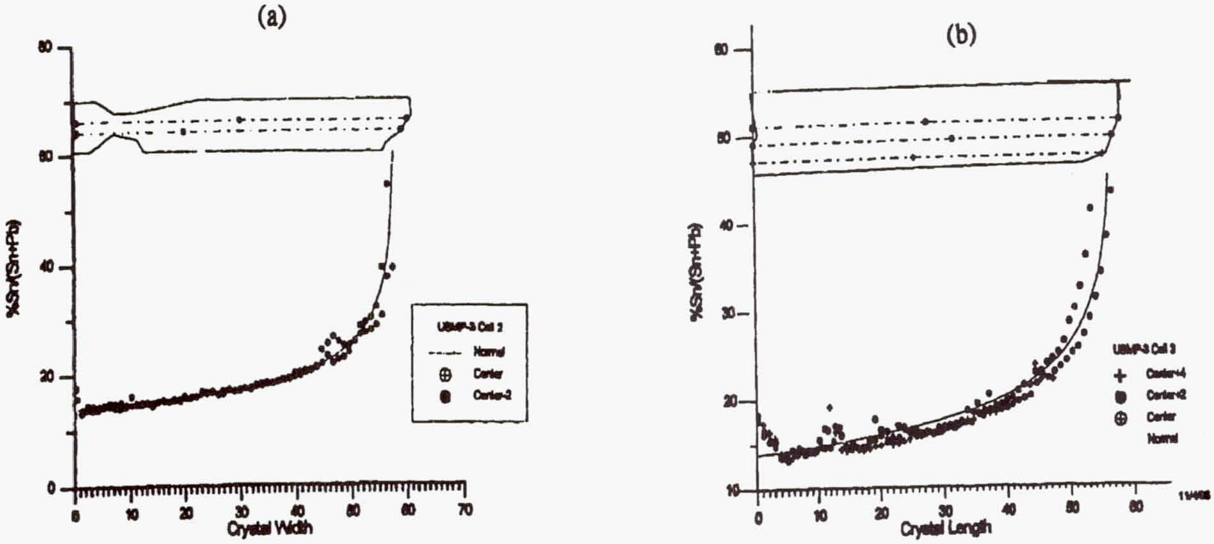

Figure 3. Fripp's Experimental Composition Profiles for Directional Solidification of PbSnTe in a) Cells #2 (Top-Cold) and b) #3 (Horizontal).

segmented ampoule. The crystals were grown in series, each in one of the three primary orientations with respect to the residual gravity vector. The growths were roughly analogous to hot-on-top, cold-on-top, and horizontal configuration. While the immediate objective of the experiment was to grow PbSnTe and establish its fundamental growth properties, another, more important objective was to gain a better understanding of the mechanisms involved in the generalized crystal growth process, particularly those affected by gravity-driven convection caused by temperature and/or solutal gradients.

The flight sample was retrieved from the AADSF at the Kennedy Space Center (KSC) in April 1996. The samples were examined, still in the Inconel cartridge, with a computer aided tomography (CAT) unit available in the KSC non-destructive test laboratory. These high voltage x-rays are capable of penetrating the PbSnTe samples and exposing any voids, large pits, and bubbles.

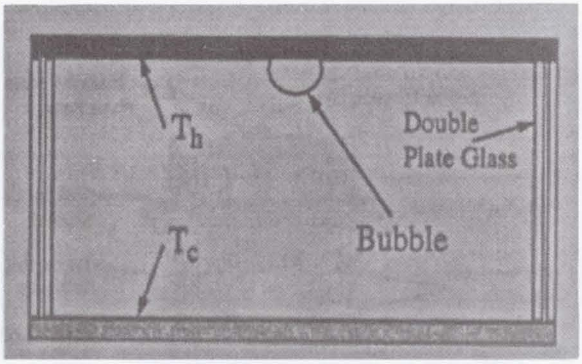

Figure 4. Schematic of The Test Enclosure

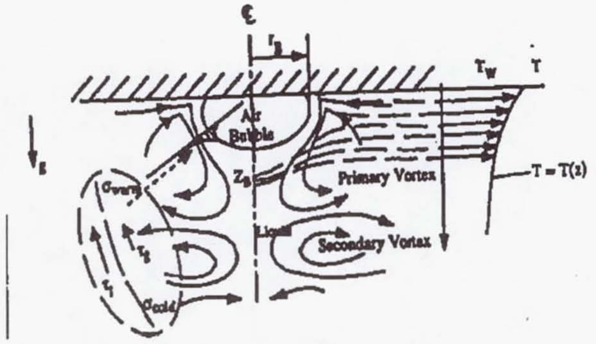

Figure 5. Bubble-Induced Thermocapillary and Natural Convective Flows

The results were totally unexpected; the crystals were cratered with large voids and riddled with meandering channels as shown in Fig. 1.

The primary objective of this flight experiment was to examine the effect of the direction of the microgravity vector on the convective mixing in the liquid during directional solidification. An excellent measurable physical parameter and a sensitive monitor of mixing in the liquid is the compositional profile in the solidified crystal. The axial compositional profiles for cells #1 and #2 and #3 are given in Figs. 2 and 3 respectively. Each cell shows evidence of considerable mixing. Fig. 2 shows the axial compositional distribution of cell #1. The anticipated spike of SnTe shows at the recalescence area at the left side of the plot, then the data flattens for what may be growth during thermal stabilization after the release of the latent heat. At 5 mm of growth, approximately the length of the produced seed after the solutal diffusion time, the composition shows signs of trying to go to diffusion growth but not making it. At approximately 25 mm of growth the curve closely approximates the fully mixed case. The axial compositional profile of the crystal in cell #2, the nominally hot-on-bottom orientation, follows the completely mixed curve for the first 45 mm of growth (after recalescence) and then exhibits deviations (see Fig. 3) that are, as yet, unexplained. Similar deviations occur in the axial compositional profile of the crystal grown in cell #3, but over a longer section (see Fig. 3). As yet, no acceleration perturbations have been related to these compositional variations. Unfortunately, any differences in convective mixing due to the alignment of the acceleration vector were also indistinguishable due to the *vigorous mixing brought about by Marangoni convection which is independent of orientation with respect to the gravity vector.*

2.2 Thermocapillary Convection Caused by a Bubble

To get a preliminary assessment of Marangoni convection caused by a bubble or void in the surrounding fluid consider an enclosure containing a liquid (silicone oil) with a bubble placed on the inside of the top wall as shown in Fig. 4. The side walls are insulated and the temperature of the top and bottom walls are uniformly maintained at T_h and T_c, respectively. Therefore, a thermally stratified state is established in the enclosure before the bubble is introduced. Once the bubble is positioned and the interface between the air and test liquid is formed, surface tension forces created by the temperature gradient along the interface will drive a thermocapillary convective flow as sketched in Fig. 4.

1-G Results: Numerical simulations shown in Fig. 6 indicate that in 1-g, this thermocapillary flow will disrupt the thermal stratification near the bubble resulting in significant temperature gradients near the bubble surface. As the thermocapillary convection gains strength, it will move the hot flu-

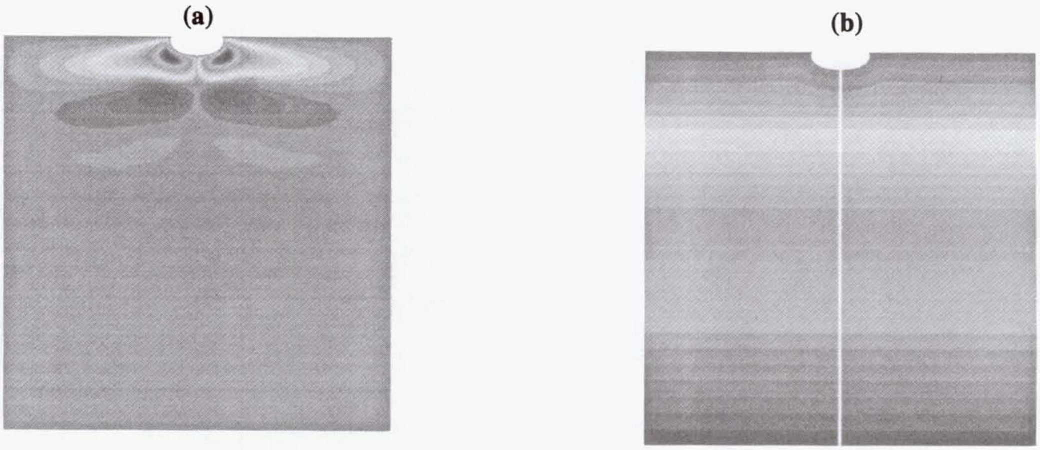

Figure 6. 1-G Numerical Predictions of Streamlines (a), Temperature Contours (b), and Bubble Shape for Ma=2440, Ra=500, Pr= 122.

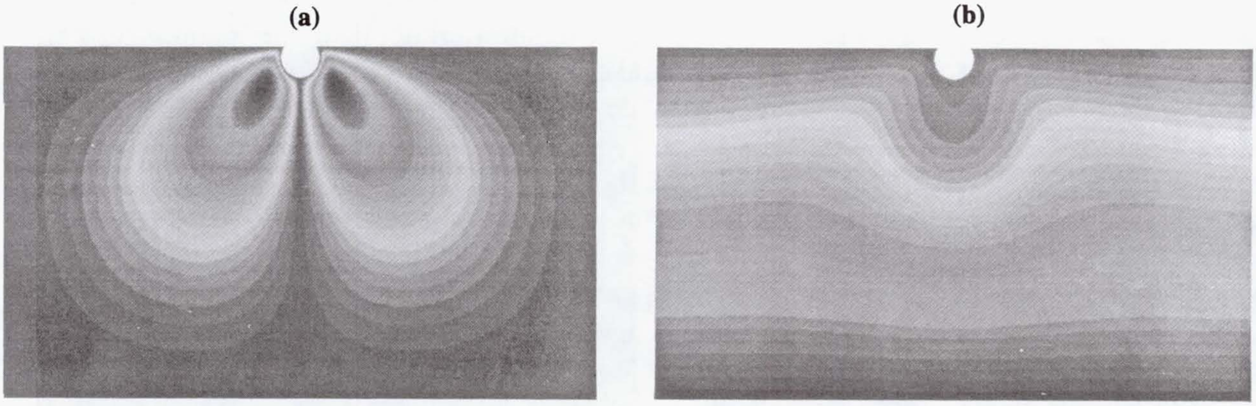

Figure 7. Low-G Numerical Predictions of Streamlines (a), Temperature Contours (b), and Bubble Shape for Ma=1830, Ra=0.25, Pr= 122.

id from the top of the cavity into the colder region below the bubble, thereby, modifying the temperature field in the lower section of the enclosure and resulting in horizontal temperature and density gradients. On earth, these density gradients will give rise to buoyancy-driven convection which will actually counteract the Marangoni flow. For small imposed vertical temperature differences, a steady-state condition will finally prevail where the vortices generated by the two counteracting forces co-exist and deform the temperature contours near the bubble as shown in Fig 6a and 6b. For larger temperature differences the fluid flow and temperature fields can go through a series of oscillatory modes which have been discussed in Kassemi and Rashidnia (1996 and 1997)

Low-G Results: Since, a low gravity environment is characterized by a reduced buoyancy force, decreased hydrostatic head, and negligible natural convection, the low-g shape of the bubble and the resulting thermocapillary flow and temperature fields will be also significantly different as shown in Fig. 7. In this case, just as in the previous situation, a vigorous thermocapillary flow is generated next to the bubble surface. This strong flow will drastically modify the temperature profiles in the enclosure. But in contrast to the terrestrial examples presented in Fig. 6, this time, a natural convective flow will not ensue due to the reduced buoyancy force. As a result, the recirculating thermocapillary vortex will grow unopposed until it nearly fills the entire enclosure at steady-state. The streamlines of Fig. 7a clearly show that the microgravity flow pattern resembles a jet-like flow emanating from around the bubble and flowing downwards into the enclosure. As a result of this intense recirculating flow, the temperature field is greatly altered as depicted in Fig 7b. *Thus, in microgravity, the shape of the bubble, and the temperature and fluid flow fields are all drastically different from their terrestrial counterparts and the unrestricted thermocapillary flow fills the entire enclosure.* In a typical solidification experiment, similar thermocapillary convection generated by a void or bubble can easily modify the temperature and velocity fields and the segregation pattern in the melt.

3. Proposed Work

The previous experimental and numerical results included in section 2.1 and 2.2 clearly underscore the following facts:

- Diffusion-Controlled growth was not possible in microgravity solidification of lead-tin-telluride and gallium arsenide when voids formed in the melt during the solidification process. This has been attributed to significant levels of mixing brought about by Marangoni convection generated by the voids.
- Preliminary work with stationary bubbles in a fluid with an imposed temperature gradient indicates that a vigorous Marangoni flow prevails in both low-g and 1-g environments. This modifies the flow structure and the temperature gradients drastically.
- The nature of convection in both 1-g and low-g depends on the magnitude of the Ma number (dictated by void size, temperature and/or concentration gradients, melt Thermophysical properties). At high Ma numbers the thermocapillary flow is time-dependent in both low-g and 1-g environments and could lead to periodic symmetric and asymmetric oscillatory modes through interactions with buoyancy.
- In the absence of buoyancy force, the Marangoni flow can grow unrestricted to affect the transport process in the entire domain.
- There is a serious gap in our knowledge with regard to bubble-induced steady and oscillatory flows and their effect on temperature and concentration fields in the melt and interface stability during 1-g and low-g solidification.
- Preliminary numerical predictions indicate that the conclusions obtained from ground-based experiments with regard to oscillatory convection generated by bubbles and its possible effects on solidification cannot be directly extrapolated to predict the behavior and effect of the Marangoni flows in space and future microgravity experiments to directly study this phenomenon are necessary.

In the context of these preliminary findings and observations, the present research program consists of two phases. The first phase has four major components:

1. Solidification experiments with SCN to directly investigate: a) the effects of Marangoni convection on the temperature, velocity, and concentration fields in the melt; and b) their impact on growth conditions and stability of the solidification front.
2. Post growth characterization of the solid to determine levels of segregation and extent of mixing.

3. Controlled flow and temperature visualization experiments with different grades of silicone oils to determine the Pr number effect which is needed for extrapolating the results of the SCN experiment to growth of low Pr (high conductivity) number materials e.g. metals and semiconductors.
4. Development of a comprehensive numerical model and simulation of the entire solidification process.

The second phase of this work is concerned with space experiments and has two major components which are as follows:

1. Numerical simulation of recent space experiments (Fripp and Matthiessen) so that existing data can be re-interpreted in terms of the separate roles played by surface tension-driven convection and buoyancy-driven convection due to residual acceleration.
2. Refine the experimental conditions, set-up, and procedures in order to design the *appropriate* space experiment and define the *optimum* parametric space for studying the effects of bubbles and voids on microgravity solidification.

4. Closure

The study of Marangoni convection generated by voids or bubbles is not only warranted because of its fundamental scientific importance in understanding the behavior of fluid flow in space, but also because of its practical significance to solidification and materials processing experiments in both 1-g and low-g environments. During the two phases of this research, an experimental set-up and procedure will be devised to study the effects of Marangoni number on the temperature velocity and concentration fields. A comprehensive numerical model will be developed and tested against the ground-based results. The verified numerical model will be used to simulate previous low-g experiments and interpret their results. The numerical model will be also used to precisely identify the parametric range of interest for a future microgravity investigation. Finally, based on the knowledge accumulated during this ground-based research, a future long duration space experiment will be designed.

5. References

Andrews, J. B., Hayes, L.J., Arikawa, Y., and, Coriell, S.R., *Microgravity Solidification of Al-In Alloys*, 35th Aerospace Sciences Meeting, AIAA, Reno, NV, January 6-10, 1997.

Fripp, A.L., and et al., *The Effect of Microgravity Direction on the Growth of PbSnTe,* AIAA paper **AIAA 97-0676**, 1997

Kassemi, M., and Rashidnia, N., *Steady and Oscillatory Thermocapillary Flows Generated by a Bubble in 1-G and Low-G Environments*, **AIAA 97-0924**, presented in the 35th AIAA Aerospace Conference, 1997.

Kassemi, M., and Rashidnia, N., *Thermocapillary and Natural Convective Flows Generated by a Bubble in 1-G and Low-G Environments*, **AIAA 96-0734**, presented in the 34th AIAA Aerospace Conference 1996.

Matthiesen D.H., and Majewski, J.A., *The Study of Dopant Segregation Behavior During the Growth of GaAs in Microgravity*, NASA Conference Publication 3272, Vol. 1, p 223, May 1994; Joint Launch + One Year Review of USML-1 and USMP-1 with the Microgravity Measurement Group

Identification of Gravity-Related Effects on Crystal Growth from Melts with an Immiscibility Gap

M. Kassemi[1], A. Sayir[2], S. Farmer[3], [1]NCMR, NASA LeRC, Cleveland OH, [2]CWRU, Cleveland, OH, [3]NASA LeRC, Cleveland OH

1. Introduction and Objective

This work involves an experimental-numerical approach to study the effects of natural and Marangoni convections on solidification of single crystals from a silicate melt with a liquid-liquid immiscibility gap. Industrial use of crystals grown from silicate melts is becoming increasingly important in electronic, optical, and high temperature structural applications. Even the simplest silicate systems like Al_2O_3-SiO_2 have had, and will continue to have, a significant role in the development of traditional and advanced ceramics. A unique feature of crystals grown from the silicate systems is their outstanding linear electro-optic properties. They also exhibit exceptionally high optical rotativity. As a result, these crystals are attractive materials for dielectric, optical, and microwave applications.

Experimental work in our laboratory has indicated that directional solidification of a single crystal mullite appears to be preceded by liquid-liquid phase separation in the melt. Disruption of the immiscible state results in crystallization of a two phase structure. There is also evidence that mixing in the melt caused by density-driven convection can significantly affect the stability of the immiscible liquid layers and result in poly-crystalline growth. On earth, the immiscible state has only been observed for small diameter crystals grown in float zone systems where natural convection is almost negligible. Therefore, it is anticipated that growth of large single crystals from silicate melts would benefit from microgravity conditions because of the reduction of the natural convective mixing. The main objective of this research is to determine the effects of transport processes on the phase separation in the melt during growth of a single crystal while addressing the following issues:

1. When do the immiscible layers form and are they real?
2. What are the main physical characteristics of the immiscible liquids?
3. How mixing by natural or Marangoni convection affects the stability of the phase separated melt?

2. Background

Very little work has been done or published with regard to solidification from immiscible liquids. High resolution digital images obtained in our laboratories at NASA Lewis demonstrate that mullite formation is preceded by a state of liquid-liquid immiscibility. To our knowledge, this is the first direct experimental evidence of liquid immiscibility reported for this system. Experimental results also reveal that mixing in the melt caused by density-driven convection can significantly affect the growth process. The transport processes affecting concentration and temperature gradients in the melt and in the growing solid are quite complicated for the silicate systems. The immiscibility of the liquid, segregation of dopant, and interface shape are not only directly affected by density-driven and surface-tension-driven convection in the melt but are also indirectly influenced by a significant amount of radiation and conduction heat transfer through the semi-transparent solid. The interaction between the various transport processes are further complicated by the observed multi-layered fluid structure which brings about various mechanical and thermal couplings across the liquid-liquid interface. Consequently, determination of the necessary conditions for growing superior quality single crystals from phase separated melts is not an easy task and requires isolating the effects of the various interacting transport processes using a combined experiments and numerical modelling approach.

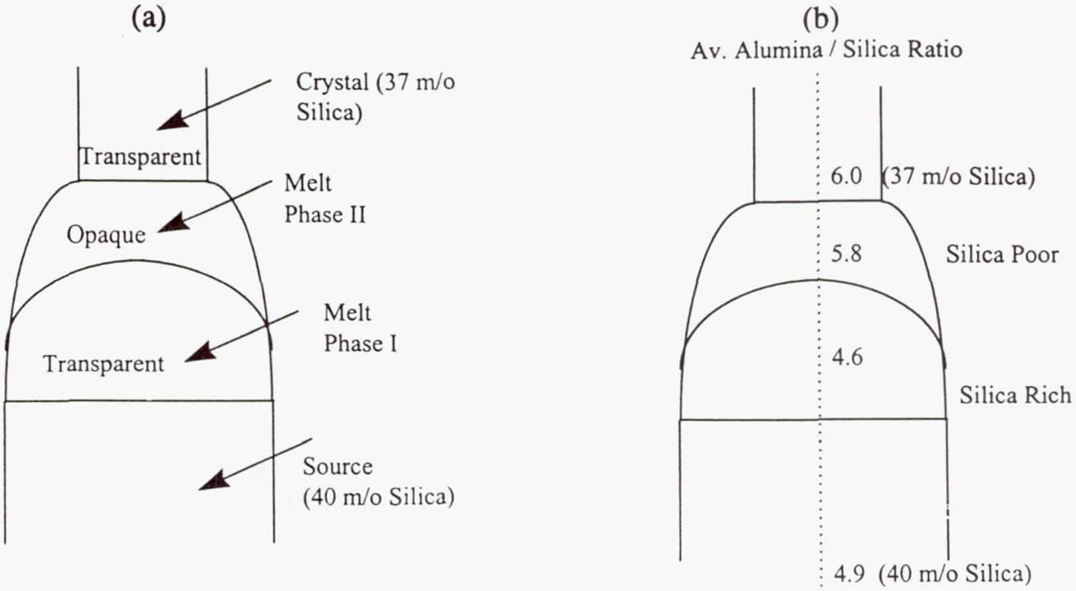

Fig. 1 a) Schematic of Phase-Separated Melt in The Float Zone Setup, and b) Qualitative Alumina/Silica Concentration Map.

3. Results and Discussion

As a first step towards gaining the necessary insight into the physical phenomena governing growth of mullites from melt, a series of tests were performed to determine the physical nature and characteristics of the melt during growth. The growth set up consists of a CO_2-laser heated float zone apparatus with operational temperatures around 1800-2200. The melting temperature of the mullite is around 1850 °C and crystal are pulled in an air atmosphere with no rotation of the crystal or source material.

Observation of Liquid-Liquid Immiscibility: Solidification experiments demonstrate that during growth of a single crystal mullite from a source material with a composition of about 33 m/o, the melt separates into two distinct phases as sketched in Fig. 1a. High resolution digital images of the melt as shown in Figs. 2 and 3 indicate that the Phase-II liquid adjacent to the crystal is less transparent to visible light than the Phase-I liquid in the interior of the melt next to the source. Optical micrographs of the cross section of the quenched molten zone also confirm the visual images by indicating a distinct difference between the scattering intensity and refractive indices of the two melt regions. The immiscibility may be brought about by structural and/or compositional differences in the melt.

Characteristics of The Two Liquid Layers: Anecdotal evidence suggests that the domed transparent Phase I liquid next to the source has a much larger viscosity than the Phase-II liquid next to the growing crystal. A qualitative map of alumina/silica concentration of the quenched solid was developed through energy disbursive spectroscopy using a field emission Hitachi SEM. The results reproduced in Fig. 2b provide a qualitative measure of the change in alumina/silica concentration through the ratio of their respective characteristic x-ray peak integrals. According to these measurements the Phase I liquid is enriched in silica as compared to the Phase-II liquid and the source.

Poly-crystalline Growth: Our numerous experimental runs suggest that phase separation in the melt is a necessary but insufficient condition for growth of a single crystal. Single crystal growth occurs at melt temperature levels around 2015 °C for small diameter (100 microns) crystals. But at lower melt temperature levels and larger diameters poly-crystalline growth prevails with a rough domed shaped interface protruding into the melt as shown in Fig. 4. SEM micrographs of the single crystal and the poly-crystalline solid are included in Fig 5. Note that poly-crystalline growth results in a solid composed of mullite with alumina-silicate glass at the grain boundaries

Seeding Experiments: A series of experiments were also performed using alumina, silica and mullite seeds to determine the effect of seeding on the liquid-liquid phase separation in the melt. When alumina seeds were used, the Phase-II liquid layer formed rapidly next to the crystal at tem-

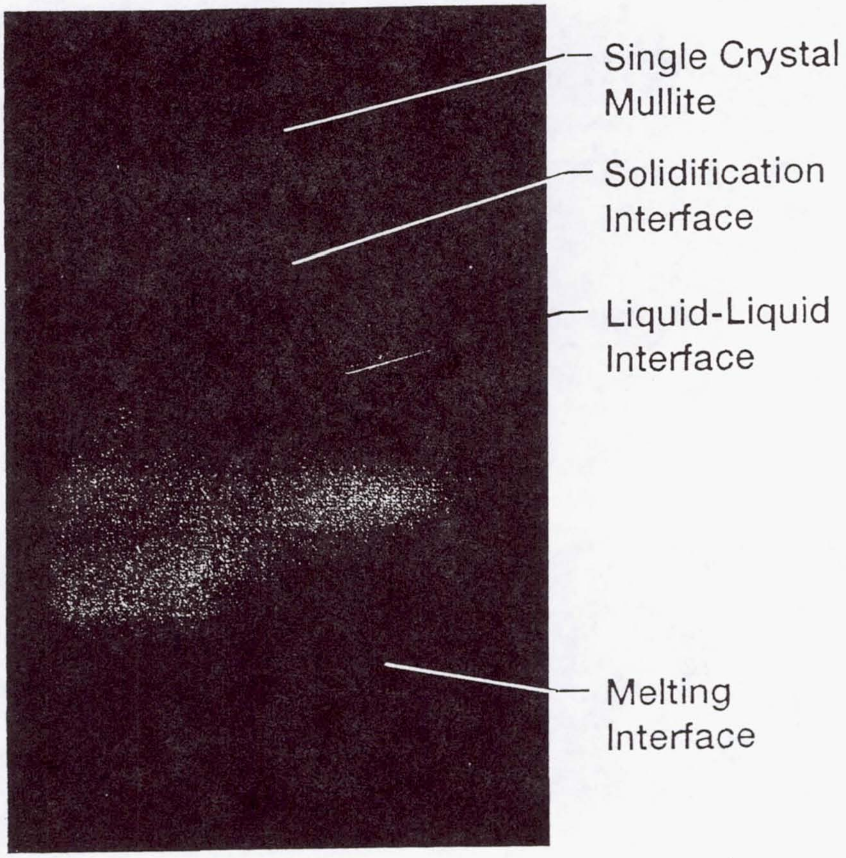

Fig. 2 High Resolution Digital Images Captured During Mullite Crystal Growth

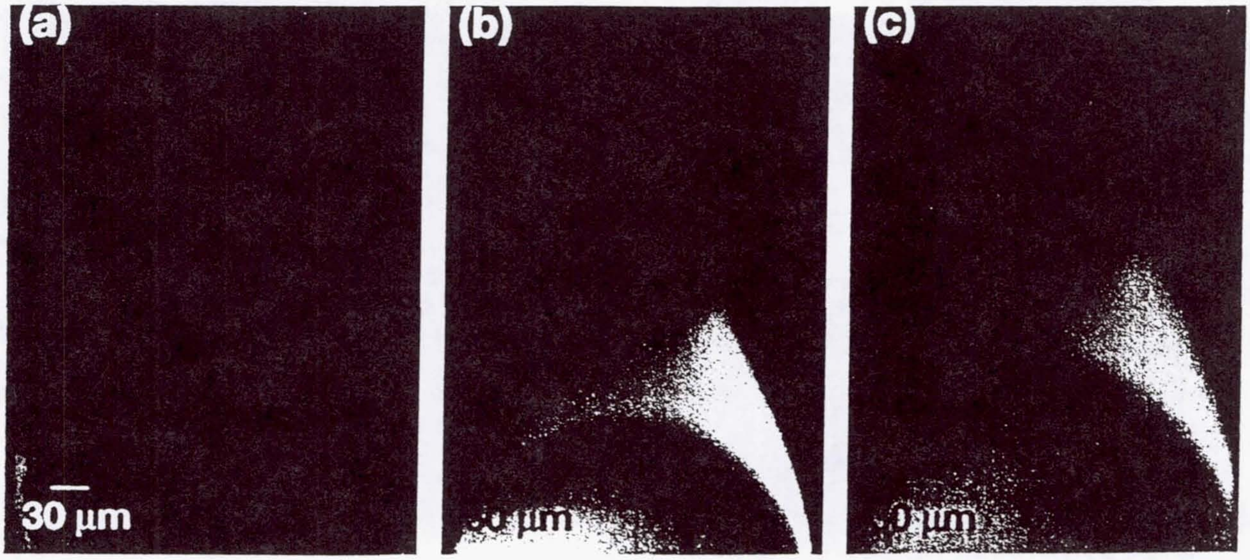

Fig. 3 a) Initiation of Single Crystal Growth, b) Subsequent Occurrence of Large Facets, c) Non-centro-symmetric Position of Crystal Fiber Relative to Melt as a Result of Faceted Growth.

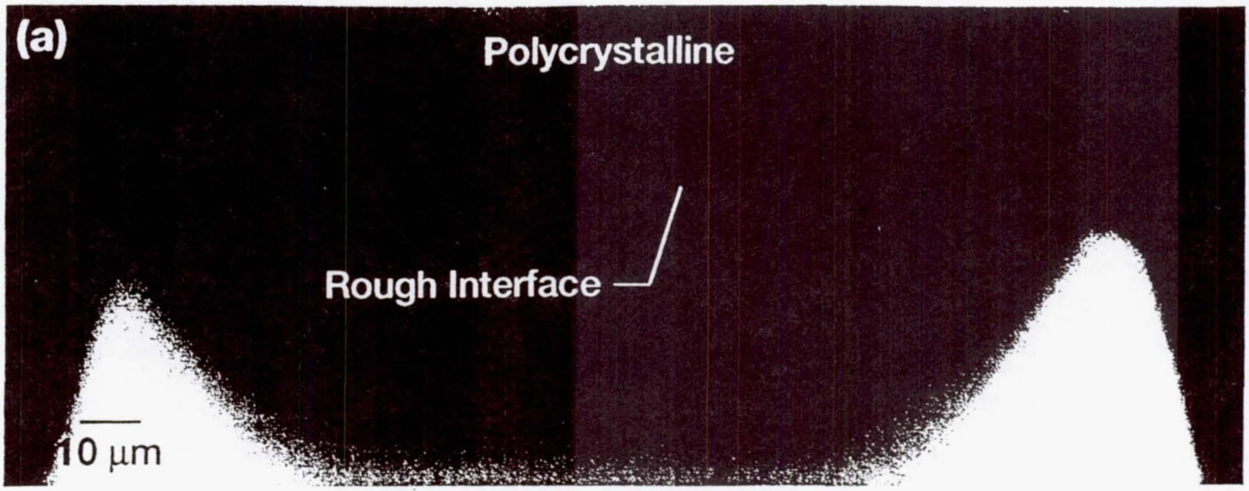

Fig. 4 High Resolution Digital Image of a Rough Domed Liquid-Solid Interface in a Poly-Crystalline Growth.

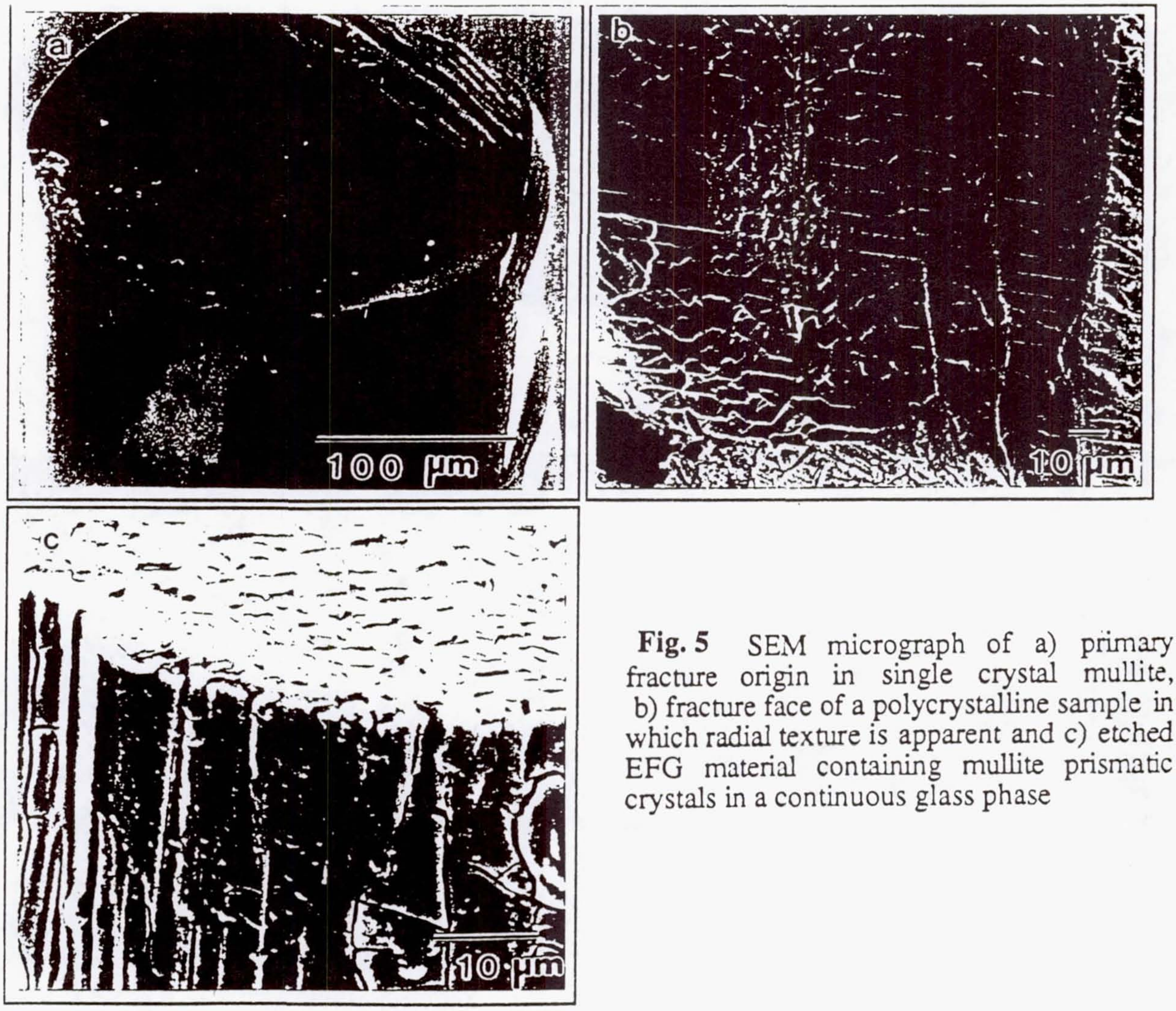

Fig. 5 SEM micrograph of a) primary fracture origin in single crystal mullite, b) fracture face of a polycrystalline sample in which radial texture is apparent and c) etched EFG material containing mullite prismatic crystals in a continuous glass phase

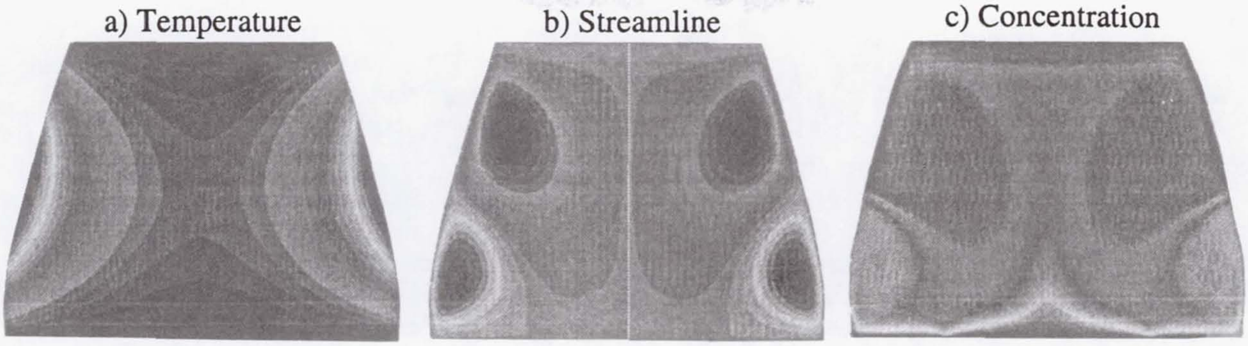

Fig. 6 a) Temperature, b) Flow, and c) Concentration Fields for a Thermocapillary Convection Dominated Case (Ma = 2.4, Ra, $2{,}4(10)^{-4}$, Pr=10, Sc=10,000).

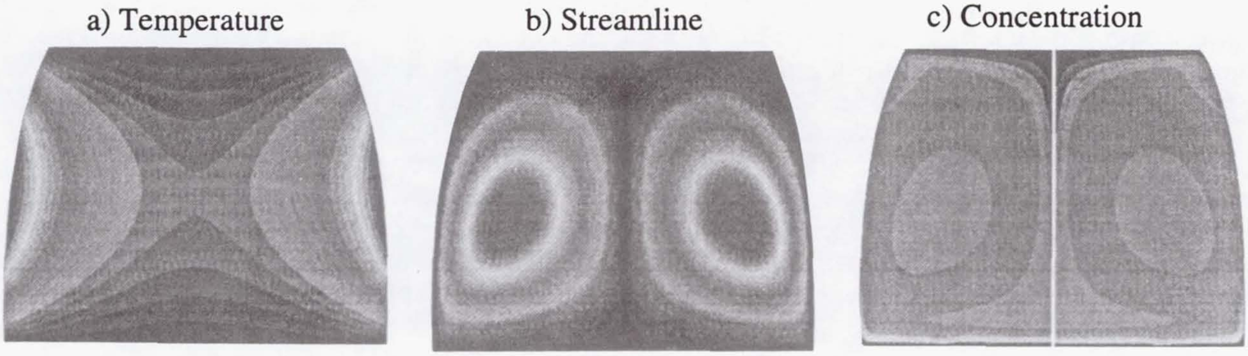

Fig. 7a) Temperature, b) Flow, and c) Concentration Fields for a Natural Convection Dominated Case (Ma = 2.4, Ra, 24., Pr=10, Sc=10,000).

perature levels around 1850 °C. When silica seed was used, the liquid-liquid phase separation did not readily take place. This might be due to excess silica in the melt. Nevertheless, It was possible to promote phase separation in two ways; either by increasing melt temperature levels or by tolerating long periods of poly-crystalline growth. It is believed that in the former case excess silica is removed by an increased evaporation rate and in the latter case excess silica is removed as the grain boundary phase. Finally, in tests with the mullite seed liquid-liquid phase separation occurred more readily compared to silica seeding but not as easily compared to alumina seeding.

Role of Transport Processes: It seems that successful growth of single crystal mullite requires a specific level of alumina concentration near the interface which in the float zone setup is determined by a dynamic balance between:

1. Evaporation of silica at the gas-melt interface
2. Rejection of silica at the crystal-melt interface
3. Transport of alumina through the phase-separated melt layers

This balance is sensitive to variations in the temperature level in the melt which controls the evaporation, diffusion, and convection rates and to variations in the melt diameter which is determines the dominant mode of convection and controls the intensity of mixing in the melt.

At small crystal diameters grown by the float zone technique, convection is not strong enough to affect the temperature field. Therefore, conduction is dominant in the melt. Radiation of course is the main heating mechanism due to the laser heating of the melt and also the main heat loss mechanism through the semitransparent crystal. There is also heat of evaporation at the gas-melt interface due to silica evaporation which is not easily quantifiable. At small diameters, Marangoni (thermocapillary) convection is dominant giving rise to concentrated vortices near the gas-melt interface which bring about only localized mixing. But at larger diameters, natural convection becomes dominant giving rise to a strong bulk flow which causes vigorous bulk mixing in the melt. Species transport takes place by convection and diffusion. Diffusion across the liquid-liquid interface is important, but at Schmidt numbers around 10,000, convection can easily modify the concentration profiles. Evaporation of silica at the melt-gas interface and rejection of silica at the melt-crystal interface have also considerable effects on the species distribution.

Numerical Simulations: A Finite element model was developed to simulate the transport processes in the float zone setup. Currently, the model includes heat, momentum, and species transport. Effects of natural and Marangoni convection, laser heating, silica rejection at the crystal-melt interface and silica evaporation at the melt-gas interface are all included. The gas-liquid interface is treated as a free surface the shape of which is determined by a force balance during the simulation. Future extensions of the model will include a rigorous formulation for the phase-separated melt and for the radiation transfer through the semi-transparent crystal.

Numerical simulations of the temperature, flow and concentration fields for the small diameter case which is dominated by thermocapillary convection are shown in Fig. 6a-c. The temperature field in Fig 6a indicates that the hottest spot occurs near the middle of the gas-melt surface where the laser beam is directed at. Transport of heat in the melt is by conduction and the resulting flow is not strong enough to modify the temperature pattern. This results in a relatively cold core in the center of the melt. At small diameters, natural convection effects are minimal and thermocapillary convection is dominant. Because the thermal coefficient of surface tension for the mullite melt is positive, the thermocapillary flow occurs from the cold region near the crystal melt interface towards the hot spot on the surface giving rise to a four-vortexed cellular pattern which provides localized mixing near the melt-gas interface as indicated in Fig. 6b. This mixing is not strong enough to affect the temperature field because of the relatively low Prandtl number, but strong enough to modify the concentration field as shown in Fig. 6c because of the large Schmidt number for the mullite melt.

Numerical simulations of the temperature, flow, and concentration fields for a larger diameter case are shown in Fig. 7a-c. This time, the flow is dominated by natural convection which results in a large buoyancy-driven vortex providing vigorous mixing in the bulk of the fluid as shown in Fig. 7b. As a result, the bottom thermocapillary vortex is completely wiped out and the top thermocapillary vortex is squeezed into a small region near the interface by the strong natural convective flow. Although the flow is not strong enough to modify the conduction dominated temperature field as indicated by comparing Figs 6a and 7a, it is strong enough to modify the concentration field drastically in the entire melt as evident in Fig. 7c. Results in Fig. 6 and 7, therefore, suggest that the relative strength of the thermocapillary to natural convection which is controlled by the ratio of the Marangoni to Raleigh numbers plays an important role in determining the flow structure in the melt.

4. Conclusion

Growth of single crystal mullite is preceded by liquid-liquid phase separation in the melt. Comparison of the numerically predicted concentration fields to the experimental measurements of the alumina/silica ratio and digital images of the phase separated melt suggests that the phase separation occurs because of structural differences. Our experiments have indicated that phase separation is a necessary but insufficient condition for single crystal growth. It seems that the phase separation is not considerably affected by the seeding material, but melt temperature levels and melt diameter play important roles by controlling the diffusion and evaporation of silica and the relative strengths of the thermocapillary and natural convection flows during growth.

Numerical simulations show that different convection patterns can prevail in the melt depending on the Raleigh to Marangoni number ratios. When natural convection is dominant, there is extensive mixing in the bulk of the melt which does not affect the temperature field noticeably but modifies the concentration fields significantly. This vigorous mixing might be responsible for the disruption of the layered melt structure at large diameters. To confirm these findings rigorously, work is underway to use an energy-based phase field method. The phase field approach together with the Navier Stokes equations provides a continuum surface tension model that can be used to focus on the interactions between the multi-layered fluid system created by the liquid-liquid immiscibility gap in the melt.

MEASUREMENT OF LIQUID-TO-SOLID NUCLEATION RATES IN UNDERCOOLED METALLIC MELTS

Joseph L. Katz
The Johns Hopkins University
Department of Chemical Engineering
Baltimore, MD 21218
Tel: 1-410-516-8484
E-mail: JLK@JHU.EDU

The main objective of this work is to obtain quantitative experimental measurements of liquid-to-crystal homogeneous nucleation rates of undercooled metallic melts. Some of the industrial melt and resolidification processes that involve nucleation phenomena heavily rely on a detailed understanding and control of either heterogeneous or homogeneous nucleation rates to produce a desired phase or microstructure. Avoiding or delaying nucleation enables the materials scientist to produce fine dispersions of second phase particles, to extend solubility limits, to refine the material's microstructure to the nanometer size range, and to synthesize novel crystalline and amorphous phases. Experimental difficulties are encountered when working with molten metals. In particular, it has not been possible to either eliminate or fully characterize the foreign surfaces presented to the melt by particles, container walls, or by suspending liquids. Thus, there is significant interest in removing these surfaces by containerless processing of metals.

This study uses a novel experimental technique that allows a small metallic droplet to be formed, solidified, and remelted in high vacuum without any physical contact. Temperature is measured by pyrometry. The same experimental apparatus should be capable of:

- exposing droplets to controlled levels of gaseous reactants and/or particulate additives in order to make quantitative measurements of their influence on crystal nucleation;
- making quantitative measurements of critical cooling rates and time-temperature-transformation diagrams for metallic glass-forming alloys;
- investigating whether there is a correlation between overheating and the undercooling limit.

This research will have several valuable outcomes: It will support the wide variety of solidification experiments of interest to microgravity investigators around the world. It can test theories for liquid-to-crystal nucleation in metallic melts. It can quantify the effect of some common trace impurities on crystal nucleation. In addition, this work, in conjunction with NASA's overall Microgravity Materials Science Program, will have a beneficial effect on countless industrial processes that involve the melting and resolidification of metals to produce useful materials.

In our experimental apparatus, droplet formation, positioning, and processing all occur in a small, evacuated chamber. The chamber is constructed of ultrahigh vacuum stainless steel and its flanges are sealed with copper gaskets. Metallic droplets are formed by electrohydrodynamically atomizing (electrospraying) a metal rod (atomizer feedstock). The tip of the sample rod is heated to its melting point by electron bombardment from a tungsten filament. An electrostatic field is established between the atomizer feedstock and an extractor electrode located below it. Molten droplets of varying sizes in the micron range are ejected from the tip of the sample rod once the force provided by the electrostatic field is strong enough to overcome surface tension effects. We successfully have electrosprayed praseodymium, gold, and zirconium sample rods, resulting in the formation of droplets with diameters in the 5 to 50 micron range.

The droplets produced during the atomization process travel downward through the vacuum chamber and into an electrodynamic levitator, where they are trapped. The electrodynamic levitator assembly consists of five electrodes: a top plate, a bottom plate, two side electrodes, and a split ring electrode (see Figure 1). By manipulating the potentials on these electrodes, all but one droplet can be released from the particle trap. DC potentials of equal magnitude, but opposite sign are placed on the top and bottom plates (disks with small holes in the center) to impart a counter-gravitational force on the metallic droplet. A negative potential is placed on the top electrode and a positive potential is placed on the bottom electrode for positively charged metallic droplets (the signs are switched for negatively charged droplets). Each side electrode is a copper spacer with a DC potential applied on it to provide horizontal positioning of the trapped particle. An AC potential is applied on the split ring electrode to provide a centering force for the droplet. Silver-coated, hollow, glass spheres and polystyrene beads successfully have been levitated in this device (in air, under manual control).

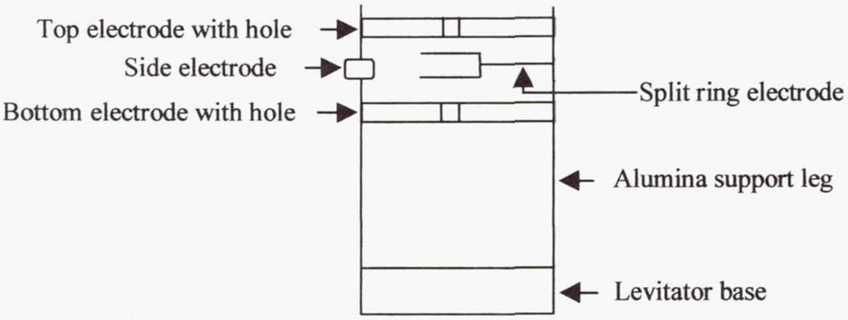

Figure 1: Front view of electrodynamic levitator assembly

We determined that a potential difference in the range of approximately 19 to 24 kilovolts between the tip of the sample rod and the extractor electrode was appropriate for the onset of droplet emission from the sample rod tip. In our first atomizer design, a potential of approximately 20 kilovolts was placed on the sample rod, while the extractor electrode (a narrow plate with a 3 millimeter diameter hole, with the tungsten filament located just below the hole) was held at ground potential. However, the metallic droplets generated with this atomizer configuration left the sample rod with too high a velocity; thus, the electrodynamic levitator was not able to capture them.

We modified the atomizer assembly by changing the design of the extractor electrode and filament arrangement (see Figures 2 and 3). Now we apply a voltage on both the extractor electrode (and filament) and the sample rod, 1.5 to 6 kilovolts on the sample rod and –15 to –23 kilovolts on the extractor electrode and its attached tungsten filament.

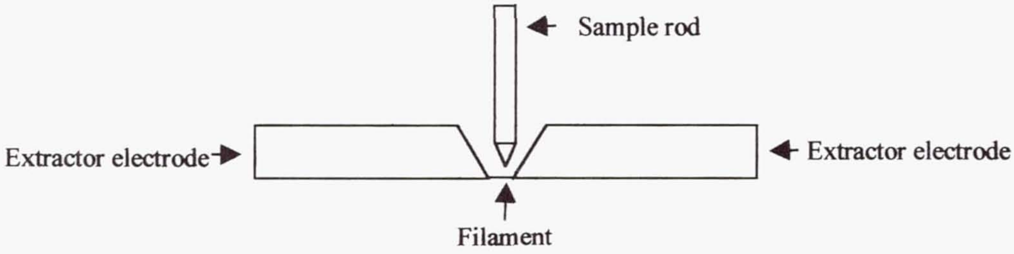

Figure 2: Front view of modified atomizer assembly

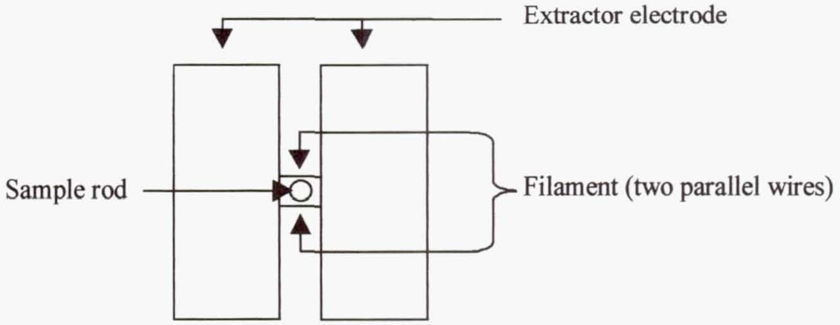

Figure 3: Top view of modified atomizer assembly

At the moment, metallic droplets that arrive at the electrodynamic levitator usually do so with too much velocity for successful capture. We are currently experimenting with higher frequency AC potentials on the split ring electrode to increase the capture capability of the levitator.

COMPOSITION EFFECTS ON PHASE FORMATION AND STABILITY

Kenneth F. Kelton
Department of Physics
Washington University
St. Louis, MO 63130
USA
Phone - 314-935-6228
FAX - 314-935-6219
email: kfk@howdy.wustl.edu

INTRODUCTION

More rapid techniques for obtaining accurate values of temperature-dependent nucleation and growth rates are needed for materials development. Small changes in stability due to composition shifts or the introduction of heterogeneous nucleation agents could be assessed quickly and experiments could be carried out remotely, such as in a microgravity environment, where the data are often taken under conditions that preclude the possibility of multiple experiments for different times at different temperatures. Differential scanning calorimetry (DSC) and differential thermal analysis (DTA) are ideally suited for these cases, yielding estimates of phase transition temperatures and enthalpies of transformation. When coupled with microstructural studies they can also give information about the mode and kinetics of transformation. The low apparatus weight and the small samples required make DSC/DTA studies ideal for supporting investigations in a reduced gravity environment. Samples processed in space, for example, might be screened quickly allowing in-flight modifications of the processing parameters. DSC/DTA investigations often suffer, however, from the lack of quantitative methods for data analysis.

Under continuing NASA support within the Microgravity Division, we have developed realistic numerical models for DSC/DTA measurements of first order phase transformations proceeding with time-dependent nucleation and cluster-size-dependent growth rates [1-3]. Account was also taken of finite sample sizes, surface crystallization and heterogeneous nucleation [3,4]. These past studies have focused on polymorphic crystallization, where the compositions of the initial and final phases are identical. Since only a limited number of phase transformations are approximately polymorphic, we are extending the models to include nucleation and growth in primary crystallizing glasses and for precipitation processes. Though growth in such cases, involving solute redistribution, has been investigated extensively, the evaluation of time-dependent nucleation rates is less clear. Previous experimental studies of compositional effects on the steady-state nucleation rate are few and interpretations of the data are sometimes difficult. Further, there are <u>no</u> previous experimental measurements of the composition dependence of the time-dependent nucleation rates. These data are essential to guide the development of a model for nucleation that can be included in our numerical models of DSC/DTA peak profiles.

In this report, results from experimental studies of the composition dependence of nucleation are presented. A model for nucleation that takes simultaneous account of the interfacial attachment processes at the growing cluster interface and diffusion into the region surrounding the developing cluster is presented and numerical results are discussed.

EXPERIMENTAL STUDIES OF COMPOSITION-DEPENDENT NUCLEATION

To guide the development of a model for nucleation in partitioning systems, experimental studies in metallic and silicate glasses and in undercooled liquid metals are underway.

a. Time-Dependent Nucleation Studies in $(Na_2O\text{-}2CaO)_{1-x}(3SiO_2)_x$ Glasses

Time-dependent nucleation rates were measured in as-quenched glasses of $Na_2O.2CaO.3SiO_2$ made with varying SiO_2 concentrations, using the two-step annealing method, for which nuclei are first produced at temperatures where growth is insignificant, and subsequently grown at higher temperatures where the nucleation rate is small [5]. The slope of the number of nuclei produced as a function of time is equal to the time-dependent nucleation rate, I(t). The induction time for nucleation, θ, is the intercept with the time axis of the portion of the graph where the number of nuclei increases linearly with time, corresponding to the steady-state nucleation rate, I^s.

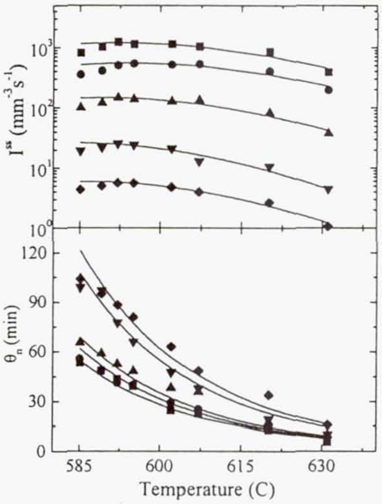

Fig. 1. Crystal steady-state nucleation rates (top) and induction times (bottom) as a function of temperature for glasses of different composition: ■ - $[SiO_2] = 0.494$; ● - $[SiO_2] = 0.5$ (stoichiometric glass); ▲ - $[SiO_2] = 0.506$; ▼ - $[SiO_2] = 0.52$; ◆ - $[SiO_2] = 0.53$. A growth anneal of 5 minutes at 700°C was used. The solid lines through the points are a fit to the steady-state nucleation rates assuming a composition-dependent interfacial energy. (From [5]).

The measured data are shown in Figure 1. To most easily indicate the amount of silica in the glass, compositions are written as $(Na_2O.2CaO)_{1-x}(3SiO_2)_x$; x=0.5 corresponds to the stoichiometric glass. The magnitudes of the steady-state nucleation rates decrease with increasing $[SiO_2]$ while the induction times increase. Changes in the growth velocity (not shown) scale inversely with changes in the induction time. The composition dependence of the nucleation rate cannot be explained by changes in the atomic mobility, as was suggested earlier by others [6], since I^s is a much stronger function of the composition than is the induction time, which scales inversely with the mobility [7]. Further, measurements of the liquidus temperature demonstrate that changes in I^s do not arise from changes in the driving free energy for crystallization [5]. If the classical theory remains correct, then, the composition dependence of the time-dependent nucleation rate arises from changes in the interfacial free energy. Detailed modeling of the time-dependent nucleation rate using the kinetic model of the classical theory [5,8] confirm this.

b. Nucleation Studies in Metallic Glasses

Most Zr-based easy metallic glass formers and many Al-rare earth (Al-RE) glasses devitrify to nanostructured materials [9,10]. The density of crystallites indicates a very high nucleation rate, 10^{19} - $10^{21}/m^3$ s, that often saturates quickly, and a low growth rate, which is strongly size dependent [11]. Because solute partitioning is central to the crystallization of these glasses, their nucleation behavior is relevant to our investigations. We recently reported the first direct measurements of time-dependent nucleation in a metallic glass by the two-step annealing method for $Zr_{65}Al_{7.5}Ni_{10}Cu_{17.5}$ metallic glasses [12]. The tendency for phase separation occurring simultaneously with nucleation and growth in the Zr-based glasses, which may also give a high density of crystallites, however, complicates the data analysis. Though phase separation is unlikely in the Al-RE glasses, the large nucleation rate in the growth regime make two-step annealing studies difficult. To get round these difficulties, annealing-induced crystal-size distributions in Al-Y-Fe glasses are being measured, and other Al-RE glasses (e.g. Al-La and Al-Sm) are under study. Our initial measurements of the size distributions for α-Al in annealed Al-Y-Fe glasses are shown in fig. 2. The rise in the density of large clusters with decreasing size signals transient nucleation. Within measurement error, the peak cluster size is independent of the annealing temperature, though the peak density is larger for the glass annealed at the higher temperature. The density decreases for small clusters, signaling either a decrease in the homogeneous nucleation rate, or a saturation of heterogeneous sites. The high cluster density at both high and low annealing temperatures makes the latter explanation unlikely. Differential scanning calorimetry studies of these glasses will be used to refine extensions being made to models of calorimetric data.

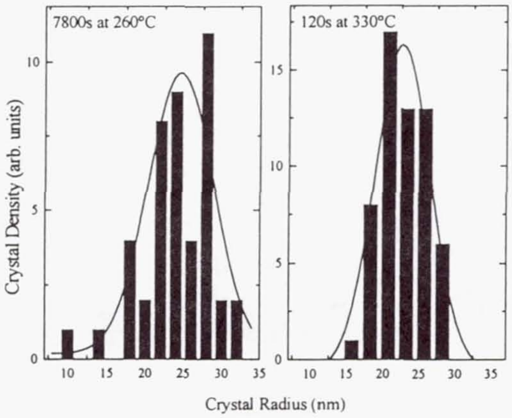

Fig. 2 - Crystal size distributions from annealed $Al_{88}Y_7Fe_5$ glass

c. Undercooling Studies in Ti-3d transition metal-Si-O alloys

Previous studies by us [13] and others [14] have shown that the interfacial energies between undercooled liquids or glasses, and quasicrystals or their crystal approximants (believed to have the same local structure as the related quasicrystal) are small. The nucleation rates, then, should depend strongly on the chemical compositions of the liquid and quasicrystal/crystal approximant. To investigate this, the microstructural evolution of undercooled Ti-Cr-Si-O, Ti-Mn-Si-O and Ti-Fe-Si-O liquids of the composition of the 1/1 crystal approximant to the icosahedral phase were studied using the NASA drop-tube facility at Marshall (in collaboration with T. Rathz and M. Robinson) and by rf-levitation at the DLR in Cologne (in collaboration with D. Holland-Moritz and D. Herlach). Although we have demonstrated that the 1/1 phase forms in all of these alloys, and is a stable phase in Ti-Cr-Si-O and Ti-Fe-Si-O, SEM backscattering studies of the solidification microstructures demonstrate that it only forms as the primary crystallizing phase in Ti-Fe-Si-O alloys. The α-Ti phase is the primary crystallizing phase in Ti-Cr-Si-O and Ti-Mn-Si-O phases.

Our determinations of the equilibrium phase diagram for Ti-Fe-Si-O show that 1/1 phases with composition $Ti_{67-71}Fe_{21-27}Si_{6-8}O_{4-10}$ are stable, forming directly from the liquid. The liquidus temperature, T_m = 1255°C, is lowest for $Ti_{68}Fe_{26}Si_6O_4$. For [Ti] < 67 at.%, only one Ti_2Fe (a=11.30 Å) phase forms with the 1/1 approximant. For [Ti] > 72 at.%, another Ti_2Fe phase with a smaller lattice constant (a=11.07 Å) forms in addition to these two phases. Below ≈ 1200°C the 1/1 phase decomposes to a phase mixture of the larger Ti_2Fe phase (a=11.30 Å) and Ti_5Si_3. Both the 1/1 and the Ti_2Fe phases, which contain strong local icosahedral order, show small undercoolings. Reduced undercooling values, $\Delta T_r = \Delta T/T_m$, obtained by levitation melting for the 1/1 phase lie between 0.11 and 0.12. As expected, the amount of undercooling increases as the composition is moved away from the stoichiometric value for the 1/1 phase.

These promising results and the small temperature range between the liquidus and the solidus near the 1/1 composition (75 to 100°C) indicate that this alloy might be a good candidate for a future space shuttle experiment, though the melting temperatures are high. Contactless measurements of the viscosity and specific heat would provide parameters needed for a quantitative analysis of the undercooling data.

NEW KINETIC MODEL FOR NUCLEATION IN PARTITIONING SYSTEMS

Experimental evidence from our glass devitrification studies [8], from precipitation processes [15] and for the devitrification of bulk metallic and Al-RE glasses [9-11] suggests that the classical theory of nucleation is inadequate in some cases to explain nucleation in partitioning systems. We have extended the classical theory of nucleation to take account of diffusion to lowest order, building upon a model proposed earlier by Russell [16]. The cluster distribution is a function of both the cluster size, n, and of the number of solute atoms in the nearest neighbor shell to the cluster, ρ. Cluster growth is based on the relative rates of exchange of solute atoms with the glass and with the cluster interior. The time-dependent nucleation rate is obtained from a numerical solution to the coupled differential equations that describe the time dependence of the cluster density, $N(n,\rho)$,

$$
\begin{aligned}
\frac{\partial N(n,\rho)}{\partial t} &= \alpha(n,\rho-1)*N(n,\rho-1) - [\alpha(n,\rho) + \beta(n,\rho)]*N(n,\rho) \\
&+ \beta(n,\rho+1)*N(n,\rho+1) + k^{+}(n-1,\rho+1)*N(n-1,\rho+1) \\
&+ k^{-}(n+1,\rho-1)*N(n+1,\rho-1) - [k^{+}(n,\rho) + k^{-}(n,\rho)]*N(n,\rho) \ .
\end{aligned}
$$

Here α and β are, respectively, the rates at which atoms enter and leave the neighborhood of the cluster and k^+ and k^- are, respectively, the interfacial attachment and detachment rates. If the solute concentration in the parent phase is high, the depletion of solute near the interface with cluster growth will be less than expected, since after atom incorporation the cluster interface moves into the neighboring region. For the discussion presented here, this complication is ignored. When the diffusive fluxes are linked with the interfacial processes underlying cluster growth an excess solute concentration in the neighborhood of sub-critical clusters can develop. This results because sub-critical clusters are on average dissolving. Atoms that diffuse to the neighborhood of those cluster interfaces tend to remain there. This is demonstrated in fig. 3, using parameters appropriate for oxygen precipitation in silicon [17]. Calculations show that the scaling behavior for I/I^s with t/θ is the same as from the classical theory of nucleation. I^s and θ are intermediate between the values for interface and diffusion limited nucleation in the classical theory.

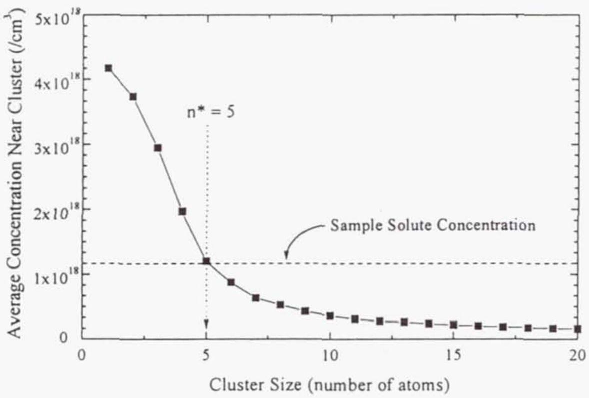

Fig. 3 - Computed average concentration of solute atoms in the neighborhood of clusters of different size. Computed for oxygen precipitation in Czochralski-grown silicon assuming an interfacial free energy of 0.38 J/m^3 and using accepted parameters [15]. The critical size, n*, at the annealing temperature is indicated.

The nucleation features in bulk metallic glasses are explained within this new model [17]. A significant population of small clusters exists in quenched glasses [3,18,19] For glasses that partition upon crystallization, those clusters are surrounded by an enhanced solute concentration. Since calculated and experimental data for polymorphic glasses demonstrate that a higher temperature distribution is retained due to kinetic freezing during the quench, clusters that are even larger than the critical size at the annealing temperature will be surrounded by a matrix rich in solute, due to the larger critical sizes at the higher temperatures. When the glasses are annealed, these clusters will grow quickly until the nearby excess solute is consumed. As is experimentally observed [11], growth will then abruptly slow down, limited subsequently by long-range diffusion. Due to the large population of small clusters, this scenario results in the high density of small crystallites. It also explains why the rate of nuclei generation drops significantly with annealing time.

* This work was supported by NASA under contract NCC 8-85.

REFERENCES

1. K.F. Kelton, J. Am. Ceram. Soc., **75,** 2449 (1992).
2. K. F. Kelton, J. Non-Cryst. Solids, **163**, 283 (1993).
3. K. F. Kelton, K. L. Narayan, L. E. Levine, T. C. Cull and C. S. Ray, J. Non-Cryst. Solids, **204**, 13 (1996).
4. K. Lakshmi Narayan, K. F. Kelton and C. S. Ray, J. Non-Cryst. Solids, **195**, 148 (1996).
5. K. Lakshmi Narayan and K.F. Kelton, J. Non-Cryst. Solids, **220**, 222 (1997).
6. P. F. James, in: Glasses and Glass Ceramics, ed. M. H. Lewis (Chapman and Hall, London, 1989). p. 80.
7. K. F. Kelton, in Solid State Physics, Vol. 45, ed. H. Ehrenreich and D. Turnbull (Academic Press, Boston, 1991), p. 75.
8. K. Lakshmi Narayan and K. F. Kelton, Acta Mat. (in press).
9. R. Busch, S. Schneider, A. Pecker and W. L. Johnson, Appl. Phys. Lett., **67**, 1544 (1995).
10. J. C. Foley, D. R. Allen and J. H. Perepezko, Scripta Materialia, **35**, 655 (1966).
11. M. Calin and U. Köster, Proceedings of ISMANAM-97, held in Barcelona, Spain (1997).
12. T. K. Croat and K. F. Kelton, MRS Proceedings, Symposium B, Boston, MA (1997).
13. J. C. Holzer and K. F. Kelton, Acta Metall. Mater., **9**, 1833 (1991).
14. D. Holland-Moritz, D. M. Herlach and K. Urban, Phys. Rev. Lett., **71**, 1196 (1993).
15. K. F. Kelton and R. J. Falster, MRS Symposium Proceedings, San Francisco, CA (1997).
16. K. C. Russell, Acta Metall., **16**, 761 (1968).
17. K. F. Kelton, Phil. Mag. Lett., **77**, 337 (1998).
18. A. L. Greer, Acta Metall., **30**, 171 (1982)
19. K. F. Kelton and A. L. Greer, J. Non-Cryst. Solids, **79**, 295 (1986).

THE TRANSIENT DENDRITIC SOLIDIFICATION EXPERIMENT (TDSE)

M.B. Koss, (518/276-2844), <kossm@rpi.edu>
M.E. Glicksman, (518/276-6721), <glickm@rpi.edu>
J.C. LaCombe, (518/276-8068), <lacomj@rpi.edu>
Materials Science and Engineering Department
Rensselaer Polytechnic Institute
Troy, NY 12180-3590

and

A. Chait, (216/433-3558), <chait@daniel.lerc.nasa.gov>
V. Pines, (216/433-6479)
Computational Microgravity Laboratory
NASA Lewis Research Center
Cleveland, OH 44135

Introduction

Dendritic solidification is one of the simplest examples of pattern formation where a structureless melt evolves into a complex crystalline microstructure. Dendrites are known to occur in the solidification of water, salts, organic materials, and most commonly and importantly, in metals and alloys. As most researchers on dendritic growth invariably note, there is considerable engineering interest in dendrites because of the role dendrites play in the determination of physical properties of cast materials. In addition, dendritic solidification has become a well-studied model in non-equilibrium physics, and computational condensed matter material physics [1].

Current theories of dendrite formation contain two independent components. The first concerns the transport of heat and solute from the solid-liquid interface into the melt. The second involves the interfacial physics that selects the unique growth velocity and tip radius of curvature from a spectrum of combinations that are consistent with the heat transfer and conservation of energy at the solid-melt interface. Until recently, neither aspect of the theory could be tested critically on the earth because of the effects of gravity-induced convection, which modifies the transport processes, and alters the growth kinetics [2,3].

Benchmark data were obtained in microgravity from two flights of the Isothermal Dendritic Growth Experiment (IDGE), using succinonitrile (SCN) [4-9]. SCN is an organic material which acts as a BCC metal analog. The data and subsequent analysis on the dendritic tip growth speed and radii of SCN dendrites demonstrated that although the theory yields predictions that are reasonably in agreement with the results of experiment, several significant discrepancies occur. However, some of the discrepancies can be understood by a consideration of the diffusion of heat from three-dimensional dendritic structures. The data and analysis for assessing the pattern selection physics are less definitive.

Current investigations by other researchers are studying, isolated single dendrites, dendritic side-branching, aligned dendritic arrays, and equiaxed dendritic growth. Some of these investigations recognize that in addition to the study of steady-state growth features, where the tip region of the dendrite grows at a constant speed, dendrites also exhibit time-dependent, non-steady features. For example, time-dependent side-branches emerge, amplify, and eventually coarsen.

The Transient Dendritic Solidification Experiment (TDSE) attempts to study fundamental aspects of time-dependent growth, while retaining the advantages of working with a single, isolated dendrite. The TDSE will also attempt to acquire benchmark microgravity data, and provide analyses on transient and time-dependent dendritic growth by employing the effect of the relatively large Clapeyron pressure-mediated melting temperature effect in SCN. A fast change in a sample's hydrostatic pressure quickly changes its liquidus temperature, and thereby provides either more or less free energy or supercooling. With this approach, we plan to observe and measure the kinetics and morphology of isolated dendrites as they evolves from one well-defined steady-state, at a pre-set supercooling, through a transient stage, to a new well-defined steady-state at the altered pressure/supercooling state.

The Clapeyron Effect

The definition of the melting temperature, T_m, is the temperature at which the liquid and solid phases co-exist in equilibrium. The melting temperature of a pure material has a well established value, which varies as a function of pressure. In materials that expand on melting (well known exceptions being water and silicon), pressure favors the solid phase as atoms or molecules are squeezed, on average, slightly closer together. Therefore, an increase in pressure does work on the solid, and raises its stability and melting temperature. This effect is classical, and can be derived from general thermodynamic principles yielding the Clapeyron equation,

$$\frac{\Delta T}{\Delta P} = \frac{T_m(v_l - v_s)}{h_f}, \qquad (1)$$

where ΔT is the change in melting temperature resulting from a change in pressure, ΔP, and v_l and v_s are the specific volumes of the liquid and solid phases, and h_f is the latent heat [10].

In principle, the Clapeyron effect, $\Delta T/\Delta P$ can be calculated from a knowledge of T_m, v_l v_s, and h_f, however, in practice, the experimental uncertainties in the determination of the specific volumes of the individual phases often leads to a large percentage uncertainty in the calculated differences in their specific volumes, which is the numerator of Eq.(1) and, hence, to large uncertainties in the pressure-induced change in the melting temperature. In the course of developing the IDGE, where small pressure changes occurred, an accurate value for $\Delta T/\Delta P$ was needed to validate procedures. We measured directly the Clapeyron effect in high-purity SCN by two independent techniques and determined that $\Delta T/\Delta P = 24.5\pm0.5$ mK/atm. Figure 1 shows the equilibrium melting point of SCN as a function of the applied pressure. These data, pressure changes up to 2 atm, directly confirm our earlier measurements of the Clapeyron coefficient using other techniques [11].

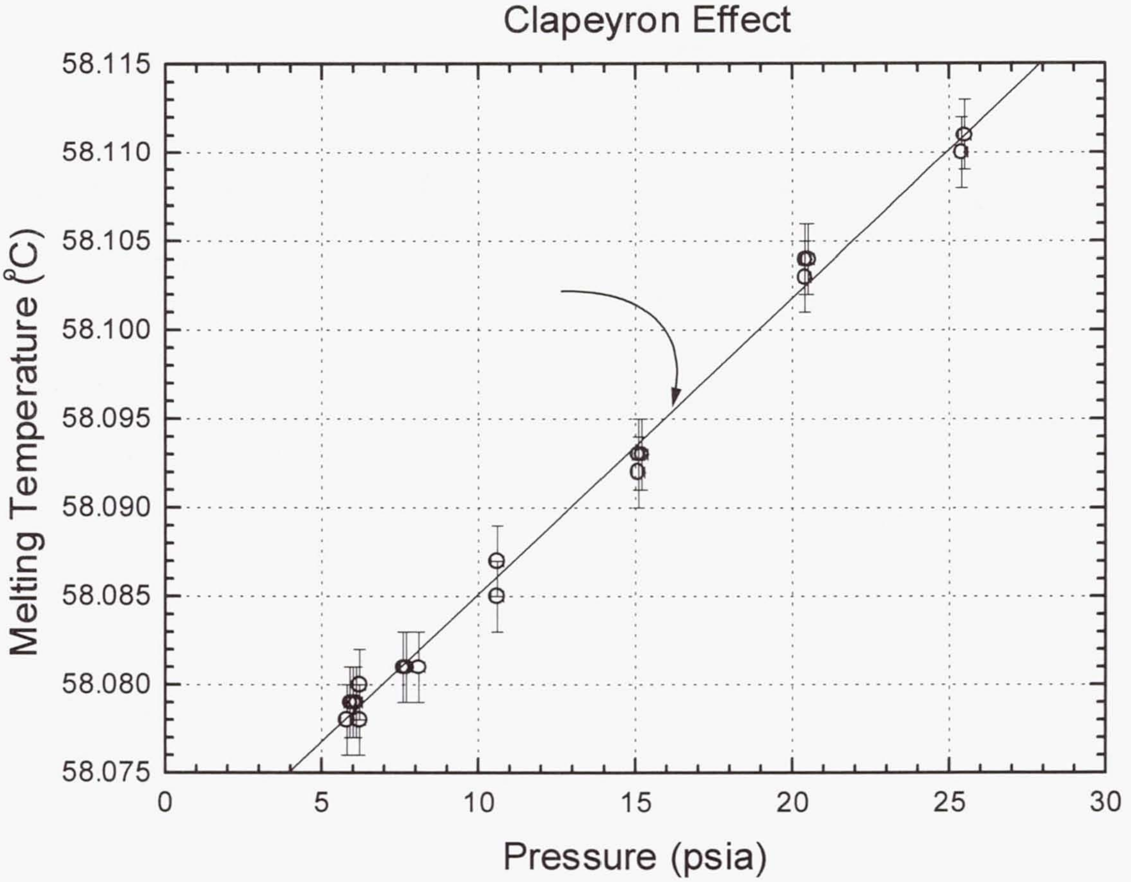

Figure 1. The Clapeyron effect in SCN.

According to Pippard [10],

> The comparison by James and William Thomson in 1849-50, of the actual pressure variation of the melting-point of ice with that predicted by Clapeyron's equation is of historical interest as being perhaps the first successful application of thermodynamics to a physical problem, and the success of this simple test undoubtedly contributed largely to the spirit of confidence which underlay and encouraged the rapid development of this subject.

As such, the Clapeyron effect is well known in Solidification theory and has been hypothesized as the explanation for cavitation induced nucleation. However, it is usually assumed that the Clapeyron effect is too small to be of interest in the solidification of metals and alloys. This is a good assumption for most materials, but not valid in the unusual case of SCN which has a Clapeyron effect that is many times larger then in most metals, and a unit supercooling that is many times smaller. Thus, the ratio of the Clapeyron Effect to the Unit Supercooling is 25 to 200 times larger for SCN then for typical metals, and indicates that pressure effects can be important in the solidification of SCN (at least for the purpose of conducting basic research).

The Transient Dendritic Growth Experiment (TDSE)

A Clapeyron coefficient as large as 24.5 mK/atm can be used in a straightforward manner to change quickly a solid-liquid interfaces equilibrium melting temperature, and, thereby, its supercooling. If this were done for an isothermal, isolated, dendrite growing at steady-state, the supercooling, and the associated free energy for dendritic growth, would be instantaneously and globally altered. This approach, would allow acquisition of a series of unique measurements on non-steady-state dendritic kinetics, and permit observations of the transient evolution of the morphology.

If a pressure-mediated melting temperature change were carried out for an isolated dendrite growing in at steady-state at some initial supercooling, the dendrite needs to respond by eventually adopting a new steady-state, appropriate to the new supercooling. If we designate in advance a particular target supercooling, we can achieve that supercooling starting at a supercoolings either above or below that supercooling, and then apply upward or downward pressure-quenching as needed. To properly calculate what that final supercooling is, one must account for the effect of the adiabatic pressure-volume work done on the melt. From the basic thermodynamics of the combined first and second laws, one can show that the temperature change in the melt temperature with pressure is,

$$\frac{\Delta T}{\Delta P} = \frac{\beta v T}{c_p}, \tag{2}$$

where β is the isothermal compressibility, v is the specific volume, T is the temperature of the melt prior to the pressurization, and c_p is the constant pressure specific heat. For SCN, this is approximately 13 mK/atm.

Thus, for the experiment, one could produce a sequence of dendritic growth runs that all terminate in a final steady-state chosen at a fixed target supercooling, but starting at a range of supercooling, at 0.025, 0.050, 0.10, 0.20, and 0.40 K above and below the common final supercooling. A particular sequence of supercooling adjustments as large as 0.4 K could be accomplished by a pressure variation in SCN of about 40 atm. This includes both the pressure mediated change in melting temperature at the interface and the adiabatic pressure-volume work temperature change of the melt. One could either start from an elevated pressure and release it (down-quench), or start from a low pressure and raise it (up-quench). For each dendritic growth run we would record the dendritic growth kinetics and morphology of the initial and final steady-states, and the transient evolution of the transition connecting the two well-defined, dynamic states. Figure 2 shows a picture that represents schematically what is described in the text.

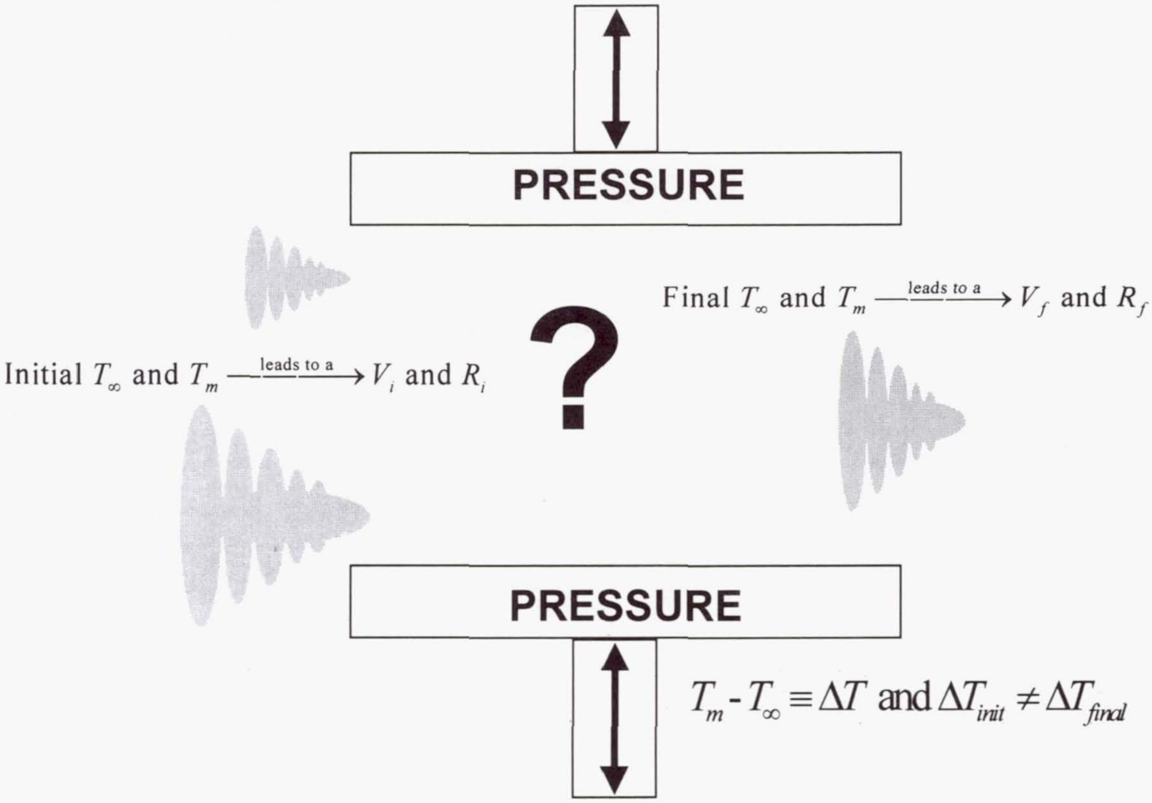

Figure 2. Schematic of Transient Dendritic Solidification Experiment (TDSE).

Preliminary Modeling Results

In addition to the experiments described above, the project has a modeling component (by the co-investigators at LeRC). The scope of this effort is to develop and conduct large scale numerical simulations of the fully transient, non-linear solidification pressurization process. These simulation use a finite-difference, operator splitting, dynamic grid generation technique to track the radius of curvature and the velocity from an initial solidification of a small spherical nucleus with arbitrary initial conditions.

For an developmental test case of an initial supercooling of 0.1 K, we simulate the growth due to an exponential pressurization over 2 seconds to 35 atm, and a final supercooling of 0.36 K, followed by an exponential de-pressurization over 2 seconds back to 1 atm.

The preliminary findings indicate that the tip velocity responds very rapidly to pressurization/de-pressurization, which reflects a rapid change in the local net heat flux corresponding to the new supercooling. Tip melting is evident following de-pressurization to accommodate a larger tip radius. The tip radius responds much more slowly for the parameter values used. The tip velocity oscillates following pressurization, but responds smoothly following de-pressurization. There is active side-branching following pressurization to accommodate reduced tip radius, and a much smoother transition to a large tip radius. This preliminary data is insufficient to determine possible hysteresis, in accordance to a two parameter selection model [12], following pressurization/depressurization cycling.

Summary and Conclusions

The study of steady-state dendritic growth has both validated many element of transport phenomena in dendritic growth, and yielded many new insights. Further development in simulation and modeling are needed, as is further understanding of the role of selection or scaling in dendritic growth. The TDSE is contributes to the further study of dendritic phenomena my carefully measuring and modeling transient effects on dendritic growth.

The major challenge encountered in measuring and analyzing the transient behavior of isothermal dendrites is defining precisely the initial conditions from which or to which the dendrite evolves. Our proposed pressure-mediated TDSE microgravity experiment, obviates this difficulty, because the transient occurs between two well-characterized steady-states, rather than between an ill-defined initial state and the final steady state. The major results expected are unique data on transient behavior that will extend the scientific bounds from the now well-understood thermal effects, and provide insight into interfacial dynamics where open questions remain.

References

1. M.E. Glicksman and S.P. Marsh, *The Dendrite*, Handbook of Crystal Growth, ed. D.J.T. Hurle, (Elsevier Science Publishers B.V., Amsterdam, 1993), Vol 1b, p.1077.
2. M.E. Glicksman and S.C. Huang, *Convective Heat Transfer During Dendritic Growth*, Convective Transport and Instability Phenomena, ed. Zierep and Ortel, Karlsruhe, (1982), 557.
3. M.E. Glicksman, E.A. Winsa, R.C. Hahn, T.A. LoGrasso, S.H. Tirmizi, and M.E. Selleck, Met. Trans. A, **19A**, 1945, (1988).
4. M.E. Glicksman, M.B. Koss, and E.A. Winsa, JOM, **47(8)**, 49, (1995).
5. M.E. Glicksman, M.B. Koss, and E.A. Winsa, Phys. Rev. Lett., **73**, 573, (1994).
6. M.E. Glicksman, M.B. Koss, L.T. Bushnell, J.C. LaCombe, and E.A. Winsa, ISIJ, **35(6)**, 604, (1995).
7. M.B. Koss, L.T. Bushnell, M.E. Glicksman, and J.C. LaCombe, Chem. Eng. Comm., **152-153**, 351, (1996).
8. L.T. Bushnell, M.B. Koss, J.C. LaCombe, and M.E. Glicksman, J. Crystal Growth, **174**, 82, (1997).
9. M.B. Koss, L.A. Tennenhouse, J.C. LaCombe, M.E. Glicksman, and E.A. Winsa, (Manuscript submitted to Metallurgical and Materials Transactions 1998).
10. A.B. Pippard, Elements of Classical Thermodynamics, Cambridge University Press, New York, 1957.
11. J.C. LaCombe, L.A. Tennenhouse, M.E. Glicksman, M.B. Koss, and E.A. Winsa, J.Crystal Growth, (Manuscript accepted for publication, 1998).
12. V. Pines, A. Chait, and M. Zlatkowski, J. Crystal Growth (Manuscript accepted for publication, 1997).

Physical Simulation of Marangoni Convection in Weld Pools

C. Limmaneevichitr and S. Kou
Department of Materials Science and Engineering
University of Wisconsin
Madison, WI 53706

ABSTRACT

Marangoni convection was observed in simulated weld pools of transparent molten $NaNO_3$. Marangoni convection was induced by touching the center of the pool surface with a hot wire to raise its temperature above that at the edge of the pool surface. The cores of the flow loops were close to the pool surface, where fluid flow was much faster and the flow lines were much more closely spaced than in the bulk pool, thus suggesting that convection in these pools was dominated by Marangoni convection. The flow loops were stable and essentially axisymmetric. When the surface temperature difference was reduced, however, convection weakened and the flow loops could not retain stability and axisymmetry.

INTRODUCTION

Marangoni convection in the weld pool can affect its depth significantly, which is often critical in welding (1). Marangoni convection in the weld pool is induced by surface-tension gradients along the pool surface, which drive the liquid at the pool surface from where the surface tension is low to where it is high (2, 3). The surface-tension gradients are induced by the temperature gradients along the pool surface. Arc heating makes the temperature of the pool surface significantly higher at the center than at the edge. In the absence of a surface-active agent, the surface tension decreases with increasing temperature, and so the melt at the pool surface flows outward from the center to the edge. In the presence of a surface-active agent, however, these phenomena can be reversed (4). Observation of Marangoni convection in a weld pool not only is limited to the pool surface because the melt is opaque, but also is complicated by the brightness of the arc.

The **objective** of the present investigation is to understand Marangoni convection in weld pools by conducting flow visualization in ground-base experiments using transparent simulated weld pools of $NaNO_3$ to reveal Marangoni convection below as well as at the pool surface.

The **benefit** of microgravity is that buoyancy convection is suppressed so that it does not interfere with the study of Marangoni convection. In the present investigation ground-base experiments are conducted in small, simulated weld pools where the effect of gravity is reduced so that Marangoni convection can dominate over buoyancy convection as in microgravity.

EXPERIMENTAL PROCEDURE

$NaNO_3$ was selected as the material for study because of its transparent melt, large temperature dependence of surface tension, and available physical properties (5-7). The apparatus for flow visualization is shown in Fig. 1. It consisted of: 1. a cylindrical inner glass container holding an essentially hemispherical pool of $NaNO_3$ melt, 2. A rectangular outer glass container holding a molten $NaNO_3$ bath to keep the pool from freezing, 3. a heat source at center of the pool surface, and 4. a light sheet of He-Ne laser passing through the meridian plane of the pool. A laser light-cut technique for flow visualization was used. The laser light sheet was produced by a 20-mw, He-Ne laser and optical lenses. Aluminum particles 20 μm in diameter was used as a tracer. Although the density of aluminum (2.7 g cm^{-3}) is greater than that of the $NaNO_3$ melt (1.9 g cm^{-3}), the settling velocity is much slower than Marangoni convection since the particles are very small in diameter. A certain amount of aluminum particles gradually settled to the pool bottom over extended periods of time.

In this preliminary stage of investigation, a hot wire of 0.76 mm diameter was used as a tentative heat source to study Marangoni convection in the absence of a surface-active agent. The bottom of the wire was allowed to touch the center of the pool surface to act as the heat source. A k-type thermocouple of 0.25 mm diameter was spot welded to the bottom of the hot wire from the side to measure its temperature. The temperature at the edge of the pool surface was measured with a second k-type thermocouple having a stainless steel sheath of 0.25 mm outer diameter. The hot wire and the second thermocouple were each mounted on a precision screw-travel stage. Two different pool sizes were studied, 6 and 10 mm in diameter at the surface. Photographs of the flow patterns were shot at the exposure time of 0.625 second.

RESULTS AND DISCUSSION

The Marangoni number is defined as $Ma = (-\partial\gamma/\partial T)(\Delta T)L/(\mu\alpha)$, where the temperature coefficient of surface tension $\partial\gamma/\partial T$ is –0.056 dyne cm^{-1} $^{o}C^{-1}$, ΔT is the temperature difference between the center of the pool surface and the edge of the pool surface, L is the characteristic length and is taken as the radius of the pool surface, the viscosity μ is 3.02×10^{-2}g cm^{-1} s^{-1}, and the thermal diffusivity α is 1.75×10^{-3} cm^2 s^{-1}.

Figure 2a shows the flow pattern in a 6 mm diameter pool with a 44.4 °C surface temperature difference (373.1 °C at center and 328.7 °C at edge; $Ma = 1.41 \times 10^4$). Essentially, the melt rises from the pool bottom along the axis of the pool to the pool surface. It continues to flow outward from the center of the pool surface, where the temperature is higher and the surface tension lower, toward the edge of the pool surface, where the temperature is lower and the surface tension higher. It then falls along the container wall to the pool bottom to start all over again. The flow is strong directionally stable enough to sustain two stable and essentially axisymmetric flow loops in the pool. The one on the right is clockwise and the one on the left counterclockwise. The cores of the flow loops are about 0.5 mm below the pool surface and 3.2 mm apart. Fluid flow is much faster near the pool surface, where the flow lines are much more closely spaced, than in the bulk pool or near the pool bottom, where the flow lines are much more widely spaced. This flow pattern is qualitatively consistent with the flow patterns of Marangoni convection computed numerically in a stationary weld pool in the absence of a surface-active agent.

Figure 2b shows the pool with the surface temperature difference reduced to 31.4 °C (356.2 °C at center and 324.8 °C at edge; $Ma = 9.99 \times 10^3$). Fluid flow in the pool slows down though the flow pattern remains essentially unchanged. With the surface temperature difference further decreased to 11.2 °C (335.3 °C at the center and 324.1 °C at the edge; $Ma = 3.56 \times 10^3$), as shown in Fig. 2c, fluid flow is no longer strong and directionally stable enough to retain an axisymmetric flow pattern. One flow loop penetrates to near the pool bottom but the other does not.

The results of 10 mm diameter pools are very similar to those described above. Figure 3a shows the flow pattern in a pool with a 48.6 °C surface temperature difference (373.7 °C at the center and 325.1 °C at the edge; Ma = 2.58×10^4). The two flow loops are stable and axisymmetric. The cores of the flow loops are about 0.8 mm below the pool surface and 6.0 mm apart.

Figure 3b shows the flow pattern in a pool with the surface temperature difference reduced to 28.4 °C (353.2 °C at the center and 324.8 °C at the edge; Ma = 1.51×10^4). As in the case of the 6 mm diameter pool, fluid flow slows down though the flow pattern remained essentially unchanged. Figure 3c shows the flow pattern in a pool with the surface temperature difference further reduced to 11.5 °C (334.5 °C at the center and 323.0 °C at the edge; Ma = 6.10×10^3). Fluid flow is weak, and the two flow loops penetrate little into the lower half of the pool, where the melt wanders around slowly. The flow pattern is neither stable nor axisymmetric.

In the configuration of a weld pool, buoyancy convection is in the same direction as Marangoni convection. Therefore, it should be checked whether the convection observed is driven primarily by Marangoni convection or buoyancy convection. The dynamic Bond number is often used as an indication of the relative strength of buoyancy convection to Marangoni convection. It is defined as $Bo = \beta\rho g\, L^2 / (-\, \partial\gamma/\partial T)$, where the thermal expansion coefficient of the melt β is $6.6 \times 10^{-4}\ {}^{\circ}C^{-1}$, and the density of the melt ρ is 1.90 g cm^{-3}, and g is the gravitational acceleration. Bo is 1.96 for the 6 mm diameter pool and 5.48 for the 10 mm diameter pool, respectively. Although $Bo > 1$ in both cases, the cores of the flow loops are very close to the pool surface, as already mentioned. This suggests that fluid flow in the pool is dominated by Marangoni convection in both cases.

In order to suppress Marangoni convection, a small drop of vacuum oil DC 704 (8) was added to the pool to contaminate the free surface of $NaNO_3$ with a thin oil film. Even at the surface temperature difference of about 50 °C, fluid flow was so slow that the flow lines in the photographs became short segments - the exposure time remained unchanged. The cores of the flow loops were significantly deeper into the pool, and the flow pattern was unstable and asymmetric. The viscosity of oil 704 drops rapidly with increasing temperature. It is about 40 cp at the room temperature, 5 cp at 100 °C and, by extrapolation, less than 1 cp at 300 °C. Since the viscosity of the $NaNO_3$ melt at its melting point 307 °C is about 3 cp, the dramatic reduction in fluid flow by the oil film cannot be due to the viscosity effect of the oil. To more clearly evaluate the role of buoyancy convection, however, it is highly desirable to conduct the experiments in microgravity.

CONCLUSIONS

Marangoni convection in weld pools can be simulated and observed in molten $NaNO_3$ pools by heating the center of the pool surface with a hot wire. As shown in these ground-base experiments, the cores of the flow loops are very close to the pool surface, where fluid flow is much faster and the flow lines are much more closely spaced than in the bulk pool. This suggests that convection in these pools is dominated by Marangoni convection. When the temperature difference between the center of the pool surface and the edge is high, the flow loops are stable and axisymmetric. When the temperature difference is reduced beyond a certain point, however, convection weakens significantly and the flow loops cannot retain its stability and axisymmetry.

REFERENCES

1. C. R. Heiple and J. R. Loper, Welding Journal, vol. 61, 97-s, 1982.
2. S. Kou, Welding Metallurgy, Wiley, New York, 1987, p. 81.
3. S. Kou, Transport Phenomena and Materials Processing, Wiley, New York, 1996, p. p.499.
4. P. Sahoo, T. DebRoy and M. J. McNallan, Metallurgical Transactions, vol. 19B, 1988, p. 483.
5. L. R. White and H. T. Davis, Journal of Chemical Physics, vol.47, 1967, p.5433.
6. G. J. Janz, Journal of Physical Chemistry, Reference Data 1, 1972, p.583.
7. F. Preisser, D. Schwabe and A. Scharmann, Journal of Fluid Mechanics, vol. 126, 1983, p. 545.
8. D. Schwabe, A. Scharmann and F. Preisser, Acta Astronautica, vol. 9, 1982, p.183.

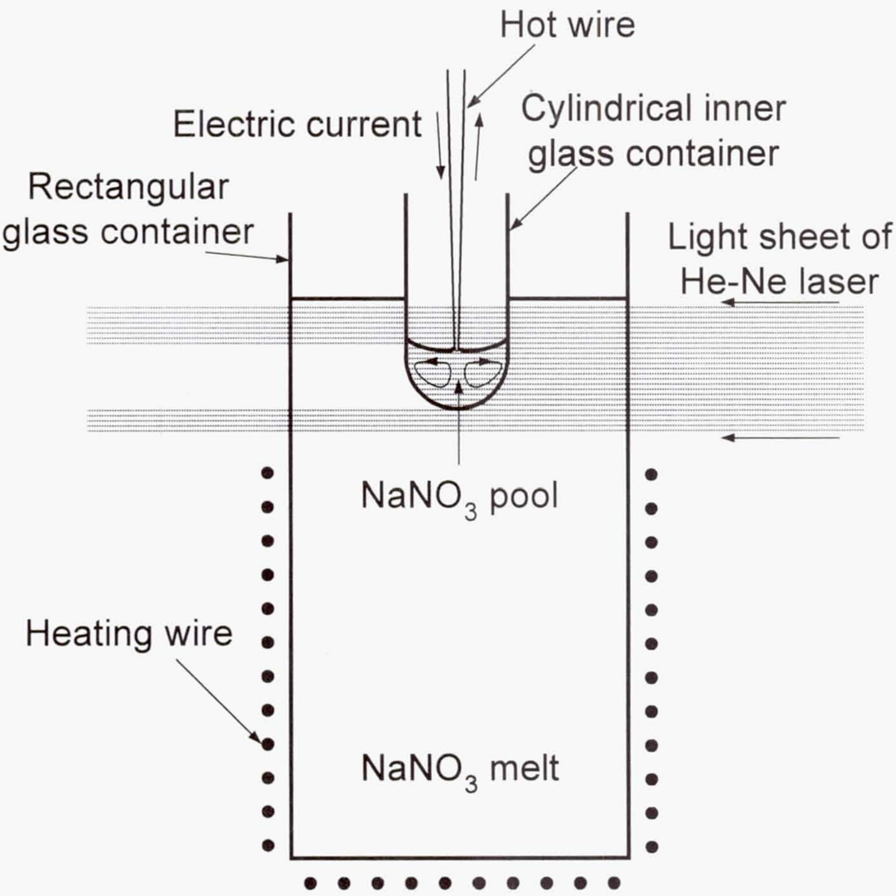

Fig 1. Apparatus for flow visualization in transparent simulated weld pool of NaNO$_3$.

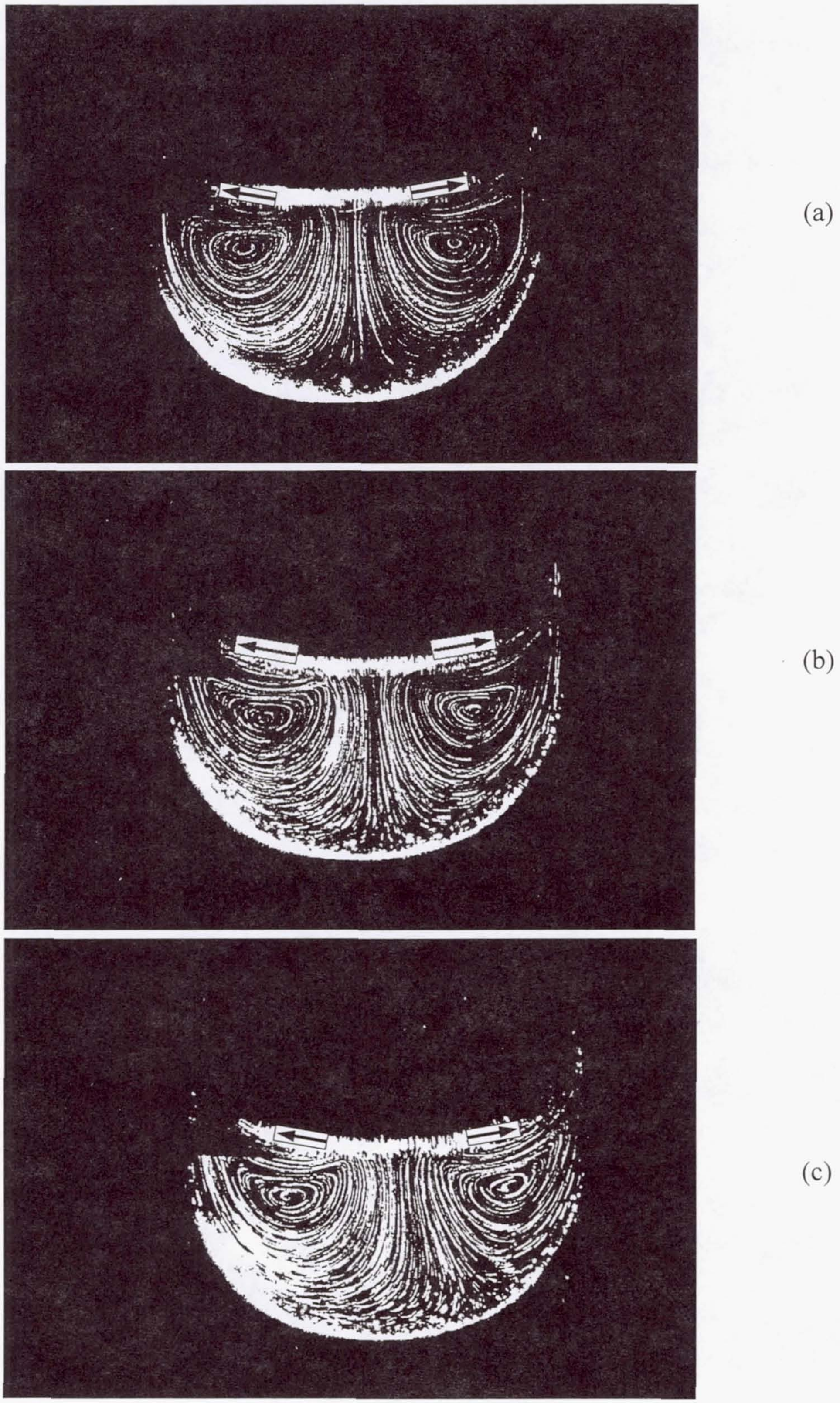

Fig.2 Flow patterns in 6 mm diameter pools with a surface temperature difference ΔT of: (a) 44.4 °C; (b) 31.4 °C; (c) 11.2 °C

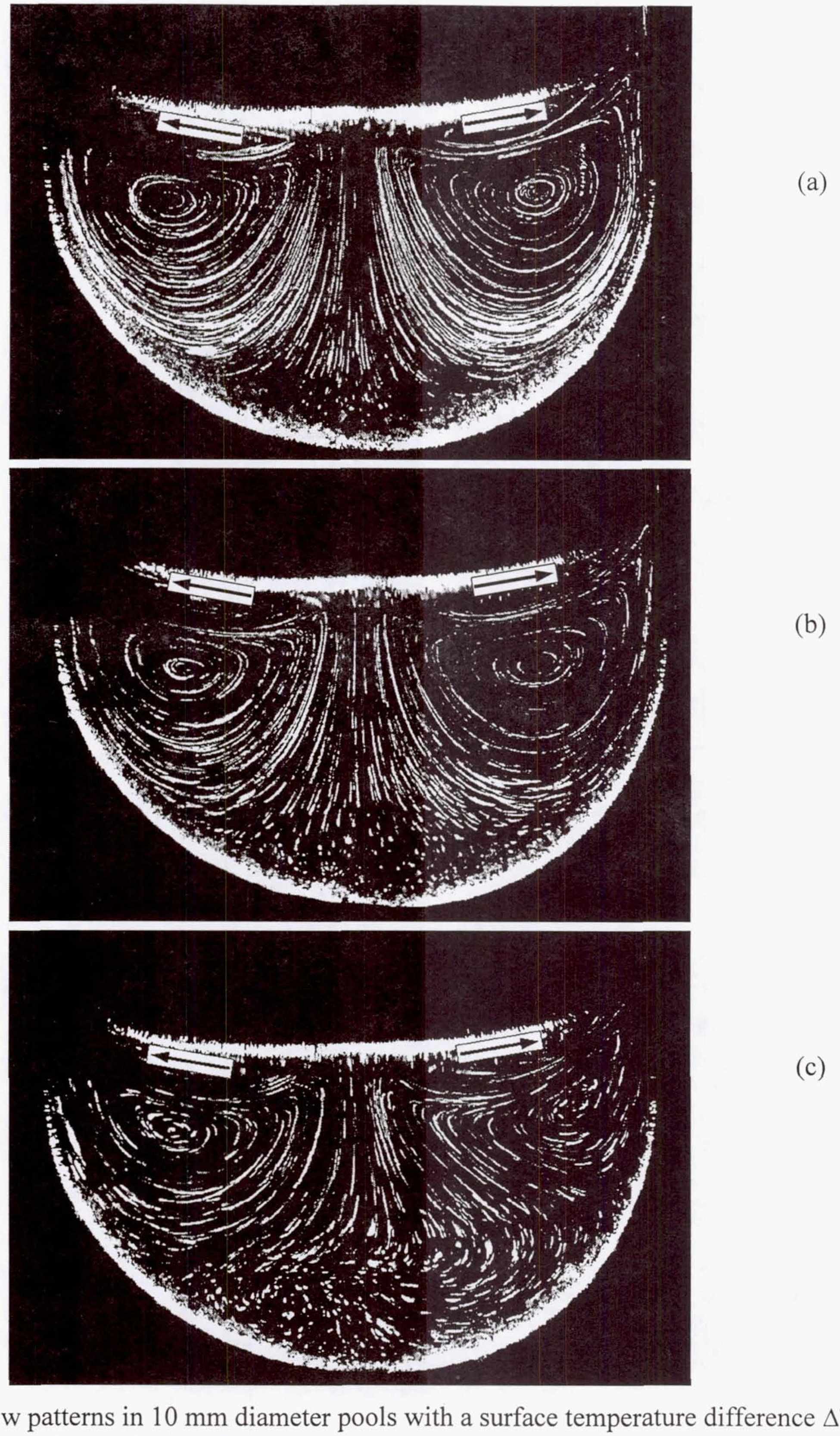

Fig.3 Flow patterns in 10 mm diameter pools with a surface temperature difference ΔT of: (a) 48.6 °C; (b) 28.4 °C; (c) 11.5 °C

INFLUENCE OF NATURAL CONVECTION AND THERMAL RADIATION MULTI-COMPONENT TRANSPORT IN MOCVD REACTORS

S. Lowry[A], A. Krishnan[B] and I. Clark[C]

The influence of Grashof and Reynolds number in Metal Organic Chemical Vapor (MOCVD) reactors is being investigated under a combined empirical/numerical study. As part of that research, the deposition of Indium Phosphide in an MOCVD reactor is modeled using the computational code CFD-ACE. The model includes the effects of convection, conduction, and radiation as well as multi-component diffusion and multi-step surface/gas phase chemistry. The results of the prediction are compared with experimental data for a commercial reactor and analyzed with respect to the model accuracy.

Keywords: Chemical Vapor Deposition (CVD), MOCVD, Computational Fluid Dynamics (CFD), Indium Phosphide, Radiation, Richardson Number

1. INTRODUCTION

Metalorganic Chemical Vapor Deposition (MOCVD) is a common technique for the growth of III-V and II-VI compound semiconductors and alloys. The uniformity and quality of these materials is tightly coupled to the composition and temperature distribution at the growth interface. As such, the understanding and control of heat and mass transport in MOCVD reactors is critical to the production of high quality materials.

The mechanisms of heat and mass transport during MOCVD are currently being investigated under a joint project between CFD Research Corporation and NASA Langley Research Center (LaRC). The research is a combined numerical/experimental study to investigate the influence of radiation and natural convection in MOCVD systems over a range of Richardson (Gr/Re^2) numbers.

2. NUMERICAL MODEL

The computational fluid dynamics code CFD-ACE is being used in the current study to model and analyze the chemistry and heat and mass transfer for selected MOCVD reactors. The code is a three-dimensional control volume Navier-Stokes code with surface and gas phase chemistry. Several advanced features essential for modeling MOCVD systems have been incorporated into the code. These include models for non-gray radiation, Soret effects, multi-component diffusion, and advanced surface chemistry models using CHEMKIN.

3. RESULTS TO DATE

The numerical studies performed thus far can be place in three categories: 1) thermal validation, 2) convection analysis, and 3) deposition predictions. These are discussed in more detail below.

Thermal Predictions

Thermal studies have been performed using data obtained by LaRC for pure gas flow in an MOCVD sled reactor. The apparatus used for these experiment is located in the Chemical Vapor Deposition Facility for Reactor Characterization at NASA Langley Research Center (Figure 1)[1]. The reactor has a circular inlet section that feeds the reactants into a rectangular duct in which is mounted a fused silica sled containing a graphite susceptor. The graphite susceptor is heated by an external Radio Frequency (RF) induction coil (not shown in Figure 1), wound around the outside of the silica test section. The reactor was operated at various flow conditions using pure nitrogen, helium, and hydrogen (Table 1). During the experiment, the temperature along the sides and top wall of the reaction chamber was measured using an infrared camera[2]. These data were subsequently used for model validation[3].

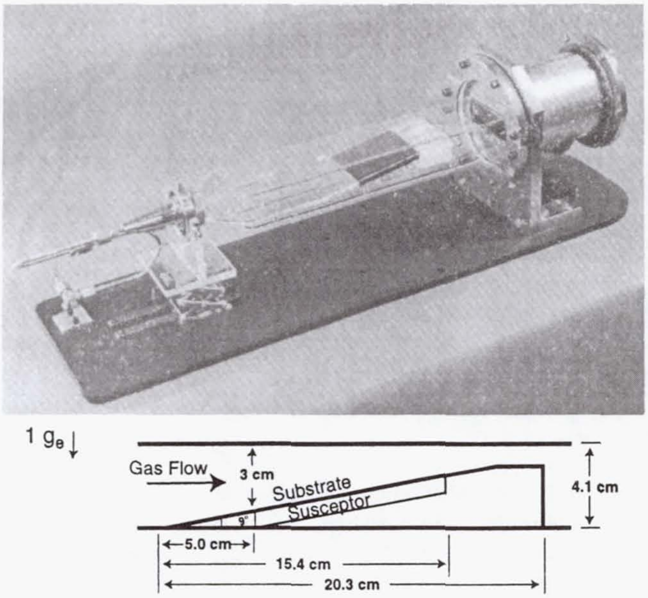

Figure 1. Experimental MOCVD Reactor at LaRC.

Table 1. Pure Gas Thermal/Flow Experiments Conducted at LaRC

$Gr/Re^2 = 27$	Hydrogen	Helium	Nitrogen
Flow Rate	9.9 lpm	N/A	9.9 lpm
Gr	200	N/A	9690
Re	2.7	N/A	18.9

$Gr/Re^2 = 41.5$	Hydrogen	Helium	Nitrogen
Flow Rate	8 lpm	8 lpm	8 lpm
Gr	200.0	171.0	9690
Re	2.2	2.0	15.3

$Gr/Re^2 = 166$	Hydrogen	Helium	Nitrogen
Flow Rate	4 lpm	4 lpm	4 lpm
Gr	200	171.0	9690
Re	1.1	1.0	7.6

$Gr/Re^2 = 664$	Hydrogen	Helium	Nitrogen
Flow Rate	N/A	N/A	2 lpm
Gr	N/A	N/A	9690
Re	N/A	N/A	3.8

$Gr/Re^2 = 2655$	Hydrogen	Helium	Nitrogen
Flow Rate	N/A	N/A	1 lpm
Gr	N/A	N/A	9690
Re	N/A	N/A	1.9

All the test cases in Table 1 were re-run using the numerical code. The model domain for these simulations consists of the entire reactor as shown in Figure 1, i.e., the chamber, the graphite susceptor, the fused silica walls, and the fused silica susceptor holder. The gray radiation model assumption was used. The temperature on the reactor wall was determined as part of the solution, rather than specified a priori. The induction heating was modeled by fixing the graphite to 873K, as set in the experiment. The results of the simulation compare well with the thermal data[3]. For the range of Richardson numbers simulated, radiation and convection were both found to play significant roles in the heat transport in the reactor. Figure 2 shows a comparison of the empirical data with the numerical predictions for Nitrogen at Ri = 41.5 where Ri is the Richardson number, defined as Gr/Re^2. (The "dips" in the experimental date are due to the RF coil obstructing the IR camera view). The agreement between the experimental data and the numerical model (e.g. to within 10 degrees for the wall temperature above the substrate) is considered to be satisfactory for first order simulations of the reactor environment. However, for very accurate analyses, additional physics, such as the non-gray radiation and the transient effects of surface emissivities need to be included. These mechanisms have been shown to be significant in commercial reactors and, as such, need to be precisely understood and modeled.

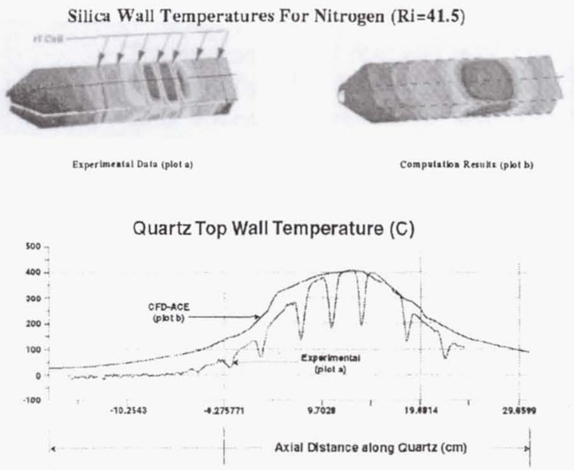

Figure 2. CFD-ACE: Thermal Prediction Validation for Nitrogen Flow in a CVD Reactor.

Flow Simulations

The parametric set of experimental test cases performed at LaRC were also analyzed numerically in terms of recirculation flows as a function of Richardson number. These parametric cases reconfirm the dependence of recirculation on the Richardson number and the existence of both longitudinal and transverse rolls for this reactor design[5-9]. Figure 3 show a comparison of the relative location and magnitude of the three dimensional recirculation zones inside the reactors as indicated by an iso-surface of reverse flow equal to one cm/sec. The results indicate the presence of recirculation. It was determined numerically that changing the reactor tilt could reduce the recirculation zones, however, since the simulations are for a non-reacting system, it is not possible to draw a correlation between the magnitude of the recirculation and the effect it would have on uniformity of deposition. This leads to the next phase of the study in which a reacting system is modeled.

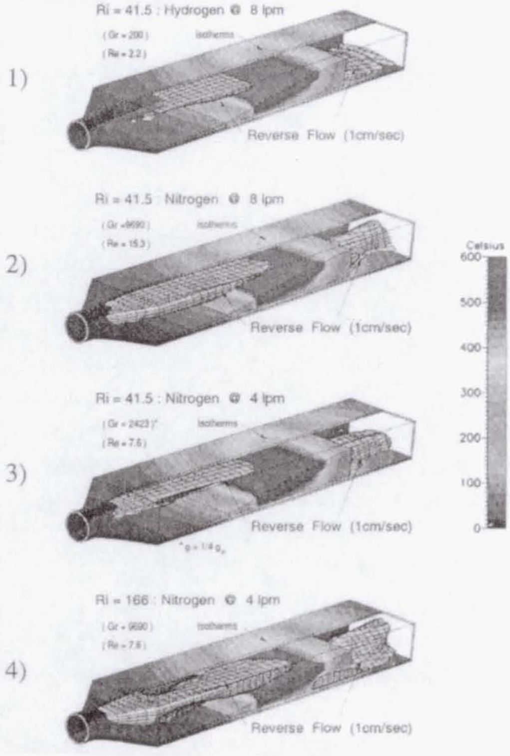

Figure 3. CFD-ACE: Recirculations Patterns for Pure Gases in an MOCVD as a Function of Ri #.

Reaction Simulation

The deposition of Indium Phosphide (InP) from the precursors Phosphine (PH_3), Trimethylindium ($In(CH_3)_3$), and Monomethylindium ($InCH_3$) was selected as the initial material for modeling. This system was selected because of the importance of InP as a semiconductor material and because of the availability of experimental data from the University of Virginia[10]. Furthermore, the data for this study were obtained using a commercial Crystal Specialties Model 425 MOCVD reactor (Figure 4) very similar in design to the test apparatus at LaRC.

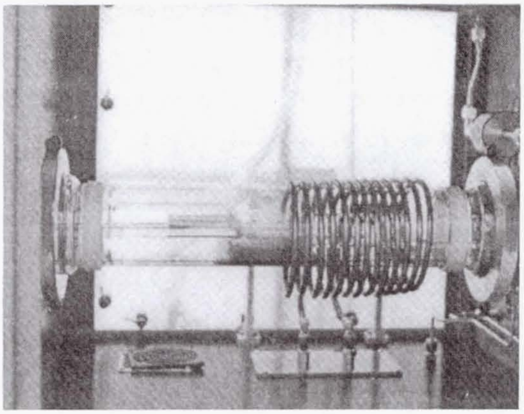

Figure 4. MOCVD Reactor at the University of Virginia.

The reaction set assumed for this system and the corresponding rate equations are shown in Tables 2 & 3 respectively [10]:

Table 2. Reaction Rates

Surface

$$In(CH_3)_3 + PH_3 \rightarrow InP(s) + 3CH_4 \tag{1a}$$

$$InCH_3 + PH_3 \rightarrow InP(s) + CH_4 + H_2$$

GasPhase

$$In(CH_3)_3 \rightarrow InCH_3 + 2CH_3 \tag{1b}$$

Table 3. Reaction Equations

$$\dot{\omega}_{InP} = \left\{A_1[TMI]e^{-E_1/RT} + A_3[MMI]e^{-E_3/RT}\right\} \tag{2a}$$

$$\dot{\omega}_{TMI} = \left\{-A_1[TMI]e^{-E_1/RT} - A_2[TMI]e^{-E_2/RT}\right\} \tag{2b}$$

$$\dot{\omega}_{MMI} = \left\{A_2[TMI]e^{-E_2/RT} - A_3[MMI]e^{-E_3/RT}\right\} \tag{2c}$$

$$\dot{\omega}_{PH_3} = \left\{-A_1[TMI]e^{-E_1/RT} - A_3[MMI]e^{-E_3/RT}\right\} \tag{2d}$$

$$\dot{\omega}_{CH_4} = \left\{3A_1[TMI]e^{-E_1/RT} + A_3[MMI]e^{-E_3/RT}\right\} \tag{2e}$$

$$\dot{\omega}_{CH_3} = \left\{2A_2[TMI]e^{-E_2/RT}\right\} \tag{2f}$$

$$\dot{\omega}_{H_2} = \left\{A_3[MMI]e^{-E_3/RT}\right\} \tag{2g}$$

The activations energies for the reaction rates are based on the experimental measurements of Buchan, et al[11] , and the pre-exponential factors were determined based on calibration with the empirical results[10].

Table 4. Activation Energies

$$A_1 = 5 \times 10^5 \quad 1/\text{sec} \tag{3a}$$

$$A_2 = 1 \times 10^{14} \quad 1/\text{sec} \tag{3b}$$

$$A_3 = 1 \times 10^9 \quad 1/\text{sec} \tag{3c}$$

Table 5. Pre-exponential Coefficients

$$E_1 = 7.6 \times 10^7 \text{J/(kgmol)} \tag{4a}$$

$$E_2 = 1.7 \times 10^8 \text{J/(kgmol)} \tag{4b}$$

$$E_3 = 1.51 \times 10^8 \text{J/(kgmol)} \tag{4c}$$

With the exception of the diffusivities, which are computed for each species based on kinetic theory, the physical properties of the mixture were assumed to be those of the predominate hydrogen. These properties were computed as follows[10]:

Table 6. Properties

Viscosity (kg / m - sec):

$$\mu = 2.907 \text{ x } 10^{-6} + 2.173 \text{ x } 10^{-8} \bullet T - 4.9167 \text{ x } 10^{-12} \bullet T^2 \tag{5a}$$

Specific Heat (J/kg - K):

$$Cp = 1.491 \text{ x } 10^4 - 1.644 \bullet T + 1.709 \text{ x } 10^{-3} \bullet T^2 \tag{5b}$$

Thermal Conductivity (W / m - K):

$$k = 9.6336 \text{ x } 10^{-3} + 3.453 \text{ x } 10^{-4} \bullet T - 1.413e - 08 \bullet T^2 \tag{5c}$$

The run conditions used for the simulation are the same as UVA InP experimental run # 83 as listed below in Table 7.

Table 7. Run Conditions

Total Flow:

7720 sccm (cm^3/min) (1.1479 e-5 kg/s)*

TMI (Trimethylindium) inlet concentration:

467e-6 mole fraction (4.844e-4 mass fraction) **

TMI flow rate: 0.048 sccm

PH3 inlet concentration:

3.88e-3 mole fraction (0.06179 mass fraction) **

PH3 flow rate: 30 sccm

Substrate temperature: 600°C (873 °K)

Pressure: 760 torr (1.013e4 nt/m^3 or 1.0 atm)

* Based on a density of 0.0893 kg/m^3 at T = 273°K and pressure = 101300 nt/m^2 (1 atm)

** Based on a mixture molecular weight of 2.1349

The Reynolds Number ($Re = UL\rho/\mu$) for this simulation is 18. This is based on a length scale of 3 centimeters which is the channel height at the leading edge of the susceptor. The viscosity is 8.983e-6 kg/m-s, based on the inlet temperature (300K) and the viscosity formula in Table 6. The corresponding mixture density, at 1.0 atmosphere and 300 K, is 0.0862 kg/m^3, as computed using the ideal gas law. The reference velocity, U, is .06255 m/s based on the above density, the cross-sectional area at the susceptor leading edge (2.743e-2 m^2), and the mass flow rate (1.1479e-5 kg/s).

The Grashof Number ($Gr = g\ \beta\ [T_{hot} - T_{cold}]\ L^3/\nu^2$) for the simulation is 16,000. The T_{hot} is the substrate temperature of 873 °K and the T_{cold} is the inlet temperature of 300 °K. For an ideal gas, the thermal coefficient of expansion (β) is equal to 1/T. For this case, β is approximated as a constant, $\beta = 1/T_{ref}$, where T_{ref} is set to the susceptor temperature (873/K). The length scale, L, and the kinematic viscosity $\nu = \mu/\rho$ (1.042 e-3 m^2/s) are the same as used for the Reynolds number and g is one earth's gravity.

The corresponding Richardson number (Gr/Re^2) is 49.

Simulation Results

Flow Pattern and Temperature Distribution: Figure 5 shows the predicted flow pattern over the sled. At the Richardson number of 49, the flow pattern is dominated by forced convection, with minor recirculation zones above the leading edge of the substrate.

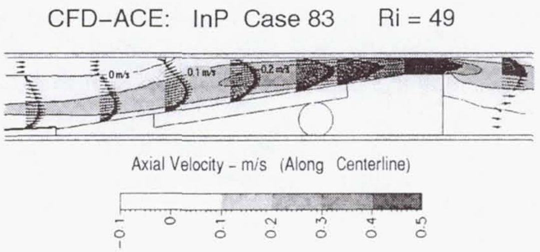

Figure 5. CFD-ACE Centerline Flow Pattern (Velocity Vectors) for UVA Case 83.

The corresponding centerline temperature contours are as shown in Figure 6.

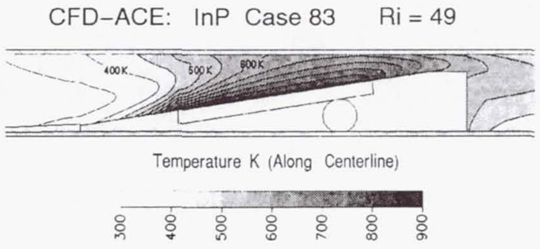

Figure 6. CFD-ACE Centerline Temperature Contours.

Predicted Deposition Rate: A full 3-D cut-away view (similar to the angle in Figure 1) of the model prediction is shown in Figure 7. The deposition rate of InP on top of the sled is indicated by the grey flooded surface contours and the x-y plot in the lower right-hand of the figure. The measured deposition rate is included in the x-y plot as a dotted line. The deposition rate along the centerline exhibits a double peak near the leading edge of the substrate, as reported by Black[10]. This is caused by the dual surface deposition mechanisms (1a and 1b) listed in Table 2. Two-dimensional studies with a refined grid do a better job of reproducing the sharpness of these twin peaks. However, even grid refinement does not increase the average deposition rate predicted over the majority of substrate. In effect, the model is under predicting the deposition rate by nearly a factor of 2.

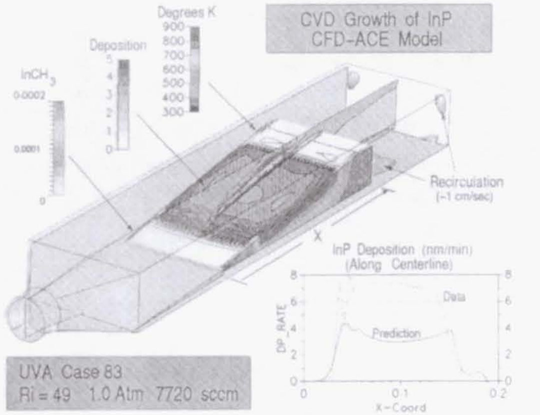

Figure 7. CFD-ACE Prediction Deposition Rates and Selected Surface Temperatures for InP at 7720 sccm at 1 atm (Ri = 49).

In an attempt to identify the cause of the discrepancy between the measured and predicted growth rates, several parametric studies were conducted to identify the sensitivity of the growth rate to the model assumptions. These include grid refinement, inlet swirl, modification of the pre-exponential coefficients (by 10%), gas radiative absorption, and substrate temperature (by 30 K). None of these were shown to increase the deposition rate significantly. This indicates that the predicted growth is diffusion limited. As shown by Figure 8, the concentration of MMI next to the substrate is severely depleted, thus limiting the growth rate. This was confirmed by increasing the reaction rate in Eq. 3c from 10^9 to 10^{20} with only a minor increase in the average growth rate.

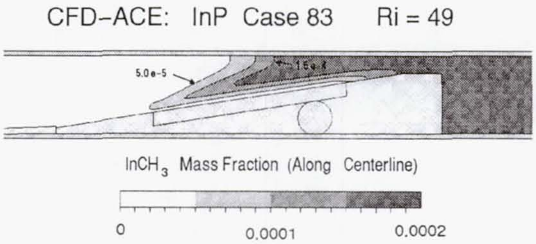

Figure 8. CFD-ACE Centerline Mass Fraction Contours.

The question therefore remains as to why the predicted growth rate of InP is less than the experimental rate. A very plausible explanation is provided by Black[10] who points out that the InP growth in the experiments is polycrystalline and that in the initial stage of growth, it is relatively sparse, as shown in Figure 9. This is in contrast with the model which computes growth rates in terms of kg/m^2-s and assumes a perfect surface. (Black's own simulation show a similar discrepancy between the experiments and predictions).

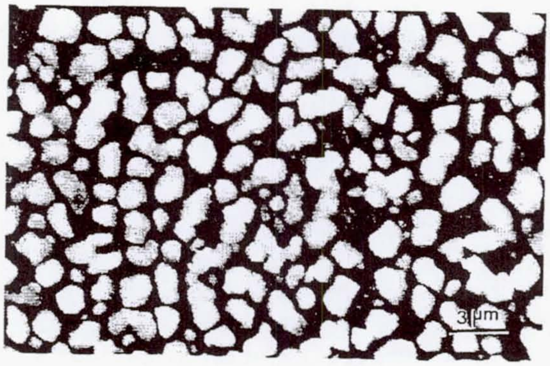

Figure 9. SEM micrograph of InP deposition on fused-silica after a growth time of 2 hours. Growth conditions the same as Run 32 (0.1 atm, 4420 sccm)[10].

The above discrepancies point to the need for both better models and well controlled experiments. Towards that end, the current model will be extended to include more rigorous chemistry models with more complex gas phase chemistry and surface reactions including surface adsorbed species[12-14]. The material to be modeled with this advanced model will be the growth of GaAs, which is well characterized and for which there are high quality data available for comparison[15-16].

4. SUMMARY/CONCLUSIONS

A full 3-D CFD model of a commercial MOCVD reactor has been developed and applied to model the growth of Indium Phosphide. The thermal predictive capability of the model has previously been validated using empirical data for pure gas flow. The model predictions for InP deposition, based on a simplified set of reaction equations are within a factor of two of the measured deposition. The empirical data itself is shown to be highly dependent on the polycrystalline structure and varies experimentally by a factor of two over a growth period of five hours. Parametric numerical studies indicates that the predicted growth rate is diffusion limited and relatively insensitive to grid refinement, increases is substrate temperature, inlet swirl, gas absorptivity, and variations in the pre-experimental factors.

The discrepancy between the predicted rate and the data is attributed to the polycrystalline nature of the growth surface and to the simplified chemistry mechanisms in the model.

The next phase of the project will study the deposition process with more complex (and realistic) chemistry models that account for surface adsorbed species. Once these improvements have been sufficiently validated, the model will then be used to better understand the combined role of radiation/convection on the MOCVD deposition process.

ACKNOWLEDGEMENTS

The authors would like to express appreciation to Professor William A. Jesser and Mr. Will Clements of the Materials Science and Engineering Department of the University of Virginia for providing data and valuable discussions on the UVA studies. This work was performed for NASA under contract NAS8-40846.

REFERENCES

1) E.J. Johnson, P.V. Hyer, P.W. Culotta, L.R. Black, I.O. Clark and M.L. Timmons (1991), "Characterization of MOCVD Fluid Dynamics by Laser Velocimetry," *J. Crystal Growth*, Vol. 109, pp. 24-30.
2) P.V. Hyer (1997), Use of Infrared Imagery in Characterization of Chemical Vapor Deposition Reactors," Infrared Physics & Tech 38, pp. 17-24.
3) M. Kannapel, S.A. Lowry, A. Krishnan, I.O. Clark, P. Hyer and E. Johnson (1997), "Preliminary Study of the Influence of Grashof and Reynolds Numbers on the Flow and Heat Transfer in an MOCVD Reactor," APIE Annual Conference, July 28-29, San Diego, CA, Vol. 3123.
4) F. Durst, L. Kadinski, Yu.N. Makarov, M. Schafer, M.G. Vasil'ev, and V.S. Yuferev (1997), "Advanced Mathematical Models for Simulation of Radiative Heat Transfer in CVD Reactors," *J. Crystal Growth*, Vol. 172, pp. 389-395.
5) A.B. Bulsar, M.E. Orazem, and J.G. Rice (1988), "The Influence of Axial Diffusion on Convective Heat and Mass Transfer in a Horizontal CVD Reactor," *J. Crystal Growth*, Vol. 92, pp. 294-310.
6) J. Ouazzani and F. Rosenberger (1990), "Three-Dimensional Modeling of Horizontal Chemical Vapor Deposition I. MOCVD at atmospheric pressure," *J. Crystal Growth*, Vol. 100, pp. 545-576.
7) D.I. Fotiadis, M. Boekholt, K.F. Jensen, and W. Richter (1990), "Flow and Heat Transfer in CVD Reactors: Comparison of Raman Temperature Measurements and Finite Element Model Predictions," *J. Crystal Growth*, Vol. 100, pp. 577-599.
8) E.P. Visser, C.R. Kleijn, C.A.M. Govers, C.J. Hoogendoorn, and L.J. Giling (1989), "Return Flows in Horizontal MOCVD Reactors Studied with the Use of TiO_2 Particle Injection and Numerical Calculations," *J. Crystal Growth*, Vol. 93, pp. 929-946.
9) P.B. Chinoy and S.K. Ghandhi (1991), "Design Considerations for the Elimination of Recirculation in Horizontal Epitaxial Reactors," *J. Crystal Growth*, Vol. 108, pp. 105-113.
10) L.R. Black (1993), "Three-Dimensional Numerical Modeling of InP MOCVD with Experimental Verification," Dissertation, University of Virginia, Department of Material Sciences and Engineering.
11) N.I. Buchan, C.A. Larsen, and G.B. Stringfellow (1988), "A Mass Spectrometric Study of the Simultaneous Reaction Mechanism of TMIn and PH_3 to Grow InP," *J. Crystal Growth*, Vol. 92, pp. 605-615.
12) K.F. Jensen, D.I. Fotiadis, and T.J. Mountziaris (1991), "Detailed Models of the MOVPE Process," *J. Crystal Growth*, Vol. 107, pp. 1-11.
13) M. Tirtowidjojo and R. Pollard (1988), "Elementary Processes and Rate-Limiting Factors in MOVPE of GaAs," *J. Crystal Growth*, Vol. 93, pp. 108-114.
14) M. Tirtowidjojo and R. Pollard (1989), "The Influence of Reactor Pressure on Rate-Limiting Factors and Reaction Pathways in MOVPE of GaAs," *J. Crystal Growth*, Vol. 98, pp. 420-438.
15) T. Bergunde, F. Durst, L. Kadinski, Yu.N. Makarov, M. Schafer, and M. Weyers (1994), "Modeling of Growth in a 5 x 3 Inch Multiwafer Metalorganic Vapour Phase Epitaxy Reactor," *J. Crystal Growth*, Vol. 145, pp. 630-635.
16) A.P. Peskin and G.R. Hardin (1998), "Gallium Arsenide Growth in a Pancake MOCVD Reactor," *J. Crystal Growth*, Vol. 186, pp.494-510.
17) T. Bergunde, J. Dauelsberg, L. Kadinski, Yu.N. Makarov, M. Weyers, D. Schmitz, G. Strauch, and J. Jurgensen (1997), "Heat Transfer and Mass Transport in a Multiwafer MOVPE Reactor: Modeling and Experimental Studies," *J. Crystal Growth*, Vol. 170, pp. 66-71.

A CFD Research Corporation, 215 Wynn Dr., Huntsville, AL 35805; sal@cfdrc.com; (256) 726-4853

B CFD Research Corporation, 215 Wynn Dr., Huntsville, AL 35805; ak@cfdrc.com; (256)726-4816

C NASA Langley Research Center, MS 473, Hampton, VA 23681

Page intentionally left blank

Orbital Processing of Eutectic Rod-like Arrays (OPERA)

David J. Larson, Jr., Lili Zheng, and Hui Zhang
Materials Science and Engineering Department
State University of New York at Stony Brook
Engineering 318
Stony Brook, NY 11794-2275

Task Objective

The objective of this program is to utilize the orbital microgravity environment to conduct unique experiments to evaluate process models that describe convective influences on solidification of regular, low volume fraction, eutectic alloys. These models include a generic model of lamellar and rod-like eutectic solidification and complementary models that concern current interface demarcation and the influences of Soret transport on eutectic and off-eutectic solidification.

Experimentally, we will directionally solidify regular eutectic structures in orbit (microgravity) and terrestrially (1-g) under magnetically damped and undamped conditions. We will simultaneously apply *in-situ* diagnostics to monitor and perturb the solidification interface velocity using current interface demarcation and to precisely monitor the temperature at the solidification interface using Seebeck measurements or subminiature thermocouple arrays. Comparative quantitative sample and data analyses will determine the relations between the velocity, interface temperature (undercooling), and structural parameters (rod diameter and interrod spacing) in microgravity (μg) and in unit gravity (1-g) under magnetically damped and undamped conditions.

Microgravity Rationale

Prior analytical convective sensitivity testing of eutectic solidification theory predicted insensitivity and prior experimental testing of this theory offered broad-based agreement, although mostly for high volume fraction lamellar eutectics that solidified without faceting at the solidification interface. Directional solidification experiments of low volume fraction eutectics under damped (microgravity or magnetic field) conditions, however, have demonstrated significant sensitivity, challenging this fundamental theory. More recent theories have been proposed which introduce: kinetic undercooling, faceting, velocity sensitivity, fluid velocity, and the possibility that the interface composition is not the same as the bulk liquid composition in order to explain the observed sensitivity. This program tests the established and proposed analytical theories and addresses the origins of the discrepancies between the experimental and analytical results. New process model(s) will be developed that will include all of the above possibilities as well as the influence(s) of the diagnostic techniques that will be employed.

Significant Results

The dominant theory that describes eutectic solidification, Jackson and Hunt, was derived for diffusion-controlled growth of alloys where both solid phases solidify metallically (i.e., without faceting at the solidification interface) and with minimum interface undercooling. Both high volume fraction (lamellar) and low volume fraction (rod-like) regular metallic arrays are treated by this theory. Many of the useful solders and brazements, however, and most of the *in-situ* composites are characterized by solidification reactions that are faceted/non-faceted in nature, rather than doubly non-faceted (metallic). Further, diffusion-controlled growth conditions are atypical terrestrially since gravitationally-driven convection is pervasive. As a consequence, it is important to determine whether these faceted/non-faceted composites behave in the same manner as their doubly non-faceted counterparts. We have selected the regular, faceted/non-faceted, low volume fraction case for investigation because of the potential for process control using directional solidification and the near-isothermality of the interface.

As a critical part of this task, a directional solidification model has been developed and validated experimentally with concomitant thermo-electric interface demarcation. This full transient model includes all of the thermo-electric contributions (Peltier, Thomson, Joule, and Seebeck) and calculates the interface shape and location as a function of time. The eutectic rod-like structure within the pulsed region and within the post-pulse transient is then approximated using the known relationship between velocity and microstructure. This model also incorporates Soret diffusion, induced and applied magnetic fields, and gravitationally-dependent convective contributions.

A separate effort has developed a generalized Jackson-Hunt theory that includes either lamellar or rod-like microstructures, asymmetric phase relations (volume fraction and redistribution coefficients), significant interface undercooling, the full Peclet (velocity) regime, surface energies, and the possibility that the interfacial composition is not the same as the bulk liquid composition.

The above models will be merged, and when completed they will provide a full model of the influences of transient and steady-state experimental conditions, as well as convective influences on directional eutectic solidification.

Experimentally, the need for homogeneous eutectic alloys is obvious. These alloys are being fabricated using rocking furnace technology and directional solidification experiments are being conducted in the Bridgman-Stockbarger geometry. The possibility of macrosegregation being introduced due to Soret Transport is being quantitatively evaluated using the process model, ground experiments, and prior off-eutectic flight results. The terrestrial experiments will continue, and a precursor μg flight experiment has been approved to precisely measure the Soret Coefficient.

The application of current pulses to the directionally solidifying sample is being developed using programmable power supplies and experiment control using Lab-View. Ampoule design is complete and preliminary experiments have been conducted. Process model validation is being pursued under one-g magnetically damped and undamped conditions.

Preliminary evaluation of interface temperature measurement has been initiated using sub-miniature thermocouple, sub-micron thermocouple, and Seebeck technologies. The compatibility of the Seebeck technique with applied magnetic fields will be evaluated and the system requirements will be quantitatively ascertained. Preliminary measurements suggest that Seebeck signals on the order of 10 μV must be processed.

Lastly, the empirical relations between microstructure, interface velocity, and interface solidification temperature are being refined under damped and undamped conditions. Improved techniques are under development for polishing the samples and quantitatively analyzing the microstructures, pattern formations and particle morphology and distribution.

Orbital Processing of High-Quality Zn-Alloyed CdTe Compound Semiconductors

D.J. Larson, Jr. - Principal Investigator
Materials Science and Engineering Department
State University of New York at Stony Brook
Stony Brook, NY 11794-2275

Co-Investigators:
M. Dudley and B. Raghothamachar - Materials Science and Engineering Department, State University of New York at Stony Brook
J.I.D. Alexander - Department of Mechanical and Aerospace Engineering, Case Western Reserve University
F.M. Carlson - Department of Mechanical and Industrial Engineering, Clarkson University
D. Gillies and M. Volz - Space Sciences Laboratory, NASA Marshall Space Flight Center
T.M. Ritter - University of North Carolina at Pembroke
D. DiMarzio - Northrop Grumman Corporation

Task Objective

The objective of this research is to investigate the influences of gravitationally-dependent phenomena (hydrostatic and buoyant) on the growth and quality of doped and alloyed Cadmium-Zinc-Telluride (CdZnTe) crystals grown by the modified seeded Bridgman-Stockbarger technique. It is hypothesized that the damping of the gravitationally-dependent buoyancy convection will substantially enhance chemical homogeneity and the near-elimination of hydrostatic pressure will enable significant reduction in defect (dislocations and twins) density.

Microgravity Rationale

The rationale for this experiment was to exploit the near-absence of hydrostatic pressure to allow the crystal to grow without forced wall contact. It was hypothesized that a crystal grown under conditions without wall contact might have substantially reduced defects due to the absence of hoop stresses during the growth and post-solidification cooling. Two geometries were employed, both of which used the balance of forces at the solid/liquid/vapor interface to minimize the likelihood of wall contact.

Significant Results

Zn:CdTe crystals were grown in unit gravity and in microgravity for comparative analysis. Two crystals were grown on the First United States Microgravity Laboratory (USML-1/STS-50) mission in 1992, and two additional crystals were grown on the Second United States Microgravity Laboratory (USML-2/STS-73) mission in 1995. The Crystal Growth Furnace (CGF) in the seeded Bridgman-Stockbarger crystal growth geometry was utilized on both missions. Crystals grown on USML-1 were found to have solidified with partial wall contact due to the near-absence of the hydrostatic pressure in microgravity, a residual g-vector that was not axial, and the non-wetting sample/ampoule wetting conditions. Crystals grown on USML-2 included: a sample/ampoule identical to the USML-1 sample/ampoule (with the addition of a restraining spring to simulate hydrostatic pressure internally) and a tapered ampoule which accomplished 2.2 cm of crystal growth without wall contact.

Infrared transmission of all ground and flight samples was found to be 63-66%, very close to the theoretical 66%, suggesting good stoichiometric control. Infrared microscopy confirmed that the primary precipitates were Te and their size (1-10 μm) and density suggested that the flight and ground-based samples experienced similar thermal histories.

Longitudinal macrosegregation, calculated using scaling analysis, was predicted to be low. Nearly diffusion controlled growth was achieved even in unit gravity and macrosegregation data could be fit with a diffusion controlled model. Radial segregation was monitored and was found to vary with fraction solidified, particularly through the shoulder region, where the sample cross-section was varying significantly. It was also disturbed in the flight samples in regions where asymmetric wall contact was noted. In regions where a steady-state was established, the radial segregation was invariant, within our experimental measurement error. Local segregation near free surfaces was investigated for evidence of thermocapillary convection using low temperature photoluminescence techniques. No evidence of compositional segregation was detected.

Flight samples were found to be much higher in structural perfection than samples processed in unit gravity under identical growth conditions. In regions where solidification had occurred without wall contact, the free surfaces evidenced virtually no twinning, although twins appeared in the flight samples in regions of wall contact and were pervasive in the ground samples. These results were confirmed using optical microscopy and synchrotron x-ray white beam topography. Full-width half-maximum (FWHM) rocking curve widths, recorded in arc-seconds, were significantly reduced from 20 a-s (1-g) to 9 a-s (μg) for the best regions of the crystals. The 9 a-s (FWHM) rocking curve value in the unconfined flight samples equals the best value reported terrestrially for this material.

Further evidence of high structural perfection was determined using low temperature photoluminescence (PL). The PL spectra exhibited well defined bound- and free-exciton peaks and donor-acceptor pair recombinations with phonon replicas of both types of features. Noticeably absent was the deep broad-band often reported at ~1.4 eV in lesser quality material.

The ground samples exhibited a fully developed (111)[110] dislocation mosaic structure, whereas dislocations within the flight samples were discrete and no mosaic structure was evident. The defect density was quantitatively reduced from 75,000 (1-g) to 800 (μg) ± 50%. Dislocation etch pit density results were confirmed using transmission synchrotron white beam and monochromated beam topography. The low defect density is thought to have resulted from the near absence of hydrostatic pressure, which allowed the molten boule to solidify with little or no wall contact. This minimized the transfer of hoop stresses during solidification and post-solidification processing.

Crystal Growth of II-VI Semiconducting Alloys by Directional Solidification

Dr. Sandor L. Lehoczky, Principal Investigator
NASA Marshall Space Flight Center
Mail Code ES75
Marshall Space Flight Center, AL 35812
Phone: (256) 544-7758
Fax: (256) 544-8762
E-mail: sandor.lehoczky@msfc.nasa.gov

Co-Investigators:
  Dr. Frank R. Szofran, NASA Marshall Space Flight Center
  Dr. Ching-Hua Su, NASA Marshall Space Flight Center
  Dr. Sharon D. Cobb, NASA Marshall Space Flight Center
  Dr. Rosalia A. Scripa, University of Alabama at Birmingham
  Dr. Yi-Gao Sha, University Space Research Association

This research study is investigating the effects of a microgravity environment during the crystal growth of selected II-VI semiconducting alloys on their compositional, metallurgical, electrical and optical properties. The on-going work includes both Bridgman-Stockbarger and solvent growth methods, as well as growth in a magnetic field. The materials investigated are II-VI, $Hg_{1-x}Zn_xTe$, and $Hg_{1-x}Zn_xSe$ ($0 \leq x \leq 1$), with particular emphasis on x-values appropriate for infrared detection and imaging in the 5 to 30 μm wavelength region. Wide separation between the liquidus and solidus of the phase diagrams with consequent segregation during solidification and problems associated with the high volatility of one of the components (Hg), make the preparation of homogeneous, high-quality, bulk crystals of the alloys an extremely difficult nearly an impossible task in a gravitational environment.

The three-fold objectives of the on-going investigation are as follows:

1. To determine the relative contributions of gravitationally-driven fluid flows to the compositional redistribution observed during the unidirectional crystal growth of selected semiconducting solid solution alloys having large separation between the liquidus and solidus of the constitutional phase diagram;

2. To ascertain the potential role of irregular fluid flows and hydrostatic pressure effects in generation of extended crystal defects and second-phase inclusions in the crystals; and,

3. To obtain a limited amount of "high quality" materials needed for bulk crystal property characterizations and for the fabrication of various device structures needed to establish ultimate material performance limits.

The flight portion of the study was to be accomplished by performing growth experiments using the Crystal Growth Furnace (CGF) manifested to fly on various Spacelab missions. The investigation complements the experiments being done on the crystal growth of $Hg_{1-x}Cd_xTe$ using the Advanced Automatic Directional Solidification Furnace (AADSF) flight instrument. The investigation consists of an extensive ground-based study followed by flight experimentation and involves both experimental and theoretical work. Just as for the AADSF-related studies. Both melt and solvent growth methods are being pursued, with the melt growth being the primary emphasis of the initial flight experiments. The combination of the two studies provides the basis for the evaluation of the influence of alloy property variations on the relative importance of various gravity- and non-gravity-related effects. Several alloy properties including the effective diffusion coefficient, segregation coefficient, thermal conductivity, microhardness, etc. are known to vary substantially with composition and from alloy system to alloy system. For example, the "effective" mass diffusion coefficients deduced from directional solidification compositional redistribution data differ by about a factor of 10, with that of $Hg_{1-x}Cd_xTe$ being the largest and $Hg_{1-x}Zn_xTe$ being the smallest. These variations will cause non-gravity-related effects to be more significant in some cases than in others.

A series of HgZnTe crystal ingots has been grown from pseudobinary melts by Bridgman-Stockbarger type directional solidification using the CGF Ground Control Experiment Laboratory (GCEL) furnace, as well as MSFC heat pipe furnaces. Several ZnTe crystals were also grown using a Te-solvent zone growth method. Various thermal boundary conditions and growth rates were employed and several of the ingots were rapidly quenched during the steady-state portion of growth to establish correlation between thermal conditions and melt/solid interface shapes. These experiments also indicated that the ingots can be successfully quenched and back melted to allow a rapid return to steady-state growth. The fitting of the measured crystal compositional distributions to appropriate theoretical models was used to obtain an estimate of the effective HgTe-ZnTe "liquid diffusion coefficient." To assist the modeling of the pertinent heat and mass transport processes, selected portions of the pseudobinary phase diagram, thermal diffusivity, melt viscosity and melt density have been measured.

A ground pre-processed and quenched sample was successfully back-melted and partially regrown in the CGF instrument during the First United States Microgravity Laboratory (USML-1) mission. The meltback interface was within 0.5 mm of the desired value. Because of the loss of power to the CGF, the experiment was prematurely terminated after approximately 39 hours into the planned 150 hour growth period. About 5.7 mm of sample had been grown at that point. Surface photomicrographs of the sample clearly showed significant topographical differences between the space- and ground-grown portions. Compositional measurements along the sample axis indicated that the desired steady-state growth for the axial composition was reached at about 3 mm into the growth because of the quenched in melt composition for steady state growth. An x-ray diffraction and SEM survey of the sample showed that both the ground and flight portions of the ingot contained only a few grains (i.e., were nearly single crystals) and the crystallographic orientation was maintained following back-melting and space growth. The interface shape, radial compositional variations, and the quenched-in dendritic structures of the flight sample all have shown an asymmetric behavior. The compositional data strongly suggest that the most likely cause was unanticipated transverse residual accelerations.

A new seeded method has been developed for the growth of HgZnTe crystal ingots from pseudobinary melt by the Bridgman-Stockbarger type directional solidification for the Second

United Sates Microgravity Laboratory (USML-2) mission. A vapor transport method developed by us was used to grow 2 cm ZnTe seed crystals in the fused silica ampoules. Then a stack of precast pseudobinary alloys of varying compositions were loaded in the remaining ampoules. The alloy compositional variation in the stack was chosen to correspond to the expected melt composition variation along the growth axis for steady-state diffusion-controlled growth conditions. A series of $Hg_{0.84}Zn_{0.16}Te$ and $Hg_{0.88}Zn_{0.12}Te$ crystals were then grown using the CGF Ground Control Experiment Laboratory (GCEL) furnace, as well as in heat-pipe furnaces. Several crystals were also grown under the influence of a 5T axial magnetic field. Detailed compositional and microstructural characterization of the samples indicated that the alloy stacks could be successfully back-melted within 0.5 mm of the seed interface to assure that growth begins under nearly steady-state growth conditions. The applied magnetic fields had a significant influence on radial alloy segregation and interface constitutional supercooling breakdown demonstrating the importance of gravity-induced fluid-flow effects.

Two $Hg_{0.88}Zn_{0.12}Te$ seeded ampoules were chosen for processing in the CGF during the Second United States Microgravity Laboratory (USML-2) mission. The results from a similar experiment that was inadvertently terminated during the previous USML-1 mission strongly indicated that residual accelerations transverse to the growth axis are detrimental for achieving the primary experiment objectives. Thus a Shuttle flight attitude that minimizes such accelerations was requested for the USML-2 mission. Just prior to launch the attitude was disallowed because of programmatic constraints and a decision was made not to perform the flight portion of the experiment under unfavorable growth conditions.

Several $Hg_{0.9}Zn_{0.1}Se$ crystals were grown by the Bridgman-Stockbarger method with and without the presence of axial magnetic fields. The measured dislocation densities were more than an order of inaptitude lower than typically observed for other II-VI alloys. This has been attributed to highly favorable growth conditions.

Page intentionally left blank

Growth of Solid Solution Single Crystals

Dr. Sandor L. Lehoczky, Principal Investigator
NASA Marshall Space Flight Center
Mail Code ES75
Marshall Space Flight Center, AL 35812
Phone: (256) 544-7758
Fax: (256) 544-8762
E-mail: sandor.lehoczky@msfc.nasa.gov

Co-Investigators:
Dr. Frank R. Szofran, NASA Marshall Space Flight Center
Dr. Donald C. Gillies, NASA Marshall Space Flight Center
Mr. Dale A. Watring, NASA Marshall Space Flight Center

The objective of the study is to establish the effects of processing semiconducting, solid solution, single crystals in a microgravity environment on the metallurgical, compositional, electrical, and optical characteristics of the crystals. The alloy system being investigated is the solid solution semiconductor $Hg_{1-x}Cd_xTe$, with x-values appropriate for infrared detector applications in the 8 to 14 mm wavelength region. Both melt and Te-solvent growth are being performed. The study consists of an extensive ground-based experimental and theoretical research effort followed by flight experimentation where appropriate. The ground-based portion of the investigation also includes the evaluation of the relative effectiveness of stabilizing techniques, such as applied magnetic fields, for suppressing convective flow during the melt growth of the crystals.

The difficulty of growing bulk crystals of the alloys, with both radial and axial homogeneity of significant lengths in Earth's gravity is well documented. Because the HgTe-rich component rejected during solidification is more dense, the vertical Bridgman-Stockbarger growth process would appear to be both gravitationally and thermally stable against convection, but this is not generally true. Due to the peculiar relationships between the thermal conductivities of the melt, solid, and ampoule, it is practically impossible to completely avoid radial temperature gradients in the growth region. In general, the presence of radial temperature gradients near the growth region will cause a curvature in the solid-liquid interface which need be neither an isothermal nor an isoconcentrational surface. Furthermore, the growth of high quality crystals usually requires a slightly convex growth interface as viewed from the melt. Under the influence of stable growth conditions, such interface geometries readily lead to lateral alloy segregation because of the tendency of the more dense HgTe-rich liquid to settle at the portions of the surface having the lowest gravitational potential. Because the alloy solidus temperature decreases with increased HgTe content, the interface temperature will be lowered in this region, causing the interface curvature to increase. Although lateral diffusion will tend to drive the interfacial melt compositions to some equilibrium values, most ground-based melt-growth experiments show large radial compositional variations that are probably a direct consequence of such an interfacial fluid flow phenomenon. In low gravity it is expected that the highly desired slightly convex growth surfaces will be easier to maintain because of the reduced tendency for stratification of the denser (HgTe rich) fluid component. At the same time, the near-elimination of radial temperature gradient-driven convection is expected to provide for a better control of the lateral compositional distribution in the melts.

It is thus expected that by growing under the influence of low-gravity conditions ($g < 10^{-6} g_0$), crystals with significantly improved crystallinity and compositional homogeneity can be prepared as compared to the best crystals that can be produced on Earth. It is also reasonable to expect that careful characterization of both the space- and ground-grown materials will lead to better insights into the peculiarities of the various growth mechanisms that will permit improvements in Earth-based processing of $Hg_{1-x}Cd_xTe$ and other compound semiconductor alloy systems.

It is believed that CdTe, $Hg_{1-x}Cd_xTe$, etc. probably possess extremely small yield strengths near their growth temperatures. If this is the case, the high dislocation density ($\sim 10^5$ cm^{-2}) usually seen in these crystals could be due at least in part, to stresses induced by the samples own weight, that is, self-induced stresses. Therefore, a second goal of these experiments is to assess the validity of this hypothesis.

Over the past several years, a detailed evaluation has been performed on the effects of growth parameters on the axial and radial compositional uniformity, defect density, and optical properties in directionally solidified $Hg_{1-x}Cd_xTe$ and other similar compounds and pseudo-binary alloys. A series of $Hg_{1-x}Cd_xTe$ alloy ingots ($0<x\leq 0.6$) has been grown from pseudobinary melts by a vertical Bridgman-Stockbarger method using a wide range of growth rates and thermal conditions. Several of the experiments were performed in transverse and axial magnetic fields of up to 5T. Precision measurements were performed on the ingots to establish compositional distributions and defect density distributions for the ingots. Correlation between growth rates and thermal conditions and growth interface shapes have been established for the alloy system. To assist the interpretation of the results and the selection of optimum in-flight growth parameters, the pseudobinary phase diagram ($0\leq x\leq 1$), liquid and thermal diffusivities ($0\leq x\leq 0.3$), melt viscosity, and the specific volumes as a function of temperature ($0\leq x\leq 0.2$) have been measured. From these measurements and other available data, the heat capacity, enthalpy of mixing, and the thermal conductivity of pseudobinary melts have been calculated using a regular associated solution model for the liquid phase. A one-dimensional diffusion model that treats the variation of the interface temperature, interface segregation coefficient, and growth velocity has been used to establish effective diffusion constants for the alloy system. Theoretical models have been developed for the temperature distribution and the axial and radial compositional redistribution during directional solidification of the alloys. These were used along with the experimental results to select the parameters for the first flight experiment flown on the Second United States Microgravity Payload (USMP-2) mission. A microscopic model for the calculation of point-defect energies, charge-carrier concentrations, Fermi energy, and conduction-electron mobility as functions of x, temperature, and both ionized and neutral defect densities has been developed. For selected samples, measurements were performed of electron concentration and mobility from 10-300 °K. The experimental data were in reasonably good agreement with theory and were successfully analyzed to obtain donor and acceptor concentrations for various processing conditions.

A five zone Bridgman-Stockbarger type "Advanced Automatic Direction Solidification Furnace (AADSF)" has been designed and developed for the flight portion of the investigation. The AADSF was successfully flown on the USMP-2 mission in March 1994 during which a 15 cm long and 0.8 cm diameter $Hg_{0.8}Cd_{0.2}Te$ alloy crystal was grown under precisely controlled residual acceleration conditions over a period of approximately 11 days. Detailed microstructural and compositional analysis has been performed for the crystal. A rate change inserted into the growth timeline sequence produced in the crystal an effective time marker for correlating orbital and residual accelerations to various crystal features and alloy compositional changes. This allowed a detailed evaluation of the effects of the magnitude and direction of residual acceleration on crystal homogeneity and perfection to be made for the first time. Circumferential variation of composition and topographic features around the boule indicated that residual acceleration vectors were present and have a large effect on the growth process. The magnitude of the measured transverse compositional variations along the growth axis showed a high degree of correlation to the direction of the residual acceleration vectors. X-ray topographs of the portion grown in the most favorable attitude (-XLV, -ZVV) indicate that this region is of significantly higher quality than usually grown on the ground. The Orbital Acceleration Research Experiment (OARE) acceleration measurement instrument record of residual acceleration vectors proved to be in excellent agreement with our results, as evidenced by the surface features of the boule. Certain attitude maneuvers of the orbiter can dramatically affect the growth stability. This is illustrated by the roll-around in tail-down attitude which reversed the direction of the residual acceleration perpendicular to the interface and caused thick compositional striations at 11 cm along the crystal. Further microstructural, optical, and electrical characterizations of the crystal promise to provide a wealth of additional information on the growth in low earth orbit of solid solution alloy crystals having a large separation between their liquidus and solidus. A series of $Hg_{0.8}Cd_{0.2}Te$ crystals were also grown under the influence of axial magnetic fields up to 5T. The application of the magnetic fields greatly reduced the radial compositional variations in the crystals, further underlying the importance of gravitationally-induced fluid flows. A new seeded method has been developed and was used for the Bridgman growth of an x=0.16 alloy input during the USMP-4 STS-mission. An <111>-B oriented CdTe seed was used along with a specially prepared alloy charge that emulated the calculated steady-state melt composition profile upon back melting. The results analysis of the results from the experiment are in progress.

Project Title: **COLLOIDAL STABILITY IN COMPLEX FLUIDS**

PI: Jennifer A. Lewis
Assistant Professor, Materials Science and Engineering
University of Illinois
105 S. Goodwin Avenue
Urbana, IL 61801
jalewis@staff.uiuc.edu

Objectives: The broad objective of this ground-based research program is to develop a fundamental understanding of factors governing the stability of complex colloidal suspensions. Such systems are utilized in numerous applications including advanced ceramics, coatings, inks, and paints. Specifically, this research aims to investigate the effects of depletion phenomena, which arise between large colloidal particles in solutions containing smaller particles, on the stability, structural evolution, and rheological properties of such complex systems.

Microgravity Relevance: This ground-based research effort will benefit from a microgravity environment because complications arising from particle-size or density-driven segregation in suspension would be minimized allowing for a broader range of experimental conditions to be probed.

Background: Colloidal processing is well known to be the optimal approach for tailoring the structure and, hence, properties of ceramic films and bulk forms. Through careful control of the interparticle interactions, suspensions can be prepared in the dispersed, weakly flocculated, or strongly flocculated state. In the dispersed state, discrete particles repel each other upon close approach when the repulsive barrier $>> kT$. In the weakly flocculated state, particles aggregate in a shallow secondary minimum (well depth $\approx 1 - 20$ kT) forming particle clusters (or flocs), with a minimum equilibrium separation distance between particles of h_o. In contrast, particles aggregate into a deep primary minimum in the strongly flocculated state forming a network of touching particle clusters at volume fractions exceeding roughly 0.05.

Depletion interactions arise between large colloids suspended in a solution containing smaller particles, known as depletants.[1-3] Such species may promote flocculation *or* stabilization of primary colloidal particles, as illustrated in Figure 1. The term, depletion, denotes the existence of a negative concentration gradient near primary particle surfaces. For rigid depletant species, their concentration is reduced at bare particle surfaces and increases to its bulk solution value at some distance away from these surfaces. This distance, known as the depletion layer thickness, is of the order of the depletant diameter ($D_{depletant}$).

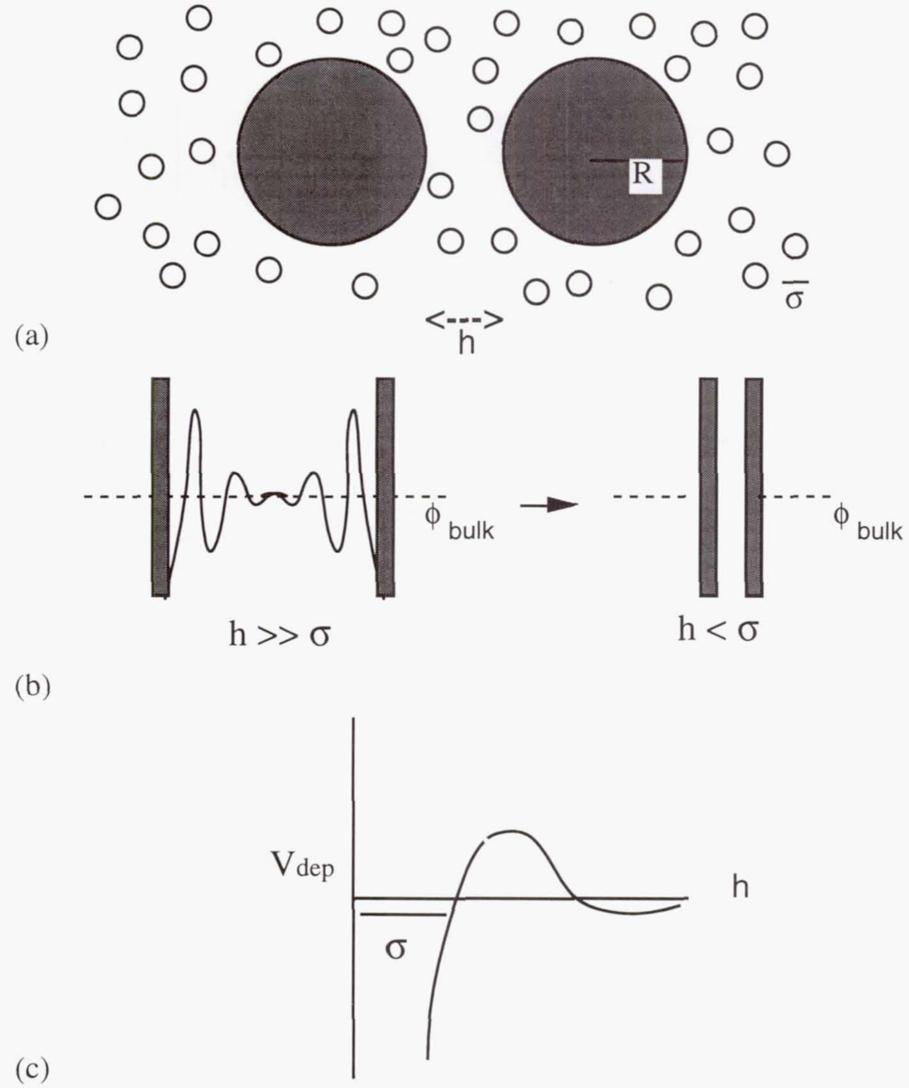

Figure 1. Schematic representation of (a) large, primary colloidal spheres interacting in a solution of smaller colloidal depletants, (b) depletant concentration profile as a function of interparticle separation distance, h, and (c) attractive, depletion potential energy resulting from such interactions ($h < \sigma$), where ϕ_{bulk} is the depletant volume fraction bulk solution.

The emergence of new and/or improved technologies hinge critically on rational improvements in wet (or suspension) processing of ceramic powders.[3] It has become increasingly clear that *relevant* ceramic systems will be complex in nature, consisting of single or multiphase particles with engineered size distributions (e.g., bimodal, trimodal) and a myriad of processing additives (e.g., soluble polymeric species, insoluble polymer lattices, etc.). However, little is known about how colloidal interactions driven by particle size differences, i.e., depletion phenomena, affect the processing-structure-property relations of particulate-derived ceramic films and bulk forms. Successful completion of this research program will establish this critical knowledge base.

Significant Results: Preliminary experiments have focused on how depletant species influence the stability and properties of model ceramic suspensions. Such systems consist of monosized silica (SiO_2, $D_{colloid}$ = 500 nm) spheres, which serve as large colloids, in an aqueous solution of monodisperse, zirconia (ZrO_2, $D_{depletant}$ = 8 nm) spheres, which serve as depletant species. The rheological behavior of these suspensions as a function of varying colloid and depletant volume fraction have been measured using controlled stress rheometers (Bohlin CVO and CS-10). In the absence of depletant species, SiO_2 suspensions (prepared at pH = 0.5) exhibited strong shear thinning behavior indicative of a weakly flocculated system, as shown in Figure 2.

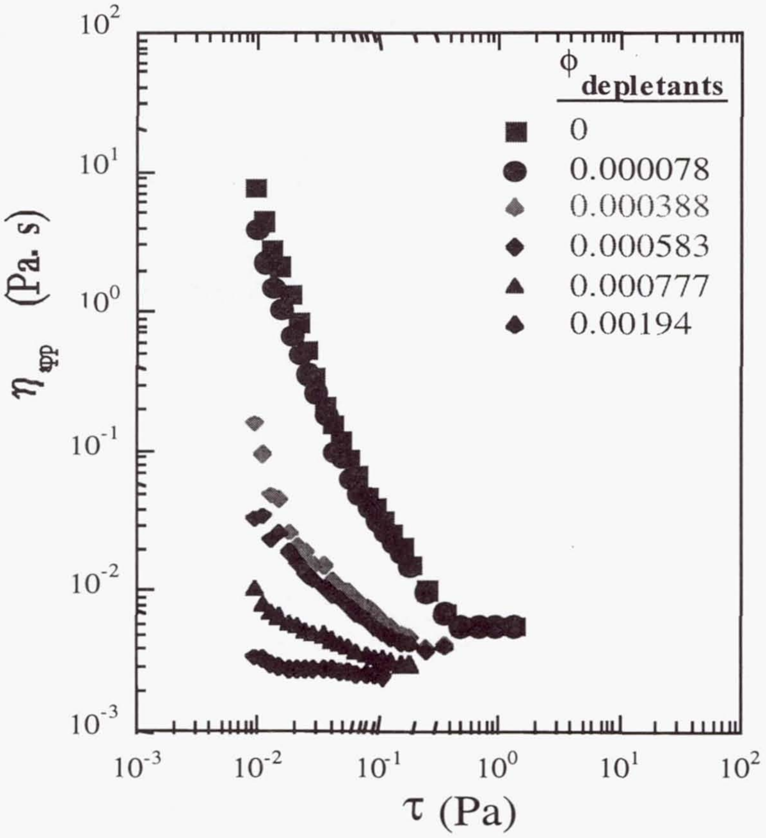

Figure 2. Log-log plot of apparent suspension viscosity versus shear stress for SiO_2 suspensions ($\phi_{colloid}$ = 0.10) of varying depletant volume fraction.

Upon the addition of depletant species, both the low shear apparent viscosity and degree of shear thinning behavior decreased dramatically indicative of improved system stability.

Sedimentation experiments were carried out the suspensions described above to probe their settling behavior as a function of depletant volume fraction. Their sediment volume as a function of settling time is given in Figure 3.

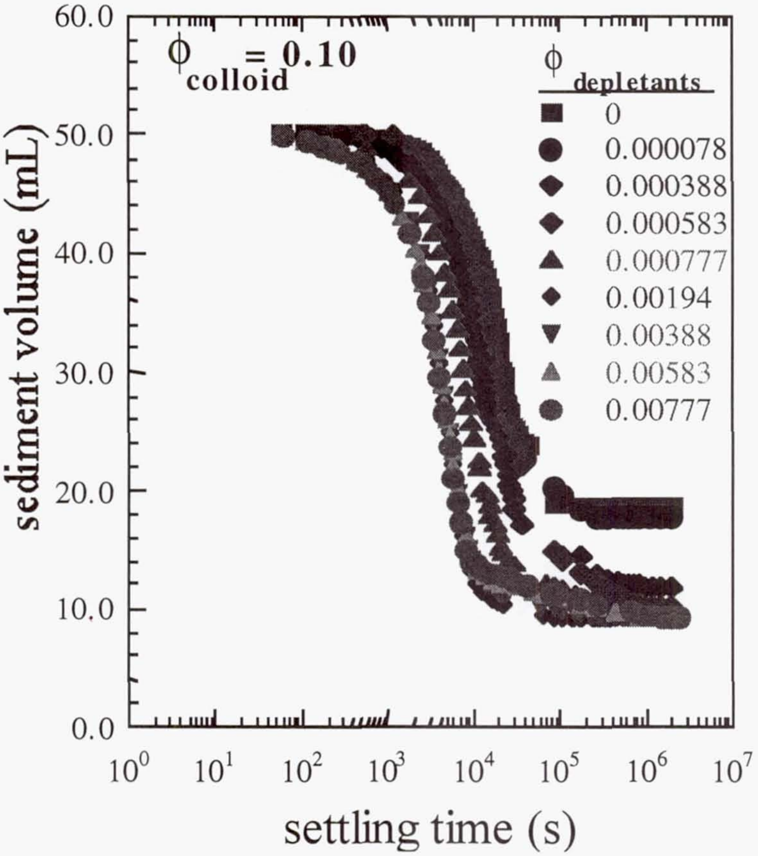

Figure 3. Semilog plot of sediment volume versus settling time for SiO_2 suspensions ($\phi_{colloid}$ = 0.10) of varying depletant volume fraction.

Their equilibrium sediment volume fraction is plotted as a function of depletent volume fraction in Figure 4. In the absence of depletant species, the suspensions settled to produce a relative open structure (packing density ~ 20% of theoretical), indicative of an unstable system. Above a critical depletant volume fraction ($\phi_{depletant}$ ~ 0.001), the suspensions settled to produce structures whose density approached that expected for random close-packing (~ 60% of theoretical) of monosized particles, indicative of a stabilized system.

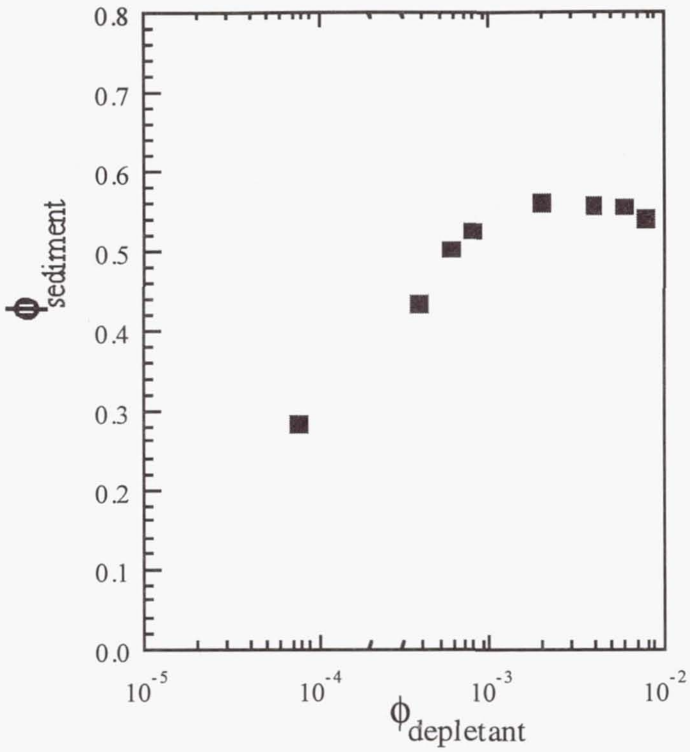

Figure 4. Semilog plot of equilibrium sediment volume fraction versus depletant volume fraction for various SiO_2 suspensions ($\phi_{colloid} = 0.10$).

Modeling of Colloidal Interactions: The stability of a given colloidal system is determined by the total interaction potential energy, To model the experimental systems described above, we account for long range van der Waals, electrostatic, short-range hydration, and depletion interactions.[1-4] The attractive van der Waals interaction potential energy, V_{vdw} , exhibits a power law distance dependence whose strength depends on the dielectric properties of the interacting colloidal particles and intervening medium. The repulsive electrostatic interaction potential energy, V_{elect}, exhibits an exponential distance dependence whose strength depends on the surface potential induced on the interacting colloidal particles and the dielectric properties of the intervening medium. Exact analytical expressions for the electrostatic potential energy cannot be given, thus analytical approximations or numerical solutions were used. The short-range hydration interaction potential energy, V_{struct}, exhibits an exponential distance dependence with a characteristic decay length of roughly 1 nm. The depletion interaction potential energy, V_{dep}, is calculated using the approach developed by Walz and Sharma[1], which predicts the depletion force between two charged spheres in a solution of smaller, charged spheres and accounts for second-order effects arising from two-body depletant interactions through a virial expansion of the single particle distribution function correct to $O\ (p_\infty{}^2)$, where p_∞ is the bulk depletant concentration.

In the absence of depletant species, the total interaction potential energy between two SiO_2 spheres ($D_{colloid}$ = 500 nm) in an aqueous solution (pH = 0.5) is shown in Figure 5(a), where V_{tot} is given by the summation of V_{vdw} , V_{elect}, and V_{struct}. In agreement with the experimentally observed behavior for such suspensions, these calculations predict that the initial system is weakly flocculated with a secondary minimum of roughly $-5\ kT$. An estimate of the depletion interaction potential energy is given in Figure 5(b) for this system, where $\phi_{\text{depletant}} = 0.1$. A repulsive barrier of ~ $2\ kT$ is predicted at these depletant concentrations. Interestingly, however, the onset of improved stabilization is observed at significantly lower $\phi_{\text{depletant}}$ suggesting either enhanced depletion effects due to the preferential segregation of such species to a region near the colloid-solution interface or their adsorption onto the colloid surfaces leading to steric effects Understanding the origin of these unusual observations is the subject of ongoing investigation.

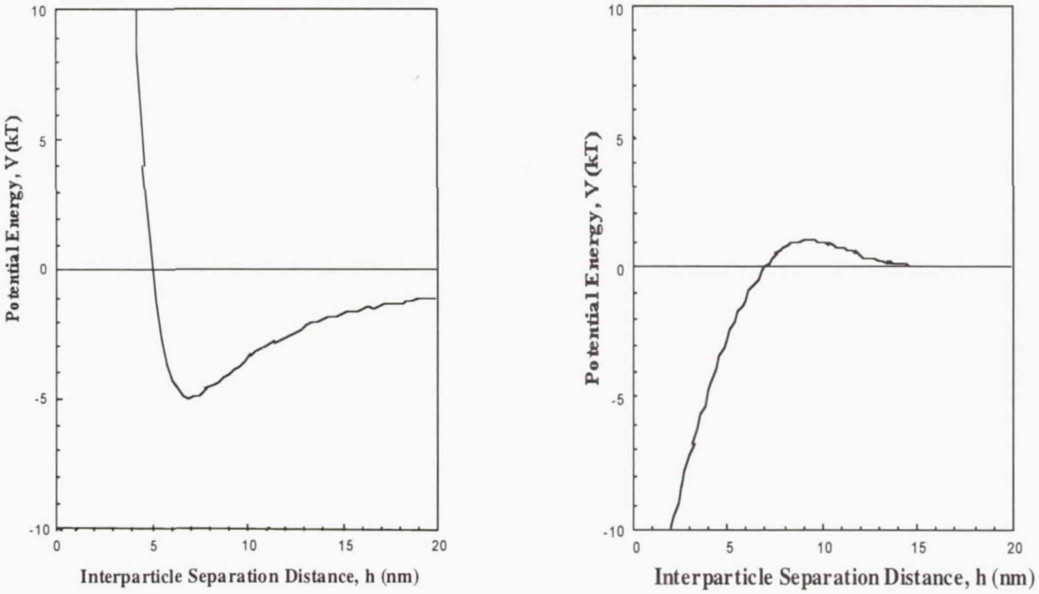

Figure 5 Modeling results of colloidal interactions in the SiO_2 system: (a) total interparticle potential calculated in the absence of depletion effects, V_{tot} ($\phi_{\text{depletant}} = 0$) and (b) the estimated depletion contribution, V_{dep} ($\phi_{\text{depletant}} = 0.1$).

References:

[1] Walz, J. Y.; Sharma, A. *J. Colloid Interface Sci.* **1994**, *168*, 485.

[2] Mao, Y.; Cates, M.E.; 1Lekkerkerker, H.N.W. *Physica A* **1995**, 222, 10-24.

[3] Ogden, A.; Lewis, J.A.; *Langmuir.* **1996**, *12*, 3413.

[4] Hunter, R.J. *Foundations of Colloid Science, Vol.1*, Oxford Science, **1989**.

A COMPARATIVE MODELING STUDY OF MAGNETIC AND ELECTROSTATIC LEVITATION IN MICROGRAVITY

Ben Q. Li
School of Mechanical and Materials Engineering
Washington State University
Pullman, WA 99164 - 2920
Phone: 509-335-7386
Fax: 509-335-4662
Email: li@mme.wsu.edu

ABSTRACT

Numerical models are developed to represent the complex electrodynamic and hydrodynamic phenomena in magnetically and electrostatically levitated droplets in microgravity environment. The numerical model development will be based on the solution of the Maxwell equations using either the boundary element technique or the coupled boundary/finite element technique and the solution of the Navier-Stokes equations and energy/mass balance equations by the finite element method. With developed models, magnetically and electrostatically levitated droplets are studied in a comparative fashion to understand the following key issues concerning their space applications: (1) viscous surface oscillation and heat transfer of droplets levitated magnetically or electrostatically, (2) turbulent flow behavior in magnetically-levitated droplets, (3) internal fluid flows and heat transfer in electrostatically levitated droplets, and (4) stability of droplets levitated magnetically or electrostatically.

I. INTRODUCTION

Magnetic levitation and electrostatic levitation are two key containerless processing technologies in materials science research for studying fundamental phenomena such as nucleation and solidification microstructure formation and for measuring thermophysical properties of molten materials under microgravity conditions, such as heat capacity, surface tension, thermal conductivity, electrical conductivity and viscosity [1-3]. In fact, there has been an operational magnetic levitation system, the TEMPUS system, specifically designed for these microgravity applications. Several flight experiments already were carried out with the system. Electrostatic levitator also has been developed and is undergoing ground-based testing and and experiments [4,5]. According to NASA's plan, one electrostatic levitation device for microgravity studies will be operational after the year 2000 and installed in the Japanese Experiment Module in the International Space Station.

The objective of this research project is to develop numerical models and to carry out extensive numerical simulations to address the above issues, with intention to develop a fundamental understanding of, and to be able to predict, the behavior of drops in electrostatic and magnetic levitators. Modeling studies will also be carried out to make a comparative assessment of the capabilities and relative advantages of magnetic and electrostatic levitation for microgravity applications. Information on the internal flow and thermal field, electromagnetic field, surface deformation and oscillation, viscous decay and sample stability will be obtained for the levitated drops as a function of various processing parameters such as the drop size, applied voltage, applied current and voltage. This information should be indispensable in providing rational guidelines for selecting the levitation process best suited for particular applications. The developed numerical models also will be useful tools to perform necessary calculations to help better plan the microgravity experiments and more accurately interpret the experimental results as well as to improve the existing electric or magnetic arrangements for levitation.

II. NUMERICAL MODELS FOR MAGNTICALLY LEVITATED DROPLETS

Numerical models have been developed to represent the electromagnetic, transport and free surface phenomena associated with levitated drops in magnetic and/or electrostatic levitation systems. The model assumes an axial symmetry. The model development is based on the finite element and boundary element computational methodologies that have been developed by our research group in the recent years [6,7]. In essence, a coupled boundary/finite element method is applied to solve the Maxwell equations. By this method, finite elements are used to discretize the droplet region where information on electromagnetic field and temperature field distributions is needed, while boundary elements are applied in the free space outside the droplet region. The finite element and boundary element regions are then coupled through the interface boundary conditions. In developing the coupled boundary and finite element code, the LU decomposition, instead of direct matrix inversion, is used to facilitate the computation of interface flux distribution, and node data are appropriately arranged to preserve the skyline structure of the finite element discretization in order to improve the computational efficiency. The code is enhanced by an iterative scheme and remeshing capability for free surface calculations. The model for fluid flow and temperature distribution in the levitated droplets is developed based on the finite element solution of the transient Navier-Stokes equations and energy balance equations with the Lorentz forces as momentum sources and Joule heating as energy sources.

Some of the calculated results are given in Figures 1 to 4. Figure 1 compares the analytical and numerical results for an aluminum sphere with a single coil placed around its equator plane. The analytical solution is given by Li [8]. Clearly, excellent agreement exists between the two approaches. Figure 2 further compares the calculated, analytical and experimentally measured lifting forces and total power absorption by a Cu sphere of 10 mm diameter immersed in TEMPUS. Once again good agreement exists between the numerically computed and experimentally measured quantities.

The calculated internal fluid flow and temperature distribution in a liquid silver sphere of 10 mm diameter magnetically positioned by TEMPUS in microgravity are shown in Figures 3 and 4. Figure 3 illustrates the temperature distribution and the fluid flow driven by the electromagnetic forces generated by both the heating and positioning coils in TEMPUS device. It can be seen that heating coils generate strong magnetically driven flows, characterized by two anti-rotating flow loops. The effect of the fluid flow also has an effect on the temperature distribution as appear in the left half of the sphere.

In Figure 4, the temperature distribution and fluid flow field are plotted for a liquid silver sphere magnetically positioned in TEMPUS in microgravity with heating coils turned off. The positioning coils produce a quadruple field that provides a magnetic potential wall for stabilizing the liquid sample. The induced Lorentz force in the sample by the quadruple field produces four rotating fluid flow loops in the liquid silver sphere. The temperature field is also different. Comparison of the Figures 3 and 4 clearly indicates that the heating coils, when in operation, have much stronger effects than the positioning coils.

III. NUMERICAL MODELS FOR ELECTROCALLY LEVITATED DROPLETS

Numerical models have also be developed to represent the electric field distribution, electrically induced droplet deformation, temperature field and fluid flow in electrostatically levitated samples. The model development is based on the modification of the models used for magnetic levitation as described above. The modification may be described as follows. Because the Maxwell equations reduce to a scalar equation for the electric potential, the boundary element method is sufficient for the solution of the potential field. Thus, only the boundary element part of the computer program is needed for the solution. The free surface deformation is calculated in the same way as for the case of magnetic levitation, except that electrostatic stress is used instead of magnetic stress. The internal fluid flow and temperature distribution in the droplet are calculated using the finite element program. For electrostatically levitated droplets, surface tension driven flows can become very important, especially when heating source can not be uniformly distributed.

Some of the results obtained from the numerical models for electrostatically levitated droplets in microgravity are given in Figures 5 to 8. Figure 5 shows the basic concept used for electrostatic levitation. In essence the sample is charged and then immersed in a static electric field. The interaction of the electric field and the charges produce a force that can be used to support the sample.

Figure 6 compares the calculated results for a conducting sphere immersed in an electric field with the analytical solutions. Clearly good agreement exists between the numerical and analytical solutions.

The calculated results for free surface deformation in an electric field are given in Figure 7. It can be seen that electric forces generate a pulling acting at the two poles and thus the sample become elongated. This is different from magnetic levitation in that the sample deformation in TEMPUS is caused by the strong squeezing forces generated at the equator.

Figure 8 shows the temperature distribution and fluid flow in a deformed silicon droplet in electric fields. The fluid flow is driven by surface tension, which is a function of temperature. The fluid is being circulated to the lower temperature region and then recirulated internally to the higher temperature region. The laser heating is assumed located around the north and south poles.

IV. FUTURE WORK

The planned work involves development of a numerical model for an axisymmetric sample undergoing free surface oscillations and viscous flow and temperature decaying under the influence of the positioning coils in magnetic levitation systems. In the TEMPUS device for surface tension and viscosity measurements, the melted sample is squeezed at the equator to induce a pre-deformed shape and then switching-off of the squeezing coils allows the sample to oscillate. During the oscillation, the position coils are still operative. The model will be capable of predicting the transient heating, temperature distribution, fluid flow and sample deformation deliberately induced by the squeezing coils. It will also be able to predict the free surface oscillation, temperature and velocity field decaying, after the squeezing coil is switched off, with the positioning coils still operative. The model development will be based on our in-house boundary/finite element code that has been developed for the electromagnetic field calculations and our on-house finite element code for fluid flow, heat transfer and free surface deformations.

Study of turbulent magnetically-driven flow is carried out using direct numerical simulations (DNS). The flow relaminarization taking place during the free surface oscillation after heating coils are switched off requires a more accurate description of turbulence. The DNS will allow an accurate representation of turbulence in the droplets and assess the error associated with the k-ε model for transitional flows and relaminarization. With DNS, information on the Reynolds stresses, turbulent intensities, instantaneous flow structure, and turbulent transport will be obtained and will be crucial for us to understand the turbulence structure in the droplets and hence flow relaminarization.

Numerical models will be developed for surface oscillation and viscous decaying of electrostatically-levitated droplets. The model will take into account the fluid flow and heat transfer as well as the electrically-induced deformation during oscillation. The code development is the same as described in Task 1 above, the difference being that the electric forces generated by the electrodes, instead of magnetic forces generated by surrounding coils, will be considered during drop oscillation. The further model development will also include the effects of the sample rotation and other types of heating sources.

Comparative study will be made of electrostatic and magnetic levitation using the models developed above. Modeling work will be carried out to compare electrostatic levitation with magnetic levitation for microgravity applications. The surface deformation, internal flow, temperature distribution and uniformity, sample stability, surface oscillation, viscous flow decaying and thermal decaying of a droplet will be studied for electrostatic levitation and compared with their counterparts for magnetic levitation. The operating conditions will include applied voltage, electrode placement and arrangement, applied current and frequency, the drop size and type of materials.

V. REFERENCES

[1] Femings, M. C., Trapaga, G. and Hyers, R. (1996) The measurement of the viscosity and surface tension of undercooled melts under microgravity conditions and supporting MHD calculations. *Microgravity Materials Science Conference*, Huntsville, AL pp. 76-77.

[2] Herlach, D. M. and Feuerbacher, B. (1986). Nucleation and undercooling. *Materials Sciences in Space*, B. Feuerbacher, H. Hamacher and R. J. Naumann, Eds., Springer-Verlag, Berlin, p. 168.

[3] Rim, W. K., Chung, S. K., Barber, D. Man, K. F., Gutt, G. and Rulison, A. (1993) An electrostatic levitator for hihg-temperature containerless materials processing in 1-g. *Rev. Sci. Instrum*, Vol. 64 (10), pp. 2961-2970.

[4] Rhihm, W. K. (1997a) Private Communication. Jet Propulsion Laboratory, California Institute of Technology, Pasadena, CA.

[5] Rhim, W. K. (1997b) Thermophysical propertiy measurements of molten semiconductors. NASA Microgravity Materials Sicence Conference, Ed. F. Szofran, D. McCauley and C. Walker, pp. 427-432.

[6] Song, S. P. and Li, B. Q. (1998). A boundary/finite element analysis of magnetic levitation systems: surface deformation and thermal phenomena. *ASME J. Heat Transf.*, Vol. 120, pp.492-504.

[7] Song, S. P., Li, B. Q. And J. A. Khadadadi (1998). Coupled boundary/finite element solution of magnetothermal problems. *Int. J. Num. Meth. Heat Fluid Flow*, Vol. 8, pp. 1369-1383.

[8] Li, B. Q. (1994). The transient magnetohydrodynamics in electromagnetic levitation processes. *Int. J. Eng. Sci*, Vol. 32, No. 8, pp. 1315-1336.

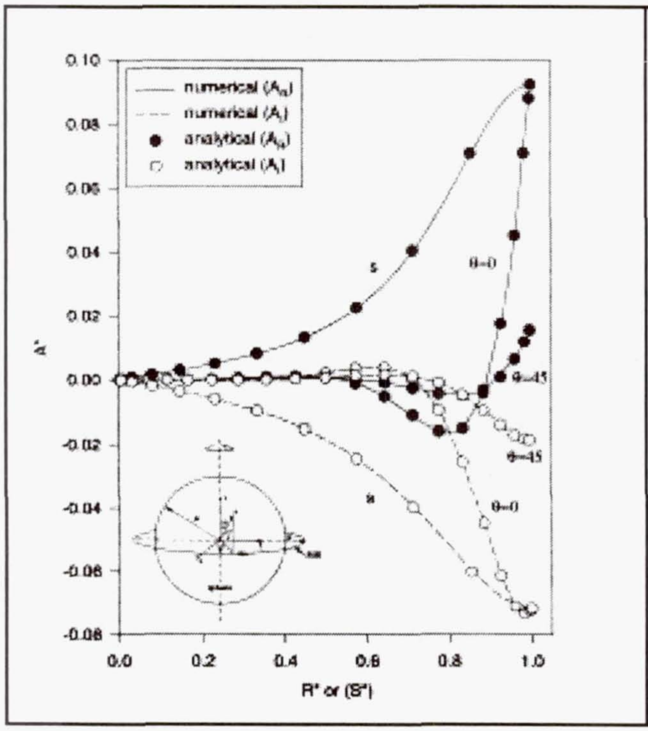

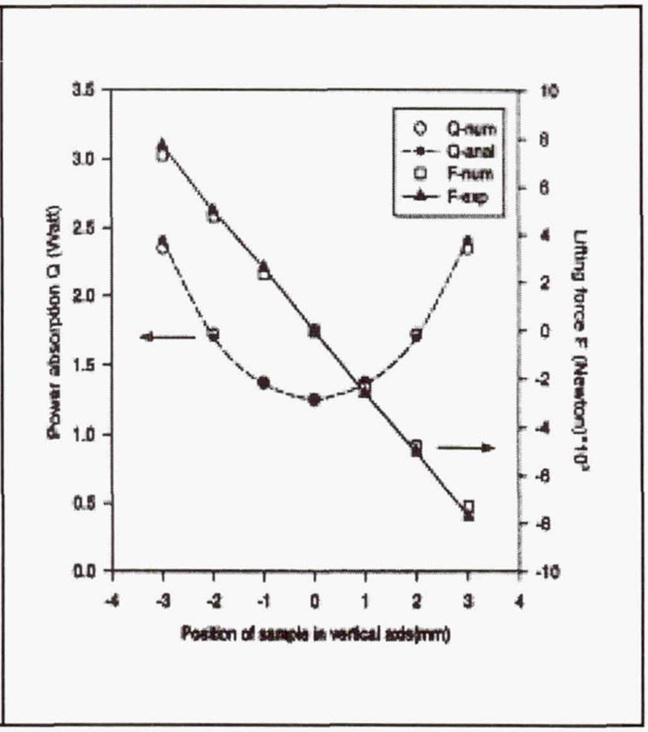

Fig. 1. Comparison of numerical and analytical solutions for magnetic vector potential A* distributions. S is the distance measured from the north pole of the sphere. R* is nondimensionalized radius.

Fig. 2. Comparison of numerical and analytical solutions and experimental measurements for global lifting force and power absorption for a Cu sphere levitated in TEMPUS device.

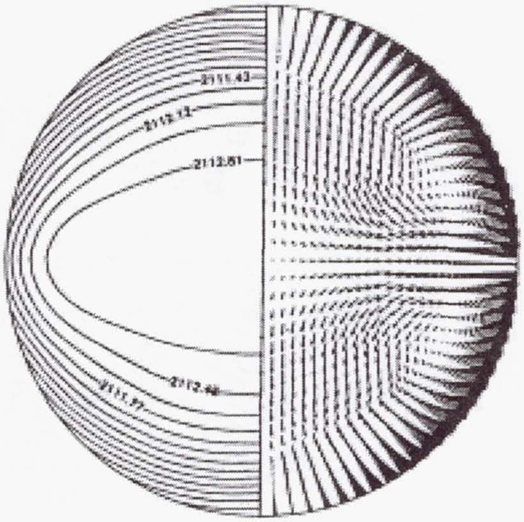

V_{max}=18.32 cm/s

Fig. 3. Numerically calculated velocity field and temperature field in a liquid silver sphere of 10 mm dia magnetically positioned in TEMPUS in microgravity with both heating and positioning coils turned on. Temperature is measured in K.

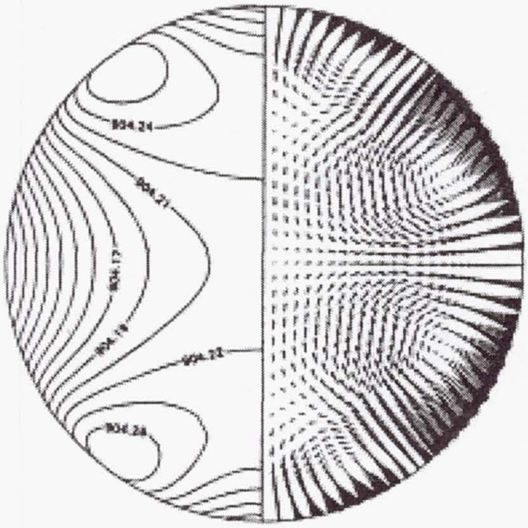

V_{max}=4.39 cm/s, steady state

Fig. 4. Numerically calculated velocity field and temperature field in a liquid silver sphere 10 mm dia magnetically positioned in TEMPUS in microgravity, with positioning coils operative only. Temperature is measured in K.

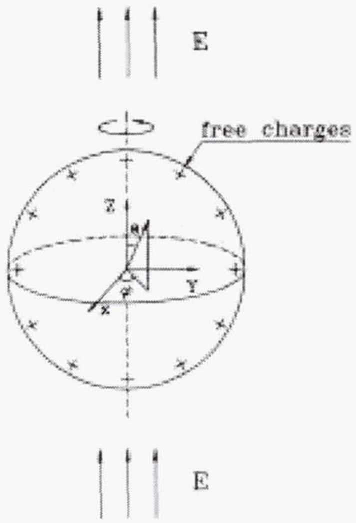

Fig.2 Schematic representation of a positively charged melt droplet levitated in an electrostatic field.

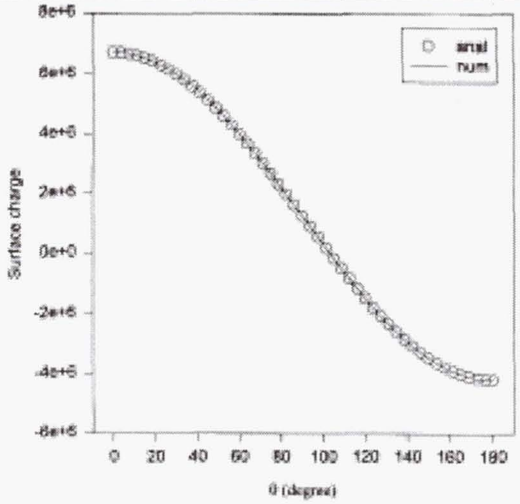

Fig.6 Comparison of numerical and analytical and results for surface charge (normalized by $\varepsilon=8.854\text{x}10^{-12}$) distribution along the surface of a 5mm diameter molten silicon sphere: applied electric field = $1.82\text{x}10^{6}$ V/m and total free charge = $8.854\text{x}10^{-10}$ C.

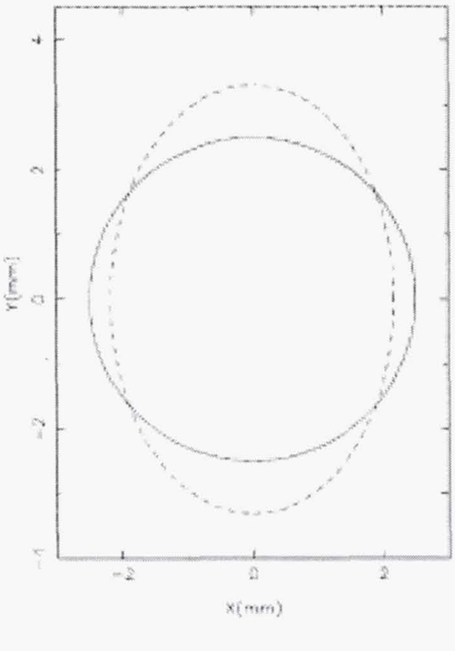

Fig.7 Electrostatically deformed free surface shape of a molten silicon drop (dashed line) in microgravity: the sample initial diameter is 5 mm, as indicated by the solid line, and the applied electric field is $2.5\text{x}10^{6}$ V/m.

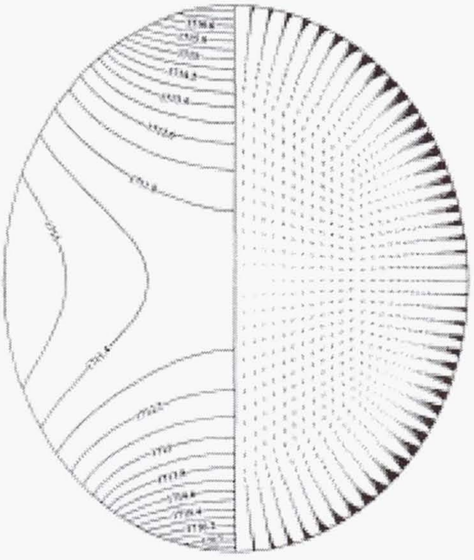

Fig.8 Temperature (in K) distribution and Marangoni convection in a Cu melt droplet electrically deformed under microgravity conditions. The maximum velocity is 4.1 cm/s. The original Cu sphere has a diameter of 3.8 mm and applied electric field is 3 x 10^{6} V/m. The laser heating power has the following characteristics: $Q=1.5 \text{ x } 10^{6} \exp(-r^{2}/0.81)$ W/m^{2}.

STUDY OF MAGNETIC DAMPING EFFECT ON CONVECTION AND SOLIDIFICATION UNDER G-JITTER CONDITIONS

Ben Q. Li
Department of Mechanical Engineering
Louisiana State University
Baton Rouge, LA 70803
Phone: 504-388-6488
Fax: 504-388-5924
Email: meli@me.lsu.edu

and

H. C. de Groh III
NASA Lewis Research Center
Cleveland, OH 44135
Phone: (216)433-5025
Fax: (216)433-5033
Email: henry@sarah.lerc.nasa.gov

ABSTRACT

As shown by NASA resources dedicated to measuring residual gravity (SAMS and OARE systems), g-jitter is a critical issue affecting space experiments on solidification processing of materials. This study aims to provide, through extensive numerical simulations and ground based experiments, an assessment of the use of magnetic fields in combination with microgravity to reduce the g-jitter induced convective flows in space processing systems. We have so far completed asymptotic analyses based on the analytical solutions for g-jitter driven flow and magnetic field damping effects for a simple one-dimensional parallel plate configuration, and developed both 2-D and 3-D numerical models for g-jitter driven flows in simple solidification systems with and without presence of an applied magnetic field. Numerical models have been checked with the analytical solutions and have been applied to simulate the convective flows and mass transfer using both synthetic g-jitter functions and the g-jitter data taken from space flight. Some useful findings have been obtained from the analyses and the modeling results. Some key points may be summarized as follows: (1) the amplitude of the oscillating velocity decreases at a rate inversely proportional to the g-jitter frequency and with an increase in the applied magnetic field; (2) the induced flow approximately oscillates at the same frequency as the affecting g-jitter, but out of a phase angle; (3) the phase angle is a complicated function of geometry, applied magnetic field, temperature gradient and frequency; (4) g-jitter driven flows exhibit a complex fluid flow pattern evolving in time; (5) the damping effect is more effective for low frequency flows; and (6) the applied magnetic field helps to reduce the variation of solutal distribution along the solid-liquid interface. Work in progress includes numerical simulations and ground-based measurements. Both 2-D and 3-D numerical simulations are being continued to obtain further information on g-jitter driven flows and magnetic field effects. A physical model for ground-based measurements is completed and some measurements of the oscillating convection are being taken on the physical model. The comparison of the measurements with numerical simulations is in progress. Additional work planned in the project will also involve extending the 2-D numerical

model to include the solidification phenomena with the presence of both g-jitter and magnetic fields.

I. INTRODUCTION

Microgravity and magnetic damping are two mechanisms applied during the melt growth of semiconductor or metal crystals to suppress buoyancy driven flow so as to improve macro and micro homogeneity of the crystals. As natural convection arises from gravity effects, microgravity offers a plausible solution to reduce the convective flow. However, recent flight experiments indicated that residual accelerations during space processing, or g-jitter, can cause considerable convection in the liquid pool, making it difficult to realize a diffusion controlled growth, as originally intended, when experiments were conducted in microgravity [1]. Further studies showed that g-jitter is a random phenomenon associated with microgravity environment and has both steady state and transient effects on convective flow [2-7].

The fact that molten metals and semiconductor melts are electrically conducting opens one more avenue to control the convective flow. Less obvious than gravity, this approach is based on the interaction of the liquid motion with an externally applied magnetic field. This interaction gives rise to an opposing Lorentz force that results in a reduction (or damping) of melt flow velocities and may be explored to suppress the unwanted g-jitter induced convection during solidification.

The objectives of this project are to: (1) determine the behavior of g-jitter induced convection in a magnetic field, (2) assess the abilities of magnetic fields to suppress the detrimental effects of g-jitter during solidification and (3) develop an experimentally verified numerical model capable of simulating transport processes and solidification phenomena under g-jitter conditions with and without a magnetic field. These goals are to be achieved through both theoretical analyses and ground based laboratory experiments. We have so far completed asymptotic analyses based on the analytical solutions for g-jitter driven flow and magnetic field damping effects for a simple one-dimensional parallel plate configuration, and developed both 2-D and 3-D numerical models for g-jitter driven flows in simple solidification systems with and without presence of an applied magnetic field [9-13]. Numerical models have been checked with the analytical solutions and have been applied to simulate the convective flows and mass transfer using both synthetic g-jitter functions and the g-jitter data taken from space flight. Some useful findings obtained from the analyses and the modeling results are reported in ref. [9-13]. Both 2-D and 3-D numerical simulations are being continued to obtain further information on g-jitter driven flows and magnetic damping effects. A physical model for ground-based measurements is completed and some measurements of the oscillating convection are being taken on the physical model. The comparison of the measurements with numerical simulations is in progress. Also, the 2-D numerical model is being modified to allow for the solidification phenomena with the presence of both g-jitter and magnetic fields.

II. ANALYTICAL SOLUTION FOR A ONE-D SIMPLE SYSTEM

This simple one dimensional analysis is intended to provide some perspective on asymptotic behavior of the magnetic damping effects on g-jitter induced flow in a parallel plate configuration. A temperature gradient is established between two infinitely large parallel plates. A g-jitter field, which is assumed to follow time harmonic oscillation but spatially independent, acts in the direction parallel to the plates. A DC magnetic field is applied perpendicularly to the plates.

Some results are selectively presented in Figures 1 to 2. Figure 1 shows the 3-D view of the natural convection distribution across the width of the channel induced by g-jitter without an applied magnetic field for different times. The quantity plotted along the vertical axis shows the velocity in the channel driven by synthetic g-jitter functions, which are assumed to follow a Fourier series in time. The fluid flow profile across the channel with applied magnetic fields illustrated in Figure 2. Clearly, as a limit, the flow can be damped entirely if a large enough magnetic field is applied. Also, a magnetic field is effective in damping flows induced by g-jitter with larger component and lower frequency. Further studies also show that the applied field is more effective in suppressing the flows associated with g-jitter with lower frequencies but only has a moderate effect on the high frequency g-jitter flows.

III. DEVELOPMENT OF 2-D FINITE ELEMENT MODEL

We have developed a numerical model for the transient fluid flow, heat transfer and solutal transport under the influence of g-jitter with and without the presence of an external magnetic field. The model development was based on the finite element solution of the transport equations with the Lorentz forces as a momentum source and entails the modification of our in-house finite element fluid flow and heat transfer code to study the g-jitter induced flow and magnetic damping effects. Our finite element code, during the course of its development, has been extensively compared with various commercial packages including FIDAP, FLOW3D, and FLUENT. The numerical model is further tested against the analytical solution for the application of magnetic damping to suppress the g-jitter induced convective flows. Figure 3 compares the numerical results and analytical solutions for a simplified parallel plate configuration. Clearly excellent agreement exists between two approaches.

The 2-D model was applied to study a simplified Beidgman-Stockbarger system for the melt growth of Ga-doped germanium single crystals. The simplification, among others, treats the solidification front being flat. Some of the results obtained from 2-D numerical model are given in Figures 4 to 6. It is seen from Figure 4 that the application of an external magnetic field reduces the convective velocities in the system studied. Figures 5 and 6 compare the time evolution of the solutal distribution along the solidification front with and with an applied magnetic field. With the magnetic field, solutal variation along the interface is much reduced. It is noteworthy that the solutal element still varies with time at a location on the interface but the amplitude of the variation is also much reduced with the applied magnetic field.

IV. DEVELOPMENT OF 3-D FINITE ELEMENT MODEL

We also have developed a 3-D numerical model for the study of transient fluid flow, heat transfer and mass transport as well as magnetic damping phenomena induced by g-jitter in microgravity with and without presence of an applied magnetic field. The model development is based on the finite element solution of the transient 3-D Navier-Stokes equations and heat/mass balance equation along with the Maxwell equations. As g-jitter in microgravity is time dependent and changes its direction because of the maneuver of space vehicles, a fully 3-D model is more appropriate.

The 3-D model described above has been applied to study the g-jitter driven flows, heat/mass transfer and magnetic damping phenomena associated with a simplified Beidgman-Stockbarger system for the melt growth of Ga-doped germanium single crystals. Again to simplify the calculations, the liquid-solid interface is assumed to be flat. Results show that , the fluid flow driven by g-jitter is very complex and also evolves in time. This can be especially true when all three g-jitter components with a composite frequency and amplitudes are considered. The temperature distribution, however, remains the same, suggesting that heat transfer in the system is primarily by conduction because of a small Prandtl number of the melt.

Figures 7 and 8 illustrate the magnetic damping effects on the g-jitter induced flows. Clearly, with the absence of the magnetic field, g-jitter induces strong recirculation in the vertical plane within which it is acting, as appear in Figure 7. With a magnetic field applied in the vertical direction, the convective flows and the recirculation loops are suppressed by the opposing Lorentz forces, as is evident in Figure 8 where the effect of inlet flow from the upper flat surface becomes more visible. Fluid flow results in other planes further indicate that with an applied magnetic field, the perturbance from g-jitter may be reduced to the level far smaller than the plug flow resulting from the inlet inertia of the fluid.

IV. WORK IN PROGRESS

The work in progress involves extensive experimental measurements and additional numerical simulations to obtain more information that will help to enhance our fundamental understanding of magnetic damping effects on g-jitter induced flow and solidification phenomena in space processing systems and to help design damping facilities for microgravity applications.

Extensive numerical simulations will be continued to study magnetic damping of g-jitter flows. Information will be obtained to quantify the effects of the field strength and direction, and the g-jitter frequency, orientation and amplitude, on the convective flows and solutal distribution and evolution in solidification systems. Solidification phenomena will be included in the 2-D model so as to better understand the effects of g-jitter and magnetic fields. Ground-based measurements will be conducted in the physical model that has just been completed and is being fine tuned. The physical measurements will be compared with the numerical model predictions. Additional experiments are also planned at NASA Lewis research center and compared with model predictions. The numerical models will be refined in light of the comparison. The refined models will be applied to carry out further studies of damping effects on velocity distribution, temperature distribution, solid-liquid interface and solute distribution during solidification with both synthetic g-jitter functions and the g-jitter data taken during space flight.

V. REFERENCES

[1] Lehoczky, S., Szofran, F. R. and Gillies, D. C. (1994). Growth of solid solution single crystals. Second United States Microgravity Payload, Six Month Sciences Report, NASA MSC.

[2] Alexander, J. I. D. (1990) *Microgravity Sci Tech.*, vol. 3, P. 52.

[3] Alexander, J. I. D. (1994). *Microgravity Sci. Tech.*, Vol. 2, p.131.

[4] Alexander, J. I. D., Amiroudine, S., Quazzani, J. and Rosenberger, F. (1991) *J. Crystal Growth*, Vol. 113, p.21.

[5] De Groh, H. C. and Nelson, E. S. (1994). On residual acceleration during space experiments. ASME Winter Annual Meeting, Chicago, IL, HTD-Vol. 290, p. 23.

[6] Nelson, E. S., (1991). An examination of anticipated g-jitter on space station and its effects on materials processes. NASA TM 103775.

[7] Sabhapathy, P. and Salcudean, M. E. (1991). *J. Crystal Growth*, Vol. 113, p. 164.

[8] B. Q. Li, "G-jitter induced flows in a transverse magnetic field," *Int. J. Heat & Mass Trans.*, Vol. 39, No. 14, pp. 2853-2860, 1996.

[9] B. Q. Li, "The effect of magnetic fields on low frequency oscillating natural convection," *Int. J. Eng. Sci.*, Vol. 34, No. 12, 1996, pp. 1369-1383.

[10] Pan and B. Q. Li, "Effect of magnetic fields on oscillating mixed convection," *Int. J. Heat & Mass Transfer*, Vol. 41, No. 17, 1998, pp. 2705-2710.

[11] B. Pan, B. Q. Li and H. C. de Groh "Magnetic damping of g-jitter induced flow in microgravity," *Spacebound-97*, Montreal, May, 1997 (published in CD-ROM, ed: R. A. Schiffman), Canadian Space Agency, Canada.

[12] B. Pan, B. Q. Li and H. C. deGroh, "Magnetic damping of g-jitter induced oscillating convection," *Joint Xth European and Vith Russain Symp. on Phys. Sci. In Mcirogravity*, June 1997, pp. 305-308.

[13] D-Y Shang, B. Q. Li and H. C. de Groh, "Magnetic damping of g-jitter driven flows: 3-D calculations," *Pan-Pacific Basin Workshop*, July 1998, accepted.

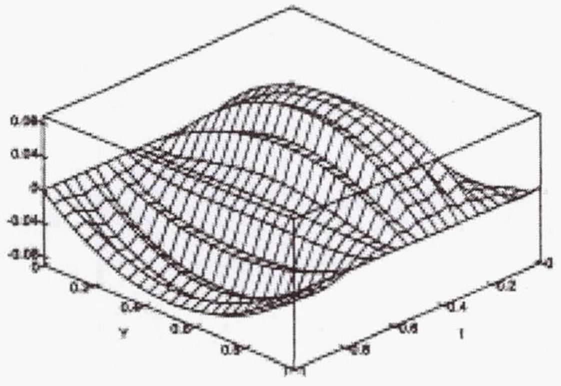

Figure 1. The flow field induced by a combination of two g-jitter components with distinct frequencies ($\Omega_2=10\Omega_1=100$) but the same magnitude ($g_2=g_1=1$, $T_2=T_1$) without a magnetic field. $t=\Omega_1\tau/2\pi$.

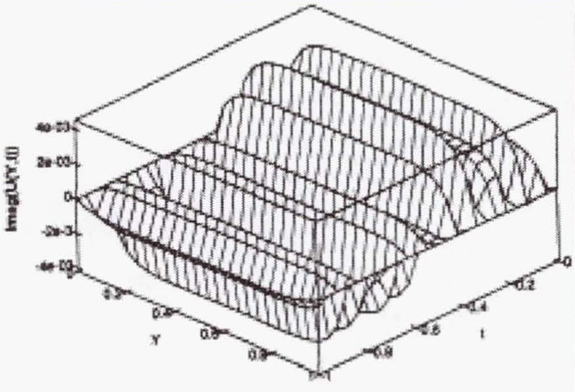

Figure 2. Effect of magnetic field on g-jitter induced flows ($\Omega_2=10\Omega_1=100$, $g_2=g_1=1$, $T_2=T_1$). Ha=20, and $t=\Omega_1\tau/2\pi$. Note that in comparison with Fig. 1, the velocity is reduced by a factor of about 10.

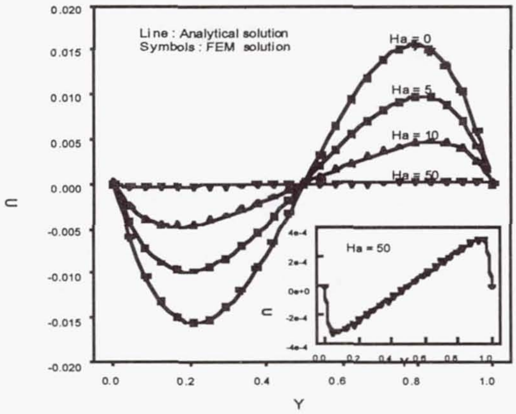

Figure 3 Comparison of the 2-D numerical and the analytical solutions for convective flows in a parallel plate channel: Y the location between the plate and U the fluid flow velocity, both nondimensionalized.

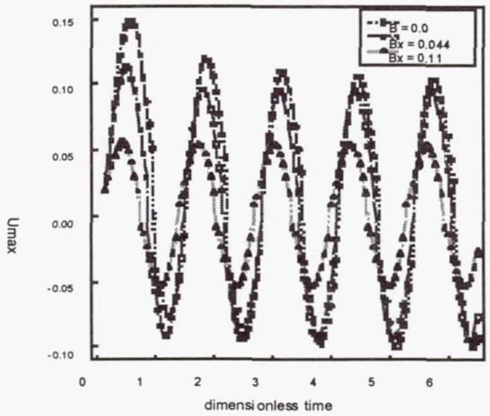

Figure 4 Dependency of maximum flow velocity in the Ga-doped germanium melt on the applied magnetic field (2-D model): single frequency g-jitter, $g=10^{-3}$ and $f_n=0.1$ acting in the x-direction.

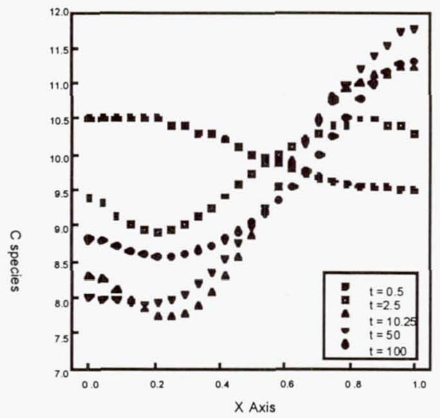

Figure 5 Concentration distribution along the interface at different times without an imposed magnetic field (2-D model): g/f – 10^{-2},10^{-3},10^{-4} g_0/1,0.1,0.01.

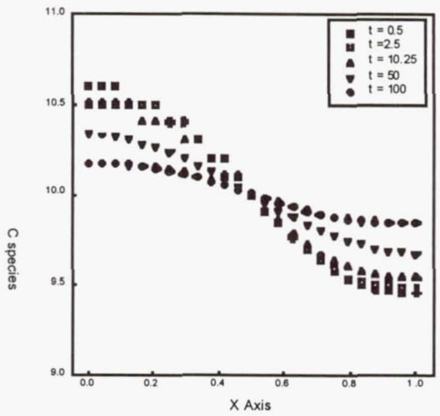

Figure 6Concentration distribution along the interface at different times with a magnetic field B_x=0.22 (2-D model): g/f – 10^{-2},10^{-3},10^{-4} g_0/1,0.1,0.01.

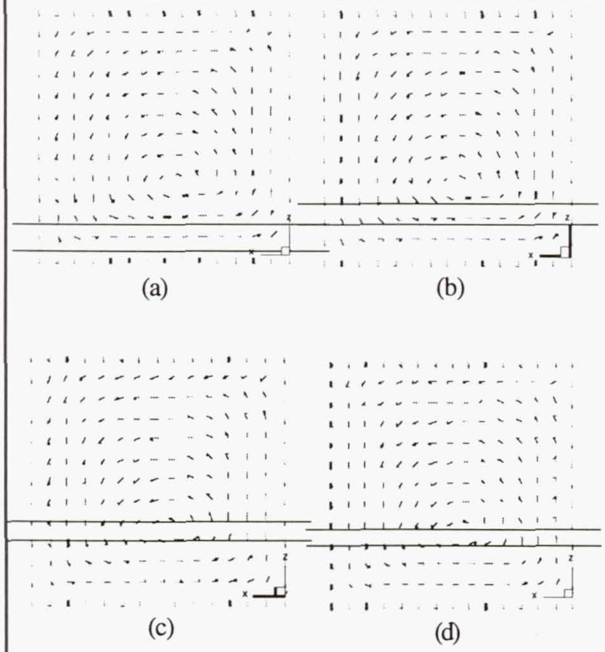

(a) (b)

(c) (d)

Figure 7 Velocity field in the x-z plane at different time steps (3-D model, viewed from the positive y-axis, g-jitter acting in the x-direction with amplitude=$1\times10^{-3}g_0$and freqneucy=0.1 Hz): (a) t=5 sec, (b) t=10 sec, (c) t=35 sec, and (d)=40 sec.

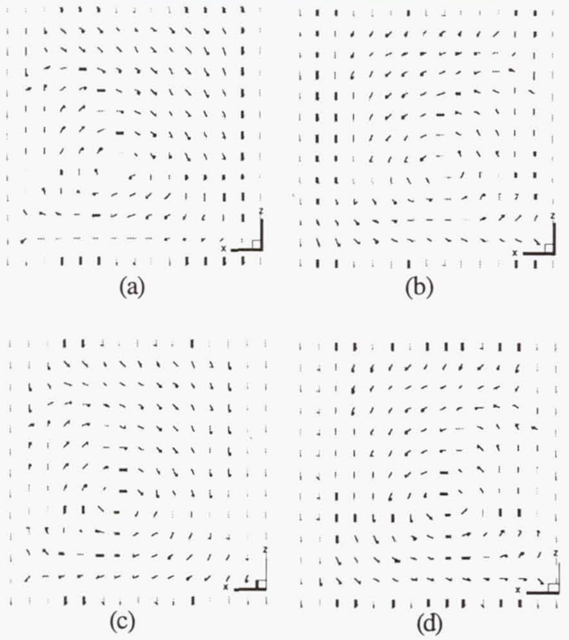

(a) (b)

(c) (d)

Figure 8 Magnetically damped velocity field in the x-z plane corresponding to Figure 7 but with an applied magnetic field in the y-direction B=0.22 Tesla.

THERMOPHYSICAL PROPERTIES OF HIGH TEMPERATURE LIQUID METALS AND ALLOYS

John Manning (Principal Investigator)
Metallurgy Division
National Institute of Standards and Technology (NIST)
Gaithersburg, MD 20899
Telephone: (301) 975-6157
and
Shankar Krishnan (Co-Investigator)
Containerless Research, Incorporated (CRI)
906 University Place
Evanston, IL 60201-2149
Telephone: (847) 467-2678

Objective

The objective of this research is to extend, for the first time, the laser polarimetry technique for measuring the normal spectral emissivity to the microsecond time regime. This will enable accurate determination of true temperature of liquid specimens at high temperatures in rapid pulse heating experiments. In addition to the measurement of other experimental quantities, the proposed project will yield data on selected thermophysical properties with unsurpassed accuracy that can be used in support of microgravity materials science research. The properties to be measured include enthalpy, specific heat capacity, heat of fusion, and electrical resistivity above the melting point of selected refractory metals and alloys.

Relevance to Microgravity

Thermophysical property values for liquid metals and alloys are needed in modeling solidification, casting design, crystal growth and in welding designs. A number of these processes (and related experiments) are currently being practiced in the reduced gravity environment of space. The present research supports these efforts by aiming to provide thermophysical measurements methodology and thermophysical data of unsurpassed accuracy on standard materials, pure elements and alloys of importance to NASA's microgravity mission.

Background

Research on materials at high temperatures, including measurements of thermophysical properties, necessitates non-contact (radiometry or optical pyrometry) for the measurement of specimen temperatures. The accurate measurement of "true" temperature is an important parameter in most experiments involving the measurement of thermophysical properties at elevated temperatures. However, due to the difficulties associated with accurate true temperature measurements (at elevated temperatures), large uncertainties exist in the reported values of the thermophysical properties of numerous materials. Ideal measurements require a blackbody configuration for the specimen that is either impractical or impossible to achieve in high temperature experiments, particularly for liquid specimens. An alternate approach is to determine the true temperature from measurements of surface radiance temperature and a knowledge of the normal spectral emissivity of the specimen surface. Pyrometric techniques are sufficiently advanced to provide the means for accurate measurements of surface radiance temperature; however, determination of normal spectral emissivity for the specific surface presents a serious difficulty.

Available data on emissivity for many materials at high temperatures are in considerable disagreement, even for pure metallic elements. In many cases, the disagreement among the literature data is believed to be largely due to differences in surface roughness and/or to problems such as specimen evaporation, surface contamination, chemical reactions, etc. This suggests that for accurate temperature determinations and thermophysical property measurements, it is essential to measure normal spectral emissivity simultaneously with the surface radiance temperature of the specimen together with other experimental quantities.

During the last decade, accurate direct measurements of normal spectral emissivity have been made possible as the result of research conducted at Rice University and Containerless Research Incorporated (CRI) [1,2]. These investigations have led to the development and application of a laser polarimetry technique for the measurement of normal spectral emissivity of levitated and pulse-heated liquids. The working principle of the laser polarimetric technique is that, when quasi-monochromatic light of linear polarization is incident on a specularly-reflecting surface at an oblique angle, the reflected light is generally elliptically polarized. By accurately measuring the polarization state of the reflected light, normal spectral emissivity can be determined.

During the past three decades, the development of subsecond pulse-heating techniques at the National Institute of Standards and Technology (NIST) [3,4] has enabled the measurement of selected thermophysical properties of a number of electrically-conducting solids at high temperatures (primarily in the range 1500 K up to and including their melting temperature). The measured properties include not only normal spectral emissivity (by employing blackbody hole methods) but also heat capacity, electrical resistivity, thermal expansion, hemispherical total emissivity, temperature and energy of solid-solid phase transformations, and melting temperature [4]. The basic technique involves rapid resistive self-heating of the specimen from room temperature to the maximum temperature of interest in less than 1 s by passing an electrical current pulse through it, and simultaneously measuring the pertinent experimental quantities with millisecond resolution.

Five years ago, NIST and CRI began a NASA-sponsored joint effort to integrate the laser polarimeter and the millisecond pulse-heating system to conduct research with the objective of validating and establishing the accuracy of the laser polarimetry method and obtaining accurate emissivity data on selected metals. An initial three-year NRA program resulted in the validation of the laser polarimetric technique and the determination of the spectral emissivity and thermophysical properties of a number of materials at temperatures up to and including the melting point [5]. Two years ago, we began the current NRA program aimed at extending the operating range of this system for the measurement of spectral emissivities and true temperature into the liquid state by integration of a microsecond pulse-heating and pyrometry system with an ultra-high speed laser polarimeter system. These studies have advanced tremendously in the last two years leading to the complete development and preliminary validation of a new ultra-high speed laser polarimeter system for the measurement of normal spectral emissivity of liquid materials with microsecond time resolution, allowing determination of true temperature and thermophysical properties in the liquid state during microsecond pulse-heating.

Accomplishments

Due to relatively long development time for the ultra-high speed laser polarimeter system, the first year of the current program involved continued studies using the millisecond pulse-heating facility. These studies provided important results on the thermophysical properties of Mo and Nb-47% Ti alloys at elevated temperatures [6,7]. The second year of this project involved the integration and use of the novel ultra-high speed laser polarimeter system developed by CRI in the microsecond pulse heating facility. Operation of the combined system (microsecond pulse heating and ultra-high speed laser polarimetry) was tested during the past year.

Figure 1 shows the experimental arrangement used to conduct the on-going NRA research work. The previous (existing) microsecond pulse heating system was modified to accommodate a new chamber, new electrical and electronic systems to control the pulse heating and provisions to accommodate the ultra-high speed polarimeter system. The laser light delivery to the polarimeter incident optics and the light collection from the polarimeter receiver was achieved through fiber optics. A single wavelength pyrometer was used to measure the radiance temperature of the specimen at an effective wavelength of 652 nm, which is close to the laser polarimeter's operating wavelength of 677 nm. The polarimeter receiver produces four output light fluxes which are transmitted to four high-speed detectors and de-modulation electronics via fiber optics. In addition, the voltage drop across a known specimen length (with the aid of voltage probes) and the current through the specimen are also recorded precisely. Further details on the polarimeter operation, the data acquisition system and data reduction, calibration of the polarimeter, and alignment issues are described in a recent publication [8]. Further details on the general principles of the operation of the microsecond pulse heating facility may be found in previous publications from NIST [9]. Figure 2 shows a close up view of the specimen geometry including the placement of the voltage probes, the electrical clamps, and the polarimeter and pyrometer measurement geometry. Specimens used in the study are typically 1.5 mm in diameter and about 50 mm long.

Figure 3 shows the first normal spectral emissivity results obtained with the new system on niobium. In these experiments, the specimen is rapidly heated, melted and heated well into the liquid region in less than 100 μs. As the specimen temperature approaches the melting temperature (T_m = 2740K), there is a rapid decrease in the emissivity. The emissivity values then remain nearly constant through the melting region and then into the liquid region. Emissivity data are obtained for approximately another 30 μs beyond the melting plateau. The pyrometer output saturates within about 10 μs beyond the plateau, but emissivity data are obtained further out in temperature.

Figure 4 shows preliminary values of the total enthalpy, heat capacity and electrical resistivity (volume uncorrected) for solid and liquid niobium as a function of true temperature. The specific heat capacity is equal to the slope of the enthalpy-temperature curve. The results for the thermophysical properties for liquid Nb in the 2800-3300K temperature range are:

Normal emissivity (at 677 nm): $\varepsilon(T) = 0.342 + 0.000015T$

Electrical resistivity: (μΩ-cm) $\rho(T) = 92.97 + 0.00273T$

$C_p = 42.4$ J/mol.K, $2800K < T < 3300K$, $\Delta H_f = 32.4$ kJ/mol

These values are in good agreement with previous results [10] obtained with a constant emissivity assumption.

Future Research Plans

This past year has resulted in the installation and successful testing of an ultra-high speed laser polarimeter system and integration with the NIST microsecond pulse heating and pyrometry facility. The preliminary results obtained on niobium show the system to be very promising. Further detailed measurements on niobium are being conducted, and we expect to submit one or two archival publications on this work in the next few months. In the next year, we hope to extend the measurements to other materials including refractory metals, such as molybdenum, tungsten, and industrially important alloys, such as Inconel 718 and 90Ti-6Al-4V from their melting point to about 1000 K above their melting point.

References

[1] S. Krishnan, *J. Opt. Soc. Am.* **A9**, 1615 (1992).

[2] S. Krishnan, P. C. Nordine, J. K. R. Weber, R. H. Hauge, and J. L. Margrave, in *Temperature, Its Measurement and Control in Science and Industry*, Vol. 6, Part II, J. F. Schooley, Ed. (Amer. Inst. of Phys., New York, 1992), p. 943.

[3] A Cezairliyan, M. S. Morse, H. A. Berman, and C. W. Beckett, *J. Res. Natl. Bur. Stand. (US)*, **74A**, 65 (1970).

[4] A. Cezairliyan, *J. Res. Natl. Bur. Stand. (US),* **75C**, 7 (1971).

[5] A. Cezairliyan, S. Krishnan, and J. L. McClure, *Int. J. Thermophys.*, **17,** 1455 (1996) .

[6] A. Cezairliyan, S. Krishnan, J. L. McClure and D. Basak, in Press, *Int. J. Thermophys.*, 1998.

[7] S. Krishnan and D. Basak, Int. J. Thermophysics, 1998, Submitted.

[8] S. Krishnan, DOC SBIR Phase II Final Report "Apparatus for spectral emissivity measurements on pulse-heated materials", 1998.

[9] A. Cezairliyan and J. L. McClure, *Int. J. Thermophys.*, **8,** 577 (1987) .

[10] A. Cezairliyan and J.L. McClure, *Int.J.Thermophys.*,**8,** 803 (1987) .

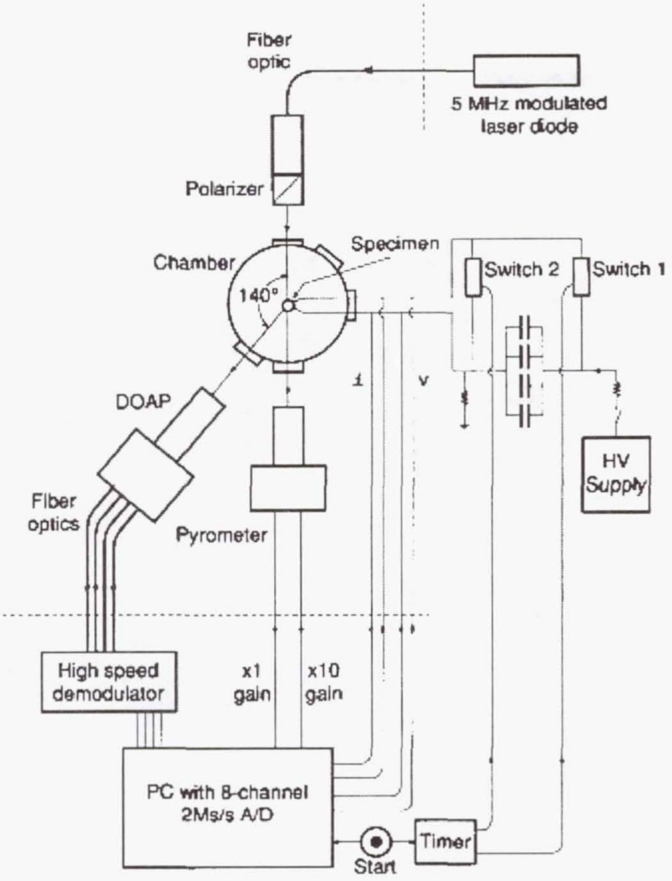

Figure 1. Functional diagram of the overall experimental arrangement including the pulse-heating system and the radiometric and polarimetric instrumentation. The polarimeter is labelled DOAP.

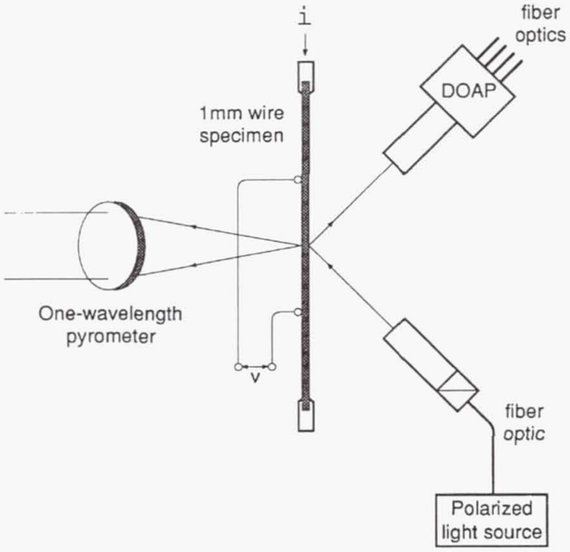

Figure 2. Schematic diagram of the specimen and the configuration of the single wavelength pyrometer, the polarimeter system and voltage probes. Dimensions are not to scale.

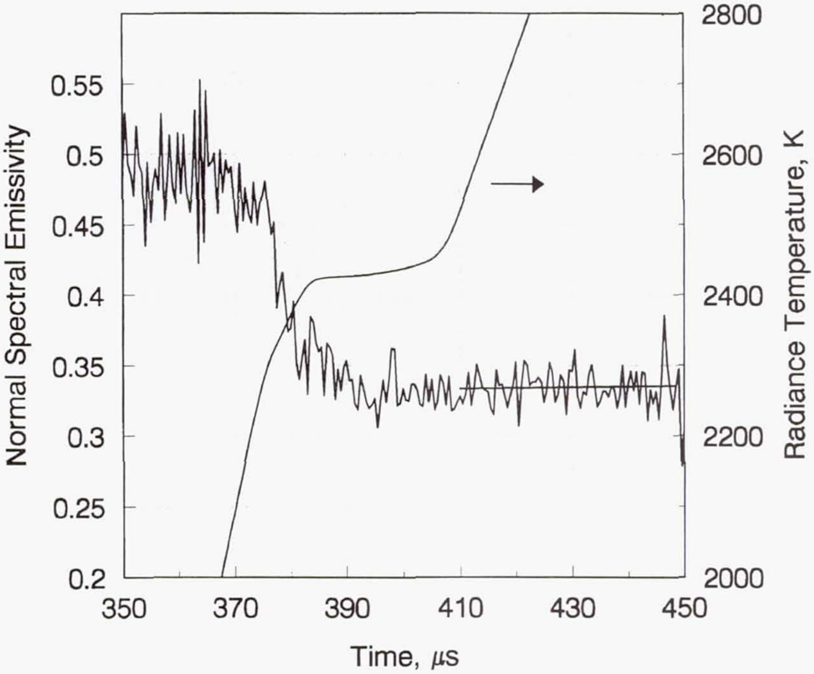

Figure 3. Normal spectral emissivity of niobium in the melting region and up to temperatures far in excess of the melting point. The line drawn through the emissivity data represents a least squares fit.

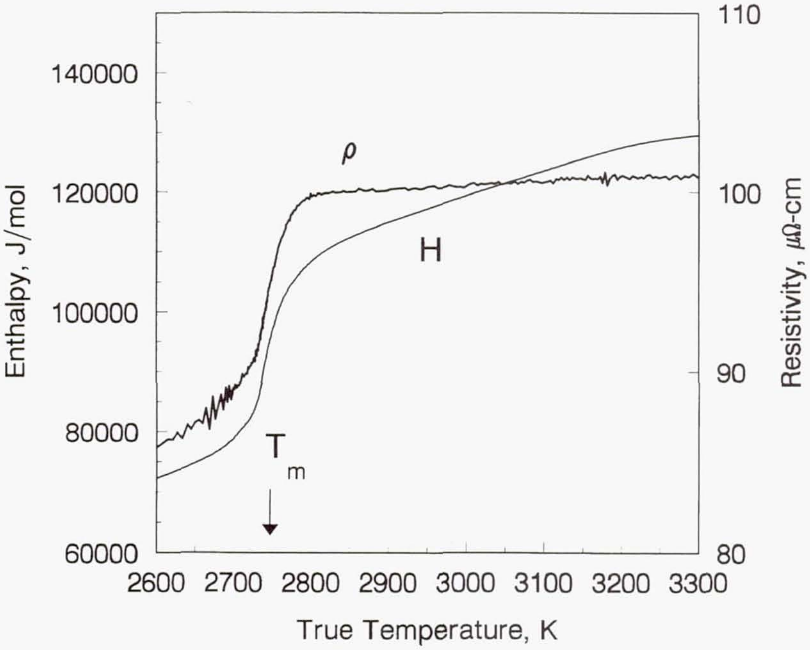

Figure 4. Preliminary values of the enthalpy and electrical resistivity of liquid niobium as a function of true temperature. These are the first results on liquid heat capacity that included a simultaneous true temperature measurements under microsecond pulse heating conditions.

DIFFUSION PROCESSES IN MOLTEN SEMICONDUCTORS

Professor David H. Matthiesen and Dr. Monica L. Kaforey
420 White Building
Case Western Reserve University
10900 Euclid Avenue
Cleveland, OH 44106
(216) 368-1366 voice
(216) 368-3209 FAX
DHM5@po.cwru.edu E-mail

1. Description of Experiment

For the reflight of the first Microgravity Science Laboratory (MSL-1R) flight of opportunity, this program of study was directed at the fundamental and applied issues pertaining to diffusion of mass in the liquid state as driven by concentration gradients (Fickian diffusion). The fundamental material systems of interest for the MSL-1 mission were the dilute binary systems of gallium (Ga), silicon (Si) and antimony (Sb) into germanium (Ge). This research program consisted of three major components: an experimental measurement portion, a continuum numerical simulation portion and an atomistic numerical simulation portion.

The experimental measurement portion was designed to provide definitive measurements of the purely diffusive component of mass transfer in molten semiconductor systems. The shear cell technique was used to directly measure the diffusion coefficients in semiconductor melts. For the Fickian diffusion case, isothermal measurements were used to determine the diffusion coefficients. An experimental matrix was used to determine the dependence of the diffusion coefficients on temperature, dopant type and column diameter. For the MSL-1 mission, the experiments contained a "check" to quantify, if any, the amount of Soret diffusion driven by the small thermal gradients in the Large Isothermal Furnace (LIF).

The shear cell technique consisted of two columns of different liquids, which are brought into contact with one another, allowed to diffuse, and then these columns were sheared into segments. Following solidification, the average concentration level of each segment was measured enabling the construction of a diffusion profile. From that concentration profile, the diffusion coefficient can be computed, and possible diffusion mechanisms may be verified.

An extensive ground based experimental matrix was conducted. However, in each of these experiments an effective diffusion coefficient was measured, which will be a combination of a purely diffusive transport and a convective transport contribution. By reducing the sample diameter, the convective transport term can be minimized. However, if the sample diameter is too small, an additional transport term due to wall effects becomes important. In the microgravity environment of near earth orbit, the convective term can be minimized and the sample diameter can be increased to minimize the wall effect, thus measuring the purely diffusive diffusion coefficient.

Post flight characterization of the flight samples will consist of measuring the average concentration of each segment using Inductively Coupled Plasma/Mass Spectroscopy (ICP/MS). In the ICP/MS technique, the sample is digested and a small number of measurements are taken from each sample. Statistical analysis of these measurements is then done to determine the precision and accuracy of these measurements. In addition, a statistical model of a perfect diffusion profile has been developed. Known error has been added to this model to determine the exact precision for which the value of diffusion coefficients can be differentiated.

Extensive continuum numerical simulation experiments have been performed using a complete thermal model of the furnace, combined with a three-dimensional model of the shear cell. These simulations (together with verification experiments) were used to determine the input control parameters for the isothermal furnace.

2. Scientific Knowledge to be Gained

The fundamental mechanisms of mass diffusion in the liquid state are not understood well enough to allow for the prediction of diffusion of one species into another or even within itself. This observation is especially true with respect to the dependence of diffusion mechanisms on temperature as well as on the dopant type. Present estimates of diffusivity in molten semiconductors can typically provide an order of magnitude estimate only, without any information on their dependency on dopant type or temperature.

The availability of these data is of paramount importance for practical reasons. The relevancy of numerical modeling for the analysis and design of ground based and space experiments is directly dependent upon the accuracy of the fundamental material properties used in these simulations. These data are also important for the correct characterization and interpretation of experimental results from ground based and space experiments.

These experiments should provide the most accurate measurements of diffusion coefficients ever made. These will be used to validate the prediction made by the numerical models and thus, it is hoped that new scientific insight into the fundamental mechanisms of diffusion as well as the structure of the liquid state in general will be found.

3. Value of Knowledge to Scientific Field

The subject of how a mass of one species diffuses through a matrix of another is, at the same time, both a very old and very new research area. That this area can encompass the small, i.e., movement of electrons in a plasma, to the very large, i.e., the depletion of the global ozone layer, merely serves to emphasize the fundamental aspects of this subject. .Most manufacturing technologies, at some stage, rely on diffusion processes in the solid, liquid or gas.

The need for precise measurements of the diffusion coefficients in molten semiconductors has been repeatedly pointed out. These data are required both to interpret the experimental results from previous space-based (and Earth-based) experiments and also to optimize newly envisioned experiments. Difficulties in experimental techniques and theoretical interpretations are cited for the lack of these data. This is a comprehensive program, which addresses both of these issues.

4. Justification of the Need for Space Environment

Terrestrial experiments designed to measure diffusion coefficients in the liquid state are hampered by convection in the melt and convection during the solidification process, both of which typically confound data interpretation. This has resulted in wide variations in the few reported data in the literature. Arnold and Matthiesen have predicted, based on numerical simulations, that for the Ga-doped Ge system, convection effects increase the measured diffusion coefficient for capillaries even as small as 2 mm in diameter. The experimental data, combined with the numerical simulations of convective effects, predict a nonexistent range of capillary diameters that allow the measurement of the actual diffusion coefficient on Earth. As a result, the microgravity environment, in which convective effects are minimized, is required.

5. Summary of Ground Based Tests

Table 1 lists the summary of ground based testing and Fig. 1 shows a plot of these results. The error bars represent 95% confidence intervals about the means. As can be seen in Fig. 1., the diffusion coefficient does increase as the capillary diameter increases, which is indicative of convection in the column.

Capillary Diameter (mm)	Diffusion Coefficient	errors
1.6000	2.2200	1.1900
1.6000	1.6000	0.090000
1.6000	1.7500	0.11000
3.0000	2.7600	0.37000
3.0000	3.1200	0.14000
1.0000	1.5900	0.50000
2.0000	0.92500	0.13800
3.0000	0.76300	0.12800
1.6000	1.6400	0.11000
3.0000	2.6400	0.41300
1.6000	1.7900	0.41300

Table 1. Summary of diffusion measurements in Ga-doped Ge.

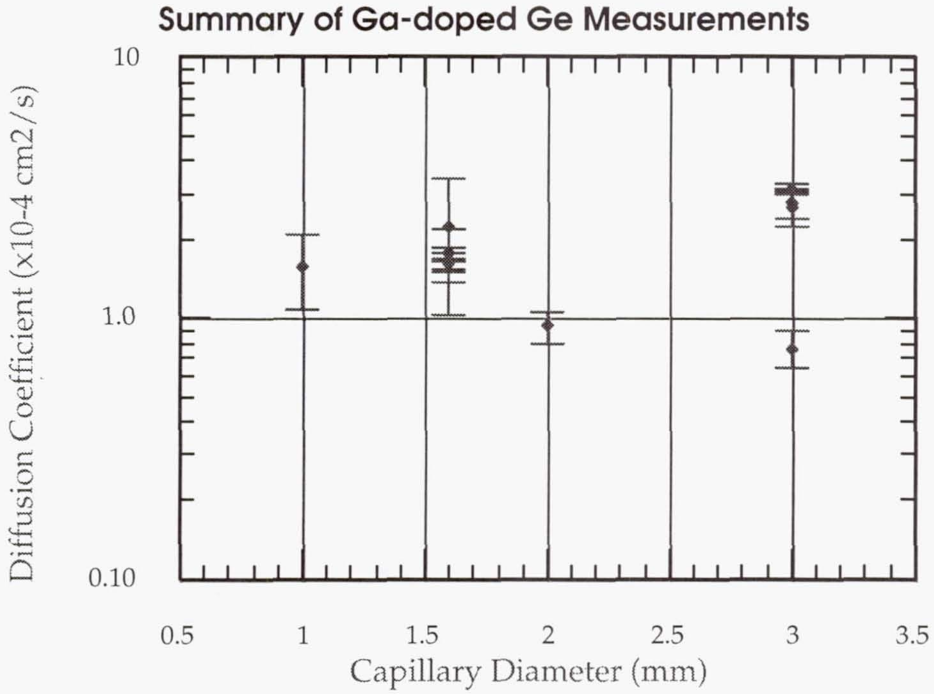

Figure 1. Plot of diffusion coefficients as a function of capillary diameter for Ga-doped Ge.

6. Results of the MSL-1R Mission

During the MSL-1R mission, 6 cartridges were processed in the LIF. Two cartridges were processed at 1000°C; three cartridges were processes at 1550°C; and one cartridge was processed at 950°C. The cartridges at 1000°C and at 950°C were thermally soaked for 6 hours and 6 minutes at which time a payload crewmember aligned the capillaries. After a 2 hour and 12 minute diffusion period, a payload crewmember rotated the cell to shear the capillaries. The cartridges at 1550°C were thermally soaked for six hours and 32 minutes and had a diffusion period of two hours and 15 minutes. After the final shear the furnace power was shut off.

Each cartridge contained one shear cell and each shear cell contained three capillaries 3 mm in diameter and 3 which were 1.5 mm in diameter. One set of capillaries consisted of one 3 mm capillary and one 1.5 mm capillary. One set was doped with gallium, one set with antimony and one set with gallium and silicon at the 1000°C temperature. For the 950°C and 1550°C temperatures, two sets were doped with gallium and one set was doped with antimony. In addition, each shear cell had six capillaries, 1 mm in diameter, which were gallium-doped germanium. These small capillaries are to be used to determine if any Soret diffusion was present.

During the MSL-1R mission several off-nominal events occurred. Because of these off-nominal events, NASA Lewis Research Center convened a Failure Review Board to investigate the cause of these anomalies and to determine what lessons could be learned from the causes of these events. Since this Board has not completed their investigation, the flight samples and the ground truth samples have not been released to the Principal Investigator.

There are three off-nominal events, which are being investigated. The first was that no downlink data was obtained from the sample thermocouple, which was located in the center of the shear cell. The cause of this was determined during the mission to be an incorrectly wired connection plug for the cartridge. The thermocouple connections on the cartridge plug were on pins J and I and the connections on the bulkhead receptacle were on pins I and H. The connector and the receptacle were each wired correctly according to their respective drawings. This anomaly was corrected during the third experiment by the payload crew using jumper cables between the connector and the receptacle.

It is clear from the description of this anomaly that one lesson to be learned is that: "flight hardware must meet flight hardware in form and function". This means that had the cartridge connector been plugged into the bulkhead receptacle and tested before flight, this error would have been found and could have been corrected.

The second off-nominal event occurred during the fourth experiment when the furnace power began to increase although the control thermocouple continued to read the same value. This indicated that the control thermocouple was reading too low, and was probably going to fail soon. It was negotiated pre-mission with NASDA that the furnace control would automatically switch to another thermocouple for control in the event of a control thermocouple failure. However, during the mission it was discovered that only if the control thermocouple would fail open-circuit would the furnace control automatically switch over. If the control thermocouple failed too low, which is a very common occurrence, the furnace power would increase and cause the furnace to over heat. An automatic shutdown occurred when the monitoring thermocouples exceeded the 1650°C temperature limit and the sample was quenched, resulting in a 100% science loss.

When the furnace control thermocouple cooled to below 270°C, the furnace reset itself and automatically turned itself on with full power. The temperature of the furnace quickly reached the melting point of the germanium. The furnace was finally turned off using payload crew intervention.

One lesson to be learned from both of these off-nominal situations is that the software to be used in flight must be thoroughly tested in flight like mission simulations.

The third off-nominal event occurred when the payload crew rotated the shear cell capillaries into alignment. The individual segments of the graphite shear cell each have individual alignment tabs. There is an 85.5° initial offset of the capillaries to allow them to melt without being in contact with each other. The initial alignment by the payload crew was thus, expected to be 85.5°. The actual procedures called for rotation to a hard stop, i.e. when all the graphite tabs aligned. The first rotation for sample one was 215° and for sample 2 it was 365°. Both of these samples were at 1000°C.

During the mission it was hypothesized that the graphite tabs were being broken. For the third sample it was requested that the payload crewmember only rotate the shear cell 85.5° and then stop without reaching a hard stop. The problem with this approach is that if the capillaries are not exactly aligned, then an unquantifiable unknown is introduced into the data set thus rendering it useless. Two samples at 1550°C and one sample at 955°C were conducted in this manner.

In the post-flight examination of the flight samples, no graphite tabs were found to be broken. Instead it was found that the stainless steel driveshaft and the tantalum transfer shaft were twisted. It is currently believed that the tolerances of the inside diameter of the stainless steel bushing and the outer diameter of the stainless steel driveshaft were incorrectly specified and did not take into account the thermal expansion of the stainless steel driveshaft. This caused the stainless steel driveshaft to bind and greatly increase the torque required to rotate the shear cell.

This error was not discovered in ground-based testing because all the bushings were machined to the largest ID tolerance and the stainless steel driveshafts were machined to the smallest OD tolerance. This situation accommodated the thermal expansion of the driveshaft. However, since the flight samples were all machined at the same time, they all contained the same problem, which was that the OD of the driveshaft and the ID of the bushing would bind at temperature.

The lesson to be learned here is that the flight samples and the ground truth samples must all be manufactured at the same time. Then the ground truth samples must be run on the ground before the flight.

Despite all of these failures, it appears at this time that the two samples run at 1000°C were fully aligned and correctly sheared, despite their twisted driveshafts, and they are expected to yield valid scientific data. Further examination needs to be done to determine if the three samples for which the initial alignment was stopped at 85.5° were fully aligned before their validity can be established.

7. Conclusions

The shear cell technique has been used to successfully measure the diffusion coefficients for Ga and Sb doped germanium. Ground-based results using capillary diameters of 1, 1.6 and 3.0 mm have indicated an increase in the diffusion coefficient with increasing capillary size. This is indicative of convection being present in the diffusion column for the ground-based experiments. Several off-nominal events occurred during the MSL-1R mission, which resulted in the loss of one experiment and the compromise of three experiments. The two experiments at 1000°C are expected to yield valid scientific data on the diffusion coefficients of Ga, Si and Sb in molten germanium.

Page intentionally left blank

THE STUDY OF DOPANT SEGREGATION BEHAVIOR DURING THE GROWTH OF GaAs IN MICROGRAVITY

Professor David H. Matthiesen, Dr. Monica L. Kaforey and Jennifer Bly
420 White Building
Case Western Reserve University
10900 Euclid Avenue
Cleveland, OH 44106
(216) 368-1336
dhm5@po.cwru.edu

1. Description of Experiment

The original proposal for the study of dopant segregation behavior during the growth of gallium arsenide (GaAs) in microgravity was a program to investigate techniques for obtaining complete axial and radial dopant uniformity during crystal growth of selenium doped gallium arsenide (Se/GaAs). The primary goal of the reflight opportunity on the Second United States Microgravity Laboratory (USML-2) was to characterize and, if possible, controllably modify the melt-solid interface shape during the growth of Se/GaAs to achieve uniform radial segregation of the dopant. The reduced effective gravitational accelerations in a microgravity environment can reduce or eliminate the driving force for buoyancy driven convection. As the level of convection is reduced, axial segregation approaches that of diffusion controlled growth. An axial segregation profile due to diffusion controlled growth will have a uniform steady state region after an initial transient. Radial segregation, however, is controlled by the shape of the melt-solid interface. In these experiments, the booster heater and gradient zone configuration of NASA's Crystal Growth Furnace (CGF) were utilized in an attempt to achieve a near planar interface shape in order to minimize radial dopant variation.

Each of the experiments used a Se/GaAs crystal grown using the Liquid Encapsulated Czochralski (LEC) technique. Each crystal was machined to a diameter of 1.5 cm and inserted into a pyrolytic boron nitride (PBN) sleeve. A graphite cup supports the cold end of the crystal. At the hot end of the crystal is a spring composed of a stack of PBN leaf springs inside a graphite spring chamber. This spring expands when the GaAs melts and keeps the graphite in electrical contact with the melt surface. The expansion of the spring also keeps the melt in contact with the wall of the container and prevents the formation of a free surface on the melt. This entire assembly is hermetically sealed inside a quartz ampoule. Electrical current is passed through the quartz ampoule using molybdenum feedthroughs. The CGF was modified to include a Current Pulse Interface Demarcation (CPID) system. This allows a current pulse to be sent through the solidifying crystal. Peltier cooling results in the incorporation of a portion of the solute boundary layer. This change in the composition of the solute can be seen as a demarcation line when a slice of the final crystal is viewed in infrared transmission. The demarcation lines show the interface shape and position at known points in time.

2. Justification for Microgravity Research

During ground based experimentation, buoyancy driven convection mixes the melt and results in a dopant distribution profile that may be described by the complete mixing theory. During experimentation in microgravity, buoyancy driven convection may be reduced such that diffusion is the dominant driving force for movement of the Se within the liquid GaAs. If this is the case, the Se distribution profile will be that described by the diffusion controlled growth theory. Diffusion controlled growth results in a concentration profile with initial and final transients and a long steady state region of constant composition in between the transients. The duration of these experiments is on the order of days. Thus, the microgravity environments available in drop towers and aircraft flying parabolic arcs are insufficient and it is necessary to do these experiments in a space environment.

3. Value of Research

The technological aspects of interface control and of transient versus steady state growth are important issues in ground-based processing of GaAs and other semiconductor materials. Experimental programs such as this one are providing an improved understanding of the interactions between process controls, such as furnace temperatures and translation rates, and the growth process, as seen via the observed interface shape and growth rate, on the resulting microstructure and material properties. Improvements in the fundamental understanding of crystal growth, whether gained during ground-based or space-based experiments, can be used to improve terrestrial crystal growth processes. Knowledge gained from this experimental program will also lead to the design of better experiments for future space station programs.

4. Ground-based Experimentation

Six crystals of Se/GaAs were successfully grown during ground-based experiments. These crystals have been examined using optical and electrical characterization techniques. The Current Pulse Interface Demarcation (CPID) system that was added to the CGF was used to successfully demarcate the interface position in the crystal at a known point in time. These positions and time intervals could later be used to calculate the actual growth rate of the crystal. The growth rate of the crystals was equal to the translation rate of the furnace for translation velocities of less than 1.5μm/s, as shown in Fig. 1. The melt-solid interface position could be moved, relative to the gradient zone of the furnace, but the interface remained concave into the solid at all positions in the furnace. The dopant distribution profiles of these crystals matched the complete mixing theory as expected.

5. Flight Experiments

Two Se/GaAs samples (primary and secondary) were processed during the USML-2 mission. The experiments were designed to minimize natural convection by processing in microgravity and to minimize surface tension driven convection through the use of a spring loaded piston designed to prevent the formation of a free surface on the molten gallium arsenide. One-piece single crystals were partially melted and regrown in microgravity. The primary sample was processed for 67 hours, 45 minutes and included 19 hours of growth at 0.5 μm/s to grow 3.42 cm and 5 hours of growth at 1.5 μm/s to grow 2.7 cm. During the second experiment, the furnace temperature was adjusted to move the melt-solid interface position towards the hot end of the furnace in order to flatten the interface shape. The second sample was processed for 50 hours, 10 minutes and included 11 hours of growth at 0.5 μm/s to grow 1.98 cm and 1 hour, 25 minutes of growth at 5.0 μm/s to grow 2.6 cm. This sample provides an order of magnitude change in growth rate and reproduces one of the growth rates used during the USML-1 mission. The cartridges containing the samples were x-rayed at Marshall Space Flight Center. The x-rays indicated that the crystals were in contact with the container along the length of the crystals and no voids were formed in the crystals.

The x-rays were also used to measure the position of the 6 thermocouples that were inside the cartridge during processing. This data is essential to correctly interpret the thermal data. These thermal data indicate that the desired thermal profiles were achieved. The absence of voids in these two samples is a result that differs from the USML-1 results. It is now believed that the voids found in the crystals grown on USML-1 resulted from the use of multi-piece initial samples. The ampoules were removed from the USML-2 cartridges and no devitrification or gross deformities were observed. The samples were removed from the ampoules, cut, and polished. Sections of the crystals were analyzed using an array of characterization methods including electrical, chemical, and optical techniques. Electrical techniques included Hall effect and capacitance-voltage measurements. Optical measurements included quantitative infrared microscopy and Fourier transform infrared spectroscopy. Chemical measurements included Secondary Ion Mass Spectrometry (SIMS). The data from these measurements were compared to current analytical and computer model based theories of crystal growth.

6. Corresponding Modeling Effort

Numerical modeling in support of the experimental program was done at the Computational Materials Laboratory at NASA Lewis Research Center. The numerical modeling results were very helpful in predicting the location of the melt-back interface relative to the furnace position for a variety of furnace temperatures and also to predicted the shape of the interface. Comparison of predictions to ground-based results are shown in Fig. 2, where it can be seen that excellent results were obtained for the seeding interface shape. The model results predicted that the interface shape would remain concave into the solid at all positions in the furnace and this was seen in the experiments.

7. Segregation Results

The segregation results for a single crystal ground-based result is shown in Fig. 3. Here the SIMS, Hall effect and FTIR data are seen to be in excellent agreement with each other. Comparison of these data with that of the theoretical complete mixing limit indicates that complete mixing segregation behavior was obtained. The segregation results for the first flight sample are shown in Fig. 4. Here it can be seen that the SIMS data indicates that a mixed segregation behavior was obtained with the dopant concentration measurements lying in between the theoretical limits.

8. Conclusions

Ground-based experimentation demonstrated that the Current Pulse Interface Demarcation (CPID) system could be used to successfully demarcate the interface position in the crystal at a known point in time. This position and time could later be used to calculate the actual growth rate of the crystal. The growth rate of the crystals was equal to the translation rate of the furnace for translation velocities of less than 1.5µm/s. The melt-solid interface position could be moved relative to the gradient zone of the furnace, but the interface remained concave into the solid at all positions in the furnace. Numerical modeling also predicted this behavior. Results from the USML-2 flight indicated that two crystals were grown successfully and that no free surfaces were formed at the surface of the crystals during the growth process. The absence of voids in either sample indicated that growth rate changes alone were not responsible for the formation of the voids seen in the USML-1 samples. The segregation results for the ground-based samples indicated that complete mixing behavior was achieved. Those of the flight samples achieved a mixed segregation behavior.

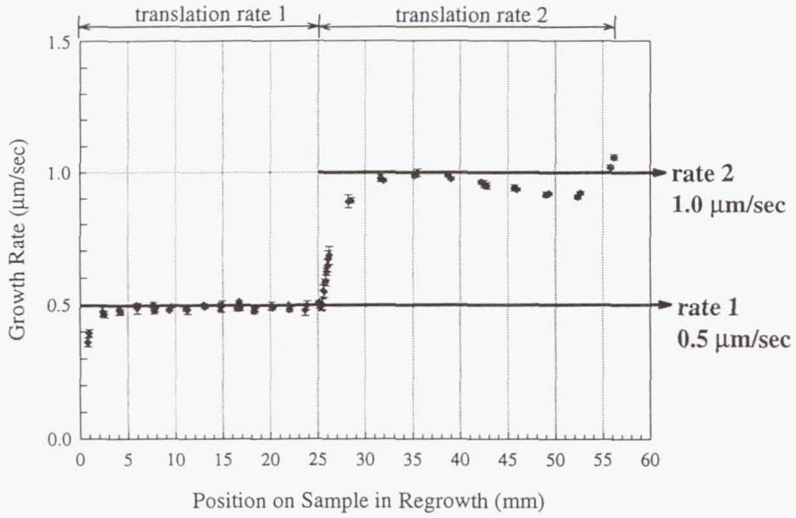

Fig. 1. Comparison of the experimentally measured microscopic growth rate with the furnace translation rates.

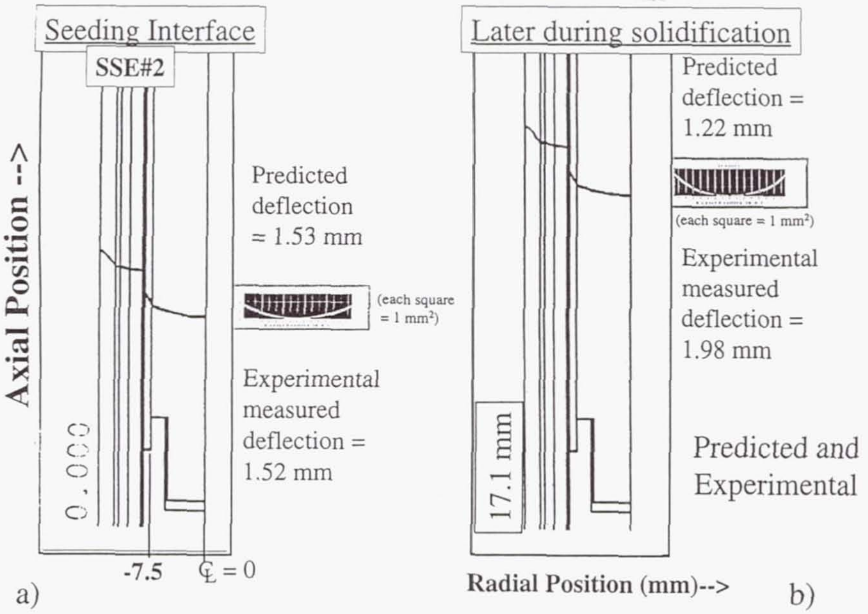

Fig. 2. Comparison of numerical simulation results with experimentally measured interface shapes: a) initial seeding interface shape and b) a position during the growth period.

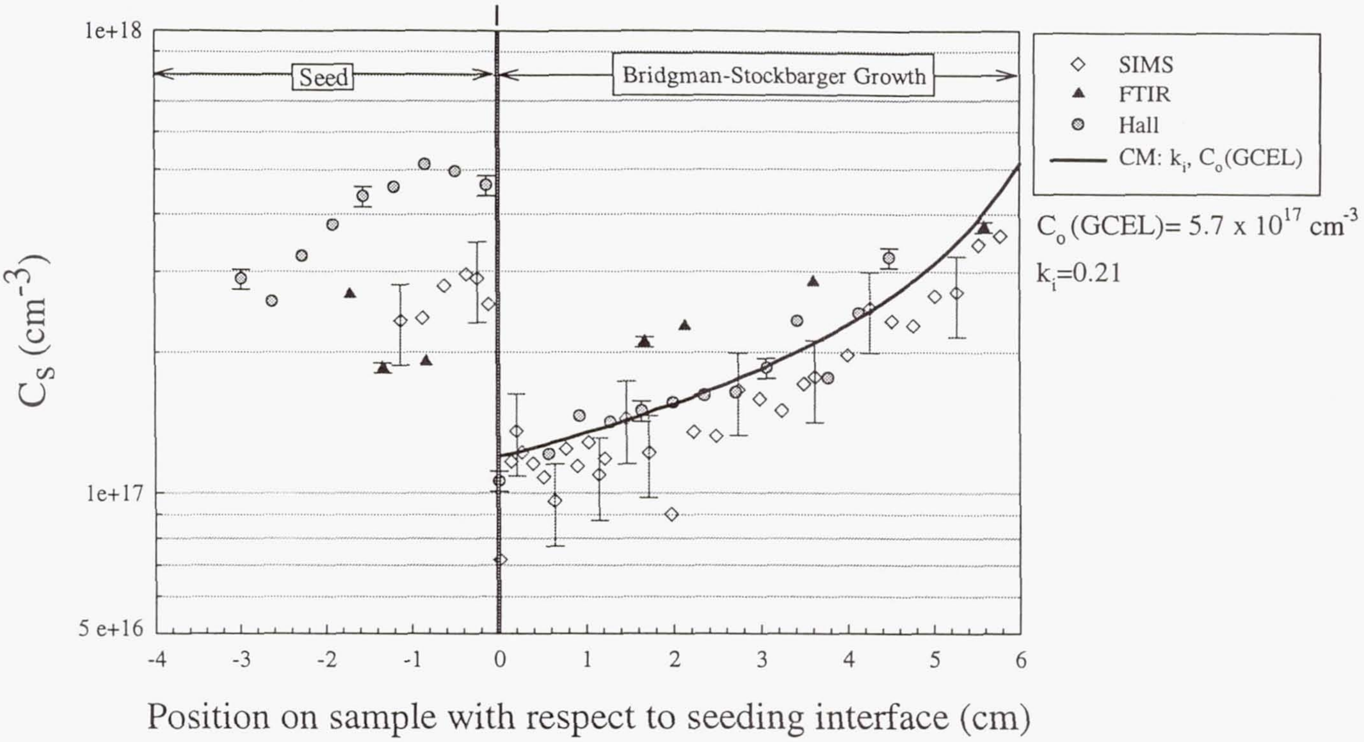

Fig. 3. Comparison of the experimentally measured selenium concentration distribution with complete mixing and diffusion controlled growth segregation behavior for ground-based sample.

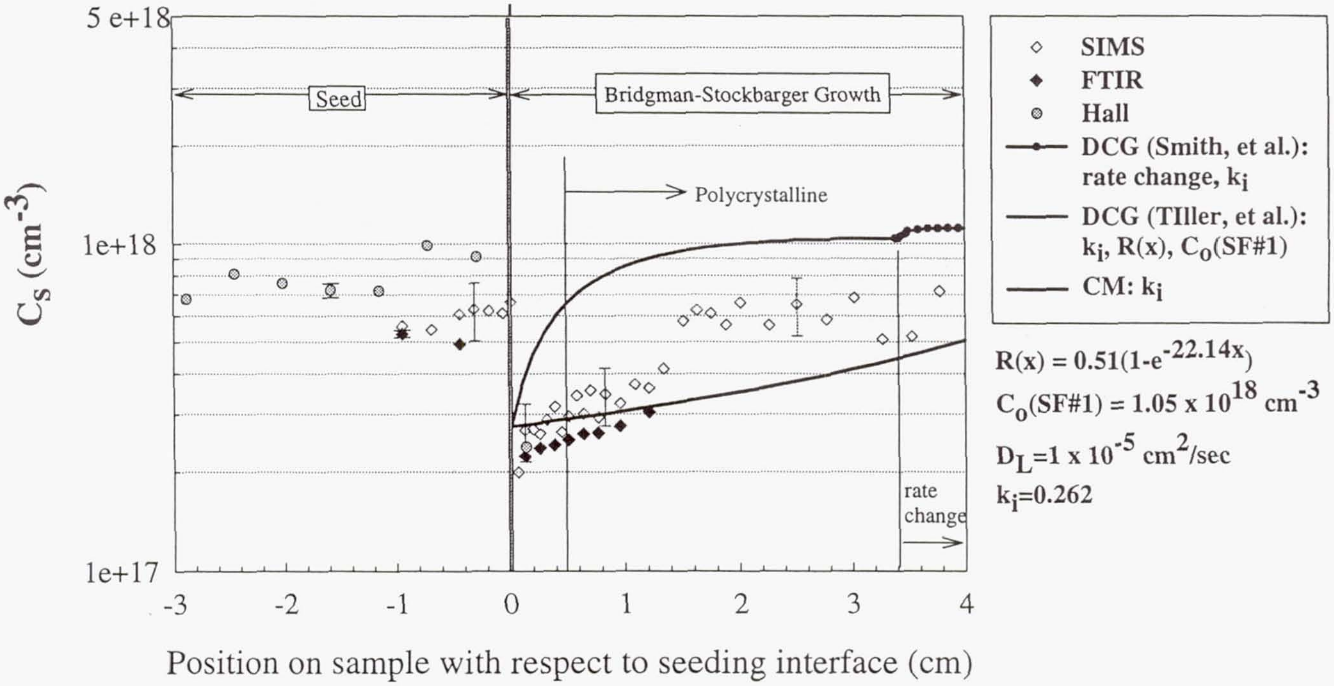

Fig. 4. Comparison of the experimentally measured selenium concentration distribution with complete mixing and diffusion controlled growth segregation behavior for flight sample #1.

High Resolution Triple Axis X-Ray Diffraction Analysis of II-VI Semiconductor Crystals

H.M. Volz[1] and R.J. Matyi[2]
[1]Materials Science Program
[2]Department of Materials Science & Engineering
University of Wisconsin
1509 University Avenue
Madison, WI 53706
Phone: (608) 263-1716
E-mail: matyi@engr.wisc.edu

The objective of this research program is to develop methods of structural analysis based on high resolution triple axis X-ray diffractometry (HRTXD) and to carry out detailed studies of defect distributions in crystals grown in both microgravity and ground-based environments.

HRTXD represents a modification of the widely used double axis X-ray rocking curve method for the characterization of grown-in defects in nearly perfect crystals. In a double axis rocking curve experiment, the sample is illuminated by a monochromatic X-ray beam and the diffracted intensity is recorded by a fixed, wide-open detector. The intensity diffracted by the sample is then monitored as the sample is rotated through the Bragg reflection condition. The breadth of the peak, which is often reported as the full angular width at half the maximum intensity (FWHM), is used an indicator of the amount of defects in the sample.

In HRTXD, both the incident and the diffracted X-ray beams are conditioned by highly perfect (and typically multiple reflection) X-ray optics to reduce the angular and spectral divergences in both beams. The importance of this arrangement can be appreciated by considering the effect of structural defects on the diffraction process. Compositional variations and/or strains in the crystal lattice will locally change the lattice parameter and will be manifested in variations from the exact Bragg condition in a direction perpendicular to the lattice planes. In contrast, the presence of a mosaic spread in the sample or local angular distortions in the diffracting planes will alter the angular position at which a misoriented region of a crystal diffracts. This effect will be manifested as redistribution of the diffracted intensity in a direction that is parallel to the reflecting planes. By conditioning the incident and diffracted X-ray beams in both angle and wavelength in a HRTXD experiment, the strong, perfect-crystal contribution to the Bragg reflection peak can be discriminated from the weaker, off-peak scatter generated by structural defects. This allows the scattering from defects to be measured directly. HRTXD also has the advantage that it can be applied to crystals with very high defect densities, unlike other methods such as transmission electron microscopy and X-ray topography.

The resulting HRTXD data are commonly plotted as equal-intensity contours as a function of parallel and perpendicular deviations from the exact Bragg condition. These so-called "reciprocal space maps" permit an assessment of the nature and density of the structural defects in the diffracting crystal to be determined either by visual examination or more quantitatively by modeling from diffraction theory. This approach is highly relevant to microgravity research because it aids in the development of our understanding of the effects of microgravity on crystal growth and the incorporation of defects.

In the present work we have analyzed the defect structures in crystals of ZnSe, $Hg_{1-x}Cd_xTe$, and $Hg_{1-x}Zn_xSe$ that were grown at the Marshall Space Flight Center. Our principal results may be summarized as follows:

ZnSe:

We have performed detailed analyses of four ZnSe crystals (ZnSe-32, -34, -37, and -43) that were grown by physical vapor transport (PVT) at the Marshall Space Flight Center by Dr. Ching-Hua Su. In general, PVT ZnSe crystals showed moderate to extensive diffuse scatter off the main Bragg peak, indicating the presence of grown-in defects. In virtually all cases the extent of the diffuse scatter was much greater than is usually observed in semiconductors such as GaAs or CdTe, suggesting that the grown-in defect density in ZnSe is greater than that seen in these more established materials.

ZnSe-34H: Figure 1 illustrates a high resolution triple axis reciprocal space map recorded from a (220) growth facet on this crystal. This particular reciprocal space map is typical of ZnSe crystals and shows many of the features seen in other crystals. The data are plotted as contours of constant values of the logarithm of the diffracted intensity. The minimum contour level, located furthest from the exact Bragg condition ($q_x=q_z=0$), is one (or 10^0) counts per second. The data are plotted in steps of $10^{0.25}$ (*i.e.* four contours per decade of intensity). The most notable feature in the plot is the extensive diffuse scatter that radiates away from the exact Bragg condition; this diffuse intensity arises from the long-range strain fields due to defects (primarily dislocations) in the crystal. In addition, a "surface streak" perpendicular to the (220) diffracting planes is also present, which is consistent both with relatively good structural perfection and a smooth surface.

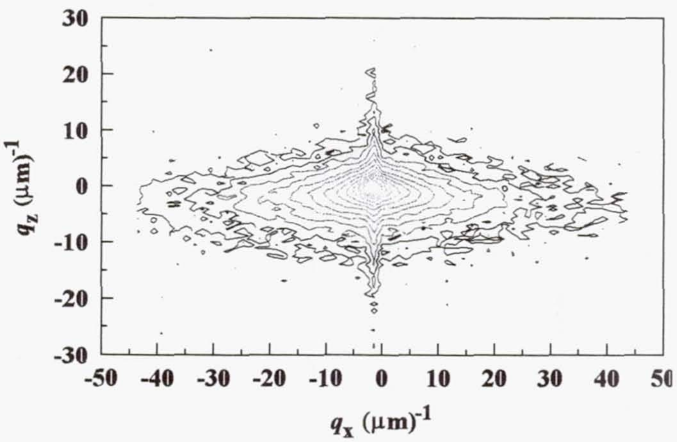

Figure 1. 220 reciprocal space map from ZnSe-34.

ZnSe-32V: A cleaved (220) wafer from crystal ZnSe-32V was examined at different locations to observe spatial variations in the defect structure. Figure 2a (next page) shows the reciprocal space map recorded when the incident X-ray beam illuminated the center of the ~10mm diameter wafer. The data suggest that the center of this particular sample possesses a surprisingly high level of structural perfection; both the intense and well-defined surface streak, combined with a low level of off-peak diffuse scatter, suggests a defect density that is comparable to high quality CdTe or moderate quality GaAs. However, when the X-ray beam was translated 5mm to the wafer periphery, the reciprocal space map shown in Figure 2b was obtained. These data show multiple diffracting regions of low structural perfection, in which the angular range of the scan

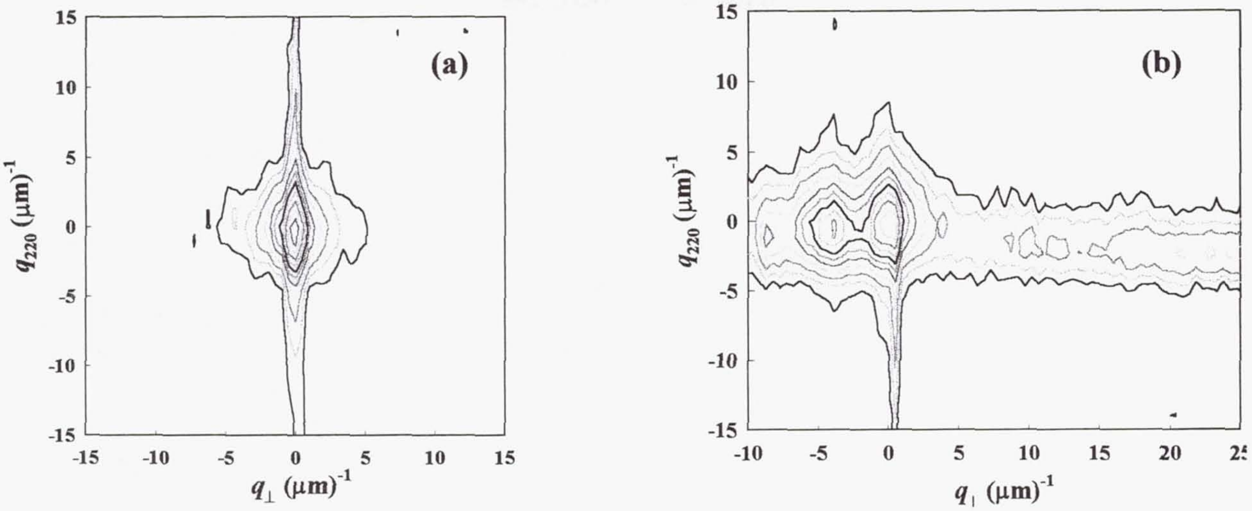

Figure 2. 220 reciprocal space maps from ZnSe-32V. (a) wafer center (b) wafer edge.

(about 0.5°) is consistent with large localized misorientations in the crystal. This interpretation is supported by synchrotron X-ray topographs recorded from this same sample by Prof. M. Dudley at SUNY -Stony Brook[1].

ZnSe-32H: Similar to ZnSe-32V, reciprocal space maps were recorded from different locations on a chemical -mechanical polished (111) wafer prepared from ZnSe-32H. In this case, the different positions were chosen to investigate the possible effect of the gravity vector on the resultant grown-in defect structure. Figures 3a and 3b show (111) reciprocal space maps that were recorded 3mm apart on the crystal surface, corresponding to data from opposite ends of the gravity vector (shown pointing towards the bottom of the page). A quantitative difference in the magnitude of the diffuse scatter from defects is evident, with the ZnSe at the bottom of the gravity vector clearly containing more of this scatter than the crystal at the top of the vector. Unfortunately, the structural perfection of the crystal is rather poor, and it is not possible to determine if the observed scattering is due to intrinsic (grown-in) defects, or if it arose from surface damage caused by the chemical-mechanical polishing process. Further work is needed to more fully resolve this issue.

ZnSe-43H: This single crystal boule had a sufficiently large growth facet to permit *x-y* spatial mapping with both double axis rocking curves and

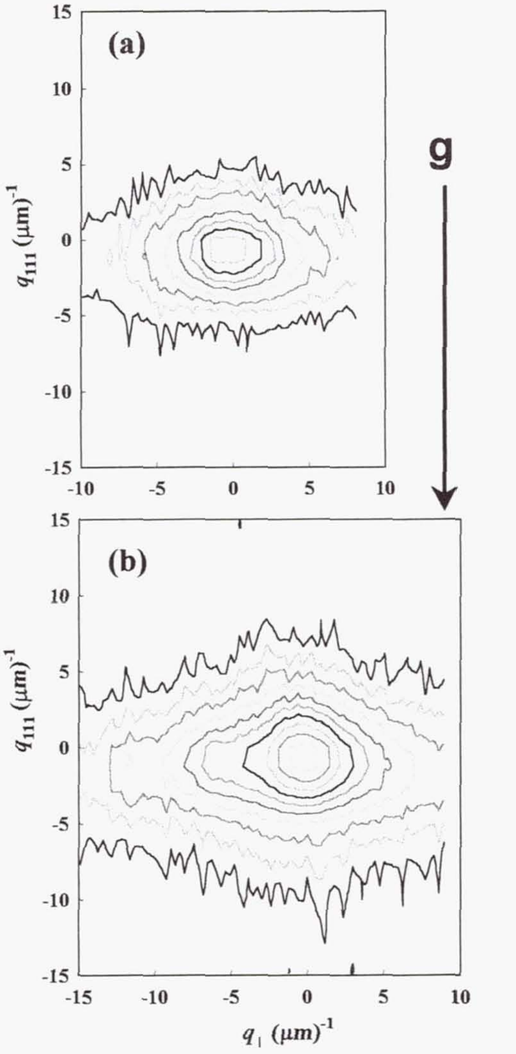

Figure 3. Reciprocal space maps from ZnSe-37. (a) top **g**; (b) bottom **g**.

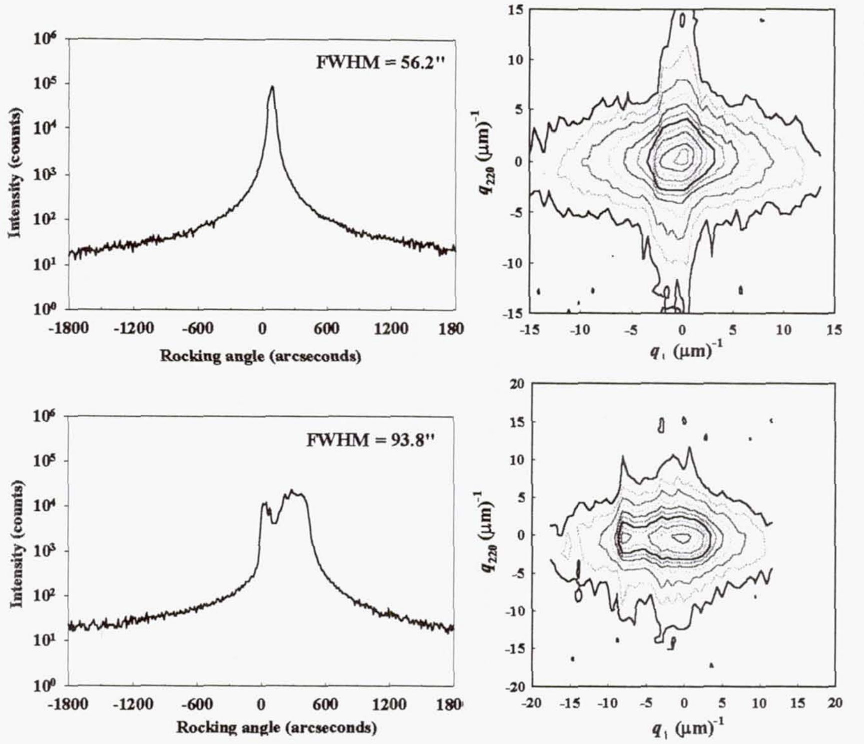

Figure 4. Rocking curves and triple axis reciprocal space maps from ZnSe-43H (see text below for details).

triple axis reciprocal space maps. Figure 4 illustrates data that were recorded at opposite ends of the (220) facet. The top pair (rocking curve and map) were recorded from a position near one edge of the facet; the bottom pair were recorded from the opposite side, about 10mm away. Synchrotron X-ray topographs recorded by M. Dudley[1] showed that the top pair were taken near an inclusion in the crystal, while the bottom pair came from a twinned region. Significant variations between the two regions are obvious. The strain field from an inclusion will broaden the reflection range (thus enlarging the rocking curve FWHM) and will generate off-peak diffuse scatter, but it should not grossly degrade the long-range structural order of the crystal. As a result, dynamical diffraction can occur as is seen in the reciprocal space map. In contrast, the presence of twinned regions and twin boundaries can significantly alter the local diffraction characteristics as slight misorientations between the twins, causing them to diffract kinematically. This is precisely what is observed in the reciprocal space map, and it explains the splitting observed in the rocking curve.

$Hg_{1-x}Cd_xTe$:

The above analysis illustrates the synergy that exists when high resolution triple axis X-ray diffraction studies are combined with X-ray topography of the same material. A recent analysis

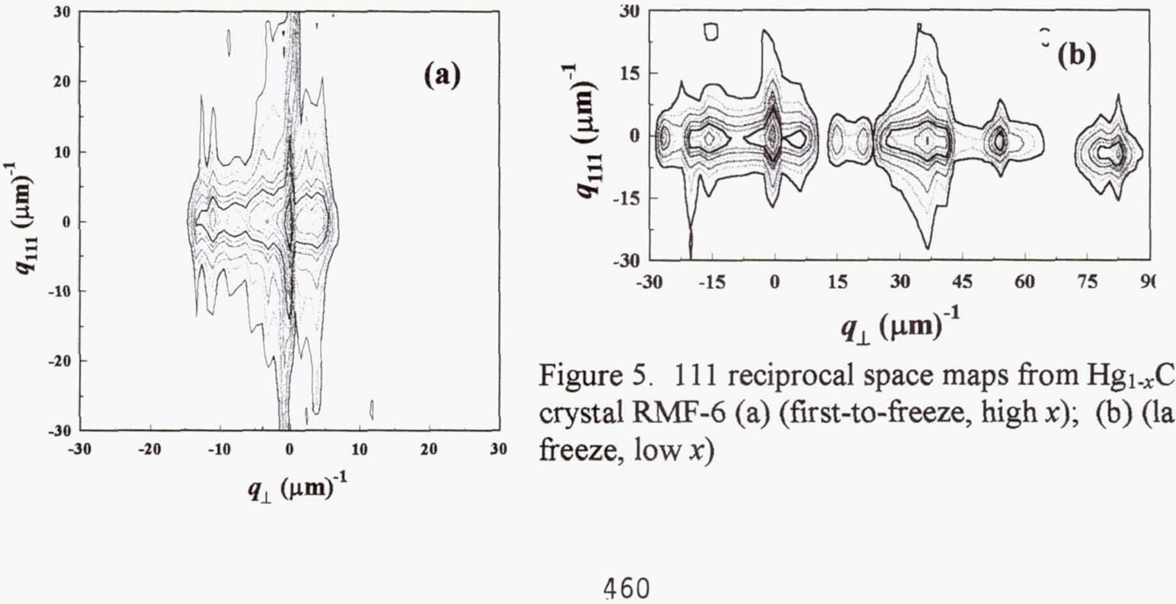

Figure 5. 111 reciprocal space maps from $Hg_{1-x}Cd_xTe$ crystal RMF-6 (a) (first-to-freeze, high x); (b) (last-to-freeze, low x)

of an $Hg_{1-x}Cd_xTe$ crystal grown at MSFC by Dr. D. Gillies by the traveling heater method from a tellurium zone further illustrates this fact. Figure 5a shows the reciprocal space maps that were recorded from the first-to-freeze (high x, low % Hg) and last-to freeze (low x, high % Hg) ends of the THM crystal. In the first-to-freeze material, the mosaic blocks are large enough to diffract dynamically, as illustrated by multiple surface streaks. This is not the case in the last-to-freeze material, Figure 5b. The mosaic spread is extremely large (note scale), with discrete mosaic blocks that approach polycrystallinity. Within each block, little evidence of a surface streak can be observed, suggesting a low degree of structural perfection. These results were confirmed by data collected from topographs recorded from adjacent samples[1].

One of the principal goals of this investigation was to see if the application of a magnetic field could reduce the density of grown-in defects. Figure 6 illustrates (111) reciprocal space maps from similar first-to-freeze and last-to-freeze sections of a $Hg_{1-x}Cd_xTe$ crystal grown with magnetic assistance. A casual examination of the reciprocal space maps reveals a significant reduction in the defect density of the crystal; in fact, the first-to-freeze region looks quite similar to what one would expect to see from nominally high quality CdTe. Although the defect density of the last-to-freeze sample was inferior to the first-to-freeze material, comparison with Figure 5b indicates that the application of the magnetic field during growth lowered the defect density in the last-to-freeze material by many orders of magnitude. All of these conclusions agree fully with those made from topographic analyses.

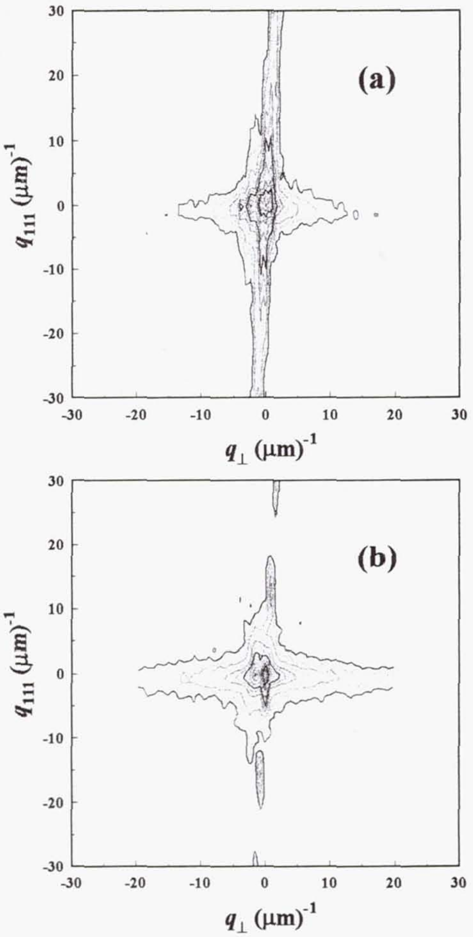

Figure 6. 111 reciprocal space maps from $Hg_{1-x}Cd_xTe$ crystal RMF-7 (a) (first-to-freeze, high x); (b) (last-to-freeze, low x)

<u>$Hg_{1-x}Zn_xSe$</u>:

Finally, a high resolution X-ray diffraction analysis has been performed on a $Hg_{1-x}Zn_xSe$ ($x \approx 0.1$) crystal grown by the Bridgman method by Dr. Su at MSFC. The (111) double axis rocking curve shown in Figure 7 exhibits multiple peaks, thus indicating a highly mosaic structure. However, it is not possible to infer much additional information from this one curve. In contrast, the triple axis reciprocal space map of the (111) reflection conveys much more. The breadth of the mosaic spread and the overall level of structural imperfection is clearly seen in the triple axis data. Somewhat surprisingly, etch pit density measurements of the defect density of this crystal returned estimates that ranged from 1×10^5 cm^{-2} to 9×10^3 cm^{-2}. These values seem extremely low given the appearance of the reciprocal space map. Possible reasons for this discrepancy are currently under investigation.

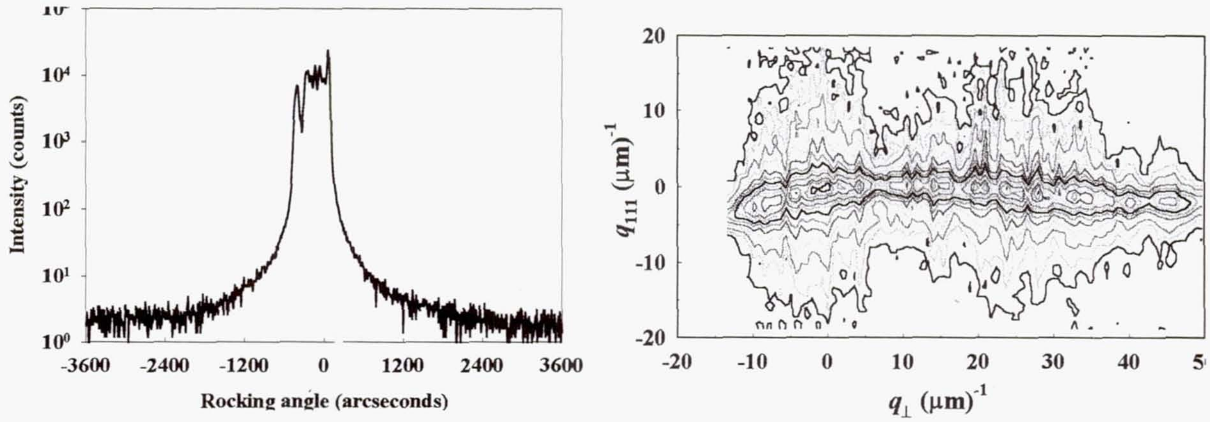

Figure 7. (111) double axis rocking curve (left) and triple axis reciprocal space map (right) from $Hg_{1-x}Zn_xSe$.

The reciprocal space map from the $Hg_{1-x}Zn_xSe$ also shows a systematic change in lattice parameter (presumably due to changes in the mercury content) as a function of angular deviation from the mean Bragg position. A calculation based on the maximum and minimum values of q_{111} in Figure 7 reveals that a 2% variation in Hg-content across the irradiated volume could account for the observed behavior. However, the reciprocal space map also suggests a possible correlation between defect structure and chemical composition of the crystal. Work is in progress to more fully understand this observation.

In conclusion, this work has shown that high resolution triple axis X-ray diffraction is an effective tool for characterizing the defect structure in semiconductor crystals, particularly at high defect densities. Additionally, the technique is complimentary to X-ray topography for defect characterization in crystals.

Acknowledgements:

The authors acknowledge Dr. S.Cobb, Dr. D. Gillies, Dr. S. Feth, and Dr. C-H. Su of the Marshall Space Flight Center for supplying the materials used in this study and for useful discussions. They also acknowledge Prof. M. Dudley (SUNY- Stony Brook) for the synchrotron X-ray topography. This work was supported by NASA under contract NCC8-48 and USRA under contract 3537-08.

References:

1. See M. Dudley and R.J. Matyi, "Combined Synchrotron White Beam X-Ray Topography and High Resolution Triple Axis X-Ray Diffraction Characterization and Analysis of Crystals Grown in Microgravity and Ground-Based Environments," in these proceedings.

Experimental Studies of the Interaction Between a Parallel Shear Flow and a Directionally-Solidifying Front

Meng Zhang
Tony Maxworthy
Department of Aerospace Engineering
University of Southern California
Los Angeles, CA 90089
Email: mengzhan@spock.usc.edu, maxworth@mizar.usc.edu

NASA Grant #: NAG3-1619

Introduction

It has long been recognized that flow in the melt can have a profound influence on the dynamics of a solidifying interface and hence the quality of the solid material[1]. In particular, flow affects the heat and mass transfer, and causes spatial and temporal variations in the flow and melt composition. This results in a crystal with nonuniform physical properties. Flow can be generated by buoyancy, expansion or contraction upon phase change, and thermo-soluto capillary effects. In general, these flows can not be avoided and can have an adverse effect on the stability of the crystal structures. This motivates crystal growth experiments in a microgravity environment, where buoyancy-driven convection is significantly suppressed. However, transient accelerations (g-jitter) caused by the acceleration of the spacecraft can affect the melt, while convection generated from the effects other than buoyancy remain important.

Rather than bemoan the presence of convection as a source of interfacial instability, Hurle in the 1960s suggested that flow in the melt, either forced or natural convection, might be used to stabilize the interface. Delves[2] considered the imposition of both a parabolic velocity profile and a Blasius boundary layer flow over the interface. He concluded that fast stirring could stabilize the interface to perturbations whose wave vector is in the direction of the fluid velocity. Forth and Wheeler[3,4] considered the effect of the asymptotic suction boundary layer profile. They showed that the effect of the shear flow was to generate travelling waves parallel to the flow with a speed proportional to the Reynolds number. There have been few quantitative, experimental works reporting on the coupling effect of fluid flow and morphological instabilities. Huang[5] studied plane Couette flow over cells and dendrites. It was found that this flow could greatly enhance the planar stability and even induce the cell-planar transition. A rotating impeller was buried inside the sample cell, driven by an outside rotating magnet, in order to generate the flow. However, it appears that this was not a well-controlled flow and may also have been unsteady.

Experimental Method

Numerous experiments have been done by other researchers to conduct morphological studies with transparent organic compound growing in a Hele-Shaw cell. The Hele-Shaw cell was used to provide a 2D solidification chamber which made in-situ observations and measurements possible. Furthermore, buoyancy-driven convection is greatly suppressed in a horizontal Hele-Shaw cell so that a microgravity environment can be simulated.

In the present experimental study, we want to study how a forced parallel shear flow in a Hele-Shaw cell interacts with the directionally solidifying crystal interface. The Hele-Shaw cell (figure 1) consists of two parallel quartz glass plates separated by a thin gap (500 μm). Each plate is ground to less than 1/4 wavelength per inch optical flatness. The bottom plate is covered with an aluminium reflective coating, which serves as a front-surface mirror. The top plate has two groups of holes through which liquid alloy can be added or removed. A parallel shear flow is formed by adding liquid into the cell through the holes on one side and removing it through the holes on the other side. The direction of the flow can be reversed by interchanging the inlet and outlet holes. The temperature distribution inside the cell is detected by an embedded Iron-Constantan thermocouple with an accuracy of 0.1°C. The thermocouple is placed next to the incoming flow.

The configuration diagram of the experimental setup is shown in figure 2. It is based on a horizontal Bridgeman furnace. Temperatures of the heater/cooler pair are controlled separately by two water circulators which have temperature stability of up to 0.01°C. A linear temperature profile is set up in the conduction stage. The Hele-Shaw cell, sitting on top of the conduction stage, is driven by a closed-loop micro-actuator to travel back and forth in the direction with the largest temperature gradient. A LEITZ interference microscope is used to observe the microstructure of the S/L interface and to measure the solute concentration field. A flow control system is used to regulate the strength and direction of the flow. This flow system is sealed in a polycarbon box and is maintained at a temperature above the melting point. All the aforementioned parts except the microscope are mounted on a pair of 3D micro-translation stages so that any part of the specimen can be focused.

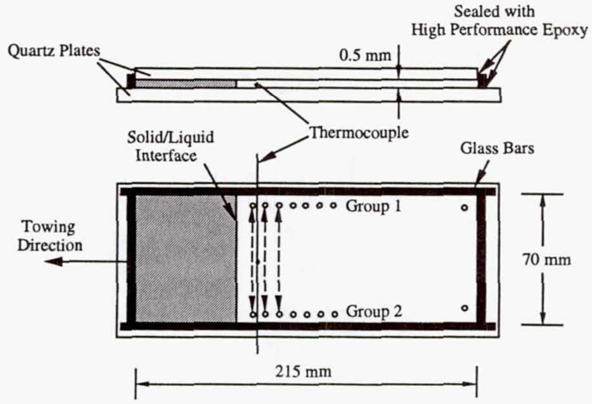

Figure 1 Hele-Shaw cell

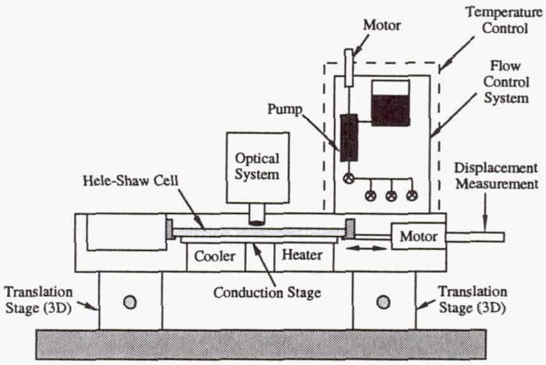

Figure 2 Diagram of the experimental setup

The transparent organic alloy SCN-1.0 Wt% acetone was used as the specimen material because: 1) it has been commonly used in past directional solidification experiment, and 2) its thermophysical properties have been well measured. A set of no-flow experiment were conducted first, during which the Hele-Shaw cell was pulled toward the cold side at some constant speeds (ranged from 3 μm/s to 10 μm/s). The interface evolution and the temperature variation served as a standard for the experiments with flow to compare with. In the second set of experiments, all the experimental condition are the same except the parallel shear flow was started when the planar interface just became unstable (called early applied flow in what follows). Since different pulling speeds will result in different time to instability and different growth rates, the flow was turned on at different times in each experiment. However, the initial cell amplitudes were < 10 μm for all the experiments with early-applied flow. In the third set of experiments, the cellular interface was developed when flow was started (called late applied flow in what follows). The flow temperature was adjusted so that no heat source or sink effect was brought in by the flow. The experiment process was observed in-situ under the interference microscope.

Results and Discussion

Figure 3.a shows the interface morphology changes in a no-flow experiment. The frame code, representing a framing rate of 1/30 second, was started when the Hele-Shaw cell began to move. Since the morphological number M (~130) is much higher than the critical value M_c (1.07) in this case, the S/L interface changed from a planar to a cellular to a dendritic structure. During the entire process, most cells grew in the normal direction to the initial planar interface. For the experiment with early-applied flow shown at figure 3.b, small perturbation existed when the flow was imposed at frame 14865. The flow direction is from top to bottom and flow speed is 15 times higher than the Hele-Shaw cell towing speed. After the flow was imposed, the existing perturbation continued to grow for a short period of time (frame 16068) and then decayed. Eventually the interface returned to a planar state. For the experiment with late-applied flow shown at figure 3.c, the cellular interface was developed when the flow was started at frame 16230. The flow has the same direction and the same strength as the previous one. Unlike the decay observed in figure 3.b, cellular structures started tilting toward the upstream direction. Later secondary dendrites appeared on the downstream side of the leading crystals while the trailing crystals were suppressed. Similar results were obtained when the experiment were repeated at various towing speeds and reversed flow direction.

To further study the parallel shear flow effect quantitatively, the amplitude and the wavelength of the cellular interface were measured at different times during growth for each experimental run. For the experiment with early-applied flow, the planar interface became unstable around a time of 465 second (figure 4.a), after this the perturbation amplitude (A) increased with time (t). Shortly after the flow was imposed at 498 second, the amplitude dropped to zero. The amplitude was 3.8 μm when the flow was turned on. The effect of flow on wavelength (λ) is not as prominent as the effect on amplitude. Figure 4.b shows that the wavelength is nearly invariant before and after the flow. For the case of late-flow experiment as shown in figure 3.c, it is difficult to quantify the

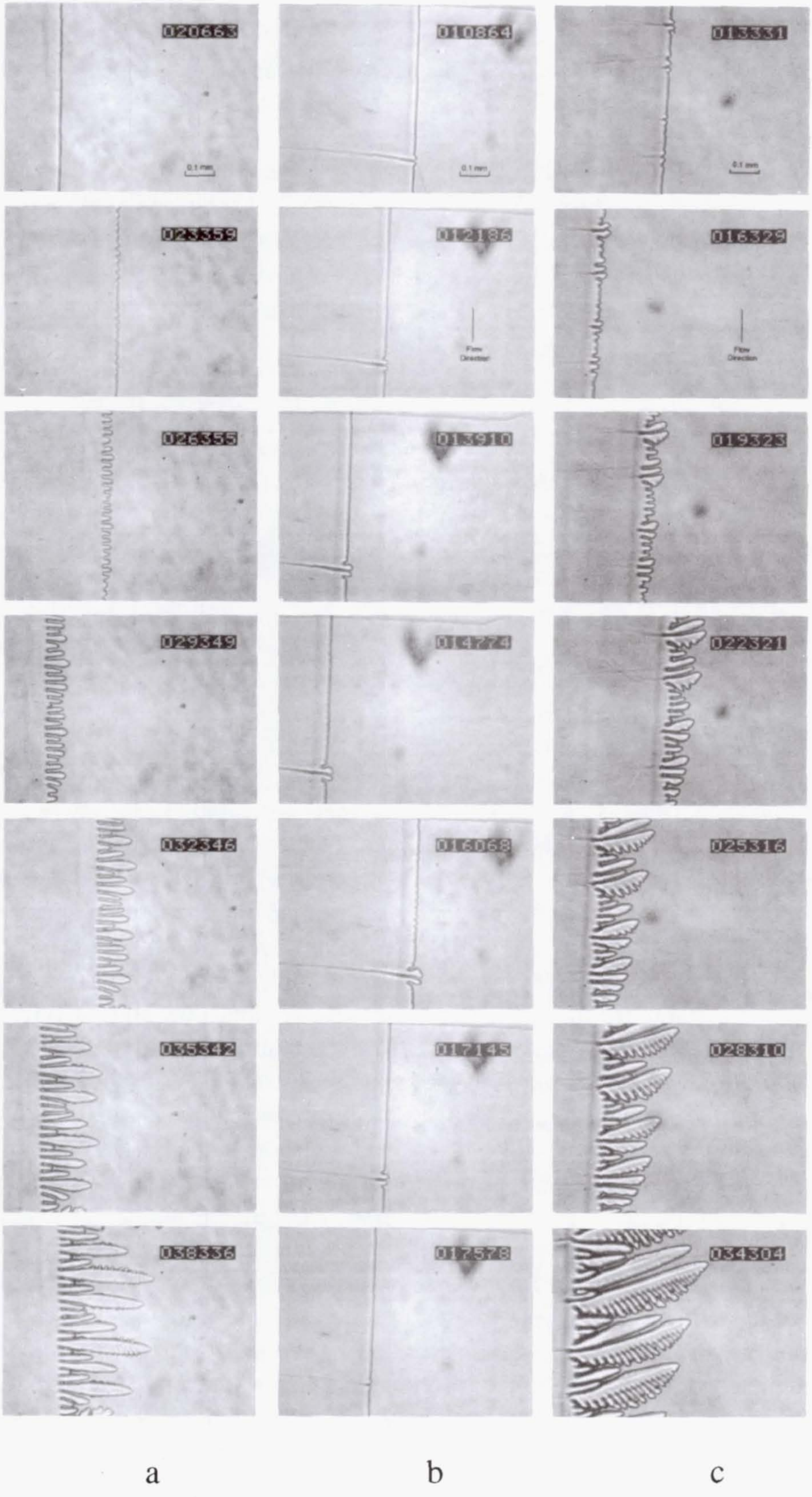

Figure 3 Effect of parallel shear flow on directional solidification interface
a. no flow; b. with early-applied flow; c. with late-applied flow
(towing speed = 4.5 μm/s, flow speed = 80 μm/s, G_T = 7.0 °C/cm)

difference in the A-t plot (figure 4.c) before and after the flow was induced. But the difference is noticeable in log(A)-t plot (figure 4.d). The exponential growth rate (slope of log(A)-t curve) is slightly reduced after the initiation of the flow. However, whether this growth rate reduction is solely from the stabilizing effect of parallel flow or not is still an open question, because the nonlinearity could play a role in slowing down the growth (for the supercritical bifurcation) as the amplitude becomes larger and larger. Again the wavelength of the cellular interface is insensitive to the imposed parallel flow.

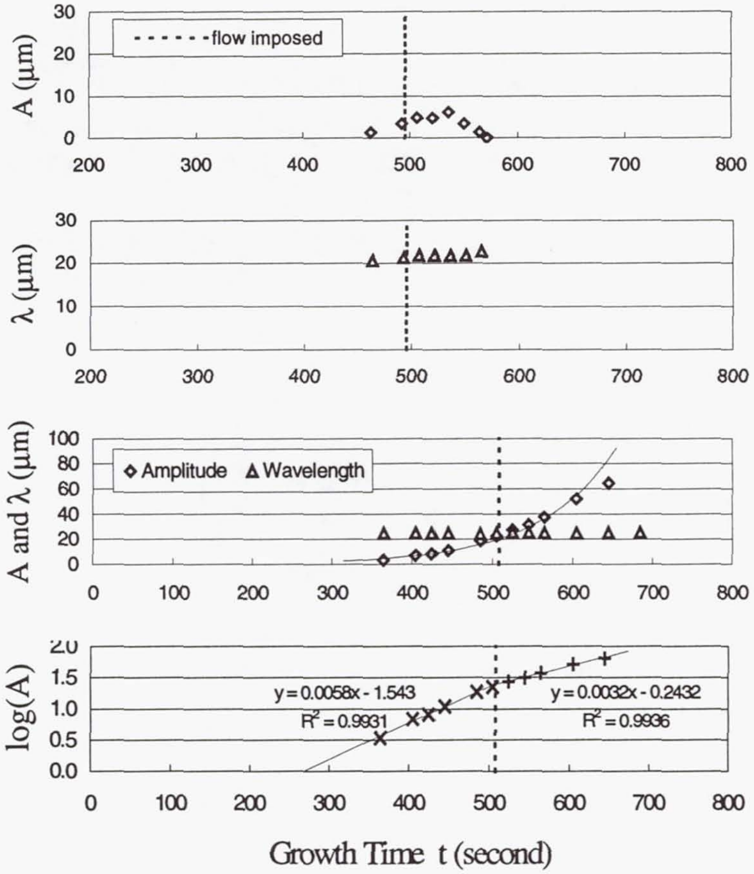

Figure 4 Effect of parallel shear flow on growth rate and wavelength
(a,b,c,d, from top to bottom)

The physical mechanism explaining these observations is a version of that discussed by Dantzig and Chao[6] using a parallel shear flow model. Since the forced parallel flow does not affect the thermal transport, it influences the interface morphology by altering the solute transport. When the parallel shear flow is applied at an interface with small amplitudes (< 10 μm in the experiment), the flow field is minimally altered by the shallow cells and is still locally parallel to the interface. This local parallel flow dramatically enhances the lateral solute transport. Therefore the parallel flow when applied early stabilizes the interface by smoothing out the lateral solute inhomogeneity at the interface. However, when the parallel shear flow is applied at the deep cellular interface, the flow field is distorted by the periodic curved interface and is no longer locally parallel to it. Flow has a stronger compressing effect on the upstream side of cells than the downstream side, which leads to an asymmetry in the concentration field with a thinner solutal boundary layer and greater concentration gradient G_c at the upstream side. Since G_c has a destabilizing effect on the interface, the upstream side of cell has a higher normal growth rate than the downstream side and as a result the cell tilts toward the incoming flow direction. It is proposed that it is the coupling effect between the interfacial morphology and the imposed parallel shear flow that leads to different crystal structures.

The interference pattern around a single crystal obtained in preliminary experiments is shown in figure 5. The originally paralleled interference fringes are distorted by the enrichment of the solute concentration as well as by the temperature gradient. This demonstrated the potential to make dynamic measurement of the solute field using an interference microscope. However, extra efforts are needed to properly resolve the interface in the interferogram.

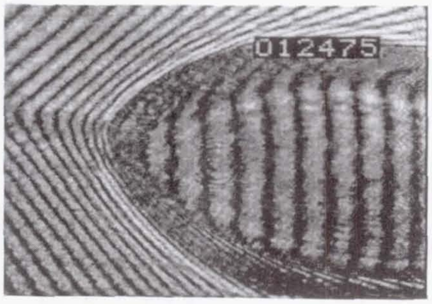

Figure 5 Interference pattern around a single crystal

Conclusion

The comparison of experimental data show that the parallel shear flow in a Hele-Shaw cell has a strong stabilizing effect on the planar interface by damping the existing initial perturbations. The flow also shows a stabilizing effect on the cellular interface by slightly reducing the exponential growth rate of cells. The left-right symmetry of cells is broken by the flow with cells tilting toward the incoming flow direction. The tilting angle increases with the velocity ratio. The experimental results are explained through the parallel flow effect on lateral solute transport. The phenomenon of cells tilting against the flow is consistent with the numerical result of Dantzig and Chao[6].

References

1. S. H. Davis, Handbook of Crystal Growth, 1B:861-897, 1993
2. R. T. Delves, J. Crystal Growth, 8:13-25, 1971
3. S. A. Forth and A. A. Wheeler, J. Fluid Mech., 202:339-366, 1989
4. S. A. Forth and A. A. Wheeler, J. Fluid Mech., 236:61-94, 1992
5. T. Huang, et al., J. Crystal Growth, 128:167-172, 1993
6. J. A. Dantzig and L. S. Chao, Proc. Instal. Symp. on Solidification Proc., 12-26,1990

A PHASE-FIELD/FLUID MOTION MODEL OF SOLIDIFICATION: INVESTIGATION OF FLOW EFFECTS DURING DIRECTIONAL SOLIDIFICATION AND DENDRITIC GROWTH

D.M. Anderson
Department of Mathematics
University of North Carolina
Chapel Hill, NC 27599, USA
(919) 962-2442

W.J. Boettinger
Metallurgy Division
NIST
Gaithersburg, MD 20899, USA
(301) 975-6160

G.B. McFadden
Math. and Comp. Sci. Div.
NIST
Gaithersburg, MD 20899, USA
(301) 975-2711

A.A. Wheeler
School of Mathematics
University of Southampton
Highfield, Southampton, SO17 1BJ, UK
44-1703-595143

Introduction

The phase-field model of solidification is extended to include the effects of fluid flow in the melt. The phase-field model is based on coupling the equations for heat flow in the liquid and solid phases with an auxiliary equation that describes the evolution of the phase-field variable, which is a non-conserved order parameter indicating the local phase, solid or liquid, at each point of the material. The solid-liquid interface is then represented by a diffuse transition layer in which the phase-field variable changes rapidly between its values in the bulk phases. The model is extended to include fluid flow by a further coupling to the Navier-Stokes equations. Preliminary studies have been performed for a model in which the solid phase is treated as a liquid of high viscosity compared to the liquid phase. The main coupling in the Navier-Stokes equations is then through an additional term in the stress tensor that depends on the gradients of the phase-field variable, representing the effects of capillary forces within the diffuse interface.

Fluid motion in the context of diffuse interface models has been treated previously[1,2] for two-fluid systems in which the flow equations are coupled to a conserved order parameter that satisfies a convective form of the Cahn-Hilliard equation, as in the Model H of Hohenberg and Halperin[3]. In this case, the capillary forces within the diffuse interface are known as the Korteweg stress[4]. Similar terms also arise in models in which the mass density is used as the conserved order parameter[5,6]; in that case the coupling is through the continuity equation rather than a Cahn-Hilliard equation. In our work, we consider coupling through the non-conserved phase-field variable in order to make contact with previous diffuse interface treatments of the solidification of a pure material, in which neither the density nor a concentration variable are appropriate order parameters. This allows us to model systems with either constant or variable density in a single component system. In addition, the phase-field variable can be used to incorporate the effects of anisotropic surface tension in the model using the appropriate generalization[7] of the Cahn-Hoffman ξ-vector[8], even if the solid is approximated by a highly viscous liquid. Related models have been derived using the formalism of two-phase flows[9], in which the phase-field variable plays a role analogous to the solid-fraction.

An important area of application is the study of flow effects on microstructure during solidification. For example, many experimental investigations, both in terrestrial and microgravity environments, have studied the selection of tip radius and velocity during dendritic growth. Previous theoretical studies of dendritic growth that include fluid motion in the liquid have been able to make predictions about how the growth rate of the tip is affected by the flow but have not, for example, been able to address the effects of fluid motion on the development of side branches. Phase-field models of solidification have been a useful tool in assessing the complicated morphologies associated with dendritic growth when diffusion (heat or solute) is the dominant growth mechanism but have not included the effects of fluid motion. This research therefore aims to provide a theoretical model which will allow the modeling and computation of complex interfacial structures in realistic growth configurations which will be able to assess the effect of flow on interfacial morphology in both a terrestrial and microgravity environment.

Our preliminary work has resulted in a derivation of the governing equations for coupled fluid flow and the phase-field evolution that is based on principles of irreversible thermodynamics. In the next section we describe the basic model, followed by a brief summary of the governing equations and entropy production term.

The Model

We consider a non-isothermal system consisting of a pure material that may exist in two distinct phases. We follow the standard phase-field methodology and introduce a phase-field variable, $\phi(\vec{x}, t)$, whose value indicates the phase of the system as a function of time, t, and position $\vec{x}$. Both phases are treated as fluids, although in the applications we will assume one phase has a much larger viscosity and interpret it as an approximation to a solid phase. In many solidification applications, a fluid model is used for the thermodynamic description of the solid phase, in that the elastic properties of the solid are ignored. We will also consider that the phase transition is first order, with an anisotropic surface energy, which would be unconventional for a fluid-fluid system, but is in keeping with our intention to model a solid-liquid system. We adopt the convention that $\phi = 0$ denotes the liquid phase and $\phi = 1$ denotes the solid phase. A solid-liquid interface is represented by a thin layer in which the phase field varies rapidly between zero and unity. The governing equations are derived by following the formalism of irreversible thermodynamics, as originally applied to the phase-field equations by Penrose & Fife et al.[10,11]. Derivations based on mechanical microforce balance laws, as developed by Gurtin et al.,[12] are also possible.

Governing Equations

We assume that the total entropy, $\mathcal{S}$, in a material volume, $\Omega(t)$, of the system is given by

$$\mathcal{S} = \int_{\Omega(t)} \left[\rho s - \frac{1}{2} \epsilon_S^2 \gamma^2 (\nabla \phi) \right] dV, \tag{1}$$

where ρ is the density and s is the entropy per unit mass. The first term in the integrand, ρs, is the classical entropy density (per unit volume) and the second is a nonclassical term associated with spatial gradients of the phase field. Here the gradient entropy coefficient ϵ_S is assumed to be a constant for simplicity, and γ is a homogeneous function of degree unity. The function γ allows for a general anisotropic surface energy of the solid-liquid interface[7]. An isotropic surface energy results from the choice $\gamma(\nabla\phi) = |\nabla\phi|$.

The total mass, $\mathcal{M}$, linear momentum, $\vec{\mathcal{P}}$, and internal energy, $\mathcal{E}$, associated with the material volume are assumed to have the form

$$\mathcal{M} = \int_{\Omega(t)} \rho \, dV, \tag{2}$$

$$\vec{\mathcal{P}} = \int_{\Omega(t)} \rho\vec{u} \, dV, \tag{3}$$

$$\mathcal{E} = \int_{\Omega(t)} \left[\rho e + \frac{1}{2}\rho|\vec{u}|^2 + \frac{1}{2}\epsilon_E^2\gamma^2(\nabla\phi)\right] dV, \tag{4}$$

respectively. Here, $\vec{u}$ is the velocity, e is the internal energy density (per unit mass) and the gradient energy coefficient ϵ_E is assumed to be constant. The thermodynamic relations

$$de = T\,ds + \frac{p}{\rho^2}\,d\rho + \frac{\partial e}{\partial\phi}\,d\phi, \tag{5}$$

$$e = Ts - p/\rho + \mu, \tag{6}$$

are assumed to apply locally, where p is the thermodynamic pressure and μ is the chemical potential.

The physical balance laws for mass, linear momentum, and internal energy are given by

$$\frac{d\mathcal{M}}{dt} = 0, \tag{7}$$

$$\frac{d\vec{\mathcal{P}}}{dt} = \int_{\delta\Omega(t)} \hat{n}\cdot\boldsymbol{m}\,dA, \tag{8}$$

$$\frac{d\mathcal{E}}{dt} + \int_{\delta\Omega(t)} \vec{q}_E\cdot\hat{n}\,dA = \int_{\delta\Omega(t)} \hat{n}\cdot\boldsymbol{m}\cdot\vec{u}\,dA, \tag{9}$$

respectively, where $\hat{n}$ is the outward unit normal to $\delta\Omega(t)$, $\boldsymbol{m}$ is the stress tensor, and $\vec{q}_E$ is the internal energy flux. The momentum balance (8) requires that rate of change of the total momentum of the material volume results from forces acting on its boundary $\delta\Omega(t)$ (note we neglect external body forces such as gravity). The energy balance (9) equates the rate of change of the total internal energy of $\Omega(t)$ plus the energy flux through its boundary to the rate of work of the forces at its boundary.

In addition, the entropy balance takes the form

$$\frac{dS}{dt} + \int_{\delta\Omega(t)} \vec{q}_S\cdot\hat{n}\,dA = \int_{\Omega(t)} \dot{s}^{prod}\,dV, \tag{10}$$

where $\vec{q}_S$ is the entropy flux and $\dot{s}^{prod}$ is the local rate of entropy production. The second law of thermodynamics is then expressed by the requirement that $\dot{s}^{prod}$ is positive.

To proceed we recast the conservation laws (7)–(10) as differential equations. These are used to express the local entropy production in terms of the fluxes $\boldsymbol{m}$, $\vec{q}_E$, and $\vec{q}_S$, as well $D\phi/Dt$. We then identify forms for these quantities which ensure that the local entropy production is positive. The fluxes that result from this procedure involve both classical contributions and non-classical contributions that depend on $\nabla\phi$. In addition, we obtain an evolution equation for the phase field.

The mass balance law (7) gives the continuity equation in its conventional form

$$\frac{D\rho}{Dt} + \rho\nabla\cdot\vec{u} = 0, \tag{11}$$

where the material derivative of ρ is denoted by $D\rho/Dt = \partial\rho/\partial t + (\vec{u}\cdot\nabla)\rho$. Similarly, the linear momentum equation takes the form

$$\rho\frac{D\vec{u}}{Dt} = \nabla\cdot\boldsymbol{m}, \tag{12}$$

where, if m_{jk} denote the components of $\boldsymbol{m}$, then $\nabla\cdot\boldsymbol{m}$ has components $\partial m_{jk}/\partial x_j = m_{jk,j}$. The energy equation is more complicated, and takes the form

$$\rho\frac{De}{Dt} + \nabla\cdot\vec{q}_E = \boldsymbol{m} : \nabla\vec{u} - \epsilon_E^2 Q_G. \tag{13}$$

where

$$Q_G = \nabla\cdot\left(\gamma\vec{\xi}\frac{D\phi}{Dt}\right) - \frac{D\phi}{Dt}\nabla\cdot\left(\gamma\vec{\xi}\right) - \gamma\nabla\vec{u} : \vec{\xi}\otimes\nabla\phi + \frac{1}{2}\gamma^2\nabla\cdot\vec{u}. \tag{14}$$

Here we have introduced the Cahn-Hoffman ξ-vector[8] for a diffuse interface[7]. If we set $\vec{p} = \nabla\phi$, it has components $\xi_j = \partial\gamma(\vec{p})/\partial p_j$; for an isotropic surface energy, this gives $\vec{\xi} = \nabla\phi/|\nabla\phi|$.

In an analogous way, the entropy balance (10) leads to the result

$$\rho\frac{Ds}{Dt} + \nabla\cdot\vec{q}_S = \dot{s}^{prod} + \epsilon_S^2 Q_G. \tag{15}$$

The continuity equation (11) and equations (5), (13) and (14) can be used to express the entropy production given by equation (15) as

$$\begin{aligned} \dot{s}^{prod} &= \frac{1}{T}\left\{\boldsymbol{m} + \epsilon_F^2\gamma\vec{\xi}\otimes\nabla\phi + \left[p - \frac{\epsilon_F^2}{2}\gamma^2\right]\boldsymbol{I}\right\} : \nabla\vec{u} + \frac{1}{T}\left\{\epsilon_F^2\nabla\cdot(\gamma\vec{\xi}) - \rho\frac{\partial e}{\partial\phi}\right\}\frac{D\phi}{Dt} \\ &\quad + \nabla\cdot\left(\vec{q}_S - \frac{\vec{q}_E}{T} - \frac{\epsilon_F^2}{T}\gamma\vec{\xi}\frac{D\phi}{Dt}\right) + \left(\vec{q}_E + \epsilon_E^2\gamma\vec{\xi}\frac{D\phi}{Dt}\right)\cdot\nabla\left(\frac{1}{T}\right), \end{aligned} \tag{16}$$

where $\epsilon_F^2 = \epsilon_E^2 + T\epsilon_S^2$.

We now make the following choices for the fluxes and $D\phi/Dt$ which ensure that $\dot{s}^{prod}$ is positive

$$
\begin{aligned}
\boldsymbol{m} &= \left[-p + \frac{\epsilon_F^2}{2}\gamma^2\right]\boldsymbol{I} - \epsilon_F^2\gamma\vec{\xi}\otimes\nabla\phi + \boldsymbol{\tau}, && (17)\\
M\frac{D\phi}{Dt} &= \epsilon_F^2\nabla\cdot(\gamma\vec{\xi}) - \rho\frac{\partial e}{\partial\phi}, && (18)\\
\vec{q}_E &= \tilde{k}\nabla\left(\frac{1}{T}\right) - \epsilon_E^2\gamma\vec{\xi}\frac{D\phi}{Dt}, && (19)\\
\vec{q}_S &= \frac{\tilde{k}}{T}\nabla\left(\frac{1}{T}\right) + \epsilon_S^2\gamma\vec{\xi}\frac{D\phi}{Dt}. && (20)
\end{aligned}
$$

Here $\boldsymbol{\tau}$ is the viscous stress tensor, which for a Newtonian fluid is given by $\mu(\nabla\vec{u} + \nabla\vec{u}^T) + \lambda(\nabla\cdot\vec{u})\boldsymbol{I}$, where μ and λ are coefficients of viscosity, $\boldsymbol{I}$ is the unit tensor, and M is a positive mobility coefficient which we take to be constant.

A constant value for the thermal conductivity k corresponds to the choice $\tilde{k} = T^2 k$. The resulting equations of motion assume the form

$$
\begin{aligned}
\frac{D\rho}{Dt} &= -\rho\nabla\cdot\vec{u}, && (21)\\
\rho\frac{D\vec{u}}{Dt} &= \nabla\cdot\boldsymbol{m}, && (22)\\
M\frac{D\phi}{Dt} &= \epsilon_F^2\nabla\cdot(\gamma\vec{\xi}) - \rho\frac{\partial e}{\partial\phi}, && (23)\\
\rho\frac{De}{Dt} &= \nabla\cdot[k\nabla T] + \epsilon_E^2\nabla\cdot(\gamma\vec{\xi})\frac{D\phi}{Dt} \\
&\quad + \left[\left(-p + \frac{1}{2}T\epsilon_S^2\gamma^2\right)\boldsymbol{I} - T\epsilon_S^2\gamma\vec{\xi}\otimes\nabla\phi + \boldsymbol{\tau}\right] : \nabla\vec{u}. && (24)
\end{aligned}
$$

The above governing equations, together with the expressions (17)–(20), are our main result. The momentum equation (22), with $\boldsymbol{m}$ given by Eqn. (17), contains a generalized version of the non-classical Korteweg stress term that provides an anisotropic solid-liquid surface tension. The energy equation also contains non-classical contributions that are proportional to ϵ_E^2 and ϵ_S^2.

These equations require that a thermodynamic potential be specified. Since we intend to apply this model to situations in which the density in each phase may be uniform, we adopt a thermodynamic formulation similar to the quasi-incompressible model of Lowengrub and Truskinovsky[13] and work with a Gibb's free energy per unit mass $g(T, p, \phi)$. This framework allows the density $\rho = \rho(\phi)$ to be specified in a way that is consistent with the underlying thermodynamics.

Conclusions

The principal objective of this research is to develop an anisotropic phase-field model for the solidification of a single-component material which incorporates flow in the melt. We will apply this model to solidification and crystal growth situations in order to investigate the effect of fluid motion in the melt on the growth characteristics as well as the microstructure formed in the solid. In particular, we will study hydrodynamic effects during directional solidification, coarsening, and dendritic growth, where complicated interface morphologies and flows may be present. Finally we will extend the model to solidification of a binary alloy with fluid flow in the melt.

References

[1] D. Jacqmin, An energy approach to the continuum surface tension method, Pro. 34th Aerosp. Sci. Meet. Exh. AIAA 96-0858, Reno: Am. Inst. Aeron. Astron. (1996).

[2] D. Jasnow and J. Viñals, Coarse-grained description of thermocapillary flow, Phys. Fluids 8 (1996) 660-669.

[3] P.C. Hohenberg and B.I. Halperin, Theory of dynamic critical phenomena, Rev. Mod. Phys. 49 (1977) 435–479.

[4] D.M. Anderson, G.B. McFadden, and A.A. Wheeler, Diffuse-interface methods in fluid mechanics, Ann. Rev. Fluid Mech. 30 (1998) 139-165.

[5] B.T. Nadiga and S. Zaleski, Investigations of a two-phase fluid, Eur. J. Mech., B/Fluids 15 (1996) 885-896.

[6] D.M. Anderson and G.B. McFadden, A diffuse-interface description of internal waves in a near-critical fluid, Phys. Fluids 9 (1997) 1870-1879.

[7] A.A. Wheeler and G.B. McFadden, On the notion of a ξ-vector and a stress tensor for a general class of anisotropic diffuse interface models, Proc. Roy. Soc. Lond. A 453 (1997) 1611-1630.

[8] D.W. Hoffman and J.W. Cahn, A vector thermodynamics for anisotropic surfaces. I. Fundamentals and application to plane surface junctions, Surf. Sci. 31 (1972) 368-388.

[9] H.J. Diepers, C. Beckermann, and I. Steinbach, A phase-field method for alloy solidification with convection, in Solidification Processing 1997, ed. J. Beech and H. Jones, Proc. 4th Decennial Int. Conf. on Solid. Process. (University of Sheffield, Sheffield, 1997) 426-430.

[10] O. Penrose and P.C. Fife, Thermodynamically consistent models of phase-field type for the kinetics of phase transitions, Physica D 53 (1990) 44-62.

[11] S.-L. Wang, R.F. Sekerka, A.A. Wheeler, B.T. Murray, S.R. Coriell, R.J. Braun, and G.B. McFadden, Thermodynamically consistent phase-field models for solidification, Physica D 69 (1993) 189-200.

[12] M.E. Gurtin, D. Polignone, J. Viñals, Two-phase binary fluids and immiscible fluids described by an order parameter, Math. Models Methods Appl. Sci. 6 (1996) 815-831.

[13] J. Lowengrub and L. Truskinovsky, Cahn–Hilliard fluids and topological transitions, Proc. R. Soc. London Ser. A. (1998) In press.

Microgravity Investigation of Dynamic Oxygen Adsorption in Molten Solder Jetting Technology

C. M. Megaridis[1], M. McNallan[2] and D. B. Wallace[3]

[1]Department of Mechanical Engineering
University of Illinois at Chicago
Chicago, IL 60607-7022
Phone: (312) 996-3436
E-mail: cmm@uic.edu

[2]Department of Civil and Materials Engineering
University of Illinois at Chicago
Chicago, IL 60607-7023
Phone: (312) 996-2436
E-mail: mcnallan@uic.edu

[3]MicroFab Technologies
Plano, TX 75074
Phone: (972) 578-8076
E-mail: dwallace@metronet.com

Background

Surface forces play a critical role in fluid dynamical phenomena which are important in materials processing. These forces are generally more important in liquid-metal systems, than in their ceramic or polymer counterparts, because of the high surface tensions of metal melts in comparison to other classes of materials. The surface tension of liquid metals has been found to be very susceptible to small amounts of adsorbed oxygen. Consequently, the kinetics of oxygen adsorption can influence the capillary breakup of liquid-metal jets targeted for use in electronics assembly applications where low-melting-point metals (such as tin-containing solders) are utilized as an attachment and/or structural material for mounting of electronic components to substrates. By interpreting values of surface tension measured at various surface ages, adsorption and diffusion rates of oxygen on the surface of the melt can be estimated.

In this newly-commenced research program, the adsorption of oxygen on the surface of an atomizing molten-metal jet will be investigated as posing a severe impediment in processing technologies involving jetting of pure tin or tin-based alloys. While the problem of interest is one of fundamental fluid transport and surface science, it is also directly related to the novel technology of dispension (printing) of microscopic solder deposits for the surface mounting of microelectronic devices. This technology, known as solder jetting [1], features deposition of solder droplets in very fine, very accurate patterns using techniques analogous to those developed for the ink-jet printing industry. The liquid-metal droplet size in the solder dispensing and deposition process is typically in the range from 50 to 100μm. This range contains the diameter of the atomizing jet which creates the droplets. Each liquid solder droplet travels in an inert environment to limit oxygen adsorption before impact on the substrate where it eventually solidifies. Typically, the distance traveled by the droplet is of the order of a few mm, impact velocities are of the order of a few m/s, initial solder superheat around 25°C, and the jetting environment temperatures are in the range from 25° to 150°C. The details of the droplet flight stage have been analyzed in [2], while the droplet impact dynamics and solidification have been investigated in [3] and [4].

A major development challenge in the commercialization of solder jetting technology stems from the need to maintain adequate control of the local inert environment around the atomizing jet and the formed droplets for a wide variety of industrial applications. To this end, the limitations of solder jetting must be quantified as a function of oxygen content in the local inert environment. Alternatively, this requires the quantification of the influence of oxygen gaseous impurities in the ambient on the dynamic surface tension properties of the employed solder melts.

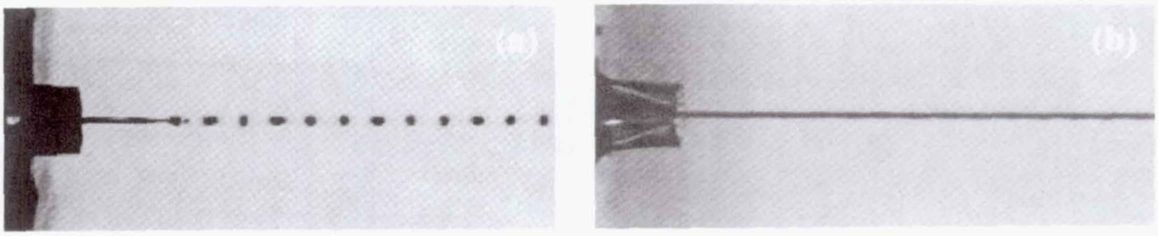

Fig. 1: Illustration of the effect of oxygen adsorption on molten-solder jetting at length scales representative of solder jet technology [5]. (a) Pure nitrogen environment, (b) Oxygen-containing ambient.

Figure 1 illustrates the problem hypothesis through two photographs showing the controlled breakup of a 50μm Indalloy-158 solder jet into 100μm droplets [5]. The jetting process in Fig. 1a takes place in a pure nitrogen atmosphere and the breakup occurs at 3mm from the orifice. The photo in Fig.1b illustrates the corresponding event when oxygen was allowed to enter the environmental chamber, and clearly depicts that atomization does not occur in the field of view (several centimeters wide). The experimental conditions for this case reveal that the surface properties of solder have been critically compromised in the presence of oxygen within a time scale smaller than 0.1ms.

Justification for Low Gravity

Typical injection velocities in solder jetting are of the order of 1m/s, while the jet breakup lengths are of the order of 1mm. Thus, the capillary jet disintegrates into droplets under the action of surface tension in about a millisecond or less. Under these circumstances, the variation of surface tension with time must be resolved at temporal scales much finer than a millisecond. This severe requirement limits the choice of surface tension measurement techniques and points to a dynamic method of high accuracy under such extreme conditions. This method has been validated for non-metallic liquids of moderate viscosity [6], and is believed to have equally good potential to provide similar data for metal melts. However, the technique also requires a high degree of spatial resolution that can be afforded only at length scales larger than those encountered in solder jetting technology. In particular, the measurement of the contractions (necks) along an excited jet becomes increasingly more difficult as the length scales get smaller. The urgent need for reliable experimental data to guide process development, forces one to resort to scaled up jets (diameters near 0.5mm or better) to afford improved spatial resolution and flexibility in conducting such experiments. While the effect of gravity on the atomization behavior of 50-100μm-diameter jets is insignificant (breakup is completed very rapidly), gravity becomes increasingly more influential in the atomization of larger solder jets that are needed for the surface tension characterization experiments. As a result, the microgravity environment appears to be necessary to conduct the jet breakup experiments relevant to the solder microdroplet dispensing technology.

To exemplify the disparity in the importance of gravity during the capillary breakup of different diameter jets, the fluid trajectory was calculated first for a set of parameters corresponding to the real solder dispension process in normal gravity (50 micron diameter jet, injection velocity of 1m/s, breakup length of 2mm). For the small diameter jet, the influence of gravity on jet trajectory remains negligible up to breakup. When a 0.5mm-diameter solder jet is used in normal gravity experiments, the breakup length increases at least by an order of magnitude, as linear theory predicts [7] and as also verified by experiments conducted in our laboratory. In the horizontal injection of a larger-diameter jet, the deviation of the jet trajectory due to gravity may exceed a few millimeters at breakup. If one further considers the significantly delayed atomization dynamics when oxygen is present locally around the solder jet [5], it becomes apparent that the axisymmetry requirement of the surface tension measurement technique cannot be satisfied for large-diameter jets positioned horizontally in a terrestrial laboratory. On the other hand, for vertical injection of a 0.5mm-diameter jet the velocity change along the direction of the gravitational field at breakup may exceed 20% of the injection velocity. Consequently, the presence of a microgravity environment is necessary for the needed controlled jet breakup experiments when 0.5mm- (or larger) diameter jets are employed to attain improved spatial resolution.

Methodology

Theoretical

The surface tension of liquid metals, including tin [8], is reduced when oxygen is adsorbed on the surface. At thermodynamic equilibrium, the effect of adsorbed oxygen on the surface tension is expressed through the Gibbs adsorption isotherm [9]

$$d\gamma/d\ln P_{O2}^{\ 1/2} = -\,R\,T\,\Gamma_O \qquad (1)$$

where γ is the surface tension of the liquid metal (N/m), P_{O2} is the partial pressure of oxygen in equilibrium with the surface (atm), R is the gas constant (J/mol K), T is the temperature (K), and Γ_O is the excess quantity of oxygen adsorbed on the surface (mol/m^2). Surface adsorption of oxygen from the gas phase can be written as

$$\tfrac{1}{2} O_2 + v^s \leftrightarrow O^s \qquad (2)$$

where v^s refers to an unoccupied site on the metal surface, and O^s denotes a site occupied by an oxygen atom. For single site occupancy, the equilibrium of reaction (2) can be expressed by the Langmuir adsorption isotherm

$$K = \exp(-\Delta G^o/RT) = \Theta_O/[P_{O2}{}^{1/2}(1 - \Theta_O)] \qquad (3)$$

where ΔG^o (J/mol) is the change in Gibbs free energy associated with reaction (2), and Θ_O is the fractional surface coverage in oxygen, given by the ratio of the surface excess of oxygen Γ_O in equilibrium with a particular oxygen partial pressure to the surface excess of oxygen at saturation $\Gamma_O{}^s$. The Langmuir and Gibbs adsorption isotherms can be combined and integrated to give an equation for the effect of adsorbed oxygen on the surface tension of the metal [10]

$$\gamma = \gamma^o - R\,T\,\Gamma_o{}^s \ln(1+KP_{O2}{}^{1/2}) \qquad (4)$$

where γ is the surface tension of the metal in equilibrium with a particular partial pressure of oxygen, γ^o is the surface tension of the pure metal, and K is the equilibrium constant defined in Eq. (3). Further expansion of the terms in Eq. (4) leads to an expression for γ [11] in terms of temperature, oxygen partial pressure, and the enthalpy and entropy changes associated with reaction (2). Experimental determination of the dependence of the surface tension of tin and solder on these parameters is necessary for an adequate understanding of the role of oxygen in the jet breakup phenomenon.

The reduction of the liquid-metal surface tension in the presence of oxygen is responsible for the change in jet behavior between oxygen-free and oxygen-containing environments (see Fig. 1). It is uncertain whether the jet breakup is completed before or after the formation of an adsorbed oxygen monolayer on the jet surface; the characteristic time for the formation of this monolayer depends not only on the adsorption kinetics, but also on the oxygen content in the gas phase. In that sense, diffusion of oxygen from the gas to the fluid surface could play a rate limiting role, which will be investigated in this work.

Experimental

This new study involves the design, fabrication and performance of drop-tower experiments in the microgravity facilities of the NASA Lewis Research Center. The planned experiments will illuminate the kinetics of oxygen adsorption on the surface of molten-solder alloys and pure tin at surface ages ranging from 0.1ms to several ms.

Jets will be formed by forcing the molten metal under pressure through a glass capillary. The jets will be excited by a time periodic electric field, illuminated stroboscopically, observed and photographed through a microscope. The oxygen adsorption tests will be conducted first in an isothermal environment and subsequently in gradually lower ambient temperatures in order to decouple the effect of temperature from the chemical effects.

The growth of axisymmetric disturbances on excited capillary jets has been used to measure the dynamic surface tension of liquids of low [12] and moderate viscosity [6]. The technique involved a complex iterative scheme between experiments and Weber's linear analysis [13], and is capable of producing accurate results for the surface tension at surface age as short as 0.1ms. Time dependent surface tension was demonstrated in [6] for dye-based inks, and significant differences between the static and dynamic values was reported in some cases. However, the technique requires detailed spatial resolution of the capillary jet breakup geometry. This can be achieved by using mm-diameter jets, which, at the same time are vulnerable to the masking effects of gravity. Hence, even though larger-diameter jets yield significantly improved resolution of fluid breakup dynamics, deviations from axisymmetry in normal gravity hinder the implementation of the surface tension measurement technique in a terrestrial laboratory. Conducting experiments in a microgravity environment (thus eliminating the unwanted influence of gravity) allows the experimental investigation of large-diameter jets in conjunction with Ronay's surface tension measurement technique [6].

Experiments in normal gravity will also define the equilibrium values of surface tension of the melts as a function of ambient oxygen concentration as well as temperature. Comparisons between equilibrium and dynamic surface tension values will provide fundamental information about the kinetics of surface adsorption on lead-tin alloys.

Expected Impact of Research

The planned research will provide a science base for the dynamic oxygen adsorption phenomena occurring in the novel solder dispensing technology, thus having a significant effect on Solder Jet development efforts. The study will allow to generate designs and operating parameters for environmental control systems that are more efficient (in terms of nitrogen usage, space allocation, and energy usage) towards the production of solder deposits of highest quality; this, in turn, will aid the successful commercialization of this innovative technique in electronic component manufacturing or other relevant technologies.

REFERENCES

1. Hayes, D. J., Wallace, D. B., Boldman, M. T. and Marusak, R. E., “Picoliter Solder Droplet Dispensing,” *Int. J. Microcircuits and Electronics Packaging*, 16:173 (1993).

2. Megaridis, C. M., “Presolidification Liquid Metal Cooling Under Convective Conditions,” *Atomization and Sprays*, 3:171 (1993).

3. Waldvogel, J.M., Poulikakos, D., Wallace, D.B. and Marusak, R.M., “Transport Phenomena in Picoliter Size Solder Droplet Dispensing on a Composite Substrate,” *ASME J. Heat Transfer*, 118:148 (1996).

4. Xiong, B., Megaridis, C. M., Poulikakos, D. and Hoang, H., “An Investigation of Key Factors Affecting Solder Microdroplet Deposition,” *ASME J. Heat Transfer*, 120:259 (1998).

5. Wallace, D. B., ‘‘Capillary Instability of a Jet of Liquid Metal,’’ *ASME J. Fluids Engineering*, 115:529 (1993).

6. Ronay, M., “Determination of the Dynamic Surface Tension of Inks from the Capillary Instability of Jets,” *J. Colloid and Interface Sci.*, 66:55 (1978).

7. Rayleigh, J. W. S. *Proc. Lond. Math. Soc.*, 10:4 (1879).

8. Passerone, A., Ricci, E., and Sangiorgio, R., “Influence of Oxygen Contamination on the Surface Tension of Liquid Tin,” *J. Materials Sci.*, 25:4266 (1990).

9. Lupis, C. H. P., *Chemical Thermodynamics of Materials*, Elsevier Science Press, (1983).

10. Belton, G. R., “Langmuir Adsorption, the Gibbs Adsorption Isotherm, and Interfacial Kinetics in Liquid Metals Systems,” *Metallurgical Transactions*, 7B:35 (1976).

11. Sahoo, P., DebRoy, T., and McNallan, M.J., “Surface Tension of Binary-Metal Surface Active Solute Systems under Conditions Relevant to Welding Metallurgy,” *Metallurgical Transactions*, 19B:483 (1988).

12. Ronay, M., “Determination of the dynamic surface tension of liquids from the instability of excited capillary jets and from the oscillation frequency of drops issued from such jets,” *Proc. R. Soc. Lond. A*, 361:181 (1978).

13. Weber, C., “Zum Zerfall eines Flussigkeitsstrables,” *Z. Angew. Math. Mech.*, 11:136 (1931).

Potential Flow Interactions with Directional Solidification

Sudhir S. Buddhavarapu[1] and Eckart Meiburg[2]

Department of Aerospace Engineering
University of Southern California
Los Angeles, CA - 90089-1191

(1) buddhava@spock.usc.edu / (213) 740-7183
(2) eckart@spock.usc.edu / (213) 740-5376

Fax : (213) 740-7774

NASA Grant # : NAG3-1619

Introduction

The effect of convective melt motion on the growth of morphological instabilities in crystal growth has been the focus of many studies in the past decade. While most of the efforts have been directed towards investigating the linear stability aspects, relatively little attention has been devoted to experimental and numerical studies. Comprehensive reviews are provided by Langer (1980), Glicksman *et al.* (1988), and Davis (1990, 1992, 1993). In a pure morphological case, when there is no flow, morphological changes in the solid-liquid interface are governed by heat conduction and solute distribution. Under the influence of a convective motion, both heat and solute are redistributed, thereby affecting the intrinsic morphological phenomenon. The overall effect of the convective motion could be either stabilizing or destabilizing.

Recent investigations by Coriell *et al.* (1984), Forth and Wheeler (1989) have predicted stabilization by a flow parallel to the interface. In the case of non-parallel flows, e.g., stagnation point flow, Brattkus and Davis (1988) have found a new flow-induced morphological instability that occurs at long wavelengths and also consists of waves propagating against the flow. Other studies have addressed the nonlinear aspects (Konstantinos and Brown (1994), Wollkind and Segel (1970)).

In contrast to the earlier studies, our present investigation focuses on the effects of the potential flow fields typically encountered in Hele-Shaw cells. Such a Hele-Shaw cell can simulate a gravity-free environment in the sense that buoyancy-driven convection is largely suppressed, and hence negligible. Our interest lies both in analyzing the linear stability of the solidification process in the presence of potential flow fields, as well as in performing high-accuracy nonlinear simulations.

Linear stability analysis can be performed for the flow configuration mentioned above. It is observed that a parallel potential flow is stabilizing and gives rise to waves traveling downstream.

We have built a highly accurate numerical scheme which is validated at small amplitudes by comparing with the analytically predicted results for the pure morphological case. We have been able to observe nonlinear effects at larger times.

Preliminary results for the case when flow is imposed also provide good validation at small amplitudes.

Linear Stability Analysis

Based on the governing equations for directional solidification, as reviewed by Davis (1992), a linear stability analysis is performed for the fully transient equations. Our results agree well with the quasistationary results predicted by Mullins and Sekerka (1962).

We then consider a uniform Hele-Shaw flow parallel to the solid/liquid interface. The analysis is similar in concept to the pure morphological case as mentioned earlier, with one additional dimensionless parameter measuring the ratio of fluid velocity to the pulling speed. We arrive at a complex algebraic equation, which is solved using a Newton iteration method. This yields the instabilty growth rates and the wave propagation velocities.

Results indicate that the effect of the uniform flow is stabilizing. This agrees with the experimental findings currently being carried out by Zhang and Maxworthy at the University of Southern California. Figure 1 indicates that the larger the uniform flow (U), the smaller the bandwidth of instability. In principle, it is possible to stabilize all wavenumbers by imposing an appropriate U over the solid/liquid interface. Results also indicate that the parallel potential flow gives rise to traveling interfacial waves. These waves travel downstream and are usually on the order of one percent of the freestream velocity. Figure 2 shows the propagation velocity for different wavenumbers.

As expected, increasing values of the Sekerka number (M) destabilize the interface by increasing the bandwidth of instability. Furthermore, higher values of the surface energy parameter (R) lead to a stabilization of the higher wavenumbers.

It is worth taking a look at the underlying physics of the process. It is well known that the driving force in the instability is the concentration gradient. In the pure morphological case, steep concentration gradients exist over the crests and flat concentration gradients in the troughs. This gives rise to an intrinsically unstable situation where the crests grow faster than the troughs, thus leading into a runaway condition.

However, when a parallel potential flow is imposed on the interface, the horizontal component of the perturbation velocity plays a major role in solute redistribution. Solute is transferred from solute-rich regions over the crests to solute-impoverished regions over the troughs. This re-arrangement evens out the differences in concentration gradients and thus brings about stability. Similarly, the vertical component of the perturbation velocity picks up solute from the windward side of the interface and dumps it on the leeward side of the interface. This generates a small downstream propagation of the interface.

Nonlinear Numerical Simulations

In order to represent the linear and nonlinear phenomena accurately, it is important to employ highly accurate computational procedures. Our numerical approach employs a high-order compact finite difference method (Lele 1992) in the pulling direction. In the compact finite difference scheme, we employ discrete approximations of central kind of sixth order accuracy away from the boundaries. At the boundaries, one-sided stencils of third order accuracy are used. A Fourier spectral method (Gottlieb and Orszag 1977) is employed in the periodic direction. The combination of these two schemes allows for the evaluation of highly accurate spatial derivatives. The calculation is advanced in time by means of a low-storage third order Runge-Kutta scheme (Wray (1991)). This combination, in conjunction with an analytical mapping leads to excellent accuracy.

To validate our numerical scheme, we performed test calculations to measure the growth of small perturbations in time for a pure morphological case. With a typical choice of 8 Fourier modes in the periodic direction and 129 finite difference grid points in the pulling direction, and for a wide range of parameters such as surface energy, stability parameter, segregation co-efficient, our results agreed to within 1% of the analytically predicted growth rates obtained from the linear stability analysis.

Subsequently we carried the simulations to longer times, where nonlinearities come into effect. We have been able to follow the interfacial growth rates to times when the depth of the grooves is comparable to their wavelengths. At late times, the interface is dominated by those wavelengths for which linear theory predicts the largest growth rates. This is indicated in Figure 3.

The next step was to incorporate the flow field into the equations. The velocity distribution is calculated by employing a boundary element technique. With this technique, one can easily simulate a potential flow. Preliminary results of interfacial growth rates at small amplitudes show excellent agreement with those predicted analytically by the linear stability. Interfacial waves are observed traveling downstream, as predicted by the linear stability analysis.

The boundary element technique mentioned above gives us the opportunity to explore a wide variety of flow configurations. Various spatial distributions of sources and sinks can be made to simulate different flow fields in order to investigate opportunities for suppressing the instabilities.

Our numerical simulations have been carried out on CRAY T90 at the San Diego Super Computing facility at the University of California, San Diego.

NOTE : In the following figures,

R (surface energy parameter) $= - [\, 2T_M\gamma Vk] / [mLDc_\infty (1-k)]$

M (Stability parameter) $= [m(k-1)/k].[c_\infty V / DG] = mG_c / G$

K (Segregation co-efficient) $= c^- / c^+$

U (non-dimensional velocity) = dimenstional velocity / pulling speed $= U^* / V$

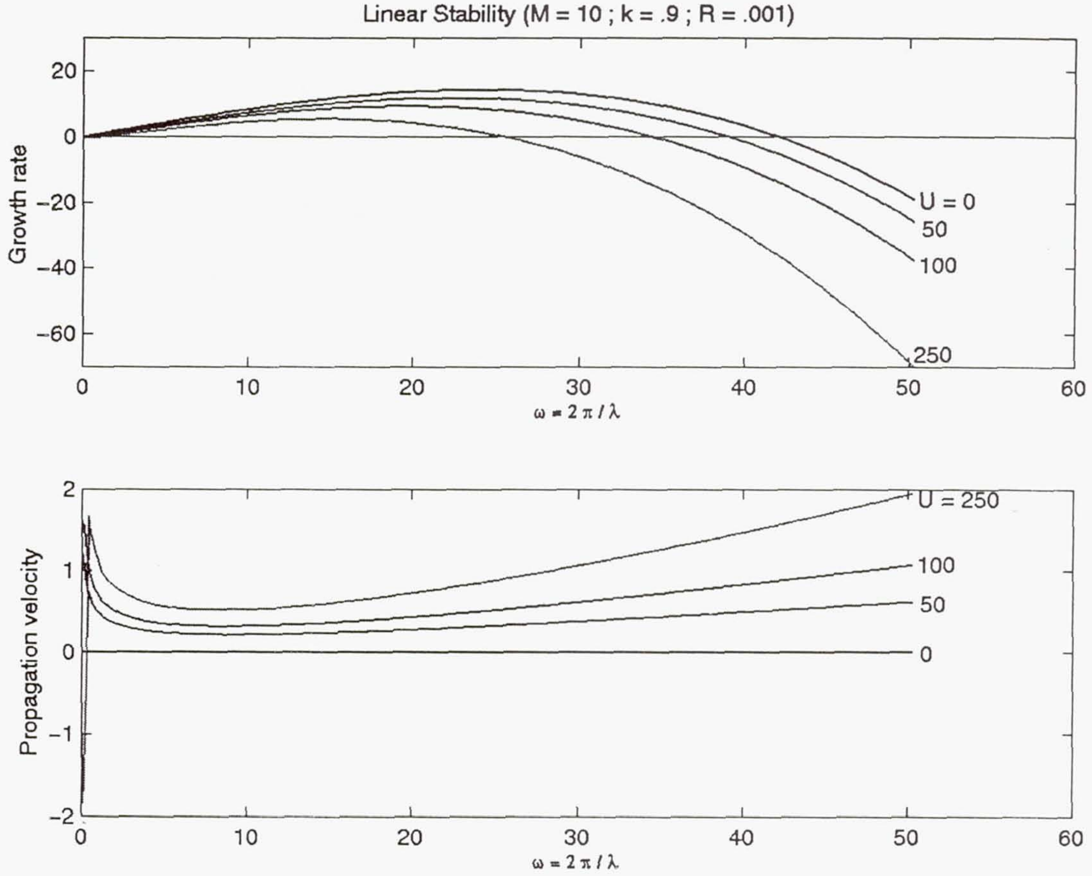
Linear Stability (M = 10 ; k = .9 ; R = .001)
Growth rate
20
0
-20
-40
-60
0
10
20
30
40
50
60
ω = 2 π / λ
U = 0
50
100
250
Propagation velocity
2
1
0
-1
-2
0
10
20
30
40
50
60
ω = 2 π / λ
U = 250
100
50
0

Figures 1-2

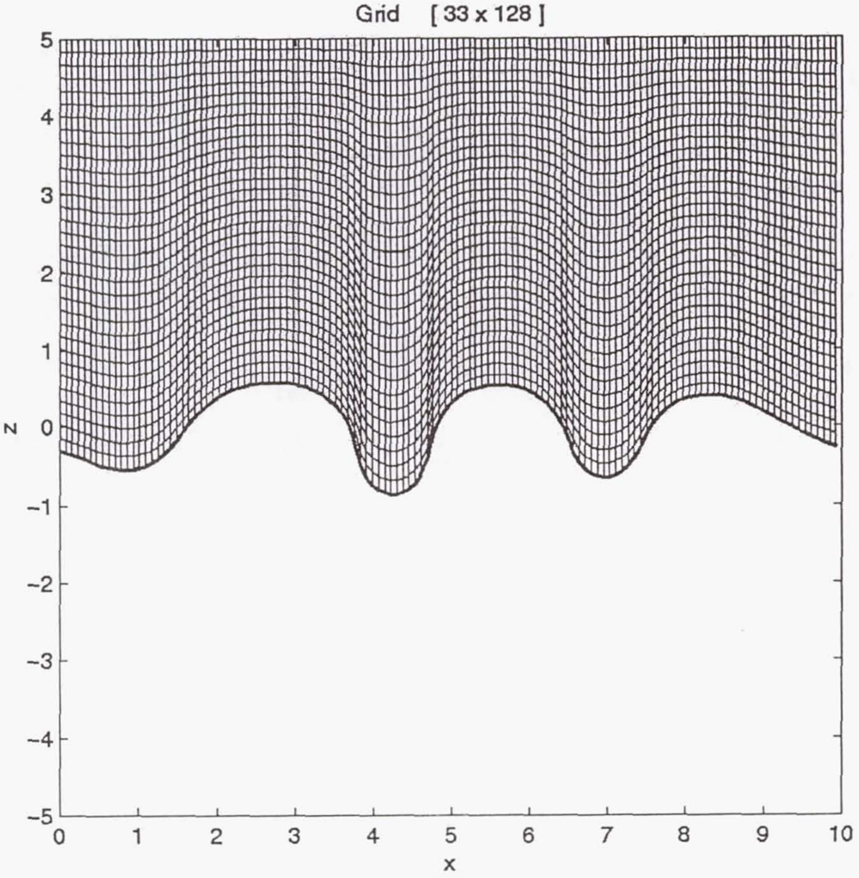

Figure 3

References

Glicksman, M.E., Coriell, S.R., and McFadden, G.B. 1986. Interaction of flows with crystal-melt interface Ann. Rev. Fl. Mech. 18, 307.

Davis, S.H. 1990 Hydrodynamic interactions in directional solidification. J. Fluid Mech. 212, 241.

Davis, S.H. 1992 Microscale coupling of solidification and flow. Proc. of the Symp. on Interactive Dynamics of Convection and Solidification. Kluwer Academic Press.

Davis, S.H. 1993 Effects of flow on morphological stability. Handbook of Crystal Growth Vol. 1 Elsevier Science Publishers.

Langer, J.S. 1980 Instabilities and pattern formation in crystal growth. Rev. of Mod. Phys., 52, 1, 1.

Coriell, S.R., McFadden, G.B., Boisvert, R.F., and Sekerka, R.F. 1984 The effect of forced Couette flow on coupled convection of morphological instability during directional solidification. J. Cryst. Growth 69, 15.

Forth, S.A. and Wheeler, A.A. 1987 Hydrodynamical and morphological stability of the unidirectional solidification of a freezing binary alloy : A simple model. J. Fluid Mech. 202, 339.

Brattkus, K. and Davis, S.H. 1988 Flow induced morphological instabilities : Stagnation point flow J. Cryst. Growth 89, 423.

Schulze, T.P. and Davis, S.H. 1996 Shear stabilization of a solidifying front : Weakly nonlinear analysis in a long-wave limit Phys. Fluids 8 (9), 2319.

Tsiveriotis Konstantinos and Brown, Robert A. 1994 Long-time-scale dynamics observed in directional solidification of a binary alloy. Phys. Rev. B 49, 18, 12 724.

Wollkind, D.J. and Segel, L.A. 1970 A nonlinear stability analysis of the freezing of a dilute binary alloy. Phil. Trans. Roy. Soc. London Ser A 268, 351

Mullins, W.W. and Sekerka, R.F. 1964 Stability of a planar interface during solidification of a dilute binary alloy. J. Appl. Phys. 35, 444.

Lele, S.K., 1992 Compact finite difference schemes with spectral-like resolution. J. Comp. Phys. 103, 16.

Gottlieb, D. and Orszag, S.A 1977 Numerical analysis of spectral methods. SIAM, Philadelphia.

Wray, A.A. 1991 Minimal storage time-advancement schemes for spectral methods.

Eshelmen, M.A., and Trivedi, R. 1987 The planar to cellular transition during the directional solidification of alloys. Acta. Metall. 35, 2443.

THERMODYNAMIC AND STATISTICAL STUDIES OF SUPERSATURATED TERNARY SOLUTIONS

Alexander F. Izmailov (izmailov@duke.poly.edu) and Allan S. Myerson (amyerson@duke.poly.edu)
Department of Chemical Engineering, Polytechnic University
Six MetroTech Center, Brooklyn, NY 11201

1. *Introduction*

It is well known that small amounts of impurity can profoundly effect nucleation and crystal growth. For example, it has been reported that Pb^{2+} acts as a nucleation agent in a $NaCl$ solution [1], whereas Co^{2+} inhibits nucleation in KNO_3 solution [1]. The effect of K^+ and Fe^{3+} ions on nucleation of ammonium-aluminum sulfates was studied in [2,3]. The study of Cr^{3+} impurities in different supersaturated solutions has demonstrated that in their presence nucleation and crystal growth are suppressed [4-6]. All these studies have been performed in bulk solutions and, therefore, have only qualitative reproducibility. In addition, no mechanistic understanding of these effects can be obtained from the normal bulk experiments. Particularly it is not possible to distinguish whether the impurity effects thermodynamics of the system in some way or alters kinetics of the nucleation and growth processes. In order to obtain reproducible quantitative results related to the effect of an impurity on nucleation, an accurate and sensitive experimental technique is required which allows preparation of stable supersaturated solutions. To the best of our knowledge the only experimental technique capable of achieving these results is based on containerless levitation of solution microdrolplets in a solvent atmosphere [7-17]. Preliminary results of the study of the impact of an impurity (Cr^{3+} ions) on nucleation of ammonium sulfate ($(NH_4)_2SO_4$) in aqueous solution by studying the dependence of water activity on $(NH_4)_2SO_4$ concentration have been reported in [18]. In this paper we present results of experimental and theoretical study of the impact of small amounts of ionic impurities such as Cr^{3+} on nucleation of $(NH_4)_2SO_4$ in aqueous supersaturated solution.

2. *The SVELT Technique. Application to the Study of Nucleation in Ternary Solutions*

The Spherical Void Electrodynamic Levitator Trap (SVELT) technique was employed in order to determine the solute activity (chemical potential) as a function of supersaturation and impurity concentration. This technique allows containerless suspension of the electrically charged microdroplets (1-$20\mu m$ in diameter) with supersaturated solution in the solvent atmosphere. The advantages of this technique provide a unique opportunity to reach extremely high supersaturations. The highest concentrations obtained in this technique are usually 5-10 times the higher than those obtained in bulk solutions [13-20] resulting in a very deep penetration into the metastable zone.

One of the objectives of the experimental study performed, was to distinguish the relative role of different impurities and their concentration on the possibility of nucleation occurrence. For this purpose microdroplets containing supersaturated solutions with impurities of known character and concentration were levitated. Therefore, the heterogeneous solution of known mean solute n_{slt} and impurity n_{imp} concentrations was prepared and injected into the SVELT chamber.

In the levitation experiments the mass m of solution microdroplet and the solvent vapor pressure in the SVELT chamber can be easily determined and directly measured, respectively. In all experiments performed in this work, we first evacuated the entire solvent from the SVELT chamber in order to determine the combined mass m_{com} of solute m_{slt} and impurity m_{imp} masses ($m_{com} = m_{slt} + m_{imp}$) by measuring the balancing *dc*-voltage $(V_{dc})_{dry}$ for the anhydrous (dry) microdroplet. After this measurement was performed, the solvent vapor was allowed back to the SVELT chamber until complete deliquescence of the dry microdroplet. In the following measurements the balancing *dc*-potential $(V_{dc})_{wet}$ and solvent vapor pressure were recorded continuously while gradually evacuating solvent vapor from the SVELT chamber by adjusting the needle valve. This procedure increases the relative solute and impurity concentrations n_{slt} and n_{imp} leaving the ratio of their masses, $r = m_{imp}/m_{slt}$, constant. Therefore, the deeper penetration into supersaturated (metastable) region takes place. Evacuation was continued at a slow rate until nucleation occured. At the nucleation point, the balancing *dc*-voltage V_{dc} drops precipitously. After nucleation the evacuation was continued to ensure that there had been no charge loss during the cycle.

The experimental procedure described above allows continuous recording of the chamber equilibrium pressure $P(T;\, n_{slt}\,,\, r)$ and the balancing *dc*-voltage V_{dc} (which retains the microdroplet at the SVELT geometric center). As a result of the solvent vapor evacuation, the balancing *dc*-voltage V_{dc} decreases steadily and the solution in the microdroplet becomes more supersaturated and eventually nucleation occurs. These measurements were repeated several (usually four) times to ensure the reproducibility of experimental results for the given solution microdroplet.

3. *Thermodynamics of Ternary Supersaturated Solutions with Electrolyte Solute and Impurity*

Let us take into account that solute ammonium sulfate, $(NH_4)_2SO_4$, and impurity, chromium sulfate $(Cr)_2(SO_4)_3$, are electrolytes. Results of our previous research papers [19,20] allow the following simple expression for the solvent chemical potential:

$$\mu_{slv}(T;\, n,\, r) = -\frac{n}{N}\,[1 + r\,\frac{(MW)_{slt}}{(MW)_{imp}}]\,k_B T - \frac{n^{\frac{3}{2}}}{3N}\,c_{slv,\,1}(T;\, r) - \frac{n^2}{2N}\,c_{slv,\,2}(T;\, r)\,. \tag{1}$$

where

$$c_{slv,\,1}(T) = c_{slt,\,1}(T) + [r\,\frac{(MW)_{slt}}{(MW)_{imp}}]^{\frac{3}{2}} c_{imp,\,1}(T)\,, \quad c_{slv,\,2}(T) = c_{slt,\,2}(T) + [r\,\frac{(MW)_{slt}}{(MW)_{imp}}]^2 c_{imp,\,2}(T)\,.$$

Therefore, expression for the relative solvent vapor humidity $RH(T;\, n_{slt},\, r) = P(T;\, n_{slt},\, r)/P_{sat}(T)$, i.e. its activity, acquires the form:

$$RH(T;\ n,\ r) = e^{-\frac{(MW)_{slv}}{1000} Nn\varphi_{slv}(T;\ n,\ r)},\quad \varphi_{slv}(T;\ n,\ r) = 1 + r\frac{(MW)_{slt}}{(MW)_{imp}} + \frac{n^{\frac{1}{2}}}{3k_B T} c_{slv,\ 1}(T;\ r) + \frac{n}{2k_B T} c_{slv,\ 2}(T;\ r)\ , \tag{2}$$

where $P_{sat}(T)$ is the solvent vapor saturation pressure at the given temperature T, $(MW)_{slv} = 18$ is the molecular weights of solvent (water). The functional parameters $p_1(T;\ r) = c_{slv,1}(T;\ r)/(3k_BT)$ and $p_2(r) = c_{slv,2}(T;\ r)/(2k_BT)$ of expression (2) are strongly dependent on solute-impurity concentration ratio r. They can be identified by direct comparison with experimental data since the relative humidity $RH(T;\ n_{slt},\ r)$ as the function of solute concentration n has been measured in our experiments for different r. Among results obtained in [19,20] for the special case of binary supersaturated electrolyte solutions we utilize and generalize to the following two for the case of ternary electrolyte solutions:

A) Within the region of solute concentrations where electrolyte solution is supersaturated (metastable) there is a particular solute association concentration $n_{ass\ ,\ max}(T;\ r)$ when the supersaturated electrolyte solution experiences a dramatic decrease to zero of its electrical conductivity. In other words, at this solute concentration the solution becomes non-conductive since all ions become associated into electrically neutral Bjerrum pairs and their associations (clusters). Further penetration into metastable zone leads back to the appearance of free ions and, thus, to non-zero conductivity. Analytical expression obtained in [20,21] for the concentration $n_{ass,\ max}(T;\ r)$ has the form:

$$n_{ass\ ,\ \max}(T;\ r) = \left[\frac{3p_1(T;\ r)}{5p_2(T;\ r)}\right]^2 . \tag{3}$$

B) Analytical expression for spinodal concentration $n_{spin}(T;\ r)$ in terms of the experimentally determinable functional parameters $p_1(T;\ r)$ and $p_2(T;\ r)$ has the form:

$$n_{spin}(T;\ r) = \frac{9}{32}\left[\frac{p_1(T;\ r)}{p_2(T;\ r)}\right]^2 + \frac{1}{2p_2(T;\ r)} + \frac{3}{4}\frac{p_1(T;\ r)}{|p_1(T;\ r)|}\sqrt{\frac{9}{64}\left[\frac{p_1(T;\ r)}{p_2(T;\ r)}\right]^2 + \frac{1}{2p_2(T;\ r)}}\ . \tag{4}$$

It is understandable that this generalizations are correct when concentration of one electrolyte (impurity) is orders of magnitude less than concentration of another electrolyte (solute), i.e. the ratio of impurity to solute concentrations $r \ll 1$.

4. *Theoretical Treatment of Experimental Data obtained for the Supersaturated Ternary Electrolyte Solutions*

In this paper we present three different sets of experimental data obtained for the water activity of the supersaturated (with respect to solute, ammonium sulfate $(NH_4)_2SO_4$) ternary electrolyte solution by means of the SVELT-based experiments. Each set of data, containing at least four trials, corresponds to different initial concentrations of impurity (chromium sulfate, $(Cr)_2(SO_4)_3$): $n_{0,imp,1} = 0.01ppm$, $n_{0,imp,2} = 0.05ppm$ and $n_{0,imp,3} = 0.1ppm$. All experiments were run at $25\ ^\circ C$ controlled with accuracy $\pm\ 0.1\ ^\circ C$.

Results for the solvent vapor activity $RH(T;\ n_{slt},\ r)$ for $n_{0,imp,1}$ concentration of chromium sulfate are presented on *Figure 1*, were solid lines represent theoretical curves obtained for each trial. Their comparison with marked lines representing experimental data demonstrate outstanding correspondence between theory and experiment: maximum relative error of this correspondence has never exceeded 3% in all experiments performed. In each set of experiments the averaged over four trials functional parameters $p_{1,ave}(T;\ r_n)$ and $p_{2,ave}(T;\ r_n)$ $(n = 1,2,3)$ were determined (*Table 1*). The averaged solvent vapor activities $RH_{ave}(T;\ n_{slt},\ r_n)$ were determined by utilizing parameters $p_{1,ave}(T;\ r_n)$ and $p_{2,ave}(T;\ r_n)$ for each initial concentration of impurities.

Table 1:

	initial Cr^{3+} concentration (ppm)	$p_{1,ave}(T,r)$	$p_{2,ave}(T,r)$	discrepency between theory & experiment (%)	$n_{ass,max,ave}(T;\ r)$ (molal)	$n_{spin}(T;\ r)$ (molal)
Set 1	*0.01*	*0.688*	*-0.085*	*2.5*	*24.78*	*50.62*
Set 2	*0.05*	*0.669*	*-0.090*	*1.9*	*19.96*	*41.70*
Set 3	*0.1*	*0.912*	*-0.132*	*2.4*	*17.21*	*34.18*

It should be noted that in all sets of data the water activity $RH_{ave}(T;\ n_{slt},\ r_n)$ in the presence of impurities is always slightly below the water activity $RH(T;\ n_{slt},\ 0)$ in their absence when ammonium sulfate supersaturations are low. Somewhere at moderately high solute supersaturations $n_{slt,cr}(r_n)$ the water activity lines $RH_{ave}(T;\ n_{slt},\ r_n)$ cross $RH(T;\ n_{slt},\ 0)$ from below. This observation is very important since it indicates that spinodal concentrations of solute should be lowered when impurities are present. Direct calculations of spinodal concentrations $n_{spin}(T;\ r_n)$ in the cases of $r_n \neq 0$ $(n = 1,2,3)$ by utilizing expression (10) have confirmed this observation (*Table 1*).

In *Table 1* the averaged association concentrations $n_{0,max,ave}(T;\ r_n)$ obtained by utilizing parameters $p_{1,ave}(T;\ r_n)$ and $p_{2,ave}(T;\ r_n)$ for each initial concentration of impurities are presented. It is important to note that in all cases $(n = 1,2,3)$ corresponding to different initial impurity concentrations there exist the following approximate equality: $n_{ass,max,ave}(T;\ r_n) \approx n_{slt,cr}(r_n)$. This means that *the ammonium and sulfate* ions become *100%* into electrically neutral Bjerrum pairs and their associations at the unique solute concentration when water activity is insensitive to the presence of impurity.

The fact that at low supersaturations $RH_{ave}(T;\ n_{slt},\ r_n) \leq RH(T;\ n_{slt},\ 0)$ can be easily understood if one takes into account that impurity ions bind some water molecules what leads to the decreased water activity. This additional binding of water molecules due to impurity leads to an increase of the relative solute supersaturation with respect to water, what explains the following facts observed in our experiments:

A) $n_{ass,\,max,\,ave}(T;\,r_n) < n_{ass,\,max,\,ave}(T;\,0)$,

B) $n_{spin}(T;\,r_n) < n_{spin}(T;\,0)$

for any $r_n > 0$ $(n = 1,2,3)$. Therefore, the formation of Bjerrum pairs between $[(NH_4)_2]^{2+}$ and $[SO_4]^{2-}$ ions in the presence of impurity is more intense than without impurity. It is also reasonable to conclude that the overall number of active (free) water molecules is a decreasing function of the number of Bjerrum pairs.

3. *Conclusions*

The results presented above raise more questions than provide answers. Explanations which we have given to the data obtained are hypothesis rather than final answers. What is important from a practical point of view is that we have found no explanation for the observation that Cr^{3+} ions serve as inhibitors of nucleation. This observation was established in bulk experiments at low solute supersaturations. In that work, however, no attention was paid to the effect of the Cr^{3+} ions on thermodynamic properties of the solution (activity of solvent, solute, etc.). In our current and forthcoming research we are planning to collect more accurate data which will allow us to address all the questionable issues discussed in this paper.

4. *References*

1. E.G.Cooke, *Krystall.Tech.* **1**, 119 (1966)
2. J.W.Mullin, and M.Kitamura, *J.Cryst.Growth* **71**, 118 (1985).
3. M.Kitamura, and J.W.Mullin, in *Proceedings of World Congress III on Chemical Engineering*, **2**, 1048 (1986).
4. M.Kitamura, T.Nakai, K.Ikemoto, and Y.Kawamura, *International Chem.Eng.* **32**, 1 (1992).
5. M.Kitamura, T.Nakai, K.Ikemoto, and Y.Kawamura, *International Chem.Eng.* **32**, 157 (1992).
6. N.Kubota, J.Fakazawa, H.Yashiro, and J.W.Mullin, *J.Cryst.Growth* **149**, 113 (1995).
7. M.D.Cohen, R.C.Flagan and J.H.Seinfeld, *J.Phys.Chem.* **91**, 4563 (1987).
8. M.D.Cohen, R.C.Flagan and J.H.Seinfeld, *J.Phys.Chem.* **91**, 4575 (1987).
9. M.D.Cohen, R.C.Flagan and J.N.Seinfeld, *J.Phys.Chem.* **91**, 4583 (1987).
11. C.B.Richardson and J.P.Spann, *J. Aerosol Sci.* **15**, 563 (1984).
12. E.J.Davis and A.K.Ray, *J.Colloid Interface Sci.* **75**, 566 (1980).
13. A.S.Myerson, H.S.Na, A.F.Izmailov and S.Arnold, in *Proceedings of the 12th Symposium on Industrial Crystallization*, p.3-013 (Poland, Warsaw, September 21-23,1993).
14. H.S.Na, S.Arnold and A.S.Myerson, *J.Cryst.Growth* **139**, 104 (1994).
15. H.S.Na, S.Arnold and A.S.Myerson, *J.Cryst.Growth* **149**, 229 (1995).
16. A.S.Myerson and S.Kim, Ind.Eng.Chem.Research **35**, 1078 (1996).

17. A.S.Myerson and A.F.Izmailov, in *Proceedings of the Conference on Crystal Growth of Organic Materials*, edited by A.S.Myerson (ACS, Washington D.C., 1996), p.222.
18. W.M.Sun and A.S.Myerson, in *Proceedings of the Conference on Crystal Growth of Organic Materials*, edited by A.S.Myerson (ACS, Washington D.C., 1996), p.249.
19. A.F.Izmailov, A.S.Myerson and H.S.Na, *Phys.Rev.* **52**, 3923 (1995).
20. A.F.Izmailov, A.S.Myerson and H.S.Na, *J.Cryst.Growth* **166**, 981 (1996).

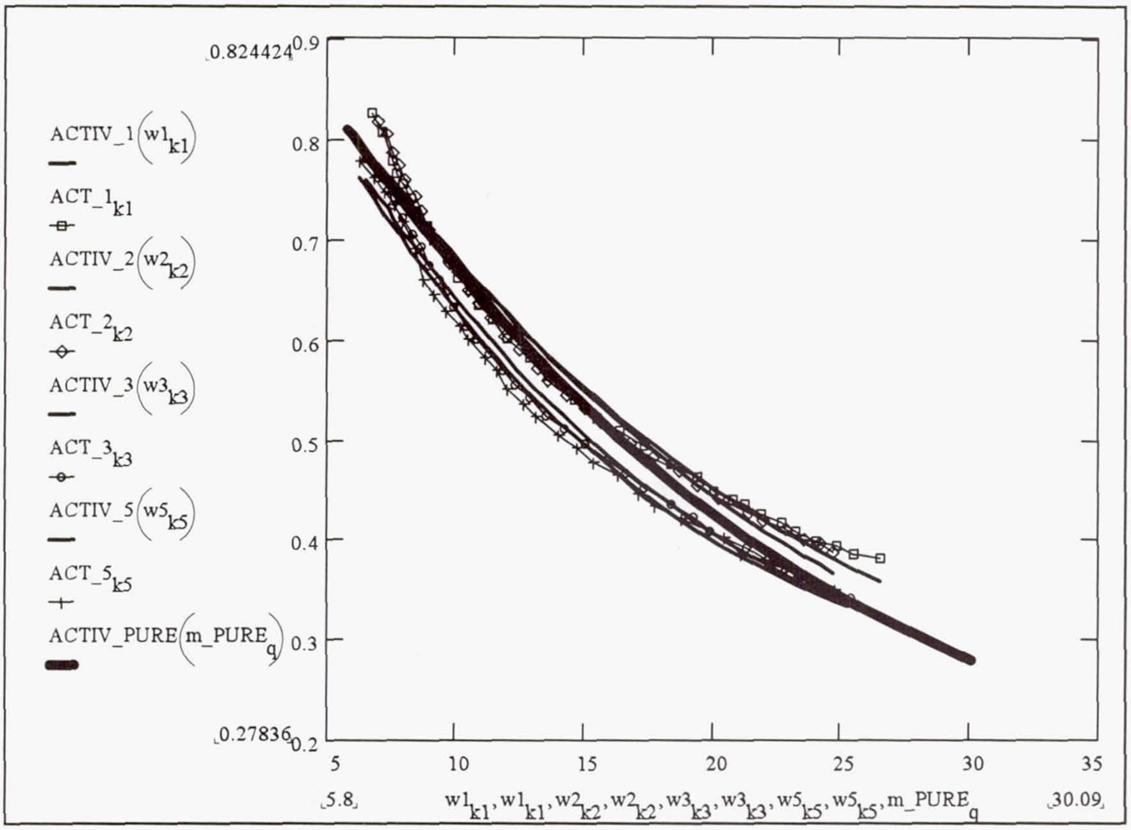

Figure 1:

Water activity versus *$(NH_4)_2 SO_4$* concentration (in molal units) in the case of initial Cr^{3+} concentration equal to *0.01ppm*. Solid lines represent theoretical curves obtained for each trial of total four trials. Marked lines represent experimental data. Thick solid line represent water activity in the absence of impurity.

Reduction of Convection in Closed Tube Vapor Growth Experiments

Robert J. Naumann
Consortium for Materials Development in Space
University of Alabama in Huntsville

Abstract

A novel method for suppressing convection during the solidification of material using closed tube physical or chemical vapor transport will be explored. Convection can be suppressed in growth from the melt by application of high magnetic fields but, unfortunately, this technique does not lend itself to vapors, which have no electrical conductivity. Since the Grashof number scales as the cube of the smallest dimension in the flow system, reduction of the size scale can be extremely effective in reducing unwanted convective flows. However, since materials of practical interest must be grown at least on the cm scale, reduction of the overall growth system is not feasible. But if the region just above the growing crystal could be restricted to a few mm, considerable reduction in flow velocity would result. By suspending an effusive barrier in the growth ampoule just above the growth interface, it should be possible to reduce the convective velocity in this vicinity to levels approaching flows in microgravity.

The effusive barrier consists of a disc just slightly smaller than the growth ampoule inside diameter. The disc will be made of a porous material, such as a glass frit, that will allow the vapor to diffuse through, but will act as a barrier to direct flow. It will be positioned at a fixed distance above the growth interface by a series of small magnets imbedded at points around its periphery. The magnets will interact with magnets of opposite polarity placed in the furnace, just outside the growth ampoule. The furnace operating temperatures for most vapor or chemical vapor growth systems are well below the Curie temperature of most magnetic materials, so this should pose no problem. We will use a transparent furnace so that the growth front will be visible. The width of the region between the growth front and the barrier can then be monitored and adjusted if necessary by either adjusting the translation rate of the sample or by moving the magnets on the outside of the furnace.

We will evaluate the effectiveness of the floating effusive barrier in vapor transport growth by growing single crystals of mercurous chloride. This choice was made for several reasons:

1. It is a technologically interesting acousto-optical material whose usefulness for device applications is still limited by structural defects that have been shown to be related to convection during the growth process by Singh and co-workers at the former Westinghouse Science and Technology Center (now Northrop-Grumman).
2. It is a relatively simple material to grow since it sublimes congruently and grows at low enough temperatures (approximately 400 °C) so that a transparent furnace may be employed to monitor the growth process.
3. The material is brightly colored and optically clear at the growth temperature so that the growth interface is easily visible and gross defects can be detected and possibly corrected during the growth process.
4. We, at the University of Alabama in Huntsville's Consortium for Materials Development in Space (UAH/CMDS), have had experience in growing this material though a previous cooperative agreement with the Westinghouse Science and Technology Center.

Growth experiments will be carried out with different spacings between the effusive barrier and the growth interface, or the barrier may be moved during an individual growth run. Altering the barrier height changes the amount of convective flows and provides a means for assessing the effects of convection on the quality of the grown material.

Characterization of the grown material will consist primarily of rocking curve data and optical scattering measurements since these are the properties that Dr. Singh and co-workers at Westinghouse found to be most affected by convection. Samples will also be submitted to the National Institute of Standards and Technology (NIST) for topographical analysis on their beam facility at the National Synchrotron Laboratory at Brookhaven. We also have a tentative agreement with the Brimrose Corporation in which they will evaluate the grown materials for potential device applications.

If sufficient improvements result, this floating barrier method could be used as a screening experiment to determine if a proposed flight experiment that involves some form of vapor transport might benefit from a reduction in conduction. Also, the technique might be used to produce a new benchmark material against which future flight results might be judged. Finally, this new growth technique may lead to the production of improved materials on Earth as a microgravity program spin-off.

After having demonstrated improvements in the growth of single crystalline material on Earth, we intend to propose a flight experiment to see if additional improvements are possible by a further reduction in convective flows.

Space- and Ground-Based Crystal Growth Using a Submerged Baffle

A. G. Ostrogorsky, P.S. Dutta, C. Marin, M. Vogel, T. Pegnier, Rensselaer Polytechnic Institute, Troy, N.Y. 12180, Tel.: (518)-276-6975; Fax.:(518)-276-6025; e-mail: ostroa@rpi.edu
Thierry Duffar (Co-Investigator), Centred'Etudes Nucleaires, Grenoble, France;
Tel.: 33-76-88-38-36; Fax: 33-76-88-51-17; e-mail: td@ecrins.ceng.cea.fr

1. Introduction

The composition of semiconductor crystals produced in space by conventional melt-growth processes is affected by minute levels of residual micro-acceleration which causes natural convection. The residual acceleration has random magnitude, direction and frequency. Therefore, the velocity field in the melt is a priori unpredictable. Virtually all crystal growth experiments conducted in microgravity have shown evidence of convective interference with segregation. Most melt growth experiments conducted in space do not yield the expected steady-state uniform composition. No composition has been reproduced. Low growth rate R and segregation coefficient k make composition particularly sensitive to residual micro-acceleration. There is no accepted formula for calculating the growth parameters in space.

The Submerged Heater Method (SHM) for directional solidification significantly reduces the level of buoyancy-driven convection [1-7]. The main feature of this method is a disk-shaped baffle which acts as a partition, creating a small zone melt at the interface.

2. Ground based experiments

Using the submerged heater/baffle we grew Ge, GaSb, and $Ga_{1-x}In_xSb$ crystals under conditions of low convection ($V \sim 20$ μm/s). Steady state segregation of Ga in Ge was not achieved. A distinct initial transient followed by steady state segregation was observed with Te-doped GaSb, Fig. 1. Similarly, a notable initial transient in In concentration was observed during growth of $Ga_{1-x}In_xSb$. We measured the diffusion coefficients by fitting Tiller's [8] equation to the initial transient in crystals grown with the submerged heater/baffle. The results are summarized in Table 1. By analyzing the above results we discovered the following important fact:

> *During growth, the diffusivity of solute in the boundary layer at the interface D_i is significantly lower than the diffusivity reported in the literature, measured in shear cells or capillaries D_{bulk}.*

Table 1. Diffusion coefficients of Te and InSb in GaSb measured from growth experiments (D_i) and shear cells (D_{cell})

Solute-solvent system	D_i [cm^2/s]	D_{cell} [cm^2/s]
Te-doped GaSb	1.0×10^{-5}	3×10^{-5} [9] 5×10^{-5} [10]
InSb in GaSb	$2\text{-}3 \times 10^{-5}$	1.2×10^{-4} [11]

The actual D_i must be lower than the values that we obtained, because of weak but still existing melt convection in ground-based experiments with the baffle. The low value of D_i can be explained by association between the atoms and clustering in the solute layer. Our conclusion is that during growth, the solute atoms or associated molecules diffuse in the solute layer against associated and/or clustered atoms of the melt. Recent melt growth of quaternary quasi-binary $(GaSb)_{1-x}(InAs)_x$ in our laboratory [12-14], provides firm evidence of such association which must reduce diffusivity. Therefore, the shape of the initial diffusion-controlled transient is related to the diffusion process in the solute layer, which is characterized by D_i at the melting point T_m. Diffusion in the bulk melt outside of the solute layer is characterized by D_{bulk} at $T_m + \Delta T$. Since in space, bulk melt has uniform composition, D_{bulk} has little direct relevance to growth in microgravity. The use of D_{cell} instead D_i may have obscured the interpretation of concentration profiles in space grown crystals.

Fig. 2 shows similar results for Ga-doped Ge. D was measured in shear cells [15] or by fitting the initial transient in Ga concentration measured in crystals grown in space [16] or under axial magnetic fields [17,18]. The shear cell provides the highest D.

3. Design

Two ampoule designs are being considered and tested. In one, the baffle is being driven by a commercial linear motion feedthrough mechanism attached to the furnace, designed to provide 10^{-11} torr. In the other design, the baffle is driven by volumetric expansion of the melt during solidification and thus does not require active motion control.

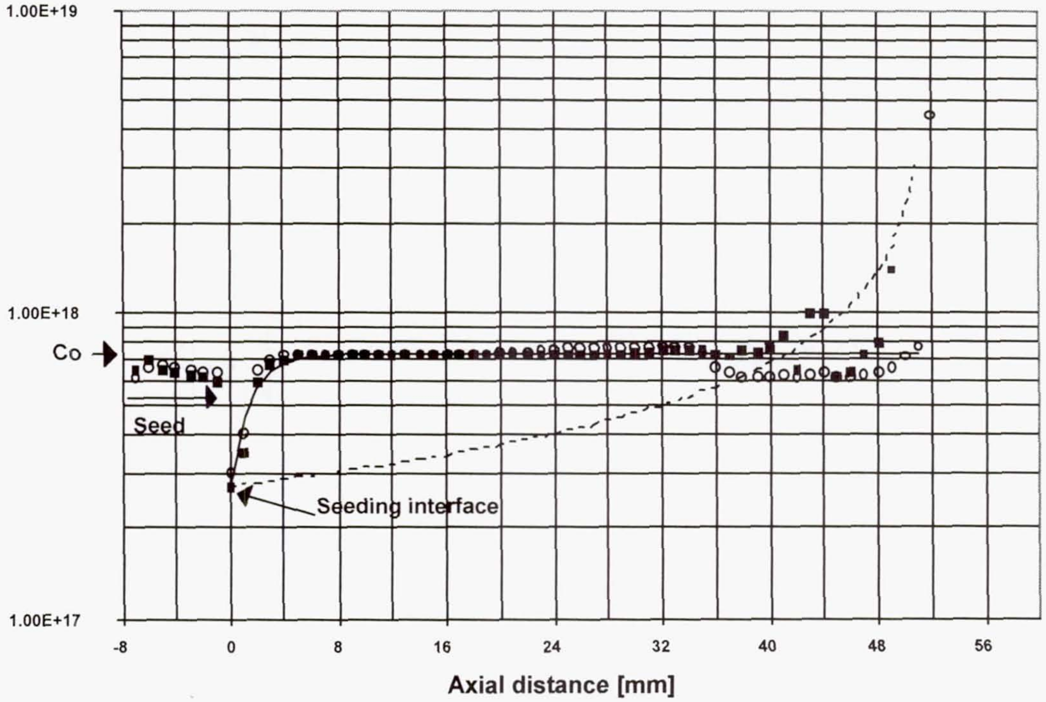

Fig. 1 Axial distribution of in Te-doped GaSb single crystal grown at 5 mm/hr, using a 20 mm diameter seed [7]. Open circles are Te concentration along the axis of symmetry; filled squares are Te concentration along the edge.

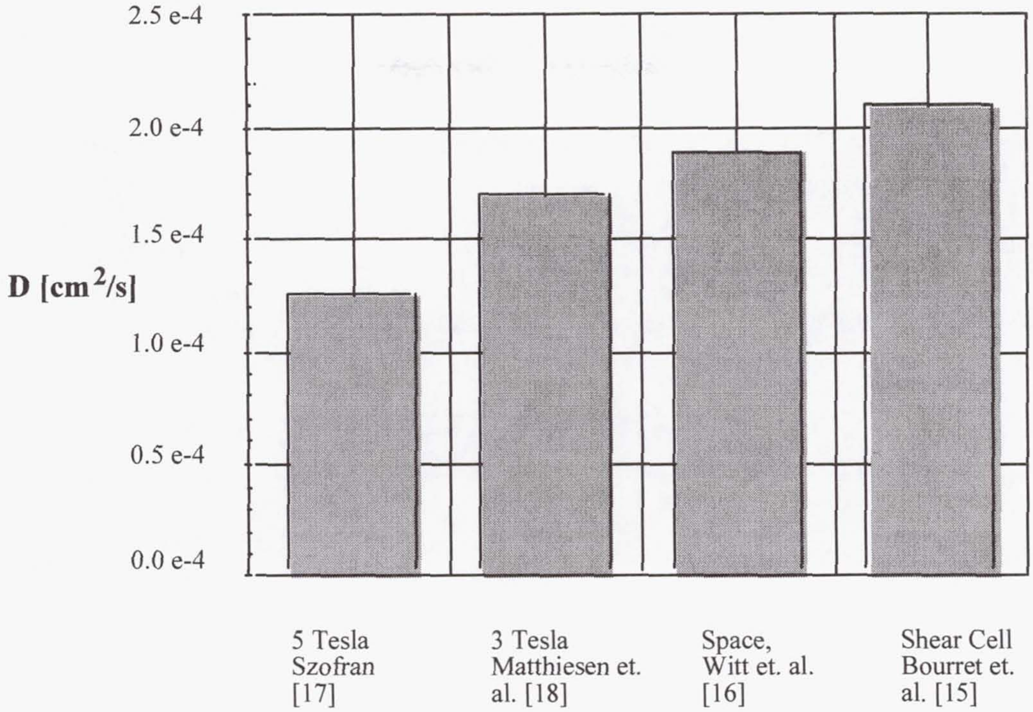

Fig. 2 Diffusion coefficient D for Ga-doped Ge in the shear cell [15] and by fitting the initial transient in concentration [16-18]. The shear cell provides the highest value of D.

---

4. Modeling

Fig. 3 shows the velocity fields and tangential velocities for several levels of residual acceleration and baffle placements. Forced convection can be best seen when no acceleration is present (figures 3j, 3k, and 3 l). Without the baffle, the velocity field is purely axial. When the baffle is placed 0.5 cm from the interface, the tangential velocity is high (5.76 μm/s). The baffle virtually eliminates the effect of residual acceleration on the velocity field in all levels tested. At 10^{-3} g_0, the tangential velocity is 5.90 μm/s, which is barely different from 5.76 μm/s at zero residual acceleration. Therefore, it can be concluded that the baffle dumps convection driven by residual acceleration.

The effect of the residual acceleration on the redistribution of solute in the melt is shown in Fig. 4. The radial segregation caused by forced convection around the baffle can be best seen when no acceleration is present (Fig. 4j, 4k, and 4 l). When the baffle is placed 0.5 cm from the interface, the radial segregation is relatively high (ξ = 49.3 %) because of radial flow caused by the baffle. However, radial segregation is not affected by the residual acceleration and therefore can be readily calculated and experimentally reproduced. As the acceleration changes from zero to 10^{-3} g_0, ξ changes only from 49.3 to 51.8 %. Therefore, residual acceleration of 10^{-3} g_0, acting parallel to the interface, will have virtually no effect on solute redistribution in the melt and crystal composition. In contrast, the conventional Bridgman configuration without the baffle is heavily affected by acceleration of 10^{-4} g_0 (ξ = 32.6 %).

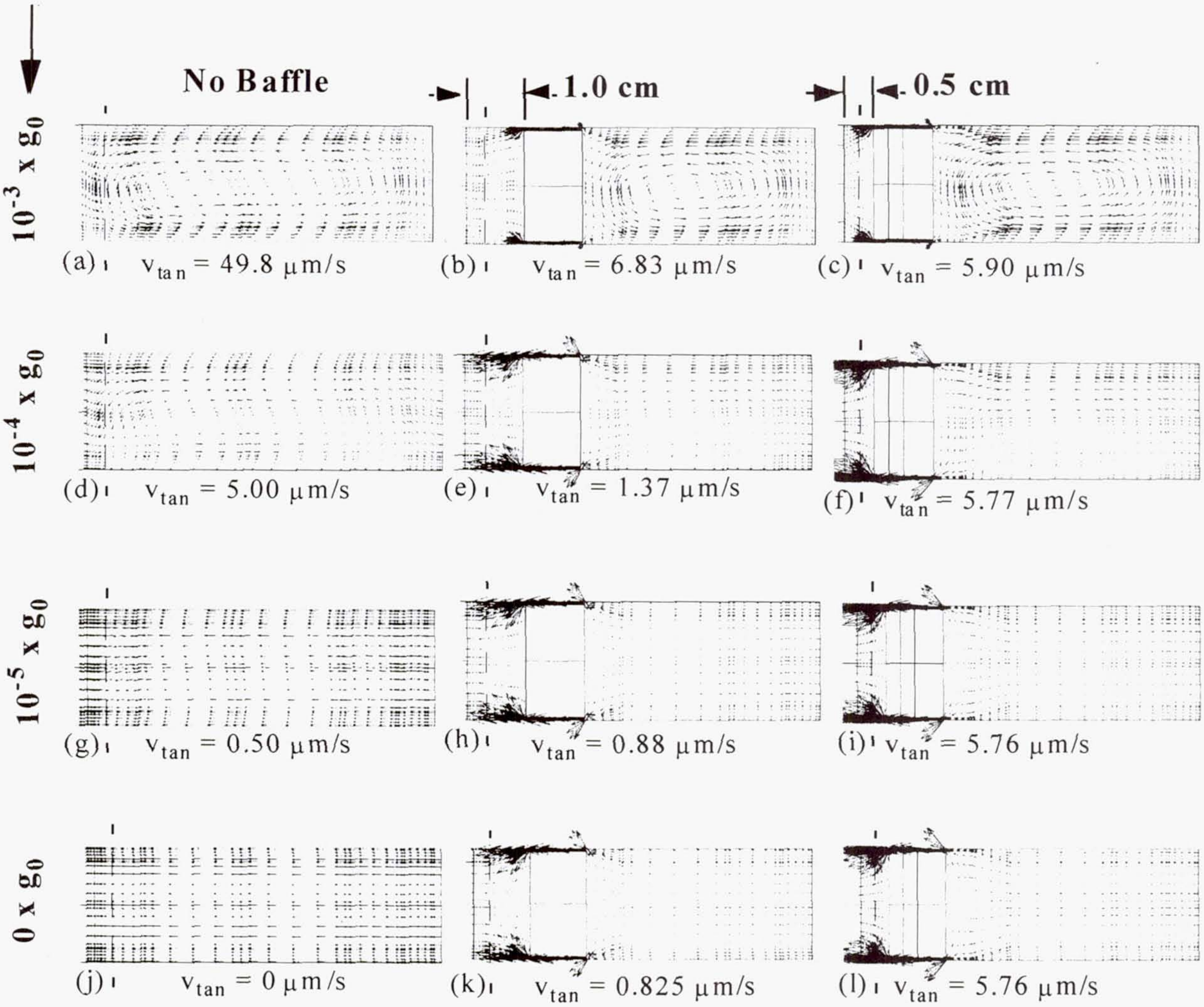

Fig. 3 Maximum tangential velocity at various levels of residual acceleration and baffle settings. v_{tan} is the highest value of velocity component parallel to and 0.25 cm from the interface. The flow at zero acceleration shows the limiting case of purely forced convection.

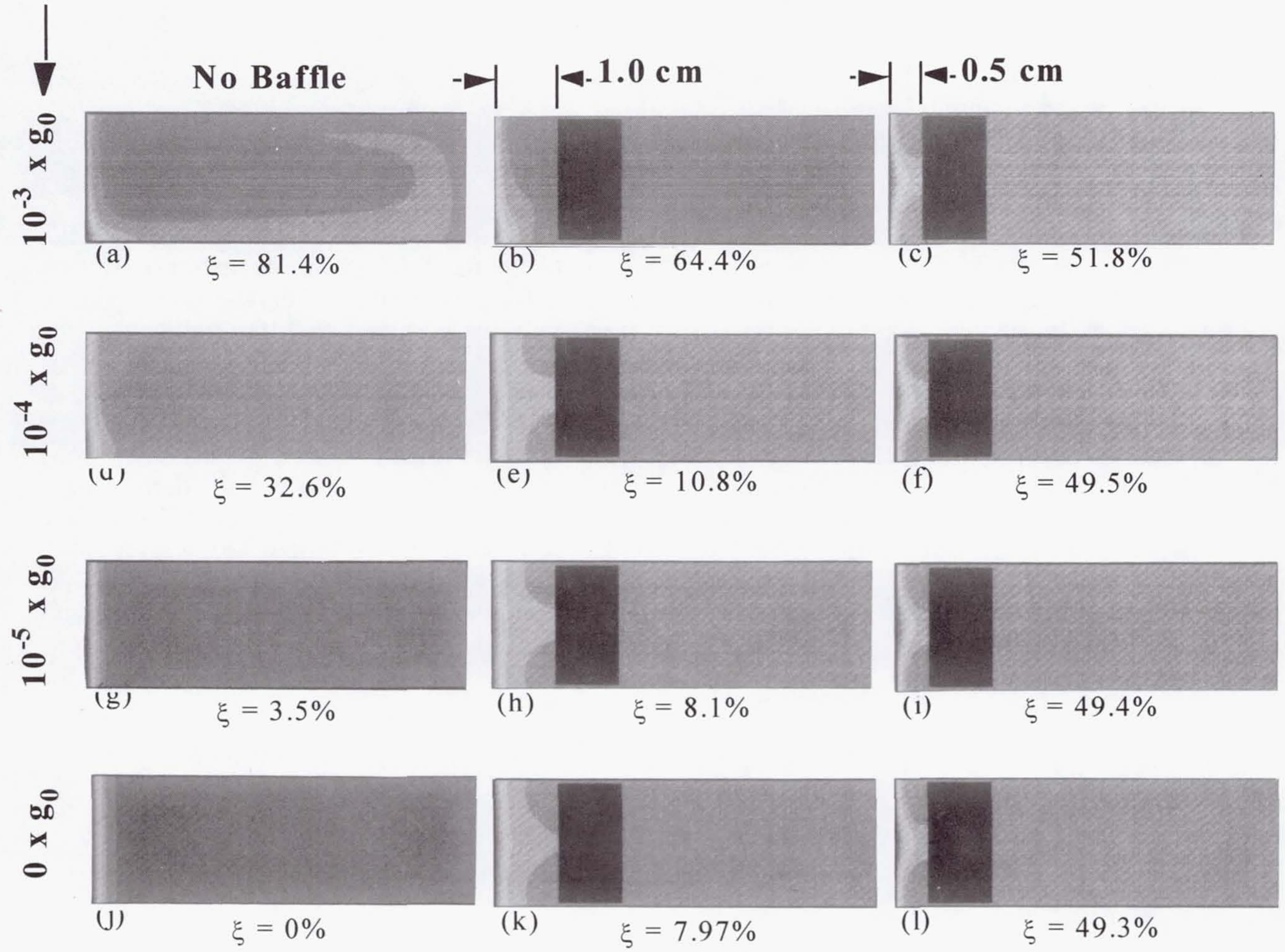

Fig. 4 Concentration field in the melt and radial segregation at the interface at various residual acceleration and baffle settings. $\xi=(C_{max}-C_{min})/C_{avg}$, all taken at the interface. The darkest shading at the interface represents the highest concentration. The segregation at zero acceleration shows the limiting case of purely forced convection.

5. Proposed flight experiments

The combined effect of microgravity and small zone melt (small L and ΔT) will generate the effective conditions of "nano-gravity" (the Rayleigh number is reduced by a factor of 10^9). The following systems will be studied: (a) Te-doped GaSb , (b) Te-doped $(GaSb)_{0.995}$ $(InSb)_{0.05}$; (c) Te-doped quasi binary $(GaSb)_{0.98}(InAs)_{0.02}$ and d) Ga-doped Ge. *The above systems were selected because of the difference in k, the growth rate R and the level of association/clustering in the solute layer which is related to* D_i.

6. Justification for the need for space environments

Space environment is needed to demonstrate that the composition of crystals grown with the submerged baffle is not altered by residual micro-acceleration. In ground-based experiments with the baffle, weak but still existing convection in the melt will alter crystal composition. The exact "reference" value of D_i measured in space, must be lower than the values that we obtained on earth.

7. Value of knowledge to scientific field

If the experiments yield the expected results, directional solidification with the baffle may become a preferred technique for crystal growth in space. The experiments will demonstrate that the baffle, without additional expense and drawbacks, will reduce the natural (i.e. free buoyancy-driven) convection in the melt to the point that it will not affect segregation. Furthermore, for the first time, we will measure precisely D_i at the growth interface, which is needed for interpretation of space experiments and modeling.

References:

[1] A.G. Ostrogorsky, J. Crystal Growth 104 (1990) 233.

[2] A.G. Ostrogorsky, F. Mosel and M.T. Schmidt, J. Crystal Growth 110 (1991) 950-954.

[3] A.G. Ostrogorsky and G. Müller, J. Crystal Growth 137 (1994) 64-71.

[4] P.S. Dutta and A.G. Ostrogorsky, J. Crystal Growth, in print.

[5] A.G. Ostrogorsky, Z. Dagojlovic, Proceedings of the Internat. Aerospace Congress, Moscow (1994).

[6] A.G. Ostrogorsky and G. Müller, J. Crystal Growth 121 (1992) 587-598.

[7] P.S. Dutta and A.G. Ostrogorsky, J. Crystal Growth, submitted.

[8] W.A. Tiller, K.A. Jackson, J.W. Rutter and B. Chalmers, Acta Metallurgica 1 (1953) 428.

[9] G. Müller, *12 Crystals, Growth, Properties and Applications,* Springer Verlag (1988).

[10] T. Duffar, C.E.A. - D.T.A. - C.E. R.E.M/3740, Report No. 15/95 Grenoble (1995)

[11] T. Duffar, personal communication; G. Müller-Vogt, ESA report.

[12] Dutta P.S., and Ostrogorsky, A.G., Patent Application pending (1998)

[13] Dutta P.S., and Ostrogorsky, J. Crystal Growth, in print (1998)

[14] Dutta P.S., and Ostrogorsky, J. Crystal Growth, submitted (1998)

[15] E. Bourret, J.J. Favier and O. Bourrel, J. Electrochem. Soc. 128 (1981) 2437.

[16] A.F. Witt, H.C. Gatos, M.Lichtensteiger, C.J. Hermn, J. Electrochem. Soc.125 (1978) 1832.

[17] F. Szofran, Personal Communication (1996 to 1998).

[18] D.H. Matthiesen, M.J. Wargo, S. Motakef, D.J. Carlson, J.S. Nakos and A.F. Witt, J. Crytsal Growth 85 (1987) 557.

Gravitational Effects On the Morphology and Kinetics of Photodepostion of Polydiacetylene Thin Films from Monomer Solutions

Mark S. Paley (USRA), PI
Basil Antar (UTSI), Co-I
William K. Witherow (MSFC), Co-I
Donald O. Frazier (MSFC), Co-I

Introduction and Objectives

The goal of this proposed work is to study gravitational effects on the photodeposition of polydiacetylene thin films from monomer solutions onto transparent substrates. Polydiacetylenes have been an extensively studied class of organic polymers because they exhibit many unusual and interesting properties, including electrical conductivity and optical nonlinearity. Their long polymeric chains render polydiacetylenes readily conducive to thin film formation, which is necessary for many applications. These applications require thin polydiacetylene films possessing uniform thicknesses, high purity, minimal inhomogeneities and defects (such as scattering centers), etc. Also, understanding and controlling the microstructure and morphology of the films is important for optimizing their electronic and optical properties. The lack of techniques for processing polydiacetylenes into such films has been the primary limitation to their commercial use.

We have recently discovered a novel method for the formation of polydiacetylene thin films using photo-deposition from monomer solutions onto tranparent substrates with UV light. This technique is very simple to carry out, and can yield films with superior quality to those produced by conventional methods. Furthermore, these films exhibit good third-order properties and are capable of waveguiding. We have been actively studying the chemistry of diacetylene polymerization in solution and the photo-deposition of polydiacetylene thin films from solution.

It is well-known that gravitational factors such as buoyancy-driven convection and sedimentation can affect chemical and mass transport processes in solution. One important aspect of polydiacetylene thin film photodeposition in solution, relevant to microgravity science, is that heat generated by absorption of UV radiation induces thermal density gradients that, under the influence of gravity, can cause fluid flows (buoyancy-driven convection). Additionally, changes in the chemical composition of the solution during polymerization may cause solutal convection. These fluid flows affect transport of material to and from the film surface and thereby affect the kinetics of the growth process. This manifests itself in the morphology of the resulting films; films grown under the influence of convection tend to have less uniform thicknesses, and can possess greater inhomogeneities and defects.

Specifically, polydiacetylene films photodeposited from solution, when viewed under a microscope, exhibit very small particles of solid polymer which get transported by convection from the bulk solution to the surface of the growing film and become embedded. Even when carried out under conditions designed to minimize unstable density gradients (i.e., irradiating the solution from the top), some fluid flow still takes place (particles remain present in the films). It is also possible that defect nulceation may be ocurring within the films or on the surface of the substrate; this, too, can be affected by convection (as is the case with crystal growth). Hence films grown in 1-g will, at best, still possess some defects. The objective of this proposal is to investigate, both in 1-g and in low-g, the effects of gravitational factors (primarily convection) on the dynamics of these processes, and on the quality, morphology, and properties of the films obtained.

Experimental Methods

The compound we have been investigating is a polydiacetylene derivative of 2-methyl-4-nitroaniline (MNA), a well-known organic nonlinear optical material. When a solution of the diacetylene monomer DAMNA in 1,2-dichloroethane is irradiated with longwave UV light through a transparent substrate, a thin polydiacetylene film (PDAMNA, see below) deposits on the surface of the substrate in contact with the solution.

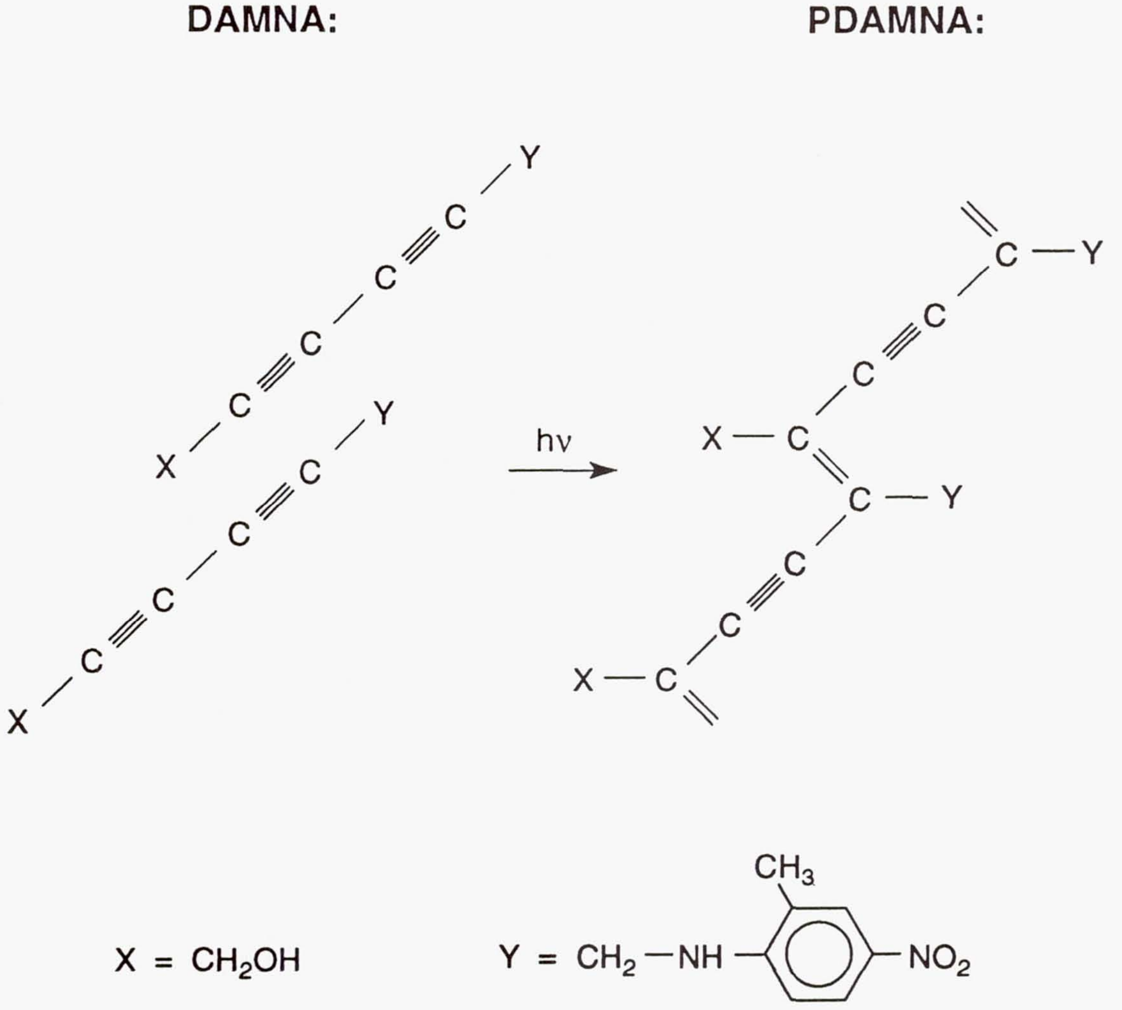

Studies on the effects of convection on photodeposition of PDAMNA films are proceeding on three fronts: numerical simulations of the fluid flow, experimental determination of the fluid flow, and in-situ spectroscopic ellipsometry studies of film deposition. Numerical simulations of the fluid flow are being conducted using FIDAP; the purpose of these studies is to ascertain the effects of variables such as cell geometry, orientation, light intensity, gravity, etc. on the pattern and intensity of the fluid flow. These studies are being complimented by experimental flow visualization studies using marker particles for simple cell geometries. Once the numerical simulations have been validated by the flow visualization studies; simulations can be performed with confidence for growth cell configurations where experimental determinations of the fluid flow are not possible.

Besides determining the fluid flow, we must also monitor film growth during PDAMNA film photodeposition in order to to discern how the fluid flow acually affects the deposition process. The technique we are employing is in-situ spectroscopic ellipsometry, which actually allows film growth to be monitored at the molecular level. Thus we should be able to observe how defects are formed in the films, whether they are transported from the bulk solution by convection, or nucleate within the film itself. We have designed and constructed a special cell for this purpose.

Preliminary Results

Kinetic studies on photodeposition of PDAMNA films from solution have shown that the rate of film growth is linear in light intensity and square root in monomer concentration. Furthermore under most growth conditions monomer is present in excess, and therefore the process is pseudo-zeroth order in concentration; i.e., the monomer concentration does not change appreciably. Thus we believe that the primary contributor to the fluid flow is thermal convection, and that solutal convection plays only a minor role. Hence at present we are only interested in studying thermal convection. Also, for the time being, we have chosen to ignore the effects of film growth on convection, the primary effect of which is to attenuate the UV light as the film thickness increases. The solution is heated via absorption of the UV radiation by the dissolved DAMNA molecules; both the solvent (1,2-dichloroethane) and the quartz cuvette are UV transparent. At the wavelength used (@366nm), it is the MNA portion of the DAMNA molecule that is responsible for the absorption, not the diacetylene. Thus we can use MNA as a model compound for DAMNA and thereby investigate thermal convection without the complication of film growth taking place. Typical monomer concentrations used for PDAMNA film photodeposition are on the order of 10^{-2} moles/liter, at these concentrations the absorption coefficient of the solution is on the order of $100 cm^{-1}$ (for both DAMNA and MNA). Because the minimum fluid element used in the numerical simulations is a cube with 0.17mm sides, this means that 99% of the radiative heating takes place within those fluid elements adjacent to the cell wall upon which the UV light is incident. Therefore in our numerical model we treat the heating of the solution as if it were being heated by a source located at the inside wall of the growth cell.

Numerical simulations of the buoyancy-driven fluid flow have been conducted for a rectangular quartz cell with dimensions 1cm x 1cm x 4cm height containing a 10^{-2} mole/liter MNA solution in dichloroethane, with a circular UV beam 5mm in diameter incident upon either a vertical face or the top face of the cell. The calculations considered the beam to be centered on the appropriate face. Computations were performed for a range of beam intensities ranging from 0.25 Watt to 4.0 Watts total power, assumed to be uniformly distributed over the 5mm UV beam. The boundary and initial conditions used were appropriate for a system is at ambient temperature in which the walls of the cell are maintained at ambient temperature throughout the run. Because the solution is dilute, the thermodynamic parameters; i.e., heat capacity, thermal expansivity, kinematic viscosity, and thermal conductivity, for the MNA solution are taken to essentially be the same as those for the pure solvent, 1,2-dichloroethane. The values of these parameters were obtained from the literature. The resulting temperature and velocity fields are obtained through numerical solution to the conservation equations for fluid dynamics. The numerical code used employs the finite element approximation for solving the equations of motion. Figure 1 shows typical flow patterns and isotherms for the two heating modes; i.e., from the top and side of the cell. Also shown in Fig. 1 is the meshing employed in the numerical computations for each heating mode.

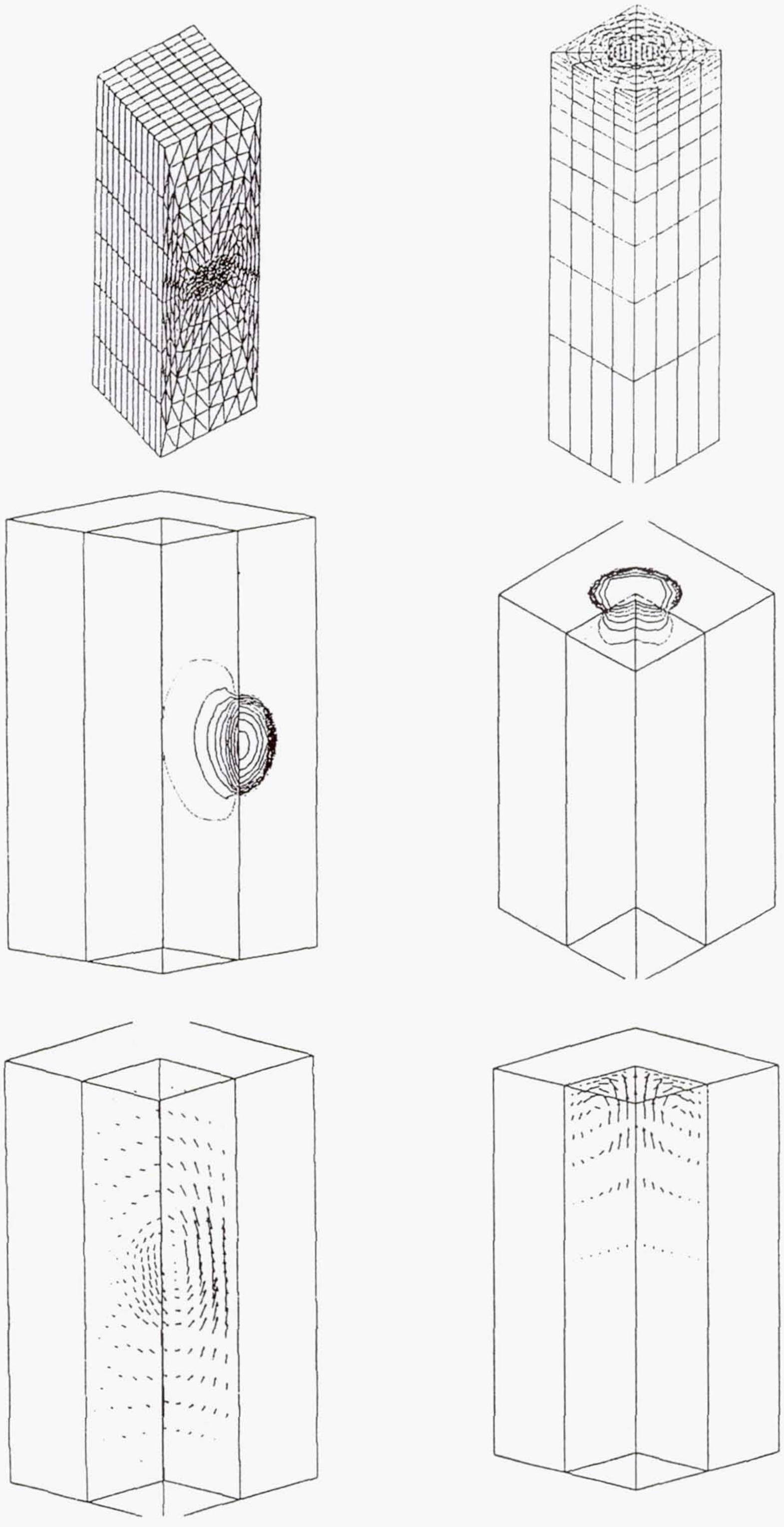

(a) (b)

Figure 1. The meshing used, the isotherms and the fluid velocity vectors for (a) side heating, and (b) top heating.

Experimental studies of the fluid flow are being conducted under the conditions described in the preceeding paragraph using poly(methacrylic acid) powder as marker particles. The flow pattern and velocities observed are in good qualitative agreement with the calculations; however, the magnitude of the experimental flow velocities (on the order of 10^{-1} cm/s) appears to be about a factor of 10 greater than the calculated velocities. We are currently in the process of finding the cause of this discrepancy, which we suspect is the manner in which the parameters were input into the code.

Preliminary measurements on PDAMNA film photodeposition using real-time in-situ spectroscopic ellipsometry have just begun using a spectroscopic ellipsometer coupled with an optical multichannel analyzer. A special cell was constructed for the purpose of studying PDAMNA film growth; the films are being grown onto glass substrates coated with a 5nm thick layer of gold. The gold is necessary in order to obtain reliable data because PDAMNA is a dielectric material; the coating is sufficiently thin that UV light can still penetrate into the solution and induce film growth. In the future the instrument configuration will be changed so that a compensator can be used, which should allow good data to be obtained without the gold coating. Also, in order to interpret the ellipsometry data, the optical constants of PDAMNA, specifically, the refractive index and the extinction coefficient, must be determined as a function of wavelength. Thus films of PDAMNA were grown on glass at several thicknesses and spectroellipsograms were obtained to determine these constants (assuming that the optical properties do not vary with thickness, which is expected to be the case).

Real-time in-situ spectroellipsograms were measured at various time intervals up to approximately 2 hours of film growth. Because of partial attenuation of the UV light by the gold, the rate of growth is quite slow. In order to determine the film thickness and/or void volume fraction, simulation of the experimental spectroellipsograms is attempted based on the optical constants of PDAMNA. These simulations are just now underway and results will be forthcoming.

Page intentionally left blank

INVESTIGATION OF CRYSTAL GROWTH OF TERNARY II-VI AND IV-VI COMPOUNDS BY PHYSICAL VAPOR TRANSPORT ("Investigation of 'Contactless' Crystal Growth by Physical Vapor Transport" and "Investigation of Convective Effects in Crystal Growth by Physical Vapor Transport")

W. Palosz

Space Sciences Laboratory, ES75, Universities Space Research Association, NASA Marshall Space Flight Center, Huntsville, AL 35812 (256) 544-1272, Witold Palosz@msfc.nasa.gov

Introduction

The subject of the research is to investigate the process of crystal growth by Physical Vapor Transport of binary and ternary/doped II-VI and IV-VI materials. Our past efforts were focused on the following specific tasks: (1) investigation of the mass transport properties of Pb(Se, Te) by Physical Vapor Transport (PVT), (2) determination of the origin and magnitude of residual gases in crystal growth systems, (3) numerical modeling of thermal field in 'contactless' PVT (cPVT) configuration, and (4) characterization of crystals grown by cPVT technique. The investigation of PVT of Pb(Se, Te) lead to identification of some specific features of this crystal growth system which may be promising both for the material applications and for microgravity research. As a part of this study, an investigation of residual gases in sealed silica glass ampoules was conducted. The relevance of this study goes beyond Pb(Se, Te) or even PVT crystal growth technique, as a presence of residual gases has an apparent effect on phenomena occuring in other important crystal growth systems (formation of voids[1], detached solidification[2]). Numerical modeling of cPVT was performed in order to better understand cPVT and to assess the relative importance of different experimental factors on the process. Crystal characterization done in this work showed the benefits of cPVT as a valuable crystal growth technique.

Physical vapor transport of Pb(Se, Te)

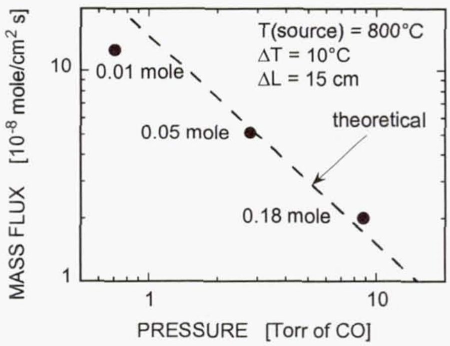

Fig. 1 Mass flux of PbTe as a function of inert gas pressure.

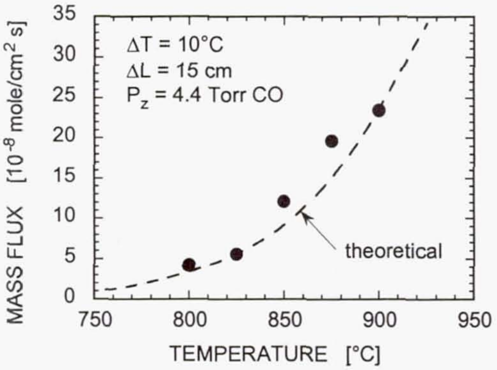

Fig. 2 Mass flux of PbTe as a function of the source temperature.

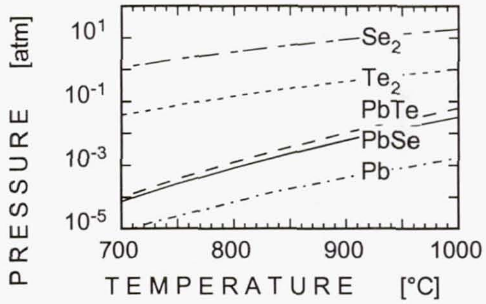

Fig. 3 Saturation pressures of PbTe, PbSe, and their components.

A number of growth experiments were performed and the mass transport rate and composition and composition distribution in the grown crystals were determined. The effect of the material preparation procedures (purification, stoichiometry adjustment, source density/compactness), thermal conditions (temperature and undercooling), inert gas pressure, and source composition on the process were determined. Theoretical thermochemical model of the system was developed and the predictions of the model were compared with the experimental results. Based on thermochemical data, the model assumes that the chalcogenides sublime molecularly and congruently, and that mass transport (crystal growth) rate is limited by diffusion. The experimental and theoretical mass transport/growth rate of PbTe as a function of the inert (residual) gas pressure and of the source temperature are shown in Figs. 1 and 2, respectively. Very good agreement obtained between the predicted and actual growth rates confirms the validity of the model and of the thermochemical and physical data used for the calculations. Equilibrium pressures of PbTe, PbSe, and their components are shown in Fig. 3. In the temperature range suitable for crystal growth (700 - 900°C), the saturation pressures of the chalcogenides differ by less than a factor of two (Fig. 3). Saturation pressures of selenium and tellurium are considerably higher than those of the chalcogenides, thus an excess of any of the chalcogens in the experimental ampoule may seriously reduce the growth rate. Saturation pressure of lead is lower than that of the chalcogenides, so even a presence of a Pb-rich phase would cause only a limited reduction of the mass transport rate in the system. Therefore, a small excess of lead in the original source material could be used to prevent a presence of excess chalcogen(s) in the ampoule and improve reproducibility of the growth conditions. Relatively small difference between saturation pressures of PbTe and PbSe suggests, that the effect of non-congruent sublimation of lead telluride-selenide on mass transport rate and on composition non-homogeneity of the crystal may be limited. Figs. 4 and 5 show the theoretically predicted dependence of the mass flux and of the crystal composition, respectively, on the source composition. The calculations were made under two alternate assumptions: ideal solid solution, and non-ideal solid solution taking activity coefficients after Sokolov[3]. As follows from Fig. 4, non-congruency of sublimation of $PbTe_{1-X}Se_X$ has only limited effect on the growth rate, what is consistent with our experimental results. The composition of the deposited material is dependent on the activity coefficients of PbTe and PbSe in the source (Fig. 5). Assuming ideal solution (activity coefficients equal unity, dashed line in Fig. 5) the deposit is always enriched in PbTe relative to the source, thus the PbSe content in the crystal is initially lower than that in the starting material, and increases as the growth proceeds. Assuming non-ideal solution conditions, the deposit is expected to be PbSe-richer at lower, and PbTe-richer (relative to the source) at higher X values, depositing with the same composition at X = 0.33 (solid line in Fig. 5). Experimental results shown in Fig. 6 confirm, that non-ideality of the $PbTe_{1-X}Se_X$ solution has the expected effect on the compositional non-homogeneity of the grown material: for low PbSe content source (X = 0.1) the initial PbSe concentration in the crystal is above 10% and decreases as the growth proceeds, while the opposite occurs for the initial source composition of X = 0.5. Our experiments showed, that homogeneity of most of the crystal at source compositions other than about X = 0.33 can be improved by using a compact (pre-melted) source: limiting the sublimation surface of the source to the cross-section area of the ampoule (as opposed to a much larger surface available for sublimation when powdered source is used) increases the surface

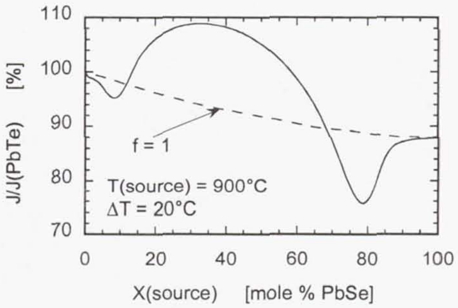

Fig. 4 Theoretical dependence of the relative mass flux on the source composition.

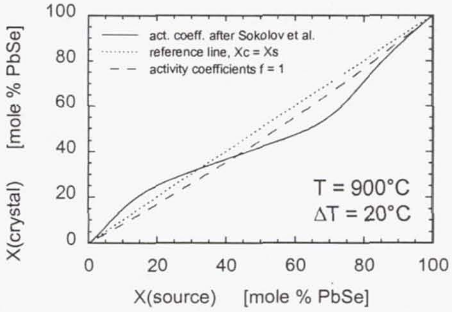

Fig. 5 Theoretical dependence of the crystal composition on the source composition.

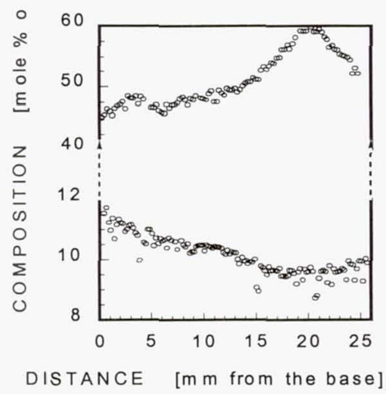

Fig. 6 Axial composition profiles. T(source) = 850°C, ΔT = 10°C, powder source.

concentration of the less volatile component of the source (PbSe) and, thus, compensates for its relatively lower partial pressure at the crystal-vapor interface. Improved homogeneity of crystals grown under such conditions is shown in Fig. 7.

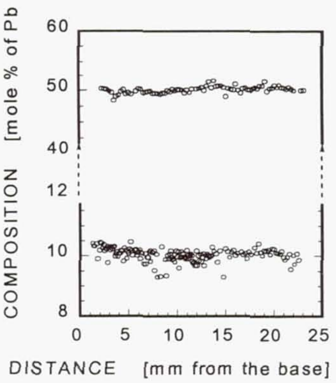

Fig. 7 Axial composition profiles. T(source) = 850°C, ΔT = 10°C, compact source.

Inert/residual gases in sealed silica glass ampoules

The gases present in sealed systems may come from the ampoule material, from the source, or from the outside of the ampoule. In addition, a diffusion through the walls of the ampoule can change the pressure and composition in the system during the course of the process. We have investigated all the above phenomena. A typical development of residual gas originating from the walls of silica glass ampoule outgassed at room temperature is shown in Fig. 8a. At high temperatures the gas, primarily hydrogen, can built up a pressure of more than 10 Torr. The amount of gas desorbed from the glass can be substantially reduced by an extensive outgassing of the ampoule at high temperature under dynamic vacuum (Fig. 8b). A major source of residual gas is the source material itself. The experimental results shown in Fig. 1 were obtained using different amounts of the source. A direct relation between the amount of the source and the residual gas pressure in the ampoules apparently exists (Fig. 1). It can also be seen, that the pressure formed in those ampoules (which were outgassed at high

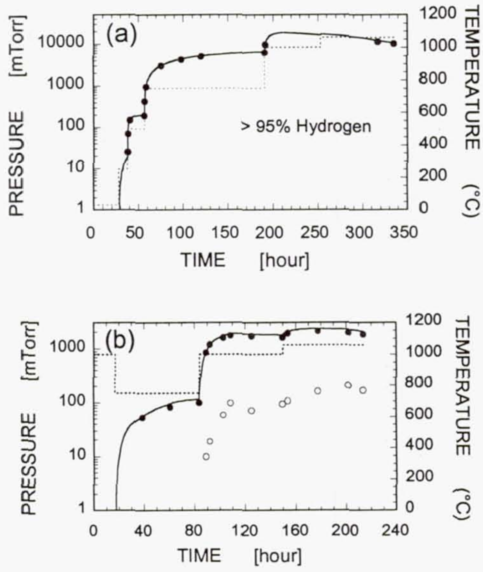

Fig. 8 Dependence of the pressure and composition of the gas accumulated in silica glass ampoule on time and temperature. A/V = 1.0. Solid circles - hydrogen, open circles - water. (a), ampoule outgassed at RT; (b), ampoule outgassed at 1000°C.

temperature under dynamic vacuum prior to loading with the source) is considerably higher than that build in empty ampoules under similar conditions (Figs. 1 and 8b). The gas generated by the source consists mostly of carbon oxides, sometimes also water, the actual composition depending primarily on the amount of residual oxide impurities in the material. The effect of diffusion through the ampoule wall is shown in Fig. 9, where $\tau_{1/2}$ is the time after which the pressure difference of a given species between the inside and outside of the ampoule decreases by ½. (The rate of the pressure change depends on the ampoule parameters: volume V, surface A, and wall thickness d[4].) As follows from Fig. 9, a substantial pressure change with time inside silica glass ampoules can occur, particularly for lighter gases (He, H_2) and higher temperatures.

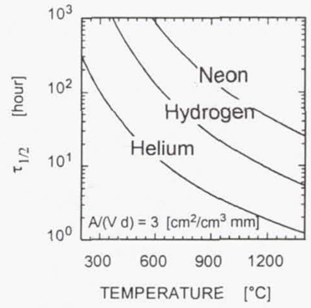

Fig. 9 Dependence of the half-time on temperature.

Numerical modeling of thermal field in 'contactless' PVT

Schematic representation of cPVT crystal growth ampoule geometry is shown in Fig. 10. Under proper conditions, most of the subliming source material deposits on the pedestal in the middle (crystal), while some of the vapors pass through the slit to the coolest (far left) end of the ampoule (deposit, Fig. 10). Maintaining the slit between the crystal/pedestal and the ampoule wall open requires the thermal conditions such, that the vapors are not supersaturated in these locations. This is conditioned primarily by the thermal field in the slit. Our simulations show, that the critical locations for supersaturation (and, thus, nucleation) are the side of the crystal/pedestal, and the inner ampoule wall surfaces in the slit, represented in Fig. 10 by lines b and c, respectively. We have analized the dependence of the temperature along those lines and their relation to the T* function in the slit (where T* is the saturation temperature of the species (PbTe, Cd+Te_2) under growth conditions) as a function of different parameters of the growth system. The results show where a parasitic nucleation can occur (the actual temperature being lower than T*). Also, they show where deposition on the wall and not on the crystal takes place (the temperature of the ampoule wall being lower than that of the adjacent crystal). An example of the temperature profile obtained numerically is given in Fig. 11. Extensive parametric studies of the system lead

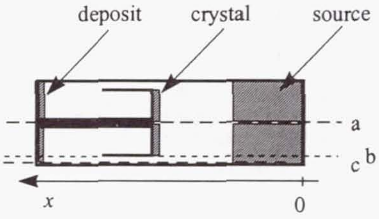

Fig. 10 Geometry of cPVT ampoule.

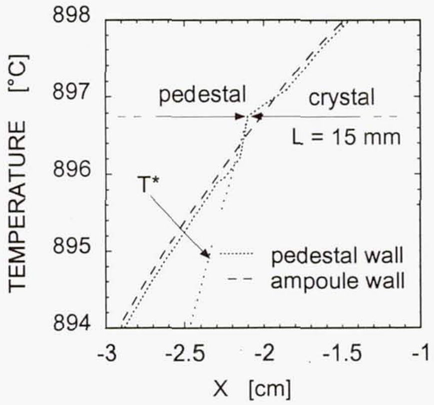

Fig. 11 Temperature profiles and saturation temperature profile in the slit.

to the following major conclusions: (1), the location prone to parasitic nucleation is in the slit just below the junction of the crystal with the pedestal, the supersaturation at that location increases with an increase in (i) the ampoule diameter, (ii) thickness of the top of the pedestal, (iii) length of the crystal, (iv) temperature gradient in the furnace, and with a decrease in thermal conductivity of the crystal; (2) preferential deposition on the ampoule wall and not on the crystal may be expected for smaller diameter crystals and a solid (as opposed to a cup shaped) pedestal.

Crystal characterization

Crystals grown by cPVT technique have been characterized using Synchrotron White Beam X-ray Topography, microprobe, chemical etching, and other techniques. It was found, that compositional non-homogeneity of the crystal and its interaction with silica glass (the growth pedestal) create a strain field in the crystal. The strain field around some precipitates was found to propagate to a distance up to three orders of magnitude larger than the size of the precipitate itself[5]. Distribution of dislocations (etch pits) was found to be dependent on the post-growth cooling rate, a tendency to polygonisation and even formation of low angle grain boundaries was found in crystals cooled-down over an extended period of time[6].

References

1. A. L. Fripp, W. J. Debnam, W. R. Rosch, and R. Narayanan, "The Effect of Microgravity Direction on the Growth of PbSnTe", http://dragon.larc.nasa.gov/microg/usmp3.html.
2. D. I. Popov, L. L. Regel, and W. R. Wilcox, J. Mater. Synthesis and Processing, 5 (1997) 283.
3. V. V. Sokolov, V. A. Dolgikh, A. S. Pashinkin, And A. V. Novoselova, Inorg. Mat. 5 (1969) 232. 32.
4. W. Palosz, J. Crystal Growth, in press.
5. W. Palosz, D. Gillies, K. Grasza, H. Chung, B. Raghothamachar, and M. Dudley, J. Crystal Growth 182 (1997) 37.
6. W. Palosz, M. A. George, E. E. Collins, K.-T. Chen, Y. Zhang, Z. Hu, and A. Burger, J. Crystal Growth 174 (1997) 733.

ANALYSIS OF CONTAINERLESS PROCESSING AND SOLIDIFICATION MICROSTRUCTURES

J.H. Perepezko, University of Wisconsin-Madison, 1509 University Avenue, Madison, WI 53706
phone: (608) 263-1678; e-mail: perepezk@nucleus.msae.wisc.edu

Objective and Application to Microgravity Knowledge Base

The main research objective is the evaluation and analysis of the undercooling and resultant solidification microstructures after containerless processing, including drop tube processing and levitation melt processing of selected alloys. The results are intended for use as an experience base for the design of future space-based microgravity experiments.

Containerless solidification processing of materials in space requires an understanding of the critical variables affecting solidification. Perhaps the most fundamental parameter in solidification processing is the level of melt undercooling prior to solidification. The containerless environment removes a major source of impurities and heterogeneous nucleation sites, allowing for a large melt undercooling. Containerless processing in ground-based drop tubes simulates the microgravity conditions via solidification of liquid droplets under free fall conditions. The enhanced liquid undercooling exposes alternate solidification pathways, allowing for the formation of novel phases and microstructures. Controlling the undercooling level provides some control of the operative solidification pathway and the resultant microstructure. The results of the ground based drop tube study are being used to identify critical processing variables and possible product phases in microgravity studies, and the analysis may be used to design and predict the science requirements for space experiments.

Research Task Description and Progress to Date

The program consists of ground based experimental studies which involve drop tube and levitation containerless processing methods in combination with detailed microstructural analyses and thermodynamic and kinetic modeling. The focus of the investigation is on the understanding and analysis of microstructural evolution during solidification of undercooled melts. The degree of liquid undercooling attainable in a laboratory scale (3 m) drop tube and levitation melting system can be altered through the variation of processing parameters such as alloy composition, melt superheat, sample size and gas environment. Rapid quenching methods are employed in order to preserve the solidifying structure for microstructural analyses. The solidification behavior is evaluated through optical metallography, SEM, TEM, thermal analysis and X-ray diffraction in conjunction with calorimetric measurements of falling droplets and a heat flow model of the processing conditions to judge the sample thermal history.

The analysis of microstructural development requires an analysis of the kinetic competition between the possible phases and structure morphologies. The classification of these kinetic transitions has been discussed previously [1-6]. Examples include the transition from growth- to nucleation-controlled microstructure development in laser-processed Al-Si alloys [3,5] and the formation of the metastable, ferromagnetic τ phase in the Mn-Al system during drop tube processing. Recently, multiple partitionlessly solidified phases have been identified in deeply undercooled Ni-V alloys [2,7]. Samples, resulting from this unexpected phase nucleation and growth behavior have been subjected to detailed microstructure analyses in order to contribute to an understanding of this novel microstructural class. Additionally, a series of experiments has been started on the similar alloy systems Co-Al and Nb-Pd.

Multiphase Partitionless Solidification

One of the main components of the current investigation is the focus on new directions for the control of microstructural evolution in shallow eutectic systems such as Ni-V and Co-Al through the high undercooling levels provided by containerless processing. In cooperation with Dr. D.M. Herlach (DLR, Cologne, Germany) bulk melts of $Ni_{100-x}V_x$ alloys were undercooled by applying an electromagnetic levitation technique. In the composition range 41-73 at.% V 15 alloys of different compositions were processed at slow cooling rates (dT/dt~10 K/s). Undercoolings up to 330 K have been achieved. Contactless temperature measurements were utilized to determine quantitatively the undercoolings prior to solidification and in combination with a fast electronic data requisition to record time resolved recalescence profiles. Analysis of multiple recalescence behavior (Fig. 1-a) allows for the assignment of primary phase identification and insight into the competition sequencing during overall solidification.

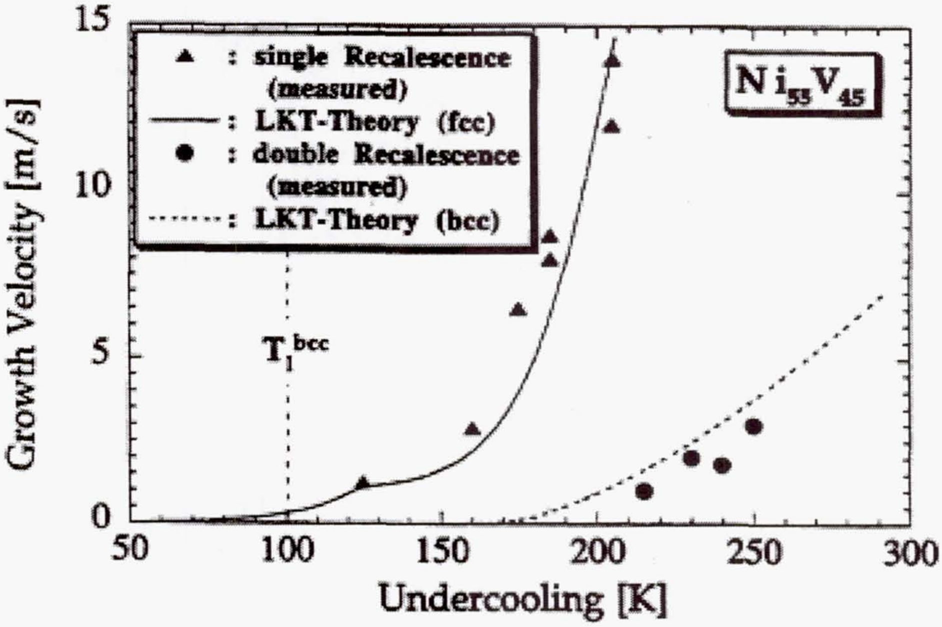

Fig. 1-a: Dendrite growth velocities as a function of undercooling (fcc stable, bcc metastable)The triangles give the growth velocity of the stable phase (fcc) while the dots represent the the growth velocities of the metastable phase (bcc). The liquidus temperature of the metastable phase is indicated by the dashed line.

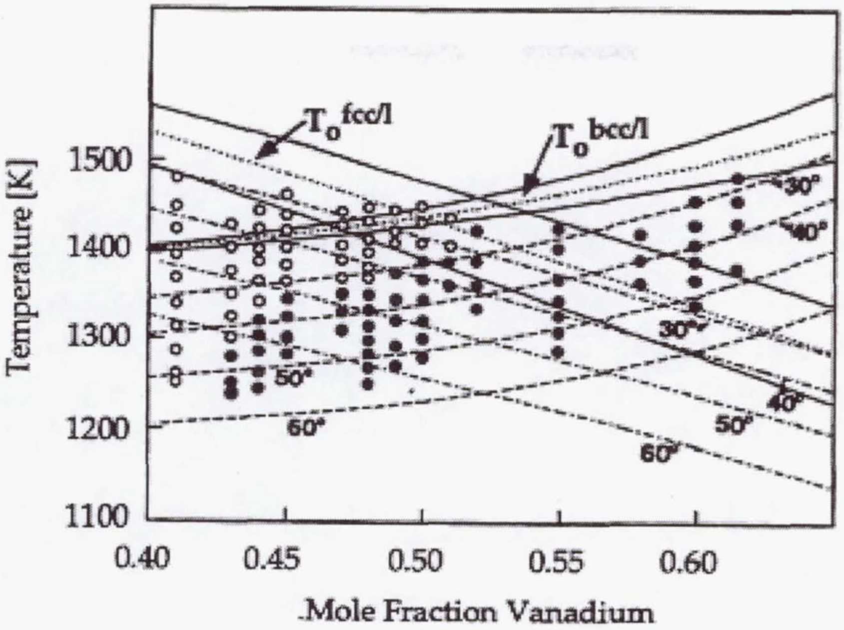

Fig. 1-b: Metastable Ni-V phase diagram including the fcc, bcc and the liquid (l) phases. The solidus and liquidus curves are represented by the solid lines and the T_0 curves are represented by dotted lines. The calculated nucleation temperatures are shown for four different contact angles (30°, 40°, 50° and 60°) for fcc (dash-dot lines) and bcc (dashed lines). The kinetics analysis indicates a transition from fcc to bcc primary solidification at a nearly constant undercooling for $\Theta_{bcc} = 30°$.

These measurements, in turn, provided information on metastable phase formation and crystal growth behavior as a function of undercooling of the alloys investigated. The comprehension of all results leads to the construction of a metastable phase diagram of Ni-V (Fig. 1-b) which describes the formation of different phases, stable or metastable, as a function of the concentration and, in addition, with the undercooling as a second "process" parameter.

SEM and TEM analyses on deeply undercooled and rapidly quenched Co-Al samples showed a complex and sensitive dependence of the phase selection sequence on the thermal history as expected for a system near a transition in kinetic competition. Figure 2 shows microstructures of Co-18.5Al which have been obtained by rapid-quenching techniques. It has been found that both the melt undercooling and the applied cooling rate in the liquid and solid states are important in developing a microstructural analysis.

Therefore the extension of the analysis of two-phase partitionless structures to similar systems can reveal new fundamental information about the nucleation and growth kinetics of competing phases and contribute to an understanding of this novel microstructural class and the key processing parameters. In the Co-Al system phase selection is being studied in both large (mm size) and small (μm size) droplets. The nucleation kinetics for the competing fcc, Co and B2 CoAl phases are being analyzed to determine the conditions needed to produce a two-phase partitionless structure. Moreover, the analysis approach will be developed further to allow for the construction of a processing map that will be essential in the design of a space experiment. This investigation will contribute to the understanding of terrestrial solidification processing and will demonstrate that microgravity materials processing can yield novel microstructures and phases that have not been observed previously with conventional terrestrial processing approaches.

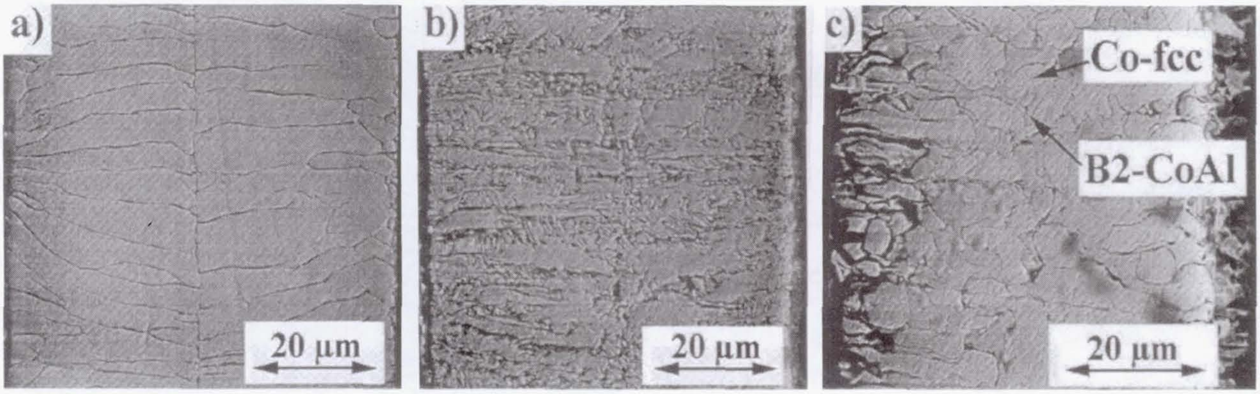

Fig. 2: SEM cross section image of the microstructure in different areas of a Co-18.5Al foil: a) CoAl-B2-area, b) B2/fcc-area, c) Co-fcc area with B2 matrix of different composition. Note that all the phases shown in a) and b) are partitionless.

Solidification of Metal-Matrix-Composites

Another central issue of the proposed program is a critical evaluation of the interaction between the crystallization front and foreign particles during the solidification of liquid undercooled metal-matrix composites. Numerous models for the interaction behavior have been proposed, but critical tests are lacking in many cases due to confounding gravitational effects such as convective flow and particle settling. In order to identify the key influence factors, a novel experimental design based upon an undercooled melt with particles has been realized to distinguish particle incorporation effectiveness as a function of interface velocity in the presence of a distribution of particle sizes.

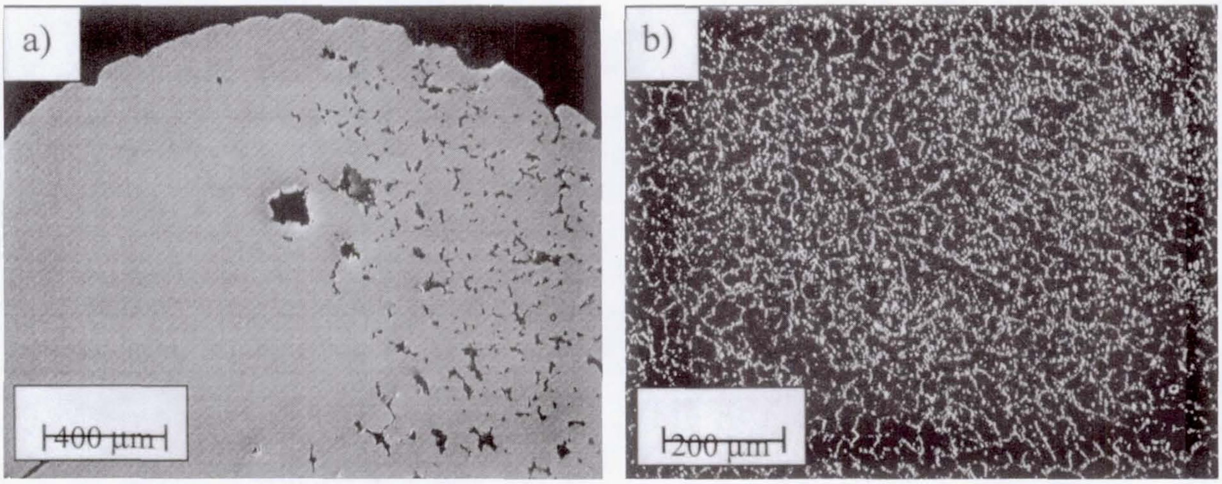

Fig. 3: The unetched microstructures of Ni-10% Ta_2O_5 samples, which undercooled a) by 37 K and b) by 194 K.

This experimental strategy allows for an assessment of various models and governing conditions that have been proposed for particle incorporation and, moreover, provides experimental experience for the incorporation behavior during multidirectional solidification.

Composites of nickel or copper with discontinuous reinforcement particles of aluminum oxide or tantalum oxide have been identified as model systems to study the incorporation behavior. In the case of Ni-Ta_2O_5, the undercooling level can exceed 200 K.

Thus, undercooling can be used effectively as a tool for controlling the rate of solidification. Additionally, the high density of tantalum oxide results in only minor buoyancy forces on the dispersed particles. Initial microstructural analyses on samples which solidified at variable levels of undercooling show a transition from particle pushing at low solidification rates to particle engulfment resulting in a homogeneous particle distribution at high growth velocities [11] (Fig. 3). Models, which predict the capability for incorporation on the basis of the ratio of thermophysical properties fail to describe such a transition and, moreover, predict pushing for all composites studied during this work. However, the experimental results are in qualitative agreement with the interaction models that predict a critical interface velocity. Yet, the quantitative comparison between the calculated critical velocities and experimental values for the pure melts indicates a large disagreement: The predicted values are about three orders of magnitude too low. But, the comparison is based on the growth velocity of the pure metallic melts. In fact, the *effective* growth velocity should be reduced due to the increased viscosity of a melt containing solid particles. Investigations on the direct measurement of the actual growth velocities of the melts with incorporated particles is in progress. Such data has not been measured up to now, but is critical for a reliable modeling of the interaction.

The theoretical treatment of the incorporation of inert particles into a solidifying melt was mostly carried out under the idealized assumptions of a planar interface interacting with perfectly smooth, spherical particles. Up to now it is not clear, if the predictions that were developed under these constraints also hold for the incorporation of irregularly shaped particles by fast growing dendrites. In order to examine the influence of the particle shape, alumina particles have been melted and solidified during free-fall in the drop tube. Thus, spherical particles have been obtained which afterwards have been used as reinforcement. Initial experiments on the Cu-Al_2O_3 system have indicated, that these particles would require even a higher growth velocity of the matrix to be engulfed. Similar experiments on the Ni-Ta_2O_5 system, where the engulfment transition has been observed on deeply undercooled samples, are underway to determine the shape dependence of the incorporation behavior more quantitatively.

Additionally, alloying of e.g. Cu with Ni (or Fe, Co) can provide a means to adjust the density of the melt such that it is equal to the density of the particles. Solidification experiments under microgravity conditions on these composites and on composites where matrix and particles have considerably different densities can be carried out to test for the influence of convective flow inside the samples on the resulting microstructure. Recent results on the incorporation behavior during dendritic solidification indicate that geometrical factors of the interface (i.e. the dendrite tip radius and the secondary arm spacing) and their dependence on temperature are important for the ability to engulf the reinforcement particles [11]. These parameters are being considered currently in a theoretical description of the incorporation process that is intended to provide a guideline for space-based studies on metal-matrix composites.

Reliable evaluation of thermal history during containerless processing is central to the proper interpretation of a solidification microstructure. In the intended studies thermal measurement of a falling droplet will be conducted using a calorimetric method. A direct thermal history capability is currently being installed as an extension to the drop tube facility. These investigations will provide a test of the solidification and heat flow models that were developed to yield insight into the mechanisms of solidification microstructure development.

Publications and Presentations*

[1] "Kinetic Competition in Undercooled Liquid Alloys", J.H. Perepezko and D.R. Allen, Mat. Res. Soc. Symp. Proc., 398, 3 (1996).

[2] "Kinetic Competition During Duplex Partitionless Solidification in Ni-V Alloys", D.R. Allen and J.H. Perepezko, Mat. Res. Soc. Symp. Proc., 398, 57 (1996).

[3] "The Development of Nucleation Controlled Microstructures During Laser Treatment of Al-Si Alloys", M. Gremaund, D.R. Allen, M. Rappaz and J.H. Perepezko, Acta Mat., 44, 2669 (1996).

[4] "Phase Selection Processes in Undercooled Ni-V Melts", J. Schroers, T. Volkmann, D. Herlach, D.R. Allen and J.H. Perepezko, Int. Jnl. Rapid Solidification , 9, 267 (1996).

[5] "Nucleation Controlled Microstructural Development in Al-Si Alloys", D.R. Allen, M. Gremaud and J.H. Perepezko, Mat. Sci. and Eng.A, 226-228,173 (1997).

[6] "Kinetic Processes in Undercooled Melts", J.H. Perepezko, Mat. Sci and Eng. A, 226-228, 374 (1997).

[7] "Two Phase Partitionless Solidification of Ni-V Alloys", D.R. Allen, H. Sieber and J.H. Perepezko, Solidification Processing 1997, Eds. J. Beech and H. Jones (Dept. Engr. Mats., Univ. of Sheffield, UK) 511 (1997).

[8] "TEM Study of the Multiple Phase Partitionless Microstructure Evolution in Rapidly Solidified Ni-V and Co-Al Alloys", H. Sieber, D.R. Allen and J.H. Perepezko, Solidification-98 Eds. S.P.Marsh, J.A.Dantzig, R.Trivedi, W.Hofmeister, M.G.Chu, E.J.Lavernia and J.-H.Chun (TMS, Warrendale, PA) 15 (1998).

[9] "Heterogeneous Nucleation During Solidification of Droplets", P.G. Höckel, H. Sieber,and J.H. Perepezko,Solidification-98 Eds.S.P.Marsh, J.A.Dantzig, R.Trivedi, W.Hofmeister, M.G.Chu, E.J.Lavernia and J.-H.Chun (TMS, Warrendale, PA) 289(!998). (TMS, Warrendale,PA) 289 (1998).

[10] "Alloy Metastability During Nucleation Controlled Reactions", J.H. Perepezko and G.Wilde, Berichte der Bunsengesellschaft fuer Physikalische Chemie 8, (1998), in press

[11] "Particle-Dendrite Interactions during Undercooled Liquid Solidification of Metal-Matrix Composites", G. Wilde, M. Byrnes and J.H. Perepezko, 10th International Conference. on Liquid and Amorphous Materials (LAM 10), Dortmund, Germany (1998), accepted.

*Publications (1,2,5-11) were also given as conference presentations.

Page intentionally left blank

COMPARISON OF STRUCTURE AND SEGREGATION IN ALLOYS DIRECTIONALLY SOLIDIFIED IN TERRESTRIAL AND MICROGRAVITY ENVIRONMENTS

D.R. Poirier, Principal Investigator, The Department of Materials Science and Engineering, The University of Arizona, Tucson, AZ 85721. Phone (520) 621-6072; FAX (520) 621-8059; poirierd@u.arizona.edu; S.N. Tewari, Co-Investigator, Chemical Engineering Department, Cleveland State University; and J.C. Heinrich, Co-Investigator, The Department of Aerospace and Mechanical Engineering, The University of Arizona

Introduction

The grant is a Flight Definition Program, so efforts have been on establishing the science base for directional solidification in low gravity. The primary purpose is to compare the structure and segregation in a binary alloy that is directionally solidified in terrestrial and low gravity environments. Models of dendritic solidification that are used to predict microstructural features upon solidification rely on the assumption of only diffusional transports. However, the thermosolutal convection masks the diffusional processes at the dendrite tips and is also responsible for macrosegregation in directionally solidified castings. Availability of microgravity provides an opportunity to obtain experimental data, where thermosolutal convection and attendant macrosegregation are negligible.

Objectives

This is a program to conduct experiments in a long-duration microgravity environment, with the objective of studying dendritic microstructures and segregation in directionally solidified dendritic alloys. The research is based on directionally solidified Pb-Sb alloys and simulations of solidification of the alloys using continuum theory of porous media. Since thermosolutal convection strongly affects transport phenomena during solidification and also leads to macrosegregates, we are convinced, therefore, that experiments in microgravity would enable us to gain scientific data on dendritic microstructures solidified without thermosolutal convection. We will characterize dendrite arm spancings, volume fraction of interdendritic liquid, and both macrosegregation and microsegregation in samples that are solidified in microgravity. The design of the microgravity experiments is guided by our on-going terrestrial experiments and computer simulations, which are being done to identify suitable growth conditions and the effect of g-jitter in microgravity experiments.

Effect of Convection of Microstructural Development

The directional solidification furnace at Cleveland State University has been used to study hypoeutectic Al-Cu and Pb-Sb alloys. Experimental studies in these systems have conclusively shown that convection affects interface morphology and segregation in terrestrial experiments. In Al-Cu, the rejected solute is heavier so that convection is not expected due to the axial gradients in temperature and composition. However, a radial gradient is always present in the directional solidification for which there is no threshold for convection. In the Pb-Sb alloy, there is significant convection because of the rejection of a lighter solute at the interface. Here we present results on the Pb-Sb alloys.

The solidifying alloys are quenched when steady growth conditions are attained, as indicated by thermocouples inserted into the samples. The quenched-liquid is distinguished from the dendritic solid during growth because the quench causes the overlying liquid and the interdendritic liquid in the upper part of the mushy zone to solidify with very fine dendrites. By taking transverse sections, the primary dendritic spacing and several other metrics of the dendrites can be measured.

The phase diagram for the Pb-Sb system has a eutectic reaction at 251.1° C and 11.2 wt % Sb. Macrosegregation along the lengths of Pb-5.8 wt % Sb and Pb-2.2 wt % Sb alloys that were directionally solidified at rates of 1 to 30 μm s^{-1} under a gradient of 14 000 K m^{-1} are shown in Figs. 1a and 1b. Fraction solidified refers to the fractional length along the ingot-sample. Thermosolutal convection has resulted in extensive transport of the solute from the mushy zone into the overlying liquid; the extent of the macrosegregation is exacerbated as solidification rate is decreased. Convection in the overlying liquid and in the vicinity of the dendrite tips still exists even at the higher growth rates.

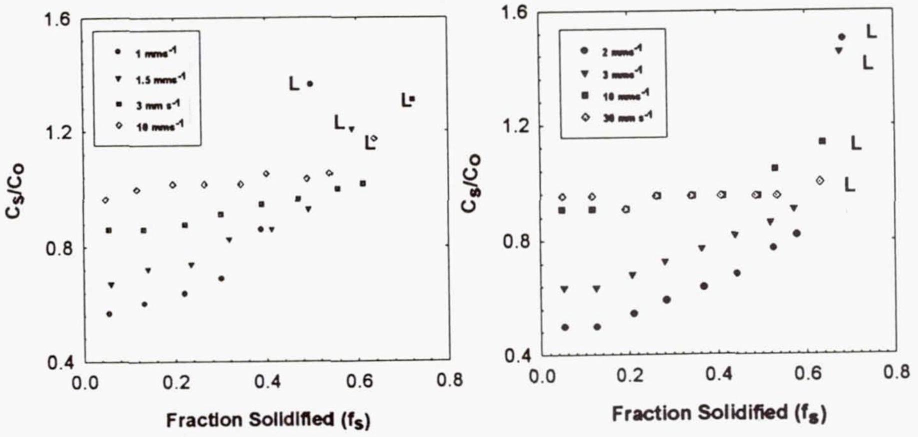

(a) (b)

Fig. 1: Macrosegregation in directionally solidified and quenched ingots: (a) Pb-5.8 wt % Sb; (b) Pb-2.2 wt % Sb. Thermal gradient is 14 000 K m^{-1}. Points marked L were in the overlying liquid when the quench was effected.

A directionally solidified and quenched ingot was examined serially with a microtome device that reveals transverse sections through the mushy zone. By rotating the images through 90°, the dendrite radii at various distances were measured and regressed to fit a parabola, resulting in a tip radius of 14.2 μm (Fig. 2). The results of repeating the procedure for twelve of the primary dendritic arms gave a mean tip radius of 19.8 ± 5.1 μm (one standard deviation), whereas the calculated value is 13 μm, using the model of Hunt and Lu [1].

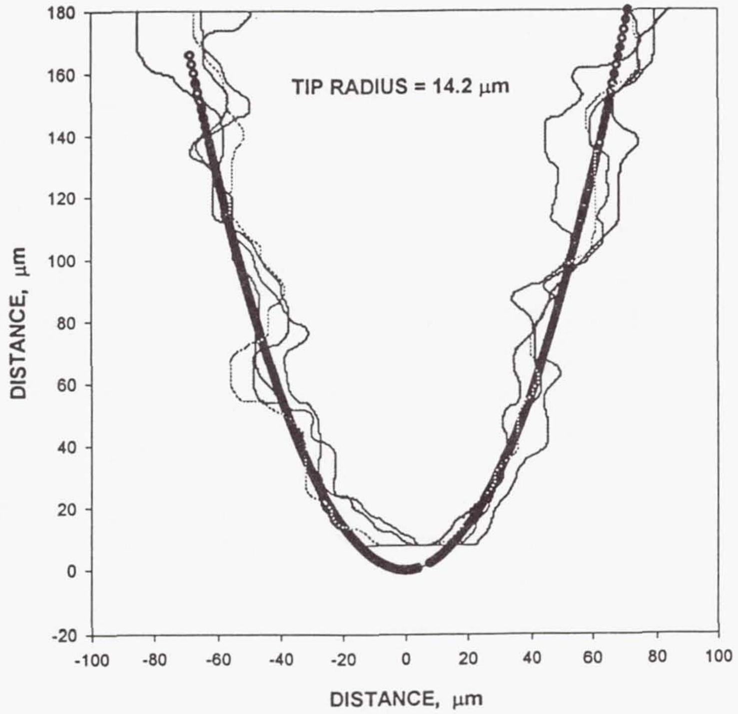

Fig. 2: Four views (rotations) of a dendritic primary arm in directionally solidified Pb=5.8 wt % Sb grown at 3 μm s^{-1} and 14 000 K m^{-1}. The heaviest curve is based on a regression of the four rotations taken every 90°.

Primary dendritic spacings in samples grown with a thermal gradient of 14 000 K m^{-1} are presented in Figs. 3a and 3b. The agreement between the predicted and measured primary spacings is poor. The discrepancy increases with slower growth speeds and decreasing thermal gradients. Similar results were also seen in series grown with thermal gradients of 4000 and 8600 K m^{-1}. The tip concentrations of Sb have been measured in some of the ingots of Pb-5.8 wt % Sb. There is reasonable agreement between measured and theoretical values for solidification rates of 3 μm s^{-1} and greater, but the agreement is poor below 3 μm s^{-1}.

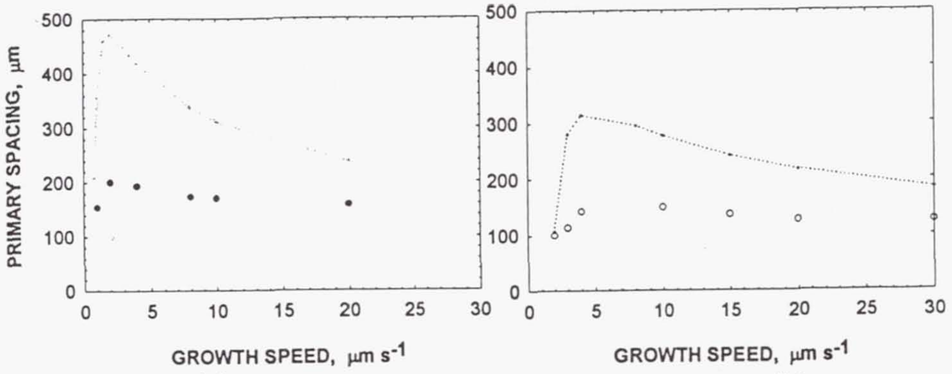

(a) (b)

Fig. 3: Primary spacings in dendritic samples directionally solidified with a thermal gradient of 14 000 K m^{-1}: (a) Pb-5.8 wt % Sb; (b) Pb-2.2 wt % Sb. The upper curves are minimum spacings calculated using the model of Hunt and Lu [1].

Mathematical Modeling and Simulation of Directional Solidification in Space

The finite element simulator calculates the velocity components, temperature, concentration, and fraction liquid in alloys that solidify with a dendritic mushy zone. Details pertaining to the numerical model and calculated results can be found in References [2-6]. The mushy zone is mathematically represented as an anisotropic porous medium of variable porosity, and it is free to develop with no predetermined shape or size. The conservation equations are solved under the following assumptions: (i) the flow is laminar; (ii) only solid and liquid phases are present, *i.e.*, no pores form; (iii) the solid and liquid phases have uniform but different densities; (iv) the density of the liquid is constant except in the buoyancy term of the momentum equations; (v) there is negligible diffusion of solute within the solid; (vi) the solid does not convect; (vii) the thermal properties are constant and equal in both the liquid and solid phases.

Initially the alloy is all liquid with a uniform concentration of solute and an imposed linear temperature distribution varying from the cooler bottom to the top. We specify the boundary fluxes and/or temperatures and allow them to vary with time if necessary. The no-slip condition for velocity is applied at the bottom, along the two side walls, and at the top of the overlying liquid. In microgravity, there can be separations from the side walls, and surface tension produces convection in the melt if the top surface is free. Experimentally these effects are suppressed by means of a solid part of the mold that is kept always in contact with the liquid (*e.g.*, with a spring-loaded plunger). In the model, therefore, we allow the top surface to drop as solidification proceeds to account for the overall shrinkage [6].

In terrestrial experiments, when flow is predominantly thermosolutal convection, the “shrinkage” (or expansion) can be neglected. But shrinkage can be an important component of the convection during solidification in microgravity. We simulated the directional solidification of a Pb-35% Sn alloy in a rectangular container 7 mm wide × 4 cm high. The temperature along the bottom of the container decreased at a prescribed rate of 0.0333 K s^{-1}, which resulted in a solidification rate of about 3 $\mu m\ s^{-1}$. The vertical boundaries were thermally insulated, and a constant thermal gradient of 10 000 K was applied at the top horizontal boundary.

When gravity $\boldsymbol{g} = 0$, the fluid motion is driven by shrinkage only. As the mushy zone advances upward, there is downward flow of the overlying liquid, which is almost fully developed. Where the downward flow encounters the mushy zone, it changes to an almost uniform speed. With $\boldsymbol{g}$ down and $\boldsymbol{g} = 10^{-4}\, g_o$, where $g_o = 9.8\ m\ s^{-1}$, two weak cells develop at the top of the mushy zone due to the interaction between the shrinkage flow and the gravitational forces. This flow is itself unstable. If perturbed, the flow slowly evolves into an unsymmetrical circulation, where one of the cells becomes dominant. With $\boldsymbol{g} = 10^{-3}\, g_o$, flow is strong enough to produce significant segregation. Hence, directional solidification should be carried out at $10^{-4}\, g_o$ or less. Even at $10^{-4}\, g_o$, however, there are weak circulation cells in the overlying liquid just above the mushy zone, and if perturbed slightly, then the convection field is not symmetrical.

Since the convection is easily perturbed at $10^{-4}\, g_o$, we ran several cases to see the effect of g-jitter on directional solidification. The alloy is Pb-23 wt % Sn, solidified in a container with a width of 6.86 mm and height of 40 mm. Initially, the container was filled with the melt at a thermal gradient in the vertical direction of 5280 K m^{-1}. At the bottom wall the temperature decreased at a prescribed rate, which gave a solidification velocity of about 10 $\mu m\ s^{-1}$.

Effects of sinusoidal variations in the gravitational acceleration were studied (Figs. 4a and b). The functions comprise a mean gravity level and two sine functions with different amplitudes and frequencies. Seven cases were run using two different sets of values for the frequencies and amplitudes and different attitudes with respect to the direction of the gravity vector.

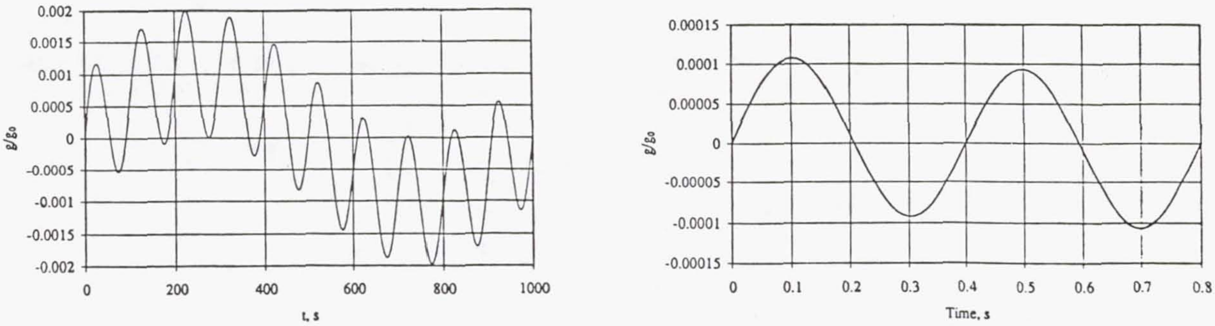

(a) (b)

Fig. 4: Functions used to simulate g-jitter: (a) first function using parameters of Ramachandran *et al.* [7]; (b) second function using parameters of Perkins [8]. Note that the amplitudes and frequencies of the two functions are very different.

Cases 1 and 2 were run using the first g-jitter function with the gravity vector antiparallel to the growth direction. The results showed that the g-jitter had almost no effect on the solidification. The flow remained dominated by shrinkage, and there were very minor fluctuations in the composition of the solid, on the order of only 0.1 wt % Sn. The results for these two cases were surprising, based on what we knew from runs made at various constant gravity levels. In those, there was no discernible effect of gravity below a level of about 10^{-5} g_o. If perturbed at and above a level of 10^{-4} g_o, then thermosolutal convection was found to be important in the overall flow. The first g-jitter function produced accelerations over one order of magnitude greater than the 10^{-4} g_o level, but no significant buoyancy effects were seen. Case 3 was a repeat of Case 2, but with the second g-jitter function. The second function has much higher frequencies and smaller amplitudes than the first. This showed almost no deviation from the case with zero gravity, which was not surprising since the second g-jitter function has much smaller amplitudes than the first.

The first three cases showed that the sinusoidal accelerations would not cause the flow to become buoyancy driven, even when the accelerations were large. However, these accelerations were all antiparallel to the direction of solidification. So the next step was to see the effects of accelerations perpendicular to the direction of solidification (Case 4) with the first g-jitter function. In the overlying liquid there was a clockwise cell and a small secondary cell just above the mushy zone. The flow was large enough to cause distortions of the mushy zone, with pockets of higher concentration of Sn. Case 5 used the second g-jitter function. This showed some similarities to the previous case, just on a smaller scale. Again we saw a large clockwise cell, but the forcing function was so small that a secondary cell did not form above the mushy zone;

instead the flow just turned to feed the solidification shrinkage. In the absence of strong buoyancy-driven convection above the mushy zone, there was no distortion of the solidification isotherms or no significant macrosegregation.

Cases 6 and 7 involved a combination of forcing in both the perpendicular and antiparallel directions. Case 6 used the second g-jitter function acting in both directions. The results were nearly identical to Case 5, where the accelerations were only in the x-direction. This seems to indicate that the accelerations in the vertical direction had little influence on the flow caused by the horizontal acceleration. Finally in Case 7, the results were similar to Case 4, where only a horizontal forcing was applied. This time, however, the vertical accelerations had a significant effect on the flow pattern. At 2000 s, the thermosolutal convection was strong enough to distort the mushy zone and to cause significant segregation.

The overall picture seems to be that even large periodic accelerations, which are antiparallel to directional solidification, have little effect. But accelerations of the form in Fig. 4a, which are also perpendicular to the directional solidification, set up convective cells at the very start of solidification that are maintained throughout solidification. Smaller and weaker cells just above the mushy zone form and react to the changes in the accelerations. These cells are driven by the higher liquid concentration at the dendrite tips and strongly impact dendritic solidification. These simulations indicate that directionally solidified samples must be aligned with the gravity vector in space experiments or the solidification furnace must be vibration-isolated within the spacecraft or space station.

References

1. J.D. Hunt and S.-Z. Lu, *Metall. Mater. Trans. 27A* (1996) 611.
2. H.-W. Huang, J.C. Heinrich and D.R. Poirier, *Model. Simul. in Mater. Sci. Eng. 4* (1996), 245.
3. S.D. Felicelli, D.R. Poirier and J.C. Heinrich, *J. Crys. Growth 177* (1997) 145.
4. D.R. Poirier, S.D. Felicelli and J.C. Heinrich, "Simulation of Transport Phenomena in Directionally Solidified Castings," in *Proceedings of the Julian Szekely Memorial Symposium on Materials Processing*, H.Y. Sohn, J.W. Evans and D. Apelian (eds.), TMS, Warrendale, PA (1997) 393-410.
5. S.D. Felicelli, J.C. Heinrich and D.R. Poirier, *Int. J. Num. Meth. Fluids 25* (1997) 1.
6. E. McBride, J.C. Heinrich and D.R. Poirier, "Numerical Simulations of Flow in Directionally Solidified Alloys in Microgravity," in *Tenth International Conference on Finite Elements in Fluids*, M. Hafez and J.C. Heinrich (eds.), The University of Arizona, Tucson, AZ (1998) 548-553..
7. N. Ramachandran, C.R. Baugher and M.J.B. Rogers, "Acceleration Environment on the Space Shuttle and Its Impact on Thermosolutal Fluid Mechanics," ASME Annual Winter Meeting, New Orleans (1993).
8. B. Perkins, private communication, NASA-MSFC, Huntsville, Alabama (1997).

FRONTAL POLYMERIZATION IN MICROGRAVITY

John A. Pojman
Department of Chemistry and Biochemistry
University of Southern Mississippi
Hattiesburg, MS 39406-5043
(601) 266-5035; 6075/fax
john.pojman@usm.edu
www-chem.st.usm.edu/japgroup/JAPGROUP.html

Introduction

Frontal polymerization is a mode of converting monomer into polymer via a localized reaction zone that propagates, most often through the coupling of thermal diffusion and Arrhenius reaction kinetics. Frontal polymerization reactions were first discovered in Russia by Chechilo and Enikolopyan in 1972.[1] They studied methyl methacrylate polymerization to determine the effect of initiator type and concentration on front velocity[2] and the effect of pressure.[3] The literature up to 1984 was reviewed by Davtyan et al.[4]

Pojman and his co-workers demonstrated the feasibility of traveling fronts in solutions of thermal free-radical initiators in a variety of neat monomers at ambient pressure using liquid monomers[5-7] and with a solid monomer.[8] The macrokinetics and dynamics of frontal polymerization have been examined in detail[9] and applications for materials synthesis considered.[10]

Basic Phenomena

Frontal polymerization reactions are relatively easy to perform. In the simplest case, a test tube is filled with the initial reactants. The front is ignited by applying heat to one end of the tube with an electric heater. The position of the front is obvious because of the difference in the optical properties of polymer and monomer. Figure 1 shows a typical front. Movies of all the phenomena described below can be viewed at our www site.

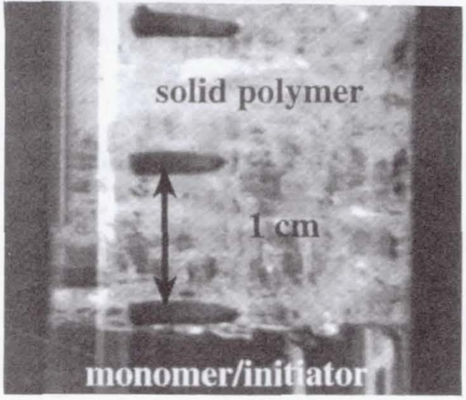

Figure 1. A descending case of frontal polymerization with triethylene glycol dimethacrylate and benzoyl peroxide as the initiator.

Under most cases, a plot of the front position versus time produces a straight line whose slope is the front velocity. The velocity can be affected by the initiator type and concentration but is on the order of a cm/min.

The defining feature of frontal polymerization is the sharp temperature gradient present in the front. Figure 2 shows three different temperature profiles for methacrylic acid for different initiators. Notice that the temperature jumps about 200 °C over as little as a few millimeters, which corresponds to polymerization in a few seconds.

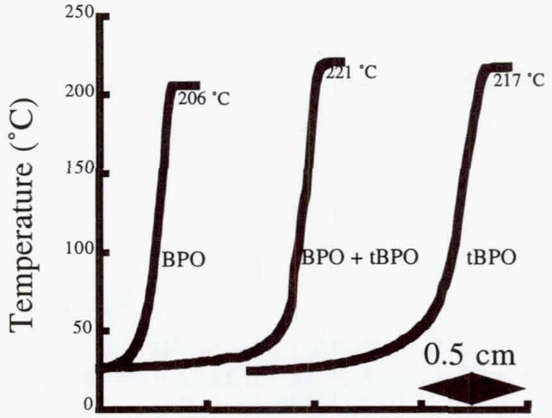

Figure 2. Temperature profiles for three different methacrylic acid polymerization fronts. The higher the energy of activation of the thermal initiator, the wider the preheat zone.

Types of Systems

We describe cases when frontal polymerization can be observed (descending fronts) under moderate pressures (<5 atm). The first case is crosslinking monomers (thermosets), including tri(ethylene glycol)dimethacrylate (TGDMA), di(ethylene glycol)dimethacrylate (DGDMA), and divinylbenzene. The free-radical polymerization of these monomers produces rigid crosslinked polymers, which sustain a sharp frontal interface (see Figure 1).

The second group of monomers form polymers that are insoluble in the monomer. Good examples are acrylic and methacrylic acids.[5, 7, 11] Insoluble polymer particles adhere to each other during their formation and stick to the reactor or test tube walls, forming a mechanically durable phase and discernible polymer-monomer interface. How well the front sustains itself depends on conversion, the polymer glass transition temperature and molecular weight distribution.

The third group of monomers includes all highly reactive monomers that produce thermoplastic polymers, which are molten at the front temperature. Such fronts decay due to the Rayleigh-Taylor instability[12, 13] (Figure 3). Although these polymers are soluble in their monomers (given sufficient time), on the time scale of the front the polymer is effectively immiscible with the monomer. Adding an inert filler such as ultra-fine silica gel (Cabosil) increases the viscosity and eliminates the front collapse. However, adding a filler prevents the production of a homogeneous product. Some monomers like styrene and methyl methacrylate require moderate pressure (20-30 atm) to eliminate monomer boiling. Higher boiling temperature monomers like butyl methacrylate, butyl acrylate and benzyl acrylate support the frontal regime at ambient pressure in test tubes.

Convective Instabilities

In the early work on frontal polymerization, the authors[1-3, 14] applied very high pressure (up to 5000 atm) to eliminate monomer (methyl methacrylate) boiling and the reaction zone decay due to the density gradient in the reaction zone (Rayleigh-Taylor instability) caused by the more dense polymer product overlying the unreacted monomer. They also managed to observe only downward traveling fronts because natural convection rapidly removed heat from the reaction zone of an ascending front leading to extinction. However, at pressures less than 1500 atm descending fronts decayed.

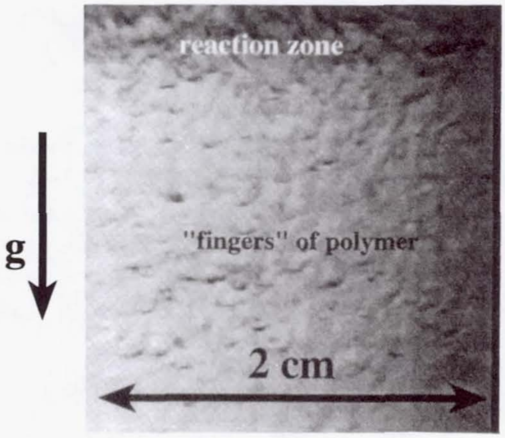

Figure 3. The Rayleigh-Taylor instability in a descending front of n-butyl acrylate polymerization.

Convection can occur with all types of monomers if the front propagates up a tube. Garbey et al. have analyzed the problem of convection in ascending frontal polymerization with a solid product and developed a modified Rayleigh number that predicts when the front will be unstable (convection will occur) and stable (front will be flat):[15, 16]

The theory predicts that for ascending fronts increased viscosity makes the front more stable with respect to convection, which is rather obvious. What is not obvious is that increasing the velocity of the ascending front also makes the front more stable. Because the monomer is converted to solid, if the front moves faster, then the liquid that is being heated is converted to product before it can move and appear as convection. These results were confirmed experimentally by Bowden et al.[17]

Recently, McCaughey et al. have confirmed the analysis of Garbey et al.[15] for ascending fronts with a liquid product by observing that fronts could be stable if the viscosity were sufficiently high or the front velocity sufficiently rapid.[18]

Convection is a serious impediment for commercial applications of frontal polymerization. Chekanov et al. found that in the frontal curing of epoxy resin, ascending fronts were extinguished by convection.[19]

Microgravity Experiments

Conquest I Sounding Rocket

In order to study poly(n-butyl acrylate) fronts, Pojman et al. added fumed silica (CAB-O-SIL, Cabot Corp.) to increase monomer viscosity.[20] However, the problem is that in increasing the viscosity of the medium could increase the molecular weight. The only way to determine the inherent molecular weight distribution that can be achieved in a front is to perform a front without CAB-O-SIL. Because of the Rayleigh-Taylor instability, the only way to accomplish this with n-butyl acrylate is to eliminate the driving force for the collapse of the more dense polymer layer, i.e., eliminate the force of gravity.

An experiment was launched on April 3, 1997 on the *Conquest I* rocket flight out of White Sands Missile Range under the Launch Voucher Demonstration Program, which was managed by the University of Alabama in Huntsville Consortium for Materials Development in Space. The flight provided at least 5 minutes of 10^{-4} g conditions.

Pojman et al. found that the molecular weight distribution of the sample polymerized in microgravity was very similar to the ground based-control experiment (Figure 4).[21] Thus, the addition of a viscosity-enhancing agent does not significantly affect the molecular properties of the sample produced frontally.

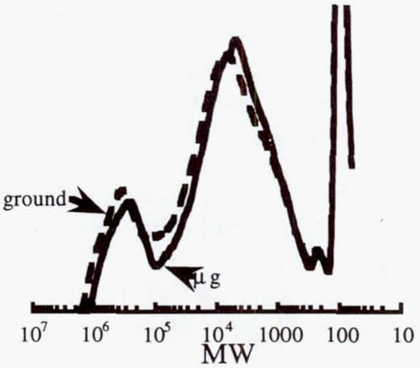

Figure 4. Gel permeation chromatogram showing the molecular weight distributions of the control and microgravity sample (relative to polystyrene standards). Adapted from Pojman et al.[21]

Visual observation after touchdown indicated that the 3.0 atm cell had large bubbles connected like a necklace in the center of the tube (Figure 5). Determining how bubbles interact with fronts in the absence of buoyancy led us to a series of KC-135 flights.

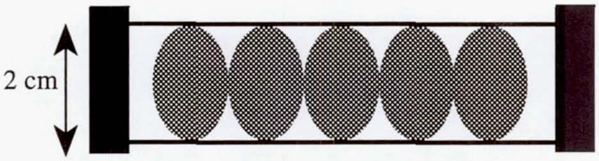

Figure 5. Approximate pattern of bubbles formed in front on *Conquest I.*

KC-135 Flights

Using the apparatus from the rocket flight, we flew fronts of benzyl acrylate and TGDMA polymerization on NASA's KC-135 aircraft. The parabolic flights afforded us approximately 20 seconds of low g (about 0.1 g) followed by a minute of 1 - 1.8 g.

Benzyl acrylate (BzA) (Monomer-Polymer and Dajac) and triethylene glycol dimethacrylate (Aldrich) were used as received. Benzoyl peroxide (97%, Aldrich) was used as the initiator with BzA, while Lupersol 231 (Atochem) was used with the TGDMA. We used 16 x 125 mm tubes (VWR #72690-022) on which a plastic cap (VWR #60826-290) could be securely screwed.

The reaction test tube was held snugly in a stainless steel mounting stand with the round sealed end of the test tube that fit into a cavity of the metal disk and the open end held by a polyethylene disk. The two disks were held together firmly with three stainless steel threaded rods. A cartridge heater was in contact with the sealed surface of the glass tube through a hole provided in the compression fitting and the metal disk. The 65 watt cartridge heater was energized with a 12 Volt DC power source for five minutes to trigger the reaction front. Because we were unable to observe the reaction in real time, we were not able to time the front to start at a specific stage of a parabola.

Liquid/Liquid Fronts

The rocket experiment indicated that bubbles can interact with the front. Because of the Rayleigh-Taylor instability discussed above, we can only study the interaction of bubbles with fronts of liquid polymer under weightless conditions.

Figure 6 shows how in weightlessness, the bubbles aggregate. When the high g arrives, the bubbles rise to the top of the tube, and the molten polymer sinks. We propose that the bubbles move toward hotter the interior of the tube via surface-tension induced convection and aggregate as they do so.

Liquid/Solid Fronts

We repeated the experiment using triethylene glycol dimethacrylate, which forms a rigid crosslinked product. We deliberately left a bubble (about 0.5 mL) when filling the tube to allow copious bubble formation. As bubbles are produced at the front in 1 g, they form long strings of small bubbles (Figue 8). It seems that existing bubbles acts as a nucleation sites for further bubbles formation.

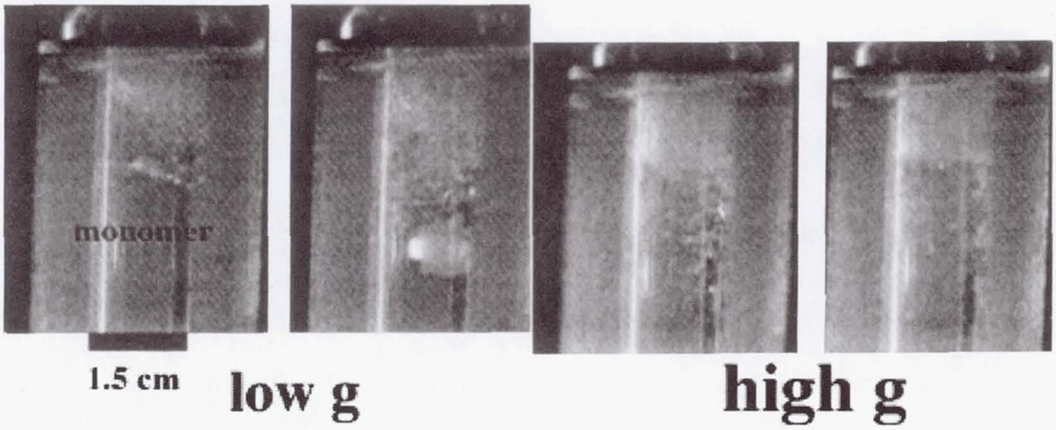

Figure 6. Fronts of benzyl acrylate polymerization in low and high g. The fronts are propagating from the top of the images on down. Time between images is 12 seconds.

However, under low g conditions, a single large bubble forms that can impede the front propagation, as can be seen in Figure 7. As the buoyant force is restored, the front grows around the bubbles, and only small bubbles are seen.

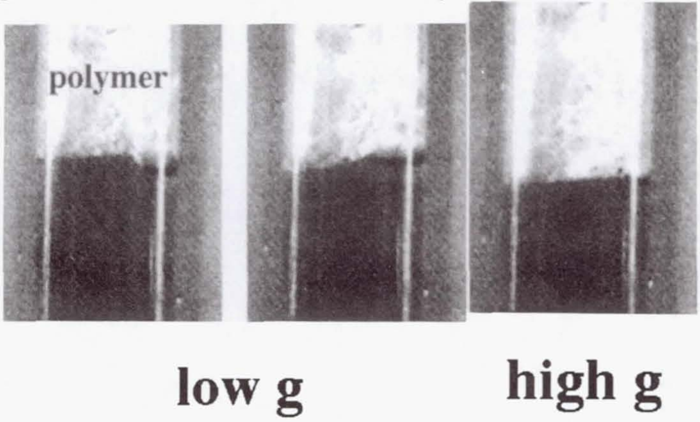

Figure 7. Images of TGDMA frontal polymerization under low and high g Time between images is approximately 10 seconds.

We propose this mechanism: Under 1 g, the buoyant force holds a bubble up against the front, and so bubbles grow in low chains. However, in low g the bubble is free to move via surface tension-induced convection. Such motion allows bubbles to aggregate into a large bubble.

Conclusions

Frontal polymerization systems, with their inherent large thermal and compositional gradients, are greatly affected by buoyancy-driven convection. Sounding rocket experiments allowed the preparation of benchmark materials and demonstrated that methods to suppress the Rayleigh-Taylor instability in ground-based research did not significantly affect the molecular weight of the polymer. Experiments under weightlessness show clearly that bubbles produced during the reaction interact very differently than under 1 g.

Acknowledgments

We thank Dr. Robert Naumann for assistance in undertaking the Conquest I flight and for loaning hardware for the KC-135 flights. We thank Dr. Patton Downey of NASA's MSFC for support and assistance with the KC-135 flights. We are grateful to James Bridges and Steve Selph (USM) for design and fabrication assistance. Support for this project was provided by NASA's Microgravity Materials Science Program (NAG8-

973), the Mississippi NASA EPSCoR program, the Air Force Office of Scientific Research and from Boston Optical Fiber, Inc.

Figure 8. Image of TGDMA sample (from front in Figure 7) showing bubble aggregation under low g.

References

(1) Chechilo, N. M.; Khvilivitskii, R. J.; Enikolopyan, N. S. *Dokl. Akad. Nauk SSSR* **1972**, *204,* 1180-1181.
(2) Chechilo, N. M.; Enikolopyan, N. S. *Dokl. Phys. Chem.* **1975**, *221,* 392-394.
(3) Chechilo, N. M.; Enikolopyan, N. S. *Dokl. Phys. Chem.* **1976**, *230,* 840-843.
(4) Davtyan, S. P.; Zhirkov, P. V.; Vol'fson, S. A. *Russ. Chem. Rev.* **1984**, *53,* 150-163.
(5) Pojman, J. A. *J. Am. Chem. Soc.* **1991**, *113,* 6284-6286.
(6) Pojman, J. A.; Craven, R.; Khan, A.; West, W. *J. Phys. Chem.* **1992**, *96,* 7466-7472.
(7) Pojman, J. A.; Willis, J.; Fortenberry, D.; Ilyashenko, V.; Khan, A. *J. Polym. Sci. Part A: Polym Chem.* **1995**, *33,* 643-652.
(8) Pojman, J. A.; Nagy, I. P.; Salter, C. *J. Am. Chem. Soc.* **1993**, *115,* 11044-11045.
(9) Pojman, J. A.; Ilyashenko, V. M.; Khan, A. M. *J. Chem. Soc. Faraday Trans.* **1996**, *92,* 2825-2837.
(10) Khan, A. M.; Pojman, J. A. *Trends Polym. Sci. (Cambridge, U.K.)* **1996**, *4,* 253-257.
(11) Pojman, J. A.; Khan, A., M.; West, W. *Polym. Prepr. Am Chem. Soc. Div. Polym. Chem.* **1992**, *33,* 1188-1189.
(12) Rayleigh, J. W. *Scientific Papers, ii*; Cambridge University Press: Cambridge, 1899.
(13) Taylor, G. *Proc. Roy. Soc. (London)* **1950**, *Ser. A. 202,* 192-196.
(14) Chechilo, N. M.; Enikolopyan, N. S. *Dokl. Phys. Chem.* **1974**, *214,* 174-176.
(15) Garbey, M.; Taik, A.; Volpert, V. *Preprint CNRS* **1994**, *187,* 1-42.
(16) Volpert, V. A.; Volpert, V. A.; Garbey, M.; Pojman, J. A. in *Gas-Phase Chemical Reaction Systems: Experiments and Models 100 Years after Max Bodenstein*; Wolfrum, J.; Volpp, H.-R.; Rannacher, R. Warnatz, J.,Ed., Springer Berlin: Heidelberg, 1996; pp 309-317.
(17) Bowden, G.; Garbey, M.; Ilyashenko, V. M.; Pojman, J. A.; Solovyov, S.; Taik, A.; Volpert, V. *J. Phys. Chem. B* **1997**, *101,* 678-686.
(18) McCaughey, B.; Pojman, J. A.; Simmons, C.; Volpert, V. A. *Chaos in press*
(19) Chekanov, Y.; Arrington, D.; Brust, G.; Pojman, J. A. *J. Appl. Polym. Sci.* **1997**, *66,* 1209-1216.
(20) Pojman, J. A.; Willis, J. R.; Khan , A. M.; West, W. W. *J. Polym. Sci. Part A: Polym Chem.* **1996**, *34,* 991-995.
(21) Pojman, J. A.; Khan, A. M.; Mathias, L. J. *Microg. sci. technol.* **1997**, *X,* 36-40.

IMPROVED CRYSTAL QUALITY BY DETACHED SOLIDIFICATION IN MICROGRAVITY

Liya L. Regel and William R. Wilcox
International Center for Gravity Materials Science and Applications
Clarkson University, Potsdam NY 13699-5814
315-268-7672; regel@agent.clarkson.edu & wilcox@agent.clarkson.edu

Introduction

Directional solidification in microgravity has often led to ingots that grew with little or no contact with the ampoule wall. When this occurred, crystallographic perfection was usually greatly improved -- often by several orders of magnitude. Unfortunately, until recently the true mechanisms underlying detached solidification were unknown. As a consequence, flight experiments yielded erratic results. Within the past four years, we have developed a new theoretical model that explains many of the flight results[1-5]. This model gives rise to predictions of the conditions required to yield detached solidification, both in microgravity and on earth.

Beginning with Skylab in 1974, many investigators found directional solidification in microgravity often yielded ingots that appear to have grown without being in intimate contact with their containers. A wide range of surface features and behavior were observed. We classify these observations into the categories shown below. Note that a given ingot might display several of these features along its length, but not all of them.

1. The ingot easily slid out of its container, whereas sticking was observed when solidification was carried out on earth under otherwise identical conditions.
2. On its surface, the ingot had isolated voids or bubbles of various sizes, depths and contact angles with the ampoule wall. (Such surface bubbles are also frequently seen on terrestrially solidified materials, but to a lesser extent.)
3. With a triangular or rectangular cross-section ampoule, the ingot had cylindrical detached surfaces in the corners and a flat surface in contact the wall over most of each face.
4. With an ampoule containing grooves machined in it, the ingot contacted only the peaks of the grooves.
5. After correcting for thermal contraction, there remained a gap of about 1 to 60 μm between the ingot and the ampoule wall around the entire periphery. Irregular narrow ridges maintained limited contact with the ampoule wall and were predominantly axial. A variety of features were seen in the detached regions, including microfacets and periodic waves or lines.
6. There was a gap of up to several mm between the ingot and the wall, typically with a wavy surface and sometimes forming an hourglass-shaped neck adjacent to the seed. Although this gap generally extended around the entire periphery, sometimes it was confined to a portion of the surface.

For semiconductors, the last portion of the ingot to freeze often replicated the surface of the ampoule, showing that contact had become intimate (as on earth). Here, we are concerned primarily with 5 and 6 above, as these differ from all prior terrestrial experience and were completely unexpected prior to Skylab. Behaviors 1 and 2 often occur on earth. Behaviors 3 and 4 are not surprising, as one would not expect non-wetting (high contact angle) liquids to penetrate cavities.

Although detached solidification has been observed predominantly with semiconductors, it has also been observed with metals and inorganic compounds. This apparent predominance may reflect only the fact that most flight experiments on directional solidification have been performed on semiconductors. Detached solidification has been observed at both fast and slow freezing rates. Sometimes it occurred with one type of dopant and not with others. The type of detachment, indeed even whether detachment occurred or not, has not been reproducible.

Some investigators have chosen to avoid detached solidification by using a spring to press a piston or plug tightly against the end of the melt. This strategy appears to have been successful. On the other hand, detachment has occurred nonetheless when a plug only lightly contacted the end of the feed ingot. We can explain these observations in a fashion similar to that used to predict the influence of gravity on detached solidification. It has been claimed that detachment is sensitive to the residual acceleration. Unfortunately there have been so few measurements of residual acceleration, particularly the average value, that one cannot judge the validity of this claim from experimental evidence alone. Our theoretical treatment leads us to believe that acceleration can enhance detachment if it is of the correct direction and magnitude.

We now discuss briefly the wide variety of properties observed in materials solidified with detachment. It is interesting to note that there was seldom any correlation between the ridges and lines sometimes observed on the surface and any internal defects or composition variation. Axial and radial variations in impurity doping ranged from that expected for diffusion-controlled solidification to that corresponding to vigorous convection. Sometimes there was a variation in composition near the detached surface. Although impurity striations were rare, they were occasionally seen near the surface. Some detached surfaces were inadvertently coated with oxide, whereas even dissolved oxygen was not detected on others. An interesting result was obtained in Wilcox's Skylab experiments on GaSb-InSb alloys[9]. Large changes in composition occurred across twin boundaries only in the detached portions of the ingots.

Generally speaking, crystallographic perfection was much greater when detached solidification occurred. Very often, twins and grain boundaries nucleated only where the ingot contacted the ampoule wall. Dislocation etch pit densities were frequently orders of magnitude less when the solidification had been detached. In semiconductors, this higher perfection has led to substantial increases in charge carrier mobility.

Models for detachment

Over the past 24 years, several models were proposed to explain detached solidification. We briefly review some of these below. When detached solidification was discovered in several

Skylab experiments, it was generally thought that the melt had lost contact from the ampoule wall because of the high contact angles of the semiconductor melts. Indeed, the phenomenon is still called "de-wetting" by some investigators[e.g.,10-12]. This view persists, in spite of microgravity experiments[13,14] and theory[15] showing that liquids do not pull away from the ampoule wall, no matter what the contact angle. The implicit assumption underlying this model is that the solid took the same shape as the liquid from which it froze. This would be like a person examining a Czochralski-grown crystal and concluding it came from a cylindrical melt of the same diameter as the crystal! In reality, the edge of a growing crystal does not even begin to follow the melt's meniscus -- it deviates by the so-called growth angle.

It is relevant to note that the voids found on the surface of Bridgman-grown crystals do not have the same shape as the gas bubbles had on the wall in the melt before solidification. In a parabolic flight experiment with InSb, gas bubbles on the wall moved when the freezing interface contacted them[15]. Such a bubble moved toward and partly onto the interface, so as to minimize the surface energy in the system. If one looks carefully at such cavities on a grown crystal, it can be seen that the angle with the ampoule changes as one moves around the periphery of the cavity. This is a manifestation of the interaction between the growing crystal and the bubble.

Some instances of detached solidification of metals in microgravity have been attributed to shrinkage during solidification. We believe this is erroneous. It is the inverse of the old discredited claim that one cannot grow semiconductor crystals by the vertical Bridgman technique because these materials expand when they freeze. To clarify the situation, let us consider the volume change that occurs as a semiconductor slowly freezes upward on earth. Solidification begins at the bottom of the ampoule, perhaps on a seed. If the density decreases upon freezing, then the top of the melt moves slowly upward to accommodate the increasing volume. Provided that enough head space remains for the entire volume change, solidification proceeds to completion without a problem. On the other hand, if the upward movement of the melt is blocked, then the ampoule breaks. The reverse situation occurs for metals that contract when they freeze. The melt surface slowly moves downward during solidification, while the melt and the solid both remain in contact with the ampoule wall.

If the coefficient of thermal expansion is greater for the ampoule than for the ingot, then during cooling from the melting point, the ingot is put under tensile stress while the ampoule is under compression[17-21]. Depending on the mechanical properties and the degree to which the solid sticks to the ampoule, the ingot may break free from the ampoule wall and form a gap, it may remain stuck and plastically deform, or it may remain stuck and break the ampoule.

Detached solidification has been attributed to a rough ampoule wall[10-12]. The idea is that a non-wetting melt cannot penetrate into cavities, especially if some residual gas is present in them. The problem with this model is that the interior of quartz growth ampoules is typically very smooth. Often it has been coated with shiny pyrolytic carbon. Artificially roughened ampoules did yield detached solidification between the peaks, while the solid was attached at the peaks[22-28].

Another proposed model invokes an oxide coating that acts as a container smaller in diameter than the ampoule. While this may have been true in some flight experiments, it has been rare. Ampoules were sealed in an inert gas and/or vacuum, sometimes with a gas getter installed. In the case of GaSb, for example, electron channeling patterns on the detached surface were sharp and showed no oxide[29,30]. No oxygen was detected by Rutherford back scattering measurements.

The meniscus model and results of recent theoretical modeling

In our new model of detached solidification a meniscus connects the edge of the ingot with the ampoule wall, similar to Czochralski growth but with much less distance between the ingot and the wall. Because of the curvature of the meniscus and the surface tension of the melt, the pressure in the gap must be greater than that in the adjacent melt. The gas filling this gap consists of one or more volatile constituents that are rejected by the growing solid. In most cases, this is the residual gas remaining in the ampoule that has dissolved in the melt. Although flight ampoules were generally sealed in a vacuum, outgassing would provide adequate gas to fill the gap. With only one known exception[23,25,27,28], the residual gas pressure has not been measured after flight experiments. In that one exception, it was about 10^{-2} torr, in spite of the use of gas getters in the sealed cartridge.

One may draw an analogy between our mechanism of detached solidification and the formation of "worm holes" or gas tubes inside growing solids. Formation of such tubes is commonly observed in ice and organic compounds. The mechanism underlying tube formation is as follows. Residual gas dissolves in the melt, e.g. air in the case of water being converted to ice cubes. The dissolved gas is much less soluble in the solid, and so accumulates at the freezing interface. When its concentration becomes large enough, a gas bubble nucleates and grows. If conditions are right, it remains at the interface and blocks the solid from growing under it. The diameter and stability of the resulting tube depends on the transport of dissolved gas into the bubble. One can regard detached solidification as the reverse geometry, i.e. the gas bubble surrounds the growing solid rather than vice versa.

Over the last several years, we have been developing our theoretical model for detached solidification. Numerical calculations were performed for InSb, which has exhibited detached solidification in numerous microgravity experiments. Steady state in the absence of buoyancy-driven convection was analyzed numerically[3]. We found that detached solidification in zero gravity is favored by a low freezing rate, increased concentration of volatile constituent, large contact angle for the melt on the ampoule wall (poor wetting), low surface tension for the melt, and a large growth angle.

Although Marangoni convection had a large effect on the local concentration field, surprisingly, it did not strongly influence the total flux of gas into the gap and, therefore, the tendency for detachment. One would expect Marangoni convection to influence the axial and radial variation in impurity doping in the crystal. Flight experiments with detachment have yielded a wide spectrum of results. In some cases, axial and radial concentration profiles corresponded to diffusion-controlled conditions. In other cases, there was clear evidence for Marangoni convection, ranging from gentle to vigorous. Why was Marangoni convection not always exhibited with detached solidification? If the gap is very narrow, our calculations show that the region of perturbed composition should also be very narrow. Thus, one might still achieve an axial concentration profile expected in the absence of convection, particularly if the freezing rate is not low. Another possible explanation for diffusion-controlled segregation with detached solidification involves a surface-active impurity that concentrates on the meniscus surface. One would expect, for example, that dissolved oxygen would concentrate on the surface of semiconductor and metal melts. Such impurities strongly inhibit the movement of a free liquid surface. For example, surfactant can stop Marangoni motion of a gas bubble in a temperature gradient and retard its rise velocity in a gravitational field. The influence of a surfactant increases as the bubble size decreases. Thus, for a given oxygen concentration in a semiconductor melt, we would expect Marangoni convection to manifest itself only for large gap widths during detached solidification.

We examined the stability of steady-state detached solidification in microgravity[4]. The shape of the meniscus is destabilizing in a fashion similar to Czochralski growth. If, for example, the crystal begins growing toward the wall, the meniscus shape tends to accelerate the change in diameter. Thus, if only the meniscus is taken into account, one predicts that both Czochralski growth and detached solidification are unstable. Since this is contrary to experimental observations, other factors must stabilize the growth. We considered gas transport and heat transfer as stabilizing mechanisms for detached solidification. We found that while gas transport into the gap is necessary for detached solidification, it is sufficient to stabilize detachment only for a short distance, on the order of the gap width. On the other hand, heat transfer strongly stabilizes detached solidification, as it does for the crystal diameter in Czochralski growth.

We considered the influence of gravity on detached solidification[5]. In the usual vertical Bridgman configuration, we must add the melt's hydrostatic head to the gas pressure in the gap required to maintain the meniscus shape (or the spring pressure when a piston is used in a microgravity experiment). At low g, the streamlines are nearly straight into the freezing interface. As g is increased, buoyancy-driven convection increases and eventually overpowers the flow due to growth. Gentle buoyancy-driven convection increases the flux of volatile species into the meniscus when it moves from the center toward the meniscus and carries segregated materials with it. At high g, the buoyancy-driven convection mixes the melt and decreases the flux into the meniscus even when the melt flow is directed radially outward along the freezing interface. Thus, for vertical Bridgman growth with a fixed convex freezing interface, there is a maximum in flux versus acceleration. On the other hand, with a concave interface, the flux decreases monotonically as acceleration increases because the convection near the interface is away from the gap. With the normal vertical Bridgman growth on earth, a slightly convex interface is indicative of the thermal field required to cause the flow favoring detachment. Thus, it is interesting to note that detached solidification was recently observed on earth for germanium with a slightly convex interface[6-8]. Use of a mirror furnace enabled observation of the ampoule in the neighborhood of the freezing interface. The appearance was exactly as expected from our model.

Future plans

We have recruited two new graduate students to work on this program. One will continue the theoretical development of the meniscus model as outlined above. The other will attempt to achieve detached solidification on Earth using a transparent, low-melting material so that the interface shape and convection in the melt can be seen.

Acknowledgment This research was supported by the United States National Aeronautics and Space Administration under Grants NAG8-1063 and NAG8-1482

References

1. W.R. Wilcox and L.L. Regel, Micrograv. Sci. Technol. 8 (1995) 56-61.
2. L.L. Regel, D.I. Popov and W.R. Wilcox, IAF-95-J.3.08, Oslo (1995).
3. D.I. Popov, L.L. Regel and W.R. Wilcox, J. Mat. Synth. & Proc. 5, 283-297 (1997).
4. D.I. Popov, L.L. Regel and W.R. Wilcox, J. Mat. Synth. & Proc. 5, 299-311 (1997).
5. D.I. Popov, L.L. Regel and W.R. Wilcox, J. Mat. Synth. & Proc. 5, 313-336 (1997).
6. F. Szofran and P. Dold, Private Communication, NASA Marshall Space Flight Center (1996).
7. F. Szofran *et al.,* in: NASA Microgravity Materials Science Conference, NASA Conference Publication 3342, Huntsville (1996).
8. Microgravity News, IntoSpace, Germany, 3 (summer 1996) 7.
9. R.A. Lefever, W.R. Wilcox, K.R. Sarma and C.E. Chang, Mat. Res. Bull. 13 (1978) 1181-1191.
10. T. Harter, T. Duffar and P. Dusserre, in: Proceedings of the VIIth European Symposium on Materials and Fluid Sciences in Microgravity, Oxford, ESA SP-295 (1990) 69-73.
11. T. Duffar and I. Harter, Ann. Chim. Fr. 16 (1991) 123-131.
12. T. Duffar, I. Paret-Harter and P. Dusserre, J. Crystal Growth 100 (1990) 171-184.
13. R. Sen and W.R. Wilcox 74 (1986) 591-596.
14. R.J. Naumann, in: Proceedings of the Joint L+1 Science Review for USML-1 and USMP-1 with the Microgravity Measurement Group, Huntsville, NASA (1993) 601-608.
15. R. Sen and W.R. Wilcox, J. Crystal Growth 78 (1986) 129-134.
16. R. Derebail, W.R. Wilcox and L.L. Regel, J. Spacecraft & Rockets 30 (1993) 202-207.
17. D.J. Larson, Jr., *et al.* in: Producibility of II-VI Materials and Devices, Proc. SPIE - Int. Soc. Opt. Eng. 2228 (1994) 11.
18. R. Shetty, W.R. Wilcox and L.L. Regel, J. Crystal Growth 153 (1995) 103.
19. T. Lee, Ph.D. Dissertation, Clarkson University (1996).
20. T. Lee, J.C. Moosbrugger, F.M. Carlson and D.J. Larson, Jr., in: L.L. Regel and W.R. Wilcox (eds.), Materials Processing in High Gravity, Plenum Press, New York (1994) 111.
21. W. Rosch and F. Carlson, J. Crystal Growth 109 (1991) 75.
22. T. Duffar, C. Potard and P. Dusserre, J. Crystal Growth 92 (1988) 467-478.

23. T. Duffar, P. Dusserre and J. Abadie, 30th COSPAR Scientific Assembly, Hamburg, (1994); Adv. Space Res. 16 (1995) 199-203.
24. T. Duffar, P. Dusserre and M.D. Serrano, Adv. Space Res. 16 (1995) 101-104.
25. M.D. Serrano *et al.*, ELGRA meeting, Madrid (1994).
26. T. Duffar, seminar, Clarkson University, Potsdam, New York (1995).
27. T. Duffar and J. Abadie, in: Preliminary Results of the D2 Mission, Norderney, European Space Agency, Paris (1994).
28. T. Duffar *et al.,* in: 9th European Symposium on Gravity Dependent Phenomena in Physical Sciences, Berlin (1995).
29. E. Lendvay, L.L. Regel *et al.*, J. Crystal Growth 71 (1985) 538-550.
30. I. Gyuro, L.L. Regel, *et al.*, Acta Astronautica 11 (1984) 361-368.

Page intentionally left blank

Thermophysical Property Measurements of Molten Semiconductors in 1-g and Reduced-g Condition

Won-Kyu Rhim, P. I.
Jet Propulsion Laboratory, California Institute of Technology
4800 Oak Grove Drive, Pasadena, California 91109, Mail Stop 183-401,
TEL: (818) 354-2925, FAX: (818) 393-5039, e-mail: won-kyu.rhim@jpl.nasa.gov
Other Participants: Mr. Takehiko Ishikawa, Dr. Paul-Francois Paradis, and Mr. Daniel Barber

Understanding and controlling the formation kinetics of variety of crystal imperfections such as point defects, non uniform distribution of doping atoms, and impurity atoms in growing crystals are very important. Theoretical (numerical) modeling of crystal growth process is an essential step to achieving these objectives . In order to obtain reliable modeling result, input parameters, i.e. various thermophysical parameters, must be accurate. The importance of accurate thermophysical properties of semiconductors in crystal growth cannot be overly emphasized. The total hemispherical emissivity, for instance, has a dramatic impact on the thermal environment. It determines the radiative emission from the surface of the melt which determines to a large extent the profile of solidified crystal. In order to understand the convection and the turbulence in a melt, viscosity becomes an important parameter. The liquid surface tension determines the shape of the liquid-atmosphere interface near the solid-liquid-atmosphere triple point. Currently used values for these parameters are rather inaccurate, and this program intends to provide more reliable measurements of these thermophysical properties. Thus, the objective of this program is in the accurate measurements of various thermophysical properties which can be reliably used in the modeling of various crystal growth processes.

In this program, thermophysical properties of molten semiconductors, such as Si, Ge, Si-Ge, and InSb will be measured as a function of temperature using the High Temperature Electrostatic Levitator at JPL. Each material will be doped by different kinds of impurities at various doping levels. Thermophysical properties which will be measured include: density, thermal expansion coefficient, surface tension, viscosity, specific heat, hemispherical total emissivity, and perhaps electrical and thermal conductivities.

Many molten semiconductors are chemically reactive with crucibles. As a result, these dispersed impurities in the melts tend to substantially modify the properties of pure semiconductors. Sample levitation done in a vacuum clearly helps maintain the sample purity. However, in the 1-g environment, all gravity caused effects such as convection, sedimentation and buoyancy are still present in the sample. In addition, large forces needed to levitate a sample in the presence of the gravity can cause additional flows in the melt. The use of the High Temperature Electrostatic Levitator (HTESL) [1] for the present research is a recent development and little is known about the flows induced by the electrostatic forces. In this ground base program, we will define the limits of HTESL technology as various thermophysical properties of molten semiconductors are measured.

Progress

(1) Thermophysical Properties of Molten Silicon

Progress has been made in measuring thermophysical properties of molten silicon and germanium. In molten silicon, the density, the ratio between the specific heat and the spherical total emissivity, the surface tension, and the viscosity have been measured. The earlier observation of the quadratic nature[2, 3] of liquid density as a function of temperature has been confirmed, indicating a certain short range ordering that might be taking place as the liquid undercools. Fig. 1 shows the density data of a high purity silicon and two boron doped silicon. Impurity effect could not be distinguished within this experimental error. Unlike most pure metals, the nonlinear increase of specific heat in undercooling silicon has also been repeatedly observed(see Fig. 2). Again, the formation of short range order must be responsible to such nonlinear behavior. If we use the literature value of $C_p(T_m) = 25.61$ J/mol/K, Fig. 2 allows us to determine the hemispherical total emissivity, ε_T, to be 0.183 which agrees closely with our earlier result of 0.18[2].

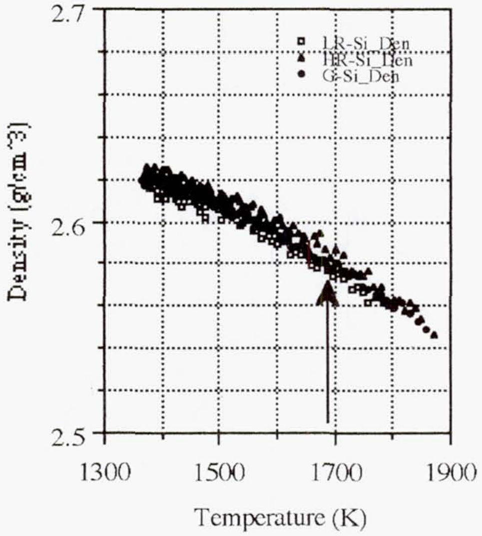

Fig. 1. Density of molten silicon.

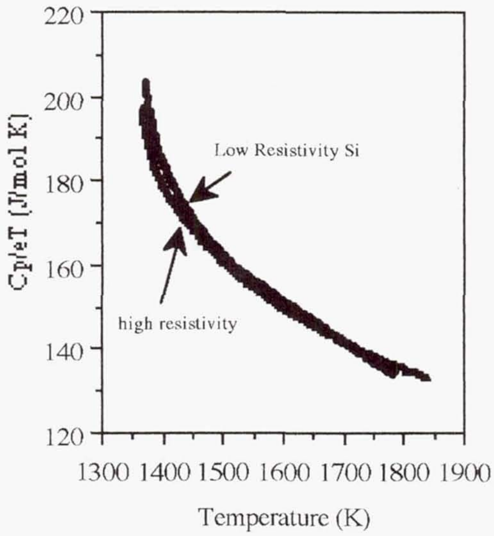

Fig. 2. C_p/ε_T vs. temperature of molten Si.

Fig. 3 and Fig. 4 are the surface tension and the viscosity data of a pure silicon and they are compared with the data by Sasaki et al.[4]. However, the sample rotation which set in during the sample heating process could not be controlled. Since the drop resonance frequency should depend on the rotation rate[5, 6], it was important to develop a sample rotation control capability to ensure the rotation frequency falls within an acceptable range.

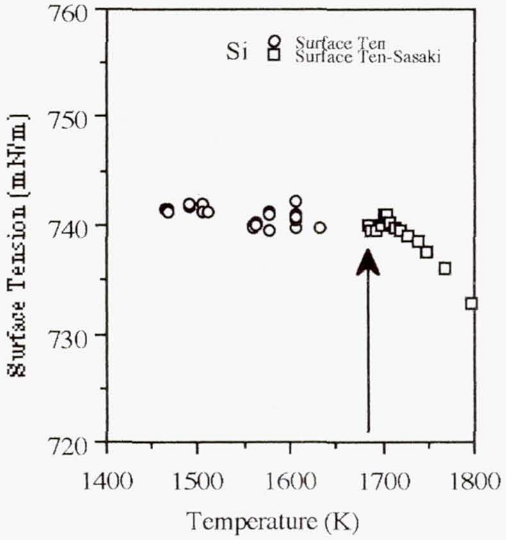

Fig. 3. Surface tension of molten silicon.

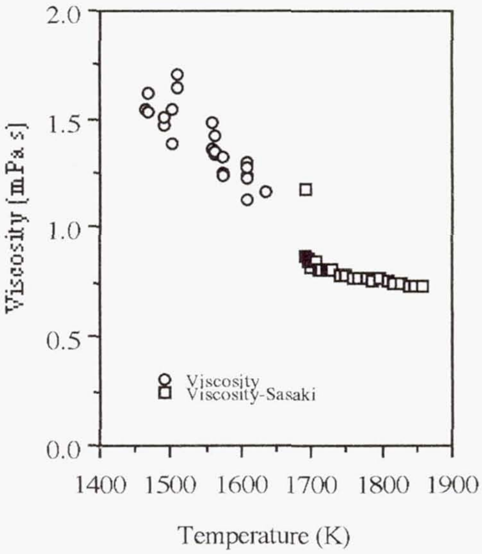

Fig. 4. Viscosity of molten silicon.

(2) Effect of Drop Rotation on Oscillation Frequency

The capability of systematically controlling rotational state of levitated samples is very important in containerless materials processing. When we want to measure surface tension through drop oscillation, we like to have a non-rotating drops. On the other hand, we like to have the drop rotating if we want to have a sample uniformly heated by a directional heating source. In general, in the absence of rotation control, levitated samples ended up showing different degrees of rotation. According to Busse's analysis[5], surface tension measurement by drop oscillation can be severely influenced by the rotational state of the drop. We had to develop a drop rotation control method to increase the accuracy of our surface tension and viscosity data.

As a result the rotation control method that was adapted to the HTESL was developed. A rotating magnetic field of appropriate frequency and strength was applied to the levitated sample in order to induce required torque. Drop oscillation was induced and frequency was measured at a preset rotational state. Fig. 5 shows the experimental data so obtained at several different rotation frequency and they were compared with the Busse's theoretical prediction[5]. From this figure, if the drop was rotating at the rate of 30 Hz, measured oscillation frequency would be about 10 % higher than that of non-rotating drop. This may translate to approximately 5 % error in measured surface tension. Fig. 6 show the effect of rotation on the damping time constant. At the present time there is no theory which can explain this quantitatively. Anyhow, this result suggests that the decay time constant is dependent to the rotational state of the drop, producing an additional source of error in the final viscosity values.

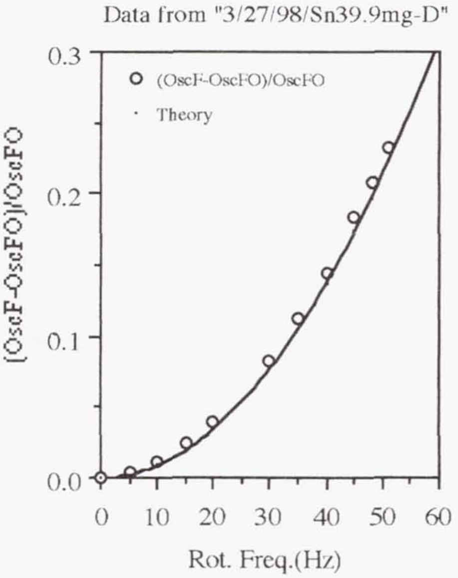

Fig. 5. Sample oscillation vs. rotation.

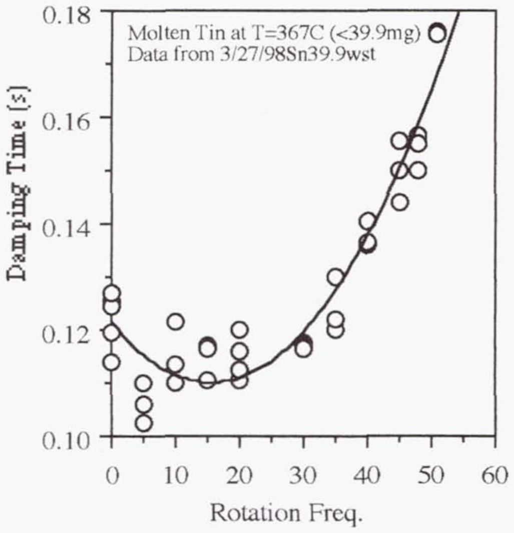

Fig. 6. Damping constant vs. rotation.

(3) Thermophysical Properties of Molten Germanium[7]

Pure germanium was melted and the density, the ratio of heat capacity to hemispherical total emissivity, the surface tension, and the viscosity were measured. Although the drop temperature was raised to ~ 200 K above the melting temperature, germanium undercooled less than 100 K. Probably it was necessary to desolve remaining impurity particles by further superheating the sample. Temperature dependence of the electrical resistivity of molten germanium was measured using the newly developed non-contact method for electrical resistivity[8]. This method was based on the fact that electrical conductivity of the rotor in an induction motor was proportional to the torque when all other parameters remained fixed. From the measured resistivity, the thermal conductivity of germanium was determined using the Wiedemann-Franz-Lorenz relationship. Considering the fact that thermal conductivity is one of the transport properties of liquids which is susceptible to gravity induced flows, this indirect approach to thermal conductivity from electrical conductivity measurement may have an important implication in terms of increased accuracy of thermal conductivity in 1-g environment.

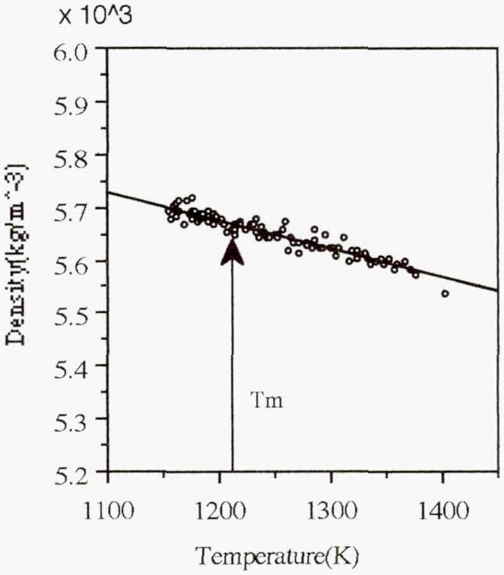

Fig. 7. Density of molten Ge vs temperature.

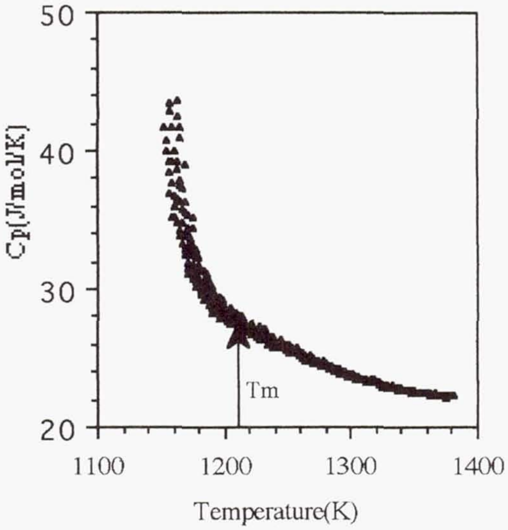

Fig. 8. Cp of molten Ge vs. temperature.

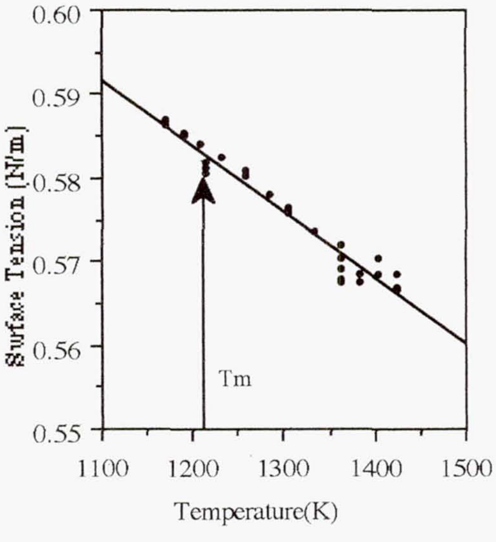

Fig. 9. Surface tension of molten Ge.

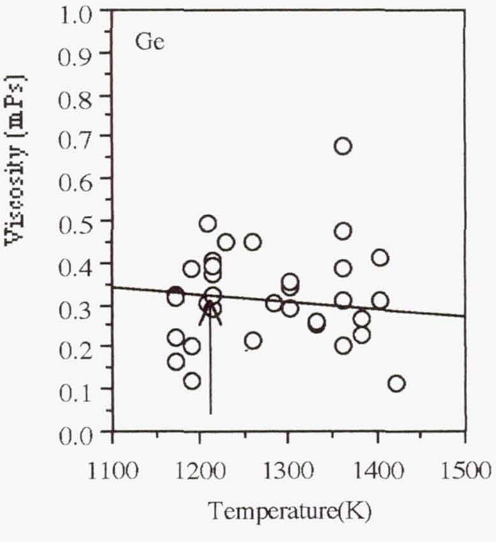

Fig. 10. Viscosity of molten germanium.

The measured liquid germanium density could be expressed by $\rho_{liq.} = 5.67 \times 10^3 - 0.542\ (T - T_m)$ Kg m^{-3} with $T_m = 1211.3$ K, the volume expansion coefficient by $\alpha = 0.9656 \times 10^{-4}\ K^{-1}$, and the hemispherical total emissivity at the melting temperature by $\varepsilon_{T,liq}(T_m) = 0.17$. Assuming constant $\varepsilon_{T,liq}(T) = 0.17$ in the liquid range which have been investigated, the constant pressure specific heat was evaluated as a function of temperature (Fig. 10). The surface tension could be expressed by $\sigma(T) = 583 - 0.08\ (T - T_m)$ mN m^{-1} and the temperature dependence of electrical resistivity of molten germanium, when $r_{liq}(T_m) = 60\ \mu\Omega cm$ was used as a reference point, could be expressed by $r_{e,liq}(T) = 60 + 1.18 \times 10^{-2} \cdot (T - 1211.3)\ \mu\Omega \cdot cm$(Fig. 11). The thermal conductivity which is determined by the resistivity data according to the Wiedemann-Franz-Lorenz law is given by $\kappa_{liq}(T) = 49.43 + 2.90 \times 10^{-2}(T - T_m)$ W/m/K(Fig. 12).

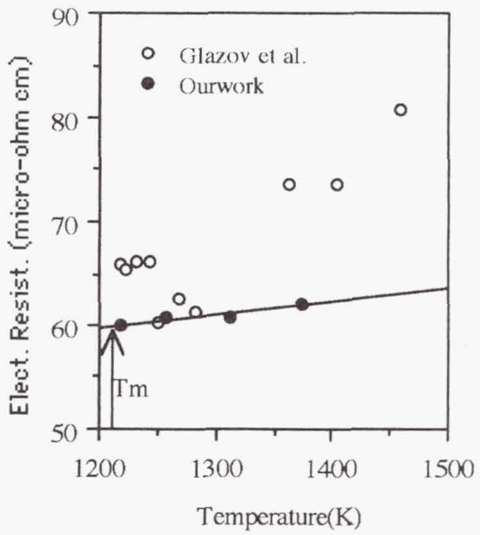

Fig. 11. Elect. resistivity of molten Ge.

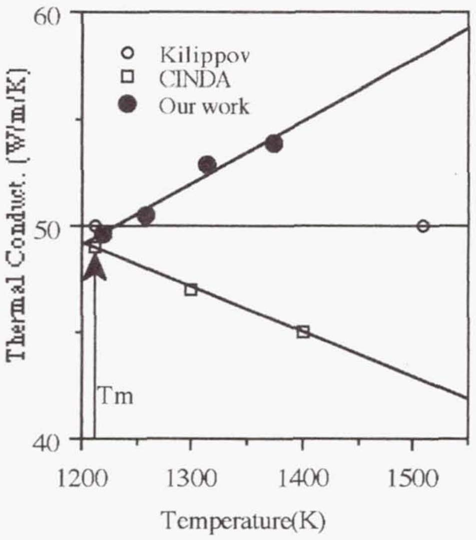

Fig. 12. Thermal conductivity of Ge.

(4) A Comment about the Viscosity Measurements

The viscosity measurement method relies on the measurement of the damping time constant of a freely oscillating drop. On the other hand, levitation of a melt in a 1-g environment requires application of a strong controlled electrostatic field to counter the weight. Any interference of a free decay process by the levitation control force can modify the decay process, and the decay constant is modified by it. The lower the viscosity is the more susceptible the decay constant will be to the external perturbation. Evidences for the range of viscosity measurable in 1-g by the JPL HTESL are being accumulated. Above their melting temperatures, both molten silicon and germanium showed viscosities that were less than 1 mPs. Examining the scatter amplitude of these data, ~ 1 mPs seems to be just about the limit.

Such susceptibility to external noise is relatively more pronounced as the viscosity of the melt decreases. In the present case, the most dominant perturbing force was coming from the levitation force whivh corrected the sample position 480 times per second. The viscosity data we obtained scattered between 0.13 mPs and 0.7 mPs. In contrast, Glazov et al.[9] reported 0.78 mPs for germanium and 1.1 mPs for silicon at the respective melting points.

(5) Upgrading of the JPL HTESL

The knowledge on spectral emissivity of a sample material at the wavelength of pyrometer is important to determine the true temperature of the sample. Without this capability, a known reference temperature is essential, and a further assumption on constant spectral emissivity over a temperature region of interest has to be made. In an environment where such a reference point does not exist, temperature information of a given alloy becomes quite uncertain. For this reason, we have purchased and integrated in the JPL HTESL a commercial instrument which measures the spectral emissivity that will help determine the true temperature. Also installed was a 100 W YAG laser which would allow the sample temperature measured even during sample heating cycle. This high power laser will be able to heat a sample higher than 2000 C. This upgrading process required construction of an almost whole new HTESL system.

Spectral emissivity measurement, laser heating and sample rotation capabilities are the three important additions in the HTESL. In summary, the new facility can measure the following properties:

(1) true temperature by measuring spectral emissivity;
(2) density (or the volume expansion coefficient);
(3) the ratio between the specific heat and the hemispherical total emissivity;
(4) surface tension of liquids within a wide viscosity range;
(5) viscosity;
(6) electrical conductivity;
(7) thermal conductivity determined from the measured electrical conductivity using the Wiedemann-Franz-Lorenz Law.

References:

[1] W. K. Rhim, S. K. Chung, D. Barber, K. F. Man, G. Gutt, A. Rulison, and R. E. Spjut: "An Electrostatic Levitator for High Temperature Containerless Materials Processing in 1-g," Rev. Sci. Instrum. 64: 2961, 1993.

[2] W. K. Rhim, S. K. Chung, and A. J. Rulison, and R. E. Spjut: "Measurements of Thermophysical Properties of Molten Silicon by a High-Temperature Electrostatic Levitator", Int. J. Thermophysics 18, 459, 1997.

[3] K. Ohsaka, S. K. Chung, W. K. Rhim, and J. C. Holzer: "Density of Si Determined by an Image Digitizing Technique in Combination with an Electrostatic Levitator", Appl. Phys. Lett. (in press).

[4] H. Sasaki, E. Tokiszaki, K. Terashima, and S. Kimura: Jpn. J. Appl. Phys. 33, 3803, 1994.

[5] F. H. Busse: "Oscillations of a rotating liquid drop", J. Fluid Mech. 142, 1-8, 1984.

[6] P. Annamalai, E. T. Trinh, and T. G. Wang, "Experimental Studies of the Oscillation of a Rotating Drop," J. Fluid Mechs., 158, 317, 1985.

[7] W. K. Rhim and T. Ishikawa: "Thermophysical Properties of Molten Germanium Measured by High Temperature Electrostatic Levitator", Proc. 5th Asian Thermophs. Properties Conf. Seoul, Korea, Aug. 30 - Sept. 2, 1998 (accepted)

[8] W. K. Rhim and T. Ishikawa: "Non-Contact Electrical Resistivity Measurement Technique for Molten Metals", Proc. First Pan-Pacific Basin Workshop and Fourth Japan/China Workshop on Microgravity Sciences, July 8-11, 1998, Tokyo, Japan (in press)

[9] V. M. Glazov, S. N. Chizhevskaya, and N. N. Glagoleva, Liquid Semiconductors (Plenum press, New York, p. 61, 1969.

Undercooling Limits and Thermophysical Properties in Glass Forming Alloys

Principal Investigator: Dr. Won-Kyu Rhim, Research Scientist, Jet Propulsion Laboratory,
M/S183-401, TEL: (818) 354-2925, FAX: (818) 393-5039

Co-Investigator: Dr. Kenichi Ohsaka, JPL, Mail Stop 183-401, TEL: (818) 354-3111
Co-Investigator: Prof. R.Erik Spjut, Harvey Mudd College, Claremont, CA 91711
(909) 607-3890

Other Participants: Mr. Takehiko Ishikawa, Dr. Paul-Francois Paradis, and Mr. Daniel Barber

Objectives of the Research

The primary objective of this program is to produce deeply undercooled metallic liquids and to identify factors that limit undercooling and glass formation. The main research objectives are:
(i) Investigating undercooling limits in glass-forming alloys and identifying factors that affect undercooling.
(ii) Measuring thermophysical properties and investigatiing the validity of the classical nucleation theory and other existing theories in the extreme undercooled states.
(iii) To investigate the limits of electrostatic levitation technology in the ground base and to identify thermophysical parameters that might require reduced-g environment.

Relation to the Gravitational Field

When experiments are conducted in a 1-g environment, all gravity caused effects such as convective flows, sedimentation and buoyancy still remain in the levitated melts. In addition, large forces that are needed to levitate a sample against gravity can cause flows in the melts. The High Temperature Electrostatic Levitator (HTESL) is a relatively recent development. Its limitations in 1-g conditions have not been fully established. Although considerably less flows are expected with electrostatic levitation, very little is known about flows induced by the electrostatic forces. The most seriously affected transport properties might be atomic diffusion, viscosity, and thermal conductivity. In this ground base program, we will identify the thermophysical properties and their temperature ranges which require reduced-g condition for their measurements.

Progress of the Research

(A) Thermophysical properties of Ni-Zr alloys (NiZr, $NiZr_2$, $Ni_{36}Zr_{64}$ and $Ni_{24}Zr_{76}$) have been extensively measured in order to investigate their alloying effect on the undercooling level and the glass formability. Properties measured were specific volume, surface tension, viscosity, and the ratio between the specific heat to the hemispherical total emissivity. What we were interested in was the effect caused by the presence of chemical short-range order (formation of the associated species) which existed in some compound forming liquid alloys.

We used the HTESL at JPL[1] to isolate samples from the contamination associated with containers and to process in a high vacuum environment, which assured consistent and repeatable undercooling levels. We selected Ni-Zi alloys, NiZr and $NiZr_2$ are compound forming alloys, and $Ni_{36}Zr_{64}$ and $Ni_{24}Zr_{76}$ are eutectic alloys. For the identification of associated species in the alloys, we measured specific volumes and viscosities of these alloys.

Figure 1 shows the specific volumes of the four alloys as a function of decreasing temperature. The melting point of each alloy is indicated by the arrow. Note that the specific volume of the $NiZr_2$ alloy is significantly smaller than those of the other alloys. Figure 2 shows the viscosity of the alloys as a function of temperature. Note that the viscosity of the compound-forming alloys are higher than those of the eutectic alloys even at temperatures well above the melting point. Table 1 shows the undercooling level, $\Delta T = T_m - T_N$, where T_m is the melting point (or eutectic temperature) and T_N is the nucleation temperature of the alloys. As a reference, the undercooling levels of the metals are also shown. Note that the undercooling level of $NiZr_2$ is smaller than those of other alloys.

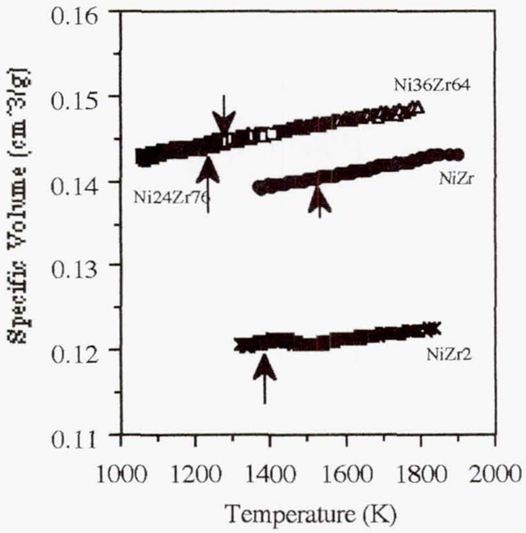

Fig. 1. Specific volume of Ni-Zr alloys

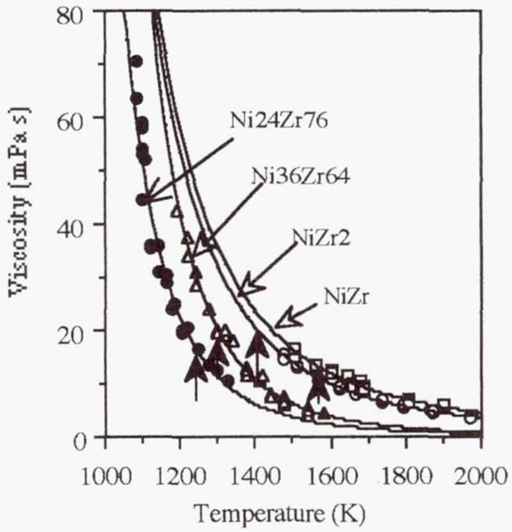

Fig. 2. Viscosity of Ni-Zr alloys

These specific volume data indicate the presence of associated species in the form of $NiZr_2$. On the other hand, the viscosity data indicate the presence of both NiZr and $NiZr_2$. As seen in Table 1, the $NiZr_2$ alloy shows significantly small undercooling compared with those of other alloys and the metals. This difference should not have arisen from the experimental conditions because the sample preparation and the experimental procedure are the same for all of the alloys. Since the $NiZr_2$ liquid alloy possesses a specific volume which is comparable to that of the compound solid, it is likely that the bonding of the species is very similar to that of the compound solid including the lattice parameters. If this is true, a drastic local structural rearrangement is not required when the liquid is transformed into the solid.

Table 1. Undercooling Level, ΔT of the alloys and metals.

Metal or Alloy	Ni	NiZr	$Ni_{36}Zr_{64}$	$NiZr_2$	$Ni_{24}Zr_{76}$	Zr
T_m or T_E (K)	1728	1533	1283	1393	1233	2130
$\Delta T/T_m$ (%)	14	11	17	6	14	15

According to classical nucleation theory, the nucleation rate, I, is given by the following form

$$I \sim \exp\left(-\frac{\sigma_{sl}^3}{\Delta G^2}\right) \qquad (1)$$

where σ_{sl} and ΔG are the liquid/solid interfacial energy and the free energy difference between the solid and liquid, respectively. Since σ_{sl} is always positive, it acts as a barrier for nucleation. The larger the σ_{sl} value, the more resistant the liquid is to nucleation, which results in a large undercooling level prior to the onset of crystallization. As is assumed above, if the $NiZr_2$ liquid has a similar local structure to the solid, distortions should be small when the two phases contact to form the interface. As a result, the interface has a small interfacial energy. Thus, the small undercooling of the $NiZr_2$ alloy can be attributed to the small interfacial energy.

Rotating Molten Metallic Drops and a New Way of Measuring Surface Tension

A new technique which is capable of systematically inducing rotation on a levitated metallic drop was developed to study the dynamics of rotating charged metallic drops and to verify a new approach for measuring the surface tension.

Molten aluminum and tin drops were levitated in a high vacuum by controlling applied electric fields, and they were systematically rotated by applying a rotating magnetic field. As the drops gradually (or step by step) gained angular momentum from their static states, their shapes evolved along an axi-symmetric branch until a bifurcation point was reached at which point in time, transformation from the axi-symmetric to tri-axial shape took place. With an assumption of "effective surface tension", which includes the effect of reduced surface tension due to the surface charges, the results agreed quantitatively well with the Brown and Scriven's prediction [2]. The normalized rotation frequencies at the bifurcation point agreed well with the predicted value, 0.559, within 2%.

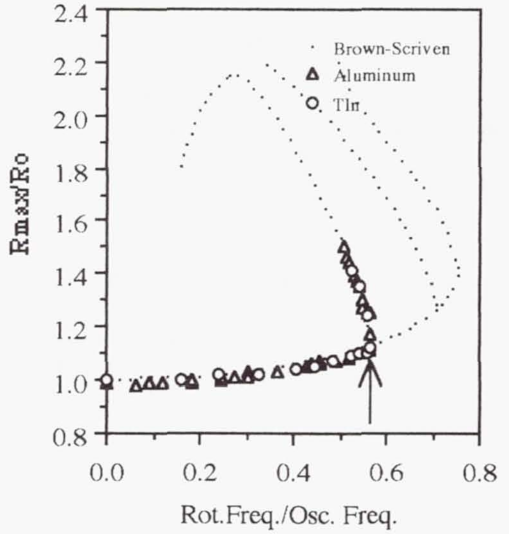

Fig. 3. Distortion vs. rotational rate

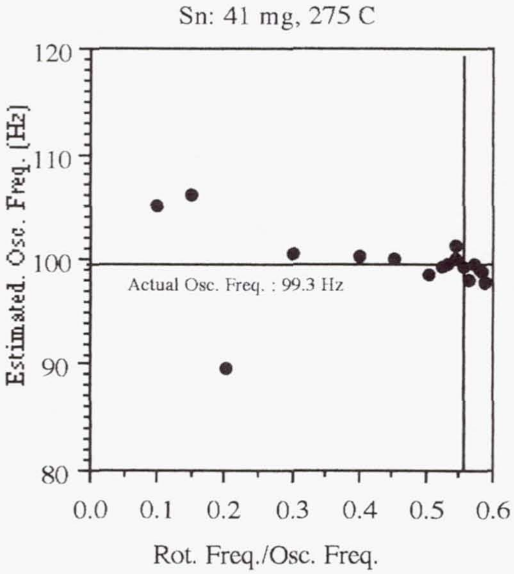

Fig.4. Effective osc. freq. vs. rot. rate

Once agreement with the theory was confirmed, we attempted to use it to explore an alternative way of measuring surface tension. This approach of measuring surface tension using drop rotation was proposed earlier by Elleman et al.[3]. For low viscosity liquids, measuring the resonant oscillation of a levitated drop is an accurate means of extracting its surface tension[4, 5]. However, for high viscosity liquids where drop oscillations cannot be induced, a new non-contact technique is needed. For example, viscosity of glass forming alloy liquids increase nearly 14 orders magnitude before their glass transition temperatures are reached. The solution to finding an alternate method for surface tension measurement can be found from Fig. 3. If a drop rotates according to the theoretical curve as shown in Fig. 3, one can determine the effective oscillation frequency at any point of the curve if the shape parameter (R_{max}/R_o) and the corresponding drop rotation frequency are known. Since the drop rotation frequency of an axi-symmetric drop is difficult to measure if the drop surface is extremely uniform, measuements of the drop rotation frequencies should be made on the triaxial branch close to the bifurcation point. Since $\omega_{rot}/\omega_{osc}= 0.559$ at the bifurcation point, and the rotation frequency can be measured, the effective oscillation frequency can be determined. Fig.4 demonstrates how effective oscillation frequency of a molten tin drop approaches actual oscillation frequency as the rotation frequency approached the bifurcation point. This approach to the surface tension measurement should be applicable to homogeneous metallic melts of broad viscosity ranges as long as the solid-body rotation condition is satisfied.

Measurement of Surface Tension of Viscosity of a Viscous Glassforming Alloy ($Zr_{41.2}Ti_{13.8}Cu_{12.5}Ni_{10.0}Be_{22.5}$)

We have attempted a preliminary demonstration of surface tension measurement using the rotation method described above. We chose a bulk glassforming alloy ($Zr_{41.2}Ti_{13.8}Cu_{12.5}Ni_{10.0}Be_{22.5}$) which was provided earlier by the Caltech's William Johnson's group. Initially the sample was heated to ~250K above the melting temperature in order to ensure that the drop oscillation could be induced in response to an applied oscillating electric field. Observed oscillations were exponentially decaying transient signals, and they were axi-symmetric $P_2(\cos\theta)$ mode. The surface tension was extracted from the drop oscillation frequency and the viscosity was calculated from the time constant of the transient oscillation [5]. As this process was continued with the temperature lowered a step at a time, we soon hit a limiting temperature below which we could not induce the oscillation within the capability of the instrument. When the rotation method for measuring surface tension was

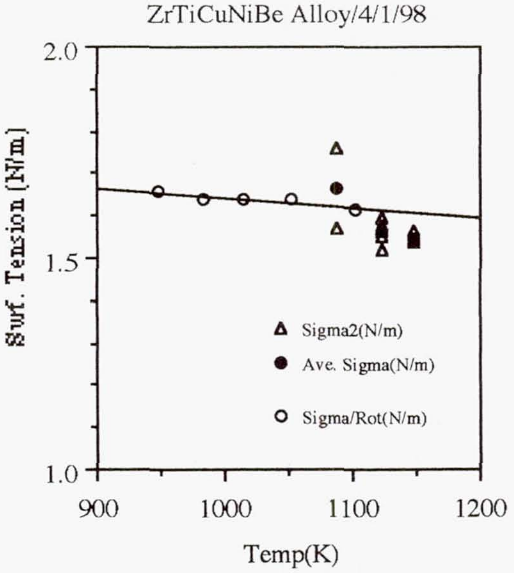

Fig. 5 Surf. tension of a bulk glassforming alloy.

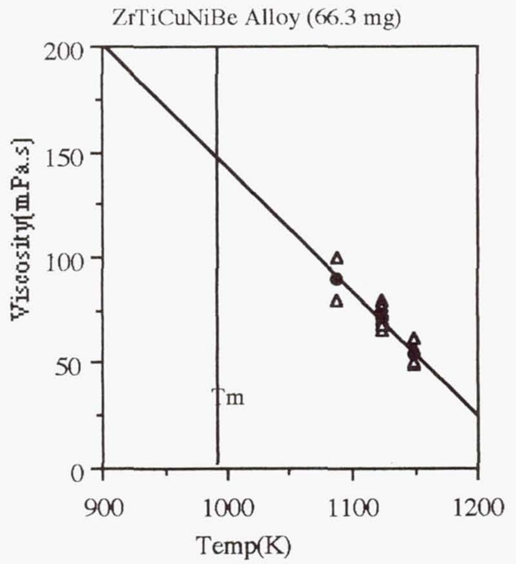

Fig. 6. Viscosity of the same alloy.

applied, we could measure the surface tension to much lower temperature as shown in Fig. 5 by open circles. Also superimposed in Fig. 5 are the surface tension data which were obtained by the transient drop oscillation method. One can observe that the uncertainty in surface tension increases rapidly with the lowered temperature. Fig. 6 shows the viscosity data obtained from the same transient oscillation signals. We noticed that the uncertainty in viscosity data does not increase nearly as rapidly as the surface tension data with lowered temperature. We also noted that the viscosity at the melting temperature is expected to be as high as 150 mPs. To our knowledge, viscosity measuring method based on the sample rotation does not exist at this time. However, its development may be possible.

A New Non-Contact Technique for Measuring Electrical (and Thermal) Conductivity[6]

Electrical conductivity is one of the most sensitive indicators of changes in the nature of chemical binding. In general, electrical conductivity is proportional to carrier density and carrier mobility. A change in the nature of the chemical binding primarily alters the carrier density, and the structural changes alter carrier mobility. Very early investigations of metals showed that the conductivity decreased approximately by a factor 2 at the melting point, while it increased in silicon and germanium as they transform from semiconducting solids to conducting liquids. The electrical conductivities of metallic liquids are of obvious importance to many liquid processing operations (e.g. electric furnace steel making and refining operations, electromagnetic stirring for melt cleanliness and microstructural control) and it is a sensitive measure for concentration fluctuation in a critically mixed liquid alloy near the critical point in the homogeneous liquid phase. The high electrical and thermal conductivity of metals in their condensed states can be attributed almost entirely to freely moving electrons, or conduction electrons. From the metallurgical point of view, relatively few studies have been carried out on the electrical properties of liquid metals and alloys. Thermal conductivity is also of significance in liquid metal processing operations.

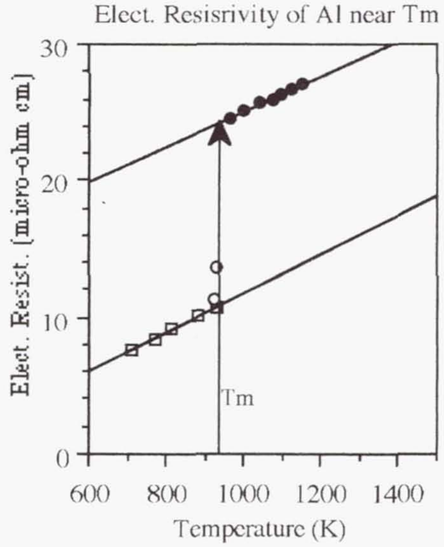

Fig. 9. Electrical resistivity if aluminum.

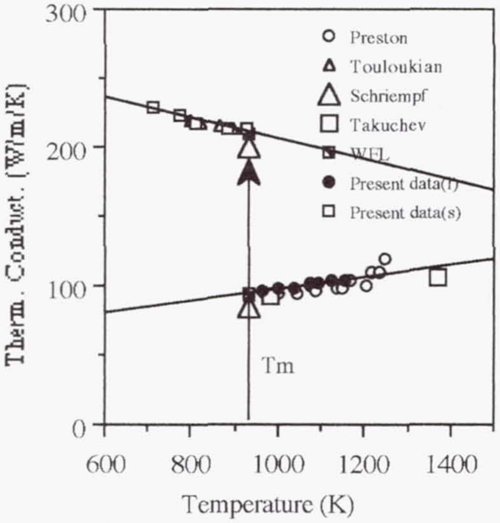

Fig. 10. Thermal conductivity determined by W-F-L Law using the data from fig. 9.

We have developed a non-contact electrical conductivity measurement technique that was adapted to the high temperature electrostatic levitator(HTESL). A rotating magnetic field was applied to a levitated drop, and the induced torque was measured. According to the theory of induction motors, induced torque should be proportional to the electrical conductivity of the liquid drop. , As it stands now, this technique measures the relative changes of electrical conductivity (or resistivity), therefore, it requires a reference point for calibration. Fig. 7 shows the electrical resistivity of aluminum around the melting temperature.

Accurately measuring thermal conductivity of molten metals is usually more difficult than the measurement of electrical conductivity. Inaccuracies in directly measured thermal conductivity are primarily caused by the difficulties in accurate heat flow measurements, and also to a certain degree, by flows taking place in a melt. However, if thermal and electric conduction take place primarily by free electrons, these two conductivity should be connected through the Wiedemann-Franz-Lorenz Law. Using this law may allow us to obtain more accurate values for thermal conductivity from accurately measured electrical conductivity. Fig. 8 shows the thermal conductivity so determined for aluminum around the melting temperature. Our results agree quite well with independently measured thermal conductivity given by the literature.

Upgrading the JPL HTESL

Upgrading effort of the JPL HTESL facility is essentially complete. The old HTESL did not have true temperature measuring capabilities. Thermophysical properties are usually measured as a function of temperature. However, without knowing true temperature, measured properties cannot be considered credible. The spectral emissivity measurements, laser heating and sample rotation capabilities are three important additions to the new HTESL. Operation of a 100 watt YAG laser was successfully tested by repeating the melting-freezing cycle of a metallic alloy. The sample rotation capability has been thoroughly tested using various solid and molten materials. In summary, the new facility can measure the following properties:

(1) true temperature by measuring spectral emissivity,
(2) density (or the volume expansion coefficient),
(3) the ratio between the specific heat and the hemispherical total emissivity,
(4) surface tension of liquids within a wide viscosity range,
(5) viscosity,
(6) electrical conductivity.
(7) thermal conductivity determined from measured electrical conductivity using the Wiedemann-Franz-Lorenz Law.

References:

[1] W. K. Rhim, S. K. Chung, D. Barber, K. F. Man, G. Gutt, A. Rulison, and R. E. Spjut: "An Electrostatic Levitator for High Temperature Containerless Materials Processing in 1-g," Rev. Sci. Instrum. 64: 2961, 1993.

[2] R. A. Brown and L. E. Scriven, "The Shape and Stability of Rotating Liquid Drops," Proc. R. Soc. Lond. A 371, 331, 1980.

[3] D. D. Elleman, T. G. Wang, and M. Barmatz: "Acoustic Containerless Experiment System: A Non-Contact Surface Tension Measurement," NASA Tech. Memo. 4069, Vol. 2, 557, 1988.

[4] W-K. Rhim, S.K. Chung, and D.D. Elleman, "Experiments on Rotating Charged Liquid Drops," Proc. 3rd International Colloquium on Drops and Bubbles (ed. T. G. Wang), AIP Conf. Proc. 197: 91, 1988 .

[5] W. K. Rhim, K. Ohsaka, and R. E. Spjut, "A non-contact technique of measuring surface tension and viscosity of molten materials using high temperature electrostatic levitator," Rev. Sci. Instrum, (accepted).

[6] W. K. Rhim and T. Ishikawa: "Non-Contact Electrical Conductivity Measurement Technique for Molten Metals", Rev. Sci. Instrum. (accepted)

Carbon-Based Reduction of Lunar Regolith (CRLR)

Dr. Eric E. Rice
Orbital Technologies Corporation (ORBITEC)
Space Center, 1212 Fourier Drive
Madison, WI 53717

Phone: (608) 827-5000
E-mail: ricee@orbitec.com

Introduction

ORBITEC is developing a new high-temperature processing technique to produce oxygen and metals from Lunar regolith via carbonaceous high-temperature reduction. The utility in this technique overcomes problematic issues inherent in traditional high-temperature processing methods that employ crucible-type containment vessels and hot-walled (i.e., resistance or inductive) furnaces. Crucible containment structures either crack from thermal and mechanical stress and/or react with the molten reaction mix, making it very unlikely that such a material could survive the repeated high-temperature thermal cycling in an economical LOX plant on the Moon. To enable *in situ* production of Lunar oxygen, high-temperature reduction of Lunar soil can be accomplished using an alternate heating source, achieving high oxygen yield and high carbon (or hydrogen, depending on the reducing source) recovery. The proposed method will allow extremely high processing temperatures (>2000 °C) and eliminate the difficult requirement of developing a containment vessel that withstands these temperatures, is impervious to prolonged chemical attack, and is capable of thermal cycling. Reduction of regolith using this heating approach will provide NASA with a manageable, practical, and efficient technique for extracting oxygen from indigenous Lunar resources for life support and propellant applications. In this effort, ORBITEC proposes to demonstrate new techniques for achieving high oxygen yield and high carbon or hydrogen recovery. It would also involve integrated designs for both a production plant and flight experiment, the latter being test-flown on a NASA reduced-gravity aircraft.

Objectives

The primary objective of this effort is to demonstrate a practical and feasible technique for heating to >2000 °C and the reduction of simulant by carbon and hydrogen, with very high recovery of carbon and hydrogen. This effort will look at both carbonaceous and hydrogen gas reduction of Lunar simulant, focusing on the first step, in either case, in the overall production of oxygen from metallic oxides. Furthermore, efficient demonstration in the first year will provide the foundation for a preliminary flight experiment designs. Demonstration of a flight experiment in 1/6-g on a NASA parabolic aircraft would further substantiate development of a technology demonstration experiment on the Moon.

As part of these overall goals, the CRLR design and development effort will focus on these technical objectives:

1. Design, develop, and fabricate a test chamber in which heating of Lunar simulant to temperatures greater than ~2000 °C can be demonstrated;
2. Determine temperature profiles, both experimentally and theoretically, within the regolith surrounding the processing zone, including transient and steady state behavior;
3. Evaluate the effects of the new heating approach on regolith heating profiles;

4. Demonstrate carbonaceous reduction of, at least, the silica, titania, and iron oxide components of Lunar simulant using three separate reducing agents, including carbon-based agents and hydrogen gas, heating to temperatures greater than ~2000 °C;
5. Design and develop a space flight experiment design that incorporates the new heating approach and is capable of acquiring samples from the Lunar surface; and,
6. Conduct low-g processing tests in a 1/6-g environment using a NASA reduced-gravity aircraft to assess the space flight experiment design, study the effect of low-g on the process, and provide data on the system's overall performance.

Project Status

It is envisioned that development of the proposed technique will ultimately lead to a scaled production plant on the surface of the Moon, providing an indigenous source of oxygen for propulsion and life support and the production of useful metal and ceramic byproducts. Before a production plant can be fully realized, several demonstrations of the technology and concept must be made in the Lunar environment. These demonstrations would most likely take the form of low-mass, low-power, experiment packages that would be part of an ISRU technology demonstration mission on the Moon that is envisioned by NASA and ORBITEC. However, the design of a space flight experiment package would require knowledge of the system's behavior and performance in the Lunar environment. Certain aspects of the Moon's environment could be simulated in the laboratory, such as the temperature extremes and its vacuum-like atmosphere. Simulation of the reduced gravity, however, would require flight-time on a NASA parabolic aircraft. Modeling of the processes also needs to be verified by experiments in 1/6-g.

It is highly desirable to investigate the proposed concept in a 1/6-g environment. It is presently unknown how the 1/6-g gravity will affect the processed regolith. It is also unknown how the transport mechanisms of carbon-based agents or hydrogen (depending on which reducing agent is used) to the hot sample surface will be influenced by 1/6-g. The lower gravity environment may affect the rate at which the reducing agent transports or diffuses into the reactant material. ORBITEC has considered the test environments available and believe that ~20 seconds, or more, of 1/6-g is sufficient time to allow for heating of small amounts of Lunar simulant material and subsequent reaction with either carbon-based agents or hydrogen gas. Drop tower tests with duration's in the 5 second time region are considered insufficient due to the initial disturbance conditions and very high cost. Thus, the environment provided by a NASA parabolic aircraft has been selected for 1/6-g simulation.

ORBITEC is currently designing and fabricating the experimental hardware for this project.

Containerless, low-gravity undercooling of Ti-Ce alloys in the MSFC Drop Tube

M. B. Robinson[a], T. J. Rathz[b], D. Li[c], G. Williams[b], G. Workman[b]
[a]NASA/Marshall Space Flight Center, Huntsville, Alabama, 35812. (256)544-7774
[b]University of Alabama, Huntsville, Alabama, 35899. (256)544-1409
[c]NASA/MSFC NRC Resident Research Associate. (256)544-9195

Introduction

Previous tests of the classical nucleation theory as applied to liquid-liquid gap miscibility systems found a discrepancy between experiment and theory in the ability to undercool one of the *liquids* before the L_1-L_2 separation occurs (1,2). To model the initial separation process in a two-phase liquid mixture, different theoretical approaches, such as free-energy gradient (3) and density gradient (4) theories, have been put forth. If there is a large enough interaction between the critical liquid and the crucible, both models predict a wetting temperature (T_w) above which the minority liquid perfectly wets and *layers* the crucible interface, but only on one side of the immiscibility dome. Materials with compositions on the other side of the dome will have simple surface adsorption by the minority liquid before bulk separation occurs when the coexistence (i.e., binoidal) line in reached. If the interaction between the critical liquid and the crucible were to decrease, T_w would increase, eventually approaching the critical consolute temperature (T_{cc}). If this situation occurs, then there could be large regions of the miscibility gap where non-perfect wetting conditions prevail resulting in *droplets* of L_1 liquid at the surface having a non-zero contact angle. The resulting bulk structure will then depend on what happens on the surface and the subsequent processing conditions.

In the past several decades, many experiments in space (5-7) have been performed on liquid metal binary immiscible systems for the purpose of determining the effects that different crucibles may have on the wetting and separation process of the liquids. Potard (5) performed experiments that showed different crucible materials could cause the majority phase to preferentially wet the container and thus produce a dispersed microstructure of the minority phase. Several other studies have been performed on immiscibles in a semi-container environment using an emulsion technique (8,9). Only one previous study was performed using completely containerless processing of immiscible metals (10) and the results of that investigation are similar to some of the emulsion studies. In all the studies, surface wetting was attributed as the cause for the similar microstructures or the asymmetry in the ability to undercool the liquid below the binoidal on one side of the immiscibility dome.

By removing the container completely from the separation process, it was proposed that the loss of the crucible/liquid interaction would produce a large shift in T_w and thus change the wetting characteristics at the surface. By investigating various compositions across the miscibility gap, a change in the type and amount of liquid wetting at the surface of a containerless droplet should change the surface nucleating behavior of the droplet – whether it be the liquid-liquid wetting or the liquid-to-solid transition. Undercooling of the liquid into the metastable region should produce significant differences in the separation process and the microstructure upon solidification. In this study, we attempt to measure these transitions by monitoring the temperature of the sample by optical pyrometry. Microstructural analysis will be made to correlate with the degree of undercooling and the separation mechanisms involved.

Experimental Details

Material Selection and Handling

Because of the limited amount of free-fall/cooling time available in the Drop Tube, a monotectic system had to be found that would provide the necessary critical and invariant temperatures to allow a sample with a reasonable diameter (5mm) to totally solidify. Other considerations were low component vapor pressures at T_{cc}, small oxygen affinity, a known phase diagram, and no toxicity. Not one system met all the requirements. The Ti-Ce (46.8 to 92.0 w/o Ce) system, prepared at the Materials Preparation Center of Ames Laboratory, USDOE, was chosen as the best trade-off. The masses of the samples ranged between 0.34 to 0.43 grams; the calculated, ideally-spherical sample diameters were 5.3 ± 0.2 mm. Drops were opened and stored under inert gas at all times. Oxygen and nitrogen levels within the samples were reported by Ames to be 150-250 ppmw and about 20 ppmw, respectively.

Low-gravity Process

The Drop Tube Facility at NASA/Marshall Space Flight Center (11) was used to provide low-gravity (hereafter labeled 0-g), containerless free-fall conditions. The 0-g samples were processed by electromagnetic (EM) levitation and heating at a frequency of 450 kHz. Once the sample was molten, the power to the coil was automatically turned off and the material allowed to freeze while in free-fall. At the bottom of the Drop Tube, the samples were funneled directly into a thick-walled pyrex tube where they were sealed under a partial pressure of inert gas. The Tube was backfilled with Ti-gettered 5-nines pure He-6%H_2 gas to a pressure of 89.5 kPa. The calculated maximum g-level induced by the drag on the sphere was 25 milli-gravity's.

An eight channel, 125 MHz per channel, 12-bit resolution data acquisition unit was used to monitor silicon detector voltages generated by the brightness of the falling sample. The recalescence temperature of the sample (and thus the amount of undercooling) was calculated knowing the initial release temperature and time (= 0), and the final time (t_{rec}) at which recalescence began. Release temperatures were kept to 2023K – 100 degrees above T_{cc} (12). For both the 0-g and 1-g studies, an Ircon Modline two-color pyrometer was used to measure the sample temperature at a rate of 100 readings per second and an accuracy of 1%.

Unit-gravity Process

The 1-g studies were performed atop the Drop Tube Facility in the same EM coil that was used to process the 0-g samples. The samples were levitated and heated to 2023K at which temperature a cooling gas was applied. A typical heating/cooling curve is presented in Figure 1. The samples were released down the Tube to allow the remaining L2 Ce-rich liquid to cool and solidify.

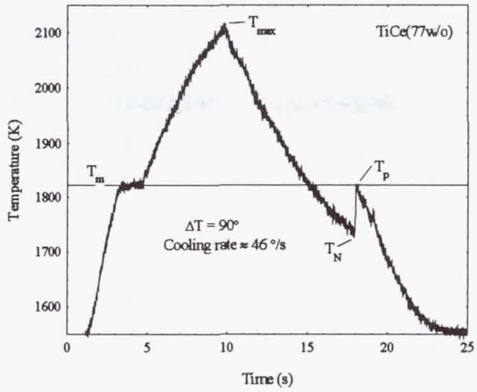

Fig. 1. Typical 1-g sample heating/cooling curve in the EM coil. Temperatures are: T_m, the monotectic, Tp, the recalescence, T_N, the nucleation, and T_{max} , the maximum.

Experimental Results

Undercooling Measurements

Sixty-one 3-nines pure Zr and 23 3-nines Ti were used as melting point calibrations for the optical pyrometer. The average Zr melting temperature was 11 degrees above and Ti was 1 degree above literature values. For the 36 1-g samples processed in the EM coil, the monotectic temperature (T_m) was reproducibly measured from the recalescence peak temperature (T_p) as 1833K with a standard deviation of 19K. From the 34 0-g sample measurements, T_m was reproducibly measured as 1830K with a standard deviation of 7K. Together, the EM coil and Drop Tube processed samples had T_m's that contrasted to the reported literature value of 1723K (12).

Liquid-to-liquid undercoolings could not be detected with the limited sensitivity of the optical pyrometer. However, Figure 2 shows the liquid-to-solid undercooling measurements placed across the miscibility gap of the Ti-Ce phase diagram. The monotectic line and the binoidal curve have been shifted to account for the measured T_m. A distinct increase in the amount of undercooling achieved in the 0-g samples versus the 1-g samples is observed. The amounts of undercooling could not be controlled in the Drop Tube – if a specimen levitated stably, melted, overheated, and released straight down the Tube without hitting the walls, large undercooling could not be avoided.

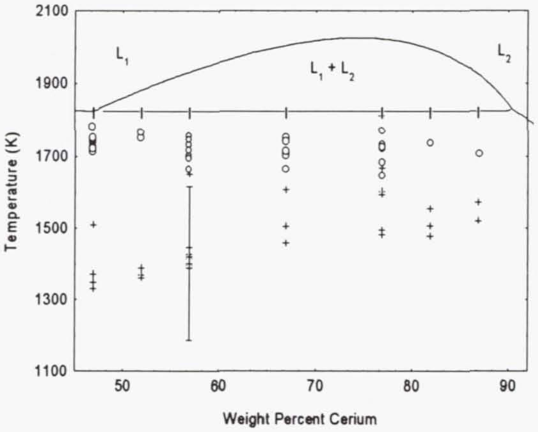

Fig. 2. Immiscibility dome of Ti-Ce phase diagram showing a composite of all the undercooling measurements taken in this study. The 0-g samples (+) showed additional undercooling over the 1-g samples (O) despite the worse-case error bars in the calculated values. The monotectic line and the binoidal curve have been adjusted for the measured T_m values (I).

Microstructure Observations

- 0-g Samples

Fig. 3a shows the general morphology seen throughout the 0-g samples: the size of the large central, concentric β-Ti sphere gets smaller as the volume percent of the Ce-rich liquid increases. At ALL compositions, a Ce-rich layer formed as the outer shell of the sample whose thickness depended on the initial volume fraction of Ce. Secondary Ce droplets were found randomly dispersed in the large β-Ti droplet. No correlation of undercooling to the remaining amount of dissolved Ce contained in the β-Ti matrix could be made.

- 1-g Samples

The 1-g samples are in contrast to the 0-g samples. The 1-g samples show the stirring/shearing effects of the EM field on the β-Ti resulting in large irregularly-shaped globules found near the surface. The Ce droplets in the β-Ti globs is found interdendritically (fig. 3b) and not randomly dispersed as in the 0-g samples. In both the 0-g and 1-g samples, blackish Ce-oxide particles were found sparsely dispersed in both the majority and minority phases.

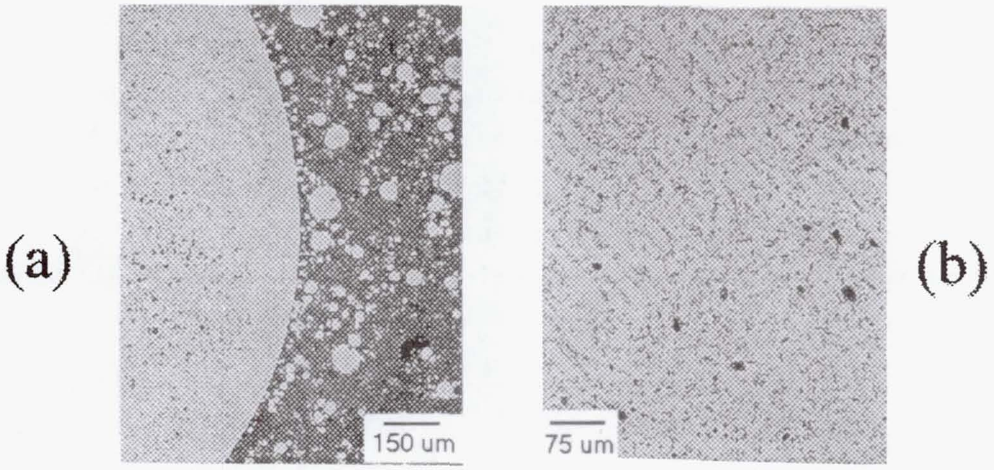

Fig. 3. Photomicrographs of (a) 0-g sample and (b)1-g sample. The dark phase is Ce-rich and the lighter is β-Ti. Black irregularly-shaped spots are Ce-oxide particles.

Discussion of Results

The large difference in the measured monotectic temperature versus literature values was extensively analyzed. Due to the speed of the pyrometer, the T_p (= T_m) of the 1-g EM samples consisted of only 1-2 points and thus had the larger degree of uncertainty. However, the Drop Tube samples' T_m upon heating consisted of the flat melting isotherm that was very reproducible across the miscibility gap. A flat melting isotherm upon heating implied that the as-cast materials from Ames Laboratories had separated and solidified with a segregated monotectic structure which metallography proved to be correct. Changes in the emissivity due to slight oxidation of the surface should be negligible due to the 2-color signal ratioing of the pyrometer. The oxygen content of the Ti-Ce after processing in the Drop Tube were analyzed by LECO Corporation and are presented in Table 1. About 500 ppmw O_2 was absorbed during the processing of the Ti-Ce in this study. The oxygen content of materials used in previous phase diagram studies (13) could not be found suggesting some inaccuracies in these phase diagrams possibly due to the addition of oxygen.

Table 1. Nitrogen and oxygen content of Zr test drops and TiCe alloys before and after processing in the Drop Tube (in ppmw).

Zr				**TiCe**			
Arc-melted		After Drop		Before Drop		After Drop	
(LECO)		(LECO)		(Ames)		(LECO)	
O2	N2	O2	N2	O2	N2	O2	N2
1173	7	1235	32	166	18	628	236

The large discrepancy between the 1-g undercoolings and the 0-g undercoolings may be attributable to several things. The 0-g temperatures in this study are a calculated number that depends on thermophysical properties values of the alloy in the undercooled state. A worse-case average error bar of ± 215 K was calculated based on the combined uncertainties of these thermophysical properties. The combined errors would still allow a large number of the Drop Tube undercoolings to be below those of the EM coil samples.

A large difference in cooling rate between the 1-g samples (40K/s) and the 0-g samples (230K/s) may effect the rate of formation of solid β-Ti nuclei and thereby the amount of undercooling. An estimate of this effect can be obtained from a modified form (14) of the classical nucleation theory where the values of ΔG_l^* are based around that given by Kelton (15) of 60kT. At the most, this correction could account for only 10K of additional undercooling.

The relatively quiescent environment of the Drop Tube allowed the 0-g samples to not be stirred as experienced by the 1-g samples in the EM field. The 1-g stirring will sweep the nucleated droplets into much larger spheres by coalescence versus a 0.1 - 2 mm/s calculated Marangoni speed. Without a sweeping effect in 0-g to hasten the coagulation of the droplets, the liquid-liquid dispersion is essentially a high temperature emulsion.

Similar microstructures were seen by Andrews (10) in containerlessly processed Au-Rh samples but only for some of his 10 v/o Au-rich samples. Both Andrews and Perepezko (8) reported a fine dispersion of the minority phase within the majority phase on one side of the miscibility gap and surface wetting of the majority phase by the less-surface energetic minority phase on the other side of the miscibility gap, as predicted by Cahn (3). Approximate calculations of the interfacial energies between the liquids L_1, L_2 and the liquid's vapors indicate that the wetting criteria $\sigma_{L1L2} < | \sigma_{L1V} - \sigma_{L2V} |$ at the monotectic temperature is easily satisfied. Thus, the minority Ce-rich phase probably wetted the majority Ti-rich phase in this study, and the minority Ti-rich phase would have formed a dispersion for the Ce-rich side of the dome if not for the lengthy time while undercooled to allow coalescence. Similar results were found by Robinson (16) in 1-g processed Co-Cu metastable immiscibles. A quiescent, 0-g environment with direct non-contact temperature measurements could help eliminate some of the questions regarding these processing effects.

References

1. B. E. Sundquist and R. A. Oriani, Trans. Faraday Soc. **63**, 561 (1967).
2. R. B. Heady and J. W. Cahn, J. Chem. Phys. **53(3)**, 896 (1973).
3. J. W. Cahn, J. Chem. Phys. **66(8)**, 3667 (1977).
4. Gary F. Teletzke, L. E. Scriven, and H. Ted Davis, J. Colloid Interface Sci. **87(2)**, 550 (1982).
5. C. Potard, AIAA paper no. 79-0173 (1979).
6. S. H. Gelles and A. J. Markworth, AIAA Journal **16**, 431 (1978).
7. T. Carlberg and H. Fredriksson, Met. Trans. **11A**, 1665 (1980).
8. J. H. Perepezko, C. Galup, K. P. Cooper in Materials processing in the Reduced Gravity Environment of Space (Guy Rindone, ed., Elsevier Science Pub. Co., Amsterdam, 1982), p. 491.
9. N. Uebber and L. Ratke, Scripta Metall. **25**, 1133 (1991).
10. J. B. Andrews, C. J. Briggs, and M. B. Robinson in Proc. 7th European Symposium on Materials and Fluid Sciences in Microgravity (Oxford, UK, ESA SP-295, 1989), p. 121.
11. T. J. Rathz, M. B. Robinson, W. H. Hofmeister, R. J. Bayuzick, Rev. Sci. Instrum. **61(12)**, 3846 (1990).
12. Binary Alloy Phase Diagram (T. B. Massalski, ed., ASM 2nd editon, 1990).
13. E. M. Savitskii and G. S. Burkhanov, J. Less-Common Metals **4**, 301(1962).
14. A. J. Rulison, W.-K. Rhim, R. Bayuzick, W. Hofmeister and C. Morton, Acta. Mater. **45(3)**, 1237(1997).
15. K. F. Kelton, Solid State Physics (F. Seitz and R. Frederick, ed., Academic Press, Inc. 1991), p75.
16. M. B. Robinson, D. Li, T. J. Rathz, and G. Williams, submitted to J. Mater. Sci.

An Overview of the Electrostatic Levitation Facility at NASA's Marshall Space Flight Center

Jan R. Rogers[1], Michael B. Robinson[1], Larry Savage[2], Wolfgang Soellner[3], and Doug Huie[4]
NASA Marshall Space Flight Center
Marshall Space Flight Center, AL 35812

[1] Mail Code ES71
[2] Mail Code ES93
[3] Raytheon
[4] Mevatec

Containerless processing represents an important area of research in microgravity materials science. This method provides access to the metastable state of an undercooled melt. Containerless processing provides a high-purity environment for the study of reactive, high-temperature materials. Reduced gravity affords several benefits for containerless processing; for example, greatly reduced positioning forces are required and therefore samples of greater mass can be studied. Additionally, in reduced gravity larger specimens will maintain spherical shape which will facilitate modeling efforts. Space Systems/LORAL developed an Electrostatic Containerless Processing System (ESCAPES) as a materials science research tool for investigations of refractory solids and melts. ESCAPES is designed for the investigation of thermophysical properties, phase equilibria, metastable phase formation, undercooling and nucleation, time-temperature-transformation diagrams, and other aspects of materials processing. These capabilities are critical to the research programs of several Principal Investigators supported by the Microgravity Materials Science Program of NASA.

NASA's Marshall Space Flight Center (MSFC) recently acquired the ESCAPES system from LORAL. MSFC is now developing a levitation facility in order to provide a critical resource to the microgravity materials science research community and to continue and enhance ground-based research in the support of the development of flight experiments during the transition to Space Station.

Page intentionally left blank

PARAMAGNETIC LIQUID BRIDGE IN A GRAVITY-COMPENSATING MAGNETIC FIELD*,†

Milind P. Mahajan, Mesfin Tsige, P.L. Taylor, and Charles Rosenblatt
Department of Physics, Case Western Reserve University, Cleveland, Ohio 44106-7079 USA

Abstract

Magnetic levitation was used to stabilize cylindrical columns of a paramagnetic liquid in air between two solid supports. The maximum achievable length to diameter ratio R_{max} was ~ (3.10 ± 0.07), very close to the Rayleigh-Plateau limit of π. For smaller *R,* the stability of the column was measured as a function of the Bond number, which could be *continuously* varied by adjusting the strength of the magnetic field.

Liquid bridges supported by two solid surfaces have been attracting scientific attention since the time of Rayleigh [1] and Plateau. For a cylindrical bridge of length *L* and diameter *d*, it was shown theoretically that in zero gravity the maximum slenderness ratio R [$\equiv L/d$] is π [1]. The stability and ultimate collapse of such bridges is of interest because of their importance in a number of industrial processes and their potential for low gravity applications. In the presence of gravity, however, the cylindrical shape of an axisymmetric bridge tends to deform, limiting its stability and decreasing the maximum achievable value of *R*. Theoretical studies have discussed the stability and possible shapes of axisymmetric bridges [2-6]. Experiments typically are performed in either a Plateau tank, in which the bridge is surrounded by a density-matched immiscible fluid [7-9], or in a space-borne microgravity environment [10]. It has been shown, for example, that the stability limit *R* can be pushed beyond π by using flow stabilization [6], by acoustic radiation pressure [7,9], or by forming columns in the presence of an axial electric field [8]. In this work magnetic levitation was used to simulate a low gravity environment and create quasi-cylindrical liquid columns in air. Use of a magnetic field permits us to *continuously* vary the Bond number $B \equiv \frac{g\rho d^2}{4\sigma}$, where *g* is the gravitational acceleration, ρ is the density of the liquid, and σ is the surface tension of the liquid in air. The dimensionless Bond number represents the relative importance of external forces acting on the liquid column to those due to surface tension. Our central result is that in a large magnetic field gradient we could create and stabilize columns of mixtures of water and paramagnetic manganese chloride tetrahydrate ($MnCl_2 \bullet 4H_2O$), achieving a length to diameter ratio very close to π.

---

* Based on NASA project *Determination of the Surface Energy of Smectic Liquid Crystals From the Shape Anisotropy of Freely Suspended Droplets*

† Part of this report is reprinted with permission from M. Mahajan, M. Tsige, C. Rosenblatt, and P.L. Taylor, *Paramagnetic Liquid Bridge in a Gravity-Compensating Magnetic Field*, **Physics of Fluids** (to be published, 1998). Copyright 1998 American Institute of Physics.

The principle of magnetic compensation of gravity is straightforward. For a material of volumetric magnetic susceptibility χ in a magnetic field H, the energy per unit volume is given by $U = -\frac{1}{2}\chi H^2$, and the force per unit volume is $-\nabla U$. To compensate gravity it is required that $\frac{1}{2}\chi\nabla H^2_{comp} \approx \rho g$, where H_{comp} corresponds to the magnetic field whose gradient just compensates gravity. For ∇H^2 larger or smaller than $2\rho g/\chi$, the liquid will rise or sag in the column, ultimately causing the column to collapse if ∇H^2 deviates too significantly from its gravity-compensating value. Thus the effective force on the column may be controlled by varying the current in the magnet.

Fig. 1 Schematic view of the experimental setup. The fluid injection system, involving a hypodermic needle that injects material from the side, is not shown.

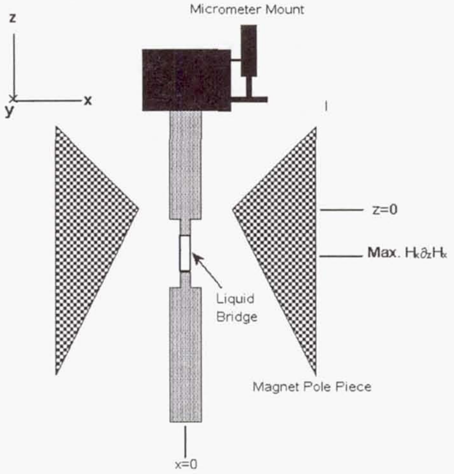

An electromagnet fitted with special Faraday pole pieces was used to produce ∇H^2 uniform to approximately 6% over the length of a 1 cm-long column. In order to determine the field profile, a Bell model 9500 Gaussmeter utilizing a Hall effect probe was used to measure H_x as a function of vertical position *z* along the symmetry plane (x = 0) of the magnet (Fig. 1). For all practical purposes, the field profile is translationally invariant along the *y*-axis, and therefore the *y* coordinate does not enter into the problem. Experimental values of both H_x and the product $H_x\partial_z H_x$ are shown as functions of *z* in Fig. 2. Note that along the plane x = 0 the z-component of field H_z vanishes, although a small component of H_z exists for $x \neq 0$. This small component may give rise to a slight distortion of the cylinder perpendicular to its symmetry axis, and will be discussed below. Nevertheless, over the small diameter of the columns $H_z\partial_z H_z$ remains small, and ∇H^2 is dominated by $H_x\partial_z H_x$; we shall therefore consider the z-component of force to be $\chi H_x\partial_z H_x$.

Fig. 2 Magnetic field H_X (right axis) and $H_X\partial_Z H_X$ (left axis) *vs.* vertical position *z* at $H = H_{comp}$. z = 0 corresponds to the position of closest approach of the pole pieces (see Fig. 1). The quantity $H_X\partial_Z H_X$ is maximum at z = -0.8 cm.

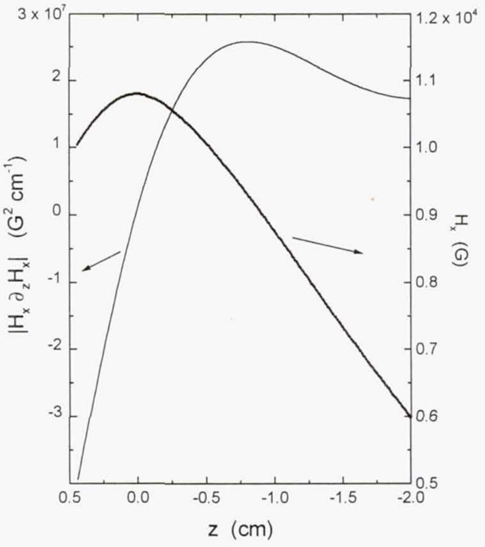

Manganese chloride tetrahydrate was obtained from Aldrich Chemicals and used as received. A high-concentration mixture of 62.5 wt.% $MnCl_2 \bullet 4H_2O$ in distilled water was prepared. By weighing a known volume of the mixture, its density was determined to be $\rho = (1.45 \pm 0.01)$ gm cm^{-3}. The surface tension σ in air was measured to be (116 ± 6) ergs cm^{-2} by the pendant drop method [11,12] To establish a confidence level for this technique, the measurements were repeated with both pure water and glycerol, where the measured values of σ were found to scatter within ±5% of accepted values in the literature.

Fig. 1 shows a sketch of the apparatus. Two ½-

inch diameter aluminum rods were machined to have cylindrical tips at their ends that are d = 0.32 cm diameter and 1.27 cm long. The pair was placed vertically in the magnet at x =0, such that the small tips faced each other. The upper rod was attached to a precision micrometer to facilitate adjustment of its position along the z-axis relative to the lower tip, and the tip of the lower rod was placed at approximately 0.4 cm below z = -0.8 cm. [z = 0 corresponds to the point where the pole pieces reach their closest approach, and z = -0.8 cm is the position of maximum $H_x \partial_z H_x$]. The lower tip was placed at this position so that the center of the liquid column would be at the approximate maximum in $H_x \partial_z H_x$. A boroscope attached to a CCD camera was positioned along the y-axis to view the liquid bridge, and the images were recorded with a video cassette recorder. The magnetic field was adjusted so that ∇H^2 approximately corresponded to ∇H^2_{comp}, and liquid was injected into the gap (typically starting at 0.1 cm) between the tips using a 25 gauge butterfly hypodermic needle and syringe. The upper tip was then translated upward using the micrometer, thereby creating a liquid cylinder between the two tips. As the upper tip was further translated, a waist formed in the column and more liquid had to be added to maintain a uniform cylinder. During this procedure the magnetic field also had to be fine-tuned to prevent sagging. This procedure was continued until a uniform cylinder of a desired length L (and thus a given slenderness ratio R = L/d) was achieved. For the longest cylinders (0.8 < L < 1.0 cm), the shape of the cylinder was found to be extremely sensitive to magnetic field: We found that if $H_x \partial_z H_x$ were to deviate from 2.57×10^7 G^2 cm^{-1} [defined as $(H_x \partial_z H_x)_{comp}$] by more than 1%, a noticeable bulge in the cylinder would appear near the top (for too large a field) or the bottom (for too small a field). Thus, knowing the density ρ and $(H_x \partial_z H_x)_{comp}$, we were able to extract the volumetric magnetic susceptibility (per cm^3) $\chi = \frac{\rho g}{\left(H_x \partial_z H_x\right)_{comp}} = (5.54 \pm 0.05) \times 10^{-5}$. We note that during the course of the experiment the relative humidity was kept near 100% to minimize evaporation of the water. Had we not done so, water evaporation would have increased the concentration of the paramagnetic salt in the column, and therefore changed the susceptibility.

Let us now turn to the stability of the column as a function of the Bond number. For our experiment the Bond number B must be redefined to include the effects of the magnetic field, *viz.*,

$$B \equiv \frac{\left(\rho g - \chi H_x \partial_z H_x\right) d^2}{4\sigma}. \tag{1}$$

As described above, columns of a given slenderness ratio *R* were created and stabilized in a magnetic field gradient, such that $(H_x \partial_z H_x)_{comp} = 2.57 \times 10^7$ G^2 cm^{-1}; this corresponds to B = 0. Then B was varied either positively or negatively by decreasing or increasing the magnetic field from its value H_{comp}. For a given *R* there was some maximum and minimum field, corresponding to a negative and positive Bond number, beyond which the column could no longer be sustained and catastrophically collapsed. In Fig. 3 we show two images of the stable bridge: One is at Bond number B approximately equal to zero. The second is at a lower field where the Bond number is just within the stability limit. [If the field is further reduced, the bridge collapses]. The Bond numbers corresponding to the limits of stability of the bridge were measured as a function of *R*, and are shown in Fig. 4. In a similar manner we also examined cylinders of smaller diameter d = 0.16 cm, finding comparable results for *R vs. B*; these are shown in Fig. 5. [Note that for d = 0.16 cm, the lower tip was placed ~ 0.2 cm below the position of maximum $H_x \partial_z H_x$, *i.e.*, below z = -0.8 cm] In both figures we also show theoretical numerical results for the stability limits calculated by Coriell *et al*. [2].

Fig. 3 Photograph of d = 0.32 cm liquid bridge with R = 2.39. a) Stable bridge with $H_X \partial_Z H_X$ adjusted to approximately $(H_X \partial_Z H_X)_{comp}$, so that B is close to zero. b) Stable bridge with $H_X \partial_Z H_X$ reduced, so that B = 0.09 (*cf.* Eq. 1). Note that when $H_X \partial_Z H_X$ is further reduced, so that B ~ 0.093, the bridge collapses.

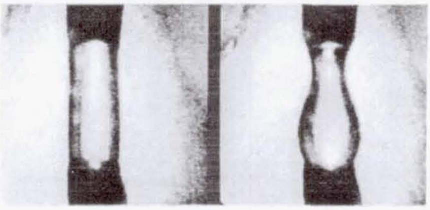

Fig. 4 Slenderness ratio *R vs.* Bond number B at the stability limits for d = 0.32 cm bridges. The region below the inverted "V" corresponds to the region of stability; outside this region the column collapses. Vertical error bars correspond to experimental uncertainty in determining *R* and horizontal error bars to uncertainty in reproducing collapse of the column at a given Bond number. The solid line represents the theoretical stability limits according to Ref. 2.

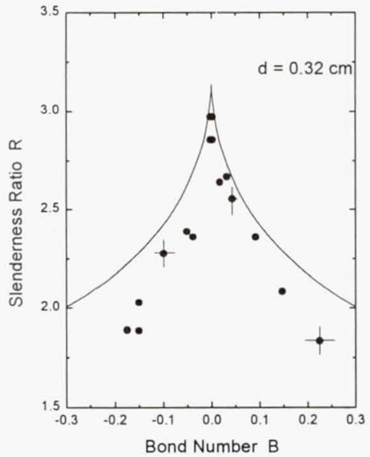

Although our experimental results for the stability limits are apparently symmetric about B = 0 and are in reasonable agreement with theory, there are clearly deviations from the theoretical curves. One problem is the uniformity of the magnetic force (see Fig. 2). Over very small length scales $H_x \partial_z H_x$ is quite uniform, although as the cylinder length approaches 1 cm there are significant variations in the magnetic force along the z-axis. For this reason it is likely that the stability of the longer columns may be compromised. It should also be remembered that although the magnetic fields corresponding to the stability limits are determined directly, the Bond number is *derived* from these fields, as well as from experimental measurements of ρ and σ. The surface tension, in particular, has a not-insignificant uncertainty. Thus, in addition to the

Fig. 5 Same as Fig. 4, except for d = 0.16 cm.

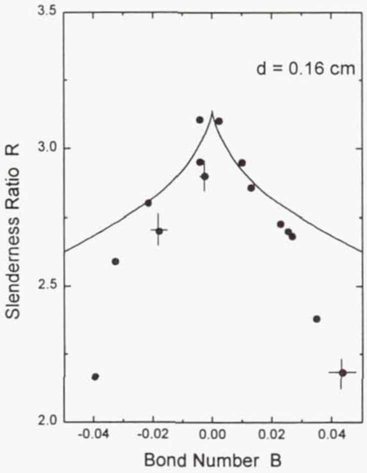

experimental error bars that appear in Figs. 4 and 5, there may be an additional *systematic* error of up to 7% in B (the abscissa). Such an error could be partially responsible for the small disagreement between experiment and theory. Additionally, we note that for the d = 0.16 cm columns the stability limits are reduced from theory at smaller *R*. We do not yet understand this phenomenon. We note, however, that as the liquid sags (rises) near the field stability limit, a thin film of liquid would often wet the sides of the lower (upper) rod, especially for shorter, smaller *R*, columns. Thus liquid would be drawn off from the column, reducing its apparent stability. This observation, in conjunction with possible inhomogeneities in the rod itself, may be partially responsible for the observed deviations. Yet another issue is the liquid volume V, where deviations from $V = \pi L d^2/4$ could affect the apparent stability [13,14] of the column. In our experiments we did not measure the volume of the bridge directly, but rather adjusted the volume to obtain an apparently right circular cylinder at B = 0. Finally, we need to consider two effects which can alter the cross section of the cylinder in the *xy*-plane from a circle to an ellipse. The dominant component of magnetic field is along the *x*-axis. We have performed a magnetic boundary value calculation, including the surface tension, to determine the distortion on an infinitely long paramagnetic column arising from a transverse magnetic field. We found that for our values of χ and H_x, the eccentricity is ~0.004 at H_{comp}, compared to zero at $H_x = 0$. This represents a tiny deviation from a circular cross-section, and would be nearly impossible to detect with our imaging scheme. An additional issue is that because H_x varies with x — we have also mapped out this variation with our Gaussmeter — there is a weak transverse force on the liquid cylinder in the x-direction. This force vanishes at the symmetry plane (x = 0), but grows linearly with *x* away from the midpoint between the pole pieces. We have calculated the distortion on the circular cross section arising from this nonuniform magnetic force, and again found that the eccentricity is of order 0.02. The effects on the stability are therefore likely to be small. Both calculations will be published elsewhere [15].

To summarize, we have demonstrated that magnetic levitation may simulate a low gravity environment to enable the formation of stable liquid bridges. Such a technique permits the continuous variation of the Bond number and obviates the need for using density-matched liquids. Despite these advantages, the inhomogeneities of the magnetic forces tend to reduce slightly the limits of stability. On the basis of these results we intend to examine the effects of a modulated magnetic field on the stability. Additionally, we may also consider the stability of *diamagnetic* fluids in much higher fields, as we have already demonstrated the principle of levitation in these systems [16].

Acknowledgments: This work was supported by the National Aeronautics and Space Administration's Microgravity Program under grant NAG8-1270.

References

1. J.W.S. Rayleigh,**The Theory of Sound** (Dover, New York, 1945), vol. 2, Chap. 20.
2. S.R. Coriell, S.C. Hardy, and M.R. Cordes, J. Colloid Int. Sci. **60**, 126 (1977)
3. J.A. Nicolás, Phys. Fluids A **4**, 2573 (1992)
4. A.Sanz and I. Martinez, J. Colloid Int. Sci. **93**, 1 (1983)
5. J.I.D. Alexander, A.H. Resnick, and L.A. Slobozhanin, Third Microfluid Physics Conference, Cleveland, Ohio, NASA Conference Publication 3338, p. 469 (1996)
6. B.J. Lowry and P. H. Steen, J. Colloid Int. Sci. **170**, 38 (1995)
7. P.L. Marston, M. J. Marr-Lyon, S. F. Morse and D. B. Thiessen, Third Microfluid Physics

Conference, Cleveland, Ohio, NASA Conference Publication 3338, p. 475 (1996)
8. S. Sankaran and D. Saville, Phys. Fluids A **5**, 1081 (1993)
9. S.F.Morse, D.B. Thiessen, and P.L. Marston, Phys. Fluids **8**, 3 (1996)
10. D. Langbein, F. Falk and R. Grobbach, Adv. Space Res. **16**, 23 (1995)
11. C.E. Stauffer, J. Phys. Chem., **69**, 1933 (1965)
12. R.-J. Roe, V.L. Bacchetta, and P.M.G. Wong, J. Phys. Chem. **71**, 4190 (1967)
13. J.M. Vega and J.M. Perales, Proc. of the 4th European Symp. on Materials Sciences under Microgravity (ESA SP-191), p. 247 (1983)
14. B.J. Lowry and P.H. SteenProc. Royal Soc. London A **449**, 411 (1995)
15. M. Tsige, M.P. Mahajan, C. Rosenblatt, and P.L. Taylor (to be published)
16. M. Mahajan, P.L. Taylor, and C. Rosenblatt, Liq. Cryst. **23**, 547 (1997)

Modeling of Macroscopic/Microscopic Transport and Growth Phenomena in Zeolite Crystal Solutions under Microgravity Conditions

Nikos A. Gatsonis, Andreas Alexandrou, Hui Shi, Bernard Ongewe
Mechanical Engineering Department
100 Institute Rd.
Worcester Polytechnic Institute, Worcester MA 02139
Phone: (508)-831-5576, 831-5147
e-mail: gatsonis@wpi.edu, andalexa@wpi.edu

Albert Sacco, Jr.
Chemical Engineering Department
242 Snell Engineering Center
Northeastern University, Boston, MA 02115
Phone: (617)-373-7910
e-mail: asacco@coe.neu.edu

Introduction

Crystals grown from liquid solutions have important industrial applications. Zeolites, for instance, a class of crystalline aluminosilicate materials, form the backbone of the chemical process industry worldwide, as they are used as adsorbents and catalysts [Meier, 1986; Barrer, 1986]. Many of the phenomena associated with crystal growth processes are not well understood due to complex microscopic and macroscopic interactions. Microgravity could help elucidate these phenomena and allow the control of defect locations, concentration, as well as size of crystals. Microgravity in an orbiting spacecraft could help isolate the possible effects of natural convection (which affects defect formation) and minimize sedimentation. In addition, crystals will stay essentially suspended in the nutrient pool under a diffusion-limited growth condition. This is expected to promote larger crystals by allowing a longer residence time in a high-concentration nutrient field. Among other factors, the crystal size distribution depends on the nucleation rate and crystallization. These two are also related to the "gel" polymerization/depolymerization rate. Macroscopic bulk mass and flow transport and specially gravity, force the crystals down to the bottom of the reactor, thus forming a sedimentation layer. In this layer, the growth rate of the crystals slows down as crystals compete for a limited amount of nutrients. The macroscopic transport phenomena under certain conditions can, however, enhance the nutrient supply and therefore, accelerate crystal growth.

Several zeolite experiments have been performed in space with mixed results. The results from our laboratory have indicated an enhancement in size of 30 to 70 percent compared to the best ground based controls, and a reduction of lattice defects in many of the space grown crystals [Sand et al., 1987; Sacco et al., 1993]. Such experiments are difficult to interpret, and cannot be easily used to derive empirical or other laws since many physical parameters are simultaneously involved in the process. At the same time, however, there is increased urgency to develop such an understanding in order to more accurately quantify the process.

In order to better understand the results obtained from our prior space experiments, and design future experiments, a detailed fluid dynamic model simulating the crystal growth mechanism is required. This will not only add to the fundamental knowledge on the crystallization of zeolites, but also be useful in predicting the limits of size and growth of these important industrial materials. Our objective is to develop macro/microscopic theoretical and computational models to study the effect of transport phenomena in the growth of crystals grown in solutions. Our effort has concentrated so far in the development of separate macroscopic and microscopic models. The major highlights of our accomplishments are described bellow.

Macroscopic Model

The crystal growth process is modeled as a multiphase (solid and fluid phases) system. The macroscopic fluid dynamics model accounts for the continuous solid and fluid phases. Throughout the process there is continuous interaction between the two phases. For the time being, the crystal growth process is modeled by an exponential law, expressed as $\dot{r} = \alpha e^{-\beta t}$, where α and β depend on microscopic fluid and chemical interactions. In the future, this model will be combined with a microscopic model based on a Monte-Carlo approach. Following [Druzhinin, 1995], the mass and momentum equations are formulated as follows.

Solid Phase

The continuity equation is

$$\frac{\partial s}{\partial t} + \nabla \cdot (s\boldsymbol{u}_s) = \dot{r}_s \qquad (1)$$

where s is solid volume fraction, $\boldsymbol{u}_s$ is solid velocity vector, $\dot{r}_s$ is rate of crystal growth divided by the density of the solid ρ_s. i.e., $\dot{r}_s = \dot{r}/\rho_s$.

The momentum equation is

$$\frac{\partial\left(s u_{s_i}\right)}{\partial t} + \nabla \cdot \left(s u_{s_i} \boldsymbol{u}_s\right) = sF_i + sg_i, \qquad i = 1,2,3. \qquad (2)$$

where F_i is the interaction force between the two phases, and, g_i the gravity acceleration component each along the coordinate direction, x_i.

Fluid Phase

The continuity equation is

$$\frac{\partial(1-s)}{\partial t} + \nabla \cdot \left((1-s)\boldsymbol{u}_f\right) = -\dot{r}_f \qquad (3)$$

where $\boldsymbol{u}_f$ is the fluid velocity vector and $\dot{r}_f$ the fluid depletion rate divided by the density of the fluid, i.e., $\dot{r}_f = \dot{r}/\rho_f$. Notice that $\dot{r}_s\rho_s = \dot{r}_f\rho_f$. The negative sign in $\dot{r}_f$ shows that fluid is depleted by supplying nutrients for the crystal growth.

The momentum equation is

$$\frac{\partial\left((1-s)u_{f_i}\right)}{\partial t} + \nabla \cdot \left((1-s)u_{f_i}\boldsymbol{u}_f\right) = -(\nabla p)_i - s\delta F_i + (1-s)g_i + (\nabla \cdot \hat{\tau})_i, i = 1,2,3. \qquad (4)$$

where δ is the density ratio ${}^{\rho_s}\!/_{\rho_f}$. p is the fluid pressure divided by ρ_f. The two phases are coupled through the interaction force F_i. In our model, ρ_s and ρ_f are assumed to be constant. $\hat{\tau}$ is the viscous stress tensor divided by the density of the fluid defined for the incompressible Newtonian fluid phase as:

$$\hat{\tau}_{ij} = (1-s)\nu\left(\frac{\partial u_{f_i}}{\partial x_j} + \frac{\partial u_{f_j}}{\partial x_i}\right) \qquad i,j = 1,2,3. \tag{4a}$$

In the above expression ν is the kinematic viscosity of the fluid phase.

Constitutive Relations

In the case of small heavy particles, the major contribution to the interaction force is from the viscous drag force [Maxey and Riley, 1983]. For particles with Reynolds number of order of unity, the viscous drag force is expressed by the following empirical formula:

$$F_i = \frac{1}{\tau_p}\left(u_{f_i} - u_{s_i}\right) f\left(Re_p\right) \tag{5}$$

Where $\tau_p = \dfrac{d^2\delta}{18\nu}$, $Re_p = \dfrac{|\boldsymbol{u}_f - \boldsymbol{u}_s|}{\nu} d$, and $f\left(Re_p\right) = 1 + 0.15\, Re_p^{2/3}$.

The following relations are used to describe the growth rate

$$\dot{r}_s = \frac{\alpha}{\rho_s} e^{-\beta t} = \alpha_s e^{-\beta t} \quad \dot{r}_f = \frac{\alpha}{\rho_f} e^{-\beta t} = \alpha_f e^{-\beta t} \tag{6}$$

Boundary and Initial Conditions

On the interior surface of the reactor, a no-slip boundary condition ($\boldsymbol{u}_f = 0$) for the fluid phase and a slip boundary condition ($\boldsymbol{u}_s \cdot \boldsymbol{n} = 0$) for crystal particle phase is imposed, here $\boldsymbol{n}$ is the unit normal vector on the surface. Initially, both phases are assumed to be stationary. The particle phase is initialized by a specified solid volume fraction distribution in the reactor. The subsequent motion of the interactive phases is induced by gravity.

Results and Discussions

Fig. 1(a) shows the solid velocity field at an intermediate time in the settling process of particles. As a result of the gravity, the particles settle to the bottom and collect around the center due to the action of fluid flow. Fig. 1(b) shows the fluid velocity field whose main feature is the recirculation region consisting of two large vortices. Fig. 1(c) represents the fluid pressure contour showing that the initial linear static pressure distribution changes mainly in the particle region. Fig. 1(d) illustrates the evolution of solid volume fraction along the centerline of the container: as time progresses, the particles shift to the bottom being slightly diffused. The maximum value decreases with time. Fig. 2. represents the effect of variable gravity levels: the larger the gravity level, the faster the particles settle. Fig. 3 shows the particle sedimentation on the bottom of the reactor: with larger gravity level, the particles settle faster.

Microscopic Model

The model is based on the Direct Simulation Monte Carlo (DSMC) method and is aimed at capturing the effects of macroscopic flow on the growth and size distribution of the growing crystals. The system include nutrients, crystals and the mean motion of the fluid in a domain that models realistic systems. The grid is based on the mean-free path (λ_{nn}) of collisions between nutrients. The length of this grid may be modified to include collisional interactions between nutrients and the fluid phase of the solution. Nutrients and crystals move and collide under the actin of gravity and fluid-drag forces.

Nucleation Process

In a zeolite solution nucleation and crystallization overlap and interact with each other. These processes have been modeled in a variety of methods [Thompson and Dryer, 1985]. The nucleation will be introduced with a Monte Carlo model that resembles closely the actual process. The nucleation sites will be created in random with a probability based on a model that describes the nucleation as a function of local thermodynamic. Another alternative is to introduce nucleation via a chemically reacting process based on a rate coefficient that depends on thermodynamic parameters. Ultimately, this issue will be resolved using experimental data.

Collisions between Nutrients

Elastic collisions between nutrients are modeled via the No-Time-Counter (NTC) method [Bird, 1994]. Collisional pairs are selected in cells and the collision probability in each computational cell is calculated based on the NTC method. The model employs the hard sphere (VHS) in evaluating collision cross sections.

Nutrient Impingement and Crystal Growth Process

The nucleation sites grow to crystals of finite size. Particle methods are ideal to model the crystallization process as well. The level of modeling however, is dictated by the computational requirements. Our approach is to describe the key physical processes with a model that will be refined through successive iterations with data comparisons. For this reason, we initially concentrate our efforts in the determination of the size distribution of the crystals.

The crystals are considered as spherical particles that grow after their attraction and attachment of nutrients. Within the framework of the DSMC, an attachment probability P_a will be evaluated in those cells in which nucleation sites or crystals exist. This probability will be calculated on concentrations or surface kinetics based on impingement rates.

Particle Weighting Scheme

Given that the crystal particles in our simulations are real particles, different particle weights have to be assigned to the crystal and nutrient 'species' respectively. The primary concern in enacting this scheme is the treatment of collisions between simulation particles that are represented by different particle weights. In this event, linear momentum and energy are not conserved by the conventional NTC elastic collision model. This is accomplished in our model using a conservative multi-weight method.

Results and Discussion

Preliminary simulations were performed in order to test the motion and collision algorithms of the code. The simulations compared the effects of gravity on settling time of crystals in the absence of fluid/particle drag. The domain is initialized with 912 spherical crystal particles in a cubic container with size 0.3 m. The spherical crystals have a diameter of 4.17×10^{-6} m, and mass of 6.63x10^{-14} kg. Results are shown in Figures 4 and 5 for 1-g and 0-g conditions respectively at 0.6 seconds after initialization. At this point, the center of gravity of the crystal particles was calculated to be at a height of 0.09 m and 0.073 m respectively for the 0-g and 1-g cases. As shown, the imposition of a gravitational force field has immediate effects on particle distribution. Future simulations will determine the extent to which this distribution gradient affects the growth rate and subsequent final size of the crystals as they compete for nutrients.

Acknowledgments
This work was performed under NASA Grant No. NAG8-1255.

References

1. W.M. Meier, "Zeolites and Zeolite-like Materials", New Developments in Zeolite Science and Technology, Proceeding of the 7th international Zeolite Conference, Tokyo, Aug., 1986.
2. R.M. Barrer, "Porous Crystals: A Perspective", New Developments in Zeolite Science and Technology, Proceeding of the 7th international Zeolite Conference, Tokyo, August, 1986.
3. Sacco, Jr., R.W. Thompson, and A.G. Dixon, ``Zeolite Crystal Growth in Space- What has been learned," AIAA 93-0473.
4. Sand, L. B., Sacco, A., Thompson, R. W., and Dixon, A. G.,``Large Zeolite Crystals: their potential growth in space", Zeolites, Vol.7, pp387-392, 1987.
5. Maxey, M.R., and James J. Riley, ``Equation of Motion for a small rigid sphere in a nonuniform flow", *Phys. Fluids 26(4),* 1983
6. Druzhinin, O.A., "On the two-way interaction in two-dimensional particle-laden flows:the accumulation of particles and flow modification", *J. Fluid Mech., Vol. 297, pp 49-76*, 1995
7. Thompson R.W. and A. Dryer, *Zeolites*, Vol. 5, 202 , 1985.
8. Bird, G., Molecular gas dynamics and the direct simulation of flows, Oxford, 1994.

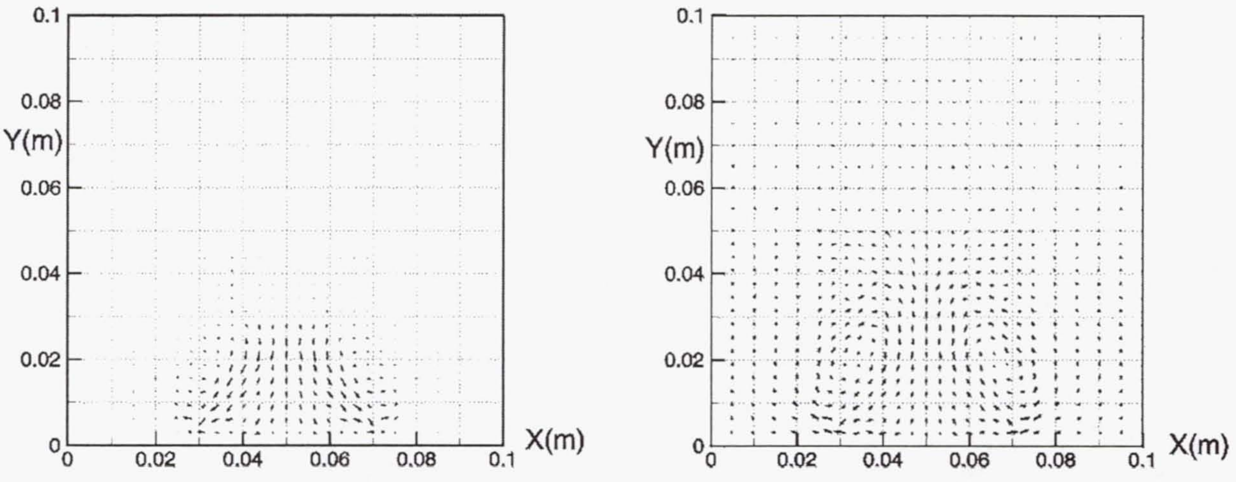

(a) Particle flux: ref. value: 0.01 m·s^{-1} →

(b) Fluid flux: ref. value: 0.1 m·s^{-1} →

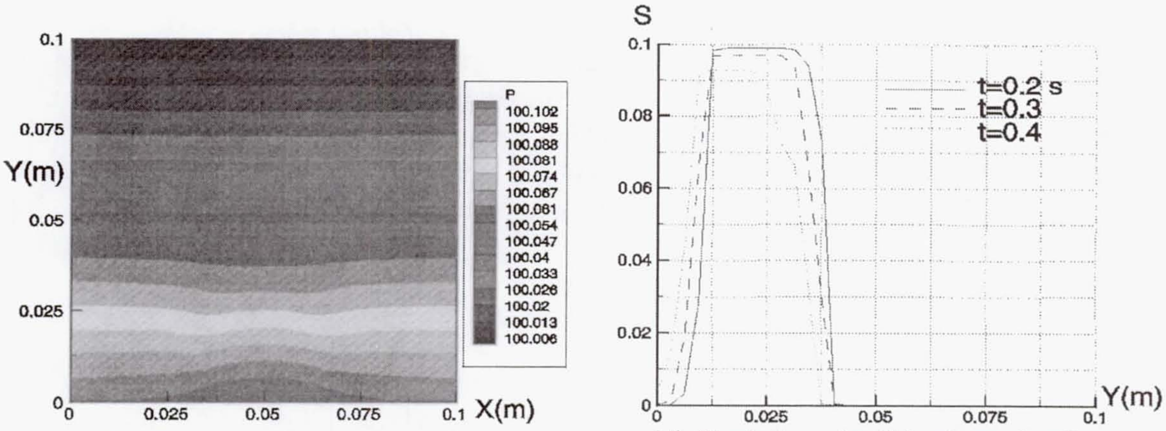

(c) Pressure contour

(d) Evolution of solid volume fraction along the centerline.

Fig. 1 Results at time 0.37 s. for a 2-D reactor. $\nu = 10^{-5}\ m^2 \cdot s^{-1}$, $g = 1.0\ m \cdot s^{-2}$, $d = 10^{-4}$ m.

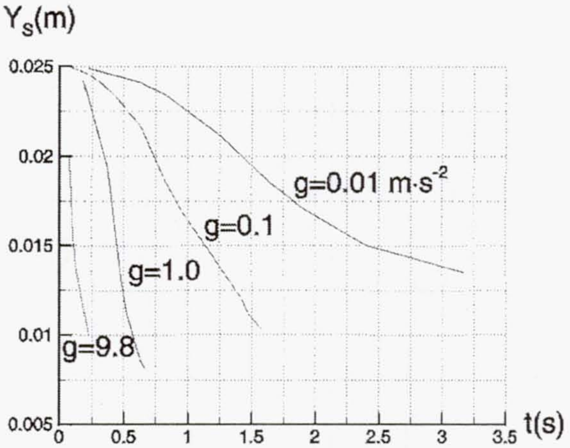

Fig. 2 Settling distance of mass center of particles versus time for variable gravities, $\nu = 10^{-5}\ m^2 \cdot s^{-1}$, $d = 10^{-4}$ m.

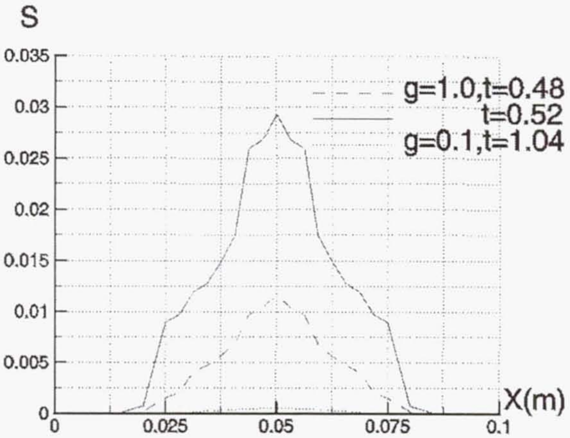

Fig. 3 Particle sedimentation on the bottom for $\nu = 10^{-5}\ m^2 \cdot s^{-1}$, $d = 10^{-4}$ m.

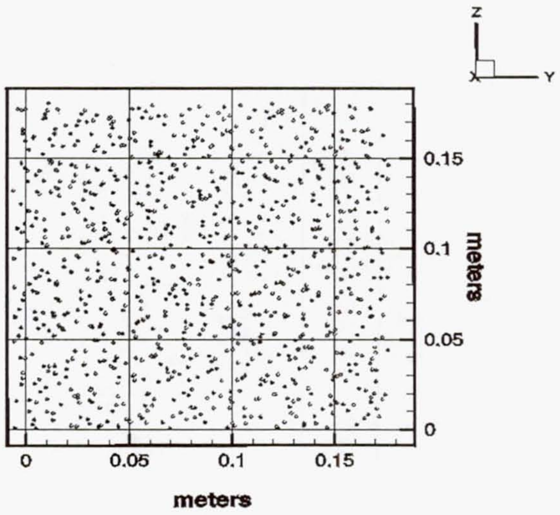

Fig. 4: Crystal particle distribution after 0.6 Seconds (0-g)

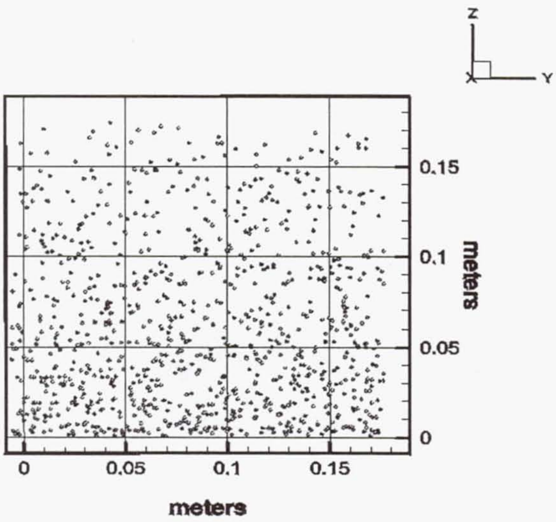

Fig. 5: Crystal particle distribution after 0.6 seconds (1-g)

PRELIMINARY INVESTIGATION ON THE EFFECTS OF GRAVITY ON WELDING BEHAVIOR OF A 304 STAINLESS STEEL

Nam Hyun Kang, Paul R. Howell, and Jogender Singh: Applied Research Laboratory and Department of Materials Science and Engineering, The Pennsylvania State University, University Park, PA 16802, 814-863-8558; hhk105@psu.edu, 814-863-3363; howell@ems.psu.edu, 814-863-9898; jxs46@psu.edu.
Samuel G. Lambrakos and Steven P. Marsh: Naval Research Laboratory, Washington DC, 202-767-2601; lambrakos@anvil.nrl.navy.mil, 202-767-1676; marsh@anvil.nrl.navy.mil

Introduction

Welding processes have been utilized widely throughout industry because of their being cost-effective and easy to employ in an assembly process. However, welding in space needs to be understood more precisely during melting and solidification, because it is difficult to precisely control the operating conditions. The important parameters which control the weld quality and shape are the interacting convection forces of a melt within the weld-pool. Three major forces for convection in laser welding are: gravity driven buoyancy flow, surface tension gradient driven thermocapillary flow, and concentration gradient driven flow. Lorentz flow driven by electromagnetic forces must also be considered for convection in gas tungsten arc welding(GTAW).

Considerable research has been conducted to understand the effects of various convection forces[1-3], and mathematical models have been developed to validate the experimental result that surface tension gradient driven flow is the dominant force in normal earth gravity of 1g [4-7]. However, few welding experiments have been performed to understand the effects of microgravity on microstructural behavior and the weld-pool shape. In addition, different results have been reported depending on the welding material and operating parameters. For example, the Soviet's electron beam welding experiments on stainless steel, Al and Ti samples reported that weightlessness did not significantly affect the welding depth [8]. Japan's GTAW of Al and 2219 Al alloy was performed under microgravity conditions; the weld bead in microgravity contained none of the ripple lines which normally exist in 1g welds [9]. In the KC-135 laser welding experiments of a stainless steel, the weld depth increased and more ripple lines were observed in microgravity than in the welds at 1g [10, 11].

The ultimate objective of the present investigation is to study the effect of heat/mass transfer in welding behavior as a function of gravitational force. The effects of gravitational force on the GTAW will be discussed for a 304 stainless steel that was produced by the KC-135 aircraft experiment at NASA.

Experimental Method

GTAW was conducted on an Fe - 18Cr - 8Ni alloy by NASA's KC-135 aircraft experiment, in which parabolic trajectories were able to simulate acceleration levels from 0.01 g to 1.8g. More specific details on the KC-135 flight experiment is contained in reference [12]. The welding experiment was started from the regime of microgravity and continued to the region of high acceleration levels. The accelerometer recording of the up/down acceleration on board is indicated in Fig 1. The base metal had a diameter of 7.5

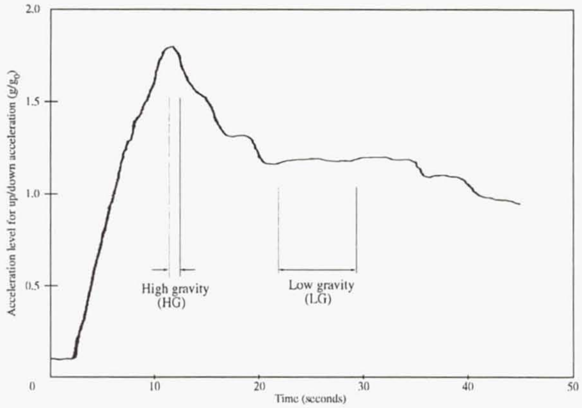

Fig 1. Accelerometer data of the up/down acceleration on KC-135 board.

cm with a 3 mm wall thickness. The welding was performed with a rotating tungsten electrode, employing 75 A direct current, 10-12 V arc voltage, and a 5 mm/sec welding speed. The exact same welding parameters were reproduced for ground-based experiments which had the objective to calibrate the data of aircraft experiment by using both horizontal ($\Omega = 0°$) and perpendicular ($\Omega = 90°$)placement of the weld-pool (Ω indicates the angle between the direction of the incident heat source and the vertical direction). Quasi-steady-state conditions were achieved within 10 seconds after starting the welding process for both experiments. Hence, the design of the KC-135 aircraft experiment is inappropriate for studying the effects of microgravity environment which was produced in the beginning region of the weld process for 5 seconds as indicated in Fig 2. However, the second peak around 14 seconds in the KC-135 aircraft experiment was determined to have a real effect of high gravity on the pool width. The fraction of the weld data for which the influence of changes in gravity was found to be significant was separated into two classes. These being welds corresponding to high gravity (HG) and welds corresponding to low gravity (LG), in which both HG and LG were higher than the normal earth gravity as shown in Fig 1. Although the transition effect due to the rapid changes in the gravity level was ignored in the HG regime at this time, the gravity levels in the whole HG region were higher than the gravity levels of the LG region. However, for a more quantitative comparison of exact gravity levels on e.g., the weld-pool shape, the interpretation of the transition effect must be considered. To study fundamental effects of gravity on the stainless steel welds, the following metallographic techniques were employed: optical microscopy (OM), scanning electron microscopy (SEM), and scanning transmission electron microscopy (STEM).

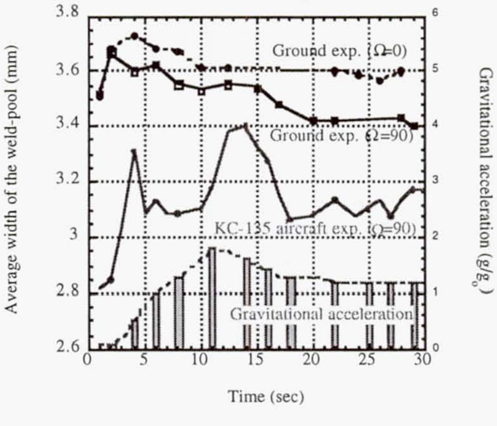

Fig 2. Weld-pool width of the KC-135 experimental with the ground experimental

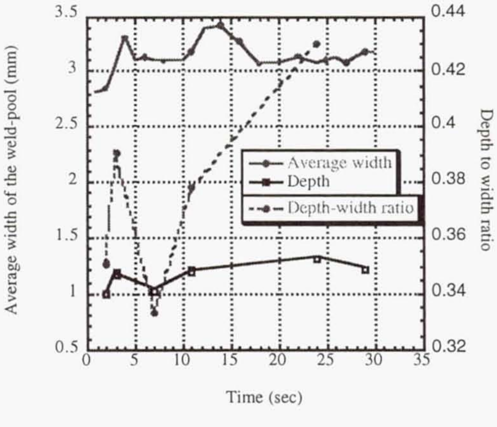

Fig 3. The effect of gravity on weld pool geometry of a 304 stainless steel

Preliminary Results

Recent analysis on Fe - 18Cr - 8Ni welds demonstrated that the weld-pool geometry was changed considerably with the variation of gravitational force during KC-135 aircraft experiment:

(i) The average width of the weld-pool was observed to increase by ~10 % and the average depth was decreased by ~10 % at high gravity (HG) compared with those at low gravity (LG) as indicated in Fig 3. The macrographs (a) and (b) in Fig 4 show the cross-section of the weld-pool developed in the two different gravity levels. The depth to width ratio of the weld-pool was observed to be ~0.38 at HG and ~0.44 at LG. The buoyancy term in the momentum conservation equation is given by:

$$F_B = g\beta(T-T_r) \tag{1}$$

where g is the gravitational acceleration, β is the coefficient of thermal expansion, and T_r is a reference temperature. The shape of the weld-pool at LG is more hemispherical than that at HG: the hemispherical shape at LG is caused by the weak buoyancy term (F_B), but at HG the more significant effect of buoyancy force (gravity-driven convection force) change the shape from a hemispherical cross section;

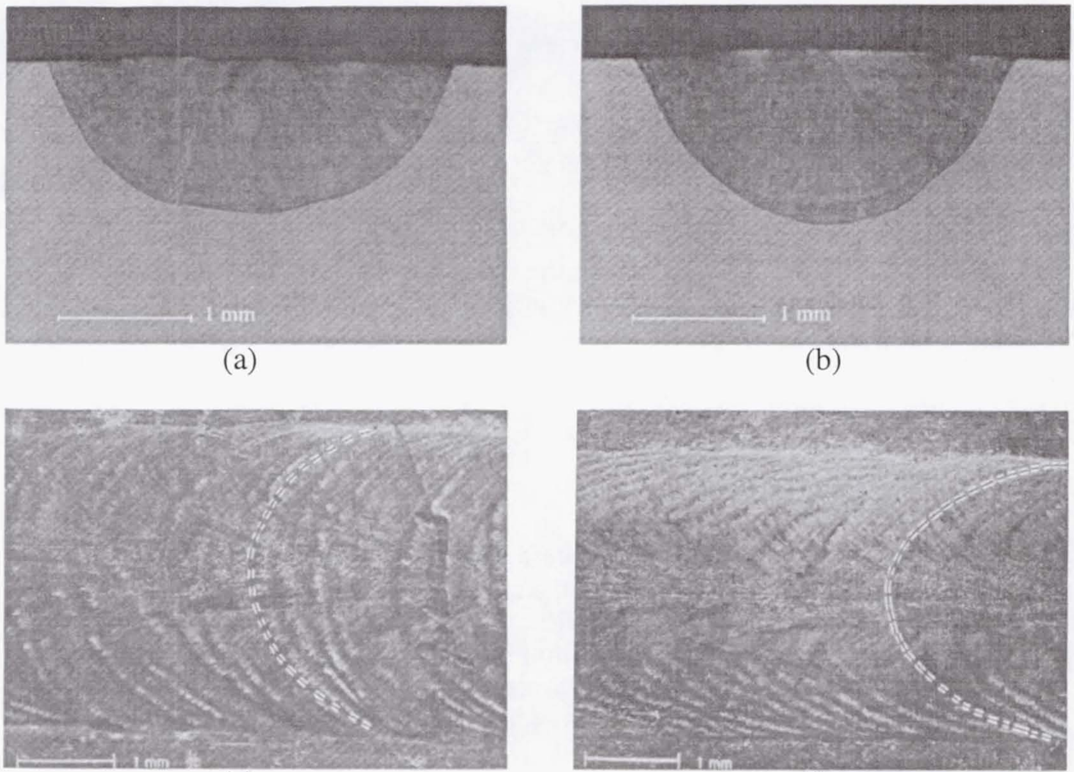

(a) (b)

(c) (d)

Fig 4. Cross-section of the weld-pool developed at (a) high gravity and (b) low gravity; top surface morphology of the weld-pool at (c) high gravity and (d) low gravity.

(ii) The top surface of the welds are shown in (c) and (d) of Fig 4 which shows two-dimensional rippling lines. Following previous work by Nishiguchi et al [13], the combined action of gravity and surface tension was used to analyze the shape of the rippling line which is given as:

$$\frac{\gamma}{R} = \frac{\gamma}{R_o} - \rho g y \qquad (2)$$

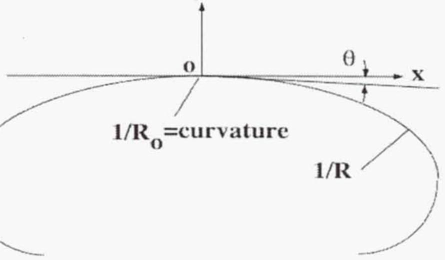

Fig 5. Two-dimensional model of the molten rippling line. (Modified from reference 13)

where R is the radius of curvature of the specific section, R_o is the radius of curvature at the origin in Fig 5, and γ is the surface tension. Qualitatively, the curvature at the center of the bead for HG was observed to be smaller than that of LG and the contact angle θ at boundary was smaller for HG than the angle for LG;

(iii) In microgravity environment, i.e., below normal earth gravity, inconsistent results were observed because steady-state was not achieved for this period.

STEM analyses across representative austenite/ferrite phase boundaries were performed to examine gravity effects on mass transfer in the melt (Fig 6). The retained δ ferrite phase was characterized by a plateau in Cr concentration profile and as a valley in Ni concentration profile. The concentration profile showed no noticeable dependence upon gravity, and more fundamental studies will be conducted after comparing the present data with the results of ground-based experiments.

Future Plans

The preliminary results showed that gravity may have a considerable effect on the geometry of Fe - 18Cr - 8Ni welds. More quantitative correlation between weld structure and actual values of the gravitational force has been purposely avoided at this time because several tasks, which are now underway, must be completed:

(i) Further filtering of the weld data for which the influence of gravity is statistically significant must be undertaken in order to examine weld structures corresponding to quasi-steady-state conditions, e.g., inertia effect on the gravitational force has to be excluded in the transition region of rapidly changing gravitational acceleration levels, even though the inertia effect is probably not significant at the transition region of HG conditions in which deceleration occurs;

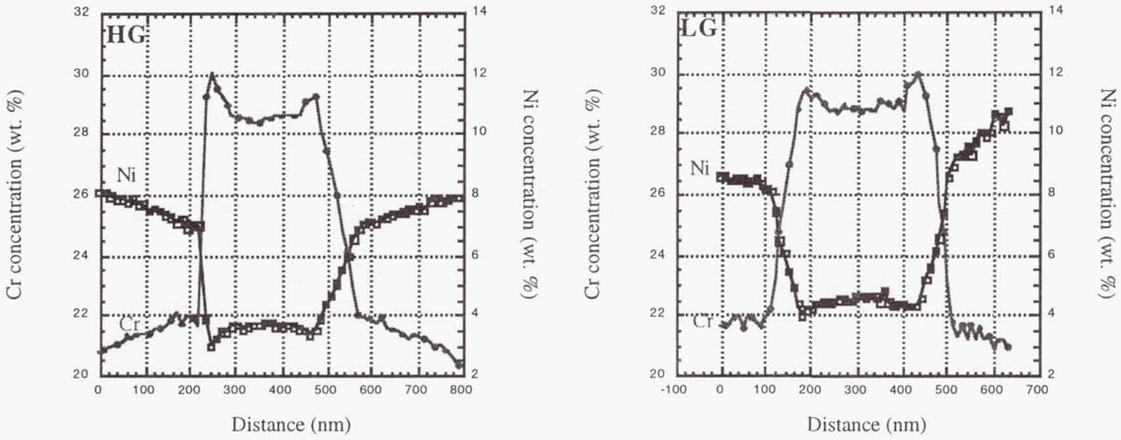

Fig 6. Measured profiles of Cr and Ni solute atoms at HG and LG.

(ii) The ground-based experiments must be compared with the KC-135 aircraft experiment. Suggested values of the acceleration level are g|cos Ω| where 0< Ω <360. These experimental data should provide a basis for filtering experimental artifacts associated with the influence of changes in gravity on other aspects of the weld process.

Based on the experimental measurements of the pool-size and the rippling lines on the free surface, an inversion modeling method will be employed to construct temperature distributions within the pool produced in different gravitational forces. This three-dimensional temperature distribution and the circulation of the melt within the pool will be used to predict the final weld microstructure and composition. Therefore, a comparison of simulations with measurements on actual welds under various gravity conditions should permit the refinement of the physical models in the simulations, thus leading to optimization of critical operating variables in the welding process. To maximize the effects of gravity on welding phenomena, new material systems which have a low surface tension and/or large difference of density, but with similar melting temperature will be selected: stainless steel has a high melt surface tension and similar density of the major alloying elements (Fe, Cr, and Ni), making it difficult to observe the effects of gravitational force on buoyancy. As candidate materials, the following alloying systems will be considered: Al-Ni (large difference of density), Ag-Cu (low surface tension), Ag-Ba and Ag-Nd (large difference of density and low surface tension).

With the parallel efforts of mathematical modeling and simulation, more fundamental studies on microstructural behavior and mass transfer will be pursued in terms of the effects of gravitational force. X-ray diffraction (XRD) and STEM will be employed for measuring the amount of retained ferrite and the concentration of alloying elements, respectively.

The laser welding technique will also be employed to compare with GTAW. The absence of an electromagnetic force in the laser weld-pool will change the interacting phenomena in the pool and the gravity effects could be calculated more easily. The long-term plan based on this research effort is to carry out KC-135 low gravity experiments in the steady-state.

Therefore, a basis for the development of a series of solidification experiments with laser welding will provide future development on the space station.

References

[1] R. A. Woods and D. R. Milner, Welding Journal, 50, 163s (1971)
[2] C. Sozou and W. M. Pickering, J. Fluid Mech., 73-4, 641 (1976)
[3] C. R. Heiple and J. R. Roper, Welding Journal, 61, 97s (1982)
[4] C. Chan, J. Mazumder, and M. M. Chen, Metall. Trans., 15A, 2175 (1984)
[5] S. Kou and D. K. Sun, Metall. Trans., 16A, 203 (1985)
[6] J. A. Hopkins, T. D. McCay, M. H. McCay, and A. H. Eraslan, Transport Phenomena in Nonconventional Manufacturing and Materials Processing, ASME 1993, p. 17
[7] J. Domey, D. K. Aidun, G. Ahmadi, L. L. Regel and W. R. Wilcox, Welding Journal, 263s, August (1995)
[8] V. F. Shulym, Proceedings of Welding in Space and the Construction of Space Vehicles by Welding, American Welding Society, Miami, FL, 12-24 (1991)
[9] K. Masubuchi and M. Nayama, Welding in Space and the Construction of Space vehicles by Welding, Proceedings of the Conference, American Welding Society, Miami, FL. 186
[10] G. L. Workman and W. F. Kaukler, Laser Welding in a Reduced Gravity Environment. AIAA Paper 846, 30th Aerospace Sciences Meeting and Exhibit (1992)
[11] K. N. Tandon and G. Wang, Laser Welding of Stainless Steel - Experiments Aboard KC-135. AIAA Paper 579, 31st Aerospace Sciences Meeting and Exhibit (1993)
[12] Basil N. Antar and Vappu S. Nuotio-Antar, *Fundamentals of Low Gravity Fluid Dynamics and Heat Transfer*, CRC Press, Inc., 15 (1993)
[13] K. Nishiguchi, T. Ohji and H. Matsui, IIW Document 212-391-77 (1977)

Flight Experiment to Study Double-Diffusive Instabilities in Silver-Doped Lead Bromide Crystals

N. B. Singh, W. R. Rosch and D. R. Suhre
Science and Technology Center, ESSD, Northrop Grumman Corporation,
1350 Beulah Road, Pittsburgh, PA 15235

S. R. Coriell
National Institute of Standards and Technology, Gaithersburg, MD 20899

W. M. B. Duval
NASA, Lewis Research Center, Cleveland, OH 44135

ABSTRACT

A detailed study on the effect of convection on crystal quality was carried out by growing lead bromide crystals in transparent Bridgman furnace. Direct observations were made on the solid-liquid interface and a new kind of instability was observed. This could be explained on the basis of toroidal flow in the AgBr-doped lead bromide sample. With the increasing translation velocity, the interface changed from flat to depressed, and then formed a cavity in the center of the growth tube. The crystal grown at the lowest thermal Rayleigh number showed the highest quality and crystal grown at the largest thermal Rayleigh number showed the worst quality. Numerical studies were carried out to provide a framework for interpreting the observed convective and morphological instabilities, and to determine the critical (limiting) concentration of dopant for a particular growth velocity and gravity level. Theoretical instability diagrams were compared with data obtained from the experimental studies. These studies provided basic data on convective behavior in doped lead bromide crystals grown by the commercially important Bridgman process.

1. OBJECTIVES:

The main objective of the present program is to understand thermosolutal convection during crystal growth of $PbBr_2$-AgBr alloys. This involves identification of the growth conditions for microgravity experiments delineating the microsegregation, observation of convecto-diffusive instabilities and comparison with theoretical models. The overall objectives can be summarized as follows:

- Observe and study the double diffusive and morphological instabilities in controlled conditions and to compare with theoretically predicted convective and morphological instability curves.
- Study the three dimensional morphological instabilities and resulting cellular growth that occur near the onset of morphological instability in the bulk samples under purely diffusive conditions.
- Understand the micro-and macro-segregation of silver dopant in lead bromide crystals in microgravity.
- Provide basic data on convective behavior in alloy crystals grown by the commercially important Bridgman crystal growth process.

2. NECESSITY OF MICROGRAVITY:

Lead bromide doped with silver can be grown under normal gravity conditions, the double diffusive nature of the convection will cause mixing of the molten charge material. This in turn will cause the solute composition in the crystal to constantly increase during growth. In semiconductor devices, where the electronic properties are a function of the crystal composition, this constant compositional variation is undesirable.

During the solidification of doped materials in Bridgman geometry, generation of destablizing temperature gradients in the melt is unavoidable, resulting in buoyancy-induced convective mixing of the liquid phase. On earth this mixing is generally very intensive and prevention of convection is important in order to minimize micro- and macro-segregation and to obtain homogeneous properties throughout the solidified material. In an actual furnace it is extremely difficult to eliminate the radial temperature gradient completely. Unavoidable gradients may give rise to flows which lead to lateral segregation in the solidified material. In binary systems, if the solute pile up ahead of the solidification front is lighter than the solvent, this would cause a positive density gradient. The net density gradient can have various profiles, depending on the properties of the melt such as thermal conductivity and diffusion coefficient or growth conditions such as growth rate and thermal gradient. Even if the net resulting temperature gradient is stable, convection can occur due to double diffusive character of solute and temperature with different diffusivities. While there have been many observations on earth of this phenomena in thin samples where convection is not important, it is nearly impossible to study three-dimensional instabilities in bulk samples on earth under purely diffusive conditions. The space experiment on transparent lead bromide-silver bromide alloys would permit a study of the various three dimensional morphologies that occur near the onset of morphological instability. Since the lead bromide-silver bromide system is transparent, experiments in space would allow the direct observation of morphological instability and the resulting cellular growth.

The present experiment on lead bromide-silver bromide alloys permits a study of various three dimensional morphologies that occur near the onset of morphological instability in a bulk crystal. Being able to see exactly what is happening during growth in low earth orbit makes this a unique system for microgravity experimentation. The system chosen here has dual advantages: (a) lead bromide is a transparent system almost ideally suitable for direct in situ observations to study solid-liquid interface phenomena and (b) lead bromide holds great promise for technological applications of acousto-optic devices and narrow band ultraviolet filters.

3. SIGNIFICANT RESULTS:

The solidification experiments with $PbBr_2$-AgBr alloys (500 and 5000ppm) showed double-diffusive instabilities at the solid-liquid interface. When the sample was held stationary, any convection present in the liquid was attributed to the radial heat losses. A systematic observations below the morphological breakdown (Fig.1) at the interface showed the development of the depression which finally ends in interfacial breakdown. When we repeated this experiment with pure lead bromide at a speeds of 2.5 cm/day the interface remained flat and did not show any instabilities. This is consistent with the predicted curve shown in figure 2. The interface got depressed in the center and then slowly formed the instability. As a function of time, the instability developed with a much larger amplitude. When the translation velocity was increased, the interface started breaking down. The flow pattern observed in the $PbBr_2$-AgBr system can be described as a “toroidal roll”.

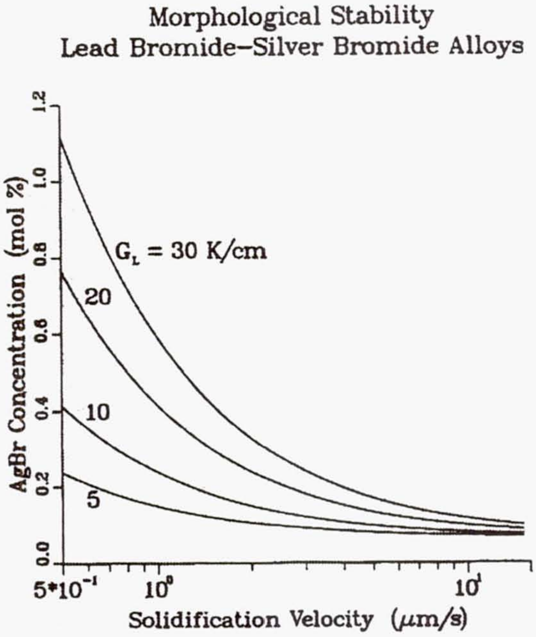
Morphological Stability
Lead Bromide–Silver Bromide Alloys

Figure 1 Predicted morphological stability curve for lead bromide-silver bromide system

A slight asymmetry of the system resulted in the displacement of the node and axis of the tours from the central axis of the tube. When the toroidal flow persisted for many hours and the tube was moving, the interface was observed to be pinched where the radial inflow converged leading to the line defect.

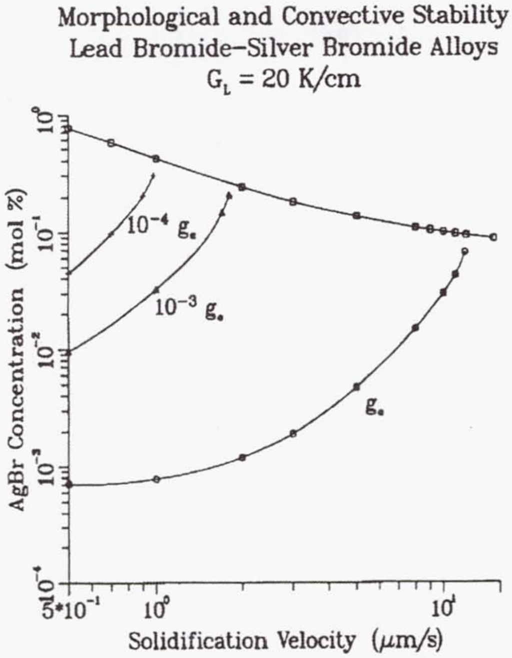

Figure 2 Morphological and convective stability curve for lead bromide-silver bromide system.

A theoretical calculation was performed (Fig. 3) to generate the concentration profile for the solute distribution and we are comparing with the experimentally measured values. We measured the diffusion coefficient and thermal conductivities of solid and liquid which were used in computing stability curves and solute distribution in the crystal. The theoretical composition profiles were calculated for the two bounding cases for 2 growth rates. Both cases assumed a crystal 8 cm in length with .5 % Ag. The diffusion coefficient is 1.7 x 10^{-5} cm^2 /s, and the k value is 0.16. The results are shown in figure 3 for the growth rate of 2 cm/day.

The first case is the well mixed solution where the composition of the liquid at the interface is identical to the composition of the rest of the liquid due to the convective mixing in the liquid. This solution gives a constantly increasing level value for the composition of silver. The second, more desirable case, is the diffusion controlled solution. Here due to a lack of mixing in the liquid, the composition at the interface is different than in the rest of the liquid. The leads to the potential of having a uniform composition of the middle portion of the crystal. Due to the slow growth rate used, the compositional boundary layer will hit the top of the crystal before the steady state composition is reached. This accounts for the jump in the composition profile seen in the 2 cm/day case.

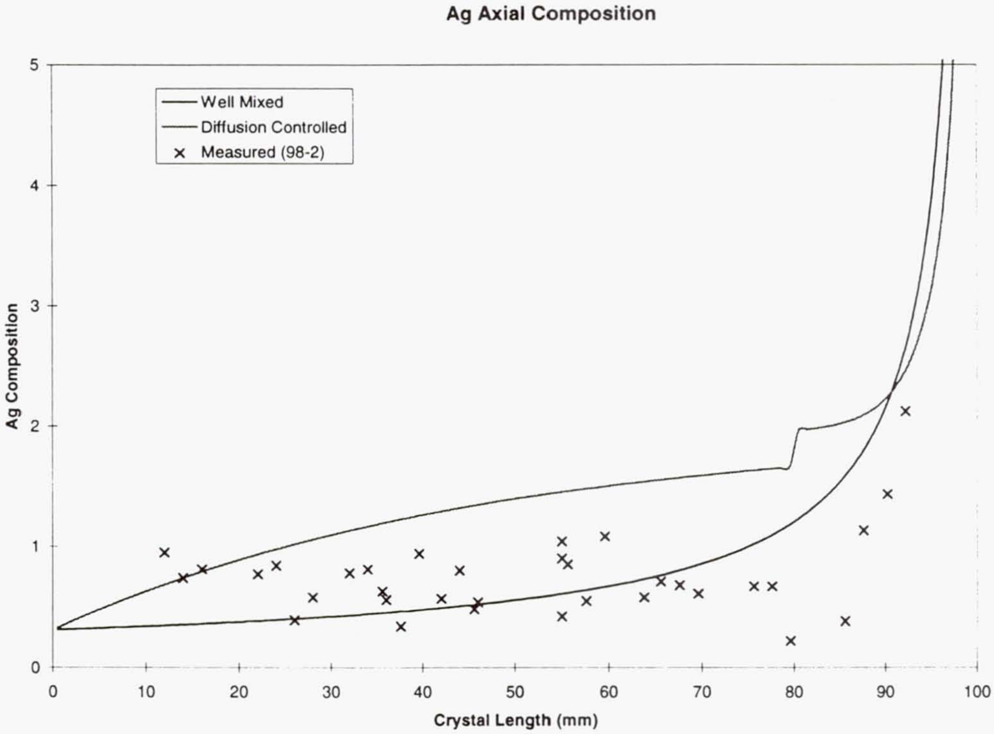

Fig. 3 Calculated and experimentally measured concentration of silver in lead bromide crystals

4. SUMMARY

Direct observations were taken during crystal growth of lead bromide samples doped with 500, 5000 and 10000 ppm silver bromide in 1-g conditions. Stationary solid-liquid interface was flat. When we started growth by moving the ampoule at a velocity lower than critical velocity of interface breakdown, the interface got depressed and the shape of depressed pit varied with the velocity. It became sharply pointed and then slowly formed the instability pulling down the central part of the interface. When the translation rate was increased, the interface broke down. The data showed that the theoretically predicted stability curve agrees well with experimentally observed values. The flow patterns can be described as a toroidal rolls.

ACKNOWLWDGMENT

Authors thank NASA Microgravity Science and Applications Division for financial support. Technical help provided by R. D. Hamacher, R. P. Storrick, C. Chamberlain and A. Stewart is sincerely appreciated.

Page intentionally left blank

TEST OF DENDRITE GROWTH THEORY AND NUCLEATION OF POLYTETRAHEDRAL PHASES FROM THE MELT

Michael J. Aziz
Division of Engineering & Applied Sciences
Harvard University
Cambridge, MA 02138
617-495-9884
aziz@deas.harvard.edu

Frans Spaepen
Division of Engineering & Applied Sciences
Harvard University
Cambridge, MA 02138
617-495-3760
spaepen@deas.harvard.edu

Introduction

Our work on *Kinetics of Nucleation and Growth from Undercooled Melts* falls in two general categories, based on the experimental techniques that are being employed. In the first category, laser heating and thin film diagnostic techniques are used to study crystal growth and liquid diffusion. In the second category, fluxing, a drop tube or vacuum processing are used to achieve undercooling of fairly large melt quantities for the study of crystal nucleation and glass formation. In this paper, we present a recent example from each category: (i) a parameter-free test of dendrite growth theory by a combination of levitation (in collaboration with D.M. Herlach's group at DLR) and pulsed-laser melting techniques[1]; and (ii) an analysis of the nucleation of polytetrahedral crystals (Laves phase) from the melt during solidification in a gas-filled drop tube[2].

Parameter-free Test of Dendrite Growth Theory

In rapid alloy solidification, the dendrite growth velocity depends very sensitively on the deviations from local interfacial equilibrium manifested by kinetic effects such as solute trapping, which is well described by the continuous growth model (CGM) of Aziz and coworkers[3]. In the dilute concentration limit of alloys, the velocity (V) dependence of the partition coefficient (k) is given by:

$$k(V) = \frac{k_e + \frac{V}{V_D}}{1 + \frac{V}{V_D}} \qquad (1)$$

Here, k_e is the equilibrium partition coefficient and V_D is a parameter called the atomic diffusive speed, which is the growth rate at which k is in mid-transition between k_e and unity.

Models for solutal dendrite growth[4] assume that the CGM holds for dendrites, and that the only differences between the highly curved dendrite tip and the planar interface are the Gibbs-Thomson depression in the melting temperature and the solution for the diffusion field ahead of the moving interface. Their predictions for the relationship between V and undercooling (ΔT) depend very sensitively on the value of the input parameter V_D for both planar and dendritic interfaces. Until this work, V_D has been used as a free parameter to fit the dendrite velocity-undercooling data. We have measured independently V_D and the dendrite velocity-undercooling function in the same alloy, which eliminates this key free parameter and provides a rigorous test of the theory. Additionally, we measured independently the bulk liquid diffusivity D_L, the remaining free parameter in the theory (through the kinetic constitutional undercooling).

A $Ni_{99}Zr_1$ alloy was chosen for a number of reasons: (i) the small equilibrium partition coefficient k_e allows strong solute trapping; (ii) precipitation of solvent-rich compounds is not favored thermodynamically; (iii) Zr is sufficiently heavier than Ni to give good resolution in Rutherford backscattering (RBS); and (iv) its high melting temperature makes it well suited for undercooling studies in an electromagnetic levitation coil.

The velocity-undercooling function was determined at DLR using electromagnetic levitation[5]. The sample is melted and undercooled, and is nucleated externally by touching it with an alumina needle. A photosensing device measures the time needed by the dendrites to propagate through the observation window of the optical system, which provides the velocity. The temperature is monitored by pyrometry, which allows the undercooling to be measured from the temperature rise upon recalescence. Figure 1a shows the data points.

The diffusive speed and liquid diffusivity were measured at Harvard by a pulsed laser resolidification technique[6]. Zr is implanted into a Ni thin film on an oxidized silicon substrate. The as-implanted profile is determined by RBS. The melt history, i.e. the position of the crystal-melt interface as a function of time, is determined by transient conductivity and transient reflectance measurements. The Zr profile after resolidification is measured by RBS, and the liquid diffusivity and diffusive speed are obtained by comparing this profile with one obtained from computer simulation. This simulation uses a Crank-Nicholson algorithm to solve the one-dimensional diffusion equation for the molten portion of the sample taking into account the segregation at the interface. Figure 2 shows contours of the χ^2 test parameter as a function of the two variables. The minimum occurs for V_D=26 m/s and D_L=2.7x10^{-9}m^2/s.

The solid line in Figure 1a shows the parameter-free agreement between theory and experiment. The dot-dashed line is the prediction for other values of D_L and V_D, which are plausible for metallic systems, but are outside the good fit of Figure 2. The agreement is clearly worse. Theses experiments are a test of marginal stability theory. Once predictions from solvability theory are available for alloys, they may also be compared with the data. We expect only minor differences in the vicinity of the critical undercooling (the transition from solutal to thermal control), which is the most important region for our purposes.

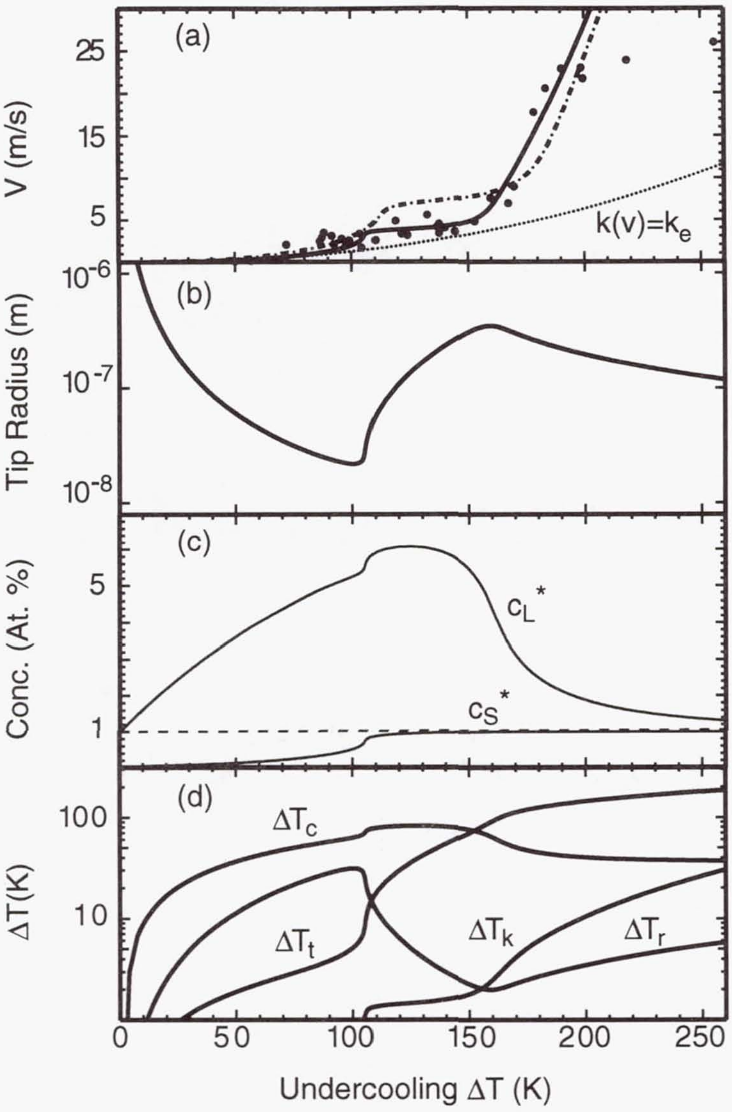

Figure 1. Dependence of total bath undercooling, ΔT, of various quantities. (From ref. 1).

(a) The dendrite growth velocity measured on $Ni_{99}Zr_1$ alloys (dots). The solid line is the parameter-free prediction of dendrite growth theory using V_D=26 m/s and D_L=2.7x10^{-9}m^2/s from Figure 2. The dotted line is the growth velocity calculated without solute trapping. The dot-dashed lines is the prediction for V_D=50 m/s and D_L=5.0x10^{-9}m^2/s, typical values for metals but not near the minimum in Figure 2. The latter two curves demonstrate the importance of an accurate knowledge of V_D and V_L for modeling dendrite growth. All curves in (b)-(d) use V_D=26 m/s and D_L=2.7x10^{-9}m^2/s.

(b) The dendrite tip radius calculated from the marginal stability analysis of growing dendrites.

(c) The concentrations of c_L* and c_S* in the liquid and the solid at the interface calculated within the dendrite growth theory.

(d) Semi-log plot of the individual contributions to the undercooling: thermal undercooling ΔT_t; constitutional undercooling ΔT_c; curvature undercooling ΔT_r; and kinetic interface undercooling ΔT_k.

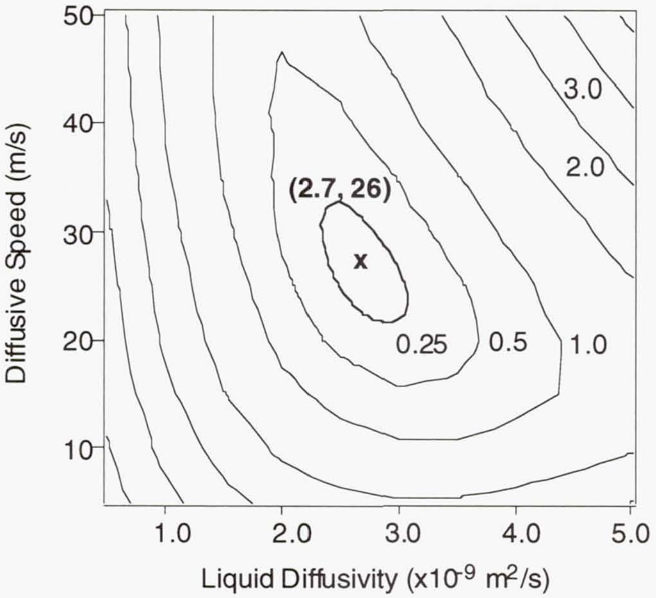

Figure 2. Contour plot of the test parameter χ^2 of the fit between simulation and experiment of the Zr profile after solidification following pulsed laser melting. The best fit is obtained for V_D=26 m/s and D_L=2.7x$10^{-9}$$m^2$/s. The dark line surrounds the region of best fit; thinner lines mark contours of less agreement. (From ref. 1).

Nucleation of Polytetraheral Crystals in a Gas-filled Drop Tube

The barrier to crystal nucleation from the melt is the interfacial tension, which has its origin in the difference between the crystalline and liquid structure[7]. The main structural characteristic of the liquid is its polytetrahedrality: it explains the prevalence of five-fold symmetric clusters and the lack of translational symmetry. In simple metals, the crystal structure contains many octahedral configurations, and the large structural discontinuity leads to large interfacial tension.

There is a category of solids, however, which also have a polytetrahedral character. They include icosahedral quasicrystals and the so-called Frank-Kasper phases[8]. Since there is less structural discontinuity between crystal and melt in these cases, one would expect a lower interfacial tension and, as a result, smaller liquid undercooling. The first experiments on quasicrystal-forming melts shows this to be the case[9].

To explore this further, we have performed solidification experiments in a $Zn_{40}Mg_{36}Ga_{24}$ which is known to form a number of polytetrahedral phases: the Laves phase, $MgZn_2$, a stable quasiperiodic phase with icosahedral symmetry[10], and a large number of icosahedral approximants. A melt of this alloy was atomized into drops, which were solidified in a helium-filled 3m drop tube. Melt temperatures were varied between 550°C and 700°C, without observable effect on the results. The solidified drops were sectioned, polished and observed by optical microscopy. Figure 3 shows a typical microstructure. The primary $MgZn_2$ dendrites are immediately recognizable from their hexagonal symmetry. That some crystals protrude into the central shrinkage cavities implies that they were fully formed before the rest of the sphere solidified.

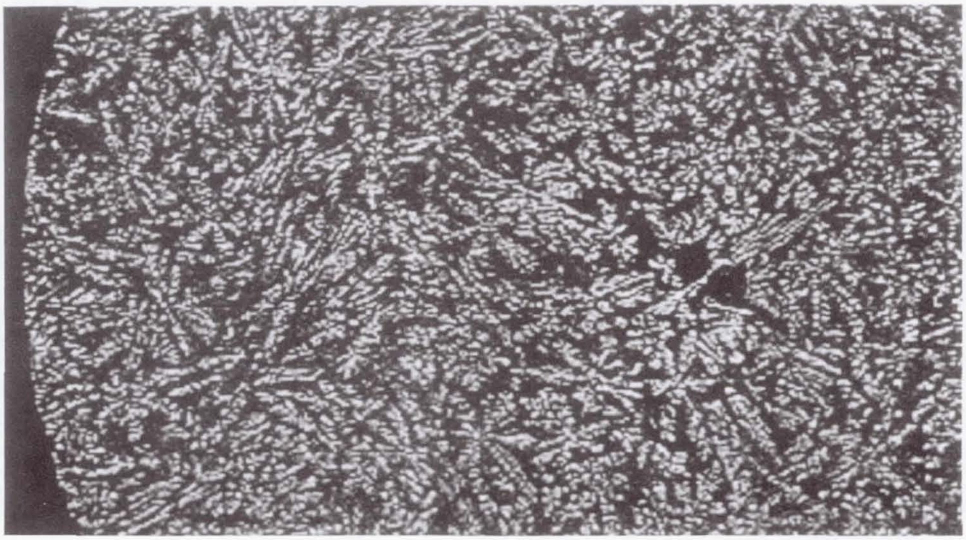

Figure 3. Microstructure of a $Zn_{40}Mg_{36}Ga_{24}$ alloy solidified in a helium-filled 3 m drop tube. The hexagonal primary dendrites are the $MgZn_2$ Laves phase. Shrinkage cavities are seen at the center. The diameter of sphere is 250 μm.

By making a large number of consecutive sections on a single drop it was possible to investigate the three-dimensional distribution of the crystals. It was found that they were uniformly distributed throughout each droplet. Spheres with diameters between 91 and 875 μm were collected and studied. The number of crystals per sphere was determined by quantifying the cross-sectional images, and was found to increase only weakly with size (from about 2,000 to 10,000).

To analyze the nucleation of these crystals, first a mathematical model was developed that combines several features: calculation of both heat and fluid flow in both the liquid and gas phases, the stochastic nucleation, in space and time of a large number of crystals in one droplet, and the growth and transport (by fluid flow) of these crystals. Classical homogeneous nucleation theory was used, and growth of the crystals was assumed to be heat-flow limited. A first test of the model was the maximum size that could be solidified for various drop heights; satisfactory agreement with the, admittedly rather scattered, data was found. The simulations were carried out as a function of the crystal melt interfacial tension, σ. Unsurprisingly, the number of nuclei, N, was found to depend strongly on σ, according to the empirical relation of the form:

$$N = a \exp(-b\sigma + d/\sigma) \qquad (2)$$

where a, b and d are fitting parameters. Up to 200 nuclei were formed in a single droplet. To obtain the 3,000 nuclei observed in a typical experiment, equation (1) requires values of σ in the range 0.002-0.003 J/m^2. This is much lower than the interfacial tension in simple metals[12], and even in quasicrystals[9]. In this case, the simulation shows that the undercooling is very small, and that the growth and recalescence are slow. The nuclei form near the droplet surface, where the temperature is lowest, and are transported throughout by fluid flow, which explains their uniform distribution. The weak dependence of the number of nuclei on the droplet diameter observed in the experiment is reproduced by the model.

References

1. Arnold C.B., Aziz M.J., Schwarz M. and Herlach D.M., submitted to Phys. Rev. B.
2. Fransaer J., Wagner A.V., and Spaepen F., in preparation.
3. Aziz M.J., J. Appl. Phys 53, 1158 (1982); Aziz M.J. and Kaplan T., Acta Metall. 36, 2335 (1988); Aziz M.J., Mater. Trans. A 27, 671 (1996).
4. Kurz W. and Trivedi R., Acta Metall 38, 1 (1990); Lipton J., Kurz W. and Trivedi R., Acta Metall 35, 957 (1987); Boettinger W.J., Coriell S.R. and Trivedi R., in *Rapid Solidification Processing: Principles and Technologies IV*, eds. Mehrabian R. and Parrish P.A. (Claitor's, Baton Rouge LA, 1988) p. 13.
5. Herlach D.M., Mat. Sci. Eng. R 12, 177 (1994); Herlach D.M., Willnecker R. and Gillessen F., *Proceedings of the 5th European Symposium on Materials Sciences under Microgravity*, ESA Sp-222, 39 (1984); Volkmann T., Wilde G., Willnecker R. and Herlach D.M., J. Appl. Phys., submitted.
6. Aziz M.J., Tsao J.Y., Thompson M.O., Peercy P.S. and White C.W., Phys. Rev. Lett. 56, 2489 (1986); Hoglund D.E., Aziz M.J., Stiffler S.R., Thompson M.O., Tsao J.Y., and Peercy P.S., J. Cryst. Growth 109, 107 (1991); Smith P.M. and Aziz M.J., Acta Metall. Mater. 42, 527 (1994).
7. Spaepen F., Acta Met. 23, 729 (1975); Spaepen F. and Meyer R.B., Scripta Met. 10, 37 (1976); Spaepen F., in **Solid State Physics** (H. Ehrenreich and D. Turnbull, eds., Academic Press, San Diego, CA, 1994) 47 , p.1.
8. Nelson D.R. and Spaepen F., **Solid State Physics** (H. Ehrenreich and D. Turnbull, eds., Academic Press, San Diego, CA, 1994) 42 , p.1.
9. Holland-Moritz D., Schroers J., Herlach D.M., Grushko B. and Urban K., Acta Mater. 46, 1601 (1998); Ebalard S., Spaepen F., Cochrane R.F. and Greer A.L., Mat. Sci. Eng. A 133, 569 (1991).
10. Ohashi W. and Spaepen F., Nature 330, 555(1987).
11. Spaepen F., Chen L.C., Ebalard S. and Ohashi W., in *Quasicrystals*, Proceedings of the Anniversary Adriatico Research Conference on Quasicrystals (World Scientific Publishing Co., Singapore, 1990), pp. 1; Ohashi W., Ph.D. Thesis, Harvard University (1989).
12. Turnbull D., J. Chem. Phys. 20, 411 (1952).

The Effect of Doping on the Fracture Toughness of YSZ in a Low Oxygen Partial Pressure Environment

K. R. Sridhar (P.I.)
Phone: (520) 621-6111, Email: sridhar@shakti.ame.arizona.edu

W. Chen (Co-P.I.)
Phone: (520) 621-6114, Email: wchen@allen.ame.arizona.edu

Department of Aerospace and Mechanical Engineering
The University of Arizona
Tucson, AZ 85721
Fax: (520) 621-8191

Introduction and Research Objectives

Solid oxide electrolyzers generate pure oxygen from oxygen bearing gases such as carbon dioxide, water, and air. These electrolyzers can generate oxygen from the carbon dioxide rich atmosphere of Mars, and also from the evolved gases obtained from hydrogen or carbon reduction of the lunar regolith. Several studies have shown that oxygen production from Martian atmosphere as a key technology that can reduce the cost of both robotic and human missions.[1,2] There is a real need for developing better electrolyzer materials that offer superior thermal and mechanical characteristics as well as improved electrical performance. The electrolyte of the electrolyzer is a ceramic solid oxide such as yttria stabilized zirconia (YSZ). In order to develop structurally robust electrolyzers that would withstand the severe vibration and shock loads experienced during the launch and landing phases of the mission, it is essential to understand the damage initiation and consequent failure mechanisms and their relation to material composition and processing parameters. The objective of this research is to understand and quantify the relation between the loading/environmental conditions and the mechanical properties such as dynamic fracture toughness and dynamic bending strength and their relations to microstructures (thus processing parameters and choice of electrode and electrolyte compositions). In this project, we will investigate the effects of dopants on both the mechanical properties (fracture toughness, four-point and bi-axial bending strengths) and the electrical performance (oxygen conductivity) of YSZ in an environment with a low oxygen concentration.

Relevance to Microgravity Program

All the major studies conducted by NASA in the recent past, such as the 90 day study and the Staford Committee report, have identified the need for utilizing space resources, i.e., “living off the land,” as an important and necessary part of future exploration of the solar system. Several studies have shown that oxygen production from the Martian atmosphere and from lunar regolith as a key technology that can reduce the cost of both robotic and human missions. The production of oxygen from carbon dioxide and water is of importance for both life support and propellant production. For example, it would be highly desirable to have a closed loop life support system with oxygen reclamation in the transit vehicle to Mars as well as for extended stays aboard the Space Station. This research addresses the material issues related to electrochemical systems in the area of ISRU. The use of local resources is especially important for a long-duration mission, high-cost/long-time transportation, or for settlement missions. Based on the knowledge learned from this research, superior materials will be developed with exceptional properties for improving the structural integrity of solid oxide electrolyzers. The improved electrolyzers would process in-situ materials to produce usable consumables for human space exploration in micro and reduced gravity environments.

Research Plans

The presence of oxygen ion vacancies in the crystal structure of YSZ allows oxygen to be separated exclusively from an oxygen bearing gas, when a DC potential is applied. The DC potential is applied to the electrolyte through porous electrodes that are applied on both sides of the YSZ electrolyte. The electrode materials are typically platinum or a perovskite such as doped lanthanum chromite. The electrochemical cell thus formed is made fairly thin (50 to 400 microns) in order to reduce the ohmic losses across the cell. Hence, the electrochemical cell is a ductile/brittle/ductile (in the case of platinum electrode), a brittle/brittle/brittle (perovskite electrodes) or brittle/brittle/ductile (hybrid electrodes) thin layered structure with the YSZ layer as the load-bearing structural member. A YSZ layer of high fracture toughness is therefore desirable to survive the severe vibration and shock loading experienced during the launch and landing phases of the mission. In addition the electrolyzer stack has to withstand high-temperature thermal cycling. The temperature at which the electrolyzer stack operates is in the range of 900 to 1000 °C, due to the enhanced oxygen ion conductivity at these elevated temperatures as well as the higher rates of thermal dissociation of carbon dioxide to carbon monoxide and oxygen. Due to the present requirement of relying on non-nuclear sources for space power, the anticipated scenario for operating the oxygen production unit will be to shut down the unit at the end of the Martian or lunar day and start back the next morning when the solar panels start producing power. The oxygen plants on Martian surface are required to operate for over 400 days and hence expected to undergo severe thermal cycling. A cracked electrolyzer will allow CO_2 to leak into the O_2 side, which is unacceptable from the mission standpoint.

Several approaches to increase the fracture resistance of YSZ by toughening are available. While m-ZrO_2 can increase the strength of YSZ it also lowers its oxygen ion conductivity. Fine particles of partially stabilized zirconia and alumina, when added in small quantities, have been shown to provide increase in bending strength without degrading the electrical properties. Only limited amount of mechanical testing has been done measuring flexural strength thus far on toughened YSZ products. In this investigation, the amounts of partially stabilized zirconia, alumina, and Alkoxide were systematically varied in the composition of YSZ. The planned doping levels are listed in Table 1.

Table 1 Planned Dopants and doping level.

Dopant	PSZ (mol%)	Alumina (mol%)	Alkoxide (mol%)	m-ZO_2 (mol%)
Level 1	1	1	1	1
Level 2	2	2	2	2
Level 3	3	3	3	3
Level 4	4	4	4	4

The resultant materials were placed in a low oxygen concentration, high temperature environment for thermal cycling. Before and after the thermal cycling, the fracture toughness of each material will be evaluated using Vickers indentation method[3] that serves as a screening method in selecting the material composition and processing parameters. The electrical conductivity will also be measured. Specimens with excellent mechanical and electrical properties will be investigated in detail to develop a more fundamental, scientific understanding of the damage and failure characteristics of solid oxide electrolyzers under dynamic loading conditions at elevated temperatures. The fracture toughness will be measured rigorously using standard four-point bending methods.[4] Quasi-static and dynamic bi-axial bending strengths will be measured as a function of material composition and processing parameters. A “ring-on-ring’ technique developed by NIST will be adopted to determine the quasi-static bi-axial flexural strength. A split Hopkinson pressure bar[5,6] will be modified to measure the corresponding dynamic strength. The effects of microstructure on two key material properties---thermal expansion coefficient and the degradation of material strength and toughness in low oxygen concentration environment---will be thoroughly investigated. Optical and electron microscopy will be employed to identify the deformation mechanisms, toughening mechanisms, and failure modes, thus relating the mechanical properties to microstructures and material processing. The effects of loading rate and low oxygen partial pressure on the microstructural evolution will also be determined. Based on the knowledge learned from this investigation, superior materials will be developed with exceptional mechanical and electrical properties for improving the structural integrity and oxygen conductivity of solid oxide electrolyzers for space missions.

1. Zubrin, R. And Price, S., “Low Cost mars Sample Return with ISPP,” NASA Contract Report NAS-9-19145, Lockheed Martin, Denver, CO. 1995.

2. Sridhar, K. R., “Mars Sample Return With ISPP,” *J. British Interplanetary Society*, **49** 435-440, 1996.

3. Lawn, B. and Wilshaw, R., “Indentation Fracture: Principles and Applications,” *J. Mat. Sci.*, **10** 1049-1081, 1975.

4. Nose, T. and Fuji, T., “Evaluation of Fracture Toughness for Ceramic Materials by a Single-Edge-Precracked-Beam Method,” *J. Am. Ceram. Soc.*, **71** 328-333, 1988.

5. Follansbee, P. S., “The Hopkinson bar,” *Mechanical Testing, Metals Handbook*, Vol. **8**, 9th ed., ASM, Metals Park, Ohio, pp. 198-217, 1985.

6. Chen, W. and Ravichandran, G., "An experimental technique for imposing dynamic multiaxial compression with mechanical confinement," *Exp. Mech.* **36** 155-158, 1996.

Particle Engulfment and Pushing by Solidifying Interfaces

Doru M. Stefanescu(1), Frank R. Juretzko(1), Brij K. Dhindaw(1), Subhayu Sen(2) and Peter A. Curreri(3)

1) The University of Alabama, Tuscaloosa, Al; 2) USRA, NASA Marshall Space Flight Center, Huntsville, Al;
3) NASA Marshall Space Flight Center, Huntsville, Al

Abstract

The scientific objectives of the work on Particle Engulfment and Pushing by Solidifying Interfaces (PEP) include: 1) to enhance the fundamental understanding of the physics of interaction between inert particles and the solidification interface, and 2) to investigate aspects of melt processing of particulate metal matrix composites in the unique microgravity environment that will yield some vital information for terrestrial applications. The proposal itself calls for a long-term effort on the Space Station. This paper reports on ground experiments performed to date, as well as on the results obtained from two flight opportunities, the LMS mission (1996) and the USMP-4 mission (1997).

Introduction

During solidification of metal matrix composites the ceramic particles interact with the solidification front. This interaction is responsible for the final microstructure. The solutal and thermal field, as well as fluid motion at the liquid/solid interface influence both interface morphology and the particle/interface interaction itself. It is thus imperative to fully understand the solidification science and transport phenomena aspects associated with the process in order to control it.

The phenomenon of interaction of particles with melt interfaces has been studied since the mid 1960's. While the original interest in the subject was mostly theoretical, researchers soon realized that understanding particle behavior at solidifying interfaces may yield practical benefits. The experimental evidence on transparent organic materials [1] demonstrates that there exist a *critical velocity* of the planar solid/liquid (SL) interface below which particles are *pushed* ahead of the advancing interface, and above which particle *engulfment* occurs.

The main objectives of the experimental and theoretical work were as follows:

- to evaluate the experimental method including sample design, thermal regime, velocity regime, analysis procedures;
- to obtain preliminary data on the critical velocity of PEP in a microgravity environment;
- to interpret these results through mathematical and computational models.

Theoretical

A previously proposed analytical model for PEP was further developed. A major effort to identify and produce data for the surface energy of various interfaces required for calculation was undertaken. The details have been reported[4]. The basic equation for calculation of the critical velocity for the particle-engulfment transition (PET) is:

$$V_{cr} = \left(\frac{\Delta\gamma_o \, a_o{}^2}{3\eta K^* R} \right)^{1/2}$$

where $\Delta\gamma_o$ is the surface energy difference between the particle-solid and particle –liquid surface energy, a_o is the atomic or molecular diameter, η is the liquid viscosity, R is the particle radius, and $K^* = K_P/K_L$ is the ratio between the thermal conductivity of the particle (K_P) and of the liquid (K_L).

Experimental

To evaluate the experimental value of PET work was conducted in the following environments:

- ground based
- low-g environment: DC-9
- μ-g environment: LMS, USMP-4

The following systems were used:

- metal/particle: Al /SiC , Al /ZrO_2 , Al-Ni /ZrO_2, Zn /ZrO_2
- transparent organic/particle: succinonitrile (pure, +0.5% water, +1% water) + polystyrene particles (0.5 to 25 μm dia.), biphenyl + glass particles (3 to 15 μm dia.)

Metal/particle systems were investigated under μ-g during the LMS mission, while transparent organic/particle couples were used during the USMP-4 mission.

Metal/Particle Systems and the LMS Mission

Directional solidification ground experiments have been carried out to determine the pushing/engulfment transition for three different metal/particle systems. The matrices were pure aluminum (99.999%), pure zinc (99.95% Zn) and Al – 4.5% Ni alloy. Spherical zirconia particles (500 μm in diameter) were incorporated in these matrices through mixing in molten state. The particles were non-reactive with the matrices within the temperature range of interest. The experiments were conducted such as to insure a planar solid/liquid interface during solidification. Particle location before and after processing was evaluated by X-ray transmission microscopy for the aluminum-base matrices. All samples were characterized by optical metallography after processing. A clear methodology for the experiment evaluation was developed to unambiguously interpret the occurrence of the PET. A full report on these findings has been published recently[2].

It was found that the critical velocity for engulfment ranges from 1.9 to 2.4 μm/s for Al/ZrO_2 and from 1.9 to 2.9 μm/s for Zn/ZrO_2. No clear PET was found for the Al-Ni/ ZrO_2 system for interface velocities down to 1μm/s.

During the LMS Mission three samples were directionally solidified in the AGHF facility, as follows: two pure aluminum (99.999%) 9 mm cylindrical rods, loaded with about 2 vol.% 500 μm diameter zirconia particles (samples FM1 and FM3); one Al-Ni loaded with the same amount and type of zirconia particles (sample FM2). To validate a cartridge-crucible-sample assembly for the Space Station experiment, two different cartridge designs were used[3]. For sample FM1 the cartridge included an alumina piston and a graphite spring. The piston-spring system compensated for melting expansion and solidification shrinkage. A simpler design was used for samples FM2 and FM3. It consisted of an expansion reservoir provided at the hot end of the crucible.

The main characteristics of the samples and furnace translation velocity are summarized in **Table 1**. For FM1 a step-wise decreasing regime was used, while for the other two a step-wise increasing regime was chosen. The SL interface velocity resulting from the different furnace translation velocities was calculated based on thermocouple data.

Table 1 Characteristics of flight samples

Flight sample	Material	Ampoule-sample	Velocity regime, μm/s
FM1	Al - ZrO_2	spring-piston	20 - 5 - 0.5
FM2	AlNi- ZrO_2	expansion reservoir	1 - 3 - 9
FM3	Al - ZrO_2	expansion reservoir	1 - 3 - 9

Both the cartridge containing the ampoule, and the ampoule after extraction from the cartridge were examined by X-ray and computer tomography (*CT*). The results of the cartridge *CT* evaluation are shown in Fig. 1. The spring-piston assembly used for sample FM1 functioned as expected. Some liquid Al leak is seen past the fore side of the piston. This leak does not seem to be significant, since no Al is seen in the 90° position of the *CT* (lower picture on Fig. 1a).

Sample FM2 was less successful. On Fig. 1b it is seen that several voids have formed along the sample. It appears that the liquid metal has fractured in that region resulting in a two-part solid sample: an upper part that is in contact with the alumina plug, and a lower part.

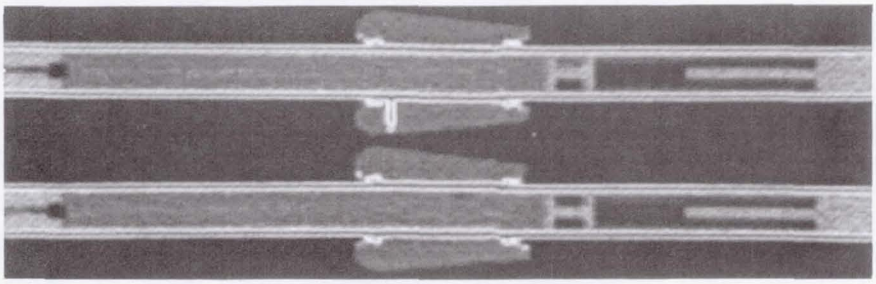

a) sample FM1

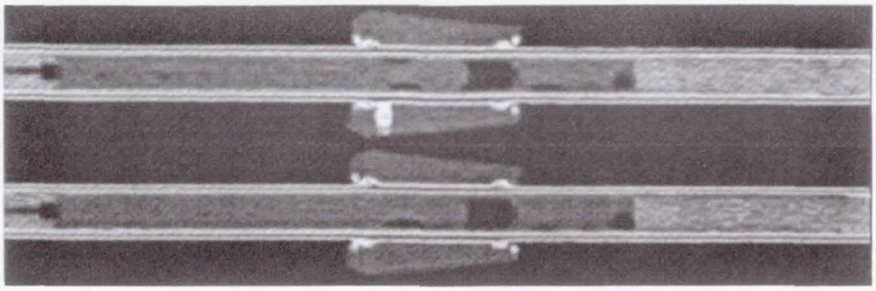

b) sample FM2

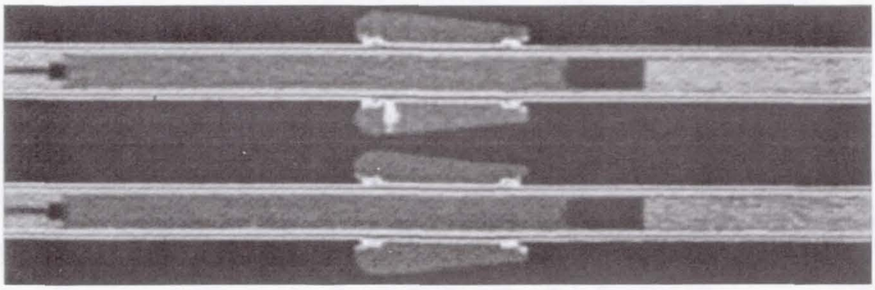

c) sample FM3

Fig. 1 *CT* images of the flight cartridge - ampoule assembly[3].

Sample FM3 behaved as expected. On Fig. 1c it is seen that the shrinkage cavity was positioned between the metal and the alumina plug. The sample itself appears to have no significant shrinkage porosity or voids. This was also confirmed through metallographic examination.

For the Al/ZrO_2 sample it was found that a PET occurred in the velocity range of 0.5 to 1 μm/s (see Fig. 2 and Fig. 3). This is smaller than the ground PET velocity of 1.9 to 2.4 μm/s. It demonstrates that natural convection increases the critical velocity. A detailed report of these results has also been published[4]. For the $Al\text{-}Ni/ ZrO_2$ system no PET was found down to the lowest velocity used during the experiment which was of 1 μm/s.

A comparison between measured and calculated critical velocity for the metallic systems studied on ground and μg are given in Table 2. It is seen that the predicted value lies within the experimentally evaluated μg value.

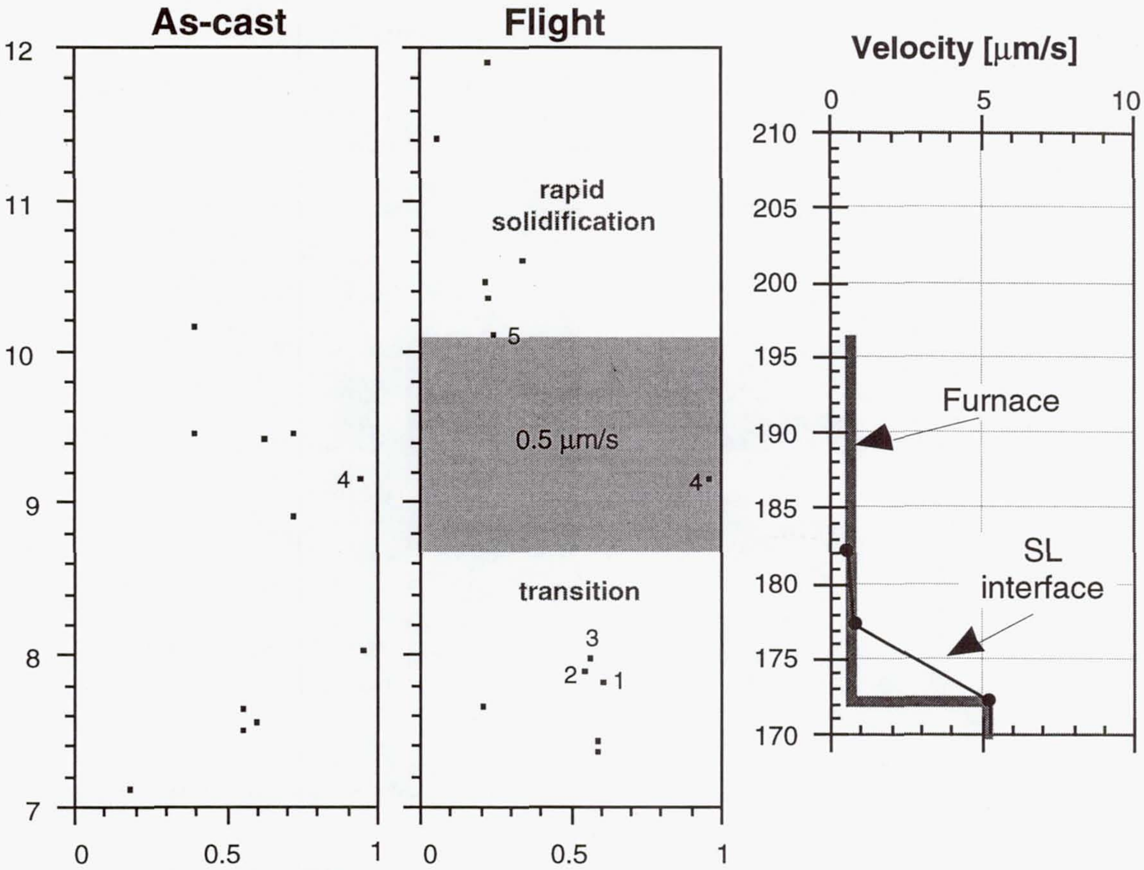

Fig. 2 Summary of XTM evaluation of particles positions in sample FM1 in the region of furnace translation rate of 0.5 μm/s [4]

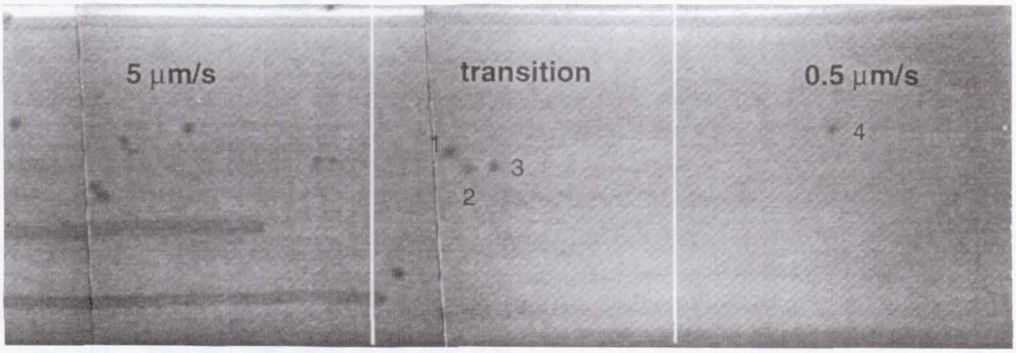

Fig. 3 XTM image of flight sample FM1. Particles are engulfed at 5 μm/s and in the transient region. No valid engulfed particles are present in the 0.5 μm/s region [4]

Table 2 Experimental and theoretical values for the critical PET velocity

Data from	Critical Velocity, μm/s	
	Al/ZrO$_2$	Zn/ZrO$_2$
Ground experiments	1.9 – 2.4	1.9 – 2.9
LMS	0.5 – 1.0	-
Model	0.775	0.672

Organic Material/Particle Systems and the USMP-4 Mission

Ground and parabolic flight experiments were also performed with a biphenyl matrix / spherical glass particles, and succinonitrile matrix / polystyrene particles. Two experimental setups were used: a horizontal gradient heating facility (HGF) for horizontal solidification, and a Bridgman-type furnace (BF) for vertical solidification. The convection level during solidification in the HGF was varied by changing the distance between the glass slides containing the composite sample. The BF was used on ground and during parabolic flights, and thus the convection level was changed by alternating low-gravity and high-gravity solidified regions. It was found that the convection level and/or particle buoyancy significantly influences the critical velocity for particle engulfment. At higher natural convection during solidification the critical velocity increases by up to 40%. At very high convection levels engulfment may become impossible because particles fail to interact with the interface. A detailed account of these experiments was previously reported[5].

In the vertical configuration Stokes settling velocity appeared to have an influence on the critical velocity for particle engulfment. This was more pronounced for thicker sample cells since the settling velocity is expected to increase with increase in sample cell thickness. The effect of Stokes velocity was to decrease the critical velocity by up to 40%. This is also illustrated by the slight increase in critical velocity when experiments were performed at lower gravity levels.

During the USMP-4 mission similar experiments on biphenyl matrix and spherical glass particles, and succinonitrile matrix with polystyrene particles were performed. The standard procedure used for the SCN/polystyrene samples consisted in directional solidification (DS) of the sample through incremental velocity changes (increase or decrease). If agglomerates or too many particles accumulated at the interface during pushing, rapid DS (10 or 15 μm/s for 30 to 50 s) was used to engulf the particles and clear the interface. Then, incremental velocity solidification was resumed.

Flight and ground experimental results together with theoretical predictions are summarized in Fig. 4. Triangles describe engulfed particles, while circles pushed particle. It is seen that a lower and upper limit for PET exists. Between these two limits, some particles are pushed and some are engulfed. It is also seen that the ground critical velocity lies significantly above the one found in *μg*, as expected.

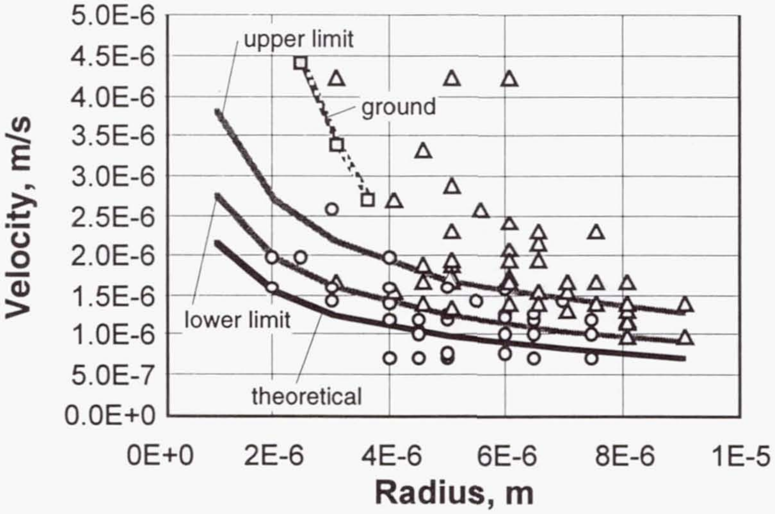

Fig. 4 USMP-4 results for SCN/polystyrene.

The theoretical critical velocity is slightly lower than the lower experimental limit. The molecular diameter calculated from the molar volume of SCN (0.081 m^3/kmol) was $a_o = 1.14 \cdot 10^{-9}$ m.

Evaluating individual particles was more difficult for the biphenyl samples because biphenyl became opaque after resolidification. Some preliminary results are given in Fig. 5.

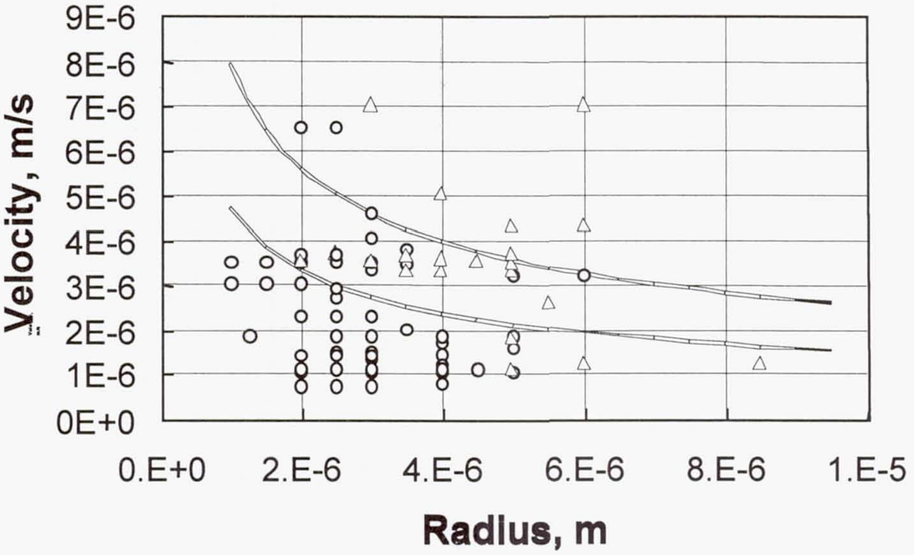

Fig. 5 USMP-4 results for biphenyl/glass.

Another procedure consisted in DS at a set velocity, after which rapid DS was used to engulf the particles. This was followed by rapid directional remelting which left behind in the liquid a band of particles (that were pushed at the set velocity). Since the liquid is transparent, it was possible to measure the particle size. In developing this method full advantage was taken of the real-time video down-link and direct interaction with the astronauts. Measurements with this procedure, as well as theoretical calculation are not available yet.

The experiments clearly demonstrated that the particles produced interface instability. For example, in one case, the interface became unstable at 2.8 µm/s when a large amount of particles were pushed ahead of the interface. However, after the interface was "cleaned" by running at 10 µm/s, the interface did not break down until the velocity reached 5.2 µm/s.

Pushing of large agglomerates of particles was systematically observed. On ground agglomerates are broken down by the convective flow and/or easily engulfed.

Additional observations were made on shrinkage flow into the interface, and on the effect of g-jitters on particle behavior at the interface. It was noticed that every time the verniers were fired particles and agglomerates were jerked along the liquid/solid interface.

References

---

[1] S.N. Omenyi and A.W. Neumann: *J. Appl. Phys.*, 1976, vol.47, no.9, pp. 3956-62

[2] F. R. Juretzko, B. K. Dhindaw, D. M. Stefanescu, S. Sen and P.A. Curreri, Metall. and Materials Trans., **29A** (1998) 1691

[3] D. M. Stefanescu, B. K. Dhindaw, F. R. Juretzko, P.A. Curreri and S. Sen, in *Life and Microgravity Spacelab (LMS) Final Report*, J. P. Downey compiler, Marshall Space Flight Center , Alabama (1998) 76

[4] D. M. Stefanescu, F. R. Juretzko, B. K. Dhindaw, S. Sen and P.A. Curreri, Metall. and Materials Trans., **29A** (1998) 1697

[5] S. Sen, B.K. Dhindaw, D.M. Stefanescu, A. Catalina and P.A. Curreri, J. Crystal Growth, **173** (1997) 574

Crystal Growth of ZnSe and Related Ternary Compound Semiconductors by Vapor Transport

Principal Investigator: Dr. Ching-Hua Su, NASA/MSFC

Co-Investigators:
Prof. R.F. Brebrick, Marquette University
Dr. A. Burger, Fisk University
Prof. M. Dudley, State Unviersity of New York
Prof. R. Matyi, University of Wisconsin
Dr. N. Ramachandran, USRA/MSFC
Dr. Yi-Gao Sha, USRA/MSFC (now at Digirad Co.)
Dr. M. Volz, NASA/MSFC

Industrial Guest Investigators: Dr. Hung-Dah Shih, Texas Instruments

I. Introduction

The materials to be studied in this project are ZnSe and the related ternary compound semiconductors such as ZnSeTe, ZnSeS and ZnCdSe. With an energy gap of 2.7 eV at room temperature and an efficient band-to-band transition, ZnSe has been studied extensively as the primary candidate for a blue light emitting diode and laser for optical displays, high density recording, and military communications. However, developments in the bulk crystal growth has not advanced far enough to provide the low price, high quality substrates needed for the thin film growth technology. The realization of routine production of high-quality single crystals of these semiconductors requires a fundamental, systematic and in-depth study on the physical vapor transport (PVT) growth process and crystal growth by vapor transport in low gravity offers a set of unique conditions for this study.

The previous results from vapor phase crystal growth of semiconductors showed improvements in surface morphology, crystalline quality, electrical properties and dopant distribution of the crystals grown in reduced gravity as compared to the crystals grown on Earth. Previously, two reasons have been put forward to account for this. The first is weight-related reductions in crystal strain and defects. These are thought to be caused by the weight of the crystals during processing at elevated temperatures and retained on cooling, particularly for materials with a low yield strength. The second, and more general, reason is related to the reduction in density-gradient driven convection. However, the detailed mechanisms responsible for the improvements and the gravitational effects on the complicated and coupled processes of vapor mass transport and growth kinetics are not well understood.

The PVT crystal growth process consists of essentially three processes; sublimation of the source material, transport of the vapor species and condensation of the vapor species to form the crystal. The latter two processes can be affected by the convection caused by gravitational accelerations on Earth. The results of some fluid dynamic analyses stated that the effects of gravity on heat transfer and mass transport in most of the PVT systems were insignificant. However, the convective flows caused by the buoyancy-driven perturbation in the transport flow field in the vicinity of the growing surface will affect the growth kinetics on the growing surface. This results in phenomena such as interface fluctuation, non-uniform step bunching, etc. which will cause non-uniformity in the incorporation of impurities and defects as well as in the deviation from stoichiometry in the grown crystal. This, in turn, will further modify the local mass transport characteristics and result in irregular flows at the vicinity of the growing surface. It is expected that the reduction in convective contamination by performing flight experiments in a reduced gravity environment will help to simplify the complexity of the coupled mass transport and growth kinetics problem. An improved comparison between the experimental results and theoretical simulations will be beneficial to any growth process involving vapor mass transport or vapor-crystal interface growth kinetics.

II. Scientific Objectives

The scientific objectives and priorities of this investigation are:

1. Grow ZnSe crystals in reduced gravity using Physical Vapor Transport (PVT) processes:

- to establish the relative contributions of gravity-driven fluid flows to (i) the non-uniform incorporation of impurities and defects and (ii) the deviation from stoichiometry observed in the grown crystals as a result of buoyancy-driven convection, irregular fluid-flows and growth interface fluctuations.
- to assess the amount of strain developed during processing at elevated temperatures and retained on cooling caused by the weight of the crystals.
- to obtain a limited amount of high quality space-grown materials for various thermophysical and electrical properties measurements and as substrates for device fabrication and thus assess device performance as influenced by a substantial reduction in gravity-related effects.

2. Perform *in-situ* and real-time optical measurements during growth to independently determine:

- the vapor concentration distribution by partial pressure measurements using optical absorption.
- the evolution of growth interface morphology and instantaneous growth velocity by optical interferometry.
- and thus help to simplify the complexity of the coupled mass transport and growth kinetics problem.

3. Evaluate the additional effects of gravity on the PVT process in the future flight experiments by examining:

- The growth kinetics on various seed orientations.
- the dopant segregation and distribution in the Cr doped ZnSe.
- the compositional segregation and distribution in the ternary compounds grown by PVT.

III. Investigation Approach

1. Mass Flux:

The main disadvantage of PVT growth technique is that the growth rate is usually low and inconsistent. Therefore, a systematic and complete study was performed to optimize the mass flux in the ZnSe PVT system.

(1) One-dimensional diffusion model:

From the results of a one-dimensional diffusion analysis, four experimentally adjustable parameters, the source temperature, the deposition temperature, the partial pressure ratio over the source (vapor phase stoichiometry) and the residual gas (CO, CO_2 and H_2O) pressure, determine the diffusive mass flux in a PVT system. However, two of these four parameters, the partial pressure ratio over the source and the residual gas pressure, are more critical than the others. These two parameters are critically dependent on the proper heat treatments of the starting materials for optimum mass flux.

(2) Thermodynamic properties:

The pertinent thermodynamic properties were determined. The partial pressures of Zn and Se_2 over ZnSe(s) were measured for several samples by the optical absorption technique and the standard Gibbs energy of formation of ZnSe(s) from Zn(g) and $0.5Se_2(g)$ was found to be independent of the sample stoichiometry. The Zn-Se phase diagram was described using an associated solution model for the liquid phase and the behavior of the thermodynamic properties of the system pertinent to the PVT process, such as the partial pressures of Zn and Se_2 along the entire three-phase curve, was calculated. The associated solution model was then extended to the Zn-Se-Te system and the thermodynamic properties, such as the partial pressures of Zn, Se_2 and Te_2 along the three-phase curve for various $ZnSe_{1-x}Te_x$ ($0 < x < 1$) pseudobinary systems were established.

(3) Mass flux measurements:

An *in-situ* dynamic technique was set up for the mass flux measurements which has the following advantages over the previous techniques; (i) the instantaneous flux (instead of an average value) was measured and (ii) multiple data points were determined from one ampoule. The mass fluxes in the ZnSe PVT system were measured on the source materials provided by various vendors and treated with different heat treatment procedures.

(4) Residual gas measurements:

The residual gas pressures and compositions in the processed ampoules were measured and it was found that (i) carbon and oxygen in the residual gas originated mainly from the ZnSe source materials and (ii) the oxygen content can be significantly reduced by hydrogen reduction treatment.

(5) Heat treatment of starting materials:

Various heat treatments were conducted to control the partial pressure ratio over the source and the effectiveness of the treatments was evaluated by partial pressure measurements. The optimum hydrogen reduction and vacuum heat treatment procedures were established for the source to maximize the mass flux in the ZnSe PVT process.

2. Crystal Growth and Characterization:

The crystal growth activities were concentrated on a novel three thermal-zone translational growth in a closed system. In order to study the effects of gravity on the various properties of the grown crystals the growth experiments were performed with the growth direction at an angle of 0° (vertical destabilized configuration), 90° (horizontal configuration) and 180° (vertical stabilized configuration) to the gravity vector direction. Self-seeded and seeded growths of ZnSe as well as the self-seeded growth of ZnSeTe and Cr doped ZnSe were conducted. The grown crystals were characterized by various techniques; including spectroscopy (atomic absorption, spark source mass spectroscopy and secondary ion mass spectroscopy), X-ray diffraction (Laue reflection, rocking curve and reciprocal lattice mapping), synchrotron radiation images from a white X-ray beam (reflection and transmission), microscopy (optical, electron, and atomic force), sample polishing and etching and optical transmission. The electrical and optical characterization was performed by optical transmission and photoluminescence measurements.

3. Effects of Gravity Vector Orientation:

The effects of gravity orientation were studied by comparing the following characteristics of the vertically and horizontally grown ZnSe crystals.

(1) Grown crystal morphology:

The morphology of the as-grown, self-seeded ZnSe crystals grown in the horizontal configuration grew away from the ampoule wall and exhibited large (110) facets which tended to align parallel to the gravitational direction. Crystals grown in the vertical configuration grew in contact with the ampoule wall over the full diameter and when the furnace translation rate was too high for the mass flux, the growing crystal surface became morphologically unstable with voids and pipes embedded in the crystal. The as-grown seeded ZnSe crystals in both the horizontal and vertical configurations showed similar characteristics in the morphology as described above for the self-seeded growth.

(2) Surface morphology:

The as-grown surfaces of the horizontally grown ZnSe and Cr doped ZnSe crystals were dominated by (110) terraces and steps. On the other hand, the as-grown surface of the vertically grown ZnSe crystals showed granular structure with tubular features (200nm OD, 75nm ID and 25nm in height) on the top. The as-grown surface of the vertically grown Cr doped ZnSe crystals showed a network of high plateaus with each island 30-70μm in diameter and 3.5μm in height. Numerous nuclei with diameters around 20-50nm and heights of 1-7nm were observed on top of these islands.

(3) Segregation and distribution of defects and impurities:

From the secondary ion mass spectroscopy mappings, for the horizontally grown self-seeded ZnSe crystal, [Si] and [Fe] showed clear segregation toward the bottom of the wafer cut axially along the growth axis. For the vertically grown seeded ZnSe crystal, [Si] and [Cu] showed segregation toward the peripheral edge of the wafer cut perpendicular to the growth axis. From the photoluminescence mappings of near band edge intensity ratios, it was determined that all of the horizontally grown crystals showed the following trends in the radial and axial segregation of [Al] and [V_{Zn}] due to the buoyancy driving force and diffusion boundary layer: [Al] segregates radially toward the top and axially toward the first grown region and [V_{Zn}] segregates radially toward the bottom and axially toward the first grown region. The as-grown surface of the seeded vertically stabilized grown crystal showed [Al], [Li and/or Na] and [V_{Zn}] segregate radially toward the center. Finally, the as-grown surface of the self-seeded vertically destabilized grown crystal showed [Al] and [V_{Zn}] segregate radially without an apparent pattern.

(4) Axial compositional variation in ZnSeTe:

The mole fraction of ZnTe in the grown $ZnSe_{1-x}Te_x$ crystals, x, was determined from precision density measurements on slices cut perpendicular to the growth axis. The vertically (stabilized) grown crystals showed less axial variations and better agreement with the source compositions than the horizontally grown crystals. The composition of the initial grown crystals and the compositional variations in the horizontally grown samples were not consistent with the one-dimensional diffusion model.

The experimental results clearly showed that the convective flows caused by the buoyancy-driven perturbation in the flow field in the vicinity of the growing surface resulted in non-uniformity in the axial and radial incorporation of impurities and defects as well as in the deviation from stoichiometry.

4. *In-situ* monitoring during growth:

In-situ and real-time measurements of (1) partial pressure using optical absorption and (2) the growth interface morphological evolution and instantaneous growth velocity using optical interferometry during growth were performed to study the coupled mass transport and growth kinetics problem. The growth furnace, optical monitoring set-up and growth ampoule design for *in-situ* optical monitoring during the PVT growth of ZnSe were constructed and optimized. Michelson and Fabry Perot optical interferometers were set up for *in-situ* monitoring of the growing surface of the crystal. The Michelson setup was flexible, i.e. the optics were easily adjusted both before and during growth, however the fringe patterns were not stable due to the thermal convection of the surrounding air. It was shown that a modification of the ampoule significantly suppressed this noise. Also, this effect is not expected to be of significant consequence in the reduced gravity environment. The Fabry-Perot interferometer provides good quality fringe patterns, but the optics is rigid and difficult to adjust during the crystal growth run. Using the interferometric techniques, the thermal expansion coefficient of ZnSe was measured between 25°C and 1080°C. Phase maps of the growing crystal surface were constructed in real-time using fringe data from both interferometric set-ups. A visual observation of the growing crystal was performed and the results can be correlated with the phase map results.

5. Transport processes modeling:

Besides the one-dimensional diffusion model, the transport process modeling also included:

(1) Two-dimensional analytical calculation:

Two-dimensional description of fluid flow using thermal conditions (no solutal effects) for a typical growth experiment was studied to estimate the maximum flow velocities for the vertical and horizontal configurations. The calculated maximum shear (perpendicular to growth direction) flow velocity was 5.2μm/s for the horizontal configuration and

0.22μm/s for the vertical configuration under 1g_o condition (where g_o is the gravity level on Earth).

(2) Two and three-dimensional numerical modeling:

Two and three-dimensional numerical simulations physical vapor transport process using finite element technique to treat both thermal and solutal induced buoyancy forces were performed. Both compressible and Boussinesq fluids were assumed for a system of multiple transport species with residual gas. The results of the two and three-dimensional calculation agreed well with the benchmark studies. The effects of gravity on the flow field were examined by plotting the differences between the calculated flow velocities for various gravity levels and that for zero gravity. The calculated maximum shear flow velocity difference under 1g_o condition was 50μm/s for the horizontal configuration and 9.4μm/s for the vertical configuration. The maximum allowable acceleration level during the flight experiments was established by taking the criterion that the maximum shear velocity should be equal to or less than 10% of the crystal growth rate. This resulted in the requirement of a maximum residual longitudinal acceleration level of 2.7×10^{-3} g_o and a transverse level of 1.0×10^{-4} g_o for the flight experiments with a growth rate of 3mm/day or 0.035μm/s.

IV. Summary

Complete and systematic ground-based experimental and theoretical analyses on the PVT of ZnSe and related ternary compound semiconductors have been performed. The analyses included thermodynamics, mass flux, heat treatment of starting material, crystal growth, partial pressure measurements, optical interferometry, chemical analyses, photoluminescence, microscopy, x-ray diffraction and topography as well as theoretical, analytical and numerical analyses. The experimental results showed the influence of gravity orientation on the characteristics of (1) the morphology of the as-grown crystals as well as the as-grown surface morphology of ZnSe and Cr doped ZnSe crystals (2) the distribution of impurities and defects in ZnSe grown crystals and (3) the axial segregation in ZnSeTe grown crystals.

REDUCTION OF DEFECTS IN GERMANIUM-SILICON

Dr. Frank R. Szofran, Principal Investigator
ES75/Space Sciences Laboratory, NASA Marshall Space Flight Center, Huntsville, AL 35812
Phone: 256-544-7777, Fax: 256-544-8762, e-mail: frank.szofran@msfc.nasa.gov

Co-Investigators:
Prof. Dr. K.W. Benz, Dr. Arne Cröll, Dr. Peter Dold
  Kristallographisches Institut der Universität, Freiburg, Germany
Dr. Sharon D. Cobb, Dr. Martin P. Volz
  ES75, Marshall Space Flight Center, Huntsville, AL
Dr. Shariar Motakef
  CAPE Simulations, Inc., Newton, MA
Prof. John S. Walker
  Dept. of Mech. and Industrial Eng., Univ. of Illinois at Urbana-Champaign, Urbana, IL

1 Objectives of the Investigation

It is well established that crystals grown without contact with a container have far superior quality to otherwise similar crystals grown in direct contact with a container. In addition to float-zone processing, detached-Bridgman growth is often cited as a promising tool to improve crystal quality, without the limitations of float zoning. Detached growth has been found to occur quite often during μg experiments and considerable improvements of crystal quality have been reported for those cases. However, no thorough understanding of the process or quantitative assessment of the quality improvements exists so far. This project will determine the means to reproducibly grow Ge-Si alloys in the detached mode.

Specific objectives include:

- measurement of the relevant material parameters such as contact angle, growth angle, surface tension, and wetting behavior of the GeSi-melt on potential crucible materials;
- determination of the mechanism of detached growth including the role of convection;
- quantitative determination of the differences of defects and impurities among normal Bridgman, detached Bridgman, and floating zone (FZ) growth;
- investigation of the influence of defined azimuthal or meridional flow due to rotating magnetic fields on the characteristics of detached growth;
- control time-dependent Marangoni convection in the case of FZ-growth by the use of a rotating magnetic field to examine the influence on the curvature of the solid-liquid interface and the heat and mass transport; and
- grow high quality GeSi-single crystals with Si-concentration up to 10 at% and diameters up to 20 mm.

2 Microgravity Relevance

At this time, the most reliable environment for obtaining and studying detached growth is reduced gravity. The proposed work seeks to compare processing-induced defects in Bridgman, detached Bridgman, and floating-zone growth configurations in Ge-Si crystals (Si $\leq$ 10 at%) 20 mm in diameter. The occurrence of detachment during growth is widely thought to be related to gas pressures in the crucible and the evolution of gases at the growth interface. Gas evolution will be strongly effected by convection in the melt, which is dominated in the Bridgman configuration by buoyancy-driven flows. Thus, terrestrial detached growth (even when reproducible) will differ significantly from microgravity detached growth and the comparison of the two will provide vastly more insight than either alone. There is also a high potential for gaining new understanding of the role of convection in defect generation. Finally, the comparison of samples grown by detached growth with float-zone samples of the same diameter is fundamental to this study because the float-zone technique is truly and completely containerless in contrast to detached Bridgman growth. Terrestrial floating zones of this material are limited to diameters of about 8 mm. Therefore, these floating-zone experiments can only be conducted in a reduced gravity environment.

3 Experimental set-up

3.1 Ampoule preparation and growth facility

Growth was performed in double-wall quartz-glass ampoules. The diameter of the seed and the growing crystal was 9 mm, the length of the seed 35 mm, and the length of the grown crystal was 41 mm. Before the starting material was filled into the ampoule, the quartz was cleaned with MUCASOL™ and H_2O (18 MΩ) and baked out under vacuum (10^{-6} mbar) at 1100°C for 2 hours. Undoped germanium (<111>-oriented) served as the seed, the feed was pill-doped with gallium with an averaged concentration of $C_0=8.2\cdot10^{18}$ at/cm^3. First, the germanium was rinsed with H_2O (18 MΩ) followed by acetone. Then it was etched for about 3 minutes with the 18:8:5 polishing etch (HNO_3 : CH_3COOH : HF).[1] After this treatment, the germanium shows a smooth and shiny surface. Then the material was put into the ampoule and baked out at 900°C for 2 hours under an alternating atmosphere of H_2 (normal pressure) and vacuum (10^{-6} mbar). Finally, the ampoule was sealed under an Argon pressure of 600 mbar (pressure at room temperature).

The growth experiment took place in a monoellipsoid mirror furnace.[2] To obtain a temperature profile suited for Bridgman growth, the lamp was moved 2 mm out of focus toward the center of the furnace.[2] The solid-liquid interface was observed by a borescope and a CCD-camera connected to a video tape recorder. With this set-up it is possible to observe and record the position of the growing interface, however, the length is restricted to ~40 to 45 mm and the temperature gradient is about 100 K/cm at the interface, increasing the development of stress and dislocations.

For growth, the ampoule was heated up within 15 minutes and kept at a constant temperature for 45 minutes to guarantee a homogeneous distribution of the dopant in the melt. The ampoule was pulled down with a constant velocity of 0.5 mm/min. No ampoule rotation was applied.

3.2 Crystal preparation and characterization

The surface of the grown crystal was analyzed by scanning electron microscopy (SEM). The sample was first cut axially (parallel to the 110-plane) for segregation measurements (4-point measurements and analysis by Nomarski Differential Interference Contrast Microscopy-NDIC). The axial slab was polished with 9 µm and 1 µm diamond paste and SYTON™ and etched with the 1:1:1 etch (H_2O_2 : CH_3COOH : HF) for 30 seconds. From the remaining part of a half cylinder, radial wafers have been cut (orientation: <111>, thickness: 3 mm), polished and etched by the Billig etch[3] (12g KOH, 8g $K_3[Fe(CN)_6]$, dissolved in 100 ml H_2O) for 8 minutes at ≈80°C.

4 Results

After growing ≈7 mm by the normal Bridgman mode with wall-contact, detachment started and continued for 27 mm. The wall-free growth took place over the whole circumference of the crystal except for some small ridges. (This topic will be discussed in more detail.) In the detached grown part, the three <111>-related growth lines (or micro-facets) showed up; one of them can be seen in figure 1 on the upper-left hand side. The remaining 7 mm of the crystal grew again with wall-contact. The transition from de-wetting to wetting behavior of the melt was visible before the solid-liquid interface reached that point. This suggests that the detachment is mainly influenced by the surface condition of the container wall. This transition did not take place across a line but over a band about 1 mm wide as seen in figure 1.

With the transition from detached to attached growth, there is an increase of the crystal diameter, as seen in figure 1. From this diameter enlargement, the dimension of the gap between detached grown crystal and container wall can be determined; at the given location it was measured to be 30 µm (see figure 1, right hand side). Therefore it can be concluded that the size of the meniscus has not exceeded some tens of micrometers, and the thermocapillary convection which can arise from such a small free surface area can be neglected or is at least not in the time-dependent state. This is in coincidence with the literature.[4] The absence of time-dependent convection has been proven by the absence of dopant striations in the detached grown part. Due to the absence of dopant striations, the interface curvature can be determined only at the transition from undoped seed to doped crystal: The phase boundary is slightly convex with a deflection toward the melt of approximately 250 µm.

The axial macrosegregation was estimated by 4-probe measurements. The dopant distribution (figure 2) falls between the theoretical curves for complete mixing and purely diffusive mass transport. For the calculation, k_0=0.087 and D=$1.9 \cdot 10^{-4}$ cm^2/s was used.[5] The reduced mixing indicates low radial temperature gradients and a rather flat solid-liquid interface. At the transition from attached to detached (x=7 mm) as well as at the reverse transition (x=34 mm), no influence of the melt-ampoule interaction on the macrosegregation (i.e. on the mixing state of the melt) is seen.

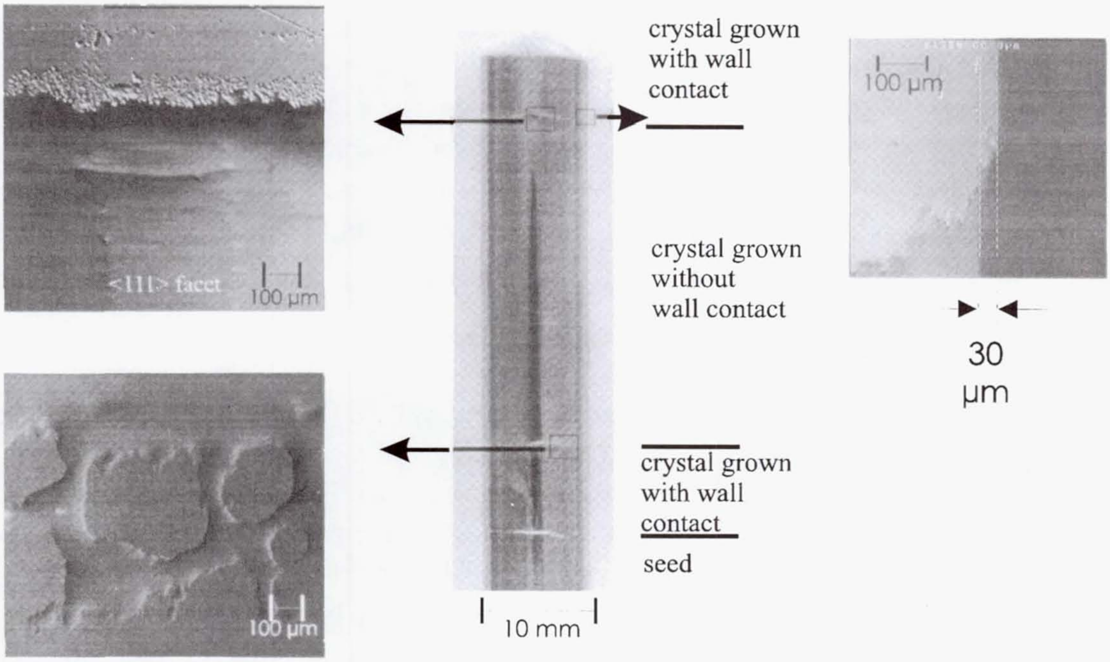

Figure 1. Photograph of the complete crystal (middle part) and SEM-images of the surface, showing the transition from detached to attached growth. Front view is on the left; side view is on the right hand side. Photos show surface as it grew, i.e. before etching.

As mentioned above, the crystal grew detached except for several small ridges, where the melt was wetting the ampoule wall. The dimension of these ridges is several tens of micrometers in width and some hundreds of micrometers in length. A similar observation was made by Witt et al.[6, 7] (and described as "Chinese wall"). This implies that the surface layer which prevented wetting of the quartz wall by the melt was not coating the ampoule entirely but was disconnected at some points. The radial EPD-distribution shows that these ridges are related to a strong increase of the defect structure. Due to the high temperature gradient during the growth process and a substantial EPD in the seed material, the overall EPD in the grown crystal is high. Nonetheless, the EPD is significantly lower in the part grown without attachment to the wall. Quantitative measurements are in progress.

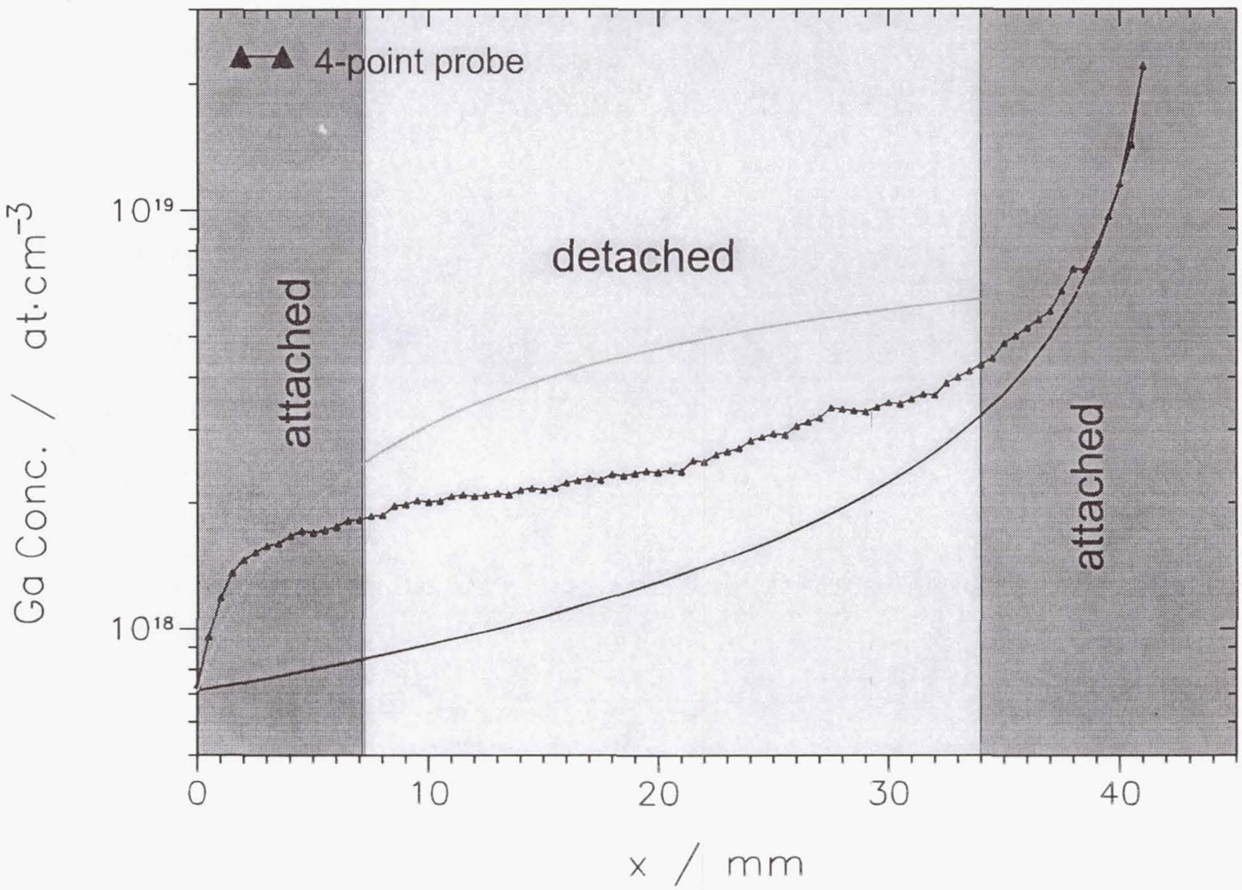

Figure 2. Axial dopant distribution, measured by 4-point probe. The detachment does not influence the macrosegregation.

5 Discussion

Without taking into account the hydrostatic pressure, the sum of the growth angle of the crystal and the contact angle of the melt (with respect to the container wall) has to be larger than or equal to 180° to realize detachment.[8] The values of these angles given in literature[8,4] suggest that this will not normally be the case. Either the surface treatment (or the coating or the status of oxidation) of the container[8] or the gas pressure at the triple point melt-crystal-container[9] can produce detached growth even if this condition is not met. Duffar et al.[8] have introduced a relationship for the gap-width between crystal and ampoule wall, the radius of the crystal, the growth angle, and the contact angle. Using this relationship, a contact angle of 174±4° (cf. 106° reported[4] for Ge on silica) is needed to obtain a gap width of about 30 μm. This relation does not consider a difference in gas pressure at the meniscus compared to the top of the melt. This condition existed in our configuration because there was gas exchange between the location of the meniscus and the top of the ampoule. The transition from attached to detached growth and vice versa, as well as the irregular transition (i.e. the simultaneous appearance of attached and detached growth at different positions of the interface), suggest that the surface condition of the quartz glass ampoule was the main source for the detachment in this case. The exact mechanism of the different wetting behavior can not be explained yet and will be the subject of systematic investigations (e.g. measurement of the contact angle with respect to surface treatment of the quartz glass). An important point is that the detached growth is possible even under normal gravity conditions, where the hydrostatic pressure assures that the melt touches the container wall.

6 Summary

For the first time, detached Bridgman growth was observed in-situ. The main results can be summarized as following:

- The gap between the detached-grown crystal and the wall of the quartz-glass ampoule was measured to be about 30 μm.
- Detached growth occurred over the whole circumference of the crystal; the crystal was in contact to the ampoule only along some small ridges.
- The transition from attached to detached and vice versa did not take place across a line but over a band about 1 mm wide.
- No dopant striations are seen in NDIC-images, indicating that the free surface of the melt meniscus does not cause time-dependent thermocapillary convection.
- No influence of the detachment is seen on the macrosegregation. The axial dopant distribution falls between the theoretical curves for complete mixing and diffusive mass transport.
- The EPD is noticeably reduced in the detached grown part (quantitative measurements in progress).

---

[1] S.K.Ghandi and J.E.Ayers, J. Electrochem. Soc. 135 (1988) 2053.

[2] P.Dold, A.Barz, S.Recha, K.Pressel, M.Franz and K.W.Benz, J. Crystal Growth (in press).

[3] E.Billig, Proc. Royal Soc., London A235,37 (1956).

[4] T.Duffar, I.Paret-Harter and P.Dusserre, J. Crystal Growth 100 (1990) 171-184.

[5] A.Rouzaud, D.Camel, J.J.Favier, J. Crystal Growth 73 (1985) 149-166.

[6] A.F.Witt, H.C.Gatos, M.Lichtensteiger, M.C.Lavine and C.J.Herman, J. Electrochem. Soc. 122 (1975) 276-283.

[7] W.R.Wilcox and L.L.Regel, Microgravity sci. technol. VIII/1 (1995) 56-61.

[8] T.Duffar, Ph.Boiton, P.Dusserre and J.Abadie, J. Crystal Growth 179 (1997) 397-409.

[9] D.I.Popov, L.L.Regel and W.R.Wilcox, J. Materials. Synthesis and Processing, Vol.5, No.4 (1997) 283-335.

MAGNETIC DAMPING OF SOLID SOLUTION SEMICONDUCTOR ALLOYS

Dr. Frank R. Szofran, Principal Investigator
ES75/Space Sciences Laboratory, NASA Marshall Space Flight Center, Huntsville, AL 35812
Phone: 256-544-7777, Fax: 256-544-8762, e-mail: frank.szofran@msfc.nasa.gov

Co-Investigators:
Prof. Dr. K.W. Benz, Dr. Arne Cröll, Dr. Peter Dold
Kristallographisches Institut der Universität, Freiburg, Germany
Dr. Sharon D. Cobb, Dr. Martin P. Volz
ES75, Marshall Space Flight Center, Huntsville, AL
Dr. Shariar Motakef, Dr. L.B. Vujisic[contributor who is not a Co-Investigator]
CAPE Simulations, Inc., Newton, MA

1 Objectives of the Investigation

The objective of this study is to (1) experimentally test the validity of the modeling predictions applicable to the magnetic damping of convective flows in electrically conductive melts as this applies to the bulk growth of solid solution semiconducting materials and (2) assess the effectiveness of steady magnetic fields in reducing the fluid flows occurring in these materials during processing. To achieve the objectives of this investigation, we are carrying out a comprehensive program in the Bridgman and floating-zone configurations using the solid solution alloy system Ge-Si. This alloy system has been studied extensively in environments that have not simultaneously included both low gravity and an applied magnetic field. Also, all compositions have a high electrical conductivity, and the materials parameters permit reasonable growth rates.

An important supporting investigation is determining the role, if any, that thermoelectromagnetic convection (TEMC) plays during growth of these materials in a magnetic field. TEMC has significant implications for the deployment of a Magnetic Damping Furnace in space. This effect will be especially important in solid solutions where the growth interface is, in general, neither isothermal nor isoconcentrational. It could be important in single melting point materials, also, if faceting takes place producing a non-isothermal interface.

2 Microgravity Relevance

During Bridgman or floating zone growth of semiconductors, generation of destabilizing temperature gradients in the melt is unavoidable, resulting in buoyancy-induced convective mixing of the liquid phase. On Earth this convective mixing is generally very intensive and interferes with segregation of melt constituents at the growth front. Crystal growth in low Earth orbit provides the opportunity to reduce the buoyancy-induced convective intensity; in some cases, mass transfer diffusion-controlled growth may be achieved if the residual acceleration direction and magnitude can be controlled. However, calculations and recent flight experiment results clearly indicate that simply reducing the steady-state acceleration to values achievable in low-Earth orbit will not provide diffusion controlled growth conditions for solid solution melts ~1cm in diameter if accelerations transverse to the growth axis are not controlled. Magnetic damping of convection in electrically conductive melts can be used to provide a higher degree of control on convection in the melt. Magnetic damping effects both buoyancy-induced and Marangoni convection and may enable diffusion controlled growth without the control of the growth direction relative to the residual steady-state acceleration. Thus our understanding of convective influences on melt-growth processes can be further advanced, and our ability to interpret space experimental results may be significantly improved.

3 Results

3.1 Vertical Bridgman Growth

3.1.1 Calculations

The calculations were performed for the entire system including the furnace, the cartridge, and the charge. In this approach, the furnace setpoints were the inputs into the model; the temperature field in the entire system, the growth interface shape, and the melt composition were the model output. Convection in the melt was modeled to be driven by thermo-solutal buoyancy forces, and the growth interface shape was calculated from the phase diagram for Ge-Si. The simulations were conducted iteratively, where at each iteration the growth interface shape was updated.

Temperature, concentration, and velocity fields are obtained as a solution of coupled axisymmetric energy, species, momentum, and mass conservation equations. Buoyancy (thermal and solutal) was incorporated using the Boussinesq approximation. The applied magnetic field was parallel to the gravity vector and the growth direction.

We have assumed that the growth rate is equal to the pull rate of 0.8μm/s, and that the segregation coefficient is constant and equal to 4.3 (which corresponds to the segregation coefficient at 5 at% Si). The set points used in the calculations resulted in a nearly constant gradient of ~43 ^{o}C/cm in the ampoule wall over the whole melt domain.

Simulation results indicate that in spite of axial solutal stabilization of convection in the melt, the effect of thermo-solutal convection on radial segregation is strong; elimination of this effect requires significant reduction of gravity to 10^{-5} to 10^{-6} levels or application of large magnetic fields close to 6T on Earth.

3.1.2 Experiments

A series of $Ge_{1-x}Si_x$ alloys, with nominal silicon concentrations of 5 at %, has been grown by the vertical Bridgman method. A seven-zone furnace was used to obtain a constant axial thermal gradient of 35° K/cm along the length of the ampoule. Such a constant axial gradient can reduce inevitable radial thermal gradients that arise as a result of differences between the thermal conductivity of the solid and liquid phases and the ampoule.[1] In order to assess the effect of ampoule thermal conductivity on interface shapes and radial segregation, alloys were grown in graphite, hot-pressed boron nitride, and pyrolytic boron nitride ampoules for comparison. All the samples reported here were solidified with a furnace translation velocity of 0.4 μm/s. For each crystal growth experiment, a static axial magnetic field of either 0 or 5 Tesla was applied.

The ampoules were loaded with 8-mm diameter Ge and Si ingots, placed on top of Ge seeds, with a <100> crystallographic orientation. After the ampoules were placed in the furnace, the furnace was lowered until part of the Ge seed was melted. The furnace was held at this position for up to 72 hours to let the melt completely homogenize. During the homogenization time, and prior to translation, crystal growth occurred until the Si concentration in the solid was in equilibrium with the

Si concentration in the melt, such that $C_S = k(C_L)C_L$, where C_S is the Si concentration in the solid, C_L is the Si concentration in the liquid, and k is the segregation coefficient. Initially, the temperature of the solid/liquid interface is the melting point of Ge. Silicon diffuses downwards towards this interface, increasing the Si concentration, and moving the phase boundary upwards with respect to the furnace. This period of regrowth has been previously described.[2] The furnace was then translated upward until the entire sample had solidified. After growth, the axial and radial concentration profiles were measured by microprobe and energy dispersive x-ray (EDX) spectroscopy. The microstructure was revealed after etching by means of Nomarski Differential Interference Contrast microscopy (NDIC).

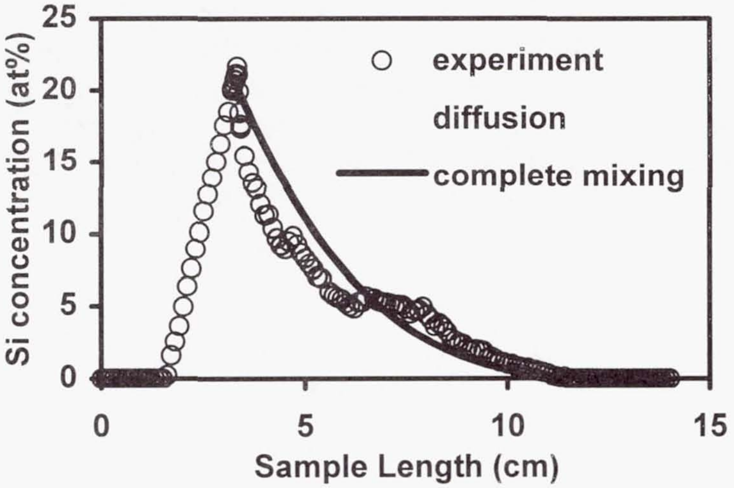

Figure 1. Axial composition profile for a $Ge_{1-x}Si_x$ alloy grown in a 5 Tesla axial static magnetic field with a furnace translation rate of 0.4 μm/s.

Figure 1 shows a typical axial segregation profile. This particular profile was obtained from a sample grown in a hot-pressed boron nitride ampoule and in a 5 Tesla field. In addition to the experimental data, the figure also shows a complete mixing curve, determined from the Pfann relation, and data from a one-dimensional diffusion model. The diffusion model takes into account the variation in segregation coefficient with respect to the liquidus composition. The Ge seed portion of the crystal is that below approximately 2 cm. The steep increase in Si concentration from 0 to 22 at % indicates the period of regrowth. The sudden drop in Si concentration indicates where furnace translation begins. All of the samples, regardless of the ampoule material and whether a 5 T field was applied, exhibit very similar behavior during the initial transient of the axial segregation profile. That is, the experimental data, in the initial transient region, are much better fit by the diffusion model than by the complete mixing model. However, after the initial transient, axial segregation profiles for all of the samples deviate at least somewhat from that expected for diffusion-controlled growth, particularly in the final transient region.

For the same sample, the largest degree of concavity in the radial segregation data is found in the initial transient region, where the change in the axial profile is also the largest. In the data examined to date, no clear distinction was observed between the radial profiles of samples grown with or without an applied field.

With the exception of the sample grown in a graphite ampoule, all samples remained single crystal up to where they reached a maximum Si concentration. The sample grown in a graphite ampoule had a highly concave interface and became polycrystalline even in the regrowth portion of the sample. In general, striations were observed in the regrowth portion of the samples. The samples remained single crystals for 1-2 mm beyond the point of maximum Si concentration where multiple grains, and in some cases large striations, were observed. An increase in the concavity of the interface shapes was also observed in this region. It is possible that the large change in lattice constant, as a result of a steep drop in Si concentration, is responsible for the deviation from single crystallinity. No clear distinction in the morphology between samples grown with or without a 5 T field was observed.

3.2 Float Zone Growth

The critical Marangoni number for silicon, which describes the transition from laminar to time-dependent flow, has been determined to be ≈150.[3] Therefore even small zone geometries result in time dependent Marangoni convection, leading to an irregular microscopic growth velocity and to dopant striations in the grown crystal.[3] Whereas the time dependency of the flow causes microscopic inhomogeneities, the time-independent, steady convection effects only the macrosegregation.[4] In this project, the influence of a static axial magnetic field (variable between B=0 and B=5 T) on the microsegregation, the macrosegregation, and the interface curvature has been analyzed. Except to note that magnetic fields tend to flatten the interface, this report will discuss only the segregation results.

3.2.1 Experimental setup and growth technique

The growth experiments were performed in a monoellipsoid mirror furnace.[5] The 8 mm diameter samples were mounted wall-free and sealed in the ampoules with argon or oxygen. B, Ga, P, As, and Sb were used as dopants. Zone heights in the range of 8 to 12 mm were established. Calculations of the temperature field have been performed,[6,7] which predict axial temperature gradients of ≈100-150 K/cm at the solid/liquid interface and a maximum temperature difference of ≈30-50 K between the interface and the half of the zone height (temperature maximum) for the case of diffusive heat transport. These values will be reduced by convection. The usual translation rate was 4 mm/min. The maximum grown length was approximately 40 mm. The furnace was positioned in the center of a superconducting solenoid. The floating zone was monitored by a borescope and a CCD-camera.

3.2.2 Preparation and characterization of the grown crystals

The grown crystals were cut lengthwise along the (110)-plane, polished, etched using the WRIGHT etch,[8] and analyzed qualitatively by NDIC (Nomarski Differential Interference Contrast Microscopy). Four-point probe and spreading resistance measurements were carried out on selected samples.

3.2.3 Results

The axial macroscopic segregation is shifted towards a more diffusion-controlled profile with higher induction. However, experiments with pill doping and oxide coated samples[9] show that even at 5 Tesla diffusion-controlled growth has not been obtained. This result is corroborated by numerical simulations.[10]

In contrast to the macrosegregation results, the magnetic field has a substantial influence on the microsegregation of the grown crystals: Crystals grown without magnetic field have strong and irregular striation patterns caused by time dependent Marangoni convection. These patterns, based on their shape and demarcation experiments, indicate the shape of the growth interface. These striations are eliminated in crystals grown in magnetic fields as low as 500 mT. Unfortunately, striation-free growth in strong axial fields is not easily reproducible, as a lot of the grown crystals (mostly the As- and Sb-doped samples) showed the unexpected appearance of striations after an initial striation-free area. The striations are never present at the start of growth. They form only after some material is crystallized; stopping the translation and then starting again repeats this sequence. Figure 2 shows an example of these structures. These striations can be quite pronounced and are often of clearly oscillatory nature (note that all the crystals were grown without rotation), in contrast to striations caused by thermocapillary convection. The strength, frequency, and position of these striations varies somewhat between experiments, or even within the same crystal. The frequency range is between 0.1Hz and 10Hz. In contrast to the residual striations detectable outside the core in the case of 100-500mT,[11,12] they are not limited to the crystal periphery. They do occur in magnetic field grown crystals coated with SiO_2 to suppress thermocapillary convection. The position of these striations often suggests a convectively mixed torus in the zone. They do not always follow the interface shape closely. Several possibilities for the origin of these effects have been considered. The most convincing explanation is thermoelectromagnetic convection (TEMC). TEMC is caused by the interaction of magnetic fields with thermoelectric currents.[13] The motion in the melt is caused by the Lorentz force resulting from the interaction of the thermoelectric current with the magnetic field. For materials with good conductivity and high thermoelectric coefficients, these currents can reach considerable values and TEMC can be the dominant source of convection. The gradient of the thermovoltage, the source of the current, may be due to temperature gradients, the difference in the Seebeck coefficient between liquid and solid, or possibly also by changes of the Seebeck coefficient due to compositional inhomogeneities. Strong effects should be expected if facets are present, due to the undercooling of the liquid in front of the facet interface. As only the current components perpendicular to the field lines lead to a Lorentz force, the TEMC in axial fields is mainly driven by radial gradients, which in turn leads to an azimuthal flow. The field also damps convection due to TEMC, so the azimuthal velocity goes through a maximum as a function of the induction.

The application of strong axial magnetic fields is an interesting tool for controlling the segregation in silicon floating zones, but one that has to be used with caution. The axial macrosegregation, usually close to the complete mixing case due to strong thermocapillary convection, can be shifted towards a

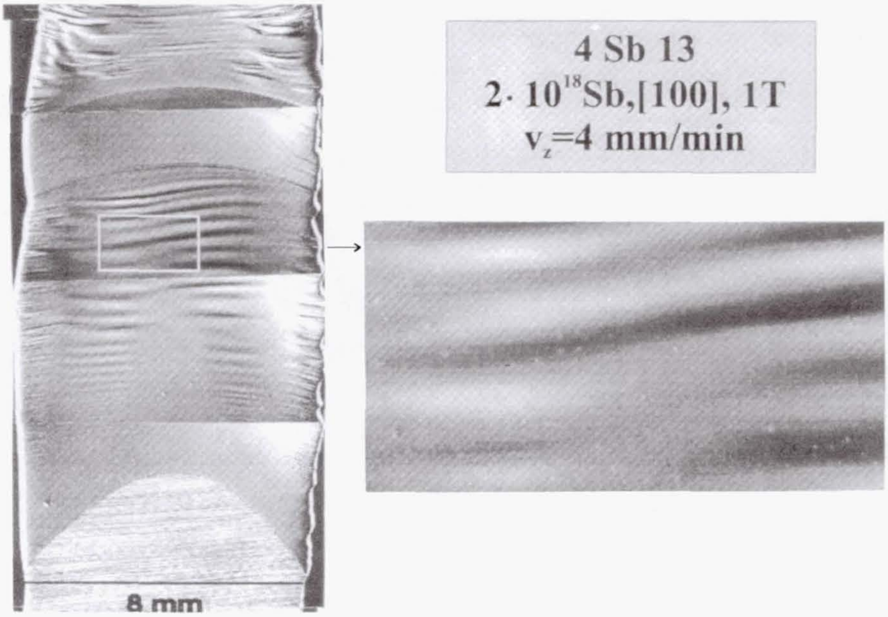

Figure 2. Silicon float-zone sample showing initial absence of striations followed by the appearance of TEMC-induced striations.

more diffusion-controlled regime, but it is not possible to attain purely diffusive conditions even with fields of 5T. This is only possible by the combination of microgravity and a coated melt surface.[9] The radial segregation is initially deteriorated by the application of axial fields < 1T due to the separation of the flow field into two areas, a quiescent center and a thin boundary layer strongly mixed by thermocapillary convection.[11,14] The thickness of the outer layer, however, is dependent on induction, and fields ≥1T are sufficient to reduce it to insignificant values.

Strong fields suppress time-dependent thermocapillary convection completely, thus eliminating the striations associated with it. However, a new type of striations was found in some of the crystals. The striations, often exhibiting strong periodicity, usually do not appear at the outset of growth, but only after some material has been grown. The explanation consistent with the experimental results is that they are caused by thermoelectromagnetic convection, originating from the interaction of thermoelectric currents with the field. A radially oriented current in an axial magnetic field leads to an azimuthal flow. In the case of axial fields, a deviation from circular symmetry (of the isotherms, the crystal position, due to faceting etc.) is necessary to generate a net current. This explains the fact that the effect is not always observed.

4 Summary

Magnetic fields up to 5 Tesla are sufficient to eliminat time-dependent convection in silicon floating zones and possibly I Bridgman growth of Ge-Si alloys. In both cases, steady convection appears to be more significant for mass transport than diffusion, even at 5 Tesla in the geometries used here. These areults are corroborated in both growth configurations by calculations.

---

[1] A. Rouzaud, D. Camel and J. J. Favier, J. Crystal Growth 73 (1985) 149-166.

[2] L. Helmers, J. Schilz, G. Bahr, and W. A. Kaysser, J. Crystal Growth 154 (1995) 60-67.

[3] A.Cröll, W.Müller-Sebert, K.W.Benz and R.Nitsche: Microgravity sci. technol. III/4 (1991) 204.

[4] W.A.Tiller, K.A.Jackson, J.W.Rutter and B.Chalmers: Acta Met.1 (1953) 428.

[5] A.Eyer, H.Leiste and R.Nitsche: J. Crystal Growth 71 (1985) 173.

[6] P.Dold, PhD-Thesis, University of Freiburg, Germany (1994).

[7] D.Langbein and H.J.Sattler, BMFT-Report BleV-R-65.424-4 (1984).

[8] M.Wright Jenkins: J. Electrochem. Soc. 124,5 (1977) 757.

[9] A. Cröll, W. Müller and R. Nitsche: J. Crystal Growth 79 (1986) 65

[10] Th. Kaiser and K.W. Benz: Submitted to J.Crystal Growth

[11] A. Cröll, P. Dold and K.W. Benz: J. Crystal Growth 137 (1994) 95

[12] P. Dold, A. Cröll, and K.W. Benz:. Submitted to J.Crystal Growth

[13] J.A. Shercliff: J. Fluid. Mech. 91/2 (1979) 231

[14] P. Dold, A. Cröll, and K.W. Benz:. Submitted to J.Crystal Growth, Th. Kaiser and K.W. Benz: Submitted to J.Crystal Growth, T.E. Morthland and J.S. Walker: J. Crystal Growth 158 (1996) 471, C.W. Lan: J. Crystal Growth 169 (1996) 269

THE FEATURES OF SELF-ASSEMBLING ORGANIC BILAYERS IMPORTANT TO THE FORMATION OF ANISOTROPIC INORGANIC MATERIALS IN MICROGRAVITY CONDITIONS

Daniel R. Talham
Department of Chemistry
University of Florida
Gainesville, FL 32611-7200
(352) 392-9016
talham@chem.ufl.edu

James H. Adair
Materials Research Laboratory
Pennsylvania State University
University Park, PA 16802-4801
(814) 863-6047
jadair@mrl.psu.edu

Hypothesis and objective.

There is a growing need for inorganic anisotropic particles in a variety of materials science applications. Structural, optical, and electrical properties can be greatly augmented by the fabrication of composite materials with anisotropic microstructures or with anisotropic particles uniformly dispersed in an isotropic matrix. Examples include structural composites, magnetic and optical recording media, photographic film, certain metal and ceramic alloys, and display technologies including flat panel displays. While considerable progress has been made toward developing an understanding of the synthesis of powders composed of monodispersed, spherical particles, these efforts have not been transferred to the synthesis of anisotropic nanoparticles.[1-3] The major objective of the program is to develop a fundamental understanding of the growth of anisotropic particles at organic templates, with emphasis on the chemical and structural aspects of layered organic assemblies that contribute to the formation of anisotropic inorganic particles.

There are two ways that anisotropically shaped particles have been produced from solution.[4] The first is crystallographically controlled growth, producing particle shapes dictated by the relative growth rate among the various habit planes. Growth rates are often controlled by the inclusion of adsorbates or "poisons" that selectively restrict the growth of certain faces. A second approach is to control nucleation and growth by the synthesis of materials in the presence of molecular templates. While this method has been successfully used to restrict the size of particles,[5-8] there have been few attempts to control particle shape. The current project applies principles from both of these approaches to achieve particle shape control by employing amphiphilic molecules assembled into specific lyotropic micellular structures as templates for the formation of anisotropic inorganic particles. An important aspect of our approach is to include careful analysis of the chemical nature of the particle/template interface, as this interaction can play an equally important role in determining the shape and orientation. As part of our studies, we make extensive use of model membrane systems prepared by Langmuir-Blodgett (LB)[9] methods in order to efficiently survey possible template systems and establish the important chemical and geometric features of the templates that influence particle growth. Our hypothesis is that uniform dispersions of anisotropic inorganic particles can be produced with templating methods if the chemical interaction between the organic template and the particle is carefully controlled.

Our initial work has now lead to LB model studies of silver and gold particles at organic templates. Silver particles are grown from silver nitrate solutions at monolayer templates formed from negatively charged surfactants. Gold particles have been formed photochemically by decomposing $AuCl_4^-$ at positively charged monolayers.[10] Plate-like platinum and silver particles have now been fabricated at lyotropic micellular templates,[11-13] and free standing bilayer templates have also been used to prepare other inorganic particles.[14,15]

Justification for Microgravity Experiments.

The advantages of a microgravity environment for studying crystallization, nucleation and growth processes are well documented.[16,17] In the present project, minimizing convectional induced fluid shear and sedimentation in the microgravity environment should allow extended structure organic templates to form rather than fragments or "rafts" that result at normal Earth's gravity. Convection limits the size of uniform template domains and also creates a non-uniform size dispersion. These imperfections in the template structures make it difficult to assess the role that the chemical and geometric identities of the template play in controlling particle size and dispersion. Reducing convection will also minimize the agglomeration of particles that are produced. Sedimentation is less of a problem than convection in the synthesis and processing of nanoscale particles or particles with nanometer scale in at least one dimension. Analysis[18] demonstrates that the displacement due to gravity becomes less dominant as the particle size becomes smaller than about 0.25 μm. In contrast, sedimentation will begin to mask template effects as particle sizes increase beyond several hundred nanometers.

Langmuir-Blodgett Template Model Studies.

Four organic surfactants with different headgroups (PO_3^{2-}, OSO_3^-, SH, COO^-) have been spread onto an aqueous silver nitrate solution. The resulting Langmuir films were then transferred onto different hydrohobic subtrates to form multilayered LB flims. Exposure of these films to formaldehyde vapor results in the formation of quasi-spherical silver particles that range in size from 10 to 20 nm within one day. Further exposure to formaldehyde vapor leads to coalescence of these nanoparticles to give three-dimensional aggregates that have been characterized by Atomic Force Microscopy (AFM) and Transmission Electron Microscopy (TEM).

The electrochemical formation of two-dimensional silver films under monolayers of the same four organic surfactants has also been studied. The reduction of silver cations to give metallic silver is achieved by applying a constant potential (from -0.2 V to -2V vs an SCE electrode used as the reference electrode) between a working electrode that just touches the surface of the aqueous subphase and a counter-electrode immersed into it. Within 1 to 10 minutes (depending on the nature of the surfactant which is used), a shiny, mirror-like, silver film can be observed at the organic monolayer-subphase interface. Optical microscopy and TEM have allowed us to determine the fractal structure of these films, which are constituted by interconnected and randomly oriented 50-100 nm silver particles. The nature of the organic surfactant, but also the organization of the Langmuir monolayer has a strong effect on the electrocrystallization process.

Gold nanoparticles[10] were generated by ultraviolet irradiation of Langmuir-Blodgett (LB) films of octadecylamine (ODA), 4-hexadecylaniline (HDA) and benzyldimethylstearylammonium chloride monohydrate (BDSAC) deposited from aqueous $HAuCl_4$ subphases. In contrast, no gold crystals were observed in irradiated LB films prepared from monolayers of dipalmitoyl-DL-α-phosphatidyl-L-serine (DPPS) and dipalmitoyl-L-α-phosphatidylcholine (DPPC). The optical properties of colloidal gold provide an opportunity to monitor the formation of gold particles with UV-visible spectroscopy. Figure 1 shows the time evolution of the absorption spectra of a 13 layer ODA LB film under UV illumination over 30 min. It can be seen that the absorption band at 330 nm, which is assigned to the $AuCl_4^-$ species, initially decreases and a strong plasmon band around 550 nm appears with increased irradiation time. At the same time, the LB film changes gradually from colorless to deep purple, indicating that the photoreduction of gold ions to zerovalent gold nanoparticles occurs very efficiently.

The absorption spectra of 11 layer films of BDSAC and HDA LB also show the gradual appearance of a plasmon band around 550 nm upon irradiation, indicating that metallic gold particles are formed and grow under UV irradiation. However, these absorption peaks are less intense than the band shown in Figure 1 for the ODA film. The reduced intensity is also obvious to the naked eye as the final purple color of the BDSAC and HDA LB films is much less pronounced than that of the ODA LB film. No change in the color of a white 10 layer DPPS LB film was observed after up to two hours of UV illumination, and there was no change in its UV-visible spectrum over that time.

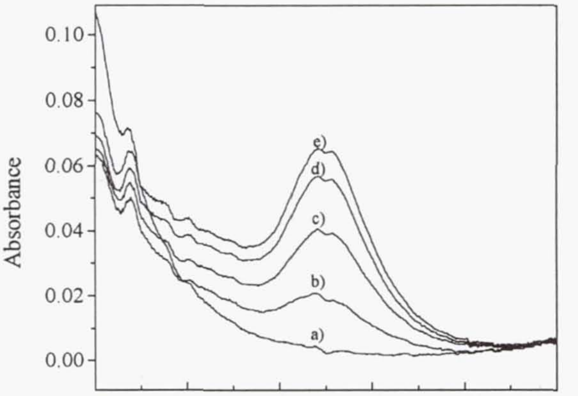

Figure 1. UV-visible absorption spectra of a 13 layer ODA LB film after exposure to UV light for: a) 0 min; b) 15 min; c) 20 min; d) 25 min; e) 30 min.

Transmission electron microscopy shows that arrays of particles ranging from 10-200 nm diameter are formed in the ODA and BDSAC films, and irregular arrays of larger particles are formed in the HDA films. AFM studies of ODA, HDA and BDSAC LB films not only confirm the results obtained by TEM in terms of size and shape of the gold crystals, but also reveal that the photoreduced metallic particles are rather thin. The surface analysis of a nine layer BDSAC LB film displayed in Figure 2 reveals a variation of the height of 15 ± 5 nm due to the presence of the gold nanoparticles. Similar values were obtained with ODA and HDA LB films. These results indicate that the gold crystals exhibit a high surface to volume ratio.

The observation of gold particles in some of the films and not others indicates that strong attractive electrostatic interactions exist between the positively charged polar heads of ODA, HDA and BDSAC and the $AuCl_4^-$ anions present in the subphase. These electrostatic forces allow the transfer of the anionic species during the LB film deposition. As the zwitterionic polar heads of DPPS and DPPC do not induce similar attractive interactions, few gold anions are transferred onto solid substrates using these lipids as templates. Moreover, comparison of the films after particle growth indicates that, under our experimental conditions, the ODA monolayer binds the $AuCl_4^-$ anions more efficiently than the BDSAC and HDA films because of a higher charge density.

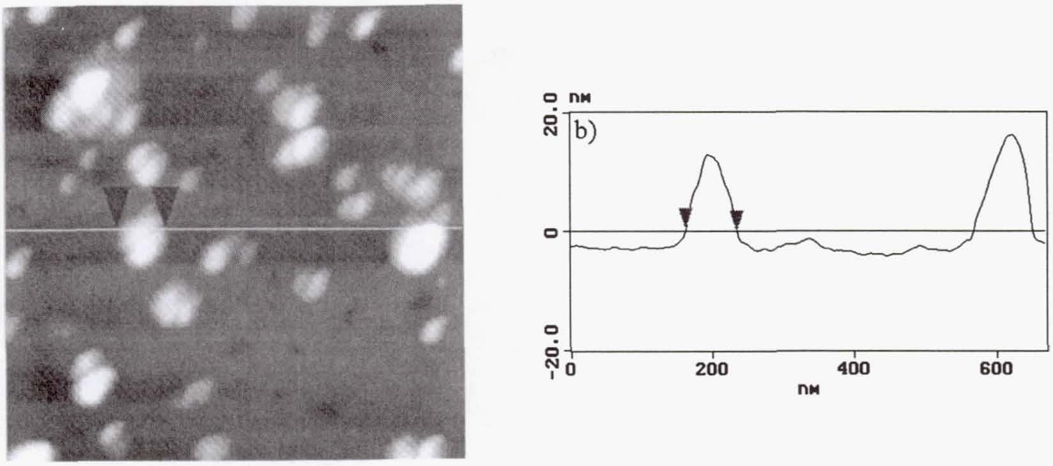

Figure 2 (left) AFM image (700x700 nm) and (right) corresponding section analysis of a 9 layer BDSAC LB film deposited onto a silicon wafer and exposed to UV light for 120 min.

Free Standing Bilayer Templates.

Templating in free standing bilayers can be used to produce metal platelets as well as the semiconductors previously described.[11-13] Figure 3 shows the effect of preparing silver and platinum particles in a bilayer system with little or no metal ion binding at the polar head group. In contrast the amine co-surfactant system (pentylamine/sodium dodecylsulfonate-toluene-water) and a bilayer composed of water and octylamine produces tabular-shaped Pt and Ag particles, respectively. A variety of metallic platelets have been prepared in the water-octylamine system including Au, Cu, and Ag/Pd alloys of special interest to the electronics community.

In addition to the templated synthesis of metal particles we have begun studies on two additional facets of self-assembled systems, enzyme catalyzed particle synthesis[14] and room temperature synthesis of metal oxides.[15] In the former work a urea-urease substrate-enzyme couple was used to synthesize aluminum basic sulfate from 15°C to 40°C by exploiting the pH increase created by the urease mediated breakdown of urea to ammonia and carbonate. Under certain conditions discrete, submicron, spherical $Al(OH)_x(SO_4)_y$ particles were produced via precipitation from homogeneous solution in contrast to the large particles of broad size distribution produced by the more traditional thermal breakdown of urea. It was shown in extended kinetic studies at 25°C that the anhydrous metal oxide is the stable phase of both undoped and Y-doped zirconia, an important material for a variety of applications including structural ceramics and high temperature fuel cells. Experiments are anticipated that will combine the enzyme-induced precipitation reactions with low temperature synthesis within bilayer self-assembly systems to produce unique particles of heretofore thermodynamically intractable materials such as Y-doped zirconia and optoelectronic materials such as $CuInSe_2$.

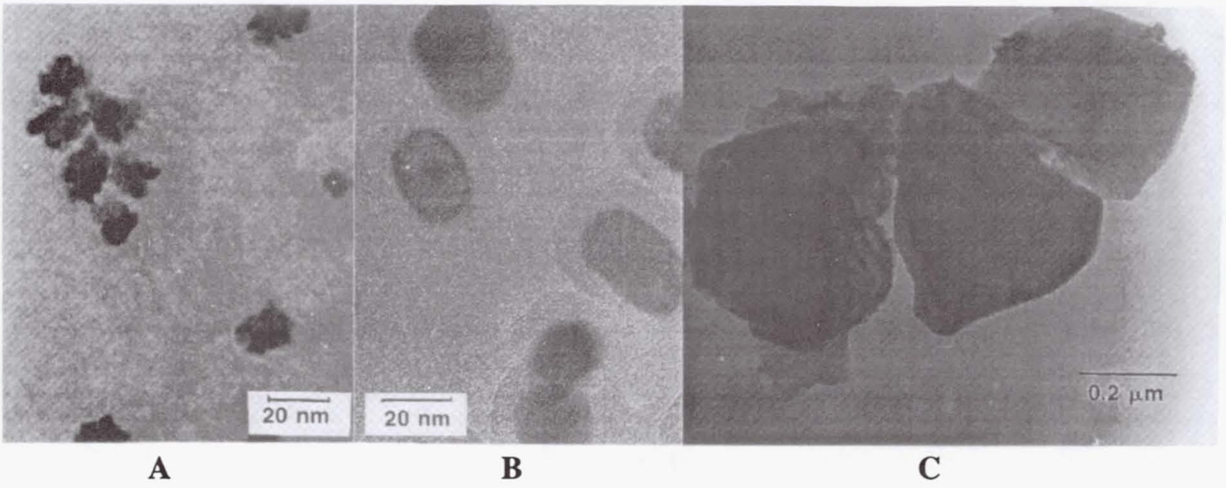

Figure 3. TEM photomicrographs of Pt and Ag particles produced in bilayer systems. (A) Pt particles produced in an AOT-heptane-water bilayer system without specific polar group templating; (B) Pt particles produced in a pentylamine/sodium dodecylsulfonate-toluene-water bilayer system with specific polar group templating and; (C) Ag particles produced in an octylamine-water bilayer with templating.

Acknowledgements. The P.I.'s would like to acknowledge coworkers T. Li and S. Ravaine. The work is supported by NASA grant NAG8-1244.

References.

(1) Hartman, P. *J. Cryst. Growth.* **1980**, *49*, 166.

(2) Adair, J. H.; Kerchner, J. A.; Bell, N. S.; Carasso, M. S. ACS Symposium Series volume No. 681, *Synthesis and Characterization of Advanced Material*, Serio, M. A.; Gruen, D. M.; Malhotra, R. (editors), American Chemical Society, Washington, DC, **1997**, pp. 82-94.

(3) Matijevic, E. In *Chemical Processing of Advanced Materials*; L. L. Hench and J. K. West, Ed.; John Wiley and Sons: 1992; pp 513-527.

(4) Calvert, P.; Mann, S. *J. Mat. Sci.* **1988**, *23*, 3801-3815.

(5) Chandler, R. R.; Coffer, J. L. *J. Phys. Chem.* **1993**, *97*, 9767-9770.

(6) Petit, C.; Lixon, P.; Pileni, M.-P. *J. Phys. Chem.* **1993**, *97*, 12974-12983.

(7) Fendler, J. H. *Chem. Rev.* **1987**, *87*, 877-899.

(8) Dameron, C. T.; Reese, R. N.; Mehra, R. K.; Kortan, A. R.; Carroll, P. J.; Steigerwald, M. L.; Brus, L. E.; Winge, D. R. *Nature* **1989**, *338*, 596-597.

(9) *Langmuir-Blodgett Films*; Roberts, G. G., Ed.; Plenum Press: New York, 1990.

(10) Ravine, S.; Fanucci, G. E.; Seip, C. T.; Adair, J. H.; Talham, D. R. *Langmuir*, **1998**, *14*, 708.

(11) Adair, J. H.; Li, T.; Kido, T.; Havey, K.; Moon, J; Mecholsky,J.; Morrone, A.; Ludwig, M. H.; Wang, L. *Materials Science and Engineering Reports*, in press.

(12) Li, T.; Moon, J.; Morrone, A. A.; Mecholsky, J. J.; Adair,J. H. submitted to *Langmuir*.

(13) Li, T.; Kido, T.; Venigalla, S.; Adair, J. H. submitted to *Langmuir*.

(14) Simpson, R. E.; Habeger, C. E.; Rabinovitch, A.; Adair, J. H. *J. Am. Ceram. Soc.* **1998**, *81*, 1377.

(15) Tsukada, T.; Venigalla, S.; Morrone, A. A.; Adair, J. H. submitted to *J. Am. Ceram. Soc.*

(16) *Materials Processing in the Reduced Gravity Environment of Space*; Doremus, R. H.; Nordine, P. C., Ed.; Materials Research Society: Pittsburgh, 1987; Vol. 87, pp 366.

(17) Vaderhoff, J. W.; Micale, F. J.; El-Aasser, M. S.; Sudol, E. D.; Tseng, C. M.; Sheu, H. R. *J. Disp. Sci. Tech.* **1984**, *5*, 231.

(18) Allen, T. *Particle Size Measurement;* 4th ed.; Chapman Hall: New York, 1990.

DYNAMIC NUCLEATION OF SUPERCOOLED MELTS and MEASUREMENT OF THE SURFACE TENSION AND VISCOSITY

E.H. Trinh and K. Ohsaka
Jet Propulsion Laboratory
California Institute of Technology

1. INTRODUCTION

We investigate the phenomenon of acoustic pressure-induced nucleation by using a novel approach involving the large amplitude resonant radial oscillations and collapse of a single bubble intentionally injected into a supercooled liquid. Using a combination of previously developed and proven techniques, the bubble is suspended in a fluid host by an ultrasonic field which supplies both the levitation capability as well as the forcing of the radial oscillations. We observe the effects of an increase in pressure (due to bubble collapse) in a region no larger than 100 μm within the supercooled melt to rigorously probe the hypothesis of pressure-induced nucleation of the solid phase. The use of single bubbles operating in narrow temporal and spatial scales will allow the direct and unambiguous correlation between the origin and location of the generation of the disturbance and the location and timing of the nucleation event. In a companion research effort, we are developing novel techniques for the non-contact measurements of the surface tension and viscosity of highly viscous supercooled liquids. Currently used non-invasive methods of surface tension measurement for the case of undercooled liquids generally rely of the quantitative determination of the resonance frequencies of drop shape oscillations, of the dynamics of surface capillary waves, or of the velocity of streaming flows . These methods become quickly ineffective when the liquid viscosity rises to a significant value. An alternate and accurate method which would be applicable to liquids of significant viscosity is therefore needed. We plan to develop such a capability by measuring the equilibrium shape of levitated undercooled melt droplets as they undergo solid-body rotation. The experimental measurement of the characteristic point of transition (bifurcation point) between axisymmetric and two-lobed shapes will be used to calculate the surface tension of the liquid. Such an approach has already been validated through the experimental verification of numerical modeling results. The experimental approach involves levitation, melting, and solidification of undercooled droplets using a hybrid ultrasonic-electrostatic technique in both a gaseous as well as a vacuum environment. A shape relaxation method will be investigated in order to derive a reliable method to measure the viscosity of undercooled melts. The analysis of the monotonic relaxation to equilibrium shape of a drastically deformed and super-critically damped free drop has been used to derive interfacial tension of immiscible liquid combinations where one of the component has high viscosity. A standard approach uses the initial elongation of a droplet through shear flows, but an equivalent method could involve the initial deformation of a drop levitated in a gas by ultrasonic radiation pressure, electric stresses, or even solid body rotation. The dynamic behavior of the free drop relaxing back to equilibrium shape will be modeled, and its characteristic time dependence should provide a quantitative means to evaluate the liquid viscosity.

2. DYNAMIC NUCLEATION OF SUPERCOOLED WATER

The ability of mechanical disturbances such as pressure waves and high-speed flow to nucleate the solid phase from a supercooled melt has been a subject of controversy for some time. The unambiguous correlation of the nucleation event to the actual mechanically-induced disturbance has been difficult to establish because the potential for heterogeneous nucleation cannot be ruled out. Thus, the ability to isolate the melt from container walls by using levitated samples would allow the elimination of one cause for heterogeneous nucleation. The spatial localization of the source of mechanical disturbance within a very small region in the supercooled melt will also allow a more convincing case for ruling out the influence of heterogeneous sites. We have used ultrasonically-trapped and radially oscillating gas bubbles with diameter ranging between 10 and 50 μm to induce pressure waves within a region localized around them. By driving these gas bubbles into the "giant" monopole resonance[1], substantial repeating pressure waves can be generated within the melt immediately outside the bubble wall. At the same time, high velocity motion of the bubble wall during its collapse cycles potentially induce high-speed flows (100-1000 m/s) within a 10 μm wide spatial region.

We have obtained evidence of dynamically-induced nucleation of ice in water supercooled to lower than -5 °C through the large-amplitude radial oscillations of 10 μm-diameter air bubbles. This was accomplished by ultrasonically trapping a gas bubble in a small thin-walled container filled with water placed within another liquid-filled ultrasonic resonator driven at 21 kHz [2]. The experimental procedure consists in introducing the thin-walled cell filled with about 3 cc of distilled and filtered water into the ultrasonic cell maintained at a temperature below 0 °C. Power input to the transducer driving the cell is subsequently adjusted to drive the bubble into large-amplitude radial mode oscillations and into the sonoluminescing region.

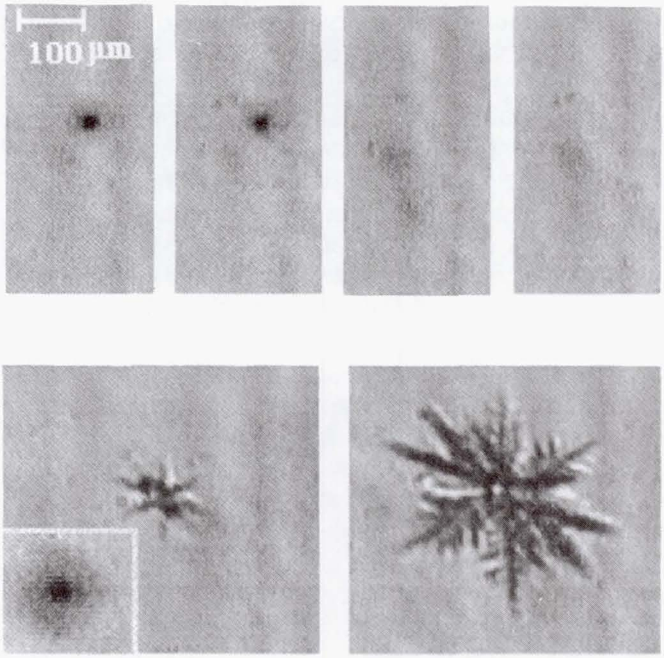

(e) (f)

Figure 1. Sequence of the onset of solidification induced by a cavitation bubble. The water temperature is -5 °C and the bubble is oscillating in the non-luminescing volume mode. The time interval between two consecutive frames is 1/30 second.

Figure 1 shows a sequence for the ice formation at -5 °C: (a) The bubble is oscillating in the non-luminescing volume mode. The cyclic variation of the bubble radius is seen as a halo around the dark core due to back lighting. The radius at maximum bubble expansion is approximately 45 μm. The inserted image at the bottom corner of (e) is for a better visualization of the cavitation bubble at the stable state. (b) The bubble seems to be distorted judging from the non-spherical halo. (c) The bubble is ejected from the stable bubble position and moved toward the six o'clock direction. (d) The bubble completely disappears. It is presumed to be shattered. (e) The ice appears in the dendritic form. (f) The dendrite grows at approximately 0.4 cm/sec. This value is comparable with the values in the literature, 0.54 cm/sec [3] and 0.39 [4] cm/sec.

Although significant velocity flows are generated by the violent bubble oscillations, the time scale of the fluid motion (on the order of microseconds) is still quite long when compared to molecular time constants (tens of picoseconds). The spatial scales of the bubble and its oscillations are also still very large when compared to the size of the fluctuating water molecular clusters described by the classical nucleation processes. Under these circumstances, we believe that pressure waves emitted during the violent periodic bubble collapses are responsible for the ice nucleation. A simple argument based on the water phase diagram and classical nucleation theory concepts suggests that a positive pressure wave up to 10 GPa is capable of nucleating the solid phase[2] because of the freezing point shift.

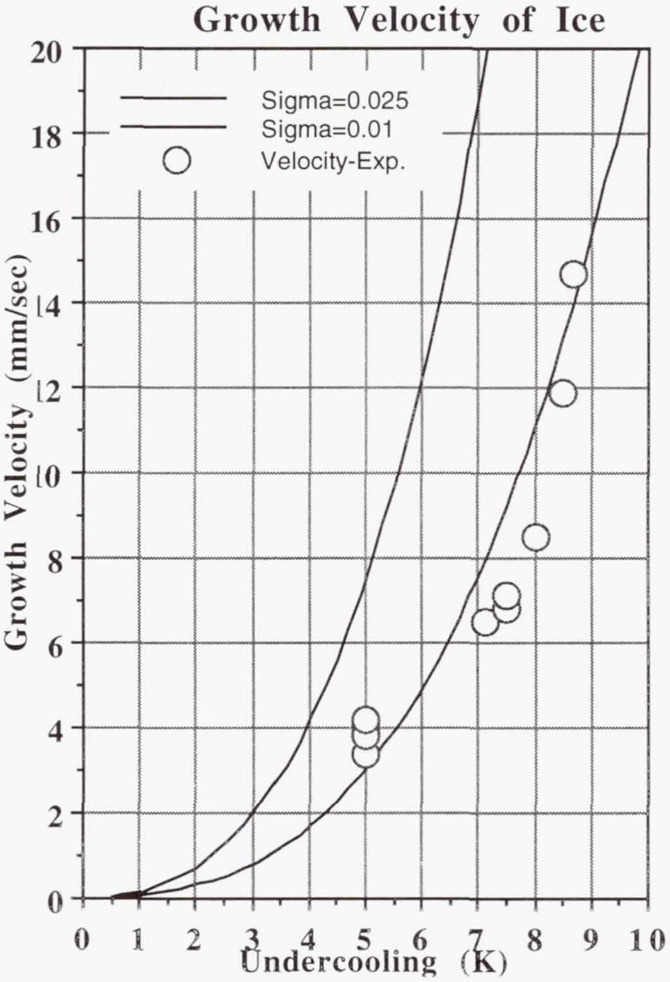

Figure 2. Dendritic growth velocity experimental results and comparison with theory.

Because the initial ice nucleus is generated within the bulk of the liquid without any seed, the dendritic free growth velocity can be measured. Figure 2 presents some preliminary results suggesting that the data can be fitted to the current theory based on a thermal diffusion model [5] with a scaling constant equal to 0.01.

3. MEASUREMENT OF THE SURFACE TENSION AND VISCOSITY

We have first addressed electrically uncharged drops that are ultrasonically levitated in air in 1-G. Due to the necessity to overcome the full impact of gravity on Earth, the high ultrasonic stresses required for the levitation of a drop also distorts its shape into an approximate oblate spheroid [6]. The systematic measurement of the shape of the levitated drop as a function of the acoustic pressure level allows the calculation of the surface tension. This method has the advantage of requiring a single measurement of the aspect ratio of a levitated drop and of the accurate determination of the sound pressure level (SPL). If an absolute measurement of the SPL is not possible, a relative method can be used by measuring the shape parameters of two drops under isothermal conditions: one with known and one with unknown surface tension . When the same acoustic sound pressure is used for levitation in both cases, the unknown surface tension can be calculated.

A second method for the measurement of surface tension for highly viscous liquids involves the accurate measurement of the dependence of the shape parameter of a levitated drop on the rotation rate. When the drop is undergoing axisymmetric solid-body rotation, the precise measurement of the rotation velocity at which the equilibrium drop shape transitions from the axisymmetric to the three-dimensional two-lobed shape (bifurcation velocity) allows the calculation of the surface tension. The bifurcation velocity has been theoretically and experimentally shown to be a unique function of the surface tension and density of the initially *spherical* drop. This bifurcation velocity depends, however, on the initial equilibrium shape of the levitated drop: due to the reduced stability, an initially oblate levitated drop will undergo transition to the two-lobed shape at lower rotation velocity than theoretically predicted for a spherical drop [7]. In order to circumvent this inconvenience, a theory for deriving the bifurcation velocity of non-spherical levitated drops must be made available, or low-gravity measurements are required. Another alternative is the Earth-based levitation and rotation of electrically charged drops using electrostatic fields [8] which yields initially quasi-spherical levitated charged drops. The detailed theoretical analysis of the effects of electric charge and field on the bifurcation velocity is then required. We are pursuing the last of these alternatives by carrying out Earth-based measurement of the bifurcation velocity of levitated drops as a function of the electric charge.

The measurement of the viscosity of super-critically damped liquid droplets could be tackled in a straightforward manner by measuring the relaxation time constant of a drop that is initially distorted from the spherical shape. An alternate approach we are currently investigating involves the shape relaxation of a rotating drop stretched to an equilibrium shape just before the onset of fission. We have thus performed some preliminary experimental measurements of the shape of rotating levitated drops as they spin down from the highly stretched configuration. The procedure involves acoustically rotating a levitated drop past the bifurcation point to a stretched two-lobed shape without inducing fission. The torque is then subsequently and abruptly released, and the drop is left to relax back to the equilibrium axisymmetric equilibrium shape. The time evolution of the relaxation process is accurately measured through video photography and the effects of viscosity through the evolution of differential flow is analyzed. An analytical model of the process is being concurrently developed.

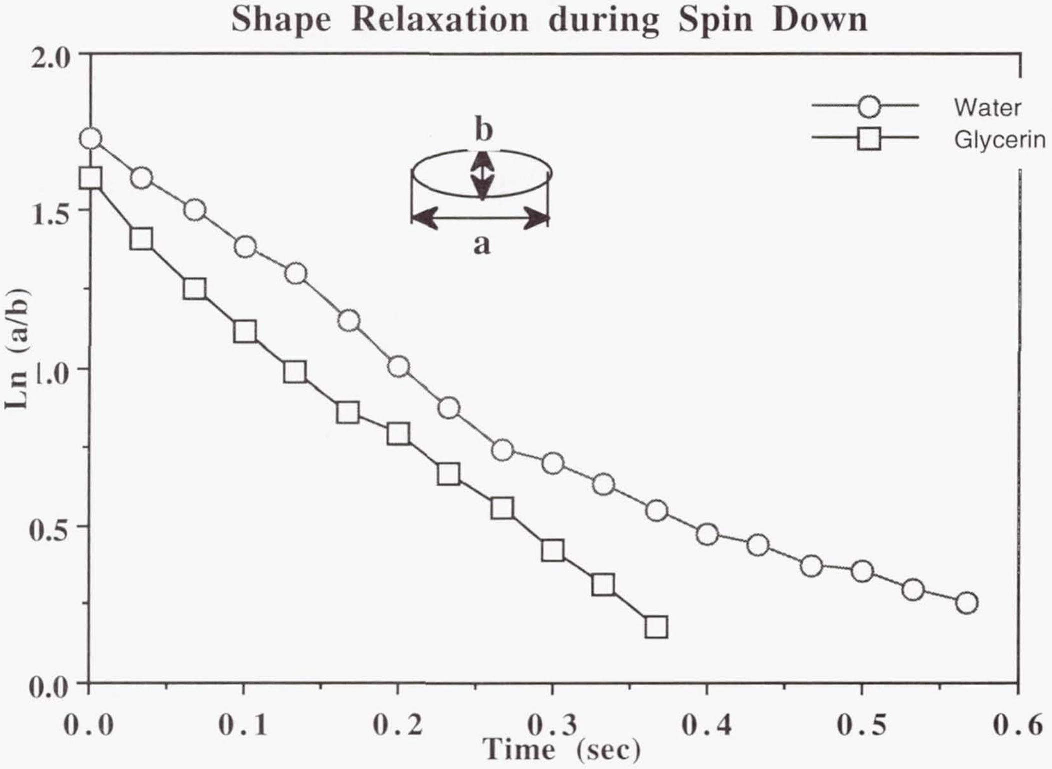

Figure 3. Aspect ratio of levitated drops of water and glycerin as they spin down from the two-lobed stretched configuration.

Figure 3 displays results of the measurement of such relaxation for water (1 cP) and glycerin (850 cP). A significance difference appears to be the double time constant for the water droplet. The sudden transition to a slower relaxation rate for water has been correlated with the transition from negative to positive curvature at the drop midsection. The overall faster relaxation time to axisymmetric shape observed for the higher viscosity liquid is attributed to the absence of differential flows.

4. SUMMARY

We have obtained some strong evidence for the correlation between high pressure pulses and the onset of nucleation of ice in supercooled water. A semi-quantitative analysis based on the effect of pressure on the displacement of the freezing point provides an explanation for such a phenomenon. We are also currently pursuing a number of potentially effective non-invasive measurement methods for the viscosity and surface tension of highly viscous supercooled liquids. Methods based on rotational dynamics appear to be the most scientifically interesting on the point of view of the fluid dynamical processes.

ACKNOWLEDGMENTS

The work described in this paper was carried out at the Jet Propulsion Laboratory, California Institute of Technology under contract with the Microgravity Research Division of the National Aeronautics and Space Administration.

REFERENCES

1. D. F. Gaitan, L. A. Crum, C. C. Church, and R. A. Roy, J. Acoust. Soc. Am. **91**, 3166 (1991)

2. K. Ohsaka and E.H. Trinh, "Dynamic Nucleation of ice induced by a single stable cavitation bubble", Applied Physics Letters **73** (6 July 1998)

3. S. H. Tirmizi and W. N. Gill, J. Cryst. Growth **85**, 488 (1987)

4. J. P. Kallungal and A. J. Barduhn, AlChE J. **23**, 294 (1977)

5. J.S. Langer and H. Muller-Krumbhaar, Acta Met. **26** (1978) 1681, 1689, 1697

6. E.H. Trinh and C.J. Hsu, J. Acoust. Soc. Am. **79**, 1335 (1986)

7. A. Biswas, E. Leung, and E.H. Trinh, J. Acoust. Soc. Am. **90**, 1502 (1991)

8. W.K. Rhim, E.H. Trinh, S.K. Chung, and D.D. Elleman "Charged drop dynamics experiments using an electrostatic-Acoustic Hybrid system", MRS Symposium Proceedings **87**, 329 (1987)

INTERFACE PATTERN SELECTION CRITERION FOR CELLULAR STRUCTURES IN DIRECTIONAL SOLIDIFICATION

R. Trivedi, Principal Investigator, Department of Materials Science and Engineering, Iowa State University, Ames, IA 50011. Phone: 5515-294-5869; FAX 515-294-4291; trivedi@ameslab.gov
S. N. Tewari, Co-Investigator, Chemical Engineering Department, Cleveland State University, Cleveland, OH, 44115,
D. Kurtze, Department of Physics, North Dakota State University, Fargo, ND, 58105.

INTRODUCTION

The aim of this investigation is to establish key scientific concepts that govern the selection of cellular and dendritic patterns during the directional solidification of alloys. We shall first address scientific concepts that are crucial in the selection of interface patterns. Next, the results of ground-based experimental studies in the Al-4.0 wt % Cu system will be described. Both experimental studies and theoretical calculations will be presented to establish the need for microgravity experiments.

The formation of cellular and dendritic patterns is important in many disciplines of science. Since the growth conditions in directional solidification can be precisely controlled and measured, it provides a powerful technique to study the underlying principles that govern the formation of ordered, disordered or chaotic patterns. The formation of a cellular or a dendritic structure is accompanied by microsegregation of solute, which results in a nonhomogeneous material. This nonhomogeneity in composition not only influences mechanical properties, but it can also generate stresses or lead to the formation of a new stable or metastable phase in intercellular region that can significantly alter the properties of the material. Thus the reliability of products made by solidification techniques such as casting and welding largely depends upon our ability to control solute segregation patterns so as to minimize stresses or to avoid the formation of undesirable phases in the intercellular region.

In the cellular structure, different cells in an array are strongly coupled so that the cellular pattern evolution is controlled by complex interactions between thermal diffusion, solute diffusion and capillarity effects. These interactions give infinity of solutions, and the system selects only a narrow band of solutions. The aim of this investigation is to obtain benchmark data that will allow us to quantitatively establish the physics of the pattern selection process. A sequence of directional solidification experiments has been proposed to quantitatively establish the fundamental principles that govern cell/dendrite microstructure selection. As the solidification velocity is increased, or the temperature gradient decreased, the interface undergoes several transitions: planar to small amplitude cells, to deep cells, and finally to dendrites. These changes in microstructures occur at low velocities where thermosolutal convection is dominant. Since reliable theoretical models are not yet possible which can quantitatively incorporate fluid flow in the selection criterion, microgravity experiments on cellular and dendritic growth are proposed to obtain benchmark data that can be quantitatively analyzed to establish the fundamental principles that govern the selection of specific microstructure and its length scales.

GROUND-BASED EXPERIMENTS

Previous ground-based study established that the conditions under which cellular and dendritic microstructures form are precisely where convection effects are dominant in bulk samples. We have performed ground-based experiments investigating the potential of several methods to reduce convection in terrestrial experiments. The methods studied include use of magnetic fields (axial and transverse) and the use of very small diameter samples of metallic alloys.

In order to see if the application of a magnetic field can suppress convection, directional solidification experiments were carried out in presence of axial and radial magnetic fields. It was observed that the application of a transverse magnetic field does not reduce the extent of solutal mixing due to convection. In addition, the transverse magnetic field introduces an anisotropy in the fluid flow that distorts the cellular mushy zone morphology. Thus, another technique was developed to reduce convection. In this technique, A series of experiments has been carried out in the Al-4wt% Cu alloy system using thin tubes of diameters varying from 6.0 mm down to 0.4 mm. A bundle of thin samples of varying diameters was placed inside the 6 mm diameter tube, and all samples were directionally solidified simultaneously in a single experiment. As a result, the thermal profile and the translation rate imposed on the samples were identical except for the degree of convection which depends on the tube diameter. Since convection effects are gradually reduced as the sample size is decreased, quantitative evaluation of convection effects on microstructural development can be obtained. The results of this series of experiments are illustrated in Fig. 1 which shows microstructures as a function of both the sample size and growth velocities at a given temperature gradient G=10 K/mm.

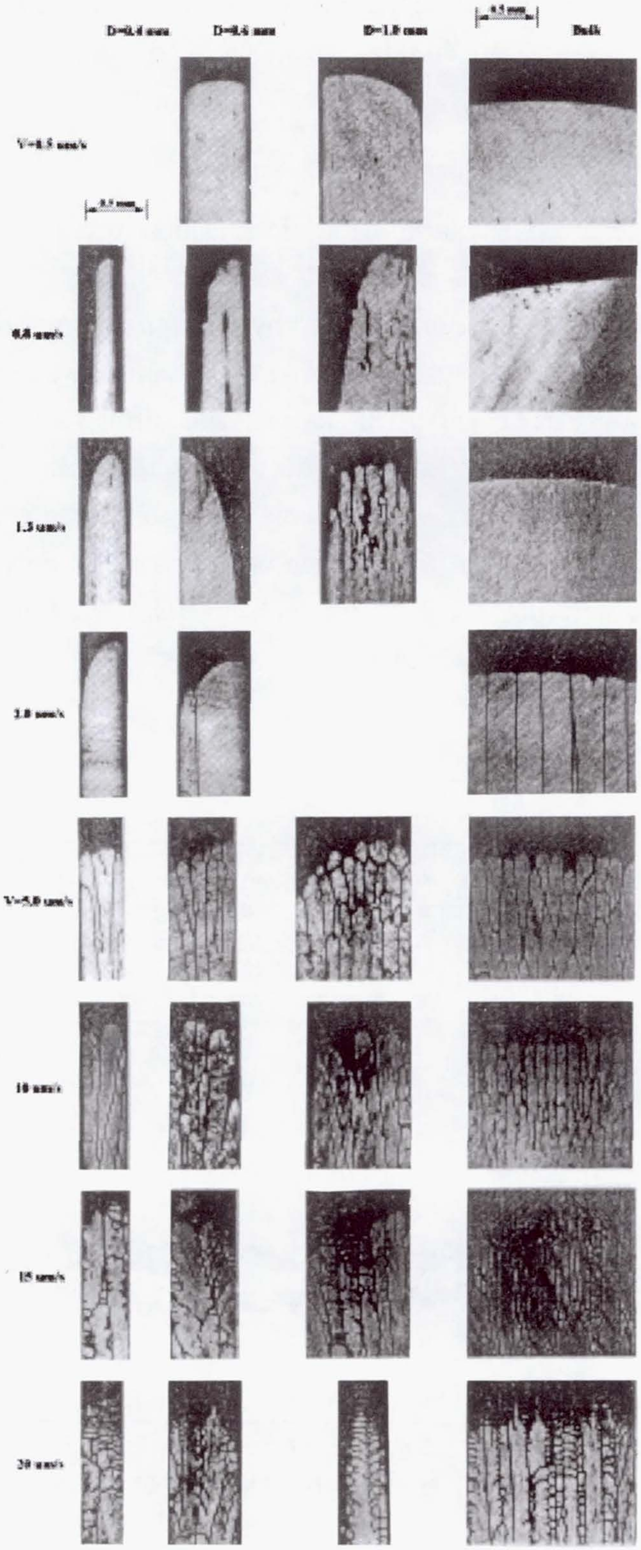

Figure 1. A matrix of microstructures with varying velocity and sample diameters in Al-4.0 wt % alloys.

Reducing the sample diameter (decreasing the extent of convection) results in the following:

- The tip temperature decreases.
- The primary arm spacing increases.
- Planar-to-cellular and cellular-to-dendritic transitions occur at lower growth speeds.

Microsegregation profiles across the cells obtained by electron-microprobe, Fig. 2, show that the solutal profile changed significantly until the diameter of the sample was reduced to 1 mm. Below this value there was no noticeable change. This suggests that diffusive growth conditions in Al-4.0 wt % Cu are approached only when the sample diameter is less than 1 mm. However, for this sample size, only very few cells were present and the constraint of the wall did not allow them to reach the steady-state configuration. A Steady state was approached only when a single cell was present at the center of a thin tube. In this case, no selection occurs and no information on the selection criterion can be obtained.

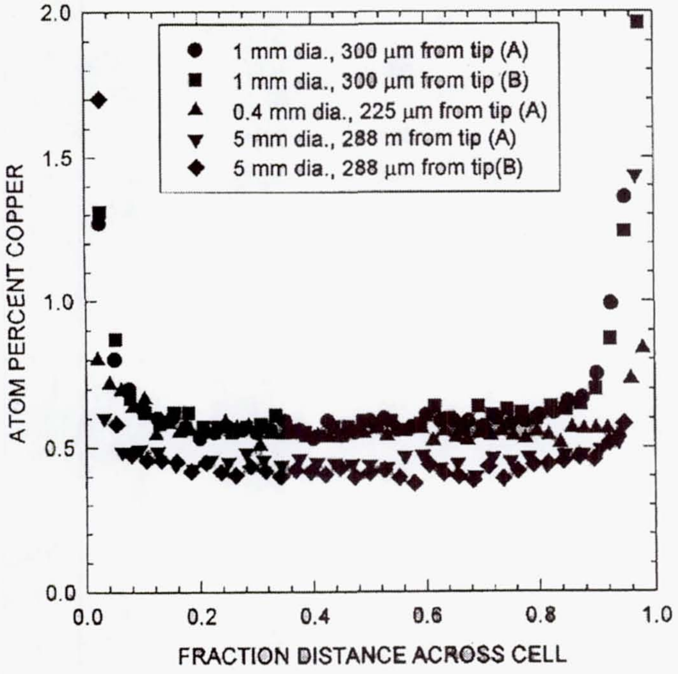

Figure 2. Microsegregation profile across cells for samples of different diameters that were directionally solidified in a single experiment.

Experimental studies were carried out for different velocities and temperature gradient values to establish the conditions under which planar to cellular and cellular to dendritic transitions occur. These transitions were found to depend upon the diameter of the tube, or upon the presence of convection. Figures 3a shows the transition conditions in large samples, whereas Fig. 3b is for small diameter samples in which diffusive growth occurs. It is seen that convection effects stabilize, or require higher velocity, for both the planar to cellular and cellular to dendritic transitions. These results in thin samples will allow us to precisely characterize experimental parameters under microgravity conditions.

These ground-based experimental studies clearly demonstrated the presence of significant convection in bulk samples. Although this experimental method permits access of the diffusive regime, this technique cannot be used to characterize microstructures for which the microstructural length scale is of the order of the sample diameter. Since sample diameters of 1mm or less is required for diffusive growth, only a single cell can form. There is no selection for the formation of a single cell, so that it is not possible to obtain diffusive growth terrestrially in bulk alloy samples that are large enough to establish the selection criterion or to obtain statistically meaningful distribution of spacing of cell/dendrite arrays.

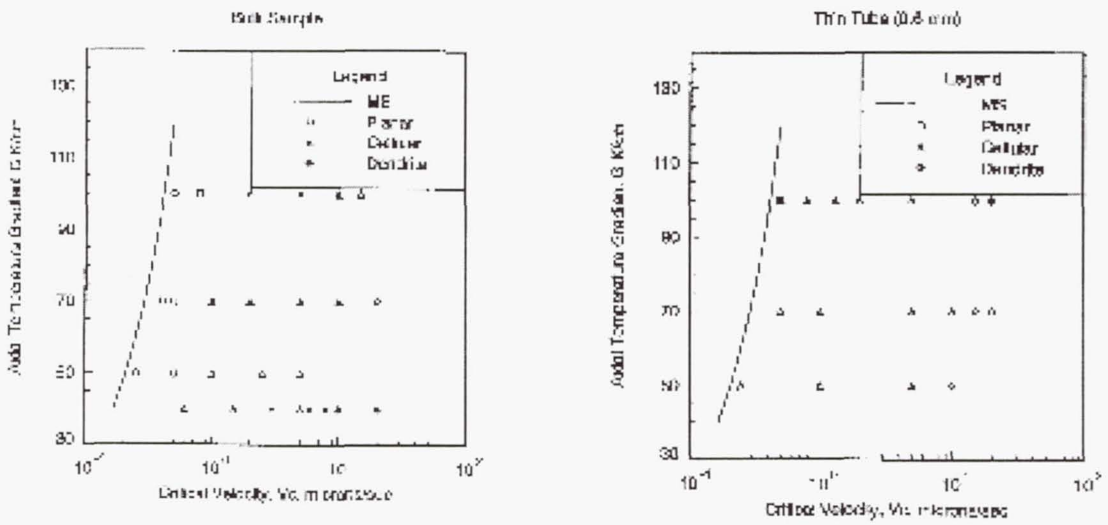

Fig. 3. Microstructures as a function of G and V. (a) Experiments in 6.0 mm tube in which significant convection is present. (b)) Experiments in 0.6 mm diameter tube in which diffusive growth conditions are present.

NUMERICAL STUDIES

In order to establish the effects of sample diameter on convection within the sample, we have developed a detailed numerical model of convection for the vertical Bridgman growth technique. A model was developed for the vertically upward solidification of a binary liquid of initial composition C_0 (in % solute) inside a two dimensional rectangular cavity. The vertical walls are rigid solid walls that represent the three-zone thermal assembly and are impervious to mass flux. The three-zone assembly consists of an isothermal cold zone wall at temperature T_c, an isothermal hot zone wall at temperature T_H, and a no-flux adiabatic zone between them. The system of coupled nonlinear equations written in coordinate frame fixed with the uniformly moving solid-liquid interface includes Boussinesq approximated Navier-Stokes equations, and the heat and solute transport equations. These equations are completely described by thermal and solutal Rayleigh numbers, the ratio of vertical to horizontal temperature gradients, the Peclet number based on growth rate, the partition coefficient, the Prandtl number, the Lewis number and the aspect ratio. Numerical calculation were carried out for conditions characteristic of solidification of Al-4.0% Cu at a growth rate of 1 μm/s in tubes of inner diameter 0.6 mm - 6 mm. These calculations show that the convective velocity is orders of magnitude larger than the diffusive velocity for samples of diameter larger than 6 mm. One needs to use sample diameter smaller than 1 mm to obtain conditions for which the convective velocity is smaller than the diffusive velocity in the Al-4.0 wt % Cu system. These calculations are in agreement with our experiments in thin samples, and both these studies clearly establish the dominant role of convection in sample diameters larger than 1 mm. The use of smaller than 1 mm diameter under terrestrial condition show that one would require microgravity level of 10^{-4} g to directionally solidify 1 cm diameter samples under diffusive conditions.

ACKNOWLEDGMENTS

P. Mazumder, E. Simsek and H. Miyahara contributed to this work. This work was supported by NASA microgravity research, Division of Materials Science, grant NASA NCC898.

Investigation of the Influence of Microgravity on Transport Mechanisms in a Virtual Spaceflight Chamber-A Ground Based Program

James D. Trolinger, PI
MetroLaser Incorporated

Roger Rangel, Co-I
University of California Irvine
Dept. of Mechanical & Aerospace Eng.

William Witherow, Co-I Jan Rogers, Co-I
Marshall Spaceflight Center,

Ravindra B. Lal, Co-I
Alabama A&M University,
Dept. of Physics

Presented at the Microgravity Materials Science Conference
July 14-16-1998
Huntsville Alabama

Background and Introduction

In January 1992, the IML-1 FES experiment produced a set of classic experimental data and a 40 hour holographic "movie" of an ensemble of spheres in a fluid in microgravity[1]. Because the data are in the form of holograms, we can study the three-dimensional distribution of particles with unprecedented detail by a variety of methods and for a wide variety of interests. The possession of the holographic movie is tantamount to having a complex experiment in space while working in an easily accessible laboratory on earth[2]. The movie contains a vast amount of useful data, including residual g, g-jitter, convection and transport data, and particle fluid interaction data. The information content in the movie is so great that we have scarcely begun to tap into the data that is actually available in the more than 1000 holograms, each containing as much as 1000 megabytes of information. This ground-based project is exploiting this data and the concept of holographic storage of spaceflight data to provide an understanding of the effects of microgravity in materials processing. This paper provides the foundation, objectives, and status of the ground based project.

Objectives

The primary objective of this project is to advance the understanding of microgravity effects on crystal growth, convection in materials processing in the space environment, and complex transport phenomena at low Reynolds numbers. This objective is being achieved both experimentally and theoretically. Experiments are making use of existing holographic data recorded during the IML-1 spaceflight. A parallel theoretical effort is providing the models for understanding the particle fields and their physics in the microgravity environment.

Virtual Spaceflight Chamber Concept:
Certain spaceflight experiments can be recorded in holograms in such a manner that having the holograms on earth is optically equivalent to being back in space with unlimited time to view the experiment[3]. Properly exploited, this concept can save a significant amount of experiment time in space by effectively bringing the experiment optically back to earth

Figure 1 illustrates the concept. Holograms of the space flight chamber are produced in space with a time resolution that is sufficient to capture any movement that is of interest to the investigator. In this case the chamber includes a growing TGS crystal surrounded by a fluid that has been seeded with polystyrene tracer particles of three sizes, 200, 400, and 600 micron diameters.

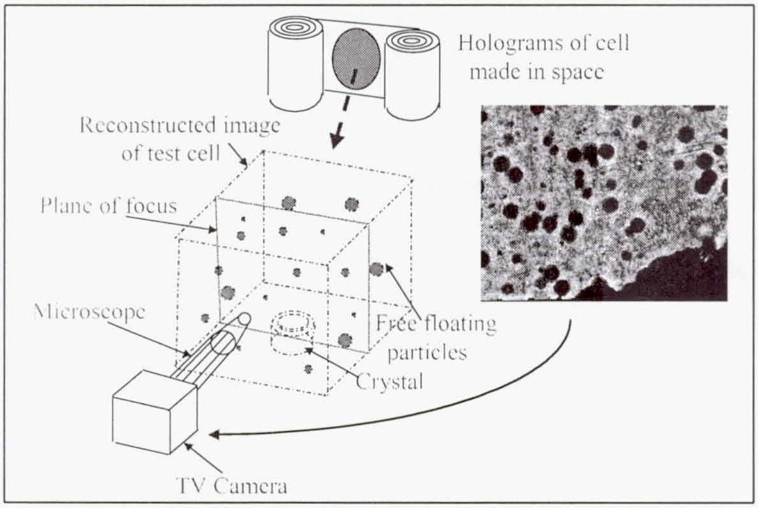

Figure 1-Virtual Space Flight Chamber Concept

When particle field data are in the form of holograms, we can study the three-dimensional distribution of particles with unprecedented detail by a variety of methods and for a wide variety of interests. The possession of the holographic movie is tantamount to having a complex experiment in space while working in an easily accessible laboratory on earth. The holographic movie contains a vast amount of useful data, including residual g, g-jitter, convection and transport data, and particle fluid interaction data. This project is further exploiting this data as well as the concept of holographic storage of spaceflight data, and is illustrating the effects of microgravity on materials processing.

The microscope scans through the entire volume under computer control, storing images throughout. The images are processed by specially developed software that locates the best focus XYZ position of each particle in each time slot. This data has been collected for all holograms for the entire IML-1 spaceflight, has been archived in CD format, and is available to other researchers who may be interested in such data. Holograms were made approximately 10 minutes apart, representing sufficient time resolution for the overall motion of particles, which is characterized by a velocity of the order of micrometers per minute.

The types of information extractable from these holograms can improve our understanding of the microgravity environment, thereby allowing NASA to better exploit its use in such applications as crystal growth from solution. The early part of this investigation has made use of existing holographic data produced in the IML-1 experiment to produce quantitative measurements of convection in the space shuttle environment, g-jitter effects on crystal growth, residual gravity, and complex transport phenomena in low Reynolds number flows. By knowing the location of all of the particles, we can select particles with specific environments for study, for example, a particle with no nearby neighbors, or a particle near the walls or the growing crystal.

Figure 2 shows an enlargement of the region containing both in-focus and out-of-focus particle images of all three sizes of particles. Particles follow a zigzag type of motion due to g-jitter. They move both under the influence of convection as well as gravity. The movement in the region of the crystal differs from that further away because of the influence of the growing crystal. The particles are used to observe micro-convection near the crystal. In addition we found the experiment useful for measuring g and g-jitter effects as well as fundamental particle/fluid physics.

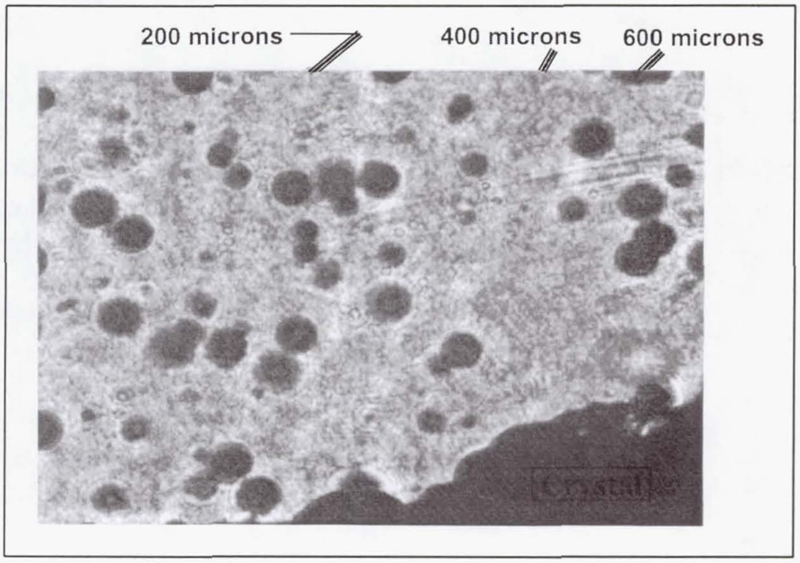

Figure 2-Particles in Microgravity

Discussion

In a microgravity environment, particles of different density can be studied side by side, since the settling rate is extremely low. Those that are denser than the fluid will move in the direction of the residual gravity, while those that are less dense move against the direction of residual gravity. Neutrally buoyant particles move only if the fluid itself moves. The particles actually cause micro-convection in the fluid. At the extremely low Reynolds numbers of these studies, a particle influences its environment out to at least 10 particle diameters. Consequently, the data interpretation requires accounting for the immediate environment of the particle. For fluid velocimetry particles with no nearby neighbors must be used. A neutrally buoyant particle that might otherwise remain motionless may move under the influence of a nearby heavier or lighter particle.

One method for extending the spatial resolution is to employ more than one particle size to reduce confusion between different tracer particles. By using several different particle sizes we improved the spatial resolution as well as the dynamic range of the velocity measurement since the terminal velocity is proportional to the square of the particle diameter, the particle/fluid density ratio, and the acceleration, g. Each factor of two in particle size quadruples the measurable velocity range. Particle size will also be used to distinguish different particle materials. In future experiments particle size can also be used to distinguish different particle materials.

A self-correcting method for measuring effects of g and g-jitter without actually determining velocity of an individual particle is to measure the relative velocity between two different particle sizes (**Figure 3**). The separation of small and large particles located close to each other is proportional to the gravity force and is not affected by registration or by convection. This is a unique way to separate the observance of convection and gravity.

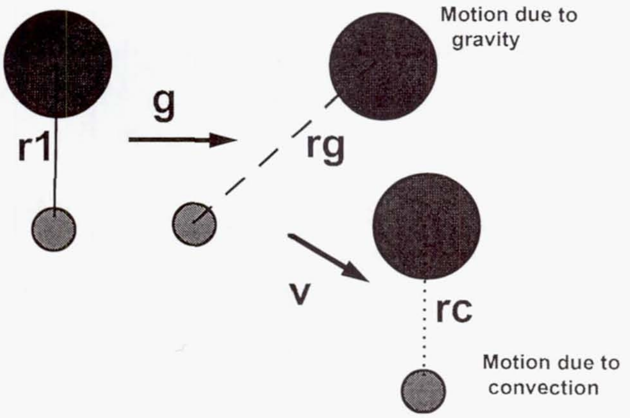

Figure 3. Motion of Large and Small Particle Pairs as Influenced by Gravity and Convection. This procedure has been the most accurate way to measure residual gravity and g-jitter, since the process cancels the effects of convection and minimizes registration errors, and the particle tracks provide a direct measure of residual g.

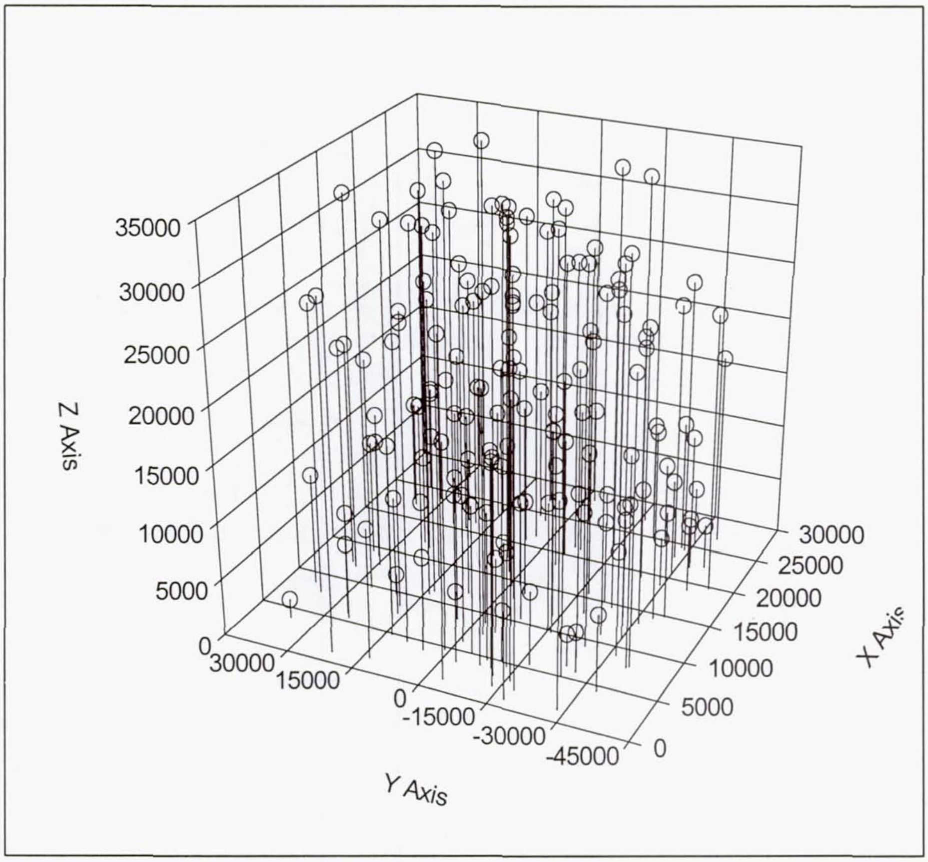

Figure 4-Distribution of Small Particles in the Chamber

Various methods have been devised to analyze and display particle mechanics data. **Figure 4** illustrates the three dimensional positions of all small particles in a hologram. By producing such data for each time slot, particle tracks are created for the entire flight. **Figure 5** illustrates particle tracks in 3D over a 10 hour time period.

We can locate a particle to within a few microns in the plane normal to viewing direction and to within about one millimeter along the direction of viewing. A major shortcoming in these data is our ability to locate a reference frame from one hologram to the next, which is about 50 microns. We are developing procedures to improve upon this measurement in subsequent experiments.

Drs. Rangel and Coimbra[4,5], using fractional derivative techniques, have discovered a new, analytical solution to the equation of motion of a particle in a fluid under conditions that are especially of interest in a microgravity environment. They applied the work to specific cases of interest for this program and have provided data to support potential flight experiments.

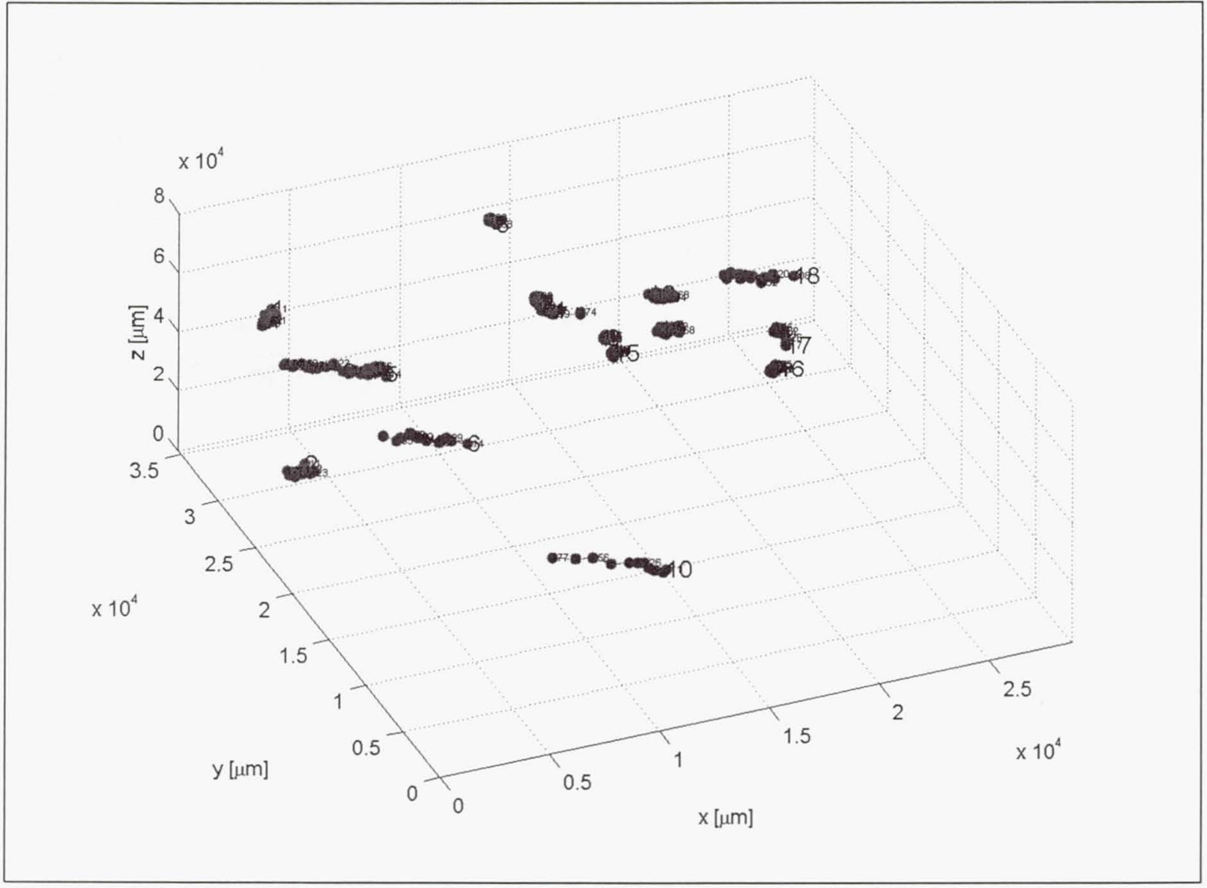

Figure 5-Particle Tracks over an 11-Hour Period

Measurements of residual g are typically in the range of 1 to 2 micro-g's, with large fluctuations of orders of magnitude. Acceleration data correlates well with SAMS on board measurements. Maneuvers are clearly defined with interesting particle movement that can be tracked throughout a maneuver.

Preliminary experiments were conducted in a KC-135 flight to gain experience with a miniaturized holocamera for low-g particle tracking studies. The experiment was designed by the entire project team and was flown by Dr. Rogers

A test cell containing various sized particles and various densities was contained in a solution. When the aircraft was on the upward movement in the parabola where g is highest, particles of density greater than the fluid sank to the "bottom" and particles lighter than the fluid rose to the "top" of the cell. When the aircraft was at the apogee where low g begins, the operator flipped the cell over 180 degrees and inserted it with force into a holder, at which time holograms were recorded continuously for the remainder of the low g portion and well into the high g portion. Based on our theoretical work, we expected that at time zero, when the cell came to a halt at its mount, the heavy particles would move from the top into the fluid and would (depending on density ratio) come to a zero velocity relative to the fluid, while the lighter particles would move upward from the bottom in a similar fashion. Data recorded from these experiments consists of approximately 120 holograms over 25 parabolas.

The holograms from the KC-135 were reconstructed to evaluate the image quality and to gain experience with use of the miniaturization techniques. A primary issue is the use of a diode laser and its ability to produce holograms of sufficient quality. These experiments suggest that the diode laser is adequate. Hologram image quality appeared as good as what would be expected from a HeNe laser. The holograms are in-line holographic recordings. Images are characterized by a collapsing diffraction pattern that remains distinct over a large depth of field.

We examined ways to simulate low g in ground-based experiments to test the experiment hardware. High viscosity solutions that have the correct optical properties provide extremely low Reynolds number flows on ground. Methylcellulose in solution can raise the viscosity of the solution by orders of magnitude.

Conclusions and Future Work

We have concluded that extremely useful data can be extracted from holograms of particle fields in microgravity. Residual gravity can be measured with unprecedented accuracy. G-jitter and microconvection can be observed and quantified. Particle interaction can be seen. A new type of particle driven convection at extremely low Reynolds numbers is observable. Improvements in the measurements required to exploit the concept completely have been identified. These include more accurate referencing between holograms, recordings from two views, and improved flexibility on hologram timing. The program is now emphasizing data types that will support the flight definition experiments.

REFERENCES

[1] J.D. Trolinger, R.B. Lal, D. McIntosh and W.K. Witherow *"Holographic Particle Image Velocimetry in the First International Microgravity Laboratory aboard the Space Shuttle Discovery"*, Applied Optics, Vol. 35, No. 4, pp. 681-689 (1 Feb. 96.).

[2] James D. Trolinger, Roger Rangel, and Ravindra Lal, *"Particle Mechanics and G-jitter Observations in the IML-1 Spaceflight"* AIAA 96-0504, 34th Aerospace Sciences Meeting, (January, 1996).

[3] James D. Trolinger, Matthias Rottenkolber, and Frank *"Development and application of holographic particle image velocimetry techniques for microgravity applications",* Journal of Measurement Sciences and Technology, Vol. 8 (1997) 1573-1583.

[4] C.F.M. Coimbra, (1997). "Analytical Study on the Unsteady Motion and Heat Transfer of Small Particles in Suspension," Ph.D. Dissertation - University of California, Irvine (In preparation).

[5] C.F.M. Coimbra, R. and Rangel *"Analytical Study on the Unsteady Motion and Heat Transfer of Small Particles in Suspension"*, Accepted for publication.

Investigation of the Influence of Microgravity on Transport Mechanisms in a Virtual Spaceflight Chamber-A Flight Definition Program

James D. Trolinger, PI
jtrolinger@metrolaserinc.com
MetroLaser Incorporated

Roger Rangel, Co-I
University of California Irvine
Dept. of Mechanical & Aerospace Eng.

William Witherow, Co-I Jan Rogers, Co-I
Marshall Spaceflight Center,

Ravindra B. Lal, Co-I
Alabama A&M University,
Dept. of Physics

Presented at the Microgravity Materials Science Conference
July 14-16-1998
Huntsville Alabama

BACKGROUND AND INTRODUCTION

A need exists for understanding precisely how particles move and interact in a fluid in the absence of gravity. Such understanding is required, for example, for modeling and predicting crystal growth in space where crystals grow from solution around nucleation sites as well as for any study of particles or bubbles in liquids or in experiments where particles are used as tracers for mapping microconvection. We have produced an exact solution to the general equation of motion of particles at extremely low Reynolds number in microgravity that covers a wide range of interesting conditions[1,2]. We have also developed diagnostic tools and experimental techniques to test the validity of the general equation[3]. This program, which started in May, 1998, will produce the flight definition for an experiment in a microgravity environment of space to validate the theoretical model. We will design an experiment with the help of the theoretical model that is optimized for testing the model, measuring g, g-jitter, and other microgravity phenomena. This paper describes the goals, rational, and approach for the flight definition program.

Objective

The first objective of this research is to understand the physics of particle interactions with fluids and other particles in low Reynolds number flows in microgravity. Secondary objectives are to (1) observe and quantify g-jitter effects and microconvection on particles in fluids, (2) validate an exact solution to the general equation of motion of a particle in a fluid, and (3) to characterize the ability of isolation tables to isolate experiments containing particle in liquids. The objectives will be achieved by recording a large number of holograms of particle fields in microgravity under controlled conditions, extracting the precise three-dimensional position of all of the particles as a function of time and examining the effects of all parameters on the motion of the particles. The feasibility for achieving these results has already been established in the ongoing ground-based NRA, which led to the "virtual spaceflight chamber" concept[4].

Tasks

The program objective will be met through the following tasks:

1. Apply and Refine the theoretical analysis to help specify the flight experiment matrix.
2. Conduct computer experiments to assist with the hardware design.
3. Collect and analyze additional data from the IML-1 holograms.
4. Produce a preliminary experiment design
5. Specify the required measurement capability.
6. Breadboard and test the experiment.
7. Perform ground feasibility demonstration.
8. Specify requirements of a flight package:
9. Conduct reviews
   a) Science Requirements Document (SRD).
   b) Science Concept Review (SCR).
   c) Requirements Definition Review (RDR).

Particle Mechanics in Microgravity

Traditionally, the study of particle motion in a fluid has considered the effect of drag and gravity.[5] The effect of drag has usually been accounted for with correlations for the drag coefficient based on the Stokes drag, corrected for higher Reynolds number effects. This approach can be shown to be approximately valid when the particles are much heavier than the displaced fluid and when the unsteadiness of the flow field is much slower than the characteristic time for steady development of the fluid layer adjacent to the particle.

More advanced investigations of the particle behavior have included additional terms in the particle equation of motion, resulting in the BBO (Basset-Bousinesq-Oseen) equation. Except for the case of particles settling in an undisturbed flow, all solutions of the more complete particle momentum equation in the Stokes regime have resorted to numerical integration of the equation. Because the numerical solution is involved, many investigations have preferred to neglect some of the more troublesome terms in the equation, even in situations where this is not justifiable.

Theoretical analysis

Recently Coimbra and Rangel have shown that an analytical solution of the complete particle momentum equation is possible. Because it is an analytical solution, it is many times more powerful than a typical numerical solution, it is easier to implement in a general fluid flow, and furthermore, the effect of the various terms in the original equation can be readily identified in the solution. A very well controlled experiment is essential to test the validity of any solution. Because the equation is valid in the Stokes regime (small Reynolds number), a microgravity environment is crucial to investigate wide ranges of particle/fluid density ratios. In a 1-g environment, heavy particles would tend to rapidly accelerate to higher Reynolds numbers, unless the particles are too small. The same thing would occur for very light particles (bubbles). Microgravity allows for a more controlled experiment. Desirable experiments would consider particles of at least two different sizes and fluids of two different viscosities. It would be important to consider isolated particles as well as interacting particles. The fluid motion must be very carefully controlled. Examples of controlled motions would be impulsive acceleration, constant acceleration, and oscillatory motion. It would be important to measure any residual gravity.

In normal gravity, viscous and gravitational forces almost always dominate the motion of a sphere. In microgravity, many common cases exist in which normally negligible terms in the equation of motion become important.[6] A complete understanding of the equations allows us to understand the motion of particles in a fluid as well as to choose experimental parameters in a new experiment to advantage, leading to special cases of the equations that will govern the design of the experiment.

COIMBRA-RANGEL SOLUTION TO THE MAXEY RILEY EQUATION OF MOTION OF A PARTICLE IN A FLUID[7]

Equation of motion for particles subjected to unsteady creeping flows

The creeping flow motion of small particles in a viscous fluid is described by the following well-known dimensionless equation (Maxey and Riley, 1983):[8]

$$\frac{dV_i}{dt} = \alpha\frac{DU_i}{Dt} - \alpha\frac{d(V_i - U_i)}{2dt} - (V_i - U_i) + (1-\alpha)\frac{\tau g_i}{U_o} - \sqrt{\frac{9\alpha}{2\pi}}\left\{\int_0^t \frac{d(V_i - U_i)}{d\sigma}\frac{d\sigma}{\sqrt{t-\sigma}} - \frac{V_i(0) - U_i(0)}{\sqrt{t}}\right\}. \tag{1}$$

In Equation (1), α is the fluid-to-particle density ratio, g_i is the acceleration of gravity, and V_i and U_i are the particle and fluid velocity, respectively. The dimensionless times t and σ were nondimensionalized by the particle's relaxation time $2a^2\rho_p/(9\mu)$, the velocities by the characteristic flow velocity U_o, and the coordinates and particle radius by the characteristic length of the flow L. Equation (1) is valid for low particle Reynolds numbers $\left(a\left|V_i - U_i\right|/\nu\right)$ and for low dimensionless number $a^2\,U_o/L\,\nu$. The particles are assumed to be small in comparison to the integral length scale of the flow, which means that the Faxen correction is negligible, thus not being included in Equation (1).[9]

Defining ϕ_i as the differential velocity $V_i - U_i$, and approximating the substantial derivative following a fluid particle (D/Dt) in the right-hand-side of Equation (1) as a time derivative along the particle's trajectory (d/dt), Eqn. (1) can be rewritten as

$$\frac{d\phi_i}{dt} = (\alpha - 1)\frac{dU_i}{dt} - \alpha\frac{d\phi_i}{2dt} - \phi_i - \sqrt{\frac{9\alpha}{2\pi}}\left\{\int_0^t \frac{d\phi_i}{d\sigma}\frac{d\sigma}{\sqrt{t-\sigma}} - \frac{\phi_i(0)}{\sqrt{t}}\right\} + (1-\alpha)\frac{\tau g_i}{U_o}. \tag{2}$$

Using fractional derivatives Coimbra and Rangel have produced an exact analytical solution to the Maxey-Riley form of the equation of motion.

Important solutions for different prescribed flow fields $U(t)$ presented in reference 23 include:

1. Gravitationally induced motion in a quiescent fluid.
2. Impulsive start at zero gravity.
3. Impulsive start in a gravity field.
4. Unperturbed fluid velocity increasing linearly in time.
5. Unperturbed fluid velocity varying as polynomial in time.
6. Unperturbed fluid velocity varying harmonically in time.

All of these cases are of great importance in spaceflight experiments.

Gravitationally induced motion in a quiescent fluid

The Coimbra-Rangel solution of the Maxey-Riley equation was used to predict the velocity and displacement for this specific case; producing solutions that can be compared with less general solutions that predict this particular case. The following figures show the preliminary results.

Figure 1 shows the behavior of the dimensionless velocities for five different values of the fluid-to-particle density ratio α. The solutions are shown for values of α equal to 100, 5, 8/5 (critical value for the general solution), 1/5, and 1/100. The particle's velocity is normalized by its own terminal velocity.

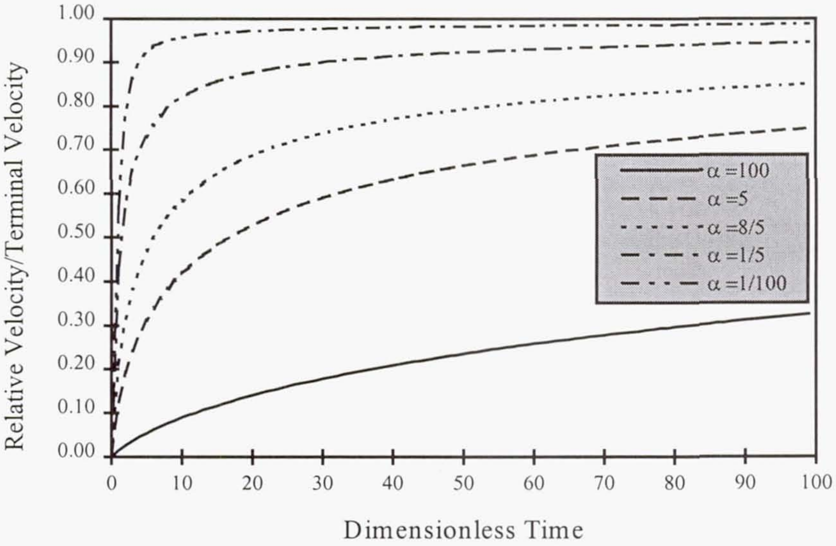

Figure 1. Exact solution for the normalized particle velocity in gravitationally induced motion through a quiescent viscous fluid.

Figure 2 shows a comparison of the Coimbra-Rangel solutions of Eqn. (1) with the solutions found when the last term (the *history term*) in the right-hand-side of Eqn. (1) is neglected. This approximation is made often because of the difficulties that arise from the inclusion of this term. As can be inferred from **Figure 2**, the approximation turns out to be a crude one unless the fluid-to-particle density ratio approaches zero.

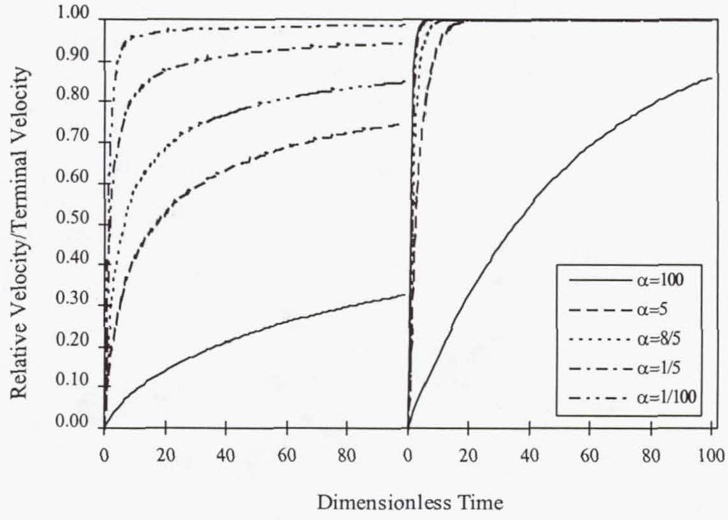

Figure 2. Comparison of exact solutions given by Equations 14, 15, and 16 (left) with solutions for the momentum equation neglecting the history term contribution (right).

Particle displacement with time for all density ratios except for the one corresponding to a very light particle, approach the near-linear behavior that is expected by particles that attain terminal velocity very soon after being released when the history term is neglected. On the other hand, when history effects are considered, the displacements diverge from the linear behavior except for the much heavier particle. This striking difference in behavior indicates that the history term should be considered in any situation departing from a value of α which is much smaller than one. The error in not considering the history effects is even more drastic when the unperturbed flow field varies with time since, in the general case, the memory effects do not decay in time as in the present case.

FLIGHT EXPERIMENT DESIGN

Since the feasibility of this experiment has already been established, one of the first milestones will be the design of a cost efficient flight experiment that will: 1) monitor and quantify the microgravity environment, 2) monitor the precise position of the particles in a distribution in a fluid, and 3) integrate the experiment with an isolation table so that a controlled force field can be applied to the particle distribution. The force field will include at least the following:

- No isolation in the Spacelab vibration environment.
- Isolation from Spacelab.
- Oscillatory motion from 1 to 10 Hz with amplitudes of a few millimeters.
- Programmed forcing functions such as steps and ramps to be determined.
- Convective fields to be introduced mechanically.

A small, windowed chamber will house the fluid and particles. The particles will include several sizes and weights, chosen in such a manner that different weights will be identifiable in the data. A holographic time history will be produced of the particle distribution, allowing particles to be precisely tracked in three dimensions in time.

Figure 3 illustrates the instrument concept, which is based upon simplicity and reliability. A laser diode will produce diverging light that illuminates one or more chambers after collimation. As the light passes through the chamber, it will pick up particle and crystal profile information and in-line holograms will be recorded on 35 mm film. Since the system is compact, two or more cells can be operated in a shoebox-sized container. By employing more than one cell, crystals can be released into the solutions at different times or, alternatively, different types of materials can be grown at the same time, comparing the influences of microgravity on two types of material.

In our previous work, we have shown that the edge of a particle or object can be located with an accuracy of better than 2 micrometers. This will be over an order-of-magnitude improvement above our work in the IML-1 spaceflight. This ability will allow the particle position to be precisely tracked, thus permitting the detection of very small motions.

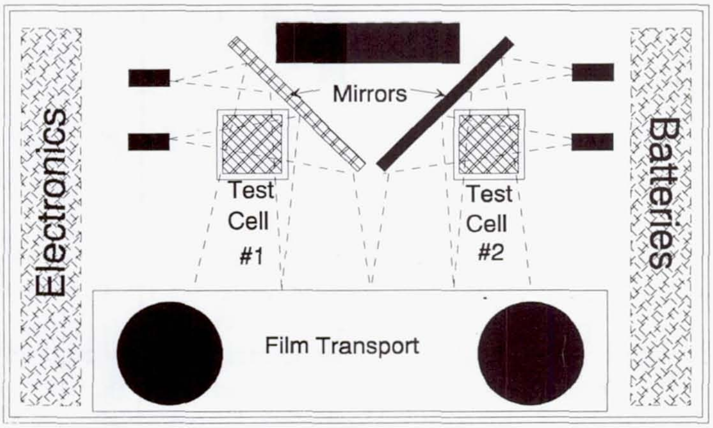

Figure 3. Flight system.

Preliminary In-line holography experiments

We have conducted preliminary experiments to select optimal components and configurations for an inline holocamera for the space flight particle tracking system. The approach was to set up a generic in-line holocamera using dimensions similar to what is anticipated in the space flight system and perform comparison experiments using the candidate components and configurations. We selected several slide mounted particle sizes for hologram evaluation (e.g. 10-100 micron diameter). Preliminary experiments suggest that diode lasers will be adequate for recording (**Figure 4**).

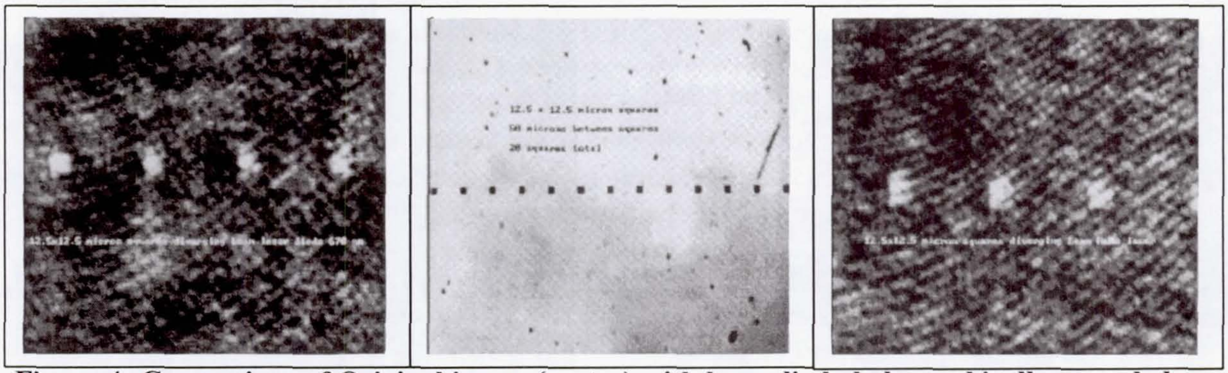

Figure 4: Comparison of Original image (center) with laser diode holographically recorded and reconstructed image (left) and HeNe laser recorded and reconstructed image (right). Particle size is 12.5 microns. Diverging wave used to record and reconstruct.

REFERENCES

---

[1] C.F.M. Coimbra, (1997). "Analytical Study on the Unsteady Motion and Heat Transfer of Small Particles in Suspension," Ph.D. Dissertation - University of California, Irvine (In preparation).

[2] C.F.M. Coimbra, R. and Rangel *"Analytical Study on the Unsteady Motion and Heat Transfer of Small Particles in Suspension"*, Accepted for publication

[3] James D. Trolinger, Matthias Rottenkolber, and Frank *"Development and application of holographic particle image velocimetry techniques for microgravity applications",* Journal of Measurement Sciences and Technology, Vol. 8 (1997) 1573-1583.

[4] Investigation Of The Influence Of Microgravity On Transport Mechanisms In A Virtual Spaceflight Chamber-A Ground Based Program; Published elsewhere in this volume

[5] P.M. Lovenlenti and J.F. Brady, "The Hydrodynamic Force on a Ridged Particle Undergoing Arbitrary Time-dependent Motion at Small Reynolds Number" J. Fluid Mech., 256, pp. 561-565, 1993.

[6] J.D. Trolinger. R.H. Rangel, R.B. Lal, "Methodologies For The Micro-Mechanics Of Microspheres In A Fluid In Microgravity". 11th International Symp on Unification of Analytical, Computational and Experimental Solution Methodologies, Danvers, Mass., 18-20 August 1993.

[7] C.F.M. Coimbra, "Analytical Study on the Unsteady Motion and Heat Transfer of Small Particles in Suspension," Ph.D. Dissertation - University of California, Irvine (In preparation) (1997).

[8] M.R. Maxey, and J.J. Riley, "Equation of Motion for a Small Rigid Sphere in a Nonuniform Flow," *Physics of Fluids*, Vol. 26, p. 883 (1983).

[9] N. Konopliv, "Gravitationally Induced Acceleration of Spheres in Creeping Flow - A Heat Transfer Analogy," *AIChE Journal*, Vol. 17, No. 6, p. 1502 (1971).

Page intentionally left blank

Coarsening in Solid-Liquid Mixtures (CSLM)

J.Alkemper, V.Snyder, P.W.Voorhees
Department of Material Science and Engineering
Northwestern University

Abstract

The CSLM experiment examines the dynamics of particle-coarsening in a two-phase mixture. The evolution of the average particle size and particle size distribution of dispersed Sn-particles in a Pb-Sn liquid was measured with respect to time. Samples were heat treated at 185°C where a mixture of liquid Pb-Sn and Sn-rich solid exist with varying volume fractions of solid. Initially, the solid was present in the form of small, dispersed particles with average sizes of ca. 10μm. Presented here are the results of the samples from the MSL-1 mission which have been analyzed at this time. Initially we concentrated our analysis on samples with 10% solid volume fraction, only a few samples with other volume fractions have been analyzed. It is found that the kinetics of the process follow the theoretical predictions within the uncertainties of the materials parameters. We also found an increasing coarsening rate with increasing volume fraction which is in agreement with existing theories. A full evaluation of the existing theories based on the results of the CSLM experiments is not possible at this point.

Objectives

There are numerous theories in the field of Ostwald Ripening, none of which has ever been verified in a quantitative manner. The predicted evolution of the average particle size was found in many experiments qualitatively (see equation 1), but a quantitative comparison was usually not possible because the thermophysical parameters were unknown. In some cases these parameters were determined from coarsening experiments through the use of one theory. However, starting from the early work of Ardell [1,2] to today [3] the measured particle size distributions (PSD) do not agree with the theoretical predictions. The objective of the CSLM experiment is to close this gap and prove or disprove the existing theories. The system of solid Sn-rich particles in a liquid Pb-Sn matrix was chosen because it allows a fast coarsening process, spherical particles, and knowledge of the necessary thermophysical parameters. The problem of particle sedimentation could be overcome through the use of microgravity (see section *Flight results compared with ground results*).

Background

In a dispersion of particles in a matrix phase where diffusion between the particles is permitted, the larger particles grow at the expense of smaller particles resulting in a reduction of interfacial area and thus minimizing the total energy. This coarsening process is known as Ostwald ripening[4]. Ostwald ripening is a phenomenon that occurs in many metallurgical systems and other systems. For example, the second-phase particles in high temperature materials used in turbine blades undergo coarsening at the operating temperature of the turbine. The coarsening process degrades the strength of the blade since alloys containing many small particles are stronger than those containing a few large ones. Other systems that show coarsening are liquid-phase sintered materials such as tungsten carbide-cobalt alloys, iron-copper alloys, dental amalgam alloys used for fillings, and porcelain.

The kinetics of the coarsening are controlled by diffusional mass flow. The classical work by Lifshitz, Slyosov[5] and Wagner[6] (LSW) predicts that the average particle size R is proportional to the cube root of time t.

$$R(t)^3 - R(0)^3 = K_{LSW}t \tag{1}$$

K_{LSW} is a constant which includes all relevant materials parameters. Unfortunately, the theory is only valid in the limit of a vanishingly small volume fraction of coarsening phase. More recent theories that include the effect of finite volume fraction, and thus particle-particle diffusional interactions, predict that the exponent of the temporal power law will not be a function of the volume fraction, but the amplitude of the temporal power law, the rate constant, will depend on the volume fraction. The dependence of the rate constant as well as the particle size distribution (PSD) on the volume fraction is different for each theory. This dependence is usually written in terms of K_{LSW} as

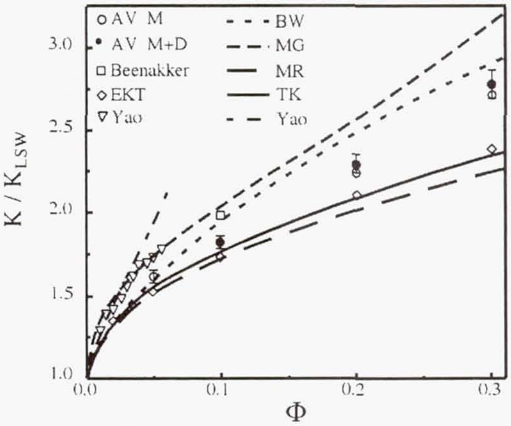

Figure 1: The dependence of the coarsening rate on the volume fraction. Shown are predictions by Akaiwa and Voorhees [7], Beenacker [8], Enomoto *et. al.* [9], Yao *et. al.* [10], Brailsford and Wynblatt [11], Marsh and Glicksman [12], Marquessee and Ross [13], and Tokuyama and Kawasaki [14].

$$K(\Phi) = K_{KLW} f(\Phi) \tag{2}$$

where Φ is the volume fraction. Figure 1 shows $f(\Phi)$ for different theories. Each of the theories shown reproduces the LSW-theory in the limit of $\Phi \to 0$. For increasing volume fractions the theories predict an increasing coarsening rate. The higher the volume fraction, the closer the particles are together leading to an increasing diffusional interaction between particles and thus increasing coarsening rate. Since most theories assume spherical, separated particles the plot stops at a volume fraction of 0.3. For higher volume fractions the particles will touch each other and can no longer be spherical. Figure 2 shows the changes in the PSD with increasing volume fraction based on the theory of Tokuyama and Kawasaki[14]. The PSD become wider and more symmetric with increasing Φ. This behavior is the same for all theories.

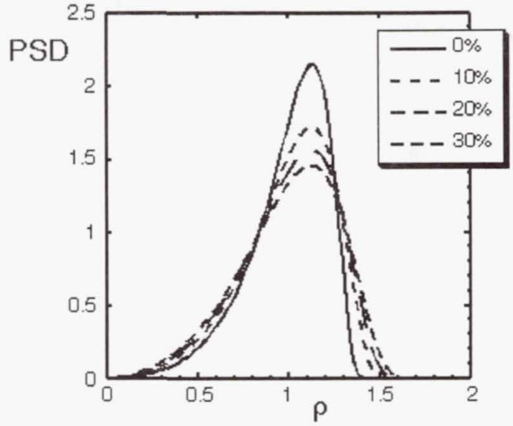

Figure 2: The PSD for different volume fractions of coarsening phase as predicted by the Tokuyama and Kawasaki theory [14]

Methods of data acquisition and analysis

Cylindrical samples of 10mm in diameter and 5mm in length were places in a sample holder plate (see figure 3) in a 3 x 3 matrix arrangement. The assembly was closed from both sides with heater plates and contained in a vacuum chamber. Each sample position in the sample holder plate was assigned to a different sample composition. The compositions of the samples were chosen to give volume fractions of solid ranging from 5% to 80% at the coarsening temperature. The experimental procedure is basically shown by figure 4: The samples are heated up to 185°C, held for a predetermined amount of time Δt, and then quenched to room temperature. This was done for different Δt. This allows the study of the coarsening behavior over time for different volume fractions of coarsening phase. During the experiments the temperature at five different locations in the sample holder plate (see figure 3) was measured and stored.

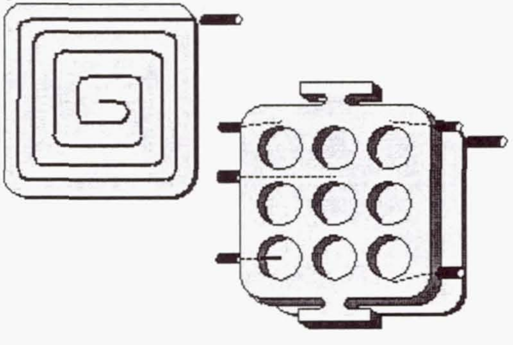

Figure 3: Sample holder plate with nine holes for the samples. Five thermistors are placed in the sample holder plate to monitor the temperature over time. Two heater plates close the assembly.

For the analysis of the microstructure the samples were cut, etched, and photographed. The cutting was done with a Reichert-Jung (Leica) Polycut E micro-milling machine. It allows the samples to be cut in predetermined steps and gives scratch-free surfaces. The etched microstructure was photographed with a digital scanning camera (Leaf Micro-Lumina) which was attached to a microscope. The pictures were taken with a resolution of ca. 2000 x 1600 pixel. In order to get a resolution of at least 100μm for a particle of average size different objectives were used. Individual images were put together to form a montage of a cross-section of a sample (see figure 5). Between 22 and 70 images were combined to give a high resolution picture of the complete cross-section. Standard image analysis routines were used for these pictures to extract the average particle size and the particle size distributions.

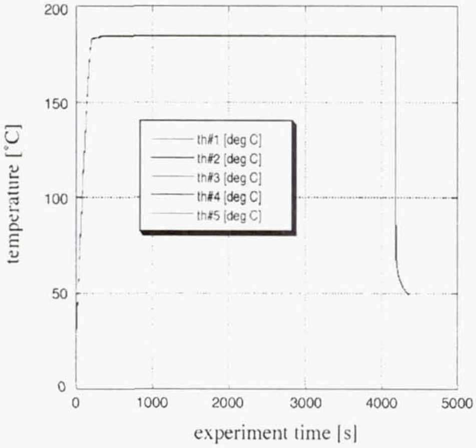

Figure 4: Temperature vs. time for one experiment. The samples were heated to 185°C (2K above the eutectic temperature), hold at that temperature for a preset amount of time and then quenched.

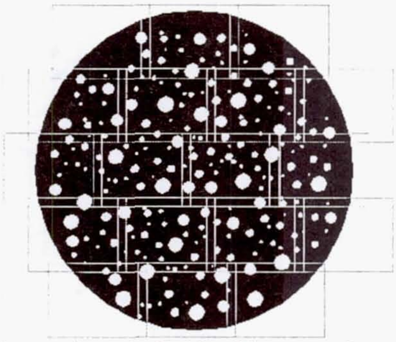

Figure 5: schematic drawing on how individual images of a cross-section were taken and later montaged to one high resolution picture of the entire cross-section.

Flight results compared with ground results

In ground based experiments the sedimentation of the Sn particles can only be avoided through the use of high volume fractions. This was done by Hardy and Voorhees [15] for different volume fractions >65%. For low volume fractions (like 10%) the sedimentation leads to a microstructure shown in figure 6a. All Sn particle are collected at the top of the sample splitting the sample into a high volume fraction region (ca. 80%) and a particle free region. In microgravity the sedimentation does not take place (figure 6b). The particles are evenly distributed throughout the sample. Valid ground data for low volume fraction samples (like 10%) does not exist for this sample system. A comparison can only be made for high volume fractions. Figure 7 shows the measured average particle sizes for the samples that have been analyzed at this time. Samples with coarsening times shorter than 545 seconds are excluded from the plot since the steady coarsening temperature had not been established for shorter times. For the samples with 10% and 20% coarsening phase equation 1 is fitted to the data giving good agreement with the experimental findings. The coarsening rates for the average particle size in the planar sections (PS) are:

$$K_{PS}(\Phi = 0.1) = 2.47 \pm 0.05\ \mu m^3/\mathrm{sec}.$$
$$K_{PS}(\Phi = 0.2) \approx 3.3\ \mu m^3/\mathrm{sec}.$$
$$K_{PS}(\Phi = 0.7) \approx 6.9\ \mu m^3/\mathrm{sec}.$$

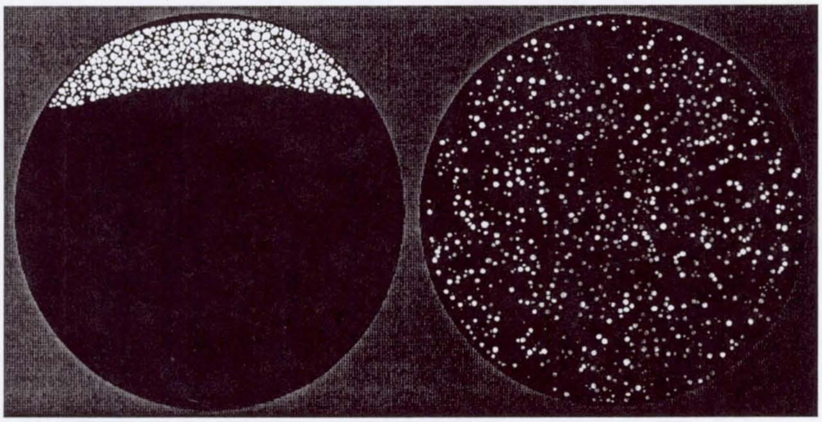

Figure 6: coarsened sample with 10% coarsening phase. The left image (a) shows a cross-section through a sample which was coarsened on ground. All Sn-particles (white) are sedimentated to the top of the sample. The right image (b) shows a sample treated the same way in space.

The values at Φ=0.7 and Φ=0.2 are rough estimates due to the limited number of data points.

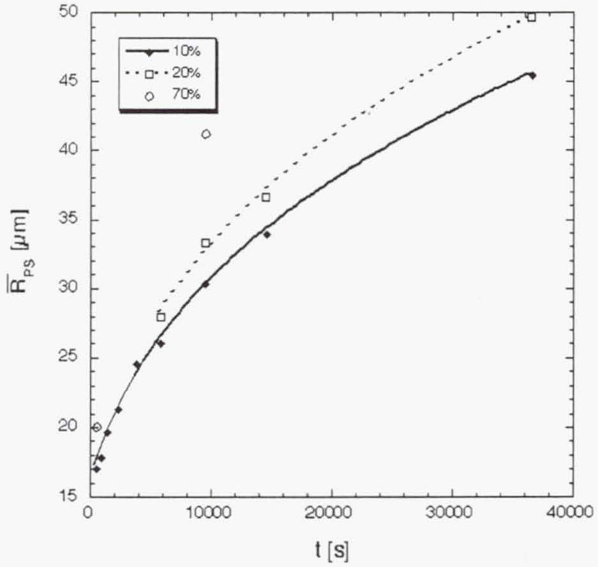

Figure 7: The average particle radii measured in planar sections for the at this time analyzed samples. The fits are done with equation 1.

Measurements of grain boundary groove experiments by Hardy *et. al.* [16] determine $K_{LSW} = 1.01\ \mu m^3/\mathrm{sec}$. Similar experiments performed as part of the CSLM experiment show a large scatter but are consistent with Hardy's results. Using the value given by Hardy we get $K(\Phi = 0.1)/K_{LSW} \approx 4.1$. This is approximately twice as high as the theories predict. Since Hardy *et. al.* used flux to reduce the oxide on the surface of the samples it is likely that this introduced impurities into the samples. These impurities may have lowered the surface tension and thus K_{LSW}. Never-the-less an agreement within a factor of two is reasonable.

Conclusions

The present results indicate the validity of the existing theories in general. They do not, however, allow us to distinguish between the different theories. This might be possible once all samples are analyzed. The coarsening rates are higher than expected. The reason is likely the uncertainty of the existing materials parameters. With respect to future plans it would be helpful to measure the materials parameters again. It is now possible to repeat the grain boundary groove experiments without the impurities which Hardy *et. al.* could not avoid. One problem encountered during the MSL-1 flight was the long time interval to reach thermal equilibrium (545 seconds). A reflight with the possibility of longer experiments will allow us to circumvent this problem.

Summary

The coarsening process of a ensemble of particles in a matrix was successfully studied. The samples are partially analyzed. The results at this point show agreement with the existing theories that describe this process to within the uncertainties of the materials parameters. A distinction between the different existing theories is not possible at this time.

Bibliography

[1] A.J. Ardell and R.B. Nicholson, J. Phys. Chem. Solids **27**, 1793-1804 (1966)
[2] P.K. Rastogi and A.J. Ardell, Acta Metallurgica **19**, 321-330 (1971)
[3] W. Bender and L. Ratke, Zeitschrift für Metallkunde **83**, 541-547 (1992)
[4] W. Ostwald, Zeitschrift für physikalische Chemie **34**, 495-503 (1900)
[5] I.M. Lifshitz and V.V. Slyozov, Journal Phys. Chem. Solids **19**, 35-50 (1961)
[6] C. Wagner, Zeitschrift für Elektochemie **65**, 581-591 (1961)
[7] N. Akaiwa and P.W. Voorhees, Physical Review E **49** (5), 3860-3880 (1994)
[8] C.W.J. Beenakker, Physical Review A **33** (6), 4482-4485 (1987)
[9] Y. Enomoto, K. Kawasaki and M. Tokuyama, Acta Met. **35** (4), 907-913 (1987)
[10] J.H. Yao, K.R. Elder, H. Guo and M. Grand, Phys. Rev. B **47** (14), 110 (1993)
[11] A.D. Brailsford and P. Wynblatt, Acta Metallurgica **27**, 489-497 (1978)
[12] S.P. Marsh and M.E. Glicksman, *Modelling of coarsening and grain growth*, TMS, Warrendale (1992)
[13] J.A. Marqusee and J. Ross, Journal of chemical Physics **80** (1), 536-543 (1984)
[14] M. Tokuyama, K. Kawasaki and Y. Enomoto, Physica **143A**, 323-338 (1986)
[15] S.C. Hardy and P.W. Voorhees, Metallurgical Transactions A **19A**, 2713-2721 (1988)
[16] S.C. Hardy, G.B. McFadden, S.R. Coriell, P.W. Voorhees and R.F. Sekerka, Journal of Crystal Growth **114**, 467-480, (1991)

MODELLING CRYSTAL GROWTH WITH MAGNETIC FIELDS

J. S. Walker
University of Illinois at Urbana-Champaign
Urbana, IL 61801
217-333-7979; jswalker@uiuc.edu

Introduction

Models have been developed for the melt motion, heat transfer and mass transport of dopants for the Bridgman and floating zone processes with both steady and rotating magnetic fields. While most modellers obtain numerical solutions of the full Navier-Stokes and energy equations, we simplify these equations by eliminating certain terms which are negligible either for strong or weak magnetic fields. Our asymptotic solutions complement the numerical solutions of the full equations. The asymptotic solutions generally require a tiny fraction of the computer time or memory needed for full solutions. Thus it is easy to treat a very large number of cases, which is important for process optimization. A good example is the buoyant convection driven by the g-jitters and other components of the residual accelerations for Bridgman crystal growth on a space vehicle. If the magnitude of the residual accelerations is less than $0.01g_o$ and there is a steady axial magnetic field with a flux density of at least 0.2T, convective heat transfer and nonlinear inertial effects are very small--certainly less than 1%. Their neglect leads to linear equations, so that the solution for any history of accelerations with chaotic g-jitters, large spikes and a DC residual acceleration, and with any time-dependent orientation, is given by the superposition of three solutions for two different unidirectional accelerations. There is a vast difference between the simplicity of the six fundamental solutions, which capture all the physical phenomena, and the generation of numerical solutions of the full equations for each acceleration history measured during each experiment in space. On the other hand, the asymptotic assumptions are not appropriate for some important experiments, and the numerical solution of the full equations is necessary. Often the two approaches have their strengths and weaknesses in complementing parameter ranges. For example, the asymptotic method may give very accurate predictions for 0.5T, have a 5% error for 0.2T, and completely miss the key physics for 0.1T. On the other hand, the numerical solution of the full equations may give very accurate results for 0.1T with only slightly more computational resources than those required without a magnetic field. However, as the field strength is increased, boundary layers become very thin, which makes the numerical solution of the full equations progressively more computationally demanding. If good results can be obtained at 0.2T, then they can be used to validate the asymptotic approach which is certainly even better for stronger magnetic fields.

Magnetic Damping of the Buoyant Convections Driven by Residual Accelerations

Models have been developed for the buoyant convections driven by residual accelerations in a Bridgman ampoule with a uniform axial magnetic field. A magnetic flux density of 0.2T is sufficient to reduce the melt velocities to such small levels that convective heat transfer and nonlinear inertial effects are negligible. As a result, the equations governing the melt motion are linear, so that accurate predictions of the melt motion for any history of residual accelerations can be obtained by the superposition of the independent solutions for (1) the steady or mean component of the residual accelerations[1], (2) g-jitters which are the random fluctuations of residual acceleration from its mean value[2,3], and (3) isolated spikes of much larger acceleration[4]. In addition the solutions for an acceleration vector whose direction is an arbitrary function of time are given by the superposition of the independent solutions for an axial acceleration and a transverse acceleration.

Magnetic Stabilization of the Thermocapillary Convections with Free Surfaces

In the floating zone process or in the Bridgman processes with the melt detached from the ampoule wall, the thermocapillary convection driven by the variations of the surface tension along the free surface is generally unstable. This instability leads to unsteady melt motions which produce undesirable striations in the crystal. A magnetic field can eliminate this instability. We have developed models for the melt motion and heat transfer in the floating zone process with an axial magnetic field[5-9] and have developed a model which predicts the minimum magnetic field strength needed to eliminate the instability[10].

Mass Transport with Magnetically Damped Melt Motions

Most previous treatments of dopant or species transport have involved the simultaneous time integration of the equations governing the melt motion, heat transfer and transport of dopants or species. Since the intrinsic time scales in these three equations differ by a factor of roughly one-thousand for most molten semiconductors and since the numerical scheme must resolve the shortest time scale associated with heat transfer, this coupled numerical integration can only simulate a few minutes of an actual crystal growth process. By recognizing that a moderately strong magnetic field reduces melt velocities sufficiently that convective heat transfer and nonlinear inertial effects are negligible, we have developed models to accurately predict the transport of a dopant during the entire period of time needed to grow a crystal[11]. The accuracy of these asymptotic models has been validated[12]. Our initial efforts have been focused on small dopant concentrations with only thermally driven buoyant convection. Our current efforts are focused on alloyed crystals where most of the buoyant convection is driven by compositional variations in the melt.

Stability of Thermoelectric Magnetohydrodynamic Flows

For most semiconductors the absolute thermoelectric powers of the solid and liquid are different. For nearly pure materials with low dopant levels a temperature variation along the crystal-melt interface can arise from the difference between the solidification temperatures for the faceted growth near the center and the atomically rough growth near the periphery. For alloyed crystals, much larger temperature variations along the interface can arise from radial variations of the mixture composition. A temperature variation along the interface and a difference between the solid and liquid absolute thermoelectric powers produces a circulation of electric current through the crystal and melt. For an axisymmetric process, these thermoelectric currents have radial and axial components. If an axial magnetic field is used to stabilize and damp the buoyant convection, the thermoelectric current in the melt interacts with the magnetic field to drive an azimuthal melt motion. The axial variations of the azimuthal velocity produce a centrifugal force which drives a secondary melt motion involving radial and axial velocities. For typical semiconductors with a strong axial magnetic field, this thermoelectric magnetohydrodynamic (TEMHD) flow involves very small radial and axial velocities, but very large azimuthal velocities. As long as the flow remains axisymmetric, it does not produce a significant change in the axisymmetric distribution of dopants or species. However, there may be an instability in the strong azimuthal flow, leading to an unsteady, nonaxisymmetric melt motion. In particular the strong azimuthal motion can be expected to generate vortices which are parallel to the magnetic field and which are convected by the azimuthal base flow. With an axial magnetic field, axial vortices act as generators on open circuit, so that the only electromagnetic damping of these vortices arises from leakage currents through the thin Hartmann layers adjacent to the crystal-melt interface and the surface parallel to it, i. e., the hot end of the ampoule or a free surface for vertical Bridgman growth or the melting end of the feed rod for the floating zone process. The vortices generated by the instability of the TEMHD flow would produce an unsteady nonaxisymmetric mass transport of dopants leading to striations in the crystal whose extent and spacing would depend on the size and convective velocity of the vortices. We have developed models for the steady, axisymmetric TEMHD flows for both the Bridgman process[13] and the floating zone process[14]. We are currently developing a linear stability analysis to determine for what magnetic field strengths the instability occurs. Unlike buoyant convection which is always stabilized by a magnetic field, the TEMHD flow is negligible for very weak magnetic fields and is stabilized by very strong magnetic fields, so that the instability only occurs for some intermediate magnetic field strengths. Some recent crystals grown by the floating zone process with a 3.0 Tesla magnetic field had a band of striations, and the scientists who grew those crystals conjectured that these striations might have arisen from an instability in the TEMHD flow. Our stability analysis will identify the range of field strengths for which the instability occurs for a given material and process and will indicate whether the observed striations could be due to this instability.

Melt Motion and Mass Transport Due to Peltier Marking

For many semiconductors, the thermal conductivity of the crystal is much less than that of the melt and is sometimes even less than that of the ampoule material. For the Bridgman process with a cylindrical ampoule, the differences in thermal conductivities may lead to a radial redistribution of the heat flux near the crystal-melt interface, and this redistribution often leads to an interface which is concave into the crystal. For the vertical Bridgman growth of alloyed or solid solution crystals, the sinking of the heavier rejected species to the center of the concave interface leads to radial variations of the solidification temperature which make the interface even more concave. Since both radial macrosegregation and large deviations from a planar interface are undesirable, much research is focused on preventing the sinking of the rejected species with a strong magnetic field and on making the interface more planar by optimizing the thermal characteristics of the Bridgman furnace. Measuring the instantaneous interface shape is a key part of experiments to achieve more planar interfaces. In the Peltier marking technique, an electric current flows axially through the crystal and melt for a very short period of time. This current changes the rate of crystal growth for this short period of time, producing a different local dopant concentration to mark the interface shape at the time of the current pulse. Without a magnetic field, Peltier marking produces a negligible effect on the mass transport of dopants and species. However, if a strong steady magnetic field is used to stabilize and damp the buoyant convection, then the brief electric current pulse interacts with the steady magnetic field to create a brief but very strong mixing in the melt near the interface. This mixing may produce a major redistribution of the rejected dopant or species from the mass diffusion boundary layer to the bulk of the melt. Since mass diffusion is very slow, the distribution of dopant or species may not return to its undisturbed state until long after the Peltier pulse. We are developing models (1) for the brief melt motion during and immediately after the Peltier pulse for the vertical Bridgman process with a strong, uniform, steady, axial magnetic field, (2) for the mass transport of species or dopants due to this melt motion, and (3) for the slow return of the dopant or species distribution to its undisturbed state after the pulse. With these models we will be able to determine the current level and duration for a Peltier pulse which will not produce macrosegregation in the crystal, and we will be able to correlate model predictions with experimental measurements for the transient mass transport after periods with predictable mixing.

Melt Motions Driven by Rotating Magnetic Fields

A periodic transverse magnetic field, which is often called a rotating magnetic field (RMF), can be used to stir the melt in order to obtain a more homogeneous crystal and may also stabilize the buoyant convection in some situations. We are currently involved in a number of modelling efforts related to the use of an RMF in the Bridgman and floating zone processes. Two key parameters are the frequency and strength of the RMF. For low frequencies, induction is negligible and the field penetrates instantly across the entire melt; for high frequencies, the field only penetrates a small distance into the melt and is confined to the skin-depth layer at the outside surface of the melt; and for intermediate frequencies, the field is highly distorted from that outside the melt and has a much smaller strength at the center of the melt. The parameter reflecting frequency is the magnetic Reynolds number, $R_\omega = \mu_p \sigma \omega R^2$, where μ_p is the magnetic permeability, σ is the electrical conductivity, ω is the circular frequency of the periodic magnetic field and R is the radius of the melt. For weak magnetic fields, the azimuthal melt velocity is much less than ωr, where r is the radial coordinate, so that the melt rotates much slower than the RMF. For this case the melt velocity is negligible in Ohm's law, so that the problem governing the RMF is decoupled from that for the melt motion, leading to sequential problems for the RMF and melt motion. For a strong magnetic field the azimuthal melt velocity is nearly equal to ωr except in boundary layers so that most of the melt motion is close to a rigid body rotation with the magnetic field. The parameter reflecting the magnetic field strength is the interaction parameter, $N = \sigma B^2 / \rho\omega$, where B is the magnetic flux density and ρ is the density. In our first study of the Bridgman process with an RMF[15], we considered a strong, low frequency RMF, i.e., $N >> 1$ and $R_\omega \leq 1$. This study showed that the crystal acts as a generator in the RMF and drives a strong electric current through the melt near the crystal-melt interface. The electric current from the crystal interacts with the RMF to accelerate the melt motion so that locally the melt rotates much faster than the RMF. This flow near the crystal-melt interface also involves nonaxisymmetric radial and axial velocities. Relative to the fixed crystal, the pattern of these radial and axial velocities rotates with the magnetic field, producing periodic convective transport of dopants or species in the mass diffusion boundary layer at twice the frequency of the field. Such a convective mass transport would produce severe rotational striations in the crystal, indicating that a strong, low-frequency RMF would lead to a very poor quality crystal. The rest of our studies of crystal growth with an RMF have considered weak magnetic fields with $N \leq 1$ and various values of R_ω. A transverse magnetic field introduces an intrinsic deviation from axisymmetry. For a weak field, previous researchers have universally assumed that the melt cannot respond to the nonaxisymmetric part of the electromagnetic (EM) body force produced by the RMF, and only treated the steady, axisymmetric melt motion driven by the azimuthal average of the EM body force. If the melt velocity is normalized by ωr, then the leading terms in an asymptotic expansion for $N << 1$ are $\mathbf{v} = N^{1/2}\mathbf{v}_a(r,z) + N\mathbf{v}_n(r,\theta,z,t) + O(N^{3/2})$, where r,θ,z are cylindrical coordinates and t is time. Here $\mathbf{v}_a$ is the steady axisymmetric velocity treated by all previous researchers. We have developed the first model for the unsteady, nonaxisymmetric perturbation $\mathbf{v}_n$ for a weak RMF. Even though it is mathematically a small perturbation of the steady axisymmetric flow, it may be very important for two reasons. First the ratio of the orders of the two flows $N^{1/2}$ is not particularly small for $B =$ 0.05 - 0.1 Tesla and a typical Bridgman process with 50 or 60 Hz. Second the azimuthal component of $\mathbf{v}_a$ is typically around one. However the radial and axial components only arise from the axial variations of the centrifugal force associated with the azimuthal component, and these axial variations are often confined to thin Ekman layers adjacent to the top and bottom boundaries, so that the radial and axial components are often quite small. Thus the numerical values of the radial and axial components of $\mathbf{v}_a$ are generally small, while the numerical values of the radial and axial components of $\mathbf{v}_n$ are always close to one because this is intrinsically nonaxisymmetric. Thus the dimensional radial and axial velocities in the unsteady nonaxisymmetric flow may actually be as large or larger than those in the steady axisymmetric flow, and these components of velocity are the important ones in the mass transport of dopants and species. In another study we are assuming that N is sufficiently small that the melt motion is negligible in Ohm's law, and we have developed a more efficient method to compute the periodic magnetic field and EM body force in the melt for moderate or large values of R_ω[16]. This method couples finite-difference numerical solutions for the field in the melt to analytical solutions for the field in the non-conducting solid and gas between the melt and the multiphase inductor producing the RMF. In our final current study we are solving for the melt motion for $R_\omega >> 1$.

Magnetic Damping of Free Surface Motions Driven by Residual Accelerations

For the floating zone process or the Bridgman process with the melt detached from the ampoule wall, the residual accelerations of the space vehicle will drive motions of the free surface. Without a magnetic field, these motions might be quite violent with deleterious effects on the crystal. A steady magnetic field provides strong electromagnetic dissipation of the kinetic energy generated by the residual accelerations. For the random g-jitters, this dissipation dramatically limits the displacements of the free surface, particularly near natural vibrational frequencies of the liquid column. For spikes of large residual acceleration, the magnetic field increases the rate of decay of the motion created by the spike. In our first model we are treating the motion of the free surface of a cylindrical liquid column due to random g-jitters with a uniform magnetic field parallel to the axis of the undeformed liquid column.

References

1. Ma, N., Homan, K. O., Walker, J. S., Physics of Fluids, 9(9), 2789 (1997).
2. Ma., N., Walker, J. S., Physics of Fluids, 8(4), 944 (1996).
3. Ma, N., Walker, J. S., J. Thermophysics & Heat Transfer, 11(2), 212 (1997).
4. Ma, N., Walker, J. S., Physics of Fluids, 9(4), 1182 (1997).
5. Morthland, T. E., Walker, J. S., J. Crystal Growth, 158, 471 (1996).
6. Morthland, T. E., Walker, J. S., Int. J. Heat & Mass Transfer, 40(14), 3283 (1997).
7. Morthland, T. E., Walker, J. S., J. Crystal Growth, 174 159 (1997).
8. Morthland, T. E., Walker, J. S., J. Fluid Mechanics, 345, 31 (1997).
9. Morthland, T. E., Walker, J. S., J. Thermophysics & Heat Transfer, 11(4), 588 (1997).
10. Morthland, T. E., Walker, J. S., J. Fluid Mechanics (1998).
11. Ma, N., Walker, J. S., J. Crystal Growth, 172, 124 (1997).
12. Ma, N., Walker, J. S., J. Crystal Growth, 180, 401 (1997).
13. Khine, Y. Y., Walker, J. S., J. Crystal Growth, 183, 150 (1998).
14. Khine, Y. Y., Walker, J. S. Submitted to J. Fluids Engineering.
15. Walker, J. S., J. Crystal Growth (1998).
16. Martin Witkowski, L., Marty, Ph., Walker, J. S., Submitted to J. Computational Physics.

PROCESS-PROPERTY-STRUCTURE RELATIONSHIPS IN COMPLEX OXIDE MELTS

Richard Weber and Paul Nordine
Containerless Research, Inc.
Evanston, IL 60201-3149
Phone: 847/467-2678
email: weber@containerless.com

Introduction and Background:

Investigation of process-property-structure relationships in high temperature liquids is essential to a scientific understanding of the liquid state and technological advances in liquid-phase processing. This research is concerned with the effects of processing variables on the behavior and properties of molten oxides. It uses containerless experimental methods to eliminate container-derived contamination, allow equilibration with controlled $p(O_2)$ atmospheres, and avoid heterogeneous nucleation by container walls to access highly non-equilibrium liquids.

Research during the first two years (June 1996-June 1998) included investigation of binary alumina-silica (Al_2O_3-SiO_2) and alumina-yttria (Al_2O_3-Y_2O_3) materials. Strong emphasis has been placed on investigation of the alumina-yttria compositions because they form melts which display an anomalous increase in viscosity when they are undercooled [1]. The alumina-yttria system is a promising candidate for low gravity experiments to measure the melt viscosity, investigate liquid phase transitions, and investigate the onset of increased viscosity in the liquid. Low gravity experiments are being developed in a separate Flight Definition project.

Accomplishments to date which are described in detail in this report were to:

1. Investigate liquid-phase processing, undercooling, and solidification of binary alumina-silica and alumina-yttria materials as a function of composition, ambient $p(O_2)$, and thermal history.

2. Investigate the anomalous increase in the viscosity observed in deeply undercooled melts.

3. Measure the enthalpy of solution of compounds formed by containerless cooling of melts and determine the enthalpy of vitrification of YAG.

4. Characterize processed materials using optical and scanning electron microscopy and X-ray diffraction analysis.

5. Develop collaborative research activities in the area of processing oxides.

6. Publish and present results.

Experimental Methods:

The compositions investigated were 40.0-90.0 mole% alumina with 10-60 mole% silica and 61.5-79.0 mole % alumina with 21.0-38.5 mole% yttria. Binary alumina-yttria materials with erbium and neodymium oxide substituted for yttrium oxide were also investigated. Spheroidal specimens *ca.* 0.3 cm. in diameter were made by laser hearth melting of high purity oxide powders [2]. The specimens were levitated in an aero-acoustic or aerodynamic levitator in argon, oxygen or metered gas mixtures [3]. Levitated specimens were heated with a cw CO_2 laser beam. Progress of the melting experiments was observed optically or with a video camera and the specimen temperature was measured using optical pyrometry.

Results:

1. Liquid-Phase Processing Experiments

Containerless processing enabled glass formation from binary alumina-silica compositions containing up to 72 mole% aluminum oxide. Compositions close to that of mullite, $Al_6Si_2O_{13}$, readily formed glass at cooling rates of approximately 200°C/s.

Compositions centered around yttrium aluminum garnet (YAG, $Y_3Al_5O_{12}$) followed different solidification paths depending on the process conditions. Melts processed in oxygen undercooled by 800-900°C and spontaneously crystallized to form YAG, or undercooled by 600-650°C and spontaneously crystallized to form a mixture of yttrium aluminum perovskite ($YAlO_3$) and aluminum oxide. Crystallization of YAG was favored if the liquid was superheated by >200°C above the equilibrium melting point for a sufficient period of time.

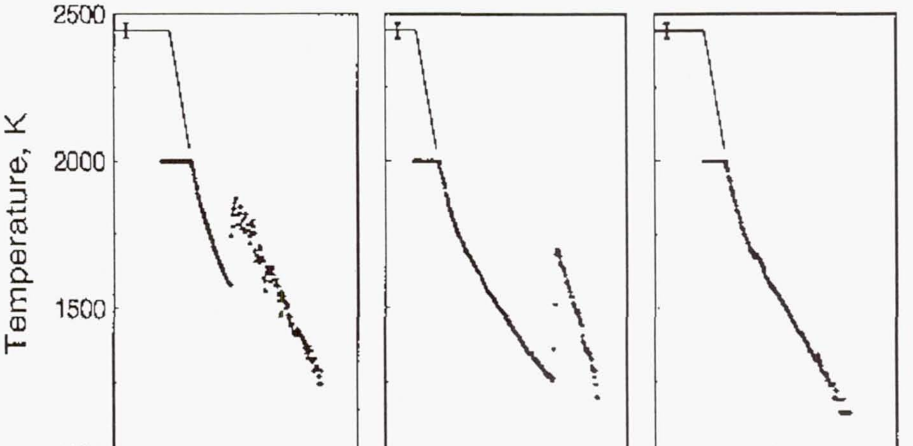

Figure 1. Cooling curves for liquid of the $Y_3Al_5O_{12}$ composition. The materials were levitated, melted, superheated and cooled under containerless conditions. Left - metastable

crystallization; center - crystallization to form YAG; right - glass formation. Solidification occurs rapidly in melts which crystallize suggesting that the liquid has low viscosity.

Stoichiometric $Y_3Al_5O_{12}$ melts processed in argon also crystallized, but formed glass if they contained a small excess of alumina or some neodymium substituted for yttrium [4]. However, glass of the stoichiometric composition could also be formed in argon at the much larger cooling rates achieved in fiber pulling experiments.

Materials containing 0.21 to 0.24 molar fraction yttrium oxide crystallized to form a mixture of yttrium aluminum perovskite and aluminum oxide [4]. Analysis of alumina-yttria phase diagrams [5,6] suggests that the solidification follows metastable extensions of the alumina and perovskite liquidus lines. The higher melting point alumina-rich phase forms first and then an extremely fine-grained mixture of perovskite and alumina fills the core of the drop. Figure 2 shows a scanning electron micrograph of a section near to the edge of a specimen containing 0.24 molar fraction yttrium oxide.

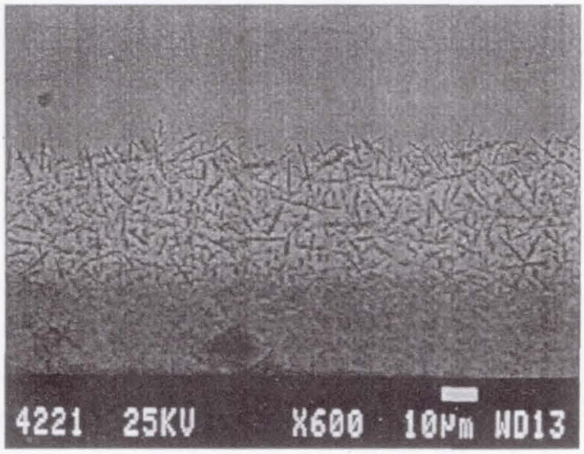

Figure 2. Scanning electron micrograph of the region near to the edge of a specimen containing 24 mole% Y_2O_3. Solidification initiated at the cooler surface of the specimen and proceeded by precipitation of aluminum oxide (dark needles). The core of the spheroid is composed of an extremely fine-grained mixture of $YAlO_3$ and Al_2O_3. A centrosymmetric void (not shown) was formed due to shrinkage of the liquid as it solidified. From the dimensions of the void, the volume decrease during solidification was estimated to be 6%.

2. Investigation of Melt Viscosity

Demonstration of glass formation for the YAG-composition shows that the viscosity of the melt increases significantly when it is undercooled. The increased viscosity of the liquid required to form glass prompted experiments to pull fibers from the undercooled melt to establish the viscosity at intermediate temperatures [1].

Figure 3 presents data on the viscosity of molten YAG as a semi-log plot of viscosity *vs* the ratio of the glass transition and absolute temperatures. The plot is based on a glass transition temperature for YAG (black square) of 1273 K. The range of viscosities shown for fiber pulling was taken to be that typically used for glass fiber manufacture, i.e. $10^{2.5}$ to $10^{3.5}$ Poise

[7] marked by the boxed region. The data for the viscosity of molten YAG at temperatures close to its melting point (near to Tg/T = 0.55) is from Fratello and Brandle [8].

The lines in Figure 3 confirm that molten YAG is an extremely fragile glass former [9] with the onset of increased viscosity occurring in the undercooled liquid at temperatures approximately 600°C below the melting point.

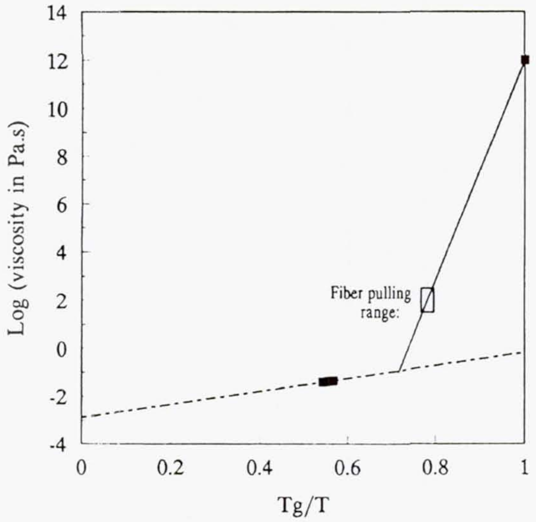

Figure 3. Log viscosity *vs.* Tg/T for YAG-composition liquid. (This figure is substantially as in Ref. [1]).

The results provide new insight into the temperature dependence of viscosity of a fragile liquid. The large crystallization velocity of the YAG-composition melts (see Figure 1) suggests the crystallization process was not inhibited by a high melt viscosity in experiments where crystalline phases were formed. In these experiments, the melt viscosity seems to be consistent with the values extrapolated from high temperature data. However, the ability to pull fibers indicates that the undercooled melt can attain much higher values of viscosity under some conditions and ultimately form glass.

3. Enthalpy Measurements on Metastable Materials

Drop solution calorimetry experiments were performed on processed materials by Dr. I-Ching Lin and Professor Alexandra Navrotsky at Princeton University [10]. We conclude that formation of the yttrium aluminum garnet phase is thermodynamically favored over a mixture of perovskite and alumina: the enthalpy for the reaction, $3\ YAlO_3 + Al_2O_3 = Y_3Al_5O_{12}$ is $\Delta H^\circ_{298} = -32.14 \pm 5.52$ kJ/mol. However, perovskite is observed to form from the undercooled melt due to kinetic limitations on attaining the garnet structure. The enthalpy of vitrification of the garnet form was calculated to be 276.47 ± 5.38 kJ/mol or 13.82 ± 0.27 kJ/g.atom. The heat of fusion of YAG was estimated to be 516 kJ/mol.

4. Characterization of Processed Material

Processed materials were examined by a variety of analytical techniques. Scanning and optical microscopy were used to investigate the morphology of bulk specimens after processing. X-ray diffraction analysis was used to determine the lattice parameters and identify crystalline phases.

5. Collaborative Research

This project has helped to develop collaborative research on the processing and properties of oxide materials with scientists at Arizona State University, Marshall Space Flight Center, Northwestern University, Princeton University, and the University of Illinois Urbana-Champaign.

6. Publication and Presentation of Results

Results were prepared for submission to peer reviewed journals and presented at international conferences, workshops, and seminars.

Plans:

The goal of the ongoing research is to understand the nature of changes in undercooled molten oxides which lead to the onset of increased viscosity. Several avenues will be pursued including: (i) further investigation of effects of ambient oxygen pressure and dopants, (ii) investigation of melt viscosity using drop oscillation techniques, (iii) investigation of the structure of undercooled molten YAG using containerless techniques in combination with synchrotron radiation, and (iv) *in-situ* measurements of the vapor species as a function of composition and process conditions to determine the component activity variations that occur in the liquid.

References:

1. J.K.R. Weber, J.J. Felten, B. Cho and P.C. Nordine, "Glass Fibers of Pure and Erbium or Neodymium-Doped Yttria-Alumina Compositions," Nature, **393**,769-71(1998).

2. J.K.R. Weber, J.J. Felten and P.C. Nordine, "New Method for High Purity Ceramic Synthesis," Rev. Sci. Instrum., **67**, 522-24 (1996).

3. J.K.R. Weber, "The Status of Containerless Processing for Materials Research and Development," Proceedings "In Space '96", Tokyo, Japan, Nov. 11-12, 1996, pp. 91-118.

4. J.K.R. Weber, B. Cho, A.D. Hixson, J.J. Felten and P.C. Nordine, "Undercooling and Solidification of Molten Al_2O_3-Y_2O_3 Mixtures ," in preparation.

5. G.T. Adylov, G.V. Voronov, E.P. Mansurova, L.M. Sigalov and E.M. Urazaeva. "Phase Diagram of Y_2O_3-Al_2O_3," Russ. J. Inorg. Chem., **33**, 1062-63 (1988).

6. I. Warshaw and R. Roy, "Stable and Metastable Equilibria in the System Y_2O_3-Al_2O_3 and Gd_2O_3-Fe_2O_3," J. Am. Ceram. Soc., **42**, 434-38 (1959).

7. K.L. Loewenstein, The Manufacturing Technology of Continuous Glass Fibres, Elsevier, Amsterdam (1973).

8. V.J. Fratello and C.D. Brandle, "Physical Properties of a $Y_3Al_5O_{12}$ Melt", J. Cryst. Growth, **128**, 1006 (1993).

9. C.A. Angell, "Formation of Glasses from Liquids and Biopolymers," Science, **267**, 1924 (1995).

10. I-C. Lin, A. Navrotsky, J.K.R. Weber and P.C. Nordine, "Thermodynamics of Glass Formation and Metastable Solidification of Molten $Y_3Al_5O_{12}$," J. Non Cryst. Sol., submitted May 1998.

MICROGRAVITY STUDIES OF LIQUID-LIQUID PHASE TRANSITIONS IN UNDERCOOLED ALUMINA-YTTRIA MELTS

Richard Weber and Paul Nordine
Containerless Research, Inc.
Evanston, IL 60201-3149
Phone: 847/467-2678
email: weber@containerless.com

Introduction and Background:

The scientific objective of this research is to increase the fundamental knowledge base for liquid-phase processing of technologically important oxide materials. The experimental objective is to define precise conditions and hardware requirements for microgravity flight experiments to test and expand the experimental hypotheses that:

1. Liquid phase transitions can occur in undercooled melts by a diffusionless transformation.

2. Onset of the liquid phase transition is accompanied by a large change in the temperature dependence of viscosity.

Recent experiments on undercooled YAG ($Y_3Al_5O_{12}$)-composition liquid demonstrated a large departure from an Arrhenian temperature dependance of viscosity. Fibers were pulled from melts undercooled by *ca.* 600° indicating that the viscosity is on the order of 100 Pa·s (1000 Poise) at 1600 K [1]. This value of viscosity is 500 times greater than that obtained by extrapolation of data for temperatures above the melting point of YAG [2]. YAG is known to be a very "fragile" glass former [3-5] and the fiber pulling experiments indicate that the onset of the highly non-Arrhenian viscosity-temperature relationship occurs at a temperature considerably below the equilibrium melting point of YAG.

Experimental results on undercooled alumina-yttria melts containing 24-30 mole % yttrium oxide suggest that a liquid phase transition occurs at rates inconsistent with diffusion limited separation processes [6]. This raises the possibility that a congruent liquid phase transition can occur in YAG composition liquid. Molecular dynamics simulations on undercooled water also show coexistence of two liquids with the same composition but different density in the undercooled state [7]. This result lends further support to the concept that polyamorphic phase transitions can occur in metastable liquids The idea that changes in melt structure and bonding associated with liquid phase transitions in molten oxides result in large changes in melt viscosity is the principal subject of this investigation.

Approach:

The research is focused on the study of undercooled pseudo-binary alumina-yttria melts. Containerless techniques are being used to access non-equilibrium liquids and allow precise control of melt chemistry at high temperatures. Although the oxides of interest are extremely stable and exhibit only small oxygen composition changes, some properties of melts are very sensitive to the ambient oxygen pressure [8] which must be controlled in order to investigate subtle effects in liquid oxides.

Properties which are being investigated are the onset and kinetics of phase transitions in the liquid and the viscosity of the undercooled liquid as a function of the temperature. The deeply undercooled molten oxides may become partially transparent so that the interior of the specimen can be observed *in-situ* to study the onset and kinetics of phase transitions, nucleation and growth.

Earth-based research is being performed under conditions that meet some of the experimental constraints to provide the design basis for microgravity experiments. Containerless experiments using aero-acoustic (AAL) [9] and electrostatic (ESL) [10] levitation techniques achieve precise control of melt chemistry, access highly undercooled melts and glassy states, and control the effects of interaction with container walls on the evolution of morphology. Microgravity experiments will obtain the control of thermal gradients, density-driven segregation, and especially of fluid flow required to test the experimental hypotheses and enable measurements of melt viscosity over a wide range of conditions.

The research is being performed in three stages. In the first stage we are using the aero-acoustic levitation facility with CO_2 laser beam heating to investigate the effects of processing conditions on the compositions of interest. In these ground-based experiments, the melts are highly stirred by the aerodynamic and acoustic levitation forces and equilibrate rapidly with the process atmosphere. Evolution of liquid phases is masked by the fluid motion in the drop, which also interferes with viscosity measurements.

In the second stage, we are performing levitation melting experiments using NASA's electrostatic levitation facility. The purpose of these experiments is to investigate the effects of greater quiescence obtained in the ESL on liquid phase transition behavior and to enable investigation of viscosity measurements on the liquids by observing relaxation of drop oscillations. These experiments will be limited to small oxygen partial pressures due to the ground-based requirement for operation in a vacuum and will encounter buoyancy- and electrostatic force-driven stirring and separation effects in melts.

The third stage of the investigation is the design of space-based microgravity experiments, in collaboration with NASA flight scientists and engineers. This work may include low gravity experiments aboard parabolic airplane flights if the ESL becomes available for this purpose. The three stages of the project will be performed in parallel with the major emphasis shifting from the first to the second and third stages over the project period.

Long term microgravity conditions are needed to meet all of the experimental requirements for detailed investigation of the phase transition phenomena:

1. Access to undercooled melts with a high degree of control of melt purity, quiescence, and the ambient oxygen partial pressure.
2. Gas-liquid equilibration at the extremely slow, diffusion limited rates allowing property measurements on a time scale that is small compared to the gas liquid equilibration time.
3. Elimination of gravity effects on buoyancy-driven convection, phase growth rate, settling time, and coalescence.
4. Fully-controlled synthesis of materials for subsequent examination and analysis.

Results:

Binary alumina-yttria materials of interest in this research are well suited to experiments in the aero-acoustic levitator. The liquid has relatively high surface tension, and can be maintained as a stable droplet over a wide range of temperatures.

Experiments in the ground-based ESL require specimens with low vapor pressure since the processing is performed under dynamic vacuum and at pressures below about 10^{-5} atmospheres (1 Pa). Thermodynamic calculations show that the pressure of gaseous species formed over an ideal solution of 3 Y_2O_3 + 5 Al_2O_3 reaches about 10^{-5} atmospheres at a temperature of 2400 K, about 150 K above the melting point of YAG. The low vapor pressure of binary alumina-yttria melts allows the ESL experiments to be performed with minor or negligible changes in chemical composition due to evaporation.

Spheroidal specimens 0.2-0.4 cm in diameter were made by melting high purity oxide powders under an argon, air or oxygen gas blanket in a laser hearth melter. Commercial single crystal sapphire spheres were used for experiments on phase-pure aluminum oxide. Specimens made in the laser hearth melter were polycrystalline and typically contained cracks and fissures which formed during solidification. Melting in air or argon atmospheres resulted in translucent spheroids often with a "milky" appearance. Material melted in oxygen occasionally "fizzed" as oxygen was evolved during solidification. These specimens were dense, opaque, and usually white in color. Larger specimens were flattened on the bottom surface where they contacted the hearth. Glassy specimens were made by levitating and melting material in an argon atmosphere. Levitation experiments are being performed in the AAL to investigate effects of processing conditions on the behavior of the binary alumina-yttria materials of interest.

The results of the first ESL experiments on the oxide materials are presented in the remainder of this section. These experiments were recently performed at NASA Marshall Space Flight Center in collaboration with Dr. Mike Robinson, Dr. Jan Rogers, Mr. Larry Savage and Mr. Wolfgang Soellner. The ESL was equipped with pyrometers to measure specimen temperature, a video camera to observe progress of the experiments, and a Residual Gas Analyzer (RGA) to measure the composition of gases in the levitation chamber.

Single crystal sapphire, polycrystalline YAG and "glassy YAG" specimens of 0.2-0.3 cm diameter and weighing 15-55 mg were easily levitated at ambient temperature. Specimens were placed on a metal specimen insertion device in the ESL and "charged" by applying a potential of several kilovolts between the vertical levitation electrodes. After about 60 seconds of charging in contact with the insertion device, the specimen levitated a few millimeters above the bottom electrode. Smaller specimens tended to “overshoot” the nominal levitation position and stick to the upper electrode or were ejected from the levitator. Smooth specimens without sharp discontinuities in their surface and weighing 25-30 mg were most stable. The heating experiments were performed on this type of specimen. Once stable levitation was achieved at ambient temperature, it could be maintained indefinitely with a levitation voltage of 8-12 kV.

Preliminary heating experiments were performed using a Nd:YAG laser. Up to 60 W of laser power was focussed onto a 0.1 cm diameter region on the specimen which was either placed on the insertion device or levitated. Transparent specimens of "glassy YAG" and single crystal sapphire did not heat significantly even at maximum laser power, but polycrystalline specimens were heated to incandescent temperatures. Subsequent heating experiments used a 25 W Synrad cw CO_2 laser beam directed onto the specimen from one side. Oxides strongly absorb CO_2 laser radiation and the available power was sufficient to melt 0.25 cm diameter sapphire specimens. At the higher temperatures, the oxides also absorbed the Nd:YAG laser energy which could be used to supplement heating.

Levitation stability decreased when the solid specimens were heated. The position control system in the ESL enhanced stability and accommodated small perturbations of the specimen without loss of levitation. If heating were performed at a high rate, the specimen fell from the levitation position when it reached an apparent temperature of 450-550°C. Once a levitated specimen had been slowly heated and then cooled to ambient temperature, it could be rapidly reheated to the highest temperature previously reached without loss of levitation stability. Careful control of the heating rate allowed the temperature to be increased to the melting point of sapphire (2327 K).

The onset of melting in sapphire specimens was accompanied by a sudden increase by a factor of 10-100 in the 16 atomic mass unit signal in the RGA spectrum indicating that oxygen was evolved. At the time of the increased oxygen signal on the RGA, the specimen also lost its charge and fell from the levitation position so that complete melting was not achieved. After the melting experiment, the levitation electrodes were covered with a thin deposit in the region near to the specimen. The electrodes were carefully cleaned before levitating a new specimen.

These were among the first ESL experiments on dielectric oxide materials at high temperatures. Preliminary results show that oxide materials levitate easily at ambient temperature. At elevated temperatures stability is reduced and it is expected that special heating techniques will be required to accomplish melting of oxides.

Plans:

Considerable R&D in the area of Electrostatic Levitation and processing of materials at high temperature is in progress at NASA MSFC. The present NRA research has and will continue to support this activity at MSFC by providing oxide specimen materials, facilities for CO_2 laser heating experiments, and participation in key ground-based experiments to define the flight experiment requirements.

Major areas of activity towards the flight definition will include:

1. Perform liquid-phase processing experiments in AAL to establish melt chemistry and precise conditions required to access high viscosity liquids.

2. Analyze results of preliminary ESL experiments, design additional ESL experiments to achieve complete melting, and investigate outgassing of oxide materials during melting.

3. Evaluate requirements for control of fluid flow to achieve viscosity measurements and control of sedimentation. Identify and analyze requirements for measurements of melt viscosity in the "free" oscillation and "critically damped" regimes.

4. Investigate phase transition in deeply undercooled melts by examining materials processed in AAL and ESL experiments.

5. Prepare documentation for the Science Concept Review and Science Requirements Definition phases of the research.

References:

1. J.K.R. Weber, J.J.Felten, B. Cho and P.C. Nordine, "Glass Fibers of Pure and Erbium or Neodymium-doped Yttria-alumina Compositions," Nature, **393**, 769-71 (1998).

2. V.J. Fratello, and C.D. Brandle, "Physical Properties of a $Y_3Al_5O_{12}$ Melt," J. Cryst. Growth, **128**, 1006-1010 (1993).

3. D. Massiot, F. Taulelle and J.P. Coutures, "Structural Diagnostic of High Temperature Liquid Phases by ^{27}Al NMR," Colloque de Phys., **C5**, 425-431 (1990).

4. P.G. Debenedetti, Metastable Liquids, Concepts and Principles, Princeton University Press (1996).

5. C.A. Angell, "Formation of Glasses from Liquids and Biopolymers, Science, **267**, 1924 (1995).

6. S. Aasland and P.F. McMillan, "Density-driven Liquid-liquid Phase Separation in the Al_2O_3-Y_2O_3 System," Nature, **369**, 633 (1994).

7. S. Harrington, R. Zhang, P.H. Poole, F. Sciortino and H.E. Stanley, "Liquid-liquid Phase Transition: Evidence from Simulations," Phys. Rev. Lett., **78**, 2409-12 (1997).

8. J.K.R. Weber, S. Krishnan and P.C. Nordine, "Effects of Melt Chemistry on the Spectral Absorption Coefficient of Liquid Aluminum Oxide," J. Am. Ceram. Soc. **78**, 3067-3071 (1995).

9. J.K.R. Weber, D.S. Hampton, D.R. Merkley, C.A. Rey, M.M. Zatarski and P.C. Nordine, "Aero-acoustic Levitation - A Method for Containerless Liquid- phase Processing at High Temperatures," Rev. Sci. Instrum., **65**, 456-465 (1994).

10. A.J. Rulison, J.L. Watkins and B. Zambrano, "Electrostatic Containerless Processing System," Rev. Sci. Instrum., **68**, 2856-63 (1997).

MOLECULAR DIFFUSION IN NONEQUILIBRIUM ALLOY FILMS AND MOLECULAR MOTION IN POLYMERIC NETWORKS

J.S. Wettlaufer
University of Washington
Seattle, Washington, 98105
206-543-7224
wett@apl.washington.edu

M. Elbaum
Weizmann Institute of Science
76100 Rehovot, Israel
972-89343537
cpelbaum@weizmann.weizmann.ac.il

H.A. Stone
Harvard University
Cambridge, Massachusetts 02138
617-495-3599
has@stokes.harvard.edu

M.G. Worster
University of Cambridge
Cambridge, CB3 9EW, England
44 1223 330850
grae@esc.cam.ac.uk

Introduction

We focus on two distinct materials science problems that arise in two distinct microgravity environments: In space and *within* the space of a polymeric network. In the former environment, we consider a near eutectic alloy film in contact with its vapor which, when evaporating on earth, will experience compositionally induced buoyancy driven convection. The latter will significantly influence the morphology of the crystallized end member. In the absence of gravity, the morphology will be dominated by molecular diffusion and Marangoni driven viscous flow, and we study these phenomena theoretically and experimentally. The second microgravity environment exists in liquids, gels, and other soft materials where the small mass of individual molecules makes the effect of gravity negligible next to the relatively strong forces of intermolecular collisions. In such materials, an essential question concerns how to relate the molecular dynamics to the bulk rheological behavior. Here, we observe experimentally the diffusive motion of a single molecule in a single polymer filament, embedded within a polymer network and find anomalous diffusive behavior.

Alloy Films

Here we consider the nature of crystallization of a two component volatile liquid in a film configuration. This geometry is important for several reasons. In the limit that the film itself is thinner than the capillary length on earth, the dominant effects influencing the equilibrium configuration are molecular diffusion, surface energy and long- and short-range intermolecular interactions. These are particularly crucial near contact lines. As the film builds in thickness, the role of gravity becomes important in both equilibrium and nonequilibrium configurations. By parity of reasoning, as a thick film thins, for example by evaporation, the influence of gravity wanes. Finally, as gravity itself vanishes we can extend the spatial range over which surface energy and long range interactions influence the behavior and we restrict our treatment of compositional evolution to diffusion and surface tension driven advection. We describe first the effect of evaporation in a pure film material and then examine the influence of a solute.

From the perspective of the bulk coexistence, the evaporation of a completely wetting one-component fluid might be considered as the reversible conjugate of the wetting process. However, as was shown earlier in the research program, attractive interactions with the substrate eliminate the reversibility by stabilizing thin films against a subsaturated vapor phase, wherein the subsaturation controls the equilibrium film thickness. A nucleation process initiated by the tails of the long range substrate potential ruptures the thick film and leaves the substrate covered by a uniform thin film which is in coexistence with the subsaturated vapor, but the thin film is decorated by droplets of evaporating fluid. These droplets stand at finite (macroscopic) contact angle and hence evaporation of a pure fluid preempts the complete wetting of the substrate[1].

The addition of another component to the fluid introduces an additional thermodynamic constraint which dramatically changes the wettability and coating properties of the system. Experimental observations made on aqueous ammonium chloride[2] motivate investigation of a model system that exhibits some of the primary features of the observed morphology. Consider an incompletely wetting droplet of solution standing on a substrate at finite contact angle as pictured from above in Figure 1. The species dependent volatility of the fluid facilitates crystallization during evaporation. Crystallization appears near the contact line of the droplet which drives the material over the substrate, but with a highly ramified interfacial region near the contact line. This contrasts with the pure case wherein evaporation leads to the nonwetting of an otherwise wetting fluid. Hence, evaporation of a nonwetting alloy leads to wetting.

The process involves a host of effects not all of which can be accounted for simultaneously in simple scaling arguments much less in analytical treatments. Evaporation acts to enrich the solution and initiates solidification within. The interaction between this process, mass conservation, and the solutal Marangoni effect drives material from the interior of the droplet into the rim and over the substrate. In contrast to the vast majority of solidification systems driven by evaporation, the phase boundary moves away from the source material in a process we describe as "extended crystallization".

This complex interplay of phenomena motivates studies in which we can isolate dominant effects in idealized configurations. Common experience dictates that a bulk container of evaporating solution will eventually be populated by crystals. What is not intuitive is that the crystals will climb up the container walls. The observations in figure 1 require interpretation in terms of a continuous film covering the crystals near the contact line. As such, we first analyze the geometry of the solid/liquid interface underlying a semi-infinite thin film of solution. The structure observed is reminiscent of morphological instabilities, but because the source of impurities lies across the film, the front evolution is essentially different, akin to an activated instability.

We focus on a region of the crystal-film interface that is small relative to the characteristic variation in the vapor pressure as depicted in figure 2. Hence, the solutal Marangoni flow that will arise in this system[3] will drive fluid into the region under consideration but the variation in surface tension over the scale of this region is small. The flow itself depends only on the coordinate normal to the solid/solution interface, $u(z) = \tau z/\mu$ where $\tau = d\gamma/dx = d\gamma/dC\, dC/dx$ is the Marangoni coefficient, wherein γ is the liquid/vapor surface tension and $C=C(x,z)$ is the solute concentration. The time independent evolution of the solute field in the film of thickness H is found by solving

$$\frac{\tau}{\mu} z \partial_x C = D \partial_{zz}^2 C \;, \tag{1}$$

subject to $C(x,z=0) = C_E$ and $C(x,z=H) = C_O$ where C_E is the equilbrium interfacial concentration at the temperature of the substrate, C_O is the equilibrium concentration at the local vapor pressure of the liquid surface, and D is the solutal diffusivity. It is the variation in the vapor pressure along the surface that gives rise to the Marangoni flow and hence by allowing a weak variation in $H=H(x)$ we account for this effect. In so doing we find a similarity solution $C=\Delta C\ \mathrm{C}(\eta)$ with similarity variable $\eta = z\ (\mathfrak{D}\ x)^{-1/3}$, in terms of ordinary functions

$$C(\eta)=\frac{\Gamma\left(\frac{1}{3}\right)-\Gamma\left[\frac{1}{3},\frac{\eta^{3}}{9}\right]}{\Gamma\left(\frac{1}{3}\right)-\Gamma\left[\frac{1}{3},\frac{\eta_{H}^{3}}{9}\right]}, \qquad \text{where } \mathfrak{D}=\frac{\mu/\tau}{D\rho^{2}/Q_{m}^{2}} \text{ and } \eta_{H}=H\ (\mathfrak{D}\ x)^{-1/3}. \qquad (2)$$

The parameter $\mathfrak{D}$ is a measure of the ratio of viscous to diffusive time scales, wherein ρ is the liquid density and Q_m is the mass flux at the liquid/vapor interface. It is fortunate that the physics of the problem suggests a spatially varying thickness because equation (1) is otherwise unseparable in a finite domain in z unless the problem is solved asympotically. Analysis of this solution shows that the flow provides material that maintains a constant film thickness in a spatial region Δx in which we would like to investigate the stability of the solid/liquid interface, but that this flow has a negligible effect on the redistribution of solute within Δx. From the perspective of the solid/liquid interface, the liquid/vapor interface is the source of solute. Hence, the solute introduced into the film at the liquid/vapor interface must diffuse through the film in order to advance the solid/liquid interface and, depending on the local temperature, any solute in excess of the local value of C_E will give rise to a local supersaturation. In the thin-film limit we have found a crystallization instability driven by this process[4]. In direct analogy with the frozen temperature approximation to the Mullins-Sekerka instability, the most dangerous mode is of zero wavenumber but the wavelength selection is weak, leaving us with the possibility of many modes manifesting themselves on the growth front. Hence, we have begun to understand why the observed contact line shown in Figure 1 becomes so highly ramified.

As the initial value of the film thickness increases, two fluid mechanical phenomena become important and can therefore influence the evolution of the solidification front. The first is Marangoni flow given by equation (2) and in a zero gravity environment, this may influence the evolution of the interface by competing with the diffusive redistribution of solute. Because the flow has a large scale directionality, there is a possibility of travelling wave instabilities, for example, as has been found in directional solidification[5]. On Earth, as the film thickens compositional convection, driven by the increased density of the fluid near the solid/vapor interface, will begin. The critical conditions for the onset of compositional convection in 1 g are well described within the framework of the Oberbeck-Boussinesq equations. As gravity vanishes, the convective stability domain diverges. Therefore, we expect that in zero gravity, the film thickness alone will determine the relative importance of diffusion and Marangoni convection in influencing the nature of the solidification instability.

Molecular Motion *within* a Polymer Network

Another sort of microgravity environment exists in other soft materials such as polymer networks. The small mass of individual molecules makes the effect of gravity negligible next to the relatively strong forces of intermolecular collisions. A trivial example is that of a simple molecule in liquid solution. With a typical length scale L of 1 nm diameter and molecular weight 100, the gravitational force mgL is of order 10^{-33} N, while the thermally driven "Brownian" forces k_BT/L have the order of 10^{-12} N. Indeed this discrepancy is retained up to the scale of one micrometer, and Brownian motion plays a dominant role in the dynamics of colloidal suspensions.

The Brownian microgravity environment is characterized by unique mechanics. Battered randomly by molecular collisions, inertia is near zero and ballistic motion is impossible. Viscosity dominates so that force is proportional to velocity rather than acceleration. In the absence of bulk flows or other external forces, the motion of any single molecule or particle is diffusive, executing a random walk with mean square displacement growing linearly with time. The assumption of ideality rests on the claim that each molecule acts independently in a randomizing field of all other molecules. They do not develop significant correlations, and in bulk they are described by simple Newtonian viscosity.

In polymers and gels the nature of thermally driven motions is considerably more subtle. In addition to molecular translations, thermal energy may couple into many types of soft bulk modes. Undulations of membranes or polymer filaments are among the most important of these modes. The soft elasticity characteristic of rubbers, foams, and even many foods depends on these undulations. While these materials have a net bulk density, their internal dynamics are dominated by thermally driven fluctuations operating at any value of gravity.

Here, we take a direct look at the diffusive motion of a single molecule in a single polymer filament, embedded within a polymer network. Of course it is impossible to image and trace in time the motion of an individual molecule. Most work concerning such topics relies on spatial-averaging methods such as light scattering. Molecular motions are inferred from observations of density fluctuations.

Our approach is to tag a point on a polymer with an optically resolvable microsphere (silica bead, 0.3 μm diameter), whose motion we follow with microscopy and video analysis tools. In order to reach observable time and length scales, we exploit particular biological polymers called microtubules. These are semi-crystalline polymers of the protein tubulin, which spontaneously forms hollow tube structures 25 nm in diameter and up to hundreds of micrometers in length. In vivo, these are ubiquitous structures present in the cells of animals and plants. For our purposes, their large diameter gives them a rigidity in the optimal range for optical measurements: they are sufficiently rigid to maintain an average direction from end to end, but still flexible enough to bend and undulate under the influence of thermal motion. (Thermal energy is distributed by equipartition into bending modes, each one costing curvature energy proportional to the fourth power of its wavenumber.) In other words, the motion of the bead should reflect the undulation of the whole polymer, in contrast to the free translational diffusion it would normally make in solution.

Experimental methods include the biochemical purification of tubulin from cow brain, development of a chemical surface treatment by which to attach beads to microtubules (in preference to free tubulin in solution), differential interference contrast microscopy, optical tweezers for manipulating the tiny beads and for verifying their proper attachment, and development of particle-tracking software for video analysis. The measurements were always of the bead position as a function of time. These were accumulated into charts of mean squared displacement vs time interval, on intervals ranging from the video rate of 25 frames per second to several seconds.

The main results are interpreted as follows[6]. At "short" times, the motion of the microtubule undulations generates a mean squared displacement which grows as $t^{3/4}$, in contrast to t^{1} for ordinary translational diffusion. At "long" times, the mean squared displacement reaches a saturation. Both the saturation amplitude and the crossover time between short and long regimes depend on the density of the polymer network. Essentially, the crossing, or "entanglement" of one filament over the next limits the undulations, dividing the polymers into segments shorter than the physical length and constraining the free oscillation of the longest wavelength modes. As a control, a bead attached to a microtubule which is not entangled in a network shows only ordinary linear diffusion on the observable time scales.

An unexpected experimental result was obtained when observing a sheared network of microtubules. The beads displayed a mean squared displacement growing as $t^{1/2}$, which is interpreted as a signature of tension in the polymer filaments to which they attached. In this case thermal energy is distributed into bending modes costing energy proportional to the square of the wavenumber.

Future Plans

Our study of the alloy films will focus on two areas. Firstly, we will investigate the role of the local shear rate in the evolution of the morphological instability. We expect that for sufficiently rapid flow, the disturbance maxima will experience a different supersaturation depending on whether they are upstream or downstream of the flow. Secondly, we would like to apply more simplified models to the droplet configuration shown in Figure 1. It is possible that one can explain the essential aspects of the spreading without having to treat the complex dynamics at the contact line. Finally, we would like to begin studying the role of long-ranged intermolecular interactions on the evolution of the surface film.

The study of polymeric networks will proceed by installation of a fast position-sensitive detector to eliminate the video-rate restriction, and introduction of a probe to the local-scale rheology of the system. We are constructing a microscope-based falling-ball viscosimeter using a bead which is heavy enough to sediment by gravity through networks of microtubules of various mesh densities. We will use the system to investigate the fluctuations in the falling bead's decent as a signal to its interaction with the network. We will then move to a network of microtubules crosslinked by smaller adhering beads, again focusing on the local-scale rheology seen by the individual particle.

References

1. M. Elbaum & S.G. Lipson, *Phys. Rev. Lett.* **72** 3562-5 (1994); M. Elbaum, S.G. Lipson, & J.S. Wettlaufer, *Europhys. Lett.* **29**, 457-62 (1995); *ibid*, **39**, 342-4 (1997).

2. R. Du & H.A. Stone, *Phys. Rev. E* **53**, 1994-7 (1996).

3. S.A. Lowry et al., *J. Cryst. Growth* **96**, 774-6 (1989).

4. J.S. Wettlaufer & H.A. Stone, *Bull. Am. Phys. Soc.*, **41** 1723 (1996).

5. Forth & A.A. Wheeler, *J. Fluid Mech.* **202**, 339-66 (1989).

6. A. Caspi, M. Elbaum, R. Granek, A. Lachish & D. Zbaida, *Phys. Rev. Lett.* **80**, 1106-9 (1998); *Bull. Am. Phys. Soc.*, **43** E13 .14 (1998).

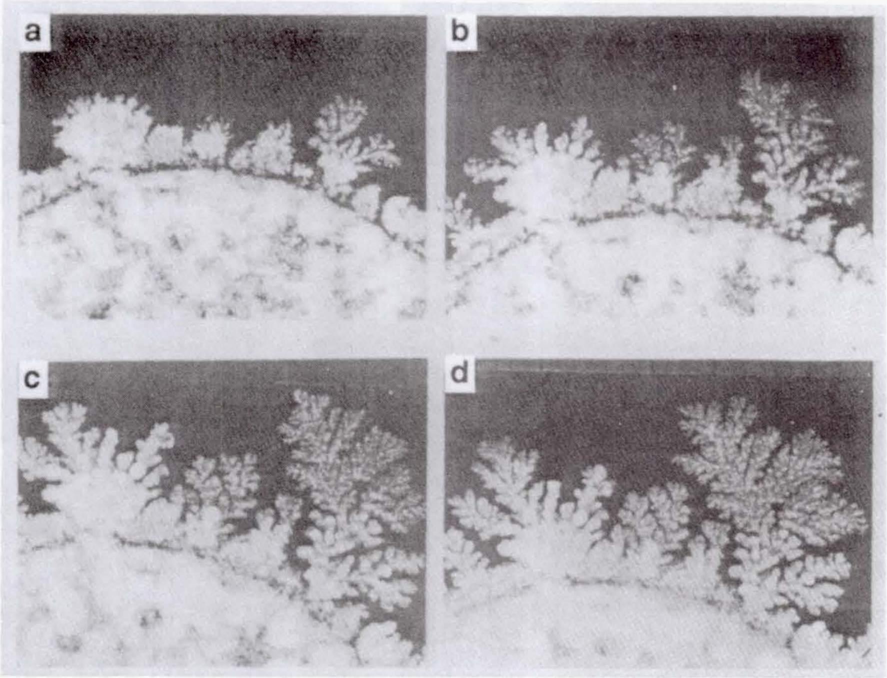

Figure 1. A droplet of aqueous ammonium chloride solution is initially placed on a petri dish in a subsaturated environment at room temperature. The droplet sits with a finite contact angle in equilibrium and begins to evaporate and crystallize. Each photograph is taken from above at equally spaced intervals, progressing from a to d, over a 24 hour period. The dark regions at the top of each photograph clearly distinguish the unwetted plastic substrate from the crystallization front.

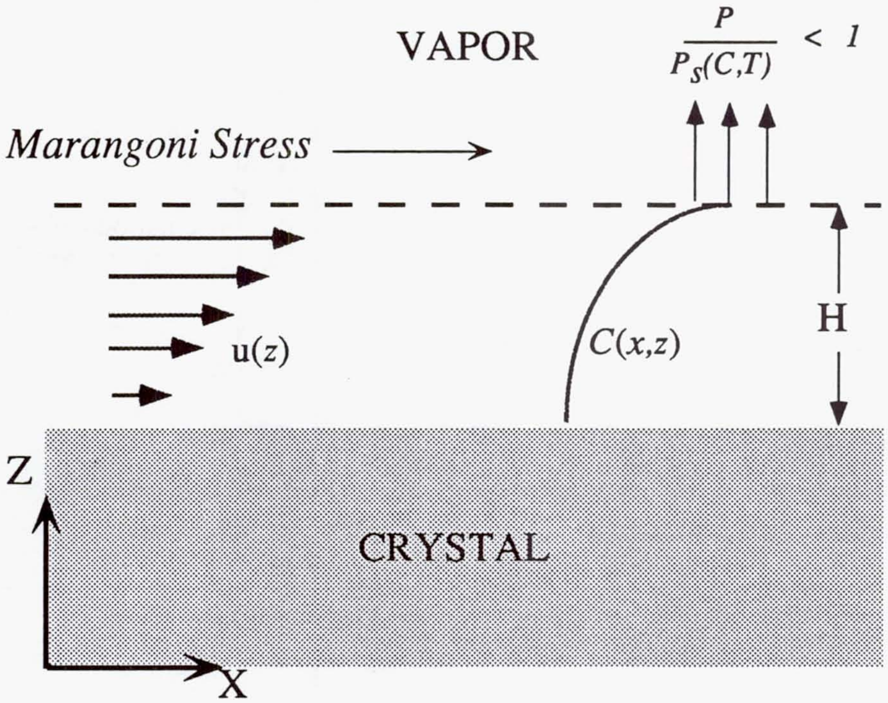

Figure 2. Schematic of the system. A solution film of thickness H overlies a crystal. The vapor pressure is lowered below saturation, $P_S(C,T)$ and it begins to evaporate. The increase in composition C is responsible for (a) supersaturation of the film and (b) a compositional Marangoni Stress driving a flow u(z).

Defect Generation in CVT Grown $Hg_{1-x}Cd_xTe$ Epitaxial Layers Under Normal and Reduced Gravity Conditions

H. Wiedemeier and Y.R. Ge
Department of Chemistry
Rensselaer Polytechnic Institute
Troy, NY 12180-3590

In order to optimize the infrared detector properties of the alloy-type semiconductor $Hg_{1-x}Cd_xTe$ in electronic devices, a high degree of compositional and structural microhomogeneity of the single crystals of this material is required. Therefore, a better understanding of the crystal growth properties and ultimate control of the defect formation are of basic scientific importance and of technological significance.

Earlier ground-based studies of the epitaxial growth of $Hg_{1-x}Cd_xTe$ on (100) CdTe substrates by chemical vapor transport demonstrated the effects of gravity-driven convection on the growth morphology and crystallinity of this material. These observations suggested that epitaxial layers of improved microhomogeneity could be grown under reduced gravity conditions.

The combined results of our First United States Microgravity Laboratory (USML-1) and Second United States Microgravity Laboratory (USML-2) experiments confirmed the above expectations and yielded $Hg_{1-x}Cd_xTe$ epitaxial layers on CdTe of significantly improved compositional and structural microhomogeneity and electrical properties relative to ground test samples. They also confirmed the considerably lower dislocation density of the $Hg_{1-x}Cd_xTe$/CdTe layer/substrate interfaces of the layers and islands. The time dependence of the morphological evolution of the growing layer and the coalescence of islands to layer reveal the inherent transient growth properties of this heterojunction system under normal and reduced gravity conditions. The combined observations show the influence of gravity-related phenomena on fluid flow at or near the growth interface.

The present investigation is concerned with the further elucidation of fluid flow interactions with deposition and growth processes. It is generally known that the compositional and structural uniformity of single crystalline layers are affected by the crystallographic orientation (off-orientation) and surface quality of the substrates, by the growth rate and temperature, and by annealing. The combined influences of these parameters on crystal growth and quality are most likely interrelated, yielding a rather complex mechanism of defect formation. The decoupling of the various origins of defect formation and their control represent major challenges in the field of crystal growth.

As a step towards these goals, new research under this project is concerned with the investigation of substrate orientation (misorientation) effects on epitaxial growth of $Hg_{1-x}Cd_xTe$ layers on CdTe. Emphasis in these studies is on the morphological evolution of the growing layers during the transient growth period of this heterojunction system. In order to correlate the results of the present investigations with those of previous epitaxial growth of $Hg_{1-x}Cd_xTe$ on (100) CdTe on ground and in microgravity, the same temperature profile, source material composition, and transport agent pressure are used.

Therefore, the effects of substrate misorientation on $Hg_{1-x}Cd_xTe$ epitaxial film growth by chemical vapor transport are being studied, for the first time, using a transient growth technique. For this purpose, (100) CdTe substrates with a misorientation of 3° towards $[0\bar{1}1]$ and growth periods of different duration are employed. The morphological evolution of the $Hg_{1-x}Cd_xTe$ films deposited on the vicinal CdTe substrates shows a transition from three-dimensional islands to two-dimensional layer growth. This trend is similar to that observed for films deposited on (100) CdTe substrates. However, there are distinct differences in the details of the surface morphology between the epitaxial growth on the vicinal and on (100) CdTe substrates. These differences include the edge morphology of individual islands, and, in particular, the formation of a long-range terrace structure of the films grown on the vicinal CdTe substrates. The formation of the terraces is related to corresponding morphological developments at the layer/substrate interface as reflected by the {011} cross-sections of this system. The pronounced terrace morphology is a direct result of the substrate misorientation, and approaches the planar surface structure of the films grown on regular (100) CdTe substrates after an extended growth time and layer thickness. In addition to the above, small differences of the surface composition and of the growth rate relative to those observed for the growth on regular (100) substrates reveal the influences of the 3° misorientation of the (100) CdTe substrates on the heteroepitaxial growth of $Hg_{1-x}Cd_xTe$. The combined results show that the interface kinetics are not fixed in the transient regime and that they are coupled to the vapor mass transport processes.

In order to further elucidate the effects of vicinal (100) CdTe faces on epitaxial growth and defect formation, investigations are in progress employing CdTe substrates with smaller misorientations than 3° from the (100) crystallographic orientation. The objectives of these studies are to correlate the morphological observations with the step density on the substrate surface, which, in turn, can be related to the degree of misorientation.

As part of the systematic investigation of the effects of substrate orientation on epitaxial growth, the transient properties of $Hg_{1-x}Cd_xTe$ film growth on (111)B CdTe substrates are being studied under vertical stabilizing and destabilizing orientations of the density gradient with respect to the gravity vector. Although the (111)B CdTe face is crystallographically quite different from the (100) and vicinal (100) faces, results to date indicate similar transient behavior of the epitaxial growth on these faces. Present data reveal measurable effects of small convective flow disturbances on the growth morphology and defect formation of this heterojunction system.

The combined results of this investigation will provide quantitative experimental data useful for the decoupling of the interactions of gravity-driven convection with surface related phenomena.

Vapor Growth of Alloy-Type Semiconductor Crystals

H. Wiedemeier, Y. R. Ge and M. A. Hutchins
Department of Chemistry
Rensselaer Polytechnic Institute
Troy, New York 12180-3590

The advantages of vapor phase techniques are very useful for the growth of high-quality $Hg_{1-x}Cd_xTe$ bulk crystals and epitaxial layers. Because of the greatly different vapor pressures of the constituents of $Hg_{1-x}Cd_xTe$, the chemical vapor transport method is employed, allowing the use of a single source material of predetermined composition in a closed container. This technique is particularly suitable for crystal growth under space flight conditions.

Extensive ground-based studies of the bulk growth and heteroepitaxy of $Hg_{1-x}Cd_xTe$ on CdTe by CVT revealed the sensitivity of this complex, ternary, alloy-type growth system to possibly even minute convective effects under vertical, stabilizing conditions. They also demonstrated the inherent transient properties of this heterojunction system. The influences of the initial compositional and structural microhomogeneity on the electrical properties of layers are observed. These observations strongly suggested measurable effects of microgravity on vapor phase crystal growth of this material. The growth of $Hg_{1-x}Cd_xTe$ epitaxial layers by chemical vapor transport on (100) CdTe during the First United States Microgravity Laboratory (USML-1) (6.4 and 8.1 hr growth) mission showed significant improvements in the crystallinity of the substrate/layer interface, of the epitaxial layer and of the surface morphology relative to ground samples. These observations indicated the effects of residual convective flow at or near the interface on crystal growth on ground. The morphological improvements of the space-grown layers are reflected in the considerably increased carrier mobilities.

In order to further elucidate the effects of fluid flow on deposition and layer growth during the transient period of this system, the Second United States Microgravity Laboratory (USML-2) mission experiments were performed for shorter growth periods (1.5 and 2.5 hr growth). This required further ground-based experiments concerning the necessary temperature-time-line conditions. The emphasis in these studies was on the observation of microgravity effects on layer growth under transient, non-steady-state conditions. The objectives included the observation of the coalescence of three-dimensional islands to two-dimensional layers, measurements of the compositional and structural uniformity, and of the electrical properties of the islands and layers grown in microgravity. The USML-1 and USML-2 experiments and ground-based studies represent the first investigations of transient crystal growth properties under normal and reduced gravity conditions.

The comparative analysis of the ground and USML-2 results showed significant differences. The as-grown surface morphology of the islands and epitaxial layer obtained in microgravity is considerably flatter relative to ground specimens. The compositional microuniformity (IR mapping) and the single crystallinity (etching, X-ray diffraction rocking curves) of the islands and epitaxial layer grown in space are measurably enhanced. These improvements yield carrier mobilities of the materials deposited under microgravity conditions which are greater by a factor of two than those of ground specimens. The significantly improved crystallinity of the space-grown substrate/layer interface relative to that of ground samples shows that any annealing effects during longer growth times (USML-1 experiments) are small.

The combined observations of the USML-1 and USML-2 experiments demonstrate the effects of even small convective flows on the growth processes of this multi-component, multi-reaction, low pressure, solid-vapor transport system. The morphological investigations of the substrate-layer interfaces (heterojunctions) strongly suggest that the formation and propagation of defects is influenced by gravity-related processes during the very initial period of deposition. The combined results show the effects of microgravity on the chemical and structural homogeneity during the transient period. These findings are of general importance for heteroepitaxial growth, independent of the particular growth method employed.

USE OF MICROGRAVITY TO CONTROL THE MICROSTRUCTURE OF EUTECTICS

William R. Wilcox and Liya L. Regel
Clarkson University, Potsdam NY 13699-5814 (wilcox@agent.clarkson.edu)
Reginald W. Smith, Queen's University, Kingston, Ontario

Introduction

The long term goal of this project is to be able to control the microstructure of directionally solidified eutectic alloys, through an improved understanding of the influence of convection.

Prior experimental results on the influence of microgravity on the microstructure of fibrous eutectics have been contradictory [1,2]. Theoretical work at Clarkson University showed that buoyancy-driven convection in the vertical Bridgman configuration is not vigorous enough to alter the concentration field in the melt sufficiently to cause a measurable change in microstructure when the eutectic grows at minimum supercooling. Currently, there are four other hypotheses that might explain the observed changes in microstructure of fibrous eutectics caused by convection:

1. Disturbance of the concentration boundary layer arising from an off-eutectic melt composition and growth at the extremum.
2. Disturbance of the concentration boundary layer of a habit-modifying impurity.
3. Disturbance of the concentration boundary layer arising from an off-eutectic interfacial composition due to non-extremum growth.
4. A fluctuating freezing rate combined with differences in the kinetics of fiber termination and fiber formation.

We favor the last of these hypotheses. Thus, the primary objective of the present grant is to determine experimentally and theoretically the influence of a periodically varying freezing rate on eutectic solidification. A secondary objective is to determine the influence of convection on the microstructure of at least one other eutectic alloy that might be suitable for flight experiments.

Influence of Electrical Current Pulsing on the Microstructure of MnBi-Bi Eutectic (Fengcui Li)

Previously, we had performed a few ground-based experiments using electric current pulses to deliberately create an oscillatory freezing rate [1,2]. Although the MnBi rod spacing appeared to increase with increasing current, we were not confident of the results because the freezing rate or pulsing conditions were varied during each experiment. With such experiments, it is difficult to be certain of the conditions under which each portion of the resulting ingot froze. Thus, we are currently performing a more thorough study in which the conditions are held constant for the duration of each experiment. New image analysis techniques were developed to yield detailed statistical information on the microstructure from numerous scanning electron micrographs. Thus far, 15 ingots have been solidified and analyzed under these conditions. The microstructures without current pulsing and at the lowest current consisted of fine, quasi-regular, semi-triangular MnBi rods. As the current was increased, increasing portions of each cross sectional slice showed other areas of less regular fibers, broken lamellae, large irregular MnBi, or completely absent of MnBi. We have confined our analysis of the microstructure to the areas showing the quasi-regular rods. The nearest neighbor distance was determined for each rod. With one exception, the standard deviation ranged from 33% to 38% of the mean nearest neighbor distance λ. The 95% confidence limits were very small compared to λ. The kurtosis and skewness were appreciable compared to the standard deviation, indicating moderate deviations from the usual bell-shaped normal distribution. Without current pulsing, the value of λ^2V was nearly the same for three different ampoule lowering velocities V. Figure 1 shows λ versus current amplitude for two different freezing rates and three different current pulsing conditions. For all conditions, λ decreased as current was increased. Note that a constant current (without pulsing) caused no significant change in λ. An alternate method of characterizing fiber spacing is to measure the fiber density ρ, i.e. the number of fibers per unit area. The values of $\rho^{-1/2}$ parallel the results shown in Figure 1, but are about 50% larger. Figure 2 shows the average percent of the cross sectional area that is MnBi. This appears to increase slightly with increasing current. (The run showing the exceptionally high value of %MnBi also exhibited an exceptionally large standard deviation for nearest neighbor distance, about 56% of the mean.)

Flight Experiments (Fengcui Li)

Originally, we had planned to fly experiments on Mir using QUELD, the Canadian gradient-freeze furnace that is installed in the Microgravity Isolation Mount (MIM). The MIM is capable of introducing controlled vibrations into an apparatus, as well as actively reducing vibrations. We had planned to take advantage of this capability. Unfortunately, because of the problems with Mir these experiments have been delayed, probably permanently. Twenty-four ampoules containing MnBi-Bi eutectic were prepared for these experiments. Several of these ampoules will be solidified at Queen's University in a ground-based copy of QUELD. We plan to determine the influence of growth rate perturbations, either by periodic mechanical shocks or heater power variations.

Influence of Accelerated Crucible Rotation on Al-Si Microstructure (Ram Ramanathan)

Experiments are underway on directional solidification of the Al-Si eutectic at different freezing rates, with and without application of accelerated crucible rotation to induce convection.

Theory of Eutectic Solidification with an Oscillatory Freezing Rate (Dimitri Popov)

For the first time, theoretical methods were developed to analyze eutectic solidification with an oscillatory freezing rate. Both a classical sharp-interface model and a phase field model are being used. A paper demonstrating the application of phase field methods to periodic structures was submitted for publication [3].

One-sided sharp-interface method. This method is based on the solution of heat and mass transfer equations separately in each phase. These solutions are connected at the freezing interface using the boundary conditions for flux conservation and continuity of temperature and concentration. At steady state with a constant freezing rate, the composition field near the interface depends on the distance d by which one phase leads the other. For both lamellar and rod eutectics, as d increases, the composition along the interface moves farther from the eutectic for both leading and trailing phases. The composition near the trailing phase becomes more uniform as d increases.

We imposed temperature fluctuations in the melt in order to generate an oscillatory freezing rate. Under some conditions there is an amplification of the amplitude of the freezing rate oscillations due to oscillations of temperature, especially if the kinetic coefficient is high. The spatially averaged composition at the interface of each phase was calculated and integrated over one period of freezing rate oscillations after the initial transient had decayed. The difference between this composition and that for a steady freezing rate was calculated and represents the excess amount of rejected component ahead of the growing phase due to freezing rate oscillations. The frequency dependence of the spatially averaged composition reveals the same high-frequency cut-off for all values of d. With increasing d, the difference in composition from the eutectic increases, as can be seen in Figures 3 and 4. That is, there is a higher supersaturation ahead of each growing phase. We believe that this high degree of supersaturation may provoke nucleation of the other phase. Therefore, a large d would be favorable for development of a finer microstructure due to freezing rate oscillations. Figure 5 shows how the concentration difference from the eutectic would diminish after nucleation of new rods or lamellae that make λ smaller.

Phase-field method. In order to be able to track the interface dynamics, particularly where the three phases (melt, α solid and β solid) come together, we initially chose the phase-field method. The governing equations were formulated using two phase-field parameters, functions of temperature and concentration. First, the necessary accuracy in the calculations of the concentration in the bulk of the phases was achieved for one dimension and one solid phase, providing the correct solution for the interfacial region. A simple lamellar eutectic structure was calculated at a constant freezing rate. As shown in Figure 6, the interface shape and the composition field ahead of the interface agree with the classic model of Jackson and Hunt. A fluctuating freezing rate and concentration ahead of the interface were obtained as a response to temperature fluctuations in the melt. The concentration change lags behind the interface velocity fluctuation, as in the one-sided model. With an oscillatory freezing rate, the majority phase tends to grow at the expense of the minority phase, and under some conditions even chokes it off and makes λ larger.

Thus we have mechanisms that can both increase and decrease λ. The challenge remains to incorporate those mechanisms in a single computational model.

Acknowledgment

We are grateful to Barbara Facemire for her interest and for arranging use of the supercomputer at Marshall Space Flight Center. This research is supported by Grant NAG8-1266.

References

1. W.R. Wilcox and L.L. Regel, Microgravity Quarterly 4, 147-156 (1994).
2. W.R. Wilcox and L.L. Regel, Acta Astronaut. 38, 511-516 (1996).
3. D.I. Popov, L.L. Regel and W.R. Wilcox, "Fourier Collocation and Fourier Galerkin Methods applied to the Phase-Field Model of Two-Dimensional Phase Transition Problems," J. Physics D: Applied Physics (submitted).

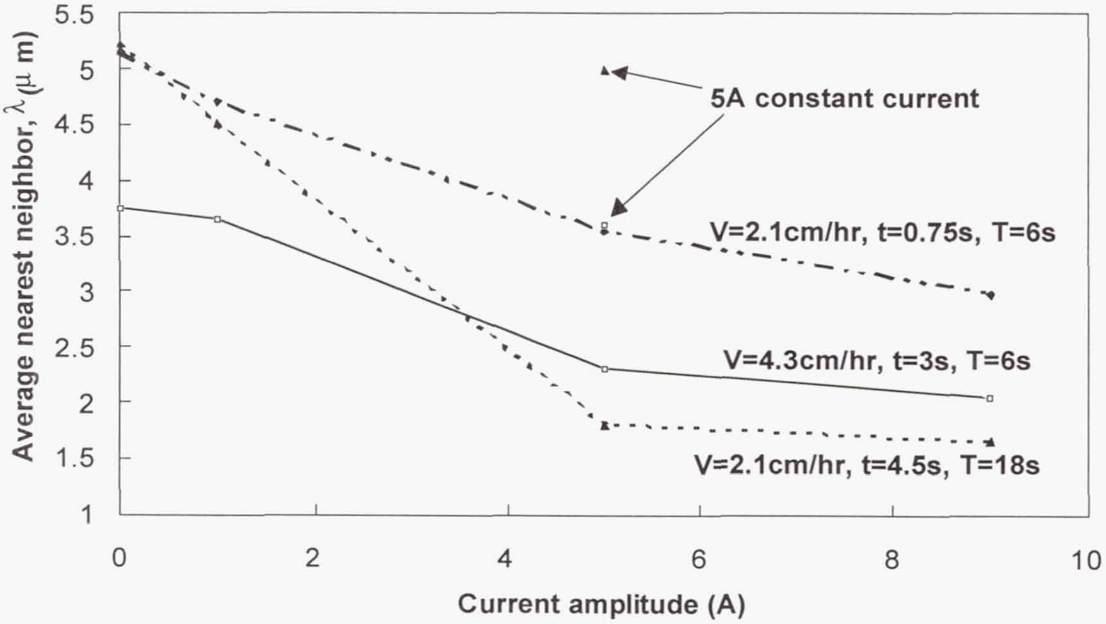

Figure 1. Average nearest neighbor distance λ of quasi-regular MnBi rods versus current amplitude, ampoule translation rate V, time t during which current is passed through the sample, and period T of current pulses. Note the two data points for a constant current of 5A (no pulsing).

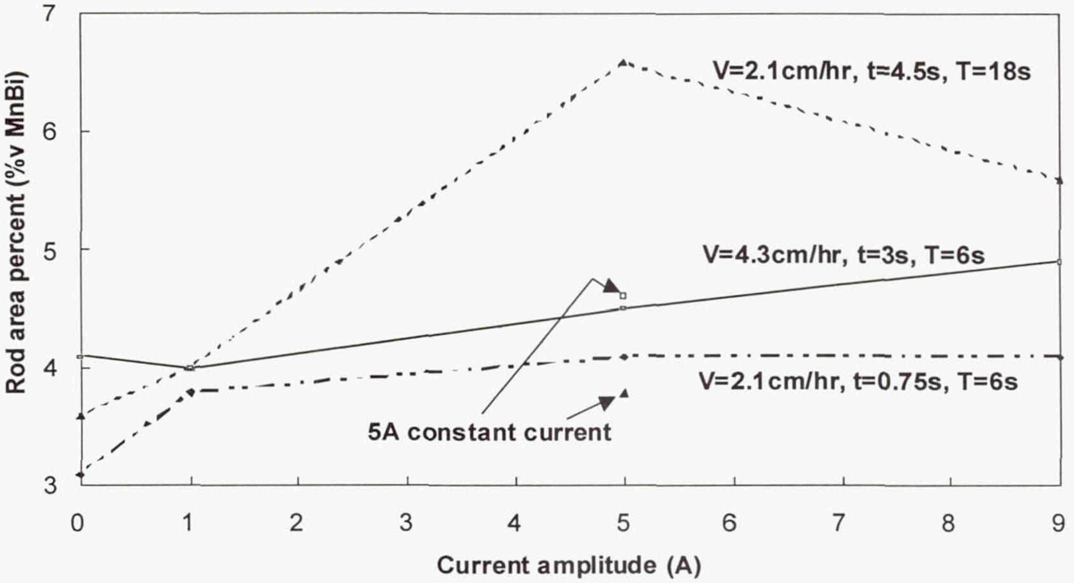

Figure 2. Average percent of the SEM quasi-regular areas that is MnBi fibers. Here V is the translation rate of the ampoule, time t during which current is passed through the sample, and period T of current pulses. Note the two data points for a constant current of 5A (no pulsing).

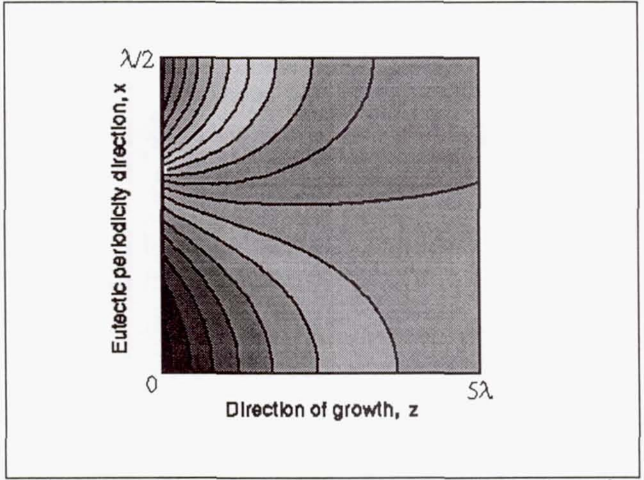

Figure 3. Composition field at an instant of time near the planar interface of a lamellar eutectic, freezing with an oscillatory rate. This solution was obtained using a sharp interface model.

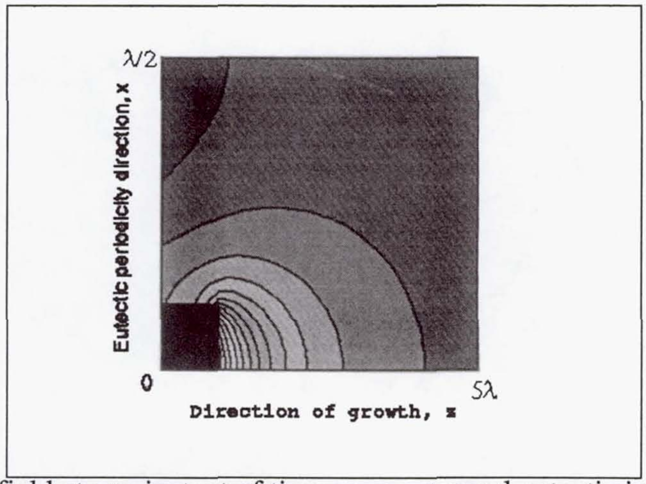

Figure 4. Composition field at one instant of time near a stepped eutectic interface, freezing with an oscillatory rate, from the sharp interface model.

Figure 6. Eutectic solidification at constant rate, modeled with the phase-field method. The α-phase has a large concentration of A (white), β has a low concentration of A (black), and the melt is at the eutectic (intermediate) concentration. Note the zones of rejection of the alien components (A rejected by β, and B rejected by α).

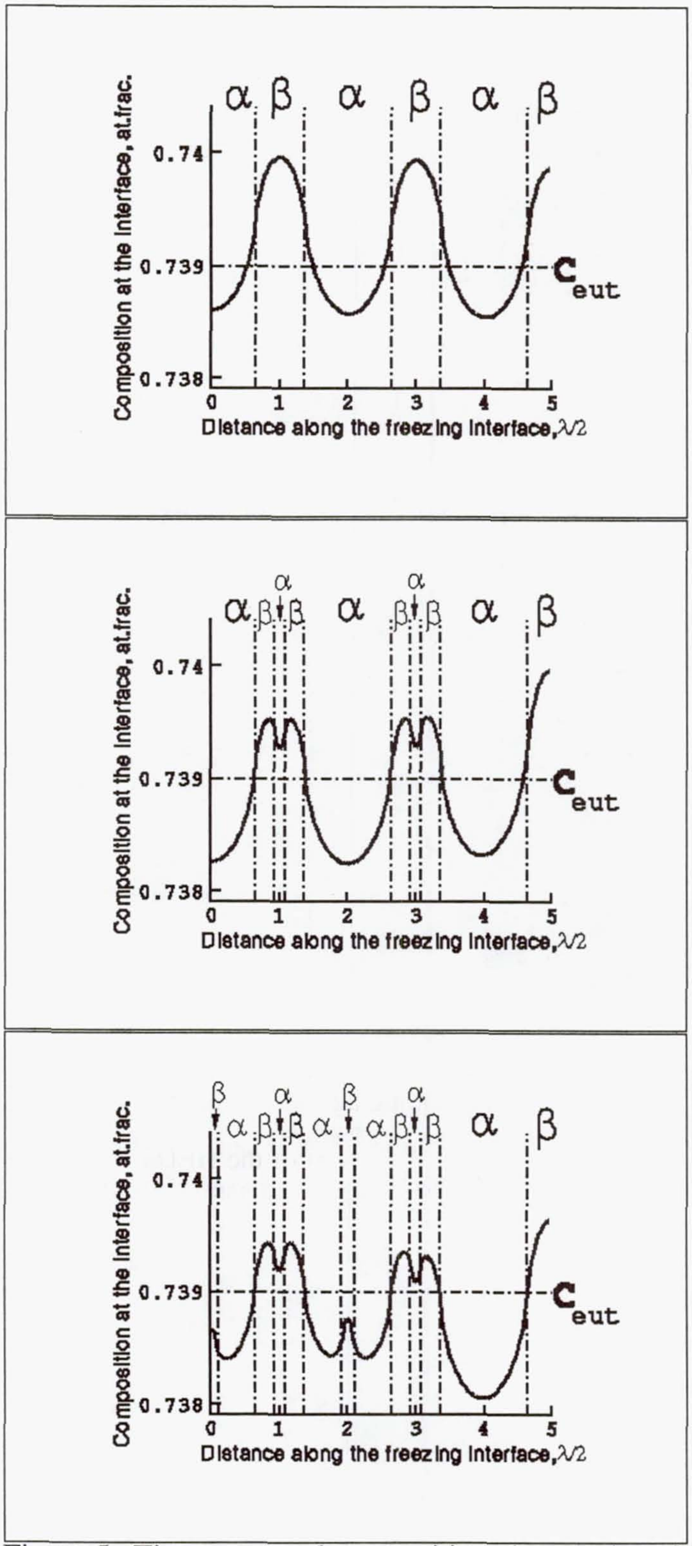

Figure 5. Time-averaged composition along an interface with an oscillatory freezing rate.
(a) – Initial state, before nucleation
(b) – After nucleation of new β
(c) – After the additional nucleation of new α

IMPROVED SPACECRAFT MATERIALS FOR RADIATION SHIELDING

J. W. Wilson,
J. L. Shinn,
R. C. Singleterry,
H. Tai,
S. A. Thibeault,
L. C. Simonsen
Ms 188B
NASA Langley Research Center
Hampton, VA 23681-0001
757-864-1414 john.w.wilson@larc.nasa.gov

F. A. Cucinotta
Ms SN3
NASA Johnson Space Center
Houston, TX 77058
281-483-0968 , francis.a.cucinotta1@jsc.nasa.gov

J. Miller
DOE Lawrence Berkeley National Laboratory
Berkeley, CA 94720
510-486-7130, miller@lbl.gov

Introduction

Solar particle events and galactic cosmic rays have the potential of producing serious radiation health effects in astronauts in the Human Exploration and Development of Space (HEDS) enterprise[1-4]. Solar particle events (SPEs) consist mainly of modest energy protons (below a few hundred MeV). Galactic cosmic rays (GCR) consist of high energy particles comprised mainly of protons but also include multiply charged ions (nuclei of chemical elements) through U with only small contributions above Ni. The SPE protons of 30 to 120 MeV are most important to astronaut exposures and fluence levels above 10^8 p/cm^2 will limit astronaut activity on rare occasions for a period of several hours to few days. A storm shelter from such events must be provided[5]. The GCR pose an ever-present low level background radiation and have great penetrating power through shield materials. The GCR ions of high charge and energy (HZE) are few in number but dominate the estimated cancer risk to astronauts in deep space[3,4,6]. The intensity of these ions must be reduced while holding secondary radiations to a minimum within the spacecraft interior where the astronaut spends most of his time[7,8]. Unlike the provision of a SPE storm shelter, shielding required against GCR is needed at all times during the mission and greatly impacts mission costs as the shielding of such a large living/work area requires a large mass of material[8]. Of course, the provision of such a large mass for GCR shielding tends to mitigate the SPE storm shelter requirement. The GCR HZE transmission characteristics of shield materials are poorly understood and the estimated excess Mars mission cost[8] for shielding against the GCR due to uncertainty in shield estimates is between \$10B and \$30B. Thus, the provision of shielding from the GCR HZE particles at minimum mission cost is a critical element of the HEDS enterprise. Unless there are cost effective means developed to protect the astronaut, there will be no HEDS missions beyond the geomagnetic field[9].

The insufficient understanding of HZE particle induced risk to astronauts is a basic challenge to shield material studies at this time. Cancer induction is related to mutational events in the cell which have been studied in mammalian cell systems as a guide to the effectiveness of HZE particle cancer induction[10,11]. There also exist data from HZE induction of harderian gland tumors in mice for which models have been derived[12]. These radiobiological models will be used as indicators for the rate of cancer risk attenuation as a function of materials selection and thickness[13]. The second challenge in seeking optimum shielding materials is that models for the nuclear interaction processes (fragmentation and secondary particle production cross sections) required for shield evaluation are not entirely developed and validated[8]. Therefore, laboratory testing of material transmission characteristics is an essential component of any materials development program. In the testing area, it is impossible to test all materials against all ions in the GCR environment due to the large number of ion types and their broad energy spectrum. Testing is limited to a few dominant ions at the most important energies. Sixty percent of the astronaut cancer risks are from the ions of C, O, Mg, Si, and Fe (with an added 30 percent from the other HZE ions and only about 8 percent from GCR protons)[14]. These five dominant ions will be the focus of laboratory testing in the most important energy range between 500 MeV per nucleon and 2000 MeV per nucleon. Such transmission tests require a complex diagnostic apparatus to identify the particles transmitted through or produced in the shield material[15]. A unique test apparatus has been developed and operated for NASA by the Lawrence Berkeley National Laboratory for use at the Brookhaven National Laboratory (BNL) AGS accelerator facility (a unique facility within the US able to simulate the GCR HZE ion beams found in space)[15-17]. Some components produced in an external shield material are themselves biologically damaging (e. g., neutrons) and multilayered neutron absorbing materials may show advantage[7,18]. A neutron shield testing facility and computational procedures are now available at Langley for the optimization of neutron absorption properties.

In the execution of this proposal, we will first examine current and developing spacecraft materials and evaluate their ability to attenuate adverse biological mutational events in mammalian cell systems and reduce the rate of cancer induction in mice harderian glands as a measure of their protective qualities. The HZETRN code[19] system will be used to generate a database on GCR attenuation in each material. If a third year of funding is granted, the most promising and mission-specific materials will be used to study the impact on mission cost for a typical Mars mission scenario as was planned in our original two year proposal at the original funding level. The most promising candidate materials will be further tested as to their transmission characteristics in Fe and Si ion beams to evaluate the accuracy of the HZETRN transmission factors[8]. Materials deemed critical to mission success may also require testing as well as materials developed by industry for their radiation protective qualities (e.g., Physical Sciences Inc.) A study will be made of designing polymeric materials and composite materials with improved radiation shielding properties as well as the possible improvement of mission-specific materials.

Shielding Methodology

The specification of the interior environment of a spacecraft and evaluation of the effects on the astronaut is at the heart of the radiation protection problem. The Langley Research Center has been developing such techniques[2,8]. The relevant transport equations are the linear Boltzmann equations for the flux density $\phi_j(\mathbf{x}, \Omega, E)$ of type j particles as

$$\Omega \cdot \nabla\phi_j(\mathbf{x},\Omega,E) = \sum\int \sigma_{jk}(\Omega,\Omega',E,E')\,\phi_k(\mathbf{x},\Omega',E')\,d\Omega'\,dE' - \sigma_j(E)\,\phi_j(\mathbf{x},\Omega,E) \tag{1}$$

where $\sigma_j(E)$ and $\sigma_{jk}(\Omega,\Omega',E,E')$ are the media macroscopic cross sections. The $\sigma_{jk}(\Omega,\Omega',E,E')$ represent all those processes by which type k particles moving in direction Ω' with energy E' produce a type j particle in direction Ω with energy E. Note that there may be several reactions which produce a particular product, and the appropriate cross sections for equation (1) are the inclusive ones. The total cross section $\sigma_j(E)$ with the medium for each particle type of energy E may be expanded as

$$\sigma_j(E) = \sigma_{j,at}(E) + \sigma_{j,el}(E) + \sigma_{j,r}(E) \tag{2}$$

where the first term refers to collision with atomic electrons, the second term is for elastic nuclear scattering, and the third term describes nuclear reactions. The microscopic cross sections and average energy transfer are ordered as follows:

$$\sigma_{j,at}(E) \sim 10^{-16}\ \text{cm}^2 \quad \text{for which } \Delta E_{at} \sim 10^2\ \text{eV} \tag{3}$$

$$\sigma_{j,el}(E) \sim 10^{-19}\ \text{cm}^2 \quad \text{for which } \Delta E_{el} \sim 10^6\ \text{eV} \tag{4}$$

$$\sigma_{j,r}(E) \sim 10^{-24}\ \text{cm}^2 \quad \text{for which } \Delta E_r \sim 10^8\ \text{eV} \tag{5}$$

This ordering allows flexibility in expanding solutions to the Boltzmann equation as a sequence of physical perturbative approximations. It is clear that many atomic collisions ($\sim 10^6$) occur in a centimeter of ordinary matter, whereas $\sim 10^3$ nuclear coulomb elastic collisions occur per centimeter. In contrast, nuclear reactions are separated by a fraction to many centimeters depending on energy and particle type. Special problems arise in the perturbation approach for neutrons for which $\sigma_{j,at}(E) \sim 0$, and the nuclear elastic process appears as the first-order perturbation.

As noted in the development of equation (1), the cross sections appearing in the Boltzmann equation are the inclusive ones so that the time-independent fields contain no spatial (or time) correlations. However, space- and time-correlated events are functions of the fields themselves and may be evaluated once the fields are known[20,21]. Such correlations are important to the biological injury of living tissues. For example, the correlated release of target fragments in biological systems due to ion or neutron collisions have high probabilities of cell injury with low probability of repair resulting in potentially large relative biological effectiveness (RBE) and quality factor[22]. Similarly, the passage of a single ion releases an abundance of low energy electrons from the media resulting of intense fields of correlated electrons near the ion path.

The solution of equation (1) involves hundreds of multi-dimensional integro-differential equations which are coupled together by thousands of cross terms and must be solved self-consistently subject to boundary conditions ultimately related to the external space environment and the geometry of the astronaut's body and/or a complex vehicle. In order to implement a solution one must have available the atomic and nuclear cross section data. The development of an atomic/nuclear database is a major task in code development.

Transport Coefficients

The transport coefficients relate to the atomic/molecular and nuclear processes by which the particle fields are modified by the presence of a material medium. As such, basic atomic and nuclear theories provide the input to the transport code data base. It is through the nuclear processes that the particle fields of different radiation types are transformed from one type to another. The atomic/molecular interactions are the principal means by which the physical insult is delivered to biological systems in producing the chemical precursors to biological change within the cells. The temporal and spatial distributions of such precursors within the cell system governs the rates of diffusive and reactive processes leading to the ultimate biological effects. The transport coefficients are developed under a related project described in a separate paper in these proceedings[23].

Transport Solution Methods

The solution to equation (1) can be written in operational form as $\phi = G\ \phi_B$ where ϕ_B is the inbound flux at the boundary, and G is the Green's function which reduces to a unit operator on the boundary. A guiding principle in radiation-protection practice is that if errors are committed in risk estimates, they should be overestimates. The presence of strong scattering terms in equation (1) provides lateral diffusion along a given ray. Such diffusive processes result in leakage near boundaries. If ϕ_Γ is the solution of the Boltzmann equation for a source of particles on the boundary surface Γ, then the solution for the same source on Γ within a region enclosed by Γ_o denoted by $\phi_{\Gamma_o}(\Gamma)$ has the property

$$\phi_{\Gamma_o}(\Gamma) = \phi_\Gamma + \varepsilon_\Gamma \tag{7}$$

where ε_Γ is positive provided Γ_o completely encloses Γ. The most strongly scattered component is the neutron field for which an 0.2 percent error results for infinite media in most practical problems[2]. Standard practice in space radiation protection replaces Γ as required at some point on the boundary and along a given ray by the corresponding Γ_N evaluated for normal incidence on a semi-infinite slab. The errors in this approximation are second order in the ratio of beam divergence and radius of curvature of the object[2], rarely exceed a few percent for space radiations, and are always conservative. The replacement of Γ by Γ_N as a highly accurate approximation for space applications has the added advantages that Γ_N is the natural quantity for comparison with laboratory simulations and has the following properties: If Γ_N is known at a plane a distance x_o from the boundary (assumed at the origin), then the value of Γ_N at any plane $x \geq x_o$ is

$$G_N(x) = G_N(x - x_o)\ G_N(x_o) \tag{8}$$

Setting $x = x_o + h$, where h is small and of fixed-step size gives rise to the marching procedures of HZETRN.

Evaluation Of Shield Effectiveness

Our prior survey of current and developing spacecraft materials will be updated and ordered according to hydrogen content per unit mass and then number of electrons per unit mass as an indicator of shielding effectiveness. The HZETRN code system will be used to evaluate the transmission of GCR through each material as a function of the material's areal density (a parameter related to total shield mass) and the rate of attenuation of adverse biological effects using four bioresponse models (cancer risk using LET-dependent quality factors, Harderian gland tumors in mice, neoplastic transformation in mice cells, and mutations in hamster cells). The materials will then be ordered according to their effectiveness per unit mass in reducing the biological hazard. Since aluminum is a current standard material for spacecraft construction, special emphasis will be given to the relative benefit of various aluminum alloy systems and aluminum matrix composites. The most promising aluminum based material systems, polymer systems, and the most promising polymer composite systems will be used in target testing at the BNL AGS facility. The targets will be prepared by the Materials Division of Langley Research Center for laboratory testing of their shield material's transmission characteristics.

Materials Database

The choice of materials will be guided as follows. Since aluminum alloys are still the primary construction technology in the space program, we will study the effects of added alloy components as to their protective qualities. For example, the Cu additive to aluminum alloy will lessen the shielding effectiveness whereas Al-Li alloy systems will have improved shielding characteristics. Aluminum metal matrix composites are favorable depending on the fiber used and boron fibers in particular may show some advantage since they absorb low energy neutrons which are always produced as a secondary reaction product. However, the boron fibers with tungsten cores need careful evaluation as the tungsten will be a strong source of secondary radiations. Neat polymers have already shown important advantages in their radiation protection properties and can be ordered in their protective abilities according to their hydrogen content although there has been little laboratory testing. The use of *in situ* polymer manufacturing and regolith composites will be examined as a mission cost effective means of habitat construction. Polymer matrix composites could be an important alternative to many aluminum based structures with anticipated improved radiation protective properties. We will examine the effects of fiber choice on protective properties as well as of polymer content. The protective value of the fibers are expected to be ordered from least effective to most effective as glass, graphite, boron, Kevlar, and polyethylene fibers. In addition, materials identified as part of mission critical elements, such as inflatable lay-ups, regolith augmentation, and consumables, will be evaluated. Materials available for habitat construction on the Martian surface will be examined. All of the materials will be quantified as to their protective abilities and trade studies in the third year will be made on the most promising materials to evaluate their effect on mission costs in the context of current uncertainty in HZE cancer risks factors.

Preliminary Transmission Characterization Tests

Water and polyethylene both satisfy the requirements of good shielding properties (High electron density and large nuclear cross section per unit mass) and have been used as targets in a number of different measurements. We discuss the 510 MeV/nucleon ^{56}Fe ion beams on CH_2 target measurements.

Transmission of Fe ions in polyethylene

The fragmentation of 510 MeV/nucleon ^{56}Fe in polyethylene was measured[16] and compared[17] to transmission properties based on the NUCFRG2 nuclear fragmentation model[24] in figure 1. The agreement between data and model is good, but the model's underprediction of the heavy fragment yield indicated that it could be improved, particularly in its treatment of nuclear structure effects. Also, in this case the uncertainties in both data and model were

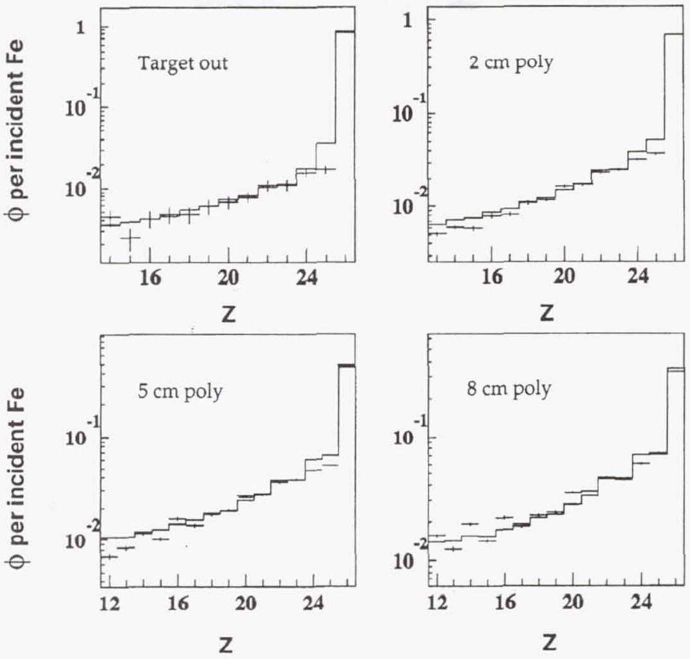

Figure 1. Comparison of measured fragment production by 510 MeV/nucleon ^{56}Fe in CH_2 with a model calculation (solid line histogram), as described in the text and in ref. [24].

small enough that the effects of higher order fragmentation could be studied. It was found that at least two generations of fragments must be included for the model transmission functions to accurately reproduce the data[2].

Validation Testing

The validity of the predicted transmission properties will be tested in the Fe and Si ion beams at the BNL AGS accelerator in the first two years. Added beam testing with C,O, and Mg beams may be accomplished in the third year. Detection systems to measure projectile fragmentation are typically of small to moderate size, depending upon the angular range covered. Figure 2 is a schematic of a detector configuration which our group has used to measure the fragmentation of 1.08 GeV/nucleon ^{56}Fe in a variety of materials at the Brookhaven National Laboratory Alternating Gradient Synchrotron (AGS)[16]. A series of solid state detectors record the energy deposited by charged particles traversing them. Convoluting the energy losses in two or more detectors makes it possible to calculate the particle's charge and energy. The solid state detector stack was augmented by plastic scintillation counters to measure the time of flight between two points. This information is needed to supplement the energy loss information in the case of the lighter charged particles.

Each individual particle event seen by the detector system is recorded during the accelerator test and off line analysis codes are used to extract information about the transmitted particle composition. Some correction to the data is required to account for multiple scattering effects for which particles are lost from the detector system.

The interactions of the high energy ions produce very penetrating secondary neutrons in the shield materials for which special inner layers of neutron absorbing materials may be placed. A fast neutron testing laboratory has been established at Langley to validate the absorption properties of materials.

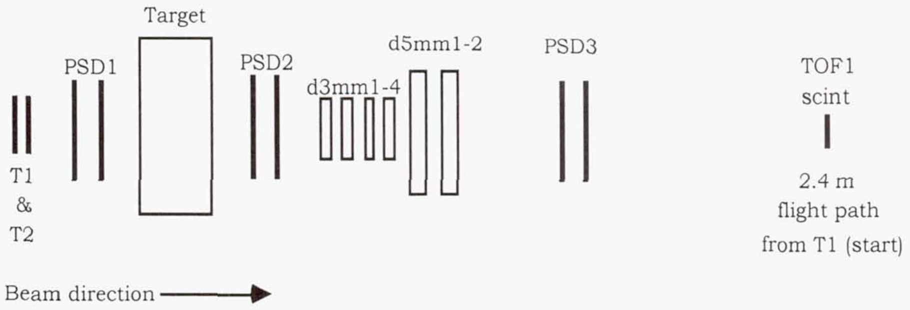

not to scale

Figure 2. Detectors used to measure fragmentation cross sections and fragment fluences from 1.08 GeV/nucleon ^{56}Fe incident on a variety of targets. The detectors include plastic scintillation counters (T1, T2, TOF1), position sensitive solid state detectors (PSD1,2,3) and 3 and 5 mm solid state energy loss detectors (d3mm1-4, d5mm1-2).

Mission Trade Studies

Mission trade studies will be performed using the developed materials data base of the radiation properties of current and developing spacecraft materials as well as mission-specific materials. The most current Mars mission scenarios and transfer vehicle configurations will be used to assess the impact of material selection on crew safety and mission cost. The calculated and experimentally validated radiation transmissions properties will be used to generate a figure of merit for each of the selected materials relative to aluminum. A methodology to incorporate the "figure of merit" results, including cancer risk using quality factors and the three bioresponse models, will be developed to establish a design procedure for the trade studies. The launch mass savings, obtained through judicious material selection, will then be evaluated for a Mars mission where parasitic shield requirements for GCR may become mission prohibitive. In addition, the effectiveness of the shield design strategy in reducing the biological effects of the GCR environment incurred by crew members will be evaluated. The remaining uncertainty associated with HZE transmission properties and bioresponse models will be included in the trade study analysis to address their impact on mission cost. By establishing a design procedure at the conceptual phase of mission development to incorporate radiation-efficient materials, based on experimentally validated transmission properties and current bioresponse models, the potentially negative impact of shielding requirements on mission go/no-go decisions can be resolved.

References

1. Anon. The Strategic Plan: NASA's Enterprise for the Human Exploration and Development of Space, January 1996.
2. J. W. Wilson, L. W. Townsend, W. Schimmerling, G. S. Khandelwal, F. Khan, J. E. Nealy, F. A. Cucinotta, L. C. Simonsen, J. L. Shinn, and J. W. Norbury, Transport Methods and Interactions for Space Radiations. NASA RP-1257, 1991.
3. NCRP; Guidance on exposures in space. NCRP report 98, 1989.
4. W.Schimmerling, et al.; Shielding against galactic cosmic rays. Adv. Space Res. 17(2):31-36; 1996.
5. Wilson, et al. Exposures to Solar Particle Events in Deep Space Missions. NASA TP-3668, 1997.
6. National Academy of Science, Radiation Hazards to Crews of Interplanetary Missions. 1996.
7. F.A.Cucinotta, et al.; Light ion components of the galactic cosmic rays: Nuclear interactions and transport theory. Adv. Space Res. 17(2):77-86; 1996.
8. J. W. Wilson, A. Konradi, J. Miller, and F. A. Cucinotta, Eds., Shielding Strategies for Human Space Exploration. NASA CP-3360, 1997.

9. N.R.Augustine and L.L. Wilkrninhz; The Augustine Report (Report of the Advisory Committee on the Future of the U.S. Space Program), U.S. House of Representatives Committee on Science, Space, and Technology, Jan. 1991.
10. W. Wilson, F. A. Cucinotta, and J. L. Shinn, Cell Kinetics and Track Structure. Published in Biological Effects and Physics of Solar and Galactic Cosmic Radiation, edited by C. E. Swenberg, G. Horneck, and E. G. Stassinopoulos. Plenum Press, pp. 295-338, 1993.
11. F.A.Cucinotta et al.; Effects of track structure and cell inactivation on the calculation of heavy ion mutation rates in mammalian cells. Int. J. Radiat. Biol. 69: 593-600; 1995.
12. F.A.Cucinotta and J.W.Wilson, Initiation promotion model of tumor prevalence in mice from space exposures. Radiat. Environ. Biophysics 34: 145-149; 1995.
13. J. W. Wilson, M. Y. Kim, W. Schimmerling, F. F. Badavi, S. A. Thibeault, F. A. Cucinotta, J. L. Shinn, and R. Kiefer: Issues in Space Radiation Protection.: Galactic Cosmic Rays. Health Phys. 68:50-58; 1995..
14. W. Schimmerling, et al., Evaluation of Risks from Space Radiations. Radiat. and Environ. Biophysics, in press.
15. Schimmerling et al, Radiat. Res. 120:36; 1989
16. C. Zeitlin, L. Heilbronn, J. Miller, S. E. Rademacher, T. Borak, T. R. Carter, K. A. Frankel, W. Schimmerling and C. E. Stronach, Heavy fragment production cross sections from 1.05 GeV/nucleon ^{56}Fe in C, Al, Cu, Pb and CH2 targets. Phys. Rev. C 56: 388-397; 1997.
17. C. J. Zeitlin, K. A. Frankel, W. Gong, L. Heilbronn, E. J. Lampo, R. Leres, J. Miller, and W. Schimmerling, A modular solid state detector for measuring high energy heavy ion fragmentation near the beam axis. Rad. Meas. **23**(1): 65-81; 1994.
18. Y. Kim et al.; Irradiation of Polymers: Fundamentals and Technological Applications. Chpt 27: Performance of polymeric materials as shielding for cosmic radiation. American Chemical Society, 1996.
19. J. W. Wilson, et al., HZETRN: Description of a Free-Space Ion and Nucleon Transport and Shielding Computer Program. NASA TP-3495, 1995.
20. J. W. Wilson, F. A. Cucinotta, F. Hajnal, Analytical Relationships of Nuclear Fields and Microdosimetric Quantities for Target Fragmentation in Tissue Systems. Health Phys. 60, 559, 1991.
21. F. A. Cucinotta, R. Katz, J. W. Wilson, R. D. Dubey, Radial dose distributions in the delta-ray theory of track structures. In: Proceedings of Two Center Effects in Ion-atom Collisions. AIP Conference Proceedings 362:245-265; 1996.
22. J. L. Shinn and J. W. Wilson, Nuclear Reaction Effects in Use of Newly Recommended Quality Factor. Health Physics, 61, 1991.
23. F. A. Cucinotta and J. W. Wilson, Evaluation Of Spacecraft Shielding Effectiveness For Radiation Protection, These proceedings.
24. J. W. Wilson et al., NUCFRG2: A semiempirical fragmentation model. Nucl. Instr. Meth. B **94**, 95 (1994).

Page intentionally left blank

Identification and Control of Gravity Related Defect Formation during Melt Growth of Bismuth-Silicate ($Bi_{12}SiO_{20}$)

Y. Zheng and A.F. Witt

Department of Materials Science and Engineering, MIT, Cambridge, MA

In the light of strong indications that a majority of critical defects formed in BSO during growth from the melt is related directly or indirectly to gravitational interference, it is suggested to use the reduced gravity environment of outer space for experimentation directed at the identification and control of these defects. The results of these experiments are expected to lead to advances in our understanding of crystal growth related defect formation in general and will establish a basis for effective defect engineering, the approach to efficient achievement of defect related, application specific properties in opto-electronic materials

Introduction

It has been established that growth of BSO from the melt requires Platinum as a confinement material. Thus, current induced growth interface demarcation, which is considered essential for studies of growth kinetics and defect formation, is complicated in conventional Bridgman geometries, because of the high electrical conductivity of the confinement material. The effectiveness of other than conventional Bridgman geometries (structured confinement walls, solidification through an orifice) is strongly dependent on the wetting behavior of the confined BSO. It is considered essential therefore, to investigate for the system under consideration the wetting behavior in contact with platinum through measurements of contact angles as well its dependence on composition of the melt and the gas phase. The approach taken to the study of the wetting behavior of high temperature melts is simple, provides for reproducible data which are consistent with published results and is applicable to implementation in a reduced gravity environment.

PRELIMINARY STUDY OF THE WETTING BEHAVIOR OF PLATINUM IN CONTACT WITH BSO MELT

Axi-symmetric Drop Shape Analysis:

Surface tension and the gravity effect determine the shape of a sessile drop. Surface tension tends to make the drop spherical while gravity tends to flatten it. Since the gravity effect is known, the surface tension can be determined by analyzing the drop shape. The three-phase contact angle (θ) can be obtained as a side-output from the drop-shape analysis, with accuracy, which is superior to that of direct angle measurements.

The shape of the sessile drop is governed by the Laplace equation. It relates the interfacial tension and curvature at the liquid-vapor (or liquid-liquid) interface to the pressure difference across it:

$$\gamma\left(\frac{1}{\boldsymbol{R}_1}+\frac{1}{\boldsymbol{R}_2}\right)=\Delta\boldsymbol{P} \qquad (1)$$

where γ is the interfacial tension, R_1 and R_2 are the two principal radii of curvature and ΔP is the pressure difference across the interface. If gravity is the only effective external force, ΔP is linear along a vertical axis z:

$$\Delta\boldsymbol{P}=\Delta\boldsymbol{P}_0+(\Delta\rho)\boldsymbol{g}\boldsymbol{z} \qquad (2)$$

where ΔP_0 is the pressure difference at a reference plane, $\Delta\rho$ is the density difference across the interface, and g is the gravitational acceleration.

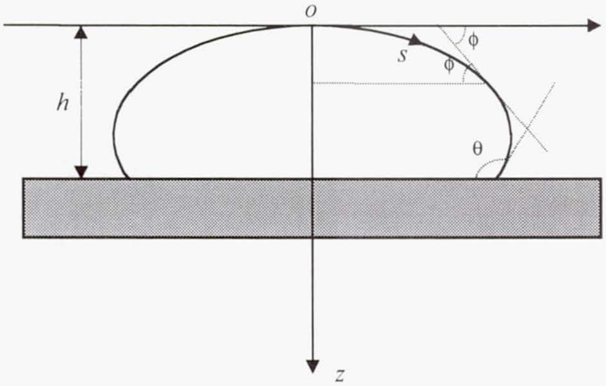

Fig. 1 Coordinate system for axi-symmetric sessile drop shape analysis.

By choosing a coordinate system as in Fig.1, we have the set of differential equations:

$$\frac{d\phi}{ds} = \frac{2}{R_0} + cz - \frac{\sin\phi}{x} \tag{1}$$

$$\frac{dx}{ds} = \cos\phi \tag{2}$$

$$\frac{dz}{ds} = \sin\phi \tag{3}$$

$$\frac{dV}{ds} = \frac{(\pi x^2 \leftarrow dz)}{ds} = \pi x^2 \sin\phi \tag{4}$$

where ***s*** is the arc length,

C is a capillary constant defined as_

____ $$c = \frac{(\Delta\rho)g}{\gamma} \tag{5}$$

The boundary conditions at the origin of the coordinate system are:

$$x(0) = z(0) = \phi(0) = V(0) = 0 \tag{6}$$

$$\left.\frac{d\phi}{ds}\right|_{s=0} = \frac{1}{R_0} \tag{7}$$

where R_0 is the radius of the drop at its apex.

The boundary conditions at the three-phase contact line is given by:

$$\phi\big|_{z=h} = \theta \tag{8}$$

$$V\big|_{z=h} = V_0 \tag{9}$$

where ***h*** is the height of the drop, and V_0 is the total drop volume.

Parameters involved are: ***c*** (or g/γ), R_0 , θ , ***h*** and V_0 .

By solving the set of differential equations (1)-(4), the shape of a drop can be uniquely generated with the parameters, ***c***, R_0 and ***h***. θ and V_0 can be calculated from equations (8) and (9). Only 2 of R_0 , θ , ***h*** and V_0 are independent parameters and any two of them are sufficient to establish the boundary conditions of the problem.

In theory, knowing the exact location of two arbitrary points on the surface of the drop as well as the origin, ***O***, the values of ***c*** and $\boldsymbol{R_0}$ can be obtained by fitting the Laplace curve to these two points.

In reality, the surface line (a projection of the surface on the 2 dimensional *X-Z* coordinate system) can be localized only with an accuracy, determined by the optical system used. Since in computational analysis each point on the line has an inevitable uncertainty at the order of 1 pixel, a significant number of points were selected from the surface line to increase the accuracy of the extracted ***c*** and $\boldsymbol{R_0}$ values. It should also be mentioned that the origin, O, (X_0, Z_0), is difficult to locate; considering this quantity, like ***c*** and $\boldsymbol{R_0}$, as optimization parameter for the curve-fitting process can avoid the problem.

Images of sessile drops were acquired using a NEC, CCD (640×480) camera fit to a stereomicroscope. For photography of BSO melts the emitted, unfiltered radiation was used; sessile drop studies of organic liquids were carried out using an external light source (Fig 2). The contour of the drop shape was obtained by applying a 'Sobel' edge operator (that finds the pixels have the maximum gradient of intensity) to the drop image monitored on the screen (Fig 3).

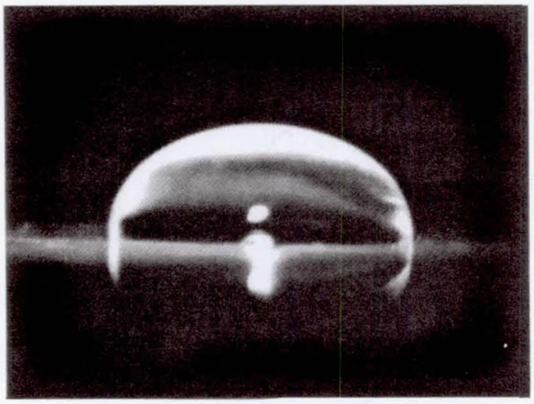

Fig. 2 Drop of glycerol on Teflon in reflection mode.

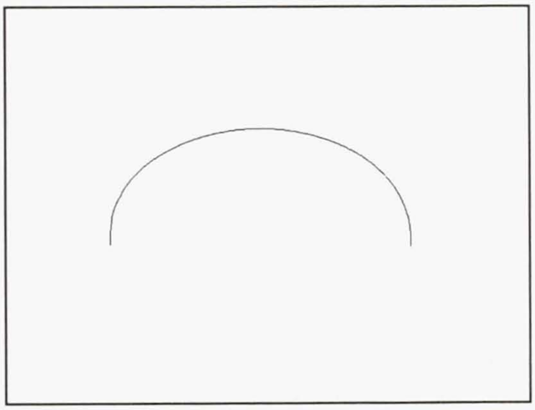

Fig. 3 Contour of the liquid-vapor interface as obtained by a 'Sobel' edge operator, applied to fig.2.

The sample points selected from the interface contour (Fig 3) were chosen to be uniformly spaced, so that every section of the curve is equally weighted during the curve-fitting process.

Experimental set-up

The determination of drop shapes and contact angles was carried out in an optical cell (with controlled ambient) with controlled heat input via a sodium heat pipe. Imaging was accomplished with an operational microscope and a CCD camera connected to a Macintosh. Image processing and analysis was done using the NIH image 1.6 software.

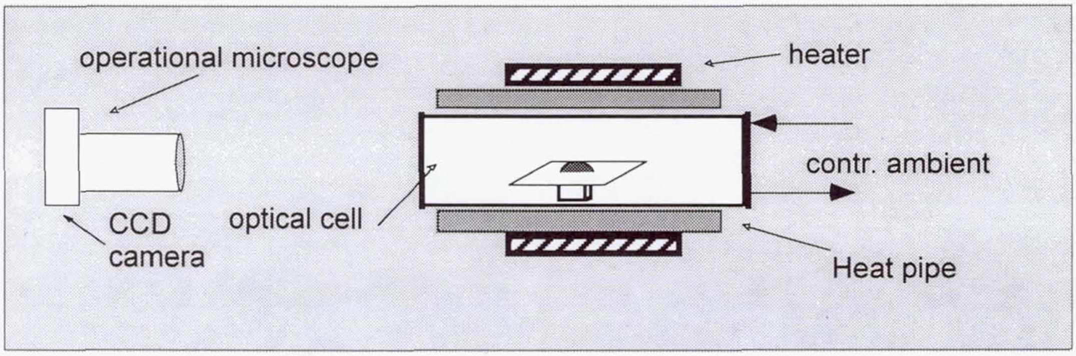

Fig.4 Schematic of optical cell used for the determination of drop shapes and contact angles.

Analysis of selected organic liquids with known surface tension

To test the viability of the adopted experimental and theoretical approach, we determined the surface tension of some organic liquids at room temperature in an argon atmosphere. The results are presented in Figs. 5, 6 and Table 1

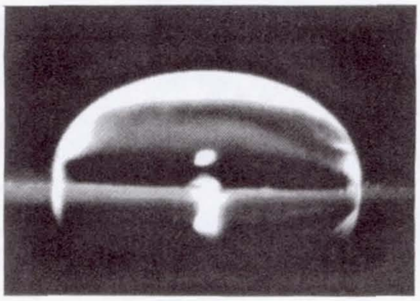

Fig. 5 Drop of glycerol on Teflon in reflection mode.

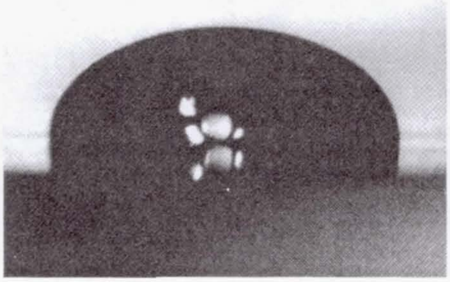

Fig.6 Drop of glycerol on Teflon in transmission mode.

Table 1 Surface tension of organic liquids according to drop shape measurements

Sessile Drop	Liquid-vapor surface tension, γ (MJ/m^2) 10 data-fitting processes for each drop		γ (mJ/m^2) from reference
	Mean	Standard deviation	
Diethylene glycol	44.2	1.7	44.77*
Glycerol (Fig. 4)	65.3	0.8	63.14**
Glycerol (Fig. 5)	62.1	0.7	

* CRC Handbook of Physics and Chemistry.

** Lange's Handbook of Chemistry

Wetting analysis on BSO:

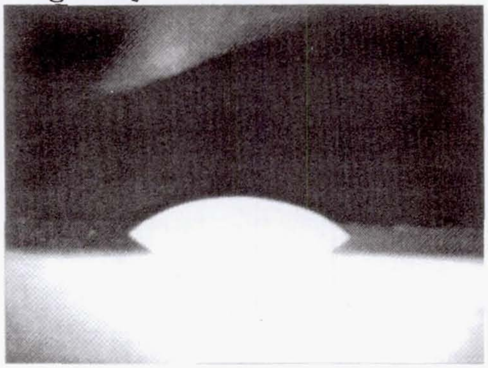

Fig. 7, BSO (I a) at $P_{O2} = 10^{-4}$ atm

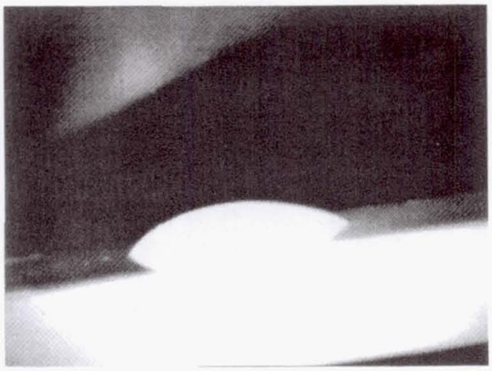

Fig. 8, BSO (I b) at $P_{O2} = 10^{-4}$ atm

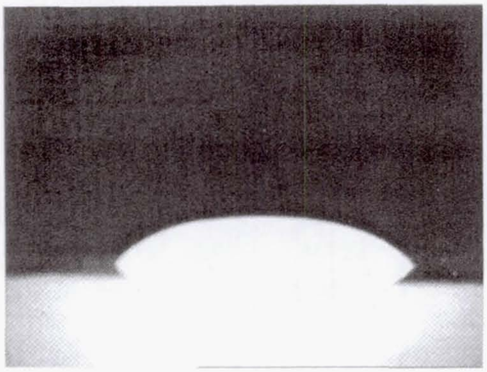

Fig. 9, BSO (II a) at $P_{O2} = 10^{-4}$

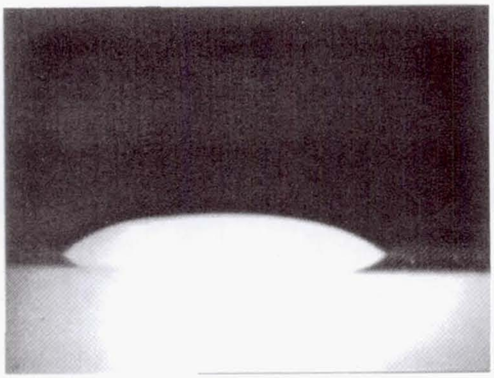

Fig. 10, BSO (II b) at $P_{O2} = 10^{-3}$ atm

Table 2 Liquid-Vapor interfacial energies and contact angles obtained by drop shape analysis:

	P_{O2} (atm)	γ (MJ/m^2)		Contact Angle			
				Left		Right	
		Mean	Std.	Mean	Std.	Mean	Std.
I a	10^{-4}	206.0	13.6	43.47°	0.48°	44.66°	0.58°
II a	10^{-4}	184.2	7.8	-*	-	51.95°	0.93°
II b	10^{-3}	207.9	10.4	-	-	39.84°	0.55°
III a	10^{-4}	194.8	5.5	48.26°	0.35°	-	-
III b	10^{-3}	204.5	10.7	40.33°	0.76°	-	-

* The contact angle was not determined because contact line was not focused well on that side of the image. (but it was well focused on the other side)

Table 3 Contact angles by direct measurement:

Sessile Drop	Contact Angle (γ)			
	Left		Right	
	Mean	Std.	Mean	Std.
I a	44.05°	0.78°	44.7°	1.3°
I b	46.86°	0.79°	39.36°	0.85°

Preliminary Results of Wetting Study

Drop shape measurement indicate that the surface tension of (undoped) BSO melts is unaffected by the oxygen partial pressure in the ambient, yielding values ranging from 195 to 206 MJ/m^2.

The contact angle (θ) is however found to vary measurably with the oxygen partial pressure, increasing from zero degrees (complete spreading) at p_{ox} of 0.2 atm to about 48^{o} at p_{ox} of 10^{-4}atm. Contact angle hysteresis is found to be small. This finding indicates that the dependence of the wetting behavior on the oxygen partial pressure is due to changes in the spreading pressure ($\gamma_{SV}-\gamma_{SL}$). The preliminary data suggest that "free" solidification is achievable in modified Bridgman geometry, provided the wetting behavior in space is not substantially different from that on the ground.

Acknowledgment: The sustained financial and intellectual support by the Life Sciences Division of the National Aeronautics and Space Administration, which made this study possible is gratefully acknowledged.

GROUND BASED EXPERIMENTS IN SUPPORT OF MICROGRAVITY RESEARCH RESULTS-VAPOR GROWTH OF ORGANIC NONLINEAR OPTICAL THIN FILMS

Dr. Maria I. Zugrav, Principal Investigator
Consortium for Materials Development in Space
University of Alabama in Huntsville
Huntsville, Alabama 35899, USA
Phone: (256) 890-6620
Fax: (256) 890-6791
E-mail: zugravm@email.uah.edu

Dr. Francis C. Wessling, Co-Investigator
Department of Mechanical and Aerospace Engineering
University of Alabama in Huntsville

Mr. William E. Carswell, Co-Investigator
Alliance for Microgravity Materials Science and Applications
University of Alabama in Huntsville

Introduction and Objectives

Ordered and oriented thin films of an organic nonlinear optical (NLO) material, N,N-dimethyl-p-(2,2-dicyanovinyl) aniline (DCVA), have been grown on disordered substrates, in space, aboard the USA Space Shuttle Endeavour on STS (Space Transportation System) -59 and STS-69. The STS-69 results extend, confirm, and are consistent with those of the STS-59. Similar experiments have been conducted in the laboratory as ground controls and have produced single crystals only. All experiments have demonstrated that the morphology of DCVA crystals is highly dependent upon gravity. The premise is that the bonds are week in nature (Van der Waals) and are significantly impacted by gravity. Hence, there is a need for a well defined ground-based program to determine the validity of this theory, that is, if the impact of gravitational forces can be overcome by other process parameters. Specifically, the ground-based studies focus on investigating the macroscopic and microscopic conditions required to prepare high-quality thin films of DCVA through the optimization and control of the growth cell orientation, growth temperature, substrate variation studies, and background pressure.

The crystal growth experiments have been performed using the Moderate Temperature Facility (MTF). An improved version of the MTF will include the capability of *in situ* observation of the growth process yielding significant understanding of the mechanisms for two different types of crystal formation, bulk crystals obtained in a normal gravity environment and ordered and oriented thin film crystals obtained in reduced gravity (thin films being achievable only in a reduced gravity environment). The three year old space-only grown DCVA thin films proved to have thermodynamic and photochemical stability. To date, vapor-deposited DCVA thin films have not been duplicated in a normal gravity environment.

The space-only grown DCVA thin films are an example of "Van der Waals epitaxy" on inorganic substrates. Understanding this new growth process is vital if we are to fully exploit its potential to incorporate highly nonlinear optically active organic materials as active opto-electronic and electro-optic components in modern integrated logic device structures.

Growth method

The crystal growth method used for the experiments on the ground and in space was the effusive ampoule physical vapor transport (EAPVT) [1-3]. This technique allows for the continuous removal to vacuum of residual impurities and other transport-limiting vapor constituents through a calibrated leak near the crystal. Consequently, mass transport rates tend to be only limited by viscous interaction with the walls and by heat transfer at the interface. Then, even for small temperature differences, ΔT, between source and crystal, the transport proceeds so rapidly that a flow-restricting capillary needs to be placed between the source and crystal to ensure high structural quality growth. The EAPVT growth method is best suited for organic NLO materials which are known to be thermally unstable and decompose at high temperatures. Hence, single crystal growth at practical rates can only be obtained in an apparatus that provides for continuous removal of any gaseous decomposition products. This consideration was essential for the design of crystal growth experiments to be conducted aboard space craft, where experiment time is at a premium.

Moderate Temperature Facility (MTF)

We have developed and built a versatile, flight qualified, MTF [4] for materials processing in space and on Earth. The four successful flights on the U.S. Space Shuttles have demonstrated the MTF materials processing capabilities. The MTF is housed in a sealed canister and consists of a mounting structure, a vacuum vent valve assembly, a backfill assembly, a controller, and the EAPVT hardware. The present configuration of the EAPVT hardware consists of six ovens. Each MTF oven contains two separate growth cells which allow the independent processing of two samples simultaneously. The oven's power consumption is less than 3 W at 140°C. This thermal efficiency was achieved by addressing all three forms of heat loss: radiative, convective, and conductive. The MTF design permits a variety of materials processing techniques to be implemented at temperatures up to 250°C, including solution, vapor, and low temperature melt crystal growth, as well as a variety of polymer reactions.

Materials preparation

DCVA, a donor/acceptor-substituted aromatic compound, was synthesized according to literature procedure [5] and characterized by melting point (454.5 K) and nuclear magnetic resonance (NMR). The product was twice recrystallized from 95% ethanol and acetonitrile to give material of at least 99.5% purity. The substrates were machined flat from oxygen-free-high-conductivity copper and aluminum rods. The final polish was done with 16 μ silicone carbide abrasive paper but, the characteristic machining marks and the central tip were still visible. These surfaces were cleaned by rubbing with Alconox detergent solution, then with deionized water, and finally with ethanol. They were exposed to the ambient atmosphere (including the moisture) for mounting the seed and assembling them into the growth cell. Consequently, the substrates were not free of adsorbed surface contaminants. In fact, the entire preparation was done as normal, for crystal growth, not expecting thin films. Seed crystals were selected from previously grown crystals.

Growth conditions

The preparatory ground-based research was complex due to the large number of parameters involved in the process of crystal growth such as: flow restriction by the capillary, effusion calibration by the leak to vacuum, ΔT of the ends of the cell, thermistors calibration, vacuum level, seed crystal preparation, temperature profile of the ampoule. The growth process of crystals is fully automated and consists of five essential sequences: outgassing and warm up, growth, backfilling, and cool-down. The terrestrial reference experiments were evacuated to ~ 10^{-4} torr through a vacuum vent valve assembly to provide the vacuum for the EAPVT process, and to reduce convective thermal transport. The flight experiments vent to the vacuum of space. During the warm-up sequence the substrate and source temperature were increased in a controlled way to avoid growth of crystals on the substrate prior to the optimum growth temperatures being reached. The backfill assembly is activated at the end of the experiment, when the growth process is complete, just before the heaters are turned off. This is done to quench the vapor transport process and avoid uncontrolled deposition during the cool-down. First, the vacuum vent valve is closed. Then, backfilling is effected by opening a valve and allowing dry inert gas to pressurize the canister until the equilibrium is achieved. A cool down sequence keeps the substrate hotter than the source, causing vapor to condense on the remaining source material instead of on the grown crystal or thin film.

Film characterization techniques

In 1994, the STS-59 flight results of the two thin film DCVA samples were considered an anomaly. However, we decided to start a systematic characterization. Since the number of samples was limited to two we have taken great care in applying the characterization techniques with the correct hierarchy, from least destructive to most destructive. The first technique to be used was, Differential Scanning Calorimetry (DSC), not for the thin film characterization but mainly for the DCVA material itself. A Perkin Elmer Model DSC-2 instrument was used to examine the thermal behavior of the DCVA source material, the Earth grown DCVA crystal, the space grown crystal (collected from a small self nucleated polycrystalline clump grown at the edge of the substrate and on top of the thin film) and a seed mounted with epoxy resin in the DSC sample holder. In the repeated scans of DSC with different operating variables such as heating and cooling rates, and consecutive heating cycles, phase transitions other than the melt were not observed between 323 and 456 K; moreover, the melting point had not changed. This means that no glassy state, polymorphism or polymerization exist in the melting-solidification cycles of DCVA. The film deposited on the substrates is the DCVA sublimed material. With these relaxing DSC results in mind, we have probed the DCVA space grown thin films with microphotography, differential interference contrast (DIC) optical microscopy, Fourier transform infrared (FTIR) spectrometry, X-ray diffraction (XRD), visible reflectance spectroscopy, stylus profilometry, and second harmonic generation (SHG) efficiency. These techniques imply a deposition of oriented and ordered thin films [6-8].

The color of the thin films is red. Observations by microphotography and DIC optical microscopy of the best thin film samples revealed a smooth and featureless surface. Craterlike and domelike features characteristic to the insufficiently clean or smooth substrate surface, were not observed at the highest magnification of the DIC optical microscopy. Usually, if there are impurity particles such as dust on the surface of the substrate, these particles tend to form holes in the film. They may act also as preferred nucleation sites that cause complete film continuity to form at an earlier stage of growth, or they may tend to repel surface diffusing admolecules. In this case a lower density of nuclei would be expected, and much more material may have to be deposited to form a pinhole-free film. A complete different topography, of a granular film, was observed at the edges of the substrate. This might be an indicative of a Volmer-Weber growth [9-12] by three-dimensional nucleation, growth and coalescence. The film grew outward, away from the substrate, more rapidly than sideways to fill the holes. Some thin film samples displayed a rough surface which might be very well an indication of the Stranski-Krastanov (layer plus island) growth [9-12] if we assume that the thickness of the film left it in the island stage of growth. There is not an easy answer concerning the growth process and additional studies will likely become necessary.

Proposed Research Plan

A ground based program is proposed to explore possible approaches to grow on Earth, from vapor, the DCVA thin films. Vapor pressure measurements [13], at various temperatures, of DCVA and other related NLO organic materials will be used in numerical calculations to separate the convection and diffusion effects in an attempt to further understand the relationship between nucleation and gravity. Vapor growth experiments altering the MTF's orientation to the gravity vector, changing the substrate temperature, modifying the temperature profile at many combinations of warm-up rates, measuring the background pressure in the MTF oven, will be carried out. The researchers hope to refine their results with electro-optical device-quality substrates so that the NLO effectiveness of the ground "to be grown" films can be quantified. It will be important to evaluate the quality of the grown films in detail and compare the results with those obtained from the previous studies [6-8].

The space experiment on STS-69 was a test experiment using changes in many growth parameters such as: substrate, source temperature, transport flux, and seeding which might influence the growth of DCVA thin films. None proved to have a major impact. Exactly reproducing all none-gravity EAPVT parameters for the unit-g experiments will be very difficult because some of them are completely different (the temperature profile) and others could not be measured (for instance the background pressure external to the growth cell).

In addition to carrying out a series of ground-based experiments aimed at understanding why the microgravity experiment results are so dramatically different from the results obtained when using the hardware on the ground, two changes need to be made to the experimental equipment. The first change is to install a fiberscope camera as part of the growth cell so that the growth of the crystals and thin films can be directly observed. At present all growth parameters are preset and nothing is known about the growth form until the experiment is complete. The ability to visualize the growth process in real-time is critical in coming to an understanding of this fundamental puzzle of why the growth form is so vastly different on Earth and in space. One barrier to using a fiberscope in the past has been that the fiberscope needs to operate in a 150°C environment. Until recently the technology has not existed to do this. Fiberscopes are typically limited to long-term operating exposures of 90°C. The technology now exists, however, to build the fiberscope we need. It will add considerable insight into the "Van der Waals " nature [14-16] of the epitaxial growth process for DCVA. The second change is to upgrade the control electronics.

References

[1] M. Ittu Zugrav, W. Carswell and F. Rosenberger, "Growth of 4-(N,N-dimethylamino)-3-acetamidonitrobenzene (DAN) single crystals by effusive ampoule physical vapor transport", Proc. Eighth American Conference on Crystal Growth, Vail, Colorado, July 1990.

[2] R. M. Banish, M. I. Zugrav, D. A. Bond and F. Rosenberger," Effusive ampoule physical vapor transport of II-VI compounds ", Proc. Eighth International Conference on Vapor Growth and Epitaxy, Freiburg, Germany, July 1994.

[3] M. Ittu Zugrav and F. Rosenberger, "Ground-based vapor crystal growth experiments", in Materials Research in Low Gravity, SPIE, 3123 (1997) 135.

[4] F. C. Wessling and W. E. Carswell, Microgravity Sci. Technol. VIII/3 (1995) 196.

[5] B. B. Corson and R. W. Stoughton, J. Am. Chem. Soc. 50 (1928) 2825.

[6] M. Ittu Zugrav, W. E. Carswell, T. M. Leslie, F. C. Wessling, and C. A. Lundquist, "Growth in space of organic thin films by physical vapor transport: Some probes and results to date", Proc. Tenth American Conference on Crystal Growth / The Ninth International Conference on Vapor Growth & Epitaxy, Vail, Colorado, August, 1996.

[7] M. Ittu Zugrav, F. C. Wessling, W. E. Carswell, T. M. Leslie, C. Watson and C. A. Lundquist, "Vapor deposited organic thin film in microgravity", Journal of Crystal Growth, 174 (1997) 130.

[8] M. Ittu Zugrav, W. E. Carswell, C. A. Lundquist, F. C. Wessling and T. M. Leslie, "Physical vapor transport experiments on board the Space Shuttle Endeavour", Materials Research in Low Gravity, SPIE, 3123 (1997) 110.

[9] R. W. Vook, "Structure and growth of thin films", International Metals Reviews 27 (1982) 209.

[10] R. W. Vook, "Nucleation and growth of thin films", Optical Engineering 23 (1984) 343.

[11] R. W. Vook, "Thin film growth", Mat. Res. Symp. Proc. 103 (1988) 3.

[12] L. I. Maissel and R. Glang, Handbook of Thin Film Technology, Mc Graw-Hill Book Co., New York, 1970.

[13] M. Ittu Zugrav and F. Rosenberger, "Towards efficient crystal growth of 4-(N,N-dimethylamino)-3-acetamidonitrobenzene (DAN) in space-Vapor pressure measurements and growth morphology studies", Space Processing of Materials, SPIE, 2809 (1996) 271.

[14] S. R. Forrest and Y. Zhang, "Ultrahigh-vacuum quasiepitaxial growth of model van der Waals thin films. I. Theory", Physical Review B49 (1994) 11297.

[15] S. R. Forrest, P. E. Burrows, E. I. Haskal, and F. F. So, "Ultrahigh-vacuum quasiepitaxial growth of model van der Waals thin films. II. Experiment", Physical Review B49 (1994) 11309.

[16] P. Fenter, P. E. Burrows, P. Eisenberger, S. R. Forrest, "Layer-by-layer quasi-epitaxial growth of a crystalline organic thin film", J. Crystal Growth 152 (1995) 65.

REPORT DOCUMENTATION PAGE

Form Approved
OMB No. 0704-0188

1. AGENCY USE ONLY *(Leave Blank)*	2. REPORT DATE February 1999	3. REPORT TYPE AND DATES COVERED Conference Publication

4. TITLE AND SUBTITLE
NASA Microgravity Materials Science Conference

5. FUNDING NUMBERS
NCC8–66

6. AUTHORS
D.C. Gillies and D.E. McCauley*, Compilers

7. PERFORMING ORGANIZATION NAMES(S) AND ADDRESS(ES)
George C. Marshall Space Flight Center
Marshall Space Flight Center, AL 35812

8. PERFORMING ORGANIZATION REPORT NUMBER
M–911

9. SPONSORING/MONITORING AGENCY NAME(S) AND ADDRESS(ES)
National Aeronautics and Space Administration
Washington, DC 20546–0001

10. SPONSORING/MONITORING AGENCY REPORT NUMBER
NASA/CP—1999–209092

11. SUPPLEMENTARY NOTES Proceedings of a conference held in Huntsville, AL on July 14–16, 1998. The conference was coordinated by the Alliance for Microgravity Materials Science & Applications (AMMSA–NASA, MSFC, UAH* & USRA**) under cooperative agreement with NASA/MSFC.
*University of Alabama in Huntsville **Universities Space Research Association

12a. DISTRIBUTION/AVAILABILITY STATEMENT
Unclassified–Unlimited
Subject Category 88
Standard Distribution

12b. DISTRIBUTION CODE

13. ABSTRACT *(Maximum 200 words)*

The Microgravity Materials Science Conference was held July 14–16, 1998 at the Von Braun Center in Huntsville, AL. It was organized by the Microgravity Materials Science Discipline Working Group, sponsored by the Microgravity Research Division at NASA Headquarters, and hosted by the NASA Marshall Space Flight Center and the Alliance for Microgravity Materials Science and Applications. It was the third NASA conference of this type in the microgravity materials science discipline. The microgravity science program sponsored approximately 125 investigations and 100 principal investigators in FY98, almost all of whom made oral or poster presentations at this conference. The conference's purpose was to inform the materials science community of research opportunities in reduced gravity in preparation for a NASA Research Announcement scheduled for release in late 1998 by the Microgravity Research Division at NASA Headquarters. The conference was aimed at materials science researchers from academia, industry, and government. A tour of the Marshall Space Flight Center microgravity research facilities was held on July 16, 1998. This volume is comprised of the research reports submitted by the principal investigators after the conference.

14. SUBJECT TERMS
microgravity, materials science, crystal growth, metals and alloys, electronic materials, optical materials, polymers

15. NUMBER OF PAGES
742

16. PRICE CODE
A99

17. SECURITY CLASSIFICATION OF REPORT Unclassified	18. SECURITY CLASSIFICATION OF THIS PAGE Unclassified	19. SECURITY CLASSIFICATION OF ABSTRACT Unclassified	20. LIMITATION OF ABSTRACT Unlimited

NSN 7540-01-280-5500

Standard Form 298 (Rev. 2-89)
Prescribed by ANSI Std. 239-18
298-102

National Aeronautics and
Space Administration
AT01S
George C. Marshall Space Flight Center
Marshall Space Flight Center, Alabama
35812